Published in Journals: Applied Sciences, Designs,
Energies, Machines and Vehicles

Topic Reprint

Advanced Electrical Machines and Drives Technologies

Volume II

Edited by
Loránd Szabó and Feng Chai

mdpi.com/topics

MDPI

Advanced Electrical Machines and Drives Technologies—Volume II

Advanced Electrical Machines and Drives Technologies—Volume II

Editors

Loránd Szabó
Feng Chai

MDPI

Basel • Beijing • Wuhan • Barcelona • Belgrade • Novi Sad • Cluj • Manchester

Editors
Loránd Szabó
Technical University of Cluj-Napoca
Cluj-Napoca
Romania

Feng Chai
Harbin Institute of Technology
Harbin
China

Editorial Office
MDPI AG
Grosspeteranlage 5
4052 Basel, Switzerland

This is a reprint of articles from the Topic published online in the open access journals *Applied Sciences* (ISSN 2076-3417), *Designs* (ISSN 2411-9660), *Energies* (ISSN 1996-1073), *Machines* (ISSN 2075-1702), and *Vehicles* (ISSN 2624-8921) (available at: https://www.mdpi.com/topics/electrical_machines_drives).

For citation purposes, cite each article independently as indicated on the article page online and as indicated below:

Lastname, A.A.; Lastname, B.B. Article Title. *Journal Name* **Year**, *Volume Number*, Page Range.

Volume II
ISBN 978-3-7258-2309-3 (Hbk)
ISBN 978-3-7258-2310-9 (PDF)
doi.org/10.3390/books978-3-7258-2310-9

Set
ISBN 978-3-7258-2305-5 (Hbk)
ISBN 978-3-7258-2306-2 (PDF)

Contents

machines

MDPI

Article

Optimal Design and Dynamic Analysis of a Spring-Actuated Cam-Linkage Mechanism in a Vacuum Circuit Breaker

Yaw-Hong Kang *, Hua-Chih Huang and Bo-Ya Yang

Department of Mechanical Engineering, National Kaohsiung University of Science and Technology, Kaohsiung City 80778, Taiwan

* Correspondence: yhkang@nkust.edu.tw; Tel.: +886-07-3814526

Abstract: This study attempted to establish an optimal design and perform dynamic analysis for a spring-actuated cam-linkage composite mechanism in a rated 12 kV, 25 kA vacuum circuit breaker (VCB). The optimal design of the VCB mechanism involves two steps: the first step involves the optimal design of the stiffness of closing springs and the cam profile, based on three-order polynomial motion curve of the follower; the second step involves the optimal design of a four-bar linkage. To minimize the surplus work in the VCB operating mechanism, the overall difference between the general output force and general resistant force of the VCB operating mechanism during the closing operation was adopted as the objective function to be minimized. Furthermore, the differential evolution algorithm with the golden ratio (DE-gr), an efficient and accuracy metaheuristic algorithm, was employed as the optimization method. The dynamic analysis of the optimal operating mechanism was conducted using a MATLAB-coded program and verified by the multibody dynamic software MSC-ADAMS. The dynamic analysis revealed that the optimal design of the VCB mechanism can considerably decrease the average closing velocity of the movable contact and the Hertz stress between the contact surface of the cam and the roller follower.

Keywords: vacuum circuit breaker (VCB); cam-linkage composite mechanism; differential evolution (DE); Hertz contact stress

Citation: Kang, Y.-H.; Huang, H.-C.; Yang, B.-Y. Optimal Design and Dynamic Analysis of a Spring-Actuated Cam-Linkage Mechanism in a Vacuum Circuit Breaker. *Machines* **2023**, *11*, 150. https://doi.org/10.3390/machines11020150

Academic Editors: Loránd Szabó and Feng Chai

Received: 20 November 2022
Revised: 13 January 2023
Accepted: 18 January 2023
Published: 21 January 2023

1. Introduction

Power circuit breakers (CBs) are the core switches of power systems that prevent accidents by instantly interrupting abnormal currents, such as over current, short circuit, and ground fault current. Therefore, CBs provide safe protection or control mechanisms for electrical equipment. Several different types of power CBs have been developed using air, oil, compressed air, SF_6 gas, and vacuum as interrupting mediums [1]. The vacuum circuit breaker (VCB), which extinguishes the arc in a vacuum interrupter and has favorable features, such as small size, high efficiency and reliability, and easy maintenance; it is often used to interrupt electric current in power transmission lines with voltages ranging from 3.6 to 38 kV [2]. The cam-linkage composite operating mechanisms are extensively employed in conventional VCBs to complete rapid opening and closing actions within several tens of milliseconds [3]. Several studies have attempted designs and/or investigated the dynamics of the operating mechanisms of CBs. Pisano et al. [4,5] experimentally investigated and analyzed the dynamic response of a high-speed cam follower system. Root et al. [6] optimized the design of the operating mechanism of Westinghouse Type R VCBs. An integrated machine program (IMP) was embedded as an analysis routine within an optimization algorithm, which was a pattern-search method coupled with a penalty function of multipliers. Jobes et al. [7] presented type synthesis and optimal dimensional synthesis of a controllable CB. Furthermore, the simulation, kinematic and dynamic analyses of the optimal mechanism were performed and validated using the multibody dynamic software Automated Dynamic Analysis of Mechanical Systems (ADAMS). Ahn et al. [3]

derived a dynamic model for a high-speed CB mechanism with a spring-actuated cam, and experimentally validated the high-speed motion behavior. The model highlighted the effects of friction on the camshaft, and the characteristics and parameters of the friction were analyzed through a nonlinear pendulum experiment and a modified simplex optimization method, respectively. Kim et al. [8] performed an optimal synthesis for a spring-actuated cam with non-constant angular velocities and an optimized cubic-spline follower motion. The dynamic characteristics of the optimal cam and follower were simulated using ADAMS, and the results indicated that the dynamic behaviors of the optimal cam were superior to those of the polynomial cam with constant angular velocity. Chen et al. [9] investigated the dynamics of a spring-type operating mechanism for a gas-insulated CB. The Lagrange equation was applied to derive the dynamic equation for the opening operation, and the equation was solved using the fourth order Runge-Kutta method. Chen [10] reported an innovative mechanism design method for achieving the feasible mechanisms that satisfied the requirements of the CB. The kinematic and dynamic equations of the mechanism were derived through the vector loop method, and the Lagrange equation was solved using the Runge-Kutta method. Based on the total energy conservation in a spring-actuated linkage system throughout its operating range, Ahn et al. [2] developed a systematic procedure to optimize the spring design parameters for achieving the desired opening and closing characteristics of the electric contacts in a VCB. The spring parameters were optimized to minimize the sum of the squares of the errors between the desired and calculated rotating velocities using the modified simplex method. Yoo et al. [11] analyzed the dynamic characteristics of the spring-actuated operating mechanism of the CB using ADAMS. Yu et al. [12] optimized the dimensional synthesis of the trigger mechanism of a 24-kV CB to minimize both the response time of the trigger hook and contact stress between the cam and roller follower. To achieve a shorter circuit breaking time, Jang et al. [13] developed a multibody dynamic model of a CB, including a switch mechanism that was optimized using a genetic algorithm (GA), and a multibody dynamic analysis of the optimum mechanism was performed using MSC-ADAMS. The opening time of the mechanism was decreased by 2.3 ms, as validated through experiments. Liu et al. [14] proposed an optimum design method for the cam design structure of a molded case circuit breaker (MCCB) and used ADAMS to perform dynamic simulations. The results indicated that the optimal cam design structure effectively prevented the movable conductor from returning when the short-circuit current was $\geq$15 kA and enhanced the interruption performance of the MCCB. Storn and Price [15] proposed a differential evolution (DE) algorithm to minimize possible nonlinear and non-differential continuous space functions. Several studies have focused on the applications of the DE algorithm and its variants for the optimal design of path-generating four-bar linkages. For example, Acharyya et al. [16], compared the optimal results obtained using the DE algorithm with those obtained using a genetic algorithm (GA) and particle swarm optimization (PSO) algorithm; they inferred that the DE method was superior to the GA and PSO methods [16]. Lin [17] used a GA-DE hybrid algorithm combined DE with a real-valued genetic algorithm. Ortiz et al. [18] used an improved DE algorithm with self-adaptive control parameters (called $IOA^{s\text{-}at}$ method). Recently, Kang et al. [19] applied the DE algorithm with a specified golden ratio (0.618:0.382) as the cross rate and mutation factor; the method is called the DE-gr method, to effectively optimize the dimensional synthesis problem of path-generating four-bar linkages. They reported that the efficiency and accuracy of the DE-gr algorithm was superior to those of the PSO, DE [16], DE-GE [17] and $IOA^{s\text{-}at}$ [18] methods.

The objective of present study is to optimally design a VCB mechanism, a spring-actuated cam-linkage operating mechanism with rated voltage 12 kV and rated short circuit current 25 kA, and to perform the dynamic analysis of the optimal VCB mechanism. The novel approach of this work is to present an objective function of optimization that minimizes the surplus output work in the VCB operating mechanism during the closing operation, such that the average closing velocity of the moving contact and the Hertz contact stress on the cam surface are decreased to satisfy the design requirements. Consequently, the

net difference between the general output force and the general resistant force of the VCB operating mechanism during the closing process was considered as the objective function to be minimized, and a DE algorithm with golden ratio (DE-gr) was employed to successfully optimize the design of the VCB operating mechanism, which are the contributions of this work.

The remainder of this paper is organized as follows: Section 2 describes the actuation principle and design of the spring-actuated cam-linkage composite operating mechanism of a VCB. Then, the characteristic forces (spring forces and active forces between different parts) and Hertz contact stress between the cam and roller follower of initial VCB mechanism design are discussed. Section 3 describes the multibody dynamic simulation of the VCB operation mechanism using MSC-ADAMS. Section 4 introduces the differential evolution (DE) algorithm and the optimization procedure. The optimal design of the cam and closing springs using the DE-gr method and the dynamic analysis of the optimal VCB mechanism were performed firstly, followed by the optimal design and dynamic analysis of the four-bar linkage and the optimal VCB mechanism, respectively. Finally, Section 5 draws the conclusions of the study.

2. Design of the VCB Operating Mechanism

2.1. Actuation Principle and Specified Motion of the VCB Operating Mechanism

A medium-voltage VCB is composed of two components: the vacuum interrupter (VI) and the operating mechanism. The operating mechanism was designed for opening and closing the electric contacts in the VI. In the VI, the electric movable contact and fixed contact were installed in a ceramic insulator envelope wherein high vacuum approximately 10^{-5} Pa was maintained. The employed operating mechanism in the present study was a spring-actuated cam-linkage composite mechanism, and the main constituent parts are illustrated in Figures 1 and 2, comprising a cam and follower mechanism, a four-bar linkage, a hook, an insulated rod, and three different springs (closing spring, opening spring, and contact spring). The movable contact for each of three phases was connected to the operating mechanism through an insulated rod and contact spring (also called a wipe spring). Figures 1 and 2 illustrate the basic configurations of the VCB operating mechanism in its opened state and closed state, respectively. In the closed state, the electric system was normally operational because the movable contact engaged with the fixed contact, and the current was connected between the primary and secondary ends; however, in the opened state, the electric current was interrupted because the movable contact separated from the fixed contact.

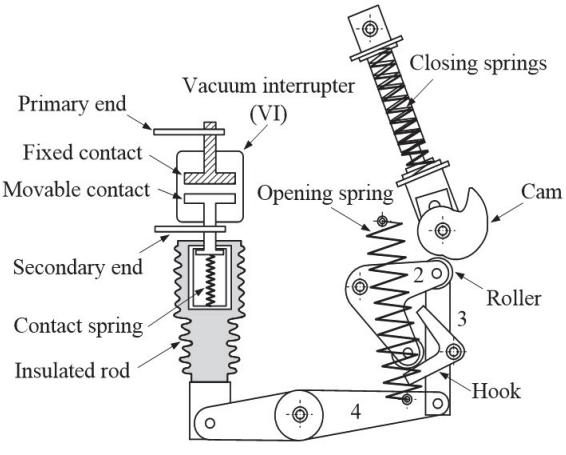

Figure 1. Opened state of a spring-actuated mechanism.

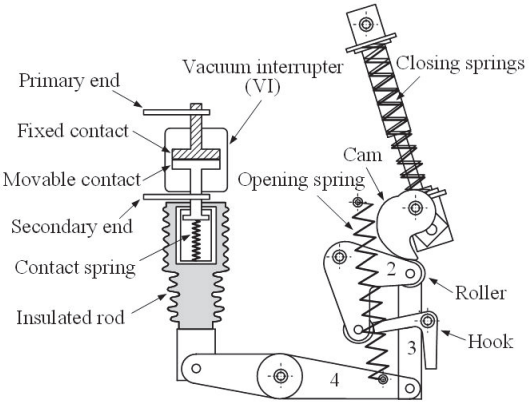

Figure 2. Closed state of a spring-actuated mechanism.

In the opened state (Figure 1), two closing springs (with different stiffness) eccentrically connected to the axis of the cam were initially compressed using a motor (not shown), and elastic energy was stored. Once a closing command was received, the closing springs were automatically or manually actuated, and the stored energy was used to drive the cam and roller follower and to drive the four-bar linkage wherein the output link would synchronously drive the insulated rod and movable contact upward. Meanwhile, the elastic energy was stored in the opening spring. When the movable contact engaged with the fixed contact, the insulated rod continued to move upward and compressed the contact spring in the VI. When the stored energy of the closing springs was exhausted, the hook automatically latched onto the roller to prevent the VCB from rebounding and completed the switching action from the opened state to the closed state.

By contrast, when an opening command was received, the contact spring and opening spring concurrently released the stored energy and the hook unlatched, thereby driving the insulated rod and movable contact rapidly downward and restoring the VCB to the opened state. The performance of the VCB was primarily affected by the materials of the electric contacts and the average closing velocity of the movable contact. The average closing velocity was defined as the average velocity of the movable contact within the last 1/3 contact stroke, and the average opening velocity was defined as the average velocity within the 3/4 range of the contact stroke from the moment of the moving contact departure [20]. If the average closing velocity of the movable contact was exceedingly high, it would cause high contact bounding, electric arc occurrence, and damage to the VCB. This studied attempted to reduce the high average closing velocity of the moving contacts for improving the performance of the VCB and to thus minimize the surplus work of the VCB operating mechanism during the closing process.

Figure 3 illustrates the status of the cam-linkage composite operating mechanism of the VCB when switching from the opened state (indicated by a dashed line) to the closed state. During cam rotation with high angular velocity, the roller followers continuously make contact with the cam, thereby preventing adverse dynamic responses. As illustrated in Figure 3, θ_c denotes the rotation angle of the cam, s_1 and s_2 (both in the positive direction with the increase in θ_c) represent the vertical displacement of points L and M on the output link of the four-bar linkage, respectively. At $\theta_c = 140^\circ$, the point L moved to the lowest position of the motion, where the overall vertical displacement was $\bar{s}_2$. Concurrently, point M moved an overall vertical distance of $\bar{s}_1$, while the movable contact moved a contact stroke s_c. Subsequently, the hook latched onto the follower link BD and prevented the opening spring from retracting the link. Within a complete revolution of the cam, the rotation angle required for the cam to effectively contact the roller and complete the closing operation was less than 180°, and the contact between the cam and the roller should be prevented in the remainder cam rotation angle. The vertical displacement (s_2) of point L

exhibited a nonlinear relationship with the rotation angle of the cam (θ_c) during the closing operation. The nonlinear motion relationship between s_2 and θ_c is illustrated in Figure 4 and depends on the characteristics of the CB, displacement range of the insulated rod, and the required average velocity of the movable contact (1.5 ± 0.2 m/s for the opening operation; 0.9 ± 0.2 m/s for the closing operation). The motion relation was specified using the cam rotation angle θ_{ci} $(i = 0, 1, 2, 3)$ at 0°, 70°, 100°, and 140°, the corresponding vertical displacements of point L were $s_{20} = 0$, $s_{21} = 0.7\,\bar{s}_2$, $s_{22} = 0.9\,\bar{s}_2$, and $s_{23} = \bar{s}_2$, respectively, and the corresponding rotation angles of the output link LE of the four-bar linkage were $\theta_{40} = 0$, $\theta_{41} = 0.7\bar{\theta}_4$, $\theta_{42} = 0.9\bar{\theta}_4$, and $\theta_{43} = \bar{\theta}_4$, respectively; $\bar{\theta}_4$ is the overall angular displacement of the output link 4. The motion relationship was similar to that between the motion of the roller follower and the cam.

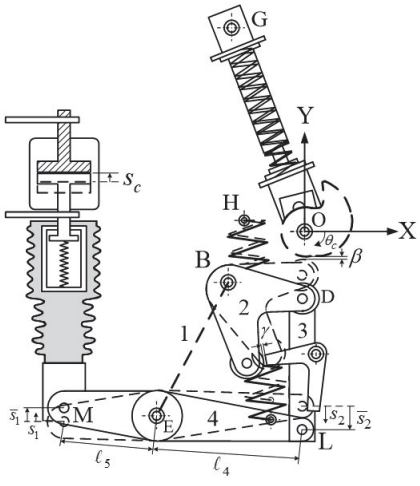

Figure 3. Sketch for closing motion of a spring-actuated operating mechanism.

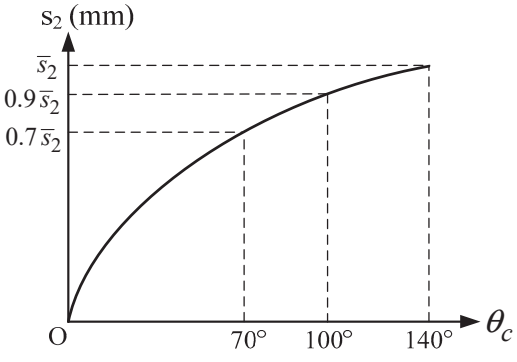

Figure 4. Specified motion relation of the VCB operating mechanism during closing process.

2.2. Cam Profile Design of the VCB Operation Mechanism

In the cam profile design, the design of the motion curve of the follower dominantly affected the output force characteristics of the VCB mechanism and the closing velocity of the movable contact, thereby influencing the overall performance of the VCB. The cam profile was designed based on the theorem of mechanisms [21], and the four-bar linkage was analyzed. Rectangular coordinate systems were used to design the cam profile (Figure 5). In Figure 5, x-y and X-Y represent the coordinate systems for the cam and the

VCB system, respectively. Point O indicates the origin of the coordinate system; x′-y′ is the coordinate system that represents the actual assembly of the cam on the VCB.

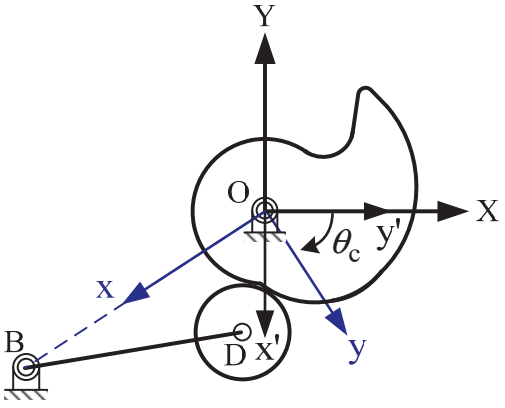

Figure 5. Coordinate systems of the cam mechanism.

The procedures of the cam profile design are described as follows:

Step 1. Assuming the oscillating angle of output link LM was very small, and the triangular proportions of the two limit positions of link LM at the opened and closed states were similar (Figure 3). Based on these, in addition to practical clearance design considerations, the instantaneous vertical displacements of points L and M, s_2, and s_1 are approximated as follows:

$$s_2 = \frac{1}{\alpha}\left(\frac{\ell_4}{\ell_5}\right)s_1 + \beta + \gamma \tag{1}$$

where, ℓ_4, ℓ_5 denote the lengths of the two sides of output link, α denotes the loss coefficient of contact, β denotes the required initial clearance between the cam and roller, and γ denotes the required initial clearance between the hook and roller. The values of α, β and γ are based on empirical knowledge.

Step 2. A known $\bar{s}_1$ condition is incorporated into Equation (1) to determine $\bar{s}_2$.

Step 3. Because the length of link 2 (ℓ_2) and the clearance (β) between the roller and cam are known, the initial angular position of input link 2 (θ_{20}) (Figure 6) of the four-bar linkage are determined as follows:

$$\theta_{20} = \tan^{-1}\left(\frac{B_y}{B_x}\right) - \cos^{-1}\left[\frac{\ell_2^2 + \ell_6^2 - (r_b + r_f + \beta)^2}{2\ell_2\ell_6}\right] \tag{2}$$

where, r_b is the radius of base circle of cam and r_f is the radius of roller follower. (B_x, B_y) is the coordinate of the pivot point B, and ℓ_6 is the distance between two pivot points B and O.

Step 4. If the preset angle of fixed link (θ_1) and initial input angle (θ_{20}) of link 2 are given, the initial output angle (θ_{40}) of link 4 are expressed as follows (Figure 6) [21]:

$$\theta_{40} = 2\tan^{-1}\left(\frac{B_0 + \sqrt{A_0^2 + B_0^2 - C_0^2}}{A_0 + C_0}\right) \tag{3}$$

where

$$A_0 = 2\ell_1\ell_4\cos\theta_1 - 2\ell_2\ell_4\cos\theta_{20}$$
$$B_0 = 2\ell_1\ell_4\sin\theta_1 - 2\ell_2\ell_4\sin\theta_{20}$$
$$C_0 = \ell_3^2 - \ell_1^2 - \ell_4^2 - \ell_2^2 + 2\ell_1\ell_2\cos(\theta_{20} - \theta_1)$$

ℓ_1, ℓ_2, ℓ_3 and ℓ_4 are the lengths of the four-bar linkage.

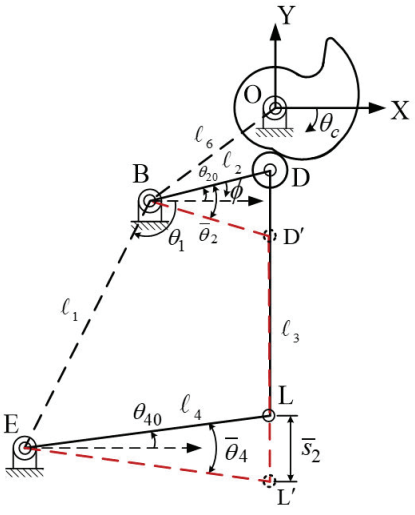

Figure 6. Cam and four-bar linkage composite mechanism.

Step 5. When the known conditions and Equation (1) are used, the overall angular displacement ($\bar{\theta}_4$) of the output link can be determined through trigonometry (Figure 6).

$$\bar{\theta}_4 = 2\sin^{-1}\left(\frac{\bar{s}_2}{2\ell_4}\right) \tag{4}$$

Subsequently, θ_{4i} $(i = 1, 2, 3)$ can be obtained using Equations (1) and (4) and the associations of θ_{ci} $(i = 1, 2, 3)$ shown in Figure 4.

Step 6. When $\bar{\theta}_4$ and θ_{4i} $(i = 1, 2, 3)$ of the four-bar linkage were determined, the corresponding angular position of link 2, θ_{2i} $(i = 1, 2, 3)$, are determined as follows:

$$\theta_{2i} = 2\tan^{-1}\left(\frac{B_i - \sqrt{A_i^2 + B_i^2 - C_i^2}}{A_i + C_i}\right) \ (i = 1, \ 2, \ 3) \tag{5}$$

where

$$\begin{aligned} A_i &= -2\ell_1\ell_2\cos\theta_1 - 2\ell_2\ell_4\cos\theta_{4i} \\ B_i &= -2\ell_1\ell_2\sin\theta_1 - 2\ell_2\ell_4\sin\theta_{4i} \qquad (i = 1, 2, 3) \\ C_i &= \ell_3^2 - \ell_1^2 - \ell_4^2 - \ell_2^2 - 2\ell_1\ell_4\cos(\theta_{4i} - \theta_1) \end{aligned}$$

Step 7. Because the oscillating follower link BD of the cam mechanism serves as the input link of the four-bar linkage, according to the specified motion of the VCB mechanism displayed in Figure 4, four angular positions of the follower link (ϕ_i, $i = 0, 1, 2, 3$) must satisfy the restriction. Therefore, a three-order polynomial displacement curve of the follower was employed to design the cam profile for preventing the occurrence of discontinuous acceleration of the follower, which may lead to transmission shock, noise, concentrated stress, and wear on the cam surface and eventually damage the cam. The three-order polynomial displacement function contains four unknown coefficients (a_0, a_1, a_2 and a_3) is expressed as follows:

$$\phi(\theta_c) = a_0 + a_1\theta_c + a_2\theta_c^2 + a_3\theta_c^3 \tag{6}$$

The relationship between the angular positions of the follower link BD (ϕ_i, $i = 0, 1, 2, 3$) and rotation angles of the cam (θ_{ci}, $i = 0, 1, 2, 3$) is expressed as follows:

$$\begin{cases} \theta_{c0} = 0, & \phi_0 = ? \\ \theta_{c1} = 70^{\circ}, & \phi_1 = |\theta_{21} - \theta_{20}| \\ \theta_{c2} = 100^{\circ}, & \phi_2 = |\theta_{22} - \theta_{20}| \\ \theta_{c3} = 140^{\circ}, & \phi_3 = |\theta_{23} - \theta_{20}| \end{cases} \tag{7}$$

Step 8. In the initial default position of the cam, a clearance β is retained between the cam and roller follower to prevent the roller from colliding with the cam at the instant of the operating mechanism to restore its default position. Therefore, at the initial default position the distance between the centers of cam and roller is $r_p = r_b + r_f + \beta$. Subsequently, the cam must be rotated counter clockwise with a small angle θ_0, covering a distance of β relative to the roller. Therefore, the actual rotation angle of the cam, θ, in the operating mechanism is $\theta = \theta_0 + \theta_c$. When $\theta_{co} = 0$, according to the geometric association illustrated in Figure 7, the initial angular position of the follower link BD (ϕ_0) is determined as follows:

$$\phi_0 = \cos^{-1}\left[\frac{\ell_2^2 + \ell_6^2 - r_p^2}{2\ell_2\ell_6}\right] - \cos^{-1}\left[\frac{\ell_2^2 + \ell_6^2 - (r_b + r_f)^2}{2\ell_2\ell_6}\right] \tag{8}$$

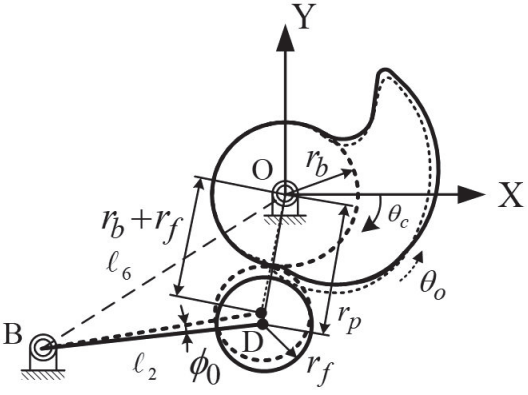

Figure 7. Initial setting of the cam mechanism with a clearance.

Step 9. From Equations (5) to (7), four simultaneous equations are used to determine the four unknown coefficients: a_0, a_1, a_2, and a_3.

Step 10. According to Figure 8, the coordinates (x_p, y_p) of the pitch curve of the cam is determined using the following equations [21]

$$\begin{aligned} x_p &= \ell_6 \cos\theta_c - \ell_2 \cos(\theta_c - \xi - \phi) \\ y_p &= \ell_6 \sin\theta_c - \ell_2 \sin(\theta_c - \xi - \phi) \end{aligned} \tag{9}$$

where

$$\xi = \cos^{-1}\left[\frac{\ell_2^2 + \ell_6^2 - \left(r_b + r_f\right)^2}{2\ell_2\ell_6}\right] \tag{10}$$

Step 11. The coordinates of the cam profile (x_c, y_c) are determined using the following equations

$$\begin{aligned} x_c &= x_p - r_f\left(\frac{dy_p}{d\theta_c}\right)\left[\left(\frac{dx_p}{d\theta_c}\right)^2 + \left(\frac{dy_p}{d\theta_c}\right)^2\right]^{-1/2} \\ y_c &= y_p + r_f\left(\frac{dx_p}{d\theta_c}\right)\left[\left(\frac{dx_p}{d\theta_c}\right)^2 + \left(\frac{dy_p}{d\theta_c}\right)^2\right]^{-1/2} \end{aligned} \tag{11}$$

where

$$\begin{aligned}\frac{dx_p}{d\theta_c} &= -\ell_6 \sin\theta_c + \ell_2\left(1 - \frac{d\phi}{d\theta_c}\right)\sin(\theta_c - \xi - \phi)\\ \frac{dy_p}{d\theta_c} &= \ell_6 \cos\theta_c - \ell_2\left(1 - \frac{d\phi}{d\theta_c}\right)\cos(\theta_c - \xi - \phi)\\ \frac{d\phi}{d\theta_c} &= \phi' = a_1 + 2a_2\theta_c + 3a_3\theta_c^2\end{aligned} \tag{12}$$

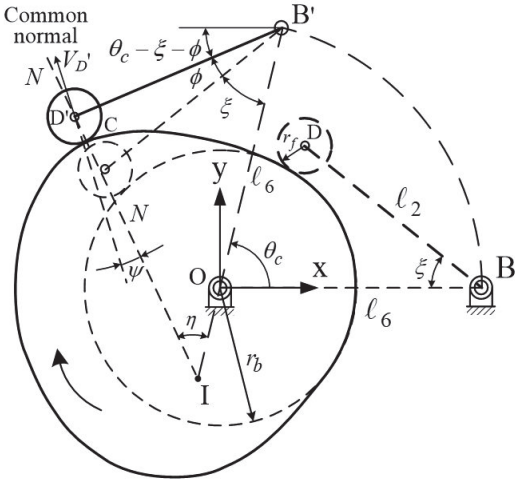

Figure 8. Disc cam with an oscillating roller follower.

Step 12. The pressure angle (ψ) of the cam, which is defined as the angle between the linear velocity (V_D) of the center of the roller follower and the common normal on the contact surfaces (Figure 8), is expressed as follows

$$\psi = \frac{\pi}{2} - \eta - \xi - \phi \tag{13}$$

As displayed in Figure 8, the intersection point, I, between the common normal of the contact surfaces and the lines joining the two rotation axes, is the instantaneous center of the follower motion relative to the cam, and can be determined using trigonometry.

$$\eta = \sin^{-1}\left[\frac{\ell_2 \sin(\xi + \phi)}{\overline{ID'}}\right] \tag{14}$$

where

$$\begin{aligned}\overline{ID'} &= \sqrt{\ell_2^2 + \left(\overline{OI} + \ell_6\right)^2 - 2\ell_2\left(\overline{OI} + \ell_6\right)\cos(\xi + \phi)}\\ \overline{OI} &= \left(\tfrac{\ell_6}{1-\phi'}\right)\phi'\end{aligned}$$

Step 13. The radius of curvature (ρ_c) of the cam profile is subsequently determined [21].

$$\rho_c = \frac{\left[\ell_6^2 - 2\ell_2\ell_6\cos(\xi + \phi)(1 - \phi') + \ell_2^2(1 - \phi')^2\right]^{3/2}}{\ell_6^2 - \ell_2\ell_6(2 - \phi')(1 - \phi')\cos(\xi + \phi) - \ell_2\ell_6(\phi'')\sin(\xi + \phi) + \ell_2^2(1 - \phi')^3} - r_f \tag{15}$$

where

$$\phi'' = \frac{d\phi'}{d\theta_c} = 2a_2 + 6a_3\theta_c$$

The radius of curvature of the cam profile is crucial for calculating the Hertz contact stress between the contact surfaces of the cam and roller follower. The Hertz contact stress

was evaluated to determine whether the contact stress and the shear stress of the cam surface were lower than the endurance contact stress and yielding shear stress, respectively.

A clearance β must be retained between the cam and the roller to prevent the roller from colliding with the cam during the operating mechanism to restore its default position.

2.3. Kinematic Analysis of the Initial VCB Mechanism Design

Figure 9 displays the schematic of a spring-actuated cam-linkage composite operating mechanism of a VCB during the closing operation. The data and design parameters of the initial design provided by the manufacturing vendor were as follows (Figures 3 and 9). Data of four-bar linkage: ℓ_1 = 139.79 mm, ℓ_2 = 70 mm, ℓ_3 = 124.7 mm, ℓ_4 = 140 mm, ℓ_5 = 90 mm, ℓ_6 = 90.6035 mm, ℓ_7 = 105 mm, and ℓ_8 = 25 mm; the overall vertical displacement of point M, $\bar{s}_1$ = 16 mm, the coordinates of fixed pivots were G(50, 200), O(0, 0), H(−57, 19), B(−72, −55), and E(−142, −176), and the angle ∠LES was 4.9°; the preset angle ∠QOX was 95°. Data of the cam mechanism: radius of base circle of the cam was $r_b = 23$ mm, radius of the roller follower was $r_f = 15$ mm, loss coefficient of the contact was α = 0.95, clearance between the roller and hook was γ = 1 mm, clearance between the cam and roller was β = 2 mm, and the default initial rotation angle was $\theta_0 = 4^\circ$. The kinematic analysis of the initial design of the VCB operating mechanism was performed during the closing operation using a MATLAB coded program.

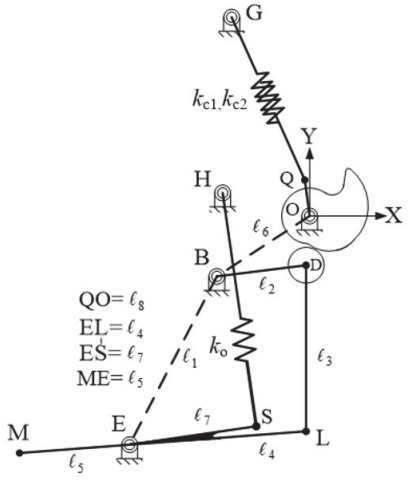

Figure 9. Sketch of the VCB operating mechanism during closing process.

According to Equations (5) to (8), the four coefficients of the three-order polynomial displacement curve of the follower were determined as follows: $a_0 = 0.015185$, $a_1 = 0.240347$, $a_2 = 0.011694$, $a_3 = -0.017243$. Figures 10–13 illustrate the results of kinematic analysis of the initial cam design. Figure 10 only displays the portions of the pitch curves and the cam profile that make continuous contact with the roller. Figure 11 (red dashed line) illustrates the angular displacement curve of the oscillating follower. Figure 12 (red dashed line) displays the pressure angle of the cam mechanism; the maximum pressure angle was less than the allowable maximum pressure angle of 45°. Figure 13 (red dashed line) depicts the radii of curvature of the cam profiles that are greater than the radius of the roller (15 mm), that is, $\rho_c > r_f$, indicating that no undercutting occurred on the cam profile. Thus, if considering only the curvature of cam profile, the initial cam design was feasible. For reducing the number of figures and facilitating the comparison between the initial cam design and optimal cam design discussed in Section 4, the relevant analyses curves (blue solid line in Figures 11–13) of the optimized cam mechanism were included into the figures of the analyses of initial design.

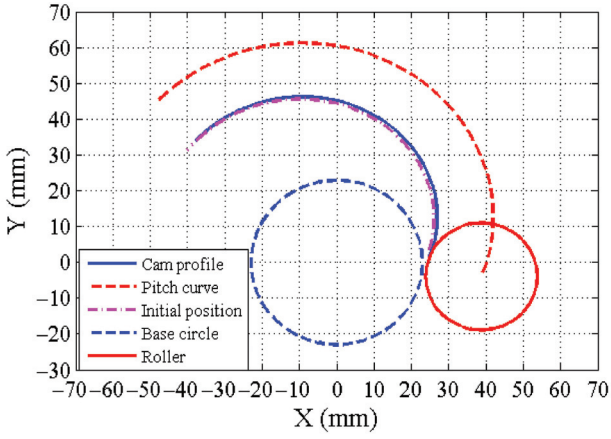

Figure 10. Initial cam profile and pitch curve (only actuated portion).

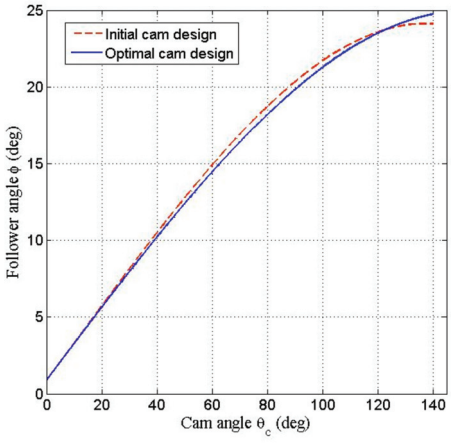

Figure 11. Angular displacement curve of the oscillating follower.

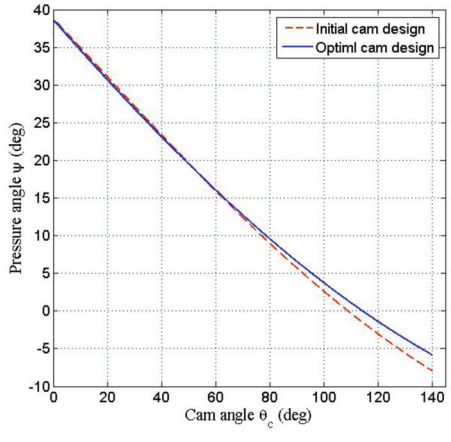

Figure 12. Pressure angle of the cam mechanism.

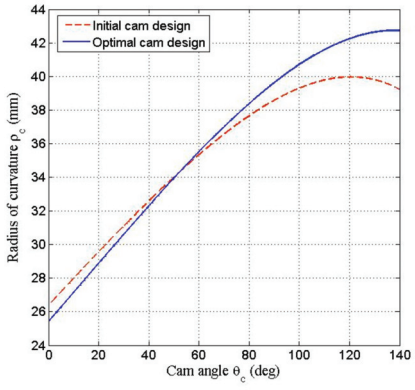

Figure 13. Radius of curvature of the cam profile.

Figure 14 (red dashed line) displays the displacement function curve of point L. Both red dashed lines in Figures 10 and 14 depict similar motion relationships. The relationship between the output and input angles of the four-bar linkage was approximately linear, as illustrated by red dashed line in Figure 15.

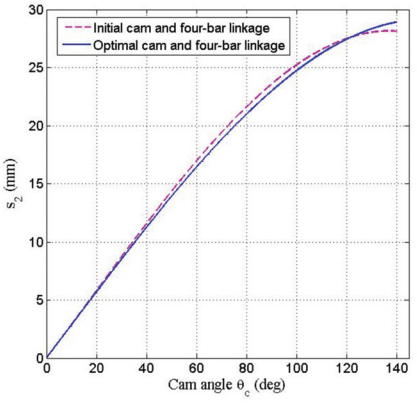

Figure 14. Displacement function curve of point L.

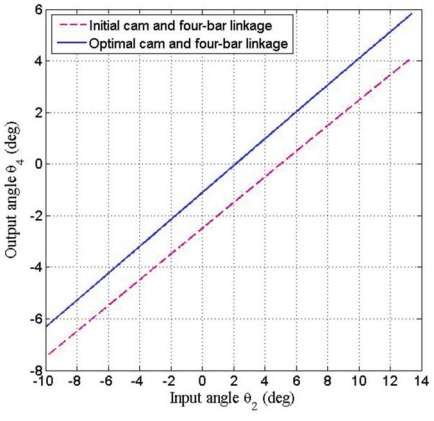

Figure 15. Output-input curve of the four-bar linkage.

2.4. Analyses of the Characteristic Forces and Hertz Contact Stress

To simplify the dynamic analysis, the following assumptions were considered: The main constituent parts of the operating mechanism, as illustrated in Figures 1 and 2, were considered rigid bodies. The weight of each part and the effects of friction on the joints were considered negligible compared with the dynamic forces acting on the parts. The closing springs, opening spring, and contact spring were linear springs. As displayed in Figure 9, the spring coefficients of two closing springs were $k_{c1} = 7.72$ N/mm and $k_{c2} = 9.33$ N/mm, and their pre-compression lengths were 140 and 100 mm, respectively. The spring force of the closing springs (F_{cs}) during the closing process are expressed as follows:

$$F_{cs} = k_{c1}(140 - \delta_c) + k_{c2}(100 - \delta_c) \tag{16}$$

where δ_c is the released length of the closing springs.

The given elastic coefficient, pre-stretched length, and default tension force of the opening spring were $k_o = 16.6$ N/mm, 33.6 mm and 247.3 N, respectively. The spring force of the opening spring (F_{os}) is expressed as follows:

$$F_{os} = k_o(33.6 + \delta_o) + 247.3 \tag{17}$$

where δ_o denotes the increased deformation of the opening spring. The known spring coefficient and pre-compression length of the contact spring (also called a wipe spring) were $k_w = 82.4$ N/mm and 17 mm, respectively. The overall compressive spring force (F_w) of the contact springs on the VCB operating mechanism in the three-phase circuit can be expressed as follows:

$$F_w = 3k_w(17 + \delta_w) \tag{18}$$

where δ_w is the increased deformation of the contact spring during the period of closing operation, the vacuum force due to the atmospheric pressure (referred to as the free-contact force, F_{fc}) between the two contacts was 160 N, indicating that the pressure applied to the movable contact was equal to the difference between the atmospheric pressure and the pressure of the VI. The free-contact force was equal to zero once the electric movable and fixed contacts were engaged. Figure 16 displays the free-body diagrams (FBDs) of various parts in VCB operating mechanism during the closing operation. The FBDs represent the cam (Figure 16a), roller and follower link (Figure 16b), and the output link connected with the insulated rod and movable contact (Figure 16c), respectively.

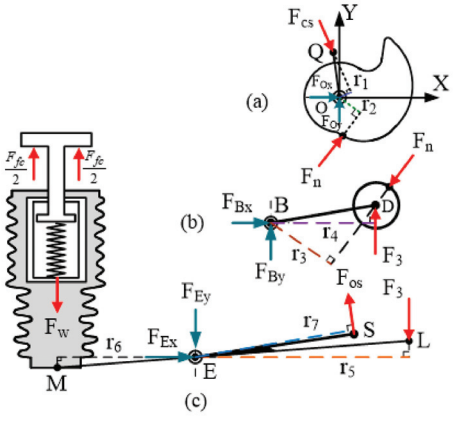

Figure 16. FBDs of various parts in the VCB operating mechanism during the closing operation.

During the closing operation, the active forces between the various parts of the mechanism were assumed to be quasi-static and were determined by applying the concept of moment equilibrium to the FBD of the various parts.

The FBD of the cam (Figure 16a) is represented by the following relationship:

$$F_n = \frac{r_1}{r_2} F_{cs} \tag{19}$$

where F_n denotes the instantaneous normal contact force between the cam and the roller follower, and r_1, r_2 represent the instantaneous perpendicular distance (or force arm) from the line of corresponding active force.

The FBD of the roller and follower link (Figure 16b) is represented by the following relationship:

$$F_3 = \frac{r_3}{r_4} F_n = \frac{r_1 r_3}{r_2 r_4} F_{cs} \tag{20}$$

where F_3 is the transmission force on the connecting link 3, and r_3, r_4 represent the instantaneous perpendicular distance from the line of corresponding active force.

As depicted in the FBD of the output link LM connected to the insulated rod and movable contact (Figure 16c), the moment exerted on the main shaft E of the output link, referred to as the driving moment (M_d), originated in two closing springs, and the resistant moment (M_r), originated in the opening spring, three contact springs, and atmospheric pressure force. The driving moment and resistance moment are expressed as follows:

$$M_d = r_5 F_3 \tag{21}$$

$$M_r = r_7 F_{os} + r_6 (F_w - F_{fc}) \tag{22}$$

where r_5, r_6 and r_7 denote the instantaneous perpendicular distance from the line of corresponding active force.

To effectively achieve a closed state, the driving moment M_d exerted on the output link should have been greater than the resistant moment M_r, $M_d > M_r$. Regarding the work done in the subsystem, as displayed in Figure 16c, the net work done on the main shaft E by the driving moment and resistant moment (assuming neglecting the effect of friction forces on joints) should be positive during the closing operation. The net done work (U_{net}) is expressed as follows:

$$\begin{aligned} U_{net} &= \int_0^{\bar{\theta}_4} (M_d - M_r) d\theta_4 \\ &= \int_0^{\bar{\theta}_4} \left[r_5 F_3 - \left(r_7 F_{os} + \left(F_w - F_{fc} \right) r_6 \right) \right] d\theta_4 \\ &= \int_0^{\bar{s}_2} F_3 ds_2 - \int_0^{\bar{s}_1} \left[\left(\frac{r_7}{r_6} \right) F_{os} + F_w - F_{fc} \right] ds_1 \\ &= \int_0^{\bar{s}_1} \left\{ \left(\frac{\ell_4}{\alpha \ell_5} \right) F_3 - \left[\left(\frac{r_7}{r_6} \right) F_{os} + F_w - F_{fc} \right] \right\} ds_1 \\ &= \int_0^{\bar{s}_1} \left\{ \left(\frac{r_1 r_3 r_5}{r_2 r_4 r_6} \right) F_{cs} - \left[\left(\frac{r_7}{r_6} \right) F_{os} + F_w - F_{fc} \right] \right\} ds_1 > 0 \end{aligned} \tag{23}$$

In Equation (23), $r_5 d\theta_4 = ds_2$, $r_6 d\theta_4 = ds_1$ and from Equation (10), $ds_2 = \ell_4 / (\alpha \ell_5)\, ds_1 = (r_5 / r_6)\, ds_1$. The first term and second term in the bracket of above equation can be referred as the general output force (F_o) and general resistant force (F_r) of the VCB operating mechanism, respectively.

$$F_o = \left(\frac{r_1\, r_3\, r_5}{r_2\, r_4\, r_6} \right) F_{cs},\ F_r = \left(\frac{r_7}{r_6} \right) F_{os} + F_w - F_{fc} \tag{24}$$

The general output force was affected by the closing spring force (F_{cs}) and the force arms ($r_1, r_2, \ldots, r_6$) were strongly affected by the cam profile and the dimensions of the four-bar linkage. The general resistant force was affected by the opening spring force (F_{os}),

contact spring force (F_w), free contact force (F_{fc}) and the force arms (r_6, r_7). Because the small rotation angle of the link LM, the change in r_6 and r_7 were considerably small and the stiffness of opening spring and contact spring were not in the design parameters, the general resistant force during the closing operation was approximately the same in the various VCB operating mechanisms designed in this study.

Equation (23) can be expressed as

$$U_{net} = \int_0^{\bar{s}_1} (F_o - F_r) ds_1 > 0 \;\cong\; \sum_{i=1}^{N_s} (F_o - F_r)_i \, \delta s_i > 0 \tag{25}$$

where *Ns* is the position number selected to calculate the forces, and δs is the small step displacement of the insulated rod. In Equation (25), the larger the value of *Ns*, the closer it is to the definite integral of Equation (23). Considering the energy loss due to the friction forces acting on the joints of the VCB mechanism, the VCB mechanism system was assumed to have a mechanical efficiency of 85% (ε = *0.85*), therefore, Equation (25) was modified as follows

$$U_{net} \cong \sum_{i=1}^{N_s} (F_{oi} - \frac{F_{ri}}{\varepsilon}) \, \delta s_i > 0 \tag{26}$$

Based on above derived equations, a MATLAB2011 coded program was developed for analyzing the characteristic forces (including spring forces, general output force, and general resistant force), and the displacement of the insulated rod during closing operation in the VCB mechanism. The program was executed using an ASUS-P43E notebook with Intel core I5-2450M 2.5 GHz CPU. The various characteristic forces, including the opening spring force (red dashed line), closing spring force (black dashed line), wipe spring force (solid green line), general resistant force (red line) and general output force (blue dashed line) during the closing operation were displayed in Figure 17. The general output force of the VCB operating mechanism is not always required to be greater than the general resistant force during the closing stroke. The area under curve (AUC) of the general output force represents the integration of the force with respect to the differential displacement of the insulated rod, indicating the output work (also referred to as driving work) in the VCB operating mechanism. Similarly, the AUC of the general resistant force indicates the resistant work in the VCB operating mechanism. This study aimed to minimize the net work done (or referred as surplus output work, equal to the difference of the driving work and the resistant work) for the CVB operating mechanism during the closing operation. Therefore, if the value of *Ns* was taken large enough, considering that the step increment of insulated rod was differential and constant, the overall differences between the general output forces and the general resistant forces (divided by mechanical efficiency) at the selected sequence positions of the insulated rod during the closing operation was considered as the objective function to be minimized, as discussed in Section 4.

Two elastic contact bodies with various curvatures cannot form a line or point contact. The contact formed in such a case is extremely small with high stress values, commonly known as Hertz contact stress [22,23]. The contact pattern between the cam and the cylindrical roller exhibited a rectangular shape as depicted in Figure 18. The contact stress distribution resembled a semi-elliptical prism of half-width b. The contact rectangular measuring 2b (width) $\times \ell$ (length), and the half-width (b) of the rectangular is expressed as follows:

$$b = \sqrt{\frac{8F_n\rho_e}{\pi \ell E_e}} \tag{27}$$

where ρ_e denotes the equivalent radius of curvature at the contact surfaces, F_n denotes the normal contact force and E_e denotes the equivalent elastic modulus, as represented by following equations:

$$\frac{1}{\rho_e} = \frac{1}{\rho_c} + \frac{1}{\rho_r} \tag{28}$$

$$\frac{1}{E_e} = \frac{1}{2}\left(\frac{1-\nu_1^2}{E_1} + \frac{1-\nu_2^2}{E_2}\right) \tag{29}$$

where E_1 and E_2 denote the elastic modulus of the cam and roller, respectively; ν_1 and ν_2 denote Poisson's ratios of the cam and roller, respectively. The maximum Hertz contact stress ($\sigma_{\max}$) is generated at the center of the contact surface between the cam and the roller follower and can be expressed as follows:

$$\sigma_{\max} = \frac{2F_n}{\pi b \ell} \tag{30}$$

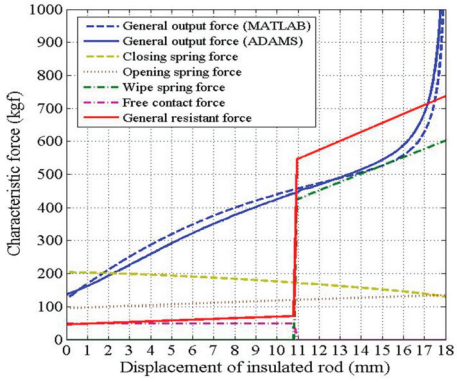

Figure 17. Characteristic forces during closing process for the initial VCB mechanism deign.

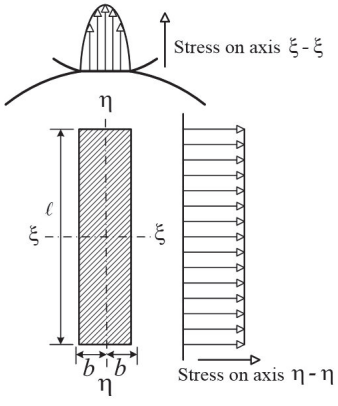

Figure 18. Contact pattern between the cam and cylindrical roller.

If the cam and roller follower are manufactured using the same steel material (Poisson's ratio $\nu = 0.3$), the maximum shear stress (τ_{max}) occurs at approximately $0.786b$ beneath the surface of the cam and can be expressed as follows:

$$\tau_{max} = 0.304\sigma_{max} \tag{31}$$

The maximum shear stress is a crucial factor that determines the surface failure of the cam that begins with an initial crack beneath the surface [23,24]. The maximum Hertz contact stress on the cam surface of the initial VCB mechanism is depicted in Figure 19, and a considerably high Hertz stress occurred near the end of closing stroke. The maximum shear stress beneath the cam surface is depicted in Figure 20. According to the Mises-Hencky shear yielding criteria [25] and Table 1, the shear yielding stress (τ_y) of the carbon

steel (S45C) is $\tau_y = 0.577\sigma_y = 1194$ MPa. Figure 20 illustrates that the maximum value of maximum shear stress was larger than the shear yielding stress, and thus the initial VCB mechanism design was not feasible.

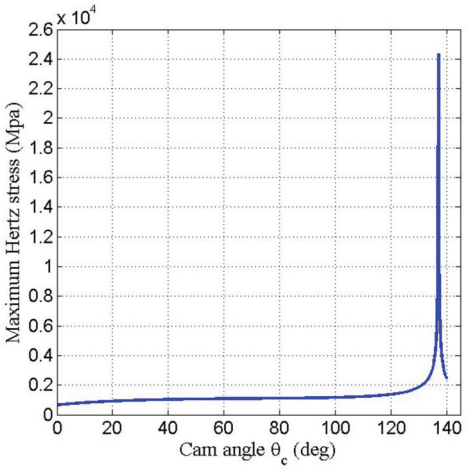

Figure 19. Maximum Hertz contact stress on the cam surface of the initial design.

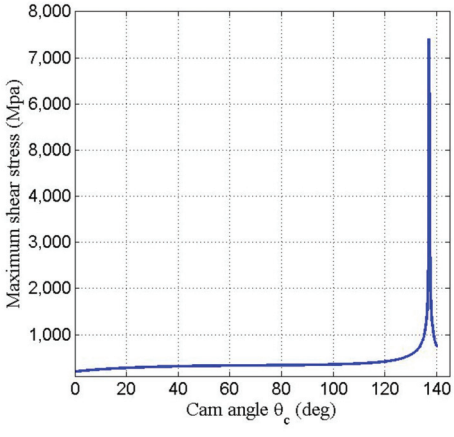

Figure 20. Maximum shear stress beneath the cam surface of the initial design.

Table 1. Materials property of the cam and electric contacts.

	Cam	**Movable/Fixed Contact**
Material type	Carbon steel (S45C)	Cu-Cr alloy
Density	7.865×10^{-6} kg/mm^3	8.96×10^{-6} kg/mm^3
Young's modulus	210 GPa	110.316 GPa
Allowable compressive yielding stress	2070 MPa	–
Ultimate tensile stress	2070 MPa	–
Brinell Hardness, H_B	705	–
Poisson's ratio	0.30	0.34

3. Multibody Dynamic Analysis by MSC-ADAMS

To elucidate the dynamic characteristics of the cam-linkage composite operating mechanism of a VCB, a three-dimensional (3D) solid model was constructed using SolidWorks software (Figure 21). The model was then converted to the .x_t format and imported into MSC-ADAMS software (Figure 22) to perform multibody dynamic analysis and simulation of the VCB operating mechanism.

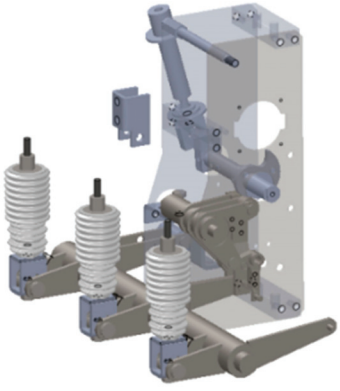

Figure 21. 3D solid model of the VCB operating mechanism.

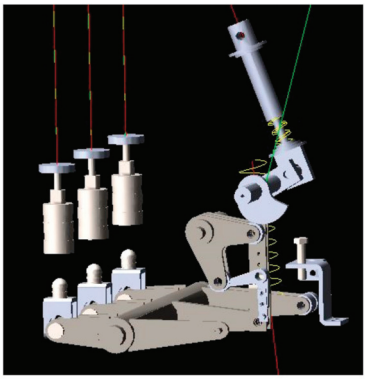

Figure 22. Simulation of the VCB mechanism by ADAMS.

3.1. Simulation Setting

Before the kinematic and dynamic analyses of the VCB mechanism were performed, various parameters including the material characteristics of various bodies, joint types connecting the various links, elastic coefficients and amount of pre-compression/pre-stretching of the springs were given, as listed in Tables 1 and 2. As displayed in Table 1, both the compressive yielding stress and ultimate tensile stress of carbon steel S45C, which was subjected to heat treatment, including quenching and tempering at 27 °C, were equal to 2070 MPa [26]. The parameters of contact conditions between the cam and roller, and the movable/fixed contacts are listed in Table 3. Finally, the free-contact force was selected according to the simulation interval using the MSC-ADAMS/Solver Command function (Table 4).

Table 2. Parameters and pre-deformed amount of the springs.

	Elastic Coefficient of Spring (N/mm)	Pre-Compressed/ Pre-Stretched (mm)	State of VCB
Closing springs	$k_{c1} = 7.72$	140 (compressed)	Opened state
	$k_{c2} = 9.33$	100 (compressed)	
Opening spring	$k_o = 16.6$	33.6 (stretched)	Closed state
Contact spring	$k_w = 82.4$	17 (compressed)	Closed state

Table 3. Parameters of contact conditions in ADAMS.

	Cam	Movable/Fixed Contact
Normal force	Impact	
Stiffness	10^5	
Force exponent	2.2	1.6
Damping	10	10^3
Penetration depth	0.1 (mm)	

Table 4. Setting of simulation time and free-contact force.

	Simulation Time (s)	Steps	Free-Contact Force	State of VCB
I	0.0000~0.0032	100	deactivate	closed
II	0.0032~0.0278	300	activate	opened
III	0.0278~0.0450	500	deactivate	closed

3.2. Multibody Dynamic Analysis

The initial default setting for multibody dynamic analysis of the VCB operating mechanism was the closed state (Figure 2). The selected simulation time, free-contact force and state of the VCB are listed in Table 4.

Figures 23–25 illustrate the results of kinematic analysis and dynamic simulation of the initial VCB mechanism design using MSC-ADAMS. The results indicated the angular displacement of the cam, the displacement of the insulated rod, and the velocities of the movable contact and insulated rod. During 0–0.0032 s, the opening spring, contact spring, and closing springs simultaneously released energy from the initial closed state. The movable contact and fixed contact separate at approximately 0.0032 s, and the opening state of the VCB is initiated. During 0.0032–0.007 s, the insulated rod and movable contact simultaneously shifted downwards, and the open circuit process was completed at 0.007 s. Concurrently, the closing springs continued to release energy. At approximately 0.0131 s, the cam contacted with the roller, exerting a downward force on the roller and actuating the insulated rod and movable contact to synchronously shift upward. At 0.0278 s, the movable contact abruptly collided with the fixed contact, thereby the velocity of the movable contact sharply decreased to zero. The insulated rod continued to move upward with an abrupt decrease in velocity, thus compressing the contact spring in the VI. The closed state was completed at approximately 0.045 s. The overall rotation of the cam from the opened state to the closed states was 140.6°, with a contact stroke of 11 mm and the overall displacement of the insulated rod was 18 mm. The simulation results indicated that the average opening velocity of the movable contact was approximately 2.5 m/s, and the average closing velocity was approximately 1.71 m/s. These results indicated that the surplus work of the VCB operating mechanism system resulted in an excessively high closing velocity of the movable contact. Furthermore, the general output force simulated using MSC-ADAMS is

illustrated in Figure 17 (blue solid line) compared with those simulated using MATLAB-coded program (blue dashed line). The values were approximated and the curve trends were consistent in both curves. The main factor causing the differences is the quasi-static assumption in this work.

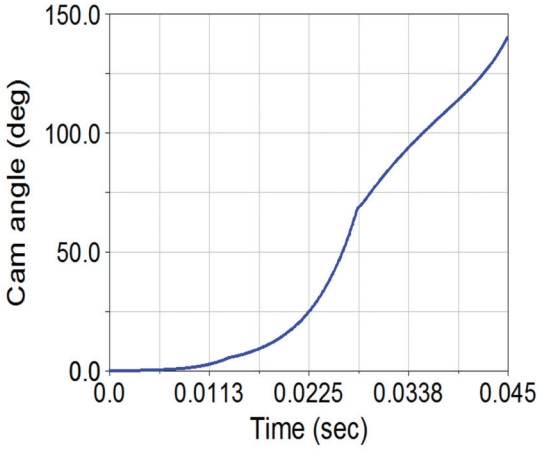

Figure 23. Angular displacement of the cam motio.

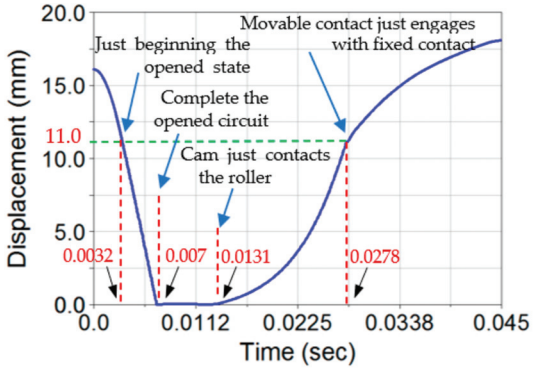

Figure 24. Displacement of the insulated rod.

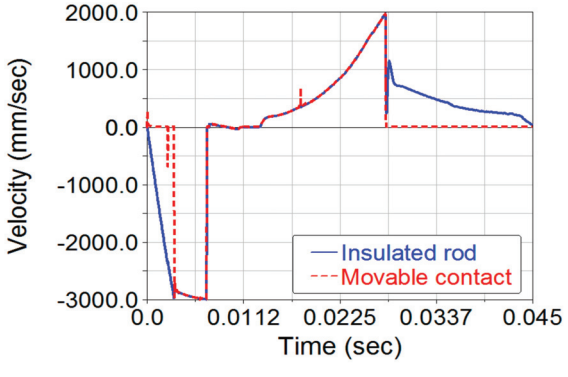

Figure 25. Velocities of the movable contact and insulated rod.

4. Optimal Design of the VCB Operation Mechanism

4.1. Differential Evolution Algorithm

Storn and Price [15] proposed the differential evolution (DE) algorithm, which is a well-known metaheuristic optimization algorithm that can be used to search for a global optimum solution in a D-dimension real variable space. The standard DE algorithm involves four basic steps: initialization, mutation, recommendation or crossover, and selection. Only the last three steps are repeated in subsequent DE iterations.

(1) Initialization

In the D-dimension real variable space, each vector, known as the genome/chromosome, forms a candidate solution of the optimization problem. The *i*-th parameter vector of the population at the current iteration (*t*) can be expressed as follows:

$$\mathbf{x}_i{}^{(t)} = [x_{i,1}{}^{(t)}, x_{i,2}{}^{(t)}, \ldots\ldots, x_{i,D}{}^{(t)}] \tag{32}$$

The initial populations (t = 1) covered the entire parameter space as much as possible through uniform random distribution within a range constrained by the prescribed minimum and maximum bounds. $\mathbf{x}_{\min} = [x_{\min,1}, x_{\min,2}, \ldots\ldots, x_{\min,D}]$ and $\mathbf{x}_{\max} = [x_{\max,1}, x_{\max,2}, \ldots\ldots, x_{\max,D}]$. Therefore, the *j*-th component of the *i*-th vector can be initialized as follows:

$$x_{i,j}{}^{(1)} = x_{\min,j} + rand_{i,j}(0,\,1)\,(x_{\max,j} - x_{\min,j}) \;\; (\mathrm{i} = 1,\,2,\,\ldots,\,\mathrm{Np};\; \mathrm{j} = 1,\,2,\,\ldots,\,\mathrm{D}) \tag{33}$$

where $rand_{i,j}(0,1)$ is a uniformly distributed random number within the interval [0, 1]. Np denotes the number of populations, *i* denotes the index of solution vector, and *j* denotes the index of the parameter in the vector.

(2) Mutation

After initialization, a donor/mutant vector $\mathbf{v}_i{}^{(t)}$ corresponding to each target vector $\mathbf{x}_i{}^{(t)}$ in the current iteration (*t*) was obtained according to outcome of the mutation operation. Figure 26 illustrates a simple DE mutation scheme ($DE/rand/1$) in the 2D parametric space. The five most frequently used mutation strategies are listed below:

$$\begin{gathered}
DE/rand/1: \\
\mathbf{v}_i{}^{(t)} = \mathbf{x}_{r1}^{(t)} + F(\mathbf{x}_{r2}^{(t)} - \mathbf{x}_{r3}^{(t)}) \\
DE/rand/2: \\
\mathbf{v}_i^{(t)} = \mathbf{x}_{r1}^{(t)} + F(\mathbf{x}_{r2}^{(t)} - \mathbf{x}_{r3}^{(t)}) + F(\mathbf{x}_{r4}^{(t)} - \mathbf{x}_{r5}^{(t)}) \\
DE/best/1: \\
\mathbf{v}_i^{(t)} = \mathbf{x}_{best}^{(t)} + F(\mathbf{x}_{r1}^{(t)} - \mathbf{x}_{r2}^{(t)}) \\
DE/best/2: \\
\mathbf{v}_i^{(t)} = \mathbf{x}_{best}^{(t)} + F(\mathbf{x}_{r1}^{(t)} - \mathbf{x}_{r2}^{(t)}) + F(\mathbf{x}_{r3}^{(t)} - \mathbf{x}_{r4}^{(t)}) \\
DE/rand\text{-}to\text{-}best/1: \\
\mathbf{v}_i{}^{(t)} = \mathbf{x}_i^{(t)} + K(\mathbf{x}_{best}^{(t)} - \mathbf{x}_i^{(t)}) + F(\mathbf{x}_{r1}^{(t)} - \mathbf{x}_{r2}^{(t)})
\end{gathered} \tag{34}$$

The indices r_1, r_2, r_3, r_4 and r_5 are randomly generated within the range [1, Np] and $r_1 \neq r_2 \neq r_3 \neq r_4 \neq r_5 \neq r_i$. $\mathbf{x}_{best}^{(t)}$ denotes the best individual vector with the best fitness function in the population at iteration t. $\mathbf{x}_{r2} - \mathbf{x}_{r3}$ represents the difference vector; the mutation weighting factor (scale factor) F is a positive control parameter used to scale the difference vector and is usually selected within [0.4, 0.99].

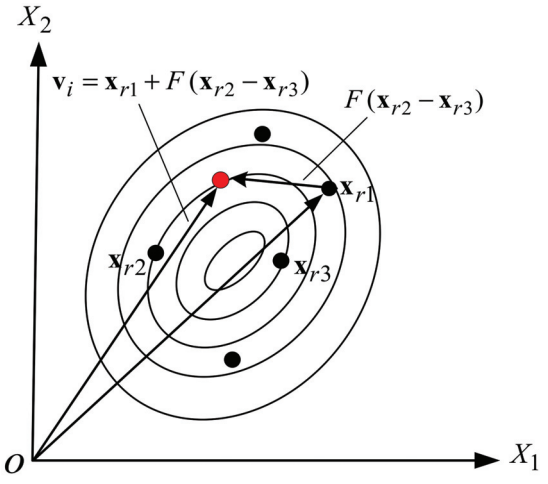

Figure 26. A simple DE mutation scheme in 2D parametric space.

(3) Crossover

Through uniform (or binomial) crossover, the components of the donor vector were combined with those of the target (parent) vector $\mathbf{x}_i{}^{(t)}$ to form a trail (offspring) vector

$$\mathbf{u}_i^{(t)} = \left[u_{i,1}^{(t)}, u_{i,2}^{(t)}, \ldots\ldots, u_{i,D}^{(t)}\right]$$
$$u_{i,j}^{(t)} = \begin{cases} v_{i,j}^{(t)} & if rand_{i,j}(0,1) \le CR or i = i_r \\ x_{i,j}^{(t)} & otherwise \end{cases} \quad (35)$$

where *CR* is a pre-defined control parameter called the crossover rate, which ranges within [0, 1]. $rand_{i,j}(0,\ 1)$ denotes a uniform random number within the range [0, 1] and ensures that the trail vector $\mathbf{u}_i{}^{(t)}$ includes at least one component from the donor vector $\mathbf{v}_i{}^{(t)}$. Element i_r is a randomly selected integer from the set [1, 2, . . . , D].

(4) Selection

Selection determines whether the target vector or the trial vector survives in the next iteration through the comparison of the corresponding objective function value.

$$\mathbf{x}_i^{(t+1)} = \begin{cases} \mathbf{u}_i^{(t)} \text{ if } f(\mathbf{u}_i^{(t)}) \le f(\mathbf{x}_i^{(t)}) \\ \mathbf{x}_i^{(t)} \text{ otherwise.} \end{cases} \quad (36)$$

where f (.) is the objective function to be minimized.

Figure 27 illustrates the flow of the DE optimization algorithm. The optimal solution of a design problem is obtained through an iterative process to determine the fitness value of the candidate solutions; the favorable solutions are retained and unfavorable solutions are discarded until the optimal solution is determined. The advantages of the DE algorithm are its simple structure, easy implementation, and ability to achieve rapid convergence.

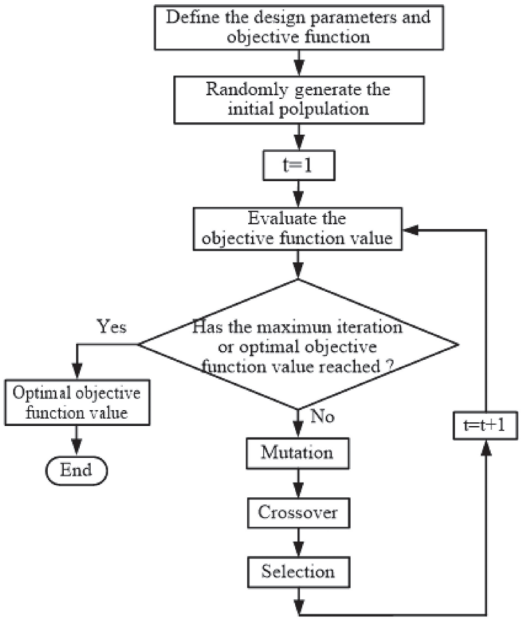

Figure 27. Flow chart of the DE optimization algorithm.

4.2. Optimum Design of Cam Profile and Stiffness of Closing Springs

To improve the output force characteristics and reduce the characteristic forces of the VCB operating mechanisms, this study adopted the overall difference between the general output force and the general resistant force of the VCB operating mechanism as the objective function. Subsequently, the DE algorithm was employed to optimize the design problem. The optimal design of the VCB operating mechanism was achieved through two steps, the first step involved the optimal design of the cam profile and elastic coefficients of the two closing springs, which was first performed at this section, and the second step involved the optimal dimensional synthesis of the planar four-bar linkage.

(1) Design variables

The design variables include the coefficients $(a_1,\ a_2,\ a_3)$ of the three-order polynomial angular displacement function of the oscillating roller follower and the spring stiffness $(k_{c1},\ \ k_{c2})$ of the two closing springs, the design variables can be expressed as a vector **X**.

$$\mathbf{X} = [x_1, x_2, x_3, x_4, x_5]^T = [a_1, a_2, a_3, k_{c1}, k_{c2}]^T \tag{37}$$

The range of the design parameters were as follows:

$$\begin{array}{l} 0 \le x_1 \le 0.5\ ,\ \ 0 \le x_2 \le 0.5\ ,\ \ -0.5 \le x_3 \le 0 \\ 4 \le x_4 \le 7.7\ ,\ 6 \le x_5 \le 9.3\ \ unit\ of\ x_4,\ \mathbf{x}_5\ (\mathrm{kN/m}) \end{array} \tag{38}$$

(2) Objective function

The optimum design the VCB mechanism is aimed to minimize the surplus work in the VCB mechanism during the closing operation. Therefore, according to Equation (26), the objective function was minimized as follows:

$$\mathrm{Min} f(\mathbf{X}) = \sum_{i=1}^{Ns} \left| F_{oi} - \frac{F_{ri}}{\varepsilon} \right| + Mh\,(\mathbf{X}) \tag{39}$$

where F_o^i, F_r^i represent the general output force and general resistant force of the mechanism at the *i*-th selected angular position of the cam; *Ns* represents the number of selected angular positions (*Ns* = 140) of the cam during the closing stroke which the cam makes contact with the follower; $h(\mathbf{X})$ denotes the penalty function; and *M* is an extremely high number ($M = 10^6$).

(3) Constraints

The specified contact stroke of the movable contact, s_c, was 11 ± 2 mm, and the maximum angular displacement ($\phi_{\max}$) of the follower link of the cam mechanism was constrained within the interval $23^\circ \leq \phi_{\max} \leq 26^\circ$. The constraint can be expressed as follows:

$$h(\mathbf{X}): \ 23^\circ \leq \ \phi_{\max} \leq 26^\circ \tag{40}$$

(4) Optimal design results

Table 5 displays the parameter settings for the optimal VCB mechanism design. This study employed the DE-gr method, which involved using a specified proportion of the crossover rate to the mutation factor, referred to as a golden ratio (0.618:0.382) [19]. Twenty-five numerical experiments were performed to obtain the best optimal solution, and each experiment had 300 generations. Table 6 lists the optimal results, indicating that the minimum value of objective function was 1.74×10^{-7}. Figure 28 displays the convergence rate of the optimization process, which rapidly converged to the optimal value in the 43rd generation. Figures 29 and 30 illustrate the dynamic analyses of the optimal VCB mechanism during the closing operation, performed using a MATLAB-coded program. Figure 29 displays the optimal cam profile and pitch curve (only actuated portion). The angular displacement curve of the oscillating follower of the optimal cam mechanism is illustrated in Figure 11 (blue solid line), it was identical to the specified motion curve displayed in Figure 4. The radius of curvature of the optimal cam profile is illustrated in Figure 13 (blue solid line). Figure 30a displays the normal contact forces (blue solid line) on the surface of the cam, Figure 30b displays the maximum Hertz contact stress (blue solid line) on surface of the cam, Figure 30c depicts the maximum shear stress (blue solid line) beneath the cam surface. The maximum Hertz contact stress and maximum shear stress in the DE-gr optimal design cam mechanism decreased considerably relative to those in the initial design. Notably, the highest Hertz contact stress and shear stress occurred at a cam rotation angle of 140° when the closing operation was completed. The shear yielding stress (τ_y) of the carbon steel (S45C) was $\tau_y = 0.577\sigma_y = 1194$ MPa. Thus, the maximum Hertz contact stress and maximum shearing stress on and beneath the optimized cam surface were lower than the contact endurance stress and yielding shear stress, respectively (see Table 1). Figure 31 illustrates the analyses of the characteristic force of the optimal VCB mechanism during closing operation. The solid blue line represents the general output force, and the area under curve (AUC) of the general output force (meaning driving work) was slightly larger than the AUC of the general resistant force (meaning resistant work) of the VCB operating mechanism. The minimum surplus work can result in a decrease in an excessively high closing velocity of the movable contact. As illustrated in Figure 31, before the electric contacts collided with the fixed contact at $s_1 = 11$ mm, the general output force was higher than the general resistant force, thereby facilitating closing operation. At $s_1 > 11$ mm the general resistant force was abruptly higher than the general output force until the closing stroke was completed. Figure 32 displays the velocity of the movable contact simulated using MSC-ADAMS. The average closing velocity was 1.17 m/s, which was lower than 1.71 m/s in the initial VCB mechanism design; the obtained average closing velocity was nearly consistent with the required average closing velocity (0.9 ± 0.2 m/s). These results of analyses indicated that the optimal design of the cam profile and closing springs achieved in this study was feasible, and the DE-gr method was effective for optimizing the VCB operating mechanism.

Table 5. Parameters setting for DE-gr optimal design of cam profile and closing springs.

	DE-Gr Algorithm
Population number	100
Iteration number	300
Crossover method	Multiple point
Crossover rate	0.618
Mutation method	DE/best/1
Mutation factor	0.382
Selection	Tournament

Table 6. Optimal results of the cam profile and closing springs design.

Design Parameters	**Initial Design**	**DE-Gr Optimization**
a_1	0.240347	0.238432
a_2	0.011694	0.000226
a_3	−0.017243	−0.011492
k_{c1} (N/mm)	7.720000	9.315336
k_{c2} (N/mm)	9.330000	7.788183
Value of objective fun.	1.75×10^3	1.74×10^{-7}

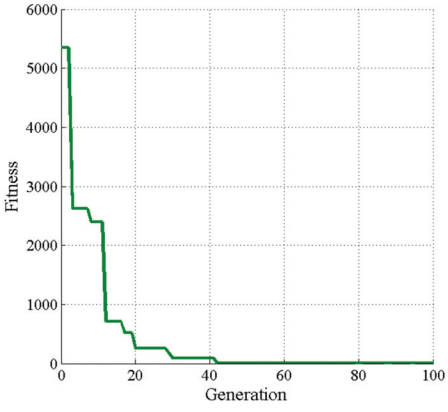

Figure 28. Convergence rate for DE-gr optimization of the cam profile and closing springs.

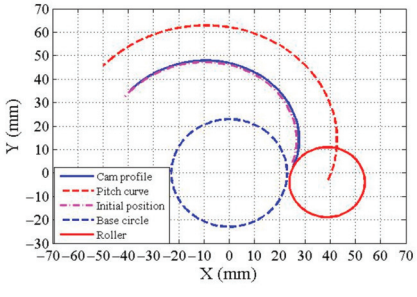

Figure 29. Optimal cam profile and pitch curve (only actuated portion).

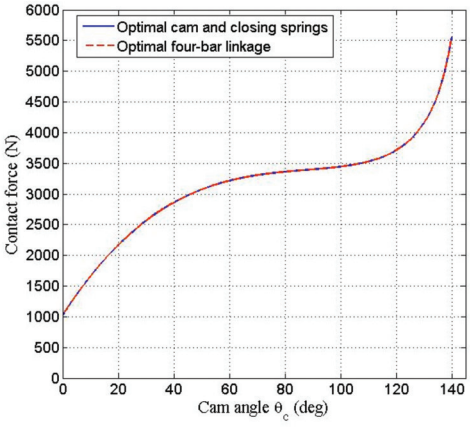

(**a**) Normal contact force on surface of cam profile

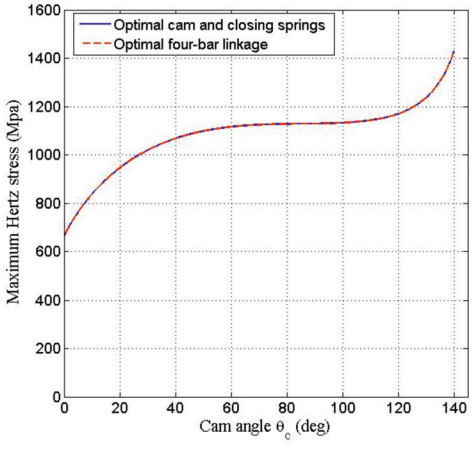

(**b**) Maximum Hertz stress on cam surface for optimal cam design and four-bar linkage design

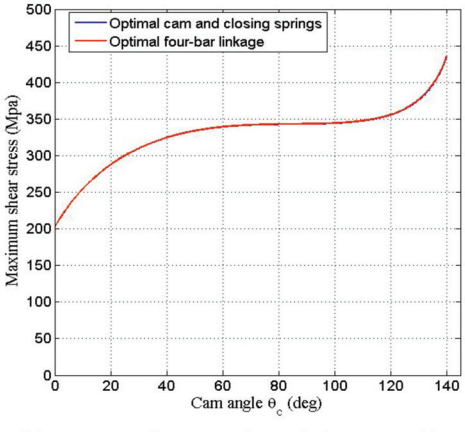

(**c**) Maximum shear stress beneath the cam profile

Figure 30. Normal contact force, Hertz stress, and maximum shear stress for the optimal VCB operating mechanism.

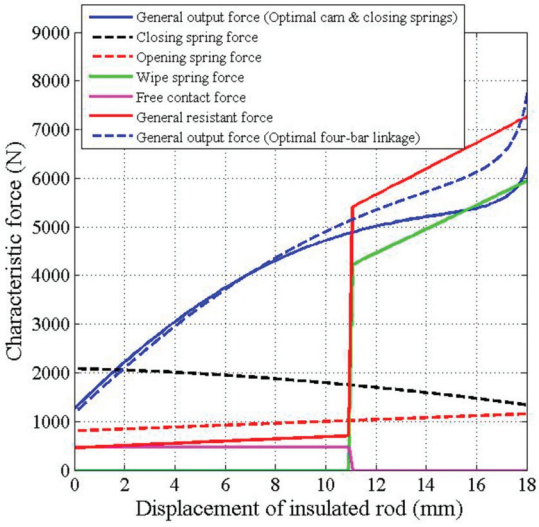

Figure 31. Characteristic forces of the optimal VCB mechanisms.

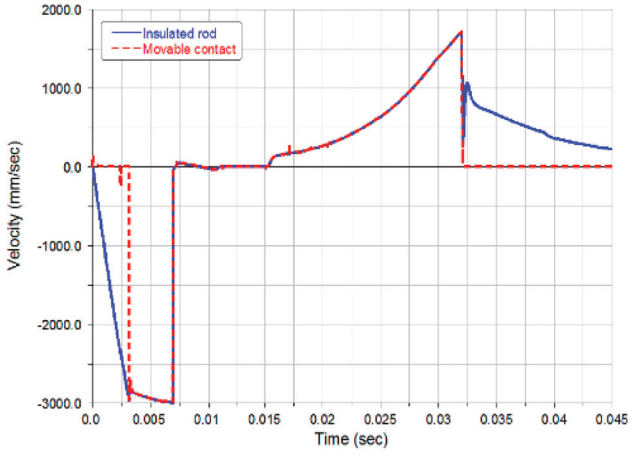

Figure 32. Velocity of movable contact and insulated rod during closing process (Simulated by MSC-ADAMS).

4.3. Optimal Synthesis of the Four-Bar Linkage

The second step of the optimal VCB operating mechanism design involved the optimal dimensional synthesis of the four-bar linkage. It was conducted based on the optimal design of the cam profile and closing springs obtained in previous step. The parameters of the DE-gr algorithm, minimum objective function, and experiment number were the same as those used in the first step of the optimal design.

(1) Design variables

The dimensions of the four-bar linkage (Figures 6 and 9), except for the length of the input link 2, the length of lever EM (ℓ_5) and the setting angle of the fixed link were used as the design variables that were expressed as a vector **X**.

$$\mathbf{X} = [x_1, x_2, x_3, x_4, x_5]^T = [\ell_1, \ell_3, \ell_4, \ell_5, \theta_1]^T \tag{41}$$

The range of the design variables of the four-bar linkage were as follows:

$$\begin{array}{l} 70 \le x_1 \le 150 \ , \quad 70 \le x_2 \le 150 \ , \quad 70 \le x_3 \le 150 \\ 50 \le x_4 \le 100 \ , \quad -\pi \le x_5 \le -0.5\pi \end{array} \tag{42}$$

(2) Objective function

The objective function was expressed as Equation (39).

(3) Constraints

The four-bar linkage was constrained by the conditions of the Grashoff mechanism [21] such that the length of the links satisfied the following requirement:

$$h(\mathbf{X}): \ r_s + r_l < r_p + r_q \tag{43}$$

where r_s, r_l represented the lengths of the shortest link and largest link, respectively, and r_p, r_q were the lengths of the other two links.

(4) Optimal design results

Table 7 lists the results of optimal design of the four-bar linkage; the value of the objective function was 7.13×10^{-10} (approximately zero). Figure 33 displays the convergence rate of the optimization of the four-bar linkage, the value rapidly converged to the optimal value in the 18th generation. The output–input curve of the optimal four-bar linkage is displayed in Figure 15 (blue solid line). The results indicated that the motion range, $[-6, 6]$, of the output link of optimal four-bar linkage was more symmetric than that of the initial design, $[-8, 4]$ (Figure 15, red dashed line), indicating that the optimization more satisfied the assumed conditions of Equations (1) and (4) and the specified motion curve shown in Figure 4. Figure 30 (shown by red dashed lines) displays the normal contact force (Figure 30a), the Hertz contact stress (Figure 30b) and maximum shear stress (Figure 30c) on and beneath the cam surface due to the optimized four-bar linkage. Obviously, the curves of normal contact force, Hertz contact stress and maximum shear stress shown in Figure 15 were consistent each other in both optimal designs. These results of stress analyses revealed that both the optimal designs were feasible. The general output force generated during the closing operation in the optimal four-bar linkage design is displayed in Figure 31 by a blue dashed line. Figure 34 indicates the comparison of the driving work (AUC of the general output force) and general resistant work (AUC of the general resistant force) among the various VCB operating mechanism designs, namely initial design, optimum design of the cam and closing springs, and optimum design of the four-bar linkage. The results of dynamic analyses of the optimal VCB mechanism in the second step revealed that they were slightly different from those of the optimum VCB mechanism with the optimal cam and closing springs in the first step. This indicates that both of the two optimal VCB mechanism designs are safe and feasible solutions, and the optimal four-bar linkage can serve as an alternative choice to replace the initial four-bar linkage while considering the layout of the VCB mechanism.

Table 7. Optimal design of the four-bar linkage.

	Initial Design	**DE-Gr Optimization**
ℓ_1	139.790000	117.263920
ℓ_3	124.700000	99.825118
ℓ_4	140.000000	133.857634
ℓ_5	90.000000	85.046620
θ_1	-121.980°	-123.967°
Obj. function value	1.74×10^{-7}	7.13×10^{-10}

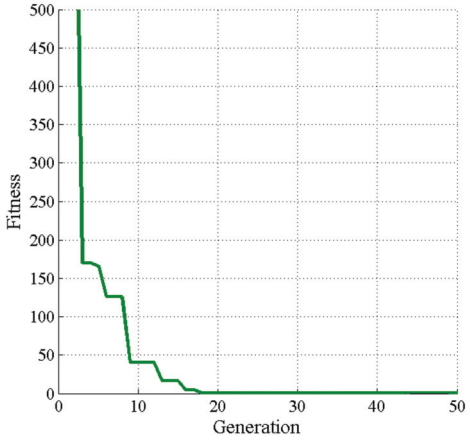

Figure 33. Convergence rate of the optimization of the four-bar linkage.

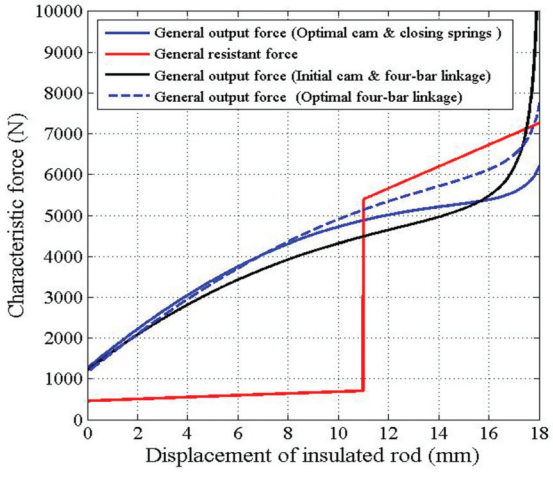

Figure 34. Comparison of the output work and resistant work among different VCB mechanisms designs.

5. Conclusions

This paper proposes a method which combines the analytical method and optimization approach for designing a spring-actuated cam-linkage operating mechanism used in a 12 kV, 25 kA VCB. The designed cam profile was based on three-order polynomial motion curve of the follower according to the specified motion of the VCB mechanism. The sum of differences between the general output force and the general resistant force of the VCB operating mechanism during the closing operation was adopted as the objective function to be minimized. Further, a DE-gr algorithm (that incorporated a golden ratio (0.618:0.382) as the ratio of crossover rate to mutation factor) was employed to optimize the design of the cam profile and elastic coefficients of closing springs, and then to optimize the design of the four-bar linkage. The dynamic analyses of the characteristic forces and the contact stress analyses of the optimal VCB operating mechanism were performed using a MATLAB-coded program. The kinematic simulation and the results of dynamic analyses were validated using the multibody dynamic software MSC-ADAMS. The optimal results revealed that the surplus output work in the initial VCB operating mechanism was effectively minimized to zero in the optimal VCB operating mechanism. Thus, the average closing velocity of the

movable contact was considerably reduced, and the maximum Hertz contact stress and maximum shear stress on and beneath the cam surface were significantly decreased. The proposed optimal design of the VCB operation mechanism helps to prevent an excessive increase in the average closing velocity of the movable contact in the VI.

Author Contributions: Y.-H.K.: Conceptualization, methodology, validation, investigation, resources, writing-original draft preparation, writing-review and editing, supervision. H.-C.H.: Investigation, writing-review and editing. B.-Y.Y.: Software, data curation, validation, formal analysis. All authors have read and agreed to the published version of the manuscript.

Funding: This research was funded by Taiwan Calsonic Co., Ltd.

Informed Consent Statement: Not applicable.

Data Availability Statement: Not applicable.

Acknowledgments: The authors would like to thank the research fund supported from Taiwan Calsonic Co., Ltd. and the valuable opinions suggested by vice-president Fan-Ming Li, and manager Chih-Chen Chang.

Conflicts of Interest: The authors declare no conflict of interest.

References

1. Flurscheim, C.H. *Power Circuit Breaker Theory and Design, Revised ed.*; Peter Peregrinus Ltd.: London, UK, 1985.
2. Ahn, G.Y.; Jeong, K.Y. Optimization of the spring design parameters of a circuit breaker to specify the specified dynamic characteristics. *Int. J. Precis. Eng. Manuf.* **2004**, *5*, 43–49.
3. Ahn, K.Y.; Kim, S.H. Modelling and analysis of a high-speed circuit breaker mechanism with a spring-actuated cam. *Proc. Inst. Mech. Eng. Part C J. Mech. Eng. Sci.* **2001**, *215*, 663–672. [CrossRef]
4. Pisano, A.P.; Freudenstein, F. An experimental and analytical investigation of the dynamic response of a high-speed cam follower system, Part 1: Experimental investigation. *ASME J. Mech. Transm. Autom. Des.* **1983**, *105*, 692–698. [CrossRef]
5. Pisano, A.P.; Freudenstein, F. An experimental and analytical investigation of the dynamic response of a high-speed cam-follower system. Part 2: A combined, lumped/distributed parameter dynamic model. *ASME J. Mech. Transm. Autom. Des.* **1983**, *105*, 699–704. [CrossRef]
6. Root, R.R.; Ragsdell, K.M. The circuit breaker-a practical example in engineering optimization. *Mech. Mach. Theory* **1983**, *18*, 229–235. [CrossRef]
7. Jobes, C.C.; Palmer, G.M.; Means, K.H. Synthesis of a controllable circuit breaker mechanism. *ASME J. Mech. Des.* **1990**, *112*, 324–330. [CrossRef]
8. Kim, J.H.; Ahn, K.Y.; Kim, S.H. Optimal synthesis of a spring-actuated cam mechanism using a cubic spline. *Proc. Inst. Mech. Eng. Part C J. Mech. Eng. Sci.* **2002**, *216*, 875–883. [CrossRef]
9. Chen, F.C.; Tzeng, Y.F. On the dynamics of a spring-type operating mechanism for a gas-insulated circuit breaker in open operation using the Lagrange equation. *Proc. Inst. Mech. Eng. Part C J. Mech. Eng. Sci.* **2002**, *216*, 831–843. [CrossRef]
10. Chen, F.C. On the design of spring-actuated mechanism for 69KV SF6 gas insulated breaker. *ASME J. Mech. Des.* **2003**, *125*, 840–845. [CrossRef]
11. Yoo, W.S.; Kim, S.O.; Sohn, J.H. Dynamic analysis and Design of a high voltage circuit breaker with spring operating mechanism. *J. Mech. Sci. Technol.* **2007**, *21*, 2101–2107. [CrossRef]
12. Yu, M.J.; Wang, L.C.; Huang, S.C. Optimal dimensional synthesis of the trigger mechanism of a high-voltage circuit breaker. *J. Chin. Inst. Eng.* **2013**, *36*, 146–156. [CrossRef]
13. Jang, J.S.; Yoon, C.G.; Ryu, C.Y.; Kim, H.W.; Bae, B.T.; Yoo, W.S. Optimization of the switch mechanism in a circuit breaker using MBD based simulation. *Sci. World J.* **2015**, *2015*, 347047. [CrossRef] [PubMed]
14. Liu, Y.Y.; Chen, D.G.; Yuan, H.W.; Ji, L.; Ma, Z. Research of dynamic optimization for the cam design structure of MCCB. *IEEE Trans. Compon. Packag. Manuf. Technol.* **2016**, *6*, 390–399. [CrossRef]
15. Storn, R.; Price, K. Differential evolution-a simple and efficient heuristic for global optimization over continuous spaces. *J. Glob. Optim.* **1997**, *11*, 341–359. [CrossRef]
16. Acharyya, S.K.; Mandal, M. Performance of EAs for four-bar linkage synthesis. *Mech. Mach. Theory* **2009**, *44*, 1784–1794. [CrossRef]
17. Lin, W.Y. A GA-DE hybrid evolutionary algorithm for path synthesis of four-bar linkage. *Mech. Mach. Theory* **2010**, *45*, 1096–1107. [CrossRef]
18. Ortiz, A.; Cabrera, J.A.; Nadal, F.; Bonilla, A. Dimensional synthesis of mechanisms using differential evolution with auto-adaptive control parameters. *Mech. Mach. Theory* **2013**, *64*, 210–229. [CrossRef]
19. Kang, Y.H.; Lin, J.W.; You, W.C. Comparative study on the synthesis of path-generating four-bar linkages using metaheuristic optimization algorithms. *Appl. Sci.* **2022**, *12*, 7368. [CrossRef]

20. Yu, L.; Geng, Y.S.; Liu, Z.Y.; Sun, L.Q.; Yao, J.J. Relationship between displacement characteristics of a 126KV vacuum circuit breaker and spring type operating mechanism. In Proceedings of the IEEE Conference 23rd Symposium on Discharges and Electrical Insulation in Vacuum, Bucharest, Romania, 15–19 September 2008; pp. 137–140.
21. Yan, H.S.; Wu, L.I. *Mechanisms*, 4th ed.; Tung Hua Books: Taipei City, Taiwan, 2014.
22. Timoshenko, S.P.; Gooder, J.P. *Theory of Elasticity*, 3rd ed.; McGraw-Hill: New York, NY, USA, 1973; pp. 403–419.
23. Budynas, R.G.; NisBett, J.K. *Shigley's Mechanical Engineering Design*, 10th ed.; McGraw-Hill Education: New York, NY, USA, 2015; pp. 138–140.
24. Norton, R.L. *Cams Design and Manufacturing Handbook*; Industrial Press: New York, NY, USA, 2002.
25. Ugural, A.S.; Fenster, S.K. *Advanced Strength and Applied Elasticity*, 4th ed.; Pearson Education Taiwan Ltd.: New Taipei City, Taiwan, 2004.
26. Zhuang, M.G. *Mechanical Design and Analysis-Part II*; Fu-Win Book Company: Tainan City, Taiwan, 1990; pp. 1705–1706. (In Chinese)

applied sciences

MDPI

Article

Research on Permanent Magnet Synchronous Motor Sensorless Control System Based on Integral Backstepping Controller and Enhanced Linear Extended State Observer

Lihuan Shao, Changfeng Zheng, Yan Zhang, Guanling Xie, Xiyu Hao and Xiaolong Zheng *

College of Electronic and Information, Hangzhou Dianzi University, Hangzhou 310018, China
* Correspondence: xlzheng@hdu.edu.cn

Abstract: The traditional sensorless control system of permanent magnet synchronous motor (PMSM) has the problems of low estimation accuracy and poor anti-interference ability. Moreover, the position estimation performance is subjected to position harmonic ripples caused by inverter nonlinearities and flux spatial harmonics. To optimize the dynamic performance of the PMSM sensorless control system, this paper proposes a sensorless control scheme that combines integral backstepping control with enhanced linear extended state observer (ELESO). The ELESO consists of two linear extended state observers (LESOs), which estimate the internal and external disturbances of the system, to improve the estimation accuracy of rotor position. Then, the integral backstepping controller processes the estimated rotor position and speed information to obtain d and q-axis voltages. The sensorless control scheme is implemented in the Matlab/Simulink and verified by experiments. The simulation and experiment show that the scheme can effectively suppress load interference and improve control accuracy.

Keywords: permanent magnet synchronous motor; sensorless control; integral backstepping control; enhanced linear extended state observer; rotor position estimation

Citation: Shao, L.; Zheng, C.; Zhang, Y.; Xie, G.; Hao, X.; Zheng, X. Research on Permanent Magnet Synchronous Motor Sensorless Control System Based on Integral Backstepping Controller and Enhanced Linear Extended State Observer. *Appl. Sci.* **2023**, *13*, 1680. https://doi.org/10.3390/app13031680

Academic Editors: Loránd Szabó and Feng Chai

Received: 6 December 2022
Revised: 25 January 2023
Accepted: 26 January 2023
Published: 28 January 2023

1. Introduction

Permanent magnet synchronous motors (PMSMs) adopt the field-oriented control (FOC) which have the advantages of small size, simple structure, high efficiency, large power density, and wide speed range. Therefore, PMSM can be widely used in aerospace, household appliances, and medical equipment fields [1]. To achieve efficient control of PMSM, a Hall sensor, optical encoder, and resolver are usually used to monitor the rotor position in time. However, this control scheme is highly dependent on the sensor, which increases the control cost. If the connection cable is too long, interference may be introduced into the system. In addition, working in high temperatures, low temperatures dirty air, and other environments will reduce the reliability of the system [2,3]. However, PMSM plays an important role in high-performance control places, so sensorless control technology came into being. The sensorless control technology discards the position sensor. By detecting the electrical signal in the motor winding, a certain control algorithm is used to estimate the rotor position and speed. Sensorless control represents the development trend of the three-phase PMSM control system. The core of sensorless control is the estimation of rotor position. Therefore, selecting an appropriate scheme to accurately estimate the real-time position of the PMSM rotor is an important part of sensorless control.

The sensorless rotor position acquisition of the PMSM mainly depends on the back electromotive force (EMF) estimation of the system [4]. As an effective position estimation method, the sliding-mode observer (SMO) has the advantages of a simple algorithm and strong robustness. In recent years, the SMO has been widely used in sensorless high-performance control of PMSM [5,6]. However, the switching function used by the traditional SMO has the problems of phase delay and speed chattering. Therefore, reducing

phase delay and speed chattering is a hot issue in SMO control. In Ref. [7], a new design of SMO was proposed to improve control accuracy. An observer is built according to the back EMF model after the back EMF equivalent signal is obtained. In this way, not only are low-pass filter and phase compensation modules eliminated but also estimation accuracy is improved. In Ref. [8], an SMO based on an adaptive super-twisting algorithm is proposed, in which the nonlinearity of the voltage source inverter (VSI) is considered. The algorithm reduces the error by compensating for the voltage distortion. Some schemes propose using the sigmoid function as a switching function to improve response speed and reduce chattering [9]. In addition, considering the double closed-loop module for processing the estimated parameters, the sliding mode controller (SMC) can replace the classical proportional-integral (PI) control algorithm. The SMC is insensitive to disturbances and parameters. In addition, it also has a fast response speed. Therefore, the SMC has been widely used in motor speed regulation systems and works with other control schemes [10–12]. In Ref. [13], a hybrid control strategy combining fuzzy SMC with load torque observer was proposed to accurately estimate load torque and suppress chattering. In Ref. [14], a fuzzy sliding mode speed controller for PMSM is proposed. The scheme combines the continuous terminal SMO, which can reach the balance point in a limited time to ensure the continuity of control and fast-tracking. Moreover, to improve the speed tracking accuracy, a neural network SMC scheme is proposed to optimize the control system [15].

Active disturbance rejection control (ADRC) has the advantages of strong anti-interference ability, weak model dependence, and a simple design process. Therefore, the ADRC has been successfully applied to motor drive systems. Extended state observer (ESO) is the core of ADRC, which was first proposed at the end of the 20th century [16]. The main idea of the ESO is to treat the unknown internal and external disturbances as the lumped disturbances of the system, thus expanding the disturbances into a new state variable [17]. Then, the new state variable can be estimated according to the output of the system. The ESO discards the low-pass filter and sliding mode function and improves the phase delay and chattering of the motor. Therefore, the ESO has extensive application prospects in motor control. In Ref. [18], a control strategy combining the ESO-based position estimation method and high-frequency current injection method was proposed. Compared with the traditional hybrid scheme, the two schemes were integrated into the same control structure, and the position observer was embedded in the current controller. The robustness of the control system is good in the full speed range. In Ref. [19], a linear active disturbance rejection controller (LADRC) design was proposed to reduce overshoot and improve dynamic response when a disturbance occurs. The ESO can effectively reduce the negative effects of phase delay and motor chattering. However, when the interference factors are caused by the system, the ESO cannot filter them out in time.

The SMC can solve the poor adaptability of the PI controller to external disturbances. However, when the state trajectory reaches the sliding mode surface, it is difficult to slide strictly along the sliding mode to the equilibrium point, resulting in chattering. In Ref. [20], using the saturation function instead of the switching function can effectively attenuate chattering. However, the traditional reaching law is difficult to suppress chattering and keep the system stable at the origin. The backstepping control considers both the control law and the adaptive law, which can make the whole closed-loop system meet the desired dynamic and static performance. Therefore, many scholars began to study the double closed-loop control based on the backstepping method to obtain a good load disturbance suppression effect. Different from the conventional feedback control methods, the backstepping control is a cascade design method. The controller aims to decompose the complex system into subsystems that do not exceed the system order. The controller designs the state variables and the Lyapunov functions for each subsystem so that the local and global stability characteristics run through each step [21]. In general, the backstepping controller makes the control process systematic and structured through reverse design. However, keeping the convergence of backstepping control and eliminating the steady-state error still needs to be concerned when the system parameters contain uncertainties.

To solve the above problems, this paper proposes a control scheme that combines an integral backstepping controller with an enhanced linear extended state observer (ELESO). Firstly, the ELESO is composed of two linear extended state observers (LESOs) cascaded, which estimate the rotor lumped interference and the internal interference of the system to eliminate the influence of the higher harmonics on position estimation. Secondly, the new Lyapunov functions are designed by adding integral terms to the backstepping controller. The integral backstepping controller can guarantee convergence and eliminate steady-state error. Moreover, the parameters of PMSM can be estimated by backstepping controller to further eliminate the internal disturbance. Finally, the effectiveness of the control algorithm is proved by simulation and experiment. The remainder of this paper is organized as follows. In Section 2, the ELESO and the integral backstepping controller are designed. In Section 3, the improved control algorithm is verified by simulation and experiment, and the results are analyzed. Finally, in Section 4, the research contents are summarized.

2. Theoretical Analysis of the Integral Backstepping Controller and the ELESO

This section will give the classical mathematical model of PMSM and important transformation formulas. The ELESO and the backstepping controller are designed according to the reference model.

2.1. The Mode of PMSM

To simplify the mathematical model of the three-phase PMSM in the natural coordinate system, the coordinate transformation includes static coordinate transformation (Clark transformation) and synchronous rotation coordinate transformation (Park transformation) [22]. After the Clark transformation and the Park transformation, the mathematical model of PMSM in the d-q synchronous rotation coordinate system is shown as follows [23]:

$$\begin{cases} \frac{di_d}{dt} = -\frac{R_S}{L_d} i_d + \frac{L_q}{L_d} n_p \omega i_q + \frac{1}{L_d} u_d \\ \frac{di_q}{dt} = -\frac{R_S}{L_q} i_q - \frac{L_d}{L_q} n_p \omega i_d - \frac{\psi_f n_p}{L_q} \omega + \frac{1}{L_q} u_q \\ \frac{d\omega}{dt} = \frac{3}{2} \frac{n_p}{J} \left(\psi_f i_q + (L_d - L_q) i_d i_q \right) - \frac{1}{J} T_L - \frac{B}{J} \omega \\ \frac{d\theta_e}{dt} = n_p \omega \end{cases} \tag{1}$$

where u_d, u_q are the stator voltages of the d and q-axis. i_d, i_q are the stator currents. R_s is the stator resistance. L_d, L_q are d and q-axis inductances. ω is the mechanical angular speed of the rotor. J is rotor inertia. B is the viscous friction coefficient. n_p is the number of pole pairs. ψ_f is the magnetic flux of the permanent magnet. T_L is the load torque.

2.2. Design of ELESO

In the static coordinate system, the voltage equation of salient pole PMSM is as follows:

$$\begin{bmatrix} u_\alpha \\ u_\beta \end{bmatrix} = \begin{bmatrix} R_s + pL_d & \omega_e(L_d - L_q) \\ -\omega_e(L_d - L_q) & R_s + pL_d \end{bmatrix} \begin{bmatrix} i_\alpha \\ i_\beta \end{bmatrix} + \begin{bmatrix} E_\alpha \\ E_\beta \end{bmatrix} \tag{2}$$

where u_α and u_β are the stator voltages in the static coordinate system. i_α and i_β are α and β-axis stator currents. $\omega_e = n_p\omega$ is the rotor's electrical angular speed. L_α, L_β are the stator inductance. p is the differential operator. E_α and E_β are the extended back EMF, which can be expressed as follows:

$$\begin{bmatrix} E_\alpha \\ E_\beta \end{bmatrix} = \left(\omega_e \left[(L_d - L_q) i_d + \psi_f \right] - (L_d - L_q) p i_q \right) \begin{bmatrix} -\sin\theta_e \\ \cos\theta_e \end{bmatrix} \tag{3}$$

It can be seen from Equation (3) that the extended back EMF contains rotor position information. Therefore, the estimation of back EMF in static coordinates will directly affect the estimation accuracy of the rotor position.

The ESO can estimate the lumped disturbance of the system accurately and efficiently. The basic form of the second-order LESO is expressed as:

$$\begin{cases} \varepsilon = z_1 - x_1 \\ \dot{z}_1 = z_2 + f + b_0 u - \beta_1 \varepsilon \\ \dot{z}_2 = -\beta_2 \varepsilon \end{cases} \tag{4}$$

where ε is the estimated error. x_1 is the actual state variable. z_1 is the estimation of x_1. z_2 is the estimated disturbance. u is the system input. f is the known disturbance, which contains the known model information of the system. b_0 is the system parameter. β_1 and β_2 are the observer gains. If the α and β-axis back EMF components with non-ideal conditions are considered as external interference, the state equation of stator current is as follows:

$$pi_x = f_{e_x} + f_x + u_x / L_d, x = \alpha, \beta \tag{5}$$

where f_{e_x} represents the lumped interference of the system, which is the sum of the external interference and the internal interference. f_x represents known model information, which can be expressed as follows:

$$\begin{cases} f_\alpha = \hat{\omega}_e (L_q - L_d) i_\beta / L_d - R_s i_\alpha / L_d \\ f_\beta = \hat{\omega}_e (L_d - L_q) i_\alpha / L_d - R_s i_\beta / L_d \end{cases} \tag{6}$$

where $\hat{\omega}_e$ is the estimated value of rotor electrical angular speed. Then, according to the definition of the state equation, the external disturbance state observer LESO1 is designed as follows:

$$\begin{cases} \varepsilon_x = \hat{i}_x - i_x \\ p\hat{i}_x = \hat{f}_{e_x} + f_x + u_x / L_d - \beta_{x1} \varepsilon_x \\ p\hat{f}_{e_x} = -\beta_{x2} \varepsilon_x \end{cases} \tag{7}$$

where $\hat{i}_x$ is the estimated value of the current. β_{x1} and β_{x2} are the gains of the LESO1. According to Equations (2) and (5), the estimated back EMF is as follows:

$$\begin{bmatrix} \hat{e}_\alpha \\ \hat{e}_\beta \end{bmatrix} = -L_d \begin{bmatrix} \hat{f}_{e_\alpha} \\ \hat{f}_{e_\beta} \end{bmatrix} \tag{8}$$

Based on the estimated back EMF, the position and the speed of the rotor under sensorless conditions can be obtained through the phase-locked loop (PLL). However, in practice, the inverter nonlinearity will generate different 5th and 7th harmonics in the phase current. As a result, (6k + 1) subharmonics will appear in the back EMF estimation, which results in six harmonic fluctuations in the estimated rotor position and speed [24]. The sixth harmonic will reduce the performance of the control system. The back EMF formula including the sixth harmonic component is as follows:

$$\begin{cases} \hat{e}_\alpha = -E_{ex} \sin(\omega_e t + \theta_e) - E_{6k\pm1} \sin((6k+1)\omega_e t + \theta_{6k\pm1}) \\ \hat{e}_\beta = -E_{ex} \sin(\omega_e t + \theta_e) + E_{6k\pm1} \cos((6k+1)\omega_e t + \theta_{6k\pm1}) \end{cases} \tag{9}$$

The rotor angle estimation error becomes:

$$\varepsilon_\theta = \theta_e - \hat{\theta}_e + E_{6k} \sin(6k\omega_e t + \theta_{6k}) \tag{10}$$

where $E_{ex} = \omega_e \cdot \psi_f$. In general, there is only the harmonic effect when $k = 1$. Therefore, after the whole FOC control finishes, the output rotor angle error will contain the sixth harmonic component. The ADRC does not require an accurate motor model. According to this characteristic, this paper proposes an internal disturbance observer LESO2 to estimate the internal disturbance of the system. The LESO2 is cascaded with the LESO1. With this scheme, the influence of higher harmonics and motor parameter changes of the system

performance can be eliminated as far as possible. At this time, the stator current model is shown as follows:

$$pi_x = f_{e_x} + f_x + u_x/L_d + f_{e_{hx}}, x = \alpha, \beta \tag{11}$$

where $f_{e_{hx}}$ represents the internal disturbance in the static coordinate system, which is the high-order harmonic back EMF. According to the current formula, the LESO2 is designed as follows:

$$\begin{cases} \varepsilon_{hx} = \hat{i}_{hx} - i_x \\ p\hat{i}_{hx} = \hat{f}_{e_x} + f_x + \hat{f}_{e_{hx}} + u_x/L_d - \beta_{x3}\varepsilon_{hx} \\ p\hat{f}_{e_{hx}} = -\beta_{x4}\varepsilon_{hx} \end{cases} \tag{12}$$

where $\hat{i}_{hx}$ is the estimated current component under the higher harmonic. ε_{hx} is the estimation error. $\hat{f}_{e_{hx}}$ is the estimated internal disturbance. β_{x3} and β_{x4} are the gains of the LESO2.

According to Equations (3) and (8), the estimated rotor position can be calculated as:

$$\hat{\theta}_e = \arctan\left(\frac{-\hat{e}_\alpha}{\hat{e}_\beta}\right) \tag{13}$$

In Equation (13), the estimated rotor position can be obtained directly. However, the arctangent function is very sensitive to noise. The position extraction method based on the arctangent function directly brings this noise into the operation, which leads to the error being amplified, thus causing greater angle estimation error. This uncertainty will reduce the accuracy and stability of the control system, especially in the middle and low speed range. Therefore, it is necessary to use the PLL to extract speed and position information from the estimated back EMF [25].

β_{x1}, β_{x2}, β_{x3} and β_{x4} are the gains of the LESO1 and the LESO2. If the gains are not properly selected, it will lead to the loss of position in the process of controller evaluation, which will lead to system instability [26,27]. Therefore, the selection of gains is an important issue. Taking the LESO1 as an example, the tracking error is defined as follows:

$$e = \begin{bmatrix} \hat{i}_x - i_x \\ \hat{f}_{e_x} - f_{e_x} \end{bmatrix} \tag{14}$$

According to Equations (5) and (7), the error state equation can be derived as:

$$\dot{e} = C_m e, C_m = \begin{bmatrix} -\beta_{x1} & 1 \\ -\beta_{x2} & 0 \end{bmatrix} \tag{15}$$

Equation (15) shows that the eigenvalues of C_m determine the behavior of the LESO1. If and only if $\beta_{x2} > 0$, Equation (15) is asymptotically stable. Therefore, the gains of the LESO1 can be selected according to the bandwidth of the LESO1 [28]. Specifically, the gains of the LESO1 are designed such that C_m has a double eigenvalue λ that is equal to the bandwidth of the LESO1 [29]. The characteristic equation is as follows:

$$|\lambda E - C_m| = \begin{vmatrix} \lambda + \beta_{x1} & -1 \\ \beta_{x2} & \lambda \end{vmatrix} = \lambda^2 + \beta_{x1}\lambda + \beta_{x2} = (\lambda + \omega_0)^2 \tag{16}$$

where ω_0 is the bandwidth of the LESO1. ω_0 should be large enough to ensure that the system can respond quickly. According to ω_0, the gains of the LESO1 can be obtained as follows:

$$\beta_{x1} = 2\omega_0, \beta_{x2} = \omega_0^2 \tag{17}$$

The gains selection of the LESO2 is similar to the LESO1.

Figure 1 is the control diagram of the ELESO. u_x is the system input, which is represented as the voltage component in the static coordinate system in the PMSM control. i_x is the current component in the static coordinate system. f_x can be calculated by combining

motor parameters with dynamic components. The three inputs act on the LESO1 and the LESO2, respectively. By subtracting the internal interference from the lumped interference, the back EMF can be obtained in the static coordinate system with high-frequency harmonics filtered. According to the estimated back EMF, the rotor position and the speed are obtained in the PLL. This scheme eliminates the low-pass filter and discrete sliding mode function and improves the phase delay and chattering problems. The ELESO can obtain high-precision estimation parameters.

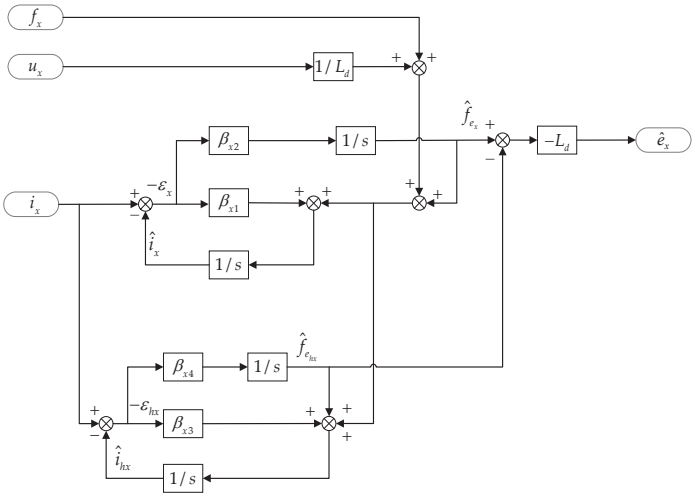

Figure 1. Block diagram of the plant controlled by the ELESO scheme.

2.3. Design of Backstepping Control

The backstepping control is used to decompose the complex nonlinear system into subsystems that do not exceed the system order, then design the corresponding Lyapunov function and intermediate virtual control quantity for each subsystem [30]. At each stage, the current Lyapunov function will be based on the state of the previous subsystem, including the current virtual control quantity to ensure system stability [31]. The control steps are mainly divided into the following steps: Firstly, the controller selects some states of the system as subsystems and designs the Lyapunov functions. According to the virtual control quantity of the subsystem, the virtual error variable is designed. A new subsystem is composed of the virtual error variable and the previous subsystem. A new Lyapunov function is designed to stabilize the new system. If the actual control quantity of the system is not obtained, the subsystem shall be designed recursively. Otherwise, the actual control quantity shall be designed to stabilize the whole system [32]. Each new system is designed on the premise that its subsystems are stable, so that the final control system can be stable.

According to the estimated position and the estimated speed of the rotor obtained by the ELESO, this paper proposes an integral backstepping control module with a speed controller and current controller cascaded. The reference values of rotor speed and d and q-axis currents are defined as ω_r, i_{dref} and i_{qref}. First, for the speed loop with a given reference speed, assuming that the control target of the system is speed tracking. Tracking error is constructed as follows:

$$e_\omega = \omega_r - \omega + e_{\omega I} \tag{18}$$

where $e_{\omega I}$ is the integral of the estimation error in the sampling time. This term is added to ensure that the system can converge even if the system parameters contain uncertainties. $e_{\omega I}$ is expressed as follows:

$$e_{\omega I} = K_\omega \int_0^t (\omega_r - \omega) dt \tag{19}$$

To make the speed tracking error approaches zero, i_{qref} is designed as a virtual control variable. The candidate Lyapunov function is constructed as follows:

$$V_\omega = \frac{1}{2} e_\omega^2 \tag{20}$$

The derivative of e_ω can be obtained by combining Equations (1) and (18):

$$\dot{e}_\omega = \dot{\omega}_r - \frac{3}{2}\frac{n_p}{J}\left(\psi_f i_{qref} + (L_d - L_q) i_d i_{qref}\right) + \frac{1}{J} T_L + \frac{B}{J}\omega + K_\omega(\omega_r - \omega) \tag{21}$$

Then, the derivative of the candidate Lyapunov function shown in Equation (20) is:

$$\dot{V}_\omega = e_\omega \dot{e}_\omega = e_\omega \left[\dot{\omega}_r - \frac{3}{2}\frac{n_p}{J}(\psi_f i_{qref} + (L_d - L_q) i_d i_{qref}) + \frac{1}{J} T_L + \frac{B}{J}\omega + K_\omega(\omega_r - \omega)\right] \tag{22}$$

To make Equation (22) negative definite, i_{qref} is taken as follows:

$$i_{qref} = \frac{J}{\frac{3}{2} n_p(\psi_f + (L_d - L_q) i_d)}\left[K_1 e_\omega + \dot{\omega}_r + \frac{1}{J} T_L + \frac{B}{J}\omega + \dot{e}_{\omega I}\right] \tag{23}$$

The result of Equation (22) is as follows:

$$\dot{V}_\omega = -K_1 e_\omega^2, K_1 > 0 \tag{24}$$

T_L is used in Equation (23). T_L is unknown in most drive control designs. Therefore, it can be estimated according to the speed information obtained in the ELESO and Equation (1) [33].

At this time, the system has achieved the goal of global progressive speed tracking. To achieve complete decoupling and speed tracking of the PMSM, the current under the synchronous rotating coordinate system can be selected as follows:

$$\begin{cases} i_{qref} = \frac{J}{\frac{3}{2} n_p(\psi_f + (L_d - L_q) i_d)}\left[K_1 e_\omega + \dot{\omega}_r + \frac{1}{J} T_L + \frac{B}{J}\omega + \dot{e}_{\omega I}\right] \\ i_{dref} = 0 \end{cases} \tag{25}$$

The current tracking error is selected as the virtual control variable. The current error is defined as follows:

$$\begin{cases} e_q = i_{qref} - i_q + i_{qe} \\ e_d = i_{dref} - i_d + i_{de} \end{cases} \tag{26}$$

where i_{de} and i_{qe} are the integral terms, which are expressed as follows:

$$i_{xe} = K_x \int_0^t (i_{xref} - i_x) dt, x = d, q \tag{27}$$

At this time, a new system is being constructed. Consider the following candidate Lyapunov function:

$$V_q = V_\omega + \frac{1}{2} e_q^2 + \frac{1}{2} i_{qe}^2 \tag{28}$$

The derivative of Equation (28) can be obtained by combining Equations (1), (24) and (26):

$$\begin{array}{l}\dot{V}_q = -K_1 e_\omega^2 + e_q\left[\frac{di_{qref}}{dt} + \frac{R_S}{L_q} i_q + \frac{L_d}{L_q} n_p \omega i_d + \frac{\psi_f n_p}{L_q}\omega - \frac{1}{L_q} u_q + K_q(i_{qref} - i_q)\right] \\ + i_{qe} K_q (i_{qref} - i_q)\end{array} \tag{29}$$

According to Equation (29), the control quantity u_q is selected as follows:

$$u_q = L_q\left[K_2 e_q + \frac{di_{qref}}{dt} + \frac{R_S}{L_q} i_q + \frac{L_d}{L_q} n_p \omega i_d + \frac{\psi_f n_p}{L_q}\omega\right] \tag{30}$$

Substituting Equation (30) into Equation (29) yields:

$$\begin{array}{l}\dot{V}_q = -K_1 e_\omega^2 - K_2 e_q^2 + (e_q + i_{qe}) K_q (i_{qref} - i_q) \\ = -K_1 e_\omega^2 - K_2 e_q^2 + (e_q + i_{qe}) K_q (e_q - i_{qe}) \\ = -K_1 e_\omega^2 - (K_2 - K_q) e_q^2 - K_q i_{qe}^2\end{array} \tag{31}$$

The result of Equation (31) is as follows:

$$\dot{V}_q \le -K_Q V_q, K_Q = \min\{K_1; (K_2 - K_q); K_q\} \tag{32}$$

For the d-axis current i_d, the target $i_{dref} = 0$. The control value is u_d. Similar to the previous subsystem construction process, the candidate Lyapunov function is defined as:

$$V_d = \frac{1}{2} e_d^2 + \frac{1}{2} i_{de}^2 \tag{33}$$

The derivative of Equation (33) yields:

$$\begin{array}{l}\dot{V}_d = e_d\left(\frac{di_{ref}}{dt} - \frac{di_d}{dt} - K_d i_d\right) + i_{de} K_d (i_{dref} - i_d) \\ = e_d\left(\frac{R_S}{L_d} i_d - \frac{L_q}{L_d} n_p \omega i_q - \frac{1}{L_d} u_d\right) + K_d (e_d + i_{de})(e_d - i_{de})\end{array} \tag{34}$$

According to Equation (34), the control quantity u_d is selected as follows:

$$u_d = L_d\left(K_3 e_d + \frac{R_S}{L_d} i_d - \frac{L_q}{L_d} n_p \omega i_q - \frac{1}{L_d} u_d\right) \tag{35}$$

Substituting Equation (35) into Equation (34) yields:

$$\dot{V}_d = -(K_3 - K_d) e_d^2 - K_d i_{de}^2 \tag{36}$$

Similar to Equation (32), $\dot{V}_d$ is represented as follows:

$$\dot{V}_d \le -K_D V_d, K_D = \min\{(K_3 - K_d); K_d\} \tag{37}$$

Through the design of the backstepping controllers, the speed controller and current controllers are cascaded to ensure that all virtual control variables will eventually converge to their reference values.

In practice, some parameters of the PMSM are not fixed. Its value changes over time. For example, the stator resistance will change as the temperature changes [34]. However, in sensorless control of using equation model, motor parameters such as resistance and inductance are used in calculation. The system operation is based on the assumption that these parameters are predetermined and conform to actual motor parameters. Therefore, the difference of motor parameters may affect the stability of the sensorless control system. To solve this problem, in [35], the author introduced the on-line parameter identification as a compensation method for motor parameter difference. Specifically, the Recursive Least

Squares method (RLS) is used as the core, and the appropriate forgetting matrix is selected to identify. The feasibility of the method is verified by simulation.

3. Simulation and Experimental Analysis

In this section, the PMSM sensorless control diagram based on the combination of the integral backstepping controller and the ELESO is shown in Figure 2. The ELESO calculates the estimated internal and external interference. The estimated rotor position and speed are obtained in PLL. D and q-axis voltages are obtained by the integral backstepping controller. After anti-Park transformation and SVPWM, the PWM signal is output to complete the whole control process. The experimental test platform is shown in Figure 3. Its components mainly include a PMSM, drive module, load, DC power supply, dynamic torque sensor, etc. The experiment uses STM32F407 chip and IR2110S driver chip as the core hardware platform to drive the 24 V on-board motor.

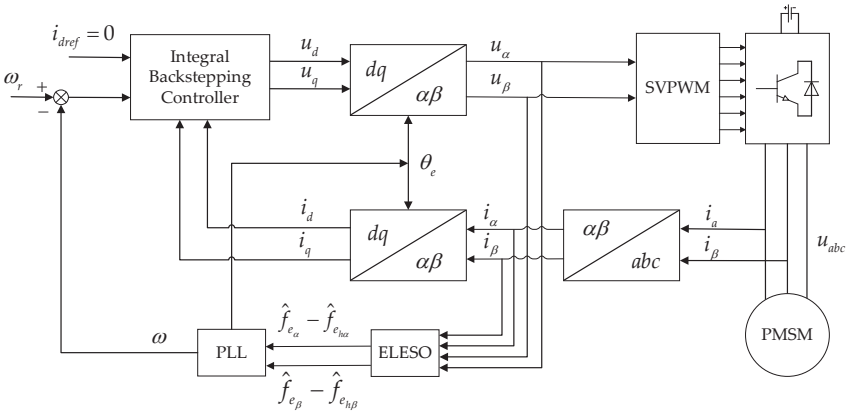

Figure 2. Block diagram of the scheme based on the integral backstepping controller and the ELESO.

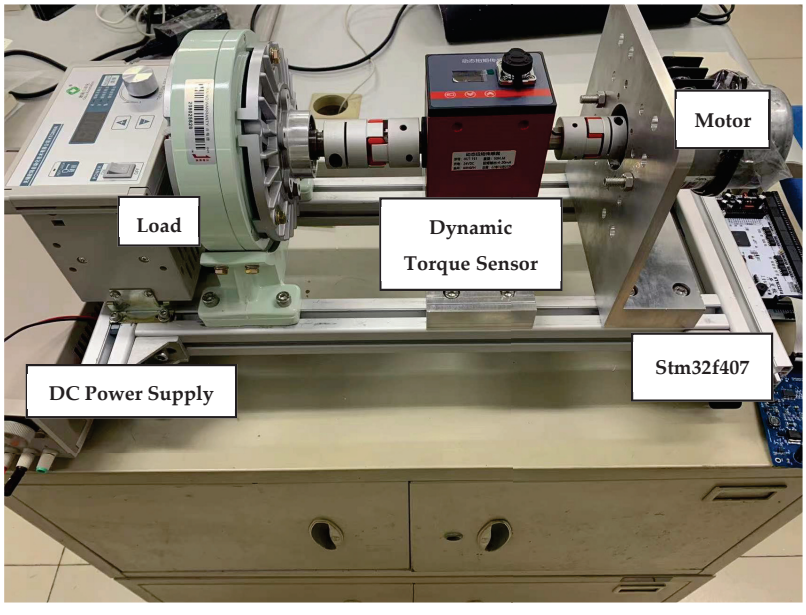

Figure 3. The experimental test platform.

3.1. Simulation Results and Analysis

Table 1 shows the parameters of the PMSM. According to the flow chart of the FOC control of PMSM, a simulation model is built in Matlab/Simulink for experimental verification. The backstepping controllers replace the traditional PI controllers and add an integral term to them. The ELESO obtains back EMF. In this paper, the control scheme combining the backstepping controller and the ESO is regarded as the old scheme, and the control scheme combining the integral backstepping controller and the ELESO is regarded as the new scheme. The new scheme is compared with the old scheme to verify the effectiveness of the new control scheme.

Table 1. PMSM parameters.

Parameters	Values
Stator resistance/Ω	1.5
Rated torque/N·m	6
d-axis inductance/mH	2.48
q-axis inductance/mH	2.95
Rated speed/rpm	1000
Moment of inertia/kg·m^2	0.0014
Flux linkage/wb	0.07
Viscous friction/B	7.2×10^{-4}
Pole pairs	4

According to the actual situation of the motor parameters, the characteristics of current tracking performance and anti-interference, the bandwidth of the LESO1 is selected as 500 Hz, and the bandwidth of the LESO2 is selected as 3000 Hz in the ELESO. In the backstepping controller, $K_1 = 4000$, $K_\omega = 200$, $K_2 = 13{,}000$, $K_q = 350$, $K_3 = 8000$, $k_d = 830$. Set the step size as 1×10^{-5} s. The motor accelerates from the static state to 500 rad/s. The rotor speed is raised to 1000 r/min at 0.5 s, and 6 N·m loads are applied to the rotor. Then, the motor runs at the rated speed.

Figure 4 shows the estimated back EMF under the old scheme. Due to the existence of harmonics, the estimated value of back EMF is not ideal. The influence of high-order harmonics on estimation accuracy is especially obvious at the low speed. According to the definition of the PLL and Equation (13), the back EMF information is finally converted into the estimated position information of the rotor. Therefore, this paper mainly shows the advantages of the new scheme from the position and speed of information.

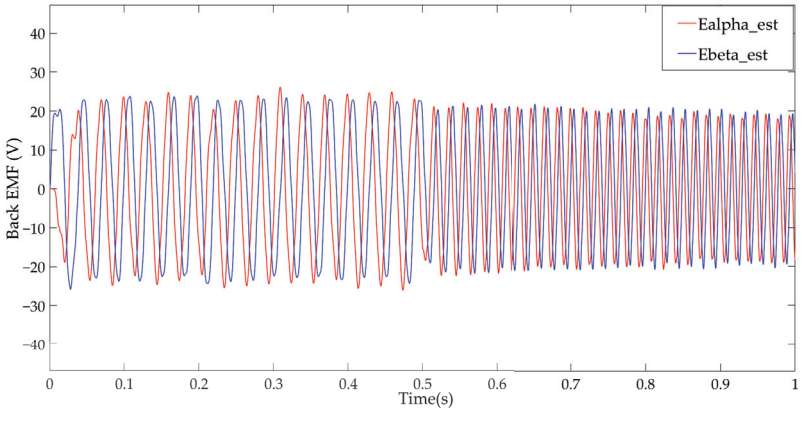

Figure 4. PMSM estimated back EMF of the control scheme of combining the backstepping controller with the ESO.

Figure 5 shows the PMSM three-phase current waveforms of the two control schemes under no-load startup. Comparing the two waveforms, it can be concluded that the scheme based on the integral backstepping controller and the ELESO has a higher sinusoidal current waveform because it filters out the higher harmonics.

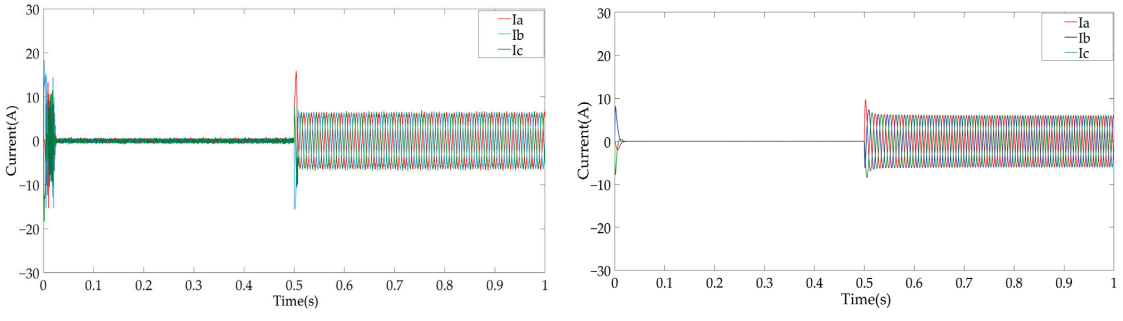

(**a**) (**b**)

Figure 5. PMSM stator three-phase current waveforms under no-load startup of the (**a**) Control scheme of combining the backstepping controller with the ESO and (**b**) Control Scheme of combining the integral backstepping controller with the ELESO.

Figure 6 shows the waveforms comparison between the estimated rotor position and the actual value under the two schemes. Combined with the rotor position error waveforms shown in Figure 7, it is obvious that the traditional scheme always has an estimation error of about 0.5 rad under no-load startup. The improved scheme will have fewer errors only at the moment of state change. With the stable operation of the motor, the position estimation error under the improved scheme is always stable at about 0 rad.

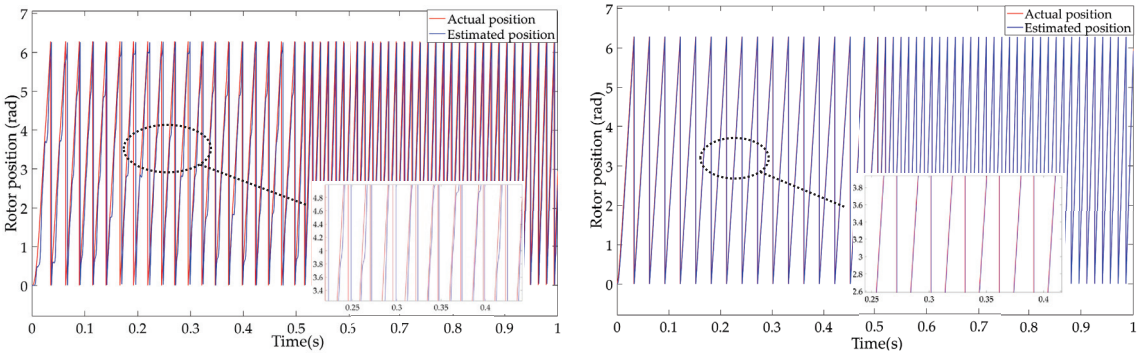

(**a**) (**b**)

Figure 6. PMSM rotor position tracking under no-load startup of the (**a**) Control scheme of combining the backstepping controller with the ESO and (**b**) Control Scheme of combining the integral backstepping controller with the ELESO.

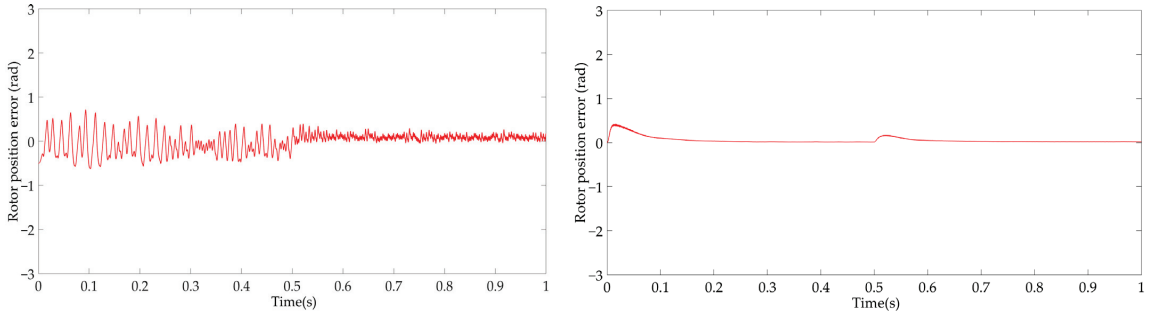

(**a**) (**b**)

Figure 7. PMSM rotor position tracking error under no-load startup of the (**a**) Control scheme of combining the backstepping controller with the ESO and (**b**) Control Scheme of combining the integral backstepping controller with the ELESO.

Figure 8 shows the d and q-axis currents of the two controllers. Due to the existence of higher harmonics, the waveforms in Figure 8a are not smooth. The high-order harmonics are filtered out in Figure 8b, so the d and q-axis currents are more stable. In addition, when the state changes in 0 s and 0.5 s, the jump amplitude of the current in Figure 8b is smaller.

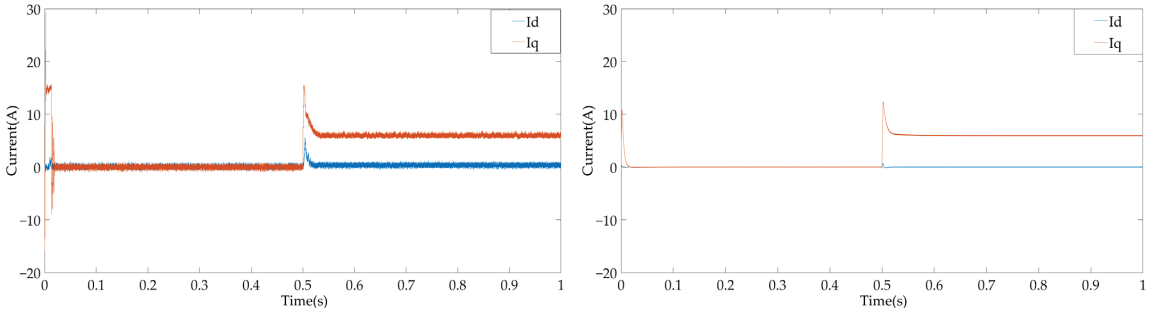

(**a**) (**b**)

Figure 8. PMSM d and q-axis currents under no-load startup of the (**a**) Control scheme of combining the backstepping controller with the ESO and (**b**) Control Scheme of combining the integral backstepping controller with the ELESO.

Figure 9 shows the rotor speed waveforms of the two controllers. The standard of rotor stability is that the rotor speed reaches the set value and can be stabilized around the set value. In Figure 9a, it takes about 0.07 s for the rotor speed to reach the set value. In Figure 9b, the waveform converges faster. The new scheme eliminates the influence of internal disturbances such as harmonic components and parameter changes. The speed waveform is smoother. The new scheme is more suitable for places with high requirements for motor speed accuracy.

According to the above waveforms, the control scheme of combining the traditional backstepping controller with the ESO does not eliminate the influence of the high-order harmonics and internal parameter changes of the motor. Therefore, the problem of jitter and poor sinusoidal performance will occur in this control scheme, especially at low speeds. The system always maintains an estimation error of about 0.5 rad, which affects the stable operation of the motor. Compared with the traditional scheme, the control scheme based on the integral backstepping controller and the ELESO has better tracking performance at a low speed. In the second stage of acceleration, the traditional control mode requires

0.06 s of reaction time, and the improved scheme only needs 0.01 s to reach the rated speed, which improves the reaction speed of the system.

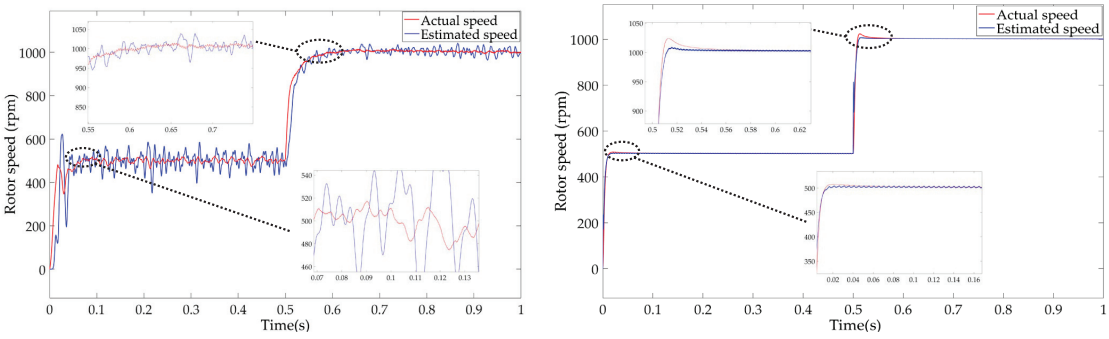

(**a**) (**b**)

Figure 9. PMSM rotor speed under no-load startup of the (**a**) Control scheme of combining the backstepping controller with the ESO and (**b**) Control Scheme of combining the integral backstepping controller with the ELESO.

The working principle of PMSM is that the magnetic field acts on the current force to make the motor rotate. When the motor is unloaded, the electromagnetic force is far greater than the force required for rotor rotation. When the motor is loaded, the resistance of the load on the rotor requires more force to rotate. Therefore, we need to conduct the motor on load starting test to verify whether the new scheme meets the expectations. Set the motor speed to the rated speed of 1000 r/min and the load to 6 N·m. The two methods are simulated, and the experimental results are analyzed.

Figure 10 shows the waveforms of the PMSM stator three-phase current under load startup test. Both schemes can obtain relatively stable three-phase waveforms under load startup, but the sinusoidal property of Figure 10a is worse than that of Figure 10b due to the existence of harmonics. In Figure 10b, the LESO2 timely estimated the harmonic components, and the external interference of the ELESO output no longer contains high-order harmonics, so the waveform is more sinusoidal.

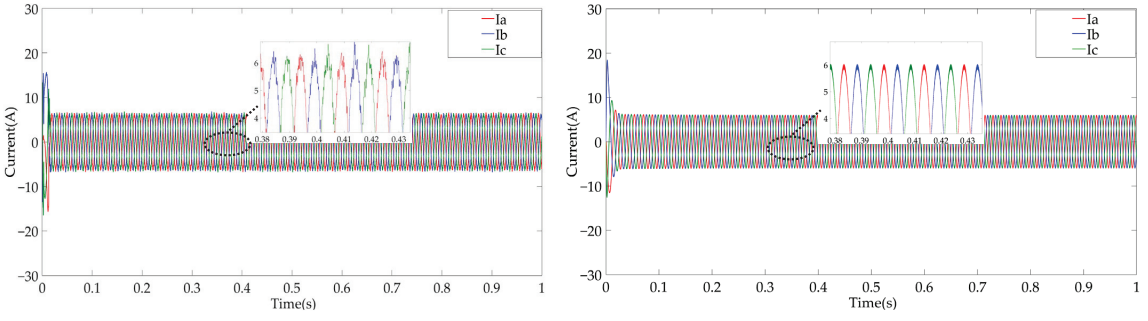

(**a**) (**b**)

Figure 10. PMSM stator three-phase current waveforms under load startup of the (**a**) Control scheme of the combining backstepping controller with the ESO and (**b**) Control Scheme of combining the integral backstepping controller with the ELESO.

Figure 11 shows the rotor position estimation waveforms under load startup. As shown in Figure 11, both control schemes can finally achieve the goal of real-time tracking.

According to the error waveforms shown in Figure 12, it can be obtained that the new scheme can converge faster. Compared with Figure 12a, the integral backstepping controller eliminates the steady-state error and further improves the system performance.

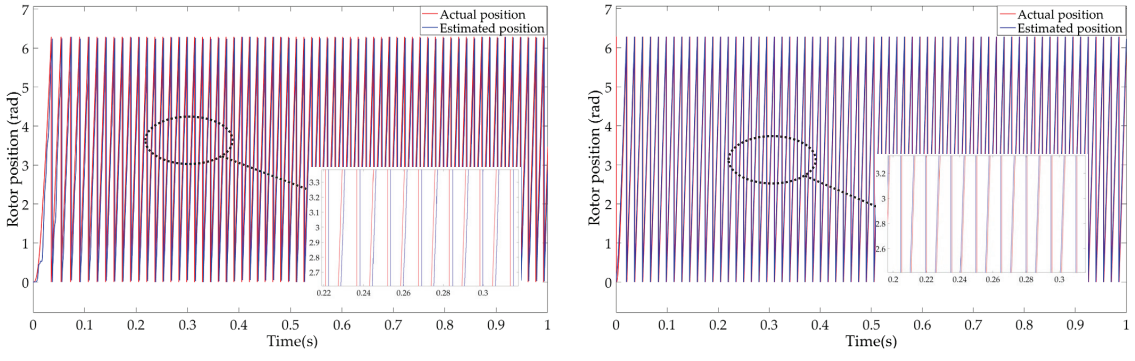

(**a**) (**b**)

Figure 11. PMSM rotor position tracking under load startup of the (**a**) Control scheme of combining the backstepping controller with the ESO and (**b**) Control Scheme of combining the integral backstepping controller with the ELESO.

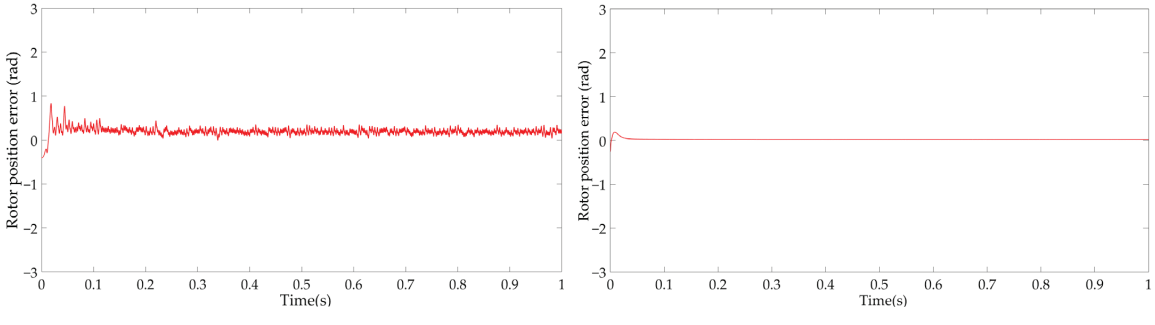

(**a**) (**b**)

Figure 12. PMSM rotor position tracking error under load startup of the (**a**) Control scheme of combining the backstepping controller with the ESO and (**b**) Control Scheme of combining the integral backstepping controller with the ELESO.

Figure 13 shows the d and q-axis currents of the two schemes under load startup. The higher harmonics are filtered out in Figure 13b, and the waveforms are smoother than those in Figure 13a. In addition, the currents in Figure 13b have a faster convergence speed and a smaller jump amplitude.

Figure 14 shows the speed-tracking waveforms of the two schemes under load startup. As shown in Figure 14a, the rotor speed reaches the set value of 0.4 s. The rotor can converge to the target speed after 0.2 s under the new system. Since high-frequency harmonics and other internal disturbances are filtered out, the speed can be stabilized at 1000 r/min thereafter. Therefore, the new system has good robustness.

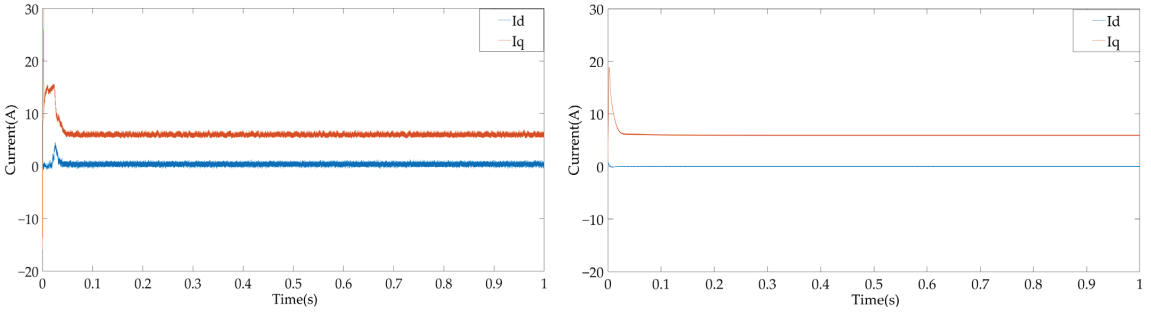

Figure 13. PMSM d and q-axis currents under load startup of the (**a**) Control scheme of combining the backstepping controller with the ESO and (**b**) Control Scheme of combining the integral backstepping controller with the ELESO.

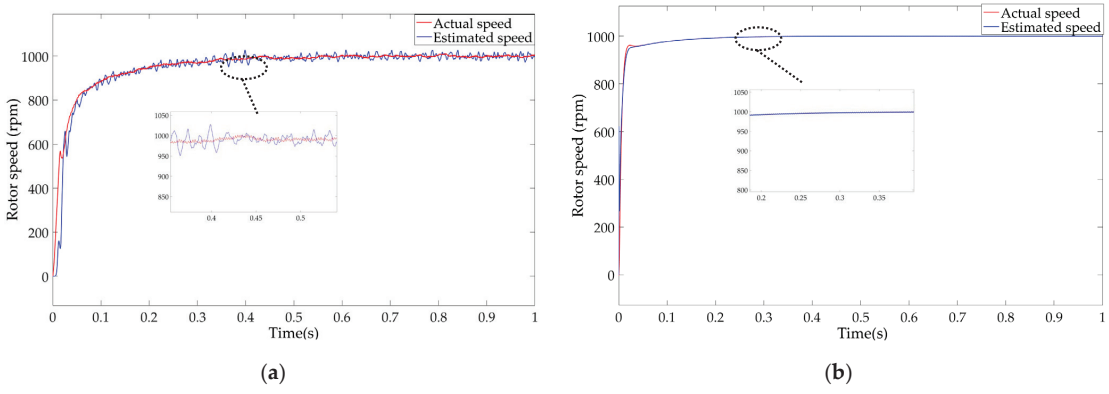

Figure 14. PMSM rotor speed under load startup of the (**a**) Control scheme of combining the backstepping controller with the ESO and (**b**) Control Scheme of combining the integral backstepping controller with the ELESO.

According to the above experimental data, when the motor starts with load, the control scheme based on the combination of the backstepping controller and the ESO, as well as the control scheme based on the combination of the integral backstepping controller and the ELESO, will eventually produce a stable waveform. However, the control scheme based on the integral backstepping controller and the ELESO can accelerate to the rated speed faster in the startup phase, which is 0.2 s faster than the traditional control scheme. The control scheme combining the backstepping controller with the ESO still has a rotor estimation error of 0.2 rad when the system is stable. Due to the estimation of the internal disturbance of the system and the addition of integral terms to the backstepping controller, the control scheme based on the integral backstepping controller and the ELESO can obtain better static stability. Through no-load acceleration and on-load starting experiments, it is verified that the PMSM sensorless control system based on the integral backstepping controller and the ELESO has better performance and stronger robustness. The simulation results realize the PMSM high-precision control without a position sensor.

3.2. Experimental Results and Analysis

The feasibility of the control scheme based on the combination of the integral backstepping controller and the ELESO is preliminarily verified through simulation. On this basis, the motor test bench shown in Figure 3 is used for experimental verification. The

magnetic particle brake and tension controller provide load to the PMSM. The dynamic torque sensor can display the change of dynamic parameters such as speed and torque of the PMSM. At zero speed and low speed, the back EMF is very small, and the rotor position cannot be accurately estimated. I-F open-loop startup is usually used to cover the startup from standstill through the low-speed area. After rotor pre-positioning, the method applies a constant q-axis current to drag the speed up to the desired speed, then switches to a medium-high speed angle observer [36].

According to the simulation results, two experiments are designed to verify the superiority of the control scheme based on the integral backstepping controller and the ELESO. These experiments also use the control scheme based on the backstepping controller and the ESO as a comparison. Firstly, PMSM starts at no load and accelerates to 500 r/min. At 0.5 s, the PMSM accelerates to 1000 r/min. When the time reaches 1 s, the load jumps to 6 N·m. Finally, the load drops to 0 N·m at 1.5 s, and the PMSM keeps running at this state. Figure 15 shows the speed waveforms under this experiment. The total duration of the experiment is set to 2 s. The timeline of the experiment is marked in Figure 15, and all the following waveforms are based on this timeline. Figure 15 clearly shows that when the system state changes, the control scheme based on the integral backstepping controller and the ELESO has a faster response speed. Figure 16 shows the actual position and estimated position of the rotor after taking the remainder under the two schemes. In Figure 16, the errors of the two schemes are small, which will be difficult to show the superiority of the improved scheme. In this paper, the position and speed information are quantified in the table for a clearer comparison. Table 2 shows the estimated and actual values of position and speed under the two schemes. According to the design of experiment 1, the appropriate time points are selected for data acquisition. In experiment 1, after the PMSM is started, the system state changes three times at 0.5 s, 1 s and 1.5 s. Table 2 shows that the control scheme based on the integral backstepping controller and the ELESO has better tracking effect in the whole process of experiment 1. The rotor position tracking error is basically stable within 0.1 rad, which is greatly improved compared with the control scheme based on the backstepping controller and the ESO. When the system state changes, the rotor speed jump amplitude of the improved scheme is lower. Moreover, when the system operates stably, especially when the load value is rated, the steady-state error of the control scheme based on the integral backstepping controller and the ELESO is smaller, and its speed can converge to the set value faster.

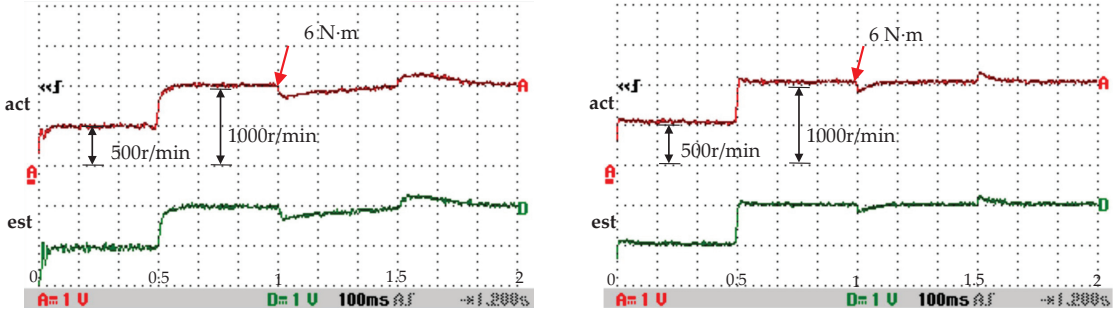

(**a**) (**b**)

Figure 15. Experiment 1 PMSM rotor speed waveforms of the (**a**) Control scheme of combining the backstepping controller with the ESO and (**b**) Control Scheme of combining the integral backstepping controller with the ELESO.

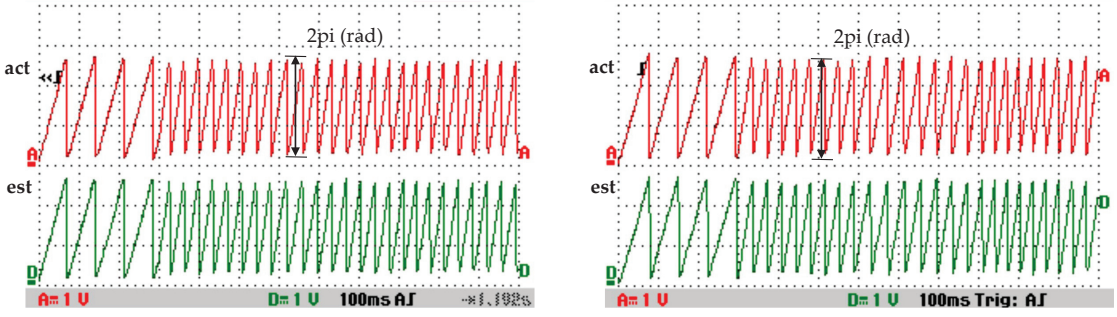

(**a**) (**b**)

Figure 16. Experiment 1 PMSM rotor position waveforms of the (**a**) Control scheme of combining the backstepping controller with the ESO and (**b**) Control Scheme of combining the integral backstepping controller with the ELESO.

Table 2. Position and speed of experiment 1.

Time (s)	Speed (a) Act/Est	Speed (a) Error	Speed (b) Act/Est	Speed (b) Error	Position (a) Act/Est	Position (a) Error	Position (b) Act/Est	Position (b) Error
0.01	363.85/137.69	226.16	500.45/501.5	−1.05	0.81/0.39	0.42	1.69/1.82	−0.13
0.05	470.00/462.84	7.16	506.67/505.13	1.54	2.16/1.48	0.68	4.52/4.61	−0.09
0.1	510.40/524.53	−14.13	503.87/502.75	1.12	1.72/1.13	0.59	4.45/4.51	−0.06
0.3	500.58/497.83	2.75	500.15/499.03	1.12	3.38/2.75	0.63	6.17/6.23	−0.06
0.55	960.06/979.30	−19.24	1015.57/1013.61	1.96	1.35/0.5	0.85	5.80/5.88	−0.08
0.6	1007.67/1005.30	2.37	1003.86/1002.66	1.2	5.99/4.68	1.31	6.14/6.19	−0.05
0.8	1001.32/1006.70	−5.38	1000.29/999.41	0.88	5.28/4.09	1.19	4.14/4.18	−0.04
1.05	873.38/870.16	3.22	945.46/945.07	0.39	1.05/0.03	1.02	4.72/5.14	−0.42
1.1	926.43/921.41	5.02	995.04/994.04	1	1.43/0.3	1.13	2.05/2.44	−0.39
1.3	967.17/931.65	35.52	999.82/998.94	0.88	1.10/0.08	1.02	6.16/6.22	−0.06
1.55	1112.68/1140.04	−27.36	1056.01/1053.08	2.93	5.98/4.58	1.4	1.14/1.21	−0.07
1.6	1110.35/1107.98	2.37	1011.21/1010.24	0.97	2.79/1.39	1.4	1.44/1.48	−0.04
1.8	1042.10/1036.18	5.92	1000.99/1000.23	0.76	2.71/1.45	1.26	3.51/3.55	−0.04

Figure 17 is the current waveforms diagram of the d and q-axis. Figure 18 shows the electromagnetic torque waveforms. In Figure 17, both schemes have obtained stable current waveforms. However, the jump amplitude of the q-axis current in Figure 17b is smaller when the speed changes. Figure 18a shows that the waveform jitter with internal interference (higher harmonics) will be very obvious. In high performance control occasions, such control performance is not allowed. The reference value of d-axis current is always 0. According to the time point selected in Table 2, the d-axis currents and electromagnetic torques are quantized in Table 3. Comparing the data of the two schemes, the d-axis current error and electromagnetic torque error of the control scheme based on the integral backstepping controller and the ELESO are 1–10% of the error of the comparison scheme. The control scheme based on the integral backstepping controller and the ELESO shows better control performance.

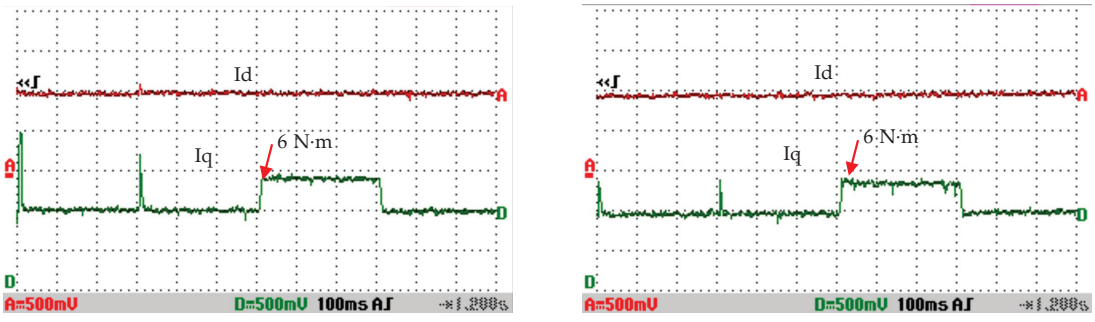

(**a**) (**b**)

Figure 17. Experiment 1 PMSM d and q-axis currents of the (**a**) Control scheme of combining the backstepping controller with the ESO and (**b**) Control Scheme of combining the integral backstepping controller with the ELESO.

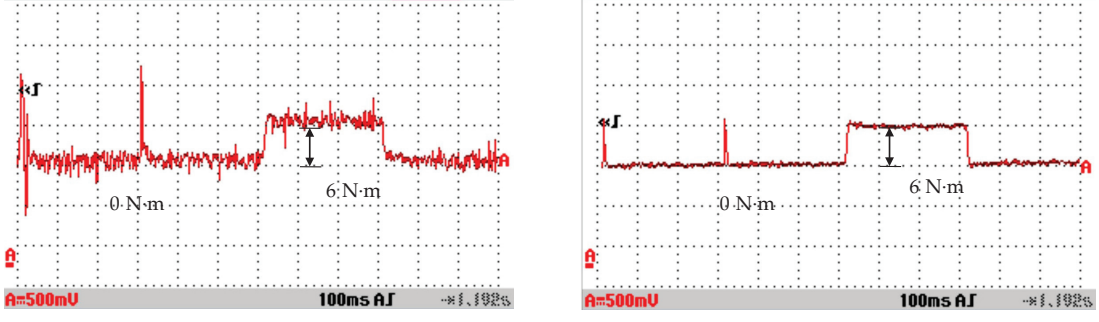

(**a**) (**b**)

Figure 18. Experiment 1 PMSM electromagnetic torque waveforms of the (**a**) Control scheme of combining the backstepping controller with the ESO and (**b**) Control Scheme of combining the integral backstepping controller with the ELESO.

Table 3. D-axis current and torque of experiment 1.

Time (s)	Id (a)	Id (b)	Torque (a)	Torque (b)
0.01	1.20	0.05	9.84	1.31
0.05	−0.27	−0.003	2.12	0.04
0.1	0.16	−0.002	0.78	0.03
0.3	−0.023	0.001	−0.60	0.01
0.55	0.50	0.002	−2.16	−0.04
0.6	0.013	−0.001	−1.57	−0.01
0.8	0.72	−0.002	2.02	0
1.05	0.60	−0.01	6.03	6.21
1.1	0.25	0.003	7.49	6.08
1.3	0.09	0.002	6.32	6.01
1.55	0.39	0.006	1.68	−0.19
1.6	0.62	0	0.64	−0.09
1.8	0.22	−0.003	0.81	−0.01

The load startup and speed jump test of PMSM are also essential steps to verify its sensorless control performance. Experiment 2 is designed as PMSM load startup and speed

jump experiment. PMSM starts at the set value of 1000 r/min and 6 N·m. Then, the speed jumps to 800 r/min at 1 s.

Figure 19 shows the speed waveforms of Experiment 2. Figure 20 shows the estimated value and actual value of the rotor position after taking the remainder. Similar to experiment 1, the relevant parameters in Figures 19 and 20 are quantified in Table 4. According to the data in Table 4, the speed in Figure 19b can reach the set value in only 0.3 s, which is much faster than the waveform in Figure 19a. Moreover, in Figure 19b, when the speed reaches the set value, PMSM can operate stably at the set value, and the steady-state error is close to 0. During the whole control process, the rotor position estimation error shown in Figure 20b is always stable around 0.4 rad. Comparing with Figure 20a, the estimation error is reduced to 30–40%.

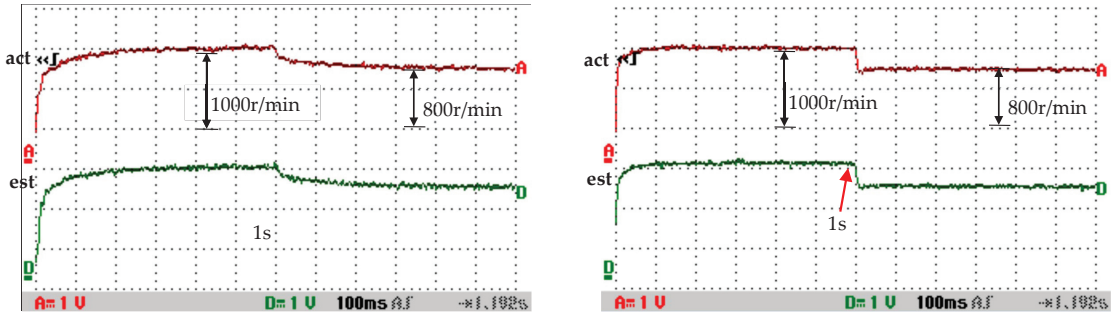

(**a**) (**b**)

Figure 19. Experiment 2 PMSM rotor speed waveforms of the (**a**) Control scheme of combining the backstepping controller with the ESO and (**b**) Control Scheme of combining the integral backstepping controller with the ELESO.

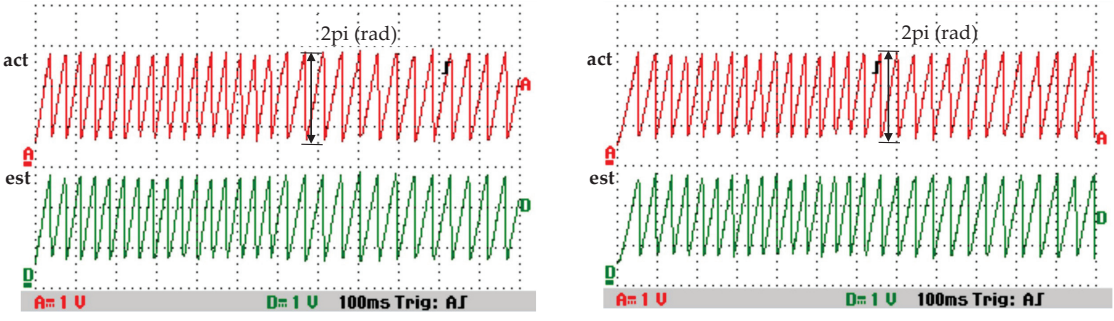

(**a**) (**b**)

Figure 20. Experiment 2 PMSM rotor position waveforms of the (**a**) Control scheme of combining the backstepping controller with the ESO and (**b**) Control Scheme of combining the integral backstepping controller with the ELESO.

Table 4. Position and speed of experiment 2.

Time (s)	Speed (a) Act/Est	Speed (a) Error	Speed (b) Act/Est	Speed (b) Error	Position (a) Act/Est	Position (a) Error	Position (b) Act/Est	Position (b) Error
0.1	812.50/814.99	−2.49	965.98/964.67	1.31	5.51/4.49	1.02	4.76/5.16	−0.4
0.3	939.87/947.73	−7.86	998.68/997.78	0.9	6.23/5.13	1.1	6.01/6.24	−0.23
0.5	970.27/987.90	−17.63	999.97/999.06	0.91	2.18/0.98	1.2	1.79/2.18	−0.39
0.7	985.96/987.44	−1.48	1000.01/999.11	0.9	1.34/0.08	1.24	3.89/4.28	−0.39
0.9	993.17/1010.23	−17.06	1000.02/999.08	0.9	1.30/0.03	1.27	5.81/6.20	−0.39
1.1	859.71/858.22	1.49	795.70/794.77	0.93	4.73/3.61	1.12	5.83/6.27	−0.44
1.3	822.55/803.84	18.71	799.83/798.87	0.96	1.13/0.2	0.93	3.70/4.14	−0.44
1.5	808.29/802.55	5.74	799.98/799.03	0.95	1.04/0.02	1.02	1.60/2.04	−0.44
1.7	799.04/803.83	−4.79	799.99/799.03	0.96	5.95/4.99	0.96	5.80/6.23	−0.43
1.9	805.53/780.67	24.86	799.99/799.02	0.97	4.05/3.04	1.01	3.70/4.14	−0.44

Figure 21 shows the current waveforms of d and q-axis under experiment 2. In Figure 21a, when the rotor speed changes, the current waveforms have a very obvious jump. Moreover, due to the existence of higher harmonics, the electromagnetic torque waveform in Figure 22a has a large fluctuation. In Figure 22b, higher harmonics are filtered, and the waveform is smoother. Table 5 shows the d-axis currents and torques data of the two schemes in Experiment 2. According to the data in Table 5, the steady-state error of d-axis current in Figure 21b is 0.001–0.002. The electromagnetic torque error in Figure 22b is stable at 0.01. Experiment 2 proves that the control scheme based on the integral backstepping controller and the ELESO has a faster response speed, lower parameters jump and smaller steady-state errors when starting and changing speed under the constant load. This is consistent with the results of experiment 1.

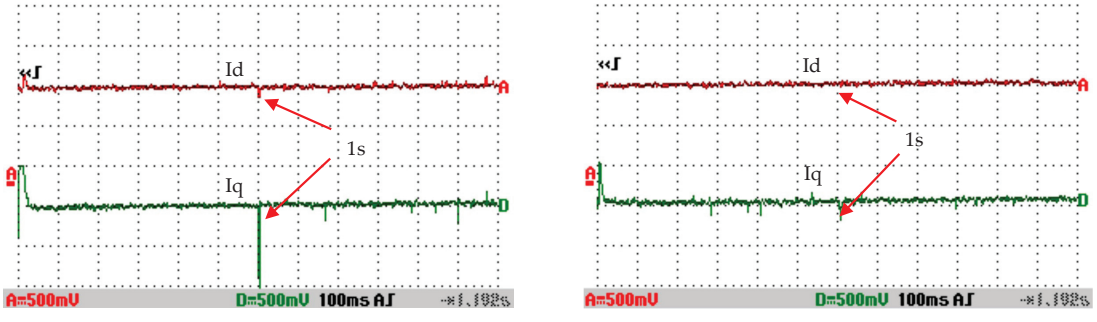

(**a**) (**b**)

Figure 21. Experiment 2 PMSM d and q-axis currents of the (**a**) Control scheme of combining the backstepping controller with the ESO and (**b**) Control Scheme of combining the integral backstepping controller with the ELESO.

In conclusion, the above experiments further verify that the control scheme based on the integral backstepping controller and the ELESO has better performance than the scheme based on the backstepping controller and the ESO. The experimental results show that the simulation results are correct. Compared with the ESO, the ELESO eliminates the interference of the higher harmonics. The backstepping controller can greatly reduce the influence of the parameter changes and the charge disturbances by introducing the integral action in each step to ensure high accuracy speed control. The scheme can be applied to places with high performance.

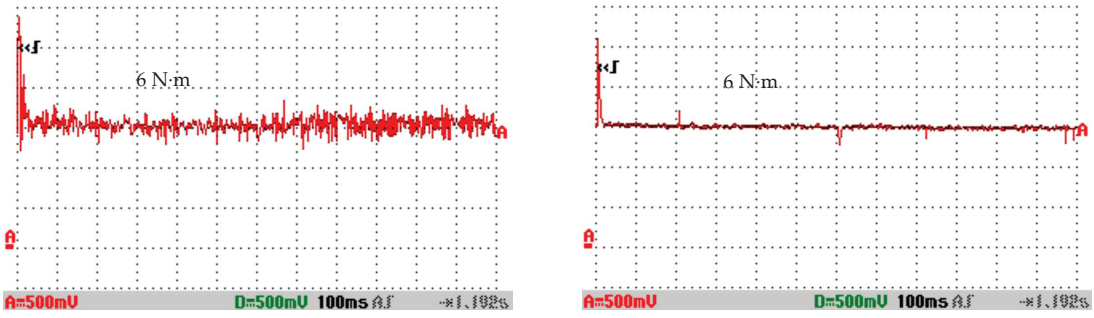

(**a**) (**b**)

Figure 22. Experiment 2 PMSM electromagnetic torque waveforms of the (**a**) Control scheme of combining the backstepping controller with the ESO and (**b**) Control Scheme of combining the integral backstepping controller with the ELESO.

Table 5. D-axis current and torque of experiment 2.

Time (s)	Id (a)	Id (b)	Torque (a)	Torque (b)
0.1	0.35	−0.002	8.84	6.06
0.3	0.50	0.002	8.49	6.02
0.5	−0.013	0.002	6.39	6.01
0.7	0.28	0.002	6	6
0.9	0.132	0.002	6.72	6.01
1.1	−0.15	0.002	3.68	6.04
1.3	−0.011	−0.001	6.57	6.01
1.5	−0.12	−0.001	6.07	6
1.7	−0.36	−0.001	4.74	6
1.9	−0.05	0	5.34	6.01

4. Conclusions

According to the characteristics of the sensorless control system, this paper proposes a sensorless control scheme that combines the integral backstepping controller with the ELESO to improve the performance of the system.

The LESO proposed by the control algorithm has the advantage of estimating the system disturbance without requiring an accurate motor model. On this basis, the algorithm improves the performance of the sensorless system by cascading another new LESO to estimate and compensate for the sixth harmonic component. Moreover, the control system provides the integral speed backstepping controller with the estimation value of the rotor speed obtained by the ELESO. The q-axis current reference value is obtained by designing a Lyapunov function. The current reference values in the synchronous rotating coordinate system are transferred to the integral current backstepping controllers to obtain the d and q-axis voltages. The reference voltages and the estimated rotor position obtained by the ELESO are transmitted to the SVPWM to realize the whole FOC sensorless control process. The acceleration and load startup experiments are carried out on the control model to verify that the improved algorithm has a faster convergence speed and more accurate position estimation. In addition, the control algorithm can effectively eliminate motor chattering and phase delay, which has good stability under static and dynamic conditions. The simulation results show that the PMSM sensorless control system based on the integral backstepping controller and the ELESO is effective and has good load interference suppression capability.

Author Contributions: Conceptualization, L.S. and C.Z.; methodology, L.S. and C.Z.; software, Y.Z. and G.X.; validation, L.S., C.Z., G.X. and X.H.; formal analysis, X.H.; resources, L.S.; data curation, C.Z.; writing—original draft preparation, C.Z.; writing—review and editing, L.S., X.Z., Y.Z. and G.X. All authors have read and agreed to the published version of the manuscript.

Funding: This research was funded by Basic Public Welfare Research Program of Zhejiang (Yanjuan Qin: LGG19F010010).

Institutional Review Board Statement: Not applicable.

Informed Consent Statement: Not applicable.

Data Availability Statement: The research data used and/or analyzed during the current study are available from the corresponding author on reasonable request.

Conflicts of Interest: The authors declare no conflict of interest.

References

1. Zhao, N.; Wang, G.; Xu, D.; Zhu, L.; Zhang, G.; Huo, J. Inverter Power Control Based on DC-Link Voltage Regulation for IPMSM Drives without Electrolytic Capacitors. *IEEE Trans. Power Electron.* **2018**, *33*, 558–571. [CrossRef]
2. Zhao, Y.; Wei, C.; Zhang, Z.; Qiao, W. A Review on Position/Speed Sensorless Control for Permanent-Magnet Synchronous Machine-Based Wind Energy Conversion Systems. *IEEE J. Emerg. Sel. Top. Power Electron.* **2013**, *1*, 203–216. [CrossRef]
3. Kim, S.-Y.; Choi, C.; Lee, K.; Lee, W. An Improved Rotor Position Estimation with Vector-Tracking Observer in PMSM Drives with Low-Resolution Hall-Effect Sensors. *IEEE Trans. Ind. Electron.* **2010**, *58*, 4078–4086. [CrossRef]
4. Liu, Y.; Zhu, J.; Wang, Z.; Liang, Y. Study of rotor position estimation algorithm based on back-EMF voltage for dual-winding fault-tolerant permanent magnet motor. *Automatika* **2022**, *63*, 496–510. [CrossRef]
5. Kim, J.; Jeong, I.; Nam, K.; Yang, J.; Hwang, T. Sensorless Control of PMSM in a High-Speed Region Considering Iron Loss. *IEEE Trans. Ind. Electron.* **2015**, *62*, 6151–6159. [CrossRef]
6. Xu, W.; Jiang, Y.; Mu, C.; Blaabjerg, F. Improved Nonlinear Flux Observer-Based Second-Order SOIFO for PMSM Sensorless Control. *IEEE Trans. Power Electron.* **2019**, *34*, 565–579. [CrossRef]
7. Qiao, Z.; Shi, T.; Wang, Y.; Yan, Y.; Xia, C.; He, X. New Sliding-Mode Observer for Position Sensorless Control of Permanent-Magnet Synchronous Motor. *IEEE Trans. Ind. Electron.* **2013**, *60*, 710–719. [CrossRef]
8. Liang, D.; Li, J.; Qu, R.; Kong, W. Adaptive Second-Order Sliding-Mode Observer for PMSM Sensorless Control Considering VSI Nonlinearity. *IEEE Trans. Power Electron.* **2018**, *33*, 8994–9004. [CrossRef]
9. Ren, N.; Fan, L.; Zhang, Z. Sensorless PMSM Control with Sliding Mode Observer Based on Sigmoid Function. *J. Electr. Eng. Technol.* **2021**, *16*, 933–939. [CrossRef]
10. Fu, D.; Zhao, X.; Zhu, J. A Novel Robust Super-Twisting Nonsingular Terminal Sliding Mode Controller for Permanent Magnet Linear Synchronous Motors. *IEEE Trans. Power Electron.* **2021**, *37*, 2936–2945. [CrossRef]
11. Xiang, L.; Yan, W.; Zhicheng, J. Global Fast Terminal Sliding Mode Control System for Permanent Magnet Synchronous Motor Drive Under Disturbances. In Proceedings of the 2018 37th Chinese Control Conference (CCC), Wuhan, China, 25–27 July 2018; pp. 3092–3095. [CrossRef]
12. Nguyen, T.H.; Nguyen, T.T.; Nguyen, V.Q.; Le, K.M.; Tran, H.N.; Jeon, J.W. An Adaptive Sliding-Mode Controller with a Modified Reduced-Order Proportional Integral Observer for Speed Regulation of a Permanent Magnet Synchronous Motor. *IEEE Trans. Ind. Electron.* **2022**, *69*, 7181–7191. [CrossRef]
13. Lu, E.; Li, W.; Wang, S.; Zhang, W.; Luo, C. Disturbance rejection control for PMSM using integral sliding mode based composite nonlinear feedback control with load observer. *ISA Trans.* **2021**, *116*, 203–217. [CrossRef]
14. Li, Z.; Wang, J.; Wang, S.; Feng, S.; Zhu, Y.; Sun, H. Design of Sensorless Speed Control System for Permanent Magnet Linear Synchronous Motor Based on Fuzzy Super-Twisted Sliding Mode Observer. *Electronics* **2022**, *11*, 1394. [CrossRef]
15. Xiong, J.-J.; Zhang, G.-B.; Wang, J.-X.; Yan, T.-H. Improved Sliding Mode Control for Finite-Time Synchronization of Nonidentical Delayed Recurrent Neural Networks. *IEEE Trans. Neural Netw. Learn. Syst.* **2020**, *31*, 2209–2216. [CrossRef]
16. Han, J. From PID to Active Disturbance Rejection Control. *IEEE Trans. Ind. Electron.* **2009**, *56*, 900–906. [CrossRef]
17. Qu, L.; Qiao, W.; Qu, L. An Extended-State-Observer-Based Sliding-Mode Speed Control for Permanent-Magnet Synchronous Motors. *IEEE J. Emerg. Sel. Top. Power Electron.* **2021**, *9*, 1605–1613. [CrossRef]
18. Du, B.; Wu, S.; Han, S.; Cui, S. Application of Linear Active Disturbance Rejection Controller for Sensorless Control of Internal Permanent-Magnet Synchronous Motor. *IEEE Trans. Ind. Electron.* **2016**, *63*, 3019–3027. [CrossRef]
19. Xi, Y.; Yu, X.; Wang, Y.; Li, Y.; Huang, J. Robust Nonlinear Adaptive Backstepping Coordinated Control for Boiler-Turbine Units. In Proceedings of the 2018 IEEE 27th International Symposium on Industrial Electronics (ISIE), Cairns, Australia, 13–15 June 2018; pp. 1167–1172. [CrossRef]
20. Nabipour, M.; Zarchi, H.A.; Madani, S.M. Variable-structure position control-a class of fast and robust controllers for synchronous reluctance motor drives. In Proceedings of the 20th Iranian Conference on Electrical Engineering (ICEE2012), Tehran, Iran, 15–17 May 2012; pp. 410–415. [CrossRef]

21. Xi, Y.; Wang, Y.A. Coordinated Control Strategy for Thermal Power Generation Units Based on the Adaptive Backstepping Method. *Zhongguo Dianji Gongcheng Xuebao* **2018**, *38*, 2070. [CrossRef]
22. Kang, Y.G.; Reigosa, D.D. Dq-Transformed Error and Current Sensing Error Effects on Self-Sensing Control. *IEEE J. Emerg. Sel. Top. Power Electron.* **2022**, *10*, 1935–1945. [CrossRef]
23. Humaidi, A.J.; Badr, H.M.; Ajil, A.R. Design of Active Disturbance Rejection Control for Single-Link Flexible Joint Robot Manipulator. In Proceedings of the 2018 22nd International Conference on System Theory, Control and Computing (ICSTCC), Sinaia, Romania, 10–12 October 2018; pp. 452–457. [CrossRef]
24. Jiang, F.; Yang, K.; Sun, S.; Xu, Y.; Liu, A. Back-EMF based Sensorless Control of PMSM with an Improved PLL for Eliminating the Position Estimation Fluctuation. In Proceedings of the 2019 22nd International Conference on Electrical Machines and Systems (ICEMS), Harbin, China, 11–14 August 2019. [CrossRef]
25. Wang, G.; Ding, L.; Li, Z.; Xu, J.; Zhang, G.; Zhan, H.; Ni, R.; Xu, D. Enhanced Position Observer Using Second-Order Generalized Integrator for Sensorless Interior Permanent Magnet Synchronous Motor Drives. *IEEE Trans. Energy Convers.* **2014**, *29*, 486–495. [CrossRef]
26. Jiang, F.; Yang, K.; Sun, S.; Zhang, H.; Tang, L.; Liu, A. An Improved Extended State Observer Based on Linear-Nonlinear Switching Strategy for PMSM Sensorless Control. In Proceedings of the 2018 21st International Conference on Electrical Machines and Systems (ICEMS), Jeju, Korea, 7–10 October 2018; pp. 1696–1702. [CrossRef]
27. Hua, X.; Huang, D.; Guo, S. Extended State Observer Based on ADRC of Linear System with Incipient Fault. *Int. J. Control. Autom. Syst.* **2020**, *18*, 1425–1434. [CrossRef]
28. Gao, Z. Scaling and bandwidth-parameterization based controller tuning. In Proceedings of the 2003 American Control Conference, Denver, CO, USA, 4–6 June 2003; pp. 4989–4996. [CrossRef]
29. Qu, L.; Qiao, W.; Qu, L. An Enhanced Linear Active Disturbance Rejection Rotor Position Sensorless Control for Permanent Magnet Synchronous Motors. *IEEE Trans. Power Electron.* **2020**, *35*, 6175–6184. [CrossRef]
30. Karabacak, M.; Eskikurt, H.I. Design, modelling and simulation of a new nonlinear and full adaptive backstepping speed tracking controller for uncertain PMSM. *Appl. Math. Model.* **2012**, *36*, 5199–5213. [CrossRef]
31. Larbaoui, A.; Belabbes, B.; Meroufel, A.; Tahour, A.; Bouguenna, D. Backstepping control with integral action of PMSM integrated according to the MRAS observer. *IOSR J. Electr. Electron. Eng.* **2014**, *9*, 59–69. [CrossRef]
32. Yang, Q.; Liu, W.; Huang, Y. Real time simulation study on backstepping sliding mode control of permanent magnet synchronous motor. In Proceedings of the 2011 International Conference on Electrical Machines and Systems (ICEMS), Beijing, China, 20–23 August 2011; pp. 1–5. [CrossRef]
33. Sun, X.; Yu, H.; Liu, X. Design and Application of Sliding Mode Controller in PMSM Position Tracking Control Based on Adaptive Backstepping. In Proceedings of the 2018 Chinese Automation Congress (CAC), Xi'an, China, 30 November 2018–2 December 2018; pp. 3507–3511. [CrossRef]
34. Nicola, C.-I.; Nicola, M.; Selișteanu, D. Sensorless Control of PMSM Based on Backstepping-PSO-Type Controller and ESO-Type Observer Using Real-Time Hardware. *Electronics* **2021**, *10*, 2080. [CrossRef]
35. Noguchi, S.; Mabuchi, H.; Suzuki, K.; Dohmaeki, H. Study of parameter variations compensation in sensorless control of PMSM. In Proceedings of the 2016 19th International Conference on Electrical Machines and Systems (ICEMS), Chiba, Japan, 13–16 November 2016; pp. 1–6.
36. Pacha, M.; Zossak, S. Improved Simple I-F Open-Loop Start-up of PMSM Drives without Speed or Position Sensor. In Proceedings of the 2019 IEEE 10th International Symposium on Sensorless Control for Electrical Drives (SLED), Turin, Italy, 9–10 September 2019; pp. 1–6. [CrossRef]

machines

MDPI

Article

Torque Ripple Suppression of Switched Reluctance Motor with Reference Torque Online Correction

Benqin Jing [1,2], Xuanju Dang [1,*], Zheng Liu [2] and Jianbo Ji [2]

[1] School of Electronic and Automation, Guilin University of Electronic Technology, Guilin 541004, China
[2] School of Electronic Information and Automation, Guilin University of Aerospace Technology, Guilin 541004, China
* Correspondence: xjd69@guet.edu.cn

Abstract: High torque ripple dramatically affects the switched reluctance motor (SRM) application. To reduce the torque ripple, a reference torque neural network (RTNN) is proposed to adjust the reference torque online. Firstly, the RTNN is built on the torque sharing function (TSF) method. Furthermore, the RTNN is designed as a single-input and -output network. As the periodic relationship between the torque ripple and the rotor angle, the rotor angle constitutes the central node parameter of the implicit function in RTNN. Therefore, one-step adjustment of the RTNN can perform well at restraining reference torque. Lastly, the torque error is used to adjust the parameters of RTNN to reduce the torque ripple. In the MATLAB environment, through the simulation comparison with fuzzy torque and PD current compensation method, the effectiveness of RTNN at torque ripple suppression is proven with different loads and speeds.

Keywords: switched reluctance motor; reference torque; TSF; neural network; torque ripple

Citation: Jing, B.; Dang, X.; Liu Z.; Ji, J. Torque Ripple Suppression of Switched Reluctance Motor with Reference Torque Online Correction. *Machines* **2023**, *11*, 179. https://doi.org/10.3390/machines11020179

Academic Editors: Loránd Szabó and Feng Chai

Received: 26 December 2022
Revised: 12 January 2023
Accepted: 17 January 2023
Published: 28 January 2023

1. Introduction

The switched reluctance motor (SRM) has the advantages of high power density, wide speed range, high reliability, and low manufacturing cost. In addition, due to the simple and robust structure, SRMs have high reliability and can operate in harsh environments [1–3]. However, due to its unique doubly salient structure, a large torque ripple will occur, which can be attributed to the nonlinear relationship between torque and current in the operation process [4,5].

Current control-based methods to reduce torque ripple mainly include current mode predictive control (MPC), torque sharing function (TSF), instant torque compensation, and current injection method.

The voltage prediction can be calculated by MPC via the micro-step method, according to the rotor voltage and flux equation [6]. Firstly, the cost function of minimum flux is designed following the flux model. Then, the MPC algorithm is employed for flux prediction and control [7]. On the basis of this idea, the predictive current control method can be further utilized [8]. An unconstrained MPC for current control can cope with the measurement noise and uncertainties within the machine inductance profile [9]. Nonetheless, the MPC Model recommendations can take a long time depending on the precise mathematical model of the SRM [10].

The TSF method has the advantage of a simple structure. The torque ripple and copper loss can reach their lowest levels by adding coefficients to the transient phase and using a genetic algorithm for optimization [11]. The torque sharing function can be further optimized according to the reference current of the torque distribution at different angles [12]. The above three methods require offline training. In comparison, the online method can adjust reference current without training. The iterative optimization method is divided into the outer loop and inner loop, the outer loop optimization of the turn-off angle to reduce copper loss, the inner loop optimization of torque ripple, the introduction of

feedback torque, and the optimization of the turn-on angle [13]. The inductance derivatives under different rotor angles and phase currents are calculated through finite element analysis, and the partial derivatives can be used to calculate the given current [14]. However, this method needs to adapt better to load changes, and improvement in the accuracy of the rotor angle is required [15]. Therefore, the accuracy of rotor angle needs to be considered [16].

To reduce torque ripple, instant torque can be employed as compensation for current. During the commutation interval, the difference between the reference and instant torque can be used to obtain the modified reference torque, which will finally translate to the reference current [17]. As the torque ripple in the commutation section is more serious, the feedback torque is used to reduce the torque ripple in the commutation section, and the effect is more pronounced [18]. The Lagrangian multiplier method can also be employed to minimize current ripple and optimize the copper loss and torque ripple [19]. As the flux change rate influences the speed and output torque, the torque error is used to adjust the reference torque of the first and second half of the transition section [20]. Changing the supply voltage can also reduce the torque ripple by avoiding torque generation in the negative torque region [21]. At the same time, the genetic algorithm and least square method can also reduce torque ripple by optimizing the opening angle and transition angle [22]. The error between the reference and the instant torque constitutes a fuzzy set to generate a reference current insensitive to rotor angles [23]. According to the current voltage and speed, the maximum output torque capacity of the current phase is calculated, and the other phase compensates for the defective part to obtain the phase reference torque of the commutation [24]. Torque error fuzzy processing, resulting in compensation current, can also reduce torque ripple [25].

A proper compensation current is essential in the current injection method. The torque error can be used as a ratio to inject into the present current, and repeat the process in the iterative learning process to obtain a proper compensation current [26]. The DC and first and second current harmonics mainly contribute to the average torque. In comparison, the fourth and fifth current harmonics significantly influence the torque ripple, but contribute much lower to the average torque [27]. Therefore, finite element analysis and current profiling adjustment can effectively reduce torque ripple through torque error [28]. To obtain the inductance value and change rate in the coefficient of torque formula, injecting high-frequency voltage is feasible [29]. The coefficient of the relationship between compensation current and torque error is complex. Reference torque, instant torque deviation, and rotor angle are input into the fuzzy controller to obtain compensation current [30]. The feed-forward plus torque compensation can reduce the dynamic response time and improve the steady-state accuracy of electromagnetic torque [31]. The fuzzy compensator adjusts the torque error, and the torque ripple can also be reduced by compensating the result to the reference torque [32].

The speed controller can generate the reference torque in TSF, but there is always a difference between the reference and instant torque. This difference is attributed to the reference current generated by the TSF, which is not the actual current required, resulting in a large torque ripple.

Based on parameter adjustment learning, neural networks can be employed for model identification and control [33]. The robustness of the system to speed control can be enhanced by introducing a neural network into the sensorless speed [34]. Similarly, the optimal control parameters of the SRM can be calculated using a dynamic SRM model, and the parameter curve can be fitted by a neural network [35]. A nonlinear flux linkage model can be trained by constructing a network of two hidden layers with two-dimensional positions, current inputs, and flux linkage output [36]. Applying the improved generalized regression neural network optimized by the fruit fly optimization algorithm to the modeling of the SRM can further improve the effectiveness and superiority of the neural network [37]. A neural network based on learning error pretreatment for flux linkage control of the SRM can effectively reduce torque ripple and has excellent repeatability [38].

Based on the above analysis, a reference torque neural network (RTNN) is herein designed to adjust the reference torque online to reduce torque ripple. The contribution of this manuscript is

(1) A RTNN is designed to correct the reference torque, employing the instant torque as feedback and rotor angle as the center of the neural network.

(2) The implicit function in the RTNN is constructed according to the total current's characteristics. Compared with the fuzzy and proportional derivative (PD) compensation, the RTNN can compensate the current more effectively, reducing the torque ripple more noticeably.

(3) The RTNN is designed for online learning and one-step adjustment, avoiding offline training.

The rest of this article is organized as follows. In Section 2, the principle of reference torque generating is introduced. Section 3 proposes the strategy of reference torque modified by RTNN. In Section 4, the performances of the proposed scheme are evaluated via simulations under different operating conditions. Finally, Section 5 concludes this article.

2. Reference Torque Generation

SRM has a double salient pole structure, its operation follows the principle of minimum reluctance, and to obtain higher energy conversion efficiency, SRM works in the magnetic saturation region, which makes the nonlinear problem of the motor more serious.

The electromagnetic torque of SRM, which is related to current and rotor angle, can be calculated from the partial derivative of the co-energy to the rotor angle, as follows:

$$T_e(i,\theta) = \left.\frac{\partial w_m^*}{\partial \theta}\right|_{i=const} \tag{1}$$

where $w_m^*(i,\theta) = \int_0^i \psi(i,\theta) * di$ is the co-energy. As the effect of magnetic saturation is very low, neglecting the saturated nature, we apply the formula as

$$w_m(i,\theta) = w_m^*(i,\theta) = \frac{1}{2} i\psi = \frac{1}{2} L i^2 \tag{2}$$

By substituting Equation (2) into Equation (1), we obtain

$$T_e(i,\theta) = \frac{1}{2} i^2 \frac{\partial L}{\partial \theta} \tag{3}$$

where i is phase current, L is phase inductance, and θ is rotor angle.

The torque distribution formula is distributed to each phase as the reference torque is obtained, as Figure 1 shows. The typical TSF includes linear TSF, sinusoidal TSF, and cubic TSF. Among them, the transition section in cubic TSF is more stable. Therefore, the cubic TSF is employed, and its distribution function is presented as Equation (4).

$$f_k(\theta) = \begin{cases} 0 & 0 \le \theta < \theta_{on} \\ 3\left(\frac{\theta-\theta_{on}}{\theta_{ov}}\right)^2 - 2\left(\frac{\theta-\theta_{on}}{\theta_{ov}}\right)^3 & \theta_{on} \le \theta < \theta_{on} + \theta_{ov} \\ 1 & \theta_{on} + \theta_{ov} \le \theta < \theta_{off} \\ 1 - 3\left(\frac{\theta-\theta_{on}}{\theta_{ov}}\right)^2 + 2\left(\frac{\theta-\theta_{on}}{\theta_{ov}}\right)^3 & \theta_{off} \le \theta < \theta_{of} + \theta_{ov} \\ 0 & \theta_{off} + \theta_{ov} \le \theta \le \tau_t \end{cases} \tag{4}$$

where θ_{on} is the on angle, θ_{off} is the off angle, θ_{ov} is the overlap angle, and τ_t is the period.

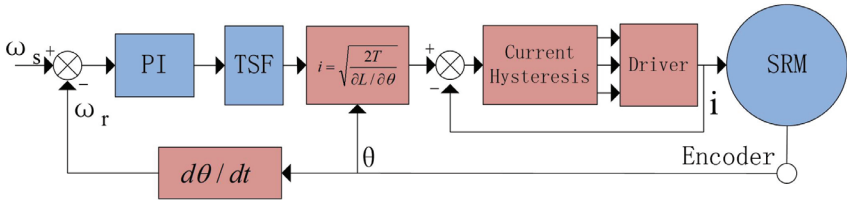

Figure 1. TSF control schematic.

The distributed torque is converted into current by Equation (5).

$$i = \sqrt{\frac{2T}{\partial L/\partial\theta}} \tag{5}$$

The reference torque of each phase is then converted into the reference current, and the given current is compared with the feedback current to control the drive circuit on and off angle, thereby realizing the motor control. In the linearized TSF control method, $\partial L/\partial\theta$, is treated as a constant value because its value varies negligibly compared to the value of the current. Current can be calculated by Equation (5). This allows the SRM to operate under different conditions. However, $\partial L/\partial\theta$ is not a constant value, its value changes with instant current and rotor angle. The improper selection of the inductive derivative will lead to a detrimental reference current, resulting in torque ripple.

3. Reference Torque Modified by RTNN

3.1. Relationship between Reference Torque and Instant Torque

It is a standard method to reduce torque ripple using the difference between instantaneous torque and reference torque, using the difference to compensate for the reference torque. However, as the compensation basis needs to be clarified, the fuzzy method must work with an unclear model [32].

Calculate the difference between the instantaneous and reference torque and form the fuzzy torque compensation according to the difference and the change in the difference. The resulting system control structure is shown in Figure 2. The designed fuzzy controller combines the artificial experience value to provide compensation torque.

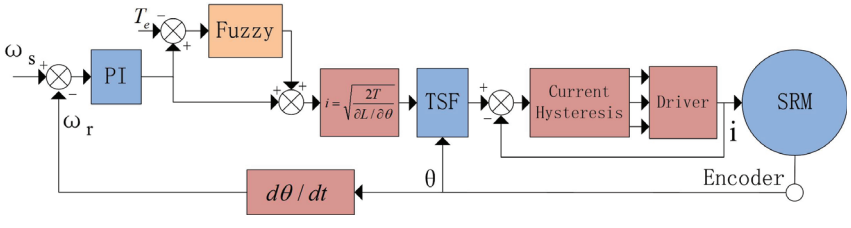

Figure 2. Reference torque compensation by fuzzy controller.

Since the final control object is current, the method of transforming torque error to the reference current is designed. The instantaneous torque is introduced to compensate for the reference current in advance, and the PD controller is used to compensate [31]. The structure designed is shown in Figure 3.

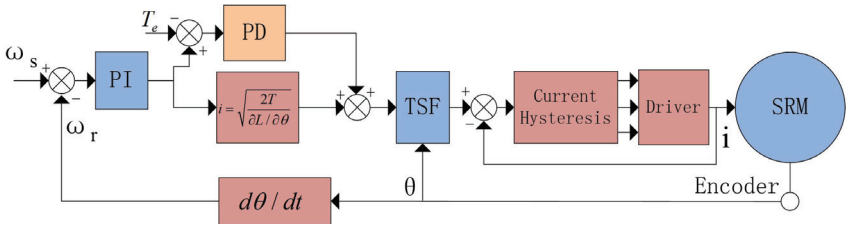

Figure 3. Compensation by PD controller.

The PD algorithm can be classified as the model-free control method. The transformation from the torque error to the compensation current does not need any SRM model, but its parameter adjustment consumes lots of time. Therefore, whether the parameter selection is reasonable or not has a significant influence on the compensation effect.

This paper considers the compensation method of parameter self-adjustment and self-learning. Due to the fact that the neural network has excellent self-learning ability, the neural network is introduced to learn the compensation amount according to the present rotor angle and torque error. The structure is shown in Figure 4.

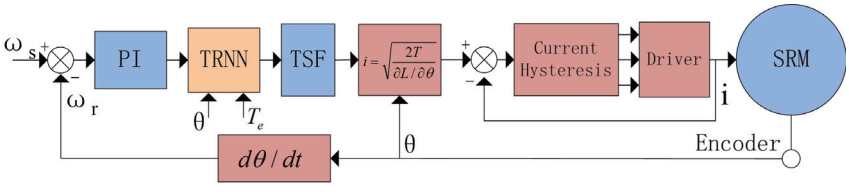

Figure 4. RTNN structure.

The RTNN is placed following the PI speed controller, which adjusts the reference torque slightly according to the present rotor angle and torque error. The subsequent process is the same as the conventional TSF method to maintain the simplicity and stability of the control structure.

In the TSF method, the reference torque is calculated according to the mechanical equation of the motor. Nonetheless, there should always be a difference between the reference and feedback torque.

To better illustrate the proposed algorithm, the speed is set as 300 rpm, and the load torque is 2 Nm; the reference and instantaneous torque curves are shown in Figure 5. The four curves, generated according to the control structure in Figure 4, from top to bottom are reference and instant torque, torque error, and rotor angle, respectively. The torque error always exists as the speed closed loop is designed according to the motor's mechanical equation, ignoring the speed fluctuation. At the same time, the reference torque lags behind the instant torque. The PI controller is also employed to compensate for the instability in the speed control, with inferior performance. Although more complex algorithms can be introduced to reduce the calculation time from the speed error to the given torque, they cannot fundamentally solve the problem.

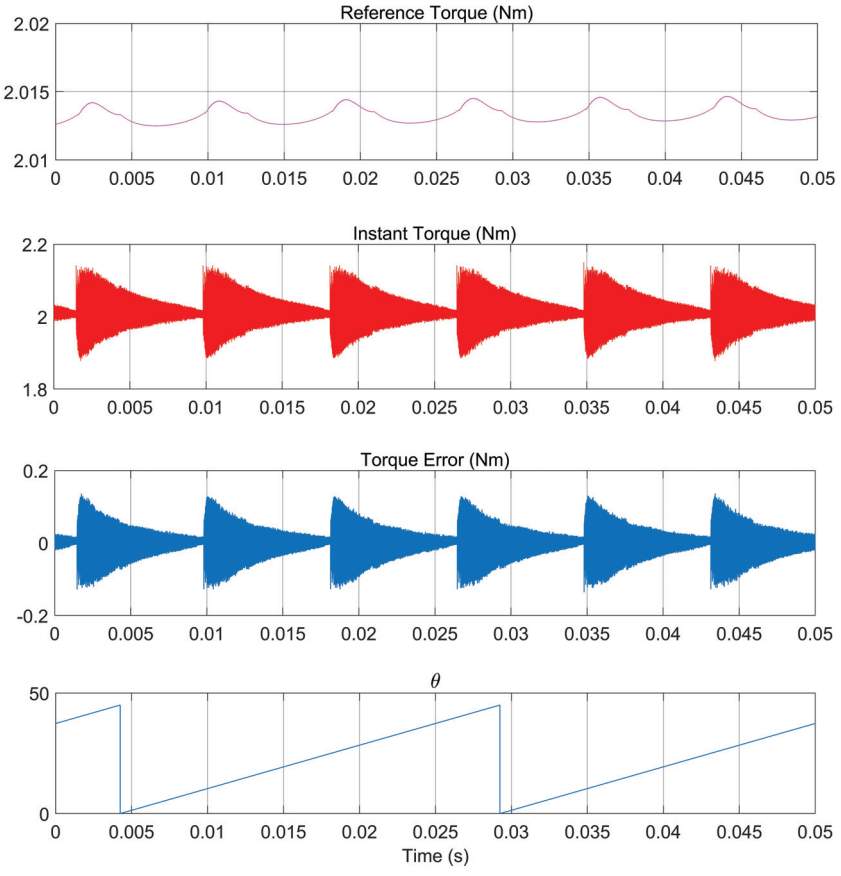

Figure 5. Curves of reference torque and instantaneous torque.

3.2. RTNN

RTNN is used in the system to fine-tune the reference torque online according to the rotor angle. The working principle of RTNN is shown in Figure 6.

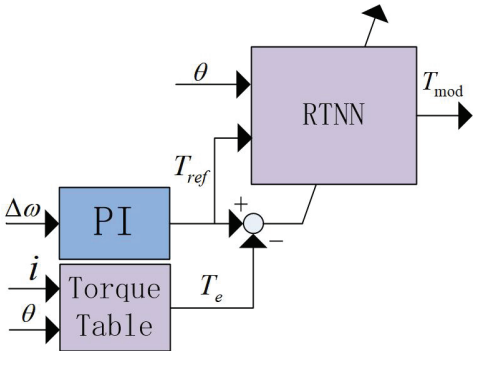

Figure 6. Framework of the RTNN.

The PI speed controller calculates the speed error to obtain the reference torque, which constitutes the input of the neural network and the rotor angle. At the same time, the instantaneous torque is obtained via a look-up table, according to the feedback current and rotor angle. Finally, the difference between the instant and the reference torque is used to adjust the internal parameters of the neural network.

The internal structure of the constructed RTNN is shown in Figure 7.

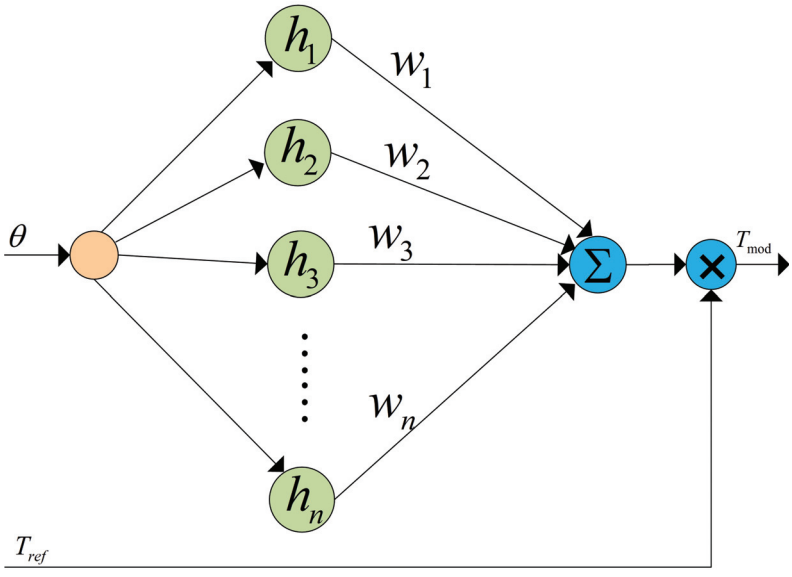

Figure 7. RTNN internal node.

The RBF neural network is a network with the radial basis function as its core. It is usually designed as a three-layer structure, including an input layer, hidden layer, and output layer. The neuron activation function of the hidden layer is composed of radial basis functions. The array operation of the hidden layer is called the hidden layer node. Each hidden layer contains a central vector c, which has the same dimension as the input vector X. The radial basis function is usually selected as the Gaussian function, which is

$$h(i) = e^{-\frac{r^2(i)}{2*b^2(i)}} \tag{6}$$

where $r(i) = \|X - c(i)\|$ is the Euclidean distance, $c(i)$ is the center vector, and $b(i)$ is the network width.

The training of the RBF network is the learning process of network parameters, including the center of the hidden layer, network width, number of hidden layer nodes, and the connection weight value from the hidden layer to the output layer. The hidden layer center is generally trained by random selection or unsupervised clustering based on data samples.

Referring to the RBF structure, the RTNN proposed in this paper is a single-input network and uses a feed-forward link. As a result, the reference torque T_{ref} does not go through the network node, but directly multiplies with the neural network output to obtain the corrected reference torque T_{mod}. Therefore, the neural network in the RTNN plays a role in adjusting the size of the reference torque according to the rotor angle.

The construction of the RTNN refers to the structure of the RBF network. The implicit function is the radial basis function, and its expression is

$$h(i) = e^{-\frac{\|\theta - c(i)\|^2}{2*b^2(i)}} \tag{7}$$

At the same time, the error back propagation algorithm is used to correct the weights and coefficients, where the error is defined as the square of the error, and the goal is to minimize the error.

$$E = \frac{1}{2}\,\text{error}^{\,2} = \frac{1}{2}(T_e - T_m)^2 \tag{8}$$

The output of the neural network is defined as T_m, and its expression is

$$T_m = \sum_{j=1}^{N} w_j * h_j \tag{9}$$

The parameter learning process of neural network is

$$\begin{cases} \Delta w(i) = \delta * \text{ error } * h(i) \\ \Delta b(i) = \delta * \frac{(\text{ error } * w(i) * h(i) * (\theta - c(i))^2}{b^3(i)} \\ \Delta c(i) = \delta * \frac{\text{error} * w(i) * h(i) * (\theta - c(i))}{b^2(i)} \end{cases} \tag{10}$$

where δ is the learning rate.

The coefficients update equation is

$$\begin{cases} w = w1 + \Delta w + \alpha(w1 - w2) \\ c = c1 + \Delta c + \alpha(c1 - c2) \\ b = b1 + \Delta b + \alpha(b1 - b2) \end{cases} \tag{11}$$

where α the momentum factor.

Thus, after RTNN correction, the final reference torque becomes

$$T_{\text{mod}} = T_{ref} * \sum_{j=1}^{N} w_j * h_j \tag{12}$$

The center point in RBF is often random and then adjusted by the error backpropagation. Unlike the random selection of hidden layer center in the traditional RBF, in the proposed method, the RBF neural network's center point significantly influences its tracking effect. Although the center value can be adjusted and changed by error feedback, the neural network is used to correct the reference torque online in this paper, the optimized adjustment needs to be completed in one step, and the one-step adjustment effect directly affects the size of the reference torque, which has a significant influence on the torque ripple.

By observing the total current during SRM operation, it is found that the total current presents a regular change in approximate sine wave. There are three peaks and troughs in one rotor angle period, as shown in Figure 8. According to this characteristic, the implicit function is customized to speed up the correction of the reference torque.

According to the characteristics of 12/8 SRM, the center point of the implicit function is initialized to

$$c = \begin{cases} 7.5, 0 \le \theta < 15 \\ 22.5, 15 \le \theta < 30 \\ 37.5, 30 \le \theta < 45 \end{cases} \tag{13}$$

Thus, after the initialization is completed, the peak points of the total current are in the middle of each phase.

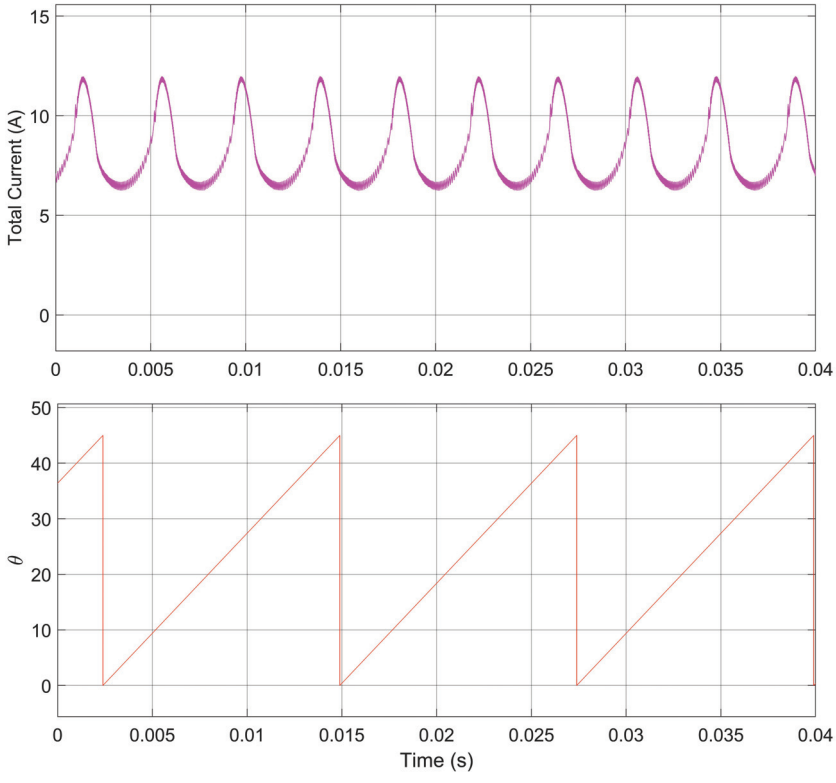

Figure 8. Relationship between total current and rotor angle.

3.3. Flow Chart of Algorithm Steps

STEP 1 Calculate the speed error according to the set speed and real speed.
STEP 2 Calculate reference torque by PI controller.
STEP 3 Measure the rotor angle and phase current.
STEP 4 Obtain the instant torque according to the torque look-up table.
STEP 5 Calculate the torque error according to the reference torque and instant torque.
STEP 6 Adjust the network weight coefficient according to torque error.
STEP 7 Calculate the modified reference torque.
STEP 8 Share the reference torque by TSF.
STEP 9 Calculate reference current.
STEP 10 Current hysteresis calculation.

The RTNN adjusts the weight and width vector of the neural network in each calculation step, as shown in Figure 9. Therefore, the output modified the reference torque periodically according to the rotor angle. RTNN is an online parameter adjustment method. Hence, its one-step adjustment results are directly used to generate the reference torque.

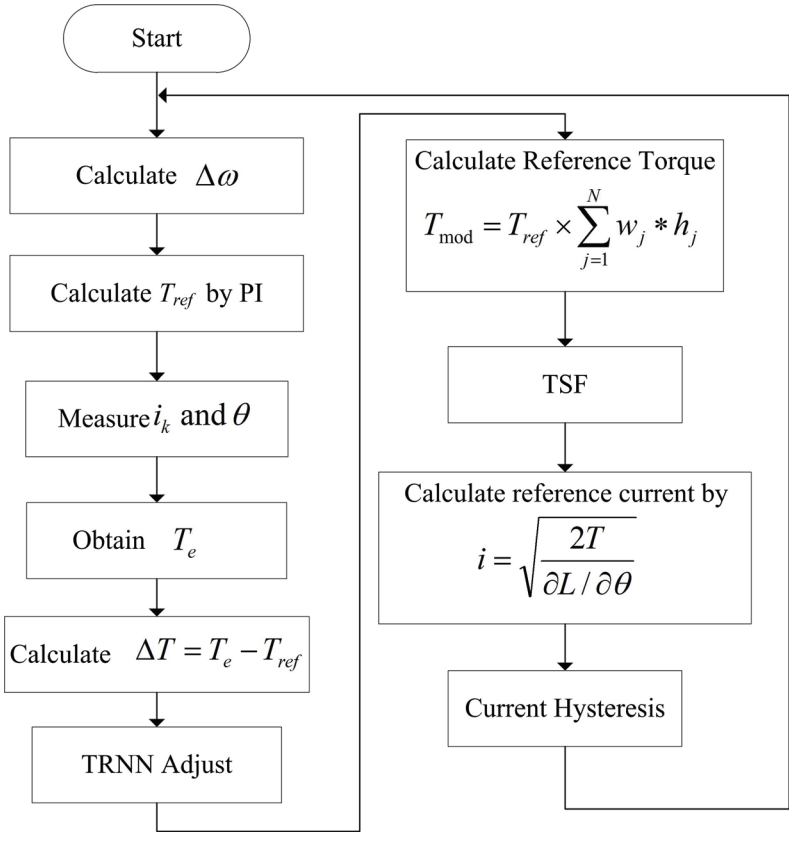

Figure 9. Algorithm flow chart.

4. Verify Simulation

To verify the proposed algorithm's correctness and compare it with the PD compensation algorithm, the simulation model of switched reluctance motor is built in MATLAB/Simulink. The SRM chosen is the 12/8 type, with rated voltage 240 V, rated speed 3000 rpm, stator resistance 0.01 Ω, stator alignment at the maximum inductance 0.00015 mH, friction coefficient 0.01 N.m.s, and inertia 0.0082 kg·m^2.

In the simulation, the inner loop is the current loop control, and the current hysteresis loop is symmetrically designed as 0.1 A. This method is compared with the fuzzy and PD compensation algorithm. In the PD compensation algorithm, the total current is obtained first, and then the total current is distributed. The proposed RTNN compensates the reference torque first, then the corrected reference torque is distributed, and finally, the torque to current conversion is performed. The distribution method used in the above three methods, whether or not the torque or current is distributed, is the cubic distribution function. As a result, the essence of the distribution of reference torque first, then torque–current conversion, and first torque–current conversion, then current distribution is the same.

In order to better measure the suppression of torque ripple under different control methods, the calculation formula of torque ripple is designed in the form of Equation (14).

$$T_{rip} = \frac{T_{max} - T_{min}}{T_{ave}} \times 100\% \tag{14}$$

where T_{rip} is torque ripple, T_{max} is maximum torque during the measuring circle, T_{min} is minimum torque during the measuring circle, and T_{ave} is average torque during the measuring circle.

Considering the response characteristics of the actual motor object, the torque table used in the simulation is based on the data obtained from the actual motor test. The instantaneous torque in the simulation is obtained by testing the actual electromagnetic torque by fixing the rotor at different rotor angles and providing different currents to measure its electromagnetic torque. The electromagnetic torque in simulation is also provided by the established torque table. It corresponds to the real-world motor output.

Thus, the RTNN proposed in this paper is compared with the fuzzy and PD compensation method. The parameters of the PD compensator were optimized and selected as $P = 1$ and $D = 0.05$. The central value in RTNN is given as above, and the other parameters are specified as $\delta = 0.006$ and $\alpha = 0.05$, The neural network node is selected to be 7, w is initialized to a 1-row 7-column matrix of 5, and b and c are initialized to a 1-row 7-column matrix of 10 and 1.5.

The load torque is set to 2 Nm, and the speed is 300 rpm. The three methods mentioned above are used to compensate respectively. The simulation results are shown in Figure 10. Figure 10a–c show the torque and current response curves using the fuzzy compensation method, PD compensation method, and the proposed RTNN method, respectively. The more significant value of torque ripple is generated during the commutation process. The torque ripples caused by the fuzzy compensation, PD compensation algorithm and the RTNN algorithm are 47.5%, 20.9%, and 13.5%, respectively. With the proposed RTNN, the torque ripple can be reduced by 71% and 35%.

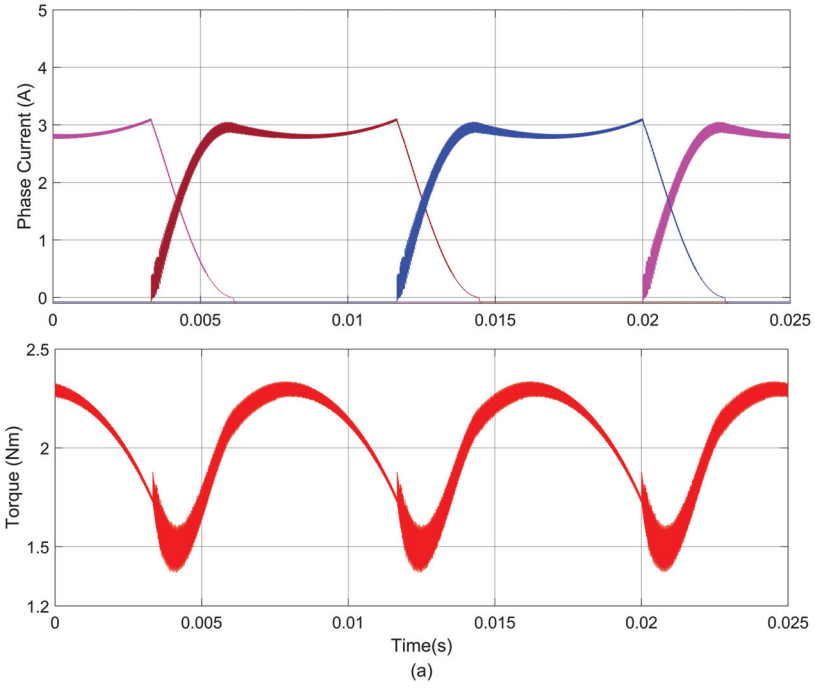

Figure 10. *Cont.*

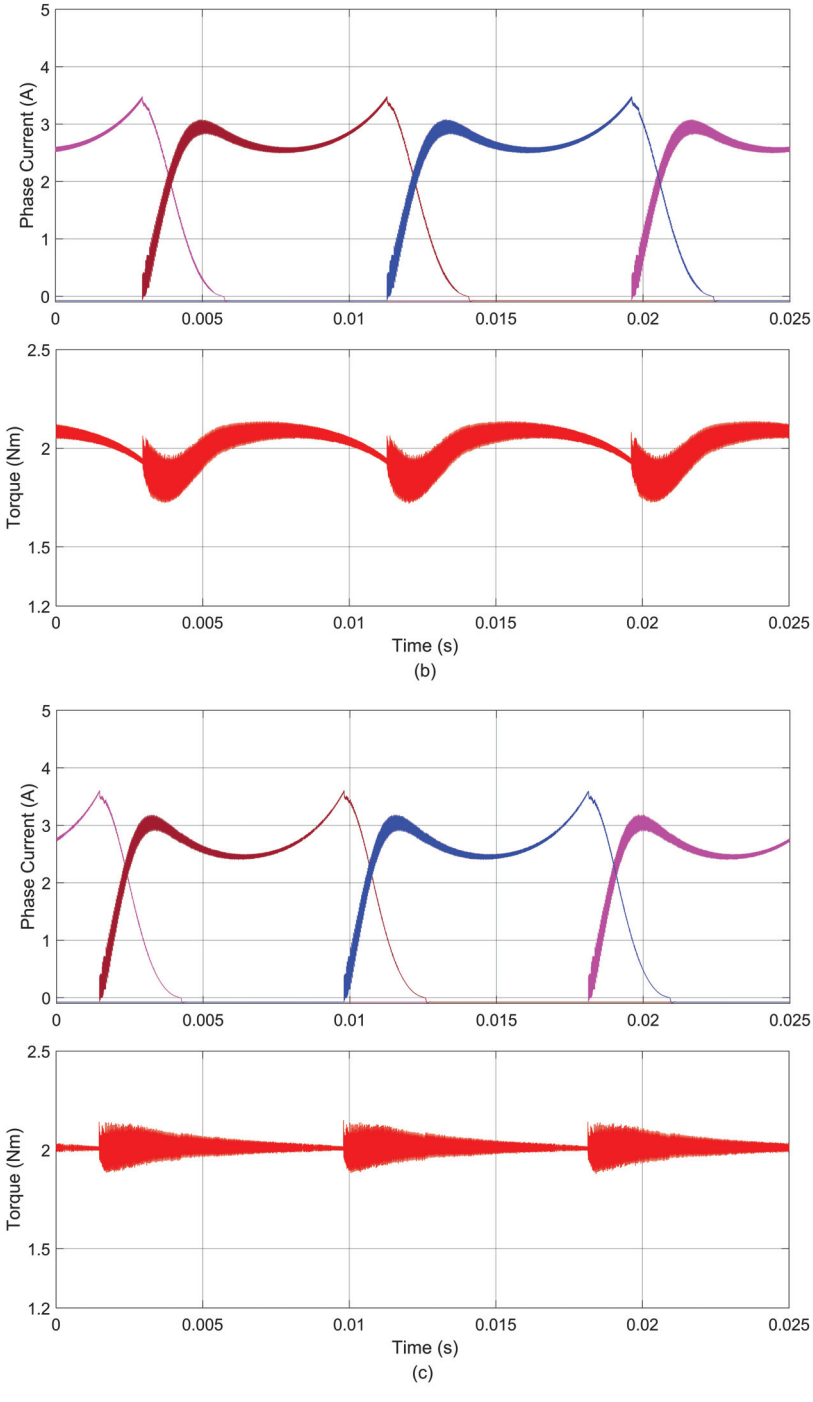

Figure 10. Phase current and electromagnetic torque at 2 Nm, 300 rpm with (**a**) fuzzy compensator, (**b**) PD compensator, and (**c**) RTNN.

The fuzzy compensation algorithm has a minimal ability to reduce torque ripple. In addition, as the reference torque lags behind the instantaneous torque, the fuzzy algorithm can not correct the lag problem by compensating the reference torque. The PD compensation algorithm cannot adjust the compensation current value according to the rotor angle due to its fixed parameters. Therefore, it only relies on the reference torque error to compensate, and the improved performance is limited. On the other hand, the RTNN method adjusts the compensation system according to the rotor angle. It fully considers that the torque ripple of SRM is enormous in the commutation process. Therefore, the reference torque is adjusted according to the torque error, and the effect of suppressing the torque ripple is noticeable.

Similarly, the load torque is changed to 5 Nm, and the speed is adjusted to 700 rpm. The fuzzy compensation, PD compensation, and RTNN methods proposed in this paper are also compared and tested. The simulation results are shown in Figure 11. The torque ripples generated by the fuzzy compensation, PD compensation algorithm, and the RTNN algorithm are 51.7 %, 15.7%, and 11.8%, respectively, and the torque ripples are reduced by 77% and 25% with the proposed RTNN. Through the performance of torque ripple, it is found that the torque ripple is reduced to varying degrees after increasing the speed and load torque.

The performance of the three methods at different operating points is shown in Figure 12, with speed changed from 100 rpm to 900 rpm, an interval of 200 rpm, and with a load torque of 1 Nm, 2 Nm, and 5 Nm, respectively. The specific torque ripple value is shown in Table 1. The numerical results show that the torque ripple of the fuzzy compensation algorithm is unchanged with the torque increase. In contrast, the torque ripple of PD and RTNN algorithms decreased. In the case of small load torque, the effect of the RTNN algorithm to reduce torque ripple is not apparent, mainly because, in this case, small control current changes will cause significant electromagnetic torque changes. Therefore, the electromagnetic torque is not easily controlled.

The advantages, disadvantages, and performance comparisons of the three algorithms are shown in Table 2. The fuzzy compensation algorithm can optimize the reference torque, which can combine well with the human experience, but searching the fuzzy rule table consumes more processor time and increases the algorithm's complexity. PD algorithm is a model-free compensation algorithm that realizes the calculation from torque error to compensation current. The computation is low, but its parameters are fixed, so the adjustment amount is fixed. The RTNN algorithm aims at optimizing the reference torque, has the ability of self-learning, needs model information, and requires rotor angle accuracy. The suppression is evident using the method proposed in this paper. The torque ripple suppression effect of the proposed RTNN method is better than that of the fuzzy and PD compensation methods under different operating conditions.

Table 1. Torque ripple comparison of the three methods (%).

Torque Load	Control Method	100 rpm	300 rpm	500 rpm	700 rpm	900 rpm
1 Nm	Fuzzy compensation	51.7	49.4	47.2	47.5	47.2
	PD compensation	29.9	26.1	23.7	25.6	23.7
	RTNN	26.3	21.8	18.8	24.1	20.3
2 Nm	Fuzzy compensation	47.3	47.5	48.3	49.4	48.1
	PD compensation	21.8	20.9	22.9	20.8	18.3
	RTNN	14.6	13.5	13.9	12.1	11.1
5 Nm	Fuzzy compensation	50.1	50.2	50.4	51.7	50.7
	PD compensation	15.8	15.8	15.6	15.7	14.8
	RTNN	8.6	10.4	8.1	11.8	12.1

Table 2. Performance comparison of the three methods.

Technique	Advantages	Disadvantages	Model Information	Computational Complexity	Optimization Object
Fuzzy compensation	Artificial experience	Costly at searching table	No	Medium	Reference torque
PD compensation	Simplicity	Fixed adjustment	No	Low	Reference current
RTNN	Learning ability	Rely on accurate rotor angle	Yes	Medium	Reference torque

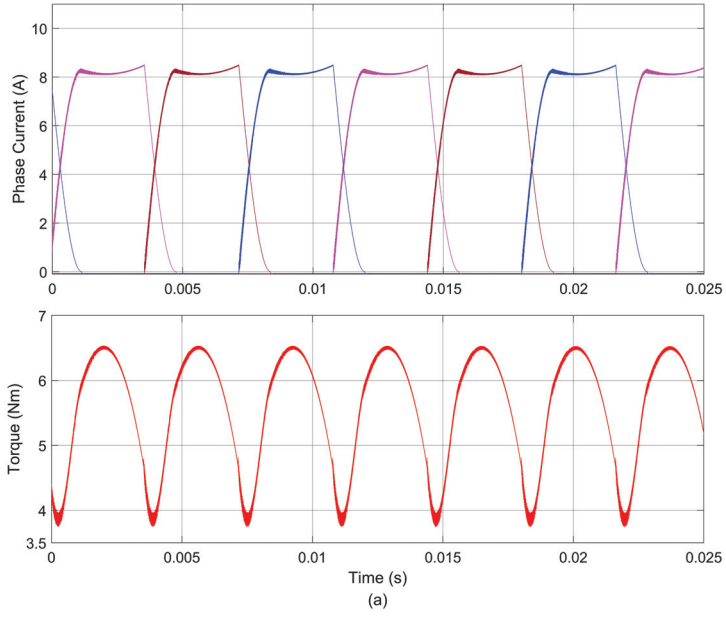

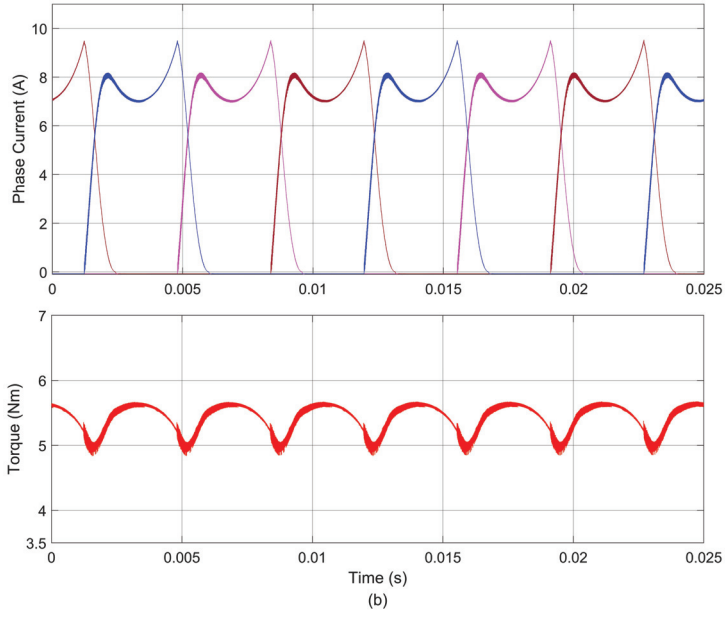

Figure 11. *Cont.*

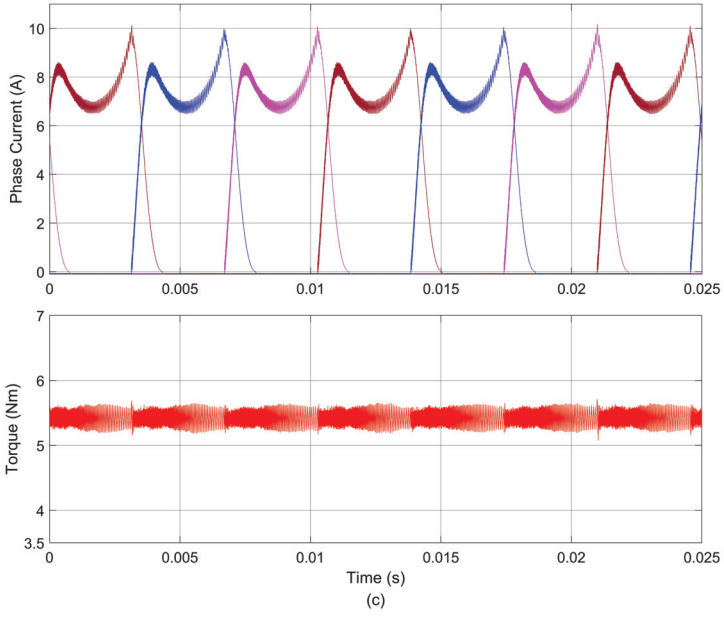

Figure 11. Phase current and electromagnetic torque at 5 Nm, 700 rpm with (**a**) fuzzy compensator, (**b**) PD compensator, and (**c**) RTNN.

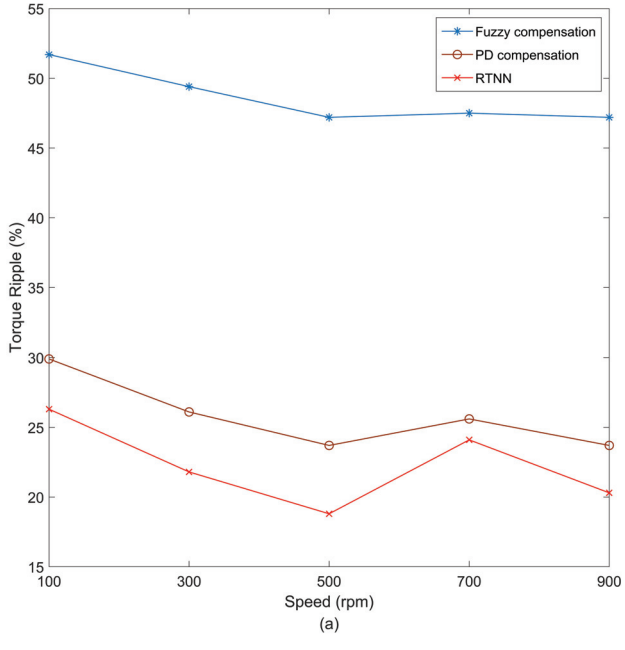

Figure 12. *Cont.*

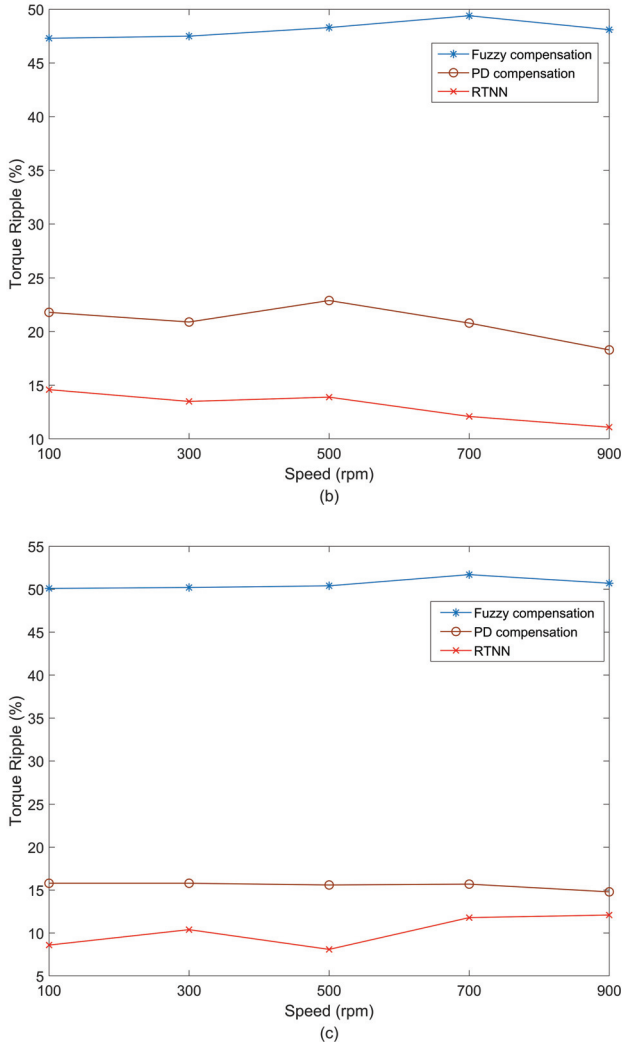

Figure 12. Torque ripple compare under different speeds with (**a**) 1 Nm torque load, (**b**) 2 Nm torque load, and (**c**) 5 Nm torque load.

5. Conclusions

To reduce the torque ripple in the SRM, this paper proposes an online neural network based on the TSF method that adjusts the reference torque online. Considering the periodic relationship between the fluctuation of torque ripple and the rotor angle, the implicit function of RTNN is directly related to the rotor angle, and the center point of the implicit function is set according to the current characteristics of SRM. Therefore, the one-step adjustment of RTNN can better suppress the torque ripple. Compared with the fuzzy torque compensation and PD current compensation methods, it is found that the torque ripple is effectively reduced under different loads and speeds.

The RTNN algorithm proposed in this paper can optimize the reference torque in one step, requiring high angle measurement accuracy. In future research, RTNN can be developed into a recurrent neural network in which the optimized value of the previous

cycle can be used to optimize the next motorcycle. Therefore, online iterative optimization can be realized, and the effect will be further improved.

Author Contributions: Conceptualization, B.J.; Data curation, B.J.; Formal analysis, B.J., X.D. and Z.L.; Investigation, B.J., Z.L. and J.J.; Methodology, B.J. and X.D.; Software, B.J., Z.L. and J.J.; Supervision, X.D., Z.L. and J.J.; Writing—original draft, B.J.; Writing—review and editing, X.D., Z.L. and J.J. All authors have read and agreed to the published version of the manuscript.

Funding: This work was financially supported partly by the National Natural Science Foundation of China under Grant 61863008 and Grant 62263009 and partly by the Fundamental Ability Enhancement Project for Young and Middle-aged University Teachers in Guangxi Province under Grant 2021KY0801.

Institutional Review Board Statement: Not applicable.

Informed Consent Statement: Not applicable.

Data Availability Statement: Not applicable.

Conflicts of Interest: The authors declare no conflict of interest.

References

1. Bostanci, E.; Moallem, M.; Parsapour, A.; Fahimi, B. Opportunities and Challenges of Switched Reluctance Motor Drives for Electric Propulsion: A Comparative Study. *IEEE Trans. Transp. Electrif.* **2017**, *3*, 58–75. [CrossRef]
2. Castano, S.M.; Bilgin, B.; Lin, J.; Emadi, A. Radial forces and vibration analysis in an external-rotor switched reluctance machine. *IET Electr. Power Appl.* **2017**, *11*, 252–259. [CrossRef]
3. Ahn, J.-W.; Lukman, G.F. Switched reluctance motor: Research trends and overview. *CES Trans. Electr. Mach. Syst.* **2018**, *2*, 339–347. [CrossRef]
4. Gan, C.; Wu, J.; Sun, Q.; Kong, W.; Li, H.; Hu, Y. A Review on Machine Topologies and Control Techniques for Low-Noise Switched Reluctance Motors in Electric Vehicle Applications. *IEEE Access* **2018**, *6*, 31430–31443. [CrossRef]
5. Fang, G.; Scalcon, F.P.; Xiao, D.; Vieira, R.P.; Gründling, H.A.; Emadi, A. Advanced Control of Switched Reluctance Motors (SRMs): A Review on Current Regulation, Torque Control and Vibration Suppression. *IEEE Open J. Ind. Electron. Soc.* **2021**, *2*, 280–301. [CrossRef]
6. Mikail, R.; Husain, I.; Sozer, Y.; Islam, M.S.; Sebastian, T. A Fixed Switching Frequency Predictive Current Control Method for Switched Reluctance Machines. *IEEE Trans. Ind. Appl.* **2014**, *50*, 3717–3726. [CrossRef]
7. Xu, A.; Shang, C.; Chen, J.; Zhu, J.; Han, L. A New Control Method Based on DTC and MPC to Reduce Torque Ripple in SRM. *IEEE Access* **2019**, *7*, 68584–68593. [CrossRef]
8. Shang, C.; Xu, A.; Huang, L.; Chen, J. Flux linkage optimization for direct torque control of switched reluctance motor based on model predictive control. *IEEJ Trans. Electr. Electron. Eng.* **2019**, *14*, 1105–1113. [CrossRef]
9. Li, X.; Shamsi, P. Model Predictive Current Control of Switched Reluctance Motors With Inductance Auto-Calibration. *IEEE Trans. Ind. Electron.* **2016**, *63*, 3934–3941. [CrossRef]
10. Valencia, D.F.; Tarvirdilu-Asl, R.; Garcia, C.; Rodriguez, J.; Emadi, A. A Review of Predictive Control Techniques for Switched Reluctance Machine Drives. Part I: Fundamentals and Current Control. *IEEE Trans. Energy Convers.* **2021**, *36*, 1313–1322. [CrossRef]
11. Li, H.; Bilgin, B.; Emadi, A. An Improved Torque Sharing Function for Torque Ripple Reduction in Switched Reluctance Machines. *IEEE Trans. Power Electron.* **2019**, *34*, 1635–1644. [CrossRef]
12. Xia, Z.; Bilgin, B.; Nalakath, S.; Emadi, A. A New Torque Sharing Function Method for Switched Reluctance Machines with Lower Current Tracking Error. *IEEE Trans. Ind. Electron.* **2020**, *68*, 10612–10622. [CrossRef]
13. Xia, Z.; Fang, G.; Xiao, D.; Emadi, A.; Bilgin, B. An Online Torque Sharing Function Method Involving Current Dynamics for Switched Reluctance Motor Drives. *IEEE Trans. Transp. Electrif.* **2022**. [CrossRef]
14. Rana, A.K.; Raviteja, A. A Mathematical Torque Ripple Minimization Technique Based on Nonlinear Modulating Factor for Switched Reluctance Motor Drives. *IEEE Trans. Ind. Electron.* **2021**, *69*, 1356–1366. [CrossRef]
15. Zhang, Z. Sensorless Back EMF Based Control of Synchronous PM and Reluctance Motor Drives—A Review. *IEEE Trans. Power Electron.* **2022**, *37*, 10290–10305. [CrossRef]
16. Lopac, N.; Bulić, N.; Vrkić, N. Sliding Mode Observer-Based Load Angle Estimation for Salient-Pole Wound Rotor Synchronous Generators. *Energies* **2019**, *12*, 1609. [CrossRef]
17. Dong-Hee, L.; Jianing, L.; Zhen-Guo, L.; Jin-Woo, A. A Simple Nonlinear Logical Torque Sharing Function for Low-Torque Ripple SR Drive. *IEEE Trans. Ind. Electron.* **2009**, *56*, 3021–3028. [CrossRef]
18. Song, S.; Hei, R.; Ma, R.; Liu, W. Model Predictive Control of Switched Reluctance Starter/Generator With Torque Sharing and Compensation. *IEEE Trans. Transp. Electrif.* **2020**, *6*, 1519–1527. [CrossRef]

19. Ye, J.; Bilgin, B.; Emadi, A. An Offline Torque Sharing Function for Torque Ripple Reduction in Switched Reluctance Motor Drives. *IEEE Trans. Energy Convers.* **2015**, *30*, 726–735. [CrossRef]
20. Ye, J.; Bilgin, B.; Emadi, A. An Extended-Speed Low-Ripple Torque Control of Switched Reluctance Motor Drives. *IEEE Trans. Power Electron.* **2015**, *30*, 1457–1470. [CrossRef]
21. Changhwan, C.; Seungho, K.; Yongdae, K.; Kyihwan, P. A new torque control method of a switched reluctance motor using a torque-sharing function. *IEEE Trans. Magn.* **2002**, *38*, 3288–3290. [CrossRef]
22. Xue, X.D.; Cheng, K.W.E.; Ho, S.L. Optimization and Evaluation of Torque-Sharing Functions for Torque Ripple Minimization in Switched Reluctance Motor Drives. *IEEE Trans. Power Electron.* **2009**, *24*, 2076–2090. [CrossRef]
23. Mir, S.; Elbuluk, M.E.; Husain, I. Torque-ripple minimization in switched reluctance motors using adaptive fuzzy control. *IEEE Trans. Ind. Appl.* **1999**, *35*, 461–468. [CrossRef]
24. Song, S.; Huang, S.; Zhao, Y.; Zhao, X.; Duan, X.; Ma, R.; Liu, W. Torque Ripple Reduction of Switched Reluctance Machine with Torque Distribution and Online Correction. *IEEE Trans. Ind. Electron.* **2022**. [CrossRef]
25. Jing, B.; Dang, X.; Liu, Z.; Long, S. Torque Ripple Suppression of Switched Reluctance Motor Based on Fuzzy Indirect Instant Torque Control. *IEEE Access* **2022**, *10*, 75472–75481. [CrossRef]
26. Sahoo, N.C.; Xu, J.X.; Panda, S.K. Low Torque Ripple Control of Switched Reluctance Motors Using Iterative Learning. *IEEE Power Eng. Rev.* **2001**, *21*, 66–66. [CrossRef]
27. Zhu, Z.Q.; Lee, B.; Huang, L.; Chu, W. Contribution of Current Harmonics to Average Torque and Torque Ripple in Switched Reluctance Machines. *IEEE Trans. Magn.* **2017**, *53*, 1–9. [CrossRef]
28. Mikail, R.; Husain, I.; Sozer, Y.; Islam, M.S.; Sebastian, T. Torque-Ripple Minimization of Switched Reluctance Machines through Current Profiling. *IEEE Trans. Ind. Appl.* **2013**, *49*, 1258–1267. [CrossRef]
29. Reddy, B.P.; Vemula, J.R.; Keerthipati, S. Torque ripple minimisation of switched reluctance motor using sense coils. *IET Electr. Power Appl.* **2020**, *14*, 614–621. [CrossRef]
30. Ma, M.; Ling, F.; Li, F.; Liu, F. Torque ripple suppression of switched reluctance motor by segmented harmonic currents injection based on adaptive fuzzy logic control. *IET Electr. Power Appl.* **2020**, *14*, 325–335. [CrossRef]
31. Cheng, H.; Chen, H.; Yang, Z.; Huang, W. Braking Torque Closed-Loop Control of Switched Reluctance Machines for Electric Vehicles. *J. Power Electron.* **2015**, *15*, 469–478. [CrossRef]
32. Ro, H.-S.; Lee, K.-G.; Lee, J.-S.; Jeong, H.-G.; Lee, K.-B. Torque ripple minimization scheme using torque sharing function based fuzzy logic control for a switched reluctance motor. *J. Electr. Eng. Technol.* **2015**, *10*, 118–127. [CrossRef]
33. Narendra, K.S.; Parthasarathy, K. Identification and control of dynamical systems using neural networks. *IEEE Trans. Neural Netw.* **1990**, *1*, 4–27. [CrossRef] [PubMed]
34. Hoai, H.-K.; Chen, S.-C.; Chang, C.-F. Realization of the Neural Fuzzy Controller for the Sensorless PMSM Drive Control System. *Electronics* **2020**, *9*, 1371. [CrossRef]
35. Rahman, K.M.; Gopalakrishnan, S.; Fahimi, B.; Rajarathnam, A.V.; Ehsani, M. Optimized torque control of switched reluctance motor at all operational regimes using neural network. *IEEE Trans. Ind. Appl.* **2001**, *37*, 904-913. [CrossRef]
36. Cao, G.; Chen, N.; Huang, S.; Xiao, S.; He, J. Nonlinear Modeling of the Flux Linkage in 2-D Plane for the Planar Switched Reluctance Motor. *IEEE Trans. Magn.* **2018**, *54*, 1–5. [CrossRef]
37. Zhang, Z.; Rao, S.; Zhang, X. Performance prediction of switched reluctance motor using improved generalized regression neural networks for design optimization. *CES Trans. Electr. Mach. Syst.* **2018**, *2*, 371–376. [CrossRef]
38. Dang, X.; Shi, Y.; Peng, H. Torque–flux linkage recurrent neural network adaptive inversion control of torque for switched reluctance motor. *IET Electr. Power Appl.* **2020**, *14*, 1612–1623. [CrossRef]

applied sciences

MDPI

Review

A Review of Innovative Electromagnetic Technologies for a Totally Artificial Heart

Mauro Andriollo, Enrico Fanton and Andrea Tortella *

Department of Industrial Engineering, University of Padova, Via Venezia, 1, 35131 Padova, Italy
* Correspondence: andrea.tortella@unipd.it; Tel.: +39-049-8277568

Abstract: A total artificial heart (TAH) represents a challenge in medical science to provide a survival perspective for patients with severe cardiac problems. Although cardiac transplantation represents the optimal therapeutic solution for end-stage heart failure, its application is limited by organ shortages. However, innovative technologies that can fit the operation and constraints of a physical heart are now under experimentation, making the target of a reliable and minimally invasive TAH much closer. The electromagnetic devices involved in system supply and actuation could potentially improve patient quality of life and expectancy. The purpose of this paper is to provide an overview of the operating principle, ratings, and key performance of the main electromagnetic components, with a particular focus on actuators that emulate the pumping effect of the heart ventricles. Linear oscillating actuators are very promising for their compactness and straightforward integration; therefore, an exhaustive overview considering both the single and the dual-mover configurations is worth being carried out. Taking a cue on the projects under development and after a detailed literature investigation, the pros and cons of the different solutions are discussed with the purpose of providing a critical analysis of the state-of-the-art.

Keywords: artificial heart; linear motion; magnetic flux; permanent magnet actuators; electromagnetic design; force calculation; wireless power transmission

Citation: Andriollo, M.; Fanton, E.; Tortella, A. A Review of Innovative Electromagnetic Technologies for a Totally Artificial Heart. *Appl. Sci.* **2023**, *13*, 1870. https://doi.org/10.3390/app13031870

Academic Editor: Feng Chai

Received: 31 December 2022
Revised: 20 January 2023
Accepted: 24 January 2023
Published: 31 January 2023

1. Introduction

In case of severe cardiac problems, the only chance of long-term survival for the patient is to use a total artificial heart (TAH) or a ventricular-assisted device (VAD). VADs help the biological heart by providing mechanical circulatory support that helps the ventricles pump blood, easing the workload of the heart in patients with advanced heart failure. They are durable devices that can assist either one ventricle (left ventricular assist device, LVAD, right ventricular assistant device, RVAD) or both ventricles (biventricular assist device, BiVAD), without explanting the natural heart. Largely diffused in the market, VADs are adopted in most cases as a bridge to transplantation (BTT) for patients who present a cardiogenic shock or have heart failure refractory to medical treatment and whose myocardial function is unlikely to recover. Alternatively, they can be used as destination therapy (DT) for patients who are not eligible for heart transplantation. In this case, it is requested to support the circulation for a period of years, allowing patients to return to their normal activities. In both BTT and DT conditions, they must be lighter and smaller to allow their implantation in as many patients as possible [1–4].

Instead, the TAH is designed to completely replace an irreversibly damaged heart, provided with an internal actuation system integrated with four artificial valves that reproduce the blood pull-in/pull-out action of the natural ventricles. An auxiliary TAH (ATAH) has been proposed with the purpose to avoid complete heart removal; at the same time, it deals with the size limitation of the thoracic cavity that prevents some patients from receiving TAH or BiVAD devices [5]. The miniaturized configuration required strict design to fulfill both the hydraulic and hemodynamic performances that required further

improvements through blood flow studies in the device chambers [6]. Integration with the natural heart to obtain the appropriate blood flow could be another issue.

In addition to fulminant myocardial infarction and dilated or ischemic cardiomyopathy, TAH therapy is currently considered a therapy option in cases of infiltrative cardiomyopathies, transplant failure, and LVAD, as well as complex congenital defects. The device can be implanted inside or outside the patient's body according to the type of technology, satisfying the physiological and mechanical constraints as accurately as possible. The main ones are [7]:

- Adequate cardiac output generation;
- Adoption of biocompatible and durable materials (the complete system must last more than 5 years);
- Limited heat generation and power consumption;
- Presence of a back-up supply unit whether the main one was not available;
- Balance the systemic and pulmonary circulations despite a wide variety of hemodynamic perturbations;
- Avoid bulky and complex equipment (external driver, percutaneous drivelines, or pneumatic hose) that can limit patient survival and quality of life.

Numerous models of TAHs have been designed and implanted over the years [2,8–13]. The SynCardia TAH (SynCardia Systems; Tucson, AZ, USA) was the first TAH to be successfully used in the world. It is a partially implantable system made of two semi-rigid polyurethane ventricles [14,15]. The artificial ventricles are available in two sizes (maximum stroke volume: 70 ml and 50 ml) according to body surface area (BSA) [9]. The AbioCor®TAH (ABIOMED) was the only fully implantable, self-contained TAH to be implanted in humans that used a mechanism to equalize the pulmonary and systemic flow [16,17]. The energy converter is situated between the ventricles and contains a high-efficiency miniature centrifugal pump that operates unidirectionally to pressurize a low-viscosity hydraulic fluid. Although the device was subsequently refined to decrease its overall size, the project was discontinued because it was deemed commercially unviable and prohibitively difficult. The Aeson®CARMAT TAH is an implantable, active electrohydraulic device with a shape close to that of a human heart [18]. It is commercially available in Europe and received FDA approval for use in the US Early Feasibility Study in 2021 [19].

Today, there are few operating units involved in the development and application of such technology, despite the high need. Severe heart disease affects approximately 64 million adults and pediatric patients annually [20]. For example, in Italy, about 1041 new patients entered the transplant list in 2021, and the average attendance is approximately 3.4 years [21]. Recent reports elaborating data from more than a decade evidence some effectiveness of TAH as BTT therapy. Between implanted patients, more than 60% were successfully bridged to transplantation and approximately 80% had one-year of survival after successful BTT [22]. Between adverse pump complications, the failure is rather infrequent due to the quite mature electrical-based technology and the implementation of fault-tolerant designs. The most common complications are patient-related risk factors or issues relating to the pump-patient interface, such as acquired von Willebrand disease, bleeding complications, infection, stroke, and pump thrombosis [1].

It should be noted that actual VADs and TAHs are designed for an adult subject, whereas cardiac issues can arise even at pediatric age. To deal with such issues, the devices should be much lighter and smaller, representing a challenge for many research institutes. A recent study on the available technology for pediatric mechanical circulatory support devices (27 devices among TAHs and VADs were analyzed in detail) showed that still no pediatric pump technology satisfies the unique and distinct design constraints and requirements to support pediatric patients [23].

The purpose of this paper is to provide an overview of the most advanced electromagnetic technologies proposed in the literature for implantable TAHs. First, a detailed description of the main TAH components is provided, considering both energy transmission and electric drive technologies. The latter are analyzed by evaluating the different

pumping modes (centrifugal or axial flows) and the bearing system to support the rotor shaft. Then, different types of linear oscillating actuators (LOAs) are presented, examining in detail the configurations applying permanent magnets (PMs), which are among the best candidates to fulfill mandatory constraints on size, weight, and efficiency. The analysis mainly focuses on single-mover configurations, applicable for both VAD and TAH applications, comparing them from an overall perspective including manufacturing, installation, and performance aspects. Yet, preliminary force results related to a dual-mover LOA are reported, which is promising for a fully integrated TAH. Finally, unconventional motor configurations are also described, where challenging features, such as contactless mechanical power transmission and linear rotary actuation, can be implemented.

2. Main TAH Projects

The first experiences focus on fluid-driven (FD) TAHs actuated by pneumatic or hydraulic devices with external drivers. Figure 1a sketches a typical arrangement where the pump injects the fluid by an alternate rotating motion that is consistent with the filling and ejection of the respective blood chambers regulated by fluid valves [13]. Electropneumatic driving systems typically resemble such an approach. The Berlin Heart project that led to EXCOR ®VAD was one of the first experiences of paracorporeal systems [1,24]. A compressor generates the pulsatile air flow driven in a forward/reverse mode by the electric motor. The pumped, air conveyed by cannulas to the heart chambers, acts on multi-laminar diaphragms separating the air and blood chambers.

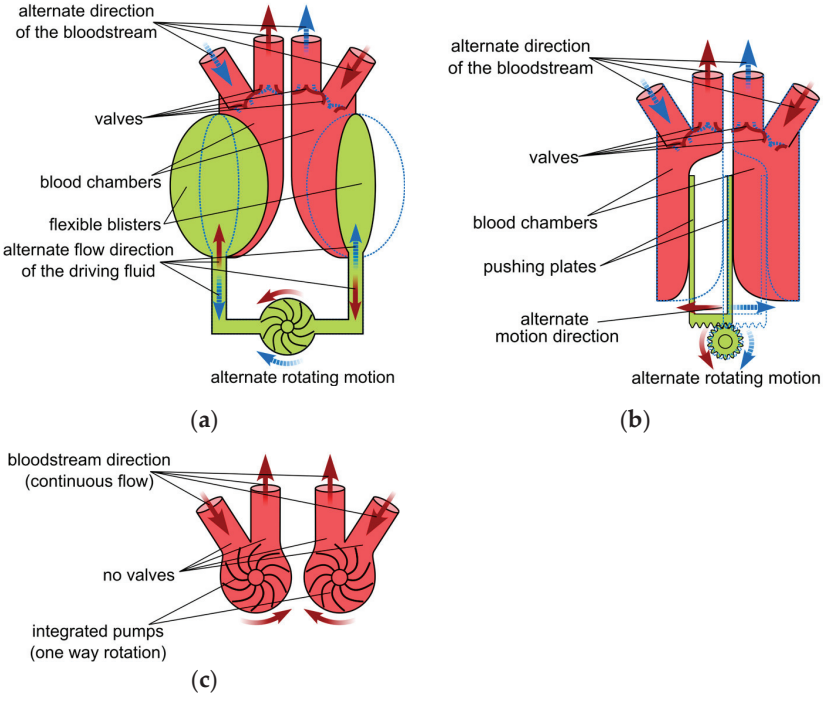

Figure 1. Main TAH types; (**a**) fluid driven; (**b**) electromechanical driven; and (**c**) continuous flow with integrated pump.

Syncardia TAH-t operates according to a similar principle. Pneumatic drivelines connect the two ventricle chambers to an external pneumatic driver system, allowing coordinated but independent pumping with control over various driving parameters [14]. In [25], a small pneumatic actuator is proposed that can be used as an extracorporeal

biventricular assist device. A brushless direct current (BLDC) electric motor drives a ball screw system clockwise or counterclockwise, moving the ball screw system and then generating a two-way airflow through the airline connectors. Two air chambers located at the opposite ends of the moving unit are connected to pusher plates. If the external blood sacs are connected to the airline connectors of the actuator, the two-way airflow is converted to a blood pumping force that pushes and pulls flexible diaphragms in the blood sacs. Although this is based on well-assessed technology, this configuration has several drawbacks, such as its bulky arrangement, noisy operation, need for percutaneous air pressure hoses, poor durability, lack of self-regulatory feedback from the circulatory system, and reduced blood compatibility. Heavily affecting the patient's quality of life, it can therefore be considered a bridging solution prior to biological heart transplantation.

A similar apparatus based on FD was implemented in the Carmat TAH (Aeson), where the external pneumatic drive is replaced by an internal electrical motor supplied by an abdominal cable connected to external batteries [1,2,18]. The main difference with the AbioCor TAH consists of the presence of four pericardial biomembranes. In every chamber, the flexible membrane acts as a divider and keeps hydraulic fluid and blood on each side. The electric motor-pump group pushes the fluid into and out of the chambers, making the membrane deflect and displace the blood. Four biological valves at the inlet and outlet provide unidirectional pulsatile blood flow. Embedded electronics, microprocessors, and integrated sensors allow auto-regulated responses for the physiological needs of the patient [19]. The large size and mass (1 kg) of the system as well as the need for a portable external power supply system continuously connected to the prosthesis represent its main disadvantages.

Hand in hand with the development of innovative biocompatible materials for membranes and pumping components [26,27], the introduction of more advanced electromagnetic devices in recent TAH projects significantly improved ergonomics, compactness, and control capability. Such features allow for a more accurate heart operation and limit the impact on daily life at the same time. Among the electromagnetic components, transcutaneous energy transmission (TET) systems represent a significant improvement, allowing the implant of long-lasting, small-size rechargeable batteries, paving the way for the prospective implantation of several types of electrical devices together with the main drive.

The first project to implement such technologies was the AbioCor TAH; the internal components consist of [17]:

- The Li-ion battery (discharge time $\approx$ 20 min);
- The controller that monitors all the implant components and transmits device performance data using radio frequency telemetry;
- The TET coil that receives high-frequency power that is transmitted across the skin from the external TET coil to recharge the internal battery;
- The electromechanical converter that includes a high-efficiency, high-speed centrifugal pump driven by an electric motor; it adjusts the speed according to the different resistances requested to emulate the systolic and diastolic phases;
- A switching valve used to alternate the direction of the hydraulic flow between the left and right pumping chambers.

Even a Japanese project developed an electrohydraulic total artificial heart (EHTAH) system using a TET, a transcutaneous optical telemetry system (TOTS) and an internal battery, which supplies the system for 40 minutes/day [28]. The blood pump actuator is composed of a diaphragm-type blood pump, consisting of a blood chamber and an oil chamber, and a reciprocating electrohydraulic actuator that creates the oil pressure used to drive the diaphragm at alternating intervals. In a revised version, the blood pump and the actuator are connected directly without going through the oil conduit by virtue of the miniaturization of the actuator and the blood pump. Despite the significant volume reduction (500 ml), the pump unit mass was approximately 2.5 kg.

Figure 1b shows the integration of the electromagnetic actuator as a replacement for the fluid pump in an electromechanical (EM) TAH [13]. It exerts a push–pull action on the plates

applied to the membrane separating two blood chambers. The linear oscillating motion is accomplished by converting the motor torque using a rotating to linear motion conversion (e.g., by a lead screw transmission) or by a linear electromagnetic actuator directly coupled to the plates. The latter solution would enhance the system reliability and efficiency, even if it requires high force density actuators. As an example, the ReinHeart project [29–32] proposes a linear oscillating actuator (LOA) that integrates two movers acting separately on each ventricle. A similar approach is adopted in a project under development at the University of Padova [33,34]. Innovative bioengineered tissues are tested to exert the pumping action of artificial ventricular membranes, separating electromagnetic LOA from blood flow at the same time. This solution prevents blood contamination and overcomes mechanical wear and reliability issues related to the rotary to linear motion conversion and likely to the presence of springs and of other auxiliary mechanical devices.

The development of more compact and unconventional magnetic configuration (e.g., axial type) enabled the conceiving of novel configurations, easing the pump integration, and enabling bearingless arrangements. As an example, the continuous-flow (CF) TAH (Figure 1c) is based on two separate blood pumps acting as a biventricular-assisted device [13]. A single or double electric motor directly drives the pumps. It operates through a continuous rotating motion in one direction without requiring valves or additional hydraulic chambers. Devices adopting this principle mock the natural heartbeat by using different speed values managed by the motor controller. The BiVACOR project represents a typical implementation of such an arrangement [35–37]. A single axial-flux motor drives the left and right impeller blades of a centrifugal pump, using actively controlled axial magnetic bearings. The axial position of the rotor is adjusted by the signal provided by suitable sensors to control blood flow in the left and right pump vanes.

The importance of innovative technologies, especially based on the introduction of novel electromagnetic devices, is recognizable in Table 1, which reports the main data of some significant TAH projects, approved or in the development stage. All projects except the SinCardia are electrically driven by an implanted motor, allowing for better control capability, reliability, and compactness of the supply system than the pneumatic actuator. Despite the rather scattered distribution and some difficulty in retrieving reliable data, the CF schemes indicatively appear to be the most convenient for the weight and volume, allowing similar performances of the other type at the same time. The only exception is related to the SynCardia TAH, which is, however, penalized by the heavy external equipment. Data on the input power and overall efficiency are more difficult to retrieve and are hardly comparable due to the different supply equipment. Moreover, such values are heavily affected by the load condition. However, percutaneous systems generally exhibit higher efficiency than TET, since the supply of implanted electrical and electronic devices by direct connection implies fewer losses than in contactless transcutaneous power transfer.

Table 1. Main data from approved or under development TAH projects.

TAH	Type	Mass (g)	Volume (mL)	Power Supply	Output (l/min)	Input Power (W)	Total Efficiency (%)
Aeson CARMAT [18]	FD	900	750	Percutaneous	2–9	N.A.	N.A.
BiVACOR [35–37]	CF	650	N.A.	Percutaneous	3–12	15.5	N.A.
Cleveland [38,39]	CF	486	160	Percutaneous	7.4	12.9	13.3
OregonHeart [40]	CF	N.A.	130	Percutaneous	7.5	10.0	17.5
Realheart [41]	EM	800	1.790	TET	2.7–8.2	N.A.	N.A.
ReinHeart [29–32]	EM	940	550	TET	5.5	12.5	10
RollingHeart [42]	EM	N.A.	704	Percutaneous	5.3	14.0	14.1
SynCardia 70cc [14]	FD	240	400	Percutaneous	9.5	N.A.	N.A.
HybridHeart [43]	FD	<900	N.A.	TET	2–8	34	6.7

3. TAH Electromechanical Components

The results of the different projects demonstrate that proper TAH operation requires a fully coordinated interaction among the various devices devoted to the supply, control, actuation, and management of all operating phases with a very high level of reliability and efficiency. This section aims to describe the components and their main functions and performances, considering a typical TAH provided with a TET supply system [44] (Figure 2).

In case of percutaneous supply, the external power source supplies the implanted one or the actuation system by cables and connectors (driveline). The components are:

- The heart unit (A), consisting of the integrated actuator and pumps or membranes installed in suitable chambers, possibly provided with valves;
- An external battery pack (B) to supply the external user interface (D), which collects information about the performance of the pumps and of the TET system and tunes the system parameters. A portable lithium-ion battery-type (Li-ion) can power the TAH from 4 to 8 h;
- An implanted auxiliary battery (C), acting as a backup unit in case of the failure of the TET system, usually consisting of a Li-ion battery with a nominal voltage of 13 to 24 V, and with enough capacity to ensure 60 minutes of nominal operation [32,44];

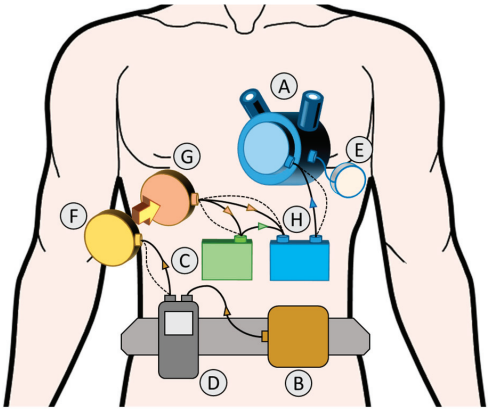

Figure 2. Typical layout of the devices forming a TET supplied TAH; solid lines: power connections; and dotted lines: data transmission cables.

- The TET system, composed of the external transmitting coil (F), which in practice is the primary winding of a transcutaneous high-frequency transformer, whose secondary is the implanted receiving coil (G). The electric power collected by G via the inductive coupling enables recharging of the implanted battery (C) and/or supplies the control circuit of the heart unit (F). A bidirectional data exchange is also present, to monitor and adjust the operating condition of the implanted devices;
- The compliance chamber (E), where blood accumulates to avoid overpressures in the ventricles and to facilitate pumping action;
- The microprocessor-based control unit (H), which regulates the operation mode of the heart unit and checks its status. Usually, the closed-loop architecture ensures adequate control robustness, tuning the control strategy according to the parameters provided by the communication cables (from the TET or heart unit sensors).

In the following section, some details of the most important TAH components are given, with particular attention on the up-to-date electromagnetic devices with enhanced performance controllability applied in recent TAH projects.

3.1. Motor Pumps and Bearings

The pumping unit for FD- and CF-TAH must be compact and efficient, manufactured with blood-compliant materials (e.g., polished titanium surfaces) and capable of minimizing common complications, such as hemolysis and thromboembolism [12]. Their design must satisfy different requirements for the operation of the LV and the RV. The pressure volume diagrams of a typical cardiac cycle show that the LV has approximately five times higher pressure during the systolic phase than the RV (140 mmHg vs. 30 mmHg); furthermore, the diastolic phase is much less demanding, as it requires near-zero pressure conditions throughout the stroke volume [45].

The first generation of implantable artificial hearts was pulsatile blood pumps, which can generate pulsatile flow rates and pressures that drive a certain amount of blood with a stroke. A sac-type squeezes and expands a polymer sac pneumatically (compressed air) or hydraulically (silicon oil). Their large size, heavy weight, and large external drive unit that limit patient mobility characterize these pumps. Differently, a pusher plate-type squeezes and expands a polymer sac with hard plates driven by electric motor/gear mechanism or by an electromagnet [46,47].

Continuous-flow pumps are mainly considered as the second generation of MCS devices, providing better efficiency and reliability. Centrifugal pumps (CFPs) or axial flow pumps (AFPs) are more commonly adopted (Figure 3) [48]. Although originally conceived for LVADs, they can also be implanted to drive TAHs. The hemocompatibility with the contact materials of the impeller/housing (biocompatible titanium and polyurethane) is generally very good without worsening the hydraulic performances. Biocompatible compounds encapsulate the electric motor to avoid any contact with possible toxic materials.

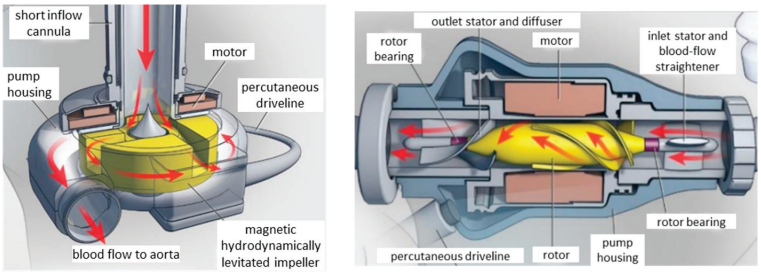

(**a**) (**b**)

Figure 3. Pump types for LVAD and TAH applications; (**a**) centrifugal flow with a magnetic bearing for impeller suspension; and (**b**) axial flow with a conventional bearing. Republished with permission of Massachusetts Medical Society.

Typically, they operate to convey a constant flow, varying the motor speed [49]. CFPs apply centrifugal force to suck the blood from the inlet and pump it tangentially to the pump housing through the outlet. In contrast, AFPs drive blood flow, both rotationally and axially, conveying it in line with the shaft axis. The CFPs are recognized to benefit from several features with respect to AFPs, some of which are worth mentioning:

- Linear dependence of the output flow on the motor current across the full range of the operating pump flow, enabling the pump operation to be monitored and controlled straightforwardly by means of the current value;
- The flat head curve (greater change in the flow rate for any given pressure gradient across the inlet and outlet of the pump) that enables the mimicking of the pulsatile flow variation between diastole and systole. Such a feature also provides a more accurate flow estimation from the pump speed and power;

- Easier integration with axial flux PM motors, resulting in a more compact rotor design, due to the disk-shaped configuration and the direct pump impeller-PM rotor coupling [36,50];
- Easier implementation of magnetic bearing suspension, allowing a larger gap between the rotor and the stator and improving reliability (absence of lubrication and sealing) and efficiency (no friction losses).

Figure 4 shows the different magnetic bearing configurations for the CFPs. In Figure 4a, the hydrodynamic thrust generated by the blood pressure on the tapered surface of the impeller combines with the alignment force acting on the fixed and rotating PMs, compensating the dependence of the magnetic force on the rotor position. The electromagnetic bearings in Figure 4b couple passive and active control actions to stabilize the rotating parts along all degrees of freedom (DOFs).

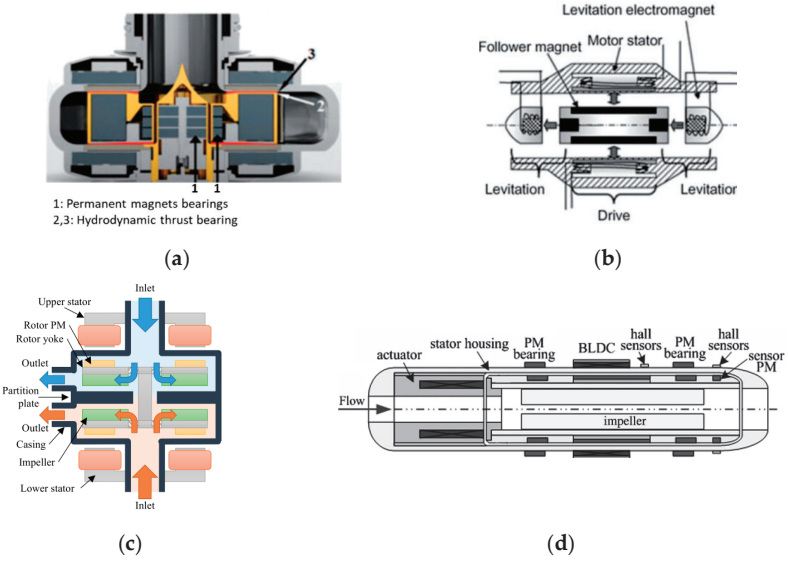

Figure 4. Magnetic bearings for blood pumps; (**a**) PM assisted by hydrodynamic thrust bearing; (**b**) electromagnetic bearings; (**c**) bearingless axial flux motor for CFPs; and (**d**) bearingless BLDC motor for CFPs. Republished with permission of IEEE.

However, the regulation of the bearing coil current by active control requires axial and/or radial gap sensors. Figure 4c shows how coupling the pump to a bearingless motor in a CF-TAH leads to a more compact design: there are eight PMs on each rotor side, facing two distinct concentrated stator windings, one of which is for motoring and axial control and the other for tilt control, thus providing full active control for all DOFs [51]. This configuration ensures a relatively large clearance between the rotating and static parts and the accurate rotor-impeller position control. The latter feature enables the flow modulation through the two ventricles to meet the different requirements of the LV and RV [36].

Unlike CFPs, the flow in AFPs cannot be accurately evaluated without a flow sensor; moreover, at a lower flow rate, the risk of tissue damage of the tissues around the inlet channel increases as a result of a higher inlet suction. Due to the high axial force component, the AFP impeller requires an adequate support bearing, whose reliability and efficiency are critical issues. Furthermore, it is difficult to reproduce natural pulsation unless a suitable rotation speed control operates the thrust modulation.

Alternatively, an oscillating pushing plate driven by a suitable-shaped bearing mounted on the motor shaft can replace the impeller [52]. Another mechanical arrangement involves the adoption of an undulation pump composed of a pump housing with a partition be-

tween the inlet and outlet ports, a disk with a slit located in the partition of the housing, an undulation shaft at the center of the pump, and a pair of seal membranes between the disk and the housing to seal the shaft from the pump room [53]. The mechanism of the undulation shaft prevents the rotation of the disk and converts the rotation of the shaft to the wave motion of the disk. A close line between the disk and the housing enables blood squeezing from the inlet to the outlet of the pump. A TAH requires two of such units that need the implementation of a rather sophisticated hierarchical control protocol [54].

More conveniently, electromagnetic bearings can compensate for axial and radial force components, as in the implementation described in Figure 4d [55]. The impeller is mounted on the inner surface of the hollow rotor, and the suspension of the rotor is based on two passive radial magnetic bearings at the ends of the impeller and an electromagnetic actuator to control the axial position. The main issue is the presence of uncompensated oscillations in the radial directions related to the actuator axial control.

Based on the implementation of magnetic bearings, a novel design concept has been proposed for the Dragon Heart at Drexel University [56]. The hybrid design integrates two blood pumps for pediatric patients, in which an axial pump impeller supports the right side of the heart and the pulmonary circulation, and a centrifugal pump impeller supports the left side of the heart and the systemic circulation (Figure 5). By such an arrangement, they share a common rotational axis with distinct fluid domains. Magnetic bearings lift the rotating impeller inside the pump housing and facilitate much wider clearances between the rotating and stationary domains, thus reducing fluid shear stress levels.

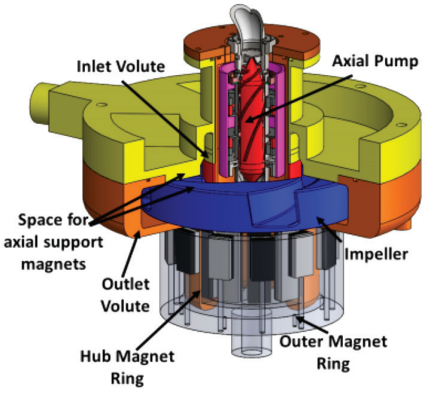

Figure 5. Design concept of the Dragon Heart pediatric TAH integrating an axial and centrifugal pump with magnetically levitated impellers [56]. Republished with permission of John Wiley and Sons.

The design is shaftless and guided by two magnetically coupled PM rings with radial magnetization: one is placed on the extended hub physically coupled to the impeller (hub PM ring), the other one is driven by an external BLDC motor (outer PM ring). The passive radial suspension denoted some limitations in combination with the hydrodynamic bearing, as high shear stresses occurred in areas with narrow fluid gaps, resulting in wear problems on the interior of the inner magnet ring. The implementation of a fully active magnetic suspension was therefore advised for future development.

An alternative to CFPs and AFPs is represented by the helical flow pump (HFP) proposed in [57], which reproduces the amplitude and frequency variations of physiological pulsation by modulating the rotation speed without requiring complex bearings due to the hydrodynamic impeller suspension. However, a minimum rotational speed is required to maintain an adequate clearance between the rotor and stator; moreover, the suitably trapezoid-shaped voltage waveform prevents instability arising due to eccentric force.

3.2. Electrical Drive

According to the different projects, the electric drive implemented in a TAH can be broadly divided into speed controller-based and position (or force) controller-based arrangements. The speed control is applied to reproduce the operation for both continuous and pulsatile flow. Three-phase or multi-phase motors are generally supplied by a voltage source inverter, often operated by space vector modulation. The PID speed controller elaborates the speed signal generated by Hall-effect sensors or sensorless, estimated in more sophisticated microcontroller-based strategies (e.g., field orientation) [36]. In the latter case, a more precise and reliable control can be achieved, for instance, by providing an active braking control to decelerate the impeller motor and then allowing energy recovery during the braking operation.

The elaboration of appropriate speed profiles enables the achievement of the pulsatile effect with a satisfactory hemodynamic response. Generally, they consist of roughly square waveforms of the desired heartbeat frequency that oscillate between two limit values. As an example, in [36] a mean aortic pressure of ≅102 mmHg and a maximum pressure slope of ≅240 mmHg/s are achieved at 30 bpm by varying the speed between 2300 and 2900 rpm. However, control parameters must be tight to the proper values, since in vivo experiments show that even slight alterations (i.e., short-term speed overshoots or control delays) can significantly alter pump outflow.

A specific controller must be expressly designed to drive the active magnetic suspension of the rotor/impeller shaft, generally operating along the axial and possibly also the radial directions, even if a passive bearing (e.g., hydrodynamic journal bearing) can be effective in controlling the radial position. In an application based on an axial flux motor, three eddy current sensors detect the axial position and send their signals to the PID controllers [35]. Accurate coordination between the controllers of the axial position and of the motor speed enables the regulation of the LV and RV outflow. The bearing control must be tuned to cope with both hydraulic forces, depending on the motor speed and the rotor position, and the inherent magnetic attractive force between the PMs and the iron core of the motor. As an example, the power to supply the windings of the hybrid PM-electromagnet bearing for the maximum axial displacement of ±0.15 mm at a speed of 2200 rpm is limited to ≅10 W. The overall consumption under the same conditions is below 15 W [35].

In the LOA configuration proposed in [32], each motor coil is generally powered by a separate DC/DC full-bridge converter, with a PWM current control and a relatively low supply voltage (between 12 V and 20 V), adequate for the low coil inductance and back-e.m.f.. The drive control enforces the predefined reference sinusoidal motion using a sensor feedback signal giving the position of the pusher plates, adjusting the supply current value to the required thrust, depending, in turn, on the blood outlet back pressure and on the pump speed. A proper motor design and an effective control strategy (e.g., field orientation) should aim to maximize the thrust/current ratio, i.e., to minimize the losses/output energy ratio, in order to avoid overheating and to extend the battery range. The electromagnetic cogging force could possibly contribute to the thrust by taking advantage of a suitable iron core design.

3.3. Energy Transmission

The TET unit enables the elimination of the percutaneous cable connection to supply the implanted equipment. Figure 6a outlines a basic layout of the external and internal circuit components involved in both power and information transmission [58,59]. The external AC source consists of a battery and a high-frequency full-bridge MOSFET inverter. Biologic tissues impose a large gap between the transmitting and receiving coils (typically g =5–15 mm), which require high-frequency operation (≥100 kHz) and ferromagnetic coil casing, also for magnetic field confinement [60]. Litz wires and ferrite magnetic pot cores are therefore needed to limit the electromagnetic losses.

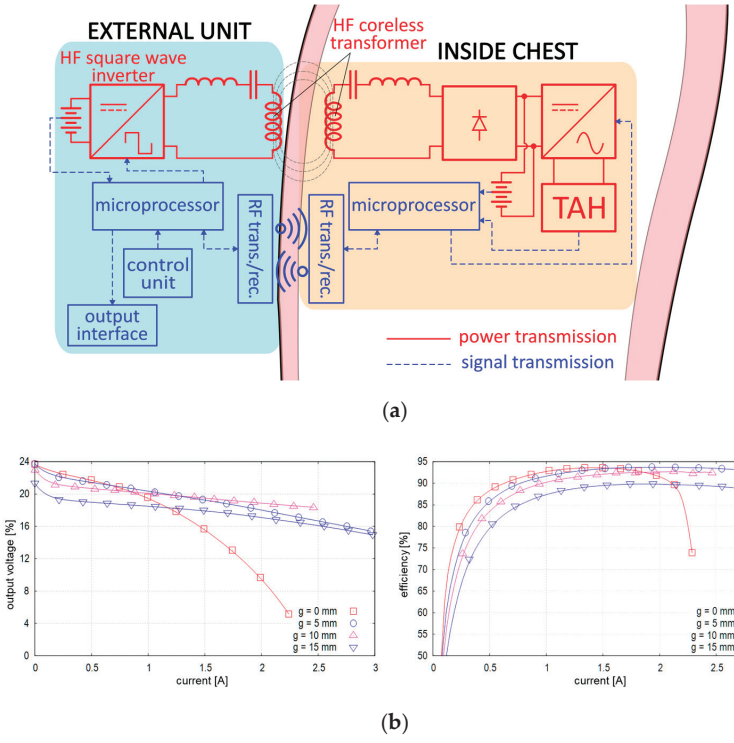

Figure 6. Layout and performances of a TET system; (**a**) scheme of the power and information circuits [59]; and (**b**) rectifier output voltage and efficiency for different air-gap values.

Using MOSFETs instead of diodes in the synchronous rectifying stage enables a remarkable reduction of conduction losses, which can be further reduced by SiC-based devices, thereby limiting the possible risks of tissue damage due to overheating. Experimental analyses of the generated waveforms showed that this converter type is less affected by deviation from the rated axial displacement (−20% variation of the output power at ±20% of the axial displacement) [61].

Figure 6b reports the typical output current/voltage characteristics for different air-gap values [60]. The voltage is stable (18 V–21 V for normal operation) for g in the 5–10 mm range; however, for $g = 0$ mm, it suddenly drops as the load increases due to the higher internal impedance. The transfer system delivers up to about 50 W, sufficient to supply the TAH during its normal operation and recharge the implanted battery at the same time. The maximum efficiency is over 90% under typical load conditions, due to properly sized series capacitors on both transformer sides compensating for leakage inductances. An integrated system that detects the temperature of the secondary coil elaborates the feedback signal of the output power, allowing one to adjust the input power in the primary coil and improving the system [59].

4. Linear Electromagnetic Actuators

Linear oscillatory actuators (LOAs) are the most promising candidates for reproducing the natural heart operation, exerting their pumping effect by the electromagnetic interaction between the m.m.f.s generated by the stator and mover components (windings or PMs). They are particularly profitable in the electromechanically driven TAH configurations shown in Figure 1b, due to the smallest amount of force transmission components and the feasibility of their complete physical separation from blood flow.

4.1. LOA Ratings

The applications of LOAs for TAH have been presented in several studies, analyzing different electromagnetic configurations and sizes, with their respective different supply characteristics and electromagnetic performances. Data collected from the literature are specifically related to single-mover TAH or LVAD applications, with the following broad ratings [62]:

- Radius/active length: 32–40 mm/20–40 mm;
- Stroke length: 8–18 mm;
- Volume: 90–180 mm^3;
- Peak force/force density (σ_f): 40–140 N/0.18–0.88 N/cm^3;
- Average LV/RV force (systolic phase): 50–70 N/15–30 N;
- Maximum values for mass/losses: 1 kg/20 W.

The different pumping force requirements evidenced by the last specification data imply distinct LOAs or additional hydraulic devices to drive both ventricles simultaneously for a full TAH operation.

4.2. PM-LOAs

Even if various potentially applicable LOA typologies could easily be borrowed from numerous short-stroke industry applications (compressors, pumps, vibrators, etc.), PM synchronous motors, regardless of the variable reluctance (VR), are the best suited to meet the requirements of high efficiency and force density for TAHs [63,64]. It is worth pointing out that the installation in a chamber separated from blood sacs avoids any contact, and then no biocompatibility issues arise with the actuator materials (e.g., PM material). Demagnetization issues can be avoided by adopting suitable NdFeB grades and PM thickness at the design stage. PM-free LOA are also considered for an LVAD actuator [65]. Their simple and inexpensive manufacturing as well as their straightforward control strategy represent significant features for possible TAH application. However, the production of high reluctance force requires a very high current density and a very small air-gap length, which is difficult to implement in miniaturized devices. As a result, σ_f tends to be too low for a TAH application. For example, the rated thrust density of the linear switched reluctance actuator analyzed in [65] is $\sigma_f \cong 0.06$ N/cm^3 at 10 A/mm^2 and with 0.2 mm air-gap length.

Tubular PM configurations are preferred because they best fit the available volume between the ventricle chambers. The most effective quadrature condition between coil m.m.f. and PM magnetic field can hardly be achieved with ordinary single-phase supply, taking into consideration the short stroke and other electromagnetic effects (e.g., longitudinal end effects, magnetic saturation, and cogging). A proper design, possibly involving the magnetic core shape, the PM magnetization pattern, and a suitable supply current switching strategy can mitigate force ripple, providing an adequate thrust average value at the same time.

PM-type LOAs can be divided into coreless moving coils (MC-LOA) and moving PMs (MM-LOA), provided or not with back iron, according to the PM magnetization pattern. In MC-LOAs, the supplied coils slide along stationary PMs, mounted on a back-iron core, or enclosed between two core flux concentrators (Figure 7a). The confinement of PM flux generally requires rather bulky cores; moreover, the moving coils should be divided into sections supplied separately with a proper sequential current control to equalize the thrust profile and limit winding losses, since the Lorenz force is proportional to the ampere-turns of the motor coil portion passed through by the PM magnetic flux [32].

In MM-LOAs, the PM mover slides alongside the stator core with a C- or E-shaped cross section, enclosing a single- or a double-coil winding. With respect to MC-LOA, the stator coil supply benefits from a faster dynamic response and lower ohmic losses. Moreover, slotted configurations can take advantage of the cogging force in the forward stroke, resulting in an effective reduction of ohmic losses, although possibly impairing the

backward stroke motion. Electromagnetic interference with other devices because of the PM flux leakage at the stroke ends and the eddy current losses in the ferromagnetic cores are other possible issues.

Alternatively, both the PMs and the coils could be placed on the stator and could interact with a passive VR mover. Such a geometry complicates small-sized stator manufacturing, and it requires very low air-gap length (0.3–0.5 mm) to enhance the modulation effect of the coil m.m.f.. However, it enables adequate thrust density and PM flux confinement. For example, in [66] a hollow-type mover is proposed that slides between two U-shaped stator rings (Figure 7b). Cogging force minimization calls for a suitable mover slotting design based on a half-period shift between the inner and outer parts. The supply of the stator coil pair by 90° phase displacement yields $\sigma_f = 0.57$ N/cm^3.

In the Vernier-type configuration, the insertion of PMs in the stator teeth slots enhances the thrust density at the expense of increased supply frequency, taking advantage of the multiplication effect of the reluctance force. In [67], the peak force using the double E-shaped stator of Figure 7c is 70 N; however, it has a significant ripple (≈30 N). The single E-shaped stator proposed in [68] enables a robust structure and a high force density by combining two different PM magnetization directions of PMs and ferromagnetic poles. The quasi-Halbach magnetization significantly enhances the thrust performance ($\sigma_f \cong 0.75$ N/cm^3) with respect to a pure radial one, halving at the same time the peak value of the cogging force.

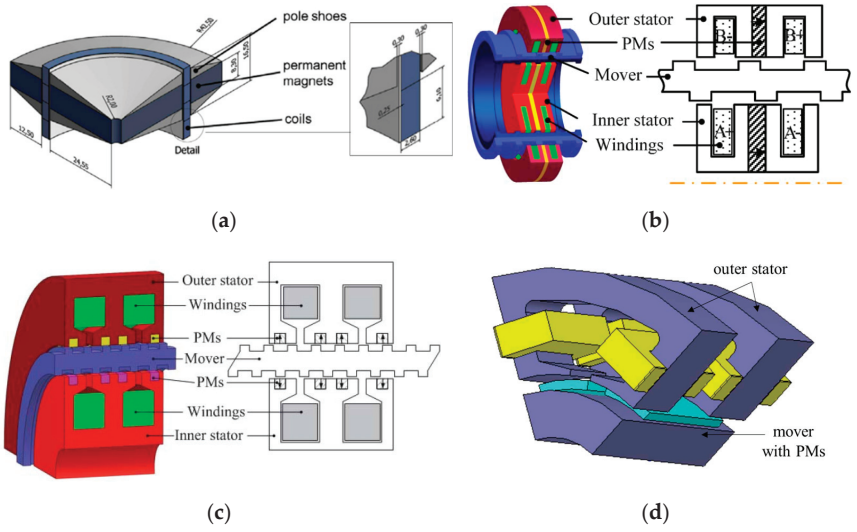

Figure 7. Examples of PM-LOA configurations; (**a**) PM stator with moving coils [30]; (**b**) double U-shaped stators with PM, windings, and VR mover [66]; (**c**) cross section of a double E-shaped stator tubular Vernier PM-LOA [67]; and (**d**) 3D schematic portion of the transverse-flux MM-LOA [69]. Republished with permission of Elsevier and IEEE.

A transverse flux configuration (Figure 7d), originally proposed for a compressor application, consists of an inner stator yoke, a concentrated armature winding enclosed between the ferromagnetic poles of two outer stators, and a six-PM mover sliding between the inner and outer stators [69]. The prevailing radial orientation of the flux lines enables the adoption of axially laminated stator yokes to reduce the eddy current losses. A single-phase sinusoidal current supply combined with the connection of the mover ends to a flexible spring gives rise to a reciprocating motion. A 100 N thrust is achieved for a 10 mm stroke length. However, the design must consider the radial forces that act on the PMs for the reliability of the system.

Despite a possible lower thrust density and an uneven thrust profile, MM-LOA are deemed to be the most convenient for the TAH application because of the easier manufacturing process and their higher suitability to comply with strict size constraints. Therefore, the main proposed configurations and related performances are discussed in the following subsections.

4.3. Single-Mover MM-LOA

According to the stator configuration, the following arrangements have been proposed:

- E-shaped stator cross section with a pair of coils supplied by opposite currents [62], [70–74];
- Single or dualrrents [71,75,76]; C-shaped stator cross section, the latter with coils supplied by opposite cu
- Stator with multiple coils to allow multiphase or fault-tolerant supply [77–79].

The latter configurations can benefit from the smooth force profile and emergency operation in case of a partial winding fault; however, the mitigation of the radial and cogging forces possibly requires slotless stator and quasi-Halbach PM magnetization, resulting in winding oversizing and higher losses due to the high equivalent air-gap.

The most common stator configurations are those with C or E shapes, combined with different types of movers, differing in the magnetization pattern, pole number, and yoke assembly. Figure 8 shows two typical configurations with the corresponding force profiles determined at constant total ampere-turns, with the outer radius, air-gap, stroke length, and ohmic losses being the same. Regarding the E-shaped stator with the interior PM (IPM) mover, the C-shaped stator with surface PM mover (Figure 8a) provides a higher peak force but suffers from higher thrust unevenness. Furthermore, the PM and mover masses are 20% and 80% higher, respectively. The optimized IPM mover provides $\sigma_f \approx 0.47$ N/cm^3.

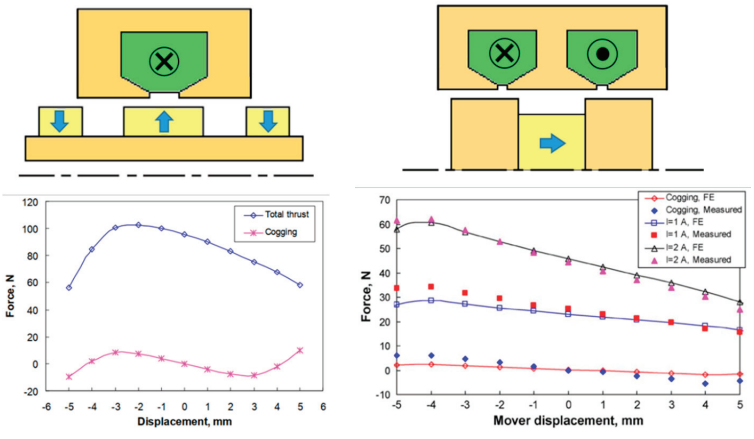

(**a**) (**b**)

Figure 8. Examples of MM-LOA and related force performances; (**a**) C-shaped stator with surface PM mover [71]; and (**b**) E-shaped stator with IPM mover [71,73] (outer radius: 32 mm, air-gap: 1 mm, and stroke: ±5 mm). Republished with permission of IEEE.

Considering additional mover PM configurations, the E-shaped configuration seems more favorable, as it limits the leakage flux along the entire stroke and yields a force density higher than that of the C-shaped one. The adoption of a quasi-Halbach type provides an even more uniform thrust profile. The application of ferromagnetic rings to the mover ends increases the average thrust, due to the higher magnetic flux [74]. On the other hand, such a design increases the mover mass and the coil inductance.

4.4. Dual-Mover MM-LOA

In general, the literature suggests integrating LOA into VAD applications, replacing the function of a single ventricle. To emulate the complete functionality of the biological heart function, the TAH must drive two distinct components. The arrangement in Figure 9a shows a dual-mover LOA enclosed in a sealed cavity between two flexible pockets, provided with non-return valves, mimicking the ventricular operation. The LOA stator interaction with two distinct movers impresses on the latter ones, reciprocating opposite synchronous motion with alternative compression and dilation of the pockets to infuse the blood flow.

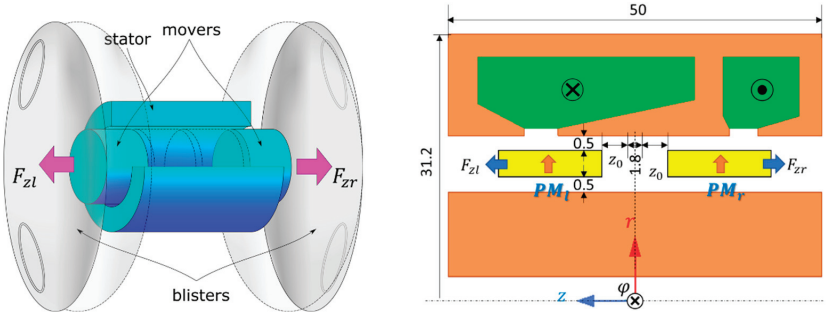

(**a**) (**b**)

Figure 9. Double-mover LOA; (**a**) working principle showing the two movers pushing the ventricular chambers; (**b**) LOA electromagnetic configuration; PM_l, PM_r: PM movers acting on the LV and RV; F_{zl}, F_{zr}: thrust acting on PM_l and PM_r; z_0: mover position with respect to the backward bound; and sizes are in mm. Republished with permission of IEEE.

Again, the tubular configuration is particularly profitable. The main features of the E-shaped stator with two PM movers (PM_l and PM_r) analyzed in [62] are:

- Identical radially magnetized NdFeB-48 PMs in a repulsive configuration;
- Two distinct coils, enclosed in the outer high permeability stator core (CoFe alloy) and supplied by reverse currents to produce opposite thrusts in the nearby movers;
- The cross sections of the LV and RV coil cross sections are proportional to the related ampere-turn $N_l I_l$ and $N_r I_r$, respectively, in turn proportioned with the corresponding rated thrust peak values $F_{zl}/F_{zr} = 70$ N/25 N;
- A fixed hollow core in the inner part to provide a return path for both the PM and winding fluxes.

High-performance magnetic materials are mandatory to satisfy the very binding limits on the overall volume (≅153 cm^3) and the active part mass (<1 kg). The moving mass is very low as well since movers have no back iron.

Figure 11 reports the thrust as a function of the mover position for different values of $N_l I_l$ and $N_r I_r$, with a maintained constant over all the stroke length (±15 mm), a maximum current density of 6 A/mm^2, and total ohmic losses of 13 W. Eddy current losses can be assumed to be negligible because of the low-frequency operation (1.3 Hz). The force profiles evidence the following aspects:

- The cogging force ($N_l I_l = N_r I_r = 0$) benefits the forward stroke for both movers;
- Inverting the LV coil supply current near the end of the stroke (see point P_1) increases the thrust, which otherwise would even become negative, producing a braking effect;
- Due to the mutual linkage between the coils, the simultaneous current inversion in both coils slightly worsens the RV thrust;
- A residual cogging force opposes the backward motion in both movers (points P_1 and $Q_{1,2,3}$), regardless of the current value.

Parametric analysis that involves the sizes of the main PM and the stator core, as well as the more convenient position z_0^* switching the current in both coils, leads to the optimized force profile shown in Figure 10.

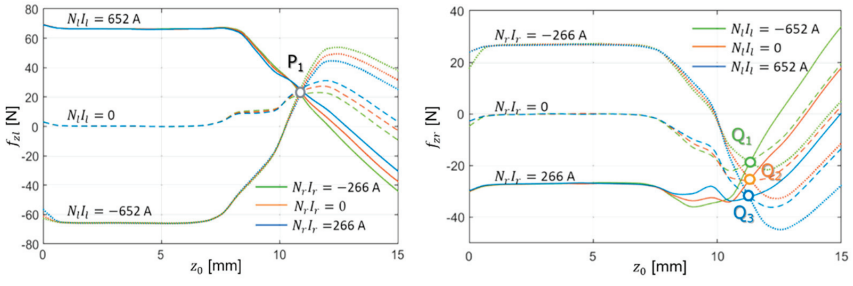

(**a**) (**b**)

Figure 10. Thrust as a function of the mover position with current switching at $z_0^* = 12.2$ mm; (**a**) LV mover; and (**b**) RV mover.

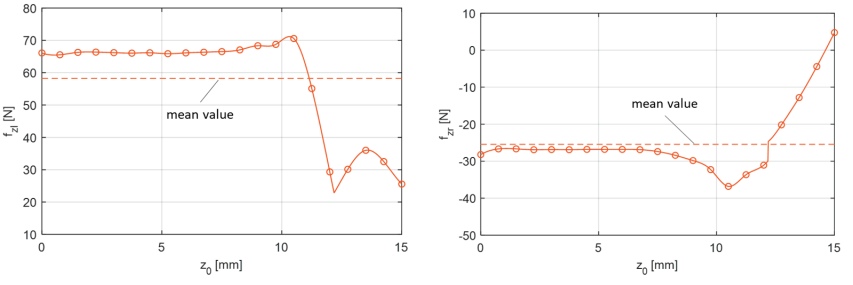

(**a**) (**b**)

Figure 11. Thrust profiles as functions of the axial mover position for different ampere-turns; (**a**) LV mover; and (**b**) RV mover.

With constant power losses being predefined, various performance indices are considered, which mainly takes into account the TAH forward stroke operation. The profiles calculated by 2D finite element analyses are sufficiently smooth for most of the forward stroke, satisfying the peak force requirements (71.2 N for the LV, −36.8 N for the RV) and with satisfactory mean values (58.2 N for the LV, −25.4 N for the RV). The supply voltage to compensate both the resistance voltage drop and the induced counter e.m.f. is lower than 20 V, therefore being consistent with the portable battery pack.

The cogging force, leading to a deadlock near the outward stroke end, represents a major concern for the backward stroke, especially for the RV mover, even if during such a phase a limited blood back-pressure aids the return motion. Therefore, the magnetic configuration should be refined to match the electromagnetic force with the counteraction of the circulatory system, as well as with the effect of the blister deflection.

5. Unconventional Electromagnetic Actuators

Other alternative configurations, aimed at overcoming issues related to the size and operation, can be grouped into two PM actuator categories. The former is based on the contactless electromagnetic interaction between the external static or rotating primary and the secondary part implanted in the chest ribs, neither requiring additional implanted batteries nor percutaneous cable connection, however, requiring very tight magnetic coupling. The latter includes actuators combining both linear and rotary (2 DOFs) motion to produce

both the pumping function and valve actuation, respectively, to manage blood flow during the TAH operating cycle. The following sections describe some examples of the two types of actuators.

5.1. Contactless Power Transfer (CPT)

Two approaches are proposed for this kind of actuators. The first one relies on external moving PMs, driven by a conventional rotary electric motor, magnetically interacting with inner PMs to produce a pumping function without using any winding. The absence of copper losses significantly limits thermal issues related to both the power transfer and the actuator operation. Other benefits are the very compact assembly, particularly profitable, for instance, for pediatric application, the ease of setting and tuning of the main drive control, and the low risk of infection transmission.

In Figure 12a, a rotating motor supplied by a separate source (i.e., external battery pack) drives a disk-type version of the actuator with an external 2-pole ring-shaped PM rotor [80].

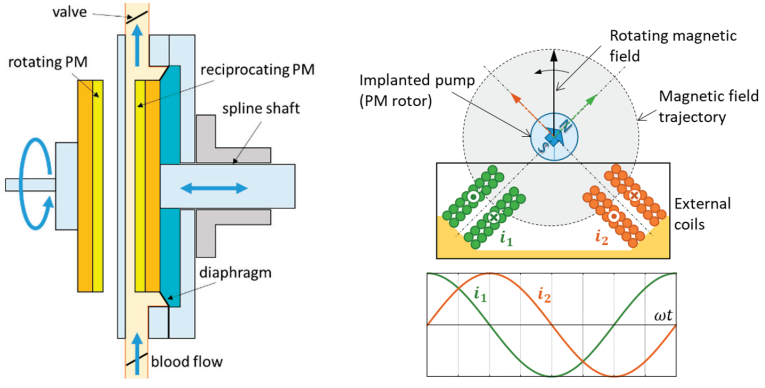

Figure 12. Configurations for the contactless mechanical power transfer; (**a**) external rotating PM disk coupled with an implanted reciprocating PM disk; and (**b**) external 2-phase coils supplied by 90° shifted sinusoidal currents interacting with a 2-pole PM rotor.

During rotation, the axially magnetized PMs alternately repel and attract the inner 2-pole PM ring, constrained to a linear reciprocating motion by mechanical coupling to a spline shaft. A diaphragm, which separates the blood flow from the oscillation chamber, prevents any contamination and hemolysis problems. The reinforcement of the air-gap flux density by an iron yoke and a proper selection of the diameter of the disk hole yields peak values of the attractive and repulsive force at least of 55 N and 15 N, respectively, with a minimum air-gap length (skin thickness included) and a disk outer diameter of 10 mm and 63 mm, respectively. Instead of rotating, in normal operations the prime motor swings through a 180° angle. The maximum output pump power is 0.65 W at an average speed of 92 rpm with a blood flow of 8 l/min. The total pumping efficiency is 32%, appreciably higher than other conventionally motor-driven TAHs.

The same principle applies by replacing the axial flux configuration with a radial flux one, where the rotating magnetic field generated by an external stator primary poly-phase winding interacts with an implanted cylindrical PM rotor. Figure 12b describes a two-phase winding arrangement in [81]. The effective interaction area is limited by the chest curvature; moreover, flux leakages are relevant because of the absence of back iron. However, no shaft or mechanical bearings are required, and the pump impeller can be integrated with the rotor without any mechanical coupling. The pump sized for pediatric VAD was successfully tested in animals that produced an average flow rate of 1.5 l/min at 50 Hz (3000 rpm) with

a 2–3 cm distance between the pump and the driving coil. Pump efficiency is approximately 20 to 40% at the average flow rate (1.7 to 2.0 l/min), with a speed ranging from 3000 rpm (50 Hz) to 6000 rpm (100 Hz).

An alternative to the configuration of Figure 12a could consist of a linear-to-linear motion transmission using external and implanted rectified PM arrays [82]. Such a configuration corresponds to a magnetic coupler, where the inner PM array is driven by the motion of the outer one. Such an arrangement is claimed to be immune to the shortcomings due to fatigue in the flexible blood pockets of most state-of-the-art bionic pneumatic or electric blood pumps. The outer active PM array is driven by a linear motor or by a rotary motor coupled to a rotary-linear motion converter. The piston enclosed in the pump casing holds the passive magnet; the casing is provided with openings on both ends connected to the aorta and the vein, respectively. A one-way valve allows blood flow from the chamber connected to the aorta to the vein, reproducing diastole in the natural heart. Simulations with NdFeB hexahedral 2-pole PMs (sizes: 30 mm × 20 mm) distanced by 60 mm evidence the feasibility of the configuration, providing 1.2 W at 70 bpm.

The effectiveness of the above solutions clearly relies on a precise alignment between the primary and the secondary, reducing the air-gap as much as possible between the two parts. Therefore, such a condition, which is quite critical during physical activities, requires a stable fixture of the external part. The linear-to-linear motion transmission also suffers from the low efficiency of the linear prime mover and of the rotating to linear motion converters.

5.2. Linear Rotary Actuator (LiRA)

Linear rotary motion can be obtained by two different approaches: magnetic conversion (MC-LiRA) from a rotating motion impressed by a conventional electric motor into a linear one by using PMs and possibly ferromagnetic parts (passive configurations), and straightforward generation of a roto-translating field in a single device (conventional LiRA) using supplied windings (active configurations).

MC-LiRAs have been conceived for different applications that require a short stroke and a high thrust [83]. The Magscrew TAH project has already implemented such an actuator [84]. The operating principle is based on the concept of a magnetic screw–nut (Figure 13a). Surface PMs with helicoidal distribution mounted on the back of the screw and on the nut move in synchronism, driven by the corresponding pole interaction. Motion control is in charge of a prime rotating motor, which must produce a clockwise and counterclockwise torque T_n to develop a reciprocating thrust force F_t. The relation to be fulfilled between the torque and force is $T_n = \tau_p/\pi \cdot F_t$ (τ_p: pole pitch). With Halbach magnetization and properly sized PMs, with an outer nut diameter of 17 mm and mover length of 12 mm, a thrust higher than 100 N is achieved. An actuator based on this concept, implemented in in vivo experiments, achieved a blood flow greater than 8 l/min and a maximum pressure of 100 mm Hg, with a device beat rate ranging from 157 to 249 bpm [85].

A field-modulated magnetic screw, proposed in [86], is based on the concept of a magnetic screw and a linear magnetic gear. An intermediate translated set of helically ferromagnetic pole pieces modulate the magnetic field produced by outer static helically shaped PM arrays (Figure 13b). Therefore, its interaction with the inner side rotating PMs enables the conversion of the torque applied to the rotor PM screw into thrust by acting on the intermediate ferromagnetic translator. The increase of the thrust to torque ratio by the gearing effect relies on satisfying the relation $n_s = p_r + p_s$, with n_s number of ferromagnetic pole pieces, p_r and p_s number of pole-pairs on the rotor, and stationary screws, respectively. Such actuators can achieve a force density of up to 20 N/cm^3, consistent with TAH requirements, even if their placement must consider the presence of the prime motor and the troublesome manufacturing of very small helicoidal parts.

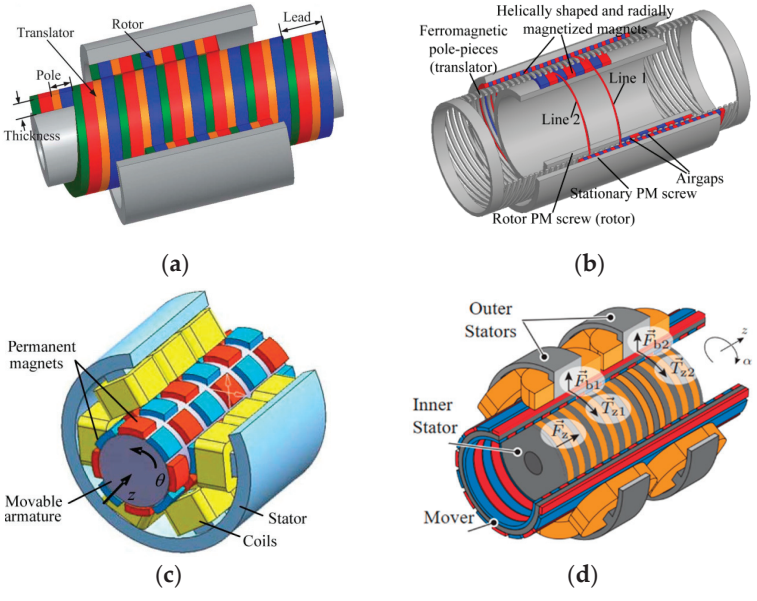

Figure 13. Linear rotary actuators; (**a**) magnetic screw–nut configuration; (**b**) field modulated magnetic screw; (**c**) linear and rotary PM actuator with stator coils; and (**d**) self-bearing linear actuator with double stator winding. Republished with permission of AIP Publishing and IEEE.

Conventional LiRAs with supplied stator winding are attractive in modern machine tools and robotics because of their ability to provide motion with two degrees of freedom. However, their inherent tubular configuration makes them suitable for TAH application; moreover, because of the possibility of the independent management of rotation and translation, their control is more straightforward and flexible than in MC-LiRAs. In this field, VR PM-free configurations are also proposed. The most significant ones rely on rotary-linear switched reluctance motors (RL-SRMs), as they benefit from simple but robust construction, low manufacturing and maintenance costs, high reliability and fault tolerance, and easy control [87]. They can present a multi-stack assembly of classical SRMs with suitably displaced rotors, where an adequate supplying sequence of the stator coils can provide the rotation or linear movement.

Alternatively, they can be provided with two separate sections: a rotating section for clockwise–counterclockwise motions in the middle and a linear section for the forward–backward movements at the actuator sides. Despite its attractiveness for some applications (pick and place machines, robotics, and automotive), RL-SRMs suffer from the main limitations of its LOA counterpart in terms of thrust density ($\sigma_f \cong 0.02$ N/cm^3 in [88]), making its application for a TAH unattractive.

Figure 13c shows a basic PM LiRA. There are 48 alternately polarized PMs, 6 in the z-direction and 8 in the θ-direction, and a stator with 18 concentrated coils, 3 in the z-direction and 6 in the θ-direction, broadly representing a 9-phase system [89]. Possibly, a salient stator inside the PM mover can exploit the Vernier effect to improve the force/mass ratio and the evenness of the torque/force profile [90].

Integrated magnetic bearings are also useful in eliminating mechanical wear problems [91]. It uses a double-stator arrangement placed concentrically inside and outside a cylindrically shaped mover (Figure 13d). The outer stator coils provide the rotating motion (torque T_{z1} and T_{z2}) and the bearing function (forces F_{b1} and F_{b2}) by an appropriate air-gap control, while the inner stator coils control the linear motion (thrust F_z).

6. Overall Comparison

To summarize the detailed overview provided in the previous sections, Table 2 reports a qualitative comparison of the designed and tested electromagnetic actuators, considering five significant properties (maturity level, compactness, manufacturing, control simplicity, and efficiency). The limited consistency of both the geometric and operational data as well as the unavailability of some information did not allow for a quantitative performance comparison. The overall evaluation points out the following considerations:

- The brushless motor (DC or AC) presents the highest maturity level because of its widespread ability in many low-rated applications, therefore ensuring high reliability and flexible control; however, in FD- and EM-TAH, the overall efficiency can suffer from the presence of gear or hydraulic converters, and in CF-TAH, the control can be more complicated in presence of magnetic bearings;
- The VR-LOA is the least suitable, as the manufacturing and control simplicity is by far offset by the limited thrust density and efficiency, the latter related to the required high current density;
- Among THE PM-LOAs, the MM one seems slightly better in terms of manufacturing simplicity, because no moving coils as well as complicated stator assembly are present;
- The CPT systems provide a promising performance and likely the most compact configuration as only the moving part is implanted; however, control issues can arise in the presence of misalignments or increased axial distancing between the external and the implanted parts;

Table 2. Overall comparison of the main actuators for TAH applications.

TAH Type	Actuator	Maturity	Compactness	Manufacturing Simplicity	Control Simplicity	Overall Efficiency
FD	Brushless motor	High	Low	Medium	High	Medium
EM	Brushless motor	High	Low	Medium	High	Medium
CF	Brushless motor	Medium	Medium	Medium	Low	High
EM	VR-LOA	Low	Low	High	High	Low
EM	MC-LOA	Medium	High	Medium	Medium	High
EM	MM-LOA	Medium	High	High	High	High
EM	PM VR-LOA	Low	Low	Low	Medium	Medium
EM	CPT	Low	High	Medium	Low	High
EM	MC-LiRA	Medium	High	Low	Medium	High
EM	Conventional LiRA	Low	Medium	Low	Low	High

- LiRAs have no distinguished merits due to their still limited development and manufacturing complexity; however, the possibility to combine mover rotation and translation could lead to the simplest operational management for a TAH (pumping and blood flow control).

7. Conclusions

In the paper, different electromagnetic technologies considered for application in a ventricle-assisted device or a totally artificial heart (TAH) are presented. The review examined the innovative solutions utilized in the most promising projects focused on the development of the total system, as well as those proposed and checked in the literature as single components. Among all the devices, the transcutaneous energy transmission (TET) system and the electromagnetic actuator are distinguished in terms of performance and durability. In view of the possible application of new high-performance materials (e.g., high-energy PMs, low core loss, high permeable magnetic materials, and Litz wire windings), very high achievable efficiency and power density are achievable, enabling compact configurations with limited losses and positively affecting both battery life and heat generation.

As for the TET, despite the inherent significant air-gap due to the biological tissue thickness, the high-frequency operation enables efficiency up to 90%. For the actuator, two solutions seem very convenient and effective. The first one, adopted in the BiVACOR project, relies on an axial flux PM motor that interacts with an axial magnetic bearing, integrating both the pumping and the pulsatile effects in a rotating motor. The other one is based on a linear oscillating actuator (LOA), acting on both artificial ventricles realized in biocompatible materials. Among the various families of PM-LOAs that can effectively mimic the heart operation, the seemingly most advanced one is applied in the ReinHeart project, but other configurations exhibit favorable features (dual-mover, linear-rotating motion, and bearingless arrangement) and are potential candidates for a future commercial TAH.

Author Contributions: Formal analysis, M.A.; investigation, E.F. and A.T.; data curation, E.F.; writing—original draft preparation, E.F.; writing—review and editing, M.A. and A.T.; supervision, M.A. and A.T.; funding acquisition, A.T. All authors have read and agreed to the published version of the manuscript.

Funding: This research was funded by the Department of Industrial Engineering–University of Padova, under the project entitled "Reliable and minimally invasive electrodynamic actuator for longer lasting artificial heart" ID TORT_BIRD2121_01.

Conflicts of Interest: The authors declare no conflict of interest.

References

1. Yang, M.; Zhang, Y. Introduction to Artificial Hearts. In *Artificial Hearts*, 2nd ed.; Yang, M., Ed.; Springer Nature: Singapore, 2020; pp. 1–19.
2. Watt, T.M.F.; Pagani, F.D. Artificial mechanical hearts and ventricular assist devices. In *Emerging Technologies for Heart Diseases*, 2nd ed.; Nussinovitch, U., Ed.; Academic Press: Cambridge, MA, USA, 2020; Volume 1, pp. 25–40.
3. Phillips, K.G.; Ranganath, N.K.; Moazami, N. Status and Availability of a Total Artificial Heart. In *Mechanical Support for Heart Failure*; Karimov, J.H., Fukamachi, K., Starling, R.C., Eds.; Springer Nature: Cham, Switzerland, 2020; pp. 191–220.
4. Jefferson, H.L.; Kent, W.D.T.; MacQueen, K.T.; Miller, R.J.H.; Holloway, D.D.; Hassanabad, A.F. Left ventricular assist devices: A comprehensive review of major clinical trials, devices, and future directions. *J. Card. Surg.* **2021**, *36*, 1480–1491. [CrossRef] [PubMed]
5. Andrade, A.; Nicolosi, D.; Lucchi, J.; Biscegli, J.; Arruda, A.C.; Ohashi, Y.; Mueller, J.; Tayama, E.; Glueck, J.; Nosé, Y. Auxiliary total artificial heart: A compact electromechanical artificial heart working simultaneously with the natural heart. *Artif. Organs* **1999**, *23*, 876–880. [CrossRef] [PubMed]
6. Andrade, A.; Fonseca, J.; Legendre, D.; Nicolosi, D.; Biscegli, J.; Pinotti, M.; Ohashi, Y.; Nosé, Y. Improvement on the Auxiliary Total Artificial Heart (ATAH) Left Chamber Design. *Artif. Organs* **2003**, *27*, 452–456. [CrossRef] [PubMed]
7. Cohn, W.E.; Timms, D.L.; Frazier, O.H. Total artificial hearts: Past, present, and future. *Nat. Rev. Cardiol.* **2015**, *12*, 609–617. [CrossRef]
8. Cole, R.M.; Arabía, F.A. Total Artificial Heart Technology: Where Are We Now? *Curr. Transpl. Rep.* **2018**, *5*, 315–318. [CrossRef]
9. Spiliopoulos, S.; Hergesell, V.; Wasler, A.; Dapunt, O. Current state of total artificial heart therapy and introduction of the most important total artificial heart systems. *Biomed. Eng. /Biomed. Tech.* **2019**, *64*, 247–250. [CrossRef]
10. Alnajar, A.; Frazier, O.H. The State of Artificial Heart Therapy. *Tex. Heart Inst. J.* **2019**, *46*, 77–79. [CrossRef]
11. Gerosa, G.; Scuri, S.; Iop, L.; Torregrossa, G. Present and future perspectives on total artificial hearts. *Ann. Cardiothorac. Surg.* **2014**, *3*, 595–602.
12. Goerlich, C.E.; Frazier, O.H.; Cohn, W.E. Previous challenges and current progress–the use of total artificial hearts in patients with end-stage heart failure. *Expert Rev. Cardiovasc. Ther.* **2016**, *14*, 1095–1098. [CrossRef]
13. Vis, A.; Arfaee, M.; Khambati, H.; Slaughter, M.S.; Gummert, J.F.; Overvelde, J.T.; Kluin, J. The ongoing quest for the first total artificial heart as destination therapy. *Nat. Rev. Cardiol.* **2022**, *19*, 813–828. [CrossRef]
14. Slepian, M.J.; Alemu, Y.; Soares, J.S.; Smith, R.G.; Einav, S.; Bluestein, D. The Syncardia™ total artificial heart: In vivo, in vitro, and computational modeling studies. *J. Biomech.* **2013**, *46*, 266–275. [CrossRef] [PubMed]
15. Essandoh, M.; Kumar, N. Total artificial heart system. *Int. Anesthesiol. Clin.* **2022**, *60*, 39–45. [CrossRef] [PubMed]
16. Dowling, R.D.; Gray, L.A., Jr.; Etoch, S.W.; Laks, H.; Marelli, D.; Samuels, L.; Entwistle, J.; Couper, G.; Vlahakes, G.J.; Frazier, O.H. The AbioCor implantable replacement heart. *Ann. Thorac. Surg.* **2003**, *75*, 93–99. [CrossRef] [PubMed]
17. Gray, L.A. Total Artificial Heart (AbioCor™). In *Treatment of Advanced Heart Disease*, 1st ed.; Baughmann, K.L., Baumgartner, W.A., Eds.; CRC Press: Boca Raton, FL, USA, 2006; pp. 459–471.
18. Mohacsia, P.; Leprince, P. The CARMAT total artificial heart. *Eur. J. Cardio-Thorac. Surg.* **2014**, *46*, 933–934. [CrossRef]
19. Carmat. Available online: https://www.carmatsa.com/en/our_product/ (accessed on 9 December 2022).

20. Lippi, G.; Sanchis-Gomar, F. Global epidemiology and future trends of heart failure. *AME Med. J.* **2020**, *5*, 1–6. [CrossRef]
21. Ministero Della Salute. Available online: https://www.trapianti.salute.gov.it/trapianti/archivioDatiCnt.jsp?lingua=italiano&anno=2022 (accessed on 9 December 2022).
22. Coyan, G.N.; Huckaby, L.V.; Diaz-Castrillon, C.E.; Miguelino, A.M.; Kilic, A. Trends and outcomes following total artificial heart as bridge to transplant from the UNOS database. *J. Card. Surg.* **2022**, *37*, 1215–1221. [CrossRef]
23. Palazzolo, T.; Hirschhorn, M.; Garven, E.; Day, S.; Stevens, R.M.; Rossano, J.; Tchantchaleishvili, V.; Throckmorton, A.L. Technology landscape of pediatric mechanical circulatory support devices: A systematic review 2010–2021. *Artif. Organs* **2022**, *46*, 1475–1490. [CrossRef]
24. Bticherl, E.S.; Hennig, E.; Baer, P.; Frank, J.; Lemm, W.; Zartnack, F. Status of the Artificial Heart Program in Berlin. *World J. Surg.* **1985**, *9*, 103–115. [CrossRef]
25. Jeong, G.S.; Hwang, C.M.; Nam, K.W.; Ahn, C.B.; Kim, H.C.; Lee, J.J.; Choi, J.; Son, H.S.; Fang, Y.H.; Son, K.H.; et al. Development of a Closed Air Loop Electropneumatic Actuator for Driving a Pneumatic Blood Pump. *Artif. Organs* **2009**, *33*, 657–662. [CrossRef]
26. Dal Sasso, E.; Bagno, A.; Scuri, S.T.G.; Gerosa, G.; Iop, L. The Biocompatibility Challenges in the Total Artificial Heart Evolution. *Annu. Rev. Biomed Eng.* **2019**, *21*, 85–110. [CrossRef]
27. Ahmed, A.; Wang, X.; Yang, M. Biocompatible materials of pulsatile and rotary blood pumps: A brief review. *Rev. Adv. Mater. Sci.* **2020**, *59*, 322–339. [CrossRef]
28. Homma, A.; Taenaka, Y.; Tatsumi, E.; Takewa, Y.; Mizuno, T.; Shioya, K.; Lee, H.S.; Tsukiya, T.; Kakuta, Y.; Katagiri, N.; et al. Development of an Electrohydraulic Total Artificial Heart System: Improvement of Pump Unit. *Electron. Commun. Jpn.* **2010**, *93*, 34–46. [CrossRef]
29. Pohlmann, A.; Leßmann, M.; Finocchiaro, T.; Schmitz-Rode, K.T.; Hameyer, K. Numerical Computation Can Save Life: FEM Simulations for the Development of Artificial Hearts. *IEEE Trans. Mag.* **2011**, *47*, 1166–1169. [CrossRef]
30. Pohlmann, A.; Leßmann, M.; Fritschi, A.; Finocchiaro, T.; Steinseifer, U.; Hameyer, K. Experimental validation of the linear drive train for a total artificial heart system. *Mechatronics* **2013**, *23*, 222–226. [CrossRef]
31. Pelletier, B.; Spiliopoulos, S.; Finocchiaro, T.; Graef, F.; Kuipers, K.; Laumen, M.; Guersoy, D.; Steinseifer, U.; Koerfer, R.; Tenderich, G. System overview of the fully implantable destination therapy—ReinHeart-total artificial heart. *Eur. J. Cardio-Thorac. Surg.* **2015**, *47*, 80–86. [CrossRef]
32. Unthan, K.; Gräf, F.; Laumen, M.; Finocchiaro, T.; Sommer, C.; Lanmüller, H.; Steinseifer, W. Design and Evaluation of a Fully Implantable Control Unit for Blood Pumps. *BioMed Res. Int.* **2015**, *2015*, 257848. [CrossRef]
33. Candela, V.; Todesco, M.; Visentin, A.; Meneghetti, G.; Fabozzo, A.; Gerosa, G.; Bagno, A. Preliminary Computational Analysis of Three Configurations for an Innovative Ventricular Chamber. *Processes* **2020**, *8*, 1358. [CrossRef]
34. Todesco, M.; Zardin, C.; Iop, L.; Palmosi, T.; Capaldo, P.; Romanato, F.; Gerosa, G.; Bagno, A. Hybrid membranes for the production of blood contacting surfaces: Physicochemical, structural and biomechanical characterization. *Biomater. Res.* **2021**, *25*, 26. [CrossRef]
35. Greatrex, N.A.; Timms, D.L.; Kurita, N.; Palmer, E.W.; Masuzawa, T. Axial magnetic bearing development for the BiVACOR rotary BiVAD/TAH. *IEEE Trans. Biomed. Eng.* **2010**, *57*, 714–721. [CrossRef]
36. Kleinheyer, M.; Timms, D.L.; Greatrex, N.A.; Masuzawa, T.; Frazier, O.H.; Cohn, W.E. Pulsatile operation of the BiVACOR TAH—Motor design, control and hemodynamics. In Proceedings of the 2014 36th Annual International Conference of the IEEE Engineering in Medicine and Biology Society, Chicago, IL, USA, 26–30 August 2014; pp. 5659–5662.
37. Greatrex, N.; Kleinheyer, M.; Nestler, F.; Timms, D. The Maglev Heart. *IEEE Spectr.* **2019**, *56*, 22–29. [CrossRef]
38. Miyamoto, T.; Horvath, D.J.; Horvath, D.W.; Kuban, B.D.; Fukamachi, K.; Karimov, J.H. Analysis of Cleveland Clinic continuous-flow total artificial heart performance using the Virtual Mock Loop: Comparison with an in vivo study. *Artif. Organs* **2020**, *44*, 375–383. [CrossRef] [PubMed]
39. Karimov, J.H.; Horvath, D.J.; Fukamachi, K. Cleveland Clinic Total Artificial Heart. In *Mechanical Support for Heart Failure*; Karimov, J.H., Fukamachi, K., Starling, R.C., Eds.; Springer Nature: Cham, Switzerland, 2020; pp. 493–504.
40. Glynn, J.; Song, H.; Hull, B.; Withers, S.; Gelow, J.; Mudd, J.; Starr, A.; Wampler, R. The OregonHeart Total Artificial Heart: Design and Performance on a Mock Circulatory Loop. *Artif. Organs* **2017**, *41*, 904–910. [CrossRef] [PubMed]
41. Fresiello, L.; Najar, A.; Brynedal Ignell, N.; Zieliński, K.; Rocchi, M.; Meyns, B.; Perkins, I.L. Hemodynamic characterization of the Realheart®total artificial heart with a hybrid cardiovascular simulator. *Artif. Organs* **2022**, *46*, 1585–1596. [CrossRef]
42. Tozzi, P.; Maertens, A.; Emery, J.; Joseph, S.; Kirsch, M.; Avellan, F. An original valveless artificial heart providing pulsatile flow tested in mock circulatory loops. *Int. J. Artif. Organs* **2017**, *40*, 683–689. [CrossRef]
43. HybridHeart. White Paper on Requirements and Constraints of Combining Technologies. Available online: https://hybridheart.eu/wp-content/uploads/2019/05/Requirements.pdf (accessed on 9 December 2022).
44. AbioCor Implantable Replacement Heart. Available online: https://www.accessdata.fda.gov/cdrh_docs/pdf4/h040006b.pdf (accessed on 9 December 2022).
45. Luo, C.; Ware, D.L.; Zwischenberger, J.B.; Clark, J.W., Jr. A mechanical model of the human heart relating septal function to myocardial work and energy. *Cardiovasc. Eng.* **2008**, *8*, 174–184. [CrossRef] [PubMed]
46. Yamane, T. How Do We Select Pump Types? In *Mechanism of Artificial Heart*, 2nd ed.; Springer: Tokyo, Japan, 2016; pp. 13–21.
47. Wang, Y.; Liang, L.; Wang, W.; Tan, Z.; Sethu, P.; El-Baz, A.S.; Giridharan, G.A. Basis of Artificial Heart Technologies. In *Artificial Hearts*, 2nd ed.; Yang, M., Ed.; Springer Nature: Singapore, 2020; pp. 31–52.

48. Rogers, J.G.; Pagani, F.D.; Tatooles, A.J.; Bhat, G.; Slaughter, M.S.; Birks, E.J.; Boyce, S.W.; Najjar, S.S.; Jeevanandam, V.; Anderson, A.S.; et al. Intrapericardial Left Ventricular Assist Device for Advanced Heart Failure. *N. Engl. J. Med.* **2017**, *376*, 451–460. [CrossRef] [PubMed]
49. Hosseinipour, M.; Gupta, R.; Bonnell, M.; Elahinia, M. Rotary mechanical circulatory support systems. *J. Rehabil. Assist. Technol. Eng.* **2017**, *4*, 2055668317725994. [CrossRef]
50. Andriollo, M.; Bettanini, G.; Tortella, A. Design procedure of a small-size axial flux motor with Halbach-type permanent magnet rotor and SMC cores. In Proceedings of the 2013 International Electric Machines & Drives Conference, Chicago, IL, USA, 12–15 May 2013; pp. 775–780.
51. Kurita, N.; Ishikawa, T.; Saito, N.; Masuzawa, T.; Timms, D.L. A Double-Sided Stator Type Axial Bearingless Motor Development for Total Artificial Heart. *IEEE Trans. Ind. Appl.* **2019**, *55*, 1516–1523. [CrossRef]
52. Slaughter, M.S.; Rogers, J.G.; Milano, C.A.; Russell, S.D.; Conte, J.V.; Feldman, D.; Sun, B.; Tatooles, A.J.; Delgado, R.M., III; Long, J.W.; et al. Advanced heart failure treated with continuous-flow left ventricular assist device. *N. Engl. J. Med.* **2009**, *361*, 2241–2251. [CrossRef]
53. Abe, Y.; Ono, T.; Isoyama, T.; Mochizuki, S.; Iwasaki, K.; Chinzei, T.; Saito, I.; Kouno, A.; Imachi, K. Development of a miniature undulation pump for the distributed artificial heart. *Artif. Organs* **2000**, *24*, 656–658. [CrossRef]
54. Saito, I.; Chinzei, T.; Abe, Y.; Ishimaru, M.; Mochizuki, S.; Ono, T.; Isoyama, T.; Iwasaki, K.; Kouno, A.; Baba, A.; et al. Progress in the Control System of the Undulation Pump Total Artificial Heart. *Artif. Organs* **2003**, *27*, 27–33. [CrossRef] [PubMed]
55. Yang, S.M.; Huang, M.S. Design and Implementation of a Magnetically Levitated Single-Axis Controlled Axial Blood Pump. *IEEE Trans. Ind. Electr.* **2009**, *56*, 2213–2219. [CrossRef]
56. Hirschhorn, M.; Catucci, N.; Day, S.; Stevens, R.M.; Tchantchaleishvili, V.; Throckmorton, A.L. Channel impeller design for centrifugal blood pump in hybrid pediatric total artificial heart: Modeling, magnet integration, and hydraulic experiments. *Artif. Organs.* **2022**, *00*, 1–15. [CrossRef] [PubMed]
57. Ishii, K.; Hosoda, K.; Isoyama, T.; Saito, I.; Ariyoshi, K.; Inoue, Y.; Sato, M.; Hara, S.; Lee, X.; Wu, S.Y.; et al. Pulsatile driving of the helical flow pump. In Proceedings of the 2013 35th Annual International Conference of the IEEE Engineering in Medicine and Biology Society (EMBC), Osaka, Japan, 3–7 July 2013; pp. 2724–2727.
58. Puers, R.; Vandevoorde, G. Recent Progress on Transcutaneous Energy Transfer for Total Artificial Heart Systems. *Artif. Organs* **2001**, *25*, 400–405. [CrossRef] [PubMed]
59. Ma, J.; Yang, Q.; Chen, H. Transcutaneous Energy and Information Transmission System With Optimized Transformer Parameters for the Artificial Heart. *IEEE Trans. Appl. Supercond.* **2010**, *20*, 798–801.
60. Miura, H.; Arai, S.; Kakubari, Y.; Sato, F.; Matsuki, H.; Sato, T. Improvement of the Transcutaneous Energy Transmission System Utilizing Ferrite Cored Coils for Artificial Hearts. *IEEE Trans. Magn.* **2006**, *42*, 3578–3580. [CrossRef]
61. Grzesik, B.; Stepien, M. Topology of TET system with soft switched converters. In Proceedings of the 2012 15th International Power Electronics and Motion Control Conference (EPE/PEMC), Novi Sad, Serbia, 4–6 September 2012.
62. Andriollo, M.; Fanton, E.; Forzan, M.; Tortella, A. Design and Analysis of a Dual Mover Linear Oscillating Actuator for a Totally Artificial Heart. In Proceedings of the International Conference on Electrical Machines (ICEM), Valencia, Spain, 5–8 September 2022.
63. Boldea, I.; Nasar, S.A. *Linear Electric Actuators and Generators*, 1st ed.; Academic Press: London, UK, 1997; pp. 91–132.
64. Finocchiaro, T.; Butschen, T.; Kwant, P.; Steinseifer, U.; Schmitz-Rode, T.; Hameyer, K.; Leßmann, M. New linear motor concepts for artificial hearts. *IEEE Trans. Magn.* **2008**, *44*, 678–681. [CrossRef]
65. Llibre, J.F.; Martinez, N.; Nogarede, B.; Leprince, P. Linear tubular switched reluctance motor for heart assistance circulatory: Analytical and finite element modeling. In Proceedings of the 2011 10th International Workshop on Electronics, Control, Measurement and Signals, Liberec, Czech Republic, 1–3 June 2011.
66. Ji, J.; Yan, S.; Zhao, W.; Liu, G.; Zhu, X. Minimization of Cogging Force in a Novel Linear Permanent-Magnet Motor for Artificial Hearts. *IEEE Trans. Magn.* **2013**, *49*, 3901–3904. [CrossRef]
67. Liu, Z.; Zhao, W.; Ji, J.; Chen, Q. A Novel Double-Stator Tubular Vernier Permanent-Magnet Motor With High Thrust Density and Low Cogging Force. *IEEE Trans. Magn.* **2015**, *51*, 1–7.
68. Ji, J.; Zhao, J.; Zhao, W.; Fang, Z.; Liu, G.; Du, Y. New High Force Density Tubular Permanent-Magnet Motor. *IEEE Trans. Appl. Supercond.* **2014**, *24*, 1–5. [CrossRef]
69. Zhang, Y.; Lu, Q.; Yu, M.; Ye, Y. A Novel Transverse-Flux Moving-Magnet Linear Oscillatory Actuator. *IEEE Trans. Magn.* **2012**, *48*, 1856–1862. [CrossRef]
70. Yamada, H.; Yano, T.; Wakiwaka, H.; Yamamoto, Y.; Nakagawa, H.; Maeda, Y. Development of high power linear pulse motor for artificial heart. In Proceedings of the 1991 Fifth International Conference on Electrical Machines and Drives (Conf. Publ. No. 341), London, UK, 11–13 September 1991; pp. 110–114.
71. Chen, X.; Zhu, Z.Q.; Howe, D.; Dai, J.S. Comparative study of alternative permanent magnet linear oscillating actuators. In Proceedings of the 2008 International Conference on Electrical Machines and Systems, Wuhan, China, 17–20 October 2008; pp. 2826–2831.
72. Zhu, Z.Q.; Chen, X.; Howe, D.; Iwasaki, S. Electromagnetic modeling of a novel linear oscillating actuator. *IEEE Trans. Magn.* **2008**, *44*, 3855–3858. [CrossRef]

73. Zhu, Z.Q.; Chen, X. Analysis of an E-Core Interior Permanent Magnet Linear Oscillating Actuator. *IEEE Trans. Magn.* **2009**, *45*, 4384–4387. [CrossRef]
74. Sun, J.; Luo, C.; Xu, S. Improvement of tubular linear oscillating actuators by using end ferromagnetic pole pieces. *IEEE Trans. Energy Conv.* **2018**, *33*, 1686–1691. [CrossRef]
75. Watada, M.; Yanashima, K.; Oishi, K.; Ebihara, D. Improvement on characteristics of linear oscillatory actuator for artificial hearts. *IEEE Trans. Magn.* **1993**, *29*, 3361–3363. [CrossRef]
76. Lu, H.; Zhu, J.; Lin, Z.; Guo, Y. A Miniature Short Stroke Linear Actuator—Design and Analysis. *IEEE Trans. Magn.* **2008**, *44*, 497–504.
77. Ahmad, Z.; Khan, H.A.; Khan, S.; Ullah, B.; Khalid, S.; Akbar, S. Design and Analysis of a Novel Dual Stator Tubular Moving Magnet Linear Actuator for Compressor Application. In Proceedings of the 2021 International Conference on Frontiers of Information Technology (FIT), Islamabad, Pakistan, 13–14 December 2021; pp. 299–304.
78. Yan, S.; Ji, J.; Wang, F.; Liu, G. New tubular fault-tolerant permanent-magnet motor for artificial heart. In Proceedings of the 2012 15th International Conference on Electrical Machines and Systems (ICEMS), Sapporo, Japan, 21–24 October 2012; pp. 1–5.
79. Birbilen, U.; Lazoglu, I. Design and Analysis of a Novel Miniature Tubular Linear Actuator. *IEEE Trans. Magn.* **2018**, *54*, 1–6. [CrossRef]
80. Saotome, H.; Shimizu, K.; Okada, T. Design of Magnetic Actuator Intended for Artificial Heart Drive. *Trans. Magn. Soc. Jpn.* **2004**, *4*, 64–66. [CrossRef]
81. Kim, S.H.; Hashi, S.; Ishiyama, K. Actuation of Novel Blood Pump by Direct Application of Rotating Magnetic Field. *IEEE Trans. Magn.* **2012**, *48*, 1869–1874. [CrossRef]
82. Xia, D. A Bionic Artificial Heart Blood Pump Driven by Permanent Magnet Located Outside Human Body. *IEEE Trans. Appl. Supercond.* **2012**, *22*, 4401304.
83. Mustafa, D.; Hussain, A. A Survey on the Design and Analysis of Magnetic Screws. In Proceedings of the 2021 IEEE Energy Conversion Congress and Exposition (ECCE), Vancouver, BC, Canada, 10–14 October 2021; pp. 3759–3766.
84. Schenk, S.; Weber, S.; Luangphakdy, V.; Klatte, R.S.; Flick, C.R.; Chen, J.F.; Kopcak, M.W., Jr.; Ootaki, Y.; Kamohara, K.; Hirschman, G.B.; et al. MagScrew Total Artificial Heart In Vivo Performance Above 200 Beats Per Minute. *Ann. Thorac. Surg.* **2005**, *79*, 1378–1383. [CrossRef] [PubMed]
85. Ji, J.; Ling, Z.; Wang, J.; Zhao, W.; Liu, G.; Zeng, T. Design and analysis of a Halbach magnetized magnetic screw for artificial heart. *IEEE Trans. Magn.* **2015**, *51*, 1–4. [CrossRef]
86. Ling, Z.; Ji, J.; Wang, F.; Bian, F. Design and analysis of a field modulated magnetic screw for artificial heart. *AIP Adv.* **2017**, *7*, 056717. [CrossRef] [PubMed]
87. Szabó, L. A Survey on Rotary-Linear Motors Used in Emerging Applications. In Proceedings of the IECON 2019-45th Annual Conference of the IEEE Industrial Electronics Society, Lisbon, Portugal, 14–17 October 2019; pp. 3257–3262.
88. Nezamabadi, M.M.; Afjei, E.; Torkaman, H. Design, Dynamic Electromagnetic Analysis, FEM, and Fabrication of a New Switched-Reluctance Motor With Hybrid Motion. *IEEE Trans. Magn.* **2016**, *52*, 1–8. [CrossRef]
89. Jin, P.; Fang, S.; Lin, H.; Zhu, Z.Q.; Huang, Y.; Wang, X. Analytical Magnetic Field Analysis and Prediction of Cogging Force and Torque of a Linear and Rotary Permanent Magnet Actuator. *IEEE Trans. Magn.* **2011**, *47*, 3004–3007. [CrossRef]
90. Krebs, G.; Tounzi, A.; Pauwels, B.; Willemot, D.; Piriou, F. Modeling of A Linear and Rotary Permanent Magnet Actuator. *IEEE Trans. Magn.* **2008**, *44*, 4357–4360. [CrossRef]
91. Miric, S.; Giuffrida, R.; Rohner, G.; Bortis, D.; Kolar, J.W. Design and Experimental Analysis of a Selfbearing Double-Stator Linear-Rotary Actuator. In Proceedings of the 2021 IEEE International Electric Machines & Drives Conference (IEMDC), Hartford, CT, USA, 17–20 May 2021.

applied sciences

MDPI

Article

Synchronous Homopolar Generator without Permanent Magnets for Railway Passenger Cars

Vladimir Prakht, Vladimir Dmitrievskii * and Vadim Kazakbaev

Department of Electrical Engineering, Ural Federal University, 620002 Yekaterinburg, Russia
* Correspondence: vladimir.dmitrievsky@urfu.ru; Tel.: +7-909-028-49-25

Featured Application: The presented results can be used in designing synchronous homopolar machines and railway undercar generators.

Abstract: The article presents the optimal design of a 35 kW brushless synchronous homopolar generator without permanent magnets for railway passenger cars. The excitation winding of the generator is located on the stator, and the toothed rotor has no windings. The generator characteristics are optimized considering the required constant power speed range. A single-objective Nelder–Mead algorithm and 2D Finite Element Analysis were used for the optimization. As a result of the optimization, power losses are significantly reduced over the entire operating range of the generator rotational speed, the current capacity of the solid-state rectifier, and the torque ripple. A comparison of the calculated characteristics of the generator under consideration with the characteristics of a commercially available undercar generator shows that the active volume is reduced by a factor of 2.1, and the losses are significantly reduced over the entire operating speed range.

Keywords: electrically excited synchronous machine; Nelder–Mead method; optimal design of electric machines; synchronous homopolar generator; synchronous homopolar machine; undercar generator

Citation: Prakht, V.; Dmitrievskii, V.; Kazakbaev, V. Synchronous Homopolar Generator without Permanent Magnets for Railway Passenger Cars. *Appl. Sci.* **2023**, *13*, 2070. https://doi.org/10.3390/app13042070

Academic Editors: Loránd Szabó and Feng Chai

Received: 31 December 2022
Revised: 1 February 2023
Accepted: 3 February 2023
Published: 5 February 2023

1. Introduction

In many countries, less than half of the railways are electrified [1,2]. Nonelectrified railway lines use diesel or diesel–electric locomotives [3]. One of the options for the electrification of passenger cars in this case is undercar generators [4,5].

Brushless synchronous homopolar machines (SHMs) with axial excitation flux and stator-fixed concentric coils of the excitation winding are known for their high reliability, due to which they find use in flywheel energy storage and traction motors, as well as in welding automotive and aircraft generators [6–9]. They can be used at high temperatures and in hazardous environments, such as drives [10] and high-power wind generators [11]. The main benefit of SHMs, in comparison with conventional generators with electrically excited rotor, is high reliability, due to the simple rotor without windings, no sliding contact, and reliable concentric excitation winding coils located on the stator. At the same time, the SHM retains the ability to control the excitation current, as in a conventional generator with an excitation winding on the rotor.

It is also a problem to ensure the cooling of a conventional generator with an excitation winding on the rotor, which has significant electrical losses. Generators with a brushless exciter are used in a number of applications, such as aircraft generators and high-power generators [12,13]. The disadvantages of such generators with a brushless exciter, compared with brushed generators, include an increase in the cost, dimensions, and weight of the machine due to the presence of a brushless exciter. Additionally, in this case, there are problems of the reliability and repair of the brushless exciter assembly.

The design of the excitation winding is much simpler and more reliable and requires much less copper that that of a conventional synchronous generator. In addition, because

the rotor does not have windings and a significant copper loss associated with them, no special measures are required to cool the rotor [14]. Another important advantage of the SHG is the high strength of the rotor to the centrifugal force and large shock loads [15].

SHMs have a complex configuration of the magnetic system, which is inconvenient for calculation and optimization, because the magnetic flux propagates in all three dimensions. The magnetic flux flows in the axial direction in laminated parts of the machine and in the transverse plane in nonlaminated parts of the machine's magnetic core. The complex three-dimensional design of the magnetic circuit causes difficulties when using conventional two-dimensional models based on the finite element analysis (FEA) to compute the characteristics of the SHM.

Because analytical models of electrical machines are usually not accurate enough due to the difficulty of taking into account the saturation of the magnetic circuit, it is necessary to use numerical models [16].

For this reason, a number of numerical calculation methods have been proposed for SHMs, taking into account the saturation of the magnetic circuit, including three-dimensional FEA [17–19], two-dimensional FEA [9,20], one-dimensional magnetic circuits, and their various combinations [21,22]. In Reference [9], a simplified SHM modeling technique was proposed, in which the features of the SHM magnetic field are taken into account in a two-dimensional model by introducing the excitation field term into the equations of the magnetic vector potential and solving the 2D magnetostatic problems complemented with an equivalent circuit equation for the excitation flux.

Articles [9,23–27] present SHM as a traction motor. Article [9] discusses a simplified methodology for estimating the characteristics of the SHM, suitable for use in multi-iteration automatic optimization, and its experimental verification. Articles [23–25] present techniques for optimizing SHMs for various traction applications. Articles [14,26] present the results of comparing the characteristics of the SHM with other types of traction motors. Article [27] presents the development of a control strategy for the traction SHM.

In References [6,17,18,20,28–30], the analysis of the SHM characteristics for various generator applications is investigated. In Reference [17], the modeling and tuning of the control system of a high-speed synchronous homopolar generator (SHG) is considered. In [18], the analytical formulas for the design and the results of 3D FEA of a high-grade SHG with a power of 10 kW and a rotation speed of 24 krpm are described. In Reference [20], the simulation of a low-power SHG with a speed of 3000 rpm at idle is considered using a 2D FEA with virtual excitation windings. In Reference [28], a theoretical evaluation of the characteristics of an SHG with a power of 500 kW with a superconducting excitation winding is presented. In Reference [30], the manual optimization of SHG performance at no-load is considered, and an experimental verification is carried out.

In References [6,29], the analysis of SHG characteristics for undercar generators is considered. In Reference [6], the modeling of a 4.5 kW undercar generator is considered, taking into account the eccentric installation of the rotor. In Reference [29], the modeling of the design of an undercarriage generator based on SHG with hybrid excitation is considered.

Based on the literature overview, it can be concluded that previous studies are limited to the manual optimization of the SHG no-load characteristics, as in [30], but do not carry out computer-aided optimization ((CAO), for example, using a genetic algorithm or the Nelder–Mead method) of the SHG on-load performance using FEA due to the fact that the 3D FEA of SHM takes too much time. At the same time, improving the performance of undercar SHGs through optimization is important to reduce their volume (and therefore cost) and power losses, which is required in practice [15].

The novelty of this article is to demonstrate that the proposed technique of CAO of the SHG on-load characteristics, based on the simplified model [9] and the Nelder–Mead method, makes it possible to reduce the volume (cost) and the power loss compared to a commercially available counterpart [31]. To overcome difficulties with the long 3D FEA time, it is proposed to use the simplified 2D SHM model presented in [9].

The optimization procedure was developed, which takes into account the operating cycle of the generator. The objectives of the optimization are to minimize losses in the generator, minimize the maximum current of the controlled rectifier, and minimize torque ripple.

The optimization procedure requires the calculation of only two operating points of the generator, which ensures a short calculation time. The target characteristics of the SHG as a result of optimization are significantly improved. The article also compares the main characteristics of an optimized SHG with a mass-produced undercar generator.

2. General Description of the SHG Design

An SHG consists of two or more SRCSs connected to each other in the axial direction by ferromagnetic structural elements. The excitation current is provided by the excitation winding located on the stator. The magnetic flux of the excitation winding is closed through the SRCSs by means of the stator housing and the sleeve on the rotor shaft [30,32]. This magnetic flux is modulated by the rotor teeth, which allows it to interact with the poles of the stator winding. In this case, half of the poles are involved. The addition of ferrite magnets to the SHG makes it possible to use all poles of the stator winding

Figure 1 shows the considered SHG design. The SHG has two stacks on the stator and two stacks on the rotor made of laminated steel. Each stack of rotor and stator is located in front of each other and forms the stator–rotor stack combination (SRSC). The stator lamination has 54 slots and 12-pole winding with a number of slots per pole and phase $q = 54/(12 \cdot 3) = 1.5$.

An excitation winding is located between the SRSCs and is attached to the nonmagnetic supporting core. The nonmagnetic supporting core has slots of the same shape as the laminated stator cores through which the armature winding coils pass. Figure 1b shows the configuration of one armature winding coil. The pitch of the armature coils is four slots. Such a distributed winding is conventional for an SHG design and is widely used in practice.

The rotor is salient-pole and has no windings. Each rotor stack has six teeth, and the teeth of the rotor stacks are shifted by 30 mechanical degrees. The SHG housing and the rotor sleeve carry the stator lamination and the rotor lamination, respectively. They are made of a solid (not laminated) steel and provide the link to the flux produced by excitation winding.

It is assumed that the generator delivers power to the DC link through a controlled rectifier with transistor switches, as shown in the diagram in Figure 2. The required DC voltage (corresponding to the amplitude line voltage of the electric machine) should not exceed 116 V. At preliminary calculations, it was found that without parallel branches, each layer of the power winding should contain only one turn. This leads to large eddy losses. Therefore, the number of parallel branches is chosen equal to the number of pole pairs six.

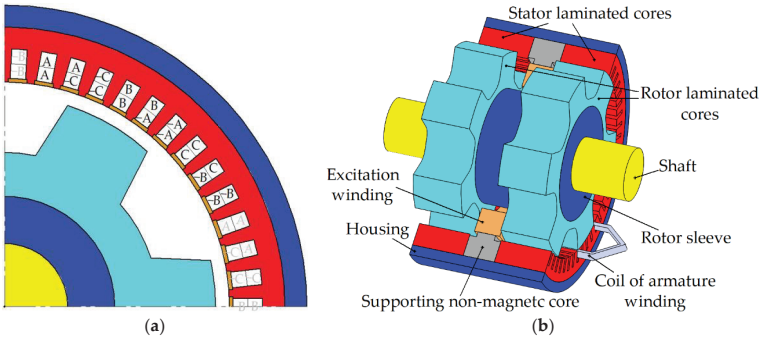

Figure 1. Sketch of the SHG geometry: (**a**) Stator cross-section and winding pattern (1/4 of the machine is shown). The uppercase letters indicate the location and direction of the sides of the coils of phases A, B, C in the slots. (**b**) General view. Only one coil of the armature winding is shown. The rest of the coils are not shown. The two-layer armature winding has 54 coils in total.

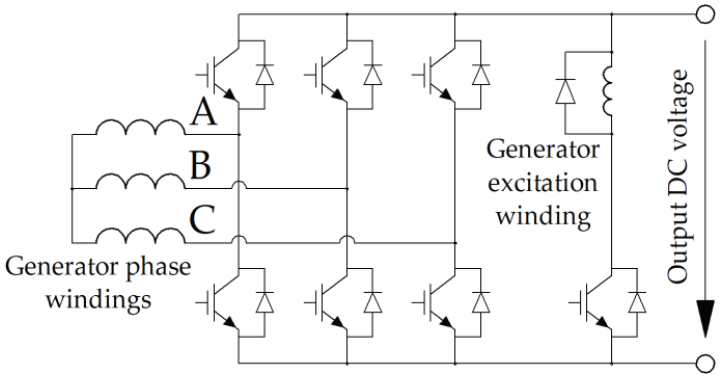

Figure 2. Schematics of the three-phase-controlled rectifier with a DC chopper to supply the excitation winding. The uppercase letters indicate the phases A, B, C of the generator.

3. Operating Points of the Generator, Variable Geometric Parameters, and Objective Function

In the traction drive, motors with a wide speed range at a constant mechanical power (CPSR) are common [25]. An unavoidable feature of CPSR is an increased load on the mechanical part (torque) at low speeds. As a natural generalization for a generator, there could be a requirement for a given range of speeds with a constant output power (active power minus the power of the excitation winding). However, at low speeds and high torques, machine saturation and losses increase, and efficiency also decreases. Therefore, even more mechanical power and even more torque are required. Therefore, in this paper, the generator with a given CPSR is considered.

The rotational speed of the undercar generator increases as the speed of the train increases. The undercar generator described in [31] provides a constant power of 35 kW in the speed range from 750 rpm to 3450 rpm. This paper describes the generator with a CPSR from n_2 = 750 rpm to n_1 = 3450 rpm and the rated mechanical power of P_{max} = 40 kW (Figure 3). It is expected that the averaged value of the output power estimates as the average losses in the modes with the speeds of 750 rpm and 3450 rpm is close to 35 kW. Mechanical losses, namely bearing and windage losses, were neglected.

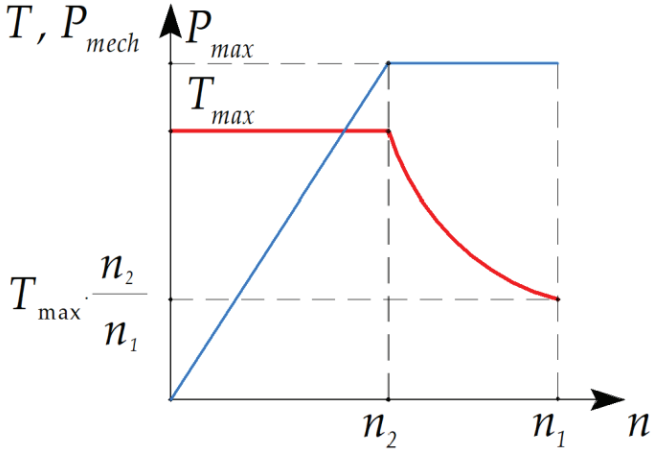

Figure 3. The dependences of the mechanical power P_{mech} (blue line) and torque T (red line) on the generator shaft on the rotation speed n.

During the optimization, it is necessary to minimize the following characteristics of the generator (the most important characteristics are listed first):

1. Average losses $<P_{loss}>$, which were estimated as the average losses in the modes with the speeds of 750 rpm and 3450 rpm;
2. Maximum value of the stator current I_{arm} (reached at 750 rpm mode);
3. Maximum symmetrized torque ripple max(*TRsym*) in both modes;
4. Maximum nonsymmetrized torque max(*TR*) in both modes.

When optimizing, both the torque ripple *TR* of a separate SRSC and the torque ripple *TRsym* resulting from the addition of the torque waveforms of all SRSCs of the SHG were considered [9].

The material for the housing and the sleeve is solid steel 1010. Because the magnetic properties of structural steel are not reported and are not guaranteed by the manufacturer, in order to guarantee that the drop of the magnetomotive force on the axial magnetic cores will be small compared to the drop on the SRSC, in the course of optimization, the flux density in the stator housing and in the rotor sleeve was limited to 1.6 T.

In this study, the single-criteria unconditional Nelder–Mead method was used to optimize the SHG design. Therefore, the objective function was given as a product of individual characteristics raised to a certain power, reflecting the importance of the characteristic. Optimization constraints cannot be set by assigning an infinite value to the optimization function if these conditions are not met, as this would lead to a rapid decrease in the volume of the simplex and convergence to an undesirable local minimum. Therefore, the maximum flux density constraint was set as a soft constraint; that is, the corresponding multiplier begins to increase rapidly if the constraint is not complied. In view of the above, the objective function is defined as follows:

$$\begin{aligned} F &= < P_{loss} > \max(I_{arm})^{0.7} \max(TRsym)^{0.025} \max(TR)^{0.01} f\left(\left(\frac{B_h}{1.6}\right)^5\right), \\ f(x) &= \begin{cases} x, x > 1, \\ 1, \textit{otherwise}, \end{cases} \end{aligned} \tag{1}$$

where $<P_{loss}>$ are the average losses (the arithmetic average of total losses at operating points at 750 and 3450 rpm); max(I_{arm}) and B_h are the values of current and magnetic flux density in nonlaminated steel in the 750 rpm operation point (the maximum values); max(*TRsym*) is the maximum value of the symmetrized torque ripple; max(*TR*) is the maximum value of the nonsymmetrized torque ripple.

To obtain a more general result, optimization was carried out under the assumption that the number of turns in the armature winding layer N_{sec} is a real number and may take noninteger values. In addition, the height and width of the winding wire can be arbitrary real numbers, without taking into account the limitations of the standard assortment [33]. The number of turns was selected so that the amplitude value of the line voltage in the 3450 rpm 40 kW mode V_{3450} (the maximum voltage mode) was equal to 116 V [14]. The number of parallel branches of the armature winding was 6. Figure 4 shows the geometric parameters of the SHG.

Table 1 shows some of the key SHG parameters that were not changed during optimization. Table 2 shows the SHG parameters that were varied during optimization. It was assumed that the shaft does not conduct any flux. The cross sections of the stator housing and the rotor sleeve conducting the same axial excitation flux were taken as equal; therefore, a change in the thickness of the stator housing also causes a change in the outer diameter of the rotor sleeve. When the thickness of the stator housing changes, the outer diameter of the stator lamination also changes.

The width and height of the rectangular armature winding wire w_x and w_y, necessary to determine the DC and AC (eddy current) losses in the armature winding, were determined based on the dependencies:

$$b_p = w_x + a_x; h_p = 2 \cdot (w_y + \Delta w) \cdot N_{sec} + a_y, \quad (2)$$

where a_x = 1.51 mm, a_y = 1.8 mm, and Δw = 0.31 mm were determined by the thicknesses of the conductor insulation and slot insulation.

The net copper fill factor of the excitation winding area was used to calculate the losses in this winding and was assumed to be 0.8. Only DC losses in the excitation winding were taken into account. As Table 2 shows, when optimizing, the electrical angle between the middle of the rotor tooth and the stator current vector ("current angle") at a speed of 3450 rpm varies. The current angle at 750 rpm was assumed to be 0.1 el. rad.

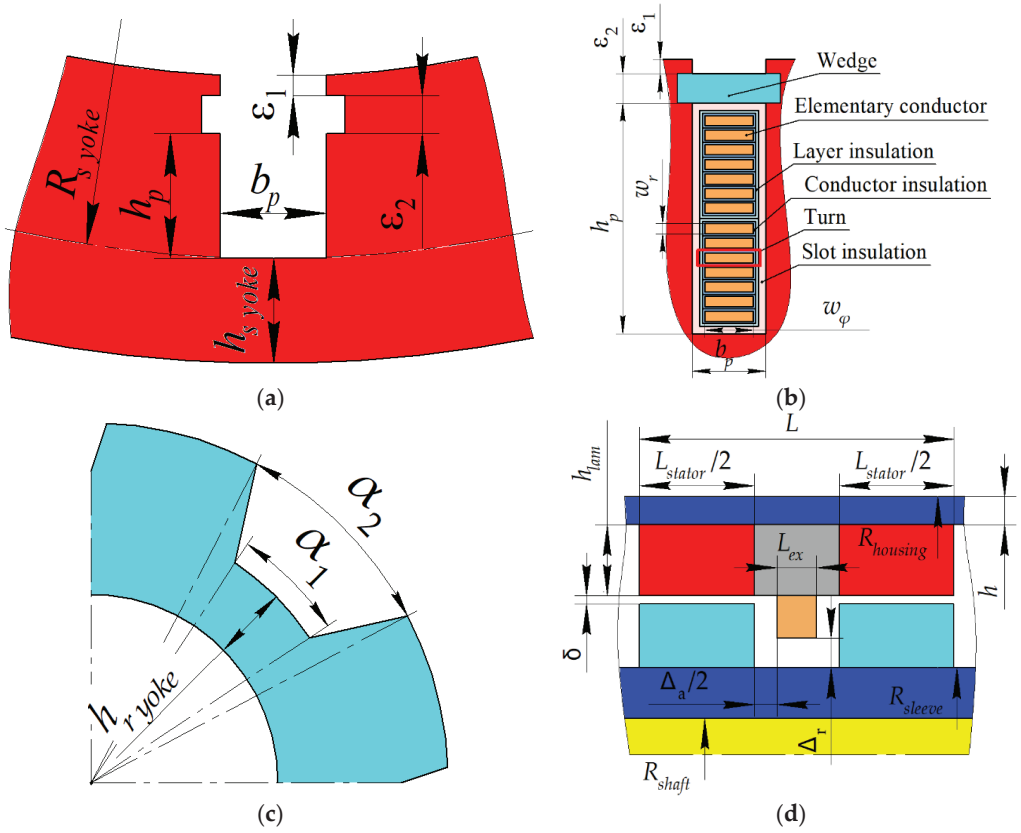

Figure 4. SHG geometric parameters. (**a**) Stator slot; (**b**) Stator winding; (**c**) Rotor core; and (**d**) Other dimensions.

To reduce the number of parameters changed during optimization, the ratio between the excitation winding current and the current in the armature winding layer was taken as constant. The ratio α_2/α_1 between the geometrical angular parameters of the rotor slot indicated in Table 2 was also taken as unchanged. Because the housing and the rotor sleeve carry out the same flux, the areas of their cross-sections were assumed to be equal.

Table 1. Some of the SHG parameters that do not change during optimization.

Parameter	Value
Machine length without end winding parts L, mm	180
Stator housing outer diameter, mm	370
Axial clearance between excitation winding and rotor, Δ_a, mm	15
Radial clearance between field winding and rotor Δ_r, mm	12
Shaft diameter, mm	40
Stator lamination yoke $H_{stator\ yoke}$, mm	12
Rotor lamination yoke $H_{rotor\ yoke}$, mm	9
Stator wedge thickness, ε_2, mm	1
Stator unfilled area thickness, ε_1, mm	1
Angle of field weakening at 750 rpm, el. degrees	0.1
Laminated steel grade	2412
Laminated steel thickness, mm	0.35

Table 2. Variable SHG optimization parameters.

Parameter	Initial Design, *x0*	Optimized Design, *x*
Stator housing thickness h, mm	15	17.1
Total stator stack length L_{stator}, mm	150	152.7
Stator slot depth, h_p, mm	20	29.8
Stator slot width, b_p, mm	5	5.6
Airgap width δ, mm	2	0.88
Rotor slot thickness, α_1	$0.5 \cdot t_z$ *	$0.554 \cdot t_z$ *
Rotor slot thickness, α_2	0.6	0.665
Angle of field weakening at 3450 rpm, electrical radian	0.6	1.13
Current ratio **	8	6.43

Notes: * The rotor tooth pitch $t_z = 360^\circ/6 = 60$ mechanical degrees; ** the current ratio is the ratio of the current in the armature winding layer to the current in the excitation winding.

Figure 5 shows a flowchart of the calculation of the output of the objective function defined by Equation (1). To find the optimized value of the vector of variable parameters x, the fminsearch(*F*, *x0*) MATLAB R2021a procedure was launched, where *F* is the objective function, according to Figure 5; *x0* is the initial vector of variable optimization parameters (see Table 2). The details of the optimization function 'fminsearch', which implements the simplex gradientless Nelder–Mead method [34], are well known and described in the documentation of the MATLAB software [35].

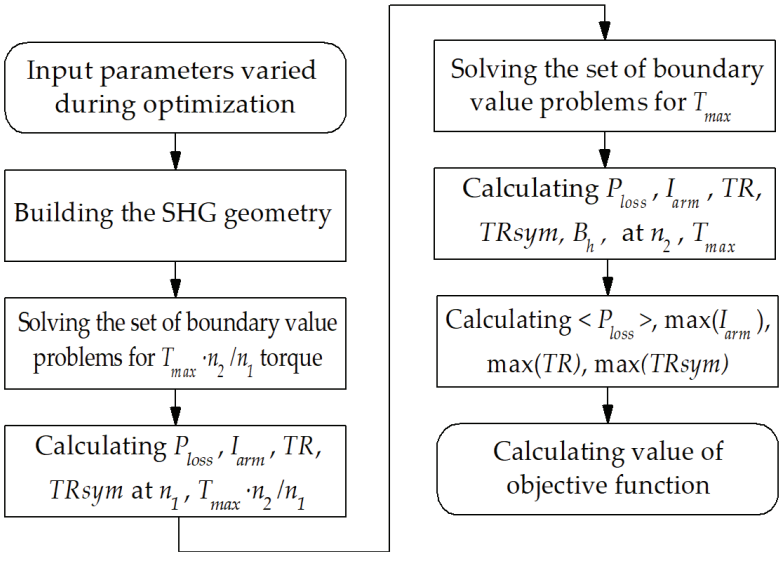

Figure 5. Objective function flowchart. The input parameters varied during optimization is shown in Table 2. The objective function is defined by Equation (1).

4. Optimization Results

The application of the Nelder–Mead method leads to the convergence of the objective function defined by Equation (1) to a certain minimum (Figure 6). In the course of optimization, the SHG average loss (Figure 7a) and the armature current amplitude (Figure 7b) were also reduced significantly. The nonsymmetrized torque ripple, that has the smallest power in the objective function (1), increased during the optimization (Figure 8a). However, the symmetrized torque ripple, which is the resultant one of the SHM as a whole, slightly decreased after the optimization (Figure 8b), which indicates that the torque waveforms of the individual SRSCs are in opposite phase and cancel each other out. Figures 9 and 10 show the geometry and 2D flux density plot of an SRSC before and after optimization.

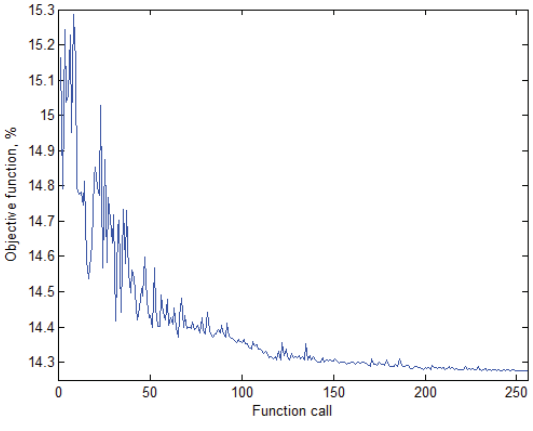

Figure 6. Change in the value of the objective function defined by Equation (1) in the course of optimization.

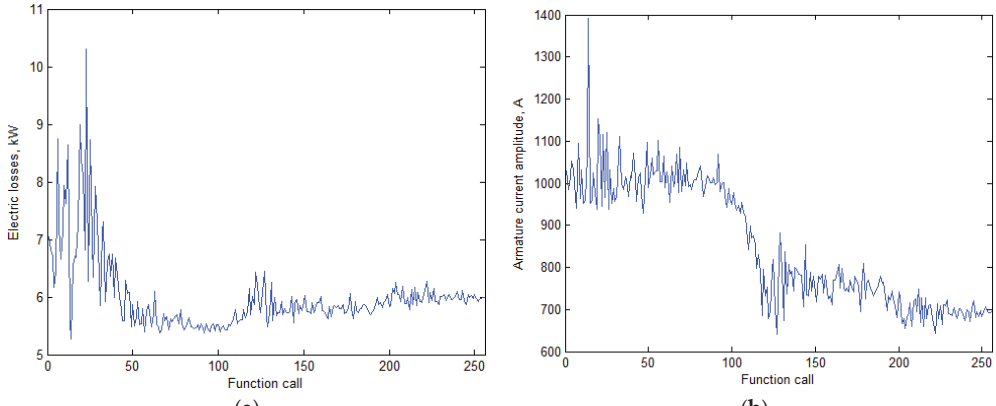

(**a**) (**b**)

Figure 7. Change in the SHG performances in the course of optimization. (**a**) average losses and (**b**) maximum armature current amplitude.

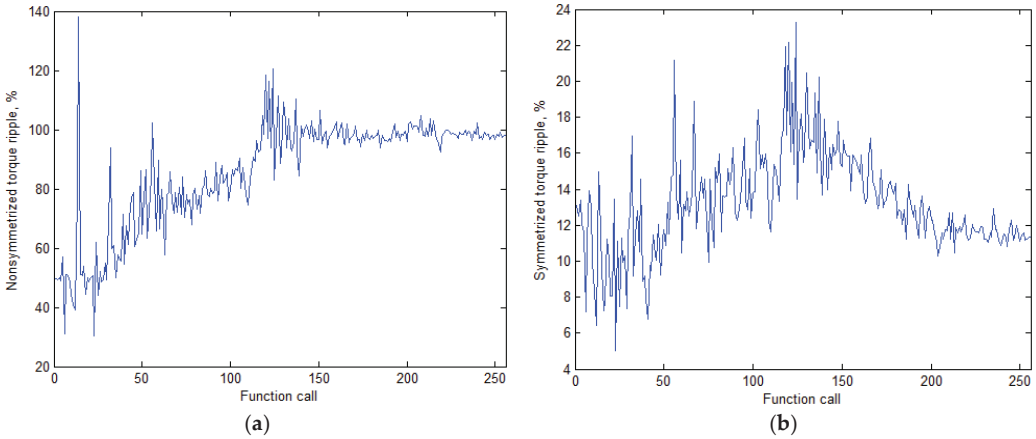

(**a**) (**b**)

Figure 8. Change in the SHG parameters in the course of optimization. (**a**) nonsymmetrized torque ripple and (**b**) symmetrized torque ripple.

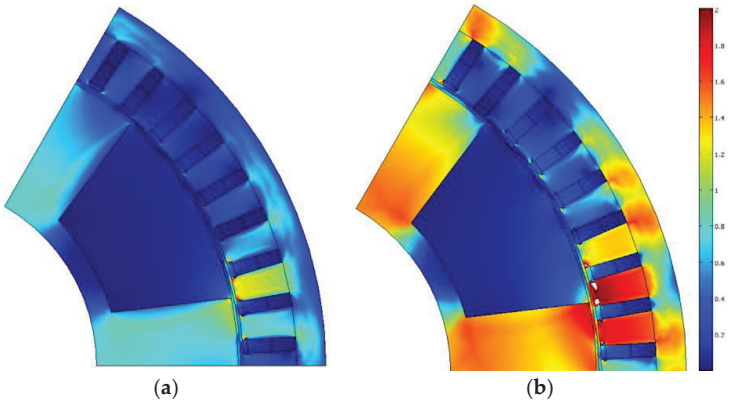

(**a**) (**b**)

Figure 9. The cross-section of the SHG initial design and its plot of flux density magnitude (T); areas of extreme saturation (>2T) are colored white: (**a**) at 3450 rpm and (**b**) at 750 rpm.

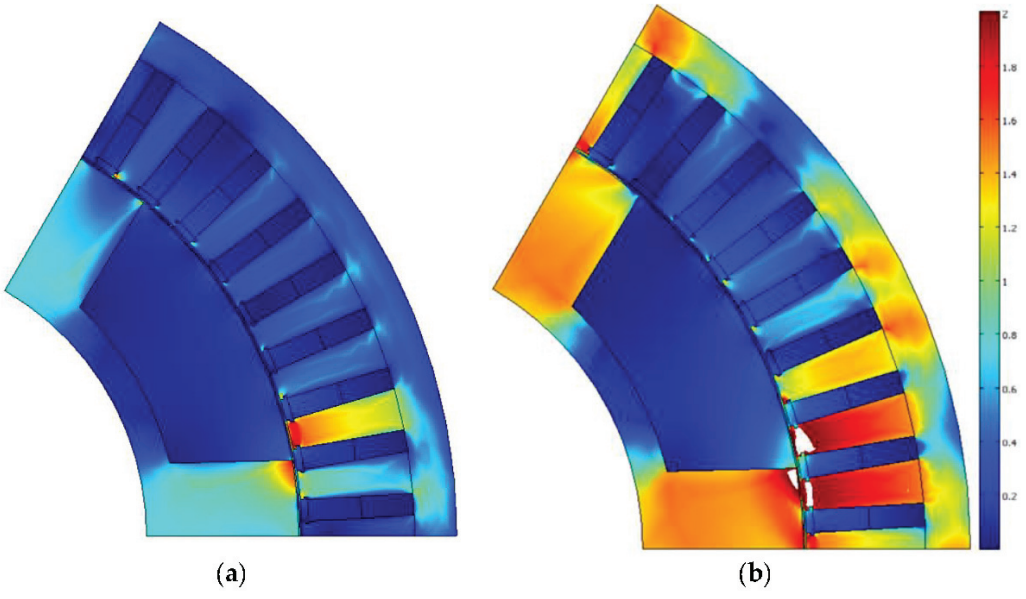

Figure 10. The cross-section of the SHG optimized design and its plot of flux density magnitude (T); areas of extreme saturation (>2T) are colored white: (**a**) at 3450 rpm and (**b**) at 750 rpm.

Comparison of the SHG parameters before and after optimization, shown in Table 3 allows us to draw the following conclusions:

(1) The losses in operating point 2 reduce by 100% (11.56 − 8.10)/11.56 = 30%;
(2) The losses in operating point 1 are much lower than those in point 2, and their increase by 3.84/2.52 = 1.5 times is not so bad. In addition, it is the price for the reduction in the required rectifier power by 100% (100.6 − 67.9)/100.6 = 32.5%, which is achieved by increasing the field weakening angle;
(3) However, average losses reduce by 100% (7.04 − 5.97)/7.04 = 15.2%;
(4) To demonstrate the ability of the SHG to produce energy at a speed lower than 750 rpm, the 300 rpm mode was calculated. To reduce saturation and losses, the torque equal to 90% of the torque in point 2 was chosen. The output power is 8.03 kW; the input power is 14.42 kW, and the generator efficiency is 56%;
(5) After optimization, the maximum symmetrized torque ripple (ripple at the shaft at low speed was reduced by 100% (13.1 − 11.3)/13.1 = 13.7%;
(6) Comparison of the initial and the optimized designs shows that as a result of optimization, the area of the stator slots for the winding increased by increasing the height and reducing the thickness of the stator tooth, which leads to a decrease in the armature winding resistance and the DC losses in the winding.

The original design has a flux density in nonlaminated parts of more than 1.6 T. Due to the introduction of an appropriate multiplier in the optimization function defined by Equation (1), in the final design, the thickness of the stator housing is increased, and the induction does not exceed 1.6 T.

The rotor sleeve radius is also automatically increased, for the housing and rotor sleeve cross-section areas are equal. The increase in the housing thickness and the stator slot depth leads to a decrease in the airgap radius, which is partially compensated by an increase in the stator stack length. Table 3 compares the SHG characteristics before and after optimization.

Table 3. Optimization results.

Parameter	Initial Design		Optimized Design	
Operating point	1	2	1	2
Rotational speed n, rpm	3450	750	3450	750
Amplitude of the armature phase current I_{arm}, A	388.6	1001.7	369.5	676.2
Efficiency η *, %	93.7	71.1	90.4	79.8
Input mechanical power P_{mech}, kW	40	40	40	40
Active electrical power P_1, kW	37.67	29.33	36.58	33.12
Output electrical power $P_1 - P_{ex}$, kW	37.5	28.4	36.2	32.0
Armature DC copper loss $P_{arm\,DC}$, kW	1.55	10.30	1.90	6.37
Armature eddy current copper loss $P_{arm\,AC}$, W	123	51	417	131
Stator lamination loss $P_{iron\,st}$, W	663	359	961	403
Rotor lamination loss $P_{iron\,rt}$, W	51	10	192	26
Excitation copper loss P_{ex}, W	129	837	368	1169
Total loss P_{loss} **, kW	2.52	11.56	3.84	8.10
Average loss $<P_{loss}>$, kW	7.04		5.97	
Number of turns in armature winding	5.14		7.75	
Required rectifier power, kW	100.6		67.9	
Power factor	0.969	0.668	1.000	0.747
Line-to-line voltage amplitude V_{arm}, V	116.0	51.3	116.0	75.3
Nonsymmetrized torque ripple, %	49.7	33.7	97.8	47.0
Symmetrized torque ripple, %	13.1	5.0	11.3	4.5
Magnetic flux density in the housing and the sleeve B_h, T	1.00	1.91	0.84	1.60

* Note: the generator efficiency was calculated as $\eta = (P_1 - P_{ex})/P_{mech}$, where P_1 is the active power in armature winding; P_{ex} is the loss in the excitation winding; P_{mech} is the input (mechanical) power. Mechanical losses, namely bearing and windage losses, were neglected; ** the total loss is the sum of all individual loss components $P_{loss} = P_{arm\,DC} + P_{arm\,AC} + P_{iron\,st} + P_{iron\,rt} + P_{ex}$.

5. Performance Comparison of the Optimized Design with a Commercially Available Undercar Generator

This section compares the characteristics of the proposed optimized design of the generator with a serially produced undercarriage generator with an excitation winding on the stator EGV.08.1 with a rated power of 35 kW [31]. Table 4 shows the comparison results of the considered generators.

The results of comparing the calculated optimized characteristics of the SHG with the characteristics of a commercially produced generator allow us to draw the following conclusions:

(1) The volume of the active part of the optimized SHG is 0.04/0.019 = 2.1 times smaller than that of a mass-produced generator. It is expected that the mass and the cost of the optimized SHG will be less than that of the mass-produced generator;

(2) The calculated efficiency of the optimized SHG neglecting mechanical losses is much greater than the efficiency of the mass-produced SHG over the entire range of operation. The mechanical losses that are mainly small losses in the bearings cannot reduce the efficiency significantly;

(3) The reduced input (mechanical) power due to the reduction of power loss of the SHG results in reducing the load on the transmission elements and wheels of the car, which will increase their lifetime.

Table 4. Performance comparison of the optimized SHG design with a commercially available undercar generator.

Parameter	EGV.08.1 (PEMZ) [31]	Optimized Design of the SHG
Output electric power, kW	35	≈35 (36.2 kW at 3500 rpm; 32.0 kW at 800 rpm)
Average output power, kW	35	34.1
Number of poles	24	12
Electric frequency at maximum speed, Hz	690	350
Stator outer diameter (excluding cooling fins) D, mm	380	370
Machine length without end winding parts L, mm	357 *	180
Active parts volume $\pi \cdot L \cdot D^2/4$, m^3	0.04	0.019
Efficiency @ 750 rpm %	72	79.8 (without taking into account mechanical losses)
Efficiency @ 3450 rpm, %	85	90.4 (without taking into account mechanical losses)
Number of phases	3	3
Cooling type	Air cooling without fan	Air cooling without fan

* Note: The length of the stator stack of a mass-produced generator was calculated taking into account its outline drawing from the manufacturer's website [31] and a sketch from the book [36], which shows that the length of the stator package is approximately 70% of the distance between the bearing shields.

6. Conclusions

This article discusses the methodology and results of optimizing a synchronous homopolar generator (SHG) with an output power of approximately 35 kW without permanent magnets for railway passenger cars. Because the rotational speed of the generator changes as the velocity of the train changes, the performance of the generator is optimized for the required speed range. To reduce the saturation and the currents at low speeds, a constant mechanical power speed range (CPSR) strategy widely used for traction motors is proposed for the undercar generator. The CPSR of the SHG is from 750 rpm to 3450 rpm.

The SHG starts to produce electric energy at the speeds much lower than the low boundary of the CPSR, which is a significant advantage when the passenger car starts with the discharged batteries. Thus, it produces 8.03 kW at 300 rpm.

An optimization procedure was adapted to use the single-criteria, unconstrained Nelder–Mead method. The optimization minimizes the SHG average power loss over the CPSR, the current capacity of the semiconductor rectifier, and the torque ripple. The optimization results show a significant improvement of the target performances of the SHG with ferrite magnets. Compared to the nonoptimized design, the following were reduced: average generator losses by 14.6%, required current capacity of the semiconductor rectifier by 24.8%, and torque ripple by 18.2%.

The calculated characteristics of the SHG were compared with the catalogue characteristics of a commercial undercar generator. The comparison shows that the volume of the SHG electromagnetic core is 2.1 times smaller than that of the commercial generator. At the same time, the calculated efficiency of the SHG is much higher than that of the commercial generator in the entire operating speed range.

In addition, the reduced input (mechanical) power due to the reduction of power loss of the SHG results in reducing the load on the transmission elements and wheels of the car, which will increase their lifetime.

Author Contributions: Conceptual approach, V.D. and V.P.; data duration, V.D. and V.K.; software, V.D. and V.P.; calculations and modeling, V.D., V.K. and V.P.; writing—original draft, V.D., V.K. and V.P.; visualization, V.D. and V.K.; review and editing, V.D., V.K. and V.P. All authors have read and agreed to the published version of the manuscript.

Funding: The research funding from the Ministry of Science and Higher Education of the Russian Federation (Ural Federal University Program of Development within the Priority-2030 Program) is gratefully acknowledged.

Institutional Review Board Statement: Not applicable.

Informed Consent Statement: Not applicable.

Data Availability Statement: Data are contained within the article.

Acknowledgments: The authors thank the editors and reviewers for careful reading and constructive comments.

Conflicts of Interest: The authors declare no conflict of interest.

References

1. Percentage of the Railway Lines in Use in Europe in 2020 which Were Electrified, by Country. Report. Statista. 2023. Available online: https://www.statista.com/statistics/451522/share-of-the-rail-network-which-is-electrified-in-europe/ (accessed on 29 January 2023).
2. Worldwide Rail Electrification Remains at High Volume. Press Release. RailwayPRO Communication Platform. 19 February. 2021. Available online: https://www.railwaypro.com/wp/worldwide-rail-electrification-remains-at-high-volume/ (accessed on 29 January 2023).
3. Liudvinavičius, L.; Jastremskas, V. Modernization of diesel-electric locomotive 2M62 and TEP-70 locomotives with respect to electrical subsystem. *Procedia Eng.* **2017**, *187*, 272–280. [CrossRef]
4. Levin, N.; Kamolins, E.; Pugachev, V.; Gusakov, A. Synchronous generator with two-channel excitation for power supply of railway passenger cars. In Proceedings of the 2012 Electric Power Quality and Supply Reliability, Tartu, Estonia, 11–13 June 2012; pp. 1–6. [CrossRef]
5. Gulbis, K.; Kamolins, E.; Brakanskis, U. Synchronous inductor generator with electrically integrated armature and field windings with improved performance. In Proceedings of the IEEE 8th Workshop on Advances in Information, Electronic and Electrical Engineering (AIEEE), Vilnius, Lithuania, 22–24 April 2021; pp. 1–6. [CrossRef]
6. Bindu, G.; Basheer, J.; Venugopal, A. Analysis and control of rotor eccentricity in a train-lighting alternator. In Proceedings of the IEEE International Conference on Power, Control, Signals and Instrumentation Engineering (ICPCSI), Chennai, India, 21–22 September 2017; pp. 2021–2025. [CrossRef]
7. Lorilla, L.; Keim, T.; Lang, J.; Perreault, D. Topologies for future automotive generators: Part I—Modeling and analytics. In Proceedings of the 2005 IEEE Vehicle Power and Propulsion Conference, Chicago, IL, USA, 7 September 2005; pp. 74–85. [CrossRef]
8. Bianchini, C.; Immovilli, F.; Bellini, A.; Lorenzani, E.; Concari, C.; Scolari, M. Homopolar generators: An overview. In Proceedings of the IEEE Energy Conversion Congress and Exposition, Phoenix, AZ, USA, 17–22 September 2011; pp. 1523–1527. [CrossRef]
9. Dmitrievskii, V.; Prakht, V.; Anuchin, A.; Kazakbaev, V. Traction Synchronous Homopolar Motor: Simplified Computation Technique and Experimental Validation. *IEEE Access* **2020**, *8*, 185112–185120. [CrossRef]
10. Severson, E.; Nilssen, R.; Undeland, T.; Mohan, N. Dual-purpose no-voltage winding design for the bearingless AC homopolar and consequent pole motors. *IEEE Trans. Ind. Appl.* **2015**, *51*, 2884–2895. [CrossRef]
11. Jeong, J.-S.; An, D.-K.; Hong, J.-P.; Kim, H.-J.; Jo, Y.-S. Design of a 10-MW-Class HTS homopolar generator for wind turbines. *IEEE Trans. Appl. Supercond.* **2017**, *27*, 1–4. [CrossRef]
12. Kutt, F.; Michna, M.; Kostro, G. Non-Salient Brushless Synchronous Generator Main Exciter Design for More Electric Aircraft. *Energies* **2020**, *13*, 2696. [CrossRef]
13. Noeland, J.; Nuzzo, S.; Tessarolo, A.; Alves, E. Excitation System Technologies for Wound-Field Synchronous Machines: Survey of Solutions and Evolving Trends. *IEEE Access* **2019**, *7*, 109699–109718. [CrossRef]
14. Prakht, V.; Dmitrievskii, V.; Kazakbaev, V.; Anuchin, A. Comparative Study of Electrically Excited Conventional and Homopolar Synchronous Motors for the Traction Drive of a Mining Dump Truck Operating in a Wide Speed Range in Field-Weakening Region. *Mathematics* **2022**, *10*, 3364. [CrossRef]
15. Levin, N.; Kamolins, E.; Pugachev, V. Unlike-Pole Inductor Generator with Electrically Integrated Armature and Excitation Windings for the Power Supply Systems of Passenger Cars. *Latv. J. Phys. Tech. Sci.* **2013**, *50*, 12–23. [CrossRef]
16. Ferrari, S.; Pellegrino, G. FEAfix: FEA Refinement of Design Equations for Synchronous Reluctance Machines. *IEEE Trans. Ind. Appl.* **2020**, *56*, 256–266. [CrossRef]
17. Cheshmehbeigi, H.; Afjei, E. Design optimization of a homopolar salient-pole brushless DC machine: Analysis, simulation, and experimental tests. *IEEE Trans. Energy Convers.* **2013**, *28*, 289–297. [CrossRef]
18. Severson, E.; Mohan, N.; Nilssen, R.; Undeland, T. Outer-rotor AC homopolar motors for flywheel energy storage. In Proceedings of the 7th IET International Conference on Power Electronics, Machines and Drives (PEMD), Manchester, UK, 8–10 April 2014; pp. 1–6. [CrossRef]

19. Hwang, Y.J. Design and Characteristic Analysis of a Homopolar Synchronous Machine Using a NI HTS Field Coil. *Energies* **2021**, *14*, 5658. [CrossRef]
20. Yang, J.; Ye, C.; Liang, X.; Xu, W.; Xiong, F.; Xiang, Y.; Li, W. Investigation of a Two-Dimensional Analytical Model of the Homopolar Inductor Alternator. *IEEE Trans. Appl. Supercond.* **2018**, *28*, 5205205. [CrossRef]
21. Ye, C.; Yang, J.; Xiong, F.; Zhu, Z.Q. Relationship between homopolar inductor machine and wound-field synchronous machine. *IEEE Trans. Ind. Electron.* **2020**, *67*, 919–930. [CrossRef]
22. Belalahy, C.; Rasoanarivo, I.; Sargos, F. Using 3D reluctance network for design a three phase synchronous homopolar machine. In Proceedings of the 34th Annual Conference of IEEE Industrial Electronics, Orlando, FL, USA, 10–13 November 2008; pp. 2067–2072. [CrossRef]
23. Dmitrievskii, V.; Prakht, V.; Anuchin, A.; Kazakbaev, V. Design Optimization of a Traction Synchronous Homopolar Motor. *Mathematics* **2021**, *9*, 1352. [CrossRef]
24. Prakht, V.; Dmitrievskii, V.; Anuchin, A.; Kazakbaev, V. Inverter Volt-Ampere Capacity Reduction by Optimization of the Traction Synchronous Homopolar Motor. *Mathematics* **2021**, *9*, 2859. [CrossRef]
25. Dmitrievskii, V.; Prakht, V.; Kazakbaev, V.; Anuchin, A. Design Optimization of the Magnet-Free Synchronous Homopolar Motor of a Subway Train. *Appl. Sci.* **2022**, *12*, 12647. [CrossRef]
26. Dmitrievskii, V.; Prakht, V.; Kazakbaev, V.; Anuchin, A. Comparison of Interior Permanent Magnet and Synchronous Homopolar Motors for a Mining Dump Truck Traction Drive Operated in Wide Constant Power Speed Range. *Mathematics* **2022**, *10*, 1581. [CrossRef]
27. Lashkevich, M.; Anuchin, A.; Aliamkin, D.; Briz, F. Control strategy for synchronous homopolar motor in traction applications. In Proceedings of the 43rd Annual Conference of the IEEE Industrial Electronics Society (IECON), Beijing, China, 29 October–1 November 2017; pp. 6607–6611. [CrossRef]
28. Kalsi, S.; Hamilton, K.; Buckley, R.G.; Badcock, R.A. Superconducting AC Homopolar Machines for High-Speed Applications. *Energies* **2019**, *12*, 86. [CrossRef]
29. Orlova, S.; Pugachov, V.; Levin, N. Hybrid Excitation of the Axial Inductor Machine. *Latv. J. Phys. Tech. Sci.* **2012**, *49*, 35–41. [CrossRef]
30. Janis, D.; Levin, N.; Orlova, S.; Pugachov, V.; Ribickis, L. Optimization of the magnetic circuit of an axial inductor machine based on the calculation and analysis of magnetic field. In Proceedings of the 13th European Conference on Power Electronics and Applications, Barcelona, Spain, 8–10 September 2009; pp. 1–8. Available online: https://ieeexplore.ieee.org/document/5278726 (accessed on 29 January 2023).
31. Synchronous Generators Type EGV. The Generators EGV Are Designed for Power Supply of a Passenger Car. Characteristics. Pskov Electric Machine-Building Plant. Available online: https://www.pemz.ru/catalog/dlya_zheleznoy_dorogi/Synchronous_generators_type_EGV/ (accessed on 30 January 2023).
32. Guo, S.; Yi, Z.; Liu, P.; Wang, G.; Lai, H.; Yu, K.; Xie, X. Analysis and Performance Evaluation of a Novel Adjustable Speed Drive with a Homopolar-Type Rotor. *Mathematics* **2022**, *10*, 3712. [CrossRef]
33. *IEC 60317-0-2:2020*; Specifications for Particular Types of Winding Wires—Part 0-2: General Requirements—Enamelled Rectangular Copper Wire. IEC: Geneva, Switzerland, 2020. Available online: https://webstore.iec.ch/publication/63495 (accessed on 30 January 2023).
34. Lagarias, J.; Reeds, J.; Wright, M.; Wright, P. Convergence Properties of the Nelder-Mead Simplex Method in Low Dimensions. *SIAM J. Optim.* **1998**, *9*, 112–147. [CrossRef]
35. Find Minimum of Unconstrained Multivariable Function Using Derivative-Free Method. MATLAB Documentation. ©1994–2023 The MathWorks, Inc. Available online: https://www.mathworks.com/help/matlab/ref/fminsearch.html (accessed on 30 January 2023).
36. Ponkratov, Y. *Electric Machines of Railway Cars*; Educational and Methodological Center for Education in Railway Transport: Moscow, Russia, 2016. Available online: https://studref.com/552936/tehnika/konstruktsii_mashin_peremennogo_toka (accessed on 30 January 2023). (In Russian)

energies

MDPI

Article

Multi-Objective Optimization Strategy for Permanent Magnet Synchronous Motor Based on Combined Surrogate Model and Optimization Algorithm

Yinquan Yu [1,2,3,*], Yue Pan [1,2,3], Qiping Chen [1,2,3], Yiming Hu [1,2,3], Jian Gao [4], Zhao Zhao [5], Shuangxia Niu [6] and Shaowei Zhou [7]

[1] School of Mechatronics and Vehicle Engineering, East China Jiaotong University, Nanchang 330013, China
[2] Key Laboratory of Conveyance and Equipment of Ministry of Education, East China Jiaotong University, Nanchang 330013, China
[3] Institute of Precision Machining and Intelligent Equipment Manufacturing, East China Jiaotong University, Nanchang 330013, China
[4] School of Electrical and Information Engineering, Hunan University, Changsha 410006, China
[5] Faculty of Electrical Engineering and Information Technology, Otto-von-Guericke University of Magdeburg, 39106 Magdeburg, Germany
[6] Department of Electrical Engineering, The Hong Kong Polytechnic University, Hong Kong 999077, China
[7] CRRC Changchun Railway Vehicles Corporation Limited, 435 Qingyin Road, Changchun 130062, China
* Correspondence: yinquan.yu@gmail.com

Abstract: When a permanent magnet synchronous motor (PMSM) is designed according to the traditional motor design theory, the performance of the motor is often challenging to achieve the desired goal, and further optimization of the motor design parameters is usually required. However, the motor is a strongly coupled, non-linear, multivariate complex system, and it is a challenge to optimize the motor by traditional optimization methods. It needs to rely on reliable surrogate models and optimization algorithms to improve the performance of the PMSM, which is one of the problematic aspects of motor optimization. Therefore, this paper proposes a strategy based on a combination of a high-precision combined surrogate model and the optimization method to optimize the stator and rotor structures of interior PMSM (IPMSM). First, the variables were classified into two layers with high and low sensitivity based on the comprehensive parameter sensitivity analysis. Then, Latin hypercube sampling (LHS) is used to obtain sample points for highly sensitive variables, and various methods are employed to construct surrogate models for variables. Each optimization target is based on the acquired sample points, from which the most accurate combined surrogate model is selected and combined with non-dominated ranking genetic algorithm-II (NSGA-II) to find the best. After optimizing the high-sensitivity variables, a new finite element model (FEM) is built, and the Taguchi method is used to optimize the low-sensitivity variables. Finally, finite element analysis (FEA) was adopted to compare the performance of the initial model and the optimized ones of the IPMSM. The results showed that the performance of the optimized motor is improved to prove the effectiveness and reliability of the proposed method.

Keywords: IPMSM; sensitivity analysis; surrogate model; Taguchi method

Citation: Yu, Y.; Pan, Y.; Chen, Q.; Hu, Y.; Gao, J.; Zhao, Z.; Niu, S.; Zhou, S. Multi-Objective Optimization Strategy for Permanent Magnet Synchronous Motor Based on Combined Surrogate Model and Optimization Algorithm. *Energies* **2023**, *16*, 1630. https://doi.org/10.3390/en16041630

Academic Editor: Gianluca Brando

Received: 19 December 2022
Revised: 10 January 2023
Accepted: 2 February 2023
Published: 6 February 2023

1. Introduction

Due to its high power factor, high torque density, high efficiency, high reliability, and other advantages, PMSM is widely used in electric vehicles, aerospace, and other vital fields [1–3]. To design an efficient and reliable PMSM, the researchers optimized both the controller and the body structure of the PMSM. The structure optimization of the PMSM is mainly divided into single-objective optimization [4,5] and multi-objective optimization [6–26] of the motor. Traditional single-objective optimization methods often consider only individual motor performance. In contrast, the overall performance of the

PMSM is affected by output torque, torque ripple, speed range, loss, temperature rise, and many other factors. In [4,5], a method for effectively weakening the tooth groove torque of the motor is proposed; however, other performance indicators, such as average torque, loss, efficiency, etc., are not taken into account. Although this single-objective optimization method can significantly improve the particular performance index of the motor, it is always premised on sacrificing other performances of the motor, which is not conducive to the overall performance improvement of the PMSM. Therefore, the current PMSM optimization study is mainly a multi-objective optimization method. In the literature [6–8], the parametric scanning method is applied to optimize the performance of the motor. This method can effectively find out the combination of design variables that meet the objective conditions, but this process requires much computation, is very time-consuming, and is not suitable for application in the case of many design variables. In order to reduce the computation time, in the literature [9–11], the Taguchi method is introduced to optimize the objective performance of the motor. This method finds the best combination of design variables based on orthogonal test design and analysis. It can effectively optimize the performance of the motor with fewer trials, and the optimization efficiency is high. Therefore, the Taguchi method is often used by designers to optimize the design of mechanical structures. However, in the case of large value ranges of design variables, the Taguchi method has a large span of adjacent value levels in the design space, and many high-quality design variables will be ignored. The optimization accuracy is insufficient. To overcome this difficulty, in the literature [12,13], the combination of fuzzy theory and the Taguchi method is introduced to convert multiple objectives to a single objective and update the value ranges of design variables in the optimization process based on the sequential Taguchi method, and then again optimize the performance of the IPMSM, thereby effectively improving the optimization accuracy. However, this method requires much manual calculation with complicated data processing.

To further improve the multi-objective optimization effect of the PMSM, in addition to the aforementioned Taguchi method, the response surface method [14,15], and the intelligent optimization algorithm [17–25], other methods are also applied in the optimization design of the motor and provide more optimization solutions to improve the performance of the motor. In the literature [14,15], the response surface method is adopted to obtain the non-linear relationship between variables and objectives and perform a comprehensive analysis to obtain the best combination of design variables of the performance of the motor. The motor optimization design based on the intelligent optimization algorithm is mainly used to build the surrogate model and then be combined with the optimization algorithm to look for the combination of variables that meet the requirements [16]. The surrogate models commonly used in optimization problems of the PMSM are the response surface method (RSM) model [17], the Kriging model [18], the support vector regression (SVR) model [19], etc. The reliability of the whole optimization is directly determined by the goodness of the surrogate model. If the surrogate model does not accurately reflect the mapping relationship between the design variables and the optimization objectives, even if it is combined with the optimization algorithm, it cannot produce accurate and effective results. The optimization algorithms commonly used in optimizing the PMSM are genetic algorithms [20], particle swarm algorithms [21], etc. In the literature [22], radial basis function (RBF) neural network and multi-island genetic algorithm (MIGA) are combined for the torque performance optimization of the motor. In the literature [23], the average torque, the torque ripple, the average suspension force, and the suspension force ripple of the motor are taken as the optimization objectives. In the optimization process, the combination of RSM and improved MOPSO is adopted. The results show that the torque Performance of the motor is improved. However, the RSM usually uses the relationship between the second-order polynomial fitting variables and the objective performance. The fitting accuracy cannot be guaranteed to be high enough when there are many variables. In the literature [24], to obtain a more accurate approximation relationship between the design variables and the optimization objectives, a variety of different surrogate models are established, analyzed,

and compared. The best-performing random forest (RF) surrogate model is selected to optimize the performance indicators of the motor in combination with NSGA-II. Although the surrogate model combined with the intelligent optimization algorithm can effectively obtain the optimal combination of design variables in the optimization design of the PMSM, as the number of design variables increases, the accuracy of the surrogate model decreases, and the convergence of the optimization algorithm is more difficult. It is a challenge to obtain the optimal value. In this case, the optimization strategy of the PMSM is very critical. By taking into account many design variables [25], the sensitivity analysis method can be used to divide the design variables into two layers of sensitivity and insensitivity and then optimize them, respectively. The results show that this strategy can effectively solve the optimization problem of many design variables. However, in that paper, only the torque performance of the motor is considered. In the literature [26], a strategy for optimizing the structure of the IPM motor based on deep learning is proposed. The process trains the model by inputting a cross-sectional image of the rotor structure of the motor and the corresponding output performance data. Then it selects the best combination of design variables based on the trained model. However, the data samples required by the method are too large, and the technique is very time-consuming.

In this paper, a multi-objective optimization strategy based on a combined surrogate model and the optimization algorithm is proposed to optimize the average torque, the torque ripple, and the loss of the IPMSM. The rest of this paper is as follows: The FEM model of the IPMSM is established, and the optimization process of IPMSM is introduced in Section 2. In Section 3, the optimization variables and objectives are determined, and the optimization variables are divided into high-sensitivity variables and low-sensitivity variables according to the comprehensive sensitivity analysis. The high-sensitivity variables are optimized by using the surrogate model in combination with NSGA-II, and the low-sensitivity variables are optimized by using the Taguchi method. In Section 4, the performances of the pre-optimization and post-optimization motors are verified and contrasted. Conclusions are drawn in Section 5.

2. IPMSM Models and Optimization Process

In this paper, an IPMSM is taken as the optimization specimen. The FEM of IPMSM is shown in Figure 1a, and the main parameters of the IPMSM are shown in Table 1. The main dimensions of the motor are set within the reasonable design range, and the PMs are inserted into the V-shaped structure rotor core.

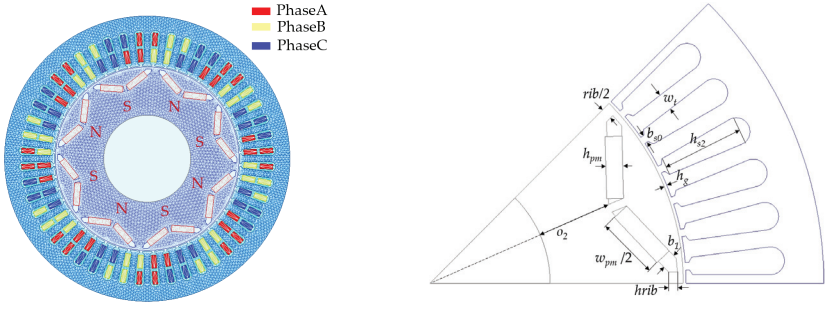

(**a**) (**b**)

Figure 1. Model of IPMSM: (**a**) grid partitioning; (**b**) 1/8 parameterization model.

Table 1. Primary parameters of the IPMSM.

Parameter	Unit	Value
Rated speed	rpm	3000
Rated power	kW	30
Rated voltage	V	336
Stator outer radius	mm	210
Stator inner radius	mm	136.5
Rotor outer radius	mm	135
Axial length	mm	210
PM	-	NdFe35
Number of poles/slots	-	8/48

The flowchart of the multi-objective optimization method of the motor proposed in this paper is shown in Figure 2. The optimization steps are present as follows:

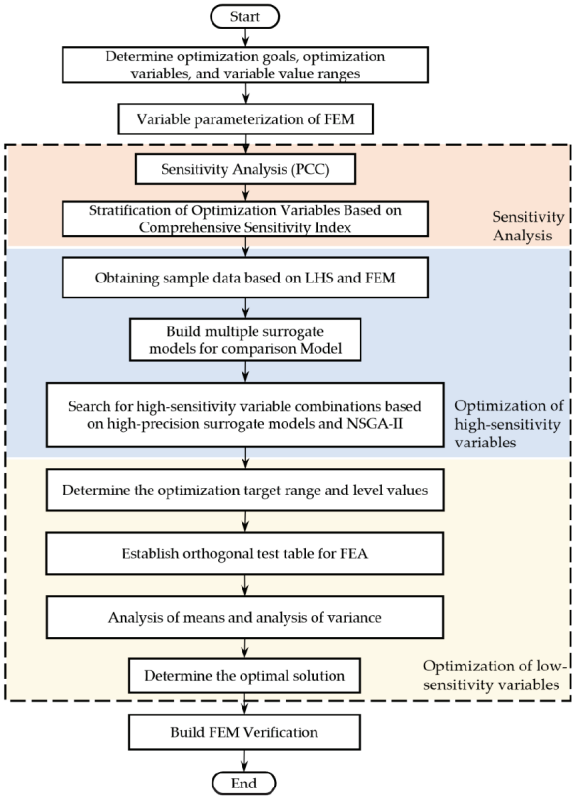

Figure 2. Flowchart of multi-objectives optimization method.

① Determining the optimization objectives and variables and establishing the parameterization model of the motor through parameterization settings.
② Performing subsequent optimizations by dividing the optimization variables into two layers of high-sensitivity and low-sensitivity according to the sensitivity value of the optimization variables toward the optimization objectives.
③ Obtaining sample datasets by using LHS and FEM for high-sensitivity optimization variables and then constructing a high-precision surrogate model based on the sample datasets.

④ Obtaining the optimal combination of high-sensitivity optimization variables based on the high-precision surrogate model and NSGA-II and optimizing the low-sensitivity optimization variables with the Taguchi method.
⑤ Evaluating the performances of the initial and optimized motors.

3. Multi-Objective Optimization of IPMSM

3.1. Determination of Optimization Variables and Optimization Objectives

3.1.1. Determination of Optimization Objectives

An electromagnetic (EM) torque is one of the vital performance indicators of the IPMSM, and the interaction of the magnetic field around the IPMSM stator current and the PM generates an electromagnetic torque. During the operation of the IPMSM, the value of the EM torque is not constant and fluctuates around the average torque. The degree of fluctuation can be expressed by torque ripple. The torque ripple is a ratio of the difference between the maximum peak value and the minimum peak value of the electromagnetic torque to the average torque. During motor operation, as the torque ripple increases, the vibration of the motor increases, and stability decreases. The calculation equation of the electromagnetic torque and the torque ripple can be expressed as [27]:

$$T_{em} = \frac{3}{2} p \left[\psi_f i_q + (L_d - L_q) i_d i_q \right] \tag{1}$$

$$T_a = avg(T_{em}) \tag{2}$$

$$T_r = \frac{T_{em\_\max} - T_{em\_\min}}{T_a} \times 100\% \tag{3}$$

where T_{em} is the electromagnetic torque; p is the polar logarithm; ψ_f is the PM chain; L_d and L_q are the d-axis and q-axis inductances of the motor, respectively; and i_d and i_q are the d-axis and q-axis currents of the motor, respectively. $T_{em\_\max}$ is the maximum peak value of the electromagnetic torque, and $T_{em\_\min}$ is the minimum peak value of the electromagnetic torque.

In the process of electromechanical energy conversion within the IPMSM, there should be a certain loss that includes copper loss, iron loss, PM eddy current loss, and additional loss, among which iron loss and copper loss are dominated. Over-loss leads to a reduction in motor efficiency and an increase in temperature, so it is significant to reduce the loss during the operation of the motor. Based on the above analysis, average torque, torque ripple, iron loss, and copper loss of the motor are selected as the optimization objectives. The iron loss of the motor can be expressed as [28]:

$$p_{fe} = p_h + p_c + p_a = k_h f B_m^{\alpha} + k_c f^2 B_m^2 + k_a f^{1.5} B_m^{1.5} \tag{4}$$

where p_h is the hysteresis loss, p_c is the eddy current loss, p_a is the abnormal eddy current loss, B_m is the magnetic density amplitude of the iron core, f is the frequency, k_h is the hysteresis loss coefficient, k_a is the abnormal eddy current loss coefficient, and α is the Stamets coefficient.

The copper loss p_{Cu} of the IPMSM can be expressed as [29]:

$$p_{Cu} = mI^2R \tag{5}$$

where m is the number of phases, I is the effective value of the phase current, and R is the phase resistance.

3.1.2. Selection of Optimization Variables

As shown in Figure 1b, the installation position of PM in the core of the motor rotor depended on the dimensions of h_{pm}, w_{pm}, rib, $hrib$, o_2, and b_1. Changes in the usage and position of the PM cause changes in the internal magnetic field intensity distribution of the motor, thus affecting the output torque performance of the motor. The stator b_{s0} in

the iron core of the stator has a great impact on the air gap magnetic conductance of the motor, which affects the tooth groove torque of the motor. The tooth groove torque causes the motor to vibrate and run unstably, which is one of the main causes of excessive torque ripple, so optimizing b_{s0} can play a role in suppressing the torque ripple of the motor. The area of each groove in the iron core of the stator is mainly determined by w_t and h_{s2}. Changes in w_t and h_{s2} affect the magnetic field distribution of the teeth and the yoke of the stator. Therefore, it has a great and certain impact on the iron loss and the copper loss, respectively, during the motor operation. On the other hand, the conversion efficiency of electromechanical energy is mainly affected by the air gap dimension between the outer surface of the rotor and the inner surface of the stator. Therefore, the length of the air gap is a crucial dimension and has a significant impact on the performance of the motor. Based on the above analysis, the structural parameters of h_{s2}, b_{s0}, w_t, h_g, rib, w_{pm}, o_2, b_1, $hrib$, and h_{pm} were selected as the variables for this optimization. The value range for each variable is presented in Table 2. To facilitate the subsequent change in the structural parameters of the motor, it is necessary to parameterize the relevant structural parameters in the FEM of the motor and as shown in Figure 1b.

Table 2. Initial values and value ranges for optimization variables.

Symbolic Representation	Initial Value (mm)	Value Range (mm)
h_{s2}	21	18–24
h_{pm}	4.5	4–5
b_{s0}	2	1.5–3
w_t	4.53	4–5
h_g	0.75	0.5–1
o_2	20	18–22
b_1	4	3.5–4
rib	6	5–7
$hrib$	2.4	2–3
w_{pm}	33	32–36

3.2. Sensitivity Analysis

Because the number of optimization variables is up to 10, if the polynomial fitting or the surrogate model is used to construct the functional relationship of these ten optimization variables and the optimization objectives simultaneously, it is not easy to ensure that the surrogate model has enough fitting quality. In particular, some non-sensitive optimization variables are easily ignored. Moreover, multi-objective optimization algorithms require more computational time when dealing with many optimization variables, even if it is difficult to converge. Therefore, it is necessary to reduce the dimensionality of the optimization variables. The original ten optimization variables are divided into two groups with low and high sensitivity. To rationally allocate the combination of the optimization variables, it is necessary to analyze the sensitivity of each optimization variable to the optimization objective and allocate the sensitivity of the optimization objectives according to the optimization variables. The sensitivity analysis step is as follows: First, the input variables (optimization variables) and the output objectives (optimization objectives) are determined, Secondly, sampling the input variable by the sample extraction method DOE (Design of Experiment). Then, the output objectives of the corresponding samples are obtained based on FEA. Finally, the sensitivities of each variable to the output objectives are calculated.

The value ranges for optimization variables are shown in Table 2. Since the motor is a strongly coupled, non-linear complex system, it is necessary to consider the interaction between the variables when sampling the sample points. In the sampling process, if a simple random sampling (SRS) method is used to sample the variables within the value ranges, the previously generated samples are not considered when developing each new model, which has large randomness and uncertainty and may not be able to obtain uniformly distributed

samples. Therefore, a stratified sampling technique LHS [30] is introduced, and the specific implementation steps are as follows:

① Distributing the range of the value for each variable into n intervals of the same length.
② Taking only one sample in each interval of each variable and taking the samples in each interval at random.
③ Randomly combining the samples sampled in step ②.

There are some variables in the IPMSM, and minor changes in these variables will have an enormous impact on the performance of the motor. Therefore, the number of samples in this sampling is selected as 100, ensuring that the distance between adjacent samples drawn for each variable is small enough. After LHS processing, the samples are sufficiently representative to consider the interaction between the variables adequately.

After obtaining a uniformly distributed sample, the output value of each sample is calculated by FEA. Then the Pearson correlation coefficient (PCC) is used to reflect the degree of sensitivity between the optimization variable and the optimization objective. The value of the PCC ranges from -1 to 1. When the PCC is greater than 0, it indicates a positive correlation between the optimization variable and the optimization objective. When the PCC is less than 0, it indicates a negative correlation between the optimization variable and the optimization objective. The absolute value of the PCC closer to 1 indicates that there is a strong correlation, and the PCC's calculation equation is:

$$\rho(X,Y) = \frac{COV(X,Y)}{\sigma_X \sigma_Y} \tag{6}$$

where *COV (X, Y)* is the covariance of the optimization variable X, and the optimization objective Y, σ_X, and σ_Y are the standard deviations of X and Y, respectively.

The sensitivity of each optimization variable to the optimization objective is calculated according to Equation (6), and the results are shown in Figure 3. Each optimization variable is different for the PCC of the different optimization objectives. For instance, the optimization variables with a significant impact on T_r are b_{s0}, w_t, h_g, *rib*, and w_{pm}. The optimization variables with an enormous impact on p_{Cu} are h_{s2} and w_t. The optimization variables with a significant impact on T_a are b_{s0}, w_t, *and* w_{pm}. The optimization variables with an enormous impact on p_{fe} are h_{s2}, w_t, and h_g. Based on the above analysis, the optimization variables that have a significant effect on each optimization objective are not identical, and it is impossible to select the key optimization variables. Therefore, it is necessary to study the sensitivity of each optimization variable as follows:

$$Sen_c(x_i) = \omega_1 |S_{T_a}(x_i)| + \omega_2 |S_{T_r}(x_i)| + \omega_3 \left| S_{p_{fe}}(x_i) \right| + \omega_4 \left| S_{p_{Cu}}(x_i) \right| \tag{7}$$

where x_i is the optimization variable; $S_{Ta}(x_i)$, $S_{Tr}(x_i)$, $S_{pfe}(x_i)$, and $S_{pCu}(x_i)$ are the sensitivity values of x_i to T_a, T_r, p_{fe}, and p_{Cu}, respectively; Sen_c (x_i) is the comprehensive sensitivity of the optimization variable x_i; ω_1, ω_2, ω_3, and ω_4 are the weight coefficients of average torque, torque ripple, iron loss, and copper loss, respectively; and $\omega_1 + \omega_2 + \omega_3 + \omega_4 = 1$. In this stage, setting the weighting ratio of torque performance and losses to 0.6:0.4, $\omega_1 = \omega_2 = 0.3$, $\omega_3 = \omega_4 = 0.2$. The composite sensitivity value of each optimization variable is studied from Equation (7) and as shown in Table 3. Stratification is performed according to the comprehensive sensitivity values of the optimization variables. Using the stratified optimization strategy can greatly improve optimization accuracy and efficiency. First, the optimization variables are sorted in the order of the comprehensive sensitivity from high to low. The first six optimization variables are classified as high-sensitivity variables, and the remaining ones are classified as low-sensitivity variables. The final high-sensitivity optimization variables are h_{s2}, b_{s0}, w_t, h_g, *rib*, and w_{pm}. The low-sensitivity ones are o_2, b_1, *hrib*, and h_{pm}.

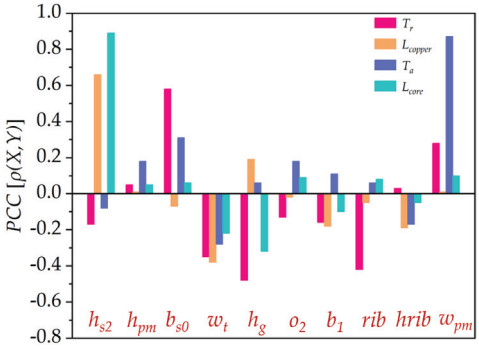

Figure 3. Sensitivity of optimization variables and optimization objectives.

Table 3. Comprehensive sensitivity values of optimization variables.

Variables	S_{Ta} (x_i)	S_{Tr} (x_i)	S_{pfe} (x_i)	S_{pCu} (x_i)	Sen_c (x_i)
h_{s2}	−0.08	−0.17	0.89	0.66	0.39
h_{pm}	0.18	0.05	0.05	0.01	0.08
b_{s0}	0.31	0.58	0.06	−0.07	0.29
w_t	−0.28	−0.35	−0.22	−0.38	0.31
h_g	0.06	−0.48	−0.32	0.19	0.26
o_2	0.18	−0.13	0.09	−0.02	0.12
b_1	0.11	−0.16	−0.1	−0.18	0.14
rib	0.06	−0.42	0.08	−0.05	0.17
$hrib$	−0.17	0.03	−0.05	−0.19	0.11
w_{pm}	0.87	0.28	0.1	0.01	0.37

3.3. Establishment of the Surrogate Model

In the high-dimensional, non-linear optimization problem, if the parametric scanning method or evolutionary algorithm is directly employed to search within the value ranges of the optimization variable, thousands of FEMs need to be built and calculated with huge time and costs. Therefore, we used the high-precision surrogate model to fit the complex relationship between the optimization variables and the optimization objectives. As a result, there is no need for many data samples to simulate a similar simulation model, which significantly improves the optimization efficiency.

To obtain a more accurate surrogate model, in this paper, six regression prediction algorithms, including (1) back propagation (BP), (2) Kriging, (3) convolutional neural network (CNN), (4) random forest (RF), (5) support vector regression (SVR), and (6) extreme gradient boosting (XGboost) are used to construct the surrogate model of optimization variables and optimization objectives. The settings of the BP neural network are: the number of layers of the BP neural network is 3. The number of neurons in the input layer is 6, the number of hidden layers is 1, and the number of neurons in each hidden layer is 5. The number of neurons in the output layer is 1. The settings of CNN are: the input layer of CNN is set to [6 1 1], the number of convolutional layers is 1, the size of the convolutional kernel is set to [3 1], and the number of convolutional kernels is 16. The activation function used in the activation layer is ReLU. The filter of the pooling layer is set to [2 1], and the step size is 2. The number of neurons in the fully connected layer is 384, and the number of neurons in the output layer is 1. Then, the evaluation indicators under the two groups of normalization and non-normalization of sample points are calculated, respectively. The total number of datasets is 300, and the dataset is divided into a training set and a test set with a ratio of 8:2. The accuracy of the surrogate models are compared by calculating the evaluation indicators. Commonly used regression model evaluation indicators are coefficient of determination (R^2), root mean square error ($RMSE$), mean absolute error

(*MAE*), mean square error (*MSE*), mean absolute percentage error (*MAPE*), and symmetric mean absolute percentage error (*SMAPE*), where *RMSE*, *Mae*, and *MSE* cannot reflect the goodness of the model when the selection range of multiple objective functions has a big difference. Therefore, the most suitable surrogate model is selected from the R^2, *MAPE*, and *SMAPE* of the main comparison models. R^2 is the evaluation indicator that best reflects the degree of fit. The closer R^2 to 1, the better the fitting. On the other hand, the smaller *MAPE* and *SMAPE*, the better the effect of the predictive model. The calculation of indicators of these three regression evaluations can be expressed as follows:

$$R^2 = 1 - \frac{\sum_{i=1}^{n} \left(y_i - \hat{y_i}\right)^2}{\sum_{i=1}^{n} \left(y_i - \bar{y}\right)^2} \tag{8}$$

$$MAPE = \frac{100\%}{n} \sum_{i=1}^{n} \left| \frac{y_i - \hat{y_i}}{y_i} \right| \tag{9}$$

$$SMAPE = \frac{100\%}{n} \sum_{i=1}^{n} \frac{|\hat{y_i} - y_i|}{(|\hat{y_i}| + |y_i|)/2} \tag{10}$$

where n is the number of samples in the test set, y_i is the actual values of the samples of the test set, $\hat{y}_i$ is the predicted values of the samples of the test set, and $\bar{y}$ is the average value of the actual values of the samples of the test set. The test results of each surrogate model are shown in Figures 4 and 5, and the specific evaluation indicators are shown in Table 4.

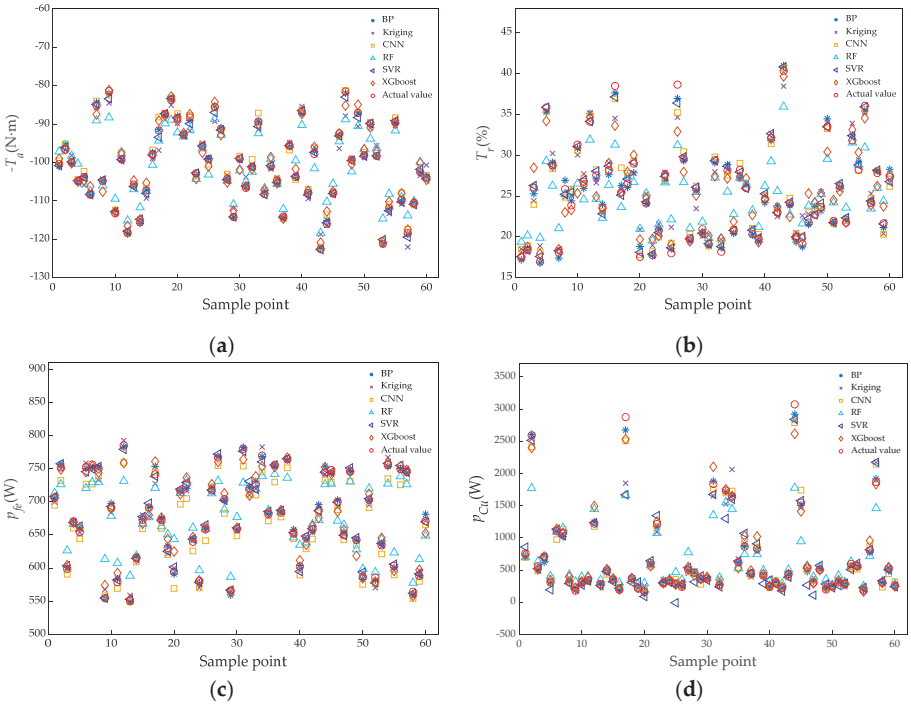

Figure 4. Prediction results of normalization of sample points: (**a**) test results of $-T_a$; (**b**) test results of T_r; (**c**) test results of p_{fe}; (**d**) test results of p_{Cu}.

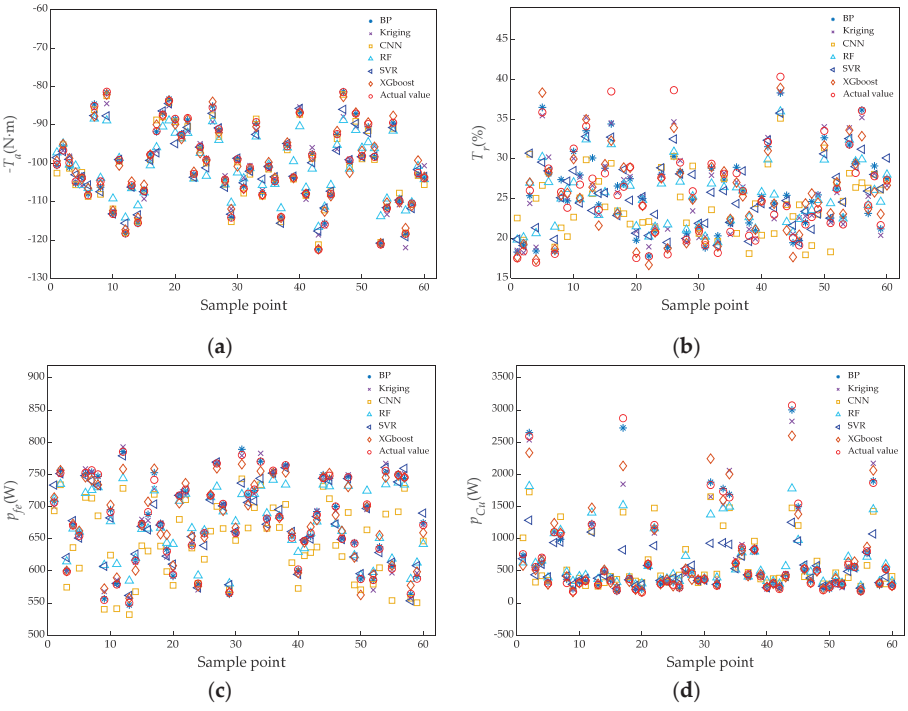

Figure 5. Prediction results of no normalization of sample points: (**a**) test results of $-T_a$; (**b**) test results of T_r; (**c**) test results of p_{fe}; (**d**) test results of p_{Cu}.

Table 4. Evaluation indicators of each surrogate model.

Surrogate Model	Evaluating Indicator	Optimization Objective							
		Normalization of Sample Data				No Normalization of Sample Data			
		$-T_a$	T_r	p_{fe}	p_{Cu}	$-T_a$	T_r	p_{fe}	p_{Cu}
BP	*MAPE* (%)	0.310	2.155	0.473	3.504	**0.308**	4.179	**0.342**	**6.038**
	SMAPE (%)	0.310	2.152	0.473	3.552	**0.308**	4.157	**0.341**	**5.832**
	R^2	0.998	0.988	0.996	0.996	**0.998**	0.923	**0.998**	**0.997**
Kriging	*MAPE* (%)	1.471	4.483	0.779	10.400	1.471	4.483	0.779	10.400
	SMAPE (%)	1.459	4.400	0.781	9.846	1.459	4.400	0.781	9.846
	R^2	0.963	0.938	0.990	0.940	0.963	0.938	0.990	0.940
CNN	*MAPE* (%)	0.824	2.921	1.856	10.757	1.113	13.347	5.041	31.017
	SMAPE (%)	0.828	2.898	1.877	10.419	1.109	13.678	5.206	28.501
	R^2	0.990	0.971	0.953	0.981	0.983	0.491	0.721	0.727
RF	*MAPE* (%)	2.684	8.386	2.767	21.774	2.886	8.314	2.675	25.023
	SMAPE (%)	2.668	8.370	2.759	19.671	2.867	8.248	2.671	22.27
	R^2	0.908	0.782	0.881	0.805	0.892	0.788	0.887	0.794
SVR	*MAPE* (%)	0.478	**1.538**	0.522	16.424	1.668	8.831	1.721	21.093
	SMAPE (%)	0.476	**1.529**	0.521	19.178	1.652	8.718	1.721	22.137
	R^2	0.996	**0.991**	0.996	0.915	0.951	0.773	0.944	0.540
XGboost	*MAPE* (%)	1.243	5.200	1.214	7.315	1.064	5.157	1.512	8.581
	SMAPE (%)	1.244	5.200	1.213	7.064	1.067	5.173	1.513	8.447
	R^2	0.979	0.895	0.975	0.975	0.983	0.908	0.967	0.946

In Table 4, the prediction accuracy of all the surrogate models except the Kriging model for the same optimization objective differs under normalized and non-normalized conditions for the training samples. The R^2 values of each surrogate model for the optimization target were compared, and the largest one was selected. If the R^2 is the same, compare MAPE and SMAPAE and select the smallest. After the comparison, the BP neural network agent model has the highest prediction accuracy for p_{Cu}, p_{fe}, and $-T_a$ under the unnormalized condition of the training samples is obtained. The SVR agent model has the highest prediction accuracy for T_r under the normalized condition of the training samples. There are the bolded parts in Table 4. Therefore, the BP neural network model and the SVR ones are adopted to construct the surrogate model of the optimization variables and the objectives.

3.4. Multi-Objective Optimization of IPMSM Based on NSGA-II and Taguchi Method

3.4.1. Optimization of High-Sensitivity Variables

When combined with the high-precision surrogate model established above, the optimal combination of design parameters is searched by using a multi-objective optimization algorithm. NSGA-II is widely used in multi-objective optimization problems due to its fast speed and strong searchability. Therefore, in this paper, the optimal combination of design parameters of the IPMSM is searched by NSGA-II. The specific implementation steps are shown in Figure 6.

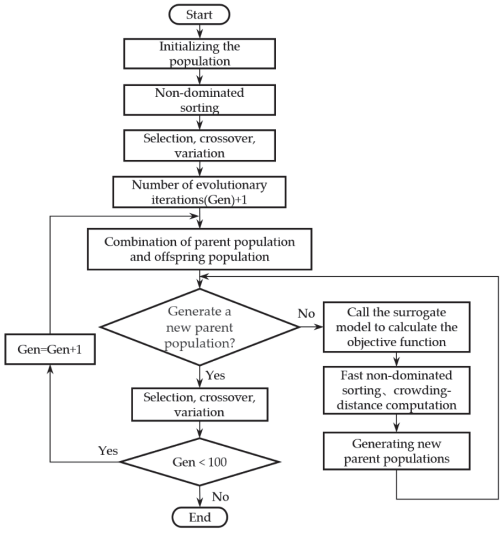

Figure 6. Optimization flowchart of NSGA-II.

The objective function is defined as:

$$\min : \begin{cases} f_1(x) = -T_a \\ f_2(x) = T_r \\ f_3(x) = p_{fe} + p_{Cu} \end{cases} \tag{11}$$

where x is the optimization variable, and the value ranges of the optimization variables are shown in Table 2. The constraint conditions are $-T_a$, T_r, and $p_{fe} + p_{Cu}$, which are smaller than the $-T_a$, T_r, and $p_{fe} + p_{Cu}$ of an initial motor, respectively:

$$\begin{cases} c_1(x) = -T_a + 91.34 < 0 \\ c_2(x) = T_r - 22.13\% < 0 \\ c_3(x) = p_{fe} + p_{Cu} - 970 < 0 \end{cases} \tag{12}$$

The Pareto solution set is obtained according to the above settings and methods, as shown in Figure 7. It can be seen that optimization objectives $f_1(x)$, $f_2(x)$, and $f_3(x)$ cannot all obtain optimal values simultaneously. To make a reasonable compromise on the three optimization objectives, four candidate points in the middle are selected for comparison according to the order of the average torque. In Table 5, candidate point 3 is the optimal one of the four candidate points. Therefore, candidate point 3 is selected as the final value of the high-sensitivity variable, as shown in a five-pointed star point in Figure 7.

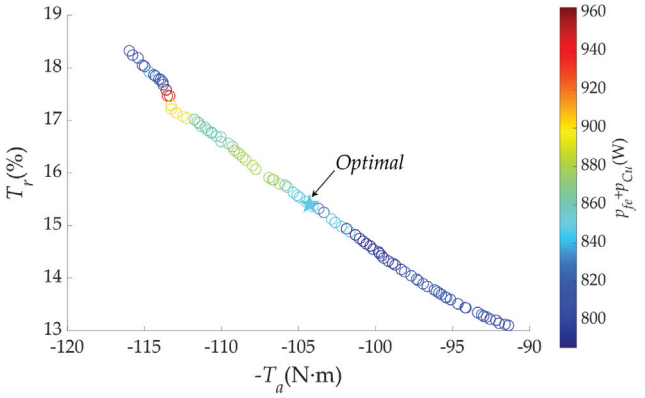

Figure 7. Pareto solution after NSGA−II optimization.

Table 5. Optimal candidate solutions.

	h_{s2} (mm)	b_{s0} (mm)	w_t (mm)	h_g (mm)	*rib* (mm)	w_{pm} (mm)	$-T_a$ (N·m)	T_r (%)	$p_{fe} + p_{Cu}$ (W)
Candidate Point1	19.31	1.87	4.75	1	7	34.55	−104.94	15.54	849.05
Candidate Point2	19.3	1.88	4.75	1	7	34.49	−104.52	15.45	849.16
Candidate Point3	19.3	1.88	4.75	1	7	34.47	−104.29	15.4	848.43
Candidate Point4	19.31	1.89	4.75	1	7	34.43	−104.07	15.36	849.62

3.4.2. Optimization of Low-Sensitivity Variables

After the high-sensitivity optimization variables are optimized, the next step is to optimize the low-sensitivity optimization variables. Since the overall impact of the low-sensitivity optimization variables on the optimization objectives is low, the optimization enhancement space is small. Therefore, the Taguchi optimization method with strong local search ability is adopted to optimize the low-sensitivity optimization variables and save computation time. The new FEM is established according to the combination of variables obtained after NSGA-II optimization. Then, the Taguchi method is used to optimize the four low-sensitivity optimization variables of o_2, b_1, *hrib*, and h_{pm}. First, the value ranges and the values of the level of the optimization variables are determined. Taking 3 level values for this optimization, the spacing between level values is equal. Each level value is named level 1, level 2, and level 3, from small to big, respectively. The specific values are shown in Table 6.

Table 6. Level values of optimization variables.

Optimization Variables	Level 1	Level 2	Level 3
o_2	18	20	22
b_1	3.5	3.75	4
hrib	2	2.5	3
h_{pm}	4	4.5	5

According to the results in Table 6, The L_9 (3^4) orthogonal test table is established and as shown in Table 7. Then, the corresponding FEM is established to calculate the four objective values.

Table 7. L_9 (3^4) orthogonal test table and FEA results.

Number of Tests	o_2	b_1	*hrib*	h_{pm}	T_a (N·m)	T_r (%)	$p_{fe} + p_{Cu}$ (W)
1	1	1	1	1	90.09	17.63	854.93
2	1	2	2	2	95.86	17.36	860.83
3	1	3	3	3	100.55	17.27	866.7
4	2	1	2	3	99.63	17.46	865.45
5	2	2	3	1	90.72	18.32	854.47
6	2	3	1	2	106.94	13.81	879.01
7	3	1	3	2	92.29	18.56	857.01
8	3	2	1	3	110.46	15.00	883.67
9	3	3	2	1	99.45	16.13	866.43

According to the established orthogonal test Table 7, the average value is analyzed, and the objective average value of each variable under different level values is calculated, as shown in Figure 8. It shows that the most favorable combination of variables for increasing T_a is o_2 (3) b_1 (3) *hrib* (1) h_{pm} (3). The most favorable combination of variables for decreasing *Tr* is o_2 (2) b_1 (3) *hrib* (1) h_{pm} (2) or o_2 (2) b_1 (3) *hrib* (1) h_{pm} (3). That for decreasing $p_{fe} + p_{Cu}$ is o_2 (1) b_1 (1) *hrib* (3) h_{pm} (1). The combinations of T_a, T_r, and $p_{fe} + p_{Cu}$ are not the same under optimal conditions. Therefore, the data in Table 7 need to be analyzed for variance. The variance calculation equation can be expressed as:

$$\bar{n} = \frac{1}{m}\sum_{k=1}^{m} n_k \tag{13}$$

$$S^2_{n(x)} = \frac{1}{L}\sum_{i=1}^{L}\left(n(x)_i - \bar{n}\right)^2 \tag{14}$$

where $\bar{n}$ is the total average value of the optimization objective n, m is the total number of trials, $S^2{}_{n(x)}$ is the variance of the optimization objectives n (x), L is the level number, and $n(x)_i$ is the objective average value when the variable x is at level i.

The variance values and proportion of variables with respect to the optimization objectives were calculated according to Equations (13) and (14) and Table 7, as shown in Table 8.

According to the comparison of the proportion values in Table 8, the rate of the impact of o_2 on $p_{fe} + p_{Cu}$ is the largest. The rate of the impact of b_1 on T_r is the largest. The rate of the impact of *hrib* on T_r is the largest, and the rate of the impact of h_{pm} on T_a is the largest. Therefore, o_2 (1) b_1 (3) *hrib* (1) h_{pm} (3) is selected as the optimal combination, and the values of motor variables optimized by the Taguchi method are shown in Table 9.

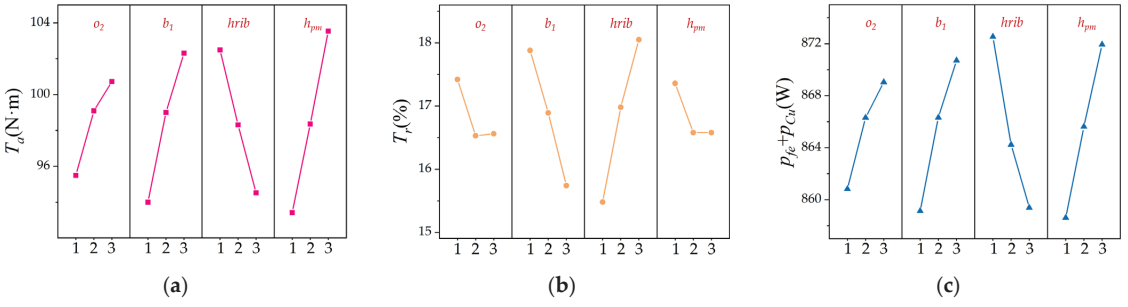

Figure 8. Impact of level values of optimization variables on optimization objectives: (**a**) impact of variable level on T_a; (**b**) impact of variable level on T_r; (**c**) impact of variable level on $p_{fe} + p_{Cu}$.

Table 8. Variance values and proportion between optimization variables and optimization objectives.

Variables	$S^2_{T_a}$	Proportion (%)	$S^2_{T_r}$ ($\times 10^{-5}$)	Proportion (%)	$S^2_{p_{fe}+p_{Cu}}$	Proportion (%)
o_2	4.78	10.82	1.70	7.77	11.68	12.48
b_1	11.67	26.43	7.70	35.21	22.80	24.36
hrib	10.61	24.03	11.11	50.80	29.46	31.48
h_{pm}	17.10	38.72	1.36	6.22	29.64	31.67

Table 9. Design variables for the initial and optimized motors.

Classification of Variables	Variable	Initial	BP + SVR + NSGA-II	BP + SVR + NSGA-II + Taguchi
High sensitivity variables	h_{s2}	21	19.3	19.3
	b_{s0}	2	1.88	1.88
	w_t	4.53	4.75	4.75
	h_g	0.75	1	1
	rib	6	7	7
	w_{pm}	33	34.47	34.47
Low sensitivity variables	o_2	20	20	18
	b_1	4	4	4
	hrib	2.4	2.4	2
	h_{pm}	4.5	4.5	5

4. Results and Discussions

In order to verify the effectiveness of the above optimization methods, the performance of the variable-optimized motor was analyzed by finite element analysis (FEA) and compared to that of the optimized motor. Figure 9a shows the electromagnetic (EM) torque of the initial IPMSM and the optimized ones in the time domain. Figure 9b shows the iron losses of the initial IPMSM and the optimized ones. Figure 9c shows the copper losses of the initial IPMSM and the optimized ones. More detailed performance parameters of the initially designed motor and optimally designed ones with different methods are shown in Table 10.

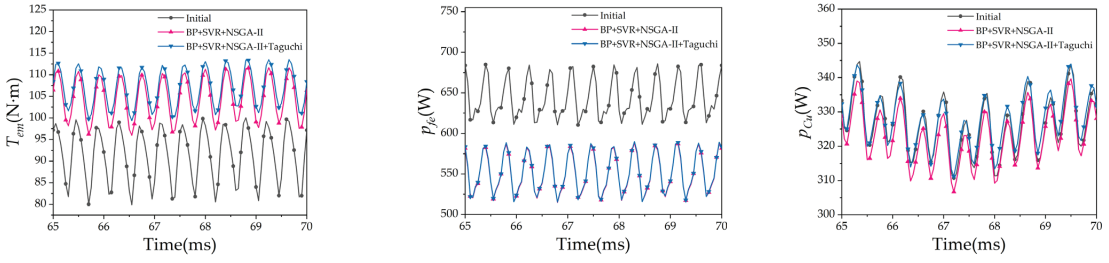

Figure 9. Performance comparison of the initial motor and the optimized motor: (**a**) comparison of T_a; (**b**) comparison of p_{fe}; (**c**) comparison of p_{Cu}.

Table 10. Performance comparison of initial motor and optimized motor with different optimization methods.

Performance	Initial	BP + SVR+ NSGA-II	BP + SVR + NSGA-II + Taguchi
T_a (N·m)	91.34	104.39	**106.96**
T_r (%)	22.13	15.03	**13.23**
T_c (N·m)	6.43	5.23	**5.09**
p_{fe} (W)	643.1	551.07	551.8
p_{Cu} (W)	326.56	323.05	327.56
Efficiency (%)	93.88	94.78	**94.84**

It can be seen that after the BP + SVR + NSGA-II solution optimizes the high-sensitivity variables of the motor, the performance of the IPMSM is greatly improved, the average torque is increased by 14.29%, the torque ripple is decreased by 32.08%, the iron loss is decreased by 14.31%, the copper loss is decreased by 1.08%, and the efficiency is increased to 94.78%.

The BP + SVR + NSGA-II + Taguchi optimization scheme is proposed due to the best performance. Compared to the motor optimized by the optimization strategy in this paper with the initial IPMSM, the average torque is increased by 17.1%, the torque ripple is reduced by 40.22%, the iron loss is reduced by 14.2%, the change in copper loss is very small, and the efficiency is increased to 94.84%.

5. Conclusions

In this paper, we propose a multi-objective optimization strategy for IPMSMs based on BP + SVR combined surrogate model with NSGA-II + Taguchi method. The average torque, torque ripple, iron loss, and copper loss of the IPMSM are used as optimization objectives to optimize the IPMSM. The verification of the numerical calculation results shows that the surrogate model constructed in this paper has very high accuracy, and the prediction results of each optimization objective have very small errors with the numerical calculation results. Compared with the performance of the initial design motor and optimized ones by other optimization strategies, the results show that the overall performance of IPMSM optimized by our proposed multi-objective optimization strategy is best. In the future, we will build the physical motor based on the results obtained in this paper to verify the effectiveness of our proposed method.

Author Contributions: Conceptualization, Y.Y. and Y.P.; methodology, Y.Y.; software, Y.P.; writing original draft, Y.Y. and Y.P. writing—review and editing, Y.Y., J.G., Q.C., Y.H., J.G., Z.Z., S.N. and S.Z. All authors have read and agreed to the published version of the manuscript.

Funding: This research was supported in part by the National Natural Science Foundation of China (Grant No. 52067006, 52162044)), in part by the Foreign expert Bureau of the Ministry of science and

technology of China (Grant No. G2021022002L), in part by long-term project of innovative leading talents in the "Double Thousand Plan" of Jiangxi Province (jxsq2019101027).

Data Availability Statement: Not applicable.

Acknowledgments: The authors would like to thank anonymous reviewers for their helpful comments and suggestions to improve the manuscript.

Conflicts of Interest: The authors declare no conflict of interest.

References

1. Guo, Y.; Si, J.; Gao, C. Improved Fuzzy-Based Taguchi Method for Multi-Objective Optimization of Direct-Drive Permanent Magnet Synchronous Motors. *IEEE Trans. Magn.* **2019**, *55*, 1–4. [CrossRef]
2. Zheng, J.Q.; Zhao, W.X.; Ji, J.H.; Li, H.T. Review on Design Methods of Low Harmonics of Fractional-slot Concentrated-windings Permanent-magnet Machine. *Proc. CSEE* **2020**, *40*, 272–280.
3. Zheng, S.; Zhu, X.; Xu, L. Multi-Objective Optimization Design of a Multi-Permanent-Magnet Motor Considering Magnet Characteristic Variation Effects. *IEEE Trans. Ind. Electron.* **2022**, *69*, 3428–3438. [CrossRef]
4. Zheng, L.; Yu, X.Z.; Wang, X.T.; Xing, X.X. Optimization and Analysis of Cogging Torque of Permanent Magnet Spherical Motor. *IEEE Trans. Appl. Supercond.* **2021**, *31*, 1–5.
5. Hao, L.; Lin, M.; Xu, D. Cogging torque reduction of axial-field flux-switching permanent magnet machine by rotor tooth notching. *IEEE Trans. Magn.* **2015**, *51*, 1–4.
6. Li, Z.; Yu, X.; Zhao, L. Multi-objective optimization of control parameters of deflectable dual-stator switched reluctance generator at low speed. *Electr. Eng.* **2022**, *104*, 2397–2406. [CrossRef]
7. Zhang, Q.; Cheng, S.; Wang, D. Multiobjective design optimization of high-power circular winding brushless DC motor. *IEEE Trans. Ind. Electron.* **2017**, *65*, 1740–1750.
8. Gao, F.Y.; Gao, J.N.; Li, M.M.; Yao, P.; Song, Z.X.; Yang, K.W.; Gao, X.Y. Optimization Design of Halbach Interior Permanent Magnet Synchronous Motor Based on Parameter Sensitivity Stratification. *J. Xi'an Jiaotong Univ.* **2022**, *56*, 180–190.
9. Husain, T.; Hasan, I.; Sozer, Y. Cogging torque minimization in transverse flux machines. *IEEE Trans. Ind. Appl.* **2018**, *55*, 385–397. [CrossRef]
10. Karimpour, S.R.; Besmi, M.R.; Mirimani, S.M. Optimal design and verification of interior permanent magnet synchronous generator based on FEA and Taguchi method. *Int. Trans. Electr. Energy Syst.* **2020**, *30*, e12597. [CrossRef]
11. Cho, S.-K.; Jung, K.-H.; Choi, J.-Y. Design Optimization of Interior Permanent Magnet Synchronous Motor for Electric Compressors of Air-Conditioning Systems Mounted on EVs and HEVs. *IEEE Trans. Magn.* **2018**, *54*, 1–5. [CrossRef]
12. Sun, X.; Shi, Z.; Zhu, J. Multiobjective design optimization of an IPMSM for EVs based on fuzzy method and sequential taguchi method. *IEEE Trans. Ind. Electron.* **2020**, *68*, 10592–10600. [CrossRef]
13. Shi, Z.; Sun, X.; Cai, Y. Robust design optimization of a five-phase PM hub motor for fault-tolerant operation based on Taguchi method. *IEEE Trans. Energy Convers.* **2020**, *35*, 2036–2044. [CrossRef]
14. Zhu, H.; Shen, S.; Wang, X. Multiobjective Optimization Design of Outer Rotor Coreless Bearingless Permanent Magnet Synchronous Motor. *IEEE J. Emerg. Sel. Top. Power Electron.* **2021**, *9*, 5489–5498. [CrossRef]
15. Chen, Y.Y.; Zhu, X.Y.; Quan, L.; Han, X.; He, X.J. Parameter Sensitivity Optimization Design and Performance Analysis of Double-Salient Permanent-Magnet Double-Stator Machine. *Trans. China Electrotech. Soc.* **2017**, *32*, 160–168.
16. Lei, G.; Zhu, J.; Guo, Y.; Liu, C.; Ma, B. A review of design optimization methods for electrical machines. *Energies* **2017**, *10*, 1962. [CrossRef]
17. Cao, Y.J.; Feng, L.L.; Mao, R.; Yu, L.; Jia, H.Y.; Jia, Z. Multi-objective Stratified Optimization Design of Axial-flux Permanent Magnet Memory Motor. *Proc. CSEE* **2021**, *41*, 1983–1992.
18. Sun, X.; Shi, Z.; Lei, G. Multi-objective design optimization of an IPMSM based on multilevel strategy. *IEEE Trans. Ind. Electron.* **2020**, *68*, 139–148. [CrossRef]
19. Gu, A.; Ruan, B.; Cao, W. A general SVM-based multi-objective optimization methodology for axial flux motor design: YASA motor of an electric vehicle as a case study. *IEEE Access* **2019**, *7*, 180251–180257. [CrossRef]
20. Tong, W.M.; Ma, X.J.; Wei, H.Y.; Wu, S.N. Multi objective optimization design of axial flux permanent magnet motor based on magnetic field analytical model and genetic algorithm. *Electr. Mach. Control.* **2022**, *26*, 39–45.
21. Lee, J.H.; Kim, J.W.; Song, J.Y. Distance-based intelligent particle swarm optimization for optimal design of permanent magnet synchronous machine. *IEEE Trans. Magn.* **2017**, *53*, 1–4. [CrossRef]
22. Hao, J.; Suo, S.; Yang, Y. Optimization of torque ripples in an interior permanent magnet synchronous motor based on the orthogonal experimental method and MIGA and RBF neural networks. *IEEE Access* **2020**, *8*, 27202–27209. [CrossRef]
23. Hua, Y.Z.; Liu, Y.C.; Pan, W.; Diao, X.Y.; Zhu, H.Q. Multi-Objective Optimization Design of Bearingless Permanent Magnet Synchronous Motor Using Improved Particle Swarm Optimization Algorithm [J/OL]. *Proc. CSEE* **2022**, 1–9. [CrossRef]
24. Pan, Z.; Fang, S. Combined random forest and NSGA-II for optimal design of permanent magnet arc motor. *IEEE J. Emerg. Sel. Top. Power Electron.* **2021**, *10*, 1800–1812. [CrossRef]

25. Zhu, X.; Shu, Z.; Quan, L. Multi-objective optimization of an outer-rotor V-shaped permanent magnet flux switching motor based on multi-level design method. *IEEE Trans. Magn.* **2016**, *52*, 1–8. [CrossRef]
26. Sasaki, H.; Igarashi, H. Topology optimization of IPM motor with aid of deep learning. *Int. J. Appl. Electromagn. Mech.* **2019**, *59*, 87–96. [CrossRef]
27. Zhu, X.; Huang, J.; Quan, L. Comprehensive sensitivity analysis and multiobjective optimization research of permanent magnet flux-intensifying motors. *IEEE Trans. Ind. Electron.* **2018**, *66*, 2613–2627. [CrossRef]
28. Zhang, Y.; McLoone, S.; Cao, W. Electromagnetic loss modeling and demagnetization analysis for high speed permanent magnet machine. *IEEE Trans. Magn.* **2017**, *54*, 1–5. [CrossRef]
29. Tang, R.Y. *Modern Permanent Magnet Machines: Theory and Design*; China Machine Press: Beijing, China, 2016.
30. Shields, M.D.; Zhang, J. The generalization of Latin hypercube sampling. *Reliab. Eng. Syst. Saf.* **2016**, *148*, 96–108. [CrossRef]

applied sciences

MDPI

Article

Analysis of Plasma Reactor Interaction with the Power Grid Depending on the Power Supply Design

Grzegorz Komarzyniec * and Michał Aftyka

Faculty of Electrical Engineering and Computer Science, Lublin University of Technology, Nadbystrzycka 38A, 20-618 Lublin, Poland
* Correspondence: g.komarzyniec@pollub.pl

Abstract: In this paper, the collaboration of a GlidArc-type plasma reactor with four dedicated power supplies was analysed. Each power supply is characterised by a different design solution. Plasma generation by electrical discharge requires a careful analysis of the power supply design, its operating characteristics, currents, voltages and frequencies. Although the power supplies tested have similar abilities and provide similar power supply parameters, different plasma reactor performance characteristics are obtained for each of them. The results indicate that some power supply parameters were overestimated or underestimated at the design stage. Some of the power supplies tested under plasma reactor load also show poor interaction with the mains. The interaction of the power supplies with the plasma reactor and the mains supply is strongly influenced by the type of plasma gas. Analyses indicate that an optimally designed power supply should combine the solutions contained in each of the power supplies tested.

Keywords: plasma reactor; GlidArc; gliding arc; power supply; plasma; electric discharge; electric arc

Citation: Komarzyniec, G.; Aftyka, M. Analysis of Plasma Reactor Interaction with the Power Grid Depending on the Power Supply Design. *Appl. Sci.* **2023**, *13*, 2279. https://doi.org/10.3390/app13042279

Academic Editors: Loránd Szabó and Feng Chai

Received: 16 January 2023
Revised: 7 February 2023
Accepted: 8 February 2023
Published: 10 February 2023

1. Introduction

Plasma is used in a number of technological processes, including cutting, sputtering of coatings, gas and surface decontamination, production of carbon nanotubes, and melting of steel. The parameters of the technological process dictate use of plasma. For technical purposes, low-temperature plasma is produced in devices called plasma reactors, of which there are many designs [1–5]. The predominant method of plasma generation in these devices is electrical discharge in a gas. Occasionally, microwave, laser, induction or capacitive plasma generators are encountered.

The possibilities for modifying plasma parameters in plasma reactors are limited [6–8]. It is possible to modify the discharge parameters by: (1) changing the shape of the electrodes, (2) changing the distance between the electrodes, (3) choosing the material from which the electrodes are made, and/or (4) choosing the shape of the discharge chamber. These methods often involve redesigning the plasma reactor and making changes to it or building a new reactor.

Additional possibilities for shaping the plasma parameters are provided by the plasma reactor's gas supply system. By: (1) controlling the inflow of plasma-generating gas, (2) selecting the chemical composition of the plasma-generating gas, and/or (3) changing the gas pressure in the discharge chamber [9–11], plasma parameters can be easily and continuously influenced.

In the main, it is the power supply system that determines the plasma parameters and the application possibilities of the plasma reactor [12–14]. Shaping the plasma parameters is possible through: (1) selecting the voltage between DC and AC, (2) selecting the frequency of the supply voltage, (3) selecting the voltage value, (4) selecting the voltage shape, (5) selecting the current value, and (6) influencing the harmonic content of the voltage and current. A power supply system that would allow the regulation of all these parameters would have a complex design, which would translate into high manufacturing costs, high

failure rates, high troubleshooting costs, susceptibility to interference, and complex operation. In most processes in which plasma reactors are used, extensive adjustment of the power supply parameters is not required. With a well-recognised and repeatable plasma process, it is possible to design a power supply that does not require any adjustment. Low manufacturing costs, low failure rates and simple operation are the most appreciated features of plasma reactor power supplies. The design of the power supply system determines the correct operation of the plasma reactor, its interaction with the power supply grid, and its impact on other equipment and people. The selection of the power system is not simple, since plasma reactors are strongly non-linear loads with stochastically varying parameters. Plasma reactors generate strongly electromagnetic interference, significant overvoltage and a large number of higher harmonics in the voltage and current [15–17]. Due to their low arc resistance, plasma reactors strongly loading the power systems [18,19].

Due to the structural diversity of plasma reactors, even within a single reactor type, and the variety of plasma processes carried out with them, it is difficult to rank these devices in terms of technical parameters. As a result, there are no guidelines for designing power systems for the entire multitude of plasma reactors.

Plasma generation by electrical discharge requires careful selection of the power supply system topology, its operating characteristics, and values of currents, voltages and frequencies [20,21]. In order to obtain good operation and control characteristics of a plasma reactor, specialised power supply systems, individually designed for a specific reactor and a specific plasma process, should be used [22,23]. From an operational, engineering and economic point of view, such an approach is unfavourable. Efforts are therefore being made to develop power systems that give the possibility of powering the widest possible range of plasma reactors, even if at the expense of lowering the efficiency of the plasma process.

In this paper, four designs of power supply systems dedicated to powering three-phase GlidArc-type plasma reactors were studied [24]. The power supplies under study were created in the Department of Electrical Engineering and Electrotechnologies at Lublin University of Technology for research projects on plasma applications in technology and industry. These power supplies have similar abilities and provide similar parameters to power the reactors but differ in design and operating principle. The differences in the design of the power supplies are due to the different requirements that were placed on them by the scope or nature of the work carried out in the various research projects, such as: regulating the frequency of the voltage supplying the reactor, increasing or decreasing the harmonic content of the voltage, increasing the dissipation reactance of the transformers, and the ability to control the discharge current. The parameters of the power supplies are selected to work with any GlidArc-type three-phase plasma reactor of no more than 9 kVA. The power supplies are designed so that any modifications to the plasma reactor (change of electrode shape, change of electrode material, change of process gas, etc.) do not affect the operation of the power supplies to an extent that would impair the reactor's power supply parameters. Despite providing a high degree of universality to the power supplies, it was noted during the course of plasma research that the power supplies have disadvantages in different areas of plasma reactor operating characteristics or applications. These observations became the genesis for a detailed study of how power supplies work with GlidArc-type plasma reactors. The control characteristics of the power supplies and their efficiency were analysed. Tests were carried out for the discharge burning in the four most commonly used plasma-forming gases: argon, helium, nitrogen, and air. The results obtained made it possible to rank the power supplies studied in terms of their efficiency in cooperation with the GlidArc plasma reactor. Attention was drawn to the advantages and disadvantages of the solutions used in the power supplies, and conclusions were drawn regarding the design of an optimal power supply system.

2. Plasma Reactor

A three-phase plasma reactor with gliding arc discharge of the GlidArc type [25] with the design shown in Figure 1 was used in the study. The reactor design parameters

are displayed in Table 1. This reactor is used for gas decontamination processes, e.g., air pollutants generated in an iron foundry during the product coating process.

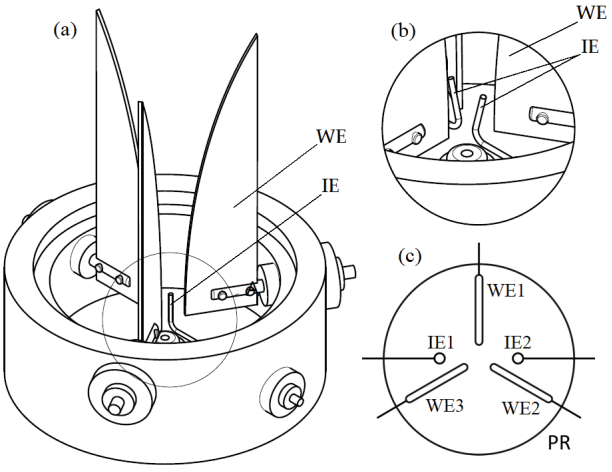

Figure 1. GlidArc-type plasma reactor, (**a**) overview drawing, (**b**) system with one ignition electrode, (**c**) system with two ignition electrodes, WE—working electrodes, IE—ignition electrodes.

Table 1. Technical parameters of the plasma reactor.

Number of working electrodes	3
Number of ignition electrodes	1 or 2
Height/width/thickness of working electrodes	140 mm/30 mm/2 mm
Working electrode spacing, bottom/top	5 mm/50 mm
Working electrode material	steel 0H18N9
Ignition electrode material	tungsten, wire ∅1 mm
Height of the discharge chamber	500 mm
Discharge chamber diameter	114 mm
Discharge chamber material	quartz glass
Material of the electrode clamping ring	aluminium PA6 (2017A)
Electrode holder and current bushings	copper DIN CuCrZr
Insulation of electrode holders	ceramics AL- 70
Gas inlet nozzle	∅5 mm

The reactor has three knife-shaped metal working electrodes arranged around the axis of the cylindrical discharge chamber with a 120° spacing between them. Each electrode is supplied from a separate phase of the three-phase grid. The supply voltage to the working electrodes should not exceed 1.5 kV at a frequency of 50 Hz, and the supply current should be less than 5 A. With such supply parameters, a plasma is obtained which has the property of decontaminating air.

With the electrodes used in the reactor and the distances between them, a voltage value of 1.5 kV is not sufficient for spontaneous ignition of the discharge. Therefore, the reactor is additionally equipped with one or two ignition electrodes made of thin metal wire. The purpose of these electrodes is to initiate an electrical discharge at the working electrodes. The ignition electrodes are supplied with voltages up to 15 kV with a minimum frequency of 50 Hz but not exceeding 20 kHz, with a current value not exceeding 350 mA. These power supply parameters are not sufficient to ignite the arc discharge at the ignition electrodes, but they do allow the electric spark to jump over. A single ignition electrode initiates the spark discharge to the working electrodes. The initiated spark channels develop into an arc discharge due to the increase in power supplied to them from the working electrodes. With two ignition electrodes, the spark discharge burns between the ignition electrodes without the involvement of the working electrodes. These discharges reduce the electrical strength of the space between the working electrodes, which allows an arc discharge to ignite between them at reduced voltage.

The operation of the GlidArc reactor is cyclic. Initiated by the ignition discharge, the right discharge burns on the working electrodes under the influence of the gas-dynamic forces caused by the plasma-forming gas flowing into the discharge chamber, and rises along the electrodes, increasing its length and volume. The nature of the discharge changes, moving from a short arc to a discharge with parameters similar to those of a glow discharge. The parameters of the generated plasma also change [26,27]. The discharge is extinguished when the power supplied from the power system cannot compensate for the energy losses of the intensively cooled and blown discharge. The end result of the plasma reactor cycle is a plasma column. As soon as the discharge is extinguished, it is rebuilt with ignition electrodes and the reactor cycle repeats. The length of the reactor cycle depends on its design parameters, the parameters of the plasma gas and the parameters of the electrical power supply system [28].

3. Electrical Power Supply System

The most important device cooperating with the plasma reactor is the power supply system. Properly selected, it guarantees stable parameters of the generated plasma, high efficiency of the plasma process and low interference generated by the plasma reactor. There are many plasma reactor power supply solutions dedicated to specific equipment or processes. The cooperation of the GlidArc plasma reactor was analysed with four different power supply systems. The power supplies under study were created in the Department of Electrical Engineering and Electrotechnologies at Lublin University of Technology for research projects on plasma applications in technology and industry. This research focused on the possibilities of using plasma generated in GlidArc-type reactors. However, there was no detailed analysis of the cooperation of this type of reactor with power supply systems.

The basic element of all the power supplies discussed is the transformer. Sometimes the transformer itself, when properly designed, makes a good power supply. Such a power supply is shown in Figure 2. The power supply design uses three single-phase transformers T_1, T_2 and T_3 connected in a YNy three-phase connection circuit. These transformers form the T-circuit supplying the working electrodes WE_1, WE_2 and WE_3 of the plasma reactor. The transformers are characterised by cores made of the amorphous material Metglas 2605SA1. The primary and secondary windings are concentrically wound in a manner typical of most transformers. A separate electrical circuit IS is used to power the IE_1 and IE_2 ignition electrodes of the plasma reactor. This circuit uses a high-frequency electronic high-voltage inverter. The parameters of the power supply circuit are given in Table 2. The letter designation TPS is adopted for this power supply.

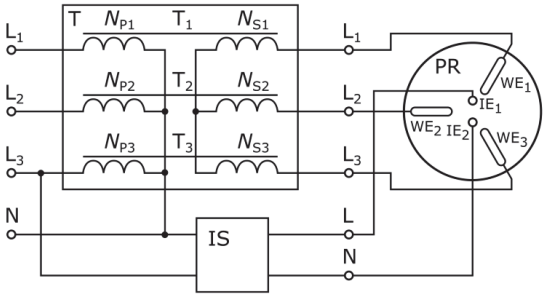

Figure 2. Transformer power system TPS, PR—plasma reactor, T—reactor working electrodes power circuit, IS—ignition electrodes power circuit, N_{P1}, N_{P2}, N_{P3}—primary windings, N_{S1}, N_{S2}, N_{S3}—secondary windings, WE_1, WE_2, WE_3—plasma reactor working electrodes, IE_1, IE_2—reactor ignition electrodes.

Table 2. Parameters of the reactor working electrode supply circuits.

Power Supply Type	TPS	ITPS	IFCTPS	PCS
Power	13.8 kVA	9 kVA	11 kVA	13.8 kVA
Supply voltage	230 V	230 V	230 V	230 V
Supply current	20 A	20 A	16 A	20 A
Output voltage	1.2 kV	1.3 kV	1.2 kV	1.2 kV
Output current	3 A	5 A	2.4 A	3 A
Output frequency	50 Hz	50 Hz	50 Hz	10 ÷ 200 Hz

An extension of the TPS power supply system is the system labelled PCS. In the PCS power supply system, transformers T_1, T_2 and T_3 are supplied by an AC/DC/AC transistor converter, as shown in Figure 3. The converter allows the frequency of the reactor supply voltage to be adjusted between 10 and 200 Hz, and the reactor discharge current to be adjusted. Chokes with an inductance of 20 mH are installed between the transformers and the converter.

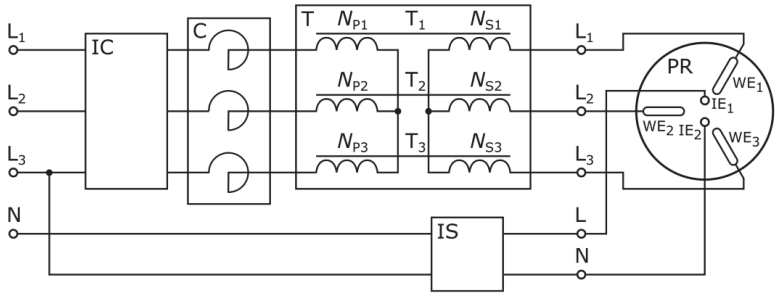

Figure 3. Converter power system PCS, PR—plasma reactor, T—reactor working electrodes power circuit, IS—ignition electrodes power circuit, C—chokes, IC—AC/DC/AC transistor converter, N_{P1}, N_{P2}, N_{P3}—primary windings, N_{S1}, N_{S2}, N_{S3}—secondary windings, WE_1, WE_2, WE_3—plasma reactor working electrodes, IE_1, IE_2—reactor ignition electrodes.

The next power supply system to be tested was a system called ITPS, consisting of three suitably connected single-phase transformers, as shown in Figure 4. Three identical transformers T_1, T_2 and T_3 were connected to form a three-phase connection system YNyn. These transformers form the power circuit for the working electrodes WE_1, WE_2 and WE_3

of the plasma reactor. The fourth transformer T_4 is used to supply the ignition electrode IE_1 of the plasma reactor. The primary and secondary windings of this transformer are included in the neutral conductors of the system of transformers T_1, T_2 and T_3. The cores of the transformers are made of ET 120-27 electrical sheet metal. The operating point of transformers T_1, T_2 and T_3 on the magnetisation characteristics of the cores was selected so that the cores operate at low saturation. As a result, a current containing the 3rd harmonic is taken from the grid. This current flows through the primary winding of transformer T_4 and a voltage of threefold frequency is induced in the secondary winding of this transformer.

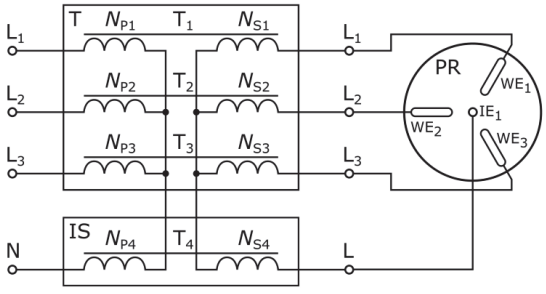

Figure 4. Integrated power system ITPS, PR—plasma reactor, T—reactor working electrode power circuit, IS—ignition electrode power circuit, N_{P1}, N_{P2}, N_{P3}, N_{P4}—primary windings, N_{S1}, N_{S2}, N_{S3}, N_{S4}—secondary windings, WE_1, WE_2, WE_3—plasma reactor working electrodes, IE_1—reactor ignition electrode.

The last power supply system tested, designated IFCTPS, uses a five-column transformer in its design (Figure 5). This system integrates the power circuit for the working electrodes of the plasma reactor and the power circuit for the ignition electrodes in a single transformer. The transformer core is made of ET 120-27 electrical sheet metal. The primary and secondary windings of the transformer are connected in a YNy three-phase connection arrangement. In typical three-phase transformer designs with five-column cores, the outer columns have no windings. In the case of the power supply in question, windings were wound on the outer columns of a five-column transformer to supply the plasma reactor ignition electrodes.

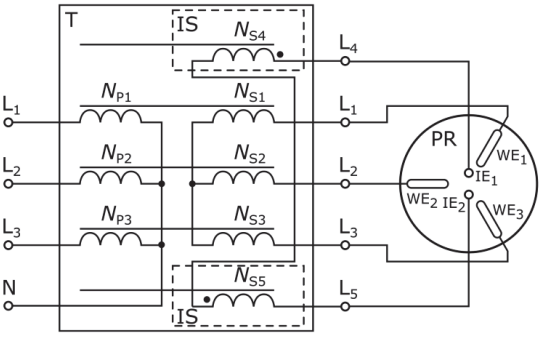

Figure 5. Power system with 5-column transformer IFCTPS, PR—plasma reactor, T—reactor working electrodes power circuit, IS—ignition electrodes power circuit, N_{P1}, N_{P2}, N_{P3}—primary windings, N_{S1}, N_{S2}, N_{S3}, N_{S4}, N_{S5}—secondary windings, WE_1, WE_2, WE_3—plasma reactor working electrodes, IE_1, IE_2—reactor ignition electrodes.

The technical parameters of the power supply circuits discussed are summarised in Tables 2 and 3. Table 2 gives the technical parameters of the plasma reactor working

electrode power supply circuits and Table 3 gives the parameters of the plasma reactor ignition electrode power supply circuits.

Table 3. Parameters of the reactor ignition electrode supply circuits.

Power Supply Type	TPS	ITPS	IFCTPS	PCS
Ignition system	electronic	transformer	transformer	electronic
Supply voltage	230 V	–	–	230 V
Supply current	250 mA	–	–	250 mA
Output voltage	15 kV	10 kV	7.6 kV	15 kV
Output current	40 mA	200 mA	350 mA	40 mA
Output frequency	20 kHz	150 Hz	50 Hz	20 kHz

4. Measurement System

In order to carry out tests on the cooperation of the plasma reactor with different types of power supply systems, a test platform was built consisting of two circuits: (1) the electricity supply and (2) the plasma gas supply.

A schematic diagram of the system for measuring electrical quantities is shown in Figure 6. Measurements were made at the inputs and outputs of the power supplies under study. Currents of all phases, phase-to-phase voltages, harmonic content in currents and voltages, active, reactive and apparent powers, and power factor were measured. The measuring system was supplied from a three-phase 400 V grid via a 23.4 kVA ATS-FAZ3-23 autotransformer. The autotransformer allows regulation of the supply voltage in a range from 0 to 450 V. The measuring system consisted of Merazet LM-3 voltmeters, Mezaret LE-3 ammeters, Mezaret LW-1 wattmeters, Tektronix DPO3054 oscilloscope, Fluke Norma 5000 power analyser, Tektronix P6015A and TCP0030 measuring probes.

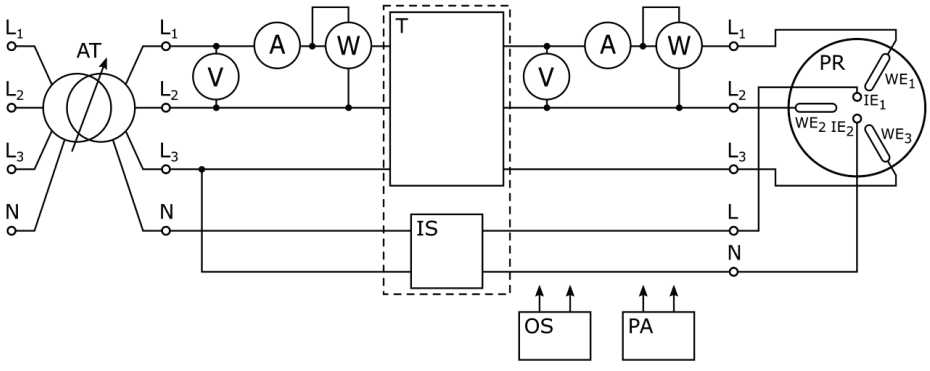

Figure 6. Measuring system for testing the cooperation of a plasma reactor with different types of power supplies, AT—autotransformer, V—voltmeter, A—ammeter, W—wattmeter, OS—oscilloscope, PA—power analyser, PR—plasma reactor, T–reactor working electrodes power circuit, IS—ignition electrodes power circuit.

An important part of the test platform is the system for supplying the plasma reactor with plasma-generating gases. The test installation consisted of four cylinders of technical gases containing argon, helium, nitrogen, and air (Figure 7). The type of plasma-generating gas introduced into the discharge chamber of the GlidArc reactor determines its performance characteristics [29]. Cylinder gas was fed to the gas inflow nozzle of the plasma reactor through Bronkhorst's EL-FLOW mass flowmeters and flow controllers: the F-202AV-M20-AAD-44-V with a flow rate of up to 15 m^3/h, the F-201AV-50K-AAD-44-V with a flow

rate of up to 2 m^3/h, and the F-201CV-1K0-AAD-44-V with a flow rate of up to 0.06 m^3/h. These regulators allow precise mixing of the gases and control of their flow through the plasmotron nozzle. The volumetric flow rate of gases entering the plasmotron nozzle was measured during the study.

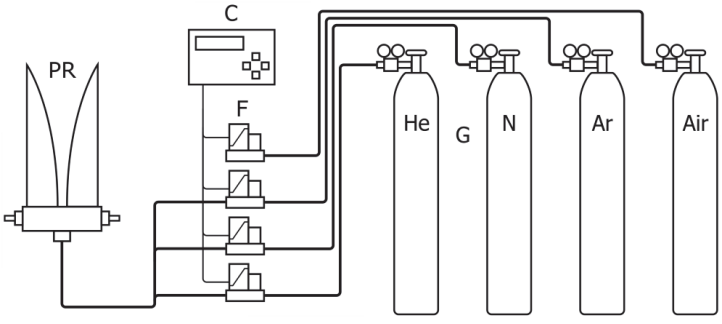

Figure 7. Plasma gas supply system, PR—plasma reactor, G—plasma gases, F—flow regulators, C—regulator setting and control system.

5. Test Results

To begin, the power supply units were tested for interaction with the grid under conditions when the outputs of the power supply units were not loaded. Measurements were carried out in the measurement system shown in Figure 6. The PR plasma reactor was disconnected from the circuit, leaving the output terminals of the L_1, L_2, L_3, L and N power supplies free.

The measurements of the electrical quantities taken from the grid by the power supply units are shown in Table 4. The table gives the rms values of the phase voltages U_1 feeding the power supplies, the currents taken by the power supplies from the mains I_1, the active power P_1, reactive power Q_1 and complex power S_1 taken, power coefficients cosφ, and the harmonic content factors in the voltage U_{1THD} and current I_{1THD}.

Table 4. Operating parameters of power supplies in no-load condition.

		ITPS	**TPS**	**IFCTPS**	**PCS**
U_1	V	237.4	238.3	234.4	234.9
I_1	A	0.998	0.012	0.068	0.826
P_1	W	67.61	7.95	14.11	335.41
Q_1	Var	707.24	3.27	37.71	476.63
S_1	VA	712.04	8.58	41.92	582.77
cosφ_1	–	0.095	0.926	0.341	0.572
U_{1THD}	%	2.54	2.45	2.68	1.93
I_{1THD}	%	51.60	34.63	41.9	87.22

The TPS power supply has the lowest grid power consumption, with a complex power consumption of 8.58 VA. Simultaneously, this power supply has the best power factor of all the power supplies tested (0.926) and has low harmonic content ratios in voltage and current of 2.45% and 34.63%, respectively. The IFCTPS power supply performs slightly poorer in terms of the aforementioned parameters. The ITPS is the worst performer. In idle operation, it takes 712.04 VA from the grid with a power factor of just 0.095. In contrast, the PCS power supply has the highest harmonic content in current at 87.22%. This power supply also takes the second highest power from the grid at 582.77 VA. From the comparison presented, it is apparent that plasma reactor power systems using conventional

transformers, with a typically chosen operating point on the magnetisation characteristic, provide the best interaction with the grid.

The most important factor in the operation of the power supplies is their response under the load of the plasma reactor in which the arc discharge is burning. Example waveforms of single-phase voltages and currents at the inputs and outputs of power supplies loaded with an operating plasma reactor, obtained from oscilloscope measurements, are shown in Figures 8–11. The waveforms were obtained for a discharge burning in argon, whose volume flow through the plasmotron nozzle was 2.8 m^3/h.

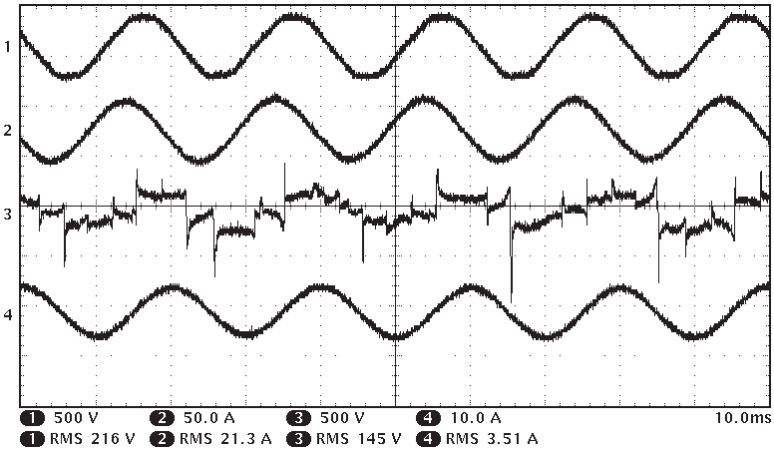

Figure 8. Current and voltage waveforms of the TPS power supply, 1—input voltage, 2—input current, 3—output voltage, 4—output current, plasma gas: argon, flow: 2.8 m^3/h.

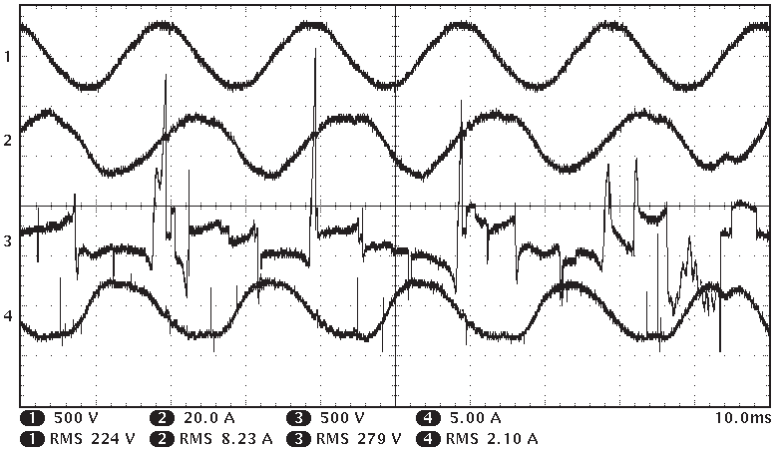

Figure 9. Current and voltage waveforms of the ITPS power supply, 1—input voltage, 2—input current, 3—output voltage, 4—output current, plasma gas: argon, flow: 2.8 m^3/h.

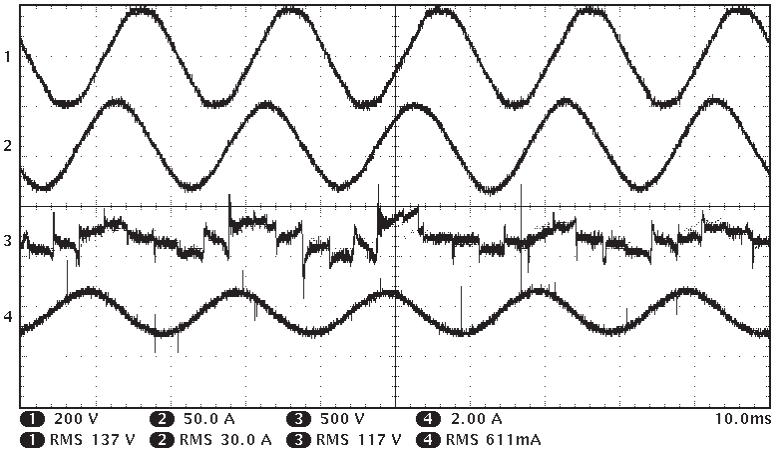

Figure 10. Current and voltage waveforms of the IFCTPS power supply, 1—input voltage, 2—input current, 3—output voltage, 4—output current, plasma gas: argon, flow: 2.8 m^3/h.

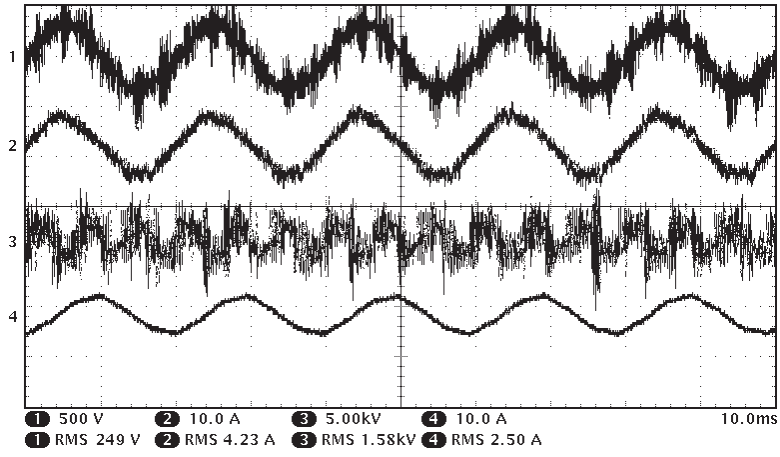

Figure 11. Current and voltage waveforms of PCS power supply, 1—input voltage, 2—input current, 3—output voltage, 4—output current, plasma gas: argon, flow: 2.8 m^3/h.

The voltage and current waveforms at the output of the TPS, ITPS and IFCTPS power supply shown in Figures 9–11 are typical of arcs burning in a three-phase system at low current and cooled intensively [30,31].

Of the gases used in measurement, argon provides the best conditions for ignition and development of a discharge in the reactor over the entire range of its flow control, and over the entire range of control characteristics of the electrical parameters of the power supplies. Despite superior argon characteristics, significant distortion of the output voltages of the tested power supplies is observed in the obtained oscillograms. Particularly large distortions are seen in the output voltage of the PCS power supply. In the case of the ITPS power supply, high value overvoltages are observed in the form of peaks accompanying the ignition of the reactor discharge. In the case of this power supply, distortion of the arc current is also evident. Poorer performance of the power packs with the plasma reactor is obtained when helium is used as the plasma-generating gas.

The plasma-generating gas that is most problematic in the interaction of the investigated power packs with the plasma reactor is nitrogen. Nitrogen is a gas with a high

ignition voltage and discharge support. Co-operation of power supplies with a reactor in which the discharge burns in nitrogen is unfavourable due to high discharge instability, a large number of disturbances in the voltage and current waveforms, and poor control characteristics. Slightly better performance is obtained with air as the plasma-forming gas. These problems arise for several reasons: (1) the design of power supplies with the assumption that the main plasma-generating gases will be argon and helium, (2) the adoption of an output voltage of power supplies not much larger than the ignition voltage of the discharge in nitrogen, (3) the limitation of the value of the discharge current which translates into a low arc temperature, (4) the susceptibility of the arc discharge to stochastic changes in position and length, and/or (5) the disturbance of the gas flow through the reactor discharge chamber caused by the reactor structural elements and the electrical discharge, worsening locally and temporarily the conditions for ignition and burning of the discharge [32,33].

Figures 12–15 show the control characteristics of the reactor supplied from the test power supplies when the discharge burns in argon, helium, nitrogen and atmospheric air. The characteristics were obtained for a volumetric gas flow rate through the plasmotron nozzle of 1.6 m^3/h.

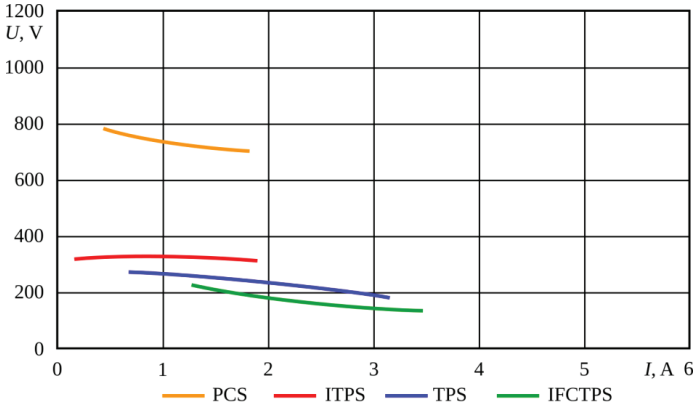

Figure 12. Control characteristics of the tested power supplies loaded with plasma reactor, plasma gas: argon, volumetric flow rate: 1.6 m^3/h.

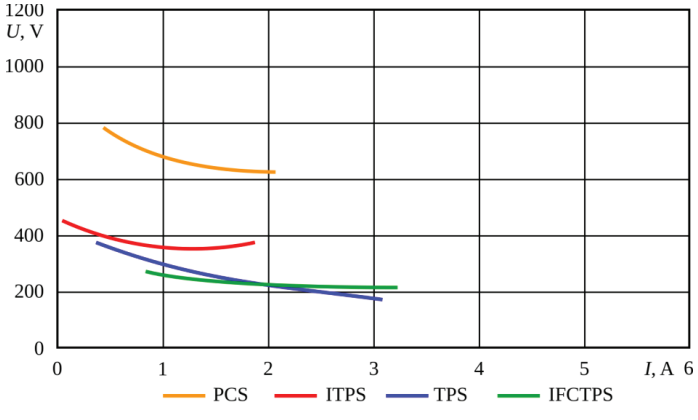

Figure 13. Control characteristics of the tested power supplies loaded with plasma reactor, plasma gas: helium, volumetric flow rate: 1.6 m^3/h.

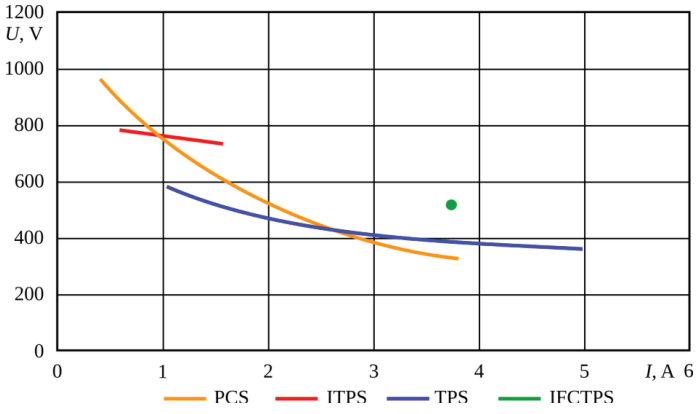

Figure 14. Control characteristics of the tested power supplies loaded with plasma reactor, plasma gas: nitrogen, volumetric flow rate: 1.6 m^3/h.

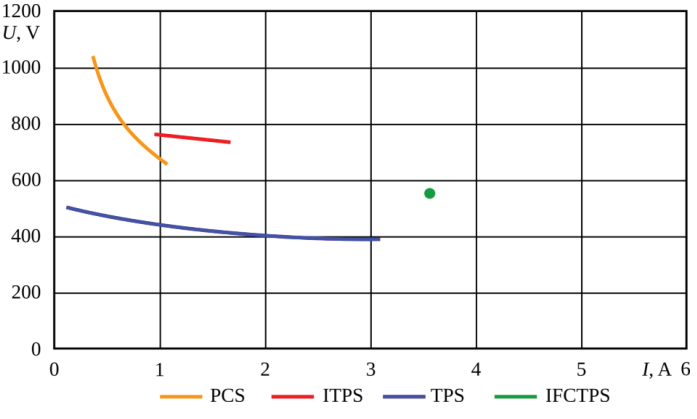

Figure 15. Control characteristics of the tested power supplies loaded with plasma reactor, plasma gas: air, volumetric flow rate: 1.6 m^3/h.

In the case of an electric discharge burning in argon, all power supplies tested showed good regulation properties (Figure 12). The IFCTPS and TPS power supply have the widest range of discharge current regulation. The worst performer in this respect is the PCS converter power supply. This power supply is also characterised by the highest value of the voltage at which the discharge in the plasma reactor burns. The value of the discharge burning voltage when the reactor is supplied from the PCS power supply is about 4 times higher compared to the IFCTPS power supply.

The low voltage values at which the discharge in the reactor burns, together with the high excess voltage supplying the working electrodes of the reactor provided by the TPS, ITPS and IFCTPS power supplies, allows the power supplied to the plasma reactor to be regulated using an autotransformer. The wide current control ranges available with these power supplies allow the plasma temperature to be influenced to suit the requirements of the plasma process being carried out. The low voltage and current values at which the discharge burns when the reactor is supplied from TPS, ITPS, and IFCTPS power supplies make it possible to obtain the low-temperature plasma required in many plasma–chemical processes.

When changing the plasma-generating gas to helium, no significant changes in the current control ranges were observed for all the power supplies tested (Figure 13). In the

case of the TPS, ITPS, and IFCTPS power supplies, there is a slight but noticeable increase in the voltage at which the electrical discharge in the plasma reactor burns. In the case of the PCS converter power supply, the helium discharge burns at voltage values similar to the burning voltage of the argon discharge.

When the discharge burns in nitrogen in the plasma reactor, the control characteristics of the ITPS and IFCTPS power supply deteriorate (Figure 14). For the ITPS power supply, the discharge burns at about twice the voltage as when argon and helium are used as plasma gases. The control range of the discharge current in the case of discharge in nitrogen is also shortened by a factor of two. Even worse is the control characteristic of the IFCTPS power supply, which is reduced to a single point. With this power supply, the discharge in the plasma reactor when the plasma gas is nitrogen burns only at 550 V and 3.75 A. The TPS and PCS power supplies have the best control characteristics for discharge in nitrogen.

Changing the plasma gas to atmospheric air does not significantly change the control characteristics of the feeders obtained for nitrogen (Figure 15), likely due to the fact that nitrogen makes up about 78% of the air composition.

The study shows that the apparent powers for which all power supplies were designed are significantly higher than the maximum arc power generated in the plasma reactor. Table 5 shows the ranges of discharge powers than can be obtained in the plasma reactor for the different plasma-generating gases and compares them with the rated powers of the power supplies tested. Analysing the percentage ratio (Table 6) of the maximum power obtained in the burning discharge in the individual gases to the power rating of the power supplies, it is found that the highest ratios were achieved for the ITPS power supply of 8.9% for argon, 7.8% for helium, 13.3% for nitrogen and atmospheric air. The worst performer in this respect is the TPS power supply where 4.3% is achieved for argon and helium, 3.6% for nitrogen, and 8% for air. For the IFCTPS and PCS power supplies, these ratios are 5.5% and 10.9% for argon, 5.5% and 5.1% for helium, 4.5% and 7.2% for nitrogen, and 10.9% and 8.7% for air, respectively.

Table 5. Power supply ratings and discharge power ranges for different plasma gases.

Power Supply Type	TPS	ITPS	IFCTPS	PCS
Rated power	13.8 kVA	9 kVA	11 kVA	13.8 kVA
Power for argon	0.2–0.6 kVA	0.1–0.8 kVA	0.4–0.6 kVA	0.1–1.5 kVA
Power for helium	0.3–0.6 kVA	0.3–0.7 kVA	0.3–0.6 kVA	0.3–0.7 kVA
Power for nitrogen	0.1–0.5 kVA	0.5–1.2 kVA	0.5 kVA	0.9–1.0 kVA
Power to the air	0.1–1.1 kVA	0.5–1.2 kVA	1.2 kVA	0.5–1.2 kVA

Table 6. Percentage ratio of maximum power obtained in the discharges to the power ratings of the Power supplies.

Power Supply Type	TPS	ITPS	IFCTPS	PCS
Argon	4.3%	8.9%	5.5%	10.9%
Helium	4.3%	7.8%	5.5%	5.1%
Nitrogen	3.6%	13.3%	4.5%	7.2%
Air	8%	13.3%	10.9%	8.7%

A comparison between the rated powers for which the power supplies are designed and the maximum discharge powers burning in the plasma reactor shows that the power supplies operate in a state of significant underloading. This underload translates into low power factor and low efficiency of the power supplies. Table 7 shows the maximum efficiencies with which each power supply operates depending on the type of plasma gas. Efficiencies are expressed as the ratio of the electrical discharge power burning in

the plasma reactor to the power taken from the grid supplying the power supplies. The TPS power supply achieves the highest efficiency of all the power supplies tested at over 70% when the electrical discharge is in nitrogen and air. The TPS power supply is also the power supply that achieves the highest average efficiency calculated for all gases. The second highest average efficiency value is achieved by the PCS power supply. The PCS power supply achieves higher efficiencies than the TPS power supply for the discharge burning in argon and helium.

Table 7. Efficiencies of power supplies for a burning discharge in different plasma gases.

Power Supply Type	TPS	ITPS	IFCTPS	PCS
Maximum efficiency for argon	25%	18%	35%	36%
Maximum efficiency for helium	26%	20%	20%	40%
Maximum efficiency for nitrogen	72%	20%	18%	20%
Maximum efficiency for air	70%	28%	25%	28%

The analysis of the harmonic content of the voltage and current drawn from the grid by power supplies loaded with the plasma reactor was carried out. For all the power supplies analysed, a large value of the I_{THD} coefficient of harmonic content in current was obtained. In contrast, a relatively small value of the harmonic content factor U_{THD} was obtained in the voltage. Table 8 shows the measured harmonic content ratios. The highest current harmonic content factor values were recorded for the PCS power supply for all plasma gases. For this power supply, the I_{THD} exceeds 146% for the air burning discharge and reaches 163% for the argon discharge. In other power supplies, the value of this coefficient strongly depends on the type of plasma gas. For example, the IFCTPS power supply achieves an I_{THD} value of 148% for discharge in nitrogen, 133% for discharge in air, only 24.7% for discharge in argon, and 19.5% for discharge in helium; 19.5% is also the lowest I_{THD} value recorded for all power supplies. In contrast, the highest value of this coefficient was recorded for the TPS power supply when the electrical discharge burned in helium.

Table 8. Harmonic content ratios.

Power Supply Type	Parameter	Gas			
		Argon	Helium	Nitrogen	Air
TPS	I_{THD}	24%	184%	92.4%	64%
	U_{THD}	3.54%	3.3%	3.83%	4%
ITPS	I_{THD}	61.2%	36.9%	77.3%	75.2
	U_{THD}	2.64%	2.43%	3.19%	1.2%
IFCTPS	I_{THD}	24.7%	19.5%	148%	133%
	U_{THD}	7.86%	4.54%	3.72%	3.71%
PCS	I_{THD}	163%	148.4%	148.3%	146.7%
	U_{THD}	5.3%	5.07%	4.78%	4.75%

6. Conclusions

The article investigates the cooperation of a plasma reactor with four types of power supplies in electricity. These power supplies were constructed at the Department of Electrical Engineering and Electrotechnologies of Lublin University of Technology for the purpose of carrying out research projects on plasma applications in technology and industry. However, no detailed research had been conducted on their interaction with the plasma reactor.

From the current analysis, it appears that all the power supplies tested exhibit poor interaction with the plasma reactor, where the discharges burn in nitrogen or in air. In nitrogen and air, the discharges burn unstably which manifests as interference in the plasma reactor's operating cycle. These disturbances are transferred to the power supplies, degrading their operational parameters. In the case of IFCTPS and ITPS power supplies, the discharge burning in nitrogen and air is also characterised by a narrow discharge power control range.

In the case of argon and helium discharges, all the power supplies tested were able to achieve cyclic and stable discharges in the plasma reactor with a wide range of power control.

The measurements show that the primary design defect of the power supplies tested is an overestimation of their power ratings in relation to the maximum discharge power burning in the reactor.

Of all the power supplies tested, the PCS converter power supply exhibits the greatest number of characteristics predisposing it to powering plasma reactors. This power supply does not have the best control characteristics of all the power supplies tested, but it guarantees correct burning of the discharge in the plasma reactor for all plasma gases. A major advantage of the PCS power supply is the ability to shape the plasma parameters by varying the frequency of the supply voltage. In the case of this power supply, an intermediate transformer has a major influence on its interaction with the plasma reactor. In the research carried out, the TPS transformer power supply system played the role of the intermediate transformer. The TPS power system had the best interaction with the plasma reactor of all the power supplies tested. When combined with the PCS, problems were generated by the electronic ignition system. This system is not only characterised by a high failure rate, but also generates high conducted interference, disturbing the operation of the AC/DC/AC converter.

From the analysis, it can be concluded that the best power supply design would be characterised by a configuration consisting of an AC/DC/AC transistor converter coupled to a five-column transformer with wound end columns. The core of such a transformer would have to be made of an amorphous material, such as the Medglas 2605SA1 type. A core made of amorphous material has a greater range of transmitted frequencies compared to ET sheet cores, which translates into better power transfer from the AC/DC/AC converter to the plasma reactor. Interaction of the IFCTPS power supply of the design presented in this paper with the transistor AC/DC/AC converter is problematic due to the low dissipation reactance of the five-column transformer and was therefore not tested. To make this cooperation possible, the phase windings of a five-column transformer would have to be made in the form of alternating primary and secondary disc windings, guaranteeing the desired dissipation reactance. With the appropriate design of the phase windings, it also seems possible to eliminate the chokes present in the output circuits of the AC/DC/AC converter.

Author Contributions: Conceptualization, G.K.; methodology, M.A.; validation, G.K. and M.A.; formal analysis, G.K.; investigation; M.A.; data curation, M.A.; writing—original draft preparation, G.K. and M.A.; writing—review and editing, G.K.; visualization, G.K.; All authors have read and agreed to the published version of the manuscript.

Funding: This research received no external funding.

Institutional Review Board Statement: Not applicable.

Informed Consent Statement: Not applicable.

Data Availability Statement: Not applicable.

Conflicts of Interest: The authors declare no conflict of interest.

References

1. Cai, X.; Fu, Z.; Xie, H.; Xue, J.; Ding, D.; Ou, N.; Zhou, G. Resonant Power Supply for Plasma Cleaning Based on Fuzzy Logic Power Tracking. *Appl. Sci.* **2022**, *12*, 4681. [CrossRef]
2. Zhang, Y.; Zeng, X.; Bai, M.; Jin, M.; Hao, W.; Gao, D.; Liu, Q.; Feng, J. The Development of 170 GHz, 1 MW Gyrotron for Fusion Application. *Electronics* **2022**, *11*, 1279. [CrossRef]
3. Jung, E.Y.; Park, C.-S.; Jang, H.J.; Iqbal, S.; Hong, T.; Shin, B.J.; Choi, M.; Tae, H.-S. Optimization of Atmospheric Pressure Plasma Jet with Single-Pin Electrode Configuration and Its Application in Polyaniline Thin Film Growth. *Polymers* **2022**, *14*, 1535. [CrossRef]
4. Renninger, S.; Rößner, P.; Stein, J.; Lambarth, M.; Birke, K.P. Towards High Efficiency CO_2 Utilization by Glow Discharge Plasma. *Processes* **2021**, *9*, 2063. [CrossRef]
5. Kavaliauskas, Ž.; Uscila, R.; Kėželis, R.; Valinčius, V.; Grigaitienė, V.; Gimžauskaitė, D.; Milieška, M. Investigations of Working Characteristics of Transferred Arc Plasma Torch Volume Reactor. *Appl. Sci.* **2022**, *12*, 2624. [CrossRef]
6. Felea, C.I.; Dragos Astanei, D. Electrical characterization of the double crossing Glidarc reactor with cylindrical symmetry. In Proceedings of the International Conference on Optimization of Electrical and Electronic Equipment (OPTIM) & 2017 Intl Aegean Conference on Electrical Machines and Power Electronics (ACEMP), Brasov, Romania, 25–27 May 2017. [CrossRef]
7. Nishime, T.M.C.; Werner, J.; Wannicke, N.; Mui, T.S.M.; Kostov, K.G.; Weltmann, K.-D.; Brust, H. Characterization and Optimization of a Conical Corona Reactor for Seed Treatment of Rapeseed. *Appl. Sci.* **2022**, *12*, 3292. [CrossRef]
8. Barkhordari, A.; Karimian, S.; Rodero, A.; Krawczyk, D.A.; Iman Mirzaei, S.I.; Falahat, A. Carbon Dioxide Decomposition by a Parallel-Plate Plasma Reactor: Experiments and 2-D Modelling. *Appl. Sci.* **2021**, *11*, 10047. [CrossRef]
9. Hnatiuc, E.; Brisset, J.L.; Hnatiuc, B. The ignition and control condition for the useful discharge in a GlidArc reactor with plane geometry and auxiliary electrodes. In Proceedings of the 12th International Conference on Optimization of Electrical and Electronic Equipment, Brasov, Romania, 20–22 May 2010. [CrossRef]
10. Burlica, R.; Hnatiuc, B.; Hnatiuc, E. The effects of gas flow-rate on electrical parameters of gliding arc discharges. In Proceedings of the XVIIth Symposium on Physics of Switching Arc, Brno, Czech Republic, 10–13 September 2007; ISBN 978-80-214-3370-0.
11. Hăisan, C.; Kříž, P.; Cerman, J.; Špatenka, P.; Hnatiuc, E. Characterization of gliding arc discharge with auxiliary electrodes. In Proceedings of the 13th International Conference on Optimization of Electrical and Electronic Equipment (OPTIM), Brasov, Romania, 24–26 May 2012. [CrossRef]
12. Rablah, B.; Laberge, M.; Zawalski, W.; Wilkie, J. Pulse power systems for plasma experiments at general fusion. In Proceedings of the 2016 IEEE International Conference on Plasma Science (ICOPS), Banff, AB, Canada, 19–23 June 2016. [CrossRef]
13. Creţu, D.; Burlică, R.; Astanei, D.; Dirlău, J.-D.; Beniugă, O. Energy efficiency evaluation of HV power supplies for non-thermal plasma generation. In Proceedings of the 8th International Conference on Modern Power Systems (MPS), Cluj-Napoca, Romania, 21–23 May 2019. [CrossRef]
14. Ivankov, A.; Capela, T.; Rueda, V.; Bru, E.; Piquet, H.; Schitz, D.; Florez, D.; Diez, R. Experimental Study of a Nonthermal DBD-Driven Plasma Jet System Using Different Supply Methods. *Plasma* **2022**, *5*, 75–97. [CrossRef]
15. Beniugă, O.; Dîrlau, J.-D.; Astanei, D.; Burlică, R. Electromagnetic field radiation generated by pulsed non-thermal plasma discharge. In Proceedings of the 8th International Conference on Modern Power Systems (MPS), Cluj-Napoca, Romania, 21–23 May 2019. [CrossRef]
16. Todirasi, G.; Hnatiuc, E.; Burlica, R.; Hnatiuc, B.; Gavril, B. Reduction of electromagnetic perturbations for cold plasma electrochemical reactors using electromagnetic screening. In Proceedings of the 12th International Conference on Optimization of Electrical and Electronic Equipment OPTIM 2010, Brasov, Romania, 20–22 May 2010; pp. 1343–1348. [CrossRef]
17. Haruni, A.M.O.; Muttagi, K.M.; Negnevitsky, M. Analysis of harmonics and voltage fluctuation using different models of arc furnace. In Proceedings of the Australasian Universities Power Engineering Conference, Perth, WA, Australia, 9–12 December 2007. [CrossRef]
18. Terzija, V.V.; Koglin, H.-J. On the modeling of long arc in still air and arc resistance calculation. *IEEE Trans. Power Deliv.* **2004**, *19*, 1012–1017. [CrossRef]
19. Ospina, G.I.; Cubillos, D.; Ibanez, L. Analysis of arcing fault models. In Proceedings of the IEEE/PES Transmission and Distribution Conference and Exposition: Latin America, Bogota, Colombia, 13–15 August 2008. [CrossRef]
20. Gao, X.; Liang, J.; Wu, L.; Wu, L.; Kawi, S. Dielectric Barrier Discharge Plasma-Assisted Catalytic CO_2 Hydrogenation: Synergy of Catalyst and Plasma. *Catalysts* **2022**, *12*, 66. [CrossRef]
21. Chi Chen, C.; Wenjie Fu, W.; Chaoyang Zhang, C.; Dun Lu, D.; Meng Han, M.; Yang Yan, Y. Dual-Frequency Microwave Plasma Source Based on Microwave Coaxial Transmission Line. *Appl. Sci.* **2021**, *11*, 9873. [CrossRef]
22. Hnatiuc, E.; Brisset, J.L.; Hnatiuc, B.; Burlica, R.; Roman, C. About electrochemical reactors with cold plasma discharges engineering. In Proceedings of the European Research in Cold Plasma Applications Conference Iasi, Iasi, Romania, 12–13 February 2007; ISBN 978-973-0-04933-6.
23. Burlica, R.; Hnatiuc, E.; Pricop, C.H.; Felea, C. A comparative study of non-thermal plasma Glidarc reactors. In Proceedings of the International Conference on Optimization of Electrical and Electronic Equipment (OPTIM), Bran, Romania, 22–24 May 2014. [CrossRef]
24. Dimitrakellis, P.; Faubert, F.; Wartel, M.; Gogolides, E.; Pellerin, S. Plasma Surface Modification of Epoxy Polymer in Air DBD and Gliding Arc. *Processes* **2022**, *10*, 104. [CrossRef]

25. Gonga, X.; Linb, Y.; Lic, X.; Wuc, A.; Zhangc, H.; Yanc, J.; Du, C. Decomposition of volatile organic compounds using gliding arc discharge plasma. *J. Air Waste Manag. Assoc. Manag. Assoc.* **2020**, *70*, 138–157. [CrossRef] [PubMed]
26. Sun, S.R.; Kolev, S.; Wang, H.X.; Bogaerts, A. Investigations of discharge and post-discharge in a gliding arc: A 3D computational study. *Plasma Sources Sci. Technol.* **2017**, *26*, 055017. [CrossRef]
27. Hnatiuc, B.; Pellerin, S.; Burlica, R.; Hnatiuc, E. Electrical and physical proprieties of a gliding arc. In Proceedings of the XVIIth Symposium on Physics of Switching Arc, Brno, Czech Republic, 10–13 September 2007; ISBN 978-80-214-3370-0.
28. Selerowicz, W.; Piechna, J.; Opalinska, T.; Ulejczyk, B. Experimental investigation of the dynamics and space range of the gliding arc in three-electrode system. *IEEE Trans. PlasmaSci.* **2011**, *39*, 2866–2867. [CrossRef]
29. El-Zein, A.; Talaat, M.; El-Aragi, G.; El-Amawy, A. Experimental model to study the characteristics of gliding arc plasma reactor with argon/nitrogen. *J. Electr. Eng.* **2015**, *15*, 64–67.
30. Emanuel, A.E.; Orr, J.A. An improved method of simulation of the arc voltage-current characteristic. In Proceedings of the 9th International Conference on Harmonics Quality of Power, Orlando, FL, USA, 1–4 October 2000; pp. 148–150. [CrossRef]
31. Felea, I.C.; Hnatiuc, E.; Astanei, D. Characterization of cold plasma glidarc reactors. In Proceedings of the International Aegean Conference on Electrical Machines and Power Electronics (ACEMP) & International Conference on Optimization of Electrical and Electronic Equipment (OPTIM), Brasov, Romania, 2–3 September 2021. [CrossRef]
32. Landfried, R.; Boukhlifa, M.; Leblanc, T.; Teste, P.; Andrea, J. Stability, spatial extension and extinction of an electric arc in aeronautical conditions of pressure under 540 V DC. *Eur. Phys. J. Appl. Phys.* **2019**, *87*, 30901. [CrossRef]
33. Terzija, V.V.; Koglin, H.-J. Testing, modeling and simulation of long arc in still air. In Proceedings of the 2001 IEEE Power Engineering Society Winter Meeting. Conference Proceedings (Cat. No.01CH37194), Columbus, OH, USA, 28 January–1 February 2001. [CrossRef]

energies

MDPI

Article

Common-Mode Voltage-Reduction Method of 7-Phase BLDC Motor Control System †

Yung-Deug Son [1], Dong-Youn Kim [2], Hyeong-Jin Kim [3] and Jang-Mok Kim [4,*]

[1] Department of Mechanical Facility Control Engineering, Korea University of Technology and Education, Cheonan 31253, Republic of Korea
[2] Department of Research and Development, Hyowon Powertech Company, Busan 46241, Republic of Korea
[3] Air Mobility Electric-Motor & Drive Research Team, Korea Electrotechnology Research Institute (KERI), Changwon 51543, Republic of Korea
[4] Department of Electrical and Electronics Engineering, Pusan National University, Busan 46241, Republic of Korea
* Correspondence: jmok@pusan.ac.kr; Tel.: +82-51-510-2366
† This paper is an extended version of our paper published in 2019 10th International Conference on Power Electronics and ECCE Asia (ICPE 2019—ECCE Asia).

Abstract: This paper describes a method for reducing the common-mode voltage in a seven-phase brushless DC motor (BLDC) drive. The conventional interleaved method used in the three-phase inverter system is extended and applied. The proposed phase-phase interleaved method is studied to apply the six-phase excitation method for controlling the seven-phase BLDC. The six-phase switching functions related with modulation index (MI) and interleaved angle are obtained, and the average of the common-mode voltage is derived mathematically. The proposed control method reduces the common-mode voltage generation by applying the optimal interleaved angle according to MI. The proposed method is verified by experimental results.

Keywords: BLDC motor; common-mode voltage; conducted EMI; interleaving PWM; seven-phase motor; switching frequency

Citation: Son, Y.-D.; Kim, D.-Y.; Kim, H.-J.; Kim, J.-M. Common-Mode Voltage-Reduction Method of 7-Phase BLDC Motor Control System. *Energies* **2023**, *16*, 2097. https://doi.org/10.3390/en16052097

Academic Editors: Loránd Szabó and Feng Chai

Received: 17 January 2023
Revised: 6 February 2023
Accepted: 18 February 2023
Published: 21 February 2023

1. Introduction

Recently, multi-phase motors have been widely used in electric propulsion, ships, and traction. The use of a multi-phase motor can reduce the torque ripple and increases the output power density compared to three-phase motors [1–3]. The use of a multi-phase motor is essential, especially in a system requiring high power with limited space, such as underwater propulsion. In addition, the multi-phase motor has the advantage of fault-tolerant control [4–9]. When one or more phases suffer a fault, the multi-phase motor can be still operated at a lower output power. For the control methods of a multi-phase motor, there are generally the hysteresis control method [7] and the vector control method [8]. The hysteresis control method is easy to implement, but it is difficult to predict the heat generated in the system because the switching frequency is variable. The vector control method has the feature of low torque ripple, but it requires complex coordinate transformation including low-order harmonics. In this paper, the current control method, namely the control principle of a three-phase BLDCM, is used. In this case, the back-electromotive force (EMF) voltage is a square wave, and the six-phase current is controlled in the square wave [9,10]. There is a hybrid-phase excitation method varying the number of excitation phases according to the operation speed and efficiency. The advantage of the BLDCM control method is that it is easy to implement. In addition, since each phase current is controlled independently, it is effective in reducing the torque ripple in the commutation period.

Generally, a motor used in underwater vehicles is operated in the high-speed region. Operation in a high-speed region causes current delay due to the increased reactance

of the stator winding and increased back-EMF voltage [11]. In addition, the insufficient number of current samplings causes some errors of the control and torque pulsation. Thus, one method to solve torque pulsation is to increase the current control frequency and the switching frequency [12]. Therefore, a superior power device, namely silicon carbide (SiC) MOSFET, is needed to achieve high-frequency switching control [13–15]. However, the use of SiC-MOSFET causes an increase in common-mode noise due to the ringing of the output voltage and rapid variation of dv/dt. Thus, this paper presents the control performance according to the switching frequency of a SiC-MOSFET inverter, and the common-mode voltage-reduction method is proposed to solve the EMI noise problem.

Figure 1 shows the loop of conduction noise. The common-mode voltage (V_{cm}) is the voltage generated by the switching operation measured between the DC neutral point and the neutral point of the motor. Normally, there are parasitic capacitor (C_s) components among the ground and case of inverter and case of motor. Thus, the current (i_g) defined as leakage current is generated by voltage variation of V_{cm}, and this current flows through C_s. This current loop is defined as a common-mode loop, which causes bearing damage in the motor drive system. Thus, the reduction of common-mode voltage is the main issue to solve in EMI problems.

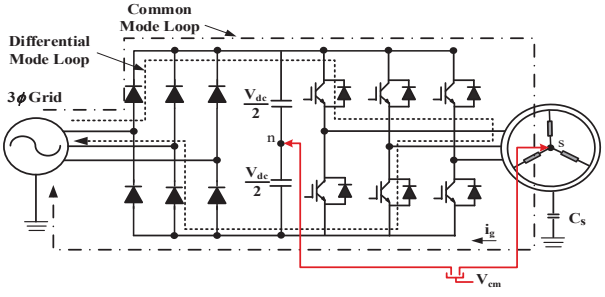

Figure 1. Loop of conduction noise in the motor drive system.

Various methods have been studied to reduce the common-mode voltage. The most effective method is to design a passive filter at the output of the inverter [16,17]. The common-mode choke is specialized in reducing the magnitude of the common-mode current [18], and applying the L-C filter between phases helps to reduce the differential mode noise [19]. Based on the passive filters, the active component is used to additionally remove the common-mode noise and reduce the filter size [20]. However, these common-mode noise reduction methods by using a passive filter are sensitive to system configuration. thus, it is difficult to apply in a system operating at various switching frequencies [21–23]. In addition, the use of passive filters significantly increases the system volume in the multi-phase motor drive system operated in limited space.

Another method to reduce the common-mode voltage is to combine the pulse width modulation (PWM). The conventional space vector pulse width modulation (SVPWM) and sinusoidal pulse width modulation (SPWM) generate the maximum magnitude of common-mode voltage at zero vector. Thus, the near-state PWM method [24] and active zero state PWM method [25] use additional vectors instead of zero vector in the 3-phase SVPWM. In multi-phase motor control, some studies have researched reducing the common-mode voltage based on the SVPWM [19–32]. These methods are suitable for vector control in synchronous coordinate frame but are not available for the hybrid-phase excitation method [9]. This represents a lack of research of the common-mode voltage reduction in multi-phase BLDC motor drive system. Therefore, in this paper, the carrier interleaving method in the three-phase inverter is extended to the six-phase hybrid excitation method [26]. In our previous work [27], the interleaving angle according to the modulation index (MI) was calculated to generate the minimum common-mode voltage. The proposed interleaved method was verified in MATLAB simulation. In this paper, the control performance of

the high-speed multi-phase motor was improved by increasing switching frequency. The use of SiC-MOSFET was able to achieve the above results. In addition, the common-mode noise generation for high switching frequency was experimentally confirmed. At last, the noise reduction method proposed in [27] was experimentally demonstrated and analyzed.

2. Basic Control Method of the 7-Phase BLDC

2.1. Mathematical Modeling

The 7-phase inverter system consists of a diode rectifier that converts AC power to DC, a DC-linked capacitor bank, a 7-phase inverter with 14 switches, and an electric motor as shown in Figure 2. A 7-phase BLDC motor is equalized with stator resistance (R_s), stator inductance (L_s), and back-EMF proportional to the motor rotational speed. The common-mode voltage (V_{cm}) represents the potential difference between the neutral point of the motor and the neutral point of the DC-linked capacitor bank, and C_s is the parasitic capacitor component that exists between the neutral point of the motor and the case of the motor. Assuming that the case of the motor is grounded, current flows through C_s when the common-mode voltage changes rapidly, which is called leakage current (i_{sg}) [17]. When the voltage is applied to the motor by the inverter operation, considering the mutual inductance component between the lines, the voltage equation can be expressed as Equation (1), where V_{xn} is the pole voltage of 7-phase inverter, i_x is the phase current of each phase, L_{ij} is the inductance of each phase, e_x is the back-EMF of each phase, and V_{sn} is the neural voltage. Self-inductance and mutual inductance are defined as Equation (2).

$$\begin{gathered} V_{xn} = R_s i_x + L_{ij}\frac{di_x(N)}{dt} + e_x + V_{sn} \\ x = \{a,\ b,c,d,e,\ f,g\}\ \ i,\ j = \{a,\ b,c,d,e,\ f,g\},\ (i \neq j) \end{gathered} \tag{1}$$

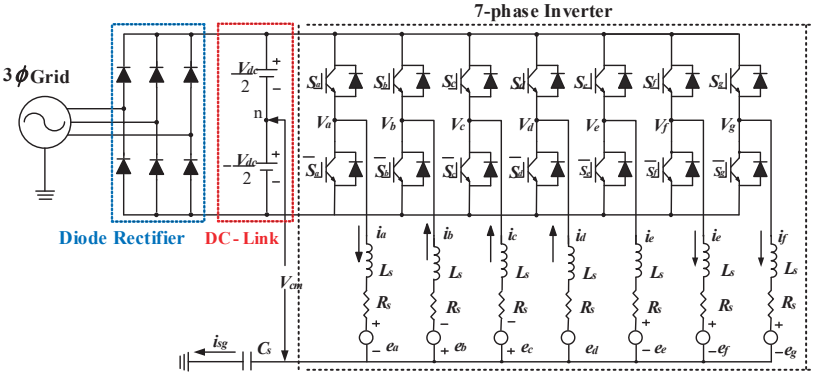

Figure 2. Equivalent model of 7-phase inverter system.

$$[L_{ij}] = \begin{bmatrix} L_s & M_{ab} & M_{ac} & M_{ad} & M_{ae} & M_{af} & M_{ag} \\ M_{ba} & L_s & M_{bc} & M_{bd} & M_{be} & M_{bf} & M_{bg} \\ M_{ca} & M_{cb} & L_s & M_{cd} & M_{ce} & M_{cf} & M_{cg} \\ M_{da} & M_{db} & M_{dc} & L_s & M_{de} & M_{df} & M_{dg} \\ M_{ea} & M_{eb} & M_{ec} & M_{ed} & L_s & M_{ef} & M_{eg} \\ M_{fa} & M_{fb} & M_{fc} & M_{fd} & M_{fe} & L_s & M_{fg} \\ M_{ga} & M_{gb} & M_{gc} & M_{gd} & M_{ge} & M_{gf} & L_s \end{bmatrix} \tag{2}$$

Since a 7-phase BLDC is in a y-connection and balanced state, the sum of seven-phase currents becomes zero, as in Equation (3). Using the Equations (1)–(3), V_{sn} can be calculated as Equation (4).

$$i_a + i_b + i_c + i_d + i_e + i_f + i_g = 0 \tag{3}$$

$$V_{sn} = \frac{1}{7}\sum_{x=a}^{g}(V_x - e_x) \tag{4}$$

The normalized output power considering the excitation method is expressed as Equation (5), where N is the number of the excited phase, E_S is the maximum value of back-EMF, and I_S is the maximum value of phase current.

$$P_{e(N)} = \sum_{n=a}^{g}(e_n i_n) = NE_s I_{s(N)} \tag{5}$$

In addition, electrical output torque can be expressed as Equation (6), where ω_m is the mechanical angular speed, and k_e is the back-EMF constant.

$$T_{e(N)} = \frac{P_e(N)}{\omega_m} = \frac{NE_s I_{s(N)}}{\omega_m} = \frac{Nk_e\omega_m I_{s(N)}}{\omega_m} = Nk_e I_{s(N)} \tag{6}$$

2.2. Basic Control Method

The position of a 7-phase BLDC is divided into fourteen sectors through seven hall sensor signals, as shown in Figure 3. The motor is driven by inducing the square wave current to the stator winding in the section where the back-EMF voltage is flat. There are 2-phase to 7-phase excitation methods depending on the number of excitation windings [9,10]. When the position is a sector 2 in a 6-phase excitation method, "A", "F", and "G" phases are positive conduction states; "B", "C", and "D" phases are negative conduction states; and "E" phase exists in a non-conduction state. Table 1 provides the conduction states depending on the position in a 6-phase excitation method.

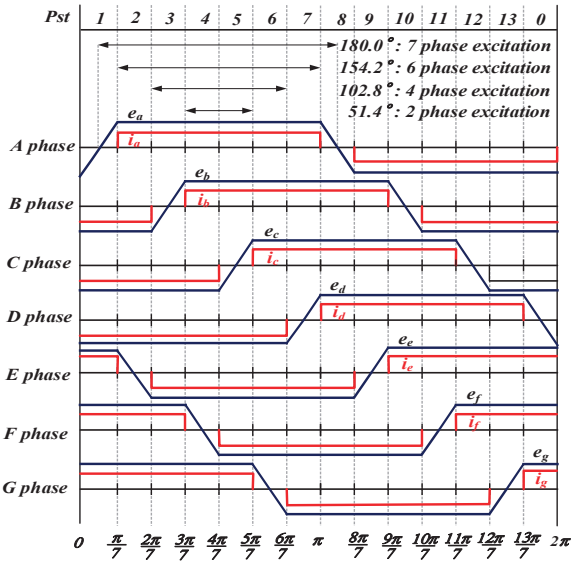

Figure 3. Excitation method of 7-phase BLDC motor.

The structure of the controller is shown in Figure 4. To control the current as a square wave, seven current controllers regulate each phase current independently, and the polarity of voltage reference is applied according to the position in Table 1. In this case, the current controller of the non-conductive phase stops the calculation and holds the value. The above control method is particularly easy to implement in fault-tolerance control and hybrid-phase excitation control [25,28,29].

Table 1. Definition of conduction phase current according to 6-phase excitation method.

Position	*Phase Current*						
	i_a	i_b	i_c	i_d	i_e	i_f	i_g
0	−	−	−	0	+	+	+
1	0	−	−	−	+	+	+
2	+	−	−	−	0	+	+
3	+	0	−	−	−	+	+
4	+	+	−	−	−	0	+
5	+	+	0	−	−	−	+
6	+	+	+	−	−	−	0
7	+	+	+	0	−	−	−
8	0	+	+	+	−	−	−
9	−	+	+	+	0	−	−
10	−	0	+	+	+	−	−
11	−	−	+	+	+	0	−
12	−	−	0	+	+	+	−
13	−	−	−	+	+	+	0

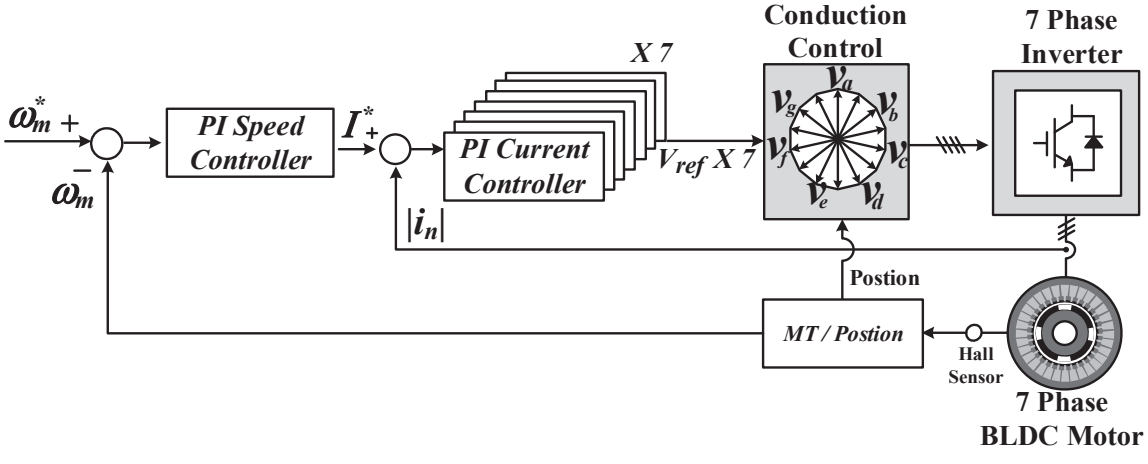

Figure 4. Structure of controller for driving 7-phase BLDC motor.

2.3. Control Characteristic According to Switching Frequency

In the seven-phase BLDCM control method, an increase of the switching frequency can have advantages in two ways. First, the ripple of the current can be reduced. It is affective on the high-speed BLDC motor with low inductance. Another advantage is the compensation for position error caused by low resolution in the high-speed region. Figure 5 shows the rotor position resolution depending on the sampling frequency. When the control frequency is 10 kHz, 30 kHz, and 50 kHz, the sampling point of position is expressed. The seven-phase control method divides rotor position in 14 sectors, and the commutation change is conducted in every sector. However, a control frequency of 10 kHz cannot immediately respond to the commutation change; then, the position error (θ_{err}) is caused by sampling delay. The control frequency of the current controller is also insufficient to control the current reference.

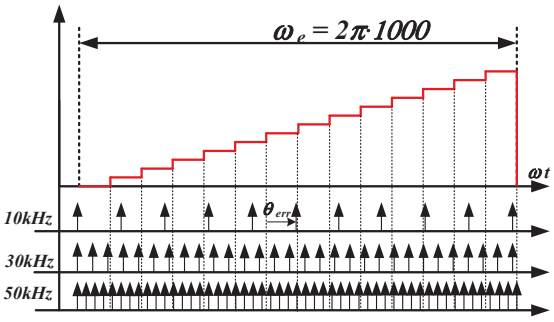

Figure 5. Rotor position resolution depending on the sampling frequency.

Figure 6 shows the effect of position error. The current of each phase should be induced at the region where the back-EMF voltage is flat. However, the position error causes torque reduction due to the area of the triangle, as expressed as "α" in Figure 7. The area "α" is proportional to the triangle region of the back-EMF voltage, and the proportional equation can be expressed as Equation (7).

$$\frac{\pi}{14} : E = \theta_{err} : \frac{14}{\pi} E\theta_{err} \tag{7}$$

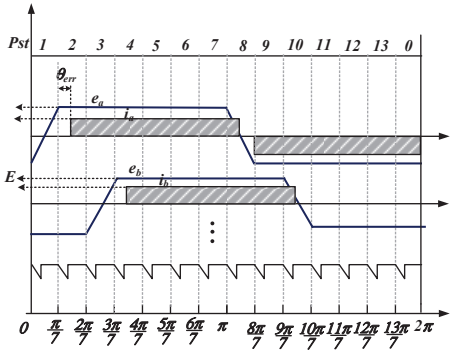

Figure 6. Torque ripple caused by position error.

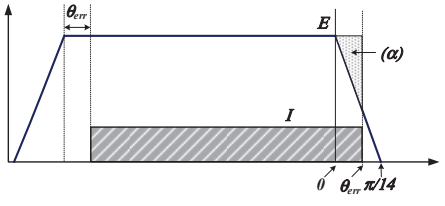

Figure 7. Torque error caused by position error.

By using (7), the amount of torque reduction (T_{loss}) can be driven as Equation (8), and output torque of Equation (6) can be expressed as Equation (9) when the position error exists.

$$T_{loss} = \frac{7}{\pi} E \cdot \theta_{err}^2 \tag{8}$$

$$T_e = \frac{6EI - \frac{7}{\pi} E \cdot \theta_{err}^2 \cdot 14}{\omega_m} \tag{9}$$

Therefore, in order to improve the control performance in the high-speed region and extend the operation region, the increase of switching frequency is essential. These days, the inverter system using SiC-MOSFET allows the possibility of using high switching frequency. However, it also comes with the problem of the EMI noise. Thus, this paper proposes a common-mode voltage-reduction method that is capable of optimizing the resulting EMI noise.

2.4. Description of the Common-Mode Voltage for the 7-Phase BLDC

The modified unipolar PWM method in [33] is used to generate the independent voltage induced to each phase winding, as shown in Figure 8. In this case, all of the voltage references are assumed to be identical for simple description. The positive and negative voltage references formed from current controller of each phase are compared with carrier wave. The positive references decide the on-time of the top switch, which is conducted in the positive conduction phases, and negative references decide the on-time of the bottom switch in the negative conduction phases. This switching method has the advantage of reducing the current pulsation by generating two output voltages in one switching period.

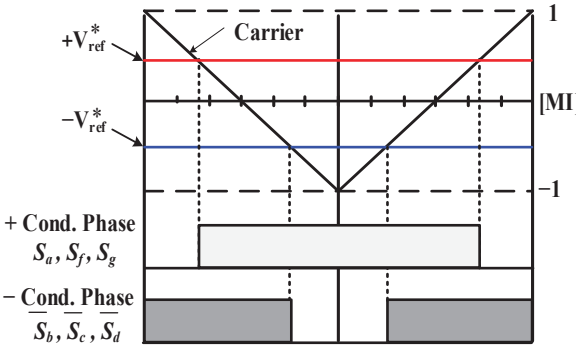

Figure 8. Modified unipolar PWM method in BLDC control.

The inverter output voltage including switching function can be expressed as Equation (10), and assuming that the sum of all phase currents and back-EMF are zero, the common-mode voltage can be calculated as Equation (11), where the switching state of non-conduction phase is excluded, and S_{state} means the number of top switches turned on. Following Equation (11), the kinds of the common-mode voltage (V_{cm}) that can be generated in the 6-phase excitation method are expressed as Equation (12). There are seven kinds of voltage that occur according to the switching states.

$$V_{xn} = \left(S_x - \frac{1}{2}\right) \cdot V_{dc}, \quad S_x = \begin{Bmatrix} 1 : switch\ on \\ 0 : switch\ off \end{Bmatrix} \tag{10}$$

$$V_{cm} = V_{sn} = \frac{V_{dc} \cdot \left(\sum_{x=a}^{g} S_x - \frac{6}{2}\right)}{6} = \frac{V_{dc}(S_{state} - 3)}{6} \tag{11}$$

$$V_{cm} = \left\{ \frac{V_{dc}}{2}, \frac{V_{dc}}{3}, \frac{V_{dc}}{6}, 0, -\frac{V_{dc}}{6}, -\frac{V_{dc}}{3}, -\frac{V_{dc}}{2} \right\} \tag{12}$$

3. Proposed Phase to Phase Interleaved Method

3.1. Definition of the Phase-Phase Interleaved in the Seven-Phase BLDCM

To reduce the common-mode voltage, the phase shift method in the three-phase inverter is extended to 6-phase excitation method [23]. Three carriers are used, and each carrier is shifted by positive k degrees ("+") and negative k degrees ("−") based on the fundamental carrier, as shown in Figure 9. The positive and negative voltage references are,

respectively, compared with "$+k$", "$-k$", and the related carrier. Moreover, the compared carrier should be changed according to the position in the 6-exciation method because the excitation phase is changed in every position. Table 2 shows the matched carrier of each phase according to the position. In Table 2, "$\pm k$"and "0°"mean the shifted angle of the carrier, and "X" means the non-conductive phase. This arrangement of the carrier waves is intended to minimize the torque ripple due to the phase shift when the position is changed. In Figure 9, the common-mode voltage is shown with a switching state. The generation pattern and magnitude of the common-mode voltage varies depending on the shift angle and MI.

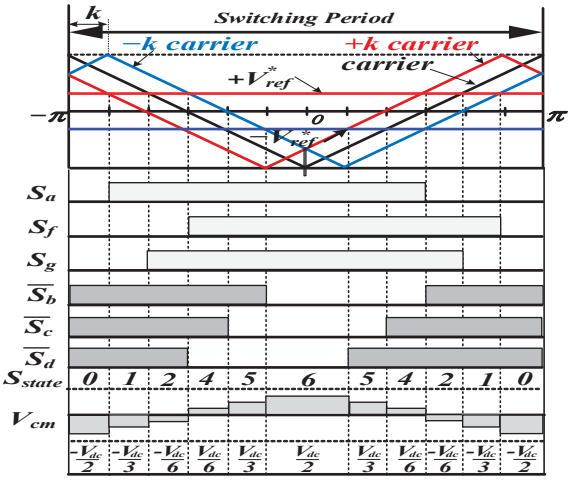

Figure 9. Switching state and common-mode voltage of phase-phase interleaved method.

Table 2. Compared carrier depending on the position.

Position	*Phase*						
	a	*b*	*c*	*d*	*e*	*f*	*g*
0	$-k$	0°	$+k$	X	$-k$	0°	$+k$
1	X	$-k$	0°	$+k$	$-k$	0°	$+k$
2	$+k$	$-k$	0°	$+k$	X	$-k$	0°
3	$+k$	X	$-k$	0°	$+k$	$-k$	0°
4	0°	$+k$	$-k$	0°	$+k$	X	$-k$
5	0°	$+k$	X	$-k$	0°	$+k$	$-k$
6	$-k$	0°	$+k$	$-k$	0°	$+k$	X
7	$-k$	0°	$+k$	X	$-k$	0°	$+k$
8	X	$-k$	0°	$+k$	$-k$	0°	$+k$
9	$+k$	$-k$	0°	$+k$	X	$-k$	0°
10	$+k$	X	$-k$	0°	$+k$	$-k$	0°
11	0°	$+k$	$-k$	0°	$+k$	X	$-k$
12	0°	$+k$	X	$-k$	0°	$+k$	$-k$
13	$-k$	0°	$+k$	$-k$	0°	$+k$	X

3.2. Switching Function Including the Shift Angle and MI for Minimum Common-Mode Voltage

The switching states of Figure 9 are newly expressed, as shown in Figure 10, to define the switching state based on the compared carrier.

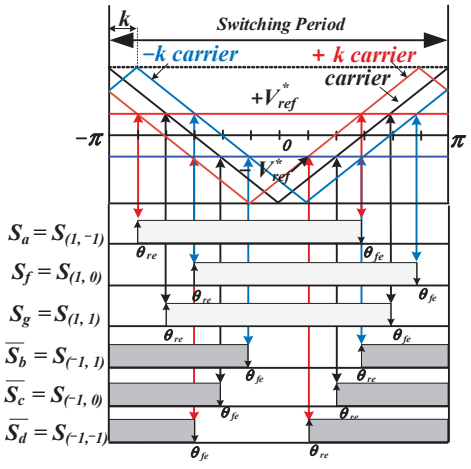

Figure 10. Revised switching state of phase-phase interleaved method in 7-phase BLDCM.

The switching state of x-phase S_x is defined as $S_{(n,m)}$ as in Equation (13). When the top switch is on, n becomes 1, and n becomes -1 when the bottom switch is on; m becomes 0, -1, and +1 according to the sign of the shifted angle of the carrier.

$$\{S_x\} \Rightarrow \left\{S_{(n,m)}\right\} n = \{-1, 1\}, \begin{cases} -1: \ Bottom\ switch\ on \\ +1: \ Top\ switch\ on \end{cases}$$
$$m = \{-1, 0, 1\}, \begin{Bmatrix} 0: & based & carrier \\ -1: & +k^{\circ} shifted & carrier \\ 1: & -k^{\circ} shifted & carrier \end{Bmatrix} \tag{13}$$

When the phase shift method is applied, the on-off point of each switching state can be expressed as Equation (14), which contains the information of MI and shifting angle (k), where θ_{re} and θ_{fe} are the rising edge and falling edge of the switching state, respectively.

$$S_{(n,m)}[\theta_{re}, \theta_{fe}] = [\frac{-\pi km}{180} - \frac{n\pi}{2}(1 + nMI), \frac{-\pi km}{180} + \frac{n\pi}{2}(1 + nMI)] \tag{14}$$

Since the switching function of equations is a periodic signal, a Fourier series of switching function is driven as Equation (18) by using the Fourier coefficient of Equations (15)–(17), and the effective integration interval is from θ_{re} to θ_{fe} in Equation (14).

$$a_0 = \frac{1}{\pi}\int_{-\pi}^{\pi} f(x)dx \tag{15}$$

$$a_a = \frac{1}{\pi}\int_{-\pi}^{\pi} f(x)\cos(x)dx \tag{16}$$

$$a_b = \frac{1}{\pi}\int_{-\pi}^{\pi} f(x)\sin(x)dx \tag{17}$$

$$\left\{S_{(n,m)}(x)\right\} = \frac{a_0}{2} + \sum_{z=1}^{\infty}\left(a_z\cos(\frac{z\pi}{2\pi}x\right) + b_z\sin(\frac{z\pi}{2\pi}x)) \tag{18}$$

where $f(x)$ is defined as 1 or -1, which means the on-state of the top and bottom switches, respectively. The range of x is from $-\pi$ to π, and z represents the precision of the switching signal. If it becomes larger, the signal is closed to the ideal square wave. By solving Equation (18), the new switching functions including the shifting angle and MI in a switching period can be expressed as Equation (19).

$$S_{(n,m)}(x) = \frac{1+MI}{2} + n\sum_{z=1}^{\infty}\frac{2}{z\pi}[\cos(mzk)\sin(\frac{z\pi(1+nMI)}{2})\cos(zx)\sin(mzk)\sin(\frac{z\pi(1+nMI)}{2})\sin(zx)] \quad (19)$$

At last, the common-mode voltage according to the switching state can be calculated as (20).

$$V_{cm} = V_{dc}\left(S_{(1,0)}(x) + S_{(1,1)}(x) + S_{(1,-1)}(x) + S_{(-1,0)}(x) + S_{(-1,1)}(x) + S_{(-1,-1)}(x)\right)/6 \quad (20)$$

3.3. Proposed Control Method for Phase Shift in 6-Excitation Method

Figure 11 shows the verification of Equations (19) and (20), which includes the specific shift angle and MI. The equations are programed by using MATLAB. As shown in Figure 10, the common-mode voltage has various patterns according to MI and shift angle. Therefore, the RMS value of V_{cm} is calculated as shown in Equation (21) to find the optimal shift angle with generation of the lowest common-mode voltage.

$$V_{cm}(rms) = \sqrt{\frac{1}{T}\int_0^T V_{cm}^2 dt} \quad (21)$$

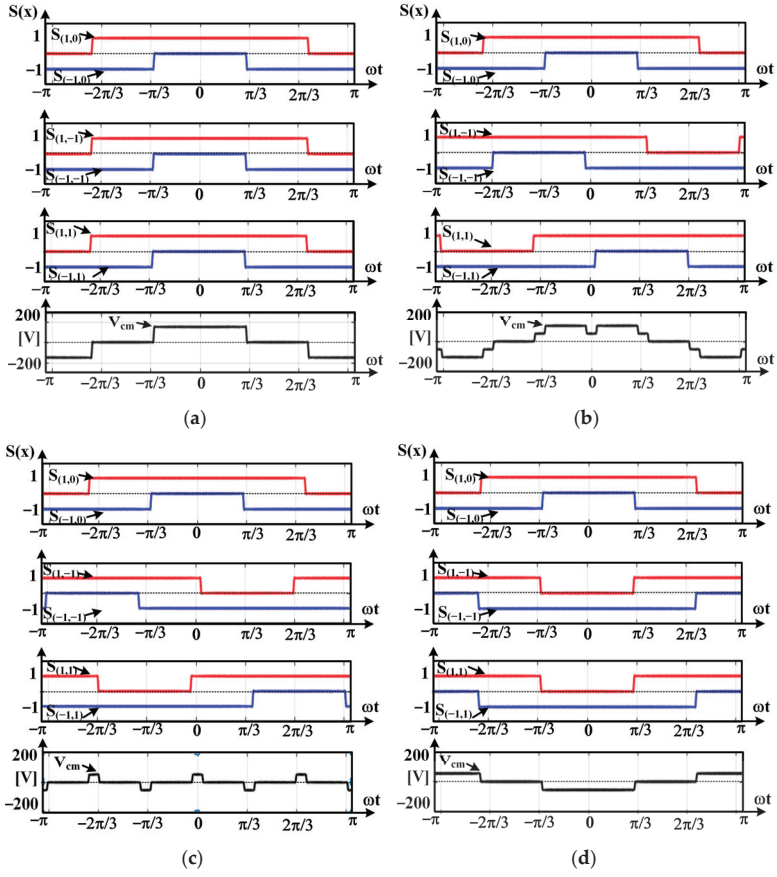

Figure 11. Pattern of common-mode voltage depending on the shift angle and MI: (**a**) k = 0°, MI = 0.4; (**b**) k = 60°, MI = 0.4; (**c**) k = 120°, MI = 0.4; and (**d**) k = 180°, MI = 0.4.

Figure 12 shows the normalized RMS value of the common-mode voltage when the conventional PWM without phase shift and phase shift method in specific angles are compared in specific angle. When the MI is lower than 0.5, a 120° shifting angle has the best performance for the generation of common-mode voltage. On the other hand, a 90° shifting angle has the lowest common-mode voltage when the MI is higher than 0.5, and the red dot indicates the point where the common-mode voltage is minimized during the operation in full range.

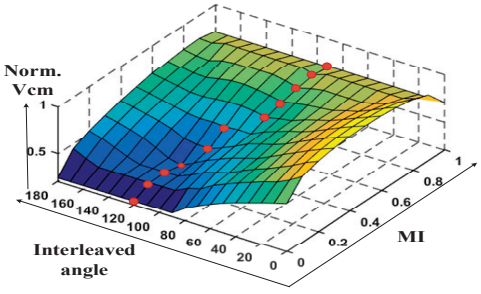

Figure 12. Amount of common-mode voltage depending on the interleave angle and MI.

Figure 13 shows the proposed interleaved method to reduce the common-mode noise in the 7-phase BLDCM operation system. When the MI was smaller than 0.5, a 90 degree interleaved method was adopted, and when the MI was larger than 0.5, a 120 interleaved method was conducted.

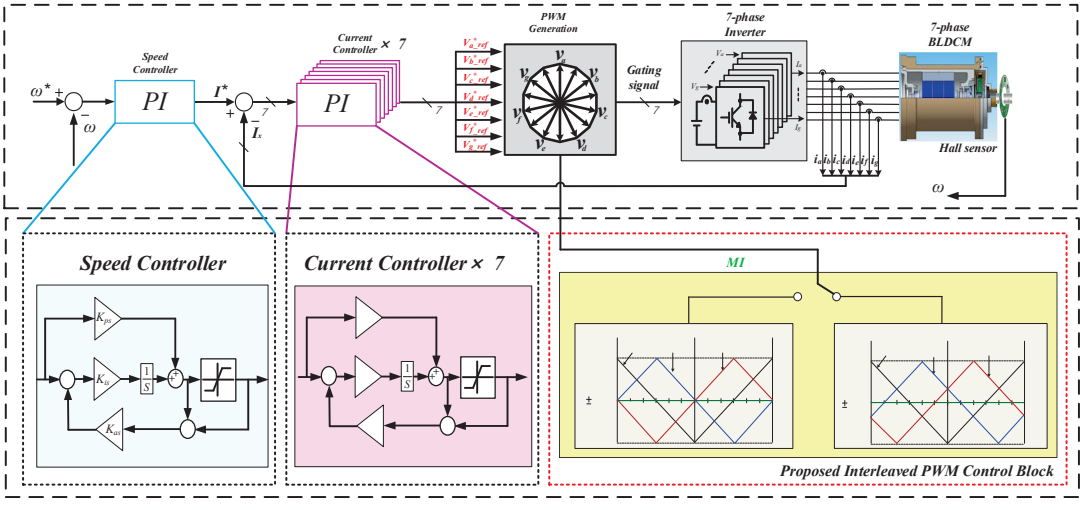

Figure 13. Proposed phase interleaved method to reduce the common-mode noise in the 7-phase BLDCM.

4. Experimental Set-Up and Results

4.1. System Configuration for SiC-MOSFET

Figure 14 shows the experimental set-up using SiC-MOSFET for high-speed control and switching frequency. A 3-phase rectifier, DC-link bank, SiC-MOSFET inverter, and developed control board are integrated in the system. The SIC-MOSFET (CAS300M12BM2) and gate driver (CGD15HB62P1) are made by CREE Inc. The dc-link and motor specification are shown in Table 3. The picture and configuration of the control board are shown in Figure 15. TMS320F28337D (DSP) and Cyclone4 (FPGA) are designed to calculate the

control algorithm in 70 kHz. TMS320F28377D has a dual core, so the control algorithm is properly distributed for reducing the calculation time, and a high-speed analog-to-digital converter (ADS5270) is used to remove the sampling delay of the phase current. All of functions to control the motor are implemented in FPGA. It can help to secure the calculation time of DSP.

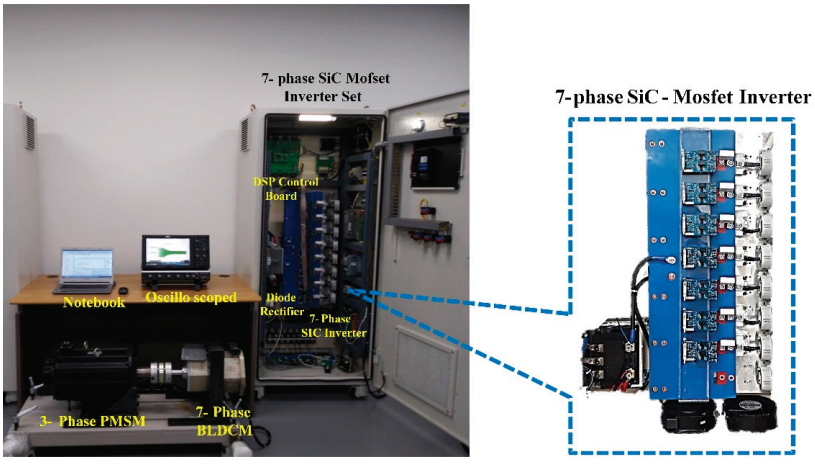

Figure 14. Experimental Configuration of SiC Inverter for 7-phase motor.

Table 3. Parameters for the experiment.

SiC-MOSFET Inverter	Part number	CAS300M12BM2 (Cree)
	Rated Voltage	1200 (V)
	Rated Current	300 (A)
	Esw	12 (mJ)
	Rds(on)	4.2 (mΩ)
	Switching frequency	10~70 (kHz)
DC-Link Bank	Capacitance	1100 (μF)
	Voltage	150 (V)
Seven-Phase BLDCM	Pole	6
	Rated speed	7000 (Rpm)
	Rated current	10 (A)
	Stator resistance	0.1 (Ω)
	Stator Inductance	1 (mH)
	Back-EMF constant	7.5 (V/krpm)

4.2. Control Performance According to Switching Frequency

In order to compare the relationship between the control frequency and control performance, the current control in 10 kHz of the conventional switching frequency is compared with 40 kHz and 70 kHz. Table 4 shows the current control cycle in a specific rotor rotation frequency and switching frequency. We already know that as a control rule, current control is required to operate at least five times within the speed control cycle. Figure 16 shows the 1.8 A current control and the speed of motor is saturated by the mechanical friction. Figure 16a shows the large torque ripple caused by commutation change in the 6-exictation method. If the switching frequency increases to 70 kHz, the torque ripple is reduced. As mentioned earlier, the control frequency affects the position error. Specially, seven-phase BLDCM is controlled by dividing the position to 14 sectors.

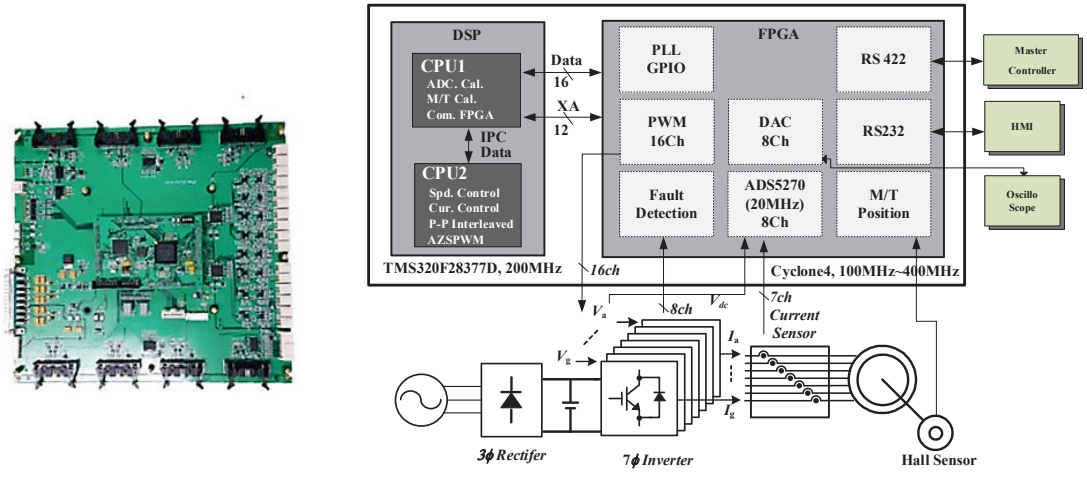

Figure 15. Configuration of SiC-MOSFET control board: (**a**) developed 7-phase control board; (**b**) block diagram of control board.

Table 4. Operation cycle according to control frequency and rpm.

Rpm	Frequency		
	10 (kHz)	**40 (kHz)**	**70 (kHz)**
4000 (Rpm)	3.5 cycle	14.2 cycle	25 cycle
7800 (Rpm)	1.8 cycle	7.3 cycle	12.8 cycle
10,400 (Rpm)	1.3 cycle	5.4 cycle	9.6 cycle

Sufficient control frequency is required in every sector. The operation cycle of the current controller can be calculated using Equation (22).

$$Operation\ Cycle = \frac{Control\ frequency}{Rpm \times \frac{P}{2\times 60} \times 14} \tag{22}$$

Figure 17 shows the speed control in 4000 rpm. Speed control in the conventional control frequency of Figure 17a shows a large current ripple caused by commutation change. Increasing the switching frequency improves the control performance through instant sampling of position changes, as shown in Figure 17b,c. In the speed control of 10 (kHz) at 7800 rpm, as shown in Figure 18a, the current cannot be controlled, and the maximum output results. This is due to the lack of frequency of operation of the current controller for one sector, as shown in Table 4, and the sampling error of the position is included. On the other hand, in the speed control of 40 kHz or 70 kHz, the phase current is controlled well.

Figure 19 shows the speed control in 10,400 rpm. In this region, the speed control of 40 kHz cannot control the phase current well. As shown in Figures 17–19, increasing the switching frequency affects the improvement of the control performance and extends the operation range. Figure 19 shows the speed control in 10,400 rpm. In this region, the speed control of 40 kHz does not control the phase current well. As shown in Figures 17–19, increasing the switching frequency affects the improvement of control performance and extends the operation range.

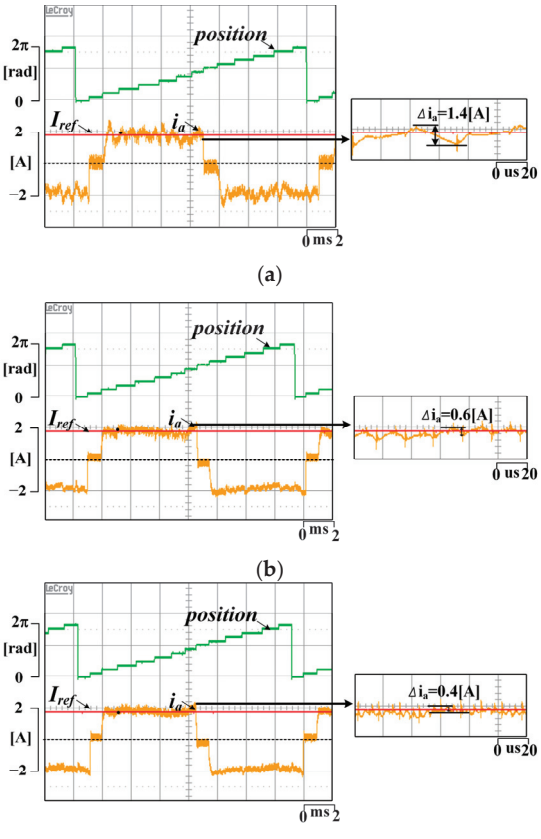

Figure 16. Comparison of current control depending on the control frequency: (**a**) 10 kHz current control; (**b**) 40 kHz current control; and (**c**) 70 kHz current control.

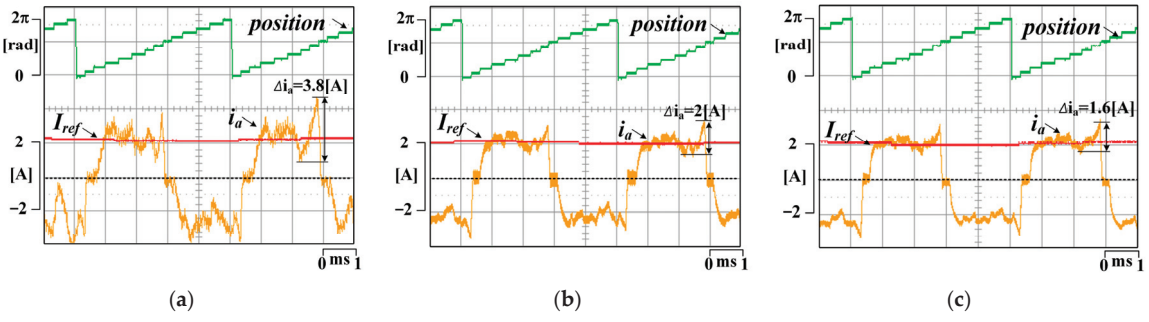

Figure 17. Speed control characteristic according to switching frequency (4000 rpm); (**a**) 10 kHz switching frequency; (**b**) 40 kHz switching frequency; and (**c**) 70 kHz switching frequency.

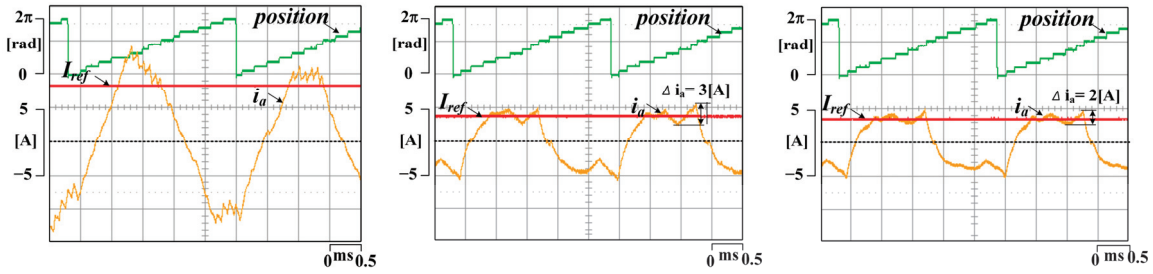

(**a**) (**b**) (**c**)

Figure 18. Speed control characteristic according to switching frequency (7800 rpm); (**a**) 10 kHz switching frequency; (**b**) 40 kHz switching frequency; and (**c**) 70 kHz switching frequency.

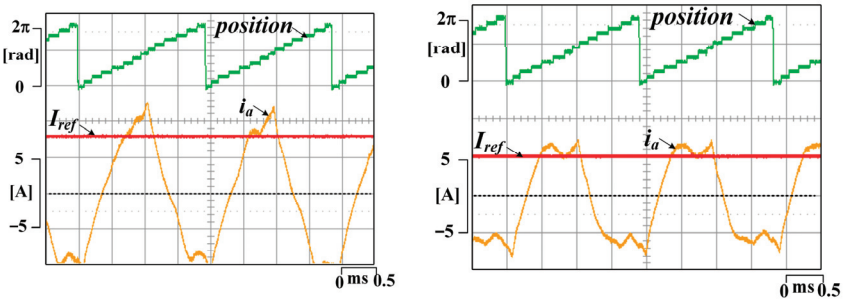

(**a**) (**b**)

Figure 19. Speed control characteristic according to switching frequency (10,400 rpm); (**a**) 40 kHz switching frequency; and (**b**) 70 kHz switching frequency.

Figure 20 shows the amount of the common-mode voltage and leakage current when the switching frequency increases. When the switching frequency increased from 14 kHz to 70 kHz, it was confirmed that the common-mode noise increased.

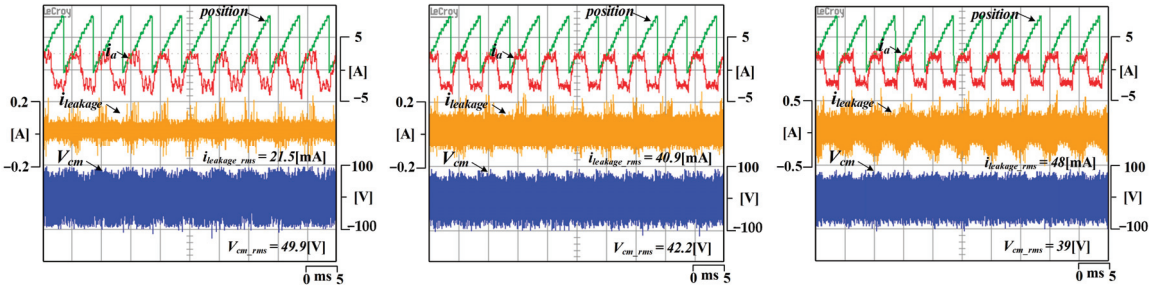

(**a**) (**b**) (**c**)

Figure 20. Relationship between switching frequency and common noise; (**a**) 14 kHz switching frequency at 4000 rpm; (**b**) 40 kHz switching frequency at 4000 rpm; and (**c**) 70 kHz switching frequency at 4000 rpm.

4.3. Common-Mode Voltage Generation According to the Interleaved Method and MI

As we know from the above experiments, increasing the switching frequency is the most important for improving the control performance, but reducing the common monde noise is more important in the current industry. Figure 21 shows the experimental results

of the proposed common-mode voltage generation according to the interleaved angle in the no-load condition. The switching frequency is controlled constantly at 40 kHz. The speed control of the 7-phase BLDCM is implemented, and the speed reference is 4000 rpm. Figure 19a shows the conventional 7-phase PWM method, and Figure 21b,c represent the 90° and 120° interleaved methods, respectively. In the no-load condition, where the modulation index (MI) is very low, the conventional PWM method has the largest common-mode voltage, and the smallest common-mode voltage appears when using 120° interleaved method.

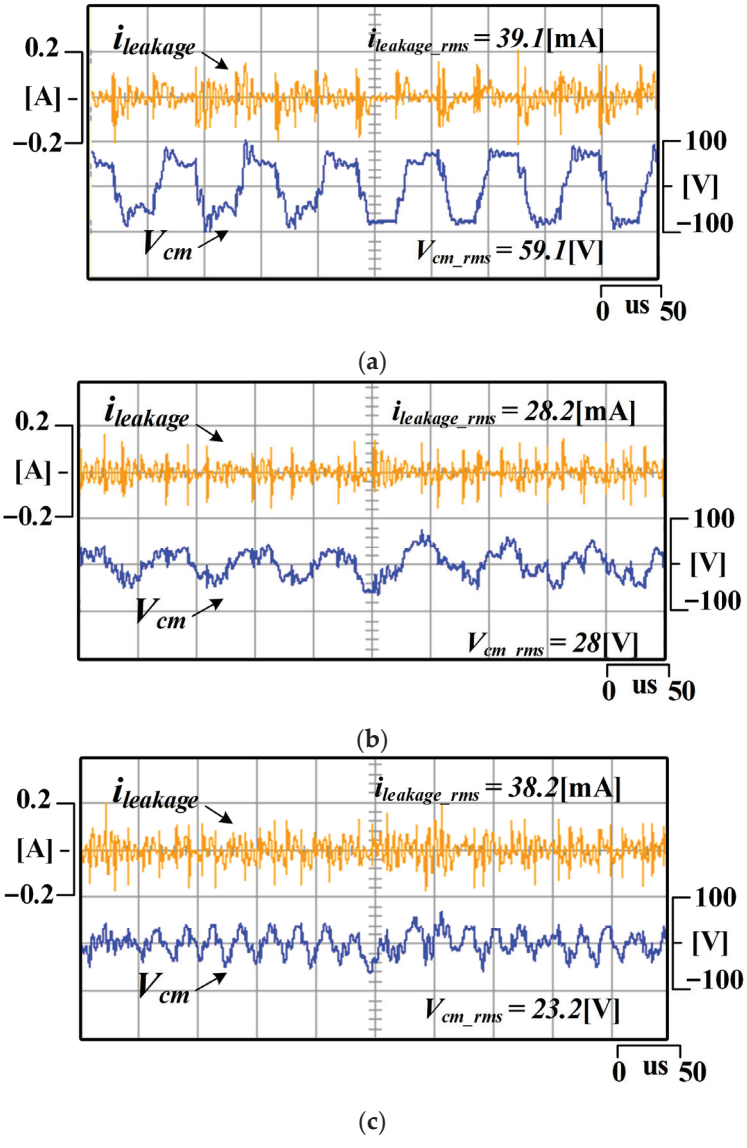

Figure 21. Comparison of common-mode voltage and leakage current depending on the 40 kHz switching frequency (4000 rpm): (**a**) conventional 7-phase PWM; (**b**) 90° interleaved method; and (**c**) 120° interleaved method.

The experimental results of the common-mode voltage and leakage current according to the PWM method and MI with the load condition are shown in Figures 22–24. The modulation index (MI) is controlled from 0.3 to 0.7 to compare results. It shows the 0.3 modulation index (MI) condition in (a), 0.5 modulation index (MI) condition in (b), and 0.7 modulation index (MI) condition in (c). As presented in Figures 22 and 23, when the modulation index (MI) condition is 0.3 and 0.5, the 120° interleaved method has the smallest common-mode voltage, and conventional 7 phase PWM has the largest common-mode voltage; as presented in Figure 24, for the 0.7 modulation index (MI) condition, the 90° interleaved method has the smallest common-mode voltage, and conventional 7-phase PWM has the largest common-mode voltage. Figure 25 shows the comparison of the common-mode noise between the conventional PMW and interleaved method. There is a little difference from the mathematical analysis due to the independent voltage reference of the 7-phase current controller. In conclusion, as observed in the experimental waveforms, the proposed method of applying the optimal interleaved angle according to MI can reduce the effect of the common-mode voltage by up to 50% compared to the conventional PWM method. Since the optimal interleaved angle is related with the modulation index (MI), a selective control method is required between the 90° interleaved method and 120° interleaved method.

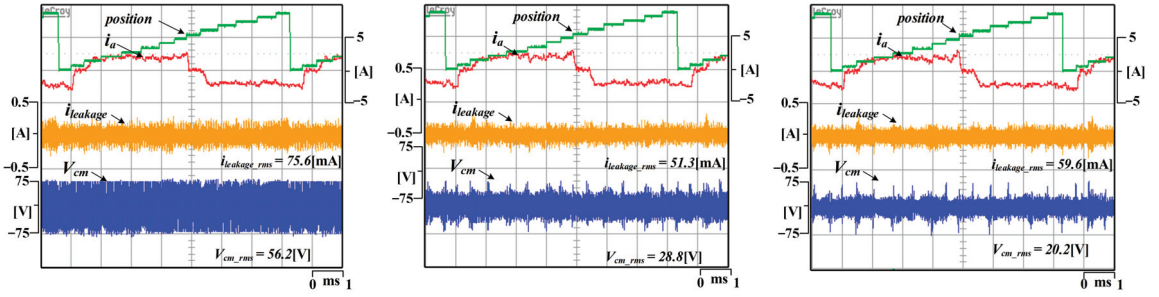

Figure 22. EMI noise characteristic according to 0.3 MI (2600 rpm) and interleaved method: (**a**) conventional 7-phase PWM; (**b**) 90° interleaved method; and (**c**) 120° interleaved method.

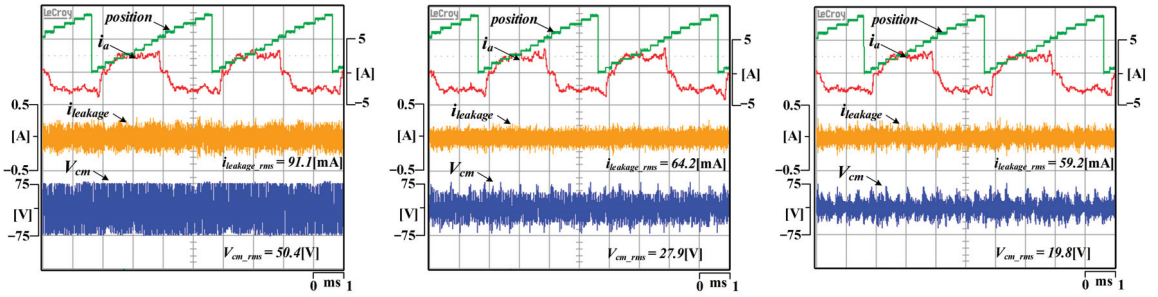

Figure 23. EMI noise characteristic according to 0.5 MI (5000 rpm) and interleaved method: (**a**) conventional 7-phase PWM; (**b**) 90° interleaved method; and (**c**) 120° interleaved method.

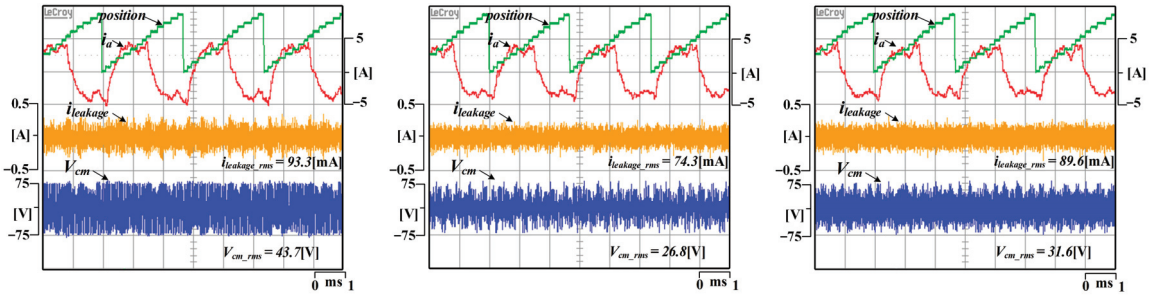

Figure 24. EMI noise characteristic according to 0.7 MI (7400 rpm) and interleaved method: (**a**) conventional 7-phase PWM; (**b**) 90° interleaved method; and (**c**) 120° interleaved method.

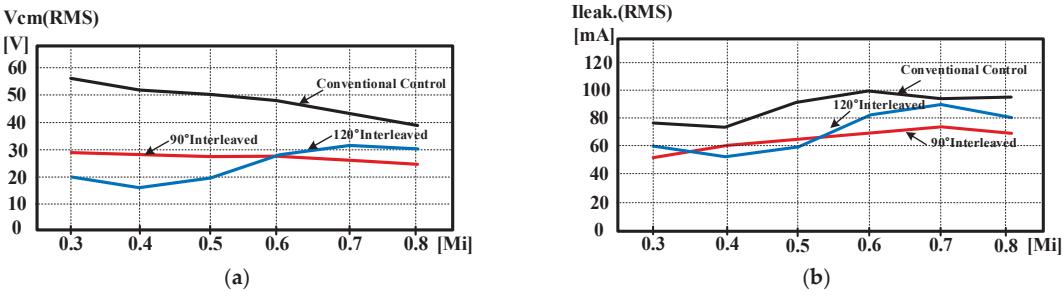

Figure 25. Common-mode noise comparison according to MI between conventional method and proposed interleaved method: (**a**) common-mode voltage and (**b**) leakage current.

5. Conclusions

This paper presents the relationship between the carrier interleaving method and modulation index (MI) with common-mode voltage in a 7-phase BLDCM control system using SiC-MOSFET for higher switching frequency. Using SiC-MOSFET can reduce current ripple and compensate for position error caused by low resolution in high-speed regions. However, increasing the switching frequency causes common-mode voltage and EMI noise. The implementation of the interleaved method in 6-excitation control is described, in which the amount of common-mode voltage was analyzed because it depends on the interleaved angle and MI. The RMS value of the common-mode voltage in a switching period was derived by mathematical equation. The paper proposes the method that operates the optimal interleaved angle according to MI for minimum common-mode voltage, and experiments about common-mode voltage were conducted to verify the optimal interleaved angle.

Author Contributions: Conceptualization, D.-Y.K. and J.-M.K.; methodology, Y.-D.S.; software, D.-Y.K.; validation, H.-J.K. and J.-M.K.; formal analysis, D.-Y.K. and J.-M.K.; investigation, D.-Y.K.; writing—original draft preparation, Y.-D.S. and H.-J.K.; writing—review and editing, Y.-D.S. and H.-J.K.; visualization, D.-Y.K.; supervision, J.-M.K. All authors have read and agreed to the published version of the manuscript.

Funding: This research received no external funding.

Data Availability Statement: Accepted and complied with.

Acknowledgments: This paper was supported by Education and Research promotion program of KOREATECH in 2022. This work was supported by the Technology Innovation Program-Materials/Parts Technology Development Program 2020 (20013335, Development of 150 kW inverter for high power motor control) funded By the Ministry of Trade, Industry & Energy (MOTIE, Korea).

Conflicts of Interest: The authors declare no conflict of interest.

References

1. Durán, M.J.; Prieto, J.; Riveros, J.A.; Guzman, H. Space-Vector PWM With Reduced Common-Mode Voltage for Five-Phase Induction Motor Drives. *IEEE Trans. Power Electron.* **2013**, *60*, 114–124.
2. Simoes, M.G.; Vieira, P., Jr. A High-Torque Low-Speed Multiphase Brushless Machine A Perspective Application of Electric Vehicles. *IEEE Trans. Ind. Electron.* **2002**, *49*, 1154–1164.
3. Gan, J.; Chau, K.T.; Chan, C.C.; Jiang, J.Z. A New Surface-Inset, Permanent-Magnet, Brushless DC Motor Drive for Electric Vehicles. *IEEE Trans. Magn.* **2000**, *36*, 3810–3818.
4. Wang, H.; Zheng, X.; Yuan, X.; Wu, X. Enhanced Natural Fault-Tolerant Model Predictive Current Control in Nine-Phase Motor Drives Under Open-Phase Fault. *IEEE Trans. Energy Convers.* **2022**, *37*, 2449–2460.
5. Moon, J.J.; Won, L.; Park, S.W.; Kim, J.M. Fault tolerant control method of seven-phase BLDC motor in asymmetric fault condition due to open phase. In Proceedings of the 2015 IEEE International conference on Power Electronics and ECCE Asia, Seoul, Republic of Korea, 1–5 June 2015.
6. Tao, T.; Zhao, W.; Du, Y.; Zhu, Y.C. Simplified fault-tolerant model predictive control for a five-phase permanent-magnet motor with reduced computation burden. *IEEE Trans Power Electron.* **2022**, *35*, 3850–3858.
7. Park, J.B.; Johnson, M.; Toliyat, H.A. A Novel Hysteresis Current Control switching Method for Torque Ripple Minimization in Multi-Phase Motors. In Proceedings of the 2014 IEEE Energy Conversion Congress and Exposition (ECCE), Pittsburgh, PA, USA, 14–18 September 2014.
8. Ryu, H.M.; Kim, J.W.; Sul, S.K. Synchronous-frame current control of multiphase synchronous motor under asymmetric fault condition of due to open phases. *IEEE Trans. Ind. Appl.* **2006**, *42*, 1062–1070.
9. Park, H.S.; Park, S.W.; Kim, D.Y.; Kim, J.M. Hybrid Phase Excitation Method for Improving Efficiency of 7-Phase BLDC Motors for Ship Propulsion Systems. *Trans J. Power Electron.* **2019**, *19*, 761–770.
10. Kim, T.Y.; Lee, B.K.; Won, C.Y. Modeling and simulation of multiphase BLDC motor drive systems for autonomous underwater vehicles. In Proceedings of the 2007 IEEE International Electric Machines & Drives Conference, Antalya, Turkey, 3–5 May 2007.
11. Lee, M.H.; Kim, H.J.; Kim, J.M. Automatic advance angle control algorithm using anti-windup feedback voltage of PI current controller for wide range speed operation of BLDCM. In Proceedings of the 2018 IEEE Applied Power Electronics Conference and Exposition (APEC), San Antonio, TX, USA, 4–8 March 2018.
12. Lai, Y.S.; Chen, J.H. A New Approach to Direct Torque Control of Induction Motor Drives for Constant Inverter Switching Frequency and Torque Ripple Reduction. *IEEE Trans. Energy Convers.* **2001**, *16*, 220–227.
13. Agarwal, A.K. An overview of SiC power devices. In Proceedings of the 2010 International Conference on Power, Control and Embedded Systems (ICPCES), Allahabad, India, 29 November–1 December 2010.
14. Lemmon, A.; Mazzola, M.; Gafford, J.; Parker, C. Stability Considerations for Silicon Carbide Field-Effect Transistors. *IEEE Trans. Power Electron.* **2013**, *28*, 4453–4459.
15. Xu, F.; Jiang, D.; Wang, J.; Wang, F.; Tobert, L.M.; Han, T.J.; Kim, S.J. Characterization of a high temperature multichip SiC JGET-based module. In Proceedings of the 2011 IEEE Energy Conversion Congress and Exposition, Phoenix, AZ, USA, 17–22 September 2011.
16. Ala, G.; Giaconia, G.C.; Giglia, G.; Piazza, M.C.D.; Vitale, G. Design and Performance Evaluation of a High Power-Density EMI Filter for PWM Inverter-Fed Induction-Motor Drives. *IEEE Trans. Ind. Appl.* **2016**, *52*, 2397–2404.
17. Akagi, H.; Hasegawa, H.; Doumoto, T. Design and Performance of a Passive EMI Filter for Use With a Voltage-Source PWM Inverter Having Sinusoidal Output Voltage and Zero Common-Mode Voltage. *IEEE Trans. Power Electron.* **2004**, *19*, 1069–1076.
18. Son, Y.C.; Sul, S.K. A New Active Common-Mode EMI Filter for PWM Inverter. *IEEE Trans. Power Electron.* **2003**, *18*, 1309–1314.
19. Son, Y.C.; Sul, S.K. Generalization of Active Filters for EMI Reduction and Harmonics Compensation. *IEEE Trans. Ind. Appl.* **2006**, *42*, 545–551.
20. Ogasawara, S.; Ayano, H.; Akagi, H. An Active Circuit for Cancellation of Common-Mode Voltage Generated by a PWM Inverter. *IEEE Trans. Power Electron.* **1998**, *13*, 835–841.
21. Hou, C.C.; Shih, C.C.; Cheng, P.T.; Hava, A.M. Common-Mode Voltage Reduction Pulse width Modulation Techniques for Three-Phase Grid-Connected Converters. *IEEE Trans. Power Electron.* **2013**, *28*, 1971–1979.
22. Hava, A.M.; Un, E. A High-Performance PWM Algorithm of Common-Mode Voltage Reduction in Three-Phase Voltage Reduction in Three-Phase Voltage Source Inverters. *IEEE Trans. Power Electron.* **2011**, *26*, 1998–2008.
23. Cacciato, M.; Consoli, A.; Scarcella, G.; Testa, A. Reduction of Common-Mode Currents in PWM Inverter Motor Drives. *IEEE Trans. Ind. Appl.* **1999**, *35*, 469–476.
24. Un, E.; Hava, A.M. A Near-State PWM Method With Reduced Switching Losses and Reduced Common-Mode Voltage for Three-Phase Voltage Source Inverters. *IEEE Trans. Ind. Appl.* **2009**, *45*, 782–793.

25. Oriti, G.; Julian, A.L.; Lipo, T.A. A New Space Vector Modulation Strategy for Common Mode Voltage Reduction. In Proceedings of the Power Electronics Specialists Conference, St. Louis, MO, USA, 27–27 June 1997.
26. Huang, J.; Shi, H. Reducing the Common-Mode Voltage through Carrier Peak Position Modulation in an SPWM Three-Phase Inverter. *IEEE Trans. Power Electron.* **2014**, *29*, 4490–4495.
27. Kim, D.Y.; Ma, J.S.; Kim, J.M. Phase to Phase Interleaved Method to Reduce the Common Mode Voltage for Seven Phase BLDCM Drive. In Proceedings of the 2019 IEEE International conference on Power Electronics and ECCE Asia, Busan, Republic of Korea, 1–7 May 2019.
28. Lee, H.D.; Sul, S.K. Common-Mode Voltage Reduction Method Modifying the Distribution of Zero-Voltage Vector in PWM Converter/Inverter System. *IEEE Trans. Ind. Appl.* **2001**, *37*, 1732–1738.
29. Zhang, D.; Wang, F.; Burgos, R.; Lai, R.; Boroyevich, D. DC-Link Ripple Current Reduction for Paralleled Three-Phase Voltage-Source Converters With Interleaving. *IEEE Trans. Power Electron.* **2011**, *26*, 1741–1753.
30. Lai, Y.S.; Shyu, F.S. Optimal Common-Mode Voltage Reduction PWM Technique for Inverter Control With Consideration of the Dead-Time Effects-Part I: Basic Development. *IEEE Trans. Ind. Appl.* **2004**, *40*, 1605–1612.
31. Quan, Z.; Li, T.W. Impact of PWM Schemes on the Common Mode Voltage of Interleaved Three-Phase Two-Level Voltage Source Converters. *IEEE Trans. Ind. Electron.* **2019**, *66*, 852–864.
32. Chen, H.; Zhao, H. Review on pulse-width modulation strategies for common-mode voltage reduction in three-phase voltage-source inverters. *IET Power Electron.* **2016**, *9*, 2611–2620.
33. Kim, H.W.; Shin, H.K.; Mok, H.S.; Lee, Y.K.; Cho, H.Y. Novel PWM Method with Low Ripple Current for Position Control Applications of BLDC Motor. *J. Power Electron.* **2011**, *11*, 726–733.

applied sciences

MDPI

Article

A Method to Determine the Torque Ripple Harmonic Reduction in Skewed Synchronous Reluctance Machines

César Gallardo [1,*], Carlos Madariaga [1], Juan A. Tapia [1] and Michele Degano [2]

[1] Department of Electrical Engineering, University of Concepcion, Concepcion 4070386, Chile
[2] Department of Electrical and Electronic Engineering, University of Nottingham, Nottingham NG7 2RD, UK
* Correspondence: cgallardos@udec.cl

Abstract: In this paper, a discrete skew methodology is presented to understand the effect of skewing angle on electromagnetic torque in SynRM design. A new approach is proposed to estimate the amplitude of each torque ripple component as a function of skewing angle. The reduction factor for each harmonic component is derived in general form, allowing for the determination of overall torque ripple waveform. The validity of the proposed method is evaluated through the examination of two SynRMs, resulting in a torque ripple reduction of up to 70%. The results obtained through the use of a proposed analytical ripple reduction estimator and FEA evaluation showed good agreement. The proposed skewing technique was applied on a previously optimized triple-barrier SynRM with a positive outcome: a consistent torque ripple reduction tackling relevant harmonic components. The analysis of harmonic distribution of torque ripple is mandatory for the selection of the optimal skewing strategy when following the proposed method, with two-step skewing recommended for mostly-purely-sinusoidal torque waveforms, and multi-step skewing recommended for machines with multiple higher-magnitude harmonic components.

Keywords: step skewing; torque ripple harmonics; finite element analysis; synchronous reluctance machines

Citation: Gallardo, C.; Madariaga, C.; Tapia, J.A.; Degano, M. A Method to Determine the Torque Ripple Harmonic Reduction in Skewed Synchronous Reluctance Machines. *Appl. Sci.* **2023**, *13*, 2949. https://doi.org/10.3390/app13052949

Academic Editors: Gang Lei, Feng Chai and Lorand Szabo

Received: 25 January 2023
Revised: 18 February 2023
Accepted: 21 February 2023
Published: 24 February 2023

1. Introduction

The operating principle of Synchronous Reluctance Motors (SynRMs), shown schematically in Figure 1, is based on the anisotropy variations of different magnetic paths, present in the rotor structure, that enable the production of reluctance torque. SynRMs are singly excited machines that can achieve good torque density, high efficiency, high-speed operation, fault tolerance capability, and low cost [1–5], making them a promising competitor of induction machines (IM). The absence of rotor windings or rotor cage translates into zero rotor copper losses, and as a result, lower rotor temperatures and higher efficiency in comparison with IMs [6]. In addition, the absence of permanent magnets simplifies the manufacturing process and reduces the overall cost with respect to other machines for the same power. Nevertheless, these advantages come at the cost of two critical drawbacks: high torque ripple and low power factor [1,7]. If the torque ripple is not minimized by design or by control strategies, it can lead to undesired mechanical vibrations and potential acoustic noise, as well as impact the current harmonics. Moreover, in high-performance applications, low torque ripple is strictly required [8], and consequently, different techniques have been developed to reduce its magnitude as much as possible. One of the main sources of the large torque ripple in SynRM is the interaction of the spatial harmonics in the magnetic motive force, generated by stator currents, and the anisotropic rotor geometry and its features [9]. There are several different design techniques presented in the literature to reduce the torque ripple in SynRMs, and they can be divided into two main categories: (i) those that aim to modify and optimize the winding configuration and slot pole combinations [10], and (ii) those that seek to optimize the rotor structure (flux barriers), the details

of its geometry, or the positioning and dimension of the iron ribs [11–15]. Among these techniques, skewing the stator or rotor structure is one of the most predominant [16–18] since it provides a reliable and straightforward solution for mitigating the torque ripple. Moreover, skewing is the most used method for suppressing torque ripple in SynRM [18].

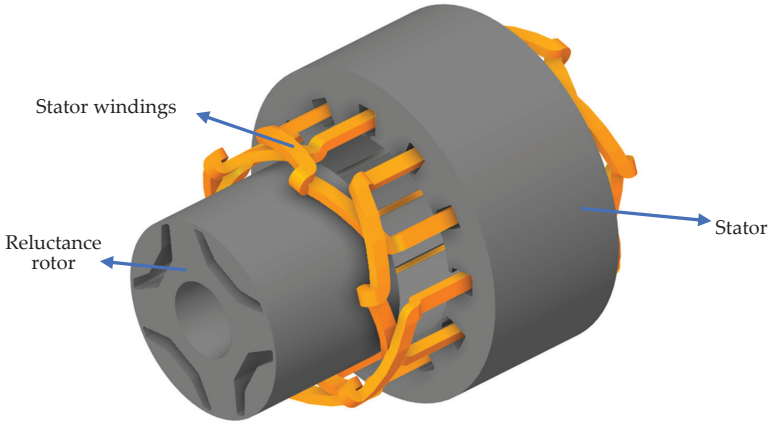

Figure 1. Three-dimensional sketch of a one-barrier four-pole synchronous reluctance motor.

Skewing techniques can be classified into two main categories: continuous skewing and discrete skewing (also called step skewing). The first one involves rotating each lamination of the stator or rotor core in regular angular distribution, between the first and the last slice equal to the skew angle [15], as depicted in Figure 2b. This can drastically reduce torque ripple, but complicates and makes the manufacturing process more expensive since each lamination of the rotor has a different position with respect to a symmetry axis, thus requiring specific tooling. In turn, the second category, considers the division of the rotor stack into a few discrete segments, as shown in Figure 2c.

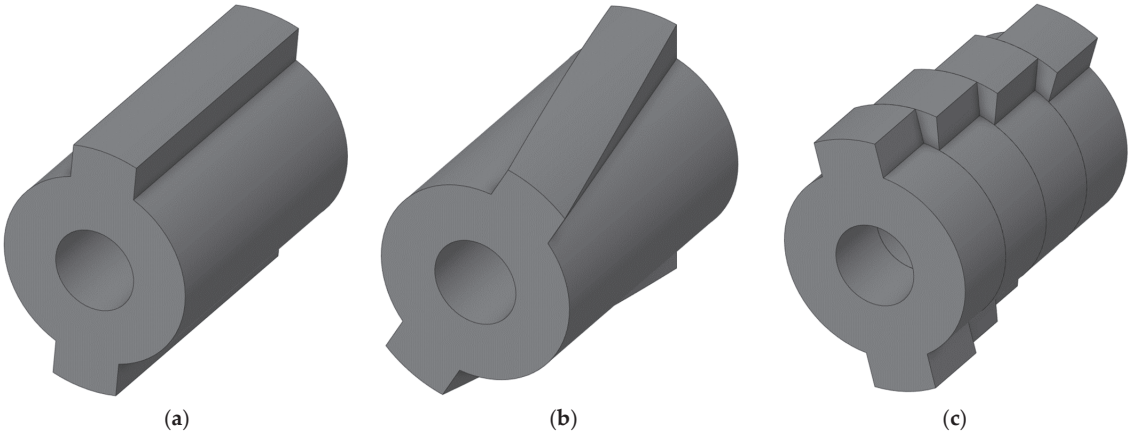

Figure 2. Three-dimensional sketches of different types of skew: (**a**) reference skewless rotor, (**b**) continuous skew, (**c**) discrete skew, also called step skew.

A considerable number of studies have addressed the rotor skewing technique using the conventional one-slot-pitch skew angle. These studies can be found in references [19–25]. In [19], the performance of a SynRM is compared when it is operated without skewing to when the rotor is skewed by one stator tooth pitch. Reference [20] investigates the effect

of rotor skewing on reducing slot harmonic torques, using a conventional skew angle of one stator slot pitch, but this reduces the average torque as well. This was confirmed in [21,22]. In [23], the equation to calculate the skew angle to suppress the stator slot harmonic component (one-slot-pitch) was presented, considering the number of slices in the calculation. The novel forced feasibility concept was introduced in [24] to improve optimization convergence and reduce overall optimization time in a SynRM design. A rotor skew was chosen as the best suited torque-ripple mitigation option by skewing the rotor at an angle of one stator slot. Recently in [25], a SynRM with salient pole rotor was continuously skewed by one stator slot pitch to improve energy conversion and reduce torque ripple. The impact of rotor skewing on torque ripple in SynRMs was analyzed in recent research [16], comparing both continuous and segmented rotor skewing. Post-optimization simulations were performed for both methods and yielded similar results, with a slight advantage to segmented rotor skewing due to the increased cost of continuous skewing. In both cases, the total skew angle was equal to one stator slot. As it may be noted from the dates of these works, the one-slot-pith skewing trend is dominant as a post-optimization process, applicable to several up-to-date machine topologies.

In turn, several papers have discussed the skewing technique for reducing torque ripple [26–32], but they lack information on the selection of the skew angle or the skewing parameters used. In [26], a rotor design with an asymmetric flux barrier was created to reduce torque ripple by splitting the rotor into two step-skewed parts. However, the paper does not mention the method used to determine the skew angle, which is assumed to be equal to the slot pitch. Reference [29] evaluates the suitability of SynRMs for electric traction applications. Skew is applied to reduce torque ripple by using a 2.5° mechanical skew angle between three stacks, resulting in an angle close to the slot pitch. In [30], the torque ripple was reduced by dividing the machine into three layers using step skew, but the skewing angle is not specified. A SynRM was optimized using topology optimization in [31], which increased the torque compared to a model optimized with parameters, but also increased the torque ripple. The skewing technique was used to reduce the torque ripple by dividing the rotor into two slices, but the specific skew angle and its determination method are not reported. In [32], the goal was to reduce torque ripple through rotor skewing while maintaining a power factor through optimization. The study found that the optimum mechanical skew angle across all machines was 2.5 mechanical degrees, very close to the slot pitch. All these works seem to match the one-slot-pith skewing trend.

Despite the prevalence of the slot pitch angle as the optimal skew angle in the literature, references [33,34] question its effectiveness in minimizing torque ripple. Reference [33] demonstrates that a torque ripple of less than 3.0% can be achieved by applying rotor skew. The optimum rotor skew angles ranged from 60–70% of a slot pitch angle for the 24-slot machine and 30–80% for the 36-slot machine. The analysis highlights that the ideal rotor skew angle heavily depends on both the stator configuration and the rotor topology. In [34], a comparison between continuous skewing and discrete skewing was performed over a SynRM. The results indicated that the torque ripple was significantly reduced even with two stacks, while only slightly decreasing in the average torque when high order torque harmonics were produced. Some results showed that the optimal skew angle differed from the traditional one-slot pitch, being either higher or lower, depending on the type of skew technique applied (continuous or discrete).

As a result, recent trends have been investigated to improve the efficacy of skewing in different topologies [17,35,36]. A new unconventional magnet step-skew method for permanent magnet synchronous motors (PMSM) is introduced in [17]. It involves varying both the length of the magnet and the skew angle between magnet segments, in contrast to the constant stack length and step-skew angle in conventional permanent magnet (PM) motors. A semi-finite element analysis (FEA) algorithm is developed showing improved performance compared to conventional step-skew. However, it comes with increased magnet manufacturing cost. In [35], a new method for parameterizing the flux barrier profiles of SynRMs and Permanent Magnet assisted Synchronous Reluctance Machina (PMa-

SynRMs) was introduced. In order to reduce torque ripple, the skew angle is obtained through a parametric FEA analysis. A discrete rotor skewing of 4° in three-step pieces is applied, which deviates from the conventional 10° angle for a 36-slot machine based on one slot pitch. In [36], the impact of step skewing on the output torque and motor inductance in a 30-slot/four-pole SynRM configuration was examined. A comparison of step skewing was made theoretically, and the study considered the effect of two harmonic orders, but did not account for the number of steps in the skewing angle calculation. Moreover, it discovered that the average torque reduction resulting from skewing is dependent on the machine operating point.

As seen, this topic has gained increased attention in the literature. A better understanding of how the optimal skewing can be achieved at the design stage is an important factor in the sizing of a SynRM. Notwithstanding and to the best of the authors' knowledge, this has not yet been investigated. In particular, the influence of a generalized multi-step skewing on the performance of SynRM, considering a torque ripple harmonic content approach and not the traditional one-slot-pitch skewing technique, has not been examined. This study aims to serve as an input of post-optimization processes in the design stage of SynRMs.

This article presents a comprehensive analytical expression for multi-step discrete skewing in SynRM. The method calculates a specific skew angle to eliminate a specific harmonic component and a mitigation factor to showcase the impact of skewing on each harmonic component. The use of this methodology ensures a suitable selection of the harmonic to be mitigated, and reduce the number of rotor steps required to effectively decrease the presence of dominant harmonics in the electromagnetic torque, in this manner improving the machine's performance. The article validates the proposed approach by analyzing two SynRM designs through FEA and includes three-dimensional (3D) FEA to consider the border effect, which is not present in two-dimensional (2D) FEA. The optimal step skew angle predicted by the analytical formula closely matches both 2D and 3D FEA results. The proposed equations are evaluated for two-step, three-step, and four-step skewing, showing promising results in mitigating the selected undesired harmonics and reducing other harmonic content collaterally. In addition, an optimized triple-barrier SynRM is post-optimized by means of the proposed method.

The paper is organized as follows: Section 2 presents the selected machines, describing their dimensions and main data. Section 3 provides the details of the proposed analytical expressions to select the step angle of N-step skewing, generalized for machines with any pole count. These expressions are assessed and validated in Section 4, which summarizes the results and discussion of several case studies evaluated by means of 2D and 3D FEA. Section 5 shows a study case of the proposed approach as a post-optimization process, reducing the torque ripple of an optimized triple-barrier SynRM. Conclusions are drawn at the end of the paper summarizing the benefits of the proposed approach and its applicability to the design of SynRM.

2. Selected Machines

With the aim of providing insight into the procedures required to use the proposed N-step skewing analytical expressions, two SynRM machines are considered as a case study and assessed in this work, as presented in Figure 3a,b, respectively. Single-layer distributed windings are considered for both machines.

Several geometrical parameters of the rotor structure of SynRM can affect the different levels of a SynRM's performance. There are several design guidelines established in the literature to choose the number of flux barriers and poles. The number of parameters increases exponentially as the number of flux barriers per pole and pole pairs increase. SynRM is designed to maximize d-axis inductance and minimize q-axis inductance, as this ensures that the machine's saliency ratio is large enough for the machines to achieve the required torque performance. On the one hand, to obtain a good saliency ratio, a small number of pole pairs is preferred, and the literature recommends adopting two-

or three-pole pairs [37]. On the other hand, the optimum number of flux barriers is defined according to the number of stator slots. In the case of a 36-slot machine, some authors do not encourage to adopt more than three flux barriers. A greater number of barriers could jeopardize the mechanical integrity of the rotor or make the design process more complex [3,38].

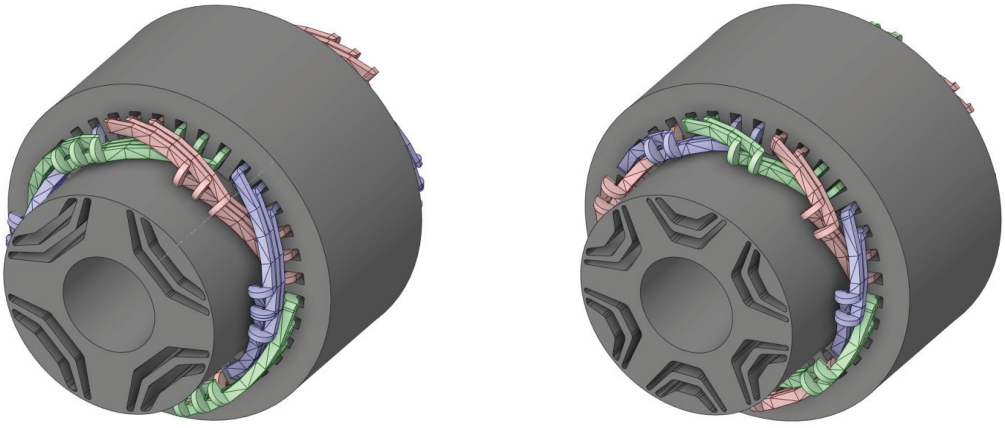

(**a**) (**b**)

Figure 3. Three-dimensional schematics of (**a**) four-pole synchronous reluctance motor with two barriers per pole; and (**b**) six-pole synchronous reluctance motor with two barriers per pole. Three-phase stator windings are highlighted in red, green, and blue, corresponding to each phase. Rotor in both machines is shown as an exploded view.

Therefore, in this paper, two machines with two- and three-pole pairs are considered, and each pole features two barriers. The common data for all machines are presented in Table 1.

Table 1. Main data of the selected machines.

Parameter	Symbol	Value	Unit
Stator outer diameter	D_{so}	245	mm
Stator inner diameter	D_{si}	161.4	mm
Rotor outer diameter	D_{ro}	160.4	mm
Rotor inner diameter	D_{ri}	70	mm
Tooth height	h_t	22.8	mm
Tooth width	b_t	9	mm
Air-gap length	g	0.5	mm
Stack length	l_{st}	120	mm
Turns per slot	N_s	20	-
Number of slots	Q_s	36	-
Speed	n	3000	rpm
Current Density	J	10	A/mm^2
Current angle	α_i^e	60	electric degrees

3. Analytical Method Derivation for Discrete Skewing

The main period of torque ripple of three-phase winding machines is 60 electrical degrees [39], which therefore dictates the period of the torque ripple harmonic of order v, derived in electrical degrees by:

$$T_{v,elec} = \frac{360^\circ}{v} \tag{1}$$

The aim of the discrete skewing is to consider N machine slices, rotated with respect to each other by a specific angle, so that each slice contributes to different torque harmonics that will ultimately modulate the torque waveform. This superposition has to be adjusted with the aim of mitigating undesired harmonic components of the resulting torque waveform. The v-th order harmonic of the torque ripple can be expressed as a term of the Fourier series expansion of the electromagnetic torque as:

$$\mathrm{T}_{\mathrm{ripple},v}(\theta_{r,e}) = A_v \cdot \cos\Big(\frac{\pi}{180}\theta_{r,e} v + \phi_v\Big), \tag{2}$$

where A_v is the amplitude of the v-th harmonic of the torque ripple, $\theta_{r,e}$ is the rotor position in electrical degrees, ϕ_v is the phase shift of the torque waveform, and $v = 1, 2, 3, \ldots$

In this sense, and following the concept of balanced multiphase systems, if the w-th harmonic of the torque ripple wants to be mitigated, then the electrical angle between each one of the N slices of the machine is proposed as:

$$\theta_{w,\mathrm{elec}} = \frac{360^\circ}{Nw} \tag{3}$$

For example, if a two-step skew is adopted, then the machine rotor will be comprised of two halves, each one contributing with torque waveforms that are shifted one with respect to the other. If the electrical shift is $\theta_{w,\mathrm{elec}}$, then the positive semi-cycles of the w-th harmonic of the torque ripple of one half of the rotor will compensate the negative semi-cycles of the other half, hence mitigating the undesired component.

The electrical angle between the N slices of the machine is translated into the skew angle (θ_s), which corresponds to the mechanical angle in which two consecutive rotor slices are rotated one with respect to the other so as to mitigate the w-th order harmonic of the torque ripple (Equation (4)).

$$\theta_\mathrm{s} = \frac{360^\circ}{pNw} \tag{4}$$

In Figure 4, the proposed methodology is schematized, comprising the decomposition of the electromagnetic torque waveform in harmonic components, the selection of a high-magnitude undesired component, and the calculation of θ_s to mitigate that undesired harmonic depending on the adopted number of slides N.

Considering the proposed skew angle, Equation (2) can be expressed in terms of a sum of the contributions of the N slices of the machine as

$$\mathrm{T}_{\mathrm{rs},\,v}(\theta_{r,e}) = \sum_{i=1}^{\mathrm{N}} \frac{\mathrm{A}_v}{N} \cos\left(\frac{\pi}{180}\theta_{r,e} v - \frac{2\pi v}{Nw}(i-1)\right) \tag{5}$$

The resulting reduction on each component of the torque ripple, considering idealized conditions and electromagnetic independency between adjacent slices can be obtained by means of the phasorial representation and consequent analysis of Equation (5). Then:

$$\mathfrak{Re}\{\mathrm{T}_{\mathrm{rs},\,v}(\theta_{r,e})\} = \sum_{i=1}^{N} \frac{\mathrm{A}_v}{N} \cos\left(-\frac{2\pi v}{Nw}(i-1)\right) \tag{6}$$

$$\mathfrak{Im}\{\mathrm{T}_{\mathrm{rs},\,v}(\theta_{r,e})\} = \sum_{i=1}^{N} \frac{\mathrm{A}_v}{N} \sin\left(-\frac{2\pi v}{Nw}(i-1)\right) \tag{7}$$

In consequence, the magnitude of the v-th harmonic of the torque ripple after applying discrete skewing following the design guidelines of Equations (3) and (4) can be expressed as

$$|\mathrm{T}_{\mathrm{rs},\,v}(\theta_{r,e})| = \frac{\mathrm{A}_v}{N}\sqrt{\left(\cos\left(-\frac{2\pi v}{Nw}(i-1)\right)\right)^2 + \left(\sin\left(-\frac{2\pi v}{Nw}(i-1)\right)\right)^2} \tag{8}$$

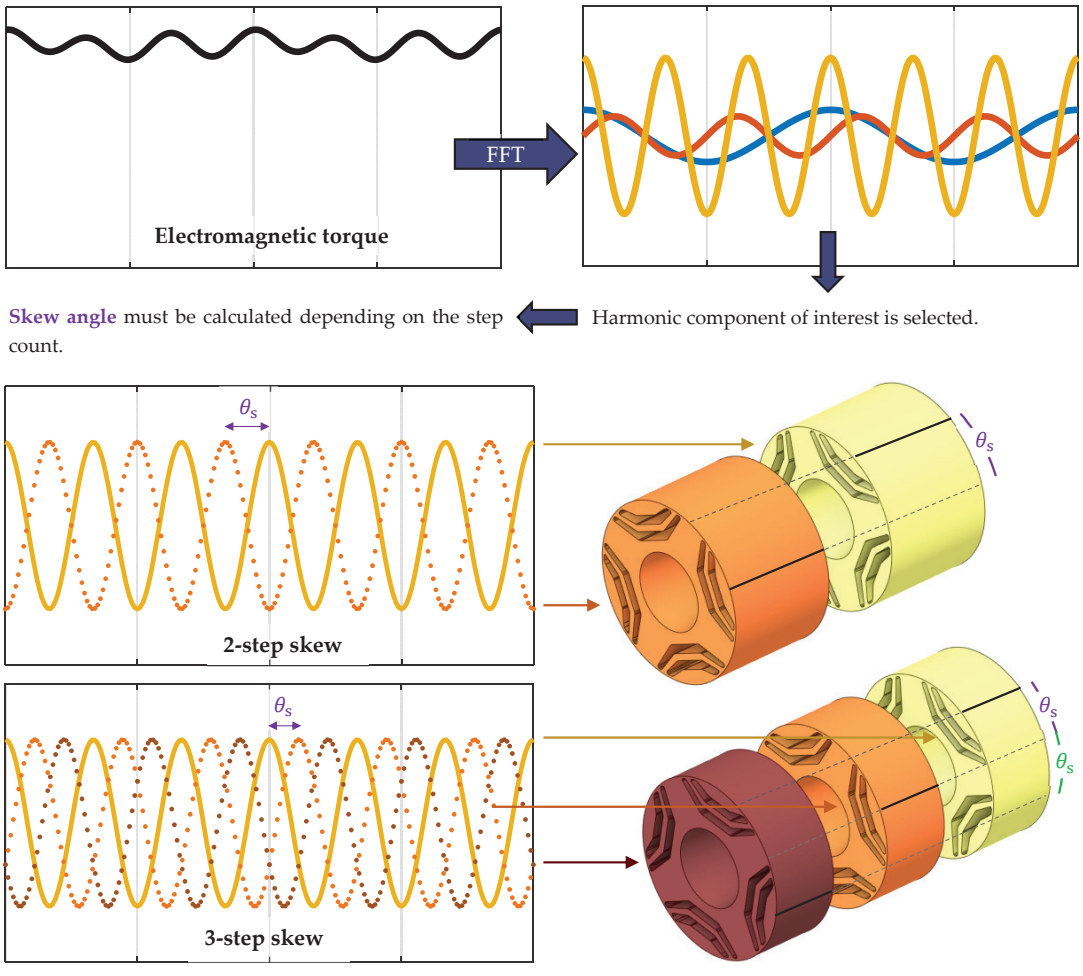

Figure 4. Schematics of the proposed methodology to calculate the skew angle θ_s to mitigate a selected harmonic of order w. Two-step and three-step discrete skew are presented, although the method can be used for any number of slides.

Finally, a skew reduction factor ($k_{rs,v}$) can be devised by obtaining the ratio between Equations (2) and (8), derived by:

$$k_{rs,v} = \frac{1}{N}\sqrt{\left(\cos\left(-\frac{2\pi v}{Nw}(i-1)\right)\right)^2 + \left(\sin\left(-\frac{2\pi v}{Nw}(i-1)\right)\right)^2} \quad (9)$$

This factor is meant to be used after the calculation of the skew angle as per Equation (4), and it allows for estimating the resulting amplitude of each torque ripple component (of order v) after applying the skew. Simplified equations for $N = 2$, 3 and 4 are provided in the following section, which are further verified and analyzed by means of 2D and 3D finite element analysis.

4. Results and Discussion: Finite Element Validation

This section shows the results obtained by applying the analytical method described in Section 3 for both four-pole and six-pole SynRMs. In order to provide the results in a clear fashion, this section is divided into four subsections. The first presents the machine evaluations without considering any type of skew, hereby called skewless machines; and the following three sections address machines with different slide number ($N = 2$, $N = 3$ and $N = 4$). All the results are obtained by means of 2D and 3D FEA simulations carried out in the commercial package ANSYS Electronic Desktop. The simulation time was chosen to evaluate a whole period of the machine's torque ripple.

4.1. FEA Evaluation Original Designs (Skewless Machines)

Figure 5 presents the electromagnetic torque waveform and spatial harmonic spectrum of both the four-pole and the six-pole SynRMs. Both 2D and 3D results are shown for comparison. From the results, the evaluation of the 2D and 3D models provide similar values, showing expected small differences, in accordance with the findings of [40]. The harmonic components of the electromagnetic torque for each machine are detailed in Figure 5b,d for the four-pole and six-pole machines, respectively. As expected, the largest harmonic component in both designs corresponds to the one generated by the stator slotting effect. Specifically, the highest magnitude harmonic of the four-pole machine corresponds to $v = 18$, and that of the six-pole machine corresponds to $v = 12$. Therefore, and according to the methodology proposed in Section 3, $w = 18$ for the four-pole SynRM and $w = 12$ for the six-pole machine. Table 2 shows the skew angle that should be considered to discrete skew the machine according to Equation 4, depending on the desired step number and aiming to mitigate the highest magnitude harmonic component. The following sections evaluate the impact of the proposed skew methodology on mitigating torque ripple for $N = 2$, $N = 3$ and $N = 4$.

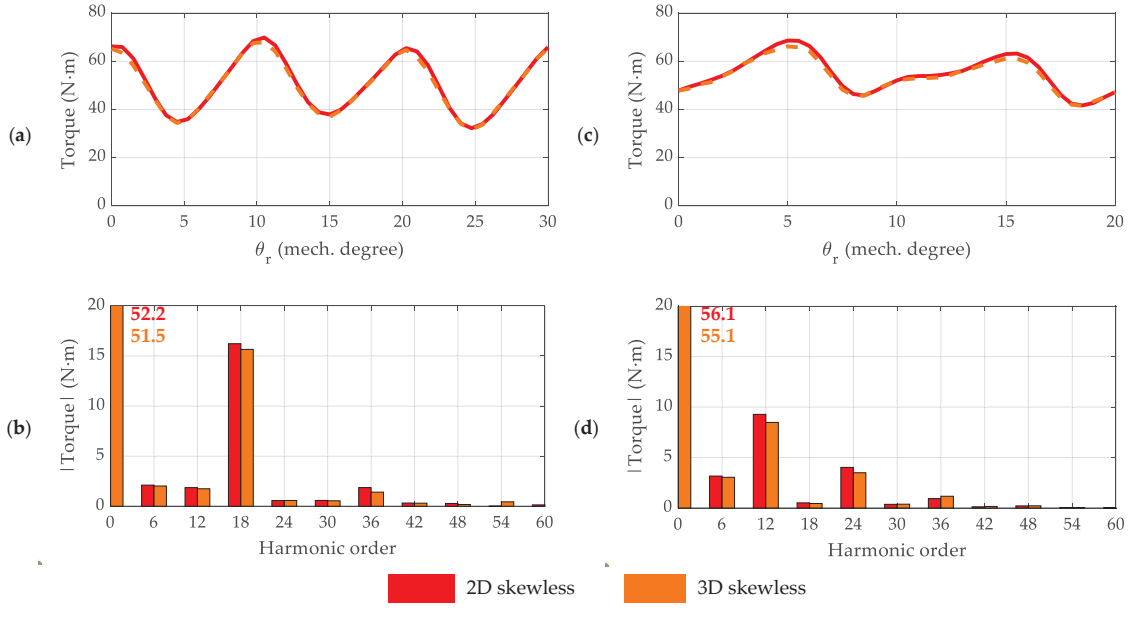

Figure 5. Electromagnetic torque waveform and spectrum of a skewless reference machine: (**a**) torque waveform of four-pole machine with two barriers per pole; (**b**) torque spatial harmonic content of four-pole machine with two barriers per pole; (**c**) torque waveform of six-pole machine with two barriers per pole; (**d**) torque spatial harmonic content of six-pole machine with two barriers per pole. Additionally, 2D and 3D simulation results are compared.

Table 2. Skew angle to reduce a specific electromagnetic torque harmonic order by discrete skew.

	Harmonic Order	Mechanical Angle for Two-Step Skew	Mechanical Angle for Three-Step Skew	Mechanical Angle for Four-Step Skew
2p2b	18th	5°	3.33°	2.5°
3p2b	12nd	5°	3.33°	2.5°

4.2. Evaluation of Torque Ripple Reduction by Means of Two-Step Discrete Skew

The comparison of the electromagnetic torque for the four-pole and six-pole machine is shown in Figure 6 when two-step skewing is applied. It can be observed that there is a significant reduction in the harmonic torque component to be mitigated, to approximately 10% of its original value.

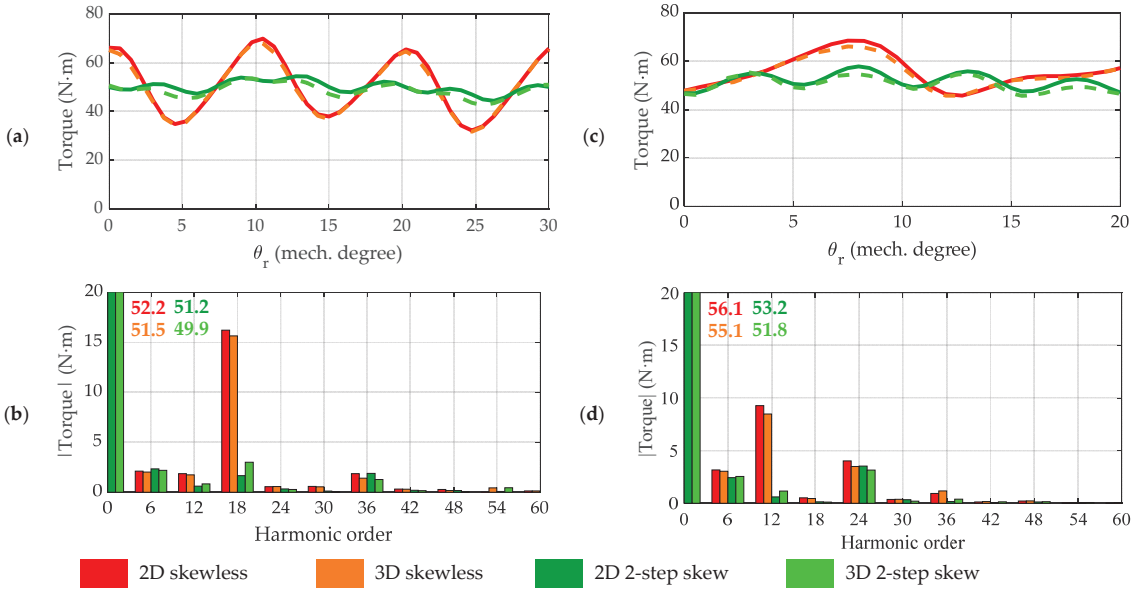

Figure 6. Comparison of electromagnetic torque waveform and harmonic content of a skewless machine vs. two-step skewed machine: (**a**) torque waveform of four-pole machine with two barriers per pole; (**b**) torque spatial harmonic content of four-pole machine with two barriers per pole; (**c**) torque waveform of six-pole machine with two barriers per pole; (**d**) torque spatial harmonic content of six-pole machine with two barriers per pole. The 2D and 3D simulation results are compared.

This agrees with the estimations obtained from the reduction factor proposed in Equation (9), which can be simplified when evaluating $N = 2$ to:

$$k_{\mathrm{rs},v} = \frac{\sqrt{2}}{2}\sqrt{1+\cos\left(\pi\frac{v}{w}\right)}. \tag{10}$$

According to Equation (10), the reduction of the main component of the electromagnetic torque (which has order $w = 18$) should be maximum ($k_{\mathrm{rs},w} = 0$). The difference lies in the fact that Equation (9) considers magnetically independent rotor slices, neglecting their interaction. Regardless of this, a significant reduction was observed in other harmonic components. In addition, for the four-pole machine it was found that the torque ripple harmonic component with $v = 12$ was also reduced to ~45% of its original value, whilst other relevant harmonics of order $v = 6$ and $v = 36$ were not significantly affected. This agrees with the estimated reduction factor proposed in Equation (10), since $k_{\mathrm{rs},6} = 0.87$,

$k_{rs,12} = 0.5$ and $k_{rs,36} = 1$. In turn, for the six-pole machine it was observed that the relevant torque ripple harmonic component with $v = 24$ was slightly reduced (to 87% of the original value), and that other relevant harmonics of order $v = 6$ and $v = 36$ were reduced to 77% and 14% of their original magnitude, respectively. This agrees with the estimated reduction factor proposed in Equation (10), since $k_{rs,6} = 0.7$, $k_{rs,24} = 1$ and $k_{rs,36} = 0$. In addition, the trend of other less relevant harmonic components of both machines matches closely with the estimations of Equation (10). These findings are summarized in Table 3.

Table 3. Torque ripple harmonic component reduction as a result of two-step skewing. The 3D results were considered and relevant harmonic components analyzed.

Harmonic Order	Four-Pole SynRM		Six-Pole SynRM	
	$k_{rs,v}$ (Analytical)	$k_{rs,v}$ (FEA)	$k_{rs,v}$ (Analytical)	$k_{rs,v}$ (FEA)
$v = 6$	0.87	0.95	0.71	0.77
$v = 12$	0.50	0.45	0.00	0.06
$v = 18$	0.00	0.10	-	-
$v = 24$	-	-	1.00	0.87
$v = 30$	-	-	-	-
$v = 36$	1.00	1.02	0.00	0.14

As an overall result of the discrete two-step skewing, the peak-to-peak value of the torque ripple was reduced. Table 4 summarizes the torque ripple as a percentage of the mean torque for the 2D and 3D simulation results, respectively. The torque ripple reduction is greater than 70% for the four-pole machine and up to 55% for the six-pole design, and an expected slight reduction of the average torque was also obtained.

Table 4. Average torque and torque ripple comparison when applying two-step skewing, by means of 2D and 3D FEA simulations.

		Skewless 2D	Skewless 3D	Two-Step Skew 2D	Two-Step Skew 3D
Four-pole SynRM	T_{avg}	51.0 Nm	50.2 Nm	50.0 Nm	48.7 Nm
	T_{rp}	73.9%	72.1%	20.2%	22.6%
Six-pole SynRM	T_{avg}	54.7 Nm	53.8 Nm	51.9 Nm	50.5 Nm
	T_{rp}	49.2%	45.9%	21.4%	19.2%

In this specific case, it can be observed that the 3D evaluation shows worse results than the 2D assessment, since in the 3D the ripple reduction is lower, and the mean torque reduction is increased, with respect to the 2D simulations. This can be ascribed to the fact that 2D simulations on ANSYS consider each slice of the machine as independent machines, when discrete skewing is applied, and the interface between slices is not taken into account, resulting in an idealization of the problem. On the other hand, the 3D simulation evaluates the rotor as a whole unit comprised of physically rotated slices, hence considering effects within the adjacent slices interface. This is further addressed in Section 4.4.

4.3. Evaluation of Torque Ripple Reduction by Means of Three-Step Discrete Skew

The comparison of the electromagnetic torque for the four-pole and six-pole machine is shown in Figure 7 when adopting a three-step discrete skew strategy.

As in the case of the two-step skewing, there is a significant reduction of up to 93% of the highest magnitude harmonic component of the torque ripple. This is in accordance with the reduction factor derived in Equation (9), further simplified for cases with $N = 3$ as per:

$$k_{rs,v} = \frac{1}{3}\left[1 + 2\cos\left(\frac{2\pi v}{3w}\right)\right] \tag{11}$$

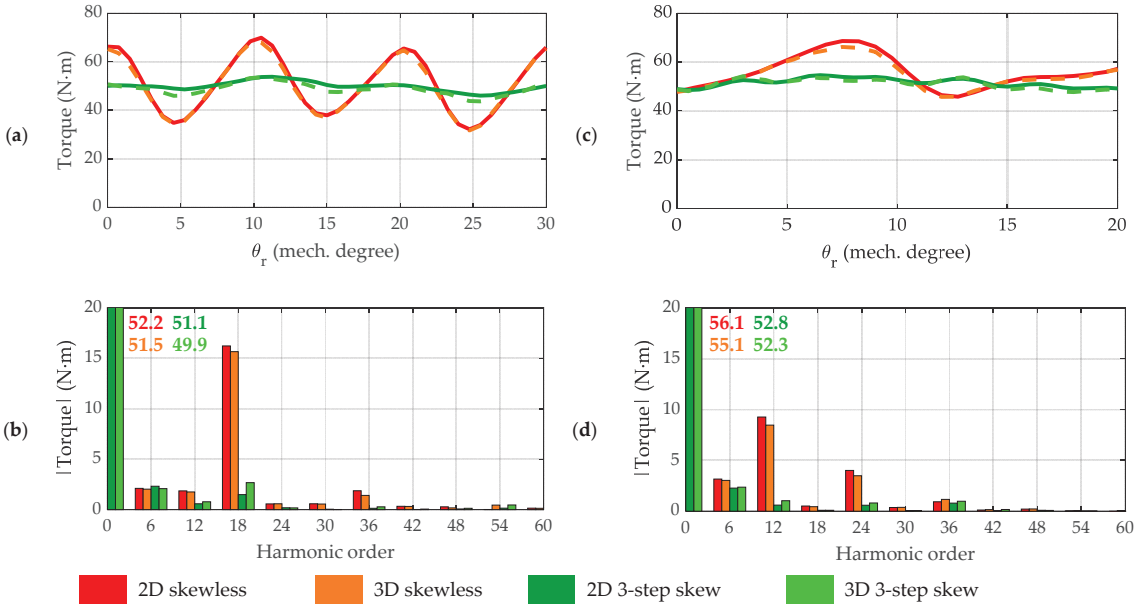

Figure 7. Comparison of electromagnetic torque waveform and harmonic content of skewless machine vs. three-step skewed machine: (**a**) torque waveform of four-pole machine with two barriers per pole; (**b**) torque spatial harmonic content of four-pole machine with two barriers per pole; (**c**) torque waveform of six-pole machine with two barriers per pole; (**d**) torque spatial harmonic content of six-pole machine with two barriers per pole. The 2D and 3D simulation results are compared.

According to Equation (11), the reduction of the highest magnitude component of the electromagnetic torque, when $v = w$, is maximum ($k_{\mathrm{rs},w} = 0$). Additionally, for the four-pole machine it was found that the torque ripple harmonic components with $v = 12$ and $v = 36$ were reduced to ~45% and ~6% of their original value, respectively, whilst the other relevant harmonic of order $v = 6$ was not significantly affected. This agrees with the reduction factor proposed in Equation (11) for $N = 3$, since $k_{\mathrm{rs},6} = 0.84$, $k_{\mathrm{rs},12} = 0.45$ and $k_{\mathrm{rs},36} = 0$. On the other hand, for the six-pole machine it was observed that the harmonic components with $v = 6$ and $v = 24$ were reduced to ~70% and ~12% of their original value, respectively, whilst the harmonic of order $v = 36$ was not visibly reduced. This agrees with the values provided by Equation (11), since $k_{\mathrm{rs},6} = 0.67$, $k_{\mathrm{rs},24} = 0$ and $k_{\mathrm{rs},36} = 1$. Although they were not relevant contributors, the trend of other harmonic components of both machines were in good agreement with the expression presented in Equation (11). These findings are summarized in Table 5.

Table 5. Torque ripple harmonic component reduction as a result of three-step skewing. The 3D results are considered and the relevant harmonic components analyzed.

Harmonic Order	Four-Pole SynRM		Six-Pole SynRM	
	$k_{\mathrm{rs},v}$ (Analytical)	$k_{\mathrm{rs},v}$ (FEA)	$k_{\mathrm{rs},v}$ (Analytical)	$k_{\mathrm{rs},v}$ (FEA)
$v = 6$	0.84	0.95	0.67	0.70
$v = 12$	0.45	0.45	0.00	0.06
$v = 18$	0.00	0.09	-	-
$v = 24$	-	-	0.00	0.12
$v = 30$	-	-	-	-
$v = 36$	0.00	0.06	1.00	0.90

As a result of the discrete three-step skewing, the peak-to-peak value of the torque ripple was considerably reduced. Table 6 presents the obtained mean torque and torque ripple (as a percentage of the mean torque) for the 2D and 3D simulations, respectively. It may be noted that the torque ripple reduction is greater than 75% in both analyzed designs and there is an expected slight reduction in the average torque.

Table 6. Average torque and torque ripple comparison when applying three-step skewing, by means of 2D and 3D FEA simulations.

		Skewless 2D	Skewless 3D	Three-Step Skew 2D	Three-Step Skew 3D
Four-pole SynRM	T_{avg}	51.0 Nm	50.2 Nm	49.9 Nm	48.7 Nm
	T_{rp}	73.9%	72.1%	15.6%	18.3%
Six-pole SynRM	T_{avg}	54.7 Nm	53.8 Nm	51.5 Nm	51.0 Nm
	T_{rp}	49.2%	45.9%	11.8%	12.7%

Similar to the case of two-step skewing, it can be appreciated that the 3D evaluation shows a worse outcome than the 2D assessment, since a lower ripple reduction and a higher mean torque reduction were achieved.

4.4. Evaluation of Torque Ripple Reduction by Means of Four-Step Discrete Skew

The comparison of the electromagnetic torque for the four-pole and six-pole machine is shown in Figure 8 when four-step skewing is applied.

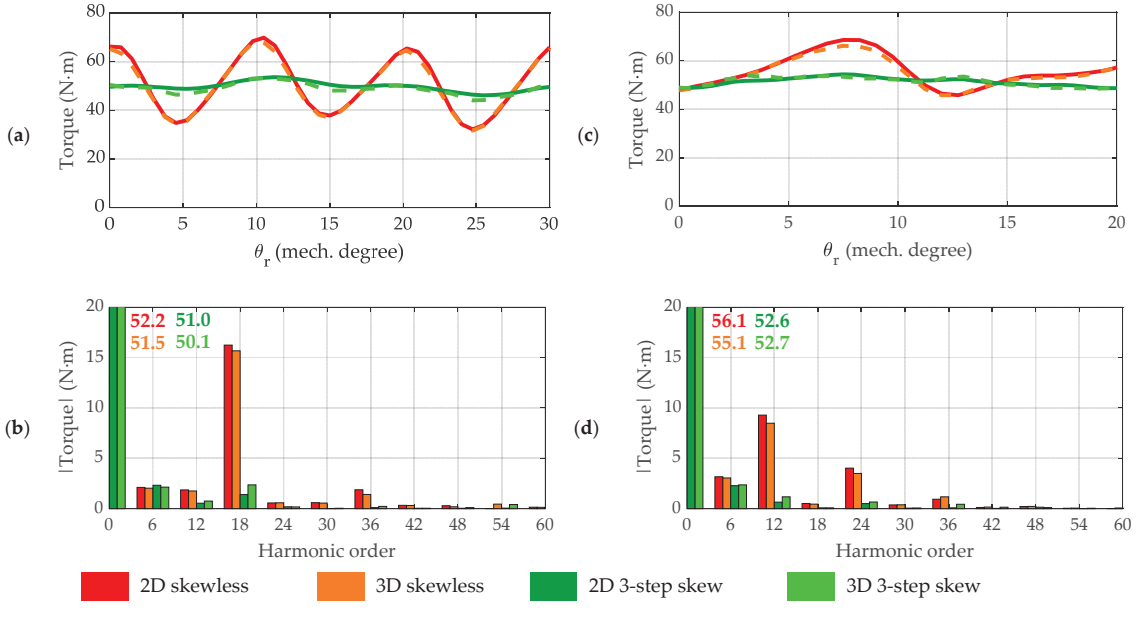

Figure 8. Comparison of electromagnetic torque waveform and harmonic content of skewless machine vs. four-step skewed machine: (**a**) torque waveform of four-pole machine with two barriers per pole; (**b**) torque spatial harmonic content of four-pole machine with two barriers per pole; (**c**) torque waveform of six-pole machine with two barriers per pole; (**d**) torque spatial harmonic content of six-pole machine with two barriers per pole. The 2D and 3D simulation results are compared.

It can be observed that there is a significant reduction in the harmonic torque component to be mitigated, approximately 10% of its original magnitude, to a similar extent to the two-step and three-step skewing. This is in agreement with the estimations obtained from

the reduction factor proposed in Equation (9), which, for the specific case of $N = 4$, can be simplified to:

$$k_{\mathrm{rs},v} = \frac{\sqrt{2}}{2}\cos\left(\frac{\pi v}{2w}\right)\sqrt{1+\cos\left(\frac{\pi v}{2w}\right)} \tag{12}$$

Based on Equation (12), the reduction of the highest magnitude component of the electromagnetic torque, when $v = w$, is maximum ($k_{\mathrm{rs},w} = 0$). Additionally, for the four-pole machine it was found that the torque ripple harmonic components with $v = 12$ and $v = 36$ were reduced to ~35% and ~5% of their original value, respectively, whilst the other relevant harmonic of order $v = 6$ was not affected. This is in agreement with the reduction factor proposed in Equation (12) for $N = 3$, since $k_{\mathrm{rs},6} = 0.84$, $k_{\mathrm{rs},12} = 0.43$ and $k_{\mathrm{rs},36} = 0$. On the other hand, for the six-pole machine, it was observed that the harmonic components with $v = 6$, $v = 24$ and $v = 36$ were reduced to ~74%, ~12% and ~6% of their original value, respectively. This is in agreement with the values provided by Equation (12), since $k_{\mathrm{rs},6} = 0.65$, $k_{\mathrm{rs},24} = 0$ and $k_{\mathrm{rs},36} = 0$. Although they are not relevant contributors, the trend of other harmonic components of both machines are in good agreement with the expression presented in Equation (12). A summary of these results is presented in Table 7.

Table 7. Torque ripple harmonic component reduction as a result of three-step skewing. The 3D results are considered, and relevant harmonic components analyzed.

Harmonic Order	Four-Pole SynRM		Six-Pole SynRM	
	$k_{\mathrm{rs},v}$ (Analytical)	$k_{\mathrm{rs},v}$ (FEA)	$k_{\mathrm{rs},v}$ (Analytical)	$k_{\mathrm{rs},v}$ (FEA)
$v = 6$	0.84	1.01	0.65	0.74
$v = 12$	0.43	0.35	0.00	0.06
$v = 18$	0.00	0.08	-	-
$v = 24$	-	-	0.00	0.12
$v = 30$	-	-	-	-
$v = 36$	0.00	0.05	0.00	0.06

Four-step skewing resulted in a severe torque ripple reduction, as summarized in Table 8, which presents the results obtained by means of the 2D and 3D evaluations, respectively. The torque ripple reduction was greater than 75% in both analyzed designs and there was an expected slight reduction of the average torque.

Table 8. Average torque and torque ripple comparison when applying four-step skewing, by means of 2D and 3D FEA simulations.

		Skewless 2D	Skewless 3D	Four-Step Skew 2D	Four-Step Skew 3D
Four-pole SynRM	T_{avg}	51.0 Nm	50.2 Nm	49.8 Nm	48.7 Nm
	T_{rp}	73.9%	72.1%	15.0%	18.3%
Six-pole SynRM	T_{avg}	54.7 Nm	53.8 Nm	51.4 Nm	51.0 Nm
	T_{rp}	49.2%	45.9%	11.2%	12.7%

Similar to the two-step and three-step skewing cases, it may be appreciated that the 3D evaluation shows a worse outcome than the 2D assessment, since a lower ripple reduction and a higher mean torque reduction were achieved. Nevertheless, the 2D and 3D results were very similar; for this reason, assessing the proposed skew technique by means of 2D simulations as a preliminary stage design can be recommended.

It is possible to observe that, when $N = 2$ and $N = 3$ are compared, there is a considerable improvement in the reduction of the torque ripple, and the behavior is different for $N = 3$ and $N = 4$, where the reduction is the same. For all cases, $N = 2$, $N = 3$ and $N = 4$, the average torque remains relatively constant. Therefore, when assessing close-to-purely-sinusoidal electromagnetic torque waveforms in a SynRM, two-step skew may then be sufficient as a single ripple component. Conversely, if there are several preponderant

harmonic components, then it is worth taking a multi-step skewing approach, to mitigate multiple harmonics at once. A study case is addressed in Section 5 covering this issue.

Consequently, it is necessary to correctly analyze the harmonic distribution of the electromagnetic torque to properly choose N, since increasing the number of steps does not always guarantee a significant reduction in torque ripple and could lead to other different manufacturing costs.

5. Study Case: Optimized SynRM for Minimum Ripple Torque

A 36-slot, six-pole, three-barrier SynRM was selected as the case study for this section. The aim was to show the applicability of the proposed method to an optimized machine, with the particularity that its torque ripple harmonic content does not have a predominant component. The machine design was optimized using ANSYS commercial software, including Electronic Desktop for electromagnetic analysis, DesignModeler for geometry parameterization, and Workbench for optimization. The optimization process was conducted using a combination of multi-objective genetic algorithms (MOGA) and FEA simulations. During the optimization process, the machine was supplied with a current of 20 A/mm^2, which is approximately three times the rated current listed in Table 9. This answers to the known fact that selecting a current between two and three times the rated current can improve the insensitivity of torque ripple to load variations [41].

Table 9. Main data of the study-case machine subject to optimization.

Parameter	Symbol	Value	Unit
Stator outer diameter	D_{so}	246	mm
Stator inner diameter	D_{si}	161.4	mm
Rotor outer diameter	D_{ro}	160.4	mm
Rotor inner diameter	D_{ri}	70	mm
Tooth height	h_t	22.8	mm
Toot width	b_t	9	mm
Air-gap length	g	0.5	mm
Stack length	l_{st}	120	mm
Number of slots	Q_s	36	-
Number of turns	N_s	20	-
Number of pole pairs	p	3	
Synchronous speed	n	5000	rpm
Rated current density	J_n	7.5	A/mm^2
Stacking factor	k_s	0.95	mm
Lamination thickness	e	0.5	mm

The objective functions were set to minimize torque ripple, maximize power factor, and maintain average torque above a specified value. The primary constraint during optimization was to keep the machine's insulation ratio within the defined limits of 0.35 to 0.45, as per the literature [42]. Geometric constraints were established to ensure feasible rotor geometries and to prevent errors or unrealistic solutions during optimization. The upper and lower limits for the rotor's geometrical parameters (objective variables) were properly defined.

The optimization results are presented in Figure 9. The optimal design was selected based on a trade-off between average torque and torque ripple, as it is not possible to achieve the lowest torque ripple and highest average torque simultaneously. In this case, the machine with the lowest torque ripple was selected.

To choose a suitable skew angle for reducing the torque ripple to acceptable values, a FFT was performed on the electromagnetic torque for one period of the torque ripple, as described in Section 3. The harmonic components of both designs under different load conditions are shown in Figure 10.

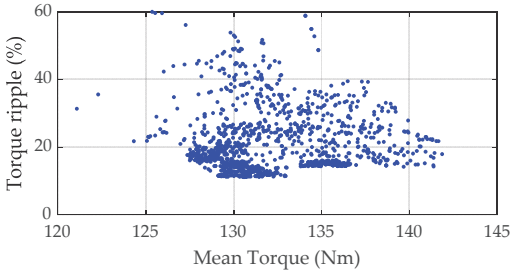

Figure 9. Designs obtained from the optimization process. The current was fixed to ~20 A/mm^2 and the current angle was defined in the optimization algorithm for MTPA.

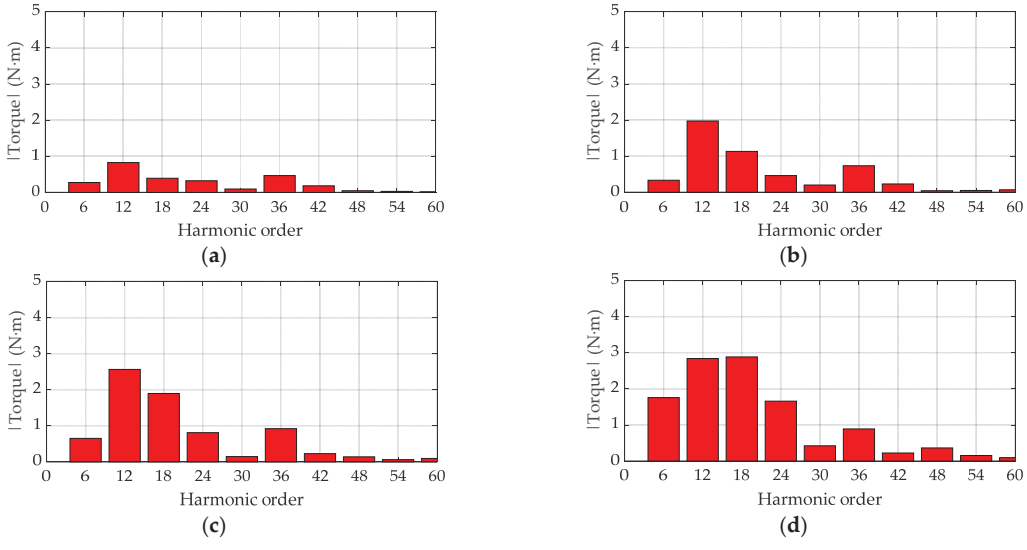

Figure 10. Harmonic components of the electromagnetic torque for the optimum design: (**a**) current density 5 A/mm^2; (**b**) current density 7.5 A/mm^2; (**c**) current density 10 A/mm^2; (**d**) current density 12.5 A/mm^2.

From Figure 10, it can be noted that, when the current density is below 10 A/mm^2, the second harmonic is predominant, which is mainly related to stator slotting. When the current density is above 10 A/mm^2, the third harmonic instead is predominant, which could render traditional methods useless based on mitigating the contribution of slotting effect on the torque ripple. In consequence, a customized skew angle is calculated from the proposed methodology, summarized in Table 10. This analysis considered the first, second, and third harmonics for mitigation using two-step, three-step, four-step, and five-step skewing.

Table 10. Skew angle to reduce a specific harmonic component of the electromagnetic torque.

Harmonic Order	Mechanical Angle for Two-Step Skew	Mechanical Angle for Three-Step Skew	Mechanical Angle for Four-Step Skew	Mechanical Angle for Five-Step Skew
6th	10°	6.66°	5°	4°
12th	5°	3.33°	2.5°	2°
18th	3.33°	2.22°	1.66°	1.33°

This case was selected for further analysis.

From Figure 10 it may be noted that some torque ripple harmonics get significantly larger as the current density increases, so it is desirable that the skewing technique used reduces these harmonics. The mitigation factor defined by Equation (9) can be used to estimate the reduction of each harmonic component. Tables 11–13 report the mitigation factor when the skew is applied to the first, second, and third harmonics, respectively.

Table 11. Value of the mitigation factor when the sixth harmonic component is selected to reduce ($w = 6$).

Harmonic Order	$k_{rs,v}$			
	Mechanical Angle for Two-Step Skew	**Mechanical Angle for Three-Step Skew**	**Mechanical Angle for Four-Step Skew**	**Mechanical Angle for Five-Step Skew**
6th	0	0	0	0
12th	1	0	0	0
18th	0	1	0	0
24th	1	0	1	0

This case was selected for further analysis.

Table 12. Value of the mitigation factor when the 12th harmonic component is selected to reduce ($w = 12$).

Harmonic Order	$k_{rs,v}$			
	Mechanical Angle for Two-Step Skew	**Mechanical Angle for Three-Step Skew**	**Mechanical Angle for Four-Step Skew**	**Mechanical Angle for Five-Step Skew**
6th	0.7	0.6	0.6	0.6
12th	0	0	0	0
18th	0.7	0.3	0.3	0.2
24th	1	0	0	0

Table 13. Value of the mitigation factor when the 18th harmonic component is selected to reduce ($w = 18$).

Harmonic Order	$k_{rs,v}$			
	Mechanical Angle for Two-Step Skew	**Mechanical Angle for Three-Step Skew**	**Mechanical Angle for Four-Step Skew**	**Mechanical Angle for Five-Step Skew**
6th	0.8	0.8	0.8	0.8
12th	0.5	0.4	0.4	0.4
18th	0	0	0	0
24th	0.5	0.3	0.2	0.2

The analysis shows that the best option for applying skew is to mitigate the first harmonic using a five-step skew. This theoretically eliminates the harmonic components, but in practice, this translates into a considerable harmonic reduction. Figure 11 shows the harmonic components of the optimal design with a five-step skew applied.

The result of applying this skewing techniques translates into a ripple reduction of up to 65%. Considerable differences can be appreciated when analyzing the response of this optimized machine and the machines evaluated in Section 4. For the case of the optimized machine, several harmonic components contributed to torque ripple, the reason for which a multi-step skewing was best suited from an electromagnetic perspective. In contrast, the machines addressed in Section 4 had a predominant torque ripple harmonic component, which could be handled by a two-step skewing.

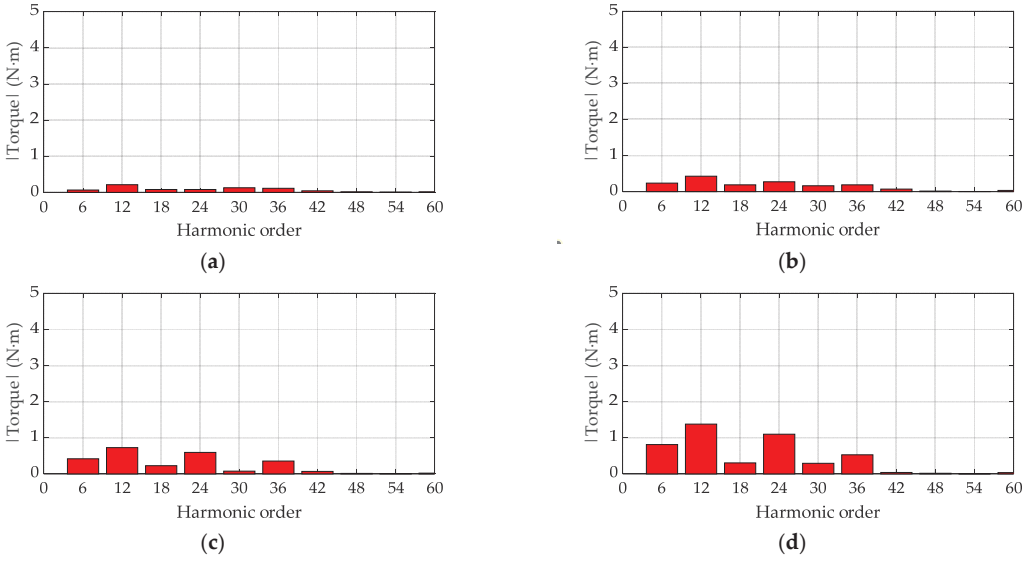

Figure 11. Harmonic components of the electromagnetic torque for the optimum design applying five-step skewing: (**a**) current density 5 A/mm^2; (**b**) current density 7.5 A/mm^2; (**c**) current density 10 A/mm^2; (**d**) current density 12.5 A/mm^2.

6. Conclusions

In this paper, an in-depth analysis of discrete-skew methodology was investigated, and an approach proposed to better understand the effect of the skewing angle and its determination during the design phase of SynRM. Following a literature review discussing the topic, the reduction factor for each harmonic component was introduced and derived in general form to estimate the resulting amplitude of each torque ripple component as a function of the skew. As a result, the overall torque ripple waveform was estimated considering the reduction of each harmonic component.

To assess the validity of the proposed method, two SynRMs were evaluated and a torque ripple reduction of up to 70% was obtained. The outcomes from the analytical expressions and FEA evaluation showed good agreement. Moreover, the proposed harmonic component reduction factor showed promising results, being able to roughly estimate the reduction of specific harmonic components of the torque ripple. The proposed skewing technique was used to mitigate the torque ripple on a previously optimized triple-barrier SynRM with acceptable results: a 65% ripple reduction was observed from 3D FEA simulations results.

By analyzing the harmonic distribution of the torque ripple, the best skewing strategy can be selected as an input of the proposed skewing technique: for mostly-purely-sinusoidal torque waveforms, a two-step or three-step skewing is advised, whilst for machines that have multiple high-magnitude harmonic components, a multi-step skewing can be recommended.

Author Contributions: Conceptualization; methodology; software; validation; formal analysis; writing—original draft preparation, C.G. and C.M.; writing—review and editing, J.A.T. and M.D.; visualization, C.G. and C.M.; supervision, J.A.T. and M.D.; funding acquisition, J.A.T. All authors have read and agreed to the published version of the manuscript.

Funding: This research was funded in part by the Agencia Nacional de Investigación y Desarrollo (ANID), Chile through grant ANIDPFCHA/Doctorado Nacional/2020-21200527, grant ANIDPFCHA/Doctorado Nacional/2020-21200350, project FONDECYT REGULAR #1201667, and project FONDEF ID21I10099.

Institutional Review Board Statement: Not applicable.

Informed Consent Statement: Not applicable.

Data Availability Statement: Data are contained within the article.

Conflicts of Interest: The authors declare no conflict of interest.

References

1. Naseer, M.U.; Kallaste, A.; Asad, B.; Vaimann, T.; Rassõlkin, A. Analytical modelling of synchronous reluctance motor including non-linear magnetic condition. *IET Electr. Power Appl.* **2022**, *16*, 511–524. [CrossRef]
2. Ibrahim, M.N.F.; Abdel-Khalik, A.S.; Rashad, E.M.; Sergeant, P. An Improved Torque Density Synchronous Reluctance Machine With a Combined Star–Delta Winding Layout. *IEEE Trans. Energy Convers.* **2018**, *33*, 1015–1024. [CrossRef]
3. Tawfiq, K.B.; Ibrahim, M.N.; El-Kholy, E.E.; Sergeant, P. Performance Improvement of Synchronous Reluctance Machines—A Review Research. *IEEE Trans. Magn.* **2021**, *57*, 1–11. [CrossRef]
4. Wang, B.; Wang, J.; Sen, B.; Griffo, A.; Sun, Z.; Chong, E. A Fault-Tolerant Machine Drive Based on Permanent Magnet-Assisted Synchronous Reluctance Machine. *IEEE Trans. Ind. Appl.* **2018**, *54*, 1349–1359. [CrossRef]
5. Villani, M.; Fabri, G.; Credo, A.; Di Leonardo, L.; Collazzo, F.P. Line-Start Synchronous Reluctance Motor: A Reduced Manufacturing Cost Avenue to Achieve IE4 Efficiency Class. *IEEE Access* **2022**, *10*, 100094–100103. [CrossRef]
6. Ozcelik, N.G.; Dogru, U.E.; Imeryuz, M.; Ergene, L.T. Synchronous Reluctance Motor vs. Induction Motor at Low-Power Industrial Applications: Design and Comparison. *Energies* **2019**, *12*, 2190. [CrossRef]
7. Fratta, A.; Toglia, G.P.; Vagati, A.; Villata, F. Ripple evaluation of high-performance synchronous reluctance machines. *IEEE Ind. Appl. Mag.* **1995**, *1*, 14–22. [CrossRef]
8. Zhao, W.; Sun, Y.; Ji, J.; Ren, Z.; Song, X. Phase Shift Technique to Improve Torque of Synchronous Reluctance Machines With Dual M-Phase Windings. *IEEE Trans. Ind. Electron.* **2021**, *69*, 5–17. [CrossRef]
9. Liang, J.; Dong, Y.; Sun, H.; Liu, R.; Zhu, G. Flux-Barrier Design and Torque Performance Analysis of Synchronous Reluctance Motor with Low Torque Ripple. *Appl. Sci.* **2022**, *12*, 3958. [CrossRef]
10. Wang, B.; Wang, J.; Griffo, A.; Sen, B. Experimental assessments of a triple redundant nine-phase fault-tolerant PMA SynRM drive. *IEEE Trans. Ind. Electron.* **2017**, *66*, 772–783. [CrossRef]
11. Sanada, M.; Hiramoto, K.; Morimoto, S.; Takeda, Y. Torque ripple improvement for synchronous reluctance motor using an asymmetric flux barrier arrangement. *IEEE Trans. Ind. Appl.* **2004**, *40*, 1076–1082. [CrossRef]
12. Credo, A.; Villani, M.; Popescu, M.; Riviere, N. Application of Epoxy Resin in Synchronous Reluctance motors with fluid-shaped barriers for e mobility. *IEEE Trans. Ind. Appl.* **2021**, *57*, 6440–6452. [CrossRef]
13. Bianchi, N.; Bolognani, S.; Bon, D.; Pre, M.D. Rotor flux-barrier design for torque ripple reduction in synchronous reluctance motors. In Proceedings of the Conference Record of the 2006 IEEE Industry Applications Conference Forty-First IAS Annual Meeting, Tampa, FL, USA, 8–12 October 2006; pp. 1193–1200.
14. Gallardo, C.; Tapia, J.A.; Degano, M.; Mahmoud, H.; Hoffer, A.E. Rotor Asymmetry Impact on Synchronous Reluctance Machines Performance. In Proceedings of the 2022 International Conference on Electrical Machines (ICEM), Valencia, Spain, 5–8 September 2022; pp. 848–854.
15. Ferrari, S.; Armando, E.; Pellegrino, G. Torque Ripple Minimization of PM-assisted Synchronous Reluctance Machines via Asymmetric Rotor Poles. In Proceedings of the 2019 IEEE Energy Conversion Congress and Exposition (ECCE), Baltimore, MD, USA, 29 September–03 October 2019; pp. 4895–4902.
16. Ban, B.; Stipetic, S. Systematic Metamodel-Based Optimization Study of Synchronous Reluctance Machine Rotor Barrier Topologies. *Machines* **2022**, *10*, 712. [CrossRef]
17. Ocak, O.; Aydin, M. An Innovative Semi-FEA Based, Variable Magnet-Step-Skew to Minimize Cogging Torque and Torque Pulsations in Permanent Magnet Synchronous Motors. *IEEE Access* **2020**, *8*, 210775–210783. [CrossRef]
18. Xu, M.; Liu, G.; Chen, Q.; Ji, J.; Zhao, W. Design and optimization of a fault tolerant modular permanent magnet assisted synchronous reluctance motor with torque ripple minimization. *IEEE Trans. Ind. Electron.* **2020**, *68*, 8519–8530. [CrossRef]
19. Vagati, A.; Canova, A.; Chiampi, M.; Pastorelli, M.; Repetto, M. Design refinement of synchronous reluctance motors through finite-element analysis. *IEEE Trans. Ind. Appl.* **2000**, *36*, 1094–1102. [CrossRef]
20. Bomela, X.B.; Kamper, M.J. Effect of stator chording and rotor skewing on performance of reluctance synchronous machine. *IEEE Trans. Ind. Appl.* **2002**, *38*, 91–100. [CrossRef]
21. Hamiti, T.; Lubin, T.; Rezzoug, A. A Simple and Efficient Tool for Design Analysis of Synchronous Reluctance Motor. *IEEE Trans. Magn.* **2008**, *44*, 4648–4652. [CrossRef]
22. Wang, Y.; Ionel, D.M.; Rallabandi, V.; Jiang, M.; Stretz, S.J. Large-Scale Optimization of Synchronous Reluctance Machines Using CE-FEA and Differential Evolution. *IEEE Trans. Ind. Appl.* **2016**, *52*, 4699–4709. [CrossRef]
23. Juergens, J.; Fricassè, A.; Marengo, L.; Gragger, J.; De Gennaro, M.; Ponick, B. Innovative design of an air cooled ferrite permanent magnet assisted synchronous reluctance machine for automotive traction application. In Proceedings of the 2016 XXII International Conference on Electrical Machines (ICEM), Lausanne, Switzerland, 4–7 September 2016; pp. 803–810.

24. Ban, B.; Stipetic, S.; Jercic, T. Minimum Set of Rotor Parameters for Synchronous Reluctance Machine and Improved Optimization Convergence via Forced Rotor Barrier Feasibility. *Energies* **2021**, *14*, 2744. [CrossRef]
25. Bernard, N.; Dang, L.; Moreau, L.; Bourguet, S. A Pre-Sizing Method for Salient Pole Synchronous Reluctance Machines with Loss Minimization Control for a Small Urban Electrical Vehicle Considering the Driving Cycle. *Energies* **2022**, *15*, 9110. [CrossRef]
26. Bianchi, N.; Bolognani, S.; Bon, D.; Pre, M.D. Rotor Flux-Barrier Design for Torque Ripple Reduction in Synchronous Reluctance and PM-Assisted Synchronous Reluctance Motors. *IEEE Trans. Ind. Appl.* **2009**, *45*, 921–928. [CrossRef]
27. Bianchi, N.; Fornasiero, E.; Carraro, E.; Bolognani, S.; Castiello, M. Electric vehicle traction based on a PM assisted synchronous reluctance motor. In Proceedings of the 2014 IEEE International Electric Vehicle Conference (IEVC), Florence, Italy, 17–19 December 2014.
28. Lazari, P.; Wang, J.; Sen, B. 3-D Effects of Rotor Step-Skews in Permanent Magnet-Assisted Synchronous Reluctance Machines. *IEEE Trans. Magn.* **2015**, *51*, 8112704. [CrossRef]
29. Hofer, M.; Schroedl, M. Comparison of a flux barrier and a salient pole synchronous reluctance machine for high rotational speeds in electric traction applications. In Proceedings of the 2017 20th International Conference on Electrical Machines and Systems (ICEMS), Sydney, NSW, Australia, 11–14 August 2017; pp. 1–6.
30. Lee, T.-H.; Lee, J.-H.; Yi, K.-P.; Lim, D.-K. Optimal Design of a Synchronous Reluctance Motor Using a Genetic Topology Algorithm. *Processes* **2021**, *9*, 1778. [CrossRef]
31. Lee, T.-H.; Lim, D.-K.; Moon, K.-Y.; Jeon, K.-W. Topology Optimization Combined with a Parametric Algorithm for Industrial Synchronous Reluctance Motor Design. *Processes* **2022**, *10*, 746. [CrossRef]
32. Baziruwiha, J.-C.; Kamper, M.J.; Botha, S. High Pole Number Epoxy-Casted Rotor Reluctance Synchronous Wind Generator. In Proceedings of the 2022 IEEE Energy Conversion Congress and Exposition (ECCE), Detroit, MI, USA, 9–13 October 2022; pp. 1–8.
33. Howard, E.; Kamper, M.J.; Gerber, S. Asymmetric Flux Barrier and Skew Design Optimization of Reluctance Synchronous Machines. *IEEE Trans. Ind. Appl.* **2015**, *51*, 3751–3760. [CrossRef]
34. Hubert, T.; Reinlein, M.; Kremser, A.; Herzog, H.-G. Torque ripple minimization of reluctance synchronous machines by continuous and discrete rotor skewing. In Proceedings of the 2015 5th International Electric Drives Production Conference (EDPC), Nuremberg, Germany, 15–16 September 2015; pp. 1–7.
35. Korman, O.; Nardo, M.D.; Degano, M.; Gerada, C. A Novel Flux Barrier Parametrization for Synchronous Reluctance Machines. *IEEE Trans. Energy Convers.* **2022**, *37*, 675–684. [CrossRef]
36. Islam, M.S.; Shrestha, A.; Islam, M. Effect of Step Skew in Synchronous Reluctance Machines for High Performance Applications. In Proceedings of the 2022 IEEE Energy Conversion Congress and Exposition (ECCE), Detroit, MI, USA, 9–13 October 2022; pp. 1–6.
37. Cai, S.; Hao, H.; Jin, M.-J.; Shen, J.-X. A simplified method to analyze synchronous reluctance machine. In Proceedings of the 2016 IEEE Vehicle Power and Propulsion Conference (VPPC), Hangzhou, China, 17–20 October 2016; pp. 1–6.
38. Ibrahim, M.N.F.; Sergeant, P.; Rashad, E. Simple design approach for low torque ripple and high output torque synchronous reluctance motors. *Energies* **2016**, *9*, 942. [CrossRef]
39. Bianchi, N.; Degano, M.; Fornasiero, E. Sensitivity Analysis of Torque Ripple Reduction of Synchronous Reluctance and Interior PM Motors. *IEEE Trans. Ind. Appl.* **2015**, *51*, 187–195. [CrossRef]
40. Fitouri, M.; Bensalem, Y.; Abdelkrim, M.N. Comparison Between 2D and 3D Modeling of Permanent Magnet Synchronous Motor Using FEM Simulations. In Proceedings of the 2020 17th International Multi-Conference on Systems, Signals & Devices (SSD), Monastir, Tunisia, 20–23 July 2020; pp. 681–685.
41. Cupertino, F.; Pellegrino, G.; Gerada, C. Design of synchronous reluctance motors with multiobjective optimization algorithms. *IEEE Trans. Ind. Appl.* **2014**, *50*, 3617–3627. [CrossRef]
42. Degano, M.; Murataliyev, M.; Shuo, W.; Barater, D.; Buticchi, G.; Jara, W.; Bianchi, N.; Galea, M.; Gerada, C. Optimised Design of Permanent Magnet Assisted Synchronous Reluctance Machines for Household Appliances. *IEEE Trans. Energy Convers.* **2021**, *4*, 3084–3095. [CrossRef]

designs

MDPI

Article

Water Pumping System Supplied by a PV Generator and with a Switched Reluctance Motor Using a Drive Based on a Multilevel Converter with Reduced Switches

Vitor Fernão Pires [1,2,3,*], Daniel Foito [1,2,4], Armando Cordeiro [2,4,5], Tito G. Amaral [1,2], Hao Chen [6], Armando Pires [1,2,3] and João F. Martins [3,7]

1 ESTSetúbal, DEE, IPS—Instituto Politécnico de Setúbal, 2914-508 Setúbal, Portugal
2 Sustain.RD, IPS—Instituto Politécnico de Setúbal, 2914-508 Setúbal, Portugal
3 INESC-ID Lisboa, 1000-029 Lisboa, Portugal
4 UNINOVA-CTS, UNL, 2829-516 Caparica, Portugal
5 Instituto Superior de Engenharia de Lisboa ISEL, DEEEA, IPL—Instituto Politécnico de Lisboa, 1549-020 Lisboa, Portugal
6 School of Electrical Engineering, China University of Mining and Technology, Xuzhou 221000, China
7 FCT, DEEC, UNL—Universidade Nova de Lisboa, 2829-516 Caparica, Portugal
* Correspondence: vitor.pires@estsetubal.ips.pt

Abstract: Pumping systems play a fundamental role in many applications. One of the applications in which these systems are very important is to pump water. However, in the real world context, the use of renewable energies to supply this kind of system becomes essential. Thus, this paper proposes a water pumping system powered by a photovoltaic (*PV*) generator. In addition, due to its interesting characteristics, such low manufacturing cost, free of rare-earth elements, simple design and robustness for pumping systems, a switched reluctance motor (*SRM*) is used. The power electronic system to be used in the *PV* generator and to control the *SRM* consists of a *DC*/*DC* converter with a bipolar output and a multilevel converter. The adopted *DC*/*DC* converter uses only one switch, so its topology can be considered as a derivation of the combination of a Zeta converter with a buck–boost converter. Another important aspect is that this converter allows continuous input current, which is desirable for *PV* panels. The topology selected to control the *SRM* is a multilevel converter. This proposed topology was adopted with the purpose of reducing the number of power semiconductors. A maximum power point algorithm (*MPPT*) associated with the *DC*/*DC* converter to obtain the maximum power of the *PV* panels is also proposed. This *MPPT* will be developed based on the concept of the time derivative of the power and voltage. It will be verified that with the increase in solar irradiance, the generated power will also increase. From this particular case study, it will be verified that changes in the irradiance from 1000 W/m^2 to 400 W/m^2 will correspond to a change in the motor speed from 1220 rpm to 170 rpm. The characteristics and operation of the proposed system will be verified through several simulation and experimental studies.

Keywords: renewable energy; photovoltaic generator (*PV*); switched reluctance motor (*SRM*); water pumping system; *DC*/*DC* converter; multilevel converter

Citation: Pires, V.F.; Foito, D.; Cordeiro, A.; Amaral, T.G.; Chen, H.; Pires, A.; Martins, J.F. Water Pumping System Supplied by a PV Generator and with a Switched Reluctance Motor Using a Drive Based on a Multilevel Converter with Reduced Switches. *Designs* **2023**, *7*, 39. https://doi.org/10.3390/designs7020039

Academic Editors: Loránd Szabó and Feng Chai

Received: 30 December 2022
Revised: 17 February 2023
Accepted: 28 February 2023
Published: 3 March 2023

1. Introduction

One of the applications in which electrical machines have been playing a very important role is related to water pumping. In fact, water pumps have been used for many purposes, such as agriculture, residences, industry and commerce. One aspect associated with these applications that has been considered, especially in recent years, is the supply of these water pumping systems from renewable energy sources. Some examples can be found in the following literature. The work proposed in [1] presents a review on solar, wind and hybrid wind–PV water pumping systems. Similarly, paper [2] also presents a review of solar-powered water pumping systems. The study presented in [3] demonstrated

a viability case study of solar/wind for water pumping systems in the Algerian Sahara regions. Research paper [4] proposes a solution for reducing carbon emissions by integrating urban water systems and solar-powered systems. One of the renewable energy sources that have been considered to be highly applicable is photovoltaic generators. In rural and remote areas, this kind of renewable energy source has even been considered to be extremely important. For example, in [5], a photovoltaic water pumping system for horticultural crop irrigation in Mozambique is proposed. A comprehensive review on solar-powered water pumping systems for irrigation developments and prospects towards green energy is presented in [6]. A case study regarding the feasibility of renewable energy sources for pumping clean water in sub-Saharan Africa is described in [7]. In [8], a PV microgrid design for rural electrification that can be applied to water pumping systems and other systems is proposed. There are several factors that must be considered in the design and application of these systems, such as, for example, the cost and reliability. Thus, besides the PV panels, in the design and choice of these systems, the power electronics and machine characteristics must be considered.

Several electrical machine types have been used for water pumping systems. Among them, one that has been recently used is the switched reluctance machine (*SRM*). This machine has been adopted due to several important characteristics, such as low manufacturing cost, free of rare-earth elements, simple design, robustness and efficiency. For example, in [9], a design and optimization model of a high-speed switched reluctance motor is proposed. A comparison of design and performance parameters in switched reluctance and induction motors is presented in [10], showing the main important characteristics of the *SRM*. It should be mentioned that some of the characteristics, such as low cost and reliability, are very interesting in pumping systems, especially for developing countries. Some examples of the importance of pumping systems in developing countries can be found in [11] applied to certain regions of India, or Latin American countries [12]. Another aspect of these pumping systems is the required power electronic converters to operate the *SRM*. Several types of power converter topologies have been proposed for this machine. One group of topologies that has been used is characterized by the application of two voltage levels to the motor windings. Some examples of two-voltage-level topologies can be found in [13]. A review of switched reluctance motor converter topologies, including two voltage levels, can also be found in [14]. Another group that is now becoming very popular is characterized by applying more than two levels to the motor winding. These topologies, designated as multilevel, present several advantages, such as reduced switching frequency, reduced current ripple, lower voltage rate of power semiconductor devices, faster motor phase magnetization and demagnetization and inherent fault-tolerant capability. For example, the review proposed in [15] summarizes several *SRM* multilevel topologies. A performance comparison of multilevel converter topologies for high-power high-speed switched reluctance machines can be found in [16]. A torque ripple analysis of several multilevel converter topologies for switched reluctance machines can be found in [17]. As well as the two-level converters, the majority of these multilevel structures present an asymmetric configuration. The first topologies were derived from the classical multilevel converters used, for example, for induction motors. In this way, the flying capacitor (*AFC*), asymmetric neutral point clamped (*ANPC*) and cascaded H-bridge were usually proposed, as described in the next references. An asymmetric three-level neutral point diode clamped converter topology for *SRM* drives is proposed in [18]. Another asymmetric neutral point diode clamped topology considering reduced component count for *SRM* drives can be found in [19]. An asymmetric flying capacitor multilevel H-bridge inverter for SRM drives can be found in [20]. A cascade multilevel converter of *SRM* drives is proposed in [21]. It is also possible to find several of these topologies in [22], now considering torque ripple minimization with multicarrier *PWM* strategies. This application also has been extended to other kinds of multilevel topologies. One of them is the *T-Type*, although the required blocking voltage of power devices is not the same. An asymmetric three-level T-Type converter for *SRM* drives applied to hybrid electric vehicles is presented in [23].

Additionally, an advanced multi-level converter for four-phase SRM drives based on the *T-Type* converter can be found in [24]. Another solution is the modular multilevel converter (*MMC*). However, since this topology consists of a higher number of power converters, it has been used for applications in which a decentralized battery energy storage system is required [25] or hybrid electric vehicle applications [26]. Meanwhile, many other topologies have been proposed. Some of them take into consideration specific applications, for example, electric vehicles or pumping systems. A comparative review of *SRM* converters for electric vehicle applications can be found in [27]. A multi-battery block module power converter for electric vehicles driven by a switched reluctance motors is proposed in [28]. A multi-purpose fault-tolerant multilevel topology for an 8/6 *SRM* drive is proposed in [29]. A novel converter topology for a photovoltaic water pump based on switched reluctance motors can be found in [30]. Additionally, a grid-interfaced solar *PV* water pumping system with energy storage is proposed in [31]. Others take into consideration specific factors, such as fast magnetizing and demagnetizing [32] or fault tolerance of the power semiconductors of the converter [33]. However, one important disadvantage is related to the higher number of power semiconductors.

In addition to the drive associated with the machine, a *DC*/*DC* converter associated with the *PV* panels must also be considered in these pumping systems. These *DC*/*DC* converters are also associated with *MPPT* (maximum power point) algorithms to constantly maintain the *PV* panels at full power. There are many *DC*/*DC* power converter topologies that have been proposed for this kind of system. Usually, these *DC*/*DC* converters are designed for a single output. Some examples where a single output is required can be found in following examples. In [34], a simplified *PWM MPPT* approach for a direct PV-fed switched reluctance motor in a water pumping system using a *DC*/*DC* converter is proposed. Other renewable energy-fed switched reluctance motors for *PV* pump applications requiring a *DC*/*DC* converter with single output can be found in [35]. A *PI* controller design for the *MPPT* of a photovoltaic system supplying *SRM* via the *BAT-inspired* search algorithm is presented in [36]. A similar solution of *MPPT* control design of a *PV* system supplying *SRM* considering the *BAT-inspired* search algorithm is proposed in [37]. An analysis and study regarding the performance of several *DC*/*DC* converters that are indicated to be used in *BLDC* motor drive applications is presented in [38]. However, several solutions have been proposed in which a dual output is required for the *SRM* drive *DC*/*DC* converters. Some examples of these type of converters can be found in the next references. A sensorless *SRM*-driven solar irrigation pump with grid support using the Vienna rectifier requiring dual output voltages is presented in [39]. A three-level quadratic boost *DC*/*DC* converter associated with an *SRM* drive for photovoltaic water pumping requiring dual output voltages is proposed in [40]. Another topology presenting dual output voltages for a four-phase *SRM*-driven solar-powered water pumping solution can be found in [41]. These solutions present boost characteristic and require two switches. Thus, in [42], another boost converter with a dual output but with only one switch is presented. *DC*/*DC* converters characterized by *buck–boost* operation were also proposed to be used for this kind of. In [43], a *DC*/*DC* buck–boost converter for a *PV* pumping system that uses an *SRM* is proposed. A similar approach was also used by [44]. However, in this case, a new configuration of a dual-output buck–boost converter was used. In [45], a *DC*/*DC* converter with dual output but based on *Luo* converters and with an advanced voltage-lift technique is proposed. A topology with similar characteristics is also proposed by [46], but in this case, a topology based on a combination of the *SEPIC* and *Cuk* converters was used. It should be noted that, in the case of motor drives with multilevel topologies, it is usual to supply them with two or more outputs. Some solutions using multilevel topologies for other types of motors can also be found in the literature. A boost multilevel *NPC*-fed asynchronous pumped storage hydro-generating unit is proposed in [47]. An isolated cascaded multilevel *qZSI* converter for a single-phase induction motor for water pump application can be found in [48]. A *PV* generator-fed water pumping system based on an *SRM* with a multilevel fault-tolerant converter is proposed in [49]. An *NPC* inverter-based solar *PV*-fed induction motor drive

for water pumping is proposed in [50]. However, one aspect of these solutions is that the design of the drive is not usually optimized taking into consideration the reduction in the power semiconductor switches and/or passive components. On the other hand, most solutions have not considered water pumping systems based on *SRM* drives connected to multilevel converters. Another aspect associated with these *PV* pumping systems is the *MPPT* algorithm that must be associated with the power electronic converters. Many different approaches have been proposed for the implementation of these algorithms. Among them, the algorithms that are most used and also considered as classical ones are the perturb and observe and the incremental conductance [51]. Other algorithms that use metaheuristic optimization techniques have also been proposed. Examples of these can be seen in works [52,53]. Although these algorithms usually allow excellent results to be obtained, their implementation usually requires some complexity.

Taking into consideration the aspects already mentioned, this paper proposes a *PV*-powered water pumping system in which an *SRM* is used. In this proposal, the *SRM* drive is composed of a multilevel converter with a reduced number of power devices [54]. On the other hand, a combined *DC*/*DC* converter associated with the *PV* panels is also proposed, which was designed with a single switch [55]. This *DC*/*DC* converter presents a buck–boost characteristic and continuous input current. Associated with this *DC*/*DC* converter, the use of an *MPPT* algorithm based on the concept of the time derivative of the power and voltage is also proposed. It should be mentioned that the adoption of this algorithm was chosen taking into consideration its simplicity and possibility to be implemented with a simple analogue electric circuit. Finally, the proposed system for the *PV*-powered water pumping system will be tested in two ways. Firstly, through a computer simulation, and secondly, using a laboratory prototype.

Regarding the organization of this paper, it consists of six sections, the first one being this introduction. In the next section, the proposed water pumping system supplied by *PV* panels and with an *SRM* drive based on a multilevel converter with reduced switches will be presented. The control system developed for this application will be presented in the third section. In the fourth section, several results that were obtained through a simulation program will be presented. These results will also be confirmed using a laboratory prototype, with the obtained results presented in Section 5. Section 6 is dedicated to the discussion of the results and comparison with other solutions. Finally, in the last section, the conclusions of this work will be presented.

2. Proposed Water Pumping System Supplied by a *PV* Generator

The proposed water pumping system will be driven by an 8/6 *SRM*. In addition, it will be fed by a renewable energy source, namely by *PV* panels. To obtain the maximum power from the *PV* generators, a *DC*/*DC* converter with dual output is proposed. To obtain the dual output, a converter derived from a combination of the Zeta converter with a *buck–boost* converter is used. This combination allows a single switch to be used. Another aspect is that the input current of the converter (output *PV* current) will be continuous. The *SRM* drive is composed of a multilevel converter that will be supplied by the dual output of the *DC*/*DC* converter. The proposed water pumping system is presented in Figure 1.

As described and presented in Figure 1, the electronics associated with the pumping system consist of two converters. These converters can be analyzed in a separated way as described in the next section.

In the context of this paper, the water pump is a mechanical device where the shaft is coupled to the SRM using an appropriate transmission. The use of a centrifugal water pump is assumed, since this is one of the most common types of pumps for transferring fluids. The centrifugal pump operates on a concept called forced vortex flow. This means that when a specific quantity of fluid is forced to rotate imposed by an external torque,

there is a rise in the rotating liquid's pressure head, which transfers the fluid from one place to another. The necessary external torque to move the impeller is given by:

$$T_{ext} = \frac{\rho g H_T Q}{\omega \eta} \tag{1}$$

where ρ is the water density in (kg/m^3), g is the acceleration due to gravity (m/s^2), H_T is the pump's total head (m), Q is the water flow rate (m^3), ω is the speed of the impeller (rad/s) and η is the efficiency of the pump. The operation limits of this application for water pumping purposes should be determined by the minimum water flow rate required and necessary head (elevation) according to pump characteristic (typical operation curve) such as speed and efficiency.

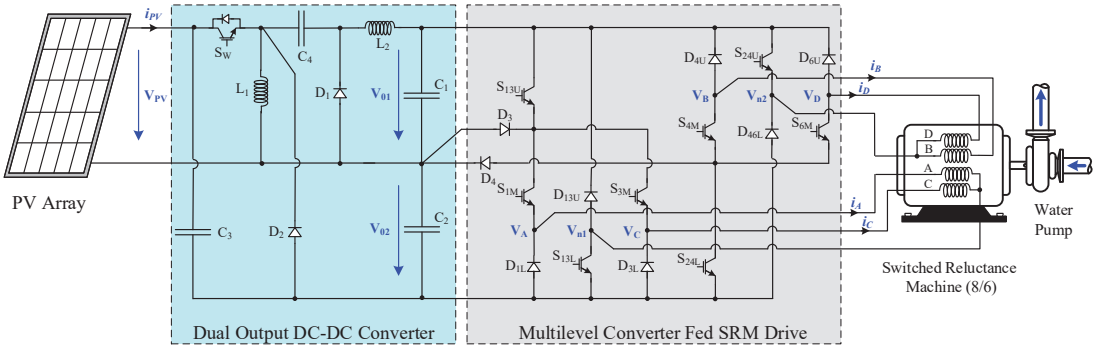

Figure 1. Water pumping system supplied by a *PV* generator and with an *SRM* using a drive based on a multilevel converter with reduced switches.

2.1. Multilevel Converter Fed SRM Drive

The proposed multilevel converter adopted in the *SRM* drive was designed with the purpose of minimizing the number of components. In this way, although allowing the application of multilevel voltages to the 8/6 *SRM*, it only requires eight transistors and eight diodes. Analyzing the possible combinations for the transistor state (*ON/OFF)* conditions, it is possible to conclude that there are five working modes associated with each motor winding, respectively (example given for motor winding *A*):

Mode 1: This mode is verified when the devices S_{13U}, S_{1M} and S_{13L} are in the *ON* condition. As shown in Figure 2a, this circuit applies the two input *DC* voltages ($V_{C1} = V_{o1}$ and $V_{C2} = V_{o2}$) to the motor winding. In this mode, the maximum positive voltage applied to the motor winding is ($+V_{C1} + V_{C2}$).

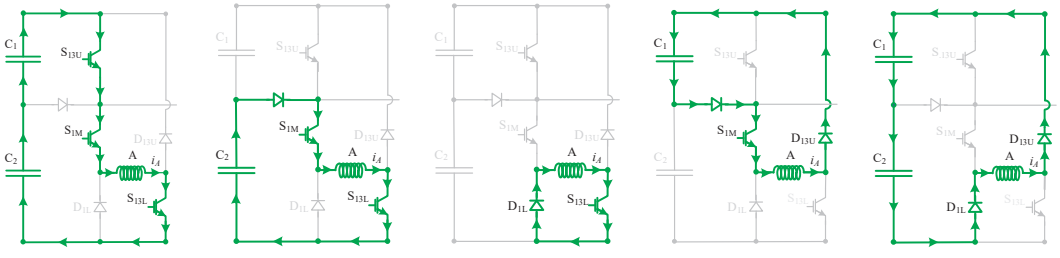

Figure 2. Operating modes associated with each motor winding: (**a**) Mode 1 → $+V_{C1}$ $+V_{C2}$, (**b**) Mode 2 → $+V_{C2}$, (**c**) Mode 3 → 0, (**d**) Mode 4 → $-V_{C1}$, (**e**) Mode 5 → $-V_{C1}$ $-V_{C2}$.

Mode 2: In this mode, the transistors S_{1M} and S_{13L} are in the *ON* condition, and the resulting circuit allows the application of the intermediate positive voltage ($+V_{C2}$) to the motor winding. Figure 2b presents the diagram of this circuit.

Mode 3: In this mode, the converter applies the zero-voltage level to the motor winding. This circuit is obtained when only S_{13L} is in the *ON* condition (see Figure 2c).

Mode 4: In this mode, the circuit allows the application of the intermediate negative voltage level ($-V_{C1}$) to the motor winding. This circuit results from the condition in which only the transistor S_{1M} is in the *ON* condition (see Figure 2d).

Mode 5: This mode is verified when none of the transistors are in the *ON* condition. As shown in Figure 2e, the circuit applies the maximum reverse voltages of the two input *DC* sources (V_{C1} and V_{C2}) to the motor winding. Therefore, the maximum negative voltage applied to the winding is ($-V_{C1} - V_{C2}$).

These operating modes can also be presented mathematically. Thus, for the development of the mathematical model, the power semiconductors are considered as ideal switches. In this way, associated with the transistors, Boolean variables are considered, as described by (2):

$$\begin{cases} \alpha_{ji} = 0 \; if \; S_{ji} \; is \; ON \\ \alpha_{ji} = 0 \; if \; S_{ji} \; is \; OFF \\ \alpha_{km} = 0 \; if \; S_{km} \; is \; ON \\ \alpha_{km} = 0 \; if \; S_{km} \; is \; OFF \end{cases} \tag{2}$$

where k = 1, 3, 4, 6, j = 13, 24 and $I = U, M$.

Using these variables, taking into consideration the possible combinations for the transistors' *ON/OFF* conditions and in accordance with the Kirchhoff laws, it is possible to obtain the mathematical expressions of the voltages applied to the motor windings, as function of the switches. These expressions are then given by:

$$\begin{bmatrix} V_{An1} \\ V_{Bn2} \\ V_{Cn1} \\ V_{Dn2} \end{bmatrix} = \begin{bmatrix} \alpha_{13U}\alpha_{1M}\alpha_{13L} - \beta_A & \alpha_{1M}\alpha_{13L} - \beta_A \\ \alpha_{4M}\alpha_{24U} - \beta_B & \alpha_{24L}\alpha_{4M}\alpha_{24U} - \beta_B \\ \alpha_{13U}\alpha_{3M}\alpha_{13L} - \beta_C & \alpha_{3M}\alpha_{13L} - \beta_C \\ \alpha_{6M}\alpha_{24U} - \beta_B & \alpha_{24L}\alpha_{6M}\alpha_{24U} - \beta_B \end{bmatrix} \begin{bmatrix} V_{o1} \\ V_{o2} \end{bmatrix} \tag{3}$$

where β is binary variable that is a function of:

$$\begin{cases} \beta_w = 1 \; if \; i_w > 0 \; and \; all \; S \; associated \; to \; winding \; w \; are \; OFF \\ \beta_w = 0 \; if \; i_w \leq 0 \; or \; all \; S \; associated \; to \; winding \; w \; are \; not \; OFF \end{cases} \tag{4}$$

where w = A, B, C, D.

According to the previous expressions, it is possible to confirm the multilevel voltage operation of the converter, namely by verifying that five different voltage levels can be applied.

2.2. Operation in Continuous Conduction Mode

Similar to the *SRM* drive that operates the motor, the *DC*/*DC* converter was also designed with a reduced component count. In this way, although the converter has the specification of having two outputs, it only requires one switch. Thus, considering that the converter operates in continuous conduction mode (*CCM*), it is possible to conclude that there are only two working modes, respectively:

Mode 1: This mode is verified when the converter switch S_w is in the *ON* state and diodes D_1 and D_2 are in the *OFF* state, resulting in the circuit configuration of Figure 3a. In this mode, both inductors (L_1 and L_2) are in charging mode, through which their currents will increase. Inductor L_1 will be charged by the input power source. On the other hand, the capacitors C_3 and C_4 will discharge their storage energy to the inductor L_2 and to the load. In this mode, capacitors C_1 and C_2 will also discharge to the load. The equations for

the inductors' voltages and capacitors' currents in this mode are as follows, where i_{load} is the nominal current of the *SRM*:

$$\begin{cases} v_{L1} = L_1 \dfrac{di_{L1}}{dt} = V_{PV} = V_i \\ v_{L2} = L_2 \dfrac{di_{L2}}{dt} = V_i + V_{C4} - V_{C1} \\ i_{C3} = C_2 \dfrac{dv_{C3}}{dt} = i_{load} + i_{C2} \\ i_{C4} = C_4 \dfrac{dv_{C4}}{dt} = -i_{L2} \end{cases} \tag{5}$$

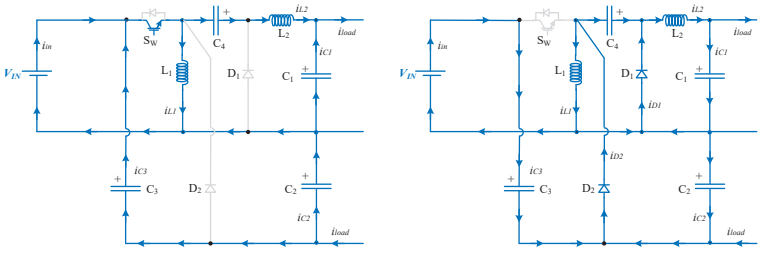

Figure 3. Operating modes of the *DC*/*DC* converter: (**a**) Mode 1: $S_W \rightarrow ON$, (**b**) Mode 2: $S_W \rightarrow OFF$.

Mode 2: In this mode, the converter switch S_w changes to the *OFF* state. In an opposite way, diodes D_1 and D_2 change to the *ON* state, resulting in the circuit presented in Figure 3b. In contrast to mode 1, in this mode, both inductors (L_1 and $L2$) will be in discharging mode. In this way, their current will decrease. The capacitors C_3 and C_4 will be in charging mode, through which inductor L_1 will discharge to such capacitors. Inductor L_2 will discharge to capacitors C_1 and C_2. The equations for the inductors' voltages and capacitors' currents in this mode are as follows:

$$\begin{cases} v_{L1} = L_1 \dfrac{di_{L1}}{dt} = V_i - V_{C3} = -V_{C4} \\ v_{L2} = L_2 \dfrac{di_{L2}}{dt} = -V_{C1} \\ i_{C3} = C_2 \dfrac{dv_{C3}}{dt} = \dfrac{i_{L1}}{2} \\ i_{C4} = C_4 \dfrac{dv_{C4}}{dt} = \dfrac{i_{L1}}{2} \end{cases} \tag{6}$$

One aspect that is possible to verify from these modes is that the *PV* current (input of the converter) will be continuous. The converter waveforms associated with the two operating modes are presented in Figure 4.

Taking into consideration both operating modes and the zero average voltage in both inductors over one cycle, the static voltage gain of this *DC*/*DC* converter can be obtained. The average voltages in the inductors are given by:

$$\begin{cases} \frac{1}{T}\int_0^T v_{L1}\, dt = \frac{1}{T}\left[\int_0^{\delta T} (V_i)\, dt + \int_{\delta T}^T (-V_{C4})\, dt\right] = 0 \\ \frac{1}{T}\int_0^T v_{L1}\, dt = \frac{1}{T}\left[\int_0^{\delta T} (V_i)\, dt + \int_{\delta T}^T (V_i - V_{C3})\, dt\right] = 0 \\ \frac{1}{T}\int_0^T v_{L2}\, dt = \frac{1}{T}\left[\int_0^{\delta T} (V_i + V_{C4} - V_{C1})\, dt + \int_{\delta T}^T (-V_{C1})\, dt\right] = 0 \end{cases} \tag{7}$$

Taking into account the expressions given by (5) and (6), the converter static voltage gain of each output and capacitor voltages can be obtained, which are given by:

$$\begin{cases} V_{o1} = V_{C1} = \frac{\delta}{1-\delta} V_i \\ V_{o2} = V_{C2} = \frac{\delta}{1-\delta} V_i \\ V_o = V_{C1} + V_{C2} = \frac{2\delta}{1-\delta} V_i \\ V_{C3} = \frac{1}{1-\delta} V_i \\ V_{C4} = \frac{\delta}{1-\delta} V_i \end{cases} \tag{8}$$

From the expressions given in (8), it is possible to see that the static voltage gains of both outputs are equal and have a *buck–boost* characteristic.

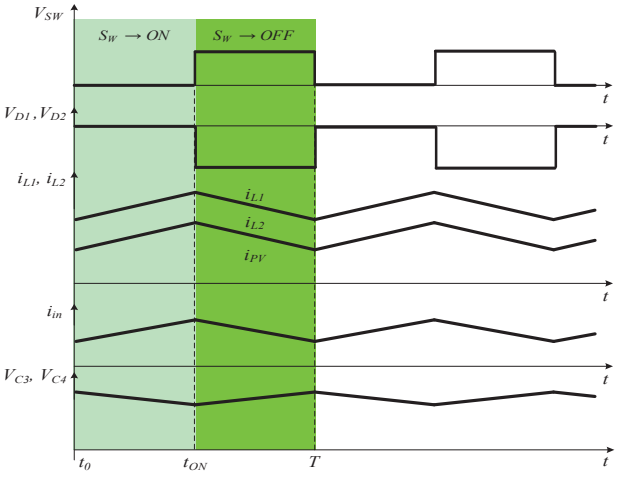

Figure 4. Waveforms associated with both operating modes.

2.3. DC/DC Component Design

This section presents the design of the components of the *DC/DC buck–boost* converter. During mode 1, the capacitor C_4 discharges according to the i_{L2} current (see Figure 3a) given by Equation (9).

$$\Delta V_{C4} = \frac{1}{C_4} \int_0^{\delta T} i_{L2}\, dt \tag{9}$$

Therefore, is possible to design the capacitor for a permissible voltage ripple. The previous equation can also be expressed as (10), where δ is the duty cycle and f_{sw} the switching frequency.

$$C_4 = \frac{i_{L2} \cdot \delta}{\Delta V_{C4} \cdot f_{sw}} \tag{10}$$

Considering that the average current over the output capacitor C_1 in each cycle is zero, the capacitor C_4 value depends on the load current, resulting in Equation (11).

$$C_4 = \frac{i_{load} \cdot \delta}{\Delta V_{C4} \cdot f_{sw}} \tag{11}$$

Inserting the duty cycle and considering Equation (8), this leads to Equation (12).

$$C_4 = \frac{i_{load}}{\Delta V_{C4} \cdot f_{sw}} \cdot \frac{V_{C1}}{(V_i + V_{C1})} = \frac{i_{load}}{\Delta V_{C4} \cdot f_{sw}} \cdot \frac{V_o}{(2V_i + V_o)} = \frac{P_{out}}{(2V_i + V_o) \cdot \Delta V_{C4} \cdot f_{sw}} \tag{12}$$

From the charge variation of C_3, it is possible to conclude that the voltage across C_3 decreases during mode 1, which leads to:

$$\Delta V_{C3} = \frac{1}{C_1}\int_0^{\delta T} i_{C3}\, dt \tag{13}$$

Similarly, one can also design the capacitor C_3 for a permissible voltage ripple as happens with capacitor C_4, Equation (14).

$$C_3 = \frac{i_{C3} \cdot \delta}{\Delta V_{C3} \cdot f_{sw}} \tag{14}$$

Considering that the average current over the output capacitor C_3 in each cycle is zero, the capacitor C_3 value depends on the load current, resulting in Equation (15):

$$C_3 = \frac{i_{load} \cdot \delta}{\Delta V_{C3} \cdot f_{sw}} \tag{15}$$

Inserting the duty cycle and considering Equation (8), this now leads to Equation (16).

$$C_3 = \frac{i_{load}}{\Delta V_{C3} \cdot f_{sw}} \cdot \frac{V_{C2}}{(V_i + V_{o2})} = \frac{i_{load}}{\Delta V_{C3} \cdot f_{sw}} \cdot \frac{V_o}{(2V_i + V_o)} = \frac{P_{out}}{(2V_i + V_o) \cdot \Delta V_{C3} \cdot f_{sw}} \tag{16}$$

In general, the differential Equation (17) represents the current evolution on a capacitor C_2.

$$i_{C2}(t) = C_2 \frac{dv_{C2}(t)}{dt} \tag{17}$$

After linearization, Equation (17) becomes Equation (18).

$$\frac{\Delta v_{C2}}{\Delta t} = \frac{i_{C2}}{C_2} \tag{18}$$

During mode 1, the instantaneous current in the capacitor C_2 is equal to the output current. Additionally, in mode 1, we have $\Delta t = \delta Tsw = \delta / fsw$, thus:

$$C_2 = \frac{i_{load}.\delta}{\Delta V_{C2} \cdot f_{sw}} = \frac{i_{load}}{\Delta V_{C2} \cdot f_{sw}} \cdot \frac{V_o}{(2V_i + V_o)} = \frac{P_{out}}{(2V_i + V_o) \cdot \Delta V_{C1} \cdot f_{sw}} \tag{19}$$

Observing Figure 4, it is possible to verify that when the power semiconductor is turned on, the charge variation ΔQ over the capacitor C_1 is equivalent to the area of a triangle with $0.5\Delta I_{L2}$ height and time base $0.5Tsw$, thus:

$$C_1 = \frac{\Delta Q}{\Delta V_{C1}} = \frac{\frac{1}{2f_{sw}} \cdot \frac{\Delta I_{L2}}{2}}{\Delta V_{C1}} = \frac{\Delta I_{L2}}{8\Delta V_{C1} f_{sw}} \tag{20}$$

Similar calculations can be performed to obtain the values of both inductors. During mode 1, the input voltage lies across L_1 and the current through it increases by ΔI_{L1}. The inductor L_1 can be obtained for a chosen current ripple according to Equation (21).

$$L_1 = \frac{V_i \cdot \delta}{\Delta I_{L1} \cdot f_{SW}} \tag{21}$$

Replacing the duty cycle given in (8), it is possible to obtain Equation (22).

$$L_1 = \frac{V_i}{\Delta I_{L1} \cdot f_{SW}} \cdot \frac{V_0}{(2V_i + V_0)} \tag{22}$$

During mode 1, the voltage across L_2 is given by Equation (5), and the current through it increases by ΔI_{L2}. The inductor L_2 can be obtained for a chosen current ripple according to (23).

$$L_2 = \frac{(V_i + V_{C4} - V_{C1}) \cdot \delta}{\Delta I_{L2} \cdot f_{SW}} \tag{23}$$

Replacing the duty cycle and other relations given in Equation (8), it is possible to obtain (24).

$$L_2 = \frac{(V_i + V_{C4} - V_{C1})}{\Delta I_{L2} \cdot f_{SW}} \cdot \frac{V_0}{(2V_i + V_0)} \tag{24}$$

The maximum reverse voltage of the converter switch S_w and maximum continuous current are given by Equations (25) and (26).

$$V_{R-SW} = V_i - V_{L1} = V_i + V_{C4} \tag{25}$$

$$I_{C-SW} = i_{L1} \tag{26}$$

When the converter switch S_w is turned on, diodes D_1 and D_2 are turned off. In this situation, the maximum reverse voltage and maximum continuous current over D_1 (during the *ON* state) are given by (27) and (28), respectively.

$$V_{R-D1} = V_{C4} - V_i \tag{27}$$

$$I_{C-D1} = i_{L1} - i_{C3} = \frac{i_{L1}}{2} \tag{28}$$

Similarly, for the diode D_2, we have Equations (29) and (30).

$$V_{R-D2} = V_{C3} \tag{29}$$

$$I_{C-D2} = i_{C2} + i_{C3} + I_{load} \tag{30}$$

To analyze the design of these components, an example of the determination of their values is now presented. The following calculations are based on Equations (8)–(30) to estimate the component values. A *DC* voltage of 40 V and a *DC* output voltage of 200 V are assumed, which results in a duty cycle of:

$$\delta = \frac{V_0}{(2V_i + V_0)} = 0.71 \tag{31}$$

Considering a switching frequency *fsw* = 10 kHz and assuming a maximum variation of 0.5 A in L_1 (ΔI_{L1}), it is possible to calculate the value of inductor L_1 based on Equation (21):

$$L_1 = \frac{40 \times 0.71}{0.5 \times 10^4} \approx 5.6 \text{ mH} \tag{32}$$

Considering the duty cycle of Equation (30), the input voltage V_i = 40 V and the voltages of capacitors C_1 and C_4 given by Equation (8), and assuming a maximum variation of 0.5 A in L_2 (ΔI_{L2}), it is possible to calculate the value of inductor L_2 based on Equation (23):

$$L_2 = \frac{(40 + 138 - 100) \times 0.71}{0.5 \times 10^4} \approx 11.2 \text{ mH} \approx 2L_1 \tag{33}$$

Assuming an output power of 1500 W and considering that C_3 and C_4 achieve a voltage variation of 2%, is possible to calculate the values of these capacitors according Equations (12) and (16):

$$C_3 = C_4 = \frac{1500}{(2 \times 40 + 200) \times 0.02 \times 138 \times 10^4} \approx 194 \text{ μF} \tag{34}$$

In the same conditions, assuming that the output capacitors C_1 and C_2 achieve a voltage variation of 1%, is possible to calculate the values of these capacitors according Equations (19) and (20):

$$C_1 = \frac{0.5}{8 \times 0.01 \times 100 \times 10^4} \approx 6.25\ \mu F \tag{35}$$

$$C_2 = \frac{1500}{(2 \times 40 + 200) \times 0.01 \times 100 \times 10^4} \approx 535\ \mu F \tag{36}$$

3. Control of the Proposed System

Another aspect that must be taken into consideration is the control of the proposed pumping system. There are several aspects that should be considered, such as the extraction of the energy from the *PV* panels and the control of the motor. The control of the extracted energy from the *PV* panels will be ensured by the *DC*/*DC* converter. Thus, since the purpose is to extract the maximum energy, an *MPPT* algorithm will be considered. This algorithm will establish the control of the *DC*/*DC* converter switch. In order to maintain the balance between the generated energy from the *PV* panels and the motor consumption, there is a voltage controller associated with the motor drive. In this way, this voltage controller will ensure that the *DC*/*DC* converter output voltages will be stable at a specific reference value. A block diagram of the control system for the proposed solution is presented in Figure 5.

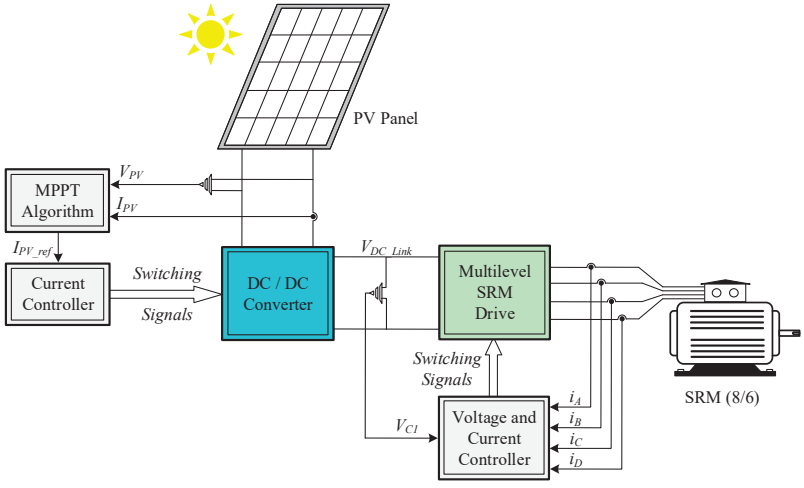

Figure 5. Control system for the proposed solution.

Regarding the *MPPT* algorithm that will ensure the harnessing of the maximum energy that the solar panels can supply, different approaches have been proposed. Among them, the algorithms that are most used are the incremental conductance and perturb and observe [51]. Other algorithms including the use of metaheuristic optimization techniques were proposed. Examples of these can be seen in works [52,53]. Although these algorithms usually allow excellent results to be obtained, their implementation usually requires some complexity. Thus, for this system, an approach considering its simplicity and possibility of being implemented with a simple analogue electric circuit will be used. This algorithm is based on the time derivative of power, as well as voltage. In this way, singularities are avoided that can be found with an algorithm based on the derivative of the power and voltage or current [56]. This algorithm will then be developed taking into consideration the typical *I*–*V* curve of the *PV* panels. In accordance with this, the *MPP* is achieved when the derivative of the voltage and power are zero. However, the movement to that point can be

achieved through the derivative of the power and voltage in order of time. Therefore, if the system is within the left side of the *MPP* and if the condition $dP/dt > 0$ and $dV/dt > 0$ is ensured, this will result in a trajectory in the direction of the *MPP*. On the other hand, if the system is within the right side of the *MPP* and if the condition $dP/dt > 0$ and $dV/dt < 0$ is ensured, this will also result in a trajectory in the direction of the *MPP*. Thus, the conditions to ensure that the system will move to the *MPP* are given by (37).

$$\begin{cases} \left(\frac{dP}{dt} > 0 \; and \; \frac{dV}{dt} > 0\right) or \left(\frac{dP}{dt} < 0 \; and \; \frac{dV}{dt} < 0\right), \; decrease \; I_{PH} \\ \left(\frac{dP}{dt} > 0 \; and \; \frac{dV}{dt} < 0\right) or \left(\frac{dP}{dt} < 0 \; and \; \frac{dV}{dt} > 0\right), \; increase \; I_{PH} \end{cases} \tag{37}$$

Starting from the conditions given by (37), the *MPPT* function regarding the derivative of voltage and power in order of time can be developed. Therefore, taking into consideration that the input current of the *DC*/*DC* converter is regulated by a hysteretic current controller, the reference current is given by the following control law:

$$i_{PV\_ref} = k \int \frac{dP}{dt} \frac{dV}{dt} \, dt \tag{38}$$

However, it is possible to simplify the previous control law even more. To do so, instead of using the derivative of the power and voltage in order of time, their signal will simply be considered. In this way, the *MPPT* only consists of a single expression given by Equation (39), which can easily be implemented through an analogue electronic circuit.

$$i_{PV\_ref} = k \int sign\left(\frac{dP}{dt}\right) sign\left(\frac{dV}{dt}\right) dt \tag{39}$$

One important aspect that must also be considered is the balance between the generated power and the power consumption of the motor. This will be ensured by the adopted voltage controller of the *SRM* drive. Therefore, this voltage controller must ensure that the output voltage of the proposed *DC*/*DC* converter remains in steady state in the reference value. To ensure this, the voltage controller will define the current references for the *SRM* drive controller. A *PI* compensator will be used for this voltage controller, as shown in Figure 6. Regarding the *PI* parameters, they have been determined through trial and error obtained from several repeated experiments.

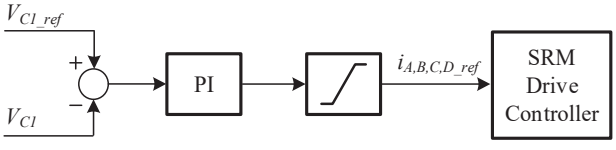

Figure 6. Voltage controller associated with the SRM drive.

4. Simulation Results

With the purpose of confirming the expected performance of the proposed solution, the system was initially implemented in a simulation software. The adopted program was one of the most used in these kinds of systems, namely the *Matlab/Simulink*. For the power electronic converters, inductors (L_1 and L_2) of 5 mH and 10 mH, respectively, and capacitors of 22 μF (C_1), 680 μF (C_2) and 220 μF (C_3 and C_4) were used. It should be mentioned that these values are based on the previous determination of these components. However, they are not completely equal, since for the experimental tests, components that exist in the laboratory were used, and the same values that were used in that part were used for comparison purposes. Regarding the machine, an 8/6 *SRM* was used. Regarding the *PV* panels used in this system, their characteristics can be seen in Table 1. The component values of the power electronic converters were obtained from the equations presented in Section 2.3, and input *DC* voltage 40 V, *DC* output voltage 200 V, 1500 W output power,

fsw = 10 kHz, a ripple limit in capacitor voltages $\Delta VC_1 = \Delta VC_2 \leq 1\%$, $\Delta VC_3 = \Delta VC_4 \leq 2\%$, and inductor current ripples $\Delta I_{L1} = \Delta I_{L1} < 10\%$ were used, which are values that are usually used by designers. However, the adopted values are higher since they have been chosen because of the existing components in our laboratory.

Several simulation tests are presented in this section. The first test was conducted with 700 W/m^2 (irradiance) and 25 °C (ambient temperature). The obtained waveforms of this test are presented in Figure 7. The waveforms of this figure are related to the voltage applied to winding A, with currents in all windings and input *DC* voltages applied to the drive (or *DC*/*DC* output voltages). From the analysis of the voltage applied the motor winding *A* (Figure 7a), the multilevel operation of the drive is noticeable, where the two positive voltage levels are clearly visible. Moreover, it is possible to see that, initially, when the winding is magnetized and at the end when it is demagnetized, the maximum voltage levels are applied. One of the voltage levels that does not appear in this waveform is the $-V_{C1}$ (Figure 2d). The reason for this is because when the demagnetization is necessary, it should be carried out as fast as possible. In this way, the negative voltage that is applied is $-V_{C1}$ $-V_{C2}$ (Figure 2e). Since there are no negative currents in this motor, there is no need to apply the negative voltage level $-V_{C1}$ (Figure 2d) to maintain a specific negative current level. On the other hand, the currents in the motor windings are clearly controlled, as visible from the waveforms presented in Figure 7b. Another aspect that can be seen is the effect of the switching action of the inverter devices on the *SRM* pulsation torque. As can be seen from Figure 7c, there are two different impacts. The first one is related to the high-frequency switching of the inverter devices originating from the hysteretic comparator. Since this hysteresis is low, the current ripple is also low, so the impact on the torque is also low. On the other hand, this high-frequency switching will affect the voltage applied to the motor windings but has a lower impact on the current. Due to this high frequency, the motor winding will behave as a low-pass filter. As a result, this will also attenuate the impact on the torque. However, the major problem appears during the transitions between the phase current, from which a pulsation torque will originate. This last problem can be attenuated using advanced control techniques. However, for this specific application, this is not significant. Finally, analyzing the waveforms of the input *DC* voltages applied to the drive (output voltages of the *DC*/*DC* converter) presented in Figure 7d, it is possible to see that they are balanced and stable at the reference value (set to 200 V). On the other hand, as shown in Figure 7e, the converter input current is continuous, which is one advantage considering the characteristics of the *PV* panels.

Table 1. Characteristics of the *PV* panels used in the proposed pumping system (in *STC*).

Parameter	Value
Voltage at MPP	37.4 V
Current at MPP	8.56 A
Power at MPP	320 W
Open-circuit voltage	46.7 V
Short-circuit current	9.10 A

Simulation tests in transient conditions were also carried out. In this condition, the system was suddenly connected considering the same values of the previous test, which can be seen in Figure 8 (notice that the voltages and currents of the capacitors and inductors are initially zero). Analyzing the output *DC*/*DC* converter voltage waveforms presented in Figure 8a, it is possible to see they started at 0 V and stabilized at 200 V (reference value) in a balanced state. It should be mentioned that until the output voltages reach the reference value, the pumping system is not operating. In this way, these results confirm the predicted operation of the voltage controller. Regarding the generated power from the *PV* panels, it is possible to see from Figure 8b that, starting from zero, it will increase immediately until

it reaches the *MPP*. On the other hand, it is also possible to confirm that after reaching the *MPP*, it will stay at that point. In this way, the predicted capability of the proposed *MPPT* algorithm is confirmed.

Another transient test that was considered was the solar irradiance variation. Thus, initially a solar irradiation of 700 W/m^2 was considered, increasing to 1000 W/m^2 at 1.2 s and returning again to 800 W/m^2 at 1.8 s. This irradiation profile is shown in Figure 9a. The waveform of the *SRM* motor speed is shown in Figure 9b. As expected, with the increment in the *PV* generated power (due to the increase in the irradiance), there is also an increment in the motor speed, and vice versa. The behavior of the voltage controller is also presented through the *DC*/*DC* output voltages shown in Figure 9c. Indeed, this figure shows that these voltages remain in the reference value, confirming that the balance between the generated power and the power consumption of the motor is ensured.

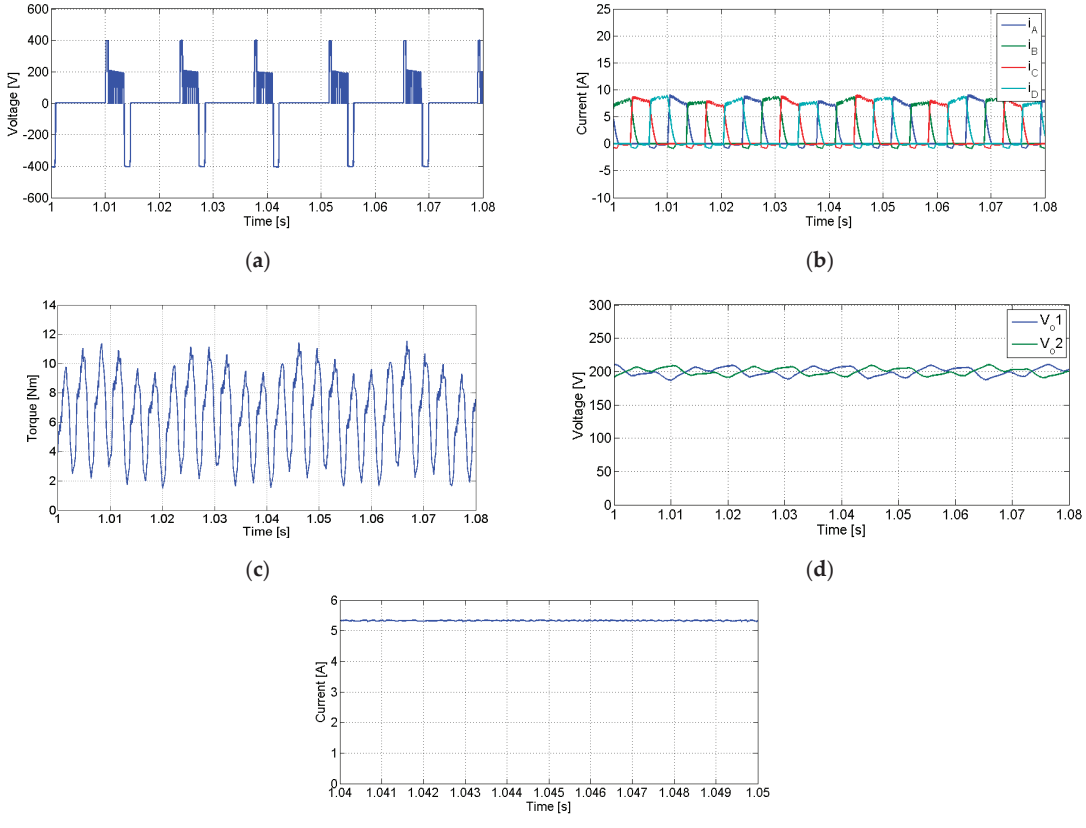

Figure 7. Obtained simulation waveforms for the tests in which an irradiance of 700 W/m^2 and an ambient temperature of 25 °C associated with the motor drive were defined: (**a**) motor winding *A* applied voltage, (**b**) currents in the motor windings, (**c**) *SRM* torque (**d**) input *DC* voltages applied to the drive, (**e**) converter input current.

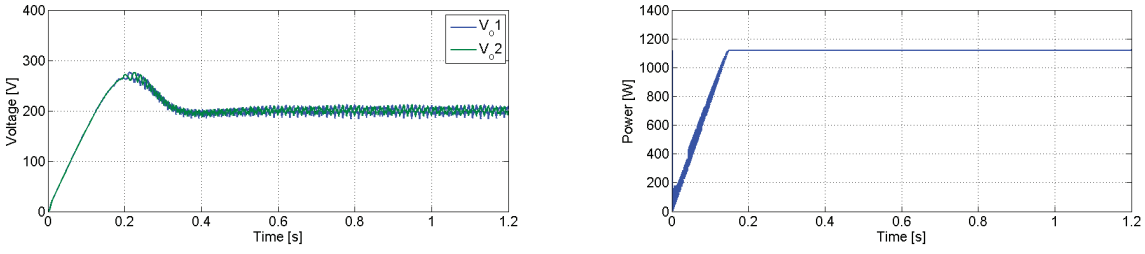

(**a**) (**b**)

Figure 8. Obtained simulation waveforms during the connection of the system (transient operation): (**a**) *DC*/*DC* output voltages, (**b**) generated *PV* power.

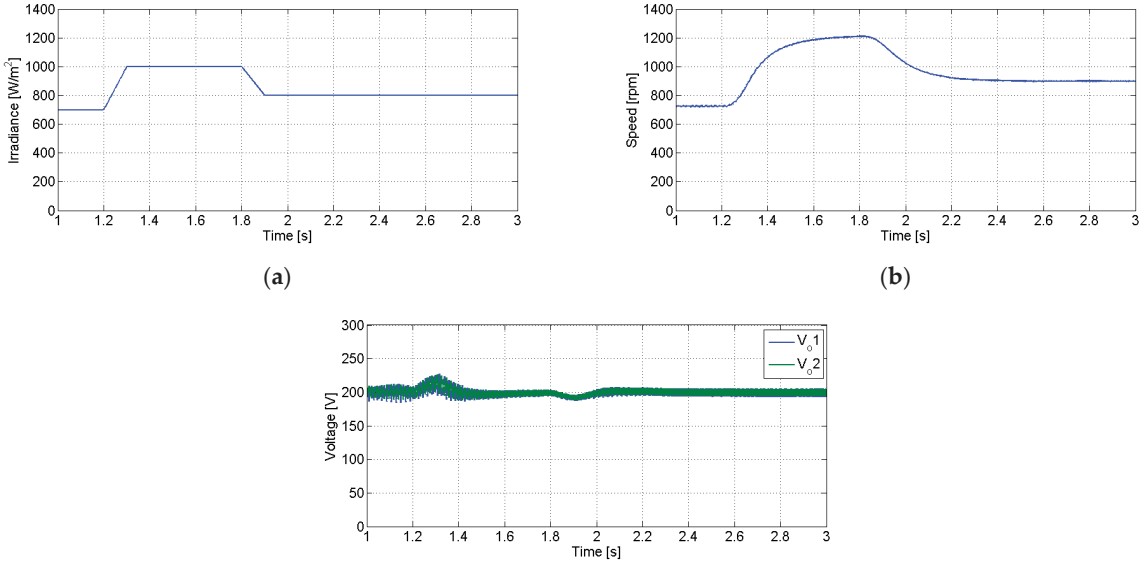

(**a**) (**b**)

(**c**)

Figure 9. Obtained simulation waveforms during the connection of the system: (**a**) solar irradiation applied to the *PV* panels, (**b**) *SRM* motor speed, (**c**) *DC*/*DC* output voltages.

Tests with respect to various irradiances applied to the *PV* panel were also carried out. Thus, in order to see the impact of these changes in the system, in Figure 10, the obtained waveforms when the irradiance changes from 1000 W/m^2 to 400 W/m^2 in steps of 200 W/m^2 are presented. In Figure 10a, the irradiance applied to the *PV* panel is presented, and Figure 10b shows the motor speed. As expected, the motor speed changes with the irradiance once the generated power also changes. In fact, the motor speed changes from 1220 rpm to 170 rpm in steps just like the irradiance. It should be stated that in pumping systems, this change in speed is generally not very important, although it must be above a specific minimum value.

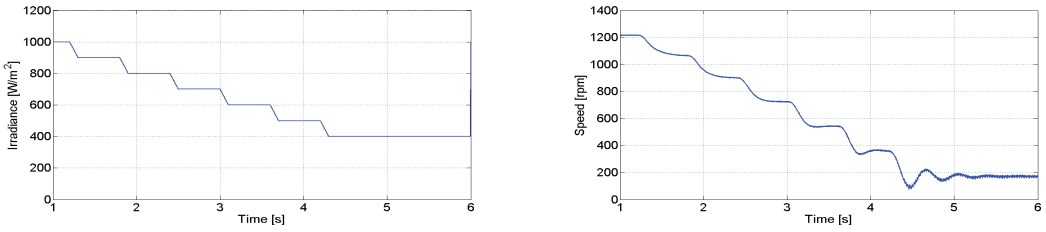

(**a**) (**b**)

Figure 10. Obtained simulation waveforms with respect to various irradiances: (**a**) solar irradiation applied to the *PV* panels, (**b**) *SRM* motor speed.

5. Experimental Results

The proposed solution was also tested using a laboratory prototype combining the power electronic converters and the *SRM*. The parameters of the components used for this prototype were the same as the ones used for the simulation tests. The *PV* panels were simulated using a controlled voltage source (EA PS8360-30 2U) in which their characteristics were programmed to obtain the typical I–V curves. An 8/6 *SRM* machine was also used. Figure 11 shows the experimental test bench with the proposed laboratorial prototype. In figure, it is possible to see: 1—the controlled voltage source (EA PS8360-30 2U); 2—the digital signal processor (DSPACE 1104) used to control the multilevel *SRM* drive and *MPPT* algorithm; 3—the gate drive circuits; 4—the *DC*/*DC* converter; 5—the multilevel *SRM* drive; 6—the auxiliary power source for the gate drive circuits; 7—the signal generator; 8—the 8/6 *SRM* machine; 9—the absolute encoder for measuring speed and rotor position; 10—the *DC* machine used to simulate the water pump; 11—the current probes and 12—the DL1540 Yokogawa oscilloscope.

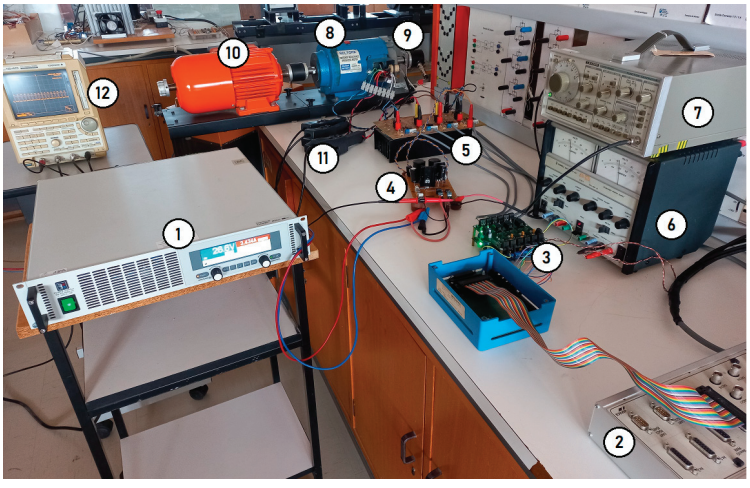

Figure 11. Photograph of the experimental test bench with the proposed laboratorial prototype: 1—controlled voltage source (EA PS8360-30 2U); 2—digital signal processor (DSPACE 1104) used to control the multilevel SRM drive; 3—gate drive circuits; 4—DC/DC converter; 5—multilevel *SRM* drive; 6—auxiliary power source for gate drive circuits; 7—signal generator; 8—8/6 *SRM* machine; 9—absolute encoder for measuring speed and rotor position; 10—*DC* machine used to simulate the water pump; 11—current probes; 12—DL1540 Yokogawa oscilloscope.

The laboratory results of the first test presented in Figure 12 were obtained in steady state considering a 700 W/m^2 irradiance and a 25 °C ambient temperature. The results shown in this figure are the voltage applied to motor winding *A* (Figure 12a) and currents in all the phases of the *SRM* (Figure 12b), as well as the output voltage (Figure 12c) and input current (Figure 12d) (applied to the *SRM* drive) of the *DC*/*DC* converter. From these waveforms, it is possible to conclude that they are similar to the ones obtained in the simulation tests. They also confirm the multilevel voltage characteristics of the *SRM* drive and continuous input current of the *DC*/*DC* converter.

Similar to the simulation tests, experimental transient tests were also performed. The first one was carried out considering the initial connection of the system. As shown in Figure 13, it is possible to conclude that the output voltage of the *DC*/*DC* converter starts at 0 V, but will rapidly achieve the desired (reference) value of 200 V. The balance of the *DC*/*DC* output capacitors voltages is also verified. It should be mentioned that, like in the simulation tests, the pumping system was only operated after the *DC*/*DC* output voltages reached the reference value.

A laboratory test in which the solar irradiance was not always constant was also performed. Thus, for this test, a first change in the solar irradiance from 700 W/m^2 to 1000 W/m^2 was implemented, then this irradiance was maintained and finally another change to 800 W/m^2 was implemented. The implemented solar irradiance, speed of the *SRM* and output voltages of the *DC*/*DC* converter results are presented in Figure 14. This figure confirms that the motor speed follows the irradiance and that the *DC*/*DC* output voltages are maintained at the reference value. These results also confirm the ones obtained in the simulation tests.

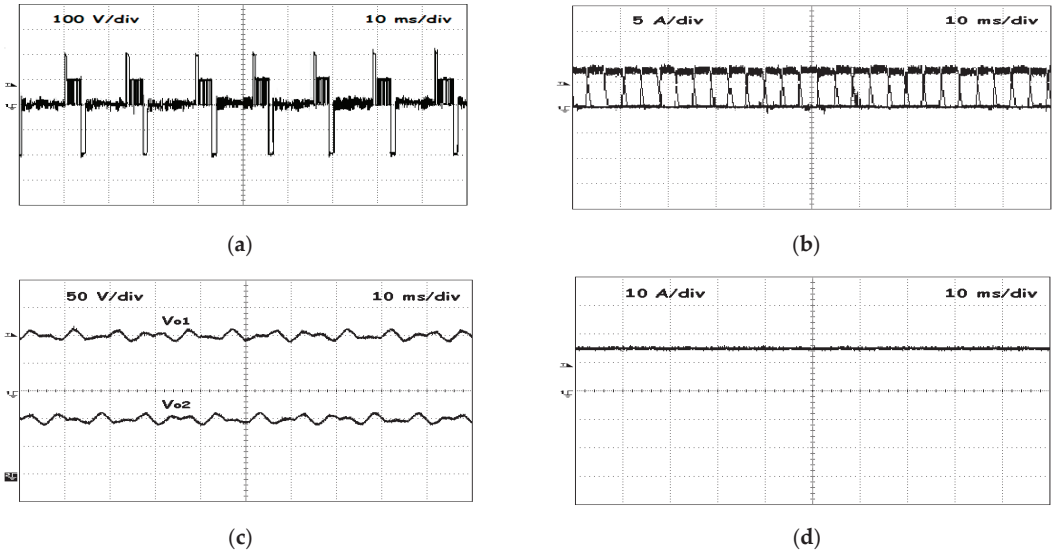

(**a**) (**b**)

(**c**) (**d**)

Figure 12. Obtained experimental waveforms for the tests in which 700 W/m^2 (irradiance) and 25 °C (ambient temperature) associated with the motor drive were defined: (**a**) voltage applied to motor winding *A*, (**b**) currents in all motor windings, (**c**) input *DC* voltages applied to the drive, (**d**) converter input current.

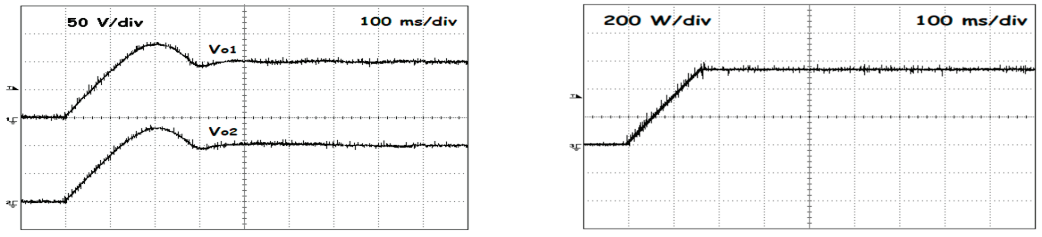

(**a**) (**b**)

Figure 13. Obtained experimental waveforms for the tests in which 700 W/m^2 (irradiance) and 25 °C (ambient temperature) during the connection of the system were defined: (**a**) *DC*/*DC* output voltages, (**b**) generated *PV* power.

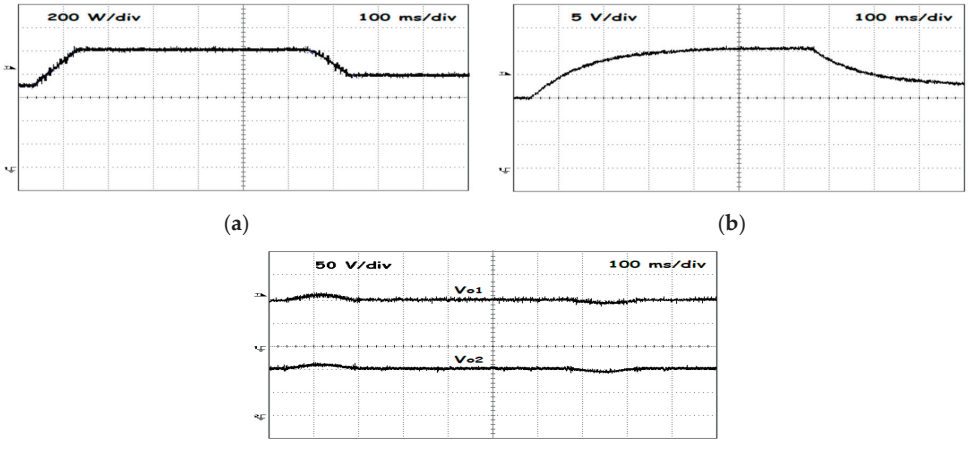

(**a**) (**b**)

(**c**)

Figure 14. Obtained experimental waveforms when the system is subject to a change in the solar irradiance: (**a**) solar irradiation applied to the *PV* panels, (**b**) speed of the *SRM* motor (22.5 V → 1000 rpm), (**c**) *DC*/*DC* output voltages.

6. Discussion

For a better analysis of the proposed system, a comparative study with other solutions is presented in this section. Since this system consists of two power electronic converters, the analysis will be focused on each of them. From the point of view of the *SRM* drive, several multilevel power converters have already been proposed. Table 2 presents the main characteristics associated with each one. As shown by this table, the asymmetric neutral point clamped (*ANPC*) [16] is the one that has more switches and diodes. This will lead to an increased cost of this drive. On the other hand, the cascaded asymmetric H-bridge [21] is the one that requires more than one independent voltage source. Thus, although requiring less diodes, this aspect will lead to an increase in the cost of this system. Among the classical multilevel structures, the T-Type [23] is considered one of the more interesting topologies. This structure requires the same number of switches, but uses a much lower number of extra diodes and does not require an extra independent voltage source. The adopted one allows for a clear reduction in the number of switches and diodes when compared with the other classical structures. Another point of view is regarding the *DC* converter associated with the *PV* panels and *SRM* drive. Another comparison is presented regarding other possible solutions. The main characteristics of each of these solutions can be seen in Table 3. From this table, it is possible to see that the one that was

adopted is among the ones that use fewer components. One of the topologies from this group that uses fewer passive components is the one from [41]. However, this topology only operates in boost mode, which can present some limitations for this kind of application. In fact, due to parasitic elements of inductors, capacitors and switching semiconductors, the voltage gain can strongly be limited, usually limited to around three times. Another interesting solution is the one from [43], although their input current is discontinuous, which, in this case, is not the best solution for *PV* panels.

Table 2. Comparison with typical multilevel power converters used in *SRM* drives.

	Topology			
Characteristics	**[16]**	**[21]**	**[23]**	**Adopted**
Number of switches	16	16	16	8
Extra diodes	32	14	8	8
Independent voltage sources	No	Yes	No	No
Cost	High	High	Medium	Low

Table 3. Comparison with *DC*/*DC* power converters used between the *PV* panels and the *SRM* drive.

						Topology	
Characteristics	**[41]**	**[42]**	**[43]**	**[44]**	**[45]**	**[46]**	**Adopted**
Voltage gain of each output	$\frac{1}{\delta}$	$\frac{1}{\delta}$	$\frac{1}{1-\delta}$	$\frac{1}{1-\delta}$	$\frac{1}{1-\delta}$	$\frac{1}{1-\delta}$	$\frac{1}{1-\delta}$
Number of switches	2	1	1	1	1	1	1
Number of diodes	3	3	2	2	4	3	2
Number of inductors	1	1	2	3	4	3	2
Number of capacitors	2	3	3	4	4	4	4
Input current	continuous	continuous	discontinuous	continuous	continuous	continuous	continuous

7. Conclusions

A water pumping system supplied by a *PV* generator and with a switched reluctance motor is presented in this paper. The purpose of this solution was to present a system with reduced costs. In this way, for the *SRM* drive, a multilevel converter with a reduced number of switches was adopted. Despite the reduced number of switches, the ability to magnetize and demagnetize the motor windings independently was maintained, as well as the provision of the DC voltage balance. For the *DC*/*DC* converter, associated with the *PV* panels and supplying energy to the motor drive, the same philosophy was adopted; it was designed with a single switch. The *DC*/*DC* converter is characterized by a dual output, which is a requirement for the *SRM* drive. On the other hand, the input current will be continuous, which is an important feature considering the use of *PV*. Associated with this converter, an *MPPT* algorithm was also implemented. The adoption of the proposed algorithm was selected due to easy implementation. In fact, it allows the use of a control law that is a function of the time derivative of the voltage and power, thus avoiding the singularities that can be found in this algorithm. Therefore, it is inclusively possible to implement this algorithm through a simple analogue circuit. The proposed system was verified through simulation and experimental tests using a laboratory prototype. These tests showed a good similarity, as well as the confirmation of the theoretical assumptions. From the theoretical assumption and performed tests, it was possible to verify that one conclusion that can be drawn from this work is that the speed of the motor is a function of the solar irradiance. This is due to the fact that by increasing solar irradiance, the generated power will also increase. In fact, tests in which the irradiance was changed from 1000 W/m^2 to 400 W/m^2 showed a change in the motor speed from 1220 rpm to 170 rpm.

Author Contributions: Conceptualization, V.F.P., H.C. and J.F.M.; methodology, V.F.P. and H.C.; simulations, V.F.P. and J.F.M.; validation, V.F.P., D.F., A.C., T.G.A. and A.P.; formal analysis, V.F.P. and J.F.M.;

investigation, V.F.P.; resources, V.F.P. and T.G.A.; data curation, V.F.P. and T.G.A.; writing—original draft preparation V.F.P., D.F. and A.C.; writing—review and editing, A.P. and A.C.; visualization, A.P. and A.C.; supervision, A.P.; project administration, J.F.M.; funding acquisition, A.P. and J.F.M. All authors have read and agreed to the published version of the manuscript.

Funding: This work was supported by national funds through the FCT—Fundação para a Ciência e a Tecnologia with reference UID/CEC/50021/2020 and UID/EEA/00066/2020.

Acknowledgments: This work was supported by national funds through the FCT—Fundação para a Ciência e a Tecnologia with reference UID/CEC/50021/2020 and UID/EEA/00066/2020.

Conflicts of Interest: The authors declare no conflict of interest.

References

1. Angadi, S.; Yaragatti, U.R.; Suresh, Y.; Raju, A.B. Comprehensive review on solar, wind and hybrid wind-PV water pumping systems-an electrical engineering perspective. *CPSS Trans. Power Electron. Appl.* **2021**, *6*, 1–19. [CrossRef]
2. Aliyu, M.; Hassan, G.; Said, S.A.; Siddiqui, M.U.; Alawami, A.T.; Elamin, I.M. A review of solar-powered water pumping systems. *Renew. Sustain. Energy Rev.* **2018**, *87*, 61–76. [CrossRef]
3. Bouzidi, B. Viability of solar or wind for water pumping systems in the Algerian Sahara regions—Case study Adrar. *Renew. Sustain. Energy Rev.* **2011**, *15*, 4436–4442. [CrossRef]
4. Liu, F.; Tait, S.; Schellart, A.; Mayfield, M.; Boxall, J. Reducing carbon emissions by integrating urban water systems and renewable energy sources at a community scale. *Renew. Sustain. Energy Rev.* **2020**, *123*, 1–14. [CrossRef]
5. Chilundo, R.J.; Neves, D.; Mahanjane, U.S. Photovoltaic water pumping systems for horticultural crops irrigation: Advancements and opportunities towards a green energy strategy for Mozambique. *Sustain. Energy Technol. Assess.* **2019**, *33*, 61–68. [CrossRef]
6. Kumar, S.S.; Bibin, C.; Akash, K.K.; Aravindan, K.; Kishore, M.; Magesh, G. Solar powered water pumping systems for irrigation: A comprehensive review on developments and prospects towards a green energy approach. *Mater. Today Proc.* **2020**, *33*, 303–307. [CrossRef]
7. Cloutier, M.; Rowley, P. The feasibility of renewable energy sources for pumping clean water in sub-Saharan Africa: A case study for Central Nigeria. *Renew. Energy* **2011**, *36*, 2220–2226. [CrossRef]
8. Mothilal Bhagavathy, S.; Pillai, G. PV Microgrid Design for Rural Electrification. *Designs* **2018**, *2*, 33. [CrossRef]
9. Kocan, S.; Rafajdus, P.; Bastovansky, R.; Lenhard, R.; Stano, M. Design and Optimization of a High-Speed Switched Reluctance Motor. *Energies* **2021**, *14*, 6733. [CrossRef]
10. Harris, M.R.; Miller, T.J.E. Comparison of design and performance parameters in switched reluctance and induction motors. In Proceedings of the Fourth International Conference on Electrical Machines and Drives Conference, London, UK, 13–15 September 1989; pp. 303–307.
11. Verma, S.; Mishra, S.; Chowdhury, S.; Gaur, A.; Mohapatra, S.; Soni, A.; Verma, P. Solar PV powered water pumping system—A review. *Mater. Today Proc.* **2021**, *46*, 5601–5606. [CrossRef]
12. Ramos, J.S.; Ramos, H.M. Solar powered pumps to supply water for rural or isolated zones: A case study. *Energy Sustain. Dev.* **2009**, *13*, 151–158. [CrossRef]
13. Ahn, J.; Lukman, G.F. Switched reluctance motor: Research trends and overview. *CES Trans. Electr. Mach. Syst.* **2018**, *2*, 339–347. [CrossRef]
14. Ellabban, O.; Abu-Rub, H. Switched reluctance motor converter topologies: A review. In Proceedings of the IEEE International Conference on Industrial Technology, Busan, Republic of Korea, 26 February 2014–1 March 2014; pp. 840–846.
15. Pires, V.F.; Pires, A.J.; Cordeiro, A.; Foito, D. A Review of the Power Converter Interfaces for Switched Reluctance Machines. *Energies* **2020**, *13*, 3490. [CrossRef]
16. Patil, D.; Wang, S.; Gu, L. Multilevel converter topologies for high-power high-speed switched reluctance motor: Performance comparison. In Proceedings of the IEEE Applied Power Electronics Conference and Exposition, Long Beach, CA, USA, 20–24 March 2016; pp. 2889–2896.
17. Deepak, M.; Janaki, G.; Bharatiraja, C. Power electronic converter topologies for switched reluctance motor towards torque ripple analysis. *Mater. Today Proc.* **2022**, *52*, 1657–1665. [CrossRef]
18. Peng, F.; Ye, J.; Emadi, A. An Asymmetric Three-Level Neutral Point Diode Clamped Converter for Switched Reluctance Motor Drives. *IEEE Trans. Power Electron.* **2017**, *32*, 8618–8631. [CrossRef]
19. Scholtz, P.A.; Gitau, M.N. Asymmetric Neutral Point Diode Clamped Topology with Reduced Component Count for Switched Reluctance Machine Drive. *Energies* **2022**, *15*, 2468. [CrossRef]
20. Yamada, N.; Hoshi, N. Experimental verification on a switched reluctance motor driven by asymmetric flying capacitor multilevel h-bridge inverter. In Proceedings of the IEEE 6th International Conference on Renewable Energy Research and Applications, San Diego, CA, USA, 5–8 November 2017; pp. 971–976.
21. Meng, R.; Wu, M. A Cascade Multilevel Converter of Switched Reluctance Motor and Its Control Timing Sequence. *Sens. Transducers* **2014**, *169*, 18–24.

22. Gengaraj, M.; Kalaivani, L.; Koodammal, K.; Krishnashini, M.; Aniana, L.; Prithi, S.D. A Comprehensive Study of Multilevel Inverter fed Switched Reluctance Motor for Torque Ripple Minimization with Multicarrier PWM Strategies. In Proceedings of the 4th International Conference on Electrical Energy Systems, Chennai, India, 7–9 February 2018; pp. 1–7.
23. Azer, P.; Bauman, J. An Asymmetric Three-Level T-Type Converter for Switched Reluctance Motor Drives in Hybrid Electric Vehicles. In Proceedings of the IEEE Transportation Electrification Conference and Expo, Detroit, MI, USA, 19–21 June 2019; pp. 1–6.
24. Lee, D.; Wang, H.; Ahn, J. An advanced multi-level converter for four-phase SRM drive. In Proceedings of the IEEE Power Electronics Specialists Conference, Rhodes, Greece, 15–19 June 2008; pp. 2050–2056.
25. Chowdhary, P.K.; Thakre, M.P. MMC based SRM Drives for Hybrid EV with Decentralized BESS. In Proceedings of the 4th International Conference on Electronics. Communication and Aerospace Technology, Coimbatore, India, 5–7 November 2020; pp. 319–325.
26. Gan, C.; Sun, Q.; Wu, J.; Kong, W.; Shi, C.; Hu, Y. MMC-Based SRM Drives with Decentralized Battery Energy Storage System for Hybrid Electric Vehicles. *IEEE Trans. Power Electron.* **2019**, *34*, 2608–2621. [CrossRef]
27. Gaafar, M.A.; Abdelmaksoud, A.; Orabi, M.; Chen, H.; Dardeer, M. Switched Reluctance Motor Converters for Electric Vehicles Applications: Comparative Review. *IEEE Trans. Transp. Electrif.* **2022**. [CrossRef]
28. Zan, X.; Xu, G.; Zhao, T.; Wang, R.; Dai, L. Multi-Battery Block Module Power Converter for Electric Vehicle Driven by Switched Reluctance Motors. *IEEE Access* **2021**, *9*, 140609–140618. [CrossRef]
29. Pires, V.F.; Foito, D.; Pires, A.J.; Cordeiro, A.; Martins, J.F. An 8/6 SRM Drive with a Multilevel Converter Based on an NPC Structure and Designed to Provide Transistor Fault Tolerant Capability. In Proceedings of the 16th IEEE International Conference on Compatibility, Power Electronics and Power Engineering, Birmingham, UK, 29 June 2022–1 July 2022; pp. 1–6.
30. Zan, X.; Wu, N.; Xu, R.; Cui, M.; Jiang, Z.; Ni, K.; Alkahtani, M. Design and Analysis of a Novel Converter Topology for Photovoltaic Pumps Based on Switched Reluctance Motor. *Energies* **2019**, *12*, 2526. [CrossRef]
31. Mishra, A.K.; Singh, B.; Kim, T. An Efficient and Credible Grid-Interfaced Solar PV Water Pumping System with Energy Storage. *IEEE J. Photovolt.* **2022**, *12*, 880–887. [CrossRef]
32. Chaurasiya, S.K.; Bhattacharya, A.; Das, S. Reduced switch multilevel converter topology to improve magnetization and demagnetization characteristics of an SRM. In Proceedings of the IEEE International Conference on Power Electronics, Smart Grid, and Renewable Energy, Trivandrum, India, 2–5 January 2022; pp. 1–6.
33. Rao, M.N.; Karthick, N.; Rao, A.M. Fault Tolerant Ability of A Multi Level Inverter Fed Three Phase Induction Motor for Water Pumping Application. In Proceedings of the 7th International Conference on Electrical Energy Systems, Chennai, India, 11–13 February 2021; pp. 212–216.
34. Koreboina, V.B.; Narasimharaju, B.L.; Kumar, D.M.V. Performance investigation of simplified PWM MPPT approach for direct PV-fed switched reluctance motor in water pumping system. *IET Electr. Power Appl.* **2017**, *11*, 1645–1655. [CrossRef]
35. Wang, X.; Gan, C.; Hu, Y.; Cao, W.; Chen, X. Renewable energy-fed switched reluctance motor for PV pump applications. In Proceedings of the 2014 IEEE Conference and Expo Transportation Electrification Asia-Pacific, Beijing, China, 31 August 2014—3 September 2014; pp. 1–6.
36. Oshaba, A.S.; Ali, E.S.; Elazim, S. PI controller design for MPPT of photovoltaic system supplying SRM via BAT search algorithm. *Neural Comput. Appl.* **2017**, *28*, 651–667. [CrossRef]
37. Oshaba, A.S.; Ali, E.S.; Abd Elazim, S.M. MPPT control design of PV system supplied SRM using BAT search algorithm. *Sustain. Energy Grids Netw.* **2015**, *2*, 51–60. [CrossRef]
38. Oliver, J.S.; David, P.W.; Balachandran, P.K.; Mihet-Popa, L. Analysis of Grid-Interactive PV-Fed BLDC Pump Using Optimized MPPT in DC–DC Converters. *Sustainability* **2022**, *14*, 7205. [CrossRef]
39. Yalavarthi, A.; Singh, B. Sensorless SRM driven Solar Irrigation Pump with Grid-Support Using Vienna Rectifier. In Proceedings of the 3rd International Conference on Energy, Power and Environment: Towards Clean Energy Technologies, Shillong, Meghalaya, India, 5–7 March 2021; pp. 1–6.
40. Cordeiro, A.; Pires, V.F.; Foito, D.; Pires, A.J.; Martins, J.F. Three-level quadratic boost DC-DC converter associated to a SRM drive for water pumping photovoltaic powered systems. *Sol. Energy* **2020**, *209*, 42–56. [CrossRef]
41. Mishra, A.K.; Singh, B. An Improved Control Technique for Grid Interactive 4-Phase SRM Driven Solar Powered WPS Using Three-Level Boost Converter. *IEEE Trans. Ind. Inform.* **2021**, *17*, 290–299. [CrossRef]
42. Sulake, N.R.; Devarasetty Venkata, A.K.; Choppavarapu, S.B. FPGA Implementation of a Three-Level Boost Converter-fed Seven-Level DC-Link Cascade H-Bridge inverter for Photovoltaic Applications. *Electronics* **2018**, *7*, 282. [CrossRef]
43. Mishra, A.K.; Singh, B. Solar Photovoltaic Array Dependent Dual Output Converter Based Water Pumping Using Switched Reluctance Motor Drive. *IEEE Trans. Ind. Appl.* **2017**, *53*, 5615–5623. [CrossRef]
44. Mishra, A.K.; Singh, B. Design of solar-powered agriculture pump using new configuration of dual-output buck–boost converter. *IET Renew. Power Gener.* **2018**, *12*, 1640–1650. [CrossRef]
45. Luo, F.L. Double-output Luo converters, an advanced voltage-lift technique. *IEE Proc. -Electr. Power Appl.* **2000**, *147*, 469–485. [CrossRef]
46. Marjani, J.; Imani, A.; Hekmati, A.; Afjei, E. A new dual output DC-DC converter based on SEPIC and Cuk converters. In Proceedings of the 2016 International Symposium on Power Electronics, Electrical Drives, Automation and Motion (SPEEDAM), Capri, Italy, 22–24 June 2016; pp. 946–950.

47. Joseph, A.; Kim, S.M.; Lee, S.; Dominic, A.; Lee, K.B. Boost multi-level NPC-fed VS large rated asynchronous pumped storage hydro-generating unit. *IET Electr. Power Appl.* **2019**, *13*, 1488–1496. [CrossRef]
48. Rahman, S.; Meraj, M.; Iqbal, A.; Tariq, M.; Maswood, A.; Ben-Brahim, L.; Al-Ammari, R. Design and Implementation of Cascaded Multilevel qZSI Powered Single-Phase Induction Motor for Isolated Grid Water Pump Application. *IEEE Trans. Ind. Appl.* **2020**, *56*, 1907–1917. [CrossRef]
49. Pires, V.F.; Foito, D.; Cordeiro, A.; Chaves, M.; Pires, A.J. PV Generator-Fed Water Pumping System Based on a SRM with a Multilevel Fault-Tolerant Converter. *Energies* **2022**, *15*, 1–19. [CrossRef]
50. Haq, S.; Biswas, S.P.; Kamal Hosain, M.; Islam, M.R.; Ashib Rahman, M.; Muttaqi, K.M. A Modified PWM Scheme to Improve the Power Quality of NPC Inverter Based Solar PV Fed Induction Motor Drive for Water Pumping. In Proceedings of the IEEE Industry Applications Society Annual Meeting, IAS 2021, Vancouver, BC, Canada, 10–14 October 2021; pp. 1–6.
51. Bollipo, R.B.; Mikkili, S.; Bonthagorla, P.K. Hybrid, optimal, intelligent and classical PV MPPT techniques: A review. *CSEE J. Power Energy Syst.* **2021**, *7*, 9–33.
52. Pathy, S.; Subramani, C.; Sridhar, R.; Thentral, T.M.T.; Padmanaban, S. Nature-Inspired MPPT Algorithms for Partially Shaded PV Systems: A Comparative Study. *Energies* **2019**, *12*, 1451. [CrossRef]
53. Radhakrishnan, R.K.G.; Marimuthu, U.; Balachandran, P.K.; Shukry, A.M.M.; Senjyu, T. An Intensified Marine Predator Algorithm (MPA) for Designing a Solar-Powered BLDC Motor Used in EV Systems. *Sustainability* **2022**, *14*, 14120. [CrossRef]
54. Pires, V.F.; Foito, D.; Pires, A.J.; Cordeiro, A.; Martins, J.F.; Chen, H. Multilevel Converter Fed SRM Drive for Single Stage PV Array Based Water Pumping. In Proceedings of the 45th Annual Conference of the IEEE Industrial Electronics Society (IECON 2019), Lisbon, Portugal, 14–17 October 2019; pp. 6495–6500.
55. Markkassery, S.; Saradagi, A.; Mahindrakar, A.D.; Lakshminarasamma, N.; Pasumarthy, R. Modeling, Design and Control of Non-isolated Single-Input Multi-Output Zeta–Buck–Boost Converter. *IEEE Trans. Ind. Appl.* **2020**, *56*, 3904–3918.
56. Pina, M.; Pires, V.F. Grid-Connected PV System Using a T-Type qZS Inverter with an Integral Time Derivative Approach to Ensure MPP and Decoupled Current Control. In Proceedings of the 2020 International Young Engineers Forum, Costa da Caparica, Portugal, 3 July 2020; pp. 38–43.

energies

MDPI

Article

Investigation of a Cup-Rotor Permanent-Magnet Doubly Fed Machine for Extended-Range Electric Vehicles

Chaoying Xia *, Jiaxiang Bi and Jianning Shi

School of Electrical and Information Engineering, Tianjin University, No. 92 Weijin Road, Tianjin 300072, China
* Correspondence: xiachaoying@126.com; Tel.: +86-182-2235-6392

Abstract: This paper investigates a cup-rotor permanent-magnet doubly fed machine (CRPM-DFM) for extended-range electric vehicles (EREVs). The topology and operating principle of the powertrain system based on CRPM-DFM are introduced. Then, the mathematical model of CRPM-DFM is established and the feedback linearization control of CRPM-DFM is given to realize the decoupling control of flux and torque. Moreover, the torque characteristic of CRPM-DFM is analyzed and the load torque boundaries with sinusoidal steady-state solution of CRPM-DFM is deduced. In addition, the MTPA control is derived to improve the efficiency of CRPM-DFM, and the efficiency of CRPM-DFM regarding various operating modes is investigated. Furthermore, the speed optimization strategy of ICE is proposed to reduce fuel consumption. Finally, the driving performance and fuel economy of the powertrain system are verified by simulation.

Keywords: cup-rotor permanent-magnet doubly fed machine; extended-range electric vehicle; speed coupler; load torque boundary; efficiency; fuel consumption

1. Introduction

In recent years, to alleviate the pressure of energy shortage and environmental pollution, new-energy vehicles have been widely used [1–3]. New-energy vehicles could be mainly arranged in three classes as follows: pure electric vehicles, hybrid electric vehicles and extended-range electric vehicles (EREVs). Pure electric vehicles can achieve zero emissions, but the disadvantages such as long charging time, high battery capacity and poor endurance are still the bottlenecks preventing the widespread applications of pure electric vehicles [4]. Hybrid electric vehicles have the advantages of high endurance ability and low battery capacity, but the powertrain system structure of hybrid electric vehicles is complex and costly. Moreover, since the main power of hybrid electric vehicles is provided by an internal combustion engine (ICE), the effects of energy conservation and emission reduction are limited [5]. EREVs with high endurance ability, middle battery capacity and lower emissions have the advantages of pure electric vehicles and hybrid electric vehicles and avoid the disadvantages of them. Therefore, EREVs have attracted extensive attention [6,7].

As shown in Figure 1, the powertrain system of EREVs includes battery packs, traction motor and a range extender composed of an ICE and a generator [8]. The range extender and the traction motor in conventional EREVs are independent mechanically. When the battery is sufficient, the vehicle operates in pure electric state; when the battery is low, the range extender supplies power to the battery and traction motor, thus increasing the range of the vehicle [9].

However, the existence of a range extender will reduce the interior space and increase the complexity and the cost of the powertrain system [10–13]. In addition, the output power of the ICE needs to be converted from mechanical power to electrical power and then from electrical power to mechanical power to drive the vehicle, which will reduce the efficiency of the system [14,15].

Citation: Xia, C.; Bi, J.; Shi, J. Investigation of a Cup-Rotor Permanent-Magnet Doubly Fed Machine for Extended-Range Electric Vehicles. *Energies* **2023**, *16*, 2455. https://doi.org/10.3390/en16052455

Academic Editors: Loránd Szabó and Feng Chai

Received: 10 January 2023
Revised: 24 February 2023
Accepted: 27 February 2023
Published: 4 March 2023

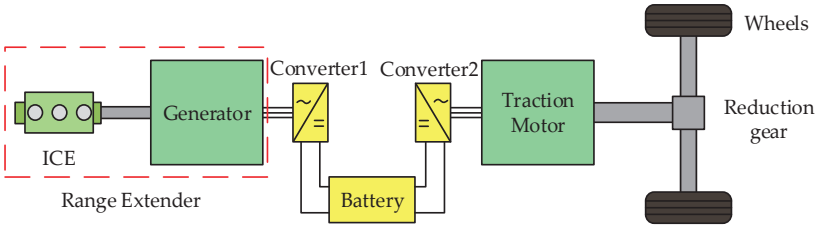

Figure 1. Structure diagram of the powertrain system of EREVs.

Dual-mechanical port machines (DPMs) can be employed to make the powertrain system more compact, which integrates the generator and the traction motor together. Nevertheless, the DPMs usually need brushes and slip rings to feed current, which causes the inevitable problems of frequent maintenance and friction loss [16]. Brushless doubly fed machines (BDFMs) have obvious advantages of flexible power flow, improved efficiency and extended torque-speed characteristics, which make them a potentially promising candidate for new-energy vehicle applications [17].

By incorporating the concept of the DPMs into the BDFMs, a cup-rotor permanent-magnet doubly fed machine (CRPM-DFM) was proposed in [18]. The CRPM-DFM integrates the generator and the traction motor together, which saves interior space, reduces vehicle weight, and improves the powertrain system's compactness. Moreover, the CRPM-DFM has no brush and slip ring, which improves the reliability and cost-effectiveness of the powertrain system. In addition, the CRPM-DFM transmits most of the output power of the ICE directly to the drive shaft in the form of electromagnetic power, which improves the efficiency of the powertrain system.

At present, there is little performance analysis of CRPM-DFM. The heat dispersion of the CRPM-DFM is studied, and a liquid cooling strategy of the CRPM-DFM is proposed in [18]. The equivalent circuit of the CRPM-DFM is given in [19]. The mathematical model of the CRPM-DFM under a two-phase rotor coordinate system has been established, and the open-loop working performance is analyzed [20]. However, different from the above studies, based on the previous work of the first author of this paper on modeling and control methods of a brushless doubly fed machine, the state space model of the CRPM-DFM in a synchronous coordinate system has been established. Then the static load capacity of the CRPM-DFM is analyzed, and the vector control strategy is proposed in [21].

To maximize the performance of CRPM-DFM, the appropriate machine control method should be designed. CRPM-DFM evolved from BDFM. The control method design of CRPM-DFM can refer to the existing research results of BDFM. The control methods of BDFM include scalar control, direct torque control and vector control [22–24]. The scalar control method has poor disturbance-rejection ability and is hardly used at present. A direct torque control method is simple, but it has the disadvantages of large computation and large torque ripple. Vector control is widely used and can be realized based on a double synchronous coordinate system and unified synchronous coordinate system, respectively. The speed adjustment range of vector control based on the double synchronous coordinate system is narrow, which is not suitable for the electric-vehicle driving field. The vector control based on the unified synchronous coordinate system is first oriented according to the magnetic field of the control machine or the power machine. Then, the variables of each machine are placed in a unified coordinate system by using the slip frequency relation between the windings of the two machines under the steady-state condition, and the BDFM is controlled by power machine stator field orientation, but there is coupling between flux and torque. To solve this problem, feedback linearization control of a brushless doubly fed motor is proposed in the literature [25]. In addition to the machine torque, the vector sum of the rotor flux of the power machine and the control machine is also selected as the control object, which realizes the decoupling control of the rotor flux and the torque. Besides, the literature [26] proposes the maximum torque per ampere (MTPA) control of

BDFM, which minimizes the stator current amplitude when the output torque is the same, thus improving machine efficiency.

The motivation of this paper is to analysis the performance of the CRPM-DFM, which includes the operating principle, torque characteristics, and efficiency of the CRPM-DFM under different operating modes. In addition, to improve the driving performance and fuel economy of the powertrain system, the control strategy of CRPM-DFM and speed optimization strategy of ICE are proposed.

This paper is organized as follows: Section 2 introduces the structure, operating principle and operating modes of the powertrain system based on CRPM-DFM. Section 3 establishes the mathematical model and derives the feedback-linearization control method of CRPM-DFM. Section 4 analyzes the torque characteristic and derives the load torque boundaries with the sinusoidal steady-state solution of CRPM-DFM. Section 5 proposes the MTPA control method and analyzes the efficiency of CRPM-DFM in different operating modes. Section 6 proposes a speed optimization strategy of ICE. Section 7 built a simulation platform of the EREVs' powertrain system based on CRPM-DFM and verifies the driving performance and fuel economy of the powertrain system. Section 8 is the summary of the whole paper.

2. The Powertrain System Based on CRPM-DFM

2.1. Structure and Operating Principle of the Powertrain System Based on CRPM-DFM

The construction of CRPM-DFM and the structure diagram of the powertrain system based on the CRPM-DFM are shown in Figure 2. It can be seen that the powertrain system based on the CRPM-DFM is constructed by an ICE, a CRPM-DFM, a bidirectional converter module, and a battery pack, where the CRPM-DFM consists of a wound stator, a rotating permanent-magnet stator and a cup rotor. The connection between the cup-rotor windings is a reverse phase sequence. The ICE is connected to the rotating permanent-magnet stator through a clutch. The reduction gear is connected to the cup rotor for driving the vehicle. The bidirectional converter is connected to the wound stator through which electrical energy is absorbed from or charged to the battery. The mechanical lock can be controlled independently, either to lock the permanent-magnet stator and cup rotor into one, or to allow them to rotate independently, in conjunction with the engagement or disengagement of the clutch, to achieve different operating modes.

The power machine is a permanent-magnet synchronous motor whose stator can be rotated, including the cup-rotor inner winding and the permanent-magnet stator and the pole number of p_p; the control machine is an asynchronous machine, including the wound stator and the outer winding of cup rotor and the pole number of p_c. Among them, there is only an electrical connection between the inner and outer windings of the cup rotor and no magnetic coupling.

When the cup rotor and permanent-magnet stator can rotate independently, the CRPM-DFM is operating in doubly fed mode. Since the rotor windings are connected in reverse phase sequence, the air-gap magnetic fields on both sides of the cup rotor rotate in reverse at the same angular velocity relative to the rotor when the CRPM-DFM is running. Therefore, the cup-rotor speed can be obtained as:

$$n_{\mathrm{r}} = \frac{p_{\mathrm{p}} n_{\mathrm{m}} + 60 f_{\mathrm{c}}}{p_{\mathrm{p}} + p_{\mathrm{c}}} \tag{1}$$

From Equation (1), the cup rotor speed can be obtained according to the power supply frequency of the wound stator and the permanent-magnet stator speed. When $f_{\mathrm{c}} > 0$, it is said that the CRPM-DFM runs in super-synchronous mode; when $f_{\mathrm{c}} < 0$, it runs in sub-synchronous mode, and when $f_{\mathrm{c}} = 0$, in synchronous mode.

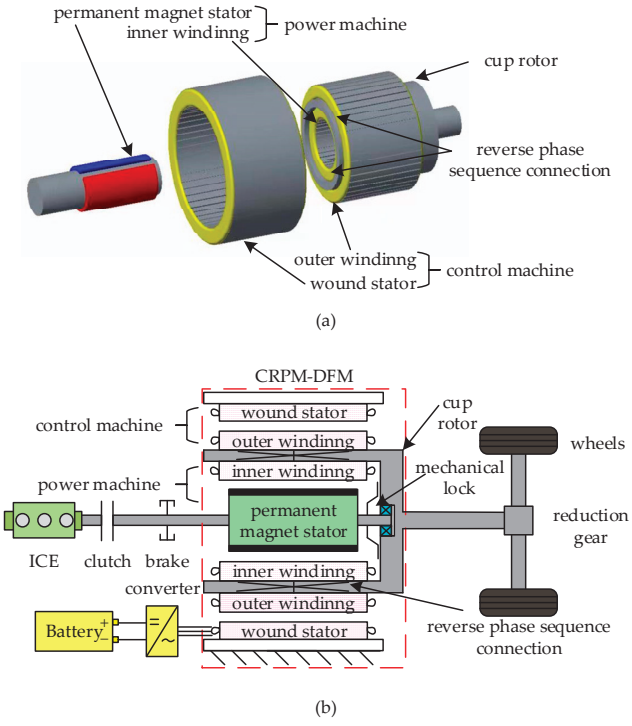

Figure 2. Construction of CRPM-DFM and structure diagram of the powertrain system. (**a**) Construction of CRPM-DFM; (**b**) structure diagram of the powertrain system based on CRPM-DFM.

The sum of the torque acting on the cup rotor by the power machine and the control machine is the output torque of the cup rotor, that is:

$$T_e = T_{ec} + T_{ep} \tag{2}$$

Ignoring the machine losses, the input and output power of the CRPM-DFM meet the following relation.

$$n_r T_e = n_m T_{ep} + \frac{60 f_c}{p_c} T_{ec} \tag{3}$$

Combining Equations (1)–(3), the relationship can be obtained that the electromagnetic torques of the power machine and control machine are proportional to their pole pairs.

$$\frac{T_{ec}}{T_{ep}} = \frac{p_c}{p_p} \tag{4}$$

It can be seen from Equations (1)–(4) that the CRPM-DFM is a speed coupler similar to a planetary gear, in that the ratio of the pole number between the power machine and control machine is equal to the ratio of the tooth number between the ring gear and sun gear, and the electromagnetic torques of the wound stator and permanent magnet stator applied to the cup rotor corresponds to the torques of the ring gear and sun gear applied to the planet carrier, respectively. When the CRPM-DFM works in super-synchronous mode (the magnetic fields of both the power machine and control machine rotate in the positive direction), the power required by the vehicle is equal to the sum of the power output of the battery and the power output of the ICE; when the CRPM-DFM works in synchronous mode (the power machine magnetic field rotates in the positive direction, and the control machine magnetic field is stationary), the power required by the vehicle is provided by the

ICE and the battery is not working; when the CRPM-DFM works in sub-synchronous mode (the power machine magnetic field rotates in the positive direction, and the control machine magnetic field rotates in the reverse direction), the power output of the ICE is equal to the sum of the power required by the vehicle and the power absorbed by the battery.

For the powertrain system based on CRPM-DFM, in doubly fed mode, the torque of the ICE is equal to the torque of the power machine. Hence, according to Equations (2) and (4), the relationship of the torques of cup rotor and ICE can be obtained.

$$\frac{T_{\text{ice}}}{T_{\text{e}}} = \frac{p_{\text{p}}}{p_{\text{c}} + p_{\text{p}}} \tag{5}$$

In the configuration of the powertrain system based on CRPM-DFM, Equation (5) has certain practical significance on how to choose the size of CRPM-DFM and ICE. In the application of EREVs, the power of ICE is relatively small. In this design, the rated power of ICE is slightly larger than the average power of the driving vehicle, and the shortage of peak power and peak torque is made up by the control machine. In addition, the control machine also needs to meet the power and torque requirements under pure electric driving mode, so $p_{\text{c}} = 3$,$p_{\text{p}} = 1$.

2.2. Basic Operating Modes of the Powertrain System Based on CRPM-DFM

When the locking device locks the rotor and the permanent magnet into one, or enables them to rotate independently, the CRPM-DFM has two working modes: asynchronous mode and doubly fed mode.

In asynchronous mode, the rotor and the permanent magnet are locked together. At this time, there is no electromagnetic induction between the rotor winding and the magnetic field generated by the permanent magnet, and the power machine does not output power. The CRPM-DFM is equivalent to an asynchronous machine with rotor series resistance and inductance. Since the permeability of the permanent magnet stator and the air is approximately equal, the air gap of the control machine is much smaller than that of the power machine. In this case, the inductance of the power machine rotor is very small, the armature reaction is weak and the magnetic circuit of power machine will not saturate because of a large current.

In doubly fed mode, the rotor and the permanent magnet rotate independently, and the torque direction of the two machines is the same, but when the power supply frequency of control machine f_{c} is greater than zero or less than zero, the power flow of the control machine is reversed, corresponding to the discharging or charging of the battery. The vehicle-requested torque is proportionally distributed to the power machine and control machine. By controlling f_{c}, the ICE speed optimization can be realized to reduce fuel consumption and restrict the fluctuation of battery SOC simultaneously.

As shown in Figure 2, the CRPM-DFM is used for a vehicle's hybrid power plant. The asynchronous mode is only used for pure electric mode to drive vehicles or brake vehicles, and to start the ICE. The doubly fed mode is only used for driving vehicles and stopping to charge batteries. Taking forward driving as an example, the conversion sequence from doubly fed mode to asynchronous mode is as follows: release the throttle $\rightarrow$ drive torque returns to zero $\rightarrow$ press the brake pedal $\rightarrow$ release the clutch $\rightarrow$ the brake makes the permanent magnet stator speed slow down to the same speed as the cup rotor $\rightarrow$ the lock device locks the permanent magnet stator and the cup rotor $\rightarrow$ the motor operates in asynchronous mode; on the contrary, the conversion sequence from asynchronous mode to doubly fed mode is as follows: release the brake pedal $\rightarrow$ brake torque returns to zero $\rightarrow$ press down the accelerator pedal $\rightarrow$ release the locking device $\rightarrow$ clutch closes $\rightarrow$ the CRPM-DFM works in doubly fed mode.

Because the control method of the asynchronous mode is the same as that of a general asynchronous motor, we will not repeat it here. The control method and characteristics of CRPM-DFM in doubly fed mode are discussed in the following part. As for the content of parking charging, only an efficiency map is provided in this paper.

3. Mathematical Model and Feedback Linearization Control of CRPM-DFM

This section establishes the mathematical model of CRPM-DFM as the basis for the following analysis and design at first. Then, to decouple the rotor flux and the torque, feedback linearization control is solved.

3.1. Mathematical Model of CRPM-DFM

By adopting the equal power transformation and considering counterclockwise rotation as positive, the relationship between each coordinate system can be obtained as shown in Figure 3.

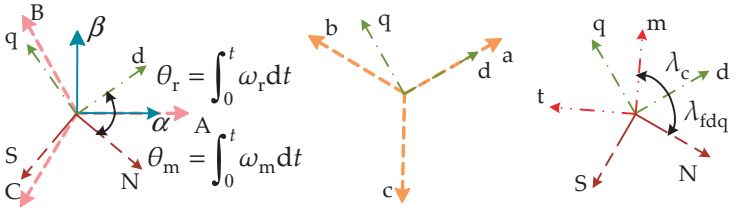

Figure 3. The relationship between the coordinate systems: (**a**) the relationship between the static stator three-phase coordinate system, the static stator two-phase coordinate system and the rotor dq coordinate system; (**b**) the relationship between the rotor dq coordinate system and the rotor three-phase coordinate system; (**c**) the relationship between the rotor dq coordinate system and the synchronous mt coordinate system.

In the rotor dq coordinate system, the voltage models of the power machine and control machine are as follows.

$$\begin{cases} \boldsymbol{u}_{cs}^{dq} = (r_{cs} + jp_c\omega_r l_{cs})\boldsymbol{i}_{cs}^{dq} + jp_c\omega_r l_{cm}\boldsymbol{i}_{cr}^{dq} + l_{cs}\dot{\boldsymbol{i}}_{cs}^{dq} + l_{cm}\dot{\boldsymbol{i}}_{cr}^{dq} \\ \boldsymbol{u}_{cr}^{dq} = r_{cr}\boldsymbol{i}_{cr}^{dq} + l_{cm}\dot{\boldsymbol{i}}_{cs}^{dq} + l_{cr}\dot{\boldsymbol{i}}_{cr}^{dq} \\ \boldsymbol{u}_{pr}^{dq} = r_{pr}\boldsymbol{i}_{pr}^{dq} + l_{pr}\dot{\boldsymbol{i}}_{pr}^{dq} + j\dot{\lambda}_{fdq}\boldsymbol{\psi}_f^{dq} \end{cases} \tag{6}$$

where $\dot{\lambda}_{fdq}$ is the electric angular velocity of the permanent magnet stator relative to the cup rotor, and $\dot{\lambda}_{fdq} = p_p\omega_m - p_p\omega_r$.

According to the inverted phase sequence of the cup rotor windings, the relation of rotor voltage and current between the control machine and the power machine in the rotor dq coordinate system is as follows.

$$\begin{cases} \boldsymbol{u}_{cr}^{dq} = \overline{\boldsymbol{u}}_{pr}^{dq} \\ \boldsymbol{i}_{cr}^{dq} = -\overline{\boldsymbol{i}}_{pr}^{dq} \end{cases} \tag{7}$$

Taking the control machine as the reference, the variables of the power machine can be redefined after taking negative conjugate transformation, as follows.

$$\begin{cases} \boldsymbol{u}'^{dq}_{pr} = -\overline{\boldsymbol{u}}_{pr}^{dq} = -\boldsymbol{u}_{cr}^{dq} \\ \boldsymbol{i}'^{dq}_{pr} = -\overline{\boldsymbol{i}}_{pr}^{dq} = \boldsymbol{i}_{cr}^{dq} = \boldsymbol{i}_r^{dq} \\ \boldsymbol{\psi}'^{dq}_{f} = -\overline{\boldsymbol{\psi}}_f^{dq} \end{cases} \tag{8}$$

According to Equations (6) and (8), the CRPM-DFM's mathematical model in the rotor dq coordinate system is as follows.

$$\begin{cases} \boldsymbol{u}_{\mathrm{cs}}^{\mathrm{dq}} = (r_{\mathrm{cs}} + \mathrm{j}p_{\mathrm{c}}\omega_{\mathrm{r}}l_{\mathrm{cs}})\boldsymbol{i}_{\mathrm{cs}}^{\mathrm{dq}} + \mathrm{j}p_{\mathrm{c}}\omega_{\mathrm{r}}l_{\mathrm{cm}}\boldsymbol{i}_{\mathrm{r}}^{\mathrm{dq}} + l_{\mathrm{cs}}\dot{\boldsymbol{i}}_{\mathrm{cs}}^{\mathrm{dq}} + l_{\mathrm{cm}}\dot{\boldsymbol{i}}_{\mathrm{r}}^{\mathrm{dq}} \\ 0 = r_{\mathrm{r}}\boldsymbol{i}_{\mathrm{r}}^{\mathrm{dq}} + l_{\mathrm{r}}\dot{\boldsymbol{i}}_{\mathrm{r}}^{\mathrm{dq}} + l_{\mathrm{cm}}\dot{\boldsymbol{i}}_{\mathrm{cs}}^{\mathrm{dq}} - \mathrm{j}\dot{\boldsymbol{\lambda}}_{\mathrm{fdq}}\boldsymbol{\psi}'^{\mathrm{dq}}_{\mathrm{f}} \end{cases} \tag{9}$$

where $r_{\mathrm{r}} = r_{\mathrm{cr}} + r_{\mathrm{pr}}$ and $l_{\mathrm{r}} = l_{\mathrm{cr}} + l_{\mathrm{pr}}$.

Equation (9) is a four-order model. After the negative conjugate operation of the variables of the power machine, all variables of CRPM-DFM rotate in the same direction with respect to the rotor dq coordinate system, which is convenient for the following research and analysis of the CRPM-DFM.

From Equation (9), the state-space model of CRPM-DFM in rotor dq coordinate system can be obtained.

$$\begin{bmatrix} \dot{\boldsymbol{i}}_{\mathrm{cs}}^{\mathrm{dq}} \\ \dot{\boldsymbol{i}}_{\mathrm{r}}^{\mathrm{dq}} \end{bmatrix} = \boldsymbol{A}^{\mathrm{dq}} \begin{bmatrix} \boldsymbol{i}_{\mathrm{cs}}^{\mathrm{dq}} \\ \boldsymbol{i}_{\mathrm{r}}^{\mathrm{dq}} \end{bmatrix} + \boldsymbol{B}^{\mathrm{dq}} \begin{bmatrix} \boldsymbol{u}_{\mathrm{cs}}^{\mathrm{dq}} \\ \boldsymbol{\psi}'^{\mathrm{dq}}_{\mathrm{f}} \end{bmatrix} \tag{10}$$

where $\boldsymbol{A}^{\mathrm{dq}} = \frac{1}{K}\begin{bmatrix} -l_{\mathrm{r}}(r_{\mathrm{cs}} + \mathrm{j}p_{\mathrm{c}}\omega_{\mathrm{r}}l_{\mathrm{cs}}) & l_{\mathrm{cm}}(r_{\mathrm{r}} - \mathrm{j}p_{\mathrm{c}}\omega_{\mathrm{r}}l_{\mathrm{r}}) \\ l_{\mathrm{cm}}(r_{\mathrm{cs}} + \mathrm{j}p_{\mathrm{c}}\omega_{\mathrm{r}}l_{\mathrm{cs}}) & -l_{\mathrm{cs}}r_{\mathrm{r}} + \mathrm{j}p_{\mathrm{c}}\omega_{\mathrm{r}}l_{\mathrm{cm}}^2 \end{bmatrix}$, $\boldsymbol{B}^{\mathrm{dq}} = \frac{1}{K}\begin{bmatrix} l_{\mathrm{r}} & -\mathrm{j}l_{\mathrm{cm}}\dot{\lambda}_{\mathrm{fdq}} \\ -l_{\mathrm{cm}} & \mathrm{j}l_{\mathrm{cs}}\dot{\lambda}_{\mathrm{fdq}} \end{bmatrix}$ and $K = l_{\mathrm{cs}}l_{\mathrm{r}} - l_{\mathrm{cm}}^2$.

The electromagnetic torque of CRPM-DFM is:

$$T_{\mathrm{e}} = T_{\mathrm{ec}} + T_{\mathrm{ep}} = p_{\mathrm{c}}l_{\mathrm{cm}}\mathrm{Im}\left\{\bar{\boldsymbol{i}}_{\mathrm{r}}^{\mathrm{dq}}\boldsymbol{i}_{\mathrm{cs}}^{\mathrm{dq}}\right\} + p_{\mathrm{p}}\mathrm{Im}\left\{\overline{\boldsymbol{\psi}'}_{\mathrm{f}}^{\mathrm{dq}}\boldsymbol{i}_{\mathrm{r}}^{\mathrm{dq}}\right\} \tag{11}$$

Both the flux and the electromagnetic torque need to be controlled. Actually, a machine control system generally has a fast-responding current loop. At this time, the CRPM-DFM is approximately powered by the current source. To obtain the mathematical model when the CRPM-DFM is supplied by the current source, the new state variable should be defined as:

$$\boldsymbol{\psi}_{\mathrm{r}}^{\mathrm{dq}} = l_{\mathrm{cm}}\boldsymbol{i}_{\mathrm{cs}}^{\mathrm{dq}} + l_{\mathrm{r}}\boldsymbol{i}_{\mathrm{r}}^{\mathrm{dq}} \tag{12}$$

The relationship between the old and new state variables is:

$$\begin{bmatrix} \boldsymbol{i}_{\mathrm{cs}}^{\mathrm{dq}} \\ \boldsymbol{\psi}_{\mathrm{r}}^{\mathrm{dq}} \end{bmatrix} = \begin{bmatrix} 1 & 0 \\ l_{\mathrm{cm}} & l_{\mathrm{r}} \end{bmatrix} \begin{bmatrix} \boldsymbol{i}_{\mathrm{cs}}^{\mathrm{dq}} \\ \boldsymbol{i}_{\mathrm{r}}^{\mathrm{dq}} \end{bmatrix} \tag{13}$$

From Equations (10) and (13), the state-space model expressed by the new state variables can be obtained:

$$\begin{bmatrix} \dot{\boldsymbol{i}}_{\mathrm{cs}}^{\mathrm{dq}} \\ \dot{\boldsymbol{\psi}}_{\mathrm{r}}^{\mathrm{dq}} \end{bmatrix} = \hat{\boldsymbol{A}}^{\mathrm{dq}} \begin{bmatrix} \boldsymbol{i}_{\mathrm{cs}}^{\mathrm{dq}} \\ \boldsymbol{\psi}_{\mathrm{r}}^{\mathrm{dq}} \end{bmatrix} + \hat{\boldsymbol{B}}^{\mathrm{dq}} \begin{bmatrix} \boldsymbol{u}_{\mathrm{cs}}^{\mathrm{dq}} \\ \boldsymbol{\psi}'^{\mathrm{dq}}_{\mathrm{f}} \end{bmatrix} \tag{14}$$

where $\hat{\boldsymbol{A}}^{\mathrm{dq}} = \begin{bmatrix} 1 & 0 \\ l_{\mathrm{cm}} & l_{\mathrm{r}} \end{bmatrix}\boldsymbol{A}^{\mathrm{dq}}\begin{bmatrix} 1 & 0 \\ -l_{\mathrm{cm}}/l_{\mathrm{r}} & 1/l_{\mathrm{r}} \end{bmatrix} = \begin{bmatrix} \frac{-l_{\mathrm{r}}^2(r_{\mathrm{cs}} + \mathrm{j}p_{\mathrm{c}}\omega_{\mathrm{r}}l_{\mathrm{cs}}) - l_{\mathrm{cm}}^2(r_{\mathrm{r}} - \mathrm{j}p_{\mathrm{c}}\omega_{\mathrm{r}}l_{\mathrm{r}})}{Kl_{\mathrm{r}}} & \frac{l_{\mathrm{cm}}(r_{\mathrm{r}} - \mathrm{j}p_{\mathrm{c}}\omega_{\mathrm{r}}l_{\mathrm{r}})}{Kl_{\mathrm{r}}} \\ \frac{r_{\mathrm{r}}l_{\mathrm{cm}}}{l_{\mathrm{r}}} & -\frac{r_{\mathrm{r}}}{l_{\mathrm{r}}} \end{bmatrix}$,

$\hat{\boldsymbol{B}}^{\mathrm{dq}} = \begin{bmatrix} 1 & 0 \\ l_{\mathrm{cm}} & l_{\mathrm{r}} \end{bmatrix}\boldsymbol{B}^{\mathrm{dq}} = \frac{1}{K}\begin{bmatrix} l_{\mathrm{r}} & -\mathrm{j}l_{\mathrm{cm}}\dot{\lambda}_{\mathrm{fdq}} \\ 0 & \mathrm{j}K\dot{\lambda}_{\mathrm{fdq}} \end{bmatrix}$.

It can be seen from Equation (14) that $\boldsymbol{\psi}_{\mathrm{r}}^{\mathrm{dq}}$ is not affected by the control machine stator voltage. Since the permeability of the permanent-magnet stator and the air is approximately equal and the air gap of the control machine is much smaller than that of the power machine, l_{pr} is very small and $l_{\mathrm{r}} \approx l_{\mathrm{cr}}$. In this case, the new state variable $\boldsymbol{\psi}_{\mathrm{r}}^{\mathrm{dq}}$ is approximately equal to the rotor flux of the control machine $\boldsymbol{\psi}_{\mathrm{cr}}^{\mathrm{dq}} = l_{\mathrm{cm}}\boldsymbol{i}_{\mathrm{cs}}^{\mathrm{dq}} + l_{\mathrm{cr}}\boldsymbol{i}_{\mathrm{r}}^{\mathrm{dq}}$, so it is also called the rotor

flux of the control machine, and it can also reflect the saturation of the rotor magnetic circuit of the control machine.

In addition, all variables in the rotor dq coordinate system are AC values, so Equation (14) is transformed into the control-machine synchronous coordinate system. After that, all variables are DC values, which is conducive to later analysis and design. The rotation transformation rule is:

$$\boldsymbol{x}^{\mathrm{dq}} = e^{\mathrm{j}\lambda_{\mathrm{c}}}\boldsymbol{x}^{\mathrm{mt}} \tag{15}$$

According to Equations (14) and (15), the mathematical model in the synchronous coordinate system can be obtained:

$$\begin{bmatrix} \dot{\boldsymbol{i}}_{\mathrm{cs}}^{\mathrm{mt}} \\ \dot{\boldsymbol{\psi}}_{\mathrm{r}}^{\mathrm{mt}} \end{bmatrix} = \hat{\boldsymbol{A}}^{\mathrm{mt}} \begin{bmatrix} \boldsymbol{i}_{\mathrm{cs}}^{\mathrm{mt}} \\ \boldsymbol{\psi}_{\mathrm{r}}^{\mathrm{mt}} \end{bmatrix} + \hat{\boldsymbol{B}}^{\mathrm{mt}} \begin{bmatrix} \boldsymbol{u}_{\mathrm{cs}}^{\mathrm{mt}} \\ \boldsymbol{\psi}_{\mathrm{f}}'^{\mathrm{mt}} \end{bmatrix} \tag{16}$$

where $\hat{\boldsymbol{A}}^{\mathrm{mt}} = \hat{\boldsymbol{A}}^{\mathrm{dq}} - \mathrm{I}\dot{\lambda}_{\mathrm{c}}$ and $\hat{\boldsymbol{B}}^{\mathrm{mt}} = \hat{\boldsymbol{B}}^{\mathrm{dq}}$.

Furthermore, under the premise that the CRPM-DFM is supplied by the current source, the stator voltage equation can be removed. Defining $\boldsymbol{\psi}_{\mathrm{r}}^{\mathrm{mt}}$ as the state variable and $\boldsymbol{i}_{\mathrm{cs}}^{\mathrm{mt}}$ as the input variable, the new two-order mathematical model can be obtained as:

$$\dot{\boldsymbol{\psi}}_{\mathrm{r}}^{\mathrm{mt}} = -\left(\frac{r_{\mathrm{r}}}{l_{\mathrm{r}}} + \mathrm{j}\dot{\lambda}_{\mathrm{c}}\right)\boldsymbol{\psi}_{\mathrm{r}}^{\mathrm{mt}} + \frac{r_{\mathrm{r}} l_{\mathrm{cm}}}{l_{\mathrm{r}}}\boldsymbol{i}_{\mathrm{cs}}^{\mathrm{mt}} + \mathrm{j}\dot{\lambda}_{\mathrm{fdq}}\boldsymbol{\psi}_{\mathrm{f}}'^{\mathrm{mt}} \tag{17}$$

By substituting Equation (12) into Equation (11), the electromagnetic torque of the CRPM-DFM expressed by the new state variable is:

$$T_{\mathrm{e}} = \frac{p_{\mathrm{c}} l_{\mathrm{cm}}}{l_{\mathrm{r}}}\mathrm{Im}\left\{\overline{\boldsymbol{\psi}}_{\mathrm{r}}^{\mathrm{mt}}\boldsymbol{i}_{\mathrm{cs}}^{\mathrm{mt}}\right\} + \frac{p_{\mathrm{p}}}{l_{\mathrm{r}}}\mathrm{Im}\left\{\overline{\boldsymbol{\psi}'}_{\mathrm{f}}^{\mathrm{mt}}\psi_{\mathrm{r}}^{\mathrm{mt}}\right\} - \frac{p_{\mathrm{p}} l_{\mathrm{cm}}}{l_{\mathrm{r}}}\mathrm{Im}\left\{\overline{\boldsymbol{\psi}}_{\mathrm{r}}^{\mathrm{mt}}\boldsymbol{i}_{\mathrm{cs}}^{\mathrm{mt}}\right\} \tag{18}$$

Finally, the CRPM-DFM's motion equation is:

$$T_{\mathrm{e}} - T_{\mathrm{L}} = J\frac{\mathrm{d}\omega_{\mathrm{r}}}{\mathrm{d}t} \tag{19}$$

3.2. Feedback Linearization Control of CRPM-DFM

Next, the synchronous coordinate system is oriented according to the rotor flux, which is $\psi_{\mathrm{r}}^{\mathrm{mt}} = \psi_{\mathrm{r}} + \mathrm{j}0$ and $|\boldsymbol{\psi}_{\mathrm{r}}| = |\boldsymbol{\psi}_{\mathrm{r}}^{\mathrm{mt}}|$. After that, Equations (17) and (18) can be written as:

$$\begin{cases} \dot{\psi}_{\mathrm{r}} = -\dfrac{r_{\mathrm{r}}}{l_{\mathrm{r}}}\psi_{\mathrm{r}} + \dfrac{r_{\mathrm{r}} l_{\mathrm{cm}}}{l_{\mathrm{r}}} i_{\mathrm{cs}}^{\mathrm{m}} - \dot{\lambda}_{\mathrm{fdq}}\psi_{\mathrm{t}}'^{\mathrm{f}} \\ 0 = \dfrac{r_{\mathrm{r}} l_{\mathrm{cm}}}{l_{\mathrm{r}}} i_{\mathrm{cs}}^{\mathrm{t}} + \dot{\lambda}_{\mathrm{fdq}}\psi_{\mathrm{m}}'^{\mathrm{t}} - \dot{\lambda}_{\mathrm{c}}\psi_{\mathrm{r}} \\ T_{\mathrm{e}} = \dfrac{l_{\mathrm{cm}}\left(p_{\mathrm{c}}\psi_{\mathrm{r}} - p_{\mathrm{p}}\psi_{\mathrm{f}}'^{\mathrm{m}}\right)}{l_{\mathrm{r}}} i_{\mathrm{cs}}^{\mathrm{t}} + \frac{p_{\mathrm{p}} l_{\mathrm{cm}}}{l_{\mathrm{r}}}\psi_{\mathrm{f}}'^{\mathrm{t}} i_{\mathrm{cs}}^{\mathrm{m}} - \frac{p_{\mathrm{p}}}{l_{\mathrm{r}}}\psi_{\mathrm{f}}'^{\mathrm{t}}\psi_{\mathrm{r}} \end{cases} \tag{20}$$

With rotor flux and electromagnetic torque as output variables, Equation (20) can be expressed in the following form:

$$\begin{bmatrix} \dot{\psi}_{\mathrm{r}} \\ T_{\mathrm{e}} \end{bmatrix} = \begin{bmatrix} -\frac{r_{\mathrm{r}}}{l_{\mathrm{r}}}\psi_{\mathrm{r}} \\ 0 \end{bmatrix} + \boldsymbol{f}(\boldsymbol{x}) + \boldsymbol{D}(\boldsymbol{x}) \begin{bmatrix} i_{\mathrm{cs}}^{\mathrm{m}} \\ i_{\mathrm{cs}}^{\mathrm{t}} \end{bmatrix} \tag{21}$$

where $f(x) = \begin{bmatrix} -\dot{\lambda}_{\mathrm{fdq}}\psi_{\mathrm{f}}'^{\mathrm{t}} \\ -\frac{p_{\mathrm{p}}}{l_{\mathrm{r}}}\psi_{\mathrm{f}}'^{\mathrm{t}}\psi_{\mathrm{r}} \end{bmatrix}$ and $\boldsymbol{D}(\boldsymbol{x}) = \begin{bmatrix} \frac{r_{\mathrm{r}} l_{\mathrm{cm}}}{l_{\mathrm{r}}} & 0 \\ \frac{p_{\mathrm{p}} l_{\mathrm{cm}}}{l_{\mathrm{r}}}\psi_{\mathrm{f}}'^{\mathrm{t}} & \frac{p_{\mathrm{c}} l_{\mathrm{cm}}}{l_{\mathrm{r}}}\psi_{\mathrm{r}} - \frac{p_{\mathrm{p}} l_{\mathrm{cm}}}{l_{\mathrm{r}}}\psi_{\mathrm{f}}'^{\mathrm{m}} \end{bmatrix}$.

When $\boldsymbol{D}(\boldsymbol{x})$ is non-singular, the control law of input-output feedback linearization can be obtained:

$$\begin{bmatrix} i_{\mathrm{cs}}^{\mathrm{m}} \\ i_{\mathrm{cs}}^{\mathrm{t}} \end{bmatrix} = \boldsymbol{D}^{-1}(\boldsymbol{x})[-\boldsymbol{f}(\boldsymbol{x}) + \boldsymbol{v}] \tag{22}$$

where $v = \begin{bmatrix} v_1 & v_2 \end{bmatrix}^T$ is the new input variable and, under the control law of Equations (21) and (22), can be written as:

$$\begin{bmatrix} \dot{\psi}_r \\ T_e \end{bmatrix} = \begin{bmatrix} -\frac{r_r}{l_r}\psi_r \\ 0 \end{bmatrix} + \begin{bmatrix} v_1 \\ v_2 \end{bmatrix} \tag{23}$$

According to Equation (23), from v_1 to the rotor flux is an inertia link, and v_2 is the same as torque, and there is no connection between the rotor flux of the control machine and torque. The reference values of the input variables are:

$$\begin{bmatrix} v_1^* \\ v_2^* \end{bmatrix} = \begin{bmatrix} \frac{r_r}{l_r}\psi_r^* \\ T_e^* \end{bmatrix} \tag{24}$$

$\boldsymbol{D}(\boldsymbol{x})$ non-singular is the premise of feedback linearization, which needs to be satisfied:

$$p_c\psi_r - p_p\psi_f'^m \neq 0 \tag{25}$$

A sufficient condition for Equation (25) is:

$$\psi_r > \frac{p_p}{p_c}\psi_{rf}^m \tag{26}$$

4. Torque Characteristic Analysis of CRPM-DFM

For the given values of speed difference between a permanent-magnet stator and cup rotor, rotor flux and load torque, feedback linearization control can give two solutions: a sinusoidal steady-state solution and non-sinusoidal steady-state solution. Taking the machine parameters in Table A1 as an example, the typical response waveforms of a sinusoidal steady-state solution and non-sinusoidal steady-state solution of the CRPM-DFM under feedback linearization control are shown in Figure 4.

Under a different permanent-magnet flux, rotor flux and speed difference, the range of torque with the sinusoidal steady-state solution is different. When the output torque exceeds the load torque boundaries, the non-sinusoidal steady-state solution exists, although the machine can still output a stable speed and torque, but the voltage and current change rate increases, and the amplitude will oscillate periodically, which requires the converter to improve the voltage and current tolerance level and provide a higher DC voltage; otherwise, the CRPM-DFM will go out of control. However, the IGBT with higher voltage and current tolerance level will increase the cost of the system. Therefore, for the powertrain system based on CRPM-DFM, the use of a non-sinusoidal steady-state solution will be avoided unless it is absolutely necessary.

The sinusoidal steady-state solution corresponds to the constant solution of Equation (20) and the constant slip frequency. For a certain permanent magnet stator speed, slip frequency and rotor flux, a set of algebraic equations can be obtained by making $\dot{\psi}_r = 0$, $T_e = T_L$ and $\dot{\lambda}_c = -\dot{\lambda}_{fdq} = \pi p_p(p_p - n_m)/30$ in Equation (20). Then, the torque range obtained when the equations have a constant solution is the torque range with the sinusoidal steady-state solution of CRPM-DFM. Therefore, by substituting the first two lines of Equation (20) into the third line of Equation (20), the load torque can be expressed as:

$$T_L = \frac{\pi p_p(n_r - n_m)}{30r_r}\left(p_c\psi_r^2 - p_p\psi_f^2 + (p_c - p_p)\psi_r\psi_f'^m\right) \tag{27}$$

According to Equation (27), because the amplitude of the m-axis component of the permanent-magnet flux cannot exceed the amplitude of the permanent-magnet flux, when

$\psi_{rf}^{m} = \psi_f$ or $\psi_{rf}^{m} = -\psi_f$, the upper and lower load torque boundaries can be obtained. Taking $n_r - n_m > 0$ as an example, the values and width of load torque boundaries are:

$$\begin{cases} T_{max} = \dfrac{\pi p_p (n_r - n_m)}{30 r_r} \left[p_c \psi_r^2 - p_p \psi_f^2 + (p_c - p_p) \psi_r \psi_f \right] \\ T_{min} = \dfrac{\pi p_p (n_r - n_m)}{30 r_r} \left[p_c \psi_r^2 - p_p \psi_f^2 - (p_c - p_p) \psi_r \psi_f \right] \\ T_{width} = \dfrac{2\pi p_p (n_r - n_m)}{30 r_r} (p_c - p_p) \psi_r \psi_f \end{cases} \tag{28}$$

From Equation (28), the upper, lower and width of load torque boundaries are proportional to the speed difference $n_r - n_m$ and inversely proportional to the rotor resistance. Because the numbers in the two square brackets in the expressions of lower and upper torque boundaries are not equal, the slopes of the lower and upper torque boundaries are different as the speed difference changes. Besides, the change of the lower and upper torque boundaries with the rotor flux amplitude of the control machine is a quadratic curve, the lower and upper torque boundaries are asymmetric, especially when $\psi_r = \psi_f$, the upper boundary is $2\pi p_p (n_r - n_m)(p_c - p_p)\psi_f^2 / 30 r_r$ and the lower boundary is 0; changing the sign of speed difference, the lower and upper torque boundaries will switch but the width remains the same.

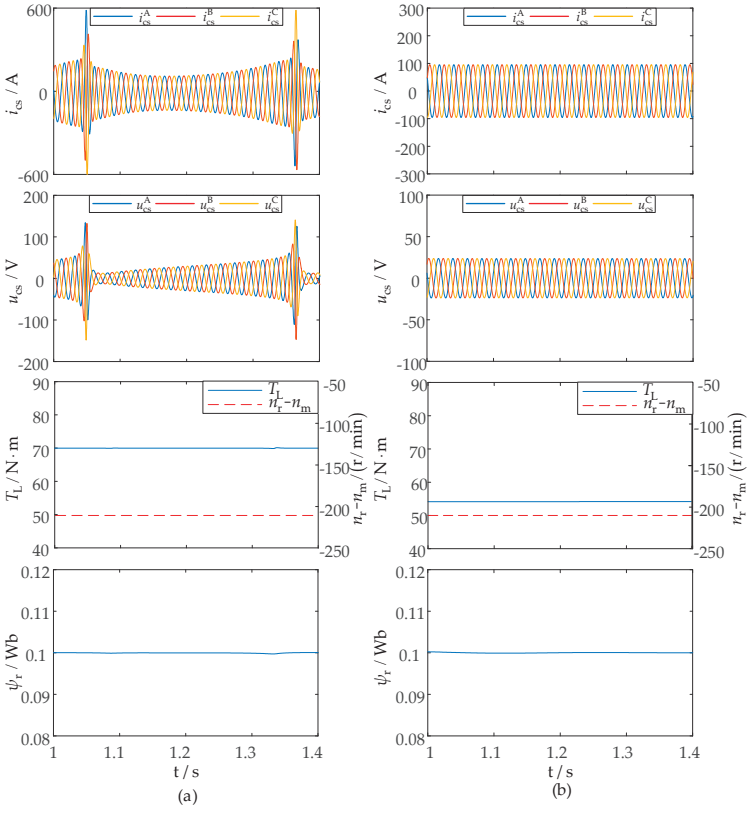

Figure 4. The response waveforms of CRPM-DFM when the non-sinusoidal steady-state solution or sinusoidal steady-state solution exists. (**a**) When the non-sinusoidal steady-state solution exists. (**b**) When the sinusoidal steady-state solution exists.

Taking the machine parameters in Table A1 as an example, and the per-unit value of torque is applied, which is $T_{Lb} = T_L/T_N$,$T_{eb} = T_e/T_N$, the load torque boundaries of CRPM-DFM are obtained, as shown in Figure 5.

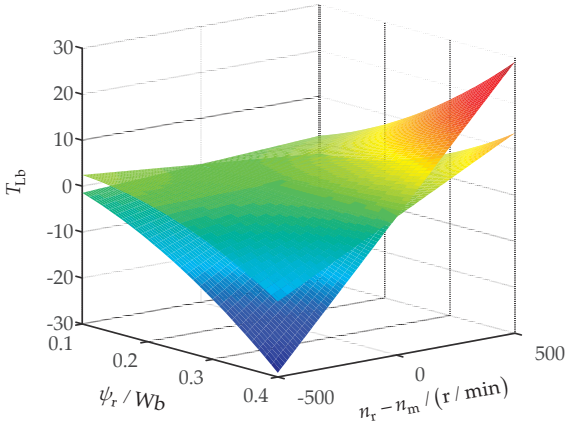

Figure 5. The upper and lower boundaries of load torque.

To further illustrate, let $n_r - n_m = \pm 1000$ r/min, $\psi_r = 0.1$Wb in Figure 5 to get the curve of Figure 6. When $n_r - n_m < 0$, the lower and upper torque boundaries of the CRPM-DFM will decrease with the increase in the amplitude of rotor flux, and even $T_{max} < 0$. When $n_r - n_m > 0$, the lower and upper torque boundaries of the CRPM-DFM will increase with the increase in the amplitude of rotor flux, and even $T_{min} > 0$, as shown in Figure 6a,b. When the amplitude of rotor flux is constant, the upper, lower and width of load torque boundaries will linearly increase with the increase of $|n_r - n_m|$; when the sign of $n_r - n_m$ changes, the lower and upper torque boundaries will switch, as shown in Figure 6c.

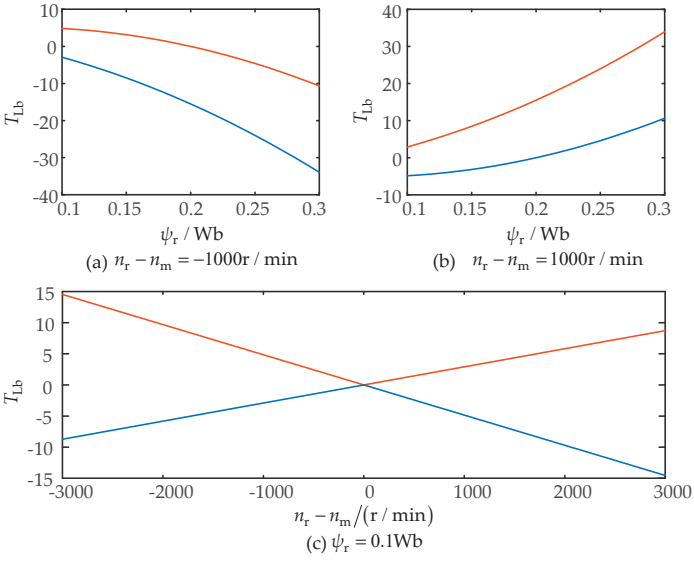

Figure 6. Influence of rotor flux and the speed difference on the load torque boundary. (**a**) Influence of rotor flux when $n_r - n_m < 0$. (**b**) Influence of rotor flux when $n_r - n_m > 0$. (**c**) Influence of the speed difference.

According to Equation (28) and Figure 6, only when the speed difference is slight will the output torque of CRPM-DFM with sinusoidal steady-state solution be limited. In most cases, the rotor flux amplitude and the speed difference can be appropriately adjusted to make the maximum output torque of CRPM-DFM with sinusoidal steady-state solution to meet the driving requirements of several times the rated torque. Only in some special cases can the CRPM-DFM be driven under a non-sinusoidal steady-state solution, such as starting the ICE when the vehicle is parked; at this time, the ICE speed and vehicle speed are both zero: $|n_r - n_m| = 0$. In addition, as described in the next section, the maximum torque per ampere (MTPA) control can effectively reduce the stator current of CRPM-DFM.

5. MTPA Control and Efficiency Analysis of CRPM-DFM

5.1. MTPA Control of CRPM-DFM

To reduce the amplitude of the control machine stator current and improve the efficiency of CRPM-DFM, the maximum-torque-per-ampere (MTPA) control strategy is presented. The results of this section show that the amplitude of the control machine stator current can be greatly reduced only by slightly adjusting the rotor flux of the control machine in the vicinity of the permanent-magnet flux. Meanwhile, because the rotor flux changes little, it will not lead to magnetic circuit saturation. The derivation of MTPA control law is as follows.

According to Equation (20), the relationship between the load torque and the m-axis component, t-axis component and amplitude of control machine stator current is:

$$\begin{cases} i_{cs}^{m} = \dfrac{l_r\dot{\psi}_r + r_r\psi_r + l_r\dot{\lambda}_{fdq}\psi_f'^{t}}{r_r l_{cm}} \\ i_{cs}^{t} = \dfrac{l_r T_e - p_p l_{cm}\psi_f'^{t} i_{cs}^{m} + p_p\psi_f'^{t}\psi_r}{l_{cm}\left(p_c\psi_r - p_p\psi_f'^{m}\right)} \\ i_{cs}^{2} = i_{cs}^{m2} + i_{cs}^{t2} = i_{cs}^{m2} + \left(\dfrac{l_r T_e - p_p l_{cm}\psi_f'^{t} i_{cs}^{m} + p_p\psi_f'^{t}\psi_r}{l_{cm}\left(p_c\psi_r - p_p\psi_f'^{m}\right)}\right)^2 \end{cases} \tag{29}$$

Next, take the partial derivatives of the amplitude of the control machine stator current with respect to i_{cs}^{m} and set it equal to zero; that is:

$$\frac{di_{cs}^{2}}{di_{cs}^{m}} = 2i_{cs}^{m} - 2p_p l_{cm}\psi_f'^{t}\frac{l_r T_e - p_p l_{cm}\psi_f'^{t} i_{cs}^{m} + p_p\psi_f'^{t}\psi_r}{l_{cm}^{2}\left(p_c\psi_r - p_p\psi_f'^{m}\right)^2} = 0 \tag{30}$$

By substituting the first line of Equation (29) into Equation (30), the following relationship can be obtained:

$$\frac{p_p\psi_f'^{t}}{p_c\psi_r - p_p\psi_f'^{m}} = \frac{\left(l_r\dot{\psi}_r + l_r\dot{\lambda}_{fdq}\psi_f'^{t} + r_r\psi_r\right)\left(p_c\psi_r - p_p\psi_f'^{m}\right)}{l_r r_r T_e - p_p l_r\psi_f'^{t}\dot{\psi}_r - p_p l_r\dot{\lambda}_{fdq}\left(\psi_f'^{t}\right)^2} \tag{31}$$

In Equation (31), ψ_r and T_e are replaced by constant values, and the necessary and sufficient condition for MTPA control when the sinusoidal steady state solution of CRPM-DFM is obtained is that the rotor flux of the control motor is given and satisfies the following relation:

$$\left(\psi_r^{*} r_r + l_r\dot{\lambda}_{fdq}\psi_f'^{t}\right)\left(p_c\psi_r^{*} - p_p\psi_f'^{m}\right)^2 = p_p\psi_f'^{t} l_r\left(r_r T_e^{*} - p_p\dot{\lambda}_{fdq}\left(\psi_f'^{t}\right)^2\right) \tag{32}$$

According to Equations (27) and (32) and $\left(\psi_f'^{m}\right)^2 + \left(\psi_f'^{t}\right)^2 = \left(\psi_f\right)^2$, the two components of the permanent-magnet flux, $\psi_f'^{m}$ and $\psi_f'^{t}$, can be removed, and the flux can be expressed as a function of the given torque and speed difference; that is:

$$\frac{r_r^2\left(p_c^2\psi_r^{*2}-p_p^2\psi_f^2+\frac{p_p r_r}{\dot{\lambda}_{fdq}}T_e^*\right)^4}{l_r^2(p_c+p_p)^2\left(\dot{\lambda}_{fdq}\left(p_p^2\psi_f^2-p_c^2\psi_r^{*2}\right)-r_r p_p T_e^*\right)^2}=(p_c-p_p)^2\psi_r^{*2}\psi_f^2-\left(p_p\psi_f^2-p_c\psi_r^{*2}-\frac{r_r T_e^*}{\dot{\lambda}_{fdq}}\right)^2 \tag{33}$$

Under the given values of T_e^* and $\dot{\lambda}_{fdq}$, the reference value ψ_r^* can be solved offline, and MTPA can be realized in open loop by the table lookup method. Figure 7 shows the variation of control-machine flux with torque and speed difference when MTPA control is adopted in the Table A1 machine parameters.

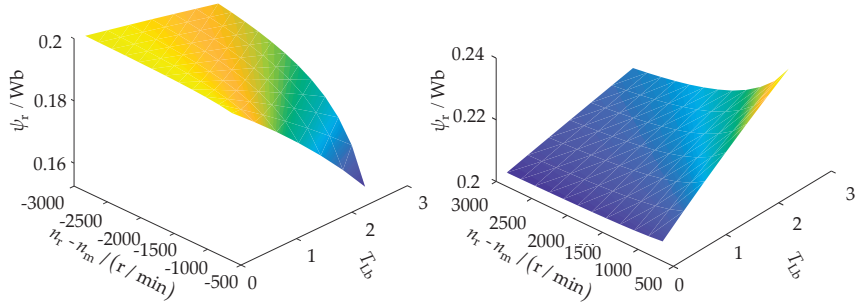

Figure 7. The reference value of rotor flux. (**a**) The reference value of rotor flux when the speed difference is negative. (**b**) The reference value of rotor flux when the speed difference is positive.

Figure 8 shows the reference value of rotor flux under MTPA control at different torque and speed differences. It can be seen that when $n_r - n_m < 0$, the amplitude of the rotor-flux reference value decreases slightly with the increase in the torque and when $n_r - n_m > 0$, the amplitude of the rotor-flux reference value increases slightly with the increase in the torque. Besides, the smaller the speed difference amplitude, the greater the flux changes. When $n_r - n_m < 0$, the amplitude of the reference value of rotor flux increases slightly with the increase in the amplitude of speed difference $|n_r - n_m|$, and when $n_r - n_m > 0$, the amplitude of the rotor-flux reference value decreases slightly with the increase of $|n_r - n_m|$. Obviously, the torque in Equation (33) should be within the lower and upper torque boundaries with the sinusoidal steady-state solution. Besides, as shown in Figures 7 and 8, the greater the torque, the greater the flux changes, and the flux changes monotonically with the torque and speed difference when $n_r - n_m < 0$, $\psi_r^* < \psi_f$ and when $n_r - n_m > 0$, $\psi_r^* > \psi_f$.

The inputs of the feedback linearization control (FLC) are the torque instruction value, which is obtained by the speed loop, and the rotor flux instruction value, which is obtained by MTPA. Then, the instruction values of the control-machine stator current are obtained from the feedback linearization control law. In addition, the synchronization angle can be obtained by integrating the angular velocity of the slip angle and the electric angular velocity of the rotor, which can be used for rotation transformation. According to the second line of Equation (20), the slip angular speed can be obtained with the rotor flux instruction value and stator current of the control machine.

$$\dot{\lambda}_c = \frac{r_r l_{cm}}{l_r \psi_r^*} i_{cs}^{t*} + \frac{\dot{\lambda}_{fdq}}{\psi_r^*}\psi_f'^m \tag{34}$$

Then, the system structure can be simplified without the flux observer.

Finally, under the control block diagram in Figure 9, the MTPA performance is verified by simulation, and the machine parameters are also shown in Table A1. Simulation results

of MTPA control are shown in Figure 10a. Simulation results of constant ψ_r^* control are shown in Figure 10b, in which Figure 9 does not contain MTPA control and $\psi_r^* = 0.186$. The permanent-magnet stator speed is 2000 r/min. The CRPM-DFM runs sub-synchronously in 1–3 s, synchronously in 3–5 s and super-synchronously in 5–7 s. The load torque is T_N in 1–7 s and $0.5T_N$ in 7–9 s. Under MTPA control and $n_r - n_m < 0$, the amplitude of the rotor-flux reference value decreases slightly with the decrease in the amplitude of speed difference, and the amplitude of the rotor-flux reference value increases slightly with the decrease in load torque, which follows the trend shown in Figure 8. The amplitude of the control-machine stator current under MTPA control is far less than that under constant ψ_r^* control.

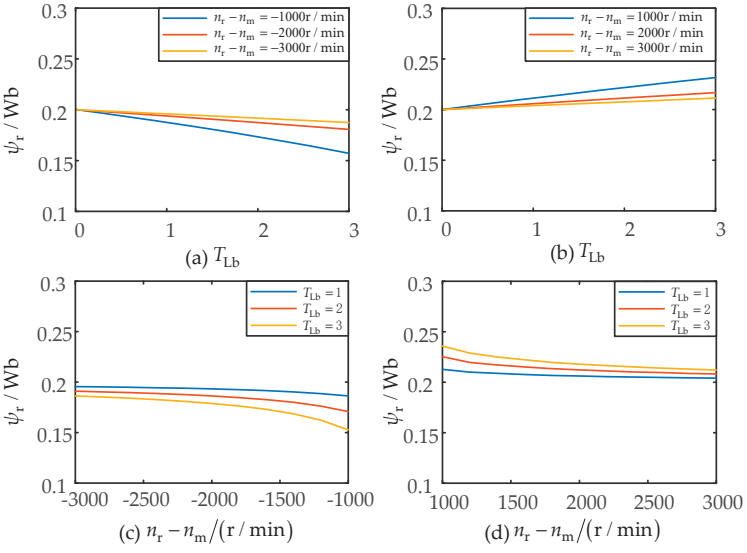

Figure 8. The reference value of rotor flux. (**a**) The relationship of the rotor flux with torque when $n_r - n_m < 0$. (**b**) The relationship of the rotor flux with torque when $n_r - n_m > 0$. (**c**) The relationship of the rotor flux with speed difference when $n_r - n_m < 0$. (**d**) The relationship of the rotor flux with speed difference when $n_r - n_m > 0$.

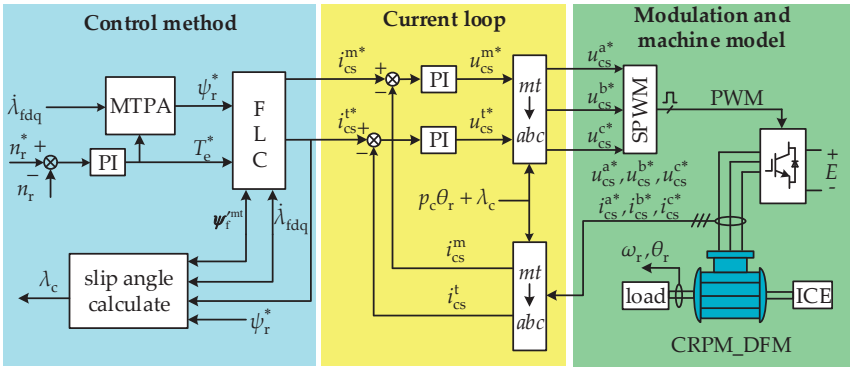

Figure 9. The control block diagram of CRPM-DFM.

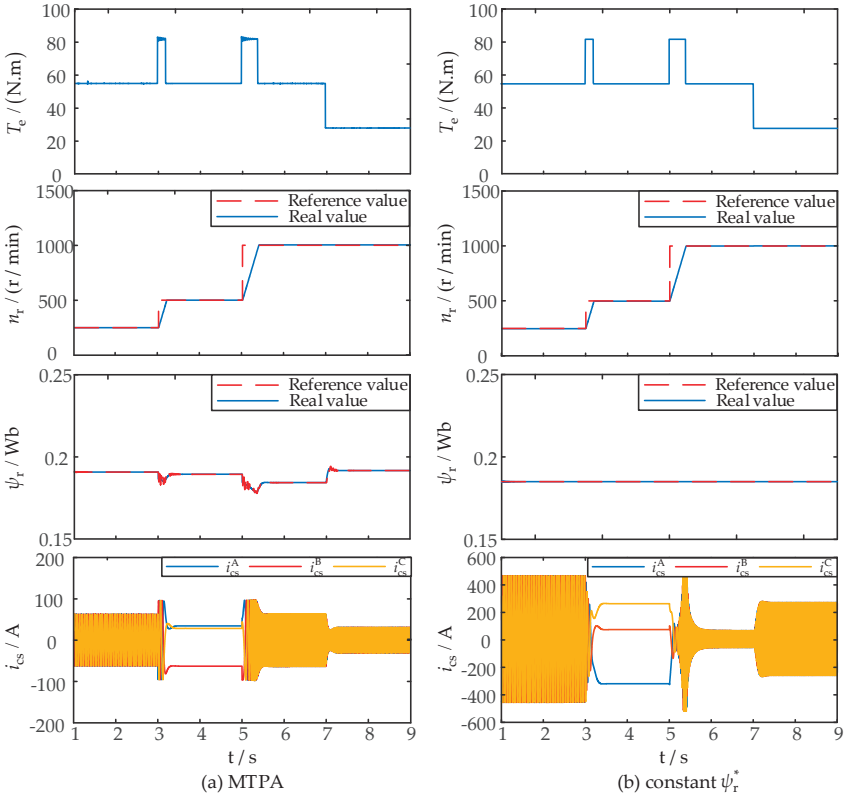

Figure 10. Simulation results: (**a**) simulation results of MTPA control; (**b**) simulation results of constant ψ_r^* control.

5.2. Efficiency Analysis of CRPM-DFM

As described in the paper, small rotor loss is the key to improving the performance of CRPM-DFM. According to the references, to reduce rotor loss, these kinds of motors all use copper conductors instead of cast aluminum conductors. In addition, to reduce eddy current loss, an interior permanent magnet is used. The efficiency maps of CRPM-DFM in different operating modes are shown in Figure 11, where the original data of all efficiency maps in this section are obtained by simulation under the MATLAB/Simulink environment, and the control block diagram is shown in Figure 9.

The CRPM-DFM has two mechanical ports and one electrical port, each of which can input power or output power. The loss of CRPM-DFM includes copper loss, iron loss, PM loss, mechanical loss and loss caused by PWM. The total loss of CRPM-DFM is equal to the difference between the input power of each port and the output power of each port; that is, the efficiency of CRPM-DFM is equal to the ratio of the sum of the output power of each port and the sum of the input power of each port. The calculation method of efficiency is as follows: in hybrid driving mode, when the cup-rotor speed n_r is less than 3000 r/min, the speed difference $n_r - n_m$ is -600 r/min, and when n_r is greater than 3000 r/min, the speed difference is 600 r/min, and the machine efficiency is the ratio of the power output of the cup rotor and the sum of the power input of the stator of the control machine and power machine; in pure electric driving mode, the machine efficiency is the ratio of the power output of the cup rotor and the power input of the stator of the control machine; in parked charging mode, the machine efficiency is the ratio of the power output of the stator of control machine and the power input of the stator of the power machine; in

regenerative braking mode, the machine efficiency is the ratio of the power output of the control-machine stator and the power input of the cup rotor.

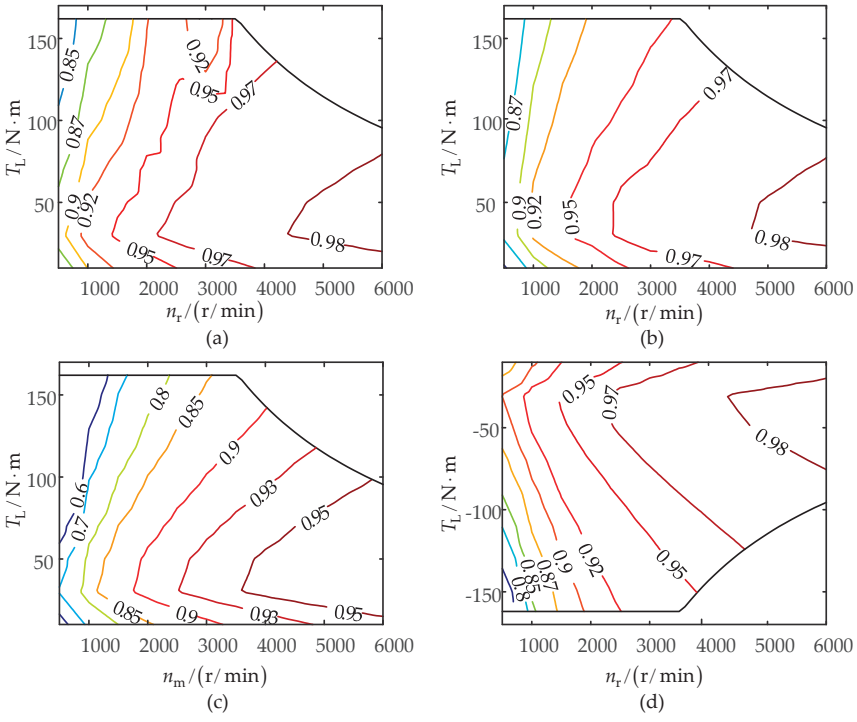

Figure 11. Efficiency maps of CRPM-DFM: (**a**) in hybrid driving mode; (**b**) in pure electric driving mode; (**c**) in parking charging mode; (**d**) in regenerative braking mode.

As can be seen from Figure 11, parked charging mode is slightly less efficient than other operating modes, but the CRPM-DFM can maintain relatively high efficiency within a wide range of speed and torque variation in different operating modes, which meets the requirements of EREVs.

6. ICE Speed Optimization Strategy

In hybrid driving mode, the CRPM-DFM works in doubly fed mode, and the vehicle-requested torque is distributed to the ICE and control machine in proportion to the pole pairs. In this case, the CRPM-DFM is equivalent to a speed coupler and the ICE speed should be optimized to adjust the power distribution of the ICE and battery. Then, the fuel consumption and battery SOC fluctuation can be reduced.

A 12 kW petrol ICE is used in this paper, and the fuel consumption map of ICE is shown in Figure 12. The optimal operating curve is a curve formed by connecting the speed and torque points corresponding to the minimum fuel consumption rate of each output power, and ICE speed n_{ice} in the optimal operating curve can be roughly expressed as a quadratic function of ICE torque T_{ice} [27], as shown in the red line in Figure 12.

$$n_{ice} = \begin{cases} 1.219T_{ice}^2 + 34.43T_{ice} + 555.7 & T_{ice} > 10 \\ 1000 & T_{ice} < 10 \end{cases} \quad (35)$$

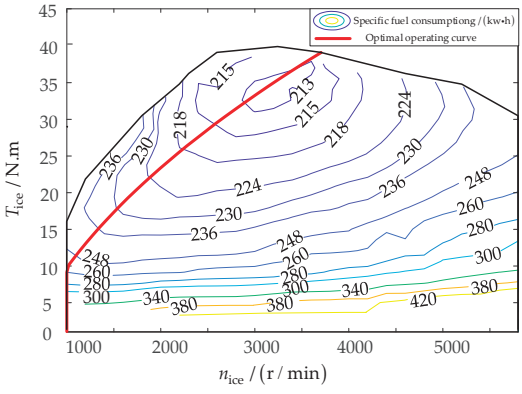

Figure 12. Specific fuel consumption map of the ICE.

Furthermore, a 30 AH nickel metal hydride (NiMH) battery with a large discharge rate is selected; to improve the performance of the battery pack and prolong its service life, battery SOC should be kept in the efficient working zone as far as possible. In this paper, the SOC maximum value is 0.7 and the SOC minimum value is 0.6.

When the vehicle is running, the pedal-torque reference value will be given; if the battery SOC is within the efficient working zone, the ICE speed can be optimized according to Equation (35) by adjusting the power supply frequency of the converter to reduce fuel consumption, unless the speed difference is too small to obtain the desired torque within the sinusoidal steady-state solution range. Therefore, the speed difference $|n_r - n_m|$ should be maintained above 600 r/min, as according to Figure 5.

In addition, a PI controller is used to restrain battery SOC fluctuation. PI controller input is the difference between the reference SOC value and actual SOC value; output is the ICE speed adjustment $n_{ice\text{-}soc}$. When the actual SOC value is higher than the reference SOC value, the ICE speed adjustment is reduced to increase the battery output power and, thus, reduce the SOC. When the actual SOC value is lower than the reference SOC value, the ICE speed adjustment is increased to reduce the battery output and, thus, increase the SOC.

Therefore, with the goal of reducing fuel consumption and SOC fluctuation, an ICE speed optimization strategy that can be applied online is proposed, and the flowchart is shown in Figure 13.

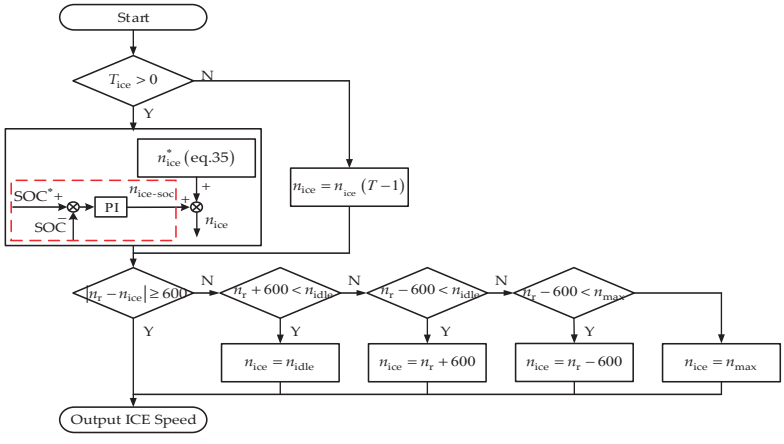

Figure 13. Flowchart of the ICE speed optimization strategy.

7. Simulation Experiments

As shown in Figure 14, an EREV powertrain system based on CRPM-DFM was built in MATLAB/Simulink to verify the driving performance and fuel economy of the powertrain system. The simulation platform consisted of a driver model, a control unit, an ICE model, a CRPM-DFM model, a battery model and a longitudinal vehicle dynamics model. Where the CRPM-DFM control strategy is shown in Figure 9 and ICE speed optimization strategy is mentioned in Section 6, the CRPM-DFM model is a mathematical model according to Equation (10), and the parameters are shown in Table A1, and ICE model is a fuel consumption map, which is shown in Figure 12. The requested pedal torque is the output of the driver model, and the requested torque is distributed to the ICE and control machine in proportion to the pole pairs. After that, the reference value of the voltage of the control-machine stator can be obtained by the CRPM-DFM control strategy, and according to the machine speed, SOC and the reference value of ICE torque, the reference value of ICE speed can be obtained by the ICE speed optimization strategy. In addition, the main parameters of EREVs are shown in Table A2.

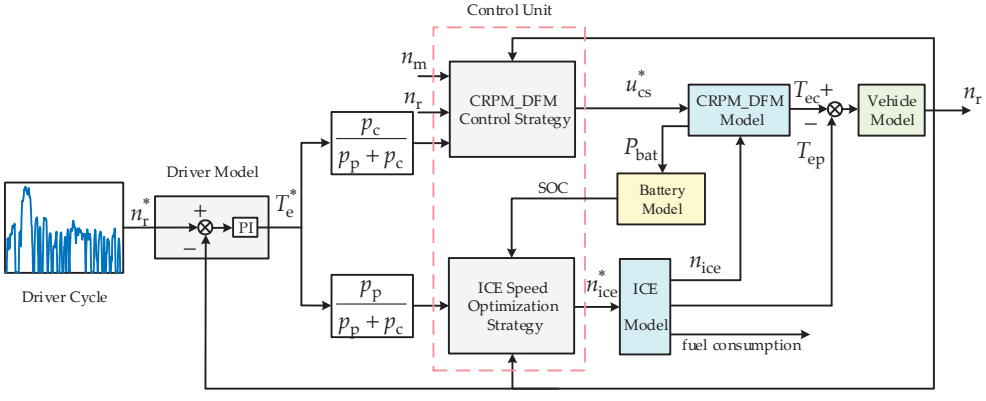

Figure 14. The system block diagram of EREV system based on CRPM-DFM.

7.1. Driving Performance Verification of the Powertrain System Based on CRPM-DFM

Abundant simulation tests were applied to validate the driving performance of the powertrain system under some typical driving cycles. Figures 15 and 16 are the simulation results under the UDDS driving cycle. It can be observed that the powertrain system based on CRPM-DFM is able to achieve the required speed, showing satisfactory driving performance, which also verifies the effectiveness of the CRPM-DFM control strategy. The ICE speed can be adjusted independently of load variations, but when the battery SOC is less than 0.65, the ICE speed needs to be properly increased to charge the battery; then, the SOC fluctuations will be reduced. In addition, the actual torque value of ICE obtained by Equation (10) is approximately equal to the theoretical torque value of ICE obtained by Equation (5), which verifies the accuracy of the torque distribution of CRPM-DFM discussed in Section 2.1.

The SOC, power, voltage and current waveforms are shown in Figure 16, and the CRPM-DFM operates within the sinusoidal steady-state solution. As an auxiliary power unit, the average output power of ICE is less than that of the battery, which accords with the characteristics of the EREVs. Besides, the SOC is limited to 0.6–0.7, which verifies the effectiveness of the ICE speed optimization strategy.

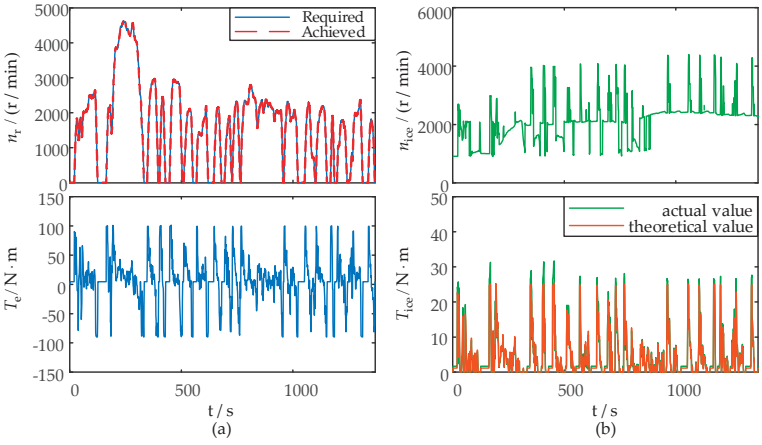

Figure 15. The torque and speed waveforms during the UDDS driving cycle: (**a**) the torque and speed waveforms of CRPM-DFM; (**b**) the torque and speed waveforms of ICE.

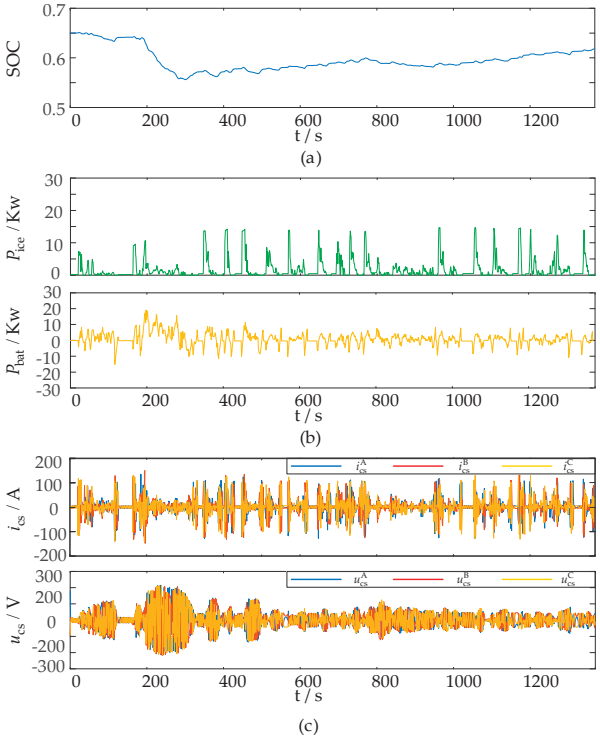

Figure 16. The SOC, power, current and voltage waveforms during the UDDS driving cycle: (**a**) the SOC waveform of battery; (**b**) the power waveforms of ICE and battery; (**c**) the current and voltage waveforms of CRPM-DFM.

7.2. Fuel Economy Verification of the Powertrain System Based on CRPM-DFM

To verify the fuel economy of the CRPM-DFM powertrain system, the fuel consumption of EREVs and conventional-engine vehicles is compared under some typical driving cycles. In the calculation of fuel consumption, not only is the fuel consumption of the ICE

considered, but also the charge deviation of the battery is converted into corresponding equivalent fuel consumption. The equivalent fuel consumption can be obtained:

$$M = m_{\text{fuel}} + \frac{E}{Q_{\text{lhv}}\eta_{\text{c}}}(\text{SOC}(t_0) - \text{SOC}(t_{\text{f}})) \tag{36}$$

where E is total battery energy (J), $Q_{\text{lhv}} = 42600$ J/g is fuel low heating value, $\eta_{\text{c}} = 0.4$ is oil-electric conversion efficiency, $\text{SOC}(t_0)$ and $\text{SOC}(t_{\text{f}})$ are the initial value and final value of the SOC, respectively, m_{fuel} is the ICE fuel consumption and M is the total fuel consumption of the vehicle.

Data of the ICE working points of EREVs are collected every 1 s, and then the ICE working points under different driving cycles are shown in the yellow points in Figure 17. Affected by the speed difference and battery SOC, a small number of operating points of ICE will deviate from the optimal operating curve, but most of the ICE operating points are near the optimal operating curve.

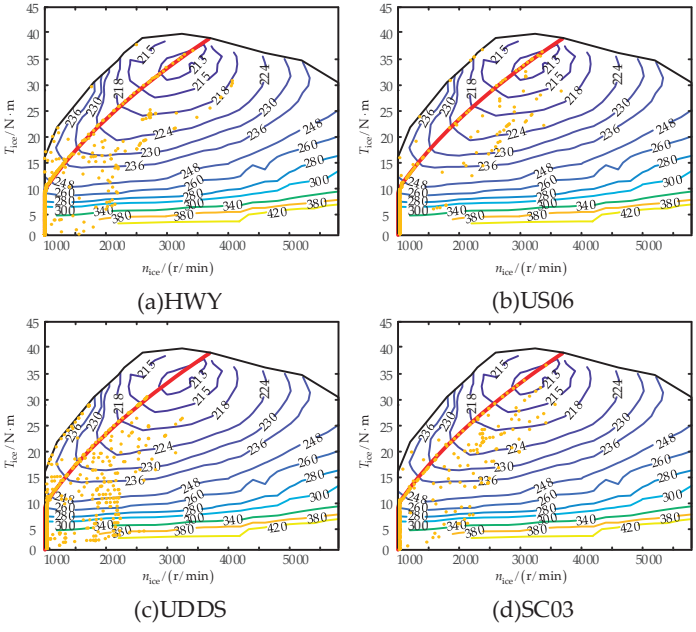

Figure 17. ICE operating points of EREVs under different driving cycles.

Fuel consumption of EREVs and conventional-engine vehicles is shown in Table 1, and it can be seen that under different driving cycles, the average oil-saving rate of EREVs is 50%, so the EREVs have better fuel economy.

Table 1. Fuel consumption results of different driving cycles (L/100 km).

Drive Cycle	Engine Vehicle	EREVs	Oil Saving Rate %
HWY	3.831	1.985	48.2
US06	4.174	2.126	49.1
UDDS	4.516	2.298	49.1
SC03	4.643	2.358	49.2

8. Conclusions

For the coupling devices of new-energy vehicles, there are three kinds: torque coupling, speed coupling and power coupling. The complexity is increased in turn, and the fuel

saving rate is also better in turn. The most prominent is the power coupling device of the two motors and mechanical planetary gear of the Prius, which can realize power coupling. The dynamic coupling device of CRPM-DFM discussed in this paper is similar to the planetary gear mechanism, which can realize the speed coupling, but there is no mechanical mechanism, and the generator and motor are integrated into one. The CRPM-DFM has high efficiency and no slip ring, and its characteristics of small size and simple structure make it suitable for the application of a vehicle's hybrid power system.

In this paper, the mathematical model of CRPM-DFM is introduced, and a high-performance control method is provided. The lower and upper limits of output torque with a sinusoidal steady-state solution and the relationship between the limits and the design parameters and operation parameters of CRPM-DFM are analyzed. To improve the efficiency of CRPM-DFM, the control strategy of maximum-torque-per-unit current is given in this paper. These results are of great significance for the application and body design of CRPM-DFM.

Obviously, the results of modeling, control method and driving characteristics of CRPM-DFM presented in this paper are not limited to the application of this paper, and the design scheme of the dynamic coupling device presented in this paper is not unique. Changes can be made in the motor-body structure and transmission mechanism design; for example, the positions of permanent-magnet stator and wound stator can be reciprocal. The motor output shaft can be equipped with a clutch to become a dual clutch design, and the output shaft can also be coupled with a motor to achieve power-coupling control, etc. These contents need to be developed in combination with the specific control requirements and drive requirements of vehicles in further research.

Author Contributions: Conceptualization, C.X.; methodology, C.X., J.B. and J.S.; software, J.B.; validation, C.X. and J.B.; formal analysis, C.X.; investigation, C.X.; resources, C.X.; data curation, C.X.; writing—original draft preparation, C.X. and J.B.; writing—review and editing, C.X. and J.B.; visualization, J.B.; supervision, C.X.; project administration, C.X.; funding acquisition, C.X. All authors have read and agreed to the published version of the manuscript.

Funding: This research received no external funding.

Data Availability Statement: Not applicable.

Conflicts of Interest: The authors declare no conflict of interest.

Nomenclature

n_r, n_m	mechanical speeds of cup rotor and the permanent-magnet stator
n_{idle}, n_{max}	idle speed and maximum speed of the internal combustion engine
ω_r, ω_m	mechanical angular speed of cup rotor and the permanent-magnet stator
f_c	frequency of the converter
λ_c, λ_{fdq}	slip angle and the rotation angle of the permanent magnet relative to the cup rotor
θ_r, θ_m	cup-rotor angle and permanent-magnet angle
p	number of pole pairs
$\boldsymbol{u}(u)$	plural form (real form) of voltage
$\boldsymbol{i}(i)$	plural form (real form) of current
$\boldsymbol{\psi}(\psi)$	plural form (real form) of flux
r	resistance
l	inductance
l_m	mutual inductance
T_e, T_L, T_N	electromagnetic torque, load torque and rated torque
J	rotational inertia
Im	imaginary part
j	unit imaginary
P_N	rated power

Superscripts

NS	N pole axis and S pole axis of the permanent magnet
ABC	static stator three-phase coordinate system
αβ	static stator two-phase coordinate system
abc	rotor three-phase coordinate system
dq	rotor coordinate system
mt	synchronous coordinate system
—	conjugate operation
′	negative conjugate operation
.	derivative of time
*	reference value
| |	amplitude

Subscripts

p	power machine
c	control machine
s	stator
r	rotor
f	permanent magnet
b	per-unit value
ice	internal combustion engine

Appendix A

Table A1. Parameters of CRPM-DFM.

Parameter	Value	Parameter	Value
P_N/kW	20	l_{cr}, l_{pr}/H	0.0031/0.0002
T_N/N · m	54	l_{cm}/H	0.003
r_{cs}/Ω	0.02	ψ_f/Wb	0.2
$r_{cr}, r_{pr}/\Omega$	0.01/0.01	p_c, p_p	3/1
l_{cs}/H	0.0031	$J/(\mathrm{kg} \cdot \mathrm{m}^2)$	0.2

Table A2. The key parameters of EREVs.

Parameter	Value	Parameter	Value
Battery pack	30 Ah/308 V	Tire radius	0.33 m
Total body mass	1000 kg	Drag coefficient	0.3
Frontal area	1.746 m^2	Rolling coefficient	0.009
ICE power	12 kW	CRPM-DFM power	20 kW

References

1. Liu, Z.E.; Hao, H.; Cheng, X.; Zhao, F.Q. Critical issues of energy efficient and new energy vehicles development in China. *Energy Policy* **2018**, *115*, 92–97. [CrossRef]
2. Husain, I.; Ozpineci, B.; Islam, M.S.; Gurpinar, E.; Su, G.J.; Yu, W.; Chowdhury, S.; Xue, L.; Rahman, D.; Sahu, R. Drive Technology Trends, Challenges, and Opportunities for Future Electric Vehicles. *Proc. IEEE* **2021**, *109*, 1039–1059. [CrossRef]
3. Puma-Benavides, D.S.; Izquierdo-Reyes, J.; Calderon-Najera, J.D.; Ramirez-Mendoza, R.A. A Systematic Review of Technologies, Control Methods, and Optimization for Extended-Range Electric Vehicles. *Appl. Sci.* **2021**, *11*, 7095. [CrossRef]
4. Aharon, I.; Kuperman, A. Topological Overview of Powertrains for Battery-Powered Vehicles with Range Extender. *IEEE Trans. Power Electron.* **2006**, *26*, 868–876. [CrossRef]
5. Niu, S.X.; HO, S.L.; Fu, W.N. Design of a Novel Electrical Continuously Variable Transmission System Based on Harmonic Spectra Analysis of Magnetic Field. *IEEE Trans. Magn.* **2013**, *49*, 2161–2164. [CrossRef]
6. Wang, Y.N.; Meng, B.M.; Shen, Y.P. Researches on Power Systems of Extended Range Electric Vehicles. *Proc. Chin. Soc. Electr. Eng.* **2014**, *34*, 4629–4639.

7. Zhang, Z.; Yu, L.; Dai, C.; Yan, Y. Investigation and development of a new brushless DC generator system for extended-range electric vehicle application. In Proceedings of the 2014 IEEE Energy Conversion Congress and Exposition, Pittsburgh, PA, USA, 14–18 September 2014; pp. 3155–3162.
8. Rahman, K.M.; Jurkovic, S.; Stancu, C.; Morgante, J.; Savagian, P.J. Design and Performance of Electrical Propulsion System of Extended Range Electric Vehicle (EREV) Chevrolet Volt. *IEEE Trans. Ind. Appl.* **2015**, *51*, 2479–2488. [CrossRef]
9. Zhou, S.; Niu, J.G.; Chen, F.X.; Fei, F.L. A Study on Powertrain Design and Simulation for Range-extended Electric Vehicle. *Automot. Eng.* **2011**, *33*, 924–929.
10. Shi, L.; Guo, Y.; Xiao, D.; Han, Z.; Zhou, X. Design, Optimization, and Study of a Rare-Earth Permanent-Magnet Generator with New Consequent-Pole Rotor for Extended-Range Electric Vehicle. *IEEJ Trans. Electr. Electron. Eng.* **2019**, *14*, 917–923. [CrossRef]
11. Zhou, L.K.; Hua, W.; Cheng, M. Analysis and optimization of key dimensions of co-axial dual-mechanical-port flux-switching permanent magnet machines for fuel-based extended range electric vehicles. *CES Trans. Electr. Mach. Syst.* **2017**, *1*, 292–299. [CrossRef]
12. Zhou, L.; Hua, W.; Wu, Z.; Zhu, X.; Yin, F. Analysis of coupling between two sub-machines in co-axis dual-mechanical-port flux-switching PM machine for fuel-based extended range electric vehicles. *IET Electr. Power Appl.* **2019**, *13*, 48–56. [CrossRef]
13. Zhou, L.K.; Hua, W. Influences of Stator Teeth Number on PM Coupling Levels of Co-Axial Dual- Mechanical-Port Flux-Switching PM Machines. *IEEE Trans. Magn.* **2019**, *55*, 8104007. [CrossRef]
14. Zhou, L.K.; Hua, W.; Zhang, G. Power distribution of a co-axial dual-mechanical-port flux-switching permanent magnet machine for fuel-based extended range electric vehicles. *AIP Adv.* **2017**, *7*, 056638. [CrossRef]
15. Xiang, Z.; Quan, L.; Zong, Z.; Gu, Y.; Yin, J. Alternative stator for new brushless dual-rotor flux-switching permanent magnet motor for extended range electric vehicles. In Proceedings of the 17th IEEE International Conference on Electrical Machines and Systems, Hangzhou, China, 22–25 October 2014; pp. 212–217.
16. Xiang, Z.; Quan, L.; Zhu, X.; Wang, L. A Brushless Double Mechanical Port Permanent Magnet Motor for Plug-In HEVs. *IEEE Trans. Magn.* **2015**, *51*, 8111104. [CrossRef]
17. Han, P.; Cheng, M.; Chen, Z. Dual-Electrical-Port Control of Cascaded Doubly-Fed Induction Machine for EV/HEV Applications. *IEEE Trans. Ind. Appl.* **2017**, *53*, 1390–1398. [CrossRef]
18. Shi, G.K.; Zhao, H.; Feng, Q. A Study on Hybrid Power System with Double Rotor Motor. *Automot. Eng.* **2007**, *29*, 97–100.
19. Ju, X.W.; Cheng, Y.; Zhao, T.X.; Cui, S.M. Torque characteristic analysis of a novel brushless dual rotor machine for hybrid electric vehicles. In Proceedings of the 22nd International Conference on Electrical Machines and Systems (ICEMS), Harbin, China, 11–14 August 2019; pp. 4365–4370.
20. Li, L.B.; Chen, P.; Shi, G.K.; Wang, H. Modeling and simulation of double-rotor motor applied to the system of hybrid electric vehicle. *Electr. Mach. Control* **2008**, *12*, 403–408.
21. Xia, C.Y.; Shi, J.N. Feedback Linearization and Maximum Torque per Ampere Control Methods of Cup Rotor Permanent-Magnet Doubly Fed Machine. *Energies* **2021**, *14*, 6402.
22. Xia, C.Y.; Hou, X.X. Study on the Static Load Capacity and Synthetic Vector Direct Torque Control of Brushless Doubly Fed Machines. *Energies* **2016**, *9*, 966. [CrossRef]
23. Zhou, D.; Spee, R.; Alexander, G.C. Experimental evaluation of a rotor flux oriented control algorithm for brushless doubly-fed machines. *IEEE Trans. Power Electron.* **1997**, *12*, 72–78. [CrossRef]
24. Shao, S.; Abdi, E.; Barati, F.; McMahon, R. Stator-Flux-Oriented Vector Control for Brushless Doubly Fed Induction Generator. *IEEE Trans. Ind. Electron.* **2009**, *56*, 4220–4228. [CrossRef]
25. Xia, C.Y.; Guo, H.Y. Feedback linearization control approach for brushless doubly-fed machine. *Int. J. Precis. Eng. Manuf.* **2015**, *8*, 1699–1709. [CrossRef]
26. Mosaddegh, H.; Zarchi, H.A.; Markadeh, G.A. Stator flux oriented control of brushless doubly fed induction motor drives based on maximum torque per total ampere strategy. In Proceedings of the 2019 10th International Power Electronics, Drive Systems and Technologies Conference (PEDSTC), Shiraz, Iran, 12–14 February 2019; pp. 84–89.
27. Cui, S. *MATLAB Based Vehicle Engineering Simulation Example*, 5th ed.; Chemical Industrial Press: Beijing, China, 2020; pp. 4–15.

applied sciences

MDPI

Article

Armature Electromagnetic Force Extrapolation Prediction Method for Electromagnetic Railgun at High Speed

Liang Jin [1,2,*], Dexin Gong [1,2], Yingang Yan [1,2] and Chenyuan Zhang [1,2]

[1] State Key Laboratory of Reliability and Intelligence of Electrical Equipment, Hebei University of Technology, Tianjin 300401, China
[2] Key Laboratory of Electromagnetic Field and Electrical Apparatus Reliability of Hebei Province, Hebei University of Technology, Tianjin 300401, China
* Correspondence: jinliang_email@163.com; Tel.: +86-138-2136-8162

Abstract: The analysis and calculation of the armature electromagnetic force is the premise of studying the dynamic characteristics of the electromagnetic railgun. Aiming at the problem of the numerical solution "pseudo-oscillation" at high speed, an extrapolation prediction method of armature electromagnetic force based on the Deep Belief Network-Deep Neural Network (DBN-DNN) is proposed. Firstly, the electromagnetic field control equation and armature dynamics equation, considering the influence of armature movement, are given, and the finite element simulation model of the electromagnetic railgun is established to analyze the dynamic characteristics and numerical solution stability of the armature electromagnetic force. Then, based on the stable numerical simulation data under different armature conductivities, a DBN-DNN method is proposed to realize the extrapolation prediction of the armature electromagnetic force under the standard conductance. Finally, the extrapolation prediction performance of the proposed method is tested by two electromagnetic railgun cases. Additionally, we further propose the training strategy of DBN-DNN parameters from solving armature electromagnetic force at low conductivity to standard conductivity. The armature electromagnetic force extrapolation prediction method for the whole launch process from low speed to high speed provides a new idea for the dynamic characteristic analysis of the high-speed electromagnetic railgun.

Keywords: electromagnetic railgun; armature electromagnetic force; deep learning; extrapolation and prediction; training strategy

Citation: Jin, L.; Gong, D.; Yan, Y.; Zhang, C. Armature Electromagnetic Force Extrapolation Prediction Method for Electromagnetic Railgun at High Speed. *Appl. Sci.* **2023**, *13*, 3819. https://doi.org/10.3390/app13063819

Academic Editor: Giuseppe Lacidogna

Received: 31 January 2023
Revised: 14 March 2023
Accepted: 15 March 2023
Published: 16 March 2023

1. Introduction

As a subversive launcher, the electromagnetic railgun is an important support for the country's major strategic needs. The armature electromagnetic force is one of the basic parameters in the launching process of the electromagnetic railgun. The systematic analysis of armature electromagnetic force is of great significance to the research on the dynamic characteristics and reliability design of electromagnetic railgun.

The numerical simulation method is an indispensable tool in the characteristic analysis, and domestic and foreign research teams have used different methods to carry out numerical simulation research on the electromagnetic railgun. References [1,2] used Maxwell and ANSYS software to simulate and analyze the electromagnetic railgun, and the research conclusions obtained had a certain guiding significance, but the influence of the armature movement was not considered. References [3–6] used MEGA and COMSOL software to study the electromagnetic field distribution characteristics considering the influence of armature movement in a 2D model, but they did not analyze the 3D model, which leads to inequality with the actual model. References [7–11] used different numerical simulation methods to establish a 3D model of the electromagnetic railgun considering the influence of armature movement, and they simulated the field distribution, emission characteristics,

frictional wear, and armature movement characteristics. Among them, the reference [7] used the controlled diffusion equation method, which considered the effects of armature movement by adding a velocity term to the electromagnetic field control equation. The velocity was reflected in the convection term of the equation, and the Peclet number (P_e) would increase as the velocity increased, and when $P_e > 1$, the numerical solution "pseudo-oscillation" may occur. Additionally, this restricted stable numerical simulation at high speeds. References [8–10] used the moving mesh method, which caused the convection term to not appear explicitly in the equation, but the velocity was reflected in the discrete mesh of the moving body at each time step. However, due to the linkage relationship between the armature position and grid change, the inversion and quality degradation of the grid at a high speed made the calculation difficult to converge, and there was a grid mismatch problem on the interface of the relative motion area. Reference [11] used the arbitrary Lagrangian–Euler method, and although the numerical simulation of electromagnetic railguns at high speed could be realized, due to the problems of angles, points, and edges in the coupling method, the calculation error was large.

The numerical simulation at high speed still has the problems of poor accuracy, difficult calculation, or even impossible calculation, and it is difficult or even impossible to achieve the accurate calculation solution of a high-speed electromagnetic railgun through the numerical simulation method alone. In recent years, AI technology has developed rapidly. Deep learning is an important method of data processing in AI. It can use flexible network structures and efficient optimization algorithms to obtain a strong representation and generalization ability for high-dimensional and nonlinear problems. Deep learning can learn the historical characteristics of numerical simulation results to predict and directly generate numerical simulation results, which has a great development potential. Reference [12] used Deep Belief Networks (DBN) to establish a cogging torque prediction and analysis model for permanent magnet synchronous motors, and the feasibility of the deep learning prediction model is verified by computational examples. Reference [13] proposed a deep neural network method aiming at the problem that traditional numerical simulation methods are computationally intensive and difficult to achieve a balance between accuracy and efficiency, which realized the rapid prediction of aerodynamic noise under the premise of maintaining accuracy. Reference [14] established a rapid calculation method of force based on Deep Neural Networks (DNN) that aimed at the difficult problem of modeling ironless permanent magnet synchronous linear motors and provided a high-precision and high-efficiency model for global optimization of motor parameters. The combination of numerical simulation and deep learning technology has attracted the attention of scholars in recent years and has led to some achievements in electromagnetics. Reference [15] used numerical simulation data and Convolutional Neural Networks (CNN) to predict two-dimensional potential distributions, and the prediction error was less than 1%. Reference [16] trained CNN in a supervised manner and learned the mapping of coils to motor magnetic field distributions, and the result showed good accuracy in magnetic field prediction. Reference [17] proposed a sequence-based modular network and an end-to-end network to predict the motor drive efficiency maps, which showed good accuracy in prediction. However, in the field of electromagnetic rail launch, there is a lack of application research combining numerical simulation and deep learning technology.

This paper combines the numerical simulation data of the electromagnetic railgun with depth learning and proposes an extrapolation prediction method of the armature electromagnetic force using the DBN-DNN model. This paper is organized as follows: Section 2 presents the governing equation, which considering the influence of armature movement, then establishes the finite element simulation model to analyze the dynamic characteristics and numerical solution stability of the armature electromagnetic force under different conductivity. Section 3 aims at the "pseudo-oscillation" problem of the numerical solution at high speed affected by P_e, proposes an extrapolation prediction method of armature electromagnetic force with standard armature conductivity, and then describes the network architecture and working principle of DBN-DNN. Section 4 uses two electro-

magnetic railgun cases to test the extrapolation prediction performance of the model and further proposes the acceleration effect of DBN-DNN model parameters when solving low conductivity transfer to standard conductivity, which improves the training efficiency of the model.

2. Numerical Simulation of Armature Electromagnetic Force

In the governing equation of the electromagnetic railgun and the finite element numerical simulation, the following assumptions are made:

1. The rail is in good contact with the armature, ignoring the unevenness of the contact interface and material wear.
2. The generation of molten aluminum at the interface during the launch will sharply reduce the sliding friction coefficient and tend to stabilize in order to simplify the calculation; it is assumed that it remains at a constant value of 0.11 throughout the launch process [18].
3. The performance parameters of armature and rail materials (such as conductivity and relative permeability) are constant values during numerical simulation, and they do not change with time and temperature.

2.1. Governing Equation

The Maxwell equations, the constitutive equation, and the $\boldsymbol{A}$-φ potential function are combined while considering the influence of the armature movement, and then the Coulomb specification is introduced. The electromagnetic field governing equation [19,20] described in stationary reference frame is obtained

$$\begin{cases} \nabla \times \left(\frac{1}{\mu}\nabla \times \boldsymbol{A}\right) + \sigma\nabla\phi + \sigma\frac{\partial \boldsymbol{A}}{\partial t} - \sigma\boldsymbol{v} \times \nabla \times \boldsymbol{A} = 0 \\ \nabla \times \left(\sigma\nabla\phi + \sigma\frac{\partial \boldsymbol{A}}{\partial t} - \sigma\boldsymbol{v} \times \nabla \times \boldsymbol{A}\right) = 0 \end{cases} \tag{1}$$

In the formula, $\boldsymbol{A}$ is the magnetic vector potential, φ is the electrical scalar potential, μ, σ, and v denote a partition function, namely, μ is the permeability, σ is the electrical conductivity, and v is the velocity, respectively. In the armature area: $\mu = \mu_{\mathrm{a}}$, $\sigma = \sigma_{\mathrm{a}}$, and $v \neq 0$; in the rail area: $\mu = \mu_{\mathrm{r}}$, $\sigma = \sigma_{\mathrm{r}}$, and $v = 0$; in the air area: $\mu = \mu_0 = 4\pi \times 10^{-7}$ H/m, $\sigma = \sigma_0$, and $v = 0$.

Then, the armature electromagnetic force $\boldsymbol{F}_{\mathrm{em}}$ is

$$\boldsymbol{F}_{\mathrm{em}} = \iiint_{\Omega} \boldsymbol{J} \times \boldsymbol{B} \mathrm{d}V \tag{2}$$

In the formula, $\boldsymbol{J}$ is the current density; $\boldsymbol{B}$ is the magnetic flux density. Under the combined action of the armature electromagnetic force $\boldsymbol{F}_{\mathrm{em}}$, the armature rail friction $\boldsymbol{F}_f$, and the air resistance $\boldsymbol{F}_{\mathrm{air}}$, the kinetic equation [21] are

$$\begin{aligned} m_{\boldsymbol{a}}\boldsymbol{a} &= \boldsymbol{F}_{\mathrm{em}} - \boldsymbol{F}_f - \boldsymbol{F}_{\mathrm{air}} \\ &= \iiint_{\Omega} \boldsymbol{J} \times \boldsymbol{B} \mathrm{d}V - \mu_f\left(\boldsymbol{F}_{\mathrm{N,em}} + \boldsymbol{F}_{\mathrm{N,p}}\right) - \tfrac{\gamma+1}{2}\rho_0\left(S\boldsymbol{v}^2 + S\boldsymbol{x}\boldsymbol{a} + \tfrac{C_f L \boldsymbol{v}^2 \boldsymbol{x}}{2}\right) \end{aligned} \tag{3}$$

In the formula, m_{a}, $\boldsymbol{a}$, and $\boldsymbol{x}$ are the mass, acceleration, and displacement of armature, respectively; μ_f is the friction coefficient; $\boldsymbol{F}_{\mathrm{N,em}}$ is the electromagnetic contact pressure; $\boldsymbol{F}_{\mathrm{N,p}}$ is the mechanical preloading pressure; γ is the specific heat ratio of the air; ρ_0 is the initial air density; S is the armature cross-sectional area; L is the perimeter of armature section; and C_f is the viscous friction coefficient.

2.2. Finite Element Model

The typical C-shaped armature and the 30 mm × 30 mm rectangular caliber electromagnetic railgun are taken as the research objects. Based on the COMSOL finite element

simulation software, the armature electromagnetic force is simulated and analyzed. The armature and rail model parameters are shown in Table 1.

Table 1. Parameters of armature and rail model.

Model Parameters	Symbol	Values
Rail length/mm	l_r	3500.00
Rail height/mm	h_r	40.00
Rail width/mm	w_r	20.00
Rail conductivity/(S/m)	σ_r	3.45×10^7
Rail permeability/(H/m)	μ_r	$4\pi \times 10^{-7}$
Armature length/mm	l_a	50.00
Armature height/mm	h_a	28.00
Armature width/mm	w_a	30.00
Armature conductivity/(S/m)	σ_a	2.20×10^7
Armature permeability/(H/m)	μ_a	$4\pi \times 10^{-7}$

The electromagnetic railgun geometric model and the mesh segmentation result are shown in Figure 1. Among them, the air region and some rail regions are not drawn. Considering the distribution characteristics of the electromagnetic field, the mesh of the rail is divided into cuboid shapes that gradually thicken from the inside to the outside and the mesh of the C-shaped armature is divided into hexahedral shapes with relatively regular regularities through the operations of "mapping", "distribution", "sweeping", "free quadrilateral grid", and "size". The air area is divided using a "free tetrahedral" grid. Through the above meshing operation, the average element mass of the armature and rail areas is 0.9171, and the average element mass of the entire model area is 0.9119. The closer this value is to 1, the better the mesh quality.

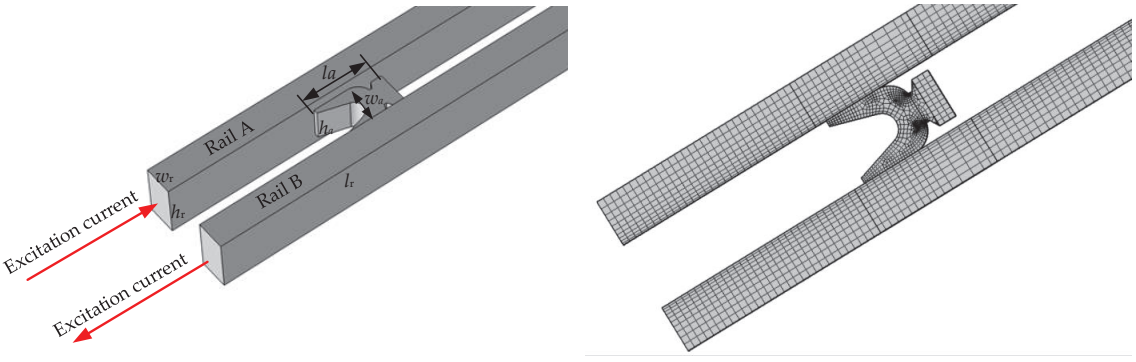

Figure 1. Electromagnetic railgun geometric model and the mesh segmentation result.

In order to observe the change in electromagnetic force more clearly with the excitation current, the trapezoidal excitation current is used closely to the project (constant current at the maximum current), as shown in Figure 2. The excitation current flows from the lower face of rail A in Figure 1, flows through the armature, and then flows out of the lower face of rail B.

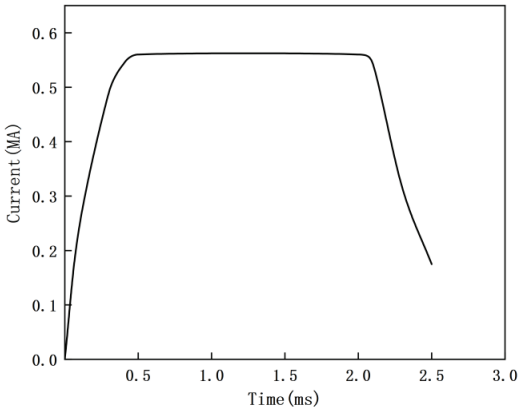

Figure 2. Waveform diagram of trapezoidal excitation current.

The material properties of the electromagnetic railgun are defined in the finite element simulation software based on Table 1. In this paper, the controlled diffusion equation method is used to numerically simulate the electromagnetic railgun, and the specific setting method is as follows: Setting the conditions for the physics fields of the "current" and "magnetic field", and then adding velocity terms by modifying the electromagnetic field control equation. The armature velocity is calculated using the physics field of "global ordinary differential and differential algebraic equations", and then so are the values of the relevant parameters in the kinetic equation, as shown in Table 2. During transient solving, we use the backward difference scheme in time. In the backward difference scheme, the equations are evaluated at the current time; therefore, it is an implicit scheme.

Table 2. Parameters of armature kinetic equation.

Parameters	Symbol	Values
Armature mass/g	m_a	125.00
Friction coefficient	μ	0.11
Mechanical preloading pressure/N	$\boldsymbol{F}_{N,p}$	5600
Specific heat ratio of the air	γ	1.4
Initial air density/(kg/m^3)	ρ_0	1.29
Armature cross-sectional area/m^2	S	0.00084
Perimeter of armature section/m	L	0.116
Viscous friction coefficient	C_f	0.003

2.3. Dynamic Characteristics and Numerical Solution Stability of Armature Electromagnetic Force

The armature electromagnetic force and movement velocity obtained by numerical simulation are shown in Figure 3. Before the armature velocity reaches 500 m/s, the stable calculation of the armature electromagnetic force and velocity can be realized; when the armature velocity increases to 500 m/s, the calculated values of the armature electromagnetic force and velocity begin to become unstable, that is, the "pseudo-oscillation" problem of the numerical solution occurs.

The numerical simulation results of the electromagnetic field on the rail section at 1.2 ms are shown in Figure 4. The rail section at 10 mm from the tail of the armature is selected as the observation angle. Under the joint action of the skin effect, proximity effect, and velocity skin effect, the magnetic flux density tends to be concentrated on the inner surface of the rail with a maximum value of 8.61 T, and the current density tends to be concentrated at two sharp corners of the inner surface of the rail, and the maximum current density is 8.84×10^8 A/m^2.

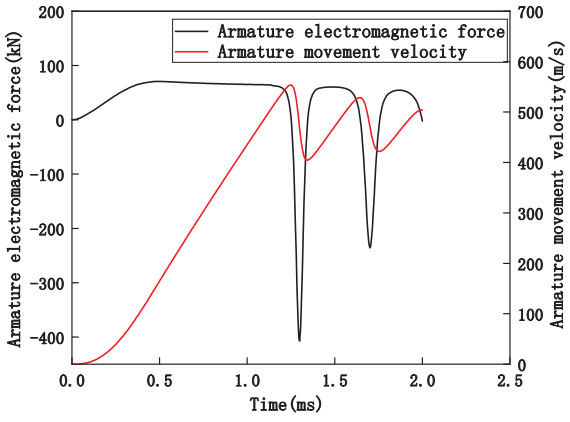

Figure 3. Calculated values of armature electromagnetic force and armature movement velocity.

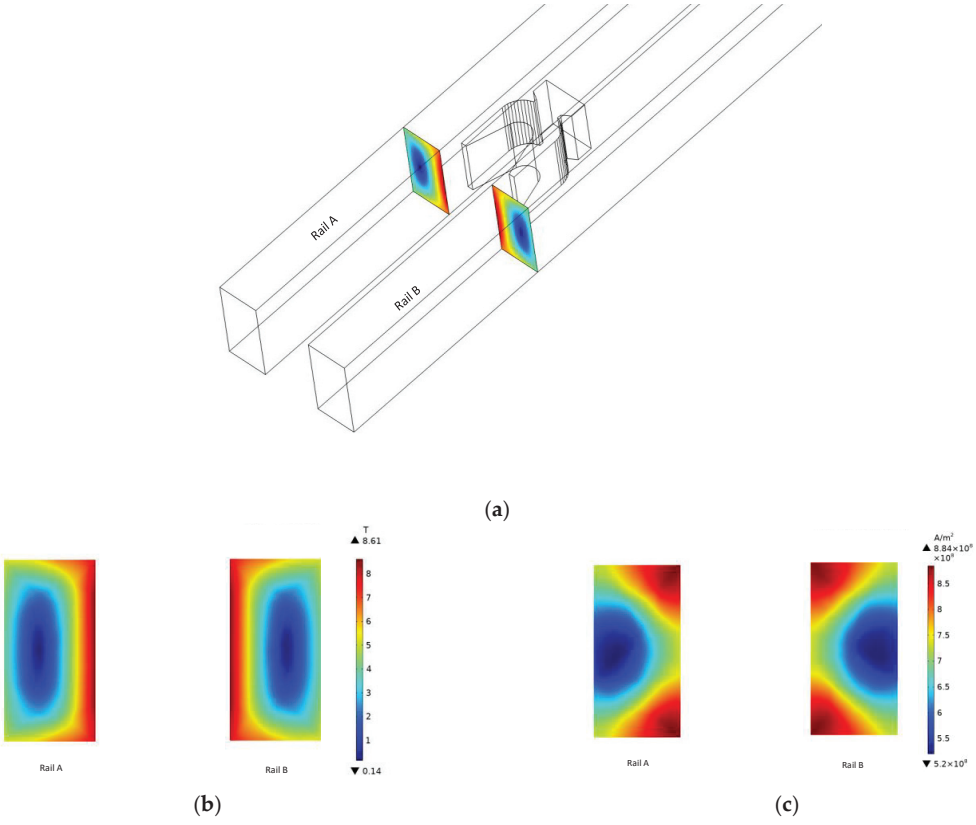

Figure 4. The numerical simulation results of the electromagnetic field on rail section at 1.2 ms. (**a**) Observation angle. (**b**) Magnetic flux density on rail section. (**c**) Current density on rail section.

The numerical simulation results of the electromagnetic field on the armature horizontal cross-section at 1.2 ms are shown in Figure 5. The horizontal cross-section in the middle of the armature is selected as the observation angle. The magnetic flux density tends to be concentrated at the throat position inside the armature with a maximum value of 16.5 T;

the current density tends to be concentrated in the inner throat and outer fillet position of the armature, and the maximum current density occurs at the armature outer fillet position of 4.35×10^9 A/m^2.

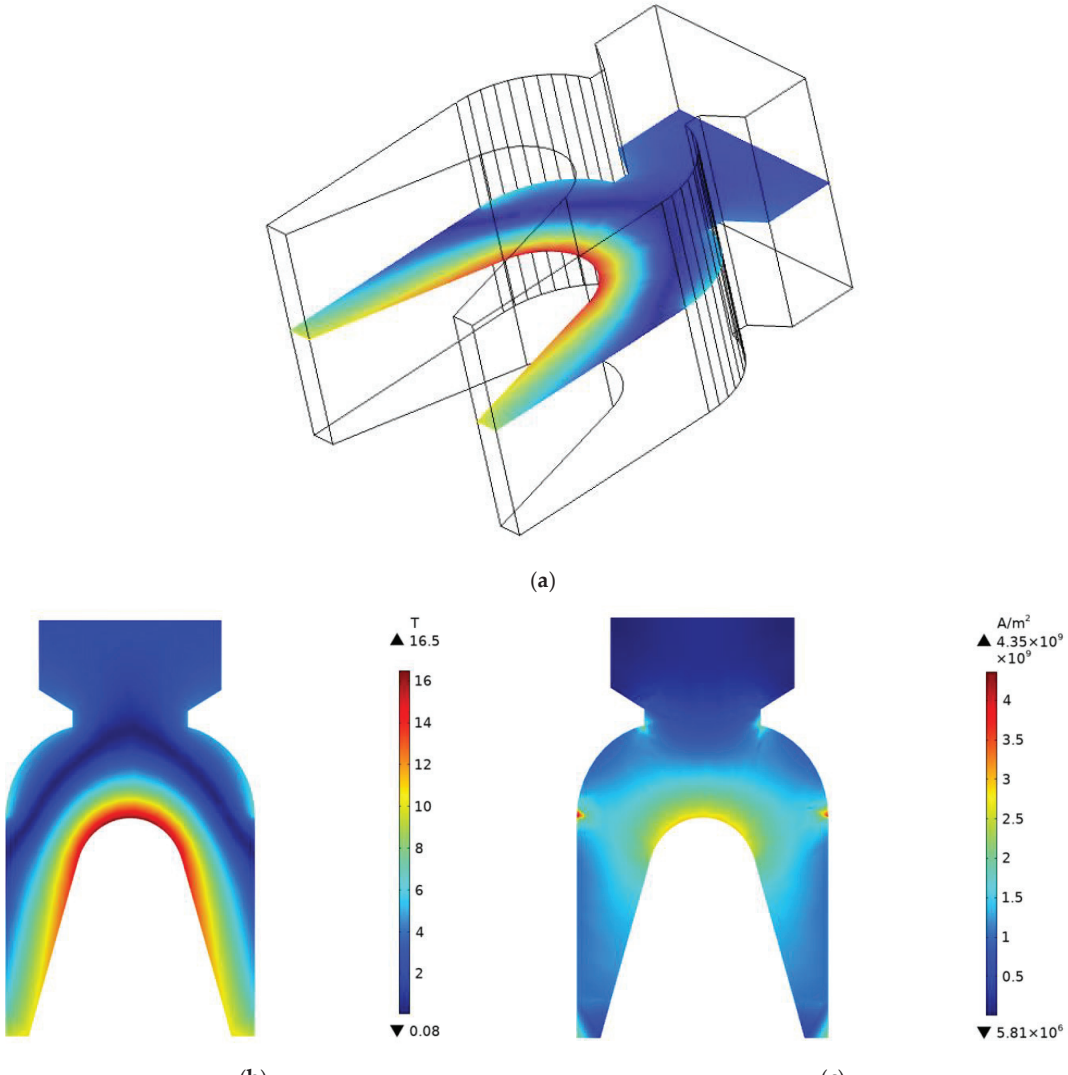

Figure 5. The numerical simulation results of the electromagnetic field on armature horizontal cross-section at 1.2 ms. (**a**) Observation angle. (**b**) Magnetic flux density on armature horizontal cross-section. (**c**) Current density distribution on armature horizontal cross-section.

The electromagnetic field governing Equation (1) of the 3D electromagnetic railgun is the convection–diffusion equation, and the velocity is reflected in the convection term of the equation. P_e is the dimensionless number that reflects the stability of the numerical solution of this equation. Additionally, the P_e is calculated as

$$P_e = \frac{convection\ rate}{diffusion\ rate} = h_c \times \frac{\sigma v}{1/\mu} = h_c \sigma v \mu \tag{4}$$

In the formula, h_c is the cell grid size. From Equation (3), we can know that P_e is proportional to the cell grid size, velocity, conductivity, and relative permeability. When $v = 500$ m/s, for $h_c = 7 \times 10^{-5}$ in the armature region, $P_e = 0.97$ is calculated based on the material properties of the armature in Table 1. With the increase in velocity, the effect of the convection term is enhanced, and the P_e number increases gradually. When $v > 500$ m/s and P_e begins to be greater than 1, the characteristics of the "principal component dominance" of the matrix of discrete equations will be weakened [22], which leads to the morbid state of the matrix and the "pseudo-oscillation" of the numerical solution, which does not exist in physics. To avoid the problem of "pseudo-oscillation" in the numerical solution, very fine meshing must be used. Under many conditions of high speed, high relative permeability, and high conductivity, the mesh component with P_e less than 1 makes the calculation too large, and the consumption of the computer resources is too high, so it is not desirable in practice.

2.4. Electromagnetic Force with Different Conductivity

Electrical conductivity is one of the factors that affect P_e, and it also affects the stability of the numerical solution. Additionally, deep learning requires the armature electromagnetic force sample data under different conductivities; under a low conductivity, the electromagnetic railgun model has low computational costs and high computational efficiencies, and we find that the armature electromagnetic force at room temperature conductivity is closer to reality by comparing the calculation results under different conductivities. Therefore, taking the rail conductivity (3.45×10^7 S/m) and armature conductivity (2.20×10^7 S/m) at room temperature as the standards for numerical simulation, the dynamic characteristics of the armature electromagnetic force at 100%, 80%, 60%, and 40% standard conductivity are analyzed.

When the armature conductivity is always the standard conductivity and only the rail conductivity changes, the armature electromagnetic force is calculated, as shown in Figure 6. The "pseudo-oscillation" of the numerical solution appears under a different rail conductivity, and the occurrence time is basically the same. The reason for this is that the rail region is stationary, and its governing equation is the diffusion equation without convection term. P_e exists in the convection–diffusion equation, so the change in the rail conductivity will not affect the stability of the numerical solution.

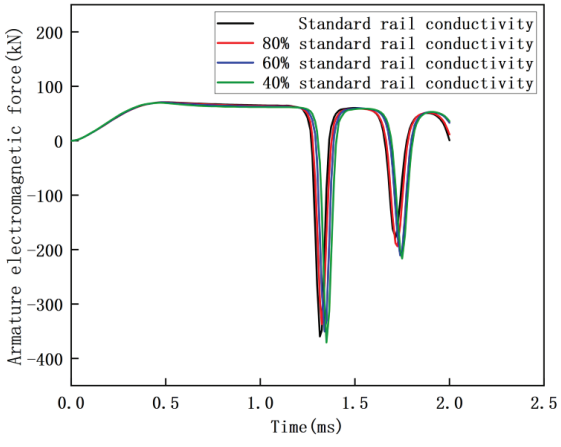

Figure 6. Armature electromagnetic force calculations when only the rail conductivity changes.

When the rail conductivity is always the standard conductivity and only the armature conductivity changes, the armature electromagnetic force is calculated, as shown in Figure 7. The governing equation of the moving armature region is the convection–diffusion equation. In the process of increasing the velocity, the lower the armature conductivity, the slower P_e of the element increases, and the later the "pseudo-oscillation" of the numerical solution appears. In the case of a 40% standard armature conductivity, the stable numerical simulation of the whole launch process can be realized.

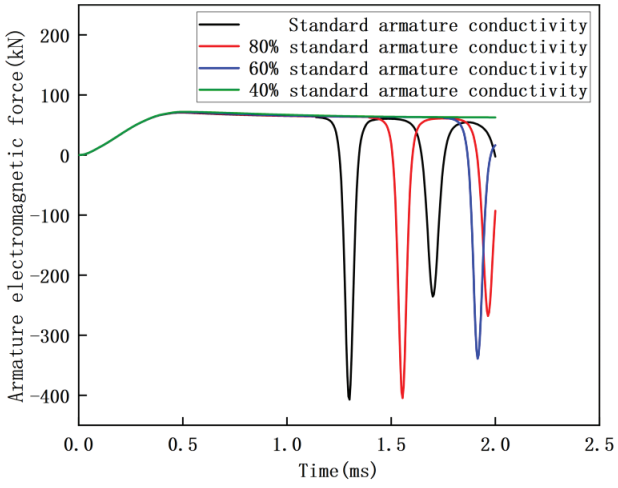

Figure 7. Armature electromagnetic force calculations when only the armature conductivity changes.

The critical velocity of the numerical simulation can be stabilized under a different armature conductivity, as shown in Table 3. Under the standard armature conductivity, the critical velocity that can stabilize the numerical simulation is 503.86 m/s. The lower the conductivity, the greater the critical velocity of the stable numerical simulation. At a 40% standard armature conductivity, the critical velocity of the stable numerical simulation increases to 956.49 m/s.

Table 3. Critical velocity for stable numerical simulation at different armature conductivities.

Armature Conductivities	Critical Velocity/(m/s)
Standard armature conductivity	503.86
80% standard armature conductivity	637.01
60% standard armature conductivity	823.30
40% standard armature conductivity	956.49

3. The Extrapolation Prediction Method

3.1. The Extrapolation Prediction Method Flow

Aiming at the problem of "pseudo-oscillation" of the numerical solution at high speed, the numerical simulation data under a different conductivity and DBN-DNN are used to realize the extrapolation prediction of the armature electromagnetic force in the stage of "pseudo-oscillation" under a standard conductivity. The extrapolation prediction method flow is shown in Figure 8.

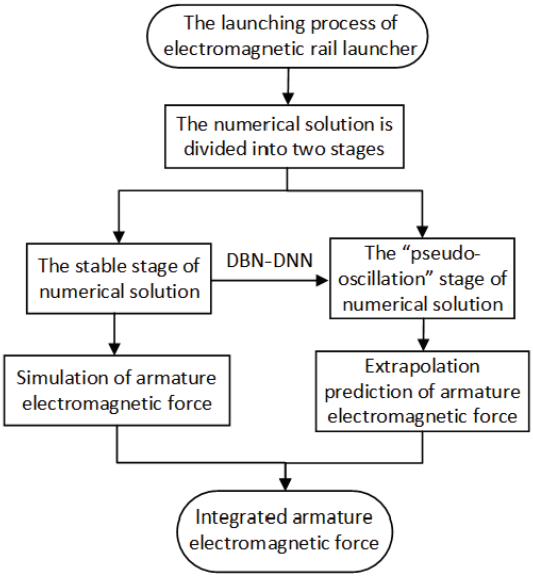

Figure 8. Flow chart of extrapolation prediction method.

1. The armature electromagnetic force under a different conductivity is numerically simulated. According to the stability of the numerical solution, the numerical solution is divided into the stable stage and the "pseudo-oscillation" stage.
2. For the stable stage, the simulation value of the armature electromagnetic force is extracted, and the sample data including the excitation current, time, velocity, armature conductivity, and electromagnetic force are obtained.
3. For the "pseudo-oscillation" stage, the sample data obtained from the stability calculation stage under a different armature conductivity are used to train the DBN-DNN model with a good effect of the feature extraction and data prediction, and then the model prediction is used to obtain the extrapolation prediction value of the armature electromagnetic force of the "pseudo-oscillation" stage under the standard armature conductivity.
4. For the comprehensive armature electromagnetic force of the whole launch process, the standard armature conductivity is obtained by superimposing the simulation value of the stability stage and the extrapolation prediction value of the "pseudo-oscillation" stage.

3.2. DBN-DNN

DBN-DNN does not need to establish the exact expression of the relationship between input and output. It can obtain the complex nonlinear mapping relationship between input and output through a lot of learning. It has the ability to express the data characteristics layer by layer and then deeply mine the data value. The DBN-DNN structure is shown in Figure 9. DBN-DNN is composed of DBN and DNN. Firstly, the whole DBN is initialized by a greedy unsupervised learning algorithm. After layer-by-layer training, the abstract feature vector learned by DBN is used as the input of DNN, which enables the network to be trained quickly, efficiently, stably, and reliably. Finally, the BP algorithm is used to train a DNN supervised to fit the label data.

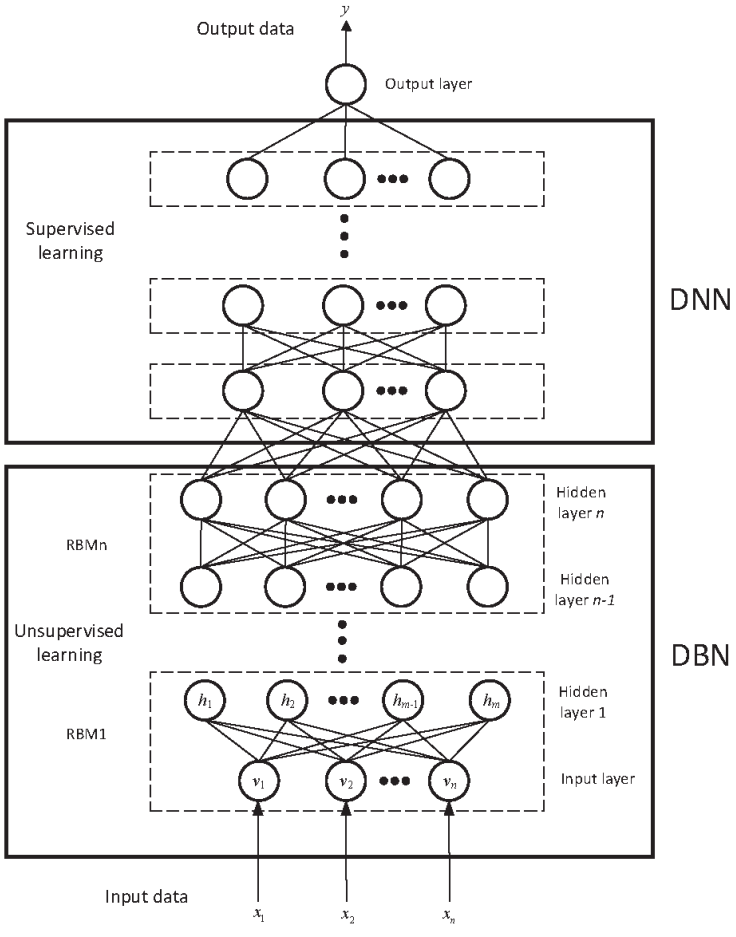

Figure 9. The structure of DBN-DNN.

DBN consists of multiple stacked Restricted Boltzmann Machine (RBM) units; each RBM consists of a visible layer and a hidden layer, and the neurons of the visible layer and the hidden layer are fully connected in both directions. The RBM is an energy model where the energy function is defined as $E_\theta(v,h)$ for a set of state quantities (v,h), and the joint probability distribution of the hidden layer and the visible layer is defined as $P(v,h)$.

$$\begin{cases} E_\theta(v,h) = -\sum_{i=1}^{n} a_i v_i - \sum_{j=1}^{m} b_j h_j - \sum_{i=1}^{n}\sum_{j=1}^{m} v_i w_{ij} h_j \\ P(v,h) = \frac{1}{Z_\theta} e^{-E_\theta(v,h)} \end{cases} \tag{5}$$

In the formula, v_i and h_j are the state vectors of the visible layer and the hidden layer, respectively; a_i and b_j are the bias vectors of the visible layer and the hidden layer, respectively; n and m are the units number of the visible layer and the hidden layer, respectively; w_{ij} is the weight between v_i and h_j; $\theta = (a_i, w_{ij}, b_j)$ is the parameters of the model; and Z_θ is the normalization coefficient.

The states of the visible and hidden layer neurons of the RBM are conditionally independent, and the probability of each neuron taking the value condition is calculated as

$$\begin{cases} P(h_j = 1|v) = \sigma(b_j + \sum_{i=1}^{n} v_i w_{ij}) \\ P(v_i = 1|h) = \sigma(a_i + \sum_{j=1}^{m} w_{ij} h_j) \end{cases} \tag{6}$$

In the formula, $\sigma(\cdot)$ is the activation function. In this paper, ReLU is used as the activation function, which can overcome the gradient disappearance and retain data information very well. On the other hand, it makes the network sparse, alleviating the overfitting problem.

In this paper, the network parameters are adjusted by the maximum likelihood estimation method, so the goal of training the RBM is to maximize the likelihood function $L(\theta)$ of the network to obtain the parameter θ, that is

$$L(\theta, v) = \prod_{i=1}^{n} p(v^i) \tag{7}$$

To simplify the calculation, it can be written in the logarithmic form shown in Equation (8). Additionally, the Contrasting Divergence (CD) algorithm [23] is used to train the RBM.

$$\begin{cases} \ln L(\theta, v) = \sum_{i=1}^{n} \ln p(v^i) \\ \theta = \text{argmax} L(\theta) = \text{argmax} \sum_{i=1}^{n} p(v^i) \end{cases} \tag{8}$$

In this paper, in the study of the electromagnetic railgun, the armature electromagnetic force is the output variable, and the excitation current, time, velocity, and armature conductivity, which affect the armature electromagnetic force, are the input variables. The armature electromagnetic force and its influence parameters obtained by numerical simulation are used to train the DBN-DNN, so that the DBN-DNN can learn the complex nonlinear mapping relationship to realize the extrapolation prediction of the armature electromagnetic force in the stage of "pseudo-oscillation". When setting the network structure, the number of hidden layers is selected as four. The number of neurons in each layer is 24, 18, 14, and 10, and the training process uses the Adaptive Moment Estimation (Adam) optimizer. To reduce the complexity of the neural networks, a dropout layer has been added. On the one hand, it can simplify the structure of the neural network and reduce the training time; on the other hand, each neuron appears with a certain probability, and a weight update no longer depends on the joint action of fixed relationship neurons, thereby improving the overfitting phenomenon of the network.

4. Case Analysis

Two cases of electromagnetic railguns with different exit velocities are used to test the extrapolation prediction performance of the model. The extrapolation prediction is realized by PyTorch [24].

4.1. Case 1

The Okaloosa Armature Tester (OAT) and MCA 103 armature published by the Florida laboratory were taken as the research objects [25,26]. The geometric dimensions and material property parameters of the model are shown in Table 4.

Table 4. Parameters of armature and rail model.

Model Parameters	Symbol	Values
Rail length/mm	l_r	220.00
Rail height/mm	h_r	31.75
Rail width/mm	w_r	6.35
Rail conductivity/(S/m)	σ_r	5.80×10
Rail permeability/(H/m)	μ_r	$4\pi \times 10^{-7}$
Armature length/mm	l_a	28.59
Armature height/mm	h_a	25.00
Armature width/mm	w_a	25.00
Armature conductivity/(S/m)	σ_a	1.86×10^7
Armature permeability/(H/m)	μ_a	$4\pi \times 10^{-7}$

The extrapolation prediction performance of the model was tested using the launch data of SLK 018. The armature has a mass of 249.72 g and flies out after accelerating in the bore for 1.0 ms. The waveform diagram of excitation current is shown in Figure 10.

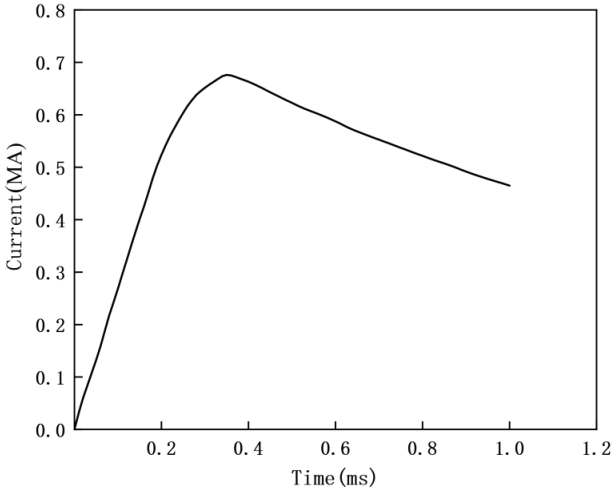

Figure 10. Waveform diagram of excitation current in case 1.

Establishing the finite element simulation model of the electromagnetic railgun. Based on the armature conductivity (1.86×10^7 S/m) in Table 3, the numerical simulation results of the armature electromagnetic force under different armature conductivities are obtained, as shown in Figure 11. Because of the short acceleration time and low flight velocity of the armature in this case, there is no "pseudo-oscillation" in the numerical solution of the armature electromagnetic force under each conductivity. Under the condition of low armature conductivity, the current distribution of the conductor is more uniform, and the armature electromagnetic force is larger.

Through the above numerical simulation, 4000 groups of required sample data are obtained. In order to eliminate the influence of the magnitude and dimension of data on the prediction accuracy and convergence speed, the sample data are normalized and divided into a training set and a test set. Among them, the training set is divided into two kinds: the sample data obtained under the standard armature conductivity and the sample data obtained under different armature conductivity. The test set is the sample data in 0.87–1 ms time under the standard armature conductivity.

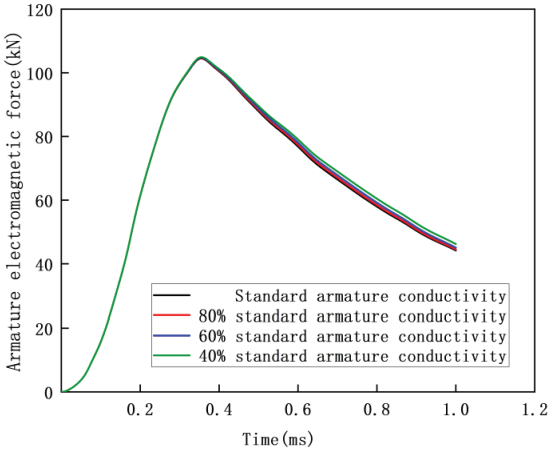

Figure 11. Simulation calculation value of armature electromagnetic force under different armature conductivities in case 1.

The above two training sets are used to train four extrapolated prediction models: Support Vector Regression (SVR), Random Forest (RF), DNN, and DBN-DNN. Then, the test set is used to test the extrapolated prediction model after training. The Mean Absolute Percentage Error (MAPE) is selected as the standard to measure the evaluation performance of the extrapolated prediction model. The value range of MAPE is [0, +∞). The smaller the value is, the higher the accuracy of the prediction model is. The calculation method is

$$MAPE = \frac{1}{N}\sum_{i=1}^{N}\frac{|y_i - \hat{y}_i|}{y_i} \times 100\% \quad (9)$$

In the formula, N is the number of samples, and $\hat{y}_i$ and yi are the predicted and simulated value of armature electromagnetic force of the sample, respectively. Considering the randomness of the performance evaluation of each extrapolation prediction model, the four extrapolation prediction models are trained and tested five times, and then the average value of MAPE is taken, as shown in Table 5.

Table 5. Average MAPE of four extrapolated prediction models.

Name	SVR	RF	DNN	DBN-DNN
When using sample data under standard armature conductivity to train the model.	6.07%	5.84%	2.38%	2.02%
When using sample data under different armature conductivity to train the model.	2.23%	2.16%	0.75%	0.52%

Compared with the training set under the standard armature conductivity, the sample data in the training set under a different armature conductivity are more sufficient, which enables the extrapolated prediction model to better grasp the overall characteristics of the data. It is more helpful to learn the mapping relationship between the excitation current, time, velocity, armature conductivity variables, and armature electromagnetic force, and the prediction effect is better.

As traditional machine learning models, SVR and RF have a limited ability to deal with input features, a restricted generalization ability, and a low prediction accuracy when solving complex problems. As a deep learning model, DNN can use deep networks and

a large number of sample data to learn the multi-level abstract features and the hidden structural representations of data, and it has a high prediction accuracy. In the DBN-DNN model, DBN completes feature extraction by pre-training the coupling relationship of input features, and it provides reasonable initial parameters for DNN training, so DBN-DNN has a greater nonlinear fitting ability and generalization ability than DNN model, and it has the highest prediction accuracy.

Through the comparison of the MAPE average of the four extrapolated prediction models under the two training sets, we know that the training set under different armature conductivities is used to train the DBN-DNN model, and then the test set is used to test the highest accuracy, and the average MAPE is the smallest, which is 0.52%. Thirty-five groups of samples are selected from its test set at equal intervals, and the calculated values of armature electromagnetic force are compared with the predicted values, as shown in Figure 12.

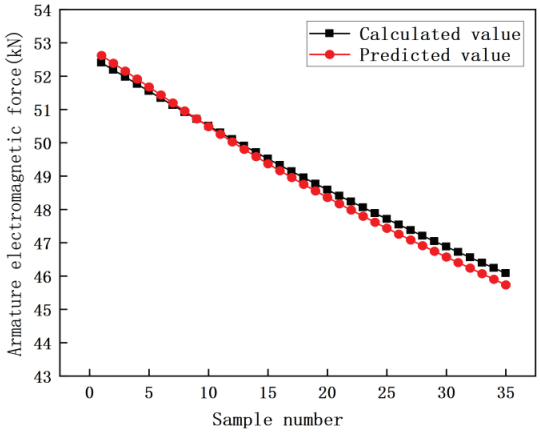

Figure 12. Comparison between the calculated value and the predicted value of armature electromagnetic force.

In Figure 11, the numerical simulation results of the armature electromagnetic force of 0–0.87 ms under the standard armature conductivity are obtained. The DBN-DNN model is trained with the sample data obtained under different armature conductivity, and then the extrapolated prediction of the armature electromagnetic force of 0.87–1 ms under the standard armature conductivity is obtained by using the test set sample extrapolation prediction. The calculated value is superimposed with the predicted values to obtain the comprehensive armature electromagnetic force of the whole launch process (0–1 ms), as shown in Figure 13.

According to the armature electromagnetic force under the standard armature conductivity in Figure 11, the calculated value of the armature velocity is obtained; according to the integrated armature electromagnetic force under the standard armature conductivity in Figure 13, the combined value of calculation and prediction of the armature velocity is obtained. The two values are similar, and they are compared with the experimental measurement value of the armature movement velocity, as shown in Figure 14. The experimental measurement value of the armature exit velocity is 247.0 m/s; the calculated value is 245.7 m/s, which is 0.53% smaller than the experimental measurement value; and the combined value of calculation and prediction is 244.9 m/s, which is 0.85% smaller than the experimental measurement value.

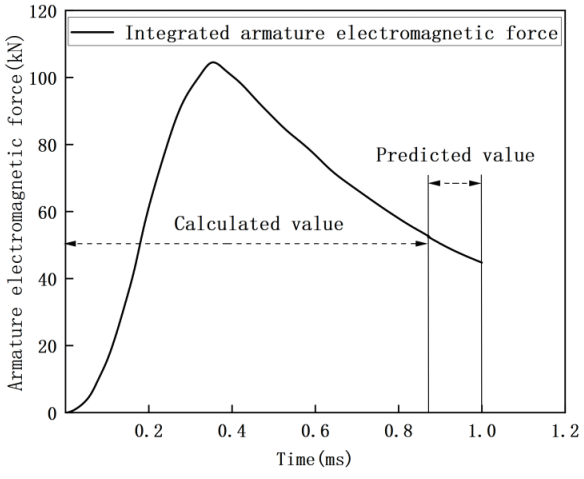

Figure 13. Integrated armature electromagnetic force under standard armature conductivity in case 1.

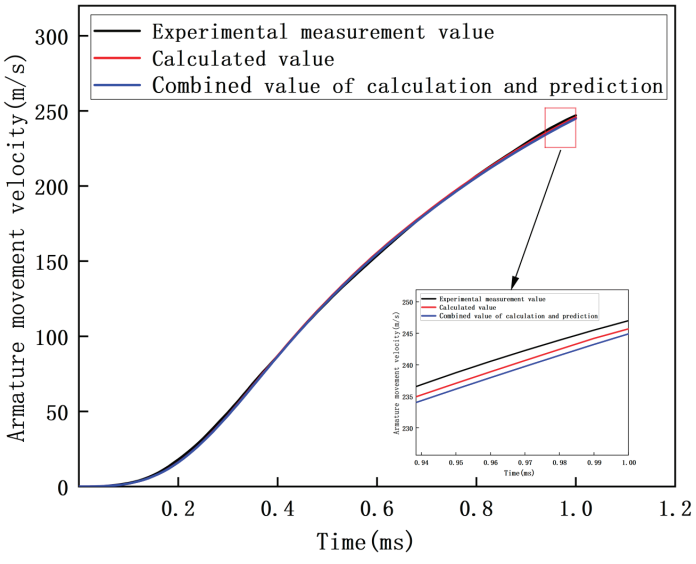

Figure 14. Comparison of armature movement velocity.

4.2. Case 2

In case 1, the armature velocity is low. In order to verify the applicability of the extrapolation prediction method under high-speed armature movement, the 40 mm × 50 mm medium-caliber railgun developed by the Agency for Defense Development (ADD) is taken as the research object [27]. Using the launch data of test number #26, where the armature mass is 300 g and it flies out after accelerating in the bore for 4.0 ms. The waveform diagram of the excitation current is shown in Figure 15.

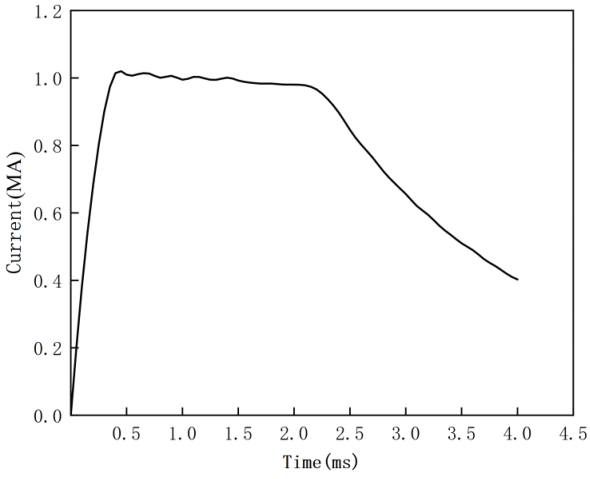

Figure 15. Waveform diagram of excitation current in case 2.

Establishing the finite element simulation model of the electromagnetic railgun. The numerical simulation results of the armature electromagnetic force under different armature conductivities are obtained when 2.50×10^7 S/m is used as the standard armature conductivity in this case model, as shown in Figure 16. Under the standard conductivity, the numerical solution of the armature electromagnetic force appears as "pseudo-oscillation" after 1.41 ms, and the lower the armature conductivity, the later the "pseudo-oscillation" occurs, and the stable numerical simulation of the whole launch process can be realized under 40% standard armature conductivity.

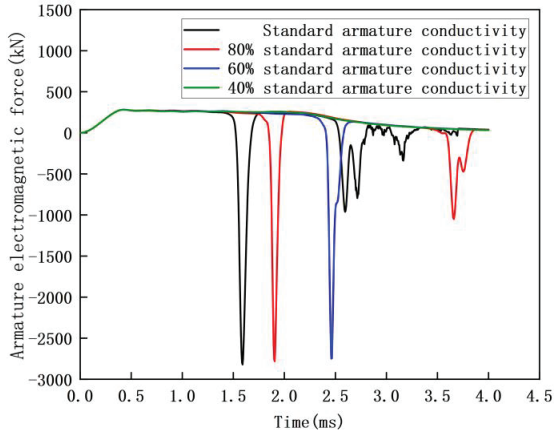

Figure 16. Simulation calculation value of armature electromagnetic force under different armature conductivities in case 2.

Through the above numerical simulation, 9500 groups of sample data under different armature conductivities of the stable stage are obtained. These sample data are normalized and divided into a training set and a test set. The training set contains the 0–1.13 ms sample data under the standard armature conductivity and all the sample data under low conductivity; the test set is the 1.13–1.41 ms sample data under the standard armature conductivity. Using the training set to train the DBN-DNN model, and then using the test

set to test the DBN-DNN model after training. The average MAPE of five training tests is 0.56%.

The DBN-DNN model, which is closest to the average value of MAPE in five training tests, is used to predict the armature electromagnetic force of the pseudo-oscillation stage (1.41–4.0 ms) under the standard conductivity, and the extrapolated prediction value of the armature electromagnetic force is obtained. Then, superimposed with the calculated value of the stable stage under the standard conductivity (0–1.41 ms) in Figure 16, the integrated armature electromagnetic force of the whole launch process (0–4.0 ms) is obtained, as shown in Figure 17.

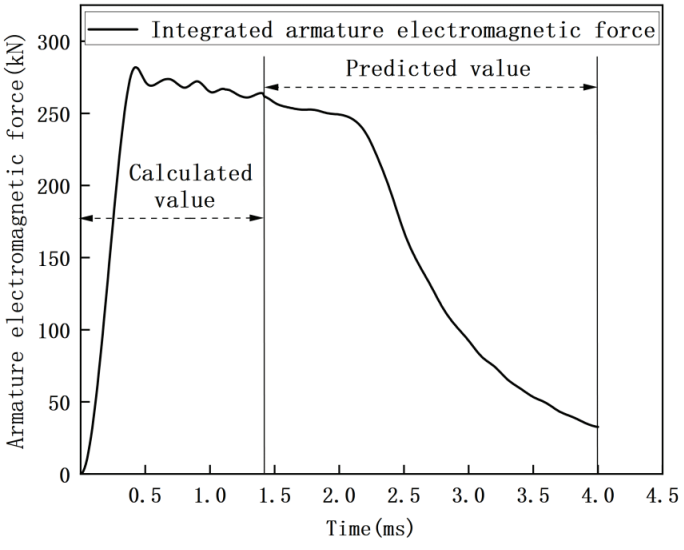

Figure 17. Integrated armature electromagnetic force under standard armature conductivity in case 2.

According to the armature kinetic equation and the integrated armature electromagnetic force under the standard armature conductivity obtained in Figure 17, the armature exit velocity is calculated as 2029.2 m/s. It is 1.03% smaller than the experimental measurement value 2050.3 m/s, which can meet the needs of practical engineering calculation and tests the performance of the armature electromagnetic force extrapolation prediction of the DBN-DNN model.

4.3. Training Strategy

The above two cases use the original training strategy: based on the stable numerical simulation sample data under different conductivities, they train the model together, and then they extrapolate the armature electromagnetic force under the standard conductivity. In order to improve the convergence speed and prediction performance of the model, this paper further proposes an improved training strategy for the transfer of DBN-DNN parameters from the armature electromagnetic force to the standard conductivity under a low conductivity. The details are as follows: First, the DBN-DNN is trained based on the numerical simulation data of 40% standard conductivity, and the current network parameters are saved after the training is completed. They are then used as the initial value of the network parameters under 60% standard conductivity. Similarly, the network parameters after training under 60% standard conductivity are taken as the initial values of network parameters under 80% standard armature conductivity. Based on this strategy, the extrapolation prediction of the armature electromagnetic force under standard armature conductivity is realized.

Using the two cases in this paper, the results of the DBN-DNN model under the two training strategies are compared, as shown in Table 6. Compared with the original training strategy, the improved training strategy reduces the MAPE value by about 20%, and the prediction effect is better; the improved training strategy improved the training speed of the model by 46.05% and 63.86%, respectively. As a whole, the training speed can be greatly accelerated by improving the training strategy, while the accuracy of the prediction model is guaranteed.

Table 6. The results of DBN-DNN model under different training strategies.

Case	Training Strategy	MAPE	Training Time/s
Case 1	Original training strategy.	0.52%	76
	Improved training strategy.	0.42%	41
Case 2	Original training strategy.	0.56%	202
	Improved training strategy.	0.45%	73

In the DBN-DNN model with an improved training strategy, the solution under different conductivities can be regarded as multiple tasks with similar control equations. Although the initial training error of the network is higher at 40% armature conductivity, the initial training error of the network at 60%, 80%, and a standard armature conductivity will gradually decrease. Additionally, the number of iterations decreases with the training process, and the training speed can become faster and faster so that the solution of the network can converge quickly under the standard armature conductivity, thus accelerating the optimization process of network parameters.

5. Conclusions

In this paper, the armature electromagnetic force of the electromagnetic railgun at high speed is analyzed and studied, and the following conclusions are drawn:

1. Due to the influence of P_e, there exists the problem of "pseudo-oscillation" in solving the convection–diffusion equation of the electromagnetic railgun at high speed, and P_e is proportional to the armature velocity and armature conductivity.
2. An extrapolation prediction method of the armature electromagnetic force at high speed is proposed, and the prediction accuracy of different models is compared to verify the advanced nature of the DBN-DNN extrapolation prediction model established in this paper.
3. In the two cases, the difference between the calculated value of the armature exit velocity and the experimental measurement value is 0.85% and 1.03%, respectively, which can meet the needs of practical engineering calculation and verify the feasibility and correctness of extrapolation prediction.
4. The training strategy of the DBN-DNN parameters is proposed when the armature electromagnetic force is transferred from a low conductivity to a standard conductivity, which ensures the prediction accuracy of the model and accelerates the training speed.

The extrapolation prediction method proposed in this paper can extrapolate the numerical results to the field of electromagnetic comprehensive performance, which is difficult or even impossible to calculate. In the next step, we will apply this method to the field, wear, vibration, and other aspects and carry out a field guidance optimization and an uncertainty optimization to achieve the performance optimization and reliability estimation of the electromagnetic railgun under extreme conditions.

Author Contributions: Conceptualization, L.J.; methodology, L.J. and D.G.; software, D.G. and C.Z.; validation, D.G. and Y.Y.; formal analysis, L.J.; investigation, Y.Y.; resources, L.J.; data curation, L.J.; writing—original draft preparation, D.G., Y.Y. and L.J.; writing—review and editing, L.J. and D.G.; visualization, D.G.; supervision, L.J. and C.Z.; project administration, L.J.; funding acquisition, L.J. All authors have read and agreed to the published version of the manuscript.

Funding: This research was funded by the Major Research Program of the National Natural Science Foundation of China, grant number 92066206, the Project of National Natural Science Foundation of China, grant number 51977148, and the Local Science and Technology Development Projects Guided by the Central Government, grant number 226Z4503G.

Institutional Review Board Statement: Not applicable.

Informed Consent Statement: Not applicable.

Data Availability Statement: All data, models generated or used during the study appear in the submitted article.

Conflicts of Interest: The authors declare no conflict of interest.

References

1. Zhang, H.; Li, S.; Gao, X.; Lu, T.; Liu, F. Distribution characteristics of electromagnetic field and temperature field of different caliber electromagnetic railguns. *IEEE Trans. Plasma Sci.* **2020**, *48*, 4342–4349. [CrossRef]
2. Liu, Y.; Guo, W.; Zhang, T.; Su, Z.; Fan, W.; Zhang, H. Influence of contacting schemes on electromagnetic force and current density distribution in armature. *IEEE Trans. Plasma Sci.* **2019**, *47*, 2726–2735. [CrossRef]
3. Rodger, D.; Leonard, P.; Eastham, J. Modelling electromagnetic rail launchers at speed using 3D finite elements. *IEEE Trans. Magn.* **1991**, *27*, 314–317. [CrossRef]
4. Rodger, D.; Leonard, P. Modelling the electromagnetic performance of moving rail gun launchers using finite elements. *IEEE Trans. Magn.* **1993**, *29*, 496–498. [CrossRef]
5. Yang, Y.; Dai, K.; Yin, Q.; Liu, P.; Yu, D.; Li, H.; Zhang, H. In-bore dynamic measurement and mechanism analysis of multi-physics environment for electromagnetic railguns. *IEEE Access* **2021**, *9*, 16999–17010. [CrossRef]
6. Li, C.; Chen, L.; Wang, Z.; Ruan, J.; Wu, P.; He, J.; Xia, S. Influence of armature movement velocity on the magnetic field distribution and current density distribution in railgun. *IEEE Trans. Plasma Sci.* **2020**, *48*, 2308–2315. [CrossRef]
7. Jin, L.; Gong, D.; Yang, Q.; Zhang, C. Characteristic analysis and verification of electromagnetic force for armature of the electromagnetic rail launcher. In Proceedings of the 2022 IEEE 20th Biennial Conference on Electromagnetic Field Computation (CEFC), Denver, CO, USA, 24–26 October 2022; pp. 1–2.
8. Hsieh, K. A lagrangian formulation for mechanically, thermally coupled electromagnetic diffusive processes with moving conductors. *IEEE Trans. Magn.* **1995**, *31*, 604–609. [CrossRef]
9. Hsieh, K. Hybrid FE/BE implementation on electromechanical systems with moving conductors. *IEEE Trans. Magn.* **2007**, *43*, 1131–1133. [CrossRef]
10. Yang, F.; Zhai, X.; Zhang, X.; Liu, H. Dynamic multiphasic coupling analysis of electromagnetic orbit launcher. *J. Proj. Rocket. Missiles Guid.* **2021**, *41*, 20–24.
11. Jin, L.; Lei, B.; Zhang, Q.; Zhu, R. Electromechanical performance of rails with different cross-section shapes in railgun. In Proceedings of the 2014 17th International Symposium on Electromagnetic Launch Technology, La Jolla, CA, USA, 7–11 July 2014; pp. 1–5.
12. Jin, L.; Wang, F.; Yang, Q.; Wang, D.; Kou, X. Typical deep learning model and training method for performance analysis of permanent magnet synchronous motor. *Trans. China Electrotech. Soc.* **2018**, *33*, 41–48.
13. Meng, H.; Xu, Z.; Yang, J.; Liang, B.; Cheng, J. Fast prediction of aerodynamic noise induced by the flow around a cylinder based on deep neural network. *Chin. Phys. B* **2022**, *31*, 545–550. [CrossRef]
14. Yang, Y.; Zhao, J.; Song, J.; Dong, F.; He, Z.; Zong, K. Structural optimization of air-core permanent magnet synchronous linear motors based on deep neural network models. *Proc. CSEE* **2019**, *39*, 6085–6094.
15. Tang, W.; Shan, T.; Dang, X.; Li, M.; Yang, F.; Xu, S.; Wu, J. Study on a Poisson's equation solver based on deep learning technique. In Proceedings of the 2017 IEEE Electrical Design of Advanced Packaging and Systems Symposium (EDAPS), Haining, China, 14–16 September 2017; pp. 1–3.
16. Khan, A.; Ghorbanian, V.; Lowther, D. Deep learning for magnetic field estimation. *IEEE Trans. Magn.* **2019**, *55*, 7202304. [CrossRef]
17. Khan, A.; Mohammadi, M.; Ghorbanian, V.; Lowther, D. Efficiency map prediction of motor drives using deep learning. *IEEE Trans. Magn.* **2020**, *56*, 7511504. [CrossRef]
18. Yang, K.; Kim, S.; Lee, B.; An, S. Electromagnetic launch experiments using a 4.8-MJ pulsed power supply. *IEEE Trans. Plasma Sci.* **2015**, *43*, 1358–1361. [CrossRef]
19. Zhang, Y.; Lu, J.; Tan, S.; Li, B.; Wu, H.; Jiang, Y. Heat generation and thermal management of a rapid-fire electromagnetic rail launcher. *IEEE Trans. Plasma Sci.* **2019**, *47*, 2143–2150. [CrossRef]
20. Fan, W.; Jiang, Y.; Wang, Y.; Liu, W.; Su, Z. Thermal measurement experiments and transient temperature distribution of rapid-fire augmented electromagnetic railgun. *IEEE Trans. Plasma Sci.* **2022**, *50*, 1351–1359.
21. Wen, Y.; Dai, L.; Lin, F. Effect of geometric parameters on equivalent load and efficiency in rectangular bore railgun. *IEEE Trans. Plasma Sci.* **2021**, *49*, 1428–1433. [CrossRef]

22. Ruan, J.; Zhang, Y.; Wang, D.; Shu, S.; Qiu, Z. Numerical simulation research and applications of electromagnetic multiphysical field for electrical equipment. *High Volt. Eng.* **2020**, *46*, 739–756.
23. Hinton, G. Training products of experts by minimizing contrastive divergence. *Neural Comput.* **2002**, *14*, 1771–1800. [CrossRef]
24. Jiang, L.; Zhang, Z. Research on image classification algorithm based on Pytorch. *J. Phys. Conf. Ser.* **2021**, *2010*, 012009. [CrossRef]
25. Price, J.; Yun, H. Design and testing of integrated metal armature sabots for launch of armour penetrating projectiles from electric guns. *IEEE Trans. Magn.* **1995**, *31*, 219–224. [CrossRef]
26. Hsieh, K.; Kim, B. International railgun modelling effort. *IEEE Trans. Magn.* **1997**, *33*, 245–248. [CrossRef]
27. Kim, S.; An, S.; Lee, B.; Lee, Y.; Yang, K. Modeling and circuit analysis of an electromagnetic launcher system for transient current waveforms. In Proceedings of the 2014 17th International Symposium on Electromagnetic Launch Technology, La Jolla, CA, USA, 7–11 July 2014; pp. 1–5.

applied sciences

MDPI

Article

Analysis of Performance Improvement of Passenger Car Synchronous Homopolar Generator with the Addition of Ferrite Magnets

Vladimir Prakht, Vladimir Dmitrievskii and Vadim Kazakbaev *

Department of Electrical Engineering, Ural Federal University, 620002 Yekaterinburg, Russia
* Correspondence: vadim.kazakbaev@urfu.ru; Tel.: +7-909-028-49-25

Featured Application: The research findings can be applied in the design of generators of various vehicles, in particular synchronous homopolar generators.

Abstract: Electric machines with hybrid excitation have increased torque density while maintaining a wide range of speed control. This article presents the results of the optimal design of a synchronous homopolar generator (SHG) with ferrite magnets on the rotor and excitation winding on the stator for passenger cars. The use of ferrite magnets on the rotor of a synchronous homopolar generator makes it possible to use the stator surface more efficiently, which in turn increases energy efficiency and reduces the dimensions of the generator. At the same time, the excitation winding on the stator provides a reliable brushless design and the ability to control the excitation flux. The problem of long-time calculation of the three-dimensional SHG structure, which is especially relevant when using multi-iterative computer optimization, is solved by using the computationally efficient Nelder-Mead method and a simplified SHG model using two-dimensional finite element analysis. It is also clear that the low torque ripple of SHG with ferrite magnets with two stator-rotor stack combinations (SRSC) is largely provided by the fact that the torque ripples of individual SRSCs are in antiphase. The problem of considering the magnetic properties of magnetic core sections made of structural low-carbon steel is discussed. It has been found that with an increase in both the saturation level of the magnetic circuit and the magnetomotive force (MMF) of the SHG excitation winding, resistance to irreversible demagnetization of ferrite magnets on the rotor can be increased by increasing their height. In addition, it is shown that there is a significant increase in performance when using the hybrid excitation, in comparison with the conventional SHG design without magnets.

Keywords: brushless; design optimization; electric machine; ferrite magnets; hybrid excitation; Nelder–Mead method; passenger car generator; synchronous homopolar generator; synchronous homopolar machine; wound field machines

Citation: Prakht, V.; Dmitrievskii, V.; Kazakbaev, V. Analysis of Performance Improvement of Passenger Car Synchronous Homopolar Generator with the Addition of Ferrite Magnets. *Appl. Sci.* **2023**, *13*, 3990. https://doi.org/10.3390/app13063990

Academic Editor: Roberto Zivieri

Received: 17 February 2023
Revised: 18 March 2023
Accepted: 19 March 2023
Published: 21 March 2023

1. Introduction

1.1. Advantages of Synchronous Machines with Electric and Hybrid Excitation without Rare Earth Magnets

Generators with rare-earth permanent magnets are widely used when operating with a controlled rectifier [1]. At the same time, many researchers are looking for alternative designs that do not contain rare earth magnets, since these magnets are expensive, and their use makes the manufacturer dependent on a few suppliers. The price of rare earth magnets can fluctuate greatly and change several times, depending on the state of the international market. The extraction of raw materials for rare earth magnets is harmful to the environment [2]. In addition, electric machines with rare earth magnets have disadvantages in operation. Nd-Fe-B rare earth magnets are not well suited for high temperature applications due to their tendency to irreversibly demagnetize at temperatures above 120 °C and strong demagnetizing fields. While more temperature resistant Sm-Co

magnets are available, due to the high cost and difficulty in machining, they are typically only used in aerospace systems [3].

The electrical conductivity of rare earth magnets is relatively high, therefore, at a high operating frequency, large eddy currents are induced in rare earth magnets, which leads to their high heating and complicates their use in high-speed applications. Magnetomotive force (MMF) from permanent magnets is uncontrollable and cannot be turned off in emergency situations, which complicates the use of the machines with rare earth magnets in many applications [4]. An alternative is wound rotor electrically excited synchronous generators (WRSG). However, their conventional designs cannot be used in many applications due to the presence of slip rings and brushes feeding the excitation winding on the rotor, which are subject to rapid wear [5]. In addition, the excitation winding on the rotor produces significant losses, which makes it difficult to cool the WRSG.

In a number of applications, for example, for turbo generators connected directly to the grid and for electric aircraft, wound rotor synchronous generators with a brushless exciter are used [6,7]. However, the use of a brushless exciter leads to an increase in the cost, size, and weight compared to traditional generators. In addition, in railway applications, the low resistance of the brushless exciter to shaking and shock loads, as well as the complexity of repairing a generator with such an exciter, are critical. Another alternative with an electrically excited brushless design is synchronous homopolar machines (SHMs).

1.2. Overview of Literature on the Design of Synchronous Homopolar Machines

On non-fully electrified rail lines, undercar generators can be used to power passenger cars. Often, synchronous homopolar generators (SHGs) without permanent magnets with concentrated excitation coils on the stator are used in this application, due to their relatively high performance and highly reliable brushless design that is resistant to shaking and shock loads and to the absence of windings on the rotor [8]. SHMs also find uses in other applications such as traction drives, flywheel storage, wind turbines, on-board generators, and welding generators [9–13]. In addition, the excitation current of the SHG is adjustable, as in a conventional electrically excited generator.

The analysis of the magnetic field of the SHG and, consequently, its optimization, is complicated by the complex three-dimensional configuration of its magnetic core. In some parts of the machine, the flux flows in the axial direction, and in others do so in the transverse plane (in the tangential and radial directions) and changes its direction to an axial one when moving from the laminated parts to the solid stator housing or magnetic sleeve on the rotor shaft.

The applicability of the traditional two-dimensional finite element model is limited, due to the three-dimensional nature of the magnetic field of the SHG. Researchers have developed a number of models that take into account the three-dimensional structure of the SHG magnetic field using one-dimensional magnetic circuits [14,15], models based on the two-dimensional finite element method (FEM) [16,17], and three-dimensional FEM models [18,19]. In [17], a technique for modeling the SGM was presented, which considers the three-dimensional structure of the magnetic field within the framework of a two-dimensional model by introducing an additional term into the equations of the vector magnetic potential, and jointly solving them with the one-dimensional equation of the axial magnetic circuit of the excitation flux. An experimental verification of this technique is carried out.

In [8,9,14,16,19–22], SHM performance analysis for generators and flywheel energy storage applications is carried out. Due to the complexity of the configuration of the magnetic system, many different methods for calculating the performance of SHG have been proposed. In [8], an SHG design using the 2D FEA mode was considered in order to improve the performance properties of a mass-produced undercar generator. Manual optimization of the number of rotor teeth, as well as the parameters of the rotor and stator teeth, was applied. Through experimental verification it is shown that the optimized design has a higher no-load EMF value. In [9], modeling of the transient process in a low-power

train-lighting alternator based on SHM is considered, taking into account the eccentricity of the rotor. In [19], the analysis of a low-power high-speed SHM with an external rotor is considered, the design of which is carried out using analytical expressions. The SHM performance at idle and at rated load is calculated using 3D FEA. In [14,16], an equivalent 2D finite element SHM model with virtual excitation on the rotor is presented, which is verified using 3D FEA and an experimental study. In [20], the design of a high-speed high-power motor/generator based on SHM is considered. The layout of a superconducting excitation winding, and a water-cooled armature winding made of Litz wire is described. For performance analysis, an approximate SHM model is used in which the magnetic field is analyzed using a 2D finite element analysis in a plane containing the axis of rotation of the machine. In [18], analysis using 3D FEM and manual optimization of the no-load electromotive force (EMF) for a three-phase SHG with a speed control range of 500–7000 rpm are presented. Characteristics of the SHM are evaluated with different combinations of stator and rotor teeth: 9/6, 15/10 and 18/12. An experimental verification was provided. In [23], the optimization of the mass and dimensions of an SHG using a genetic method and a lumped parameter model is presented. It is noted that the use of 3D FEA in SHM optimization is complicated by a large calculation time. In [24,25], methods for analyzing transient processes in SHGs using ordinary differential equations are proposed. In [26,27], methods for analyzing the thermal state of an SHG are proposed. In [28], the features of SHG modeling with a superconducting excitation winding are discussed.

Despite the SHM advantages, the losses in SHM with the same dimensions are significantly higher than in conventional WRSG due to less efficient use of the rotor surface [5]. Since ferrite magnets are much cheaper than rare earth magnets, have a wider range of suppliers and are environmentally friendly, it is attractive to improve the performance of the SHG by adding ferrite magnets. Ferrite magnets are also well suited for use in high-temperature applications and have extremely low electrical conductivity, which makes them suitable for high-speed applications [22].

In [21,22], a design of an SHG with ferrite magnets for powering passenger cars is presented. It is shown that the addition of ferrite magnets makes it possible to increase the efficiency and reduce the mass and dimensions of the SHG. In [21], the calculation of the electromotive force (EMF) of SHG with ferrite magnets at idle is carried out; however, the calculation of the performances under load and the analysis of irreversible demagnetization were not carried out. In [22], a design of SHG with ferrite magnets is described in more detail.

1.3. The Problem and Aim of the Study

The review of the literature shows that the performance optimization of SHG with ferrite magnets under load has never been presented.

The purpose of the study is to increase the performance and reduce the weight and dimensions of synchronous homopolar generators for passenger cars operated on non-electrified and partially electrified railways. The novelty of this article lies in the development of a technique for optimizing the on-load performance of SHG with ferrite magnets as a railway undercar generator. The cost function is constructed, and a relevant example of the optimized design is obtained. The optimization of the SHG with ferrites minimizes losses, semiconductor rectifier current, torque ripple, and the volume of irreversibly demagnetized permanent magnets. In addition, a comparative analysis of the characteristics of the optimized SHG with ferrite magnets and an SHG without permanent magnets, the optimized characteristics of which were obtained in [29], is presented.

2. Main Features of the Considered Design of the SHG with Ferrite Magnets

As Figure 1 shows, the SHG has two laminated steel stator-rotor stack combinations (SRSCs). In the axial direction, the excitation magnetic flux is transmitted through the non-laminated stator housing, in which the stator laminated stacks are installed, and through the rotor sleeve, on which the laminated rotor stacks are installed. The three-phase

armature winding is placed in 54 stator slots and has 12 poles with the number of slots per pole and per phase $q = 54/(12 \cdot 3) = 1.5$.

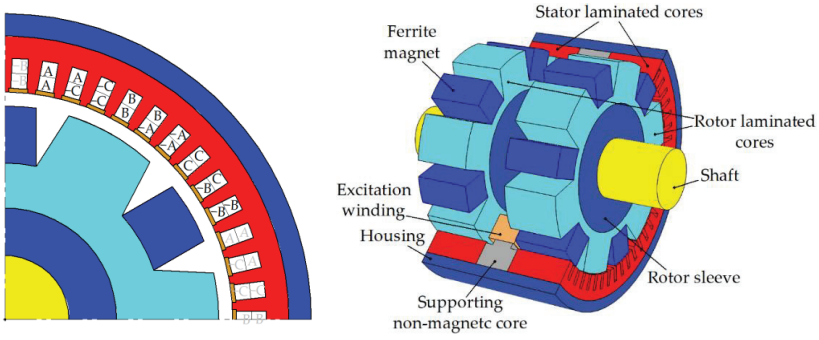

Figure 1. SHG approximate geometry: (**a**) Cross-section and stator armature winding configuration (1/4 of the generator cross-section is shown, the other parts are symmetrical); (**b**) General view. One half of a stator cutout is shown. Rotor is shown without cutout. The armature winding placed in the stator slots is not shown.

The excitation winding is placed in an axial gap between the two generator SRSCs. The laminated rotor stacks are of salient pole design. The rotor has no windings and has low-energy ferrite magnets in the slots of the rotor stacks. Each rotor lamination has six teeth. The tooth shift of the two rotor laminations relative to each other is 30 mechanical degrees.

Figure 2 shows the scheme for rectifying the output current of the generator to the network of the car. The generator feeds the network of the car, and also recharges the battery. The rectifier uses controlled transistor switches that provide vector control of the generator armature winding current. The concentric coil of the excitation winding is located between the pairs of rotor and stator stacks and is fixed on the supporting non-magnetic core. The DC-link voltage (close to the maximum amplitude of the line-to-line voltage of the generator) must not exceed 116 V. The semiconductor converter also includes a single-phase breaker for powering the excitation winding of the generator.

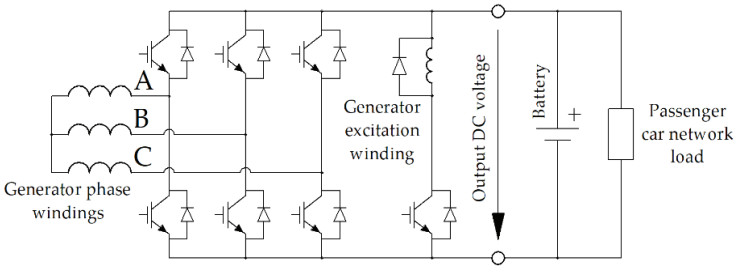

Figure 2. Scheme of rectifying the output current of the generator to the car network. Capital letters denote the phases A, B, C of the generator.

At the preliminary calculations, it was established that without parallel paths, each layer of the armature winding should contain one turn. However, this led to large eddy current losses in the armature winding, so the number of parallel paths was chosen to be six, that is, equal to the number of pole pairs.

3. SHG Mathematical Model

The SHG magnetic core has two SRSCs linked to each other in the axial direction by the stator housing and the rotor sleeve made of non-laminated low-carbon steel. The excitation

winding fixed on the stator induces the excitation flux, which passes through the SRSCs, the stator sleeve on the rotor shaft, and the stator housing [8,30] (see Figure 3). The modulation of the magnetic field by the teeth of the rotor allows this magnetic flux to interact with the poles of the armature winding on the stator. In the absence of magnets, only half of the poles would be involved in the torque production. The addition of permanent magnets between the teeth of the rotor makes all poles of the armature winding to usable [31,32].

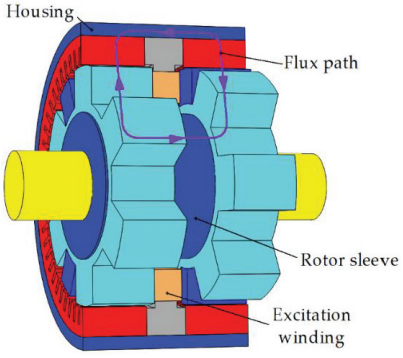

Figure 3. Excitation winding flux path through the stator housing, the SRCSs, and the rotor sleeve.

The developed mathematical model consists of a set of g boundary 2D magnetostatic problems for a magnetic field in the cross section of an SRCS and a magnetic circuit equation with lumped parameters in the axial direction. The range of considered rotor position angles is chosen taking into account the symmetry with respect to a shift by a third of the electric period and cyclic phase permutation and is equal to a third of the electric period. One third of the electric period is divided into g sections and boundary value problems are considered for the beginning of each section. In this study, g = 24.

As in conventional electric machines, the magnetic field in a good approximation can be assumed to be uniform along the axis and lying in the transverse plane. Therefore, the equations traditional for 2D problems of magnetostatics are solved [17]:

$$\begin{aligned} \frac{\partial B_x}{\partial x} + \frac{\partial B_y}{\partial y} &= 0; \\ \frac{\partial H_y}{\partial x} - \frac{\partial H_x}{\partial y} &= J_z, \end{aligned} \tag{1}$$

where J_z is the z-component of the current density, which is not equal to zero only in the stator slots filled with a winding; B_x and B_y are the components of the magnetic flux density; H_x and H_y are the components of the magnetic field.

A distinctive feature of SHM is the presence of a magnetic monopole, i.e., excitation flux flowing in on the inner boundary of the rotor and flowing out of the outer boundary of the stator (or vice versa). Then, the general solution of the Gauss law for magnetism (1) can be expressed as follows:

$$\begin{aligned} B_x &= \frac{\partial A_z}{\partial y} + \frac{\phi\, x}{2\pi(x^2+y^2)}; \\ B_y &= -\frac{\partial A_z}{\partial x} + \frac{\phi\, y}{2\pi(x^2+y^2)}. \end{aligned} \tag{2}$$

where A_z is the z-component of the vector magnetic potential; ϕ is the linear density of the magnetic charge. Only the component of the vector magnetic potential A along the z-axis is different from zero. In these equations, the first terms on the right side of these equations are common for a magnetostatic problem. The second terms determine the linear flux density of the magnetic monopole, which is set based on the following relation:

$$\Phi = \phi \cdot L_{stator}/2. \tag{3}$$

where L_{stator} is the total stator laminated stack length.

The calculation area is one sector corresponding to the pole pitch of the generator, with periodic boundary conditions P_I and P_{II} on the boundaries of this sector, as shown in Figure 4. The change in the rotor angular position is modeled not by changing the geometry of the calculation area, but by changing the connecting boundary condition on a circular line lying in the middle of the air gap between the rotor and stator.

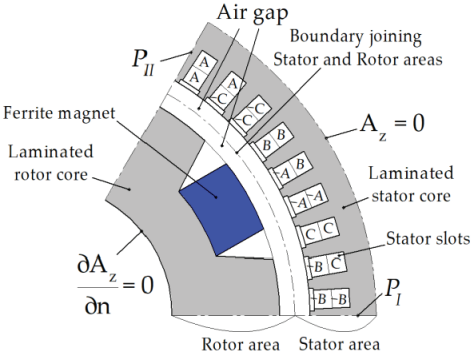

Figure 4. Computational domain.

The equations of magnetostatics are complemented by constitutive equations. For the rotor and stator stacks, the magnetization curve *H(B)* is set. For magnets, the residual magnetic flux density and the magnetic permeability are set. For the areas of the armature winding, the current density is set, and the flux coupled to the winding is calculated, which is necessary to calculate the voltage in the armature winding.

The rotor rotates together with the rotating field, and there are practically no eddy currents in its stack and sleeve. Since the rotor sleeve is ferromagnetic, the normal derivative of A_z is equal to zero at the inner boundary of the rotor package (the Neumann boundary condition).

On the contrary, the magnetic flux is frozen into the stator housing, and the normal component of the magnetic flux density at the outer boundary of the stator stack is represented only by the monopole field. Thus, for the outer boundary of the stator stack, the Dirichlet boundary condition $A_z = 0$ is accepted.

Due to the fact that the field is frozen into the stator housing, we will assume that the magnetic charge does not change in time, and when calculating the MMF drop on a pair of rotor and stator stacks, we will use the average value for all boundary value problems. MMF can be calculated as a curvilinear integral of magnetic field along any trajectory from the inner boundary of the rotor stack to the outer boundary of the stator stack. Radial segments can be chosen as such trajectories. However, due to the discreteness of the finite element method, such integrals will have a small accuracy. Therefore, it is better to average over the azimuthal angle the values of these integrals. Therefore, the MMF drop on one pair of rotor and stator stacks is determined by the formula:

$$F = \frac{p}{2\pi g} \sum_{i=0}^{g-1} \iint \frac{H_{xi} \cdot x + H_{yi} \cdot y}{x^2 + y^2} \, dS, \tag{4}$$

where the double integral $\int\int$ is taken over the entire computational domain.

The magnetic circuit equation in the axial direction has the form [17]:

$$N \cdot I_{exc} = 2 \cdot F + F_{housing} + F_{sleeve}, \tag{5}$$

where I_{exc} is the excitation winding current; N is the number of turns of the excitation winding; F is the drop in MMF on one SRCS; $F_{housing} = \lambda \cdot H_{housing}$ $(\Phi / S_{housing})$ is the MMF drop on the stator housing; $F_{sleeve} = \lambda \cdot H_{sleeve}$ (Φ / S_{sleeve}) is the MMF drop on the rotor

sleeve; $H_{housing}$ and H_{sleeve} are the dependences of the magnetic field on the magnetic flux density in the stator housing and in the rotor sleeve, respectively; $S_{housing}$ and S_{sleeve} are the cross-sectional areas of the housing and sleeve; λ is the axial distance between the SRCSs.

The torque created by one SRCS and the EMF induced in the armature winding of one SRCS are called nonsymmetrized. The torque and EMF of the whole machine are equal to the sum of the torque and the EMF of each SRCS. To find the torque and EMF of the whole machine, there is no need to calculate them for each SRCS. It is assumed that the torque of the second SRCS is equal to that of the first SRCS, and the EMF is equal to that of the first SRCS with a sign '−' when the rotor is shifted by half the electric period [17]. Further, the torque ripple of the whole machine is referred to as symmetrized torque ripple. The torque ripple as a single SRVS is referred to as nonsymmetrized torque ripple.

The iron loss is a key component of the total loss. Therefore, it is also evaluated for each intermediate design obtained during the optimization, i.e., at each step of optimization (each call of the objective function) based on the solution of g boundary problems. A conventional algorithm for calculating iron losses is used [33].

4. Selection of the Objective Function and Optimization Parameters

Like traction motors, an undercar generator is an electrical machine, operating over a wide range of speeds at a constant required output power. However, in the case of a generator, a constant electrical output is required. The rotational speed of an undercar generator increases along with the velocity of the train. The operating speed range of the considered undercar generator is from 750 to 3450 rpm. The generator must produce about 35 kW in this speed range [34]. In order to simplify the optimization procedure, it was assumed that the mechanical power of the generator does not change and is equal to P_{max} = 40 kW > 35 kW in the entire considered speed range, roughly taking into account the generator loss. Two boundary points are considered in the optimization: the speed n_1 = 3450 rpm at the torque of $T_{max} \cdot n_2/n_1$ = 111 N·m and the speed n_2 = 750 rpm at the torque of T_{max} = 510 N·m (Figure 5).

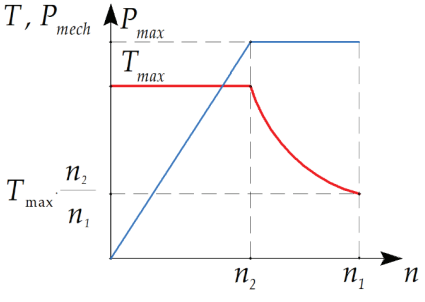

Figure 5. The required torque and mechanical power of the generator as a function of speed.

Manufacturers of passenger car generators [34] have been requested to increase their energy efficiency, and it is necessary to limit the reactive current and torque ripple. In addition, in order to avoid the failure of the generator, it is necessary to prevent irreversible demagnetization of the permanent magnets on the rotor.

Thus, the goals of optimization in descending order of importance are to minimize the following quantities:

1. Average losses <P_{loss}> which are estimates as the average losses in the modes with the speeds of 750 rpm and 3450 rpm;
2. Upper limit of the phase armature current I_{arm};
3. Symmetrized torque ripple max($TRsym$) in the entire operating speed range;
4. Non-symmetrized torque ripple max(TR) in the entire operating speed range;
5. Volume of irreversibly demagnetized magnets at maximum current at a speed of 750 rpm.

Structural steel 1010 (non-laminated steel used for the manufacture of machine parts) is the material of non-laminated parts of the magnetic circuit. Since the exact magnetization curve and saturation knee point of this steel are not exactly known and are not specified by the manufacturer to ensure that the drop in the magnetomotive force on the stator housing and rotor sleeve is small compared to the drops on the SRSCs, the flux density in these parts is limited to 1.6 T.

In this study, the single-criterion unconditional Nelder-Mead method is used to optimize the SHG design, which is well known [35] and is included in the basic MATLAB software package ("fminsearch" function).

Since the Nelder-Mead method is a single-criteria method, in order to achieve the set of optimization goals, the objective function is set as the product of individual goals raised to a certain power, reflecting their significance. Since the Nelder-Mead method is an unrestricted method, the constraints are also given as separate multipliers of the objective function. To avoid reducing the size of the simplex too quickly and slowing down or stalling the optimization process as a result, the corresponding multipliers increase rapidly rather than discretely, unless constraint conditions ("soft constraints") are met. The objective function used is:

$$F = < P_{loss} > \max(I_{arm})^{0.7} \max(TRsym)^{0.025} \max(TR)^{0.01} f\left(\left(\frac{B_h}{1.6}\right)^5\right) f\left(\left(\frac{S_{demag}}{S_{mag}}\right)^{300}\right);$$
$$f(x) = \begin{cases} x, x > 1 \\ 1, otherwise \end{cases}, \quad (6)$$

where <P_{loss}> is the average total loss (arithmetic mean of total losses P_{loss} at the two considered operating points);

max(I_{arm}) is the maximum armature current that occurs at the 2nd operating point (the maximum torque; 750 rpm); max($TRsym$) is the maximum value of the symmetrized torque ripple; max(TR) is the maximum value of the nonsymmetrized torque ripple; B_h is magnetic flux density in the stator housing and rotor sleeve at the 2nd operating point; S_{demag} is the area of the demagnetized magnets; S_{mag} is the total area of the magnets. Furthermore, for greater clarity, the natural logarithm (6) is used.

In Equation (6), constants/weights 1, 0.7, 0.025 and 0.01 determine the importance of certain objectives. These values just reflect the approximate relative priority of each of the optimization goals, based on the experience of the authors in designing similar machines. The most important target has a weight of one. The most important optimization objective is to reduce the average loss, so the corresponding <P_{loss}> multiplier is raised to the highest power. The constant 0.7 means that a 1% reduction in the current at 750 rpm is considered as valuable as a 0.7% reduction in the average loss. The objectives of reducing symmetrized and unsymmetrized torque ripples are substantially less important. The constants 0.025 and 0.01 mean that other things being equal, designs with lower torque ripples are preferable.

The last two multipliers of function (6) set the soft constraints of flux density in non-laminated parts of the magnetic core and the area of irreversibly demagnetized ferrite magnets. The constants 5 and 300 control the steepness of the constraints. Too small values of these constants can lead to constraint violations, i.e., to an unacceptable design. Calculations show that the optimized design satisfies the constraints (flux density in these parts is no more than 1.6 T; demagnetizing force is 3.9 kOe). Too large values cause fast reduction of the volume of the simplex, which slows down optimization.

In order to simplify the optimization procedure, as well as the possibility of using the results for different types of winding wires with different standard sizes (for example as specified in [36]), it is assumed that the number of turns in the layer of the armature winding, as well as the width and height of the wire are arbitrary positive real numbers. The number of turns is selected so as to fit with the amplitude value of the line voltage V_{3450} in the 40 kW; 3450 rpm (maximum voltage) operating point is equal to 113 V [5]. The number of parallel branches is assumed to be equal to six. The parameters that define the design of the generator are illustrated in Figure 6.

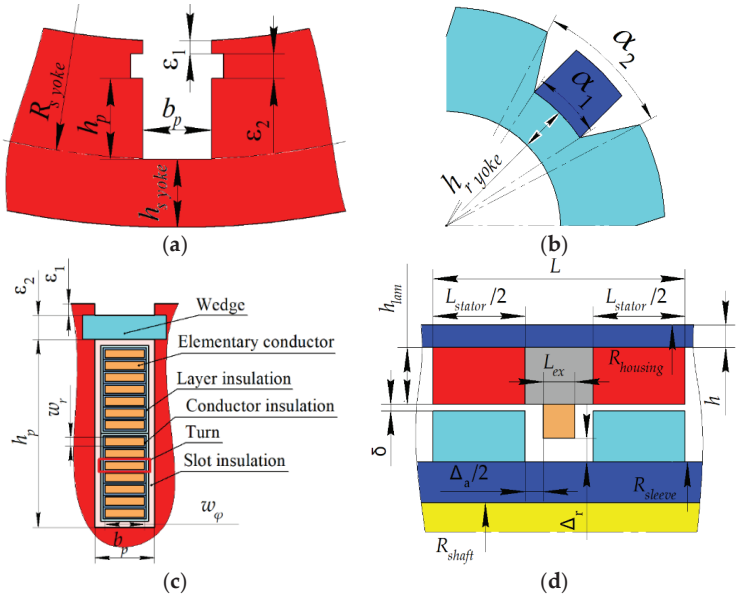

Figure 6. Parameters of the SHG geometry. (**a**) Stator core parameters; (**b**) Rotor core parameters; (**c**) Armature winding parameters; (**d**) Parameters in the axial plane.

The main unchangeable parameters of the generator are shown in Table 1. Table 2 shows the values of the parameters of the SHG varied during the optimization for the initial design, as well as the design obtained as a result of optimization. Because the Nelder-Mead method is an unconstrained optimization method, ranges of optimization parameters are not provided.

Since the Nelder-Mead method is a local search method, the initial design is not completely random. To obtain the initial design, a manual optimization with several attempts was carried out. The parameters varied manually to achieve better performance, to mitigate the saturation or the violation of the constraints. Some principles used are as follows:

- To mitigate the saturation, the thickness of the most saturated parts of the magnetic core must be increased. For example, to decrease saturation, the most saturated parts of the magnetic core should be thickened;
- To decrease the total loss, it is useful to inspect the losses in individual parts of the machine;
- To decrease the loss in the armature winding or in the excitation one, we can try to increase their cross-section area, etc.

The rotor shaft is made of non-magnetic material. Since the same magnetic flux flows through the stator housing and the rotor sleeve, their cross sections are assumed to be equal. For this reason, a change in the thickness of the stator housing also leads not only to a change in the outer diameter of the stator lamination, but also to a change in the outer diameter of the rotor sleeve.

Table 1. Main unchangeable parameters of the generator.

Characteristics	Values
Length of all laminated stacks plus the axial clearances between them for installing excitation coils L, mm	150
Outer diameter of the stator housing, mm	370
Axial clearance between excitation coils and a rotor stack Δ_a, mm	15
Radial clearance between excitation coils and the rotor sleeve Δ_r, mm	12
Diameter of the rotor shaft, mm	40
Back iron width of stator lamination $H_{stator\ yoke}$, mm	12
Back iron width of rotor lamination $H_{rotor\ yoke}$, mm	9
Thickness of the stator wedge, ε_2, mm	1
Stator tooth tip height ε_1, mm	1
Current angle at 750 rpm, electrical radian	0.1
Grade of electrical steel	2412
Thickness of electrical steel, mm	0.35

Table 2. Initial and optimized vectors of the variable optimization parameters.

Characteristics	Initial Design, $x0$	Optimized Design, x
Housing thickness h, mm	15	11.07
Total stator stacks length L_{stator}, mm	130	128.3
Stator slot depth h_p, mm	20	27.9
Stator slot width b_p, mm	5	6.37
Airgap width δ, mm	2	0.91
Rotor slot thickness, α_1	$0.5 \cdot t_z$ *	$0.481 \cdot t_z$ *
Rotor slot thickness, α_2	$0.6 \cdot t_z$ *	$0.689 \cdot t_z$ *
Angle of field weakening at 3450 rpm, electrical radian	0.6	0.93
Current ratio ** @ 750 rpm	8	14.54
Current ratio ** @ 3450 rpm	8	9.76

Notes: * $t_z = 360/6 = 60°$ (mechanical) is the rotor tooth pitch; ** the current ratio is the ratio between the current in a layer of the armature winding and the excitation current.

The net fill factor of the armature slot with copper is assumed to be 0.8. The width w_x and the height w_y of the rectangular wire of the armature winding, which are taken into account when estimating its DC losses and eddy current losses, include the thicknesses of conductors and insulation [5]:

$$b_p = w_x + a_x; h_p = 2 \cdot (w_y + \Delta w) \cdot N_{sec} + a_y, \quad (7)$$

where $a_x = 1.51$ mm, $a_y = 1.8$ mm, $\Delta w = 0.31$ mm take into account the thicknesses of the rectangular busbar insulation and the thickness of the slot insulation.

When calculating losses in the excitation winding, eddy current losses are not taken into account. At the maximum torque, the angle between the center of the rotor tooth and the stator current vector ("current angle") is taken unchanged and equal to 0.1 electric radians as shown in Table 1. The current angle at maximum speed is also an optimization parameter as shown in Table 2.

Figure 7 illustrates the order of calculations when calling the objective function F (6). The optimization procedure 'fminsearch'of MATLAB software, which implements the simplex gradientless Nelder-Mead method [35], is well known, and its details are described

in [37].The optimization procedure fminsearch(F, $x0$) is launched to find the vector x of optimized values of the generator parameters, where $x0$ is a vector with initial values of the generator parameters (see Table 2).

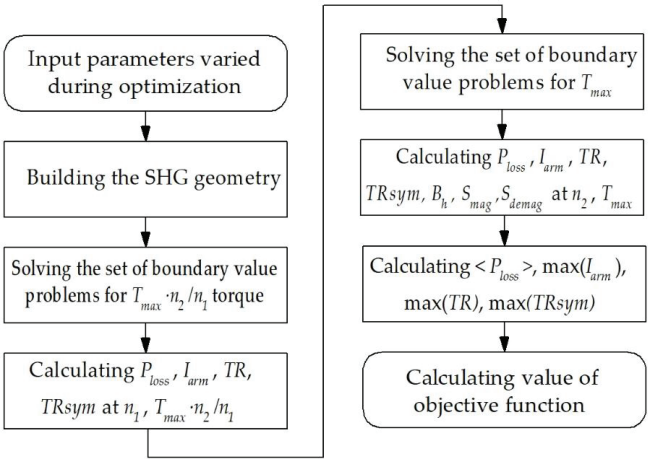

Figure 7. Order of the SHM performance calculation during one step of the optimization. The objective function is defined by Equation (6). The input parameters are shown in Table 2.

5. Optimization Progress and Comparative Analysis of the Generator Performances before and after Optimization

As a result of optimization, the value of the objective function (6) converges to a minimum (Figure 8). The volume of the simplex can quickly decrease during optimization, and further optimization slows down. Therefore, after the 180th function call, the Nelder-Mead method was restarted. The optimal solution found was used as the initial approximation. The linear dimensions of the simplex at the restart were reduced by four times compared to the initial simplex. One function call takes approximately 20 min using a laptop with two cores, 2.70 GHz processor and 16 GB of RAM.

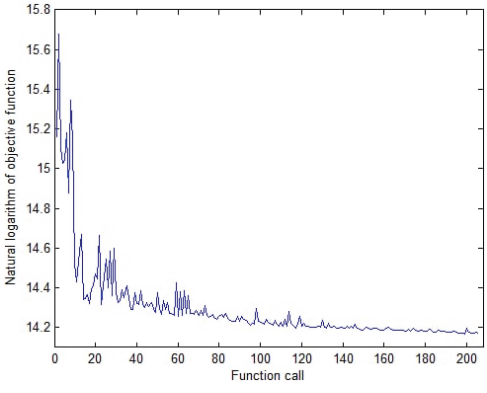

Figure 8. Progress of the objective function (6) during optimization.

The average generator loss (Figure 9a) and the upper limit of the output current (Figure 9b) were significantly reduced through optimization. The non-symmetrized torque ripple, which is the lowest priority optimization target, according to the objective function (6), increased its value (Figure 10a). However, the noise and vibrations caused by the generator in the mechanism joining it with the wheels are determined by the symmetrized

torque ripple, which was reduced (Figure 10b). A decrease in the symmetrized ripple with an increase in the non-symmetrized one indicates that the torque waveforms of individual pairs of rotor and stator stacks are in antiphase. In this way, the torque ripples of the individual SRSCs cancel each other out, as seen from Figure 11.

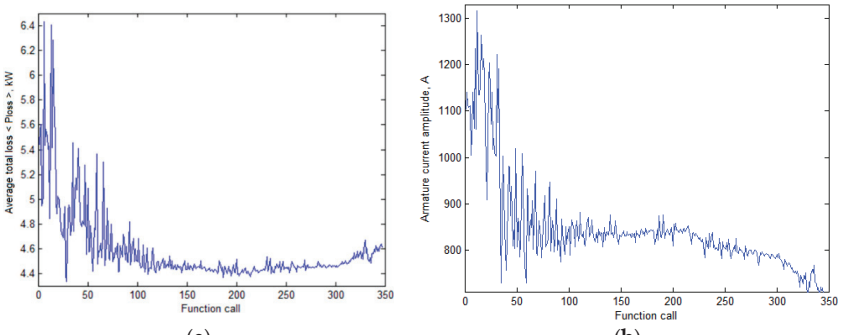

(**a**) (**b**)

Figure 9. Change of the generator parameters during optimization: (**a**) Average losses; (**b**) Maximum magnitude of the armature winding current.

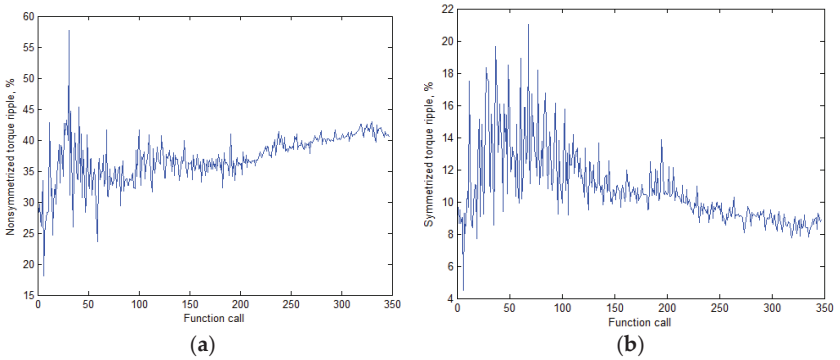

(**a**) (**b**)

Figure 10. Change of the generator parameters during optimization: (**a**) Nonsymmetrized torque ripple; (**b**) Symmetrized (output) torque ripple.

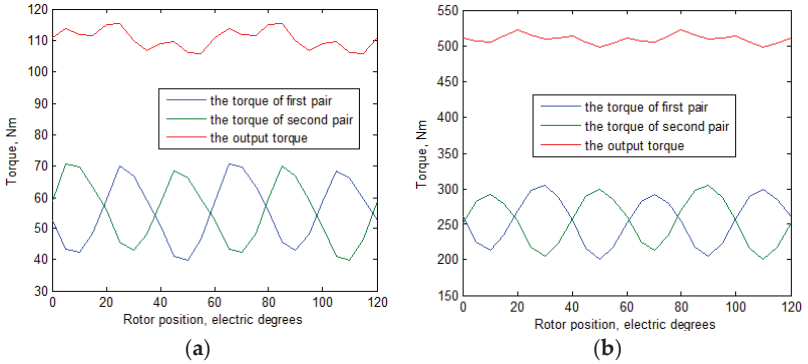

(**a**) (**b**)

Figure 11. The torque ripple of the individual SRSC and the symmetrized (output) torque ripple after optimization: (**a**) at 3450 rpm; (**b**) at 750 rpm.

Figures 12 and 13 show the geometry and 2D flux density plot of an SRSC before the first start of the optimization procedure and after optimization, correspondingly. Table 3 compares the performances of the SHG with ferrite magnets before and after optimization.

Table 3. Generator characteristics before and after optimization.

Characteristics	Initial Design		Optimized Design	
Loading case, *i*	1	2	1	2
Rotational speed *n*, rpm	3450	750	3450	750
Armature phase current amplitude I_{arm}, A	408	1035	375	700
Efficiency, % *	94.5	78.0	92.7	84.4
Mechanical power on the generator shaft P_{mech}, kW	40	40	40	40
Shaft torque, N·m	111	510	111	510
Output electrical power P_1, kW	37.97	32.36	37.22	34.90
Armature DC copper loss $P_{arm\ DC}$, kW	1.12	7.21	1.29	4.51
Armature eddy-current copper loss $P_{arm\ AC}$, W	123	46	402	157
Stator laminated steel loss $P_{iron\ st}$, W	756	379	960	411
Rotor laminated steel loss $P_{iron\ rt}$, W	33	9	121	24
Excitation copper loss P_{ex}, W	187	1170	151	1123
Total loss P_{loss}, kW **	2.22	8.81	2.93	6.22
Average losses $<P_{loss}>$, kW	5.51		4.58	
Turns number in the armature slot	4.41		6.82	
Required rectifier power, kW	104.0		70.3	
Power factor	0.926	0.804	0.989	0.854
Line-to-line voltage amplitude V_{arm}, V	116.0	44.9	116.0	67.4
Nonsymmetrized torque ripple, %	35	28	56	41
Symmetrized torque ripple, %	9.8	4.3	8.6	4.5
Flux density in the non-laminated parts of the magnetic core, T	0.4	1.3	0.1	1.5

Notes: * the generator efficiency was calculated as $\eta = (P_1 - P_{ex})/P_{mech}$, where P_1 is the active power in armature winding; P_{ex} is the losses in the excitation winding; P_{mech} is the input (mechanical) power. The bearing loss and the loss due to air friction are not considered when calculating the efficiency; ** The total loss is calculated as the sum of the following $P_{loss} = P_{arm\ DC} + P_{arm\ AC} + P_{iron\ st} + P_{iron\ rt} + P_{ex}$.

Comparison of Figures 12 and 13 shows that as a result of optimization, the height and area of the stator slots has increased significantly. The air gap has become much smaller. The thickness of the rotor teeth and the thickness of the magnets in the rotor slots have been significantly reduced. Comparison of Figure 14a,b demonstrates that after optimization, the maximum demagnetization force has been slightly reduced from 3 kOe to about 2.9 kOe, while the coercive force of the magnets is greater than 3.9 kOe. It can be concluded that the proposed design does not create a risk of demagnetization of the permanent magnets.

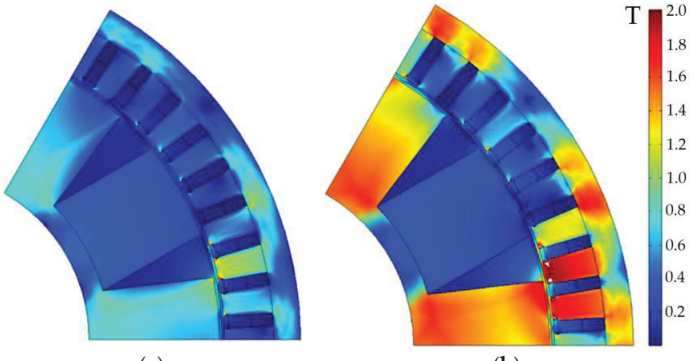

Figure 12. Pole-sector geometry of the generator for the initial design. White color shows areas with flux density more than 2 T: (**a**) Maximum speed; (**b**) Maximum torque.

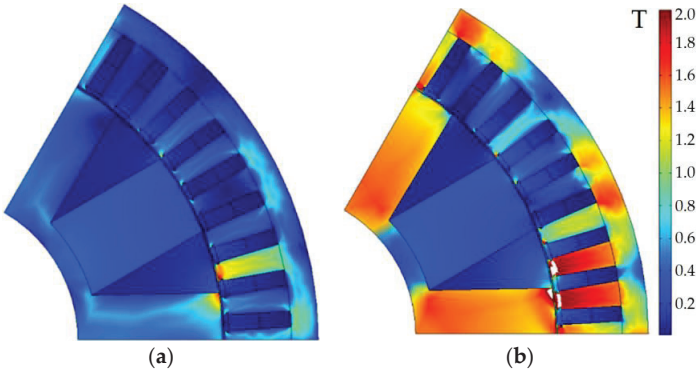

Figure 13. Pole-sector geometry of the generator for the optimized design. White color shows areas with flux density more than 2 T: (**a**) Maximum speed; (**b**) Maximum torque.

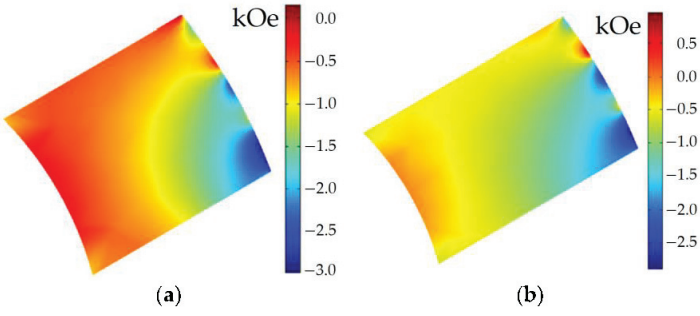

Figure 14. Field of the demagnetizing force (kOe) acting on the permanent magnet of the rotor at the maximum torque (at 750 rpm): (**a**) Before optimization, minimum value is −3.0 kOe; (**b**) After optimization, minimum value is −2.9 kOe.

Comparison of the SHG characteristics before and after optimization presented in Table 3 allows us to draw the following conclusions:

1. Average losses were reduced by 100% (5.51 − 4.58)/5.51 = 16.9%;
2. The armature current at the maximum torque was reduced by 100% (957.7 − 700)/957.7 = 26.9%;
3. Output (symmetrized) torque ripple at maximum torque at 750 rpm was reduced by 100% (9.8 − 8.6)/9.8 = 12.2%;
4. The coercive force of the applied grade of ferrite magnet (Y30H-2) is 3.9 kOe [38], which is much greater than the demagnetizing magnetic field in the optimized design;
5. The optimized SHG with ferrite magnets is more saturated than the initial one. However, the risk of demagnetization of ferrite magnets does not increase because the increase in the height of the magnet after optimization compensates for the increased MMF of the excitation coil;
6. After optimization, due to the soft restriction introduced in function (6), the flux density in the non-laminated parts does not exceed 1.6 T.

6. Comparison of SHG Characteristics without Magnets and with Ferrite Magnets

One of the goals of the study is to evaluate the increase in the performance of SHG with ferrite magnets by comparing its characteristics with a similar homopolar generator without magnets, the optimization results of which are presented in [29]. Tables 4 and 5 compare the performance and design features of these two generator configurations. The data of the SHG without magnets are given according to the final optimization results

obtained in article [29]. The data of the SHG with ferrite magnets are in line with the optimized design from Table 3.

Table 4. Characteristics of generators without magnets and with ferrite magnets.

Characteristics	SHG without Magnets		SHG with Ferrite Magnets	
Loading case, i	1	2	1	2
Rotational speed n, rpm	3450	750	3450	750
Armature phase current amplitude I_{arm}, A	369.5	676.2	375	700
Efficiency, %	90.4	79.8	92.7	84.4
Mechanical power on the generator shaft P_{mech}, kW	40	40	40	40
Shaft torque, N·m	111	510	111	510
Output electrical power P_1, kW	36.58	33.12	37.22	34.90
Armature DC copper loss $P_{arm\ DC}$, kW	1.90	6.37	1.29	4.51
Armature eddy-current copper loss $P_{arm\ AC}$, W	417	131	402	157
Stator laminated steel loss $P_{iron\ st}$, W	961	403	960	411
Rotor laminated steel $P_{iron\ rt}$, W	192	26	121	24
Excitation copper loss P_{ex}, W	368	1169	151	1123
Total loss P_{loss}, kW	3.84	8.10	2.93	6.22
Average losses	5.97		4.58	
Turns number in the armature slot	7.75		6.82	
Required rectifier power, kW	67.9		70.3	
Power factor	1	0.747	0.989	0.854
Line-to-line voltage amplitude V_a, V	116.0	75.3	116.0	67.4
Nonsymmetrized torque ripple, %	97.8	47.0	56	41
Symmetrized torque ripple, %	11.3	4.5	8.6	4.5
Flux density in the rotor sleeve and in the stator housing, T	0.84	1.60	0.1	1.5

Table 5. Comparison of the cost and geometric characteristics of the considered configurations.

Characteristics	SHG without Magnets	SHG with Ferrite Magnets
Stator laminated steel weight, kg	34.2	28.0
Rotor laminated steel weight, kg	15.6	17.1
Copper weight of armature winding, kg	17.8	14.7
Copper weight of excitation winding, kg	2.44	2.62
Weight of ferrite magnets, kg	-	7.88
Weight of structural steel of the rotor sleeve and stator housing, kg	53.2	29.2
Total weight of the active materials and the structural steel, kg	123.24	99.5
Stator laminated steel cost, USD	34.2	28.0
Rotor laminated steel cost, USD	15.6	17.1
Copper cost of armature winding, USD	124.6	102.9
Copper cost of excitation winding, USD	17.1	18.3
Cost of ferrite magnets, USD	-	145.5
Cost of the structural steel, USD	53.2	29.2
The total cost of the active materials (permanent magnets, copper, electrical steel) and low carbon steel of the stator housing of the rotor sleeve, USD *	244.7	341.0
Length of all stacks of the stator laminated steel, mm	152.7	128.3
Length of all laminated stacks plus the axial clearances between them for installing excitation coils, mm	180	150
Laminated stator external diameter, mm	370	370
Air gap, mm	0.88	0.91

* Note: when calculating the cost of materials, it is assumed that the price of copper is $7 per kilogram; the price of electrical steel and the price of the structural steel are $1 per kilogram; the price of ferrite magnets of Y30H-2 grade is $18.46 per kilogram [38].

According to the results of comparative analysis of the characteristics of the SHG with ferrite magnets and without magnets, shown in Tables 4 and 5, the following conclusions can be drawn:

1. The average losses for the generator with ferrite magnets have been reduced, in comparison with the generator without magnets, by 100% (5.97 − 4.58)/5.97 = 23.4%;
2. The maximum armature current for the SHG with ferrite magnets is slightly higher than that for the SHG without magnets, by 100%(700 − 676.2)/676.2 = 3.5%. This is due to the fact that the optimization result is a compromise between the minimum losses and the minimum current, and the losses $<P_{loss}>$ in the objective function (6) have a larger weight coefficient;
3. The output torque ripple at maximum speed for a generator with ferrite magnets is reduced by 100% (11.3 − 8.6)/11.3 = 23.9% compared to a generator without magnets;
4. Due to the addition of ferrite magnets, the length of the magnetic core of the generator, taking into account the axial clearance for installing excitation coils, can be reduced by 100% (180 − 150)/150 = 16.7%;
5. Due to the contribution of the ferrite magnets to the resulting excitation flux, the MMF of the excitation winding can be reduced; in addition, the MMF generated by the excitation winding and the magnets in the non-laminated parts are opposite. All of these factors make it possible to significantly reduce the cross-section of non-laminated parts and reduce their weight by about two times;
6. When adding ferrite magnets, the total mass of the materials of the electromagnetic core of the generator is reduced by 100% (123.24 − 99.5)/23.24 = 19.3%;
7. An SHM without magnets allows the control technique in which the current ratio is equal throughout the entire constant mechanical power speed range (CPSR). In an SHM with (ferrite) magnets, the magnets' contribution in the machine excitation does not reduce at high speed. Therefore, the excitation current must decrease more rapidly than armature current does with an increase of speed. In the considered SHG with ferrite magnets, the current ratio at 3450 rms is 1.5 times less than that at 750 rpm;
8. When the car battery is discharged, the power supply of the excitation winding of the SHG without magnets is lost, and there is a risk that the generator cannot be started due to lack of excitation. In the undercar SHG with ferrite magnets, even in the absence of current in the excitation winding, some excitation is created by permanent magnets. Therefore, even with a discharged car battery, SHG with ferrite magnets can provide the car with energy and recharge the battery;
9. The total cost of the materials of the electromagnetic core (electrical steel, copper, ferrite magnets, non-laminated steel) for SHG with ferrite magnets is 341/244.7 = 1.4 times more than for SHG without magnets, because of adding the cost of ferrite magnets.

In general, as a result of comparing the characteristics of the SHGs with ferrite magnets and without magnets, it can be concluded that the use of the SHG with ferrite magnets in this application is promising; since the efficiency of the generator has been improved significantly, the dimensions and weight have also been significantly reduced, with a relatively small increase in cost.

7. Discussion

Based on the findings of the study, the following implications can be made regarding the appropriate design of the SHG with ferrite magnets:

- Computer-aided optimization of the SHG design with ferrite magnets, which has a complex three-dimensional structure of the magnetic system, applying widely used methods, such as 3D FEM and multicriteria optimization algorithms, is complicated by very high computational costs [23]. This problem can be solved by applying the computationally efficient Nelder-Mead method and the simplified SHG model with ferrites presented in this article;

- With an increase in the level of saturation of the magnetic circuit and the magnitude of the MMF of the excitation winding, the resistance to demagnetization of ferrite magnets on the rotor can be increased by increasing their height;
- It is advisable to restrict the flux density in non-laminated sections of the magnetic core made of structural low-carbon steel to a value low enough to ensure a small drop in MMF, despite the fact that magnetic properties of low-carbon steels are not regulated.

8. Conclusions

This article evaluates the improvement in performance of a synchronous homopolar machine by adding ferrite magnets to the rotor in the case of a 35 kW passenger car generator considering its operating speed range. For a fair comparison, the characteristics of the generator configurations with ferrite magnets and without magnets are optimized using the same method. The single-criterion unconstrained Nelder-Mead algorithm and the two-dimensional finite element method are used.

The following optimization objectives were selected: decreasing the average losses over the entire range of operating speeds, decreasing the installed power capacity of the solid-state rectifier, and the reduction of the torque ripple. As a result of optimization, the characteristics of the generator have been significantly improved. Compared to the non-optimized design, the following were reduced: average generator loss by 16.9%, upper limit of the solid-state rectifier current by 26.9%, symmetrized (output) torque ripple by 12.2%.

The non-symmetrized torque ripple, which has the lowest power in the objective function defined by Equation (6), became higher after optimization. Despite this, the output (symmetrized) torque ripple even decreased after optimization, indicating that the torque waveforms of the individual stator-rotor stack combinations (SRSCs) are in opposite phases and cancel each other out.

When comparing the SHG characteristics with and without ferrite magnets, we can conclude that the addition of ferrite magnets significantly improves the target characteristics: average generator losses are reduced by 23.4%; torque ripple is reduced by 23.9%; the total weight of active materials, stator housing, and rotor sleeve is reduced by 19.3%; and the length of the electromagnetic core is reduced by 16.7%. The current rating requirement for a semiconductor rectifier for the SHG with ferrite magnets is slightly higher than that for an SHG without magnets by 3.5%. At the same time, the cost of materials for the generator without magnets is 1.4 times less, since ferrite magnets are not used in it.

In general, as a result of comparing the characteristics of the SHGs with ferrite magnets and without magnets, it can be concluded that the use of the SHG with ferrite magnets in this application is promising, since the efficiency of the generator has been improved significantly, and the dimensions and weight have also been significantly reduced, with a relatively small increase in cost.

The limitation of the proposed approach is that the optimization of electromagnetic characteristics of the SHG is carried out without taking into account thermal and hydrodynamic (ventilation) processes. In future work, the comparison between the SHM with ferrite magnets and other types of electrical machines for passenger car generators and other applications will be carried out. Also, the presented SHM model with ferrite magnets will be supplemented by considering thermal and hydrodynamic processes.

Author Contributions: Conceptual approach, V.D. and V.P.; data curation, V.D. and V.K.; software, V.D. and V.P.; calculations and modeling, V.D., V.K. and V.P.; writing—original draft, V.D., V.K. and V.P.; visualization, V.D. and V.K.; review and editing, V.D., V.K. and V.P. All authors have read and agreed to the published version of the manuscript.

Funding: The research funding from the Ministry of Science and Higher Education of the Russian Federation (Ural Federal University Program of Development within the Priority-2030 Program) is gratefully acknowledged.

Institutional Review Board Statement: Not applicable.

Informed Consent Statement: Not applicable.

Data Availability Statement: Data are contained within the article.

Acknowledgments: The authors thank the editors and reviewers for careful reading and constructive comments.

Conflicts of Interest: The authors declare no conflict of interest.

References

1. Jung, S.; Jung, H.; Hahn, S.; Jung, H.; Lee, C. Optimal Design of Direct-Driven PM Wind Generator for Maximum Annual Energy Production. *IEEE Trans. Magn.* **2008**, *44*, 1318–1338. [CrossRef]
2. Lima, I.; Filho, W. *Rare Earth Industry*; Elsevier: Amsterdam, The Netherlands, 2015.
3. Fang, S.; Wang, Y.; Liu, H. Design study of an aerospace motor for more electric aircraft. *IET Electr. Power Appl.* **2020**, *14*, 2881–2890. [CrossRef]
4. Liaw, C.; Soong, W.; Welchko, B.; Ertugrul, N. Uncontrolled generation in interior permanent-magnet Machines. *IEEE Trans. Ind. Appl.* **2005**, *41*, 945–954. [CrossRef]
5. Prakht, V.; Dmitrievskii, V.; Kazakbaev, V.; Anuchin, A. Comparative Study of Electrically Excited Conventional and Homopolar Synchronous Motors for the Traction Drive of a Mining Dump Truck Operating in a Wide Speed Range in Field-Weakening Region. *Mathematics* **2022**, *10*, 3364. [CrossRef]
6. Kutt, F.; Michna, M.; Kostro, G. Non-Salient Brushless Synchronous Generator Main Exciter Design for More Electric Aircraft. *Energies* **2020**, *13*, 2696. [CrossRef]
7. Noeland, J.; Nuzzo, S.; Tessarolo, A.; Alves, E. Excitation System Technologies for Wound-Field Synchronous Machines: Survey of Solutions and Evolving Trends. *IEEE Access* **2019**, *7*, 109699–109718. [CrossRef]
8. Janis, D.; Levin, N.; Orlova, S.; Pugachov, V.; Ribickis, L. Optimization of the magnetic circuit of an axial inductor machine based on the calculation and analysis of magnetic field. In Proceedings of the 2009 13th European Conference on Power Electronics and Applications, Barcelona, Spain, 8–10 September 2009; pp. 1–8. Available online: https://ieeexplore.ieee.org/document/5278726 (accessed on 12 January 2022).
9. Bindu, G.; Basheer, J.; Venugopal, A. Analysis and control of rotor eccentricity in a train-lighting alternator. In Proceedings of the 2017 IEEE International Conference on Power, Control, Signals and Instrumentation Engineering (ICPCSI), Chennai, India, 21–22 September 2017; pp. 2021–2025. [CrossRef]
10. Lorilla, L.; Keim, T.; Lang, J.; Perreault, D. Topologies for future automotive generators. Part I. Modeling and analytics. In Proceedings of the 2005 IEEE Vehicle Power and Propulsion Conference, Chicago, FL, USA, 7 September 2005; pp. 74–85. [CrossRef]
11. Bianchini, C.; Immovilli, F.; Bellini, A.; Lorenzani, E.; Concari, C.; Scolari, M. Homopolar generators: An overview. In Proceedings of the 2011 IEEE Energy Conversion Congress and Exposition, Phoenix, AZ, USA, 17–22 September 2011; pp. 1523–1527. [CrossRef]
12. Severson, E.; Nilssen, R.; Undeland, T.; Mohan, N. Dual-purpose no-voltage winding design for the bearingless AC homopolar and consequent pole motors. *IEEE Trans. Ind. Appl.* **2015**, *51*, 2884–2895. [CrossRef]
13. Jeong, J.-S.; An, D.-K.; Hong, J.-P.; Kim, H.-J.; Jo, Y.-S. Design of a 10-MW-Class HTS homopolar generator for wind turbines. *IEEE Trans. Appl. Supercond.* **2017**, *27*, 2669140. [CrossRef]
14. Ye, C.; Yang, J.; Xiong, F.; Zhu, Z.Q. Relationship between homopolar inductor machine and wound-field synchronous machine. *IEEE Trans. Ind. Electron.* **2020**, *67*, 919–930. [CrossRef]
15. Belalahy, C.; Rasoanarivo, I.; Sargos, F. Using 3D reluctance network for design a three phase synchronous homopolar machine. In Proceedings of the 2008 34th Annual Conference of IEEE Industrial Electronics, Orlando, FL, USA, 10–13 November 2008; pp. 2067–2072. [CrossRef]
16. Yang, J.; Ye, C.; Liang, X.; Xu, W.; Xiong, F.; Xiang, Y.; Li, W. Investigation of a Two-Dimensional Analytical Model of the Homopolar Inductor Alternator. *IEEE Trans. Appl. Supercond.* **2018**, *28*, 2802480. [CrossRef]
17. Dmitrievskii, V.; Prakht, V.; Anuchin, A.; Kazakbaev, V. Traction Synchronous Homopolar Motor: Simplified Computation Technique and Experimental Validation. *IEEE Access* **2020**, *8*, 185112–185120. [CrossRef]
18. Cheshmehbeigi, H.; Afjei, E. Design optimization of a homopolar salient-pole brushless DC machine: Analysis, simulation, and experimental tests. *IEEE Trans. Energy Convers.* **2013**, *28*, 289–297. [CrossRef]
19. Severson, E.; Mohan, N.; Nilssen, R.; Undeland, T. Outer-rotor AC homopolar motors for flywheel energy storage. In Proceedings of the 7th IET International Conference on Power Electronics, Machines and Drives (PEMD 2014), Manchester, UK, 8–10 April 2014; pp. 1–6. [CrossRef]
20. Kalsi, S.; Hamilton, K.; Buckley, R.G.; Badcock, R.A. Superconducting AC Homopolar Machines for High-Speed Applications. *Energies* **2019**, *12*, 86. [CrossRef]
21. Orlova, S.; Pugachov, V.; Levin, N. Hybrid Excitation of the Axial Inductor Machine. *Latv. J. Phys. Tech. Sci.* **2012**, *49*, 35–41. [CrossRef]
22. Ketner, K.; Dirba, J.; Levins, N.; Orlova, S.; Pugachev, V. Inductor Machine with Axial Excitation. LV Patent LV13971B, 20 November 2009. (In Latvian)

23. Yu, K.; Jiang, L.; Guo, S.; Xi, C.; Xie, X. An Optimized Design Method of Homopolar Inductor Alternator Based on Genetic Algorithm. *IEEE Trans. Plasma Sci.* **2023**, *51*, 544–552. [CrossRef]
24. Yao, J.; Zhao, Y.; Zhao, Y.; Zhang, X.; Guo, T.; Yu, K.; Wang, Z. Calculation and Analysis of Transient and Sub-Transient Processes in Homopolar Inductor Machine. In Proceedings of the 25th International Conference on Electrical Machines and Systems (ICEMS), Chiang Mai, Thailand, 29 November–2 December 2022; pp. 1–6. [CrossRef]
25. Wu, Y.; Yang, B.; Fan, X.; Fan, X.; Liu, H. Modeling and Simulation of Homopolar Inductor Alternator System. In Proceedings of the 25th International Conference on Electrical Machines and Systems (ICEMS), Chiang Mai, Thailand, 29 November–2 December 2022; pp. 1–4. [CrossRef]
26. Ye, C.; Deng, C.; Yang, J.; Dai, Y.; Yu, D.; Zhang, J. Study on a Novel Hybrid Thermal Network of Homopolar Inductor Machine. *IEEE Trans. Transp. Electrif.* **2023**, *9*, 549–560. [CrossRef]
27. Glowacki, J.; Sun, Y.; Storey, J.; Huang, T.; Badcock, R.; Jiang, Z. Temperature Distribution in the Field Coil of a 500-kW HTS AC Homopolar Motor. *IEEE Trans. Appl. Supercond.* **2022**, *32*, 3128347. [CrossRef]
28. Hwang, Y. Design and Characteristic Analysis of a Homopolar Synchronous Machine Using a NI HTS Field Coil. *Energies* **2021**, *14*, 5658. [CrossRef]
29. Prakht, V.; Dmitrievskii, V.; Kazakbaev, V. Synchronous Homopolar Generator without Permanent Magnets for Railway Passenger Cars. *Appl. Sci.* **2023**, *13*, 2070. [CrossRef]
30. Guo, S.; Yi, Z.; Liu, P.; Wang, G.; Lai, H.; Yu, K.; Xie, X. Analysis and Performance Evaluation of a Novel Adjustable Speed Drive with a Homopolar-Type Rotor. *Mathematics* **2022**, *10*, 3712. [CrossRef]
31. Boldea, I.; Tutelea, L. Claw Pole and Homopolar Synchronous Motors: Modeling, Design, and Control. In *Reluctance Electric Machines. Design and Control*, 1st ed.; CRC Press: Boca Raton, FL, USA, 2018; pp. 179–200. [CrossRef]
32. Bimbhra, P. Homopolar Inductor Alternators. In *Generalized Theory of Electrical Machines*, 5th ed.; Khanna Publishers: Delhi, India, 2012; pp. 387–393.
33. Stumberger, B.; Hamler, A.; Trlep, M.; Jesenik, M. Analysis of interior permanent magnet synchronous motor designed for flux weakening operation. *IEEE Trans. Magn.* **2001**, *37*, 3644–3647. [CrossRef]
34. Synchronous Generators Type EGV. The Generators EGV Are Designed for Power Supply of a Passenger Car. Characteristics. Available online: https://www.pemz.ru/catalog/dlya_zheleznoy_dorogi/Synchronous_generators_type_EGV/ (accessed on 15 December 2022).
35. Nelder, J.; Mead, R. A Simplex Method for Function Minimization. *Comput. J.* **1965**, *7*, 308–313. [CrossRef]
36. IEC. *Specifications for Particular Types of Winding Wires—Part 0-2: General Requirements—Enamelled Rectangular Copper Wire*; IEC 60317-0-2:2020; IEC: Geneva, Switzerland, 2020. Available online: https://webstore.iec.ch/publication/63495 (accessed on 15 December 2022).
37. Find Minimum of Unconstrained Multivariable Function Using Derivative-Free Method. MATLAB Documentation. © 1994–2023 The MathWorks, Inc. Available online: https://www.mathworks.com/help/matlab/ref/fminsearch.html (accessed on 18 January 2022).
38. Hard Ferrite Magnets, Product Information, IBSMagnet. 2020. Available online: https://ibsmagnet.com/products/dauermagnete/hartferrit.php (accessed on 13 January 2022).

energies

MDPI

Perspective

Perspectives on Electric Machines with Cryogenic Cooling

Fabrizio Marignetti *,† and Guido Rubino †

Department of Engineering, University of Cassino and South Lazio, 03043 Cassino, Italy
* Correspondence: marignetti@unicas.it; Tel.: +39-0776-299-3716
† These authors contributed equally to this work.

Abstract: Cryogenic cooling is a well-established and expanding technology. In the field of electric machines, it allows the construction of more efficient machines with a high power density. This paper addresses the main cooling technologies and their impact on cryogenic machine construction, providing perspective for their use in future electrical machines. Although cost and safety issues of cryogenic systems are still holding back the uptake of cryogenic electric motors and generators, research in this field should provide significant improvements and promote their use at different levels.

Keywords: cryogenic cooling system; superconducting machine; temperature impact; electrical resistance measurement; performance

Citation: Marignetti, F.; Rubino, G. Perspectives on Electric Machines with Cryogenic Cooling. *Energies* **2023**, *16*, 2994. https://doi.org/10.3390/en16072994

Academic Editors: Loránd Szabó and Feng Chai

Received: 3 February 2023
Revised: 17 March 2023
Accepted: 20 March 2023
Published: 24 March 2023

1. Introduction

Electric machines with cryogenic cooling are still in the research and development phase. Cryogenic cooling has been shown to improve the performance and efficiency of electric machines by reducing winding resistance, eddy current losses [1], and core losses [2]. However, this technology is still not widely adopted in the industry due to its high cost and complexity. In addition, technological challenges still need to be overcome, such as the need for specialized insulation materials that can withstand the extreme temperatures of cryogenic cooling. Overall, research is underway in this area to develop more efficient and cost-effective ways to implement cryogenic cooling in electric generators, electric vehicles, and ships, and in other fields requiring small electric machine sizes with significant power. In general, cryogenic cooling systems used for electrical machines [3] usually use cryogenic fluids and particular cooling techniques. The paper has two main purposes:

- To provide a short review of superconducting machines (SCMs) with a description of different technologies used for cryogenic motors and generators. In particular, the cooling systems, cryogenic fluids, and materials used for cryogenic electrical machines will be treated;
- The second objective is to illustrate the perspective of electric machines with cryogenic cooling where possible research paths are suggested for the next few years.

Overall, the paper provides an aid to engineers and designers to build a clear picture of the techniques and materials used for cryogenic electric motors and evaluate this technology's prospects.

2. Superconducting Machines

In recent years, the world of research and industry has focused on researching the reduction of CO_2 emissions using all-electric solutions with ever-greater efficiencies [4]. Superconducting machines (SCMs) have the potential to offer higher power densities, higher efficiency, and reduced size and weight compared to traditional electric machines.

2.1. Applications of Superconducting Electric Machines

Superconducting electric machines have promising prospects for various applications. Some of these applications include:

- Electric propulsion: The development of superconducting machines for electric cars is still in the research and development phase, while for naval applications there were prototypes built in 2018 by General Atomics Electromagnetic Systems (GA-EMS) for the US Navy with 36.5 megawatts of power [5] and that of the companies Northrop Grumman and Rolls-Royce, which in 2019 announced that it had developed a prototype superconducting generator for use in naval propulsion systems [6]. Studies on electric ship propulsion [7] have shown that superconducting synchronous motors can achieve efficiency levels greater than 99% at full load, allowing traveling longer distances. The efficiency remains constant even at low loads, which is particularly important for ship propulsion, as ships employ around 30% of the maximum power at cruise speed. Additionally, the use of superconductors provides the potential to reduce the weight and volume of the motor, which can have a significant impact on the overall weight and size of the propulsion system;
- Wind turbines: Superconducting generators could increase the power output of wind turbines [8], especially offshore ones, by reducing the size and weight of the generator and increasing the efficiency [9]. In the year 2019, by the EU H2020 EcoSwing project [9], the world's first rotor for a 3.6 MW wind generator was successfully tested. The compatibility of the technology has been demonstrated with all the real impacts present in an operating environment such as variable speeds, network failures, electromagnetic harmonics, vibrations, etc., and with the volume of the active parts 50% lower, therefore lighter than the permanent magnet machines;
- Aeronautics: The development of superconducting aircraft motors is still in the research and development phase, and there are currently no commercial superconducting aircraft motors available on the market. However, there has been a growing interest in using superconducting technologies in aircraft propulsion systems due to their potential for high efficiency, power density, weight savings, and reduced emissions [10–12]. In 2020 the ASuMED project [13] was successfully closed and demonstrated on a prototype the advantages of a new fully superconducting motor with about 1 MW of power at 10,000 rpm a thermal loss $< 0.1\%$ with a power density of 20 kW/kg 99.9% motor efficiency. Currently, there is a major Airbus project named ASCEND (advanced superconducting and cryogenic experimental powertrain demonstrator) [14,15] aimed at developing a hybrid-electric demonstrator aircraft which is at an advanced stage;
- Industrial applications: Superconducting motors and generators could be used in various industrial applications, including compressors, pumps, and conveyors, where high power density, efficiency, and reliability are required. Several research activities are currently underway which aim to make this technology reliable. In this paper, the problems and the current technologies used to overcome them will be dealt with in Section 2.9;

Although superconducting electric machines offer the potential for significant improvements in efficiency, power density, and reliability compared to traditional electric machines, challenges remain, including cost, materials availability, and integration with existing systems. Those challenges will be dealt with in the following.

2.2. Types of Superconducting Machines

Superconducting windings have zero electrical resistance at very low temperatures, which allows for very high current densities and high efficiency [16]. There are three main types of superconducting machines:

1. Superconducting synchronous machines (SCSMs): These are synchronous machines that use superconducting windings in their rotor or stator. They can be used as generators [8] or motors [17], and provide high power density, high efficiency, and high power factor. Studies have shown that SCSMs can achieve efficiency levels of 99% at full load [7], compared to conventional motors that typically operate at around 94–96% efficiency;

2. Superconducting induction machines (SCIMs): These are induction machines that use superconducting windings in their rotor. They have high efficiency and power density, especially in applications that require high torque and low speed operation, but their power factor is lower than that of SCSMs. Studies have shown that SCIMs can achieve efficiency levels greater than 98% at full load [18], compared to conventional induction machines that typically operate at around 80–90% efficiency;
3. Superconducting homopolar machines (SCHMs): They have been considered for high speed applications [19] and ship propulsion [19]. However, technical problems, mainly related to the complexity of their brushes, have kept these machines at the concept level.

Losses in SCSMs and SCIMs are caused by mechanical friction, electrical resistance within the windings, eddy current effects, and hysteresis.

In addition to power loss, SCMs have several advantages over traditional electric machines:

- High power density: Superconducting windings allow for very high current densities, meaning that the machine can be made smaller and more compact;
- High power factor: Superconducting windings have a very low reactance, meaning that the machine has a high power factor;
- Low noise and vibration: Superconducting machines have low iron losses and winding losses, meaning that they produce less noise and vibration.

However, SCMs also pose some challenges that need to be overcome before they can be widely adopted in the industry. These challenges include the need for low temperatures to maintain superconductivity, the cost and complexity of cryogenic cooling systems, and the need for specialized insulation materials that can withstand low temperatures.

2.3. Cooling Systems of Superconducting Machines

Usually, the selection of the cooling systems for superconducting machines is conducted based on the personal or technical experience of the machine engineers and designers. An incorrect calculation of the cooling system makes the electric machine unreliable or with a high fault rate. The fluids commonly used for both AC and DC electric machines are liquid nitrogen (LN2) or liquid helium (LHe). Cooling systems for superconducting machines are essential to maintain the superconducting state of the materials used in the windings, which typically require temperatures below the critical temperature of the superconducting material.

The most common cooling systems for LN2 or LHe used in superconducting machines are:

1. *Cryocoolers*: A refrigerator designed to reach cryogenic temperatures below −153 °C (120 K) is often called a cryocooler. These are refrigeration systems that use a closed-loop cooling system to maintain the low temperatures required for the superconducting materials [20]. They can be based on Gifford–McMahon [21], pulse tube, or Stirling cycle technology [22]. These cooling systems are typically used in low-power superconducting devices and systems.
2. *Forced-flow cooling*: In this method, LHe [23] or LN2 is circulated through the superconducting windings to cool them. The liquid is cooled in a heat exchanger before being recirculated. Recently a new technique called rotary cryocooler was placed inside the rotating shaft which is used for cryogenic cooling of the rotor coil [24]. The most common solution is to use a rotating cryostat to cool the rotor of the machine as shown in Figure 1;
3. *Immersion cooling*: This method involves immersing the superconducting windings in a bath of LHe or LN2 [25]. This method is more efficient than forced-flow cooling but it is also more complex and difficult to implement Figure 2;
4. *Pumped Two-Phase (P2P) cooling* [26]: This method uses helium (He) or nitrogen (N) in both liquid and gas phases to cool the superconducting windings. The liquid phase absorbs heat, and the gaseous phase carries the heat away Figure 3;

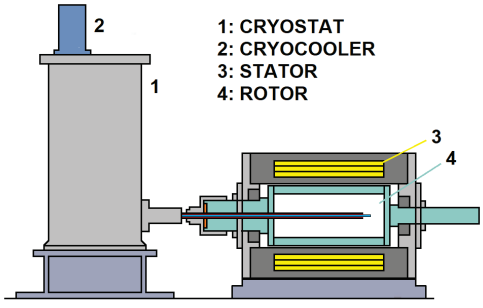

Figure 1. Electric machine with rotating cryostat for rotor cooling.

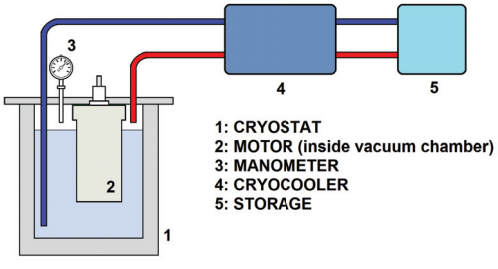

Figure 2. Electric machine cooled in the cryostat.

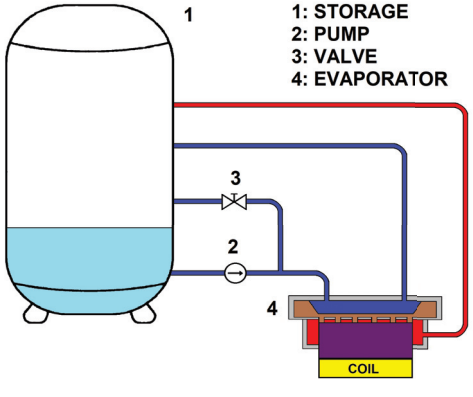

Figure 3. Typical structure of the pumped two-phase (P2P) cooling.

5. *Spray cooling* [27]: LN2 is sprayed onto the stator winding to cool it. This method is also less effective than immersion cooling, but it is simpler to implement;

The choice of the cooling system depends on the specific requirements of the application and the design of the superconducting machine. Figure 4 shows the map of cryocooler applications in the plane of cooling capacity as a function of temperature. Cryocoolers are commonly used in low-power superconducting devices and systems, while forced flow or immersion cooling is used in high-power systems such as superconducting generators or motors.

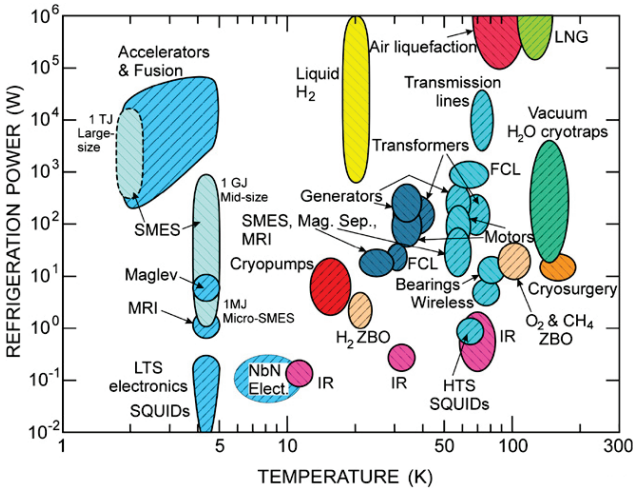

Figure 4. Map of cryocooler applications in the plane of refrigeration power versus temperature [28].

In recent years the aircraft industry has been studying new cooling systems for the electric machine that use hydrogen (H) [29] although it is not as common as other cryogenic cooling methods. There are several ways to use hydrogen as a cooling agent for electric machines:

1. Direct injection cooling: H2 is directly injected into the winding of the machine, where it cools the winding by absorbing heat;
2. Forced-flow cooling: H2 is circulated through the machine's windings using a pump, where it absorbs heat and then is cooled in a heat exchanger before being recirculated;
3. Two-phase flow cooling: H2 is circulated through the machine's windings in a two-phase flow, where it exists both as a liquid and a gas. The liquid phase absorbs heat, and the gaseous phase carries the heat away.

The use of hydrogen as a cooling agent for electric machines has some advantages such as being a clean, environmentally friendly, and non-toxic coolant. However, the technology is still in the development phase, which means that it is not yet widely adopted and it has some technical challenges such as leakage, safety, and reliability issues. Additionally, hydrogen is flammable, which requires special safety precautions to be taken when handling and storing it.

2.4. Cryogenic Fluids

A fluid, to be considered "cryogenic", must be able to operate below the threshold of –153 °C (120 K), as established by the scientific community and widely accepted and used by various industries and fields of study. Cryogenic fluids can be used in various applications, such as cooling, refrigeration, and transportation of materials at extremely low temperatures. The most common types include:

1. *Liquid nitrogen (LN2)*: Nitrogen exists as a liquid at temperatures below −195.8 °C (77 K). It is relatively inexpensive, abundant, and non-toxic. It is commonly used as a coolant in various applications, such as in cryogenic cooling systems for electric machines, cryogenic storage for biological samples, and food freezing;
2. *Liquid helium (LHe)*: Helium exists as a liquid at temperatures below −268.9 °C (4.25 K). It is less abundant and more expensive than liquid nitrogen, but it has a much lower boiling point, which makes it useful in applications that require even lower temperatures. It is commonly used in cryogenic cooling systems for superconducting machines, particle accelerators, and in cryocoolers;

3. *Liquid hydrogen (LH2)*: Hydrogen exists as a liquid at temperatures below −252.87 °C (20.28 K). It is an efficient coolant and has high thermal conductivity and low viscosity. It is used in a variety of applications as a coolant [30], such as in fuel cells, rocket propulsion, and in the aerospace industry;
4. *Liquid neon (LNe)*: Neon (Ne) exists as a liquid at temperatures below −246 °C (27 K). it is similar to liquid helium and liquid hydrogen in terms of cooling performance.

Like liquid nitrogen, liquid helium can be used as a cooling agent for electric machines to improve their performance and efficiency. By using LN2 or LHe, the winding resistance of the machine can be reduced, which leads to a lower copper loss and an increase in the power factor. Additionally, soft materials with high internal resistivity, such as soft magnetic composites (SMCs), can reduce the eddy current loss in the stator core. It has been experimentally proven that the magnetizing characteristic does not change significantly in the range between 77 K and 300 K (−196.15 °C and 26.85 °C), while the presence of the magnetic material increases the useful component of the flux density [31,32]. The overall effect is an increase in the machine's efficiency, which can lead to energy savings.

LN2 cooling can have significant advantages in improving the efficiency of electric machines, but it also requires significant infrastructure and handling precautions. LN2 can be dangerous to handle, and it requires specialized storage and transfer equipment. LHe cooling has similar advantages and disadvantages to LN2 cooling. Like LN2, LHe is a cryogenic fluid, also requiring specialized equipment. LHe is more expensive than LN2, and has a much lower boiling point (Table 1) making it more difficult to handle and requiring more complex insulation materials. Additionally, LHe is a rarer element than Nitrogen. LHe cooling is typically only used in high-performance or high-power machines, such as high-field superconducting magnets in particle accelerators, or cryocoolers. The scientific community is directing research into alternative fluids such as LH2 by developing new, more reliable storage technologies. Hydrogen has a lower liquefaction point and higher thermal conductivity than nitrogen or neon used in available cryogenic systems [33]. Therefore, applying hydrogen to cryogenic systems can be a viable alternative to increase efficiency and stability.

Table 1. Chemical–physical properties of most common fluids in cryogenic cooling systems [34].

Coolant	Critical Temperature (K)	Critical Pressure (kPa)	Density (g/L @ Room Temperature)	Boiling Temperature (K)	Molar Gas (g/mol)	Latent Heat (J/kg)	Specific Heat Ratio of Liquid Phase	Viscosity ($NSm^{-2} \times 10^{-5}$)	Toxic	Flammable
N_2	126.2	3390	1.25	77.35	14.01	199.000	1.4	1.69	No	No
H_e	5.19	228.32	0.178	4.22	4	23.300	1.66	3.16	No	No
H_2	32.938	1285.8	0.089	20.28	2.01	58.000	1.405	1.34	No	Yes
N_e	44.4918	2678.6	0.9	27.1	20.17	331.700	1.66	1.17	Yes	No

For completeness, other cryogenic fluids are also listed [35], but have limited use. Among these we find: fluorine (F), which has a boiling point of −188 °C (85 K), but is highly toxic and is extremely reactive, as it reacts with all other elements except light inert gases; argon (Ar) has a boiling point of −186 °C (87 K) and is a non-toxic, extremely stable, odorless chemical element. However, due to its specific weight, argon tends to stagnate in rooms, therefore storing large quantities of argon in small, closed rooms is dangerous in the event of leaks. Methane (CH4) has a boiling point of −161 °C (112 K), and is normally stable, but burns read. It rapidly or completely vaporizes at atmospheric pressure and normal ambient temperature, so it is dangerous in the event of a leak. Air has a boiling point of −194 °C (79 K), and oxygen has a boiling point of −183 °C (90 F) even if they are part of the cryogenic fluids, but there are problems of use.

2.5. Materials Used for a Cryogenic Electric Machine

The materials used in electric motors for cryogenic cooling systems must be able to withstand the extremely low temperatures and the high thermal stresses caused by the

rapid temperature changes associated with the cryogenic cooling process. Some of the materials that are commonly used in electric motors for cryogenic cooling systems include:

1. *Copper*: copper (Cu) is commonly used as the conductor material in the resistive windings of electric motors for cryogenic cooling systems [36,37]. It has good electrical conductivity and is relatively inexpensive. If cooled with LN, the resistivity of copper drops by 90%, therefore, cooling of resistive windings can be considered [38]. However, copper also has a relatively high coefficient of thermal expansion which can make it difficult to use in some applications;
2. *Aluminum*: aluminum (Al) is also used as a conductor material in the windings of electric motors for cryogenic cooling systems [39]. It has good electrical conductivity and a lower coefficient of thermal expansion than copper, which makes it easier to use in some applications;
3. *Superconductors*: Superconductors are materials that have zero electrical resistance at very low temperatures. They are used in the windings of superconducting motors for cryogenic cooling systems. They include materials such as niobium–titanium (NbTi) and niobium–tin (Nb3Sn) [31,40] that are used at temperatures below −269 °C (4 K), and high-temperature superconductors (HTS) such as yttrium barium copper oxide (YBCO) [41] that are used at temperatures above −269 °C (4 K). Superconducting wires are generally composites: the superconducting filament or tape covers non-superconducting matrix material, such as copper or silver. The matrix material provides mechanical support for the superconducting filament;
4. *Insulation materials*: Insulation materials such as polyimide (PI), polyamide–imide (PA) [42], and epoxy [43] are used to insulate the windings of electric motors for cryogenic cooling systems. These materials must be able to withstand the extremely low temperatures and the high thermal stresses associated with the cryogenic cooling process;
5. *Cryogenic steels*: In cryogenic applications, steels have become the preferred/dominant structural material for cryogenic applications. The choice is due to the combination of strength and toughness, and to obtain greater resistance to cryogenic temperatures in recent years, research has led to the development of a wide range of steels tailored with additives for specific applications [44,45];
6. *Bearings*: The use of cryogenic bearings in electric motors can have some disadvantages with mechanical bearings, such as difficult lubrication and short life. The use of superconducting magnetic bearing (SMB) [46,47], compared to traditional bearings, means a longer life due to reduced friction and vibration.However, manufacturing cryogenic bearings in electric motors comes with many challenges, such as the need for specialized materials and manufacturing processes, high cost, and lack of experienced field personnel.

Figure 5 shows the thermal conductivity of materials as the temperature varies [48].

The study concludes that welding on (typically soft) metals, at cryogenic temperatures (e.g., liquid nitrogen), its yield strength increases many times within −196.15 °C (77 K). Consequently, if the rig survives cooling in liquid nitrogen, not much will happen (mechanically) for further cooling to liquid helium temperature [49].

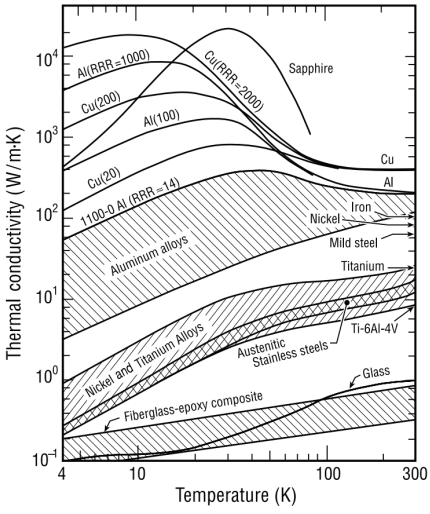

Figure 5. Thermal conductivity of selected classes of materials (ASM 1983) [48].

2.6. Cold and Cryogenic Power Electronics

The latest generation electric motors are usually equipped with power electronics that can be cooled with cryogenic systems. In general, cold power electronics or cryogenic power electronics (CPE) refers to the technology of using power electronic devices and systems that are operated at low temperatures, such as cryogenic temperatures, to improve their performance and efficiency. The main advantage of CPE is that it allows for the reduction of power losses in electronic devices, which leads to an increase in efficiency and power density. CPE uses temperatures below −20 °C (253.15 K), such as liquid nitrogen or liquid helium, to operate electronic devices and systems. The characteristics of various power devices at cryogenic temperatures were studied by Leong [50], and the behavior at various temperatures are summarized in net chart Figure 6. The chart represents the behavior of the semiconductor switch. The 100% represents the optimal regions for the usage, while lower values correspond to the regions where the behavior of the switches shows inadequate behavior.

- Si N-channel MOSFETs in the range, of 20–50 K, show little degradation in ON-state, and negative temperature dependence, while the optimum range of operation is between 60 K and 80 K;
- Si P-channel MOSFETs show non-ohmic behavior due to negative temperature below 60 K, while their optimum operating temperature is over 90 K;
- SiC MOSFETs show no improvements compared to higher temperatures, and their temperature dependence changes its sign around 50 K;
- GAN HEMTS is almost independent of the temperature below 50 K and slightly dependent on the temperature over that temperature;
- GaAs Schottky diodes show not negligible improvements at high currents.

Consequently, silicon N-channel power MOSFETs are most suitable for cryogenic applications as they can achieve extremely low on-state resistance and reasonable breakdown voltages. Other researchers have analyzed power devices at cryogenic temperatures and agreed with this study, but added that the power modules have silicone gels material inside them which makes them less suitable for cryogenics [51]. Consequently, the best modules are those made of ceramics or materials that resist cryogenics.

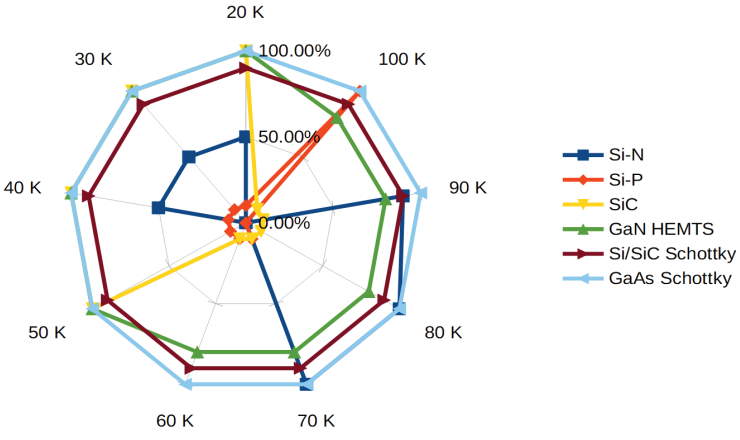

Figure 6. Behavior of the semiconductor switch at cryogenic temperatures (Data adapted from [50]).

2.7. Cryocooler Performance

The efficiency of a cryocooler is a measure of how much energy is required to achieve a given cooling capacity. This parameter is typically measured in coefficient of performance (COP) or terms of the specific cooling power (SCP). The cooling capacity of a cryocooler is the amount of heat that can be removed from the cooled object per unit of time. This parameter is typically measured in watts (W) or watts per hour (Wh). Cryocoolers are designed for specific applications, so the performance parameters vary depending on the specific application. The cryocooler performance is also affected by the environment and the cooling demand of the system, so it is important to match the cryocooler to the specific application. The five kinds of cryocoolers most commonly used to provide cryogenic temperatures for various applications are the Joule–Thomson, Brayton, Stirling, Gifford–McMahon, and pulse tube cryocoolers [28]. A comparison of cryocooler efficiencies near 80 K (the largest application area for small cryocoolers) is given in Figure 7.

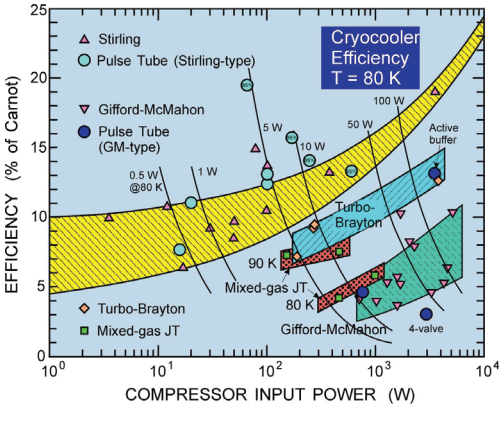

Figure 7. Cryocooler's actual performance at 80 K [28].

For higher operating temperatures the efficiency of the cryocooler will be higher, as shown in Figure 8.

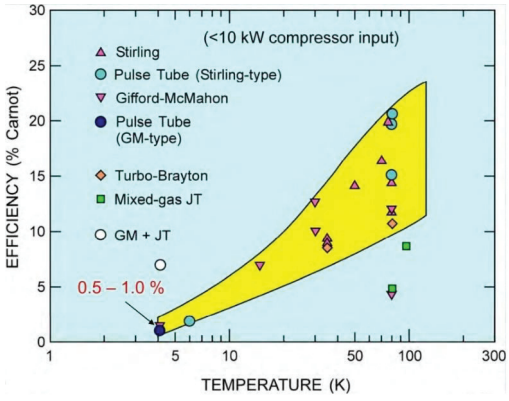

Figure 8. Efficiency of small cryocoolers <10 kW [28].

Efficiencies at 80 K can reach about 20% Carnot for the best cryocoolers (for space), while commercial cryocoolers typically achieve 10–15% Carnot. For low-temperature superconducting (LTS) at 4 K we have the minimum efficiency with a value of about 1%. Various modeling studies [52] have shown that regenerators, optimized for He-3 at a pressure of about 0.5–1.0 MPa can increase efficiencies at 4 K.

2.8. Mathematical Model of Machines with Cryogenic Cooling

Cryogenic and standard electric machines have many common mathematical relationships because they both operate based on the principles of electromagnetic induction. The main difference is that cryogenic machines operate at very low temperatures, where the resistance of the motor windings is greatly reduced due to the superconducting properties of the materials used. Here are some common parts in the mathematical relationships between cryogenic machines and standard machines:

- *Electromagnetic equations*: The basic equations that describe the behavior of electric machines, such as Faraday's law, Ampere's law, and Gauss's law, apply to both cryogenic and standard machines. These equations relate the magnetic field, current, voltage, and other parameters of the machine;
- *Circuit equations*: The circuit equations that describe the behavior of electric circuits, such as Kirchhoff's laws and Ohm's law, also apply to both cryogenic and standard machines. These equations relate the current, voltage, and resistance of the circuit components;
- *Motor equations*: The equations that describe the behavior of electric motors, such as the stator and rotor equations, the torque equation, and the power equation, are also common to both cryogenic and standard machines. However, in cryogenic machines, modifications may be needed to account for the superconducting properties of the materials used;
- *Cooling equations*: Cryogenic machines require cooling systems to maintain their low operating temperatures, so equations that describe the behavior of heat transfer and thermodynamics may be needed to model the cooling system. These equations may be modified to account for the unique properties of cryogenic cooling, such as the use of liquid nitrogen or helium or other as the coolant.

Overall, the main difference in the mathematical relationships between cryogenic and standard machines is that cryogenic machines require modifications to account for their superconducting properties and cooling systems. However, the basic principles of electromagnetic induction, circuit theory, and motor theory still apply to both types of machines. It must be considered that, to avoid saturation of the cores and further reduce losses, very often superconducting machines have no teeth or cores, meaning that the flux lines distribution is more complicated than in traditional machines. A rough comparison

between the power densities of standard and superconducting machines can be made based on the air gap power. The air gap power of an induction machine without stator teeth, with less distortion of the induction distribution at the air gap and reduced synchronous reactance (0.3–0.5 per unit) is:

$$S_d = \frac{\pi^2}{60\sqrt{2}} \cdot n \cdot B_m \cdot K \cdot D^2 \cdot L \quad (1)$$

where n is the number of conductors in the slot; B_m is the maximum value of the magnetic induction at the air gap; K is the linear armature current density; D is the bore diameter; L is the active length of machine.

In radial-flux machines, the electric loading is proportional to the slot height:

$$K = J_a \cdot h_a \quad (2)$$

where J_a is the armature current density, and h_a is the slot depth of armature.

On the other hand, in superconducting machines, the excitation flux density is proportional to the height of the excitation coils:

$$B_m \propto h_e \quad (3)$$

where h_e is the height of the excitation coil.

Substituting, we have:

$$P \propto D^2 \cdot L \cdot h_a \cdot h_e \cdot J_a \quad (4)$$

In standard machines, the electric loading reaches around 60,000 A/m and Bm is limited by the saturation of the magnetic circuit. In superconducting machines, the Bm increases with the height of the rotor coil, namely with the machine diameter, thus Bm reaches $0.8T$ for standard motors and $1.5 - 2T$ for larger cryogenic motors. Therefore, for standard motors, the torque density varies linearly with the third power of the characteristic length, while, for superconducting machines, it depends on the fourth power of this dimension:

$$P \propto D^4 \quad (5)$$

This means that superconducting machines are more advantageous at high powers.

2.9. Problems in the Uses in Industrial Applications

The use of cryogenic electric machines for practical industrial applications can offer many advantages, such as high efficiency, high density of power, and small size and weight. However, several restrictions and challenges must be considered. Some of these include:

- *Material compatibility*: Cryogenic temperatures can cause materials to become brittle, which leads to corrosion or mechanical failure. It is important to select materials compatible with cryogenic temperatures and perform regular inspections and maintenance to ensure materials do not deteriorate over time;
- *Cryogenic fluid leaks*: Cryogenic fluids such as liquid nitrogen and liquid helium are potentially hazardous, and leaks can be dangerous to personnel and equipment;
- *Temperature gradients*: Cryogenic cooling systems can create significant temperature gradients in the equipment being cooled. This can cause thermal stresses and mechanical deformation, which can lead to equipment failure over time;
- *Thermal expansion*: Cryogenic temperatures can cause materials to contract, which can lead to stress and deformation in the machine. This can cause parts to become misaligned and lead to mechanical failure;
- *Electrical insulation*: Cryogenic temperatures can cause electrical insulation materials to become brittle, which can lead to electrical breakdown and failure. It is important to use materials that are designed for use in cryogenic environments and to perform regular insulation testing;

- *AC loss*: Traditionally, the major obstacle to the diffusion of superconducting machines is considered the AC loss behavior of the superconducting windings [53]. Superconductive windings are commonly said to not tolerate high frequencies, as the AC loss increase may lead to thermal instability and, finally to quenching. Quench is a local phenomenon that may lead to winding disruption. This factor has limited the application of superconducting windings to field windings. Today, the availability of rare-earth barium copper oxide (REBCO) superconductors with high critical temperatures, allows the superconductor tape to withstand higher frequencies, opening the way to new machine configurations, with AC superconductive windings. The most common HTS belongs to the REBCO family. In particular, the most used rare earth in HTS is yttrium, which is used in the YBCO superconductor. Unfortunately, the fabrication technology of HTS is complex and expensive, although new production processes produce generations of HTS with increased reliability and cost-effectiveness. Recently, a new technique for fabricating MgB2 based superconductors, called reactive Mg-liquid infiltration [54], has been exploited to evaluate spirals and ring coil windings [55]. An extensive characterization of HTS coils can be found in [31]. The frequency dependence of the coil resistivity with the frequency, in the range 10–100 Hz can be approximated as:

$$R_{coil} = K_{sc} * f \quad (6)$$

  where R_{coil} = resistivity of coil, K_{sc} = constant typical of each superconductor type, f = frequency;
- *Complexity of the cooling system*: Cryogenic cooling systems can be complex, requiring specialized equipment and expertise to design, install, and maintain.
- *Energy consumption*: Cryogenic cooling systems can consume a significant amount of energy, therefore before use, it is necessary to make an overall energy balance of the equipment or system to determine if it is cost-effective for that application;

In addition, cryogenic electric machines also suffer from vibrations and stray magnetic fields affecting the metal part. Vibration is a significant problem due to the high stiffness and brittleness of materials at cryogenic temperatures. At these temperatures, the mechanical properties of materials change, making them more susceptible to cracking and breaking under mechanical stress. This can lead to a decrease in machine performance and reliability. Furthermore, the operating frequency of the machine can influence the behavior of superconducting materials, making it important to design the machine to operate at specific frequencies. To address these issues, the design of cryogenic electric machines must take into account the effects of vibration and frequency on machine performance and reliability. This can include the use of specialized materials and coatings to reduce vibration and improve mechanical stability, as well as the use of specific operating frequencies to optimize machine performance. Furthermore, particular care must be taken in the design of the cryostat due to the stray magnetic fields affecting the metal parts. In the presence of magnetic fields, the choice of materials for cryostat construction becomes more limited. Magnetic fields can induce electrical currents in certain materials, which can generate heat and cause the materials to lose their superconducting properties if they are being used for that purpose. Therefore, in applications where magnetic fields are present, the cryostat must be constructed using materials that are not magnetically conductive. Some materials that are commonly used in cryostats in the presence of magnetic fields include:

- *Non-magnetic stainless steel*: Non-magnetic stainless steel, such as grade 304 L, is commonly used in cryostat construction for applications where magnetic fields are present. This material has low magnetic permeability, which means it is not easily magnetized by an external magnetic field;
- *Aluminum alloys*: Certain aluminum alloys, such as 5083 and 6061, are non-magnetic and are commonly used in cryostat construction for applications where magnetic fields are present. These alloys have low magnetic permeability and are also lightweight and relatively inexpensive;

- *Titanium alloys*: Certain titanium alloys, such as Ti-6Al-4V and Ti-3Al-2.5V, are non-magnetic and are commonly used in cryostat construction for applications where magnetic fields are present. These alloys have low magnetic permeability and are also corrosion-resistant and strong;
- *Copper alloys*: Some copper alloys, such as Cu-Ni alloys (such as Monel) and brass, have low magnetic permeability and are suitable for use in cryostats in the presence of magnetic fields. However, copper alloys can be more expensive than other materials and may corrode in the presence of certain cryogenic fluids.

Thus, the choice of materials for cryostat construction in the presence of magnetic fields depends on a variety of factors, including the strength and orientation of the magnetic field, the specific application, and the required performance characteristics of the materials. It is important to select materials that are not magnetically conductive and that can withstand the stresses and thermal cycling that occur during operation.

Sealing rings in a cryogenic motor can be affected by the presence of stray magnetic fields. These fields can induce eddy currents in the sealing ring, which can lead to heating and a reduction in the sealing efficiency. To prevent the effects of stray magnetic fields, non-magnetic materials are typically used for the sealing rings in cryogenic motors. Materials such as non-magnetic ferrofluid gaskets [56] are often used, which perform very well from this point of view, even if very expensive. These materials have low magnetic permeability and can withstand the cryogenic temperatures of the motor.

Overall, a cryogenic electric machine for use in industrial environments requires careful planning, design and maintenance to ensure safe and reliable operation. The choice of motor materials depends on various factors, including the required magnetic field strength, temperature, and mechanical stress. The material properties also play a significant role in determining the efficiency and performance of the motor. It is important to carefully consider the selection of materials to optimize the performance of the superconducting motor in the presence of magnetic fields to cryogenic temperatures.

3. Prospective Electric Machines with Cryogenic Cooling

The use of electric machines with cryogenic cooling is an active area of research and development. The main perspective is to increase the efficiency and performance of electric machines, which can lead to energy savings and reduced environmental impact. However, some challenges need to be overcome before this technology can be widely adopted in the industry. The challenge we should face in the next 10 years will be to transfer a part of the research to the industries, providing a consolidated design technique for cryogenic engines. Furthermore, the technical personnel currently working in the electric motor industries do not have the training or specialization to operate in this sector. A lot of work will be asked of universities, to integrate courses for cryogenic design, and highly specialized courses for the issue of installation/safety licenses to work in this field.

In addition, there are other challenges to be faced in the field of industrial research:

1. *High-temperature superconductors* (HTS): The research in this field is producing new superconductors with higher critical temperatures. The use of these HTS materials in cryogenic motors could allow for operation at higher temperatures, which would reduce the cost and complexity of the cooling systems;
2. Improved cooling systems: Research is ongoing to develop more efficient and cost-effective cryogenic cooling systems for electric motors, such as two-phase flow cooling systems and immersion cooling systems;
3. Improved insulation materials: Researchers are exploring new insulation materials that can withstand the low temperatures and high thermal stresses associated with cryogenic cooling, which could improve the performance and reliability of cryogenic motors;
4. Intelligent control systems: The use of advanced control systems and artificial intelligence algorithms to optimize the performance of cryogenic motors in real-time;

5. Cryogenic energy storage (CES): Cryogenic energy storage is a promising technology that uses cryogenic temperatures to store energy in the form of liquid hydrogen or liquid helium. This technology could be used in conjunction with cryogenic motors to improve the overall efficiency and performance of the system;
6. Superconducting magnetic energy storage (SMES): Superconducting magnetic energy storage is a new technology that stores electricity from a source within the magnetic field of a coil made of superconducting wire with almost zero energy loss. This technology could bring many benefits to electric motors, for example during the braking phase we could recover a part for the next restart;
7. Advanced materials and manufacturing techniques: The use of advanced materials, such as carbon nanotubes, and manufacturing techniques, such as 3D printing, could allow for the development of more efficient and reliable cryogenic motors;
8. Cryogenic motors with integrated power electronics: Combining cold power electronics and superconducting machines can provide several advantages which lead to an increase in system efficiency with a reduction in power losses. It can also increase the power density of the system, allowing for smaller and more compact designs. Additionally, by operating the power electronics and machines at low temperatures, the system may produce less noise and vibration.

As listed, there are still many issues to be addressed before this technology can reach a wider range of applications. On the other hand, cryogenic cooling systems are complex and expensive to implement and require specialized insulating materials that can withstand the extreme temperatures of cryogenic fluids. The cost of cryogenic fluids, the complexity of the cooling system, and the need for specialized insulation materials are factors slowing market uptake. Furthermore, until all the technological challenges (especially those relating to safety systems in the event of accidental losses or losses caused by third parties, reliability issues in static or dynamic conditions, durability, and predictive maintenance) are addressed, cryogenic electric motors represent a technology that will only operate in the high-level industrial or research field. Despite these challenges, the use of cryogenic cooling in electric motors is an active area of research, and this technology is expected to become increasingly cost-effective in a few years, encouraging its use.

Overall, while the technology is still evolving, cryogenic electric motors have the potential to improve the efficiency and performance of electric motors and other electrical systems in the future, but they still require further research and development to overcome the challenges and make them more cost-effective and practical for wide-scale adoption.

Furthermore, it must be considered that cryogenic motors need special accessories, such as cables fault current limiters (FCL) and fast-acting circuit breakers (FACBs). The use of cryogenic cooling can be extended to these devices to improve motor performance, reduces size, and improves efficiency. The use of cryogenic cables leads to lower energy losses and therefore they achieve a higher power density, and as this technology does not produce heat, it is considered environmentally friendly. The use of cryogenic FCLs and FACBs can provide several advantages, achieving higher efficiency due to reduced power losses, and higher reliability as they are less subject to wear with higher power density in a compact size.

4. Conclusions

This article has summarized the most recent developments in technologies and findings that can boost the application of superconducting motors and generators. Large superconducting machines are currently used primarily in ship propulsion and wind power generation. However, the new generations of HTS, efficient cooling systems and means, and other devices such as superconducting protection systems should help to spread this technology further, opening new technological scenarios with more efficient and powerful machines in the near future. However, for cryogenic electric motors to become a large-scale industrial product, there is still a lot of work to be carried out in various areas, such as research, industry, and regulatory issues. However, the significant

benefits of cryogenic electric motors are increased efficiency and power density, resulting in a reduction in mass.

Author Contributions: Conceptualization, F.M. and G.R.; formal analysis, F.M. and G.R.; investigation, F.M. and G.R.; resources, F.M. and G.R.; data curation, F.M. and G.R.; writing—original draft preparation, F.M. and G.R.; writing—review and editing, F.M. and G.R.; visualization, F.M. and G.R.; supervision, F.M. and G.R. All authors have read and agreed to the published version of the manuscript.

Funding: This research received no external funding.

Data Availability Statement: The data presented in this study are available on request from the corresponding author.

Conflicts of Interest: The authors declare no conflict of interest.

Abbreviations

The following abbreviations are used in this manuscript:

AC	alternating current
Al	aluminum
Ar	argon
ASCEND	Advanced Superconducting and Cryogenic Experimental powertraiN Demonstrator
Cu	copper
CES	cryogenic energy storage
CH4	methane
COP	coefficient of performance
CO_2	carbon dioxide
CPE	cryogenic power electronics
Cu	copper
DC	direct current
F	fluorine
FACBs	fast-acting circuit breakers
FCL	fault current limiters
GA-EMS	General Atomics Electromagnetic Systems
H	hydrogen
H2	chemical formula for hydrogen (dihydrogen)
He	chemical formula for helium
HTS	high-temperature superconductors
LH2	liquid hydrogen
LN2	liquid nitrogen
LHe	liquid helium
LNe	liquid neon
LTS	low-temperature superconducting
N	nitrogen
N2	chemical formula for nitrogen (dinitrogen)
NbTi	niobium-titanium
Nb3Sn	niobium-tin
Ne	chemical formula for neon
PA	polyamide-imide
PI	polyimide
P2P	pumped two-phase cooling
REBCO	rare-earth barium copper oxide
SCHMs	superconducting homopolar machines
SCIMs	superconducting induction machines
SCMs	superconducting machines
SCP	specific cooling power
SCSMs	superconducting synchronous machines
SMB	superconducting magnetic bearing
SMC	soft magnetic composites

SMES	superconducting magnetic energy storage
YBCO	yttrium barium copper oxide

References

1. Bucho, L.F.; Fernandes, J.F.; Costa Branco, P.; Biasion, M.; Vaschettc, S.; Cavagnino, A. Losses analysis of induction motors under ambient and cryogenic conditions. In Proceedings of the IEEE Energy Conversion Congress and Exposition ECCE, Virtual, 10–14 October 2022; pp. 1–7. [CrossRef]
2. Biasion, M.; João Fernandes, F.P.; da Costa Branco, P.J.; Vaschetto, S.; Cavagnino, A.; Tenconi, A. A comparison of cryogenic-cooled and superconducting electrical machines. In Proceedings of the IEEE Energy Conversion Congress and Exposition ECCE, Singapore, 24–27 May 2021; pp. 4045–4052. [CrossRef]
3. Qingsong, W.; Yu, W.; Shuangxia, N.; Xing, Z. Advances in thermal management technologies of electrical machines. *Energies* **2022**, *15*, 3249. [CrossRef]
4. Kalsi, S.; Weeber, K.; Takesue, H.; Lewis, C.; Neumueller, H.; Blaugher, R. Development status of rotating machines employing superconducting field windings. *Proc. IEEE* **2004**, *92*, 1688–1704. [CrossRef]
5. Systems, G.A.E. GA-EMS Delivers High-Temperature Superconducting Motor to U.S. Navy for Advanced Propulsion System Testing. In *General Atomics Electromagnetic Systems*; General Atomics: San Diego, CA, USA, 2018.
6. Rolls-Royce. *Rolls-Royce Develops Superconductive Generator for Naval Use*; Rolls-Royce: London, UK, 2019.
7. Torrey, D.; Parizh, M.; Bray, J.; Stautner, W.; Tapadia, N.; Xu, M.; Wu, A.; Zierer, J. Superconducting synchronous motors for electric ship propulsion. *IEEE Trans. Appl. Supercond.* **2020**, *30*, 5204708. [CrossRef]
8. Tomé-Robles, D.J.; Nilssen, R.; Nøland, J.K. Comparison of AC superconducting multiphase symmetric winding topologies for wind power generators with PM rotors. *IEEE Trans. Appl. Supercond.* **2022**, *32*, 5202715. [CrossRef]
9. Bergen, A.; Andersen, R.; Bauer, M.; Boy, H.; ter Brake, M.; Brutsaert, P.; Bührer, C.; Dhallé, M.; Hansen, J.; ten Kate, H.; et al. Design and in-field testing of the world's first ReBCO rotor for a 3.6 MW wind generator. *Supercond. Sci. Technol.* **2019**, *32*, 125006. [CrossRef]
10. Nøland, J.K.; Mellerud, R.; Hartmann, C. Next-generation cryo-electric hydrogen-powered aviation: A disruptive superconducting propulsion system cooled by onboard cryogenic fuels. *IEEE Ind. Electron. Mag.* **2022**, *16*, 6–15. [CrossRef]
11. Chen, R.; Niu, J.; Ren, R.; Gui, H.; Wang, F.; Tolbert, L.; Choi, B.; Brown, G. A cryogenically-cooled MW inverter for electric aircraft propulsion. In Proceedings of the AIAA/IEEE Electric Aircraft Technologies Symposium EATS, New Orleans, LA, USA, 26–28 August 2020; pp. 1–10.
12. Da Silva, F.F.; Fernandes, J.F.P.; da Branco, P.J.C. Barriers and challenges going from conventional to cryogenic superconducting propulsion for hybrid and all-electric aircrafts. *Energies* **2021**, *14*, 6861. [CrossRef]
13. European Commission. Advanced Superconducting Motor Experimental Demonstrator (ASuMED). Horizon 2020. 2017. Available online: https://cordis.europa.eu/project/id/723119 (accessed on 15 January 2023).
14. Airbus. ASCEND: Advanced Superconducting and Cryogenic Experimental PowertraiN Demonstrator. 2021. Available online: https://www.airbus.com/en/newsroom/stories/2021-03-cryogenics-and-superconductivity-for-aircraft-explained (accessed on 29 March 2021).
15. Ybanez, L.; Colle, A.; Nilsson, E.; Berg, F.; Galla, G.; Tassisto, M.; Rivenc, J.; Kapaun, F.; Steiner, G. ASCEND: The first step towards cryogenic electric propulsion. *IOP Conf. Ser. Mater. Sci. Eng.* **2022**, *1241*, 012034. [CrossRef]
16. Bucho, L.F.D.; Fernandes, J.F.P.; Biasion, M.; Vaschetto, S.; Cavagnino, A. Experimental assessment of cryogenic cooling impact on induction motors. *IEEE Trans. Energy Convers.* **2022**, *37*, 2629–2636. [CrossRef]
17. Sugimoto, H.; Tsuda, T.; Morishita, T.; Hondou, Y.; Takeda, T.; Togawa, H.; Oota, T.; Ohmatsu, K.; Yoshida, S. Design of an axial flux inductor type synchronous motor with the liquid nitrogen cooled field and armature HTS windings. *IEEE Trans. Appl. Supercond.* **2007**, *17*, 1571–1574. [CrossRef]
18. Liu, B.; Badcock, R.; Shu, H.; Fang, J. A superconducting induction motor with a high temperature superconducting armature: Electromagnetic theory, design and analysis. *Energies* **2018**, *11*, 792. [CrossRef]
19. Kalsi, S.; Hamilton, K.; Buckley, R.G.; Badcock, R.A. Superconducting AC homopolar machines for high-speed applications. *Energies* **2019**, *12*, 86. [CrossRef]
20. Kim, Y.; Ki, T.; Kim, H.; Jeong, S.; Kim, J.; Jung, J. High temperature superconducting motor cooled by on-board cryocooler. *IEEE Trans. Appl. Supercond.* **2011**, *21*, 2217–2220. [CrossRef]
21. Radenbaugh, R. Refrigeration for superconductors. *Proc. IEEE* **2004**, *92*, 1719–1734. [CrossRef]
22. Kasthurirengan, S.; Srinivasa, G.; Karthik, G.S.; Ramesh, K.P.; Shafi, K.A. Experimental studies on a two stage pulse tube cryocooler reaching 2.5 K. *AIP Conf. Proc.* **2008**, *985*, 85. [CrossRef]
23. Montoya, R.Á.; Delgado, S.; Castilla, J.; Navarrete, J.; Contreras, N.D.; Marijuan, J.R.; Barrena, V.; Guillamón, I.; Suderow, H. Methods to simplify cooling of liquid helium cryostats. *HardwareX* **2019**, *5*, 00058. [CrossRef]
24. Dyson, R.W.; Jansen, R.H.; Duffy, K.P.; Passe, P.J. High efficiency megawatt machine rotating cryocooler conceptual design. In Proceedings of the AIAA/IEEE Electric Aircraft Technologies Symposium EATS, Indianapolis, IA, USA, 22–24 August 2019; pp. 1–15. [CrossRef]

25. Redmond, J.H.; Bott, F.W. Development of cryogenic electric motors. In *Proceedings of the SAE World Congress Exhibition*; SAE International: Warrendale, PA, USA, 1964. [CrossRef]
26. Laskaris, T. A two-phase cooling system for superconducting AC generator rotors. *IEEE Trans. Magn.* **1977**, *13*, 759–762. [CrossRef]
27. Guechi, M.; Desevaux, P.; Baucour, P.; Espanet, C.; Brunel, R.; Poirot, M. Spray cooling of electric motor coil windings. *J. Comput. Multiph. Flows* **2016**, *8*, 95–100. [CrossRef]
28. Radebaugh, R. Cryocoolers: The state of the art and recent developments. *J. Phys. Condens. Matter* **2009**, *21*, 164219. [CrossRef]
29. Stautner, W.; Xu, M.; Mine, S.; Amm, K. Hydrogen cooling options for MgB2-based superconducting systems. *AIP Conf. Proc.* **2014**, *1573*, 82. [CrossRef]
30. Dezhin, D.; Dezhina, I.; Ilyasov, R. Superconducting propulsion system with LH2 cooling for all-electric aircraft. *J. Phys. Conf. Ser.* **2020**, *1559*, 012143. [CrossRef]
31. Messina, G.; Yazdani-Asrami, M.; Marignetti, F.; della Corte, A. Characterization of HTS coils for superconducting rotating electric machine applications: Challenges, material selection, winding process, and testing. *IEEE Trans. Appl. Supercond.* **2021**, *31*, 5200310. [CrossRef]
32. Marignetti, F.; Carbone, S.; Delli Colli, V.; Attaianese, C. Cryogenic characterization of copper-wound linear tubular actuators. *IEEE Trans. Ind. Electron.* **2012**, *59*, 2167–2177. [CrossRef]
33. Nam, G.D.; Sung, H.J.; Ha, D.W.; No, H.W.; Koo, T.H.; Ko, R.K.; Park, M. Design and analysis of cryogenic cooling system for electric propulsion system using liquid hydrogen. *Energies* **2023**, *16*, 527. [CrossRef]
34. Yazdani-Asrami, M.; Sadeghi, A.; Atrey, M.D. Selecting a cryogenic cooling system for superconducting machines: General considerations for electric machine designers and engineers. *Int. J. Refrig.* **2022**, *140*, 70–81. [CrossRef]
35. Barron, R.F. *Cryogenic Systems (Monographs on Cryogenics)*; Oxford University Press: Oxford, UK, 1985.
36. Simon, N.; Drexler, E.; Reed, R. Properties of copper and copper alloys at cryogenic temperatures. *NIST Monogr.* **1992**, *177*, 10017.
37. Manolopoulos, C.D.; Iacchetti, M.F.; Smith, A.C.; Miller, P.; Husband, M. Litz wire loss performance and optimization for cryogenic windings. *IET Electr. Power Appl.* **2022**.
38. Marignetti, F. On liquid-nitrogen-cooled copper-wound machines with soft magnetic composite core. *IEEE Trans. Ind. Appl.* **2010**, *46*, 984–992. [CrossRef]
39. Ho, J.; Oberly, C.; Gegel, H.; Griffith, W.; Morgan, J.; O'Hara, W.; Prasad, Y. A new aluminum-base alloy with potential cryogenic applications. In *Advances in Cryogenic Engineering Materials*; Clark, A.F., Ed.; Springer: Boston, MA, USA, 1986; pp. 437–442. [CrossRef]
40. Kopylov, S.E.; Bragin, A.V.; Khrushchev, S.V.; Shkaruba, V.A.; Tsukanov, V.M.; Mezentsev, N.A. Development of ultra low resistance splicing of Nb3Sn and NbTi superconducting wires. *IEEE Trans. Appl. Supercond.* **2021**, *31*, 9000905. [CrossRef]
41. Liu, J.H.; Song, S.S.; Gou, C.C.; Zhou, J.B.; Wang, L.; Dai, Y.M.; Fang, Y.T. Development of YBCO insert for a 25 T all superconducting magnet. In Proceedings of the IEEE International Conference on Applied Superconductivity and Electromagnetic Devices ASEMD, Shanghai, China, 20–23 November 2015; pp. 433–434. [CrossRef]
42. Cook, J.T.; Hones, H.M.; Mahon, J.R.; Yu, L.; Krchnavek, R.R.; Xue, W. Temperature-dependent dielectric properties of polyimide (PI) and polyamide (PA) nanocomposites. *IEEE Trans. Nanotechnol.* **2021**, *20*, 584–591. . [CrossRef]
43. Wang, M.Y.; Du, B.X.; Han, X.T.; Li, Z.L. Effects of magnetic field on partial discharge in epoxy resin for superconducting coil insulation. *IEEE Trans. Appl. Supercond.* **2021**, *31*, 4702603. [CrossRef]
44. Anoop, C.R.; Singh, R.K.; Kumar, R.R.; Jayalakshmi, M.; Prabhu, T.A.; Tharian, K.T.; Murty, S.V.S.N. A review on steels for cryogenic applications. *Mater. Perform. Charact.* **2021**, *10*, 20200193. [CrossRef]
45. Sonar, T.; Lomte, S.; Gogte, C. Cryogenic treatment of metal a review. *Mater. Today Proc.* **2018**, *5*, 25219–25228. [CrossRef]
46. Supreeth, D.K.; Bekinal, S.I.; Chandranna, S.R.; Doddamani, M. A review of superconducting magnetic bearings and their application. *IEEE Trans. Appl. Supercond.* **2022**, *32*, 3800215. [CrossRef]
47. Liwang, A.; Guomin, Z.; Wanjie, L.; Guole, L.; Naihao, S.; Liye, X.; Liangzhen, L. Research on a superconducting magnetic bearing system for submerged cryogenic disk motor-pump. *IEEE Trans. Appl. Supercond.* **2018**, *28*, 5202505. [CrossRef]
48. Reed, R.P.; Clark, A.F. Thermal conductivity and thermal diffusivity. In *Materials at Low Temperatures*; Park, A.I.M., Ed.; American Society for Metals: Geauga County, OH, USA, 1983; Chapter 4.
49. Ekin, J. *Experimental Techniques for Low-Temperature Measurements: Cryostat Design, Material Properties and Superconductor Critical-Current Testing*; Oxford University Press: Oxford, UK, 2006. [CrossRef]
50. Leong, K.K. Utilising Power Devices below 100 K to Achieve Ultra-Low Power Losses. Ph.D. Thesis, University of Warwick, Warwick, UK, 2011.
51. Graber, L.; Saeedifard, M.; Mauger, M.; Yang, Q.; Park, C.; Niebur, T.; Pamidi, S.; Steinhoff, S. Cryogenic power electronics for superconducting power systems. In Proceedings of the Madison CEC ICMC, Madison, WI, USA, 9–13 July 2017; Indico Cern 2017.
52. Radebaugh, R.; Huang, Y.; O'Gallagher, A.; Gary, J. *Calculated Performance of Low Porosity Regenerators at 4 K with He4 and He3*; ICC Press: The Hague, The Netherlands, 2008.
53. Smith, J.; Keim, T. Applications of superconductivity to AC rotating machines. In *Superconducting Machines and Devices: Large Systems Applications*; Springer: Boston, MA, USA, 1974; pp. 279–345. [CrossRef]

54. Giunchi, G. MgB2 superconductive inserts: Products between bulks and wires. *IEEE Trans. Appl. Supercond.* **2011**, *21*, 1564–1567. [CrossRef]
55. Marignetti, F.; Cavaliere, V.; Giunchi, G.; Messina, G.; Attaianese, C.; Della Corte, A. Use of MgB2 superconductors for excitation field in synchronous machines—Part II: Inserts. *IEEE Trans. Appl. Supercond.* **2013**, *23*, 8002606. [CrossRef]
56. Wal, K.; Ostayen, R.; Lampaert, S. Ferrofluid rotary seal with replenishment system for sealing liquids. *Tribol. Int.* **2020**, *150*, 106372. [CrossRef]

energies

MDPI

Article

Fault-Tolerant Control of Induction Motor with Current Sensors Based on Dual-Torque Model

Yongda Li and Pingping Gong *

School of Electrical Engineering, Guangxi University, Nanning 530004, China; 2012301030@st.gxu.edu.cn
* Correspondence: gongpp@gxu.edu.cn

Abstract: The safety of direct torque control (DTC) is strongly reliant on the accuracy and consistency of sensor measurement data. A fault-tolerant control paradigm based on a dual-torque model is proposed in this study. By introducing the vector product and scalar product of the stator flux and stator current vector, a new state variable is selected to derive a new dual-torque model of induction motor; it is combined with a current observer to propose a dual-torque model fault-tolerant control method. This technology calculates torque and reactive torque directly, reducing the system's reliance on sensors, avoiding sensor-noise interference, and improving torque response speed while suppressing torque ripple. In addition, to improve system dependability and safety, a fault-tolerant control method is devised by combining the model with an adaptive virtual current observer. Ultimately, experiments validate the suggested method's effectiveness and feasibility.

Keywords: induction motor; torque control; fault diagnosis; fault-tolerant control

Citation: Li, Y.; Gong, P. Fault-Tolerant Control of Induction Motor with Current Sensors Based on Dual-Torque Model. *Energies* **2023**, *16*, 3442. https://doi.org/10.3390/en16083442

Academic Editors: Loránd Szabó and Feng Chai

Received: 16 March 2023
Revised: 11 April 2023
Accepted: 12 April 2023
Published: 14 April 2023

1. Introduction

Induction motors are commonly used in industries such as electric vehicles and hybrid electric vehicles, and reliability and efficiency are hard indicators for motor drive system control in electrified transportation [1,2]. Secondly, in order to improve the energy efficiency of the vehicle, the design of the motor drive system should take into account the reduction in the harmonic content of the motor feed current; to avoid the risk of mechanical resonance of the drive shaft system and to improve the reliability of the vehicle, the electromagnetic torque ripple must be minimized [3,4]. Compared to fieldoriented control (FOC), direct torque control (DTC) offers faster response times, higher accuracy, and better dynamic characteristics. However, DTC is noisy and insensitive to changes in motor parameters, and its main problems are that the switching frequency is high and not fixed and the torque fluctuation is large [5]. In the literature [6], the dot and fork products of the stator and rotor magnetic chain vectors and the squared signal of the magnetic chain amplitude are selected as the state variables of the motor system, the linearized mathematical model of the motor is reconstructed, and the feedback linearization-based direct torque control strategy of the induction motor is proposed to improve the robustness and steady-state control accuracy of the system; in the literature [7], the dot and fork products of the stator magnetic chain vector and the stator current vector are selected as the system state variables to define the state–space transformation equations that are not affected by any motor parameters, giving a formal derivation of the induction motor DTC method to improve the control accuracy. From the perspective of instantaneous power control at the machine end, an indirect active/reactive power control method was explored in the literature [8]. The induction motor drive system designed based on this control algorithm outperforms FOC and DTC for some specific tasks in terms of torque, speed, current response, and the speed regulation range.

In addition, the reliability of electric and hybrid electric vehicles is heavily dependent on the reliability of electronic equipment [9,10]. In the case of electric vehicles, vehicle

stability depends on the accuracy and reliability of sensor measurement data. These sensors include current sensors, voltage sensors, and speed sensors. Current sensors are particularly prone to failure, and causes of failure include noise, gain drift, saturation, and connection problems [11]. Consequently, researchers have focused strongly on sensorless technology and on fault-tolerant control in the event of sensor failure, with the aim of reducing the number of current sensors used [12,13]. In this research, we offer a fault-tolerant control model based on a dual-torque model, as well as fault diagnosis and fault-tolerant control techniques for the model. This concept attempts to increase the dependability and stability of electric and hybrid electric cars by reducing the dependency on current sensors.

Rapid diagnosis and localization of current sensor faults are crucial for implementing fault-tolerant control in induction motors [14]. Existing diagnostic methods include observer-based, data-driven, and coordinate transformation methods. For example, a simple and effective current sensor fault diagnosis method is proposed in [15]. The fault diagnosis is carried out according to the change of the corresponding characteristic quantity before and after the current sensor fault. Only the phase current information that can be directly collected is needed. This method also has a relatively simple calculation process, so it is very suitable for real-time fault diagnosis. The authors of [16] used a Luenberger observer and the state equation of a permanent magnet synchronous motor to diagnose current sensor faults. A full-order adaptive state observer is proposed in [17], which can identify the rotor resistance online and greatly improve the AC accuracy of the observer. This method also uses the residual between the measured value and the estimated value as the basis for fault diagnosis. The authors in [18] design an observer that does not need to measure the load, so the fault diagnosis method is no longer affected by load mutation and load increase and decrease, thus improving the reliability of the method.

After fault diagnosis of a current sensor, if a fault is found to exist, a fault-tolerant control is required to maintain the normal operation of the system. Two categories of fault-tolerant control of current sensors are currently available: switching the control system from high-performance dual-loop control to single or open-loop control [19]; and estimating the current by building an observer, replacing the faulty phase current with the estimated current, and achieving closed-loop control after detecting the fault [20–22]. For example, the author of article [23] switches the whole vector control to the variable voltage and variable frequency (VVVF) system when the current sensor fails, realizing the open-loop control without current information. Therefore, the motor can still run until it stops, avoiding the loss caused by sudden shutdown. However, this open-loop control sacrifices the control performance of the induction motor. The second method can guarantee control performance and is more widely applied. For example, the authors in [20] estimate currents using a flux observer and replace a faulty phase current to achieve closed-loop control, thus achieving fault-tolerant control of an induction motor drive system. Article [21] proposes a method for sensor fault diagnosis, isolation, and fault tolerance of an induction motor based on the extended Kalman filter. This method has good robustness, but needs to build two additional current observers for fault-tolerant control, resulting in heavy computational burden. Article [22] has constructed three parallel full-order adaptive current observers with three-phase current to realize fault diagnosis and fault-tolerant control of one or any two induction motor current sensors; however, this scheme requires a high-performance computing unit to meet its high computational burden need. The authors of [24] introduce a dual-torque model of an induction motor based on rotor magnetic flux and stator currents, combining a nonlinear control method. The electromagnetic torque depends not on the absolute positions of the rotor magnetic flux and stator current vector in stationary and rotating coordinate systems but on their relative positions. The authors of [25,26] have applied the definition and model of the dual-torque induction motor, which is described in [24] to estimate the motor speed while improving the stability of motor operation and reducing torque ripples. Most of the research in fault-tolerant control focuses on the speed-sensorless control methods; the current sensor fault diagnosis and fault-tolerant control algorithms mostly use the current observer to replace the current sensor. Although

sensorless control can avoid the system fault to a certain extent, it will cause complexity and slow response speed in the system.

In order to enhance the reliability of induction motor drive systems, we present an approach that combines a current sensor fault-tolerant control strategy with the dual-torque model. By utilizing the dual-torque control model introduced in [24], we select state variables with the vector product (torque) and scalar product (reactive torque) of the stator magnetic flux and stator current vectors, and, consequently, derive a dual-torque induction motor model. Based on this model, we design a fault diagnosis and fault-tolerant control scheme for induction motors. The proposed method is designed to enable the motor to maintain its rotation, in response to a command, in the event of a current sensor failure. Moreover, it reduces the complexity of the algorithm effectively. To validate the proposed approach, experiments are conducted on an induction motor driven by a dual-level inverter, which is controlled by dSPACE (DS1104). Overall, this study offers a valuable contribution to the field of fault-tolerant control of induction motor drive systems. The proposed method provides a practical and reliable solution for diagnosing and controlling current sensor faults, thereby ensuring stable system operation.

Traditional Direct Torque Control

For traditional DTC, the αβ component of the stator voltage in the two-phase stationary coordinate system can be obtained using the Clarke transformation as [27]:

$$\begin{bmatrix} u_\alpha \\ u_\beta \end{bmatrix} = \frac{2}{3}\begin{bmatrix} 1 & -\frac{1}{2} & -\frac{1}{2} \\ 0 & \frac{\sqrt{3}}{2} & -\frac{\sqrt{3}}{2} \end{bmatrix}\begin{bmatrix} u_a \\ u_b \\ u_c \end{bmatrix} \tag{1}$$

The stator flux and stator currents are used as state variables to create a mathematical model of an induction motor in a stationary coordinate system. Such a model can result in stator flux and current, and so:

$$\frac{\mathrm{d}\vec{\psi}_s}{\mathrm{d}t} = -R_s\vec{i}_s + \vec{u}_s \tag{2}$$

$$\frac{\mathrm{d}\vec{i}_s}{\mathrm{d}t} = \frac{1}{\sigma L_s}\left(\frac{R_r}{L_r} - \mathrm{j}\omega\right)\vec{\psi}_s - \left(\frac{R_r}{\sigma L_s} - \mathrm{j}\omega\right)\vec{i}_s + \frac{1}{\sigma L_s}\vec{u}_s \tag{3}$$

In the stationary coordinate system, based on the induction motor and flux equations, the model for the rotor flux current can be derived as follows:

$$\begin{array}{l} \frac{\mathrm{d}\psi_{r\alpha}}{\mathrm{d}t} = -\frac{1}{T_r}\psi_{r\alpha} - \omega\psi_{r\beta} + \frac{L_m}{T_r}i_{s\alpha} \\ \frac{\mathrm{d}\psi_{r\beta}}{\mathrm{d}t} = -\frac{1}{T_r}\psi_{r\beta} + \omega\psi_{r\alpha} + \frac{L_m}{T_r}i_{s\beta} \end{array} \tag{4}$$

In the above equations, the equivalent resistance is $R_\gamma = (R_r L_s)/L_r + R_s$; the leakage coefficient is $\sigma = 1 - L_m^2/(L_s L_r)$; $\vec{u}_s$ is the stator voltage vector; $\vec{i}_s$ and $\vec{i}_r$ are the stator and rotor current vectors, respectively; $\vec{\psi}_s$ and $\vec{\psi}_r$ are the stator and rotor flux vectors, respectively; R_s and R_r are the stator and rotor resistances, respectively; L_s and L_r are the stator and rotor inductances, respectively; L_m is the mutual inductance; ω is the rotor electrical angular velocity; and the rotor time constant is $T_r = L_r/R_r$ [28]. A traditional DTC structure block diagram is shown in Figure 1.

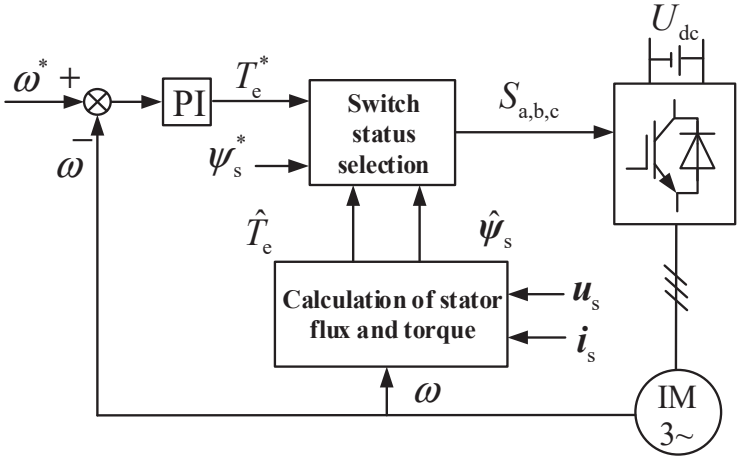

Figure 1. Traditional direct torque control (DTC) structure block diagram.

2. Dual-Torque Model for an Induction Motor

According to the mirror power theory proposed in [29], the reactive power of the original system is physically interpreted as the active power of its mirror system, which proves that the original system is the same as the mirror system in terms of its passive nature and explains the physical meaning of reactive power, giving a theoretical pavement for further research on the physical abstraction of reactive power-based motor control methods. The radial motion is slower compared to the tangential motion; that is, the change in amplitude is slower compared to the change in phase, which is a slow time scale variable. To fill the absence of this key variable, a variable, reactive torque T_R, is introduced in this paper, and since the phase change is faster compared to the amplitude change, the two variables are of different time scales; their separation is designed to be more conducive to improving the control performance of the system.

An independent flux closed-loop negative-feedback-control outer loop is added to improve the robustness and control accuracy against parameter variations. Figure 2 presents a structural diagram of the dual-torque DTC method, which mainly consists of a speed and flux outer loop PI controller, stator flux estimation, and calculations of torque T_e and reactive torque T_R. The reference values of T_e and T_R are obtained from the speed outer loop PI controller and the flux outer loop PI controller, respectively.

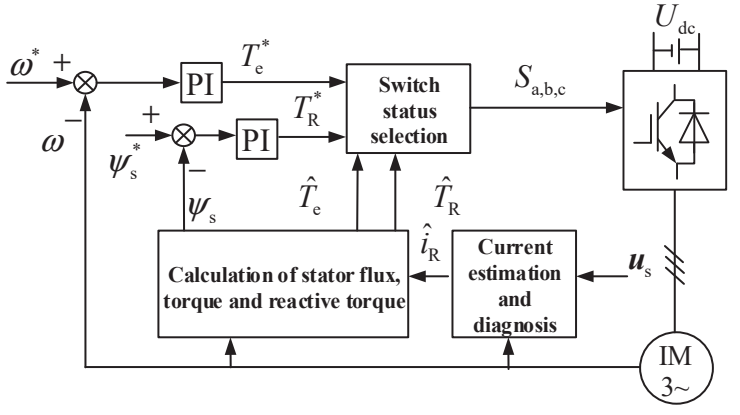

Figure 2. Structure block diagram of DTC dual-torque model current sensorless.

2.1. Dual-Torque Model for an Induction Motor

Building on the approach for obtaining a model of an induction motor through rotor flux linkage and stator current described in [24], this study introduces three state variables based on stator flux linkage and stator current, as described by Equations (5)–(7). Consequently, the dual-torque model of the induction motor is derived using stator flux linkage.

$$\psi_s^2 = \psi_{s\alpha}^2 + \psi_{s\beta}^2 \tag{5}$$

$$\tau_s = \psi_{s\alpha} i_{s\beta} - \psi_{s\beta} i_{s\alpha} \tag{6}$$

$$\eta_s = \psi_{s\alpha} i_{s\alpha} + \psi_{s\beta} i_{s\beta} \tag{7}$$

In the above, τ_s is the cross product of the stator flux and stator current vectors, known as the normalized torque; and η_s is the dot product of the stator flux and stator current vectors, representing the normalized reactive torque.

Typically, a 5th-order model is needed to fully characterize the dynamic and static behaviors of an induction motor. Because the flux linkage angle is only used for observer design, the method proposed in this paper requires only a 4th-order model, which can fully capture the dynamic and static characteristics of the induction motor by utilizing the state variables defined in Equations (5)–(7). By taking the derivatives of the variables defined in Equations (5)–(7), we obtain:

$$\frac{d\omega}{dt} = \frac{n_p}{J}\left(\frac{3}{2} n_p \tau_s - T_L\right) \tag{8}$$

$$\frac{d\psi_s^2}{dt} = -2R_s\eta_s + 2u_{\eta s} \tag{9}$$

$$\frac{d\tau_s}{dt} = -\frac{R_s L_r + R_r L_s}{\sigma L_s L_r}\tau_s - \frac{1}{\sigma L_s}\omega\psi_s^2 + \frac{1}{\sigma L_s}u_{\tau s} + \left(\omega\eta_s - \frac{\eta_s}{\psi_s^2}u_{\tau s} + \frac{\tau_s}{\psi_s^2}u_{\eta s}\right) \tag{10}$$

$$\begin{array}{c} \frac{d\eta_s}{dt} = -\frac{R_s L_r + R_r L_s}{\sigma L_s L_r}\eta_s + \frac{R_r}{\sigma L_s L_r}\psi_s^2 + \frac{1}{\sigma L_s}u_{\eta s} \\ +\left(-\omega\tau_s + \frac{\tau_s}{\psi_s^2}u_{\tau s} + \frac{\eta_s}{\psi_s^2}u_{\eta s} - R_s\frac{\tau_s^2+\eta_s^2}{\psi_s^2}\right) \end{array} \tag{11}$$

$$\begin{array}{c} \sigma\frac{d\eta_s}{dt} = -\frac{R_s L_r + R_r L_s}{L_s L_r}\eta_s + \frac{R_r}{L_s L_r}\psi_s^2 + \frac{1}{L_s}u_{\eta s} + \\ \sigma\left(-\omega\tau_s + \frac{\tau_s}{\psi_s^2}u_{\tau s} + \frac{\eta_s}{\psi_s^2}u_{\eta s} - R_s\frac{\tau_s^2+\eta_s^2}{\psi_s^2}\right) \end{array} \tag{12}$$

In the above:

$$\begin{array}{l} u_{\tau s} = \psi_{s\alpha} u_{s\beta} - \psi_{s\beta} u_{s\alpha} \\ u_{\eta s} = \psi_{s\alpha} u_{s\alpha} + \psi_{s\beta} u_{s\beta} \end{array} \tag{13}$$

In Equation (12), the leakage coefficient σ is much lower than 1. Therefore, when considering the dynamic characteristics of the slow-timescale variation of the stator flux, the derivative term of the fast variable η_s related to the leakage coefficient σ and several terms inside the parentheses in Equations (3)–(15) can be ignored, so that:

$$0 = -\frac{R_s L_r + R_r L_s}{L_s L_r}\eta_s + \frac{R_r}{L_s L_r}\psi_s^2 + \frac{1}{L_s}u_{\eta s,slow} \tag{14}$$

$$u_{\eta s,slow} = -\frac{R_r}{L_r}\psi_s^2 + \left(R_s + \frac{L_s}{L_r}R_r\right)\eta_s \tag{15}$$

Substituting Equation (15) into Equation (9), we get:

$$\frac{d\psi_s^2}{dt} = -\frac{2R_r}{L_r}\psi_s^2 + \frac{2L_s R_r}{L_r}\eta_s \tag{16}$$

According to Equation (16), we calculate:

$$T_R = \frac{3}{2} n_p \eta_s = \frac{3n_p}{2L_s} \psi_s^2 + \frac{3n_p L_r}{4L_s R_r} p\psi_s^2 \tag{17}$$

The equation indicates that p is a differential operator. According to Equation (17), there is a linear dynamic relationship between the reactive torque T_R and the square of the stator flux, and T_R can be used to adjust the stator flux, which is the dynamic control variable of the stator flux.

2.2. Fault Diagnosis of Dual-Torque Vector Control of Induction Motors

To improve traditional model-based diagnosis methods, most researchers have replaced the observer to adjust the control performance of fault-tolerant control after a fault occurs. Diagnosis results are mostly based on a determination of α phase or β phase current error, based on the principle of coordinate transformation. However, the phase current error cannot directly determine which phase of a three-phase current sensor has failed; so, an additional judgment module needs to be added.

Traditional fault-tolerant control of current sensors uses the fault detection method expressed in Equation (18), in which the estimated value of the current components on the αβ axis is used to replace the measured value after a fault occurs [30].

$$\begin{cases} \left| i_{s\alpha} - \hat{i}_{s\alpha} \right| > \varepsilon_1 \\ \left| i_{s\beta} - \hat{i}_{s\beta} \right| > \varepsilon_1 \end{cases} \tag{18}$$

where $i_{s\alpha}$ is the stator current component on axis α; $\hat{i}_{s\alpha}$ is the estimated stator current component on axis α, and $i_{s\beta}$ are the stator current component on axis β and the estimated stator current component on axis β, respectively. The threshold value ε_1 is determined manually.

$$\begin{cases} \left| i_A - \hat{i}_A \right| > \varepsilon_2 \\ \left| i_B - \hat{i}_B \right| > \varepsilon_2 \\ \left| i_C - \hat{i}_C \right| > \varepsilon_2 \end{cases} \tag{19}$$

Three current sensors are utilized to capture the currents of phases A, B, and C, respectively. The sum of the three phase currents is employed to detect potential faults in the current sensors. i_A and $\hat{i}_A$ denote the measured and estimated stator current components on axis A; i_B and $\hat{i}_B$ represent the measured and estimated stator current components on axis B; i_C and $\hat{i}_C$ indicate the measured and estimated stator current components on axis C; and ε_2 is the threshold value. At present, there is no uniform standard for selecting the threshold value. Most of them are based on experience. In this study, after many simulations and experiments, we finally selected i_{sq} with a threshold value of 11%.

We then design a current observer to obtain estimated values of the currents in phases A, B, and C. These values can be compared with the measured values to determine whether there is a fault in any of the current sensors. If a fault is detected, the estimated value of the current in the corresponding phase can be used to replace the measured value from the faulty sensor. It is possible to diagnose the faulty phase currents of phase A and phase B and, for the diagnosed phase current with a faulty sensor, replace the sensor measurement value with the observer's estimated value. Finally, calculate the phase C current using the diagnosed and corrected phase A and phase B currents. The fault diagnosis flowchart is shown in Figure 3.

An adaptive virtual current observer is meant to recreate the stator current using the observer principle. This method replaces the measured current with an estimated current, allowing operation without current sensors, making it a fault-tolerant control scheme in the event of current sensor failure. Operating without current sensors can eliminate the effects of sensor measurement noise and reduce current and torque ripples. The flow chart of current estimation is shown in Figure 4.

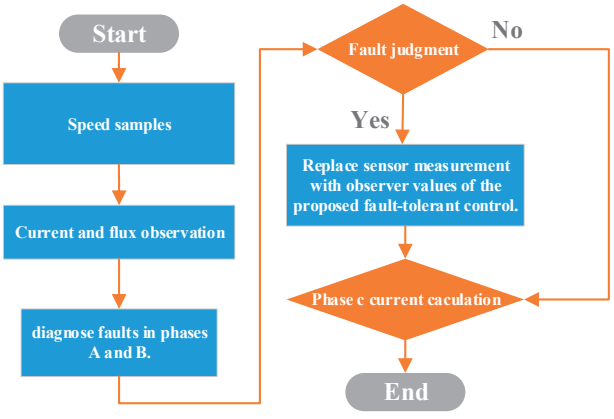

Figure 3. Flow chart of fault diagnosis.

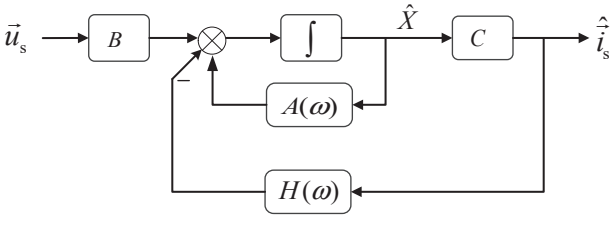

Figure 4. Current estimation structure diagram.

The Equations (1) and (2) can now be expressed, beginning thus:

$$\begin{cases} \dot{X} = AX + BU \\ Y = CX \end{cases} \tag{20}$$

In the above formula: $X = \begin{bmatrix} \vec{i}_s & \vec{\psi}_s \end{bmatrix}^T$, $A = \begin{bmatrix} j\omega - \frac{R_Y}{\sigma L_s} & \frac{1}{\sigma L_s}\left(\frac{1}{T_r} - j\omega\right) \\ -R_s & 0 \end{bmatrix}$, $B = \begin{bmatrix} \frac{1}{\sigma L_s} & 1 \end{bmatrix}^T$, and $U = \vec{u}_s$, $Y = \vec{i}_s$, $C = \begin{bmatrix} 1 & 0 \end{bmatrix}$.

The virtual current observer may be expressed using the Luenberger observer theory as follows:

$$\begin{cases} \dot{\hat{X}} = A\hat{X} + BU + HY - H\hat{Y} \\ \hat{Y} = C\hat{X} \end{cases} \tag{21}$$

In the above formula:

$$X = \begin{bmatrix} \hat{\vec{i}}_s & \hat{\vec{\psi}}_s \end{bmatrix}^T,\ \hat{Y} = \hat{\vec{i}}_s,\ H = \begin{bmatrix} H_1 + jH_2 & H_3 + jH_4 \end{bmatrix}^T$$

Modify Equation (21) because there is no input for the current sensor measurement signal, as follows:

$$\begin{cases} \dot{\hat{X}} = A\hat{X} + BU - H\hat{Y} \\ \hat{Y} = C\hat{X} \end{cases} \tag{22}$$

The error system can be calculated by subtracting system (22) from system (20):

$$\Delta\dot{X} = (A - HC)\Delta X + HY \tag{23}$$

In the above formula:

$$\Delta X = X - \hat{X}$$

Under the stable pole position of the observation system matrix $A - HC$, the estimated value can converge to the real stator current and flux, according to Lyapunov stability theory. As a result, the observer's characteristic equation is as follows [31]:

$$\det[s - (A - HC)] = s^2 + \left(\frac{R_\gamma}{\sigma L_s} + H_1 + jH_2 - j\omega\right)s + \left(\frac{1}{T_r} - j\omega\right)\frac{R_s + H_3 + jH_4}{\sigma L_s} \quad (24)$$

The dynamic equation of the observer is defined as follows:

$$\Delta(s) = s^2 + \left(\frac{R_\gamma}{\sigma L_s} - j\omega\right)hs + \left(\frac{1}{T_r} - j\omega\right)\frac{R_s h^2}{\sigma L_s} \quad (25)$$

In the above, h is a proportional constant. The following equation can be used to compute the gain matrix H. By comparing the identical s-order terms in Equations (24) and (25), we obtain:

$$\begin{cases} H_1 = h\frac{R_\gamma}{\sigma L_s} - \frac{R_\gamma}{\sigma L_s} \\ H_2 = \omega - h\omega \\ H_3 = h^2 R_s - R_s \\ H_4 = 0 \end{cases} \quad (26)$$

3. Dynamic Response Performance Test

An experimental platform for an induction motor fed by a dual-level inverter based on the dSPACE controller DS1104 is introduced here. When building the experimental platform for traditional induction motor control systems, most of them use a microcontroller or DSP as the main controller, which requires a lot of time and effort to convert the model originally built in MATLAB/Simulink simulation software to computer language programming. However, manual programming is not always reliable and relatively easy to implement for complex algorithms that are more difficult. dSPACE controllers are the perfect solution to this problem. The semiphysical experimental platform built on the dSPACE DS1104 controller can be seamlessly linked to MATLAB/Simulink simulation software. Through the real-time interface (RTI) module and real-time code generation (RTW) module, the system simulation model built in Simulink can be quickly converted into executable C code, compiled and linked, and then the executable file is downloaded to the internal supporting system. After compiling and linking, the executable file is downloaded to the internal DSP controller, and then the program is executed to achieve real-time verification of the control algorithm. The dSPACE DS1104 is the core single-board hardware used to build the dSPACE semiphysical real-time simulation test platform, with which a common PC can be used to build a powerful development system. Batteries are used to power the converter, both to obtain a stable and high-quality DC voltage and to protect the motor.

The experimental platform is shown in Figure 5, and the motor parameters are set out in Table 1.

Table 1. Induction Motor Ratings and Parameters.

Symbol	Quantity	Value
P_N	Rated shaft power	2.2 kW
U	Rated voltage	380 V
f	Rated frequency	50 Hz
ω	Rated speed	1422 r/min
n_p	Pole pairs	2
R_s	Stator resistance	3.4 W
R_r	Rotor resistance	2.444 W

Table 1. *Cont.*

Symbol	Quantity	Value
L_s	Stator inductance	0.2724 H
L_r	Rotor inductance	0.2715 H
L_m	Mutual inductance	0.2631 H
J	Machine inertia	0.005 kg m^2

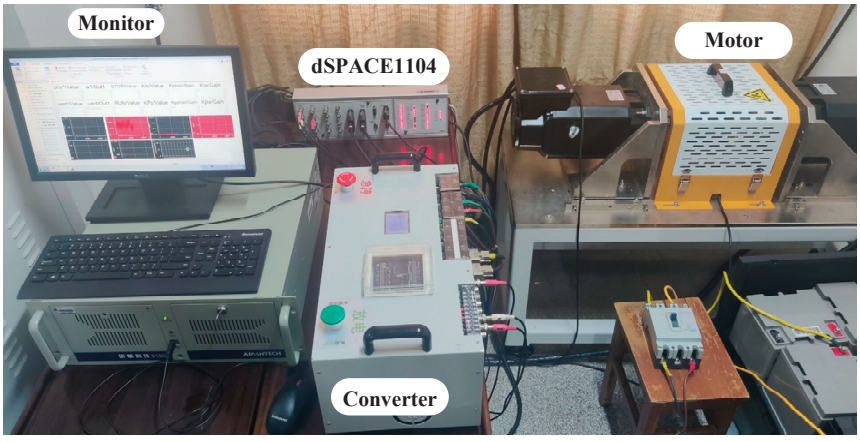

Figure 5. Experimental Platform.

3.1. Positive and Reverse Dynamic Response Performance Test

Firstly, under the rated excitation and load conditions, forward and reverse experiments are conducted, and the motor is started at a speed of 200 r/min. When it is in normal operation, a command is given to change the speed from 200 r/min to −200 r/min. The experimental results are shown in Figure 6. The dynamic operating characteristics of the dual-torque DTC are observed and compared with DTC. The experimental results showed that, compared with the DTC, the dual-torque DTC could track the set value quickly and accurately under rated load conditions. Nevertheless, when the speed is changed, the magnetic flux of DTC is influenced and displays visible variations, with the highest ripple of stator flux amplitude reaching 0.2 Wb, indicating that the torque of dual-torque DTC in magnetic flux decoupling control performance is better than DTC.

3.2. Transient Torque Step Response Characteristics

Quantitative analysis and comparison of the steady-state performance of the system are conducted using the root–mean–square error calculation formula. The calculation formula for torque ripple can be expressed as follows:

$$T_{e\_ripple} = \sqrt{\frac{1}{N}\sum_{n=1}^{N}\left(T_e(n) - \overline{T}_e\right)^2} \tag{27}$$

where T_{e_ripple} represents the torque ripple; $T_e(n)$ represents the torque value of the nth sampling point; $\overline{T}_e$ represents the average value of torque during the set time period; and N is the number of samples in the specified time.

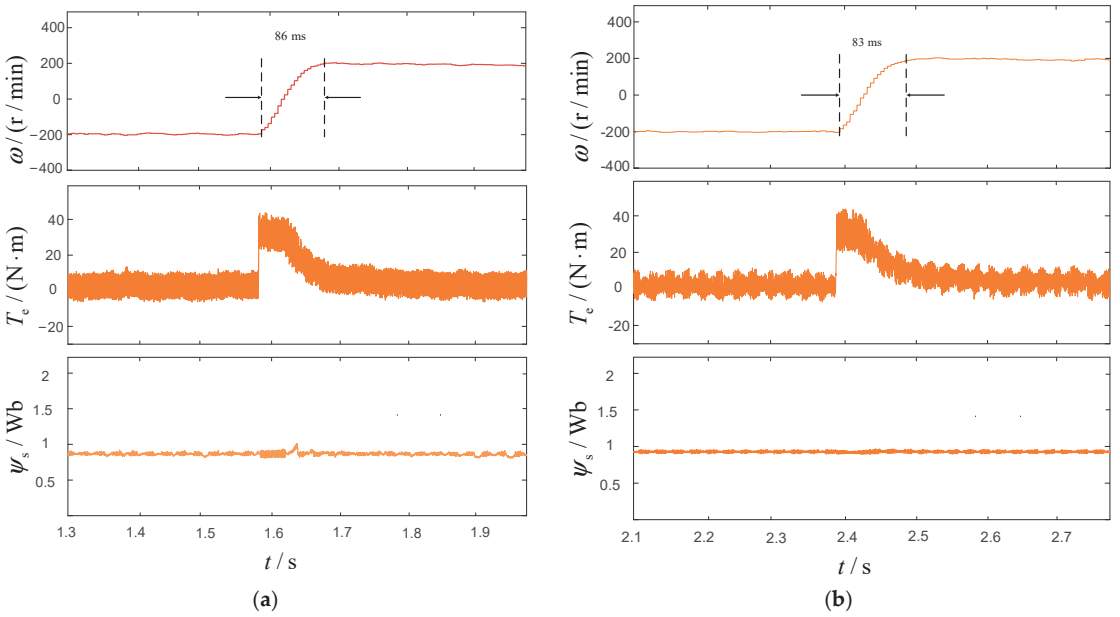

Figure 6. Speed acceleration from −200 r/min to 200 r/min under no-load state: (**a**) DTC; (**b**) The proposed method.

The transient torque step response characteristics of the two methods are compared and tested, as shown in Figure 7. The torque step reference value is 30 N·m. The time taken for the torque to increase from a 0% to 100% steady-state value is used as the response time of the torque. As shown in Figure 7, the torque increase rate of DTC is 1.87 (N·m)/100 μs, and the torque increase rate of the dual-torque DTC is 2.08 (N·m)/100 μs, indicating that the torque response speed of the dual-torque DTC method is higher. In addition, by using Equation (27) to calculate the transient torque ripple during speed changes, it is found that the ripple of the dual-torque DTC is slightly smaller. This is because the dual-torque DTC directly calculates torque and reactive torque, avoiding noise interference from current sensors and improving the torque response speed.

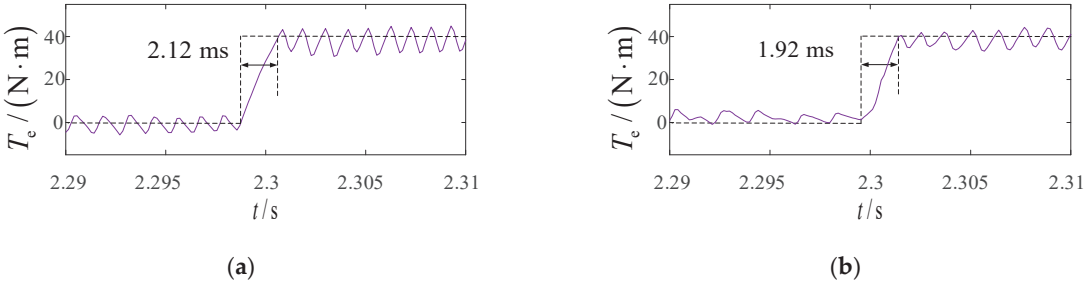

Figure 7. Torque acceleration from 0% to 100% steady-state value: (**a**) DTC; (**b**) The proposed method.

3.3. Operating Capacity at Low Speed with Load

In the preceding studies, the dynamic performance of the standard DTC technique and the dual-torque DTC method for induction motors are compared. In the following experiment, we sought to compare the steady-state performance of these two methods when the motor is operated at low speed with a load. The induction motor is operated at a

stable speed of 150 r/min with a load of 15 N·m. The waveforms of the stator current and torque for both methods are observed and compared.

Figure 8 shows the experimental torque waveforms of the two methods under low-speed conditions with a load. It can be seen from the figure that the torque ripple of the conventional DTC is slightly higher than that of the dual-torque DTC. A quantitative examination indicates that the torque ripple of the traditional DTC technique is 3.029 Nm, whereas the torque ripple of the dual-torque DTC approach is 2.748 Nm, representing a 9.3% decrease over the conventional DTC method. As a result, the dual-torque DTC efficiently suppresses torque ripples.

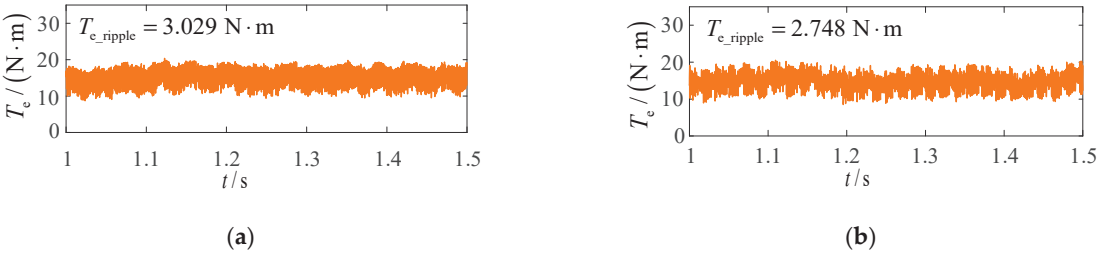

(**a**) (**b**)

Figure 8. Steady state torque waveform: (**a**) DTC; (**b**) The proposed method.

Figure 9 shows the stator current waveforms at a speed of 150 r/min with a load of 15 N·m. The fast Fourier transform algorithm is used to analyze the harmonic content of the current waveform. The total harmonic distortion (THD) of the stator current for the conventional DTC method is 24.52%; for the dual-torque DTC method it is 20.31%. Compared with the conventional DTC method, the THD of the stator current is reduced by 17.2% using the dual-torque DTC method.

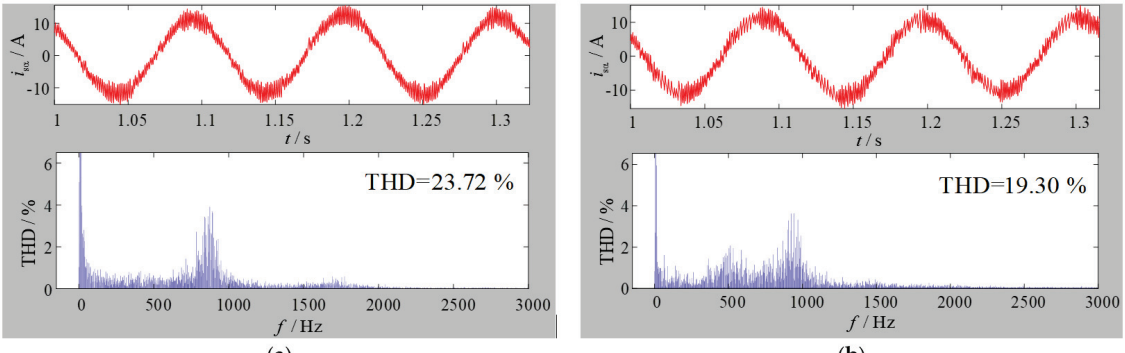

(**a**) (**b**)

Figure 9. Harmonic analysis of stator current: (**a**) DTC; (**b**) The proposed method.

In order to improve the persuasiveness of the experimental results, the torque ripple of the motor under no-load stable operation at different speeds is calculated using both methods, and the respective results are compared, as shown in Figure 10. From the torque ripple calculation results in the figure, it can be seen that the torque ripple of the dual-torque DTC method is lower than that of the conventional DTC method at different speeds. The results of the above series of steady-state experiments indicate that, compared with the conventional DTC method, the steady-state performance of the induction motor control system using the dual-torque DTC method is improved to a certain extent, and that the proposed method is feasible.

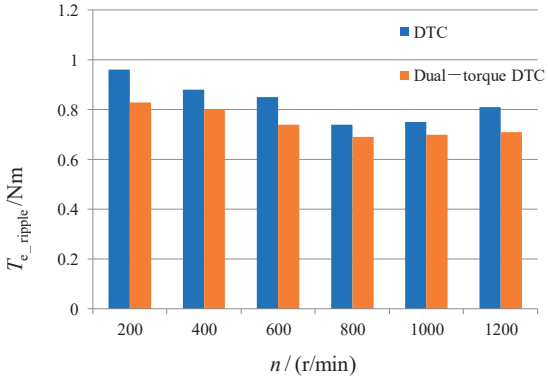

Figure 10. Torque ripple at different speeds.

3.4. Parameter Adaptation Experiment

Variation in motor parameters can affect the control performance of the system, and severe parameter mismatch may even cause the motor system to fail to operate properly. To test the robustness of the dual-torque DTC method, the rotor resistance is increased by 50% in rated excitation and no-load conditions, and the motor speed is varied from −300 r/min to 300 r/min. The experimental results are shown in Figure 11. It can be seen that the waveforms of speed, current, flux, and torque are all normal, without any obvious distortion. The experimental results show that the dual-torque DTC can still maintain normal and stable operation of the motor system when the rotor resistance of the motor changes; its dynamic response speed and steady-state control performance are comparable to those of the conventional DTC. That is, within a certain range of parameter errors, both methods can maintain the normal and stable operation of the motor system, and the robustness of the dual-torque DTC system is good.

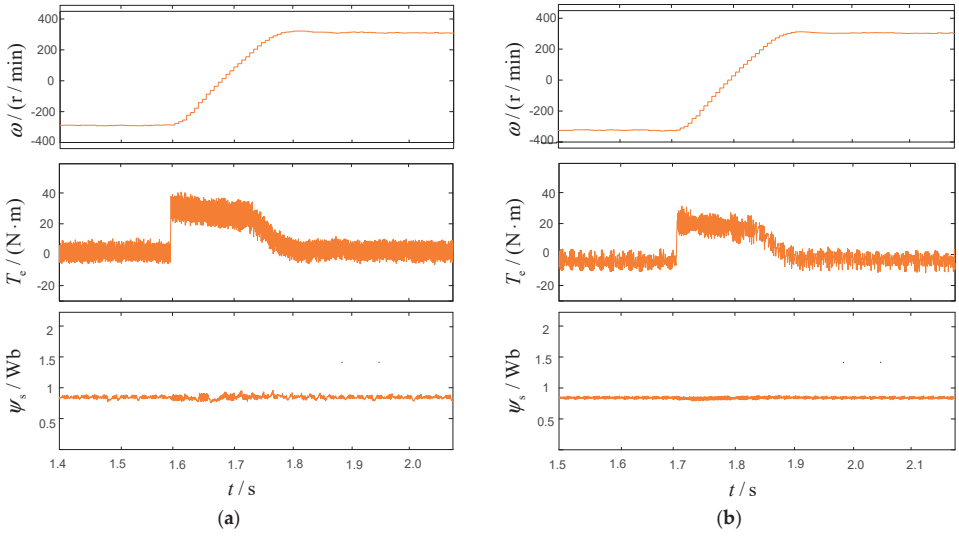

Figure 11. Rotor resistance increases by 50%: (**a**) DTC; (**b**) The proposed method.

Figure 12 shows the experimental results of stator resistance mismatch; it can be seen that the dual torque model has better torque stability than DTC after the stator resistance change, and that the proposed method is more robust.

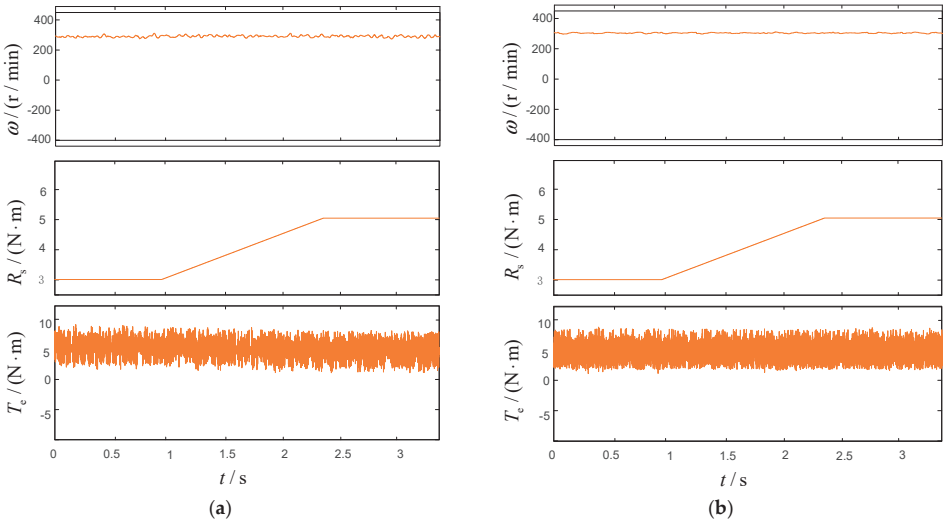

Figure 12. Experimental results of stator resistance mismatch: (**a**) DTC; (**b**) The proposed method.

3.5. Fault-Tolerant Control Experiment

The induction motor is operated at a stable speed of 200 r/min with a load of 20 N·m. To validate the effectiveness of the proposed current sensor fault-tolerant control for the dual-torque DTC model, the dSPACE system is utilized to simulate sensor faults by manipulating the output values of the sensors. In order to simulate faults, the measurement value of phase A current sensor input to the control system is changed to 0 at 0.7 s; the system is able to use the estimated value of the current observer to replace the measured value of the current sensor, ensuring the safe operation of the motor and maintaining the given speed. After that, the current measurement values of both the A-phase and B-phase current sensors are changed to 0 at 0.6 s, and the system still operates safely. The dynamic characteristics of the induction motor under fault are then observed, and the results are presented in Figure 13. As can be seen from the figure, the system could accurately detect the sensor fault and utilize the estimated value of the observer to replace the sensor measurement value, ensuring the smooth operation of the induction motor after the sensor fault. Hence, the proposed method is practical and effective.

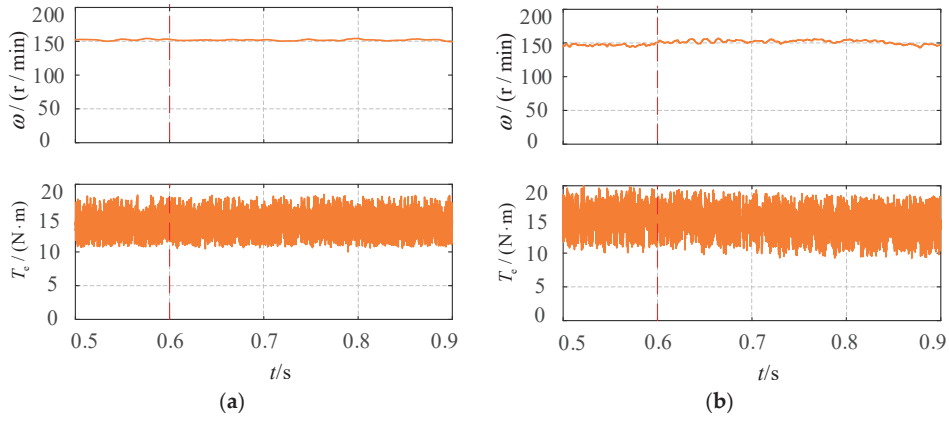

Figure 13. Fault-tolerant control experiment: (**a**) Phase A fault; (**b**) Phase A and B fault.

4. Conclusions

In this paper, a dual-torque DTC method is proposed to address the issues of fault tolerant control of current sensors. This method introduces torque and reactive torque as state variables and derives a dual-torque model of the induction motor using stator flux and stator current. The proposed method offers the following advantages:

The dual-torque signal is directly calculated through current and direct current voltage feedback signals, enabling direct dual-torque control of the induction motor and improving speed stability, thereby reducing current and torque ripples. Moreover, the proposed method combines the model with an adaptive virtual current observer to design a fault-tolerant control scheme that decreases measurement noise of current sensors and ensures safe rotation of the motor, thus enhancing system safety and reducing the torque ripple.

In conclusion, our experimental results demonstrate that the dual-torque DTC method achieves levels of dynamic and steady-state control performance similar to the conventional DTC method. The dual-torque DTC method achieves superior response speed, lower torque ripples, and total harmonic distortion of the stator current. The proposed method shows great potential for improving the control performance and reliability of induction motor drive systems.

Author Contributions: Conceptualization, Y.L.; methodology, Y.L.; software, Y.L.; validation, Y.L.; writing—original draft, Y.L.; writing—review and editing, P.G. All authors have read and agreed to the published version of the manuscript.

Funding: This research received no external funding.

Data Availability Statement: Data is unavailable due to privacy or ethical restrictions.

Conflicts of Interest: The authors declare no conflict of interest.

References

1. Ronanki, D.; Singh, S.A.; Williamson, S.S. Comprehensive Topological Overview of Rolling Stock Architectures and Recent Trends in Electric Railway Traction Systems. *IEEE Trans. Transp. Electrif.* **2017**, *3*, 724–738. [CrossRef]
2. Un-Noor, F.; Padmanaban, S.; Mihet-Popa, L.; Mollah, M.; Hossain, E. A Comprehensive Study of Key Electric Vehicle (EV) Components, Technologies, Challenges, Impacts, and Future Direction of Development. *Energies* **2017**, *10*, 1217. [CrossRef]
3. Wu, C.; Sehab, R.; Akrad, A.; Morel, C. Fault Diagnosis Methods and Fault Tolerant Control Strategies for the Electric Vehicle Powertrains. *Energies* **2022**, *15*, 4840. [CrossRef]
4. Gao, H.; Zhang, W.; Wang, Y.; Chen, Z. Fault-Tolerant Control Strategy for 12-Phase Permanent Magnet Synchronous Motor. *Energies* **2019**, *12*, 3462. [CrossRef]
5. Liu, C. Emerging Electric Machines and Drives—An Overview. *IEEE Trans. Energy Convers.* **2018**, *33*, 2270–2280. [CrossRef]
6. Lascu, C.; Jafarzadeh, S.; Fadali, M.S.; Blaabjerg, F. Direct Torque Control with Feedback Linearization for Induction Motor Drives. *IEEE Trans. Power Electron.* **2017**, *32*, 2072–2080. [CrossRef]
7. Sorchini, Z.; Krein, P.T. Formal Derivation of Direct Torque Control for Induction Machines. *IEEE Trans. Power Electron.* **2006**, *21*, 1428–1436. [CrossRef]
8. Forestieri, J.N.; Farasat, M.; Trzynadlowski, A.M. Indirect Real- and Reactive-Power Control of Induction Motor Drives. *IEEE J. Emerg. Sel. Top. Power Electron.* **2018**, *6*, 2109–2125. [CrossRef]
9. Burriel-Valencia, J.; Puche-Panadero, R.; Martinez-Roman, J.; Sapena-Bano, A.; Pineda-Sanchez, M.; Perez-Cruz, J.; Riera-Guasp, M. Automatic Fault Diagnostic System for Induction Motors under Transient Regime Optimized with Expert Systems. *Electronics* **2018**, *8*, 6. [CrossRef]
10. Gonzalez-Prieto, A.; Aciego, J.J.; Gonzalez-Prieto, I.; Duran, M.J. Automatic Fault-Tolerant Control of Multiphase Induction Machines: A Game Changer. *Electronics* **2020**, *9*, 938. [CrossRef]
11. Xiaodong, S.; Krishnamurthy, M. Survivable Operation of Induction Machine Drives with Smooth Transition Strategy for EV Applications. *IEEE J. Emerg. Sel. Top. Power Electron.* **2014**, *2*, 609–617. [CrossRef]
12. Adamczyk, M.; Orlowska-Kowalska, T. Postfault Direct Field-Oriented Control of Induction Motor Drive Using Adaptive Virtual Current Sensor. *IEEE Trans. Ind. Electron.* **2022**, *69*, 3418–3427. [CrossRef]
13. Azzoug, Y.; Sahraoui, M.; Pusca, R.; Ameid, T.; Romary, R.; Cardoso, A.J.M. High-performance vector control without AC phase current sensors for induction motor drives: Simulation and real-time implementation. *ISA Trans.* **2021**, *109*, 295–306. [CrossRef]
14. Rangari, S.C.; Suryawanshi, H.M.; Renge, M. New Fault-Tolerant Control Strategy of Five-Phase Induction Motor with Four-Phase and Three-Phase Modes of Operation. *Electronics* **2018**, *7*, 159. [CrossRef]
15. Chakraborty, C.; Verma, V. Speed and Current Sensor Fault Detection and Isolation Technique for Induction Motor Drive Using Axes Transformation. *IEEE Trans. Ind. Electron.* **2015**, *62*, 1943–1954. [CrossRef]

16. Kommuri, S.K.; Lee, S.B.; Veluvolu, K.C. Robust Sensors-Fault-Tolerance with Sliding Mode Estimation and Control for PMSM Drives. *IEEE/ASME Trans. Mechatron.* **2018**, *23*, 17–28. [CrossRef]
17. Freire, N.M.A.; Estima, J.O.; Cardoso, A.J.M. A New Approach for Current Sensor Fault Diagnosis in PMSG Drives for Wind Energy Conversion Systems. *IEEE Trans. Ind. Appl.* **2014**, *50*, 1206–1214. [CrossRef]
18. Verma, V.; Chakraborty, C.; Maiti, S.; Hori, Y. Speed Sensorless Vector Controlled Induction Motor Drive Using Single Current Sensor. *IEEE Trans. Energy Convers.* **2013**, *28*, 938–950. [CrossRef]
19. Liu, Y.; Stettenbenz, M.; Bazzi, A.M. Smooth Fault-Tolerant Control of Induction Motor Drives with Sensor Failures. *IEEE Trans. Power Electron.* **2019**, *34*, 3544–3552. [CrossRef]
20. Manohar, M.; Das, S. Current Sensor Fault-Tolerant Control for Direct Torque Control of Induction Motor Drive Using Flux-Linkage Observer. *IEEE Trans. Ind. Inform.* **2017**, *13*, 2824–2833. [CrossRef]
21. Zhang, X.; Foo, G.; Don Vilathgamuwa, M.; Tseng, K.J.; Bhangu, B.S.; Gajanayake, C. Sensor fault detection, isolation and system reconfiguration based on extended Kalman filter for induction motor drives. *IET Electr. Power Appl.* **2013**, *7*, 607–617. [CrossRef]
22. Yu, Y.; Zhao, Y.; Wang, B.; Huang, X.; Xu, D. Current Sensor Fault Diagnosis and Tolerant Control for VSI-Based Induction Motor Drives. *IEEE Trans. Power Electron.* **2018**, *33*, 4238–4248. [CrossRef]
23. Yu, Y.; Wang, Z.; Xu, D.; Zhou, T.; Xu, R. Speed and Current Sensor Fault Detection and Isolation Based on Adaptive Observers for IM Drives. *J. Power Electron.* **2014**, *14*, 967–979. [CrossRef]
24. Zhang, X.; Yan, K.; Cheng, M. Two-Stage Series Model Predictive Torque Control for PMSM Drives. *IEEE Trans. Power Electron.* **2021**, *36*, 12910–12918. [CrossRef]
25. Ravi Teja, A.V.; Verma, V.; Chakraborty, C. A New Formulation of Reactive-Power-Based Model Reference Adaptive System for Sensorless Induction Motor Drive. *IEEE Trans. Ind. Electron.* **2015**, *62*, 6797–6808. [CrossRef]
26. Sun, W.; Yu, Y.; Wang, G.; Li, B.; Xu, D. Design Method of Adaptive Full Order Observer with or Without Estimated Flux Error in Speed Estimation Algorithm. *IEEE Trans. Power Electron.* **2016**, *31*, 2609–2626. [CrossRef]
27. Cho, Y.; Bak, Y.; Lee, K.-B. Torque-Ripple Reduction and Fast Torque Response Strategy for Predictive Torque Control of Induction Motors. *IEEE Trans. Power Electron.* **2018**, *33*, 2458–2470. [CrossRef]
28. Krzemiński, Z. Nonlinear Control of Induction Motor. *IFAC Proc. Vol.* **1987**, *20*, 357–362. [CrossRef]
29. Zhong, Q.-C. The Ghost Operator and Its Applications to Reveal the Physical Meaning of Reactive Power for Electrical and Mechanical Systems and Others. *IEEE Access* **2017**, *5*, 13038–13045. [CrossRef]
30. Foo, G.H.B.; Zhang, X.; Vilathgamuwa, D.M. A Sensor Fault Detection and Isolation Method in Interior Permanent-Magnet Synchronous Motor Drives Based on an Extended Kalman Filter. *IEEE Trans. Ind. Electron.* **2013**, *60*, 3485–3495. [CrossRef]
31. Li, H.; Lu, Z.; Li, Z. Transient analysis of load switches of self-excited induction generators based on Lyapunov stability theory. *IEEJ Trans. Electr. Electron. Eng.* **2017**, *12*, 337–346. [CrossRef]

machines

MDPI

Article

Stall Torque Performance Analysis of a YASA Axial Flux Permanent Magnet Synchronous Machine

Jordi Van Damme [1,2,*], Hendrik Vansompel [1,2] and Guillaume Crevecoeur [1,2]

[1] Department of Electromechanical, Systems and Metal Engineering, Ghent University, 9000 Ghent, Belgium; hendrik.vansompel@ugent.be (H.V.); guillaume.crevecoeur@ugent.be (G.C.)
[2] Flanders Make@UGent-MIRO, 9052 Ghent, Belgium
* Correspondence: jordi.vandamme@ugent.be

Abstract: There is a trend to go towards low gear-ratio or even direct-drive actuators in novel robotic applications in which high-torque density electric motors are required. The Yokeless and Segmented Armature Axial Flux Permanent Magnet Synchronous Machine is therefore considered in this work. In these applications, the motors should be capable to deliver high torque at standstill for long periods of time. This can cause overheating of the motors due to a concentration of the losses in a single phase; hence, it becomes necessary to derate the motor torque. In this work the influence of the slot/pole combination, the addition of a thermal end-winding interconnection and the equivalent thermal conductivity of the winding body on the torque performance at standstill will be studied both experimentally via temperature measurements on a prototype stator, and via a calibrated 3D thermal Finite Element model. It was found that both a good choice of the slot/pole combination and the addition of a thermal end-winding interconnection have a significant influence on the torque performance at standstill, and allow up to 8% increase in torque at standstill in comparison to a reference design.

Keywords: axial flux; end winding; slot/pole combination; stall torque

Citation: Van Damme, J.; Vansompel, H.; Crevecoeur, G. Stall Torque Performance Analysis of a YASA Axial Flux Permanent Magnet Synchronous Machine. *Machines* **2023**, *11*, 487. https://doi.org/10.3390/machines11040487

Academic Editors: Loránd Szabó and Feng Chai

Received: 3 April 2023
Revised: 16 April 2023
Accepted: 17 April 2023
Published: 18 April 2023

1. Introduction

Owing to its high torque density and energy efficiency, Yokeless and Segmented Armature (YASA) Axial Flux Permanent Magnet Synchronous Machines (AFPMSM) have proven their benefits in several application areas such as transportation and wind energy generation [1,2]. This axial flux motor topology consists of two rotors and a central stator, as illustrated in Figure 1. Motivated by the merits in these applications, more recently, this machine topology was also considered for use in quasi-direct-drive and direct-drive actuators of novel robotic applications [3,4].

In some robotic applications however, the electric motor has to generate its maximum torque at (quasi-)standstill during a significant fraction of the load cycle. This is, e.g., the case in force-controlled robotic grippers [5] (See also Figure 1), or when a robot has to hold a vertical load against gravity for a long time [6]. This leads to a concentration of the losses in a single phase of the motor. For the worst-case commutation position: twice the rated conduction losses are dissipated in a single phase when the motor produces its rated torque at standstill. Although the sum of the conduction losses of all phases in this case does not exceed the rated conduction losses, due to the uneven loss distribution, this can eventually lead to overheating of the motor at standstill. This problem is well-known in academic and industrial literature [6,7]. To avoid overheating, the stall torque, i.e. the maximum torque that a motor can produce under certain cooling conditions in steady-state at standstill, is typically lower than the rated torque.

Alternatively, brakes can be used to generate a stall torque and hold a load. There exist various kind of brakes [8], and most of them use an electromagnetic actuator such as

a solenoid to engage or disengage friction discs. These friction discs provide the required holding torque without consuming energy. Hence, they can generate a higher stall torque. However, in certain applications, e.g., force-controlled robotic grippers where soft objects need to be grasped, the force of the gripper needs to be precisely controlled in order to avoid damage to the soft object [5]. Traditional grippers that use brakes cannot be used in this case since they rely on applying a sufficiently large torque to hold the object and then engage their holding brake. This would harm the soft object. To conclude, brakes can generate much higher stall torques; however, they are not usable in every application.

So far, no solutions have been presented yet to overcome the problem of overheating at standstill. Researchers have predominantly focussed on strategies that improve the overall thermal performance of YASA AFPMSMs through either an improved cooling (i.e., liquid instead of air cooling [9,10]), through impregnating the windings [2] or through the introduction of radially inward heat extraction fins [1]. Although these strategies are very effective in increasing the total dissipated power losses, they are less effective in mitigating local overheating due to the uneven loss distribution caused by high torque at (quasi-)standstill. The problem of uneven temperature distribution due to partial immersion of the stator in an oil-cooled outer rotor radial flux machine was discussed in [11]. Oil storage slots were presented as an effective solution to reduce the local overheating. Although the presented solution appears to be very effective at rated speed, at (quasi-)standstill, the oil flows under the action of gravity to the bottom half of the motor, which drastically reduces its cooling effectiveness.

In this work, the problem of overheating during standstill due to the uneven loss distribution will be analysed. Based on physical insights from previous studies on the thermal behaviour of YASA AFPMSMs [1,2,9], three key design parameters have been identified that potentially have a significant impact on the redistribution of the heat from the phase with the highest losses to the phases with lower losses. The influence of these three key design parameters on the stall torque performance is studied in this work (See Figure 1):

1. *Slot/pole combination:* This aspect influences both the fundamental winding factor and back-emf constant, which directly impact the torque. It also influences the number of adjacent slots belonging to the same phase. As heat has to flow from the phase with the highest losses to phases with lower losses, it can be expected that the number of adjacent slots influences the thermal performance under uneven loss distribution.
2. *Thermal end-winding interconnection:* From previous studies, it is known that the end-winding at the inner diameter is often the hottest area of a YASA AFPMSM [2,10]; therefore, a good thermally conducting ring which interconnects all end-windings can redistribute the heat from the phase with the highest losses to the other phases.
3. *Equivalent winding body thermal conductivity:* Since in a YASA AFPMSM there is no iron stator yoke which has a good thermal connection with all slots, the equivalent thermal conductivity of the winding body can have a significant influence on the heat transfer between phases.

Note that also the axial flux machine topology can have an influence on the results, especially in the double stator, single rotor or single stator, single rotor topologies where the stator has an iron yoke providing a good thermal connection between the coils. However, this analysis falls beyond the scope of this work. The focus in this work is on the single stator, double rotor topology, which is known to have a higher torque density and energy efficiency [1,2].

The analysis results in this work will lead to a better understanding of the stall torque performance and can be used in the design of motors for applications where high torque at (quasi)-standstill is important. Other applications might also benefit from the results. For example, in [12,13], the problem of local overheating due to unbalanced supply voltage or inter-turn short circuits in induction motors was analysed. The studied key design parameters in this work can also improve the performance in these applications by redistributing the heat from the location with a higher loss concentration. However, this is beyond the scope of this article.

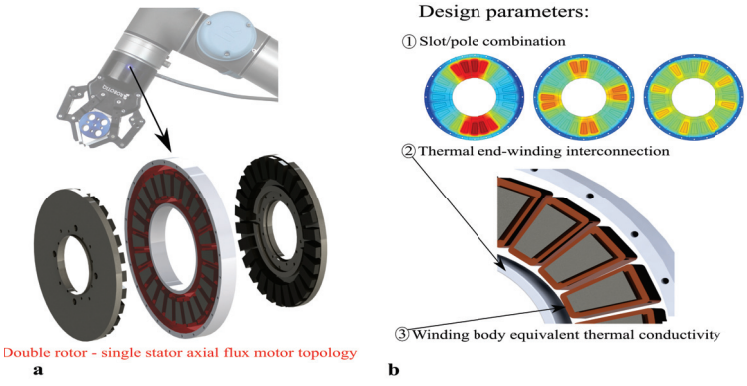

Figure 1. (**a**) The motor in a force controlled gripper has to generate high torque at (quasi)-standstill [14]. (**b**) Overview of the studied parameters in this work that potentially have a significant impact on the stall torque performance.

To study the influence of the aforementioned design parameters on the stall torque performance, a prototype YASA AFPMSM shown in Figure 2 is considered. Its main specifications are given in Table 1. The influence of the key design parameters will first be studied experimentally, the corresponding measurements will also be used to identify a 3D thermal Finite Element (FE) model. This model will allow to further analyse and improve the understanding of the experimental findings.

This paper is organised as follows: first, the three studied parameters are described in detail and illustrated for the prototype YASA AFPMSM in Section 2. Subsequently, the experimental setup is described in Section 3.1. The 3D thermal FE model is outlined in Section 3.2. Finally, the results of the experimental and simulation parameter study are presented in Section 4.

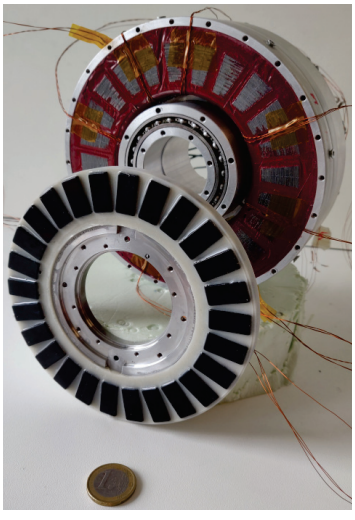

Figure 2. Prototype Yokeless and Segmented Armature Axial Flux Permanent Magnet Synchronous Machine used throughout this work; it has two rotors and a single stator. For visualization purposes only a single rotor is shown here. Its specifications are given in Table 1.

Table 1. Specifications of the test case YASA AFPMSM.

Parameter	Symbol	Value	Unit
Three-phase inverter DC bus voltage	V_{DC}	48	V
Maximum speed	Ω_{max}	300	rpm
Number of pole pairs	N_p	13	/
Number of slots	Q_s	24	/
Number of phases	n_{ph}	3	/
Number of turns per tooth coil	n_{turns}	35	/
Outer diameter stator iron core	D_o	138.5	mm
Inner diameter stator iron core	D_i	98.5	mm
Axial length stator iron core	h_{stat}	15	mm
Axial slot length	h_{slot}	10	mm
Total axial length (incl. housing)	l_{tot}	62.5	mm
Slot width	b_{slot}	6	mm
Airgap thickness	h_{air}	1.5	mm
Magnet height	h_{mag}	5	mm
Rotor yoke height	h_{mag}	6	mm

2. Design Parameters Affecting Tangential Heat Transfer

2.1. Loss Distribution

From previous work on thermal analysis of YASA AFPMSMs, it is known that there is no heat transfer between adjacent tooth coils under a uniform loss distribution and cooling [2]. However, when the motor produces torque at (quasi-)standstill, the phase currents are (quasi-)DC currents whose magnitude depends on the rotor position. Since the actual standstill rotor position is very application-specific and can vary with the operating scenario, the design should account for the worst-case standstill rotor position. This is the position where $I_u = 2 \cdot I_v = 2 \cdot I_w = \sqrt{2} \cdot I_{nom,RMS}$ [6]. With I_u, I_v, I_w the (quasi-)DC phase currents and $I_{nom,RMS}$ the rated motor RMS current. Recall that for this worst-case position, the conduction losses in phase U equal twice the rated conduction losses and that the total conduction losses in the windings equal the rated conduction losses. A heat transfer between phases can be expected in this case, i.e., a heat transfer in the tangential direction. This worst-case scenario will be considered throughout this work. Note that phase *U* was chosen arbitrarily as the phase with the highest losses in this work.

2.2. Slot/Pole Combination

The slot/pole combination influences the stall torque performance in different ways. The (stall) torque is given by [15]:

$$T = 3 \cdot \xi \cdot k'_\phi \cdot I, \tag{1}$$

with ξ, the fundamental winding factor, k'_ϕ, the back-emf constant and I the RMS phase current. A first way is via the fundamental winding factor. It is given by the product of the pitch factor ξ_p and distribution factor ξ_d. For a 3-phase, fractional slot concentrated two layer winding, the fundamental winding factor is given by:

$$\xi = \xi_p \cdot \xi_d = \sin\left(\frac{N_p \pi}{Q_s}\right) \cdot \frac{\sin\left(\frac{\pi}{6}\right)}{z \cdot \sin\left(\frac{\pi}{6 \cdot z}\right)} \tag{2}$$

where z is the numerator of q reduced to the lowest terms:

$$q = \frac{Q_s}{6 \cdot N_p} = \frac{z}{n}. \tag{3}$$

Table 2 gives the number of poles that result in a fundamental winding factor higher than 0.866 for a stator with 24 slots.

Table 2. Number of poles with $\xi > 0.866$ for a stator with 24 slots.

Q_s		Number of Poles (p)							
		16	**18**	**20**	**22**	**26**	**28**	**30**	**32**
24	ξ	0.866		0.933	0.9495	0.9495	0.933		0.866
	k'_ϕ	0.324		0.353	0.358	0.354	0.346		0.329
	$k_\phi = k'_\phi \cdot \xi$	0.281		0.329	0.340	0.336	0.323		0.285

The second way is via the back-emf constant k'_ϕ:

$$k'_\phi = \frac{E_p}{\xi \cdot \Omega}, \tag{4}$$

with E_p the no-load back-emf (RMS value) of a phase at the mechanical speed Ω. The back-emf constant for different slot/combinations is determined using the analytical model for the flux density distribution in the iron core from [16,17], the results can be found in Table 2. The prototype YASA AFPMSM has 24 slots, 26 poles and a fundamental winding factor equal to 0.9495. Although 22 and 26 poles result in the highest fundamental winding factor, other pole pair numbers will also be considered since these have a different winding diagram. The winding diagram indicates which coils belong to each phase. A different slot/pole combination results in a different winding diagram and thus a different number of adjacent coils belonging to the same phase. It can be expected that the distance between the centre of a phase with high losses and a phase with lower losses, respectively, will influence the tangential heat transfer. This is the third way via which the slot/pole combination influences the heat transfer in the tangential direction. Figure 3 gives the winding diagrams and the number of adjacent coils belonging to the same phase n for the feasible slot/pole combinations from Table 2.

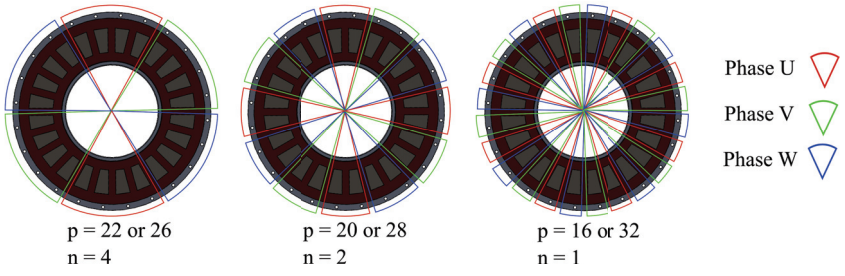

Figure 3. Winding diagrams and the number of adjacent coils belonging to the same phase n for the feasible slot/pole combinations from Table 2.

2.3. Thermal End-Winding Interconnection

In Figure 4 the thermal end-winding interconnection ring (1) is shown. The concept is illustrated here for an epoxy potted YASA AFPMSM stator which is cooled via its housing at the outer diameter (3). The end-winding interconnection ring is therefore located at the inner diameter of the stator. In order to act as a highway for redistributing the heat between phases, it consists of a good thermally conducting material, e.g., aluminium or aluminium-oxide.

In [18], a copper foam end-winding interconnection ring filled with phase change material was proposed for an outer-rotor radial flux machine to improve its peak load capabilities. Different from the proposed end-winding ring in this work, the ring in [18] interconnects the end-windings of the outer-rotor radial flux machine at the coldest axial face of the motor, i.e., the face where most heat leaves the motor. Therefore, the ring only acts as a thermal buffer during peak loads, but it is less effective in redistributing the heat between phases since it is located at the colder axial side of the motor. Although the concept

of a thermal end-winding interconnection ring for redistributing the heat is illustrated in this work for a YASA AFPMSM, it is also applicable for radial flux machines.

Figure 4. Yokeless and Segmented Armature Axial Flux Permanent Magnet Synchronous Machine: (1) Thermal end-winding interconnection ring (2) Concentrated winding tooth coil (3) Aluminium housing (4) Epoxy impregnation (5) Permanent magnet rotor.

At standstill no eddy-currents are induced in the end-winding ring; however, if the application both requires standstill and high speed operation, eddy current losses can occur in the end-winding ring if the electrical frequency is sufficiently high. The eddy current losses can be limited by choosing aluminium-oxide, or copper or aluminium foam instead of a solid aluminium ring. Therefore, this aspect will not be studied in further detail in this work.

2.4. Equivalent Winding Body Thermal Conductivity

A winding body consists of different materials with different thermal properties, this is often represented by equivalent thermal conductivities that depend on the thermal conductivities and volume fractions of the constituting materials [19]. Additionally, a winding body has anisotropic thermal properties due to its stranded or layered nature. Therefore, two different equivalent thermal conductivities are defined: one for the direction along the conductor and one for the direction perpendicular to the conductor. Typically, the latter is the lowest one. In previous works, it was shown that the equivalent thermal conductivity perpendicular to the conductor can be much larger for a winding body consisting of anodised aluminium [4,19]. Since the thermal conductivity of a winding body can have large influence on the thermal properties of the stator [2], it is expected that this can also have an influence on the tangential heat transfer. Therefore, the effect of the equivalent thermal conductivity of a winding body on the heat transfer in the tangential direction, and thus the stall torque performance, will be studied in this work. To this end, a YASA AFPMSM stator consisting of conventional concentrated winding tooth coils with round enamelled copper wire will be compared to a geometrically identical stator with anodised aluminium foil, which has superior equivalent thermal conductivities in both directions [4].

3. Materials and Methods

3.1. Experimental Setup

To study the influence of the slot/pole combination, the thermal end-winding interconnection and the winding body equivalent thermal conductivity on the heat transfer in the tangential direction and eventually on the stall torque performance, the experimental setup shown in Figure 5 is used. It consists only of the stator of the prototype YASA AFPMSM motor from Figure 2. The rotor is not considered in this work since at standstill the rotor losses and convective heat transfer between stator and rotor is negligible [20]. Moreover, this allows to study different slot/pole combinations with a single stator. This avoids the need to manufacture multiple rotors and/or stators and eliminates the vari-

ability in the measurements caused by variability in the rotor/stator properties due to manufacturing imperfections.

Since it was assumed that the convective heat transfer between rotor and stator is negligible, both the top and bottom airgap surface of the stator are insulated with thermal insulation wool and XPS insulation (see (4) and (5) on Figure 5). All heat leaves the stator at the outer diameter via forced convection over the housing surface. The airflow is generated by two cooling fans (see (3) on Figure 5) located above the stator.

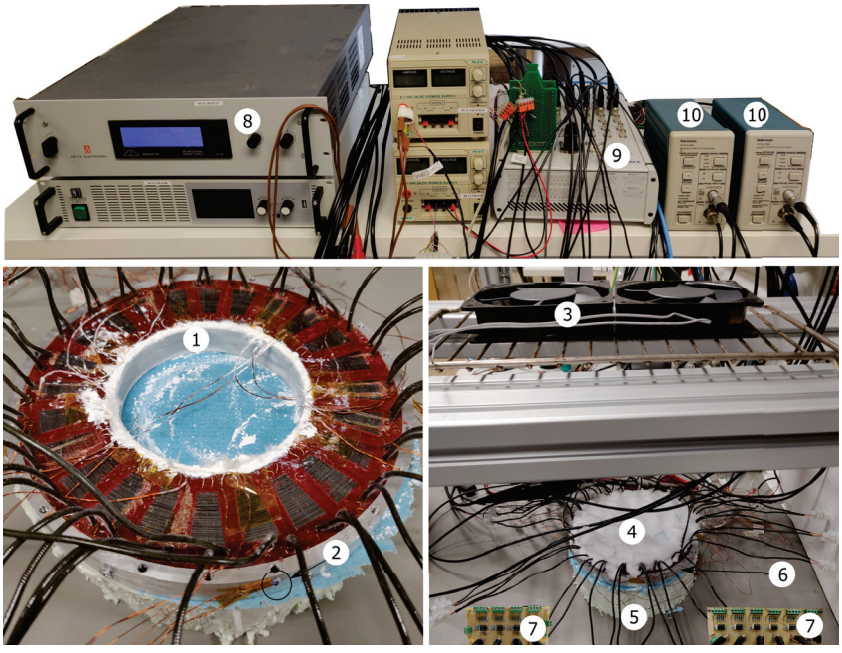

Figure 5. Experimental test setup. (left) Detailed view of prototype stator (1) thermal end-winding interconnection (2) PT100 temperature sensor on aluminium housing (right) Overview of setup: (3) cooling fans (4) thermal insulation wool (5) Expanded Polystyrene Insulation (XPS) (6) prototype stator between insulation (7) PT100 temperature sensor signal conditioning board (8) DC power supply (9) dSPACE MicroLabBox® real time control and data processing unit (10) Tektronix® TCPA 300 current amplifier.

As already mentioned in Section 2.1, only the worst-case uneven loss distribution has to be considered. This is the position where $I_u = 2 \cdot I_v = 2 \cdot I_w = \sqrt{2} \cdot I_{nom,RMS}$ [6]. To emulate this worst-case situation, phase U is connected in series with a parallel connection of phases V and W, as shown in Figure 6. All coils belonging to the same phase are connected in series. A programmable DC power supply is used to inject a constant current in phase U. This way, the same loss distribution is obtained, as if the motor would produce a certain torque at standstill.

To study the influence of the equivalent winding body thermal conductivity, two geometrically identical stators were constructed: one with enamelled round copper wire as conductor and one with anodised aluminium foil as conductor. Figure 7 shows a single tooth coil for both conductor types and Table 3 provides the detailed specifications for each tooth coil. Note that both tooth coils have the same number of turns and approximately the same resistance. This means both coils produce approximately the same losses for a given current (and thus torque). The main reason for this is the larger cross-section of the aluminium foil conductor, which is possible due to a more space-efficient stacking of the foil and a thinner electrical insulation layer. For mechanical stability reasons both stators

were impregnated in an epoxy resin; therefore, they exhibit the same appearance after impregnation and only one stator is shown in Figure 5.

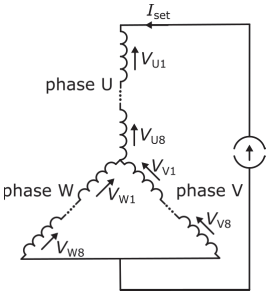

Figure 6. Phase connection to emulate worst-case loss distribution.

Figure 7. Prototype tooth coils. Left: enamelled copper wire tooth coil, Right: anodised aluminium foil tooth coil.

Since both terminals of each coil are accessible, all slot/pole combinations of Figure 3 can be realised experimentally. It also enables the measurement of the voltage over every single tooth coil and thus the determination of the dissipated power in each tooth coil. This enables the consideration of the difference in resistance between tooth coils due to a different average coil temperature.

To study the influence of a thermal end-winding interconnection, a removable aluminium ring with a thickness of 3.5 mm is used at the inner diameter of the stator (see (1) on Figure 5). Thermal paste is used to ensure a good thermal contact between the ring and the end-winding region. Since the stator with round enamelled copper wire and the stator with anodised aluminium foil are geometrically identical, the ring fits in both stators.

Every single tooth coil of both stator variants is instrumented with a PT100 temperature sensor at the inner diameter of each iron core segment (see Figure 8). This is the hotspot location in a stator in case of uniform losses [2]. Additionally, PT100 temperature sensors have been placed at certain locations at the outer diameter of the aluminium housing as well (e.g., see (2) in Figure 5). Due to spatial periodicity in the worst-case loss distribution, it is not necessary to measure the temperature of every tooth coil. For the slot/pole combinations that result in 4 and 2 adjacent tooth coils ($n = 4$ or 2), it is sufficient to consider only one quarter of the stator. For $n = 1$, 1/8th of a stator is even sufficient. To account for variations in the thermal properties between coils due to manufacturing imperfections, the hotspot temperature (i.e., the temperature in the centre of phase *U*) in two different spatial periods of the stator is measured. At the same angular location as the hotspot, also the temperature at the outer diameter of the housing is measured.

Table 3. Specifications of the prototype tooth coil.

Enamelled Copper Wire (Grade I, IEC 60317-13)	**Symbol**	**Value**	**Unit**
Number of turns	n_{turns}	35	/
Nominal outer diameter	$d_{\text{Cu,o}}$	0.8425	mm
Conductor diameter	$d_{\text{Cu,i}}$	0.8	mm
Winding length (incl. terminals)	l_{Cu}	276	cm
measured DC resistance (@ 25 °C)	$R_{\text{DC,Cu}}$	94.54 ± 0.37 [1]	mΩ
Height laminated iron core	h_{core}	20	mm
Weight of tooth coil	$m_{\text{Cu+SiFe}}$	31.3	g
Resistivity copper	ρ_{Cu}	1.72×10^{-8}	Ωm
Resistance temperature coeff.	α_{Cu}	3.93×10^{-3}	K^{-1}
Fill factor	$f_{\text{Cu,coil}}$	49	%
Dielectrical strength (IEC 60317-0-1)	E_{max}	87	$V_{\text{RMS}}/\mu\text{m}$
Price/kg		16.64	EUR/kg
Anodised aluminium foil			
Number of turns	n_{turns}	35	/
foil width	h_{Al}	10	mm
total foil thickness	$t_{\text{Al,tot}}$	86	m
thickness Al_2O_3 layer	t_{AlOx}	4.6	m
Foil length (excl. terminals)	l_{Cu}	250	cm
Cu terminal length (dia. 0.9 mm)	l_{term}	40	cm
measured DC resistance (@ 25 °C)	$R_{\text{DC,Al}}$	95.83 ± 0.6 [1]	mΩ
Height laminated iron core	h_{core}	20	mm
Weight of tooth coil	$m_{\text{Al+SiFe}}$	25.8	g
Resistivity aluminium	ρ_{Al}	2.74×10^{-8}	Ωm
Resistance temperature coeff.	α_{Al}	4.03×10^{-3}	K^{-1}
Fill factor	$f_{\text{Al,coil}}$	75	%
Dielectrical strength (ISO 2376)	E_{max}	26.5	$V_{\text{RMS}}/\mu\text{m}$
Price/kg		685 [2]	EUR/kg

[1] mean and standard deviation over 24 tooth coils. [2] Note that this is the cost for a small order quantity of 2 kg; for larger order quantities, the cost will be lower.

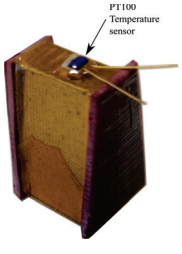

Figure 8. Indication of the PT100 temperature sensor location.

Besides temperature measurements, also the voltage over every single tooth coil in the half stator of Figure 5 is measured. The currents in phase *U* and *V* are measured using a Tektronix® TCPA 300 current amplifier. A dSPACE MicroLabBox® platform was used for data-acquisition. All signals were sampled at 1 kHz.

3.2. 3D Thermal FE Model

To support the analysis of the experimental data, a 3D thermal FE model is developed in this section. To support the experimental data analysis, the model will first be calibrated using experimental data to find the model parameters that result in a good agreement between model predictions and measurements.

3.2.1. Geometry

As already mentioned in Section 3.1, it is sufficient to consider only one quarter of a full stator due to the periodicity in the worst-case loss distribution. The full geometry of the FE model thus consists of 6 adjacent tooth coils. Figure 9 depicts a single tooth coil of the modelled geometry of the 3D thermal FE model. It consists of a winding body of either round enamelled copper wire or anodised aluminium foil (5) wound on a laminated iron core (2). A mica sheet (3) with a thickness of 0.2 mm is used as inter coil insulation and a solid aluminium-oxide pad (6) is used as electrical insulation between coil and housing (phase-to-ground insulation). Optionally, a thermal end-winding interconnection ring (1) can be included in the model as well. The coil assembly was potted in a low viscosity epoxy resin.

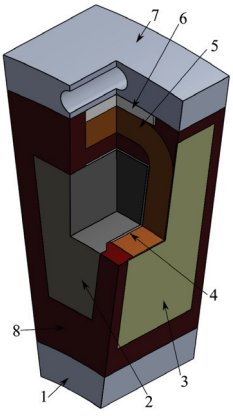

Figure 9. Concentrated winding tooth coil: (1) Aluminium thermal end-winding interconnection ring; (2) Laminated iron core; (3) Mica inter coil insulation sheet; (4) Mica slot liner; (5) Winding body; (6) Aluminium-oxide thermal pad; (7) Aluminium housing; (8) Epoxy potting.

3.2.2. Thermal Interfaces

The gap between the end-winding and the thermal end-winding ring is filled with epoxy. This gap is modelled in full detail and can be varied from 0 to 3.7 mm.

Since the phase-to-ground insulation consists of a rigid, non-deformable material (aluminium-oxide), the low viscosity potting resin also flows in the small gaps between the winding body and the housing. Since it is not feasible to model these gaps in full detail, a fill factor f_{pad} is introduced:

$$f_{\text{pad}} = \frac{t_{\text{AlOx-pad}}}{t_{\text{AlOx-pad}} + t_{\text{gap,equi}}}, \tag{5}$$

with $t_{\text{AlOx-pad}}$ as the thickness of the aluminium-oxide pad between winding and housing and $t_{\text{gap,equi}}$ the equivalent thickness of the gaps filled with epoxy. The phase-to-ground insulation will be modelled as an amalgam of aluminium-oxide and epoxy resin. The fill factor will be used for the calculation of the equivalent thermal conductivity in Section 3.2.3.

3.2.3. Anisotropic Material Modelling

The winding body, the laminated iron core and the phase-to-ground insulation exhibit anisotropic thermal properties since these bodies consist of strands or laminations of different materials with different thermal properties. As already explained in Section 2.4, this will be modelled via two equivalent thermal conductivities. One for the direction along the strand or lamination k_1 and one for the direction perpendicular to the strand or out of the lamination plane k_2.

For the epoxy impregnated, enamelled copper wire winding body, the equivalent thermal conductivities are calculated through the use of the Hashin and Shriktman approximation [19]:

$$k_{1,\mathrm{wi}}^{\mathrm{Cu}} = f_{\mathrm{wi}}^{\mathrm{Cu}} \cdot k_{\mathrm{Cu}} + (1 - f_{\mathrm{wi}}^{\mathrm{Cu}}) \cdot k_{\mathrm{Ep}} \tag{6}$$

$$k_{2,\mathrm{wi}}^{\mathrm{Cu}} = k_{\mathrm{Ep}} \cdot \frac{(1 + f_{\mathrm{wi}}^{\mathrm{Cu}}) \cdot k_{\mathrm{Cu}} + (1 - f_{\mathrm{wi}}^{\mathrm{Cu}}) \cdot k_{\mathrm{Ep}}}{(1 - f_{\mathrm{wi}}^{\mathrm{Cu}}) \cdot k_{\mathrm{Cu}} + (1 + f_{\mathrm{wi}}^{\mathrm{Cu}}) \cdot k_{\mathrm{Ep}}} \tag{7}$$

For the anodised aluminium foil winding body, a two-step approach is followed: first, the equivalent properties of the anodised foil are calculated and subsequently, these properties are used to calculate the properties of an impregnated anodised aluminium foil winding body.

Step 1:

$$k_{1,\mathrm{afol}} = f_{\mathrm{afol}} \cdot k_{\mathrm{Al}} + (1 - f_{\mathrm{afol}}) \cdot k_{\mathrm{AlOx,film}} \tag{8}$$

$$k_{2,\mathrm{afol}} = \frac{k_{\mathrm{Al}} \cdot k_{\mathrm{AlOx,film}}}{(1 - f_{\mathrm{afol}}) \cdot k_{\mathrm{Al}} + f_{\mathrm{afol}} \cdot k_{\mathrm{AlOx,film}}}, \tag{9}$$

where k_{Al} and k_{AlOx} are the thermal conductivity of aluminium and aluminium-oxide film, respectively. The fill factor for this combination is defined as:

$$f_{\mathrm{afol}} = \frac{t_{\mathrm{Al,tot}} - 2 \cdot t_{\mathrm{AlOx}}}{t_{\mathrm{Al,tot}}}, \tag{10}$$

where $t_{\mathrm{Al,tot}}$ is the thickness of the anodised aluminium foil and t_{AlOx} the thickness of the aluminium-oxide insulation film on the foil.

Step 2:

$$k_{1,\mathrm{wi}}^{\mathrm{Al}} = f_{\mathrm{wi}}^{\mathrm{Al}} \cdot k_{1,\mathrm{afol}} + (1 - f_{\mathrm{wi}}^{\mathrm{Al}}) \cdot k_{\mathrm{Ep}}, \tag{11}$$

where $f_{\mathrm{wi}}^{\mathrm{Al}}$ is the fill factor of the impregnated winding body, $k_{1,\mathrm{afol}}$, the equivalent thermal conductivity of the anodised foil in the plane of the foil and k_{Ep}, the thermal conductivity of the epoxy resin. For the thermally poor conducting direction, the equivalent thermal conductivity can be calculated using the series material model from [19]:

$$k_{2,\mathrm{wi}}^{\mathrm{Al}} = \frac{k_{2,\mathrm{afol}} \cdot k_{\mathrm{Ep}}}{(1 - f_{\mathrm{wi}}^{\mathrm{Al}}) \cdot k_{2,\mathrm{afol}} + f_{\mathrm{wi}}^{\mathrm{Al}} \cdot k_{\mathrm{Ep}}}, \tag{12}$$

where $k_{2,\mathrm{afol}}$ is the equivalent thermal conductivity of the anodised foil perpendicular to the plane of the foil.

The laminated iron core is an amalgam of electrical steel sheets and a thin adhesive layer to bond the sheets together. The equivalent thermal conductivities are also calculated using the series-parallel model from [19]:

$$k_{1,\mathrm{core}} = f_{\mathrm{core}} \cdot k_{\mathrm{FeSi}} + (1 - f_{\mathrm{core}}) \cdot k_{\mathrm{Ep}} \tag{13}$$

$$k_{2,\mathrm{core}} = \frac{k_{\mathrm{FeSi}} \cdot k_{\mathrm{Ep}}}{(1 - f_{\mathrm{core}}) \cdot k_{\mathrm{FeSi}} + f_{\mathrm{core}} \cdot k_{\mathrm{Ep}}}, \tag{14}$$

where f_{core} is the fill factor of the laminated iron core and k_{FeSi} the thermal conductivity of electrical steel.

As already mentioned in Section 3.2.2, the phase-to-ground insulation will be modelled as an amalgam of aluminium-oxide and epoxy resin. The equivalent thermal conductivities are again calculated using the series-parallel model from [19]:

$$k_{1,\mathrm{pad}} = f_{\mathrm{pad}} \cdot k_{\mathrm{AlOx}} + (1 - f_{\mathrm{pad}}) \cdot k_{\mathrm{Ep}} \tag{15}$$

$$k_{2,\mathrm{pad}} = \frac{k_{\mathrm{Ep}} \cdot k_{\mathrm{AlOx}}}{(1 - f_{\mathrm{pad}}) \cdot k_{\mathrm{AlOx}} + f_{\mathrm{pad}} \cdot k_{\mathrm{Ep}}}. \tag{16}$$

3.2.4. Boundary Conditions

As already explained in Section 3.1, convective heat transfer at the airgap surface is neglected. It is assumed that all heat is dissipated via forced convection over the housing at the outer diameter.

3.2.5. Transient Model Calibration

To calibrate the 3D thermal FE model, the coils of both the stator with round enamelled copper wire and the stator with anodised aluminium are configured to emulate a 24 slot, 22 or 26 poles combination as depicted in Figure 10. Initially, the stator is in thermal equilibrium with its environment. A constant current $I_{\mathrm{set}} = 4A$ is then injected in phase U which corresponds to 21 W dissipated power in the motor. For 100 min, the hotspot and corresponding housing temperatures of selected coils, all coil voltages, and the phase currents are recorded. The voltage and current measurements are used to calculate the power losses at every time step, these serve as inputs for the FE model transient simulation. These transient experiments are performed once for a stator without thermal end-winding interconnection ring and once for a stator with thermal end-winding interconnection ring. The results from both the simulation with the 3D thermal FE model and the measurements are given in Figures 11 and 12. The numbering of the temperature signals corresponds to the numbering of the tooth coils in Figure 10. The parameters used for the simulations are given in Table 4. Due to the temperature limit of the used epoxy resin, the maximum hotspot temperature was kept below 80 °C. It can be concluded that the simulations are in good agreement with the measurements for both the round enamelled copper wire stator and the anodised aluminium foil winding stator, and for the case with and without thermal end-winding interconnection ring. The 3D thermal FE model can thus reliably be used to support the experimental data analysis in order to obtain a better understanding of the measurement results.

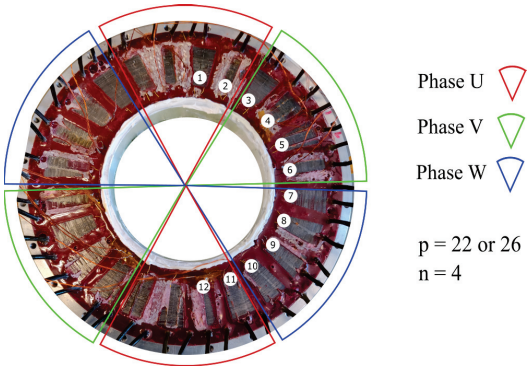

Figure 10. Indication of the PT100 temperature sensor location.

Table 4. Thermal Finite Element Model Parameters.

Parameter	Value	Unit
k_{Cu}	385	W/mK
k_{Al}	237	W/mK
k_{Ep}	0.37	W/mK
$k_{\mathrm{AlOx,film}}$	1.6	W/mK
k_{AlOx}	20	W/mK
k_{FeSi}	28	W/mK
$f_{\mathrm{wi}}^{\mathrm{Cu}}$	0.49	[/]
f_{afol}	0.89	[/]
$f_{\mathrm{wi}}^{\mathrm{Al}}$	0.75	[/]
f_{core}	0.98	[/]
f_{pad}	0.88	[/]
$k_{1,\mathrm{wi}}^{\mathrm{Cu}}$	189	W/mK
$k_{2,\mathrm{wi}}^{\mathrm{Cu}}$	1.08	W/mK
$k_{1,\mathrm{afol}}$	212	W/mK
$k_{2,\mathrm{afol}}$	14.3	W/mK
$k_{1,\mathrm{wi}}^{\mathrm{Al}}$	159	W/mK
$k_{2,\mathrm{wi}}^{\mathrm{Al}}$	1.37	W/mK
$k_{1,\mathrm{core}}$	27.4	W/mK
$k_{2,\mathrm{core}}$	0.37	W/mK
$k_{1,\mathrm{pad}}$	17.6	W/mK
$k_{2,\mathrm{pad}}$	2.72	W/mK

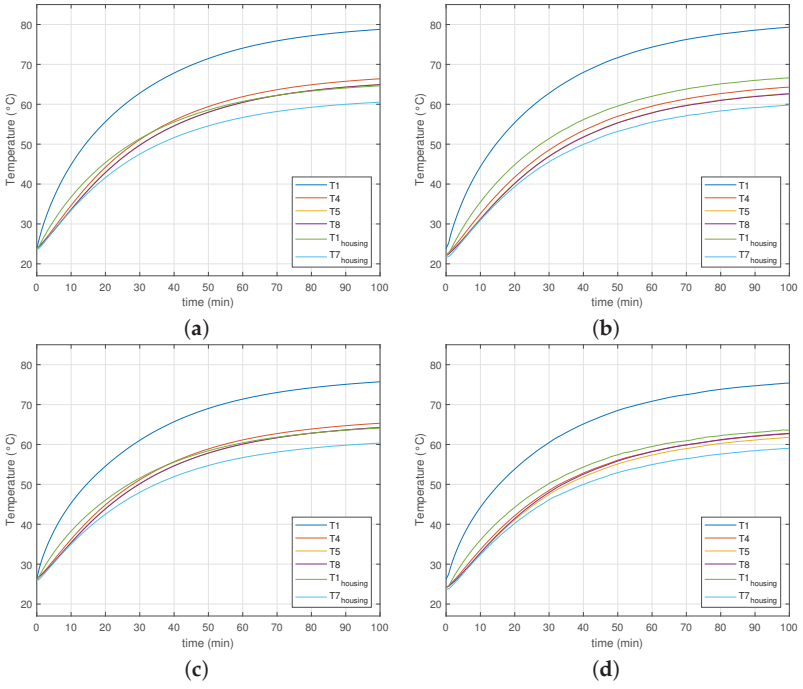

Figure 11. Transient temperature evolution at selected locations (see Figure 10) in a stator with round enamelled copper wire for a 24 slot, 22 or 26 pole combination. (**a**) Simulated temperatures | stator without end-winding ring. (**b**) Measured temperatures | stator without end-winding ring. (**c**) Simulated temperature | stator with end-winding ring. (**d**) Measured temperatures | stator with end-winding ring.

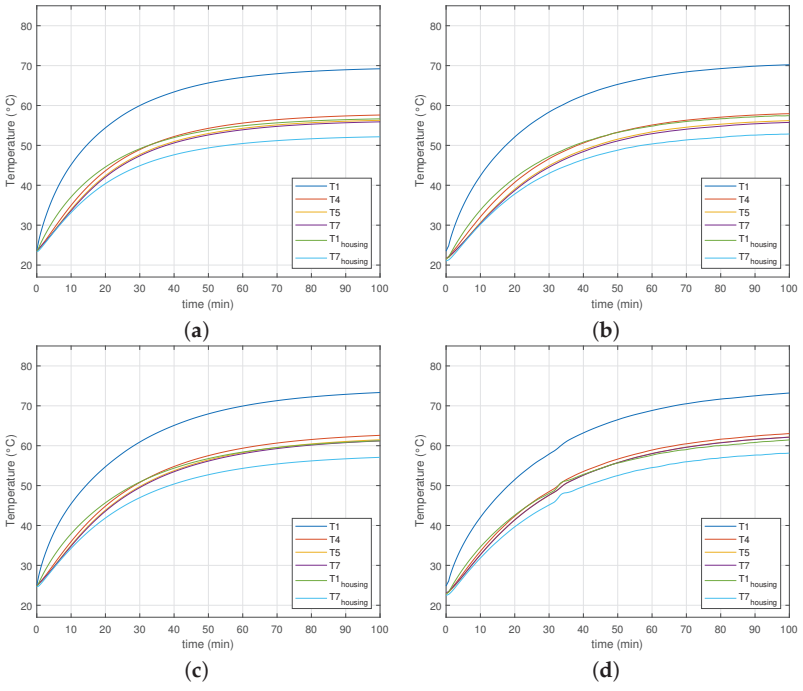

Figure 12. Transient temperature evolution at selected locations (see Figure 10) in a stator with anodised aluminium foil winding for a 24 slot, 22 or 26 pole combination. (**a**) Simulated temperatures | stator without end-winding ring. (**b**) Measured temperatures | stator without end-winding ring. (**c**) Simulated temperatures | stator with end-winding ring. (**d**) Measured temperatures | stator with end-winding ring.

3.2.6. Steady-State Temperature Distribution

Using the calibrated model from Section 3.2.5, the steady-state temperature distribution can be calculated. This is illustrated for the scenario from Figure 11a, i.e., the stator with round enamelled copper wire without thermal end-winding interconnection, with a 24 slots, 22 or 26 poles combination in Figure 13.

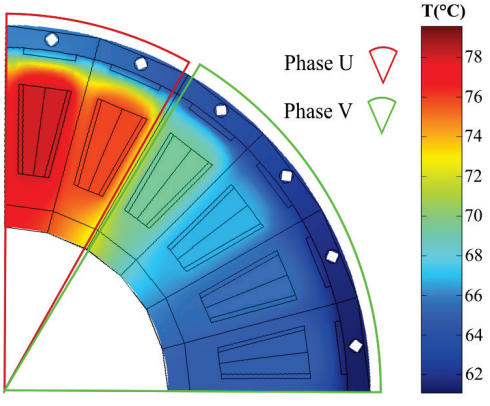

Figure 13. Steady-state temperature distribution in the stator with round enamelled copper wire without thermal end-winding interconnection, with a 24 slots, 22 or 26 poles combination.

As expected, the highest temperatures are found in the coils belonging to phase U since the losses in phase U are four times higher than in phase V. It can also be observed that there is a temperature difference between the coils of phase U clearly proving the presence of a heat flux in the tangential direction, i.e., heat is redistributed from coils with higher losses to coils with lower losses.

4. Results

4.1. Experimental Results

To study the influence of the slot/pole combination, thermal end-winding interconnection and equivalent winding body thermal conductivity on the stall torque performance, 10 experiments are performed in which the slot/pole combination, the presence of a thermal end-winding ring and the conductor material are varied. Table 5 specifies the test conditions for each experiment.

Table 5. Measured thermal resistance between hotspot and housing surface.

n	Thermal End-Winding Connection (Yes/No)	Al/Cu	$R_{\mathbf{hotspot}}$ (K/W)	$\frac{Q_{\mathbf{stall}}}{2 \cdot Q_{\mathbf{uniform,s24p22}}}$
4	No	Cu	7.89	0.534
4	Yes	Cu	7.29	0.578
2	No	Cu	6.44	0.655
2	Yes	Cu	6.34	0.665
1	No	Cu	4.86	0.866
1	Yes	Cu	4.90	0.860
4	No	Al	7.33	0.536
4	Yes	Al	6.43	0.611
	uniform losses	Cu	8.42	
	uniform losses	Al	7.86	

To emulate a stall torque loss distribution, the stator coils are connected as shown in Figure 6. A constant current $I_{\text{set}} = 4A$ is injected in phase U, which corresponds to 21 W dissipated power in the motor. The stall torque temperature distribution will be compared with the temperature distribution under uniform losses. To emulate this scenario, all coils of the stator are connected in series and a constant current $I_{\text{set}}^{\text{uniform}} = 2.8A = 4/\sqrt{2}A$ is injected into this ring network, also resulting in 21 W dissipated power. After 100 minutes, thermal steady-state is reached and the hotspot and corresponding housing temperatures, coil voltages and phase currents are recorded. The recorded values are used to calculate the thermal resistance between the hotspot and the housing at the same angular position (θ^*) as:

$$R_{\text{hotspot}} = \frac{T_{\text{hotspot}}(\theta^*) - T_{\text{housing}}(\theta^*)}{Q_{\text{coil},U}} \qquad (17)$$
$$Q_{\text{coil},U} = V_{\text{coil},U} \cdot I_U,$$

where $T_{\text{hotspot}}(\theta^*)$ is the temperature in the hotspot of a coil (see Figure 8) in the centre of phase U, $T_{\text{housing}}(\theta^*)$ is the temperature of the housing (see (2) in Figure 5) at the same angular location θ^*, $Q_{\text{coil},U}$ is the dissipated power in this coil, which is the product of the voltage $V_{\text{coil},U}$ over and the current I_U through the coil. The thermal resistance is preferred as a metric to compare the experimental results over the absolute or relative temperature since this metric is less sensitive to variations in ambient conditions (e.g. ambient temperature and housing convective heat transfer coefficient). As already mentioned in Section 3.1, two hotspot and housing temperatures are measured in different spatial periods of the stator, the average of thermal resistance of both is given in Table 5. Note that the thermal resistance in all cases is lower compared to the thermal resistance in case of uniform losses. This could be expected since a part of the losses of phase U are dissipated via the other phases, hence the decrease in the effective thermal resistance of phase U. Although the thermal resistance is lower in case of uneven loss distribution, the temperature is still higher

in comparison to a uniform loss distribution because two times more losses are dissipated in phase U in case of uneven loss distribution. Therefore, the maximum stall torque is lower than the maximum torque at low speed. Low speed means sufficiently high such that a uniform loss distribution can be assumed, but low enough such that iron and mechanical losses can be neglected. The ratio of the maximum stall torque over the torque at low speed will be used as a performance metric to quantify the stall torque performance of a motor. This ratio can also be interpreted as a 'torque derating factor at standstill':

$$\frac{T_{\text{stall}}}{T_{\text{uniform,ref}}}, \tag{18}$$

where $T_{\text{uniform,ref}}$ is the maximum torque under uniform losses at low speed for a reference scenario. The calculation of the torque derating factor as well as the definition of the reference scenario will be discussed in detail in the following paragraphs.

4.1.1. Influence of Slot/Pole Combination

To study the influence of the slot/pole combination, $T_{\text{uniform,ref}} = T_{\text{uniform,s24p22}}$ with $T_{\text{uniform,s24p22}}$ the maximum torque under uniform losses at low speed for a stator without end-winding ring and for the slot/pole combination with the highest $\xi \cdot k'_{\phi}$, i.e. 24 slots and 22 poles. This factor is now calculated using the measured thermal resistance from Table 5 and the fundamental winding factor and back-emf constant from Table 2:

$$\frac{T_{\text{stall}}}{T_{\text{uniform,s24p22}}} = \frac{\xi \cdot k'_{\phi} \cdot I_{\text{stall}}}{\xi_{\text{s24p22}} \cdot k'_{\phi,s24p22} \cdot I_{\text{uniform,s24p22}}}. \tag{19}$$

The currents can be expressed in terms of the dissipated power losses in phase U:

$$Q_{U,\text{stall}} = R_U \cdot (1 + \alpha \Delta T_{\text{stall}}) \cdot I^2_{U,\text{stall}} \tag{20}$$

and

$$Q_{U,\text{uniform,s24p22}} = R_U \cdot (1 + \alpha \Delta T_{\text{uniform,s24p22}}) \cdot I^2_{U,\text{uniform,s24p26}} \tag{21}$$

and since for the worst-case standstill position $I_{U,\text{stall}} = \sqrt{2} \cdot I_{\text{stall}}$, Equation (20) becomes:

$$Q_{U,\text{stall}} = R_U \cdot (1 + \alpha \Delta T_{\text{stall}}) \cdot (\sqrt{2} I_{\text{stall}})^2, \tag{22}$$

with α, the resistance temperature coefficient, ΔT_{stall} and $\Delta T_{\text{uniform,s24p22}}$, the difference between the winding temperature and the reference temperature at which the winding resistance R_U was determined. To obtain a fair comparison between the cases in Table 5, it is assumed that $\Delta T_{\text{stall}} = \Delta T_{\text{uniform,s24p22}}$ and R_U is assumed the same for all slot/pole combinations of the stator with round copper wire in Table 5, Equation (19) now becomes the following:

$$\frac{T_{\text{stall}}}{T_{\text{uniform,s24p22}}} = \frac{\xi \cdot k'_{\phi}}{\xi_{\text{s24p22}} \cdot k'_{\phi,s24p22}} \cdot \sqrt{\frac{Q_{\text{stall}}}{2 \cdot Q_{\text{uniform,s24p22}}}} \tag{23}$$

$$\frac{Q_{\text{stall}}}{Q_{\text{uniform,s24p22}}} = \frac{\frac{\Delta T_{\text{stall}}}{R_{\text{hotspot,stall}}}}{\frac{\Delta T_{\text{uniform,s24p22}}}{R_{\text{hotspot,uniform,s24p22}}}} = \frac{R_{\text{hotspot,uniform,s24p22}}}{R_{\text{hotspot,stall}}}. \tag{24}$$

The ratio $\frac{Q_{\text{stall}}}{Q_{\text{uniform,s24p22}}}$ can now be found using the thermal resistance measurements from Table 5. The assumption of equal temperature difference between hotspot and housing in the 'stall torque case' and the 'uniform losses reference case' $\Delta T_{\text{stall}} = \Delta T_{\text{uniform,s24p22}}$ entails that the hotspot temperature in both cases is the same if the housing temperature is the same. The same hotspot temperature means that in both cases the motors operate at their thermal limit.

To study the influence of the slot/pole combination on the stall torque performance, the coils of the stator of the prototype YASA AFPMSM (Figure 5) are allocated to a phase as shown in Figure 3 and their terminals are connected according to Figure 6. Experiments are performed as described in Section 4.1. First, the ratio $Q_{\text{stall}}/Q_{\text{uniform,s24p22}}/2$ is considered. This ratio is also given in Table 5 and can be interpreted as the ratio of the total losses that can be dissipated in a motor producing torque at standstill over the losses that can be dissipated in a motor with uniform loss. To have a fair comparison, in both cases, the losses result in the same temperature difference between hotspot and housing. The results from Table 5 are visualised in a bar plot in Figure 14. It is clear that the number of adjacent coils belonging to the same phase has a large influence on the ratio $Q_{\text{stall}}/Q_{\text{uniform,s24p22}}/2$. For the case $n = 4$, which corresponds to 24 slots and either 22 or 26 poles, even 47% less power can be dissipated to obtain the same difference between hotspot and housing as compared to the case of a uniform loss distribution. The slot/pole combinations with $n = 1$ exhibit the best thermal performance because losses from phase U can be very effectively dissipated via the tooth coils from phases V and W due to the large surface area between the phases since every tooth coil from phase U has two neighbouring tooth coils from other phases.

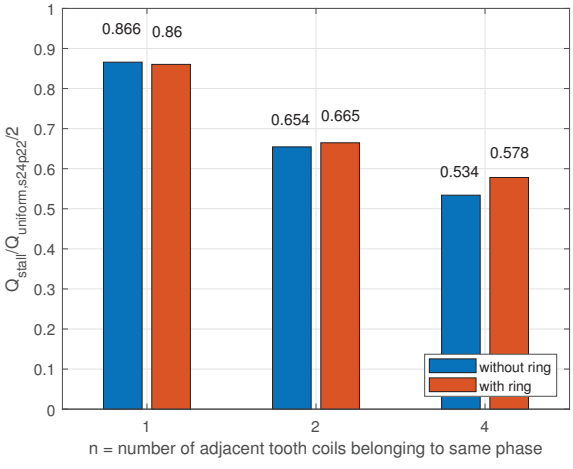

Figure 14. Measured ratio of the losses that can be dissipated in under stall torque conditions over the losses that can be dissipated in case of uniform loss distribution for various slot/pole combinations (see Figure 3) and for the cases with and without thermal end-winding interconnection.

The superior thermal performance of the slot/pole combinations with $n = 1$ does not necessarily imply superior stall torque performance. The torque derating factor $T_{\text{stall}}/T_{\text{uniform,s24p22}}$ for various slot/pole combinations is shown in Figure 15. It can be seen that the combination of 24 slots and 20 poles exhibits the highest stall torque performance because this combination combines good thermal performance (see Figure 14) with a good winding factor and back-emf constant. The stall torque of this slot/pole combination is 8.5%, which is higher than the slot/pole combination in the prototype YASA AFPMSM (24 slot, 26 poles). However, the differences between slot/pole combinations in terms of the stall torque performance are less pronounced than in terms of the thermal performance (see Figure 14).

4.1.2. Influence of Thermal End-Winding Interconnection

To study the influence of a thermal end-winding interconnection on the stall torque performance, a solid aluminium ring is inserted at the inner diameter of the stator prototypes and the same experiments as described in Sections 4.1 and 4.1.1 are repeated. The results in terms of the thermal performance were already given in Table 5 and are shown in Figure 14. The addition of a thermal end-winding ring results in 0.6% up to 4% increase

in thermal performance for $n = 1$ and $n = 4$, respectively, compared to the case without end-winding ring. This confirms that a thermal end-winding interconnection contributes in redistributing the heat from phase *U* to the other phases. The influence is more pronounced for $n = 4$ because in this case the surface area for heat transfer between phases is limited and thus, adding a thermal end-winding interconnection has more impact on the thermal performance. However, compared to the influence of the slot/pole combination on the thermal performance or stall torque performance, the influence of an end-winding ring is lower. A possible explanation for this is the presence of a large gap (2 mm) filled with epoxy between the end-winding and the end-winding interconnection ring. The influence of this gap will be studied in more detail in Section 4.2.1.

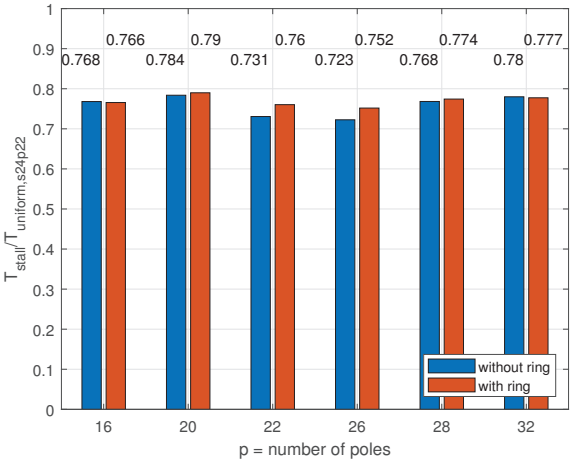

Figure 15. Measured torque derating factor $T_{\text{stall}}/T_{\text{uniform,s24p22}}$ for various slot/pole combinations and for the case with and without thermal end-winding interconnection.

4.1.3. Influence of Equivalent Winding Body Thermal Conductivity

The influence of the equivalent thermal conductivity of the winding body is studied by comparing a stator with round enamelled copper wire as conductor and a stator with anodised aluminium foil as conductor. The experiments as described in Section 4.1 are performed on both stators for $n = 4$ (see Figure 3), once without the end-winding interconnection and once with the end-winding interconnection. The outcome of the experiments was already given in Table 5. $T_{\text{uniform,ref}}$ in the torque derating factor $T_{\text{stall}}/T_{\text{uniform,ref}}$ is now defined as $T^{\text{x}}_{\text{uniform,s24p22}}$ with $\text{x} \in \{\text{Al,Cu}\}$ i.e., the maximum torque under uniform losses at low speed for either the stator with anodised aluminium foil winding or with round enamelled copper wire, without end-winding ring and the slot/pole combination with the highest $\xi \cdot k'_{\phi}$, i.e., 24 slots and 22 poles. The results are visualised in Figure 16.

No significant difference can be observed between the two conductor types. Although, it was expected that the stator with anodised aluminium foil winding would have a better stall torque performance due to its higher equivalent thermal conductivity in the direction out of the plane of the foil, i.e., $k^{\text{Al}}_{2,\text{wi}}$. However, since no explanation can be given at this point, this aspect will be further investigated with the aid of the 3D thermal FE model in Section 4.2.2.

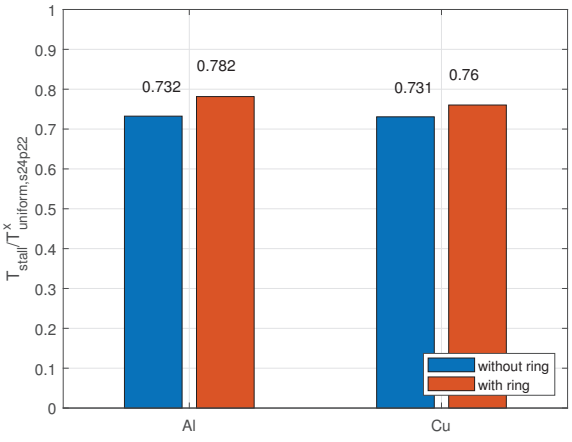

Figure 16. Measured torque derating factor $T_{stall}/T^{x}_{uniform,s24p22}$ with x $\in$ {Al,Cu}for different conductor types, for $n = 4$, and for the case with and without thermal end-winding ring.

4.2. Experimental Data Analysis through Simulation

4.2.1. Influence of Gap between End-Winding and End-Winding Interconnection Ring

It was mentioned in Section 4.1.2 that the addition of a thermal end-winding interconnection ring had less influence on the stall torque performance in comparison to the choice of the slot/pole combination. The presence of a gap filled with epoxy in between the end-winding and the ring was mentioned as a possible explanation. To study whether a higher stall torque performance can be obtained through the addition of a thermal end-winding ring if this gap is thinner, the calibrated 3D thermal FE model from Section 3.2.5 will be used here. The gap between the end-winding and the end-winding ring is decreased to its minimal value, the power losses in each tooth coil recorded during the experiments described in Section 4.1 are used as inputs for the simulation. The torque derating factor $T_{stall}/T_{uniform,s24p22}$ is again calculated using the simulated steady-state temperature distribution for various slot/pole combinations for the stator with copper wire winding for both the case without end-winding ring and the case with a minimal gap between the end-winding and end-winding ring. The results are given in Figure 17a.

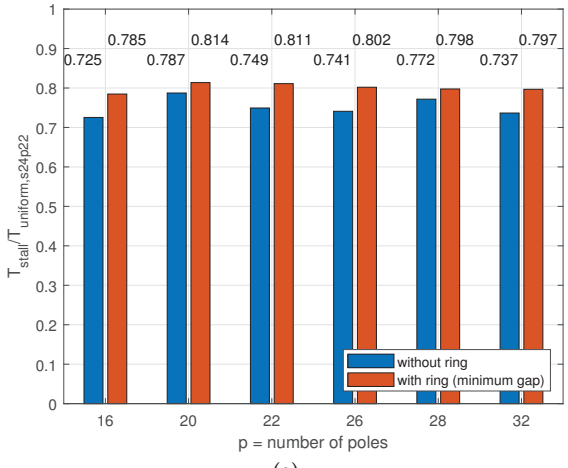

(**a**)

Figure 17. *Cont.*

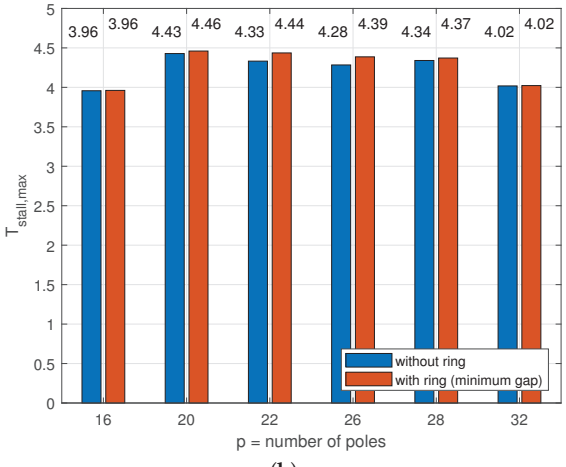

(**b**)

Figure 17. Simulated (**a**) torque derating factor $T_{\text{stall}}/T_{\text{uniform,s24p22}}$ and (**b**) maximum stall torque for various slot/pole combinations and for the case without thermal end-winding interconnection and with a thermal end-winding interconnection with a minimum gap between the end-winding and the ring. (**a**) Simulated torque derating factor $T_{\text{stall}}/T_{\text{uniform,s24p22}}$. (**b**) Simulated maximum stall torque (@ $T_{\text{hotspot}} = 150$ °C).

The addition of a thermal end-winding interconnection ring with minimum gap between end-winding and ring allows to increase the stall torque performance by up to 8.2%, whereas this was only 4% with a gap of two millimetres as mentioned in Section 4.1.2.

To compare the actual stall torque values for the different cases, the maximum stall torque for the various cases is shown in Figure 17b. The maximum stall torque is defined as the torque that results in a hotspot temperature of 150 °C. This torque was calculated using the current that results in a hotspot temperature of 150 °C, Equation (1) and the values from Table 2. The current was found iteratively using the thermal FE model. It can be seen that there is a difference of 0.5 Nm in maximum stall torque between the slot/pole combinations 24/16 and 24/22.

4.2.2. Analysis of Equivalent Thermal Conductivity of Winding Body

The study of the influence of the equivalent winding body thermal conductivity is one of the main goals of this work; however, the experimental results from Section 4.1.3 did not allow us to draw strong conclusions. No clear difference in stall torque performance between the stator with copper wire winding and the stator with anodised aluminium foil could be found. It was expected that the higher equivalent thermal conductivity of the anodised foil in the direction out of the plane of the foil [4,19] would lead to a better tangential heat transfer. This could not be proven experimentally.

By varying the winding fill factor in the 3D thermal FE model, the equivalent winding body thermal conductivity can be varied. The fill factor will be varied by ±20% with respect to its nominal value in the 3D thermal FE model and the torque derating factor $T_{\text{stall}}/T^{\text{x}}_{\text{uniform,s24p22}}$ with x $\in$ {Al,Cu} is again calculated based on the simulated steady-state temperature distribution. The recorded power losses from the experiments in Section 4.1.3 were used as inputs for the simulations. The results are visualised in the barplot in Figure 18.

It can be concluded that for both the aluminium winding and copper winding stators, the fill factor and the the equivalent winding body thermal conductivity has no significant influence on the stall torque performance.

It is important to note, however, that increasing the fill factor increases both the maximum stall torque T_{stall} and the maximum torque under uniform losses at low speed

$T^{x}_{\text{uniform,s24p22}}$ in the ratio $T_{\text{stall}}/T^{x}_{\text{uniform,s24p22}}$ with x $\in$ {Al,Cu}, but it will not allow a higher maximum stall torque as compared to its maximum torque under uniform losses at low speed.

Similarly to in Section 4.2.1, the actual stall torque values for the different cases are compared in Figure 18. It can be seen that, also at elevated temperatures, the winding body thermal conductivity does not have a significant influence on the stall torque values. This is because the winding body thermal resistance is not dominant in the thermal path from heat source to heat sink. Therefore, changes in the thermal conductivity do not have a significant impact on the thermal performance and thus, has no impact on the stall torque performance either. It could already be seen in Figures 11 and 12 that the temperature difference between hotspot and housing was much smaller than the difference between hotspot and ambient, confirming that the thermal resistance between housing and ambient is dominant in this case.

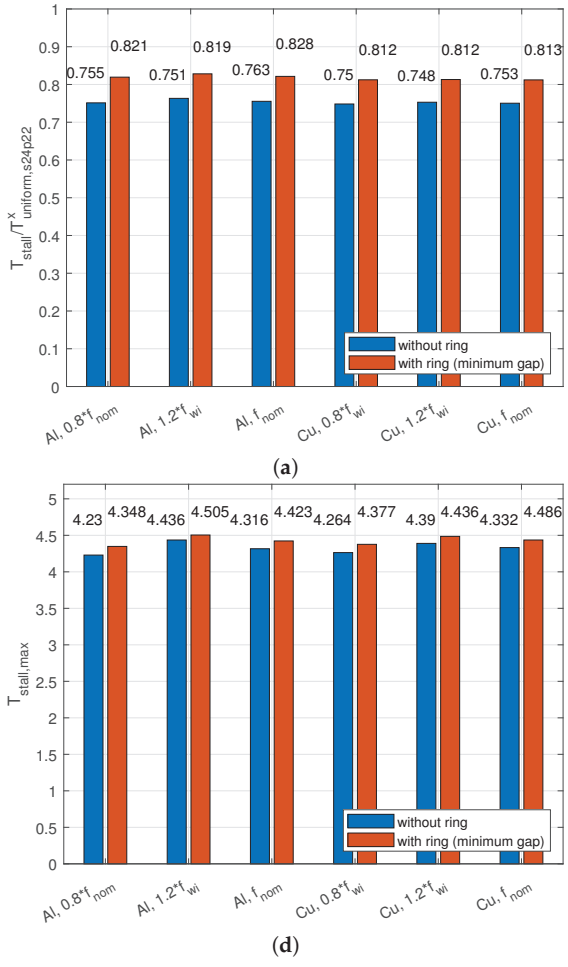

Figure 18. Simulated (**a**) torque derating factor $T_{\text{stall}}/T^{x}_{\text{uniform,s24p22}}$ with x $\in$ {Al,Cu} and (**b**) maximum stall torque, for different values of $f^{\text{Al}}_{\text{wi}}$, for different conductor types, for a 24 slots and 22 or 26 poles combination, and for the case with and without thermal end-winding ring. (**a**) Simulated torque derating factor $T_{\text{stall}}/T_{\text{uniform,s24p22}}$. (**b**) Simulated maximum stall torque (@ $T_{\text{hotspot}} = 150\ ^{\circ}\text{C}$).

4.2.3. Influence of Cyclic Loading

There are no applications in which a motor operates sufficiently long at standstill and maximum stall torque to reach thermal steady state. More frequently, as in the case of a force-controlled robotic gripper, the load cycle of the motor consists of a long period of high torque at standstill, e.g. when the gripper is holding a soft object and short periods of low torque and high speed when the gripper is opening and closing. Since the term stall torque is frequently used in motor datasheets, it is also used as a metric here, as it is a well known and easy-to-understand term. However, it would be interesting to study the impact of a load cycle on the stall torque performance. To this end, the thermal FE model is used to simulate the following load cycle which corresponds to a realistic gripper scenario: (1) gripper grasps object at start location: high speed, gradually increasing current (duration: 4 s); (2) gripper holds object while it is moved to end position: standstill, maximum current (duration: 26 s); (3) gripper releases object at end position: high speed, gradually decreasing current (duration: 4 s); (4) gripper without object returns to start position: standstill, no current (duration: 26 s). Hence, the duty cycle for this load cycle is 50%. A scenario with uniform loss distribution as would be the case if the motor rotates when generating torque and a scenario with non-uniform loss distribution as is the case for a motor generating torque at standstill are compared. For both scenarios, the torque that results in a peak hotspot temperature of 150 °C is determined. The hotspot temperature variations for both scenarios are given in Figure 19. Larger temperature variations can be found for the case with non-uniform loss distribution since the variation of the losses is larger in case of a non-uniform loss distribution. The torque derating factor for this load cycle is then calculated as the ratio of the maximum stall torque over the maximum torque in case of uniform losses, i.e. when the losses are uniform during phase (2). The derating factor for a load cycle is compared to the derating factor for a continuous load scenario, but no difference could be observed, this allows to conclude that the stall torque derating factor for continuous load can reliably be used also in cyclic load applications.

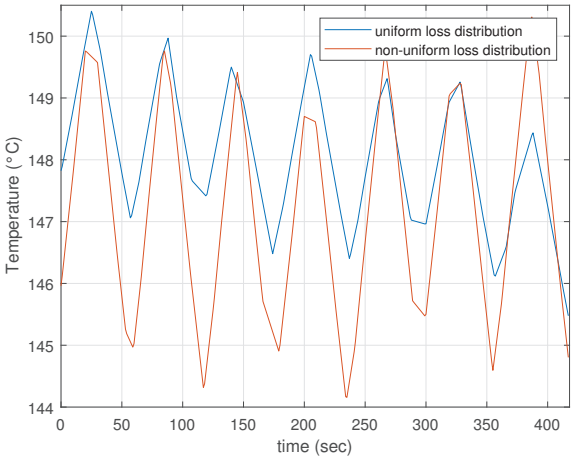

Figure 19. Simulated hotspot temperature variations for a load cycle with a duty cycle of 50% for a case with uniform losses (e.g., when the motor is rotating when producing torque) and for a case with non-uniform losses (e.g., when the motor is at standstill when producing torque).

5. Conclusions

In this work, the stall torque performance of a YASA AFPMSM motor was analysed. More specifically, the influence of the slot/pole combination, the addition of a thermal end-winding interconnection ring and the equivalent thermal conductivity of the winding body were studied. To this end, prototype YASA AFPMSM stators were manufactured and instrumented with temperature sensors. A uniform and an uneven loss distribution were

imposed on the stators by injecting DC currents to emulate a low-speed and a standstill situation, respectively. The steady-state hotspot temperatures and losses were recorded and used to calculate the thermal resistance between hotspot and housing. These thermal resistances, the fundamental winding factor and the back-emf constants were then used to calculate the stall torque performance metric introduced in this work. This metric was determined for various slot/pole combinations, a stator with/without thermal end-winding interconnection and for a stator with anodised aluminium foil winding and a stator with copper wire winding to study the impact of the equivalent thermal conductivity of the winding body.

It was concluded that only the slot/pole combination and the addition of a thermal end-winding interconnection can have a significant impact on the stall torque performance (with up to 8% increase in the stall torque performance metric). The equivalent thermal conductivity of the winding body has no impact on the stall torque performance, specifically; however, a higher fill factor leads to superior thermal properties and thus, to both a higher maximum stall torque and a higher maximum torque at low speed.

Author Contributions: Conceptualization, J.V.D.; methodology, J.V.D. and H.V.; software, J.V.D. and H.V.; validation, J.V.D.; formal analysis, J.V.D.; investigation, J.V.D.; resources, J.V.D.; data curation, J.V.D.; writing—original draft preparation, J.V.D.; writing—review and editing, H.V. and G.C.; visualization, J.V.D.; supervision, H.V. and G.C.; project administration, J.V.D.; funding acquisition, J.V.D., H.V. and G.C. All authors have read and agreed to the published version of the manuscript.

Funding: J. Van Damme was awarded a Ph.D. Fellowship Strategic Basic Research (SB) from the Research Foundation Flanders (FWO) in 2019 (Grant Number: 1S87322N). This research was also financially supported by Flanders Make vzw in the research project FiberMech.

Data Availability Statement: The study did not report any data.

Acknowledgments: The authors would like to acknowledge Tony Boone and Vincent Gevaert for their assistance in the manufacturing of the YASA AFPMSM prototypes.

Conflicts of Interest: The authors declare no conflict of interest.

References

1. Vansompel, H.; Hemeida, A.; Sergeant, P. Stator heat extraction system for axial flux yokeless and segmented armature machines. In Proceedings of the 2017 IEEE International Electric Machines and Drives Conference (IEMDC), Miami, FL, USA, 21–24 May 2017, pp. 1–7. [CrossRef]
2. Vansompel, H.; Leijnen, P.; Sergeant, P. Multiphysics Analysis of a Stator Construction Method in Yokeless and Segmented Armature Axial Flux PM Machines. *IEEE Trans. Energy Convers.* **2019**, *34*, 139–146. [CrossRef]
3. Waldhof, M.; Echle, A.; Parspour, N. A Novel Drive Train Concept for Personalized Upper Body Exoskeletons with a Multiphase Axial Flux Machine. In Proceedings of the 2019 IEEE International Electric Machines & Drives Conference (IEMDC), San Diego, CA, USA, 12–15 May 2019; pp. 2160–2166. [CrossRef]
4. Van Damme, J.; Vansompel, H.; Crevecoeur, G. Anodised Aluminium Foil Winding Axial Flux Machine for Direct-Drive Robotic Applications. *IEEE Trans. Ind. Electron.* **2022**, 1–10. [CrossRef]
5. De Clercq, T.; Sianov, A.; Crevecoeur, G. A Soft Barometric Tactile Sensor to Simultaneously Localize Contact and Estimate Normal Force with Validation to Detect Slip in a Robotic Gripper. *IEEE Robot. Autom. Lett.* **2022**, *7*, 11767–11774. [CrossRef]
6. Gill, H. *AC Servo Motor System the Difference Between Continuous Ratings and Holding Continuous Loads*; Technical report; Kollmorgen: Radford, VA, USA, 2018.
7. Pfaff, G.; Weschta, A.; Wick, A.F. Design and Experimental Results of a Brushless AC Servo Drive. *IEEE Trans. Ind. Appl.* **1984**, *IA-20*, 814–821. [CrossRef]
8. Robotics and Automation. Technical Report, Mayr Antriebstechnik, 2022. Available online: https://www.mayr.com/branchen/broschueren/robotik-und-automation/img_006_v00_en_30_06_2021.pdf (accessed on 12 April 2023).
9. Camilleri, R.; Howey, D.A.; McCulloch, M.D. Predicting the Temperature and Flow Distribution in a Direct Oil-Cooled Electrical Machine with Segmented Stator. *IEEE Trans. Ind. Electron.* **2016**, *63*, 82–91. [CrossRef]
10. Mohamed, A.H.; Vansompel, H.; Sergeant, P. An Integrated Modular Motor Drive With Shared Cooling for Axial Flux Motor Drives. *IEEE Trans. Ind. Electron.* **2021**, *68*, 10467–10476. [CrossRef]

11. Tang, Z.P.; Wang, Y.C.; Zhou, F.; Yu, F.Y.; Gieras, J.F.; Shen, J.X. Study on Heat Dissipation of Low-Speed Outer Rotor Permanent Magnet Motor Based on Multi-phase Flow Model. In Proceedings of the 2021 International Joint Conference on Energy, Electrical and Power Engineering, Frankfurt, Germany, 17–19 September 2021; Cao, W., Hu, C., Huang, X., Chen, X., Tao, J., Eds.; Springer Nature: Singapore, 2022; pp. 607–620.
12. Gnacinski, P. Effect of unbalanced voltage on windings temperature, operational life and load carrying capacity of induction machine. *Energy Convers. Manag.* **2008**, *49*, 761–770. [CrossRef]
13. Adouni, A.; J. Marques Cardoso, A. Thermal Analysis of Low-Power Three-Phase Induction Motors Operating under Voltage Unbalance and Inter-Turn Short Circuit Faults. *Machines* **2021**, *9*, 2. [CrossRef]
14. Universal Robots-Robotiq. Available online: https://robotiq.com/cobot-brands/universal-robots accessed on (4 January 2023).
15. Melkebeek, J. *Electrical Machines and Drives: Fundamentals and Advanced Modelling*; Springer: Cham, Switzerland, 2018.
16. Di Stefano, R.; Marignetti, F. Electromagnetic Analysis of Axial-Flux Permanent Magnet Synchronous Machines with Fractional Windings with Experimental Validation. *IEEE Trans. Ind. Electron.* **2012**, *59*, 2573–2582. [CrossRef]
17. Vansompel, Hendrik. Design of an Energy Efficient Axial Flux Permanent Magnet Machine. Ph.D. Thesis, Ghent University, Ghent, Belgium, 2013.
18. Li, B.; Yuan, Y.; Gao, P.; Zhang, Z.; Li, G. Cooling structure design for an outer-rotor permanent magnet motor based on phase change material. *Therm. Sci. Eng. Prog.* **2022**, *34*, 101406. [CrossRef]
19. Simpson, N.; Wrobel, R.; Mellor, P.H. Estimation of Equivalent Thermal Parameters of Impregnated Electrical Windings. *IEEE Trans. Ind. Appl.* **2013**, *49*, 2505–2515. [CrossRef]
20. Howey, D.A. Thermal Design of Air-Cooled Axial Flux Permanent Magnet Machines. Ph.D. Thesis, Imperial College London, London, UK, 2010.

energies

MDPI

Article

An Influence of Spatial Harmonics on an Electromagnetic Torque of a Symmetrical Six-Phase Induction Machine

Andriy Kutsyk [1,2,*], Mariusz Korkosz [1], Mykola Semeniuk [2] and Marek Nowak [1]

[1] Faculty of Electrical and Computer Engineering, Rzeszow University of Technology, 35-959 Rzeszow, Poland; mkosz@prz.edu.pl (M.K.); mnowak@prz.edu.pl (M.N.)
[2] Institute of Power Engineering and Control System, Lviv Polytechnic National University, 79-013 Lviv, Ukraine; mykola.b.semeniuk@lpnu.ua
* Correspondence: a.kutsyk@prz.edu.pl

Abstract: The analyses of the influence of spatial harmonics on the electromagnetic torque of the multi-phase induction machine and reducing this influence are important tasks to ensure the high efficiency of the induction machine. Designing the machine to consider the influence of spatial harmonics is essential to ensure the desired mechanical and energy characteristics. In the case of the sinusoidal winding supply of the induction machine, the magnetomotive force has high spatial harmonics, which are caused by the machine-winding design. The interaction between the 5th, 7th, 11th and 13th spatial harmonics of the winding function and the first time-harmonic of the winding supply causes the appearance of the 6th and 12th harmonics in the electromagnetic torque of the machine. A prototype of the symmetrical six-phase induction machine and the experimental study for the influence of spatial harmonics on the harmonic content of the stator currents in different machine modes are given in this paper. The mathematical model of the six-phase induction machine has been developed using the average voltages in integration step method. The introduction of the harmonic components into the magnetization inductance in the mathematical model of the six-phase induction machine for taking into account the spatial harmonics of the machine-winding function is proposed in this paper. The adequacy of the mathematical model was confirmed by comparing the simulation and experimental results. The harmonic content of the electromagnetic torque, which is caused by spatial harmonic influence, is analyzed.

Keywords: multiphase induction machine; space harmonics; high harmonic content; method of average voltages in integration step

Citation: Kutsyk, A.; Korkosz, M.; Semeniuk, M.; Nowak, M. An Influence of Spatial Harmonics on an Electromagnetic Torque of a Symmetrical Six-Phase Induction Machine. *Energies* **2023**, *16*, 3813. https://doi.org/10.3390/en16093813

Academic Editors: Loránd Szabó and Feng Chai

Received: 17 March 2023
Revised: 24 April 2023
Accepted: 26 April 2023
Published: 28 April 2023

1. Introduction

Multiphase machines play an important role in modern e-mobility due to different advantages: increasing the efficiency and reducing the losses of induction machines [1,2] and permanent magnet synchronous machines [3], decreasing the electromagnetic torque pulsation [4,5], reducing the harmonic content DC link current when the machine is supplying from the multi-leg inverter [6,7] and improving the system reliability [8]. Multiphase machines are significantly more fault-tolerant than three-phase machines. There are different fault-tolerance strategies for the operation of the five-phase machine [9] and six-phase machine [10]. This active fault-tolerance control is very important for the development of high-performance electric drives in electrical vehicles [11]. Reference [12] notes the fault tolerance of the multi-winding switched reluctance motor. The main idea of all fault-tolerance strategies is that the multiphase machine can continue to work with a rotating field as long as three phases are operated.

References [8,13] discuss the spatial harmonics of the IM magnetomotive force (MMF). The design of IM stator windings does not provide perfectly sinusoidal MMF distribution due to the presence of spatial harmonics. The shape of the magnetizing force in the air

gap is close to rectangular and its composition includes harmonics from the series $6k \pm 1$ ($k = 0, 1, 2, 3 \ldots$). At the same time, according to the results of the analysis carried out in [13] for IM and in [14] for synchronous machines, the 5th, 7th, 11th and 13th harmonics are the most influential (the amplitude of the 17th harmonic is 7 times smaller than the 13th and 64 times smaller than the first).

The shorter end-winding length in IM design can reduce the influence of spatial harmonics. However, the spatial harmonics are not completely eliminated [15–17].

As shown in [18], reducing the influence of time and spatial harmonics on the electromagnetic torque (torque ripple minimization) is important for increasing the IM efficiency. The spatial harmonic content caused by the IM winding design is analyzed in [19]. This type of harmonic causes magnetic noise and vibration [20].

On the other hand, publications [21–23] note that higher spatial harmonics in machines have a positive effect. In particular, rotor speed, mechanical defects such as rotor eccentricity, damaged rotor rings and short circuits in windings can be determined based on the information about the spatial harmonics of the machine.

There are two types of stator winding structure used for six-phase induction machines (6PIMs): an asymmetrical stator winding structure with two three-phase windings spatially shifted by 30 electrical degrees, and a symmetrical stator winding structure with two three-phase windings spatially shifted by 60 electrical degrees. The advantage of the asymmetrical 6PIM is the elimination of the 6th harmonic of electromagnetic torque, which is caused by the interaction between the 5th and 7th spatial harmonics of the winding function and the 1st harmonic of the stator current in the case of the sinusoidal supply voltage [24]. The symmetrical 6PIM provides better opportunities from the perspective of control influence forming [25–27].

The block diagram of the symmetrical 6PIM is shown in Figure 1. Two three-phase windings with a spatial displacement of 60 electrical degrees ($\beta = 60°$) are supplied from power transformers PT1 and PT2. Three-phase voltages for the secondary windings of power transformers PT1 and PT2 are shifted by 60 electrical degrees. This is achieved by appropriately connecting the secondary windings of the power transformers.

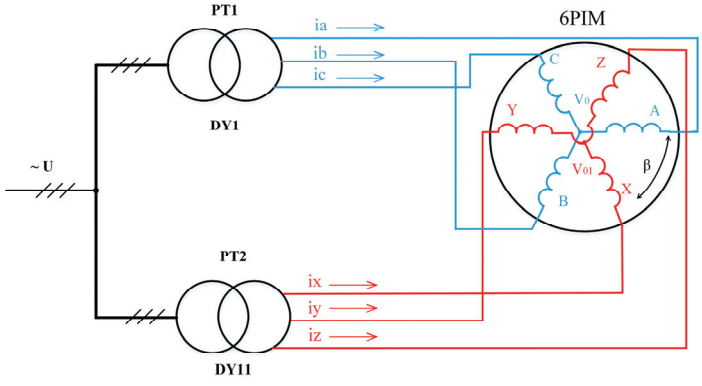

Figure 1. Symmetrical six-phase induction machine.

The harmonic composition of the magnetomotive force caused by the influence of the spatial harmonics of machine windings is known. However, there is no sufficiently simple analytical description for the higher harmonics of the 6PIM electromagnetic torque caused by the interaction between the spatial harmonics of the machine windings and the time harmonics of the supply current. An analytical description is very important to identify ways to improve the electromechanical compatibility of the 6PIM with the load, particularly in eliminating the corresponding harmonics of the electromagnetic torque. Therefore, one of this paper's tasks is to develop an analytical description of the appearance of the higher

harmonics in the 6PIM electromagnetic torque caused by the interaction between the spatial harmonics of the machine windings and the time harmonics of the stator current.

Mathematical models based on the finite element method (FEM) are usually used for the analysis of the IM electromagnetic processes, taking into account spatial harmonics [28–30]. These models enable the analysis of the electromagnetic processes in steady-state modes of the IM and have a low-speed response. There are FEM models of the IM that cooperate with other simulation tools to take into account the space harmonics in the transient analysis [31]. The complexity of the mathematical description in field-oriented mathematical models and low calculation performance prevent the use of such models for the study of transient processes in multi-engine systems with semiconductor converters. In this regard, it is necessary to create fast-action mathematical models that would take into consideration the influence of spatial harmonics and enable the study of electromagnetic and electromechanical transient and steady-state processes in multi-engine complexes with semiconductor converters. This is the second task of the paper.

This paper presents an experimental study of the influence of the spatial harmonics of the winding function on the harmonic content of symmetrical 6PIM currents, the development of a 6PIM fast-action mathematical model that takes into account the influence of spatial harmonics, and an analysis of the influence of spatial harmonics on the harmonic content of the 6PIM electromagnetic torque.

The structure of this paper is as follows. An analytical description of the MMF and electromagnetic torque of the symmetrical 6PIM, taking into account space harmonics, is included in Section 2. Section 3 presents the mathematical model of the symmetrical 6PIM, taking into account space harmonics. The experimental test bench with the prototype of the symmetrical 6PIM is given in Section 4. Section 5 presents the experimental and simulation results of the symmetrical 6PIM. The conclusions are finally summarized in Section 6.

2. An Analytical Description of the 6PIM MMF and Electromagnetic Torque Taking into Account Spatial Harmonics

For an analytical description of the symmetrical 6PIM MMF, this section considers the sinusoidal supply of the 6PIM.

It is known that MMF in the air gap of a three-phase winding ABC contains, in addition to the first harmonic, higher harmonics, with the 5th, 7th, 11th and 13th harmonics having the most influence [13,14]. Taking this into account, the expressions for the MMF of phases A, B and C are written as follows:

$$\begin{gathered} F_A = w_A i_A = [w_1 \cos\eta + w_5 \cos 5\eta + w_7 \cos 7\eta + w_{11} \cos 11\eta + w_{13} \cos 13\eta]\ I_{m1} \cos(\omega t), \\ F_B = w_B i_B = [w_1 \cos(\eta - \rho) + w_5 \cos(5\eta - 5\rho) + w_7 \cos(7\eta - 7\rho) + w_{11} \cos(11\eta - 11\rho) + w_{13} \cos(13\eta - 13\rho)]\ I_{m1} \cos(\omega t - \rho), \\ F_C = w_C i_C = [w_1 \cos(\eta + \rho) + w_5 \cos(5\eta + 5\rho) + w_7 \cos(7\eta + 7\rho) + w_{11} \cos(11\eta + 11\rho) + w_{13} \cos(13\eta + 13\rho)]\ I_{m1} \cos(\omega t + \rho). \end{gathered} \quad (1)$$

where w_A, w_B, and w_C—distribution function of winding coils $w(\eta)$; w_i—magnitude of the winding function's harmonics (i = 1, 5, 7, 11, 13); η—spatial angle in electric degrees; I_{m1}—magnitude of the phase current; $\omega = 2\pi f$—angular frequency of the current; and $\rho = 2\pi/3$.

The MMF for the first three-phase winding ABC of the symmetrical 6PIM is determined:

$$\begin{gathered} F_{ABC} = F_A + F_B + F_C, \\ F_{ABC} = \tfrac{3}{2}[w_1 I_{m1} \cos(\eta - \omega t) + w_5 I_{m1} \cos(5\eta + \omega t) + w_7 I_{m1} \cos(7\eta - \omega t) + w_{11} I_{m1} \cos(11\eta + \omega t) + w_{13} I_{m1} \cos(13\eta - \omega t)]\ . \end{gathered} \quad (2)$$

Expression (2) is obtained taking into account the trigonometric transformations described in [24].

The MMF for the second three-phase winding XYZ of the symmetrical 6PIM is determined according to the following expression:

$$\begin{gathered} F_{XYZ} = \tfrac{3}{2}[w_1 I_{m1} \cos(\eta - \omega t + \beta - \alpha) + w_5 I_{m1} \cos(5\eta + \omega t + 5\beta + \alpha) + w_7 I_{m1} \cos(7\eta - \omega t + 7\beta - \alpha) + \\ w_{11} I_{m1} \cos(11\eta + \omega t + 11\beta + \alpha) + w_{13} I_{m1} \cos(13\eta - \omega t + 13\beta - \alpha)]. \end{gathered} \quad (3)$$

where β—the spatial displacement between the first three-phase winding ABC and the second three-phase winding XYZ of the 6PIM in electrical degrees, and α—the phase shift between the supply voltages of the 6PIM three-phase windings.

The resulting MMF in the air gap of the 6PIM is determined according to the following expression:

$$F = F_{ABC} + F_{XYZ} = \frac{3}{2}I_{m1}w_1[\cos(\eta - \omega t) + \cos(\eta - \omega t + \beta - \alpha)] + \frac{3}{2}I_{m1}w_5[\cos(5\eta + \omega t) + \cos(5\eta + \omega t + 5\beta + \alpha)] + \frac{3}{2}I_{m1}w_7[\cos(7\eta - \omega t) + \cos(7\eta - \omega t + 7\beta - \alpha)] + \frac{3}{2}I_{m1}w_{11}[\cos(11\eta + \omega t) + \cos(11\eta + \omega t + 11\beta + \alpha)] + \frac{3}{2}I_{m1}w_{13}[\cos(13\eta - \omega t) + \cos(13\eta - \omega t + 13\beta - \alpha)]. \quad (4)$$

Taking into account that spatial displacement between the winding ABC and the winding XYZ of the symmetrical 6PIM is 60 electrical degrees ($\beta = \frac{\pi}{3}$) and the phase shift between the supply voltages of the symmetrical 6PIM is 60 electrical degrees ($\alpha = \frac{\pi}{3}$), Expression (4) is written as:

$$F = 3\,I_{m1}w_1\cos(\eta - \omega t) + 3I_{m1}w_5\cos(5\eta + \omega t) + 3I_{m1}w_7\cos(7\eta - \omega t) + 3I_{m1}w_{11}\cos(11\eta + \omega t) + 3I_{m1}w_{13}\cos(13\eta - \omega t). \quad (5)$$

The magnitude of the MMF of the symmetrical 6PIM is determined by substitution $\eta = \omega t$ according to the following expression:

$$F_m = 3I_{m1}w_1\cos(0) + 3I_{m1}(w_5 + w_7)\cos(6\omega t) + 3I_{m1}(w_{11} + w_{13})\cos(12\omega t). \quad (6)$$

The 5th and 7th spatial harmonics of the winding function lead to the appearance of the 6th time harmonic in the magnitude of the MMF and, accordingly, in the electromagnetic torque of the symmetrical 6PIM according to Expression (6). Similarly, the 11th and 13th spatial harmonics lead to the appearance of the 12th time harmonic in the magnitude of the MMF and in the electromagnetic torque of the symmetrical 6PIM.

Note that the obtained expressions correspond to the sinusoidal supply of 6PIM windings. In the case of the non-sinusoidal supply of 6PIM windings (using Voltage Source Inverters), the expression for the MMF will contain additional components caused by the influence of time harmonics on the winding supply. The interaction between the time harmonics of the winding supply and the spatial harmonics of the winding function is analytically analyzed in [24].

3. Mathematical Model Description of Symmetrical 6PIM Taking into Account Spatial Harmonics

The mathematical model of the symmetrical 6PIM was developed using the average voltages in integration step (AVIS) method. The main principles of the AVIS method are given in [32,33]. A feature of this method is its high calculation performance and numerical stability. It enables the creation of fast-response mathematical models, which can work in real-time mode with the interaction of physical objects (hardware-in-the-loop technology). Examples of such models for electrical drives with a three-phase IM are presented in [34,35], and power systems with wind turbines are discussed in [36]. Reference [37] presents mathematical models of electrotechnical systems with synchronous machines and technology for use in testing synchronous generator excitation systems. The AVIS method is used for creating models of power systems with nonlinear elements [38]. The specified examples testify to the adequacy of the chosen method and its efficiency for the modeling of electromagnetic and electromechanical processes in electrotechnical systems.

The universal equation for an electrical branch, which contains active resistance R and inductance L, is written according to the AVIS method [32]:

$$U - u_{R0} - u_{C0} - \sum_{k=1}^{m-1}\left(\frac{R\Delta t^k}{(k+1)!}\cdot\frac{m-k}{m+1}\right)\frac{d^k i_0}{dt^k} + \left(\frac{R}{m+1}\right)(i_0 - i_1) + \frac{1}{\Delta t}(\psi_0 - \psi_1) = 0 \quad (7)$$

where i_0—the branch current at the beginning of the integration step; m—the order of the polynomial that describes the current curve in the integration step (order of the method);

$U = \frac{1}{\Delta t}\int\limits_{t_0}^{t_0+\Delta t} udt$—the average values in the integration step of the branch voltage; u_{R0}—the voltage on the active resistance at the beginning of the integration step; ψ_0, ψ_1—the flux linkages at the beginning and at the end of the integration step; and Δt—the integration step.

Applying Equation (7) of the 2nd order AVIS for the stator and rotor windings of the IM, and taking into account that an increase in the flux linkages in the integration step is determined as $\Delta\vec{\psi}_{am} = \mathbf{L}_{am1}\vec{i}_1 - \mathbf{L}_{am0}\vec{i}_0$, the vector equation is written as:

$$\vec{U} - \mathbf{R}\vec{i}_0 + \left(\frac{\mathbf{R}}{3} + \frac{\mathbf{L}_{am0}}{\Delta t}\right)\vec{i}_0 - \frac{\mathbf{R}\Delta t}{6}\frac{d\vec{i}_0}{dt} - \left(\frac{\mathbf{R}}{3} + \frac{\mathbf{L}_{am1}}{\Delta t}\right)\vec{i}_1 = 0. \quad (8)$$

where $U = \frac{1}{\Delta t}\int\limits_{t_0}^{t_0+\Delta t} u_{am}(t)dt$—the vector of the average voltages in the integration step; $u_{am} = (u_A, u_B, u_C, u_X, u_Y, u_Z, u_a, u_b, u_c)^T = (u_A, u_B, u_C, u_X, u_Y, u_Z, 0, 0, 0)^T$—the instantaneous voltages; $\vec{i}_0 = (i_{A0}, i_{B0}, i_{C0}, i_{X0}, i_{Y0}, i_{Z0}, i_{a0}, i_{b0}, i_{c0})^T$, $\vec{i}_1 = (i_{A1}, i_{B1}, i_{C1}, i_{X1}, i_{Y1}, i_{Z1}, i_{a1}, i_{b1}, i_{c1})^T$—the vector of currents at the beginning and the end of the integration step; $\mathbf{R} = \mathrm{diag}(R_A, R_B, R_C, R_X, R_Y, R_Z, R_a, R_b, R_c)$—the matrix of active resistances; $\mathbf{L}_{am0} = \mathbf{L}_{am}(\gamma_{R0})$, $\mathbf{L}_{am0} = \mathbf{L}_{am}(\gamma_{R1})$—the matrix of inductances at the beginning and the end of the integration step; and γ_{R0}, γ_{R1}—rotation angle at the beginning and the end of the step.

In order to determine the IM currents using the AVIS method of the 2nd order, time derivatives of the currents are used. The following equation can be written to find these derivatives:

$$\vec{U} = \mathbf{R}\vec{i} + \frac{d\vec{\psi}_{am}\left(\vec{i}, \gamma_R\right)}{dt}. \quad (9)$$

Taking into account that the flux linkages in Expression (9) are functions of the currents and rotation angle, the time derivatives of flux linkages are determined as:

$$\frac{d\vec{\psi}_{am}\left(\vec{i}, \gamma_R\right)}{dt} = \frac{\partial\vec{\psi}_{am}\left(\vec{i}, \gamma_R\right)}{\partial\vec{i}}\frac{d\vec{i}}{dt} + \frac{\partial\vec{\psi}_{am}\left(\vec{i}, \gamma_R\right)}{\partial\gamma_R}\frac{d\gamma_R}{dt} = \mathbf{L}_{am}\frac{d\vec{i}}{dt} + \frac{\partial\mathbf{L}_{am}}{\partial\gamma_R}\vec{i}\,ap\Omega = \vec{E}_{TR} + \vec{E}_{ROT}. \quad (10)$$

where p—the number of pole pairs; Ω—the rotation speed; and $\vec{E}_{TR}$, $\vec{E}_{ROT}$—the electromotive force of transformation and electromotive force of the rotation (components of the stator electromotive force).

According to Formulas (9) and (10), the expression for the derivatives of currents is:

$$\frac{d\vec{i}}{dt} = \left(\vec{U} - \mathbf{R}\vec{i} - \frac{\partial\mathbf{L}_{am}}{\partial\gamma_R}\vec{i}\,ap\Omega\right)\mathbf{L}_{am}^{-1}.$$

The expression for the rotation angle and rotation speed is written as:

$$\begin{array}{l} \frac{d\gamma_R}{dt} = p\Omega, \\ \frac{d\Omega}{dt} = \frac{T_e - T_L}{J}. \end{array} \quad (11)$$

where T_L—the load torque; T_e—the electromagnetic torque of 6PIM; and J—the inertia.

The equation for electromagnetic torque is written as:

$$T_e = \frac{3}{2}pL_m(i_{r\beta}i_{s\alpha} - i_{r\alpha}i_{s\beta}). \quad (12)$$

where $i_{s\alpha}, i_{s\beta}, i_{r\alpha}, i_{r\beta}$—the stator and rotor winding currents in the αβ reference frame determined by the following expressions:

$$\begin{aligned} i_{s\alpha} &= \tfrac{2}{3}\left[i_A \cos(0) + i_B \cos(\rho) + i_C \cos(2\rho) + i_X \cos\left(-\tfrac{\pi}{3}\right) + i_Y \cos\left(-\tfrac{\pi}{3} + \rho\right) + i_Z \cos\left(-\tfrac{\pi}{3} + 2\rho\right)\right], \\ i_{s\beta} &= \tfrac{2}{3}\left[i_A \sin(0) + i_B \sin(\rho) + i_C \sin(2\rho) + i_X \sin\left(-\tfrac{\pi}{3}\right) + i_Y \sin\left(-\tfrac{\pi}{3} + \rho\right) + i_Z \sin\left(-\tfrac{\pi}{3} + 2\rho\right)\right], \\ i_{r\alpha} &= \tfrac{2}{3}[i_a \cos(\gamma_R) + i_b \cos(\gamma_R - \rho) + i_c \cos(\gamma_R - 2\rho)], \\ i_{r\beta} &= \tfrac{2}{3}[i_a \sin(\gamma_R) + i_b \sin(\gamma_R - \rho) + i_c \sin(\gamma_R - 2\rho)]. \end{aligned} \tag{13}$$

The matrix of inductances for the 6PIM is written as:

$$\mathbf{L}_{am}(\gamma_R) = \begin{bmatrix} \mathbf{L}_{s1s1} & \mathbf{L}_{s1s2} & \mathbf{L}_{s1r} \\ \mathbf{L}_{s1s2}^T & \mathbf{L}_{s2s2} & \mathbf{L}_{s2r} \\ \mathbf{L}_{s1r}^T & \mathbf{L}_{s2r}^T & \mathbf{L}_{rr} \end{bmatrix}, \tag{14}$$

where the matrix of the self and mutual inductances for the stator (s1 and s2) and rotor windings (r) are:

$$\mathbf{L}_{s1s1} = \mathbf{L}_{s2s2} = \begin{bmatrix} 2L_m/3 + L_{\sigma1} & -L_m/3 & -L_m/3 \\ -L_m/3 & 2L_m/3 + L_{\sigma1} & -L_m/3 \\ -L_m/3 & -L_m/3 & 2L_m/3 + L_{\sigma1} \end{bmatrix}, \mathbf{L}_{rr} = \begin{bmatrix} 2L_m/3 + L_{\sigma2} & -L_m/3 & -L_m/3 \\ -L_m/3 & 2L_m/3 + L_{\sigma2} & -L_m/3 \\ -L_m/3 & -L_m/3 & 2L_m/3 + L_{\sigma2} \end{bmatrix}, \tag{15}$$

the matrix of mutual inductances between the stator windings are:

$$\mathbf{L}_{s1s2} = \frac{2}{3}\begin{bmatrix} L_m \cos\left(\frac{\pi}{3}\right) & L_m \cos\left(\frac{\pi}{3} + \rho\right) & L_m \cos\left(\frac{\pi}{3} - \rho\right) \\ L_m \cos\left(\frac{\pi}{3} - \rho\right) & L_m \cos\left(\frac{\pi}{3}\right) & L_m \cos\left(\frac{\pi}{3} + \rho\right) \\ L_m \cos\left(\frac{\pi}{3} + \rho\right) & L_m \cos\left(\frac{\pi}{3} - \rho\right) & L_m \cos\left(\frac{\pi}{3}\right) \end{bmatrix}, \tag{16}$$

and the matrix of mutual inductances between the stator and rotor windings are:

$$\begin{aligned} \mathbf{L}_{s1r} &= \tfrac{2}{3}\begin{bmatrix} L_m \cos(\gamma_R) & L_m \cos(\gamma_R + \rho) & L_m \cos(\gamma_R - \rho) \\ L_m \cos(\gamma_R - \rho) & L_m \cos(\gamma_R) & L_m \cos(\gamma_R + \rho) \\ L_m \cos(\gamma_R + \rho) & L_m \cos(\gamma_R - \rho) & L_m \cos(\gamma_R) \end{bmatrix}, \\ \mathbf{L}_{s2r} &= \tfrac{2}{3}\begin{bmatrix} L_m \cos\left(\gamma_R - \frac{\pi}{3}\right) & L_m \cos\left(\gamma_R - \frac{\pi}{3} + \rho\right) & L_m \cos\left(\gamma_R - \frac{\pi}{3} - \rho\right) \\ L_m \cos\left(\gamma_R - \frac{\pi}{3} - \rho\right) & L_m \cos\left(\gamma_R - \frac{\pi}{3}\right) & L_m \cos\left(\gamma_R - \frac{\pi}{3} + \rho\right) \\ L_m \cos\left(\gamma_R - \frac{\pi}{3} + \rho\right) & L_m \cos\left(\gamma_R - \frac{\pi}{3} - \rho\right) & L_m \cos\left(\gamma_R - \frac{\pi}{3}\right) \end{bmatrix}. \end{aligned} \tag{17}$$

As was shown in Section 2, the presence of spatial harmonics leads to the appearance of time-harmonic components in the magnitude of the MMF in the air gap according to Expression (6). To take these harmonics to account, this paper proposes to define the magnetizing inductance of the 6PIM by introducing the time-harmonic components according to the following equation:

$$L_m = L_0 + L_6 \cos(6\omega t) + L_{12} \cos(12\omega t). \tag{18}$$

where L_0—the magnitude of the zero harmonic; L_6—the magnitude of the 6th harmonic; and L_{12}—the magnitude of the 12th harmonic.

4. Experimental Test Bench

The prototype of the symmetrical 6PIM was created by the authors and has been used to analyze the spatial harmonic influence and verify the adequacy of the developed mathematical model. The scheme of the machine-winding distribution in the stator slots is shown in Figure 2. The parameters of 6PIM are: nominal power—1.5 kW, synchronous speed—3000 rpm.

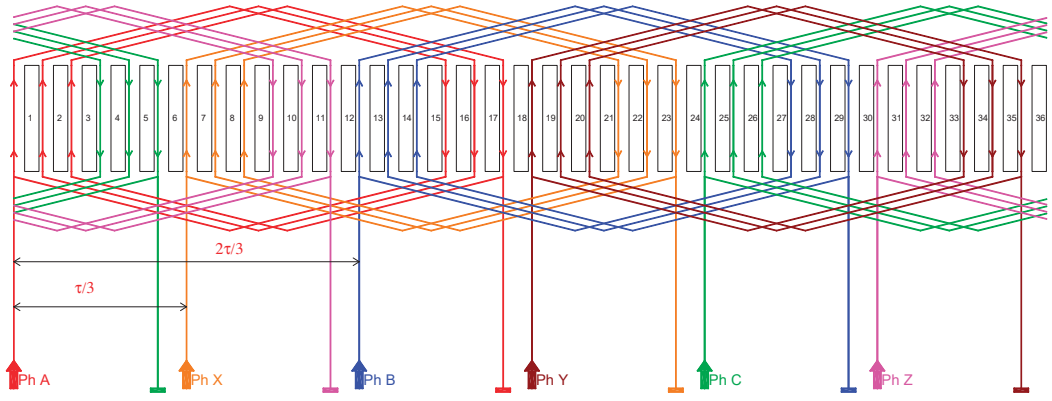

Figure 2. Winding scheme of the symmetrical 6PIM.

The experimental test bench is developed for the experimental study of the symmetrical 6PIM. The test bench consists of the prototype of the symmetrical 6PIM, power transformers PT1 and PT2, which supply the stator windings of the machine, a permanent magnet synchronous generator and an electrical DC load (Figure 3). The three-phase voltages of the PT1 and PT2 secondary windings are shifted by 60 electrical degrees.

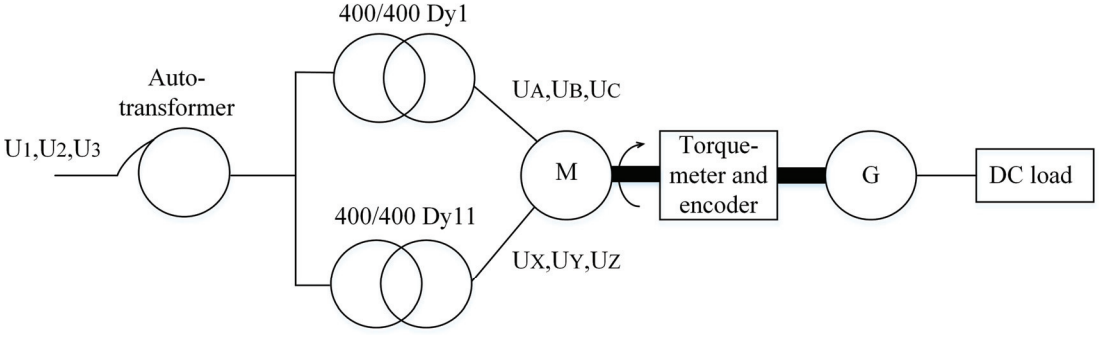

Figure 3. Block diagram of the experimental test bench with symmetrical 6PIM.

A prototype of the symmetrical 6PIM is shown in Figure 4.

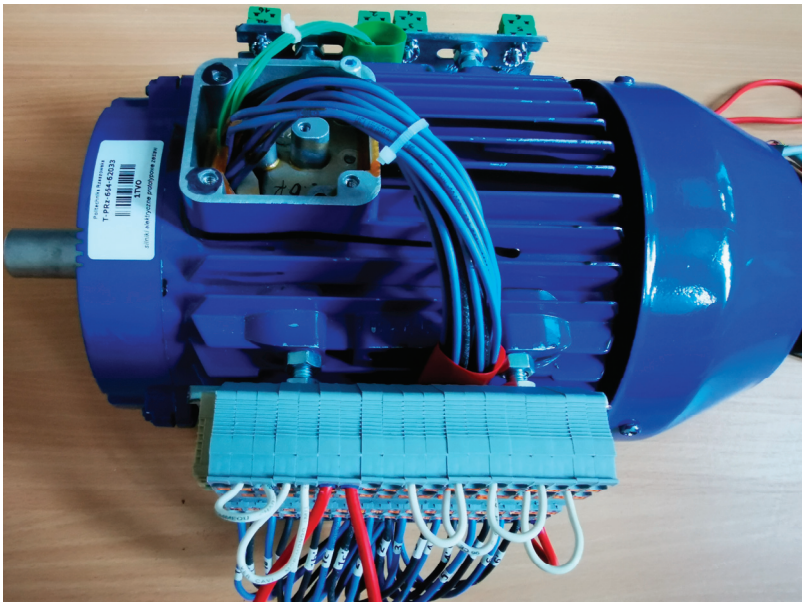

Figure 4. Prototype of the symmetrical 6PIM.

5. Experimental and Simulation Results

For checking the adequacy of the developed mathematical model of the symmetrical 6PIM, a comparison of the experimental results and the results of the mathematical modeling of the stator currents for normal and fault modes is conducted. The normal modes of the 6PIM are the 10% load (Figure 5) and the nominal load (Figure 6). The fault mode of the 6PIM is the three-phase ABC open fault (Figure 7). In this case, the winding supply voltage is purely sinusoidal. The 6PIM parameters used for the simulation are: $P_N = 1.5$ kW, $U_N = 400$ V, $I_N = 1.43$ A, n = 2812 rpm, $T_N = 5.04$ Nm, $L_{\sigma 1} = 0.06$ H, $L'_{\sigma 2} = 0.01$ H, $L_m = 1.3$ H, $R_1 = 8.0$ Ohm, $R'_2 = 4.0$ Ohm, and J = 0.015 kg·m^2.

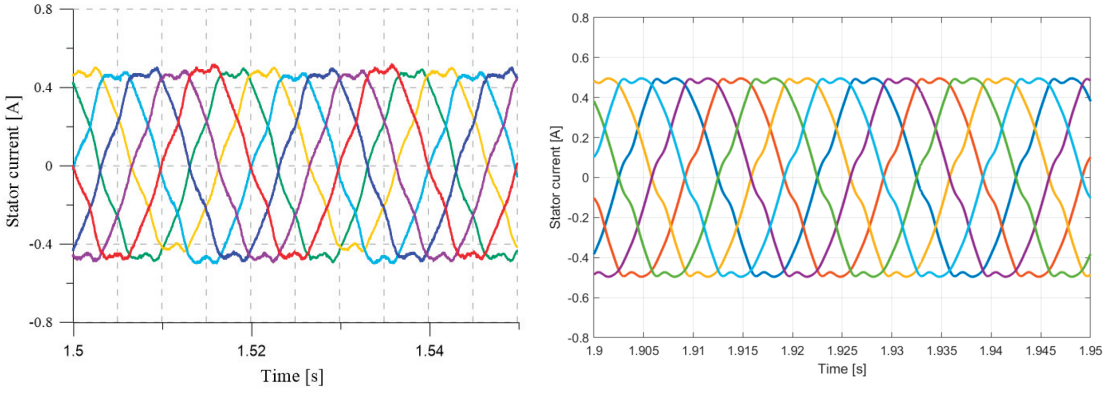

(**a**) (**b**)

Figure 5. Stator current of the 6PIM for the 10% load: (**a**) the experiment, (**b**) the simulation (the phase currents of the windings are marked with different colors here and further).

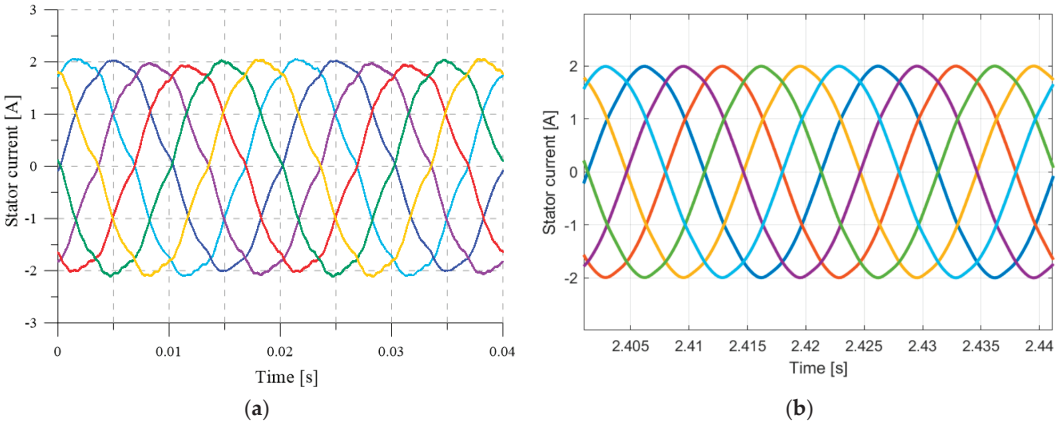

Figure 6. Stator currents of the 6PIM in the steady-state mode for the nominal load: (**a**) the experiment, (**b**) the simulation.

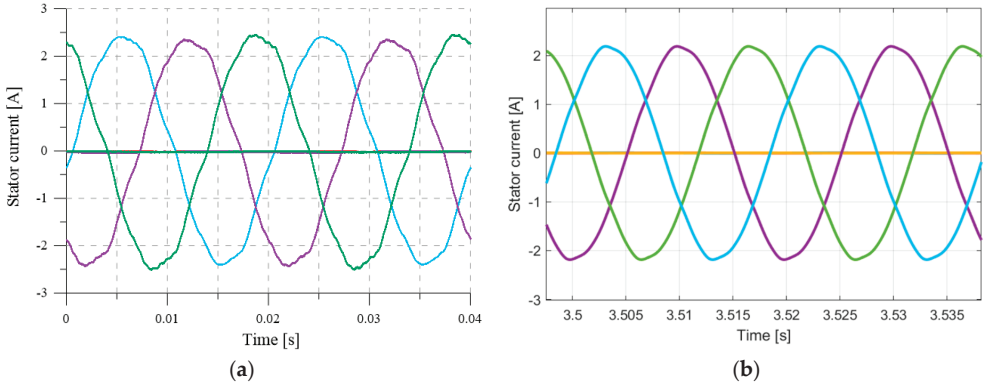

Figure 7. Stator currents of the 6PIM in the steady-state mode for the 50% load and three-phase ABC open fault: (**a**) the experiment, (**b**) the simulation.

The non-sinusoidal shape of the stator current of the 6PIM in all specified modes in the case of the sinusoidal winding supply voltage is explained by presence of the spatial harmonics winding distribution (magnetic flux in the air gap) and, accordingly, the non-sinusoidal stator electromotive force. In this case, the experimental and simulation results show that the high harmonic content of the stator current depends on the machine load (the load increase improves the current curve). The current curve is improved in the case of illumination of the influence for the one three-phase winding.

A detailed comparison of the experimental results and the results of the calculation using the developed mathematical model (Figure 8) shows the high coincidence of the instantaneous values of the currents, which confirms the adequacy of the model and the method used in terms of identifying the spatial harmonic influence on the electromagnetic processes. The maximum deviation of the calculated values from the experimental values occurs for the 10% machine load when the current distortions are at their maximum (Figure 8a). However, this deviation is not greater than 10%, which is an acceptable result.

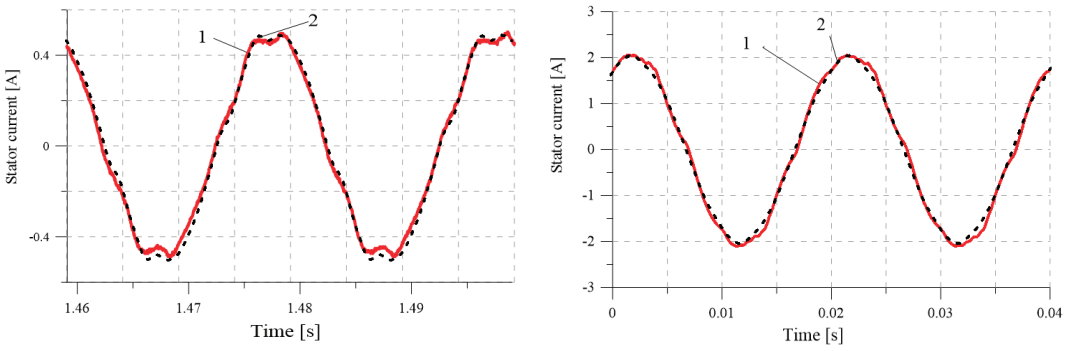

Figure 8. Stator currents of 6PIM in the steady-state mode: (**a**)—for the 20% load, (**b**)—for the nominal load, 1—the experimental result (red solid line), 2—the simulation result (black dashed line).

The deviation of the simulation and experimental results for the nominal load is smaller, at 3% (Figure 8b). The maximum deviation of the simulation and experimental results for the single winding mode (three-phase ABC open fault) is 8%.

The harmonical analysis for the stator current of the symmetrical 6PIM shows the presence of the 5th, 7th and 11th, and 13th harmonics (higher harmonics can be neglected) in the stator current in all modes (Figures 9 and 10), which are caused by the presence of spatial harmonics in the winding function. The high harmonic magnitude depends on the load. The magnitude of the 5th harmonic is 4.18 from the first (fundamental) harmonic for the 10% machine load and 0.86% from the first harmonic for the nominal load (Figure 9). The magnitude of the 5th harmonic is 1.18% from the first harmonic for the three-phase ABC open fault (Figure 10).

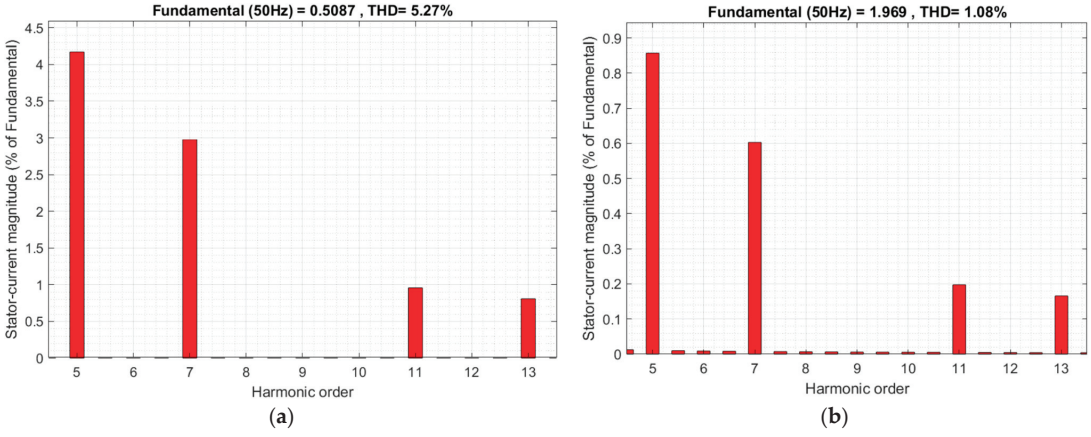

Figure 9. High harmonic spectrum of the 6PIM stator current (**a**)—for the 10% load, (**b**)—for the nominal load.

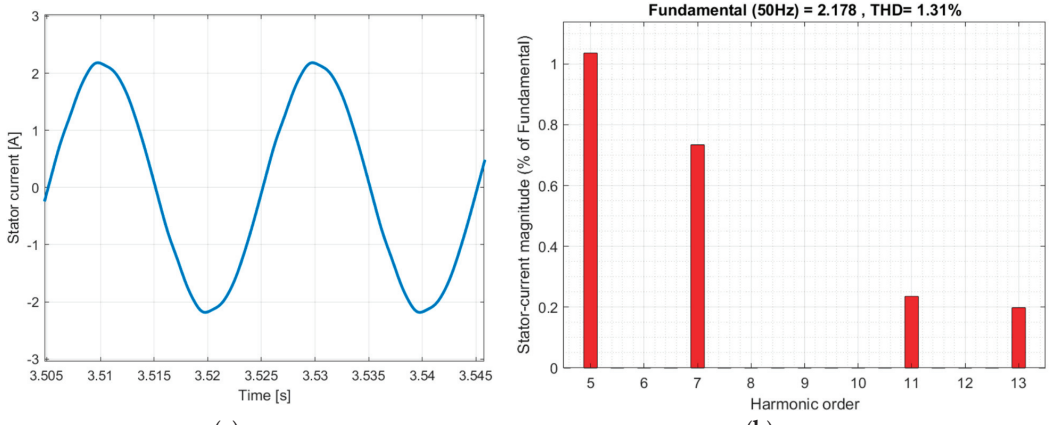

(**a**) (**b**)

Figure 10. (**a**) Stator current of the 6PIM for the 50% load and the three-phase ABC open fault and (**b**) the high harmonic spectrum.

The non-sinusoidal stator current causes the ripples of the 6PIM electromagnetic torque. The curve and harmonic analyses of the 6PIM electromagnetic torque for the described modes are shown in Figures 11–13.

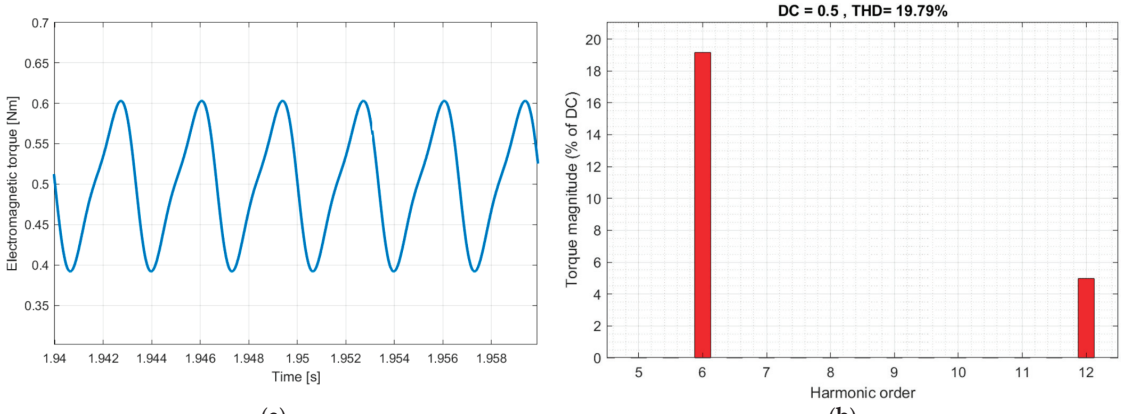

(**a**) (**b**)

Figure 11. (**a**) Electromagnetic torque of the 6PIM for the 10% load and (**b**) the high harmonic spectrum of the electromagnetic torque.

The harmonical analyses for the electromagnetic torque of the symmetrical 6PIM shows the presence of the 6th and 12th harmonics in the electromagnetic torque that agrees with the analytical description in Section 2. It is of note that the magnitude of the 6th harmonic is 19.16% from the zero harmonic for the 10% load mode (Figure 11) and 2.25% from the zero harmonic for the nominal load (Figure 12). The magnitude of the 6th harmonic is 2.51% from the zero harmonic for the three-phase ABC open fault and 50% load (Figure 13).

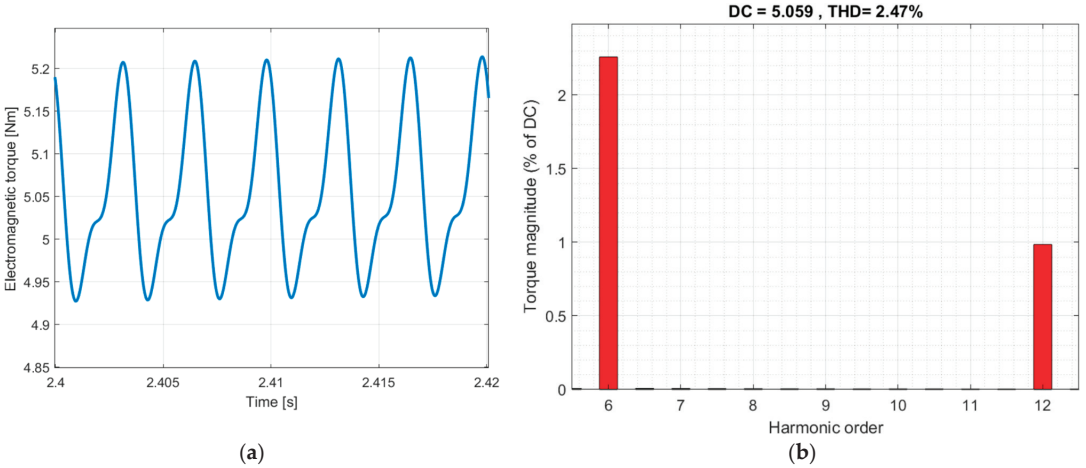

Figure 12. (**a**) Electromagnetic torque of the 6PIM in the steady-state mode for the nominal load and (**b**) the high harmonic spectrum of the electromagnetic torque.

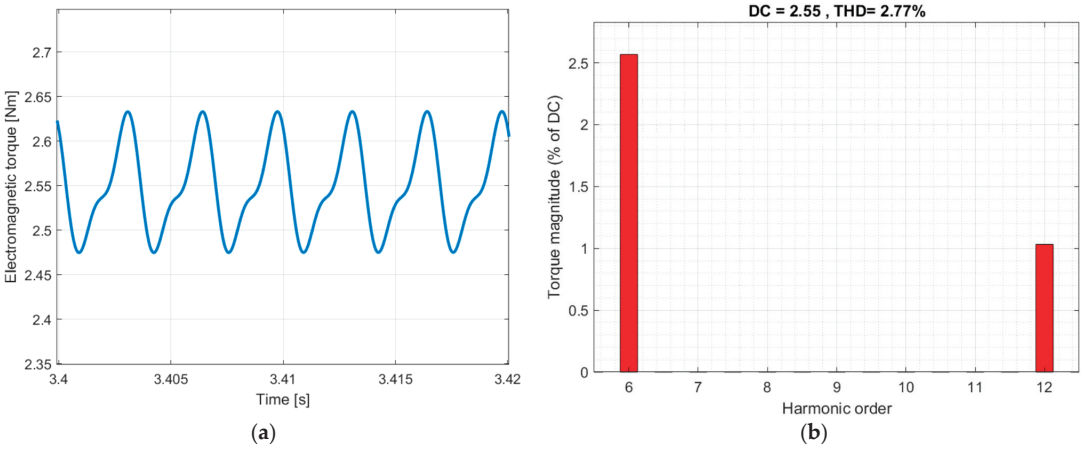

Figure 13. (**a**) Electromagnetic torque of the 6PIM in the steady-state mode for the 50% load and the three-phase ABC open fault and (**b**) the high harmonic spectrum of the electromagnetic torque.

The harmonic spectrum of the stator current and the electromagnetic torque for the 10% load mode of the symmetrical 6PIM is shown in Table 1.

The comparison results of the total harmonic distortion (THD) in the stator current and the electromagnetic torque of the symmetrical 6PIM are shown in Table 2.

The simulation results for the start-up of the symmetrical 6PIM with nominal load are shown in Figures 14 and 15. As in the case of the three-phase IM, there are significant pulsations of the electromagnetic torque; their magnitude is four times greater than the nominal value of the torque (Figure 14).

Table 1. Harmonic spectrum of the stator current and the electromagnetic torque for 10% load mode of the 6PIM (missing harmonics are not shown in the table).

Harmonic Order	Stator Current Harmonic Magnitude, %	Electromagnetic Torque Harmonic Magnitude, %
0	0	100
1	100	0
5	4.17	0
6	0	19.18
7	2.98	0
11	0.96	0
12	0	4.92
13	0.81	0
17	0.02	0
18	0	0.12

Table 2. THD of the 6PIM stator current and electromagnetic torque.

Mode of 6PIM	THD,%	
	Stator Current	Electromagnetic Toque
10% load mode	5.27	19.79
nominal load	1.08	2.47
50% load and three open-phase ABC fault	1.13	2.77

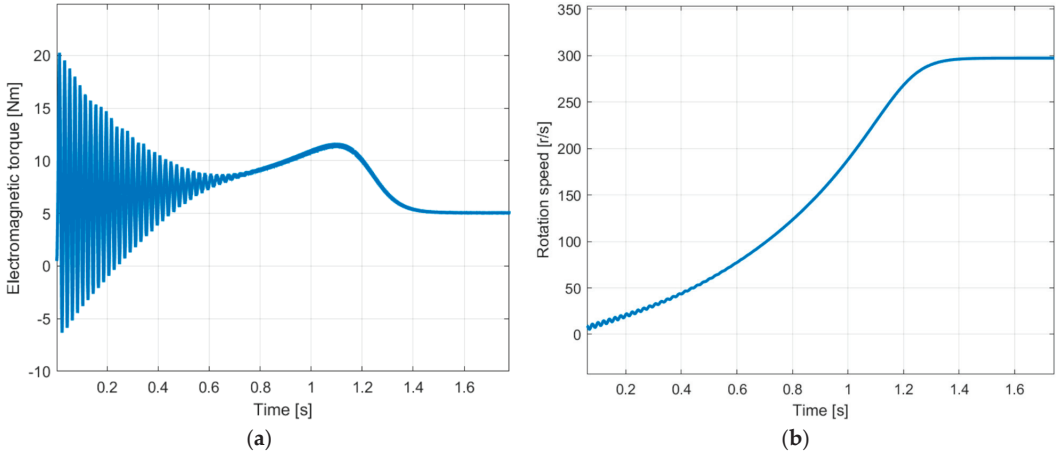

(**a**) (**b**)

Figure 14. (**a**) Electromagnetic torque and (**b**) rotation speed of the 6PIM in the transient mode for the nominal load.

The stator and rotor currents of the 6PIM are shown in Figure 11.

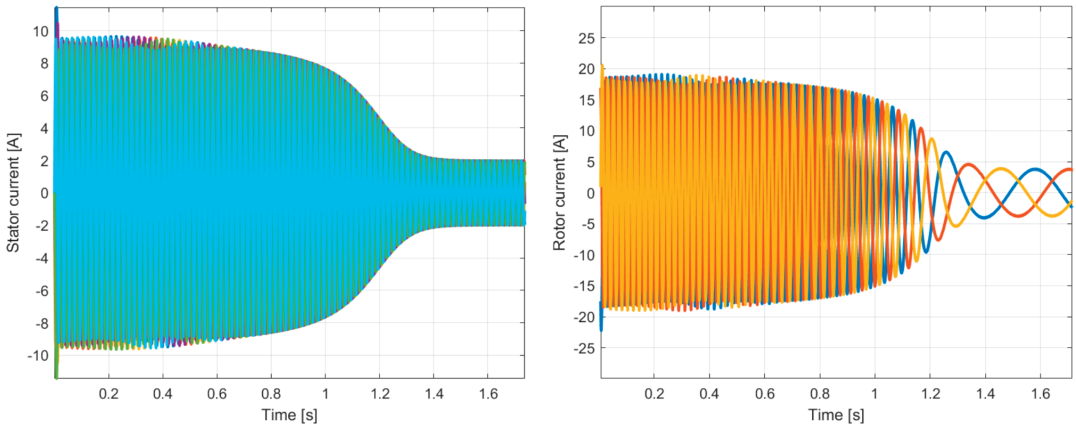

(**a**) (**b**)

Figure 15. (**a**) Stator currents and (**b**) rotor currents of the 6PIM in the transient mode for the nominal load.

6. Conclusions

The design of the IM does not allow the sinusoidal spatial distribution of the winding coil to be provided. This distribution is described as the winding function, which contains the first (fundamental) harmonic and the 5th, 7th, 11th and 13th harmonics. It is analytically shown that the interaction between the 5th and 7th spatial harmonics of the winding function of the symmetrical 6PIM and the 1st time harmonic of the winding supply leads to the appearance of the 6th time harmonic in the magnitude of the MMF and in the electromagnetic moment. Similarly, the interaction between the 11th and 13th spatial harmonics of the winding function and the 1st time harmonic of the winding supply leads to the appearance of the 12th time harmonic in the magnitude of the MMF and in the electromagnetic moment.

The experimental study of the prototype of the symmetrical 6PIM shows the distortion of the 6PIM currents in the case of the sinusoidal winding supply. This distortion is caused by the influence of spatial harmonics. The analysis of the harmonic content has proven the presence of the 5th, 7th, 11th and 13th harmonics in the stator current. The THD of the stator current is increased in the case of a reduction in the IM load. The THD of the stator current is reduced in the case of a three-phase ABC open fault.

The developed mathematical model for the electrical circuits of the symmetrical 6PIM using the AVIS method is characterized by a high calculation speed and takes into account the influence of the spatial harmonics by introducing the harmonic components into the model parameters. The adequacy of the mathematical model was proven by the comparison of the experimental and simulation results for the stator currents. The maximum deviation of the instantaneous values for the experimental and simulation results is 10%.

The greatest influence of the spatial harmonics on the IM electromagnetic torque is noticeable for small loads (for the investigated machine, THD = 19.79 by 10% load). This requires the use of methods for compensate for the influence of spatial harmonics in 6PIM due to the winding design and the winding supply scheme, which may be the subject of further research.

Author Contributions: Conceptualization, A.K. and M.K.; data curation, M.S.; formal analysis, A.K.; funding acquisition, M.K.; investigation, M.K. and M.S.; methodology, M.S.; project administration, M.K.; resources, M.K. and M.N.; software, M.S.; supervision, M.K.; validation, A.K. and M.K.; visualization, M.K.; writing—original draft, M.S.; writing—review and editing, A.K. All authors have read and agreed to the published version of the manuscript.

Funding: This research was financed in part by the statutory funds (UPB) of the Department of Electrodynamics and Electrical Machine Systems, Rzeszow University of Technology, and in part by the Ministry of Education and Science of the Republic of Poland within the "Regional Initiative of Excellence" program for the years 2019–2023. Project number 027/RID/2018/19; amount granted: PLN 11 999 900.

Data Availability Statement: Not applicable.

Conflicts of Interest: The authors declare no conflict of interest.

References

1. Levi, E. Editorial—Special Issue on Multi-Phase Motor Drives. *EPE J.* **2004**, *14*, 4.
2. Levi, E. Advances in converter control and innovative exploitation of additional degrees of freedom for multiphase machines. *IEEE Trans. Ind. Electron.* **2016**, *63*, 433–448. [CrossRef]
3. Shchur, I.; Jancarczyk, D. Electromagnetic Torque Ripple in Multiple Three-Phase Brushless DC Motors for Electric Vehicles. *Electronics* **2021**, *10*, 3097. [CrossRef]
4. Barrero, F.; Duran, M.J. Recent advances in the design, modeling and control of multiphase machines—Part 1. *IEEE Trans. Ind. Electron.* **2016**, *63*, 449–458. [CrossRef]
5. Bojoi, R.; Farina, F.; Profumo, F.; Tenconi, A. Dual-Three Phase Induction Machine Drives Control—A Survey. *IEEJ Trans. Ind. Appl.* **2006**, *126*, 420–429. [CrossRef]
6. Levi, E.; Barrero, F.; Duran, M.J. Multiphase machines and drives—Revisited. *IEEE Trans. Ind. Electron.* **2016**, *63*, 429–432. [CrossRef]
7. Bojoi, R.; Caponet, M.C.; Grieco, G.; Lazzari, M.; Tenconi, A.; Profumo, F. Computation and measurements of the DC link current in six-phase voltage source PWM inverters for AC motor drives. In Proceedings of the Power Conversion Conference, Osaka, Japan, 2–5 April 2002; pp. 953–958. [CrossRef]
8. Levi, E. Multiphase Electric Machines for Variable-Speed Applications. *IEEE Trans. Ind. Electron.* **2008**, *55*, 1893–1909. [CrossRef]
9. Guzman, H.; Gonzalez, I.; Barrero, F.; Durán, M. *Open-Phase Fault Operation on Multiphase Induction Motor Drives. Induction Motors—Applications, Control and Fault Diagnostics*; IntechOpen: London, UK, 2015. [CrossRef]
10. Munim, W.N.W.A.; Duran, M.J.; Che, H.S.; Bermúdez, M.; González-Prieto, I.; Rahim, N.A. A Unified Analysis of the Fault Tolerance Capability in Six-Phase Induction Motor Drives. *IEEE Trans. Power Electron.* **2017**, *32*, 7824–7836. [CrossRef]
11. Benbouzid, M.E.H.; Diallo, D.; Zeraoulia, M. Advanced Fault-Tolerant Control of Induction-Motor Drive for EV/HEV Traction Applications: From Conventional to Modern and Intelligent Control Techniques. *IEEE Trans. Veh. Tech.* **2007**, *56*, 519–528. [CrossRef]
12. Gan, C.; Li, X.; Yu, Z.; Ni, K.; Wang, S.; Qu, R. Modular Seven-Leg Switched Reluctance Motor Drive With Flexible Winding Configuration and Fault-Tolerant Capability. *IEEE Trans. Transp. Electrif.* **2022**. [CrossRef]
13. Xiaodong, L.; Yilmaz, L. Harmonic analysis for induction motors. In Proceedings of the IEEE CCECE/CCGEIJ, Ottawa, ON, Canada, 7–10 May 2006; pp. 172–176. [CrossRef]
14. Park, S.-H.; Chin, J.-W.; Cha, K.-S.; Ryu, J.-Y.; Lim, M.-S. Investigation of AC Copper Loss Considering Effect of Field and Armature Excitation on IPMSM With Hairpin Winding. In Proceedings of the IEEE Transactions on Industrial Electronics, Singapore, 16–19 October 2023. [CrossRef]
15. Kabir, M.A.; Jaffar, M.Z.M.; Wan, Z.; Husain, I. Design and experimental evaluation of a multilayer AC winding configuration for sinusoidal MMF with shorter end-turn length. In Proceedings of the 2017 IEEE Energy Conversion Congress and Exposition, Cincinnati, OH, USA, 1–5 October 2017; pp. 5834–5839. [CrossRef]
16. Toliyat, H.A.; Lipo, T.A. Analysis of concentrated winding induction machines for adjustable speed drive applications-experimental results. *IEEE Trans. Energy Convers.* **1994**, *9*, 695–700. [CrossRef]
17. El-Refaie, A.M.; Shah, M.R. Comparison of Induction Machine Performance with Distributed and Fractional-Slot Concentrated Windings. In Proceedings of the 2008 IEEE Industry Applications Society Annual Meeting, Edmonton, AL, Canada, 5–9 October 2008; pp. 1–8. [CrossRef]
18. Neto, L.M.; Camacho, J.R.; Salerno, C.H.; Alvarenga, B.P. Analysis of a three-phase induction machine including time and space harmonic effects: The a, b, c reference frame. *IEEE Trans. Energy Convers* **1999**, *14*, 80–85. [CrossRef]
19. Abdel-Khalik, A.S.; Masoud, M.I.; Ahmed, S.; Massoud, A.M. Effect of Current Harmonic Injection on Constant Rotor Volume Multiphase Induction Machine Stators: A Comparative Study. *IEEE Trans. Ind. Appl.* **2012**, *48*, 2002–2013. [CrossRef]
20. Stincescu, R.B.; Viarouge, P.; Cros, J.; Kamwa, I. A general approach of space and time harmonics interactions in induction motors. In Proceedings of the IEEE International Electric Machines and Drives Conference, Hartford, CO, USA, 17–20 May 1999; pp. 366–368. [CrossRef]
21. Sapena-Bano, A.; Martinez-Roman, J.; Puche-Panadero, R.; Pineda-Sanchez, M.; Perez-Cruz, J.; Riera-Guasp, M. Induction machine model with space harmonics for the diagnosis of rotor eccentricity, based on the convolution theorem. *Int. J. Electr. Power Energy Syst.* **2020**, *117*, 105625. [CrossRef]

22. Sapena-Bano, A.; Martinez-Roman, J.; Puche-Panadero, R.; Pineda-Sanchez, M.; Perez-Cruz, J.; Riera-Guasp, M. Induction machine model with space harmonics for fault diagnosis based on the convolution theorem. *Int. J. Electr. Power Energy Syst.* **2018**, *100*, 463–481. [CrossRef]
23. Lin, F.; Zuo, S.; Deng, W. Impact of rotor eccentricity on electromagnetic vibration and noise of permanent magnet synchronous motor. *J. Vibroeng.* **2018**, *20*, 923–935. [CrossRef]
24. Kutsyk, A.; Korkosz, M.; Semeniuk, M.; Bogusz, P.; Lozynskyy, A.; Kozyra, J.; Łukasik, Z. Electromagnetic and Electromechanical Compatibility Improvement of a Multi-Winding Switch Control-Based Induction Motor—Theoretical Description and Mathematical Modeling. *Energies* **2022**, *15*, 8038. [CrossRef]
25. Gonzalez-Prieto, A.; Gonzalez-Prieto, I.; Yepes, A.G.; Duran, M.J.; Doval-Gandoy, J. Symmetrical Six-Phase Induction Machines: A Solution for Multiphase Direct Control Strategies. In Proceedings of the 22nd IEEE International Conference on Industrial Technology, Shanghai, China, 22–25 August 2021; pp. 1362–1367. [CrossRef]
26. Vukosavic, S.N.; Jones, M.; Levi, E.; Varga, J. Rotor fux oriented control of a symmetrical six-phase induction machine. *Electr. Power Syst. Res.* **2005**, *75*, 142–152. [CrossRef]
27. Nabi, H.P.; Dadashi, P.; Shoulaie, A. A novel structure for vector control of a symmetrical six-phase induction machine with three current sensors. In Proceedings of the 10th International Conference on Environment and Electrical Engineering, Rome, Italy, 8–11 May 2011; pp. 1–5. [CrossRef]
28. Mezani, S.; Laporte, B.; Takorabet, N. Complex finite element computation of induction motors with consideration of space harmonics. In Proceedings of the IEEE International Electric Machines and Drives Conference, Madison, MI, USA, 1–4 June 2003; Volume 1, pp. 264–268. [CrossRef]
29. Oliveira, F.T.; Donsion, M.P. A finite element model of an induction motor considering rotor skew and harmonics. *Renew. Energy Power Qual. J.* **2017**, *15*, 119–122. [CrossRef]
30. Carbonieri, M.; Bianchi, N.; Alberti, L. Induction motor mapping using rotor field-oriented analysis technique. In Proceedings of the 2019 IEEE Energy Conversion Congress and Exposition, Baltimore, ML, USA, 29 September–3 October 2019; pp. 2321–2328. [CrossRef]
31. Leonardo, L.D.; Popescu, M.; Tursini, M.; Parasiliti, F.; Carbonieri, M. Transient Modeling of Induction Motors considering Space Harmonics. In Proceedings of the 2020 International Conference on Electrical Machines, Gothenburg, Sweden, 23–26 August 2020; pp. 2553–2559. [CrossRef]
32. Plakhtyna, O.; Kutsyk, A.; Lozynskyy, A. Method of average voltages in integration step: Theory and application. *Electr. Eng.* **2020**, *102*, 2413–2422. [CrossRef]
33. Plakhtyna, O.; Kutsyk, A.; Semeniuk, M. An analysis of fault modes in an electrical power-generation system on a real-time simulator with a real automatic excitation controller of a synchronous generator. *Elektrotehniski Vestn. Electrotech. Rev.* **2019**, *86*, 104–109.
34. Kutsyk, A.; Lozynskyy, A.; Vantsevitch, V.; Plakhtyna, O.; Demkiv, L. A Real-Time Model of Locomotion Module DTC Drive for Hardware-In-The-Loop Implementation. *Przegląd Elektrotechniczny* **2021**, *97*, 60–65. [CrossRef]
35. Kuznyetsov, O. Mathematical model of a three-phase induction machine in a natural abc reference frame utilizing the method of numerical integration of average voltages at the integration step and its application to the analysis of electromechanical systems. *Math. Probl. Eng.* **2019**, *2019*, 4581769. [CrossRef]
36. Kłosowski, Z. The analysis of the possible use of wind turbines for voltage stabilization in the power node of MV line with the use of a real-time simulator. *Przegląd Elektrotechniczny* **2015**, *1*, 20–27. (In Polish)
37. Kutsyk, A.; Semeniuk, M.; Korkosz, M.; Podskarbi, G. Diagnosis of the Static Excitation Systems of Synchronous Generators with the Use of Hardware-In-the-Loop Technologies. *Energies* **2021**, *14*, 6937. [CrossRef]
38. Lozynskyy, A.; Kozyra, J.; Łukasik, Z.; Ku´smi´nska-Fijałkowska, A.; Kutsyk, A.; Paranchuk, Y.; Kasha, L. A Mathematical Model of Electrical Arc Furnaces for Analysis of Electrical Mode Parameters and Synthesis of Controlling Influences. *Energies* **2022**, *15*, 1623. [CrossRef]

machines

MDPI

Article

Design and Implementation of a Low-Cost and Low-Power Converter to Drive a Single-Phase Motor

Hudson V. Coutinho [1], Jose A. Toledo [1], Leonardo A. R. Silva [2] and Thales A. C. Maia [3,*]

[1] Graduate Program in Electrical Engineering, Universidade Federal de Minas Gerais, Av. Antônio Carlos 6627, Belo Horizonte 31270-901, MG, Brazil; huvico@ufmg.br (H.V.C.); jtoledoj@ufmg.br (J.A.T.)
[2] Department of Telecommunications and Mechatronics Engineering, Universidade Federal de São João del-Rei, Rod. MG 443 Km 7, Ouro Branco 36420-000, MG, Brazil; leonardo@ufsj.edu.br
[3] Departament of Electrical Engineering, Universidade Federal de Minas Gerais, Av. Antônio Carlos 6627, Belo Horizonte 31270-901, MG, Brazil
* Correspondence: thales@ufmg.br

Abstract: This research introduces a cost-effective converter for single-phase machines, aiming to enhance efficiency and reduce energy consumption in retrofit applications. Single-phase motors commonly found in household appliances often suffer from low efficiency, resulting in wasted energy. To tackle this problem, a dedicated converter was proposed to replace the existing capacitors and improve the motor performance. This study presents a proof of concept for retrofit applications, discussing the converter design methodology and prototype evaluation. Additionally, a cost analysis comparing single-phase and three-phase motors is included. It aims to demonstrate the long-term cost savings and improved energy efficiency of the proposed converter. The findings highlight the converter's potential as a promising solution for enhancing energy efficiency and decreasing costs in single-phase motor applications.

Keywords: efficiency; household appliances; low-cost converter; market survey; single-phase induction motor; power electronics; micro-power module

Citation: Coutinho, H.V.; Toledo, J.A.; Silva, L.A.R.; Maia, T.A.C. Design and Implementation of a Low-Cost and Low-Power Converter to Drive a Single-Phase Motor. *Machines* **2023**, *11*, 673. https://doi.org/10.3390/machines11070673

Academic Editors: Loránd Szabó and Feng Chai

Received: 4 May 2023
Revised: 11 June 2023
Accepted: 19 June 2023
Published: 21 June 2023

1. Introduction

Fossil fuels represent the primary source of energy worldwide, accounting for approximately two-thirds of global energy production [1]. The consumption rates of these fuels have been steadily increasing, particularly in countries experiencing industrial and demographic expansion, with annual growth rates ranging from 1% to 2% [2]. Nevertheless, this surge in demand has resulted in a corresponding escalation in CO_2 emissions [3], intensifying global apprehensions regarding climate change and prompting renewed endeavors to enhance energy efficiency, including that of electric motors.

Electric motors play a crucial role in global energy demand, accounting for approximately 40% of energy consumption [4]. Among various types of motors, single-phase motors represent approximately 9% of industrial demand [5] and nearly half of residential electric consumption [6,7]. They are commonly used in appliances such as washing machines, refrigerators, and air conditioners, as well as in air compressors, pumping systems, and other types of machinery [5,8]. However, their efficiency and torque ripple are compromised at a low load due to load variation [9].

Single-phase motors suffer from a low starting torque and low efficiency, resulting in significant energy waste. Even motors with 1 horsepower or more exhibit an efficiency of only 78% [10]. As a result, in many instances, single-phase motors are oversized in order to meet the high starting torque requirements, leading to low-load operation and a reduced efficiency. Therefore, enhancing the efficiency of these applications is critical in order to reduce energy consumption.

The utilization of frequency inverters and innovative control methods has the potential to significantly enhance performance and reduce losses [11]. By adopting this technology, energy consumption can be reduced by up to 30%. Studies have demonstrated that air conditioners can achieve efficiencies of up to 51.7% depending on the duty cycle and climatic conditions [12,13]. However, it is important to note that this solution is more suitable for new equipment that employs three-phase permanent magnet motors and may not be financially feasible for retrofit applications utilizing single-phase motors.

According to the literature, employing a frequency inverter with rotation measurement can lead to a significant reduction in energy consumption, such as up to 43% with a single-phase motor [14]. However, the incorporation of a rotation sensor may increase costs, and the availability of symmetrical coils can be limited. To address these challenges, a more versatile control approach has been proposed, capable of handling asymmetrical coils [15–17] and enabling sensorless control by estimating the motor's variables [18].

Replacing a single-phase motor with a three-phase motor may not be an attractive option for several reasons. Firstly, many existing single-phase motors are still in good operating condition [19]. Secondly, residential power supply is typically provided in a single phase, not in three phases. Therefore, utilizing a dedicated frequency inverter for driving a single-phase motor can be a viable alternative, provided that the cost of the converter is low, compatible with the power level, and offers a good performance.

With the continuous decline in the cost of semiconductors [20], the development of inexpensive and specialized converters to enhance the energy efficiency and performance of single-phase motors is becoming increasingly feasible. These converters have the potential to replace the capacitors commonly used with single-phase motors as they contribute to the overall cost without providing substantial improvements. By adopting these new converters, significant advancements can be made in terms of cost-effectiveness and energy savings, leading to even greater benefits.

This paper presents a design methodology for a low-cost and low-power converter dedicated to driving single-phase motors, with the aim of improving the efficiency of household appliances. The research includes a simulation and experimental validation of the prototype on a test bench, as well as a market survey to evaluate the feasibility of the proposed converter in comparison to the price difference between single-phase and three-phase motors. The primary focus of the work is to provide a technological proof of concept with a specific emphasis on retrofit applications, while also presenting the methodology for converter development.

2. Problem Statement and Relevance

Single-phase induction motors are extensively utilized in low-power applications, representing nearly 90% of all electric motors in the global stock, with an estimated 2 billion motors rated up to 750 W [21]. These motors are commonly found in various household appliances, including refrigerators, air conditioners, washing machines, dryers, microwaves, heat pump systems, and hydraulic pumping equipment. In rural areas, where consumers bear the cost of electrification, the supply of electricity is typically limited to single-phase power, making these motors indispensable for irrigation and artesian well systems.

Single-phase motors are favored not only for their compatibility with household appliances [6,7] but also due to their cost-effectiveness compared to three-phase motors. However, single-phase motors have inherent limitations in terms of efficiency and are susceptible to high torque ripple as a result of their operating principle [9].

2.1. Motors Benchmarking

To evaluate the economic feasibility, a simplified price analysis of single-phase and three-phase motors based on the Brazilian market is presented. The objective was to assess the power range suitable for a single-phase converter. For this market survey, Figure 1 shows the prices of 161 motors with 4 poles and power ranging from 1/4 to 10 hp, among 4 different brands. It is important to note that there is a significant price

variation due to various motor classifications based on the degree of internal protection (IP). To obtain a median value from a homogeneous set, the IP classification was not considered in this analysis.

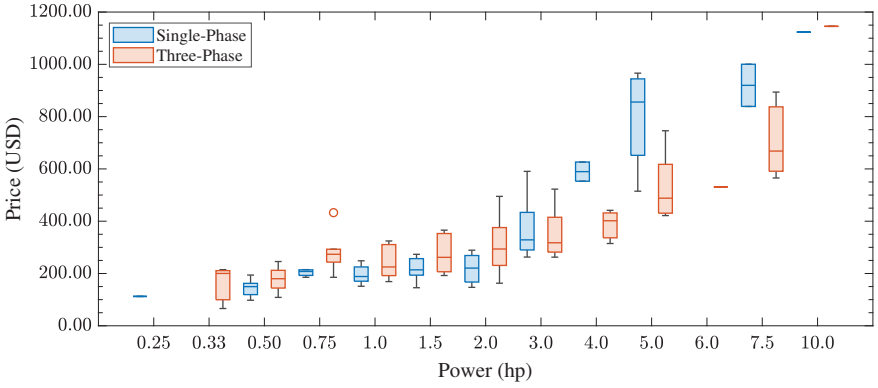

Figure 1. Comparative study of prices of single- and three-phase four-pole motors for different powers, computed on 12 October 2022.

Figure 2a shows the median prices for each shaft power and for each motor type, whereas Figure 2b shows the price difference between both motors type for some shaft power. It is noteworthy that, for low power ratings up to 2 hp, the single-phase motor is more affordable than the three-phase motor, thus reinforcing the notion that single-phase motors remain economically advantageous for such applications.

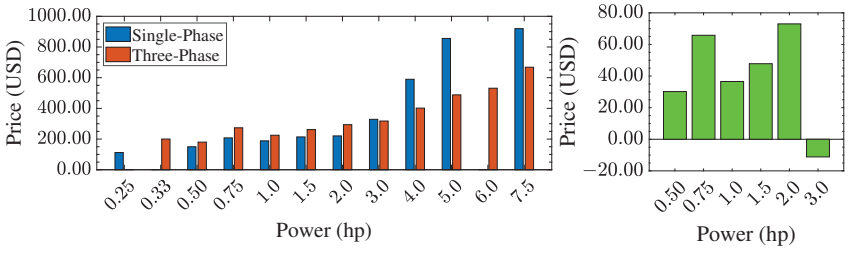

Figure 2. Price comparison between the power of four-pole single- and three-phase motors. (**a**) Median price. (**b**) Price difference.

It is worth noting that, even in households with access to a three-phase power supply, which represent a minority, the addition of a cheap converter is justified by the price difference between low-power single-phase and three-phase motors. It is more advantageous to drive a single-phase motor using the converter compared to directly starting a three-phase motor. For instance, in the case of a 1 hp motor, converters priced up to USD 37.00 become financially appealing.

It is important to emphasize that the market survey presented solely considers the equipment acquisition cost and does not account for the operating cost, which is ultimately borne by the consumer. However, when considering the efficiency gains and potential energy savings, the overall return on investment is expected to be even more favorable.

2.2. Motor and Converter Technologies

To operate a single-phase motor using the voltage grid, a capacitor is required to induce a phase-shift in the current, enabling the generation of a rotating magnetic field [22]. However, variations in the capacitor's aged value can cause cogging torque, thereby

reducing the motor's efficiency even under rated load conditions. Furthermore, the motor may experience efficiency losses if the load falls below its rated value.

In typical scenarios, single-phase motors are directly powered by the mains voltage. However, achieving speed control necessitates voltage variation through the use of a rheostat, which is inefficient and reduces the available torque. To enhance efficiency and drive flexibility, static converters can be employed. These converters allow for speed and torque variation in the motor through control strategies aimed at optimizing efficiency or maximizing torque [14,23,24].

The three most commonly used converter topologies for driving single-phase motors are the dual half-bridge, three half-bridge, and dual full-bridge configurations [25]. By employing a space vector pulse width modulation (SVPWM) technique, the converter can generate voltage space vectors within the regions depicted in Figure 3. These regions encompass the range of desired voltage V^* that can be synthesized by the converter, which differs from the three-phase case.

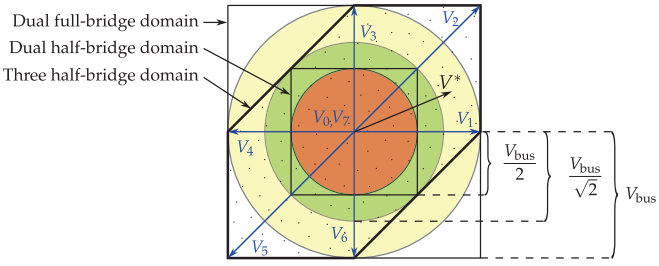

Figure 3. Illustrative drawing of three different domains applied to the single-phase converter.

In the case of the three half-bridge topology, there are eight possible switching combinations that result in voltages V_0 to V_7. By appropriately sequencing these voltages during the switching period, the desired voltage can be achieved. To maintain a constant motor torque, the voltage V^* should remain within the domain circle. For instance, with the three half-bridge converter, it is capable of synthesizing any voltage within the shaded region. However, to ensure constant torque, the voltage should not exceed the limit defined by the green circle.

The dual half-bridge topology is a cost-effective option as it utilizes only four switches. It employs a DC voltage bus with two capacitors that create a central neutral point, which is connected to the winding's neutral point. However, this topology has the drawback of providing a low output voltage magnitude of $V_{bus}/2$ (represented by the red circle in Figure 3) and is unable to generate a zero-voltage vector. Additionally, to achieve symmetrical voltages, the capacitors must be identical, which can be challenging due to the different physical characteristics of the auxiliary and main motor windings. This results in asymmetric currents flowing through the capacitors and leads to different voltages across each capacitor. Therefore, compensation techniques are necessary in the switching control to address this issue [18].

Another topology option is to use a full-bridge configuration for each winding, which requires eight switches. Although this topology is more expensive compared to others, it effectively utilizes the DC bus voltage and generates a first-order output voltage magnitude of V_{bus} (represented by the yellow circle in Figure 3). Furthermore, each coil is fed independently, resulting in an uncoupled system. This topology has been studied in various works, such as [26,27]. Additionally, an elliptical SVPWM technique has been proposed to generate any unbalanced two-phase output voltage for feeding an asymmetrical bi-phase induction motor. This technique helps to reduce pulsations in electromagnetic torque, leading to an improved speed control [28].

In this paper, the most commonly used topology, shown in Figure 4, was employed. This topology utilizes three half-bridges with six switches to achieve an output voltage

magnitude of $V_{bus}/\sqrt{2}$ (represented by the green circle in Figure 3) [29]. This topology has been widely studied and applied in various academic papers, including those focused on field-oriented control strategies [14], direct torque control in symmetrical two-phase motors [30], rotor-flux-oriented control considering asymmetric coils and torque cogging elimination [18] (without cost and efficiency analysis), and slip frequency control with constant V/f using a feedback encoder [31].

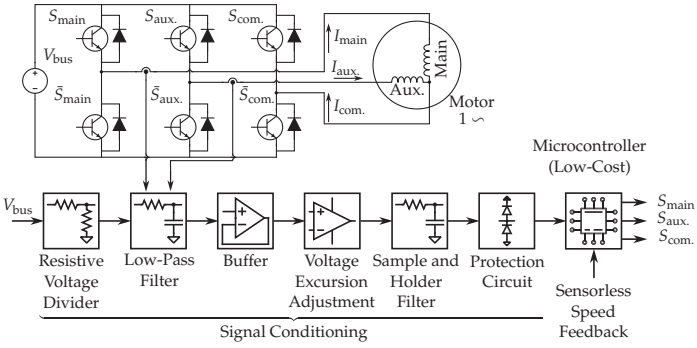

Figure 4. Illustrative schematic of the power converter components that are integrated to drive a single-phase motor.

It is worth noting that, in the presented topology, the common leg functions as a virtual neutral point and carries a higher current compared to the other legs due to the summation of the two currents [28]. This characteristic should be taken into consideration when sizing the electronic switches to ensure that they can handle the required current. Furthermore, power modules integrated with the six switches are widely available, enabling the design of a compact and simplified converter, which adds to the attractiveness of this topology for converter design.

3. Methodology

When designing a converter, it is necessary to determine the voltage and current requirements in order to calculate the rated output and input power, as well as the switching frequency and operation mode. The specification of components is based on factors such as voltage drop, thermal behavior, and impedance. The design methodology is an interactive process, as illustrated in Figure 5, that involves iterative checks on operating parameters, transients, and thermal behavior to meet the cost target and ensure proper functionality.

The steps discussed earlier were evaluated in the specification of the converter topology. The schematic diagram shown in Figure 4 is divided into two sections: the power circuit and the signal circuit. The rectified voltage from the DC bus is supplied to the input of the three-phase IGBT integrated module, along with the six PWM signals that control the activation of the switches. Two output currents from the converter are measured using Hall effect sensors, and the corresponding voltage signals are conditioned and made available to the signal circuit. These voltage signals are then processed and prepared for use at the inputs of a microcontroller, along with the measurement of the DC bus voltage. The microcontroller performs signal processing and generates the PWM signals to control the electronic switches.

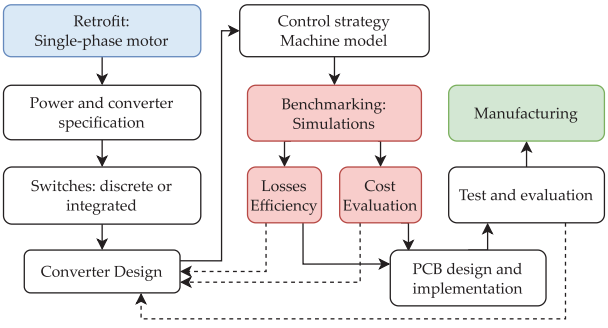

Figure 5. The main steps of the converter design methodology for achieving a satisfactory design result for manufacturing.

4. Converter Design

In this work, the objective was to design a cost-effective converter that fulfills the specific requirements outlined in Table 1. The converter is intended to be used for powering low-power household appliances. To achieve this objective, the converter design was optimized to minimize costs while ensuring that all the necessary requirements were met.

Table 1. Requirements for the converter design.

Group	Requirement
Cost	Meets the Low-Cost Features
Specifications	Works on a mains voltage up to 220 Vac/60 Hz Feeds a load of up to 1 hp
Switches	Integrated three-phase IGBT module with heat sink
Sensors	Measures two output currents with Hall sensors Measures the voltage bus with a resistive divider
Control	Conditions the output signals to microcontrollers Maximum switching of 5 kHz

4.1. Specification of the DC Bus Components and IGBT Module

Indeed, the DC bus plays a crucial role in power electronics systems, and its design should not be overlooked. To address issues such as total harmonic distortion (THD) and power factor improvement, more advanced filtering techniques can be employed. These filters help to reduce harmonics and improve the overall quality of the input power waveform [32]. Additionally, at higher power levels, the presence of leakage inductance between the grid and the rectifier input can result in significant voltage drops. It is important to consider these factors during the design process to ensure the proper functioning and efficiency of the converter.

The choice of an integrated diode rectifier bridge for converting the 127–220 AC voltage into DC voltage is a common and practical solution. The specified current rating of 25 A at 60 Hz indicates the capability of the rectifier bridge to handle the expected current requirements of the load, which, in this case, corresponds to a load of 1 hp.

When designing the filter, the cost of the capacitor is an important consideration. Research has shown that the cost of a capacitor is directly proportional to its volume [33]. Additionally, the rated voltage of the capacitor also affects its volume. Consequently, a converter designed to operate at a lower DC bus voltage will require a smaller and more affordable capacitor compared to a higher voltage level. In this case, an electrolytic capacitor with a voltage rating of 450 V was selected, taking into account its availability and affordability.

An integrated module with IGBTs was chosen for the converter design due to its suitability for household appliances, cost-effectiveness, and compact size. The selected module features three half-bridge IGBTs with reverse conduction capability provided by a monolithic diode. It is rated for a maximum current of 20 A, which meets the requirements for driving low-power household appliances. By utilizing this integrated module, the design achieves the desired functionality while optimizing space utilization and cost efficiency.

4.2. Specification of the Heat Sink

Proper thermal calculation is crucial for designing the heat sink of static switches and evaluating the thermal conditions during operation to prevent semiconductor failure and damage. It is important to note that the maximum output power in a steady state is determined by the switching frequency and output current of the converter.

Estimating the junction temperature of the devices can be accomplished by modeling the current and voltage transients in the switches and analyzing the thermal effects during overload pulses. However, the calculation can be simplified by focusing on steady-state conditions, which provide a good approximation of the device's thermal behavior [34].

The designed converter model underwent simulation to obtain the current and voltage values in each IGBT for the steady-state condition, as well as the switching times. The total losses were calculated using the IGBT parameters provided in the datasheet. To model the thermal conditions in the steady state, a thermal circuit, as shown in Figure 6, was employed [35,36]. Subsequent simulations were conducted to determine the required thermal resistance of the heat sink in order to maintain the junction temperature within a safe limit of 140 °C, as depicted in Figure 7.

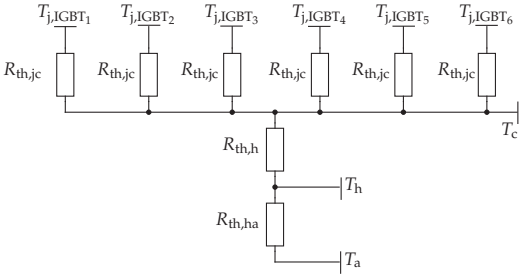

Figure 6. Simplified thermal equivalent circuit applied to the thermal analysis.

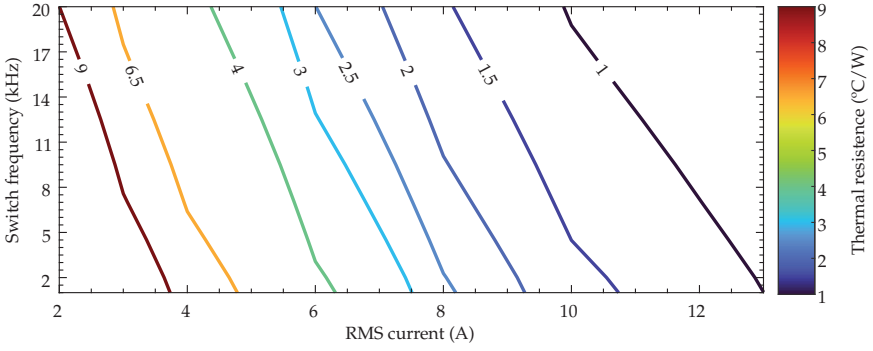

Figure 7. Maximum thermal resistance depending on switching frequency and output current.

Based on the results presented in Figure 7, a heat sink with dimensions of 56 × 30 × 20 mm and a thermal resistance of 5.33 °C/W was selected. Subsequent simulations were conducted to observe the junction temperature in the steady state as a function of output current and switching frequency, considering the chosen heat sink. The results are illus-

trated in Figure 8. It should be noted that using a fan in conjunction with the heat sink can reduce the equivalent thermal resistance and enhance thermal exchange with the environment, thereby allowing for a higher output current. However, increasing the switching frequency reduces the maximum current that the converter can sustain.

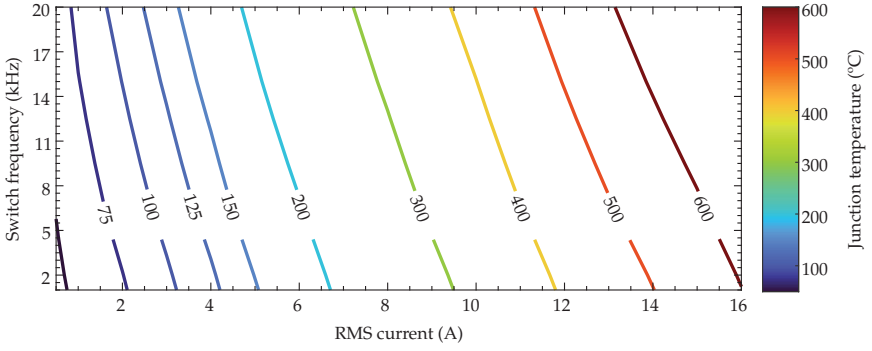

Figure 8. Maximum junction temperature depending on switching frequency and output current.

4.3. Specification of the DC Bus and Output Current Signals Conditioning Circuit

The circuit schematics are depicted in Figure 9. To condition the voltage, a resistive voltage divider was employed, followed by a low-pass filter to filter out any high-frequency components. The resulting signal was then buffered and fine-tuned by the excursion adjustment circuit. Subsequently, the processed output voltage was fed into the microcontroller for further processing. The circuit diagram specifically designed for voltage measurement is shown in Figure 9a.

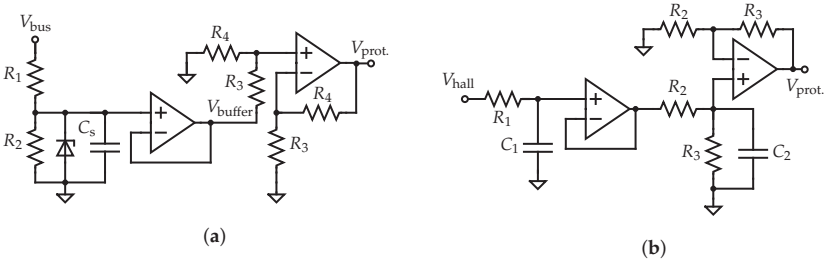

Figure 9. Schematic of a voltage and current signal conditioner circuit to measure the DC bus voltage and the main and auxiliary winding currents. (**a**) Voltage conditioner. (**b**) Current conditioner.

To ensure the reliability and prevent excessive voltage-related failures of the surface mount device (SMD)-type resistors, the resistive divider R_1 was constructed using resistors connected in series. This arrangement effectively reduces the voltage across the terminals of each resistor. Furthermore, a capacitor was incorporated into the resistive divider to filter out high-frequency components and minimize noise above the cut-off frequency. To provide additional protection against voltage surges, a Zener diode was included in the circuit. This diode acts as a voltage clamp, limiting the maximum voltage that can be applied to the circuit and offering an extra layer of safeguarding.

The system utilizes Hall effect transducers to measure two of the output currents, whereas the third current is estimated by summing the other two measurements. One notable advantage of these transducers is their ability to provide electrical isolation between the measured circuit and their output. This feature eliminates concerns related to common-mode voltage and enhances the accuracy and reliability of the current measurements.

As depicted in Figure 9b, the transducer voltage V_{hall} first undergoes low-pass filtering before being buffered. Subsequently, the buffered voltage is adjusted by the voltage excursion adjustment circuit to ensure accurate measurement within the desired range.

The resulting output voltage is then accessible to the microcontroller for further processing, similar to the bus voltage measurement described earlier.

4.4. Specification of the Protection Circuit and Auxiliary Voltage Sources

To safeguard the microcontroller pins and prevent damage, a protection circuit with a diode clamper was incorporated. This circuit limits the voltage levels applied to the microcontroller, preventing potential overvoltage situations. Furthermore, a sample-and-hold capacitor was integrated into the circuit design to minimize any signal interference and provide stable voltage levels during sampling.

In order to provide the necessary auxiliary voltage to power both modules and microcontrollers, an AC/DC converter module was employed. By utilizing pre-designed modules, the design time and costs associated with developing a custom power supply circuit were significantly reduced. This makes the use of modules an attractive option, allowing for a streamlined and cost-effective implementation in this application.

4.5. Design of the Control Loop

To minimize torque pulsation in single-phase motors, it is crucial to implement a control strategy that specifically addresses motor asymmetry. One effective approach is rotor flux-oriented control, which involves a mathematically derived treatment of motor currents. The references [18,37] provide detailed insights and results regarding the implementation of this control strategy, enabling other researchers to further investigate and clarify the expected performance under various operating conditions. These references serve as valuable resources for understanding and optimizing the control loop for reducing torque pulsation in single-phase motors.

The torque produced by the motor depends on various factors, including the number of pole pairs (P), the rotor inductance (l_r), the mutual inductance ($\mathcal{M}$), the stator current (i_s), and the rotor flux (ϕ_r). The torque can be defined as follows:

$$T_\mathrm{e} = \frac{P}{l_\mathrm{r}}(\mathcal{M}_\mathrm{q} i_\mathrm{sq} \phi_\mathrm{rd} - \mathcal{M}_\mathrm{d} i_\mathrm{sd} \phi_\mathrm{rq}). \tag{1}$$

It is worth noting that the oscillatory term can be effectively compensated for by setting the ratio of the rotor flux components $|\phi_\mathrm{rd}|/|\phi_\mathrm{rq}| = 1$ and the ratio of the stator current components $|i_\mathrm{sd}|/|i_\mathrm{sq}| = \mathcal{M}_\mathrm{d}/\mathcal{M}_\mathrm{q}$. This compensation approach is based on the turns ratio (k) between the auxiliary and main windings and allows for the adjustment of current amplitudes.

For the purpose of this study, the introduction of auxiliary currents i_sd1 and i_sq1, as well as the correction factor $k = \mathcal{M}_\mathrm{d}/\mathcal{M}_\mathrm{q}$, allows for addressing the asymmetry in the motor system. By assuming that the imposed motor currents are given by $i_\mathrm{sd} = i_\mathrm{sd1}$ and $i_\mathrm{sq} = k \cdot i_\mathrm{sq1}$, we can substitute them into Equation (1) to obtain an equivalent torque equation that resembles a symmetrical motor system. The resulting equation

$$T_\mathrm{e} = \frac{P}{l_\mathrm{r}} \mathcal{M}_\mathrm{d} (i_\mathrm{sq1} \phi_\mathrm{rd} - i_\mathrm{sd1} \phi_\mathrm{rq}) \tag{2}$$

eliminates torque pulsation and yields a rotor behavior that is similar to that of a three-phase machine referenced on the dq axis.

This control strategy for a motor system utilizing field orientation of the rotor flux was simulated. In this method, the control input references are the motor torque and flux. The direct and quadrature motor currents were subsequently calculated and imposed by the converter, as illustrated in Figure 10.

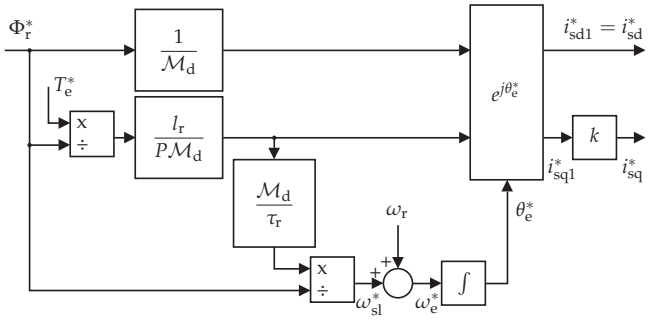

Figure 10. Block diagram of the field-oriented controller used in closed-loop torque control in an asymmetric single-phase motor.

This strategy was simulated to evaluate the efficiency map by considering a symmetrical and an asymmetrical motor (Figure 11a), as well as a capacitor-start motor (Figure 11b), including converter losses. The results are presented in Figure 11c. It is observed that there is an efficiency gain of up to 10%, depending on the load driven, when comparing a capacitor-driven motor and a control-loop-driven motor, considering both symmetric and asymmetric motor configurations. Additionally, it is noted that the symmetric motor outperforms the asymmetric motor in terms of efficiency across the entire power range.

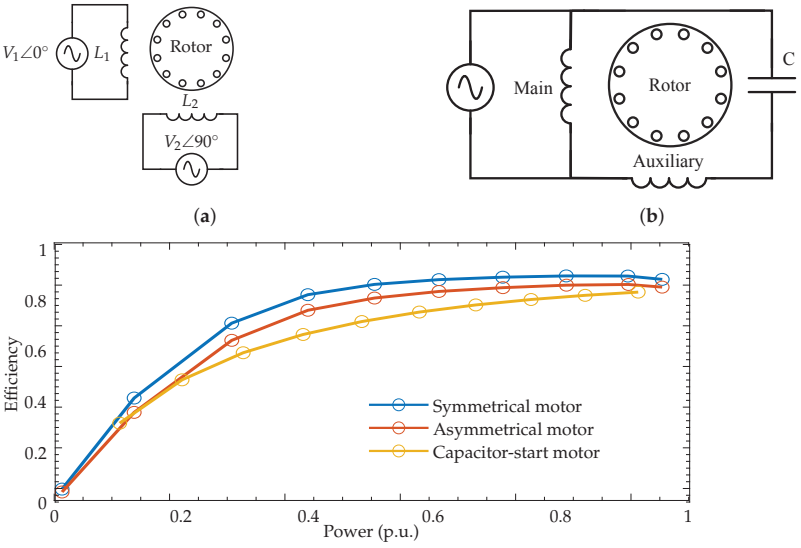

Figure 11. Comparison of the performance between an auxiliary capacitor drive and an inverter in function of the shaft load. (**a**) Symmetric and asymmetric motor. (**b**) Capacitor-start motor. (**c**) Motors efficiency map.

5. Experimental Results

The implemented converter, with a volume-to-power ratio of 660 mm^3/W, was used for the experimental tests shown in Figure 12. The test setup includes a 1 hp, 127 Vac, 2-pole single-phase induction machine manufactured by Eletroplas, a hydraulic pump, a LaunchPad from Texas Instruments with a TMS320F28379D processor, a multimeter for current and voltage measurement, a personal computer with Code Composer Studio, and an oscilloscope Hantek, model 6022bl.

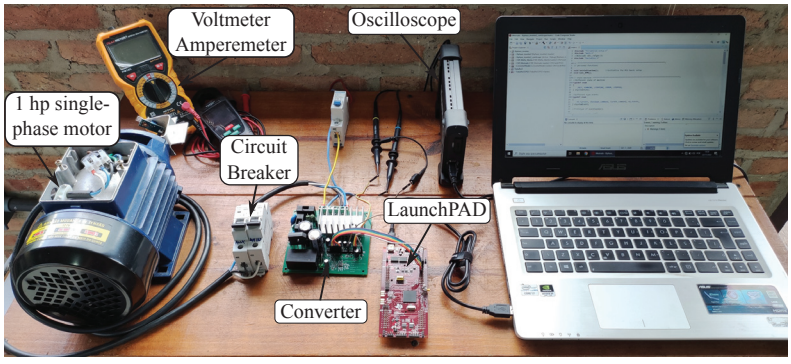

Figure 12. Complete setup used to collect the experimental results.

Initially, the motor was directly connected to the grid using its auxiliary capacitor, which drove the hydraulic pump coupled to its shaft. The steady-state grid voltage and current, as well as the auxiliary and main winding currents, are plotted in Figure 13. It was observed that the current distortion, caused by magnetic saturation, resulted in a significant THD in both the motor and grid currents. Table 2 presents the third, fifth, and seventh harmonic orders relative to the fundamental, as well as the calculated total THD.

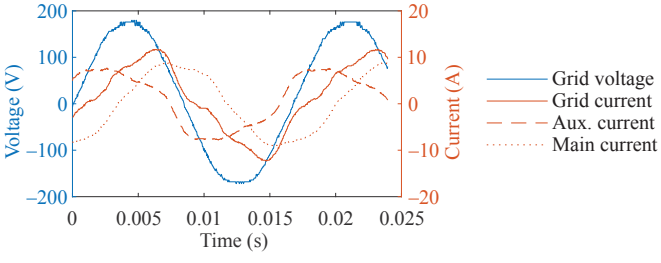

Figure 13. Grid voltage and current and auxiliary and main winding currents in a direct start using the auxiliary capacitor.

Table 2. Current magnitude of third, fifth, and seventh harmonic orders relative to the fundamental and total THD from main and auxiliary windings with rated load.

	With Inverter		**Direct Start**		
Order	**Main**	**Aux**	**Main**	**Aux**	**Grid**
3	14.73%	15.52%	4.95%	16.40%	15.27%
5	4.26%	4.06%	4.94%	7.79%	10.10%
7	1.22%	2.18%	0.94%	1.97%	0.65%
THD	16.06%	20.82%	7.30%	18.39	18.48%

Magnetic core saturation is often attributed to various factors, including the use of low-quality magnetic materials, inadequate design or operational conditions, and the presence of non-linear loads. These factors contribute to the saturation of the magnetic flux, resulting in increased core losses and a diminished magnetic performance. Consequently, the motor tends to draw a higher current than required.

Subsequently, the converter was connected to the 127 V/60 Hz grid source to operate the motor coupled with a hydraulic pump. In this experiment, an open-loop control strategy was employed with a 5 kHz PWM frequency for IGBT switching. The reference vector voltage was selected to follow a circular trajectory within the maximum allowable range, as depicted in Figure 3. The experimental outcomes, presented in Figure 14, display the main and auxiliary currents and voltages signals.

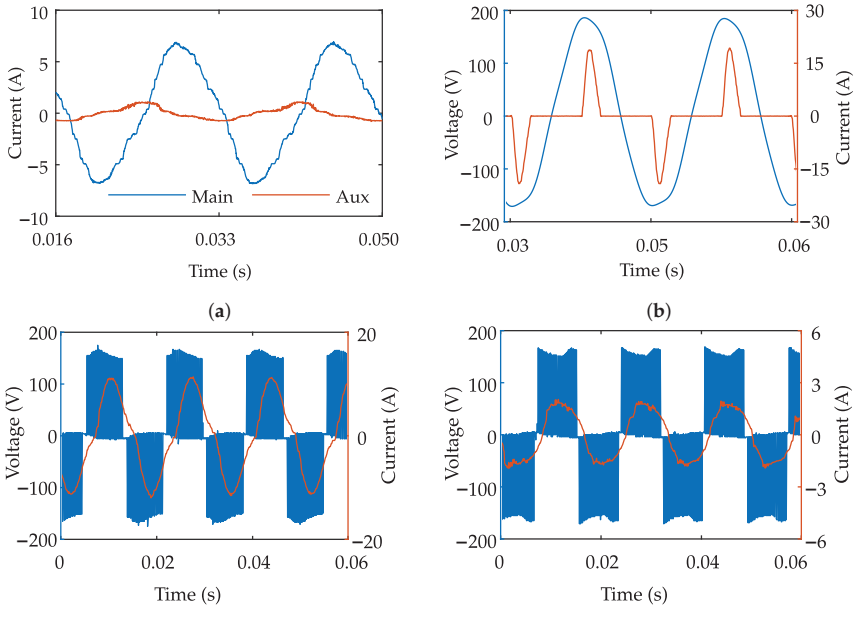

Figure 14. Current and voltage signals from converter driving the single-phase motor with a 5 kHz switching frequency. (**a**) Main and auxilary currents, no load. (**b**) Grid voltage and current, full pump load. (**c**) Main voltage and current, full pump load. (**d**) Aux. voltage and current, full pump load.

Initially, the motor was started with no load, using an open-loop V/f constant ramp until it reached a steady state, as presented in Figure 14a. Subsequently, a load was added to the rotor shaft by fully opening the discharge valve of the pump, allowing for water circulation. The signals corresponding to the full pump load are depicted in Figure 14b–d. The line current waveform shown in Figure 14b is typical of a full bridge rectifier but suffers from high peaks of 20 A and high THD due to the proposed low-cost solution [38]. The current waveforms in Figure 14c,d exhibit distortion due to the poor quality of the motor's magnetic material, as evidenced by the presence of third and fifth harmonics in Table 2.

The voltage fluctuations on the DC bus impose limitations on the achievable voltage vector domain and contribute to the harmonic content, creating a trade-off between THD and the utilization of the DC bus in the designed converter. To mitigate this distortion and improve the input current waveform toward a sine waveform, a DC voltage bus control method can be employed.

The current measurements also indicate the presence of high-frequency components, which are attributed to capacitive coupling between the measurement circuits and the PWM signals with high rates of the change in voltage (dV/dt) in the power circuits. These findings contribute valuable insights into the motor's behavior and the effectiveness of the control strategy within the specific experimental conditions of this study.

The grid supplied an approximate power of 519 W, whereas the converter delivered 478 W to the motor, with 7.4 A to the main winding and 1.3 A to the auxiliary winding. The converter itself consumed around 40 W, resulting in an efficiency of approximately 92%. It is important to note that the power did not reach the rated level, potentially due to limitations imposed by the characteristic curve of the pump.

6. Converter Cost

The estimated total cost of the designed converter is USD 27.81, as calculated from the itemized costs listed in Table 3. This cost does not include the microcontroller and its power supply. The most expensive components in the converter include the IGBT module, the PCB with SMD components, the current sensors, the DC capacitors, the AC-DC 15 V module, and the 3 V regulator. It is important to focus on reducing the cost of these components to enhance the overall cost-effectiveness of the converter.

Table 3. Components cost of the implemented converter.

Description	Part Number	Quantity	Price (USD)	
			Unity	Total
IGBT Power Module	IGCM20F60GA	1	6.80	6.80
PCB with SMD components	-	1	5.87	5.87
Hall Effect Current Sensor	ACS712ELCTR-20A-T	2	1.44	2.88
Aluminum Electrolytic Capacitors	450 V 220 µF	2	1.18	3.36
Power Modules AC-DC 15 V	TAS5-15-WEDT	1	2.80	2.80
Linear Voltage Regulators 3 V	TPS79730DCKT	1	2.19	2.19
Bridge Rectifiers	KBU2510	1	0.79	0.79
Aluminum Electrolytic Capacitors	35PX100MEFC6.3X11	10	0.06	0.63
Through-Hole Fuse Holders	FH1-200CK-B	2	0.29	0.57
Screw Terminal	JL500-50008GT1	1	0.51	0.51
Heat Sink	HS 5620	1	0.50	0.50
Diodes of General Purpose	BAS321,115	10	0.05	0.49
Unidirectional DO-201 TVS	1.5KE20A/B	2	0.19	0.38
Shunt Resistor 0.01 Ω (5 W)	-	2	0.18	0.37
Radial Leaded Varistors	STE14D431K1EN0FQB0R0	2	0.18	0.36
Operational Amplifier	LM358D	3	0.04	0.13
Unidirectional SOD-123F TVS	SMF5.0A	2	0.03	0.07
Aluminum Electrolytic Capacitors	KS226M035D07RR0VH2FP0	5	0.01	0.06
				27.81

In an open-loop control application, it is indeed possible to eliminate the current sensors and the 3 V regulator, leading to cost savings of approximately USD 5.00 per converter. This demonstrates the significance of thoroughly evaluating the design requirements and selecting components that fulfill those requirements at the lowest feasible cost. By further optimizing the converter's design and selecting components judiciously, it is possible to achieve additional cost savings without compromising performance and reliability.

The estimated cost provided was based on the prototype design, and it is reasonable to expect a significant reduction in cost when scaling up to mass production. Mass production typically benefits from economies of scale, streamlined manufacturing processes, and the bulk purchasing of components, resulting in lower per-unit costs. Therefore, the proposed solution becomes even more attractive in terms of cost-effectiveness when produced in large quantities.

7. Conclusions

This paper presents the design process of an affordable converter specifically tailored for driving low-power single-phase motors commonly found in household appliances. Recognizing the limited availability of converters for such motors, the design stages were meticulously examined and refined to ensure cost reduction. Through simulation and experimental validation, a prototype was successfully developed, achieving an efficiency of 92%. This low-cost converter holds great potential as a viable solution for retrofit applications seeking efficiency enhancements.

In contrast to the conventional approach of utilizing a direct motor drive in appliances to avoid additional costs associated with power converters, this study showcases the feasibility of constructing a cost-effective converter for single-phase motors. Furthermore,

employing such a converter can result in operational efficiency improvements and potentially enable the downsizing of the motor thanks to better power utilization within the system. Consequently, the investment in the converter can be justified over time through energy savings or the use of a smaller and more economical motor.

The thermal analysis conducted during the design process played a vital role in determining the operational limitations of the converter. Despite the IGBT module having a rated current capacity of 20 A, the actual maximum current was constrained by the cooling effectiveness of the module. The design did not incorporate a fan, relying solely on a heat sink for thermal dissipation. However, by incorporating a fan along with the heat sink, the thermal design can be enhanced, enabling the converter to drive more powerful motors with increased efficiency and reliability.

The suboptimal quality of single-phase motors often leads to the occurrence of magnetic core saturation during their operation. This saturation phenomenon gives rise to the generation of significant harmonic components in both the grid current and motor current, consequently leading to a reduction in overall efficiency and the presence of torque pulsations. By employing higher-quality magnetic materials in the construction of single-phase motors, it is possible to enhance their efficiency. Furthermore, the implementation of advanced control techniques, such as field-oriented control, can effectively mitigate the adverse effects of harmonic distortion and torque pulsations, thereby improving the overall performance of the motor.

Future work will encompass several aspects to further enhance the understanding and performance of the single-phase motor drive. This includes developing a comprehensive model of the single-phase machine to accurately represent its torque and rotation control characteristics. Additionally, the implementation of a back-to-back assembly will be pursued to validate the control algorithms and investigate the energy efficiency of the drive utilizing the designed converter.

The planned research will involve studying the motor's performance under various operating conditions, including normal operation as well as critical scenarios such as sudden load changes, power supply variations, and speed fluctuations. Detailed analysis will be conducted to examine efficiency, torque output, and speed waveforms in each scenario, providing valuable insights into the drive's performance.

In addition, there are plans to develop and implement a control strategy for the DC bus voltage to regulate and stabilize its level. Furthermore, the closed-loop control approach mentioned in this paper for mitigating torque pulsation will be implemented on the microcontroller. The objective is to assess the effects of this control approach on even harmonics and their correlation with motor asymmetry. Through the study and optimization of the control strategy, it is anticipated that the overall performance and efficiency of the single-phase motor drive system can be further improved.

Author Contributions: Conceptualization, H.V.C., J.A.T., L.A.R.S. and T.A.C.M.; Methodology, H.V.C., J.A.T., L.A.R.S. and T.A.C.M.; Software, H.V.C.; Validation, H.V.C.; Investigation, H.V.C.; Writing—original draft, H.V.C.; Writing—review & editing, J.A.T. and L.A.R.S.; Supervision, T.A.C.M.; Project administration, T.A.C.M. All authors have read and agreed to the published version of the manuscript.

Funding: This research received no external funding.

Data Availability Statement: Data sharing not applicable.

Conflicts of Interest: The authors declare no conflict of interest.

References

1. Rivera-Durán, Y.; Berna-Escriche, C.; Córdova-Chávez, Y.; Muñoz-Cobo, J.L. Assessment of a Fully Renewable Generation System with Storage to Cost-Effectively Cover the Electricity Demand of Standalone Grids: The Case of the Canary Archipelago by 2040. *Machines* **2023**, *11*, 101. [CrossRef]
2. Ritchie, H.; Roser, M. Energy Production and Consumption: Our World in Data. 2022. Available online: https://ourworldindata.org/energy-production-consumption (accessed on 11 March 2022).

3. BP. *Statistical Review of World Energy*; Technical Report; BP: London, UK , 2022.
4. Tiwari, D.; Miscandlon, J.; Tiwari, A.; Jewell, G.W. A Review of Circular Economy Research for Electric Motors and the Role of Industry 4.0 Technologies. *Sustainability* **2021**, *13*, 9668. [CrossRef]
5. Sauer, I.L.; Tatizawa, H.; Salotti, F.A.; Mercedes, S.S. A Comparative Assessment of Brazilian Electric Motors Performance with Minimum Efficiency Standards. *Renew. Sustain. Energy Rev.* **2015**, *41*, 308–318. [CrossRef]
6. Abrahão, K.C.F.J.; Souza, R.G.V. Estimativa da evolução do uso final de energia elétrica no setor residencial do Brasil por região geográfica. *Ambiente Constr.* **2021**, *21*, 383–408. [CrossRef]
7. EPE. *Anuário Estatístico de Energia Elétrica 2020—Ano Base 2019*; Technical Report, Empresa de Pesquisa Energética (EPE): Brasilia, Brazil, 2020.
8. de Rossiter Corrêa, M.B.; Jacobina, C.B.; Lima, A.M.N.; Silva, E.R.C. Motor Drive System For Single-phase Induction Motors—An Evaluation. *Eletrônica Potência* **2003**, *8*, 79–88. [CrossRef]
9. Um, D.Y.; Park, G.S. Comparison of Electromagnetic Characteristics of Single-Phase Induction Motor between Balanced and Unbalanced Operation under Different Loads. *Energies* **2021**, *14*, 919. [CrossRef]
10. Chasiotis, I.; Karnavas, Y.; Scuiller, F. Effect of Rotor Bars Shape on the Single-Phase Induction Motors Performance: An Analysis toward Their Efficiency Improvement. *Energies* **2022**, *15*, 717. [CrossRef]
11. Tan, D. Power Electronics: Historical Notes, Recent Advances and Contemporary Challanges. *Eletrônica Potência* **2020**, *25*, 386–394. [CrossRef]
12. Marangoni, F.; Tellini, T.; Moreno, R.P.R.; Ferreira, S.O.; Konopatzki, E.A. Comparativo Econômico entre Condicionadores de Ar com Tecnologias Convencional e Inverter. In Proceedings of the Encontro Nacional de Engenharia de Produção, Fortaleza, Brasil, 13–16 October 2015; p. 20.
13. Lim, J.; Yoon, M.S.; Al-Qahtani, T.; Nam, Y. Feasibility Study on Variable-Speed Air Conditioner under Hot Climate Based on Real-Scale Experiment and Energy Simulation. *Energies* **2019**, *12*, 1489. [CrossRef]
14. Nied, A.; Oliveira, J.; Stival, L.H.R.C.; Polli, H.B. Improving Washing Machine Performance Using Single-Phase Induction Motor Field-Oriented Control. In Proceedings of the IECON 2013—39th Annual Conference of the IEEE Industrial Electronics Society, Vienna, Austria, 10–13 November 2013; pp. 2917–2922. [CrossRef]
15. Correa, M.B.R.; Jacobina, C.B.; Lima, A.M.N.; Silva, E.R.C. A Three-Leg Voltage Source Inverter for Two-Phase AC Motor Drive Systems. In Proceedings of the 2001 IEEE 32nd Annual Power Electronics Specialists Conference (IEEE Cat. No. 01CH37230), Vancouver, BC, Canada, 17–21 June 2001; Volume 3, pp. 1458–1463. [CrossRef]
16. Jacobina, C.B.; Correa, M.B.R. Induction Motor Drive System for Low Power Applications. *IEEE Trans. Ind. Appl.* **1999**, *35*, 52–61. [CrossRef]
17. Chuan-Sheng, L.; Jonq-Chin, H.; Po-Cheng, C. Improvement of Driver Efficiency for the Single-Phase Motor. In Proceedings of the 2012 IEEE International Symposium on Industrial Electronics, Hangzhou, China, 28–31 May 2012; pp. 664–667. [CrossRef]
18. Correa , M.B.R.; Jacobina, C.B.; Lima, A.M.N.; Silva, E.R.C. Rotor-flux-oriented control of a single-phase induction motor drive. *IEEE Trans. Ind. Electron.* **2000**, *47*, 832–841. [CrossRef]
19. Dragotto, E. *Cost-Benefit Analysis of a Refrigerator Replacement Program for Low-Income Households in Brazil*; United States Agency for International Development: Washington, DC, USA, 2007; p. 38.
20. Byrne, D.M.; Oliner, S.D.; Sichel, D.E. How Fast Are Semiconductor Prices Falling? In *Finance and Economics Discussion Series (FEDS)*; Board of Governors of the Federal Reserve System: Washington, DC, USA, 2017. [CrossRef]
21. Waide, P.; Brunner, C.U. *Energy-Efficiency Policy Opportunities for Electric Motor-Driven Systems*; OECD Publishing: Paris, France, 2011. [CrossRef]
22. Boldea, I.; Nasar, S.A. *The Induction Machines Design Handbook*, 2nd ed.; The Electric Power Engineering Series; CRC Press/Taylor & Francis: Boca Raton, FL, USA, 2010.
23. Doncker, R.W.; Pulle, D.W.J.; Veltman, A. *Advanced Electrical Drives: Analysis, Modeling, Control*; Power Systems; Springer: Dordrecht, The Netherlands; Heidelberg, Germany, 2011. [CrossRef]
24. Zahedi, B.; Vaez-Zadeh, S. Efficiency Optimization Control of Single-Phase Induction Motor Drives. *IEEE Trans. Power Electron.* **2009**, *24*, 1062–1070. [CrossRef]
25. Jang, D.h. PWM Methods for Two-Phase Inverters. *IEEE Ind. Appl. Mag.* **2007**, *13*, 50–61. [CrossRef]
26. Kumsuwan, Y.; Premrudeepreechacharn, S.; Kinnares, V. A Carrier-Based Unbalanced PWM Method for Four-Leg Voltage Source Inverter Fed Unsymmetrical Two-Phase Induction Motor. *IEEE Trans. Ind. Electron.* **2013**, *60*, 2031–2041. [CrossRef]
27. Kumar, B.; Srinivas, S. Space Vector Based PWM of Dual Full-Bridge VSI Fed Two-Phase Induction Motor Drive. In Proceedings of the 2014 IEEE 23rd International Symposium on Industrial Electronics (ISIE), Istanbul, Turkey, 1–4 June 2014; pp. 667–672. [CrossRef]
28. Kumar, B.; Srinivas, S. Elliptical Space Vector PWM for Dual H-bridge VSI Fed Two-Phase Induction Motor Drive. In Proceedings of the 2016 IEEE International Conference on Power Electronics, Drives and Energy Systems (PEDES), Trivandrum, India, 14–17 December 2016; pp. 1–5. [CrossRef]
29. Konarik, R.; Pridala, M.; Jarabicova, M.; Sedo, J.; Laskody, T. Topologies of Converters for Two-Phase AC Motors. In Proceedings of the 2017 18th International Scientific Conference on Electric Power Engineering (EPE), Kouty nad Desnou, Czech Republic, 17–19 May 2017; pp. 1–6. [CrossRef]

30. Meshram, S.M.; Fadnis, A.Y. Direct Torque Control of Three-Leg Inverter Driving Two-Phase Induction Motor. In Proceedings of the 2015 IEEE Power, Communication and Information Technology Conference (PCITC), Bhubaneswar, India, 15–17 October 2015; pp. 242–247. [CrossRef]
31. Piyarat, W.; Hothongkham, P.; Charumit, C.; Kinnares, V. Simple Speed Control of an Asymmetrical Type Two-Phase Induction Motor Drive. In Proceedings of the ECTI-CON2010: The 2010 ECTI International Confernce on Electrical Engineering/Electronics, Computer, Telecommunications and Information Technology, Chiang Mai, Thailand, 19–21 May 2010; p. 5.
32. Gupta, R. A Study of AC/DC Converter with Improved Power Factor and Low Harmonic Distortion. *Int. J. Comput. Sci. Eng.* **2012**, *4*, 1017–1029.
33. Lazaro, A.; Barrado, A.; Pleite, J.; Vazquez, R.; Vazquez, J.; Olias, E. Size and Cost Reduction of the Storage Capacitor in AC/DC Converters under Hold-up Time Requirements. In Proceedings of the IEEE 34th Annual Conference on Power Electronics Specialist, 2003. PESC '03, Acapulco, Mexico, 15–19 June 2003; Volume 4, pp. 1959–1964. [CrossRef]
34. Freescale Semiconductor. *Thermal Analysis of Semiconductors Systems*; White Paper; Freescale Semiconductor: Austin, TX, USA, 2008.
35. Künzi, R. Thermal Design of Power Electronic Circuits. In Proceedings of the 2014 CAS - CERN Accelerator School: Power Converters, Baden, Switzerland, 7–14 May 2014. [CrossRef]
36. Wintrich, A.; Nicolai, U.; Tursky, W.; Reimann, T. *Application Manual Power Semiconductors*, 2nd ed.; ISLE Verlag: Ilmenau, Germany, 2015.
37. Correa, M.; Jacobina, C.; Silva, E.; Lima, A. Vector control strategies for single-phase induction motor drive systems. *IEEE Trans. Ind. Electron.* **2004**, *51*, 1073–1080. [CrossRef]
38. Busatto, T.; Rönnberg, S.K.; Bollen, M.H.J. Comparison of Models of Single-Phase Diode Bridge Rectifiers for Their Use in Harmonic Studies with Many Devices. *Energies* **2021**, *15*, 66. [CrossRef]

applied sciences

MDPI

Article

Comparison of Differential Evolution and Nelder–Mead Algorithms for Identification of Line-Start Permanent Magnet Synchronous Motor Parameters

Aleksey Paramonov [1], Safarbek Oshurbekov [1], Vadim Kazakbaev [1], Vladimir Prakht [1], Vladimir Dmitrievskii [1] and Victor Goman [2,*]

[1] Department of Electrical Engineering, Ural Federal University, 620002 Yekaterinburg, Russia; paramonov.aleksey@inbox.ru (A.P.); safarbek.oshurbekov@urfu.ru (S.O.); vadim.kazakbaev@urfu.ru (V.K.); va.prakht@urfu.ru (V.P.); vladimir.dmitrievsky@urfu.ru (V.D.)

[2] Electromechanical Engineering Technology Department, Abu Dhabi Polytechnic, Abu Dhabi 111499, United Arab Emirates

* Correspondence: vvg_electro@hotmail.com

Featured Application: The findings of this study can be applied in the design and experimental investigation of line-start permanent magnet motors.

Abstract: Line-start permanent magnet synchronous motors (LSPMSMs) are of great interest to researchers because of their high energy efficiency, due to the growing interest of manufacturers in energy-efficient units. However, LSPMSMs face some difficulties in starting and synchronization processes. The LSPMSM lumped parameter model is applicable to estimating the successfulness of starting and further synchronization. The parameters of such a model can be determined using computer-aided identification algorithms applied to real motor transient processes' curves. This problem demands significant computational time. A comparison between two algorithms, differential evolution and Nelder–Mead, is presented in this article. The algorithms were used for 0.55 kW, 1500 rpm LSPMSM parameter identification. Moreover, to increase computational speed, it is proposed to stop and restart the algorithms' procedures, changing their parameters after a certain number of iterations. A significant advantage of the Nelder–Mead algorithm is shown for the solving of the considered problem.

Keywords: line-start permanent magnet synchronous motor; Nelder–Mead algorithm; differential evolution algorithm; electric motors; energy efficiency class; energy saving; motor starting

Citation: Paramonov, A.; Oshurbekov, S.; Kazakbaev, V.; Prakht, V.; Dmitrievskii, V.; Goman, V. Comparison of Differential Evolution and Nelder–Mead Algorithms for Identification of Line-Start Permanent Magnet Synchronous Motor Parameters. *Appl. Sci.* **2023**, *13*, 7586. https://doi.org/10.3390/app13137586

Academic Editors: Loránd Szabó and Feng Chai

Received: 6 May 2023
Revised: 21 June 2023
Accepted: 25 June 2023
Published: 27 June 2023

1. Introduction

A significant share of industrial mechanisms, including pumps, fans, air blowers, and compressors, are driven by electric motors, which are connected directly to a power grid without intermediate power converters and are launched using a direct start [1–3]. The vast majority of these motors are induction motors (IMs) [1–3]. Despite all the well-known induction motors' advantages, they expose significant losses during the rotor winding, which diminishes their energy efficiency class [4].

Line-start permanent magnet synchronous motors (LSPMSMs) do not have noticeable rotor winding losses at steady state, which increases their energy efficiency class in comparison to induction motors. LSPMSMs are available on the market and mostly are employed in pump and fan units [5–7]. Figure 1 shows a comparison of IM and LSPMSM designs.

LSPMSMs are of great interest to researchers because of their high energy efficiency due to the growing interest of manufacturers in energy-efficient units [8–11]. The LSPMSM model's performance can be improved by using computer-aided design optimization procedures [12–14].

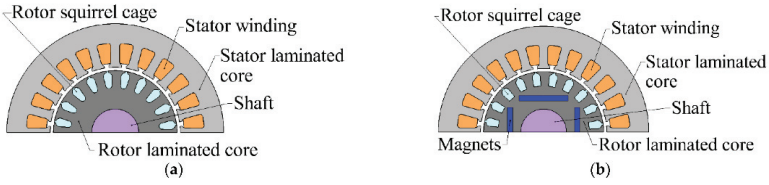

Figure 1. Sketches of electric motors. (**a**) Induction motor (IM); (**b**) synchronous motor with the direct start from the network and permanent magnets (LSPMSM).

There are studies investigating LSPMSM performance at unbalanced voltage [15]. In [16], the LSPMSM steady-state torque was evaluated by transient analysis using a neural network. Article [17] is devoted to LSPMSM modelling, using a bond graph model [18]. Article [19] discusses the latest LSPMSM design techniques. Article [20] presents an experimental comparison of a 4-pole 5.5 kW LSPMSM with axial and radial fluxes. There are also studies on the effect of LSPMSM rotor design on additional losses [21].

LSPMSMs face some difficulties in starting and synchronization processes, especially with loads with a high moment of inertia [22–24]. An LSPMSM lumped parameter model [25] was applied to estimate the successfulness of starting and further synchronization, which has been extremely beneficial for the experimental verification of LSPMSM characteristics. However, experimental parameter identification is related to significant obstacles.

Evaluation of electrical parameters can be done using a finite element model (FEM) based on known motor constructive parameters [26]. However, this approach requires knowledge of the geometrical details of the motor core, winding data, and the materials it is composed of. This requires access to motor design documentation or irreversible disassembly of motor parts for study purposes, which is not always possible.

In the case that the motor constructive parameters are unknown, there are several approaches for determining equivalent circuits parameters applicable for IMs [27–33] and LSPMSMs [25,26,34,35]: (1) steady-state experiments, such as no-load tests, locked rotor tests, etc., allow individual motor parameters to be determined [25]; (2) computer-aided identification algorithms make it possible to use the transient response to estimate multiple motor parameters, as explained in [34].

Measurement techniques of individual LSPMSM parameters using steady-state experiments include: the stator winding DC resistance estimation; the leakage inductance estimation on sinusoidal voltage operation with rotor extraction; the locked rotor test for rotor resistance and inductance estimation; the DC step-voltage test to estimate the LSPMSM total inductances; and the open-circuit test used for the permanent magnet flux linkage estimation [25]. However, such an approach demands a very high measurement accuracy and relies on many assumptions. The presence of the mutual inductance of the stator winding and the rotor squirrel cage makes it impossible to measure the total inductances at a locked rotor. Further, the total inductances measurement using the DC step-voltage test has low accuracy because of the nonlinear nature of the motor total inductances, which is the result of the presence of main-path saturation and cross saturation in the motor magnetic circuit.

According to Newton's second law, the rotor moment of inertia can be measured as a coefficient between dynamic torque and angular acceleration. However, it demands a laboratory test bench with a prime mover and a torque sensor or a frequency converter with a specific testing algorithm, which are not always available [36].

These difficulties can be overcome by computer-aided identification methods that require only phase currents and speed measurement during the motor start-up process.

There are many computer-aided identification algorithms; for example, the Kalman filter, the model reference adaptive system, the least squares method, artificial neural networks, the genetic algorithm, the differential evolution algorithm, particle swarm

optimization, etc. [27,34,35]. For example, in [34], the identification of LSPMSM parameters based on the time plots of current and speed during start-up using the differential evolution algorithm is discussed.

It can be concluded that, due to the disadvantages of other methods, such as the need to know the motor design parameters in the case of using FEA or a large number of assumptions in the case of parameter estimation through steady-state experiments, computer identification is a promising method for estimating the parameters of the LSPMSM model. However, a detailed comparison of the effectiveness of various computer identification algorithms for determining the parameters of LSPMSM has not yet been carried out.

This article presents a comparison between the differential evolution (DE) [37,38] and Nelder–Mead (NM) algorithms [39,40] for lumped parameter LSPMSM model identification. The novelty of this article lies in the results of comparing the DE and NM algorithms for the considered specific problem. Moreover, it shows the advantages of the NM algorithm over the DE algorithm. Its practical impact lies in revealing a more accurate and computationally efficient algorithm for the identification of LSPMSM parameters.

The comparison was carried out on the example of transients calculated for the LSPMSM model with given parameters. The results of the study show that the differential evolution algorithm demonstrates relatively low parameter identification accuracy and longer computational time. However, it can be used to determine the initial approximation for the algorithms with better convergence. The Nelder–Mead algorithm is confirmed as more computationally efficient for the considered problem.

Moreover, it is proposed to stop and restart identification procedures for both algorithms, changing their tuning parameters, when the rate of convergence shows a significant decrease.

The purpose for identifying the parameters of the LSPMSM in our study is to obtain a tool that correctly predicts the success/failure of starting and synchronizing the LSPMSM for various moments of inertia and for the various dependencies of the load torque on the speed. We have added this explanation to the article.

2. Mathematical Model of the Motor

The transient processes for the LSPMSM start-up are calculated using the LSPMSM mathematical model.

When modelling the LSPMSM, it is assumed that:

- The magnetic fields generated by the stator and rotor windings have a sinusoidal spatial distribution;
- The magnetic permeability of the steel is constant;
- The stator and rotor windings are symmetrical;
- Each winding is powered by a separate source;
- The mains voltage phasor is constant throughout the entire starting process, and an increase in the motor current does not cause a decrease in its amplitude;
- The magnetic core losses are not taken into account.

The system of ordinary differential LSPMSM equations to be solved is represented as:

$$\begin{gathered}
\mathrm{d}\lambda_{\mathrm{sd}}/dt - p\cdot\lambda_{\mathrm{sq}}\cdot\mathrm{d}\varphi/dt + R_s\cdot I_{sd} = U_{sd};\\
\mathrm{d}\lambda_{\mathrm{sq}}/dt + p\cdot\lambda_{\mathrm{sd}}\cdot\mathrm{d}\varphi/dt + R_s\cdot I_{sq} = U_{sq};\\
\mathrm{d}\lambda'_{\mathrm{rd}}/dt + r'_d\cdot I'_{rd} = 0;\\
\mathrm{d}\lambda'_{\mathrm{rq}}/dt + r'_q\cdot I'_{rq} = 0;\\
I'_{rd} = (\lambda'_{\mathrm{rd}} - \lambda_{\mathrm{sd}})/L_{\sigma d};\\
I'_{rq} = (\lambda'_{\mathrm{rq}} - [\lambda_{\mathrm{sq}} - \lambda'_0])/L_{\sigma q};\\
I_{sd} = \lambda_{\mathrm{sd}}/L_{sd} - I'_{rd};\\
I_{sq} = (\lambda_{\mathrm{sq}} - \lambda'_0)/L_{sq} - I'_{rq};\\
T = 3/2\cdot Z_p(\lambda_{\mathrm{sd}}\cdot I_{sq} - \lambda_{\mathrm{sq}}\cdot I_{sd});\\
J\cdot\mathrm{d}^2\varphi/dt^2 = T - T_{load},
\end{gathered} \tag{1}$$

where U_{sd} and U_{sq} are the stator voltages along the d and q axes; I_{sd}, I_{sq}, $I'_{rd,}$ and I'_{rq} are the stator and rotor currents; L_{sd}, L_{sq}, $L_{rd,}$ and L_{rq} are the stator and rotor total inductances; $L_{\sigma d}$ and $L_{\sigma q}$ are the rotor leakage inductances; λ_{sd}, λ_{sq}, $\lambda'_{rd,}$ and λ'_{rq} are the stator and rotor flux linkages; λ'_0 is the permanent magnet flux linkage; R_s is the stator resistance; Z_p is the number of motor pole pairs; r'_{rd} and r'_{rq} are the rotor resistances; φ is the mechanical rotational angle equal to the integral of the motor speed ω; T is the motor torque; T_{load} is the loading torque; J is the total moment of inertia. All initial conditions are equal to zero, except for the stator flux along the q-axis $\lambda_{sq\,0} = \lambda'_0$.

Figure 2 shows the implementation of equation system (1) in Simulink. According to Figure 2a, the LSPMSM fed directly from the mains ("Discrete 3-phase Source"), was mechanically coupled to the load. The load was simulated as a summation of a constant torque T_c and component $\omega \cdot F$ that represented a bearings frictional torque, which depended on speed linearly, as is shown in Figure 3b.

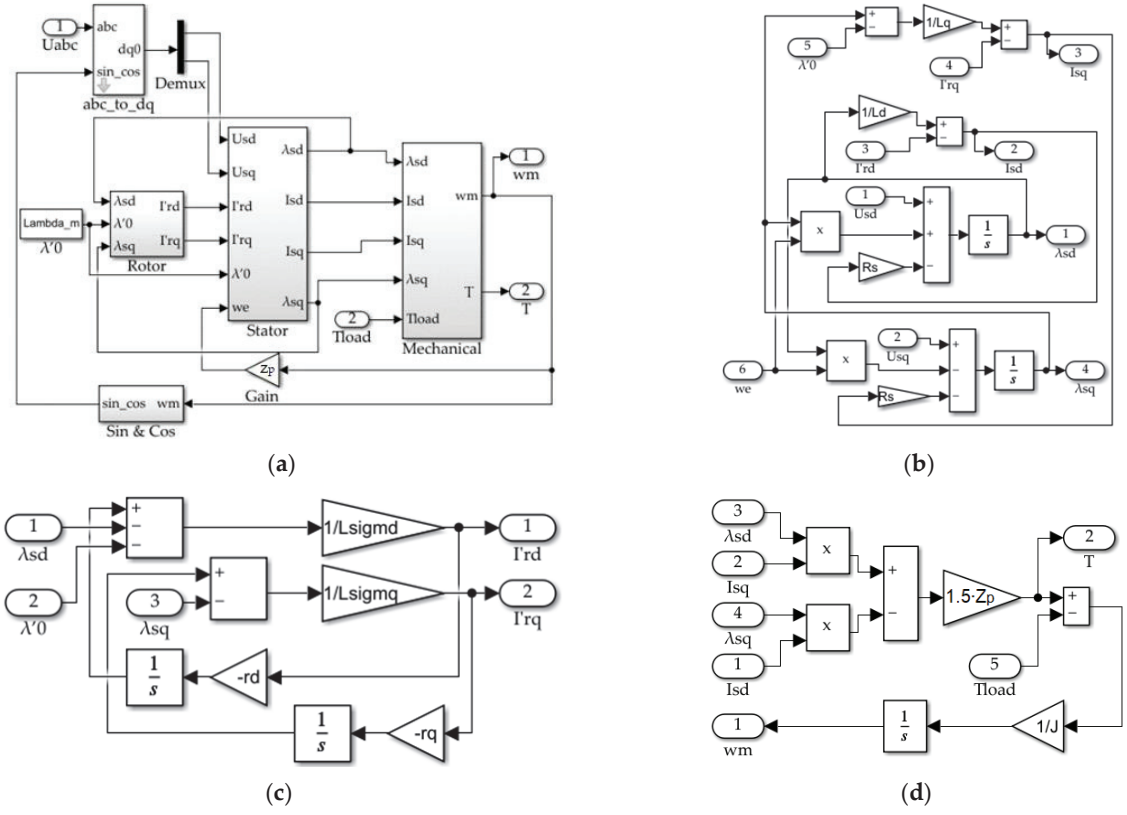

Figure 2. Simulink model of the LSPMSM motor in the d-q axes. (**a**) General view of the model; (**b**) calculation of stator currents; (**c**) calculation of rotor currents; (**d**) torque calculation.

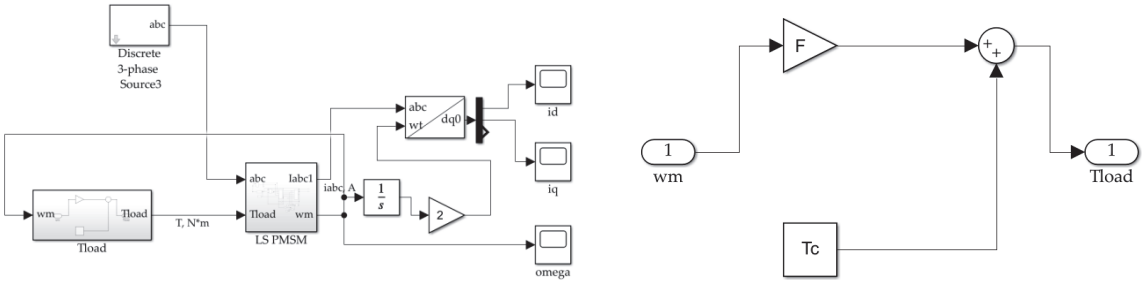

(**a**) (**b**)

Figure 3. Simulink model of the LSPMSM motor fed from 3-phase 380 V, 50 Hz grid. (**a**) General view; (**b**) load torque model.

The LSPMSM parameters (rated power 550 W, rated speed 1500 rpm) given in Table 1 were taken as the motor parameters.

Table 1. The LSPMSM parameters (rated power 550 W, rated speed 1500 rpm).

Parameter	Value
Motor rated power, kW	0.55
Motor rated line-to-line voltage, V	380
Root-mean-square (RMS) rated stator current, A	1.11
Rated power factor	0.85
Rated frequency f, Hz	50
Pole pair number Z_p	2
Stator phase resistance R_s, Ohm	15.3
Total direct inductance L_d, H	0.26
Total quadrature inductance L_q, H	0.15
Leakage direct inductance $L_{\sigma d}$, H	0.038
Leakage quadrature inductance $L_{\sigma q}$, H	0.051
Rotor direct resistance r'_d, Ohm	9.24
Rotor quadrature resistance r'_q, Ohm	10.1
Permanent magnet flux linkage λ'_0, Wb	0.76
Motor inertia moment J, kg·m^2	0.003
Bearing friction and windage coefficient F, N·m/(rad/s)	10^{-4}

It is known that the operating temperature significantly affects the resistance and rotational speed of induction motors [41]. At the same time, the heating of the LSPMSM is much less due to lower losses, and it does not have any slip. This makes it possible to not consider the influence of temperature when identifying its parameters [34].

Figure 4 represents the LSPMSM phase currents and angular frequency transient processes at $T_c = 0$ N·m and $F = 10^{-4}$ N·m/(rad/s). Figure 4a shows the time plots of the components of the stator current along the direct (d) and quadrature axis (q) in a coordinate system fixed relative to the rotor. Figure 4b shows the time plot of the mechanical angular frequency of the rotor. Figure 5 shows the directions of the d and q axes relative to the magnetization direction of the permanent magnets. The transient waveforms were selected for the study because these values (phase currents and angular frequency) can be easily measured in experiments with the real LSPMSMs. Figure 4 shows that the LSPMSM starting time was 0.7 s. The steady-state phase current amplitude was 1.58 A. The starting inrush current was 15.8 A. During the starting process, the motor reached the synchronous speed of 157.09 rad/s (1500 rpm) at 0.06 s for the first time; however, further, it accelerated to a higher speed because of inertia. Later, the motor decelerated as a result of synchronous torque action. These oscillations were repeated several times with the decreasing amplitude caused by dumping factors such as asynchronous torque and load frictional torque.

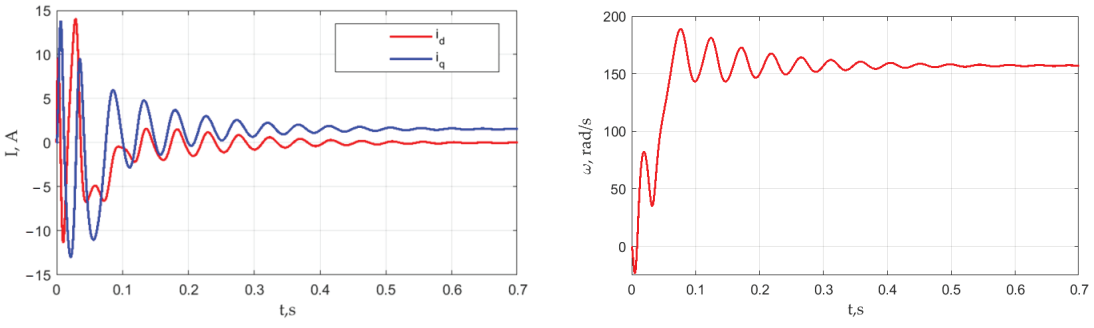

(**a**) (**b**)

Figure 4. LSPMSM starting simulation results: (**a**) *d* and *q*-axis stator currents; (**b**) motor speed ω.

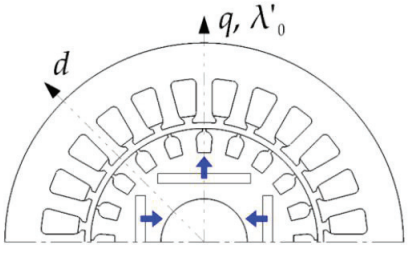

Figure 5. Axes *d* and *q* of the rotor relative to the permanent magnet magnetization direction (indicated by blue arrows).

3. General Algorithm of the Motor Parameters Identification

The flow chart of the motor parameters identification algorithm is shown in Figure 6. It is valid for both DE and NM. During the initialization stage, a set of identifiable parameters, their constraints and initial conditions, parameters of the objective function that do not change during optimization (amplitude and frequency of the supply voltage, number of poles, stator resistance, etc.), as well as a settings identification algorithm (number of iterations, maximum optimization function execution time, coefficients that impact the optimization process, number of individuals in a population for DE, etc.) were defined. Since the Nelder–Mead method is an unconstrained method, the constraints were applied only if DE was used. DE is a bound-constrained global search algorithm that requires setting up quantities and names of the variables, their constraints, and an initial approximation, as well as accuracy if the solving problem demands it.

In the basic identification loop, using the identification algorithm (DE or NM), the next estimate of the identified parameters was calculated, which was the input of the objective function. In the objective function, the simulation of the Simulink model was called using the function "sim" [42], whose inputs were the name of the model, its initial state, etc., and the output was the vector of simulation results of the Simulink model.

An objective function, $F_{value,}$ that should be minimized during the basic identification cycle was calculated as an integral of the squared deviations of the angular frequency ω^m and the currents i_d and i_q for separated time samples, calculated at the current values of the identifying parameters of reference transient processes functions shown in Figure 4:

$$F_{value} = k_{id} \cdot q_{id} + k_{iq} \cdot q_{iq} + k_{\omega} \cdot q_{\omega}, \quad (2)$$

where k_{id} = 20, k_{iq} = 20 and k_{ω} = 1 are the weight coefficients according to [34]; q_{id}, q_{iq} and q_{ω} are the error functions. These error functions are defined as follows:

$$q_{id} = \frac{1}{t_2 - t_1} \int_{t_1}^{t_2} [i_d^m(t) - i_d(t)]^2 dt; \tag{3}$$

$$q_{iq} = \frac{1}{t_2 - t_1} \int_{t_1}^{t_2} \left[i_q^m(t) - i_q(t) \right]^2 dt; \tag{4}$$

$$q_{\omega} = \frac{1}{t_2 - t_1} \int_{t_1}^{t_2} [\omega^m(t) - \omega(t)]^2 dt, \tag{5}$$

where $i_d{}^m$, $i_q{}^m$ and ω^{m} are simulation results of the d- and q-axis stator currents and angular frequency, respectively, obtained using motor parameters given in Table 1.

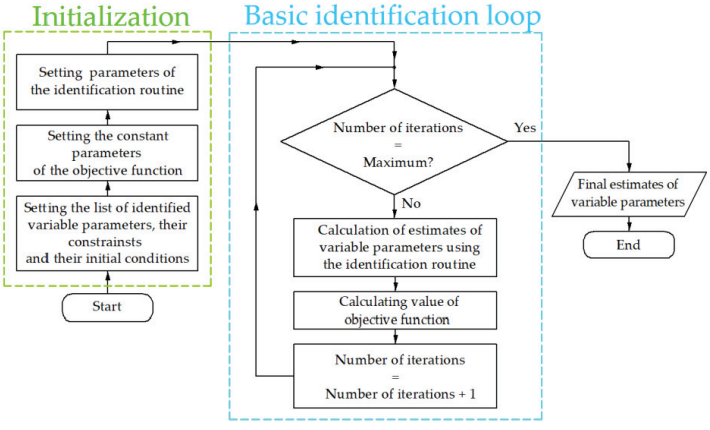

Figure 6. One-stage identification algorithm flow chart.

The basic identification loop ended after the specified number of iterations had been completed. The parameter estimate obtained after this was the result of identification.

4. Identification Algorithms

As was stated earlier, the implementation results of the two algorithms (DE and NM) were compared for the LSPMSM parameter identification problem. DE is a multidimensional optimization algorithm which belongs to the stochastic optimization algorithms group. DE is the result of further development of the genetic algorithm [38]. According to the original definition, DE can be described as follows. Initially, a set of vectors called generation is created. N-dimensional points where a minimized objective function $f(x)$ is determined are considered as vectors. The algorithm creates a new generation of randomly combined vectors from the previous generation. The number of vectors is the same for each generation, and this is one of the algorithm parameters.

A new generation of vectors Is generated as follows. For each previous generation vector $x_{i,}$ three different random vectors, v_1, v_2, and $v_{3,}$ are selected among the previous generation except vector x_i itself. As a result, a mutated vector (6) is generated:

$$v = v_1 + F_v (v_2 - v_3), \tag{6}$$

where F_v is one of the method parameters, which is a positive real number in the range (0, 2). It is recommended to vary this value when an objective function approaches a minimum [31].

Then, the crossover procedure is implemented on mutated vector v. The procedure consists of the replacement of some of the vector's coordinates by initial vector x_i coordinates. Each replacement is performed with some probability, which is another parameter of the algorithm. The result after the crossover procedure vector is called a trial vector. If this vector is «better» than the initial vector x_i, which means that an objective function value was reduced, then x_i is replaced by the trial vector in a new generation. Otherwise, the previous x_i vector remains as an initial vector.

The NM is an unconstrained optimization algorithm applicable to the function of several variables [40]. The algorithm searches for a local optimum and can «stick» in one of the local optima. Different initial simplex shapes can be changed to find the better minimum if necessary.

The NM is used to find the unconstrained minimum of a function of n variables defined elsewhere in $\mathbb{R}^n$.

The algorithm parameters are listed below:

- Reflection coefficient $\alpha > 0$.
- Contraction coefficient $0 < \beta < 1$.
- Expansion coefficient $\gamma > 1$.

Usually, units $\alpha = 1$, $\beta = 0.5$, and $\gamma = 2$ are selected.

The algorithm contains the following steps enumerated to highlight function calls:

1. Preparation. Initially, $n + 1$ points are selected: $x_i = (x_i^1, x_i^2, \ldots, x_i^n)$, $i = 1 \ldots (n + 1)$, where $x_1 = (x_1^1, x_1^2, \ldots, x_1^n)$ is an initial parameter vector, $x_2 = (x_1^1 \cdot (1 + \delta), x_1^2, \ldots, x_1^n)$, $x_3 = (x_1^1, x_1^2 \cdot (1 + \delta), \ldots, x_1^n) \ldots, x_{n+1} = (x_1^1, x_1^2, \ldots, x_1^n \cdot (1 + \delta))$, δ is the initial simplex coefficient. These vectors constitute the n-dimensional space simplex. Objective function values are calculated at the points $f_1 = (x_1), f_2 = f(x_2), \ldots, f_{n+1} = f(x_{n+1})$.
2. Sorting. Three points are selected among simplex vertices: x_h where function value f_h is the greatest, x_g where f_g is the next to the greatest, and x_l where f_l is the least function value. The further steps' aim is at least the diminishing of f_h.
3. A centroid of the aforementioned points of the simplex excluding x_h is determined as $x_c = 1/n \sum_{(i \neq h)}(x_i)$. Calculation of $f_c = f(x_c)$ is not mandatory.
4. Reflection. The reflection $x_r = (1 + \alpha)x_c - \alpha x_h$ of x_h with respect to x_c with coefficient α and the value of the function $f_r = f(x_r)$ at x_r is to be calculated.
5. Expansion. Then f_r is compared with the values f_h, f_g, and f_l:

   If $f_r < f_l$, the selected search direction is successful, and the search step can be increased using the expansion operation. A new point $x_e = (1 + \gamma)\, x_c - \gamma x_r$ and the function value $f_e = f(x_e)$ are to be calculated.

   If $f_e < f_r$, the simplex expands up to this point: set x_h equal to x_e and f_h equal to f_e, and then finish the current iteration (go to Step 6).

   However, if $f_r < f_e$, an expansion is too wide: set x_h equal to x_r and f_h equal to f_r, and then finish the current iteration (go to Step 6).

   If $f_l < f_r < f_g$, the point selection is acceptable; the new one is better than the two previous points. Set x_h equal to x_r and f_h equal to f_r, and then finish the current iteration (go to Step 6).

   If $f_g < f_r < f_h$ then set x_h equal to x_r and f_h equal to f_r.
6. Contraction. Determine the point $x_s = \beta x_h + (1 - \beta)\, x_c$ and the function value at this point $f_s = f(x_s)$. If $f_s < f_h$ set x_h equal to x_s and f_h equal to f_s, then go to Step 6.
7. Shrinking. If $f_s > f_h$, that means that the initial points were more successful. Perform simplex global contraction (homothety) to the point with the least value of $x_i = x_l + (x_i - x_l)/2$, $I \neq l$. The function values at these points are to be calculated.

8. The last step is the convergency check-up. It can be done by simplex vertices dispersion evaluation. The mutual proximity of the simplex vertices assumes their proximity to the searching objective function minimum. If the desired accuracy is not reached, the algorithm can be continued from Step 2.

5. Comparison of the LSPMSM Parameters Identification Results Obtained by DE and NM

The results of the DE and NM implementation are described in this section. The implementation was performed for the considered LSPMSM lumped-parameters identification problem.

It is known that it is recommended to change optimization algorithm coefficients when approaching the minimum. This was coefficient F_v for the DE and coefficient δ for the NM. This made it possible to speed up the identification process, and also to get out of local minima. Considering that the NM algorithm tends to a local optimum, it is advisable to restart the algorithm after it gets stuck. Due to this reason, when the algorithms reached a certain number of iterations, the algorithms were stopped and restarted with the new initial approximation. Further in the article, we describe how the optimization stage means a stage during which the algorithm works from start to intermediate or end stops.

Figure 7 shows the three-stage optimization flow chart. The internal structure of the "Initialization" and "Basic identification cycle" blocks is shown in Figure 6. NM-3 stands for the Nelder–Mead optimization in three stages. The DE-3 stands for differential evolution in three stages. One stage for the NM consisted of 400 iterations, and the coefficient δ was equal to 0.3, 0.01, and 0.005 for the first, second, and third stages, accordingly. One stage for the DE consisted of 18 iterations with 120 individuals in each generation, and the coefficient F_v was equal to 0.8, 0.4, and 0.04 for the first, second, and third stages, accordingly. The δ and F_v values were determined experimentally. The boundary conditions, initial approximation and required accuracy for the DE are presented in Table 2.

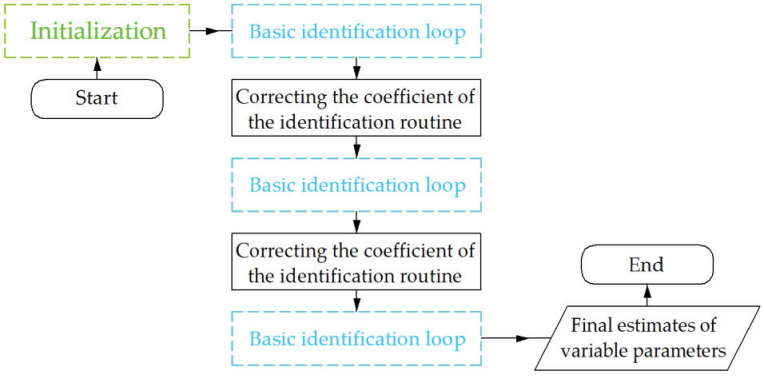

Figure 7. Three-stage identification algorithm flow chart.

Table 2. The boundaries, accuracy, and initial approximation of the identified parameters.

Parameter	Lower Boundary	Upper Boundary	Accuracy for DE-Based Algorithms	Initial Approximation
L_d, H	0.1	1	0.001	0.513
L_q, H	0.1	1	0.001	0.301
$L_{\sigma d}$, H	0.01	0.1	0.001	0.0762
$L_{\sigma q}$, H	0.01	0.1	0.001	0.0814
r'_d, Ohm	5	12	0.01	8
r'_q, Ohm	5	12	0.01	9
λ'_0, Wb	0.5	1	0.01	0.5
J, kg·m^2	0.001	0.01	0.001	0.006

It should be noted that the DE created an initial population according to the normal distribution in the range represented in Table 2 where the number of individuals was equal to the number of initial parameters. The initial population was the same for both DE and DE-3.

The DE algorithm supposes the generation of random numbers. Therefore, to estimate the results' repeatability, the identification was performed six times. Table 3 shows the results for six consecutive runs of the DE and DE-3. At the same time, the NM and NM-3 were started only once, because random number generation is not supposed in these algorithms.

Table 3. Final values of the objective function/number of iterations for different algorithms.

Number of a DE Run	DE	DE-3	NM	NM-3
1	3.473/5383	0.423/3323	0.0095/2661	0.0016/1200
2	11.973/5399	0.627/3314		
3	10.974/5398	0.388/3457		
4	7.525/5399	0.462/3475		
5	16.68/3996	0.177/3547		
6	3.288/5135	0.196/3942		
Mean deviation	8.986	0.379	-	-
RMS deviation	5.236	0.17	-	-

Based on Table 3, it can be concluded that the NM algorithm provides the final value of the objective function 3.28/0.0095 = 345 times fewer than DE. In addition, NM demands the number of iterations 5383/2661 $\approx$ 2 times fewer than the DE. The NM-3 algorithm provides the final value of the objective function 0.379/0.0016 = 237 times fewer than DE-3. In addition, NM-3 demands the number of iterations 3332/1200 $\approx$ 3 times fewer than the DE-3. Table 4 represents the LSPMSM parameters' values determined by the considered algorithms and real parameters. The best result out of six performed repetitions for the DE and DE-3 is shown in Table 4.

Table 4. Identification results obtained by the considered algorithms and real motor parameters.

Parameter	Real Value	DE	DE-3	NM	NM-3
L_d, H	0.26	0.244	0.253	0.256	0.257
L_q, H	0.15	0.162	0.155	0.150	0.15
$L_{\sigma d}$, H	0.038	0.039	0.038	0.038	0.038
$L_{\sigma q}$, H	0.041	0.042	0.044	0.041	0.041
r'_d, Ohm	9.24	10.23	8.90	9.24	9.26
r'_q, Ohm	10.1	9.70	9.69	10.09	10.1
λ'_0, Wb	0.76	0.76	0.75	0.76	0.76
J, kg·m^2	0.003	0.003	0.003	0.003	0.003
Objective function value	-	3.288	0.177	0.0095	0.0016
Number of iterations	-	5135	3547	2661	1200

Figure 8 shows the objective function values for the considered optimization algorithms with the number of objective function calls, starting from the 120th NM call (1st generation for DE). Table 5 shows the mean values and RMS deviation of identified parameters obtained using the DE and DE-3 algorithms.

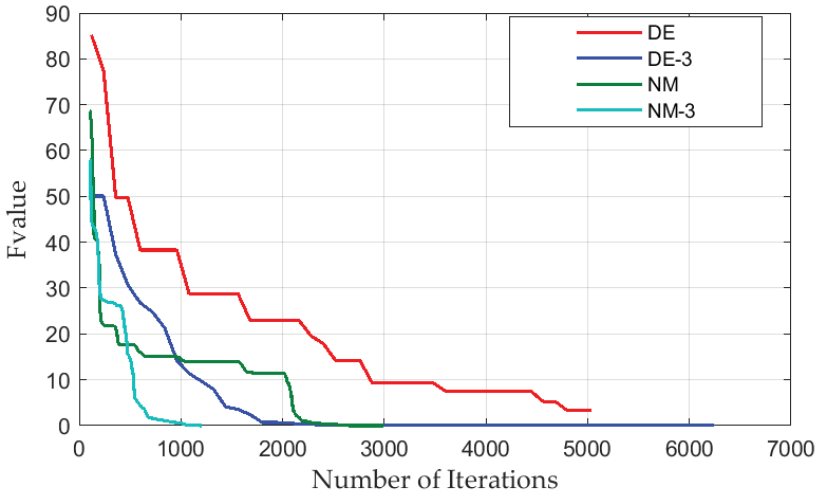

Figure 8. The objective function values vs. the number of iterations for DE, DE-3, NM, and NM-3 algorithms.

Table 5. Identification results obtained by the considered algorithms in comparison with real motor parameters.

Parameter	Real Value	DE Identified Value	DE RMS Deviation	DE-3 Identified Value	DE-3 RMS Deviation
L_d, H	0.26	0.301	0.111	0.264	0.012
L_q, H	0.15	0.142	0.017	0.156	0.0022
$L_{\sigma d}$, H	0.038	0.04	0.0047	0.04	0.0015
$L_{\sigma q}$, H	0.041	0.039	0.0104	0.045	0.0015
r'_d, Ohm	9.24	10.12	0.99	8.79	0.138
r'_q, Ohm	10.1	10.52	0.78	9.86	0.286
λ'_0, Wb	0.76	0.748	0.017	0.7433	0.0052
J, kg·m^2	0.003	0.003	0.00	0.003	0.00

The faster convergence of DE-3 compared to DE and NM-3 compared to NM confirms the effectiveness of the "stop and restart" technique used.

6. Identification with a Random Initial Approximation

The results of the considered identification algorithms were estimated at a random selection of the initial approximation. To perform that, the identification with six different random initial approximations was conducted. The random values were selected from the parameter ranges shown in Table 2.

Table 6 presents the results, such as the final values of the objective function and the number of iterations for the considered identification algorithms at six different initial approximations. Furthermore, Table 6 shows the mean and RMS deviations of the objective function values, calculated for six different initial approximations. Tables 7 and 8 show the mean and RMS deviations of the parameters calculated by the considered algorithms. Figure 9 represents the dependencies of the objective function values on the number of objective function calls (iterations) for the best initial approximation.

With a fortunate choice of the initial approximation, when using the NM and NM-3 algorithms, the final value of the objective function deviated from the minimum value by a negligibly small amount (as a result of the identification, the objective function was reduced by four or more orders of magnitude). Using NM-3 required 2–3 times fewer function calls than NM (see Figure 7, Table 6).

Table 6. The results of 6 executions for the considered identification algorithms with a random initial approximation: the objective function final values and the number of iterations.

Execution No.	DE	DE-3	NM	NM-3
1	3.3/5399	0.4/3891	7.8×10^{-10}/3002	6.5/1203
2	6.4/5396	0.61/3511	7.7×10^{-13}/2674	6.5×10^{-4}/1203
3	4.1/5396	0.4/3891	8.3×10^{-13}/2195	2.1×10^{-4}/1203
4	10.6/5398	0.34/3951	4.7×10^{-12}/2809	1.8×10^{-10}/1203
5	5.4/5395	0.61/3511	8×10^{-13}/2770	5.5×10^{-3}/1203
6	4.8/5400	24/2878	8×10^{-13}/2650	1.7×10^{-9}/1203
Mean deviation	5.8	4.4	1.3×10^{-10}	1.1
RMS deviation	2.6	9.6	3.2×10^{-10}	2.7

Table 7. Deviations of the LSPMSM parameters obtained using the NM identification algorithm with a random initial approximation.

Parameter	Real Value	NM Identified Value	NM RMS Deviation	NM-3 Identified Value	NM-3 RMS Deviation
L_d, H	0.26	0.256	0.06	0.253	0.0093
L_q, H	0.15	0.15	0.01	0.159	0.02
$L_{\sigma d}$, H	0.038	0.038	0.07	0.039	0.0023
$L_{\sigma q}$, H	0.041	0.041	0.03	0.043	0.0067
r'_d, Ohm	9.24	9.24	4.9	8.99	0.59
r'_q, Ohm	10.1	10.09	6	9.6	1.2
λ'_0, Wb	0.76	0.76	0.21	0.75	0.023
J, kg·m^2	0.003	0.003	0.00	0.003	0.0001

Table 8. Deviations of the LSPMSM parameters obtained using the DE identification algorithm with a random initial approximation.

Parameter	Real Value	DE Identified Value	DE RMS Deviation	DE-3 Identified Value	DE-3 RMS Deviation
L_d, H	0.26	0.272	0.056	0.29	0.12
L_q, H	0.15	0.143	0.017	0.147	0.012
$L_{\sigma d}$, H	0.038	0.042	0.0064	0.035	0.0011
$L_{\sigma q}$, H	0.041	0.035	0.0104	0.042	0.0005
r'_d, Ohm	9.24	10.03	0.98	9.1	0.055
r'_q, Ohm	10.1	11.1	1.2	10.03	0.97
λ'_0, Wb	0.76	0.76	0.014	0.77	0.012
J, kg·m^2	0.003	0.003	0.00	0.003	0.00

With successful parametric identification, the objective function was reduced by about an order of magnitude when using DE and by two orders of magnitude when using DE-3. In addition, DE-3 required about two times fewer function calls than DE.

Although NM is a local search algorithm, and DE is a global one, in both cases, being stuck in a local minimum was possible (for example, see NM-3, start 1 and DE-3 start 6 in Table 6). Further, DE and DE-3 required more objective function calls compared to NM and NM-3.

From the above, we can conclude that in the considered application the Nelder–Mead method provides significant advantages over differential evolution. Therefore, it is preferable to run NM multiple times to find the best initial approximation rather than using DE. This does not preclude the use of DE to automatically find an initial approximation for NM.

The faster convergence of DE-3 compared to DE and NM-3 compared to NM confirms the effectiveness of the "stop and restart" technique used in the case of a random initial approximation, as well. Furthermore, even though NM is an unrestricted method, the results of identification using NM and NM-3 satisfy the conditions that all identified

parameters (L_d, L_q, $L_{d\sigma}$; $L_{q\sigma}$; r'_d; r'_q, λ'_0; J) are greater than zero; $L_d > L_q$; $L_d >> L_{d\sigma}$; $L_q >> L_{q\sigma}$, which confirms the ability of NM to successfully solve the problem under consideration.

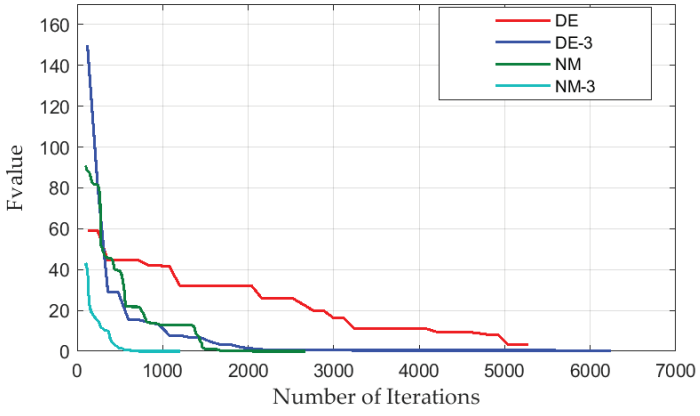

Figure 9. The best objective function values vs. iterations for the random initial approximations.

7. Conclusions

The study is devoted to the comparative analysis of various computer-aided iterative identification methods based on optimization algorithms such as the differential evolution (DE) and the Nelder–Mead (NM) in LSPMSM lumped-parameter model identification. The comparison was carried out on the example of transients calculated for the LSPMSM model with given parameters.

Comparing the DE and NM algorithms at the same initial approximation, it can be concluded that the NM algorithm provided the final value of the objective function, proportional to the deviation of the identified parameters, 345 times fewer than DE. In addition, NM demanded the number of iterations to be two times fewer than DE. Comparing the DE and NM algorithms with a random initial approximation, it can be concluded that the NM provided the final value of the objective function $4.5 \cdot 10^{10}$ times fewer than DE.

It can be concluded that, even though NM is an unrestricted local search method, it is able to successfully solve the problem under consideration, being more computationally efficient and accurate than DE. In this case, the DE method can be used at the initial stage of identification to find a suitable initial approximation for the NM. For a more accurate identification of the parameters, when a suitable initial approximation has already been found, the NM should be used.

In addition, in this study, it is proposed to stop and restart the considered identification procedures with a change in the algorithm parameters after a certain number of iterations and use the previously obtained results as a new initial approximation. Such multistage optimization (three stages have been found to be enough) leads to an increase in the computational speed and accuracy for both DE and NM. In this case, the NM algorithm provided the final value of the objective function 237 times fewer and required the number of iterations to be three times fewer than the DE with the same initial approximation. With a random initial approximation, in this case, the NM provided the final value of the objective function four times fewer than DE.

Although the article demonstrates the validity of the presented results only in the case of identifying the parameters of the LSPMSM model based on the results of simulated transients, in the future, the results will be used, and the conclusions will be verified when solving the problem of parametric identification of a real LSPMSM based on real transients.

Author Contributions: Conceptual approach, A.P., V.K. and V.P.; data curation, A.P. and S.O.; software, A.P., S.O. and V.K.; calculations and modelling, A.P., S.O., V.D., V.K. and V.P.; writing—original draft, A.P., S.O., V.D., V.K., V.G. and V.P.; visualization, A.P. and V.K.; review and editing, A.P., S.O., V.D., V.K., V.G. and V.P. All authors have read and agreed to the published version of the manuscript.

Funding: The work was partially supported by the Ministry of Science and Higher Education of the Russian Federation (through the basic part of the government mandate, Project No. FEUZ-2023-0013).

Institutional Review Board Statement: Not applicable.

Informed Consent Statement: Not applicable.

Data Availability Statement: Data are contained within the article.

Acknowledgments: The authors thank the editors and reviewers for their careful reading and constructive comments.

Conflicts of Interest: The authors declare no conflict of interest.

Glossary

List of Abbreviations

DE	Differential evolution
DE-3	Differential evolution (three stages)
IM	Induction motor
LSPMSM	Line-start permanent magnet synchronous motor
NM	Nelder–Mead method
NM	Nelder–Mead method (three stages)

List of Mathematical Symbols

f	Mains voltage frequency, Hz
F	Bearing friction and windage coefficient, N·m/(rad/s)
F_v	Parameter of differential evolution
F_{value}	Objective function value
i_{abc}	Mains phase currents, A
I_{sd}, I_{sq}	Stator currents, A
I'_{rd}, I'_{rq}	Rotor currents, A
J	Moment of inertia of the motor, kg·m^2
k_{id}, k_{iq}, k_ω	Weight coefficients of the objective function
L_{sd}, L_{sq}	Stator total inductances, H
$L_{\sigma d}$, $L_{\sigma q}$	Rotor leakage inductances, H
q_{id},q_{iq}, q_ω	Error terms in the objective function
r'_d, r'_q	Rotor resistances, Ohm
R_s	Stator resistance, Ohm
t	Time variable
T	Motor shaft torque, N·m
T_c	Constant component of the loading torque, N·m
T_{load}	Loading torque, N·m
U_{abc}	Mains phase voltage, V
U_{sd}, U_{sq}	Stator voltages along d and q axes, V
v	Mutated vector of differential evolution
v_1, v_2, v_3	Random vectors of differential evolution
x	Previous generation vector
Z_p	Number of motor poles
α, β, γ, δ	Parameters of Nelder–Mead method
λ'_{rd}, λ'_{rq}	Rotor flux linkages, Wb
λ_{sd}, λ_{sq}	Stator flux linkages, Wb
λ'_0	Permanent magnet flux linkage, Wb
φ	Mechanical rotational angle, rad
ω	Angular frequency of the rotation of the motor shaft, rad/s

References

1. Kurihara, K.; Rahman, M. High-Efficiency Line-Start Interior Permanent-Magnet Synchronous Motors. *IEEE Trans. Ind. Appl.* **2004**, *40*, 789–796. [CrossRef]
2. Kazakbaev, V.; Paramonov, A.; Dmitrievskii, V.; Prakht, V.; Goman, V. Indirect Efficiency Measurement Method for Line-Start Permanent Magnet Synchronous Motors. *Mathematics* **2022**, *10*, 1056. [CrossRef]
3. Addendum to the Operating Instructions: AC Motors DR.71.J-DR.100.J with LSPM Technology, 21281793/EN, 09/2014, SEW Eurodrive. Available online: https://download.sew-eurodrive.com/download/pdf/21343799.pdf (accessed on 19 December 2022).
4. de Almeida, A.T.; Ferreira, F.J.T.E.; Baoming, G. Beyond Induction Motors—Technology Trends to Move Up Efficiency. *IEEE Trans. Ind. Appl.* **2014**, *50*, 2103–2114. [CrossRef]
5. Catalogue of Super Premium Efficiency SynchroVERT LSPM Motors. Available online: https://www.bharatbijlee.com/media/14228/synchrovert_catalogue.pdf (accessed on 19 December 2022).
6. WQuattro, Super Premium Efficiency Motor, Product Catalogue, WEG Group—Motors Business Unit, Cod: 50025713, Rev: 03, Date (m/y): 07/2017. Available online: https://static.weg.net/medias/downloadcenter/h01/hfc/WEG-w22-quattro-european-market-50025713-brochure-english-web.pdf (accessed on 19 December 2022).
7. KT-420-5, Operation of Bitzer Reciprocating Compressors with External Frequency Inverters, Bitzer, 01. 2022. Available online: https://www.bitzer.de/shared_media/html/kt-420/Resources/pdf/279303819.pdf (accessed on 19 December 2022).
8. Do, N.; Le, T.; Ngo, X. Effect of Permanent Magnet Structure on The Performance of LSPMSM with a Power of 22 kW and 3000 rpm. *IOP Conf. Ser. Earth Environ. Sci.* **2022**, *1111*, 012047. [CrossRef]
9. Zhao, W.; Tian, M.; Wang, X.; Sun, Y. Analysis of the Synchronization Process and the Synchronization Capability for a Novel 6/8-Pole Changing LSPMSM. *IEEE Trans. Magn.* **2020**, *56*, 1–6. [CrossRef]
10. Melfi, M.J.; Umans, S.D.; Atem, J.E. Viability of Highly Efficient Multi-Horsepower Line-Start Permanent-Magnet Motors. IEEE Trans. *Ind. Appl.* **2015**, *51*, 120–128. [CrossRef]
11. Isfahani, A.H.; Vaez-Zadeh, S.; Rahman, M.A. Evaluation of synchronization capability in line start permanent magnet synchronous motors. In Proceedings of the 2011 IEEE International Electric Machines & Drives Conference (IEMDC), Niagara Falls, ON, Canada, 15–18 May 2011; pp. 1346–1350. [CrossRef]
12. Dinh, B.M. Optimal Rotor Design of Line Start Permanent Magnet Synchronous Motor by Genetic Algorithm. *Adv. Sci. Technol. Eng. Syst. J.* **2017**, *2*, 1181–1187. [CrossRef]
13. Yan, B.; Yang, Y.; Wang, X. Design of a Large Capacity Line-Start Permanent Magnet Synchronous Motor Equipped With Hybrid Salient Rotor. *IEEE Trans. Ind. Electron.* **2020**, *68*, 6662–6671. [CrossRef]
14. Palangar, M.F.; Mahmoudi, A.; Kahourzade, S.; Soong, W.L. Simultaneous Efficiency and Starting Torque Optimization of a Line-Start Permanent-Magnet Synchronous Motor Using Two Different Optimization Approaches. *Arab. J. Sci. Eng.* **2021**, *46*, 9953–9964. [CrossRef]
15. Ferreira, F.; de Almeida, A.; Cistelecan, M. Voltage Unbalance Impact on the Performance of Line-Start Permanent-Magnet Synchronous Motors. In Proceedings of the 6th International Conference EEMODS, Nantes, France, 14–17 September 2009; pp. 123–137.
16. Gnaciński, P.; Muc, A.; Pepliński, M. Influence of voltage subharmonics on line start permanent magnet synchronous motor. *IEEE Access* **2021**, *9*, 164275–164281. [CrossRef]
17. Farooq, H.; Bracikowski, N.; La Delfa, P.; Hecquet, M. Estimation of Steady-State Torque of Line Start Permanent Magnet Synchronous Motor Using Reluctance Network Approach. In Proceedings of the International Conference of the IMACS TC1 Committee, Nancy, France, 17–20 May 2021; pp. 603–616. [CrossRef]
18. RMahmoudi, A.; Roshandel, E.; Kahourzade, S.; Vakilipoor, F.; Drake, S. Bond graph model of line-start permanent-magnet synchronous motors. *Electr. Eng.* **2022**, *1*, 1–15. [CrossRef]
19. Zohra, B.; Akar, M. Design Trends for Line Start Permanent Magnet Synchronous Motors. In Proceedings of the 3rd International Symposium on Multidisciplinary Studies and Innovative Technologies, ISMSIT, Ankara, Turkey, 11–13 October 2019. [CrossRef]
20. Eker, M.; Zöhra, B.; Akar, M. Experimental performance verification of radial and axial flux line start permanent magnet synchronous motors. *Elect. Eng.* **2023**, *1*, 1–12. [CrossRef]
21. Song, H.; Wang, R.; An, A.; Qiu, H. Influence of rotor magnetic circuit structure on eddy current loss of high voltage line-start permanent magnet synchronous motor. *Int. Trans. Electr. Energy Syst.* **2021**, *31*, 1–10. [CrossRef]
22. Paramonov, A.; Oshurbekov, S.; Kazakbaev, V.; Prakht, V.; Dmitrievskii, V. Study of the Effect of Throttling on the Success of Starting a Line-Start Permanent Magnet Motor Driving a Centrifugal Fan. *Mathematics* **2022**, *10*, 4324. [CrossRef]
23. Wang, D.; Wang, X.; Chen, H.; Zhang, R. Matlab/Simulink-Based Simulation of Line-start PMSM Used in Pump Jacks. In Proceedings of the 2nd IEEE Conference on Industrial Electronics and Applications, Harbin, China, 23–25 May 2007; pp. 1179–1181. [CrossRef]
24. Paramonov, A.; Oshurbekov, S.; Kazakbaev, V.; Prakht, V.; Dmitrievskii, V. Investigation of the Effect of the Voltage Drop and Cable Length on the Success of Starting the Line-Start Permanent Magnet Motor in the Drive of a Centrifugal Pump Unit. *Mathematics* **2023**, *11*, 646. [CrossRef]
25. Maraaba, L.S.; Al-Hamouz, Z.M.; Milhem, A.S.; Twaha, S. Comprehensive Parameters Identification and Dynamic Model Validation of Interior-Mount Line-Start Permanent Magnet Synchronous Motors. *Machines* **2019**, *7*, 4. [CrossRef]

26. Dmitrievskii, V.; Prakht, V.; Kazakbaev, V.; Oshurbekov, S.; Sokolov, I. Developing ultra premium efficiency (IE5 class) magnet-free synchronous reluctance motor. In Proceedings of the 6th International Electric Drives Production Conference (EDPC), Nuremberg, Germany, 30 November–1 December 2016; pp. 2–7. [CrossRef]
27. Zhan, X.; Zeng, G.; Liu, J.; Wang, Q.; Ou, S. A Review on Parameters Identification Methods for Asynchronous Motor. *Int. J. Adv. Comput. Sci. Appl.* **2015**, *6*. [CrossRef]
28. Deng, A.; Zou, J.; Shao, Z.; Huang, G.; Shi, L.; Deng, W.; Antong, D. Improvement on asynchronous motor system identification based on interactive MRAS. In Proceedings of the 27th Chinese Control and Decision Conference (CCDC), Qingdao, China, 23–25 May 2015; pp. 448–453. [CrossRef]
29. Balara, D.; Timko, J.; Zilkova, J.; Lešo, M. Neural networks application for mechanical parameters identification of asynchronous motor. *Neural Netw. World* **2017**, *27*, 259–270. [CrossRef]
30. Kryukov, A.; Suslov, K.; Ilyushin, P.; Akhmetshin, A. Parameter Identification of Asynchronous Load Nodes. *Energies* **2023**, *16*, 1893. [CrossRef]
31. Yang, T.-G.; Gui, W.-H. Stator resistance identification for induction motor based on particle swarm optimization neural network observer. *Dianji Yu Kongzhi Xuebao/Electr. Mach. Control.* **2015**, *19*, 89–95. [CrossRef]
32. Wang, L.; Liu, Y. Application of Simulated Annealing Particle Swarm Optimization Based on Correlation in Parameter Identification of Induction Motor. *Math. Probl. Eng.* **2018**, *2018*, 1869232. [CrossRef]
33. Guangyi, C.; Wei, G.; Kaisheng, H. On Line Parameter Identification of an Induction Motor Using Improved Particle Swarm Optimization. In Proceedings of the 26th Chinese Control Conference, CCC, Zhangjiajie, China, 26–31 July 2007; pp. 745–749. [CrossRef]
34. Marčič, T.; Štumberger, B.; Štumberger, G. Differential-Evolution-Based Parameter Identification of a Line-Start IPM Synchronous Motor. *IEEE Trans. Ind. Electron.* **2014**, *61*, 5921–5929. [CrossRef]
35. Su, G.; Wang, P.; Guo, Y.; Cheng, G.; Wang, S.; Zhao, D. Multiparameter Identification of Permanent Magnet Synchronous Motor Based on Model Reference Adaptive System—Simulated Annealing Particle Swarm Optimization Algorithm. *Electronics* **2022**, *11*, 159. [CrossRef]
36. Kaššay, P.; Grega, R. Measuring Mass Moment of Inertia of a Rotor—Two Simple Methods Using No Special Equipment. In *Current Methods of Construction Design: Proceedings of the ICMD 2018*; Springer International Publishing: Basel, Switzerland, 2020; pp. 303–315. [CrossRef]
37. Markus Buehren. Differential Evolution. MATLAB Central File Exchange. 2023. Available online: https://www.mathworks.com/matlabcentral/fileexchange/18593-differential-evolution (accessed on 3 March 2023).
38. Price, K.; Storn, R.; Lampinen, J. *Differential Evolution: A Practical Approach to Global Optimization*; Springer: Berlin/Heidelberg, Germany, 2005.
39. Fminsearch. MathWorks. Available online: https://www.mathworks.com/help/matlab/ref/fminsearch.html (accessed on 20 June 2023).
40. Nelder, J.; Mead, R. A Simplex Method for Function Minimization. *Comput. J.* **1965**, *7*, 308–313. [CrossRef]
41. Wang, H.; Ge, X.; Liu, Y.-C. Second-Order Sliding-Mode MRAS Observer-Based Sensorless Vector Control of Linear Induction Motor Drives for Medium-Low Speed Maglev Applications. *IEEE Trans. Ind. Electron.* **2018**, *65*, 9938–9952. [CrossRef]
42. Simulate Simulink Model. MATLAB Documentation. © 1994–2023 The MathWorks, Inc. Available online: https://www.mathworks.com/help/simulink/slref/sim.html (accessed on 20 June 2023).

machines

MDPI

Article

Discontinuous PWM Strategy with Frequency Modulation for Vibration Reduction in Asynchronous Machines

Antonio Ruiz-González [1], Juan-Ramón Heredia-Larrubia [2,*], Francisco M. Pérez-Hidalgo [1] and Mario Jesus Meco-Gutiérrez [1]

[1] Electrical Engineering Department, University of Malaga EII, Doctor Ortiz Ramos s/n, 29071 Málaga, Spain; afruiz@uma.es (A.R.-G.); fmperez@uma.es (F.M.P.-H.); mjmeco@uma.es (M.J.M.-G.)
[2] Electronic Technology Department, University of Malaga EII, Doctor Ortiz Ramos s/n, 29071 Málaga, Spain
* Correspondence: jrheredia@uma.es

Abstract: The aim of this paper is to present our research into the reduction of vibrations in induction motors. The use of power inverters results in the generation of electrical harmonics, which increase the level of the mechanical vibrations of electrical machines. To reduce these harmonics, we present a discontinuous pulse-width modulation (PWM) control strategy based on carrier-wave modulation applied to multilevel inverters. Using the proposed modulation technique, the amplitude of the electrical harmonics is reduced, as compared to other conventional techniques. These current harmonics produce the MMF (magnetomotive force) harmonics in the air gap, which are one of the main sources of vibrations. The control strategy makes it possible to vary the electrical spectrum at the output of a multilevel inverter by modifying a control parameter of the carrier wave in the PWM, thus avoiding the natural frequencies of mechanical resonance. The proposed technique also has the feature of attenuating the total harmonics distortion of the voltage of the multilevel inverters, as well as the achievement of a higher RMS value of the output voltage for the same DC level. Laboratory results for an induction motor with different modulation strategies, applied in a multilevel inverter and compared to the strategy presented, are attached.

Keywords: induction motors; multilevel inverters; vibrations; PWM techniques

Citation: Ruiz-González, A.; Heredia-Larrubia, J.-R.; Pérez-Hidalgo, F.M.; Meco-Gutiérrez, M.J. Discontinuous PWM Strategy with Frequency Modulation for Vibration Reduction in Asynchronous Machines. *Machines* **2023**, *11*, 705. https://doi.org/10.3390/machines11070705

Academic Editors: Loránd Szabó and Feng Chai

Received: 25 May 2023
Revised: 27 June 2023
Accepted: 28 June 2023
Published: 3 July 2023

1. Introduction

The induction motor is the most widely used type of mechanical drive equipment in industrial environments, and it has positioned itself as an important component in fields such as smart transport and machine manufacturing [1]. These devices need to be controlled using power converters that regulate their torque and speed. These converters generate a pure non-sinusoidal power supply that produces electrical harmonics. These harmonics produce vibrations and noises in the motors, and they can deteriorate them and reduce their life cycles [1,2]. Vibration is a key component in the operation of the motor. If vibration sources are not detected early on, this will lead to the gradual deterioration of the machine, reaching a point where irreparable damage occurs, resulting in motor shutdown, potentially causing accidents.

The steady-state vibration of the engine can be influenced by several sources in addition to those originating from the electromagnetic field. Thus, vibrations originating from the mechanical base of the system, the type of anchoring to the ground, or other devices that are mechanically connected to the motor can be the sources of such vibrations [3]. Additionally, high-voltage switching through pulse-width modulation (PWM) of the motor controllers produces harmonics which generate MMF that, in turn, cause undesired torques during operation.

Considerable focus has been placed on vibrations caused by electromagnetic phenomena, particularly those resulting from harmonics. The slotting effect and the magnetic

interaction between the stator and rotor have received significant attention in this regard. In [4], a model is introduced to precisely calculate the electromagnetic parameters associated with vibroacoustic phenomena. This model treats each spatial harmonic generated by the stator winding MMF individually, employing the current-sheet approach to determine the radial and tangential forces present in squirrel-cage induction motors.

The proposal of the present work is to offer a possible solution for avoiding these harmonics, and therefore vibrations, in a motor, for which the use of multilevel power converters (MLI), together with an optimized control technique, is proposed.

The multilevel inverter is a power converter that provides a suitable solution for synthesizing an output voltage to reduce the harmonic content of voltage and current in medium- and high-power systems [5]. The most common topologies of these converters consist of connecting individual inverters, "called stages", to provide an output voltage that is the result of associating the voltages of the different stages. The advantages of multilevel converters over two-level converters include a lower dv/dt, lower switching losses, a higher fault-tolerance capability, and better output waveform quality [6]. Due to this last advantage, the output filter will also have a smaller volume.

There is a wide range of multilevel inverter topologies [7,8], with the most prevalent voltage source topology being the neutral-point diode converter (NPC) [9], some of them having parallel structures for high-power motors [10]. Other relevant types of topologies would be the flying capacitor converter (FCC) [11] and the modular multilevel converter (MMC) [12,13]. Finally, the cascaded H-bridge converter (CHB) [14], with different control techniques [15] and with symmetrical and asymmetrical power supplies [16], is more applicable as the number of levels increases.

In this research paper, we have opted to use a cascaded H-bridge multilevel inverter for our comparative analysis (see Figure 1), which boasts several advantages over alternative topologies (NPC and FCC). The CHB inverter possesses modularity and enhanced controllability due to the identical structure of each stage. Furthermore, it enables the attainment of multiple levels using minimal components. These alleviate switching losses in the utilized devices, thereby augmenting circuit reliability and efficiency [17]. Consequently, this topology finds extensive utilization in industrial applications [8].

One of the applications of the CHB inverter is the provision of power to high-power motors, which is supplied at elevated voltages to minimize current in the windings. This necessitates multiple stages for each phase. It is widely recognized that using such devices for the speed or torque control of AC electrical machines can lead to increased vibrations.

Regarding modulation techniques, the literature offers numerous options for MLI control. The most commonly employed techniques include carrier-based PWM [18], space vector modulation [19,20], and selective harmonic elimination [21,22]. Carrier-based modulation has given rise to highly popular techniques for MLIs, such as phase-shifted pulse-width modulation (PS–PWM) and carrier-level shift pulse-width modulation (LS–PWM) [23,24]. Other techniques involve modifying the carrier-signal frequency and modulating the signal harmonics' amplitudes to reduce losses and enhance the electrical parameters of the modulated waveform [25]. In [26], an LS–PWM technique is utilized, where the reference signal is vertically shifted to derive the switching signal for the MLI. As a level shift exists between the carrier signals, higher voltage distortion occurs, which is not the case with PS–PWM.

In summary, all electric drives contribute to increased vibrations in electromagnetic circuits [27]. However, the level of these vibrations can be mitigated depending on the control technique and topology employed [28,29]. Here, the proposed strategy focuses on cascaded or H-bridge inverters and utilizes an efficient PS–PWM technique. This technique not only ensures a balanced power distribution among the cells but also results in reduced voltage distortion and the effective suppression of harmonic current distortion. These characteristics play a crucial role in attenuating the vibrations generated by the motor. The vibration results and quality parameters of the inverter output waveform obtained through the proposed modulation technique have been compared with results from other techniques documented in the scientific literature, which have shown promising outcomes. Specifi-

cally, the compared techniques include amplitude-shifted modulation in the carrier waves (Figure 2a), phase-shifted modulation in the carrier waves (Figure 2b), and phase-shifted modulation with harmonic injection into the modulating wave (Figure 2c). To the best of our knowledge, there is currently no recent research in the technical literature on reducing vibrations in induction motors using multilevel converters and PS–PWM techniques.

The remainder of the present paper is structured as follows: Section 2 provides an introduction to the vibration frequencies anticipated when feeding an induction motor with either a sinusoidal source or an inverter generating specific sets of harmonics.

In Section 3, the proposed technique for controlling multilevel inverters is presented, outlining its fundamental principles. The generation of the signals applied to the IGBT gate terminals and the waveform at the inverter's output, based on the control parameter, is described. Additionally, the section illustrates the relationship between the instantaneous frequency of the carrier wave and the modulating signal in relation to the control parameter.

Subsequently, Section 4 presents and analyzes the laboratory results. It showcases the equipment required to generate the control waves for the tested strategies, including the vibration meter setup and the signal analyzer used to record voltage and current waveforms, along with their corresponding electrical spectra. Lastly, Section 5 summarizes the conclusions drawn from the research.

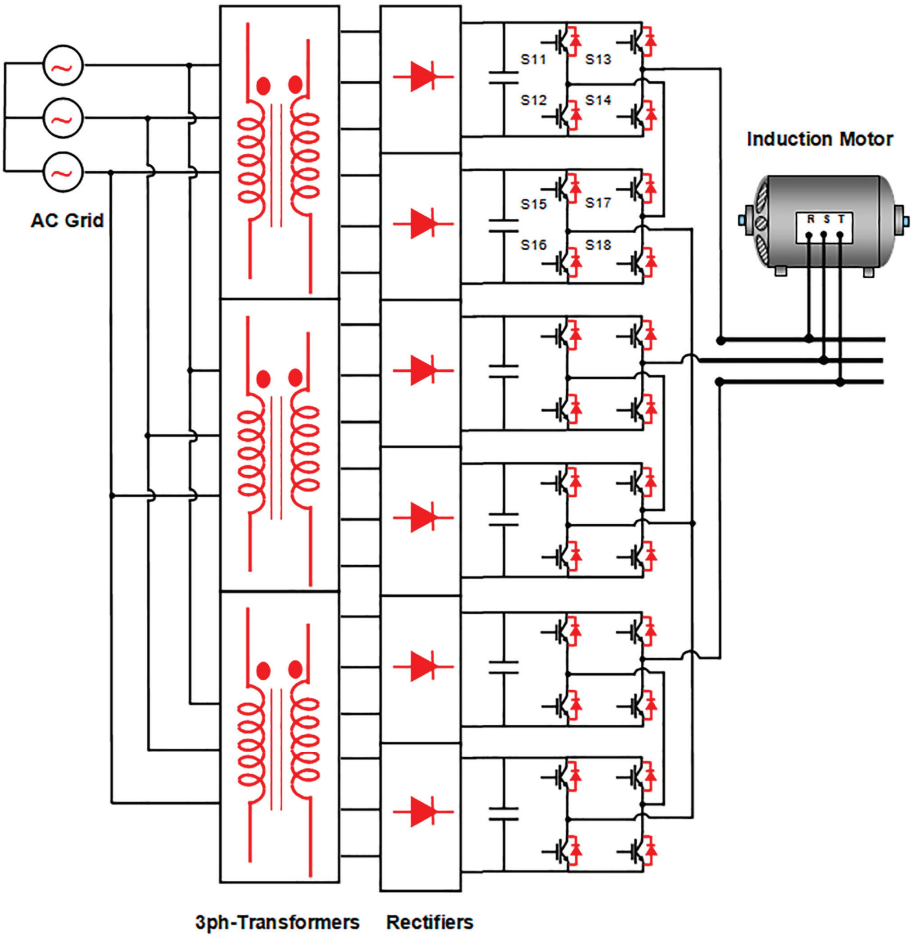

Figure 1. CHB multilevel power inverter.

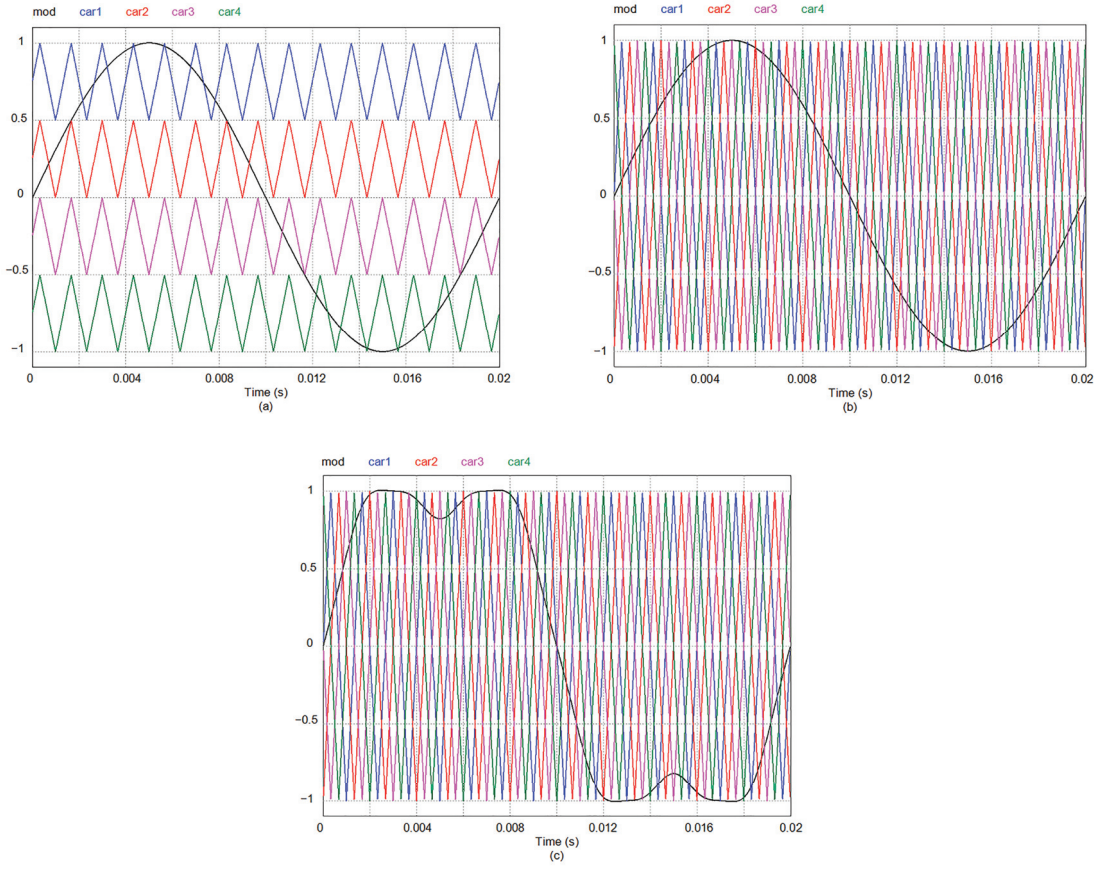

Figure 2. Multilevel inverter modulation: (**a**) with amplitude shift; (**b**) with phase shift; (**c**) with phase shift and injection of harmonics.

2. Natural Frequencies and Axial Stress Generating MMFs on the Stator

There are two sources of vibrations that occur in an electrical machine, depending on their origin. The first type is composed of axial forces of aerodynamic and mechanical origin and by the eccentricities of its axis (mainly, the fan, bearing, activation of mechanical resonances, and the phenomenon of magnetostriction). They are low-frequency, depend on the degree of saturation in the magnetic circuit of the machine, and the load level has a limited effect on them. Electrical harmonics of the spatial type, due to the restriction of the maximum number of slots and coils (size functions), are another source of vibrations and noise. On the other hand, when an inverter is used to power the motor, the produced electrical harmonics are a new source of vibrations. This last source of vibrations will be a function of the modulation technique used with the power switches of these inverters, the carrier frequency, and the speed set for the motor shaft. These vibrations depend on the current and, therefore, on the load level. When any of these electrical harmonics activate a natural resonance frequency of the engine, the level of vibration can be critical to the lifetime of the machine.

The calculation of the natural resonance frequencies of an induction motor structure can be carried out with the equations found in the technical literature [30]. If the stator length is greater than its mean diameter, D_c, good results are obtained for these frequencies

by considering the electrical machine as a cylinder of infinite length. For circumferential modes of vibration where $m \geq 0$, the frequency can be expressed as follows:

$$f_m = \frac{P_m}{\pi D_c}\sqrt{\frac{E_c}{\rho_c(1-\nu_c^2)}} \tag{1}$$

where ν_c is Poisson's ratio, E_c is the modulus of elasticity, and P_m is the root of the equation of movement. Circumferential mode forces m to zero, and therefore, $P_m = 1$. For $m \geq 1$,

$$P_m = \frac{1}{2}\sqrt{(1+m^2+k^2m^4)^{\pm\sqrt{(1+m^2+k^2m^4)^2-4k^2m^6}}} \tag{2}$$

and the dimensionless thickness parameter is

$$\kappa^2 = \frac{h_c^2}{3D_c^2} \tag{3}$$

where h_c is the stator thickness. On the other hand, a housing with a bell-shaped end behaves like a cylinder with both ends mechanically constrained. There will be two axes of displacement: a radial one with circumferential vibrational modes, m, "breathing" $m = 0$, elliptical $m = 1$, etc., and another axial one with modes n being equal to 1 onwards. The characteristic equation of the movement of a cylinder of finite length, L_f, supported on legs according to the Donnell–Mushtari theory [30], will be of the following type:

$$P_{mn}^6 - C_2 \cdot P_{mn}^4 + C_1 \cdot P_{mn}^2 - C_0 = 0 \tag{4}$$

where P_{mn} are the roots of the equation of motion. The housing resonance frequencies have the same structure as those in Equation (1). Three groups of roots correspond to the displacement in the three orthogonal directions in Equation (4), for which the smallest real root determines the natural deflection frequency of the frame, with that being:

$$C_2 = 1 + +\frac{1}{2}(3-\nu)(m^2+\lambda^2) + \kappa^2(m^2+\lambda^2)^2 \tag{5}$$

$$C_1 = \frac{1}{2}(1-\nu)[(3+2\nu)\lambda^2 + m^2 + (m^2+\lambda^2)^2] + \frac{3-\nu}{1-\nu}\kappa^2(m^2+\lambda^2)^2 \tag{6}$$

$$C_0 = \frac{1}{2}(1-\nu)[(1-\nu^2)\lambda^4 + \kappa^2(m^2+\lambda^2)^4] \tag{7}$$

$$\lambda = 0.5n\pi\frac{(D_f - h_f)}{L_f - L_0} \tag{8}$$

$$\kappa = \frac{h_f^2}{12R_f^2} \tag{9}$$

$$L_0 = L_f\frac{0.3}{n+0.3} \tag{10}$$

where C_2, C_1, and C_0 are the coefficients of the polynomial described in (4), R_f is the average radius of the casing, D_f is the average diameter of the casing, h_f is the thickness of the casing, L_f is its length, ν is its Poisson's ratio, and ρ is the density. The circumferential vibrational modes, m equal to 0 onwards (natural numbers), should be calculated for each axial vibrational mode, n.

If the motor is fed from a balanced three-phase power supply, the only harmonics that appear are spatial harmonics. The most significant of these spatial harmonics are the tooth

harmonics. They are present when the machine is fed with a three-phase network, and they depend on the number of phases and poles and the winding factor of each harmonic:

$$\nu = k\left(\frac{s_1}{p}\right) \pm 1 \tag{11}$$

with p being the number of pairs of poles, s_1 being the number of stator slots, and k equaling the natural numbers from 1 onwards. The amplitude of the vibrations, A, shall be proportional to the products of the terms of the flux densities:

$$A = f\left(B^2(\alpha, \mathrm{t})\right) \tag{12}$$

where B is the magnetic flux density in the magnetic circuit of the machine, α is the angular position with respect to a reference, and t stands for time, such that the amplitude and frequency of these vibrations must consider the product of all the harmonic terms of the induction in the machine. Other harmonics are due to the phenomenon of magnetostriction and bearing rollers.

When the machine is powered by a power inverter, the radial forces resulting from the electrical harmonics are caused by the interaction between the stator harmonics and their corresponding time harmonics, resulting in a specific frequency:

$$f_r = 2\mathrm{f}\cdot(2\mathrm{k}m_1 \pm 1) \tag{13}$$

where f is the frequency of the fundamental component of the modulated waveform, k is the series of natural numbers, and m_1 is the number of phases of the stator. Similarly, the harmonic decomposition of the rotor currents will result in vibrations at specific frequency values:

$$f_r = 2\mathrm{f}\cdot(2\mathrm{k}m_1 \pm 1)\cdot\left(\frac{s_2}{p} \pm 1\right) \tag{14}$$

with s_2 being the number of rotor slots. In addition, frequency vibrations are generated as a result of the mutual influence between the frequency of the carrier signal, $\mathrm{f_c}$, with the time harmonic frequency of the modulating wave. Its vibrational mode is zero, and therefore, the possibility of producing high vibrations is greater since these are reduced with the order of the vibrational mode. Their frequencies can be obtained as follows:

$$f_r = \left|\pm\left(\mathrm{n}\cdot\mathrm{f_c} \pm \mathrm{n}'\cdot\mathrm{f}\right) - \mathrm{f}\right| \tag{15}$$

where f_r is the frequency of the force density. If n is even, n′ is odd, and if n is odd, n′ will be even. Therefore, electrical harmonics can be expected at the following frequencies: $\mathrm{f_c} \pm 2\mathrm{f}$, $\mathrm{f_c} \pm 4\mathrm{f}$, $2\mathrm{f_c} \pm \mathrm{f}$, $2\mathrm{f_c} \pm 3\mathrm{f}$, and so on. In other words, it can be anticipated that the vibrational harmonics generated by the inverter will manifest themselves at frequencies that are either slightly above or below the frequency of the electrical spectrum of the modulated wave applied to the electric motor. When an electrical harmonic is present at a frequency of f, the corresponding vibrational harmonic will manifest itself at a frequency of either (f + 1) or (f − 1). This is due to the axial force densities being derived from the multiplication of all the flux densities within the air gap.

Power inverters manipulate the voltage level and frequency in the stator of the machine, resulting in an electrical spectrum characterized by amplitudes and frequencies that are contingent upon the modulation technique employed. The existence of these harmonics will produce energy losses, reduced efficiency, and pulsating torques that translate into vibrations in the machine. One common approach to mitigating the adverse effects of these electrical harmonics is to raise the frequency of the carrier signal. However, this frequency is constrained by the maximum switching frequency of the circuit breakers and, in turn, increases the losses incurred by the inverter. Another approach, enabled by the decreased cost of power switches, is to interconnect multiple elementary stages in a series,

each utilizing one or more separate sources. This arrangement reduces the number of switching for each IGBT and enables a higher carrier frequency in the PWM technique, thereby amplifying the voltage and power capacities of the electrical machine.

In the case of high power and voltage requirements, minimizing switching losses becomes crucial. This is achieved by minimizing the frequency of the carrier wave in the inverter modulation. However, this strategy amplifies the likelihood of mechanical resonances in the system caused by the time harmonics generated by the inverter. Hence, for such applications, the control strategy assumes special significance.

3. New HIPWM–FMTC Strategy Applied to Multilevel Inverters

The HIPWM–FMTC (harmonic injection PWM–frequency-modulated triangular carrier) technique generates the output voltage of an inverter by comparing a modulating wave that injects harmonics with a triangular carrier wave that is frequency-modulated. The frequency of the carrier waveform is not constant but varies based on a periodic function, specifically a squared cosine, which is synchronized with the phase of the modulating waveform. The employed strategy involves increasing the number of switching pulses when the slope of the modulating waveform is at its maximum or minimum and then gradually reducing it to zero when the slope is at its lowest (near the maximum and minimum phases). However, the total number of pulses in a complete period is maintained in relation to any conventional PWM technique. This strategy is commonly referred to in the technical literature (within the context of three-level inverters) as the HIPWM–FMTC (harmonic injection PWM–frequency-modulated triangular carrier) technique [31].

A modified version of the HIPWM–FMTC technique has been proposed, which introduces a parameter that interrupts the triangular carrier wave during certain time slots of the modulating wave. This modification allows for an increase in the instantaneous switching frequency in some time slots while eliminating switching in others [32]. When applied to multilevel inverters, this technique is referred to as HIPWM–FMTC truncated or HIPWM–FMTCt [33]. The effect of overmodulation to improve the HIPWM–FMTC technique in three-level inverters has also been investigated [34]. The instantaneous pulsation of the carrier wave, denoted as ω_i, becomes a discontinuous function that is synchronized with the modulating wave ω_m. It can be defined as follows:

$$\omega_i = \frac{d\theta}{dt} = A_M \cdot \omega_m \left[cos^2 \omega_m t - K \right] \tag{16}$$

The modulating wave and the instantaneous pulse of the carrier wave, ω_i, need to be synchronized functions, as depicted in Figure 3. The parameter K, which represents the truncation level, is a real number ranging from 0 to 1, and it is independent of $\overline{M}$, which represents the number of pulses per period. On the other hand, A_M is a parameter that determines the middle of the maximum frequency of the carrier wave. By selecting appropriate values for A_M, K, and the frequency modulation order, $\overline{M}$, the instantaneous maximum frequency can be adjusted. The combination of these parameters (A_M and K) enables the modification of the electrical spectrum without altering the value of $\overline{M}$. Thus, after setting a value for $\overline{M}$, each value of K will correspond to a specific value of A_M. It is important to note that when Equation (12) yields negative values, ω_i will be nullified during those intervals.

Note that the frequency modulation order, $\overline{M}$, is the mean value of a periodic function $M(t)$, thus, the instantaneous frequency modulation order, which will be null between t_1 and t_2 and between t_3 and t_4 for each period of the modulating wave to avoid such switching. During a period of the modulating wave, both M and $\overline{M}$ will be the same value:

$$\overline{M} = \frac{1}{T_m} \int_0^{T_m} A_M \left[cos^2(\omega_m t) - K \right] dt \tag{17}$$

where T_m is $2\pi/\omega_m$. The frequency modulation order, $\overline{M}$, must be set to a natural number, and if the motor is three-phase, it must be set to an odd value that is a multiple of 3.

The primary objective is to ensure that the maximum instantaneous frequency of the triangular carrier wave aligns with the points where the modulating sine wave exhibits the steepest slope (0 and π radians). The frequency of the carrier wave gradually decreases following a quadratic cosine function around these phases and eventually reaches zero within a specific time interval determined by the truncation factor, as described by Equations (12) and (13). In the case of $K = 0$, the carrier wave frequency theoretically becomes zero only at the phase values of the modulating wave: $\pi/2$ and $3\pi/2$. In other words, the instantaneous pulsation of the carrier wave is never eliminated. As K increases from 0 to 1 (excluding 1, which would imply an infinite instantaneous carrier wave frequency), the proposed technique ensures that the carrier frequency becomes zero for progressively longer time intervals centered around the T/4 and 3T/4 of the period of the modulating wave. The frequency of the carrier waveform increases precisely around the 0 and T/2 of the period of the modulating wave, which correspond to the points of its steepest slopes. This approach is adopted because the modulating wave undergoes faster slope changes at these phase values, thereby providing a more accurate representation of the carrier wave's shape in the modulated waveform. As shown in Figure 3, $K = 0.55$ and $\overline{M} = 15$ ($A_M = 111.15125$); for slightly less than half of the period, there will be a modulated triangular carrier, and during the other, slightly more than half, of the period, switching will be canceled. The maximum excursion of the carrier frequency will be $A_M \cdot \omega_m \cdot (1 - K) = 50.01806 \cdot \omega_m$. Therefore, t_1 is 2.3426 ms, and t_2, t_3, and t_4 will be 7.6574, 12.3426, and 17.6574 ms, respectively. For other values of K, regardless of the value of M, the times t_1 to t_4 will change. For example, for $K = 0.5$, they will be 2.5, 7.5, 12.5, and 17.5 ms.

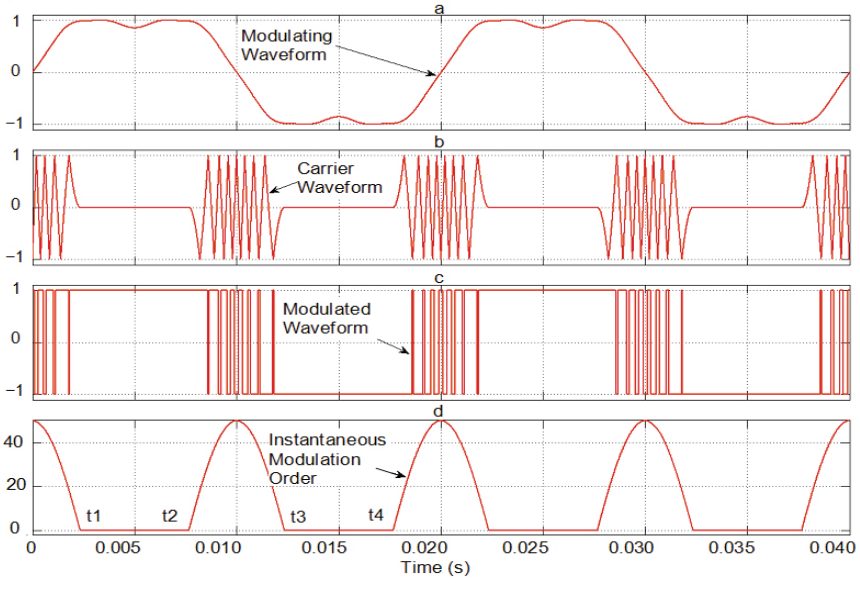

Figure 3. Simulation of the proposed PWM generation: (**a**) modulating waveform for f = 50 Hz; (**b**) HIPWM–FMTCt carrier ($K = 0.55$ and $A_M = 111.15125$); (**c**) phase voltage for an H-bridge; (**d**) instantaneous modulation order.

By employing this technique, the maximum frequencies of the carrier will be up to π times $\overline{M}$ depending on K, instead of $\overline{M}$, as would be the case in a sinusoidal PWM technique. In Figure 3, the area beneath the curve of the instantaneous modulation order corresponds to $\overline{M} = 15$ and $K = 0.55$. It is possible to identify the modulating, carrier, and modulated functions, as well as the function of the instantaneous modulation order. In

Figure 4a, the combined modulating and carrier functions can be observed as a function of time. Figure 4a,b illustrate the signals driving the gates of the 2-stage H-bridge transistors corresponding to one phase of the multilevel inverter shown in Figure 1. The pulse train that triggers the S1_1 base is generated by comparing the modulating signal with the phase 0° harmonic injection with the phase 0° carrier. Similarly, the pulse train that triggers the base of S1_3 is obtained by comparing the modulating signal with the 180° phase harmonic injection with the 0° phase carrier. The pulses resulting from the comparison between the modulator and the 0° and 90° phase carrier stimulate S1_5. Finally, the 180° phase modulator, as compared to the 90° phase carrier, generates the pulses that drive the gate of S1_7. The timing of these signals is shown in Figure 4c.

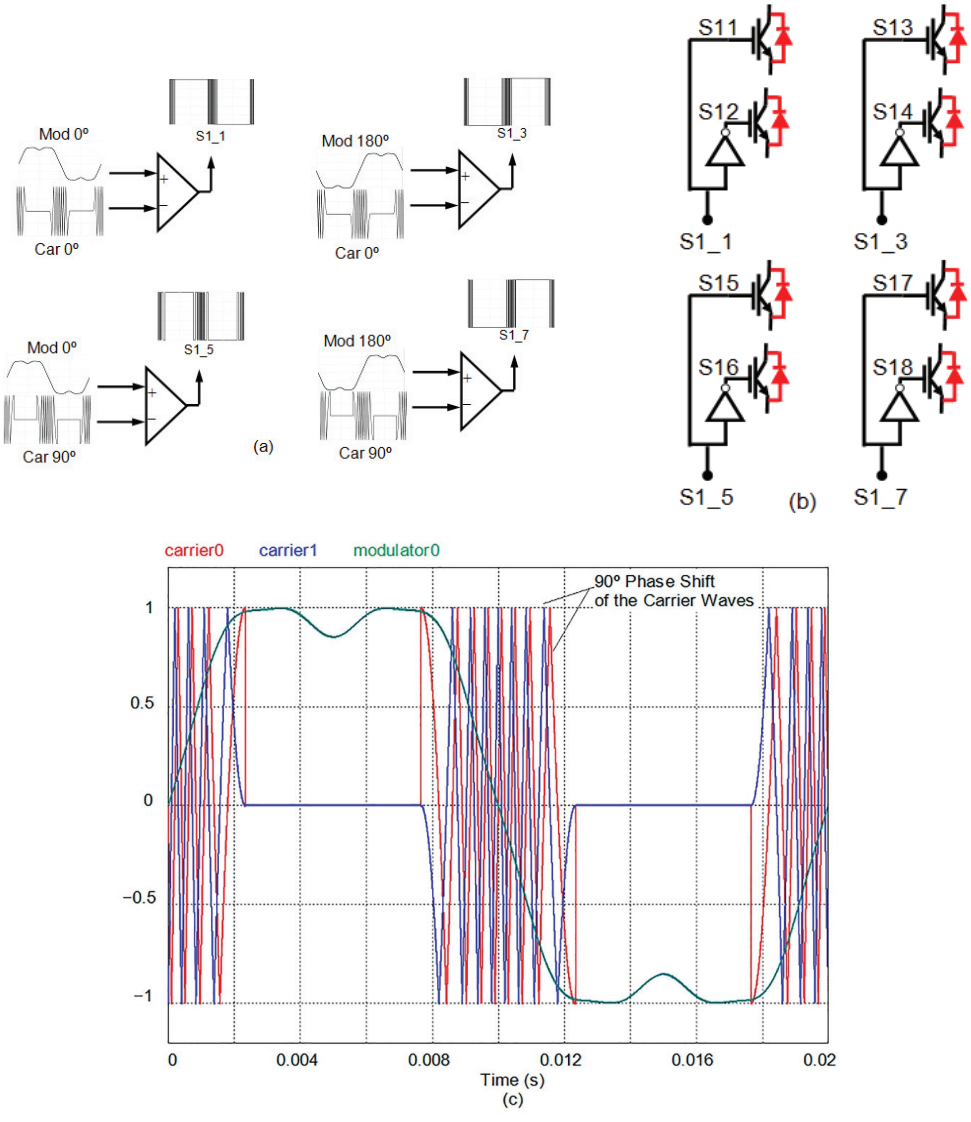

Figure 4. (**a**) Single-phase pulse generation; (**b**) gate signals for IGBTs; (**c**) modulator and carrier waveforms for f = 50 Hz, $\overline{M}$ = 15 for the proposed technique (K = 0.55 and A_M = 111.1513π).

Table 1 shows how some variables evolve against K when ω_m are set to 100π rad/s while $\overline{M}$ is fixed at 11 and 15, respectively. The variables presented are t_1 (a quarter of the time that makes possible the per-period switching of the output waveform), A_M, and $A_M \cdot (1 - \mathrm{K})$, with the latter being the instantaneous modulation order of maximum frequency. The maximum carrier frequency is f_m multiplied by $A_M \cdot (1 - K)$. Figure 5a shows the simulation of two periods of the three-line voltage of the modulated waves, where it can be seen how the switching frequency is higher for values close to zero. Moreover, it decreases until the commutations in the maximum and minimum values disappear. Figure 5b illustrates how the amplitude of the 17th harmonic, as a percentage of the fundamental, changes with respect to the K-value. This is true for the fundamental term as well as for the rest of the harmonics.

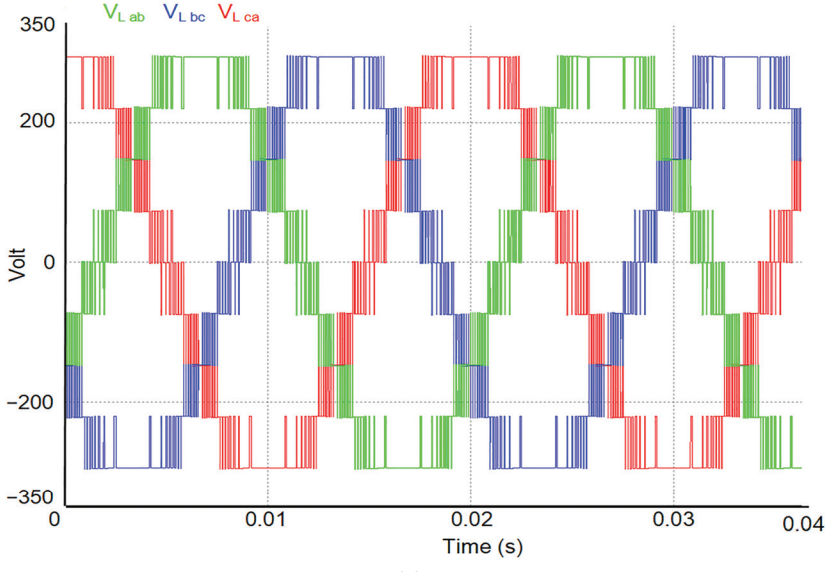

(**a**)

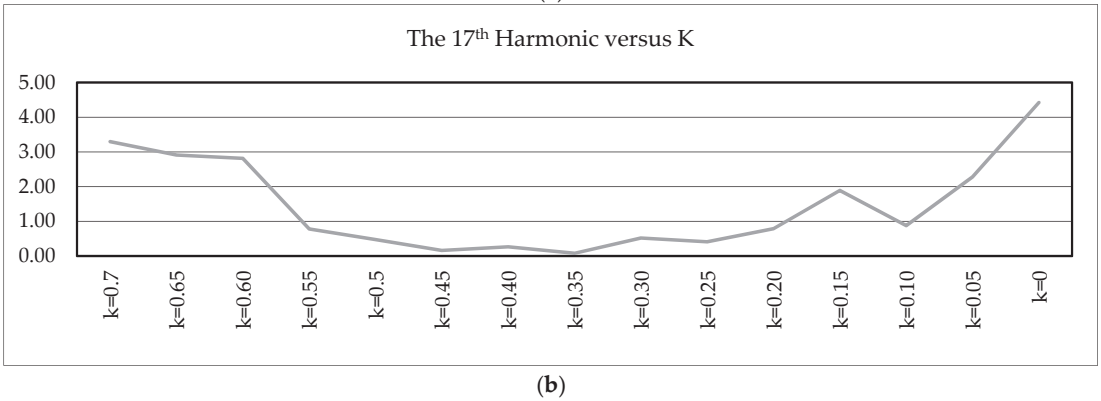

(**b**)

Figure 5. (**a**) Modulated line voltage waveforms with HIPWM–FMTCt strategy (K = 0.55, f = 50 Hz, and $\overline{M}$ = 15); (**b**) amplitude for the 17th harmonic with respect to the K-value.

Table 1. A_M, t_1, and $A_M \cdot (1 - K)$ for different values of K with $M = 11$ and $M = 15$.

K	A_M ($M = 11$)	A_M ($M = 15$)	t_1 (ms)	$A_M \cdot (1 - K)_{M = 15}$
0.2	32.4700	44.27732	3.5242	35.4218
0.3	40.4314	55.13370	3.1550	38.5935
0.4	51.8016	70.63850	2.8207	42.3831
0.45	59.4751	81.10240	2.6599	44.6063
0.5	22π	30π	2.5000	47.1239
0.55	81.5109	111.1513	2.3426	50.0181
0.6	97.9098	133.5134	2.1835	53.4054
0.7	152.6484	208.1569	1.8480	62.4471
0.8	283.9854	387.2528	1.5153	77.4506

4. Results

An AEG^{TM} 380/220 V, 1000 W, and 4-pole asynchronous motor with $s_1 = 36$ slots in the stator and $s_2 = 26$ slots in the rotor was used to measure vibrations in the laboratory. The multilevel inverter was built on the basis of GUASCH S.A.^{TM} modules, which have GPT-IGBT transistors. The GUASCH S.A.^{TM} GPT-IGBT module was used to implement the multilevel inverter. It offers a power stack of insulated gate bipolar transistors (IGBTs) for motor control. The power system consists of three-phase bridge rectifiers, capacitor banks, IGBTs with forced-air-cooled heat sinks, opto-coupled drivers, output phase current sensors, DC-link current, and a voltage sensor. The maximum voltage that the DC-link can withstand must not exceed 750 V, and the maximum RMS current in each phase is 32 A.

The hardware system for generating control signals for each of the H inverters that make up the multilevel inverter is based on the NI9154 card from National Instruments^{TM}, on which a Labview^{TM} platform has been developed for generating the PWM techniques that control the different H-bridges of the multilevel inverter. A Chauvin Arnoux^{TM} C.A. 8336 was used to measure the output current harmonics of the multilevel inverter. To measure the vibrations of the machine, a sensor PCB^{TM} Piezotronics Accelerometer model number 333B50 was connected to a METRAVIT Symphonie model 01 dB sound-level meter. Figure 6a illustrates the multilevel power inverter and the NI9155 control equipment, and Figure 6b illustrates the sensor on the AEG^{TM} asynchronous motor.

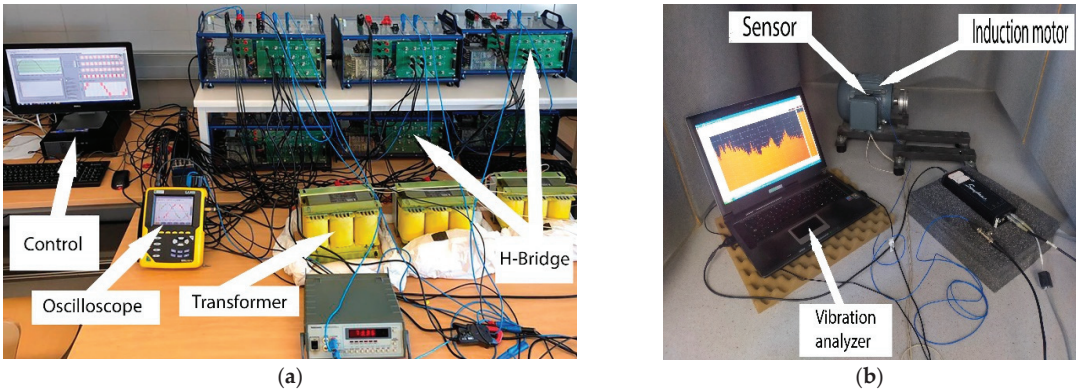

(**a**) (**b**)

Figure 6. Implementation: (**a**) multilevel inverter, NI9154 network analyzer, National Instruments^{TM} NI9154 board with Labview^{TM} system for control of the multilevel inverter bridges; (**b**) motor with PCB^{TM} Piezoelectric Accelerometer model 333B550 and vibration analyzer.

Figures 7–10 illustrate the waveforms and amplitudes of the current spectra (%) of the different PWM techniques, SPWM-I, SPWM-II, and SPWM-III, and the HIPWM–FMTCt technique with $K = 0.55$ presented in this paper.

The SPWM-I technique corresponds to PWM with an amplitude-shifted triangular carrier wave. This is, perhaps, the most common technique in the technical literature on multilevel inverters. Figure 7a shows the output waveform of the multilevel inverter, and Figure 7b shows the harmonics electrical spectrum of the output current of this waveform. The fundamental harmonic, in terms of the percentage of output voltage, is maintained at 220 V RMS.

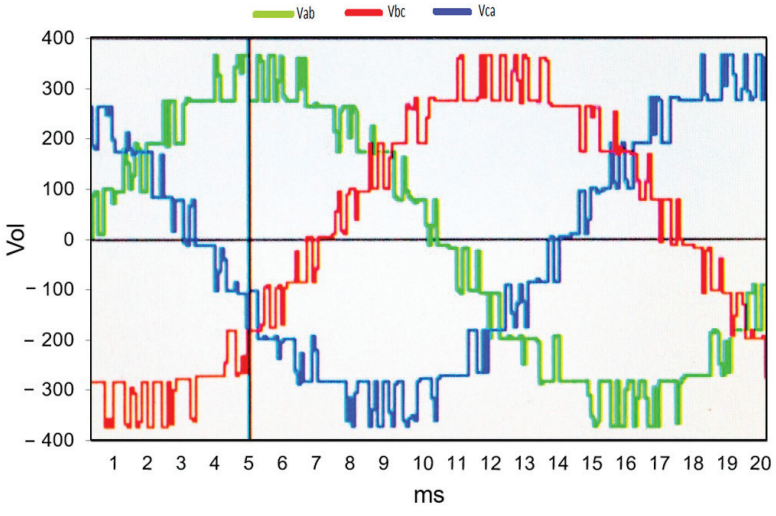

(**a**)

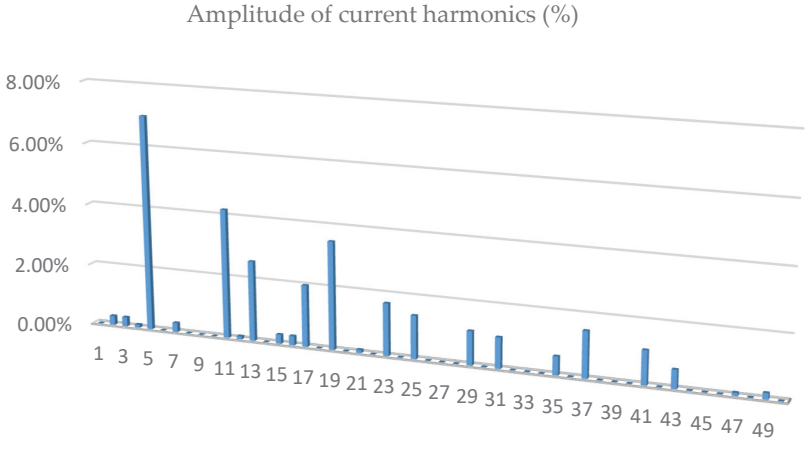

(**b**)

Figure 7. (**a**) Line voltage output (220 V RMS) with SPWM-I strategy; (**b**) amplitude of current harmonics (%): V = 220 V RMS of the fundamental term.

The following SPWM-II technique corresponds to a phased-shift for the triangular wave carriers and a sine modulator wave. As in the previous technique, Figure 6a,b correspond to the inverter output voltage waveform and the harmonics electrical spectrum in percentage terms of the current, respectively. The output voltage is maintained at 220 V RMS.

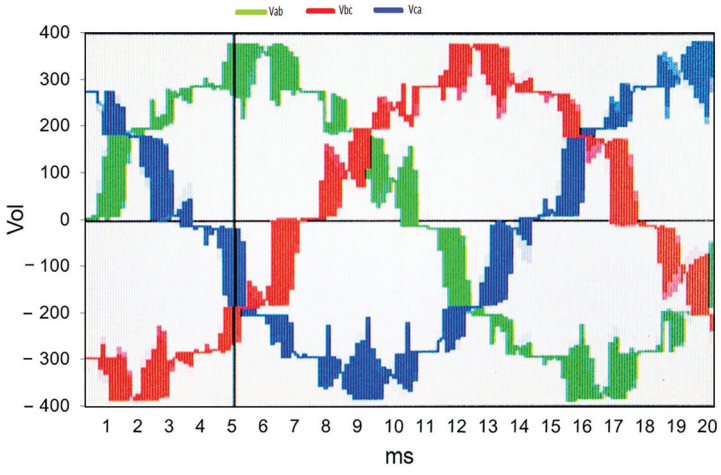

(**a**)

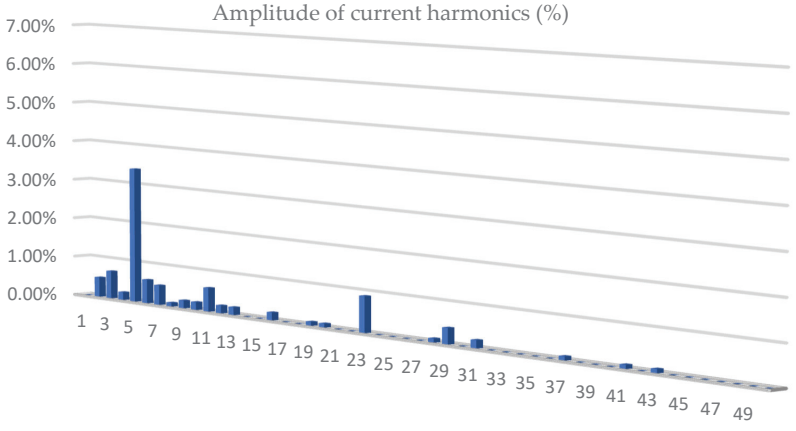

(**b**)

Figure 8. (**a**) Line voltage (220 V RMS) of the multilevel inverter with SPWM-II strategy; (**b**) amplitude of current harmonics (%): V = 220 V RMS of the fundamental term.

The SPWM-III technique uses a triangular carrier, and harmonics are injected into the modulating waveform. Figure 9a shows the modulated waveforms for the line signal of the multilevel inverter with SPWM-III, and Figure 9b shows the electrical spectrum of the output current (%) of the SPWM-III multilevel inverter (V = 220 V RMS of the fundamental term).

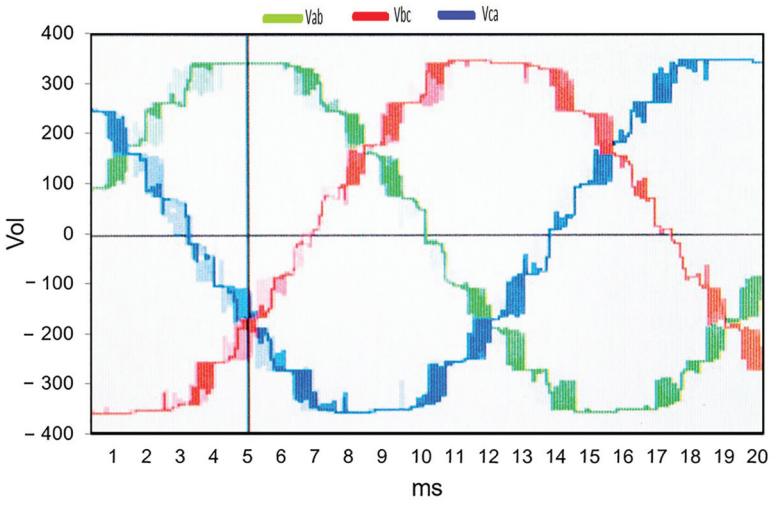

(**a**)

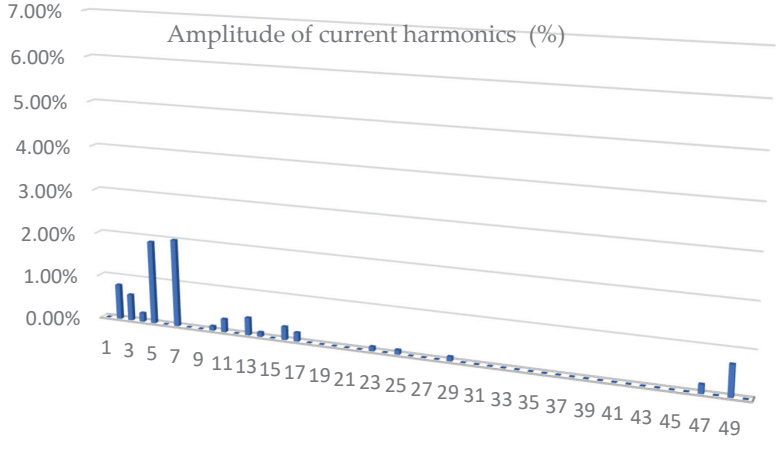

(**b**)

Figure 9. (**a**) Line voltage output of the multilevel inverter with SPWM-III technique; (**b**) percentage amplitude of current harmonics (V = 220 V RMS of the fundamental term).

The proposed technique is HIPWM–FMTCt, which has the characteristic of modulating and truncating the frequency of the carrier wave. Figure 10a,b show the output of the inverter voltage and the percentage electrical spectrum of the output current, as in the previous techniques. The same value of the base term is maintained, as in the previous techniques, at 220 V RMS. For these graphs, a value for $K = 0, 55$ has been chosen as this is the best value of K for reducing vibrations within the field of the measurements made.

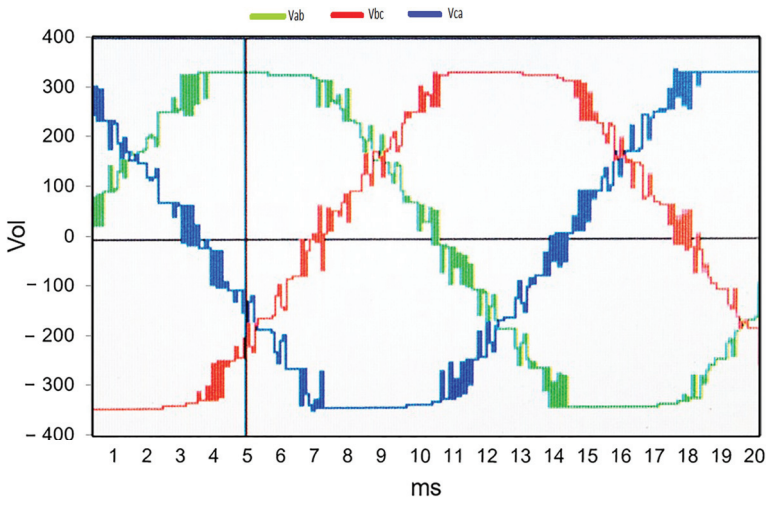

(**a**)

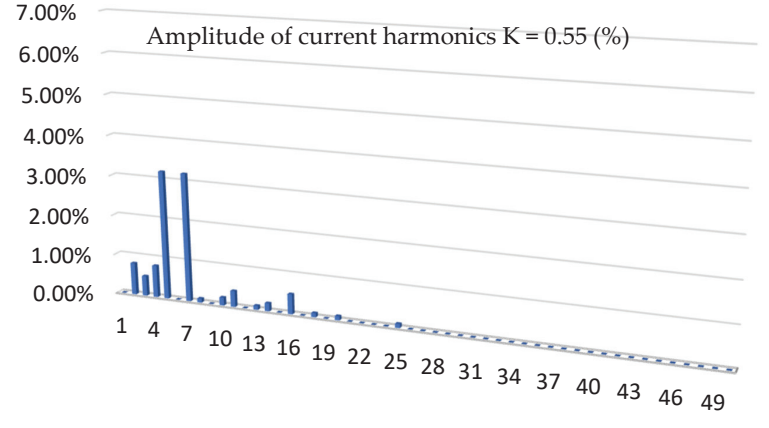

(**b**)

Figure 10. (**a**) Line voltage output of the multilevel inverter with technique HIPWM–FMTCt, with K = 0.55 and M = 15; (**b**) percentage amplitude of current harmonics (V = 220 V RMS of the fundamental term).

By means of the hammer test, it was possible to identify the most significant resonance frequencies of the machine. The vibration graph shows that, after the test, the resonance frequencies coincided with the calculations made using Equations (1)–(10) with the construction parameters of the machine, which are as follow: modulus of elasticity, E_c: 200 × 10^9 Pa; density, ρ : 7700·9.8 N/kg; D_c: 0.176 m; stator slots, s_1: 36; tooth height, h_t: 0.008 m; stator thickness, h_c: 0.01 m; tooth width, c_t: 0.0087 m; stator length, L_i: 0.25; and stator diameter, D_c: 0.186 m.

As can be clearly seen in Table 2 (calculated values) and Figure 11 (hammer test results), there are resonance frequencies measured at 1600 Hz, which correspond to the calculated 1571 Hz, as well as to the calculated frequency of 2921 Hz (see Table 2), which practically

coincide with the experimental result. The calculated housing resonance frequencies exceeded 10 kHz, outside the measurement range, and have therefore not been provided.

Table 2. Radial frequencies calculated for the induction motor.

m	Frequency (Hz)	Frequency (Hz)	Frequency (Hz)
1	0.45×10^2 0.995×10^3 0.6533×10^4	0.229×10^3 0.1571×10^4 0.8519×10^4	0.547×10^3 0.2921×10^4 0.4619×10^4
0	2.9206×10^3		

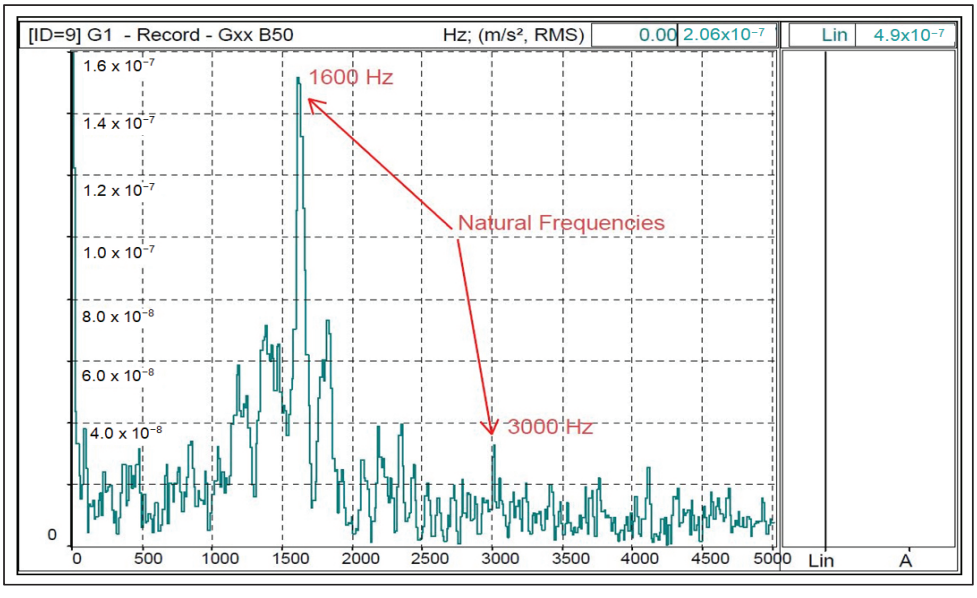

Figure 11. Natural frequency testing with an impact hammer acceleration (m/s^2) versus frequency with two natural frequencies detected.

The vibration results as a function of the frequency of the mains-fed motor and the multilevel inverter are shown below for the SPWM-I, SPWM-II, SPWM-III, and HIPWM–FMTCt techniques. This last technique will only be presented for $K = 0.55$, for which the vibration level RMS is lowest. The RMS power supply value for all techniques was 220 V RMS. The average frequency of the carrier signals was 750 Hz.

Figure 12 shows the vibrations due to spatial harmonics (tooth harmonics), which are the most significant, as mentioned in Section 2, and which are clearly distinguishable with the sinusoidal power supply. The frequency of the spatial harmonic will be $\nu \pm 1$, as Equation (11) shows. With the motor used, the harmonic frequencies of the vibrations produced by these tooth harmonics appear above the values of 18 ± 1 (17,19) and 36 ± 1 (35,37), with p = 2 and $s_1 = 36$. These vibrations will appear in all of the graphs since they are a consequence of the constructive characteristics of the machine. For the 50 Hz power supply, vibrations are identified for 900 Hz and 1800 Hz.

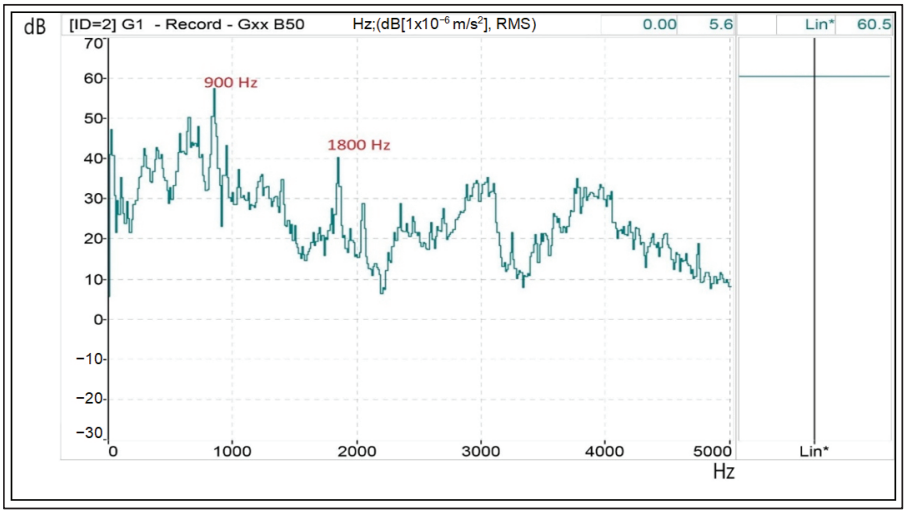

Figure 12. Tooth harmonics on a spectral vibration diagram—dB/Hz—when the motor is supplied by the three-phase network. (Lin*: measured on a linear scale without weighting adjustment A).

Figure 13 shows the results of the SPWM-I strategy, with M = 15. In addition to the vibrations caused by using a sinusoidal power supply, time harmonics also can be identified. One can observe electrical harmonics 19 (1·750 + 2·50 Hz), 37(2·750 + 7·50 Hz), and 31 (1550 Hz), which activate the natural resonance of 1500 Hz. These electrical harmonics generate vibrational frequencies of 1000 Hz, 1500 Hz, and 1800 Hz, respectively, if the most significant ones are indicated.

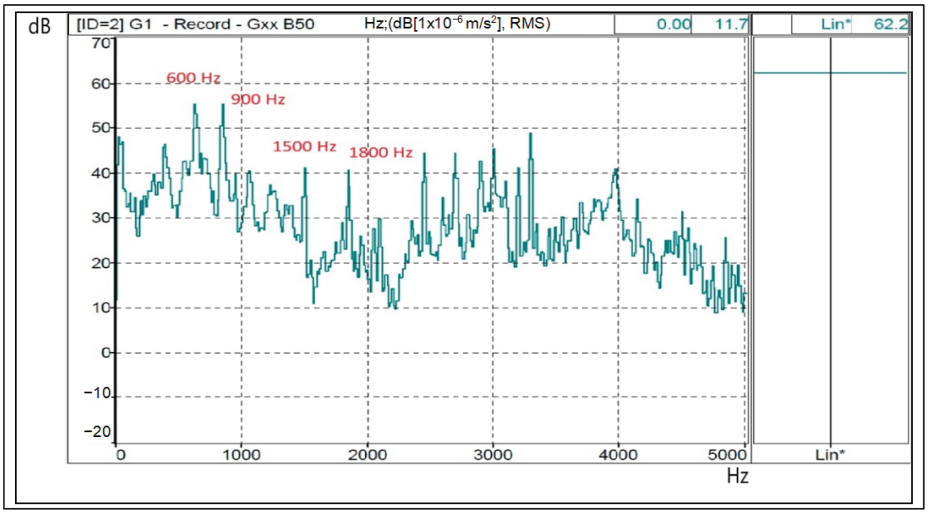

Figure 13. Mechanical resonances (1500 and 3000 Hz), tooth (900 and 1800 Hz) and electrical harmonics on a spectral vibration diagram—dB/Hz—when the motor is supplied from the multilevel inverter with the SPWM-I technique. (Lin*: measured on a linear scale without weighting adjustment A).

Figure 14 shows the results of the SPWM-II strategy, with M = 15. In addition to the vibrations caused by space harmonics, time harmonics also appeared. It can be observed that electrical harmonics 11, 17, 23, and 29 activate the natural resonance of 1500 Hz.

These electrical harmonics generate vibrational frequencies of 600 Hz, 900 (this harmonic coincides with one of harmonic of tooth), 1500 Hz, and 1900 (second-order tooth harmonic).

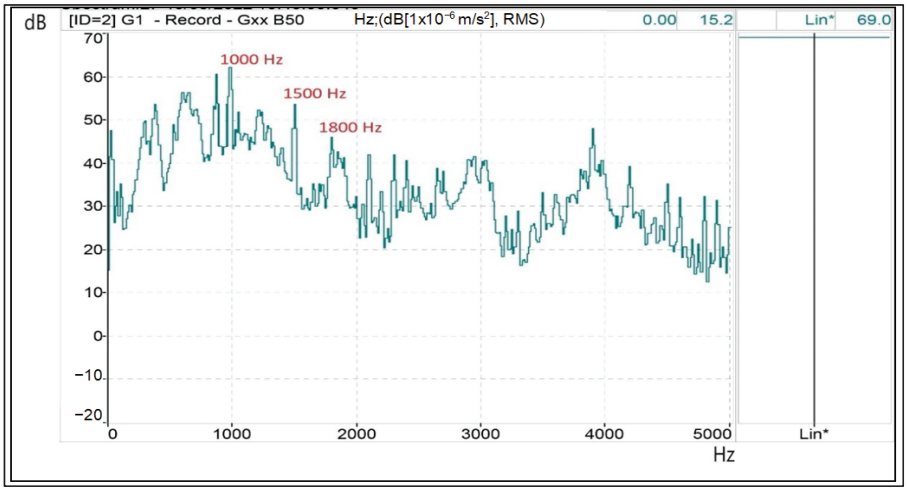

Figure 14. Mechanical resonances (1500 and 3000 Hz), tooth (900 and 1800 Hz) and electrical harmonics (900 Hz) on a spectral vibration diagram—dB/Hz—when the motor is supplied from a multilevel inverter with the SPWM-II technique. (Lin*: measured on a linear scale without weighting adjustment A).

In Figure 15, we find a vibration spectrum as a function of frequency in the results for the SPWM-III technique that is very similar to the previous one. In addition to the vibrations caused by space harmonics, time harmonics also appeared. It can be observed that electrical harmonics 11, 17, 23, and 29 activate the natural resonance of 1500 Hz. These electrical harmonics generate vibrational frequencies of 600 Hz, 900 (this harmonic coincides with one of harmonic of tooth), 1500 Hz and 1900 (second tooth harmonic).

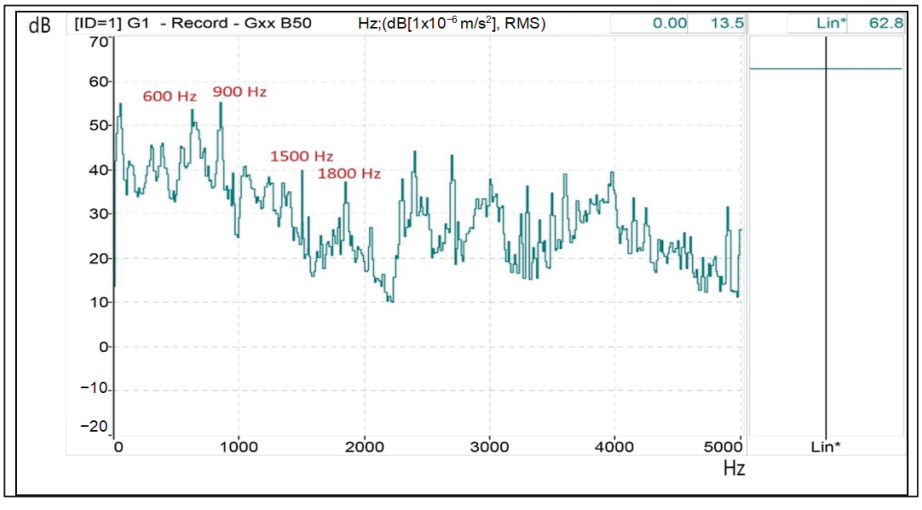

Figure 15. Mechanical resonances (1500 and 3000 Hz), tooth (900 and 1800 Hz) and electrical harmonics (600 and 900 Hz, mainly) on a spectral vibration diagram—dB/Hz—when the motor is supplied from a multilevel inverter with the SPWM-III technique. (Lin*: measured on a linear scale without weighting adjustment A).

Finally, Figure 16 depicts the results of the proposed HIPWM–FMTCt technique, with $K = 0.55$ and $\overline{M} = 15$. It can be seen that vibrations similar to the three previous ones appear, but the vibration is lower, and the natural resonance frequencies of 1500 Hz and 3000 Hz have not been activated due to the adjustment made to parameter K.

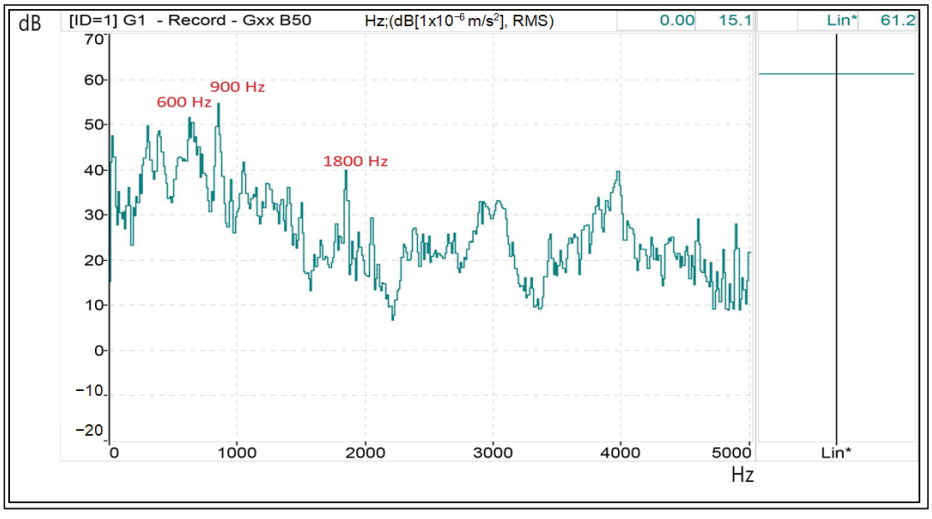

Figure 16. Tooth harmonics (900 and 1800 Hz) and electrical harmonics (600 and 900 Hz, mainly) on a spectral vibration diagram—dB/Hz—when the motor is supplied from a multilevel inverter with the SPWM-III technique with $K = 0.55$. (Lin*: measured on a linear scale without weighting adjustment A).

Table 3 shows a summary of the most important results obtained in the laboratory setup. The third column shows the linear value of the accelerometer measurement in dB using 1×10^{-6} m/s^2 as a reference. With the proposed technique and a truncation factor of 0.55, 1 dB less is measured than with the lowest value of the SPWM techniques used for comparison. The RMS line voltage setting at its fundamental term for all of them was 220 V. For that line voltage, the fourth column shows the measured percentage level for the voltage THD. It can be seen that the best value has been obtained by setting the truncation level K to a value of 0.45. Finally, the last column shows how the RMS voltage level at the inverter output can be adjusted by taking the DC-Link voltage at 75 V as a reference.

Table 3. Experimental Results for $\overline{M} = 15$ and $M = 15$.

Type of PWM/Power Supply	Level of Truncation	Level of Vibrations dB 220 V RMS Fund. Term	THD Voltage (%) 220 V RMS Fund. Term	V_{RMS}(V) DC-Link 75 V
Power supply		60.5		
SPWM-I		69.0	15.0	187
SPWM-II		62.2	4.52	190
SPWM-III		62.8	5.73	226

Table 3. *Cont.*

Type of PWM/Power Supply	Level of Truncation	Level of Vibrations dB 220 V RMS Fund. Term	THD Voltage (%) 220 V RMS Fund. Term	V_{RMS}(V) DC-Link 75 V
HIPWM–FMTCt	K = 0.30	63.1	8.58	220
	K = 0.40	62.9	7.05	223
	K = 0.45	62.8	4.01	226
	K = 0.50	62.6	4.25	231
	K = 0.55	61.2	4.51	229
	K = 0.60	62.3	5.03	228
	K = 0.65	62.7	5.24	230
	K = 0.70	63.0	5.52	230
	K = 0.75	63.2	6.87	231
	K = 0.80	63.8	7.39	231

5. Conclusions

The vibrations produced by an induction machine depend on, among other parameters, the constructive alignments, the electrical harmonics of the power supply, and the degree of saturation of the hysteresis cycle of its magnetic circuit. The use of power inverters to drive them increases the level of vibrations due to the electrical harmonics produced. Among the various sources of vibration production, particularly important are those produced at the natural resonance frequencies of the mechanical structure, which can shorten its useful life. In the present work, a theoretical–practical study of the resonance frequencies of an engine has been described. It has been demonstrated that, by adjusting the control variable of a discontinuous modulation technique, it is possible to avoid the activation of these resonance frequencies, as well as to reduce the vibration level measured with respect to other known techniques (maintaining the frequency modulation order for all the techniques tested). The maximum switching frequencies of the carrier wave for the described technique have also been calculated for two different frequency modulation orders—M = 15 and M = 11—and the results obtained with M = 15 are presented. Measurements were carried out to evaluate both the electrical and vibration results. The main objective of this study was to select values of K that minimize the magnetic harmonic field (MMF) in the air gap, thus reducing the vibrations caused by the motor. If the objective is to reduce the total harmonic distortion (THD) or to increase the root-mean-square (RMS) value of the output voltage, which for the same transferred power will result in a lower current, the most appropriate K value can also be determined. With a K value of 0.55, vibrations are minimized. When K is set to 0.5, there is an improvement in THD, while higher K values cause an increase in RMS values at the inverter output. Within a K range of 0.5 to 0.6, lower vibrations were observed than were with other modulation techniques described in the technical literature. The proposed technique effectively reduces vibrations by not activating mechanical resonances and spatial harmonics with a high winding factor.

Author Contributions: A.R.-G.: conceptualization, methodology, and writing—original draft preparation; F.M.P.-H., J.-R.H.-L. and M.J.M.-G.: simulation and data collection; A.R.-G., F.M.P.-H., J.-R.H.-L. and M.J.M.-G.: hardware implementation, validation, writing—review and editing; F.M.P.-H.: funding acquisition. All authors have read and agreed to the published version of the manuscript.

Funding: This research was funded by National Plan Project ENE-19744C0302, Spain.

Data Availability Statement: The authors confirm that the data supporting the findings of this survey paper are available within the related research papers cited in this article.

Conflicts of Interest: The authors declare no conflict of interest.

References

1. Song, P.; Liu, Y.; Liu, T.; Wang, H.; Wang, L. A Novel Suppression Method for Low-Order Harmonics Causing Resonance of Induction Motor. *Machines* **2022**, *10*, 1206. [CrossRef]
2. Liu, H.; Liu, Q.; Zhang, W.; Miao, Y.; Liu, P. Random PWM Technique for Acoustic Noise and Vibration Reduction in Induction Motors used by Electric Vehicles. *Trans. China Electrotech. Soc.* **2019**, *34*, 1488–1495.
3. Devillers, E.; Le Besnerais, J.; Lubin, T.; Hecquet, M.; Lecointe, J. An Improved 2-D Subdomain Model of Squirrel-Cage Induction Machine Including Winding and Slotting Harmonics at Steady State. *IEEE Trans. Magn.* **2018**, *54*, 8100612. [CrossRef]
4. Kocabas, D.A. Novel winding and core design for maximum reduction of harmonic magnetomotive force in AC motors. *IEEE Trans. Magn.* **2009**, *45*, 735–746. [CrossRef]
5. Salem, A.; Van Khang, H.; Robbersmyr, K.G.; Norambuena, M.; Rodriguez, J. Voltage Source Multilevel Inverters with Reduced Device Count: Topological Review and Novel Comparative Factors. *IEEE Trans. Power Electron.* **2021**, *36*, 2720–2747. [CrossRef]
6. Leon, J.I.; Kouro, S.; Franquelo, L.G.; Rodriguez, J.; Wu, B. The Essential Role and the Continuous Evolution of Modulation Techniques for Voltage-Source Inverters in the Past, Present, and Future Power Electronics. *IEEE Trans. Ind. Electron.* **2016**, *63*, 2688–2701. [CrossRef]
7. Yuan, X. Ultimate Generalized Multilevel Converter Topology. *IEEE Trans. Power Electron.* **2021**, *36*, 8634–8639. [CrossRef]
8. Rodriguez, J.; Lai, J.S.; Peng, F.Z. Multilevel inverters: A survey of topologies, controls, and applications. *IEEE Trans. Ind. Electron.* **2002**, *49*, 724–738. [CrossRef]
9. Rodriguez, J.; Bernet, S.; Steimer, P.K.; Lizama, I.E. A survey on neutral-point-clamped inverters. *IEEE Trans. Ind. Electron.* **2010**, *57*, 2219–2230. [CrossRef]
10. Matsui, K.; Kawata, Y.; Ueda, F. Application of parallel connected NPC-PWM inverters with multilevel modulation for AC motor drive. *IEEE Trans. Power Electron.* **2000**, *15*, 901–907. [CrossRef]
11. Huang, J.; Corzine, K.A. Extended operation of flying capacitor multilevel inverters. *IEEE Trans. Power Electron.* **2006**, *21*, 140–147. [CrossRef]
12. Debnath, S.; Qin, J.; Bahrani, B.; Saeedifard, M.; Barbosa, P. Operation, Control, and Applications of the Modular Multilevel Converter: A Review. *IEEE Trans. Power Electron.* **2015**, *30*, 37–53. [CrossRef]
13. Deng, F.; Lü, Y.; Liu, C.; Heng, Q.; Yu, Q.; Zhao, J. Overview on submodule topologies, modeling, modulation, control schemes, fault diagnosis, and tolerant control strategies of modular multilevel converters. *Chin. J. Electr. Eng.* **2020**, *6*, 1–21. [CrossRef]
14. Malinowski, M.; Gopakumar, K.; Rodriguez, J.; Perez, M.A. A survey on cascaded multilevel inverters. *IEEE Trans. Ind. Electron.* **2010**, *57*, 2197–2206. [CrossRef]
15. Corzine, K.A.; Wielebski, M.W.; Peng, F.Z.; Wang, J. Control of cascaded multilevel inverters. *IEEE Trans. Power Electron.* **2004**, *19*, 732–738. [CrossRef]
16. FKhoucha, K.; Lagoun, M.S.; Kheloui, A.; Benbouzid, M.E.H. A Comparison of Symmetrical and Asymmetrical Three-Phase H-Bridge Multilevel Inverter for DTC Induction Motor Drives. *IEEE Trans. Energy Convers.* **2011**, *26*, 64–72. [CrossRef]
17. Yu, Y.; Konstantinou, G.; Hredzak, B.; Agelidis, V.G. Power Balance Optimization of Cascaded H-Bridge Multilevel Converters for Large-Scale Photovoltaic Integration. *IEEE Trans. Power Electron.* **2016**, *31*, 1108–1120. [CrossRef]
18. Tolbert, L.M.; Habetler, T.G. Novel multilevel inverter carrier-based PWM method. *IEEE Trans. Ind. Appl.* **1999**, *35*, 1098–1107. [CrossRef]
19. Yao, W.; Hu, H.; Lu, Z. Comparisons of Space-Vector Modulation and Carrier-Based Modulation of Multilevel Inverter. *IEEE Trans. Power Electron.* **2008**, *23*, 45–51. [CrossRef]
20. Lin, H.; Chen, R.; Li, R.; Zhu, L.; Yan, H.; Shu, Z. A Flexible and Fast Space Vector Pulse Width Modulation Technique for Multilevel Converters. In Proceedings of the 22nd International Conference on Electrical Machines and Systems (ICEMS), Harbin, China, 11–14 August 2019; pp. 1–4. [CrossRef]
21. Dahidah, M.S.; Konstantinou, G.; Agelidis, V.G. A review of multilevel selective harmonic elimination PWM: Formulations, solving algorithms, implementation and applications. *IEEE Trans. Power Electron.* **2014**, *30*, 4091–4106. [CrossRef]
22. Zolfagharian, O.; Dastfan, A.; Marzebali, M.H. Selective Harmonic Elimination Technique Improvement for Cascaded H-Bridge Multilevel Converters Under DC Sources Uncertainty. *IEEE J. Emerg. Sel. Top. Power Electron* **2023**. [CrossRef]
23. Darus, R.; Konstantinou, G.; Pou, J.; Ceballos, S.; Agelidis, V.G. Comparison of phase-shifted and level-shifted PWM in the modular multilevel converter. In Proceedings of the 2014 International Power Electronics Conference (IPEC-Hiroshima 2014-ECCE ASIA), Hiroshima, Japan, 18–21 May 2014; pp. 3764–3770.
24. Subki AS, R.A.; Manap, Z.; Tumari, M.Z.; Jidin, A.Z.; Saat, S.; Abidin, A.F.Z.; Saealal, M.S. Analysis on three phase cascaded H-bridge multilevel inverter based on sinusoidal and third harmonic injected pulse width modulation via level shifted and phase shifted modulation technique. *Int. J. Power Electron. Drive Syst.* **2021**, *12*, 160.
25. Sadegh Orfi, M.; Sarvi, M.; Vlaabjerg, F.; Daravi, P. Improved harmonic injection pulse-with modulation variable frequency triangular carrier scheme for multilevel inverters. *IET Power Electron.* **2020**, *13*, 3146–3154. [CrossRef]

26. Chavarria, J.; Biel, D.; Guinjoan, F.; Meza, C.; Negroni, J.J. Energy-Balance Control of PV Cascaded Multilevel Grid-Connected Inverters Under Level-Shifted and Phase-Shifted PWMs. *IEEE Trans. Ind. Electron.* **2013**, *60*, 98–111. [CrossRef]
27. Ermolaev, A.; Erofeev, V.; Plekhov, A.; Titov, D. Magnetic Vibration in Induction Motor Caused by Supply Voltage Distortion. *Energies* **2022**, *15*, 9600. [CrossRef]
28. Poorfakhraei, A.; Narimani, M.; Emadi, A. A review of modulation and control techniques for multilevel inverters in traction applications. *IEEE Access* **2021**, *9*, 24187–24204. [CrossRef]
29. Seshadri, A.; Lenin, N.C. Review based on losses, torque ripple, vibration and noise in switched reluctance motor. *IET Electr. Power Appl.* **2020**, *14*, 1311–1326. [CrossRef]
30. Gieras, J.F.; Wang, C.; Cho Lay, J. *Inverter-Fed Motors in Noise of Poliphase Electric Motors*; CRC Press, Taylor&Francis Group: Boca Raton, FL, USA, 2006.
31. Meco-Gutierrez, M.J.; Perez-Hidalgo, F.; Vargas-Merino, F.; Heredia-Larrubia, J.R. A New PWM Technique Frequency Regulated Carrier for Induction Motors Supply. *IEEE Trans. Ind. Electron.* **2006**, *53*, 1750–1754. [CrossRef]
32. Ruiz-Gonzalez, A.; Meco-Gutierrez, M.J.; Vargas-Merino, F.; Heredia-Larrubia, J.R.; Perez-Hidalgo, F. Pulse width modulation technique with harmonic injection in the modulating wave and discontinuous frequency modulation for the carrier wave to reduce vibrations in asynchronous machines. *IET Power Electron.* **2019**, *12*, 2865–2872. [CrossRef]
33. Ruiz-Gonzalez, A.; Heredia-Larrubia, J.R.; Meco-Gutierrez, M.J.; Perez-Hidalgo, F.M. Pulse-Width Modulation Technique with Harmonic Injection in the Modulating Wave and Discontinuous Frequency Modulation for the Carrier Wave for Multilevel Inverters: An Application to the Reduction of Acoustic Noise in Induction Motors. *IIEEE Access* **2023**, *11*, 40579–40590. [CrossRef]
34. Yegane, M.S.O.; Sarvi, M. An improved harmonic injection PWM-frequency modulated triangular carrier method with multiobjective optimizations for inverters. *Electr. Power Syst. Res.* **2018**, *160*, 372–380. [CrossRef]

energies

MDPI

Article

Intelligent Backstepping Control of Permanent Magnet-Assisted Synchronous Reluctance Motor Position Servo Drive with Recurrent Wavelet Fuzzy Neural Network

Faa-Jeng Lin [1,*], Ming-Shi Huang [2], Yu-Chen Chien [1] and Shih-Gang Chen [2]

[1] Department of Electrical Engineering, National Central University, Taoyuan 32001, Taiwan; 110521077@cc.ncu.edu.tw
[2] Department of Electrical Engineering, National Taipei University of Technology, Taipei 10608, Taiwan; simonh@ntut.edu.tw (M.-S.H.); csg12388@gmail.com (S.-G.C.)
* Correspondence: linfj@ee.ncu.edu.tw; Tel.: +886-3-422-7151 (ext. 34532)

Abstract: An intelligent servo drive system for a permanent magnet-assisted synchronous reluctance motor (PMASynRM) that can adapt to the control requirements considering the motor's nonlinear and time-varying natures is developed in this study. A recurrent wavelet fuzzy neural network (RWFNN) with intelligent backstepping control is proposed to achieve this. In this study, first, a maximum torque per ampere (MTPA) controlled PMASynRM servo drive is introduced. A lookup table (LUT) is created, which is based on finite element analysis (FEA) results by using ANSYS Maxwell-2D dynamic model to determine the current angle command of the MTPA. Next, a backstepping control (BSC) system is created to accurately follow the desired position in the PMASynRM servo drive system while maintaining robust control characteristics. However, designing an efficient BSC for practical applications becomes challenging due to the lack of prior uncertainty information. To overcome this challenge, this study introduces an RWFNN as an approximation for the BSC, aiming to alleviate the limitations of the traditional BSC approach. An enhanced adaptive compensator is also incorporated into the RWFNN to handle potential approximation errors effectively. In addition, to ensure the stability of the RWFNN, the Lyapunov stability method is employed to develop online learning algorithms for the RWFNN and to guarantee its asymptotic stability. The proposed intelligent backstepping control with recurrent wavelet fuzzy neural network (IBSCRWFNN) demonstrates remarkable effectiveness and robustness in controlling the PMASynRM servo drive, as evidenced by the experimental results.

Keywords: permanent magnet-assisted synchronous reluctance motor (PMASynRM); maximum torque per ampere (MTPA); finite element analysis (FEA); backstepping control (BSC); recurrent wavelet fuzzy neural network (RWFNN); intelligent backstepping control recurrent wavelet fuzzy neural network (IBSCRWFNN)

Citation: Lin, F.-J.; Huang, M.-S.; Chien, Y.-C.; Chen, S.-G. Intelligent Backstepping Control of Permanent Magnet-Assisted Synchronous Reluctance Motor Position Servo Drive with Recurrent Wavelet Fuzzy Neural Network. *Energies* **2023**, *16*, 5389. https://doi.org/10.3390/en16145389

Academic Editors: Loránd Szabó and Feng Chai

Received: 14 June 2023
Revised: 10 July 2023
Accepted: 13 July 2023
Published: 14 July 2023

1. Introduction

The permanent magnet synchronous motor (PMSM) is an electric motor type that has found extensive applications in diverse fields, including electric vehicles, industrial automation, robotics, and aerospace plane [1,2]. Compared to conventional induction motors, PMSM exhibits high efficiency exceeding 90%, resulting in substantial energy savings. It also possesses a high magnetic field strength and low internal resistance, enabling PMSM to achieve a higher power density and greater output power within a relatively smaller volume. Moreover, PMSM offers excellent torque-speed performance and sensitive current control ability, making it ideal for precision applications such as automatic control systems [3–5]. Despite its advantages, rare-earth elements such as NdFeB can be costly and raise concerns regarding the supply chain monopoly and trade wars. Additionally, high-performance applications using PMSM face challenges such as operating

at the region of flux-weakening control with large direct-axis current and the potential for uncontrolled generator mode due to the flux linkages generated by permanent magnets (PM). These drawbacks limit the potential benefits of PMSM and should be taken into account when considering their use in specific applications. Hence, there is a need to decrease the utilization of rare-earth PMs.

Due to their rapid dynamic response, wide speed range, affordability, and high efficiency, the synchronous reluctance motor (SynRM) has gained significant popularity and is now utilized in numerous applications. Unlike induction motors and PMSM, SynRM offers inherent advantages by eliminating the need for permanent magnetic materials, cages, and excitation windings. This not only enhances its robustness but also reduces its overall cost, making it an attractive alternative [6–9]. However, SynRM has limited overload capability compared to other types of motors, meaning that it may not be suitable for applications that require high levels of torque for short periods of time. Based on the aforementioned reasons, a relatively new machine, known as the permanent magnet-assisted synchronous reluctance motor (PMASynRM), has been developed to address the challenges associated with the scarcity of rare-earth PMs. One approach to mitigating these difficulties involves reducing the amount of rare-earth PMs used in the rotor or replacing them with ferrite magnets [10–13]. Maximum torque per ampere (MTPA) has been widely utilized as a control strategy in PMSMs and SynRMs control to maximize output torque [14–19]. In [17,18], the MTPA control strategy has been implemented in the control of IPMSMs and SynRMs to determine the ideal current angle for maximizing the output torque based on a given stator current. Moreover, in [19], an MTPA control with nonlinear simultaneous equations was derived from the Lagrange multiplier method, which could be solved by numerical algorithms. The MTPA control technology enables the production of equivalent torque with minimal current. It achieves this by identifying the ideal current angle that maximizes output torque at a given stator current while also minimizing copper loss during the process. However, PMASynRM has inherent drawbacks, such as nonlinear and time-varying control characteristics, which make achieving high-performance servo applications and the traditional MTPA quite challenging [20].

The backstepping control (BSC), despite its advantages in providing a recursive and systematic design methodology for nonlinear feedback control, may encounter undesired chattering phenomena due to the presence of a sign function. Several approaches, such as adaptive control [21] and intelligent control [22], have been proposed for integration with BSC to overcome this issue and enhance control performance. In [21], a PMSM drive system was targeted, and an adaptive backstepping (ABS) control approach was introduced as a solution. The purpose of this method is to achieve precise tracking responses by utilizing the robustness properties of the ABS control. In [22], to overcome the limitations posed by the nonlinear and time-varying control natures of a SynRM, a robust position controller was devised for a SynRM servo drive system. This was achieved through the introduction of an intelligent BSC approach, employing a recurrent feature selection fuzzy neural network. In addition, to improve control performance and facilitate model-free controller design, intelligent control methods, including fuzzy mechanisms, NNs, and FNNs, have been widely used as universal approximators in various studies. Among these, the FNN has been particularly popular due to its combined advantages of neural networks and fuzzy logic and has been applied in various fields, such as photovoltaic systems, robotics, and motor control [23–25]. In fact, the FNN's robustness and convenience have garnered attention for controlling permanent magnet linear synchronous motors [25]. Moreover, the recurrent neural network (RNN) is capable of mapping and storing temporal information dynamically [26,27], utilizing time delays from earlier states, and approximate information can be obtained from internal feedback states. This makes RFNN a better option for dynamic performance than the pure feedforward FNN. Furthermore, the wavelet transform is an influential and effective technique used for the analysis of intricate time-varying signals. It offers numerous advantages and capabilities, making it a valuable tool in signal processing [28], and has been extensively studied for its applications that combine

the learning capabilities of artificial neural network (ANN) and wavelet decomposition. Recently, researchers have proposed integrating wavelet functions into FNNs to create the wavelet fuzzy neural network (WFNN) with the goal of improving adaptive and learning capabilities for complex engineering problems [29]. By analyzing non-stationary signals to identify local details, reducing data complexity and handling uncertainty through fuzzy logic, and leveraging NNs' self-learning characteristics to improve model accuracy, the WFNN is capable of describing nonlinear systems with uncertainties and possesses a fast learning capability. Additionally, this study proposes an intelligent control system using the capabilities of FNN, RNN, and WNN, where an online trained recurrent wavelet fuzzy neural network (RWFNN) [30] is utilized to enhance control performance.

High-performance applications of PMASynRM are limited due to nonlinear and time-varying control features. Therefore, the purpose of this article is to develop a high-performance PMASynRM servo drive that simultaneously achieves robust position control and high energy efficiency by using intelligent backstepping control recurrent wavelet fuzzy neural network (IBSCRWFNN) control with MTPA. To address the issue of MTPA, a Maxwell 2D simulation tool is employed in the design process of the PMASynRM. Then, the optimal current angle command for MTPA control is subsequently analyzed using finite element analysis (FEA), and apply the result by a lookup table (LUT) method to ensure proper functionality. Moreover, the PMASynRM servo drive is controlled by using the BSC to solve the presence of unavoidable uncertain system dynamics in the PMASynRM servo drive system. However, the bound of lumped uncertainty in the BSC is difficult to determine in real-life situations. To overcome this issue, the suggested method involves approximating the BSC using the RWFNN. Furthermore, this research incorporates an adaptive compensator to account for potential deviations resulting from the approximation of the RWFNN. In addition, the utilization of the Lyapunov stability method to generate online learning algorithms [22] for the IBSCRWFNN is proposed, ensuring robust performance in position control. The rest of this study is organized as follows: in Section 2, the focus will be on describing the modeling of the position servo drive system for PMASynRM with MTPA control based on the results of FEA. In Section 3, the PMASynRM servo drive is controlled by using the BSC to solve the presence of unavoidable uncertainties. To overcome the difficulty of the BSC, the RWFNN is discussed in Section 4. In Section 5, the Lyapunov stability method is proposed to generate online learning algorithms for the IBSCRWFNN. Section 6 will present the experimental results of the PI control, BSC, and the proposed IBSCRWFNN control. Finally, the research findings are thoroughly discussed in Section 7, presenting the conclusive remarks.

2. Modeling of PMASynRM Position Servo Drive System

2.1. Modeling of PMASynRM Servo Drive System

The stator voltage equations of PMASynRM in the *d*-*q* reference frame can be formulated as follows:

$$v_d = R_s i_d + \frac{d}{dt}\lambda_d - \omega_e \lambda_q \tag{1}$$

$$v_q = R_s i_q + \frac{d}{dt}\lambda_q + \omega_e \lambda_d \tag{2}$$

where R_s is the stator resistance; v_d and v_q are the *d*-axis and *q*-axis voltage; i_d and i_q are the *d*-axis and *q*-axis stator currents; λ_d and λ_q are the *d*-axis and *q*-axis flux linkages; ω_e is the rotor electrical angular velocity. Furthermore, the flux linkage equations in the *d*-*q* reference frame are represented in the following:

$$\lambda_q = L_q i_q \tag{3}$$

$$\lambda_d = L_d i_d + \lambda_m \tag{4}$$

The equations above denote the d-axis and q-axis inductances as L_d and L_q, respectively, and λ_m as rotor PM flux. Neglecting magnetic saturation, the resulting electromagnetic torque in the d-q reference frame of PMASynRM can be represented by the following equation:

$$T_e = \frac{3}{2}\frac{P}{2}[\lambda_m i_q + (L_d - L_q) i_q i_d] \quad (5)$$

where P is the pole number. Both PMASynRM and PMSM have electromagnetic torque consisting of reluctance torque and PM torque. However, in the case of PMASynRM, the reluctance torque plays the main driving role owing to the substantial disparity between the inductance values of the d-axis and q-axis inductances. The expression for the mechanical dynamic equation of the PMASynRM is as follows:

$$T_e = J\frac{d\omega_r}{dt} + B\omega_r + T_L \quad (6)$$

J represents the inertia coefficient; B represents the damping coefficient; ω_r is the speed response; T_L represents the external load and friction torque.

2.2. PMASynRM Position Servo Drive System

The PMASynRM utilized in this study is a 4-pole, 36-slot motor with a power rating of 4.5 kW, voltage rating of 214 V, current rating of 9.4 A, a rated speed of 1500 rpm, and a maximum torque of 25 Nm. The mechanical designed parameters for the PMASynRM and the specifications of the servo drive system are outlined in detail in Tables 1 and 2.

Table 1. Mechanical designed parameters of PMASynRM.

Parameters	Values
Pole number	4 pole
Slot number	36 slot
Air gap length	0.3 mm
Rotor inner diameter	31 mm
Rotor outer diameter	94.4 mm
Stator inner diameter	95 mm
Stator outer diameter	160 mm
Stack length	150 mm

Table 2. Specifications of PMASynRM servo drive.

Parameters	Values
Power rating	4.5 kW
Phase voltage rating	214 V
Phase current rating	9.4 Arms (delta)
Speed rating	1500 rpm
Torque rating	25 Nm
d-axis inductance	19.6 mH
q-axis inductance	84.3 mH
Stator resistance	1.01 Ω
Inertia coefficient	0.0069 Nm/(rad/s^2)
Damping coefficient	0.0013 Nm/(rad/s)
Magnetic flux	0.0854 Wb
DC-link	540 V
Sampling time of current/speed and position loop	0.1 ms/1 ms
Switching frequency	20 kHz
Encoder	2500 counts/turn

A typical PMASynRM position servo drive with coordinate transformation includes proportional position control, PI speed control, LUT for current angle, and PI current controllers, as illustrated in Figure 1. θ_r^* is the position command; θ_r is the position response; θ_e is the rotor electrical position; ω_r^* is the speed command. The d-q axis current commands are represented by i_d^* and i_q^* respectively. The three-phase currents are denoted by i_a, i_b, and i_c. Similarly, the d-q axis voltage commands are represented by v_d^* and v_q^* respectively. By utilizing Hall current sensors with a transformation ratio of 1 V/6.67 A with an analog-to-digital converter (ADC), it is very effective to measure the three-phase currents. By implementing the space vector pulse width modulation (SVPWM) technique, control of the voltage source inverter (VSI) can be achieved. The VSI operates at a switching frequency of 20 kHz. Moreover, the VSI employs a silicon carbide (SiC) power MOSFET, which has a voltage rating of 900 V and a current rating of 36 A. Furthermore, using a load driver in torque control mode to control an industrial PMSM as the load for the PMASynRM, the performance of the position servo drive system for the PMASynRM is evaluated. In addition, a torque meter is connected to measure the torque output. The QEP interface is used to connect the encoder to the DSP, as illustrated in Figure 1.

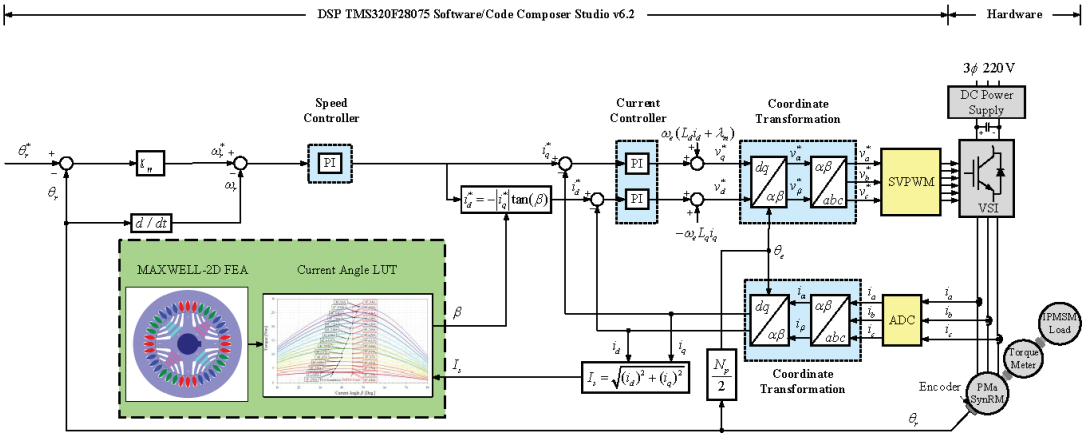

Figure 1. PI Controlled PMASynRM position servo drive.

2.3. Speed and Position Controllers Design

The speed and position controllers discussed in this article utilize PI controllers. These controllers are designed based on the controlled plants' small signal models. The speed controller depicted in Figure 2, where s is the Laplace operator, assumes ideal conditions where $T_L = 0$ and sets $i_d^* = -5$A. By referring to Equations (7) and (8), as well as Table 2, the torque constant can be deduced as $K_t = 1.2267$.

$$T_e = K_t i_q^* \tag{7}$$

$$K_t = \frac{3}{2}\frac{P}{2}[\lambda_m + (L_d - L_q)i_d^*] \tag{8}$$

Moreover, the bode diagrams of the speed-controlled plant and the loop gain are shown in Figure 3. The design requirements for the speed controller include a desired bandwidth (BW) $f = 20$ Hz and phase margin (PM) $\phi_m = 70°$. The graphical representation in Figure 3 reveals that the controlled plant necessitates compensation of -3.01 dB and $-20.1°$. The obtained result of the PI speed controller is

$$K_P + \frac{K_I}{s} = 0.664 + \frac{30.5385}{s} \tag{9}$$

where K_P is a proportional gain; K_I is an integral gain; s is the Laplace operator. Furthermore, the position controller depicted in Figure 4 utilizes a proportional controller K_{PP}. In addition, the bode diagrams of the position-controlled plant and the loop gain are shown in Figure 5. The design requirements for the speed controller include a desired bandwidth (BW) f = 2 Hz and phase margin (PM) $\phi_m = 70°$. The graphical representation in Figure 5 reveals that the controlled plant necessitates compensation of 21.8 dB and $-19.5°$. Since the position controller consists of a single constant term, it can only compensate for the gain through a proportional gain K_{PP} as follows:

$$K_{PP} = 12.3 \tag{10}$$

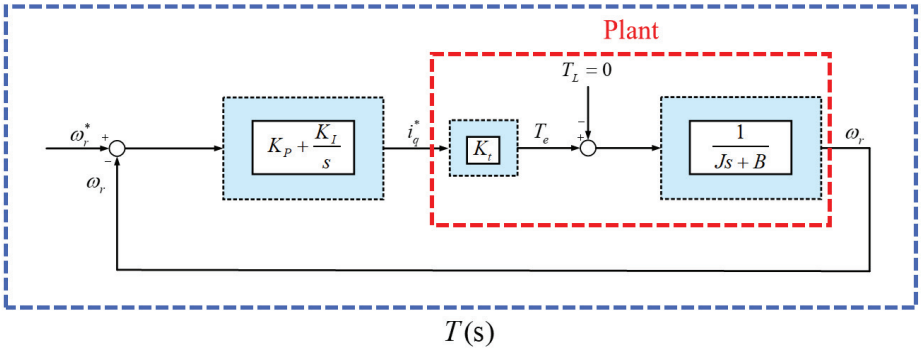

Figure 2. PI speed controller.

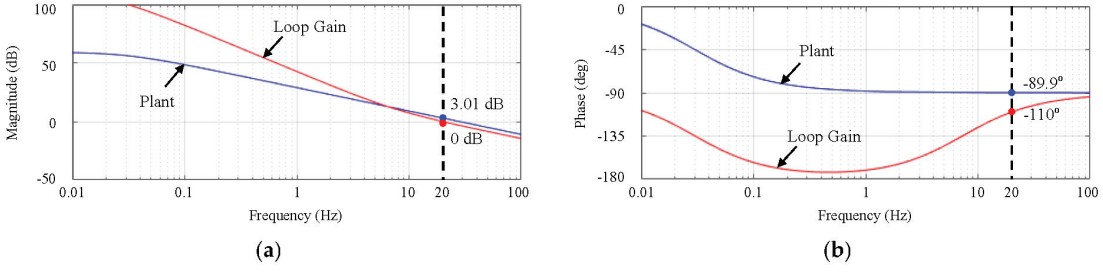

Figure 3. Bode diagrams of speed controller. (**a**) Magnitude; (**b**) Phase.

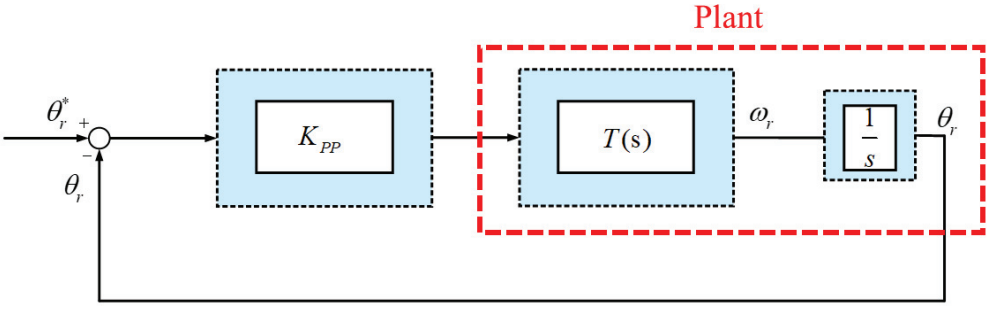

Figure 4. Proportional position controller.

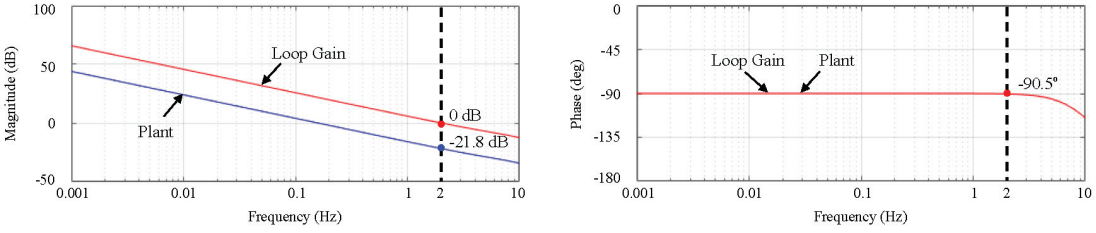

Figure 5. Bode diagrams of position controller. (**a**) Magnitude; (**b**) Phase.

3. BSC System

To rewrite the ideal dynamic equation using Equations (5) and (6), it can be expressed as follows:

$$\dot{\omega}_r = -\frac{\overline{B}}{\overline{J}}\omega_r + \frac{3P\left[\overline{\lambda}_m + \left(\overline{L}_d - \overline{L}_q\right)i_d^*\right]}{4\overline{J}}i_q^* - \frac{T_L}{\overline{J}} = A_m\omega_r + B_m i_q^* + C_m T_L \tag{11}$$

where $A_m = -\frac{\overline{B}}{\overline{J}}$; $B_m = \frac{3P\left[\overline{\lambda}_m + \left(\overline{L}_d - \overline{L}_q\right)i_d^*\right]}{4\overline{J}}$; $C_m = -\frac{1}{\overline{J}}$; The symbol "$^-$" represents the nominal value. Considering the presence of uncertainties necessitates a rewrite of the dynamic Equation (11) as follows:

$$\dot{\omega}_r = (A_m + \Delta A_m)\omega_r + (B_m + \Delta B_m)U + (C_m + \Delta C_m)T_L = A_m\omega_r + B_m U + F \tag{12}$$

where $U = i_q^*$ is the torque current command, the time-varying parameter variations are indicated by ΔA_m, ΔB_m, and ΔC_m. Moreover, F represents the lumped uncertainty, which is defined as follows:

$$F = \Delta A_m\omega_r + \Delta B_m U + (C_m + \Delta C_m)T_L,\ |F| \le F_b \tag{13}$$

and F_b is defined as lumped uncertainty bound. Furthermore, the following definitions are used for the error in position tracking and its derivative:

$$e_1 = \theta_r^*(t) - \theta_r(t) \tag{14}$$

$$\dot{e}_1 = \dot{\theta}_r^*(t) - \dot{\theta}_r(t) \tag{15}$$

The term $\dot{\theta}_r^*(t) = \omega_r^*(t)$ can be regarded as a virtual control input, and the following stabilizing function λ_1 is defined:

$$\lambda_1 = -c_1 e_1 - \omega_r^*(t) \tag{16}$$

The constant c_1 is a positive value, and the first Lyapunov function is selected as

$$V_1 = \frac{1}{2}e_1^2 > 0 \tag{17}$$

The function V_1 is positive definite. In addition, the definition of the virtual control error is as follows:

$$e_2 = \omega_r(t) + \lambda_1 = \omega_r(t) - c_1 e_1 - \omega_r^*(t) \tag{18}$$

Obtaining the derivative of V_1 can be performed as follows:

$$\dot{V}_1 = e_1\dot{e}_1 = e_1(-e_2 - c_1 e_1) = -e_1 e_2 - c_1 e_1^2 \tag{19}$$

Assuming that $e_2 = 0$ is satisfied, then the derivative of V_1 will be negative. Additionally, the derivative of e_2 can be obtained as

$$\dot{e}_2 = \dot{\omega}_r(t) + \dot{\lambda}_1 = \dot{\omega}_r(t) - c_1\dot{e}_1 - \dot{\omega}_r^*(t) \tag{20}$$

The replacement of Equation (12) with Equation (20) yields the following equation:

$$\dot{e}_2 = A_m\omega_r(t) + B_m U + F - c_1\dot{e}_1 - \dot{\omega}_r^*(t) \tag{21}$$

Then, the selection of the second Lyapunov function is performed as follows:

$$V_2 = \frac{1}{2}e_1^2 + \frac{1}{2}e_2^2 = V_1 + \frac{1}{2}e_2^2 > 0 \tag{22}$$

where V_2 is a positive-definite function. The derivative of V_2 can be obtained by

$$\begin{aligned} \dot{V}_2 = \dot{V}_1 + e_2\dot{e}_2 &= -e_1e_2 - c_1{e_1}^2 + e_2\dot{e}_2 = -c_1{e_1}^2 + e_2\left(-e_1 + \dot{e}_2\right) \\ &= -c_1{e_1}^2 + e_2\Big(A_m\dot{\theta}_r(t) + B_m U + F - c_1\dot{e}_1 - \dot{\omega}_r^*(t) - e_1\Big) \end{aligned} \tag{23}$$

To ensure system stability based on Lyapunov's condition, $\dot{V}_2$ must be negative semidefinite. Consequently, utilizing Equation (23), a BSC control law is proposed as follows [22]:

$$U_{BSC} = {B_m}^{-1}[-A_m\dot{\theta}_r(t) + c_1\dot{e}_1 + \dot{\omega}_r^*(t) + e_1 - c_2e_2 - F_b\mathrm{sgn}(e_2)] \tag{24}$$

where c_2 is a positive constant; $\mathrm{sgn}(\cdot)$ is a sign function. The dynamic Equation (12) of the PMASynRM position servo drive system indicates that the implementation of the BSC law, as outlined in Equation (24), ensures system stability. By substituting Equation (24) into Equation (23), we can derive the resulting equation as follows:

$$\begin{aligned} \dot{V}_2 &= -c_1e_1^2 + e_2[-c_2e_2 - F_b\mathrm{sgn}(e_2) + F] \\ &= -c_1e_1^2 - c_2e_2^2 - |e_2|F_b + e_2F \\ &\le -c_1e_1^2 - c_2e_2^2 - |e_2|F_b + |e_2||F| \\ &\le -c_1e_1^2 - c_2e_2^2 - |e_2|(F_b - |F|) \\ &\le -c_1e_1^2 - c_2e_2^2 \le 0. \end{aligned} \tag{25}$$

Thus, parametric uncertainty and external torque disturbance do not affect the stability of the BSC system. Figure 6 illustrates the control system's capability to maintain stability even in the presence of disturbances. However, it is worth noting that the use of a sign function can lead to chattering phenomena. A boundary layer approach can be employed to mitigate this issue by substituting the sign function with a saturation function. This substitution helps reduce the occurrence of chattering phenomena.

$$sat(e_2) = \begin{cases} 1 & e_2 > \phi \\ \frac{e_2}{\phi}, & -\phi \le e_2 \le \phi \\ -1 & e_2 < -\phi \end{cases} \tag{26}$$

The saturation function is denoted as *sat*; the boundary layer is set as $\phi > 0$. Thus, the BSC control law (24) is modified as follows:

$$U_{BSC} = {B_m}^{-1}[-A_m\dot{\theta}_r(t) + c_1\dot{e}_1 + \dot{\omega}_r^*(t) + e_1 - c_2e_2 - F_b sat(e_2)] \tag{27}$$

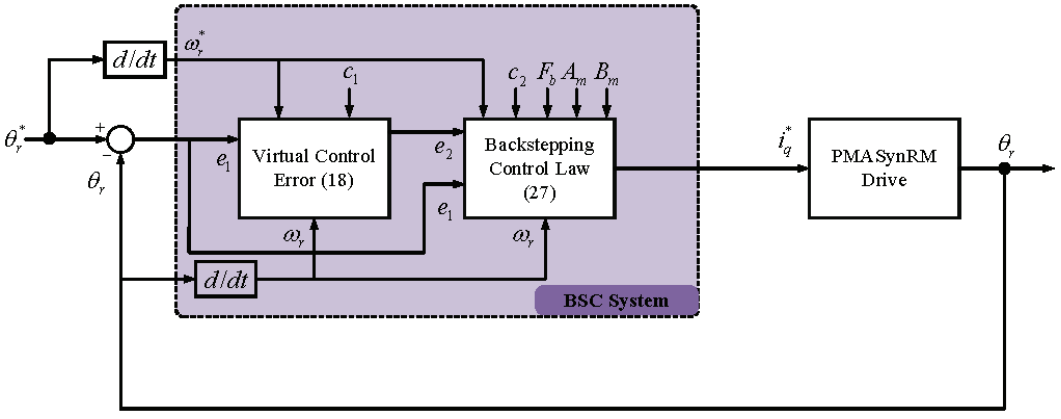

Figure 6. Control block diagram of BSC controlled PMASynRM position servo drive.

4. IBSCRWFNN System

The BSC system can ensure system stability when $|F| \leq F_b$. However, the lumped uncertainty is unknown in the real world, making it challenging to determine the upper bound F_b. Moreover, asymptotic stability is a crucial requirement for position servo drives. In order to overcome the limitations associated with the BSC law described in Equation (27), an RWFNN controller [30] is proposed. The primary objective of designing the RWFNN controller is to achieve improved performance by providing an effective approximation of the BSC law. The control block diagram of the IBSCRWFNN system is shown in Figure 7. The control law for the IBSCRWFNN system is designed as follows to achieve asymptotic stability in position servo drives.

$$U = \hat{U}_{RWFNN} + \hat{U}_c \tag{28}$$

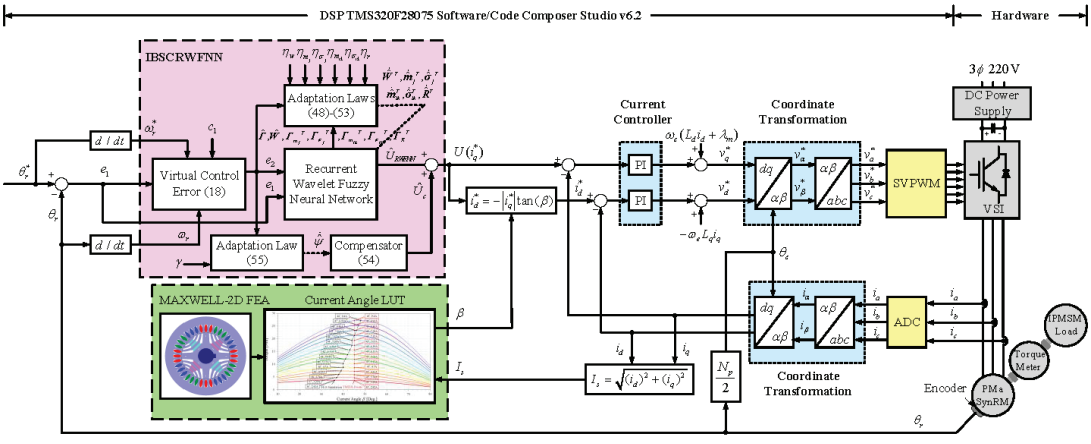

Figure 7. IBSCRWFNN controlled PMASynRM position servo drive.

The RWFNN controller, represented by $\hat{U}_{RWFNN}$, plays a crucial role in learning the BSC law to handle unknown system dynamics. Simultaneously, the compensator, denoted as $\hat{U}_c$, is specifically designed to minimize the approximated error introduced by the RWFNN controller. This combination of $\hat{U}_{RWFNN}$ and $\hat{U}_c$ effectively addresses the unknown system dynamics and improves the overall performance of the control system.

Furthermore, the network structure is represented in Figure 8.

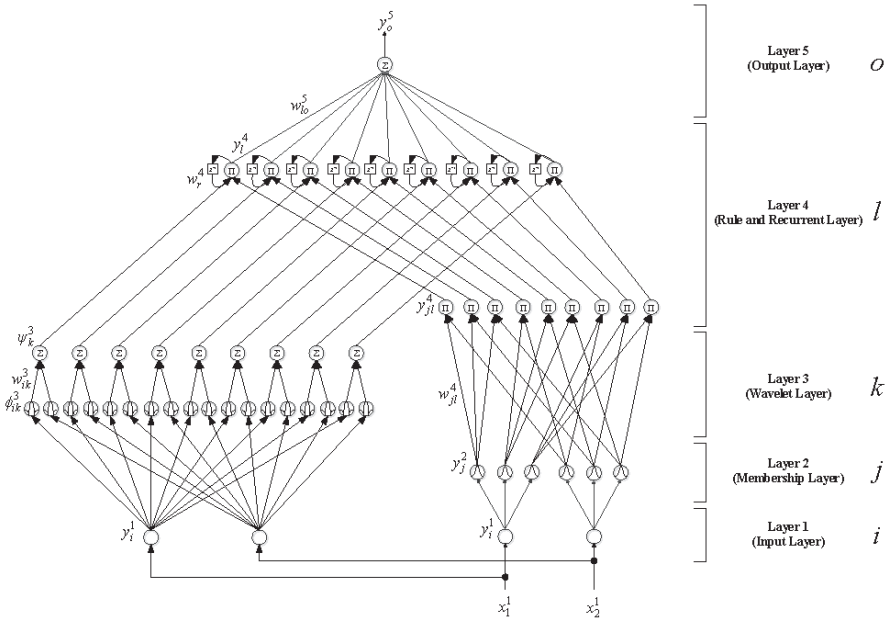

Figure 8. Network structure of RWFNN.

Figure 9 illustrates the flowchart outlining the proposed RWFNN controller. The detailed description of the operational mechanisms in the proposed RWFNN is as follows:

1. Measuring:

Utilizing the eQEP module in the DSP, the position response is measured with the assistance of an incremental encoder that has a resolution of 2500 counts/rev. Then, the RWFNN controller receives and utilizes $e_1 = \theta_r^*(t) - \theta_r(t)$ and $e_2 = \omega_r(t) + \lambda_1$ for generating control signals.

2. RWFNN Input Layer:

Two input signals are fed into this layer of the proposed RWFNN controller: the tracking error of the rotor position $x_1^1 = e_1$ and the virtual control error $x_2^1 = e_2$. To describe the input and output of each node i in this layer, the following expression is used:

$$net_i^1(N) = x_i^1(N) \tag{29}$$

$$y_i^1(N) = f_i^1\left(net_i^1\left(N\right)\right) = net_i^1(N),\ i = 1,\ 2 \tag{30}$$

The network inputs are represented by $net_i^1(N)$, where the superscript and subscript correspond to the layer and node numbers, respectively. N denotes the sampling iteration number, while $y_i^1(N)$ is the output of node ith. The unity function is denoted as $f_i^1(\cdot)$.

3. RWFNN Membership Layer:

Layer 2 takes the outputs of layer 1 as its inputs. Additionally, the membership function utilized in this layer is the Gaussian function. The following elucidate the correlation between the input and output of each node in a comprehensive manner:

$$net_j^2(N) = -\frac{\left(x_i^2(N) - m_j^2\right)^2}{\left(\sigma_j^2\right)^2} \tag{31}$$

$$y_j^2(N) = f_j^2\left(net_j^2(N)\right) = \exp(net_j^2(N)),\ j = 1, 2, \ldots,\ 6 \tag{32}$$

The input is denoted by $x_i^2(N) = y_i^1(N)$; the mean and standard deviation of the Gaussian function for node jth are represented by m_j^2 and σ_j^2 respectively; the output of node jth is denoted by $y_j^2(N)$; $f_j^2(\cdot)$ is an exponential function.

4. RWFNN Wavelet Layer:

The propagation of signals in the wavelet layer is illustrated below:

$$\phi_{ik}^3(x) = \frac{1}{\sqrt{\left|\sigma_{ik}^3\right|}}\left[1 - \frac{\left(x_i^1(N) - m_{ik}^3\right)^2}{\left(\sigma_{ik}^3\right)^2}\right] \times \exp\left[\frac{\left(x_i^1(N) - m_{ik}^3\right)^2}{\left(\sigma_{ik}^3\right)^2}\right],\ k = 1, 2, \ldots,\ 9 \tag{33}$$

$$\psi_k^3(N) = \sum w_{ik}^3 \phi_{ik}^3(x) \tag{34}$$

The input to node ith from layer 1, directed towards the wavelet function of node kth, is represented as ϕ_{ik}^3, and the connective weight as w_{ik}^3. In the wavelet layer, the output of node kth is represented by ψ_k^3. The dilation and translation variables of the wavelet function are expressed as m_{ik}^3 and σ_{ik}^3, respectively.

5. RWFNN Rule and Recurrent Layer:

The layer comprises a rule layer and a recurrent layer. Each node l, denoted as $\prod$, performs a multiplication operation on the input signals and outputs their product. Additionally, the nodes in the rule and recurrent layer employ a multiplication operation on the output signals derived from the membership layer, wavelet layer, and recurrent layer. This dynamic mapping process enhances the overall mapping capability of the system. The nodes are summarized as follows:

$$y_{jl}^4(N) = \prod w_{jl}^4 y_j^2,\ l = 1, 2, \ldots,\ 9 \tag{35}$$

$$net_l^4(N) = y_{jl}^4 \psi_k^3 w_r^4 y_l^4(N-1) \tag{36}$$

$$y_l^4(N) = f_l^4\left(net_l^4\left(N\right)\right) = net_l^4(N) \tag{37}$$

The output of the lth node in this layer is represented by $y_l^4(N)$. The calculation involves the utilization of the connecting weight, denoted as w_{jl}^4, between layer 2 and layer 4, and the recurrent weight is denoted by w_r^4. $y_l^4(N-1)$ denotes the previous output of node lth in this layer, and the unity function is denoted as $f_l^4(\cdot)$. Each node in the network incorporates a feedback loop using the recurrent technique to achieve dynamic mapping and higher sensitivity to previously obtained data.

6. RWFNN Output Layer:

The inputs to layer 5 are obtained from the outputs of layer 4 and compute the final output by summing them up. In this layer, the output $y_o^5(N)$ is mathematically expressed as follows:

$$net_o^5(N) = \sum_l^9 w_{lo}^5 x_l^5(N),\ o = 1 \tag{38}$$

$$y_o^5(N) = f_o^5\left(net_o^5\left(N\right)\right) = net_o^5(N) \tag{39}$$

The output of the rule layer is represented as $x_l^5(N) = y_l^4(N)$. The connective weight is represented by w_{lo}^5. The final output of the RWFNN is depicted as $y_o^5(N)$. The unity function is denoted as $f_o^5(\cdot)$.

7. Online Network Parameters Learning:

All the adaptation laws of online network parameters learning will be given in Theorem 1 in the following section.

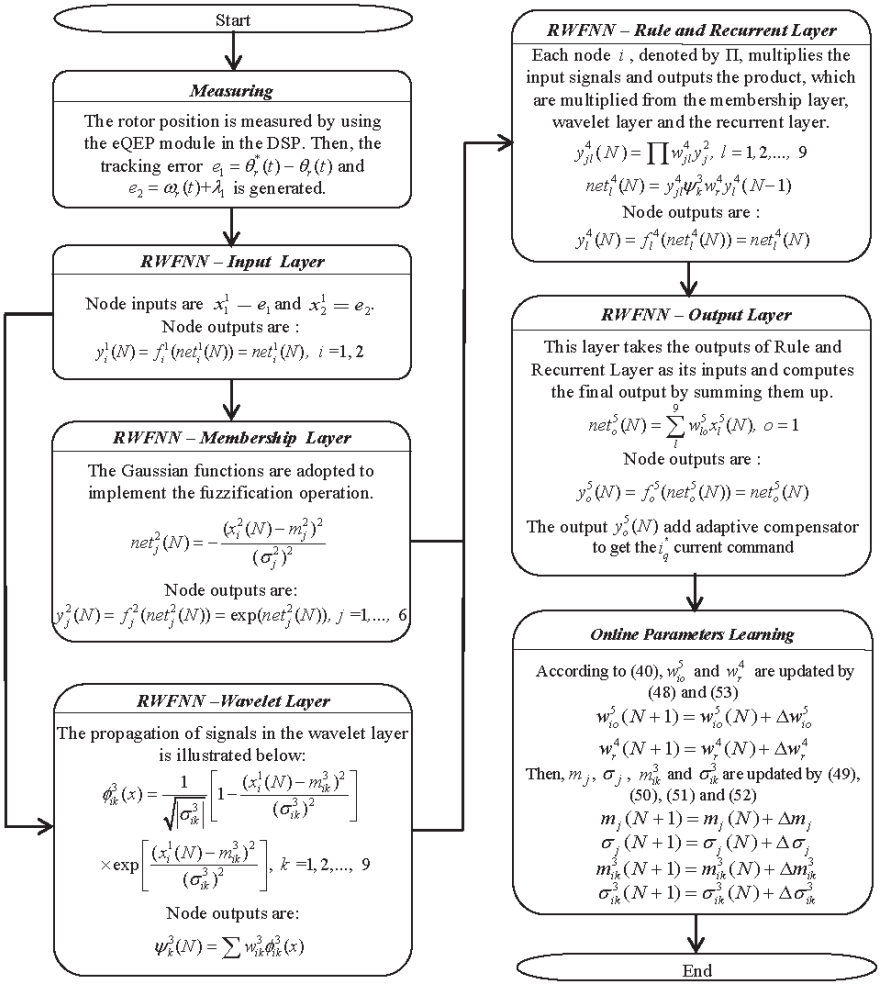

Figure 9. RWFNN flowchart for position control.

5. Stability Analysis of IBSCRWFNN System

The structure of the five-layer RWFNN, as illustrated in Figure 8, can be expressed as

$$
\begin{aligned}
&U_{RWFNN}(e_1, e_2, \boldsymbol{W}, \boldsymbol{m}_j, \boldsymbol{\sigma}_j, \boldsymbol{m}_{ik}, \boldsymbol{\sigma}_{ik}, \boldsymbol{R}) \equiv \boldsymbol{W\Gamma} \\
&\boldsymbol{W} = \left[w_1^5\ w_2^5\ w_3^5\ w_4^5\ w_5^5\ w_6^5\ w_7^5\ w_8^5\ w_9^5\right] \in R^{1\times 9} \qquad \boldsymbol{\Gamma} = \left[x_1^5\ x_2^5\ x_3^5\ x_4^5\ x_5^5\ x_6^5\ x_7^5\ x_8^5\ x_9^5\right]^T \in R^{9\times 1} \\
&\boldsymbol{m}_j = \left[m_1^2\ m_2^2\ m_3^2\ m_4^2\ m_5^2\ m_6^2\right]^T \in R^{6\times 1} \qquad \boldsymbol{\sigma}_j = \left[\sigma_1^2\ \sigma_2^2\ \sigma_3^2\ \sigma_4^2\ \sigma_5^2\ \sigma_6^2\right]^T \in R^{6\times 1} \\
&\boldsymbol{m}_{ik} = \left[m_1^3\ m_2^3\ \cdots m_{18}^3\right]^T \in R^{18\times 1} \qquad \boldsymbol{\sigma}_{ik} = \left[\sigma_1^3\ \sigma_2^3\ \cdots \sigma_{18}^3\right]^T \in R^{18\times 1} \\
&\boldsymbol{R} = \left[w_{r1}^4\ w_{r2}^4\ w_{r3}^4\ w_{r4}^4\ w_{r5}^4\ w_{r6}^4\ w_{r7}^4\ w_{r8}^4\ w_{r9}^4\right] \in R^{1\times 9}
\end{aligned}
\tag{40}
$$

The universal approximation property guarantees the existence of an optimal U^*_{RWFNN} for any nonlinear function. Consequently, a designed optimal U^*_{RWFNN} is employed to learn the BSC law U_{BSC} in order to achieve the following:

$$U_{BSC} = U^*_{RWFNN}(e_1,\, e_2,\, \boldsymbol{W}^*,\, \boldsymbol{m}_j^*,\, \boldsymbol{\sigma}_j^*,\, \boldsymbol{m}_{ik}^*,\, \boldsymbol{\sigma}_{ik}^*,\, \boldsymbol{R}^*) + \varepsilon = \boldsymbol{W}^*\boldsymbol{\Gamma}^* + \varepsilon \tag{41}$$

The reconstructed error is represented by ε, which is the minimum value; $\boldsymbol{W}^*$, $\boldsymbol{m}_j^*$, $\boldsymbol{\sigma}_j^*$, $\boldsymbol{m}_{ik}^*$, $\boldsymbol{\sigma}_{ik}^*$, and $\boldsymbol{R}^*$ are the optimal values of $\boldsymbol{W}$, $\boldsymbol{m}_j$, $\boldsymbol{\sigma}_j$, $\boldsymbol{m}_{ik}$, $\boldsymbol{\sigma}_{ik}$, and $\boldsymbol{R}$ respectively. Additionally, the control law illustrated in Equation (28) can be expressed as

$$U = \hat{U}_{RWFNN}(e_1, e_2, \hat{\boldsymbol{W}}, \hat{\boldsymbol{m}}_j, \hat{\boldsymbol{\sigma}}_j, \hat{\boldsymbol{m}}_{ik}, \hat{\boldsymbol{\sigma}}_{ik}, \hat{\boldsymbol{R}}) + \hat{U}_c = \hat{\boldsymbol{W}}\hat{\boldsymbol{\Gamma}} + \hat{U}_c \tag{42}$$

where $\hat{\boldsymbol{W}}$, $\hat{\boldsymbol{m}}_j$, $\hat{\boldsymbol{\sigma}}_j$, $\hat{\boldsymbol{m}}_{ik}$, $\hat{\boldsymbol{\sigma}}_{ik}$, and $\hat{\boldsymbol{R}}$ represent the estimated values of $\boldsymbol{W}$, $\boldsymbol{m}_j$, $\boldsymbol{\sigma}_j$, $\boldsymbol{m}_{ik}$, $\boldsymbol{\sigma}_{ik}$, and $\boldsymbol{R}$ correspondingly. The equation below is obtained by subtracting (41) from (42):

$$\begin{aligned}
\widetilde{U} &= U_{BSC} - U \\
&= U_{BSC} - \hat{U}_{RWFNN}(e_1,\, e_2,\, \hat{\boldsymbol{W}},\, \hat{\boldsymbol{m}}_j,\, \hat{\boldsymbol{\sigma}}_j,\, \hat{\boldsymbol{m}}_{ik},\, \hat{\boldsymbol{\sigma}}_{ik},\, \hat{\boldsymbol{R}}) - \hat{U}_c \\
&= U^*_{RWFNN}\left(e_1,\, e_2,\, \boldsymbol{W}^*,\, \boldsymbol{m}_j^*,\, \boldsymbol{\sigma}_j^*,\, \boldsymbol{m}_{ik}^*,\, \boldsymbol{\sigma}_{ik}^*,\, \boldsymbol{R}^*\right) + \varepsilon \\
&\quad -\hat{U}_{RWFNN}(e_1,\, e_2,\, \hat{\boldsymbol{W}},\, \hat{\boldsymbol{m}}_j,\, \hat{\boldsymbol{\sigma}}_j,\, \hat{\boldsymbol{m}}_{ik},\, \hat{\boldsymbol{\sigma}}_{ik},\, \hat{\boldsymbol{R}}) - \hat{U}_c \\
&= \boldsymbol{W}^*\boldsymbol{\Gamma}^* + \varepsilon - \hat{\boldsymbol{W}}\hat{\boldsymbol{\Gamma}} - \hat{U}_c \\
&= \widetilde{\boldsymbol{W}}\boldsymbol{\Gamma}^* + \hat{\boldsymbol{W}}\widetilde{\boldsymbol{\Gamma}} + \varepsilon - \hat{U}_c
\end{aligned} \tag{43}$$

where $\widetilde{\boldsymbol{W}} = \boldsymbol{W}^* - \hat{\boldsymbol{W}}$ and $\widetilde{\boldsymbol{\Gamma}} = \boldsymbol{\Gamma}^* - \hat{\boldsymbol{\Gamma}}$. A linearization technique is employed to convert the RWFNN into a partially linear form. This technique involves obtaining the Taylor series expansion of $\widetilde{\boldsymbol{\Gamma}}$, which can be expressed as

$$\widetilde{\boldsymbol{\Gamma}} = {\boldsymbol{\Gamma}_{m_j}}^T\widetilde{\boldsymbol{m}}_j + {\boldsymbol{\Gamma}_{\sigma_j}}^T\widetilde{\boldsymbol{\sigma}}_j + {\boldsymbol{\Gamma}_{m_{ik}}}^T\widetilde{\boldsymbol{m}}_{ik} + {\boldsymbol{\Gamma}_{\sigma_{ik}}}^T\widetilde{\boldsymbol{\sigma}}_{ik} + {\boldsymbol{\Gamma}_R}^T\widetilde{\boldsymbol{R}} + \boldsymbol{N}_h \tag{44}$$

where $\widetilde{\boldsymbol{m}}_j = \boldsymbol{m}_j^* - \hat{\boldsymbol{m}}_j$, $\widetilde{\boldsymbol{\sigma}}_j = \boldsymbol{\sigma}_j^* - \hat{\boldsymbol{\sigma}}_j$, $\widetilde{\boldsymbol{m}}_{ik} = \boldsymbol{m}_{ik}^* - \hat{\boldsymbol{m}}_{ik}$, $\widetilde{\boldsymbol{\sigma}}_{ik} = \boldsymbol{\sigma}_{ik}^* - \hat{\boldsymbol{\sigma}}_{ik}$, $\widetilde{\boldsymbol{R}} = \boldsymbol{R}^* - \hat{\boldsymbol{R}}$; the high-order term is represented by $\boldsymbol{N}_h$. In addition,

$${\boldsymbol{\Gamma}_{m_j}}^T = \begin{bmatrix} \frac{\partial x_1^5}{\partial m_1} & \frac{\partial x_1^5}{\partial m_2} & \cdots & \frac{\partial x_1^5}{\partial m_6} \\ \frac{\partial x_2^5}{\partial m_1} & \frac{\partial x_2^5}{\partial m_2} & \cdots & \frac{\partial x_2^5}{\partial m_6} \\ \vdots & \vdots & \ddots & \vdots \\ \frac{\partial x_9^5}{\partial m_1} & \frac{\partial x_9^5}{\partial m_2} & \cdots & \frac{\partial x_9^5}{\partial m_6} \end{bmatrix} \in R^{9\times 6} \qquad {\boldsymbol{\Gamma}_{\sigma_j}}^T = \begin{bmatrix} \frac{\partial x_1^5}{\partial \sigma_1} & \frac{\partial x_1^5}{\partial \sigma_2} & \cdots & \frac{\partial x_1^5}{\partial \sigma_6} \\ \frac{\partial x_2^5}{\partial \sigma_1} & \frac{\partial x_2^5}{\partial \sigma_2} & \cdots & \frac{\partial x_2^5}{\partial \sigma_6} \\ \vdots & \vdots & \ddots & \vdots \\ \frac{\partial x_9^5}{\partial \sigma_1} & \frac{\partial x_9^5}{\partial \sigma_2} & \cdots & \frac{\partial x_9^5}{\partial \sigma_6} \end{bmatrix} \in R^{9\times 6}$$

$${\boldsymbol{\Gamma}_{m_{ik}}}^T = \begin{bmatrix} \frac{\partial x_1^5}{\partial m_1} & \frac{\partial x_1^5}{\partial m_2} & \cdots & \frac{\partial x_1^5}{\partial m_{18}} \\ \frac{\partial x_2^5}{\partial m_1} & \frac{\partial x_2^5}{\partial m_2} & \cdots & \frac{\partial x_2^5}{\partial m_{18}} \\ \vdots & \vdots & \ddots & \vdots \\ \frac{\partial x_9^5}{\partial m_1} & \frac{\partial x_9^5}{\partial m_2} & \cdots & \frac{\partial x_9^5}{\partial m_{18}} \end{bmatrix} \in R^{9\times 18} \qquad {\boldsymbol{\Gamma}_{\sigma_{ik}}}^T = \begin{bmatrix} \frac{\partial x_1^5}{\partial \sigma_1} & \frac{\partial x_1^5}{\partial \sigma_2} & \cdots & \frac{\partial x_1^5}{\partial \sigma_{18}} \\ \frac{\partial x_2^5}{\partial \sigma_1} & \frac{\partial x_2^5}{\partial \sigma_2} & \cdots & \frac{\partial x_2^5}{\partial \sigma_{18}} \\ \vdots & \vdots & \ddots & \vdots \\ \frac{\partial x_9^5}{\partial \sigma_1} & \frac{\partial x_9^5}{\partial \sigma_2} & \cdots & \frac{\partial x_9^5}{\partial \sigma_{18}} \end{bmatrix} \in R^{9\times 18}$$

$${\boldsymbol{\Gamma}_R}^T = \begin{bmatrix} \frac{\partial x_1^5}{\partial w_{r1}} & \frac{\partial x_1^5}{\partial w_{r2}} & \cdots & \frac{\partial x_1^5}{\partial w_{r9}} \\ \frac{\partial x_2^5}{\partial w_{r1}} & \frac{\partial x_2^5}{\partial w_{r2}} & \cdots & \frac{\partial x_2^5}{\partial w_{r9}} \\ \vdots & \vdots & \ddots & \vdots \\ \frac{\partial x_9^5}{\partial w_{r1}} & \frac{\partial x_9^5}{\partial w_{r2}} & \cdots & \frac{\partial x_9^5}{\partial w_{r9}} \end{bmatrix} \in R^{9\times 9}$$

Rewriting (44), $\boldsymbol{\Gamma}^*$ can be calculated as follows:

$$\boldsymbol{\Gamma}^* = \hat{\boldsymbol{\Gamma}} + \tilde{\boldsymbol{\Gamma}} = \hat{\boldsymbol{\Gamma}} + \boldsymbol{\Gamma}_{\boldsymbol{m}_j}{}^T \tilde{\boldsymbol{m}}_j + \boldsymbol{\Gamma}_{\sigma_j}{}^T \tilde{\sigma}_j + \boldsymbol{\Gamma}_{m_{ik}}{}^T \tilde{\boldsymbol{m}}_{ik} + \boldsymbol{\Gamma}_{\sigma_{ik}}{}^T \tilde{\sigma}_{ik} + \boldsymbol{\Gamma}_R{}^T \tilde{\boldsymbol{R}} + \boldsymbol{N}_h \tag{45}$$

Substituting (44) and (45) into (43), expressing the estimated error in Equation (46) can be performed in the following manner:

$$\begin{aligned}
\tilde{U} &= \tilde{\boldsymbol{W}}\boldsymbol{\Gamma}^* + \hat{\boldsymbol{W}}\,\tilde{\boldsymbol{\Gamma}} + \varepsilon - \hat{U}_c \\
&= \tilde{\boldsymbol{W}}\Big(\hat{\boldsymbol{\Gamma}} + \boldsymbol{\Gamma}_{m_j}{}^T \tilde{\boldsymbol{m}}_j + \boldsymbol{\Gamma}_{\sigma_j}{}^T \tilde{\sigma}_j + \boldsymbol{\Gamma}_{m_{ik}}{}^T \tilde{\boldsymbol{m}}_{ik} + \boldsymbol{\Gamma}_{\sigma_{ik}}{}^T \tilde{\sigma}_{ik} + \boldsymbol{\Gamma}_R{}^T \tilde{\boldsymbol{R}} + \boldsymbol{N}_h\Big) \\
&+ \hat{\boldsymbol{W}}\Big(\boldsymbol{\Gamma}_{m_j}{}^T \tilde{\boldsymbol{m}}_j + \boldsymbol{\Gamma}_{\sigma_j}{}^T \tilde{\sigma}_j + \boldsymbol{\Gamma}_{m_{ik}}{}^T \tilde{\boldsymbol{m}}_{ik} + \boldsymbol{\Gamma}_{\sigma_{ik}}{}^T \tilde{\sigma}_{ik} + \boldsymbol{\Gamma}_R{}^T \tilde{\boldsymbol{R}} + \boldsymbol{N}_h\Big) + \varepsilon - \hat{U}_c \\
&= \tilde{\boldsymbol{W}}\hat{\boldsymbol{\Gamma}} + \tilde{\boldsymbol{W}}\boldsymbol{\Gamma}_{m_j}{}^T \tilde{\boldsymbol{m}}_j + \tilde{\boldsymbol{W}}\boldsymbol{\Gamma}_{\sigma_j}{}^T \tilde{\sigma}_j + \tilde{\boldsymbol{W}}\boldsymbol{\Gamma}_{m_{ik}}{}^T \tilde{\boldsymbol{m}}_{ik} + \tilde{\boldsymbol{W}}\boldsymbol{\Gamma}_{\sigma_{ik}}{}^T \tilde{\sigma}_{ik} + \tilde{\boldsymbol{W}}\boldsymbol{\Gamma}_R{}^T \tilde{\boldsymbol{R}} + \tilde{\boldsymbol{W}}\boldsymbol{N}_h \\
&+ \hat{\boldsymbol{W}}\boldsymbol{\Gamma}_{m_j}{}^T \tilde{\boldsymbol{m}}_j + \hat{\boldsymbol{W}}\boldsymbol{\Gamma}_{\sigma_j}{}^T \tilde{\sigma}_j + \hat{\boldsymbol{W}}\boldsymbol{\Gamma}_{m_{ik}}{}^T \tilde{\boldsymbol{m}}_{ik} + \hat{\boldsymbol{W}}\boldsymbol{\Gamma}_{\sigma_{ik}}{}^T \tilde{\sigma}_{ik} + \hat{\boldsymbol{W}}\boldsymbol{\Gamma}_R{}^T \tilde{\boldsymbol{R}} + \hat{\boldsymbol{W}}\,\boldsymbol{N}_h + \varepsilon - \hat{U}_c \\
&= \tilde{\boldsymbol{W}}\hat{\boldsymbol{\Gamma}} + \hat{\boldsymbol{W}}\boldsymbol{\Gamma}_{m_j}{}^T \tilde{\boldsymbol{m}}_j + \hat{\boldsymbol{W}}\boldsymbol{\Gamma}_{\sigma_j}{}^T \tilde{\sigma}_j + \hat{\boldsymbol{W}}\boldsymbol{\Gamma}_{m_{ik}}{}^T \tilde{\boldsymbol{m}}_{ik} + \hat{\boldsymbol{W}}\boldsymbol{\Gamma}_{\sigma_{ik}}{}^T \tilde{\sigma}_{ik} + \hat{\boldsymbol{W}}\boldsymbol{\Gamma}_R{}^T \tilde{\boldsymbol{R}} + \tilde{\boldsymbol{W}}\boldsymbol{\Gamma}_{m_j}{}^T \tilde{\boldsymbol{m}}_j \\
&+ \tilde{\boldsymbol{W}}\boldsymbol{\Gamma}_{\sigma_j}{}^T \tilde{\sigma}_j + \tilde{\boldsymbol{W}}\boldsymbol{\Gamma}_{m_{ik}}{}^T \tilde{\boldsymbol{m}}_{ik} + \tilde{\boldsymbol{W}}\boldsymbol{\Gamma}_{\sigma_{ik}}{}^T \tilde{\sigma}_{ik} + \tilde{\boldsymbol{W}}\boldsymbol{\Gamma}_R{}^T \tilde{\boldsymbol{R}} + \boldsymbol{W}^*\boldsymbol{N}_h + \varepsilon - \hat{U}_c \\
&= \tilde{\boldsymbol{W}}\hat{\boldsymbol{\Gamma}} + \hat{\boldsymbol{W}}\boldsymbol{\Gamma}_{m_j}{}^T \tilde{\boldsymbol{m}}_j + \hat{\boldsymbol{W}}\boldsymbol{\Gamma}_{\sigma_j}{}^T \tilde{\sigma}_j + \hat{\boldsymbol{W}}\boldsymbol{\Gamma}_{m_{ik}}{}^T \tilde{\boldsymbol{m}}_{ik} + \hat{\boldsymbol{W}}\boldsymbol{\Gamma}_{\sigma_{ik}}{}^T \tilde{\sigma}_{ik} + \hat{\boldsymbol{W}}\boldsymbol{\Gamma}_R{}^T \tilde{\boldsymbol{R}} - \hat{U}_c + H
\end{aligned} \tag{46}$$

The H, which is named as the uncertain term, can be expressed as follows:

$$H = \tilde{\boldsymbol{W}}\boldsymbol{\Gamma}_{m_j}{}^T \tilde{\boldsymbol{m}}_j + \tilde{\boldsymbol{W}}\boldsymbol{\Gamma}_{\sigma_j}{}^T \tilde{\sigma}_j + \tilde{\boldsymbol{W}}\boldsymbol{\Gamma}_{m_{ik}}{}^T \tilde{\boldsymbol{m}}_{ik} + \tilde{\boldsymbol{W}}\boldsymbol{\Gamma}_{\sigma_{ik}}{}^T \tilde{\sigma}_{ik} + \tilde{\boldsymbol{W}}\boldsymbol{\Gamma}_R{}^T \tilde{\boldsymbol{R}} + \boldsymbol{W}^*\boldsymbol{N}_h + \varepsilon \tag{47}$$

Theorem 1. *Given the PMASynRM servo drive system described in (12), the proposed IBSCR-WFNN achieves absolute asymptotic stability under the following condition.*

1. *Implementation of the IBSCRWFNN control as illustrated in (28);*
2. *Adoption of the RWFNN adaptation law as described in (48)–(53);*
3. *The compensators, illustrated in Equations (54) and (55), are developed with an adaptive law.*

$$\dot{\hat{\boldsymbol{W}}}^T = -\eta_w e_2 \hat{\boldsymbol{\Gamma}} \tag{48}$$

$$\dot{\hat{\boldsymbol{m}}}_j^T = -\eta_{m_j} e_2 \hat{\boldsymbol{W}} \boldsymbol{\Gamma}_{m_j}{}^T \tag{49}$$

$$\dot{\hat{\sigma}}_j^T = -\eta_{\sigma_j} e_2 \hat{\boldsymbol{W}} \boldsymbol{\Gamma}_{\sigma_j}{}^T \tag{50}$$

$$\dot{\hat{\boldsymbol{m}}}_{ik}^T = -\eta_{m_{ik}} e_2 \hat{\boldsymbol{W}} \boldsymbol{\Gamma}_{m_{ik}}{}^T \tag{51}$$

$$\dot{\hat{\sigma}}_{ik}^T = -\eta_{\sigma_{ik}} e_2 \hat{\boldsymbol{W}} \boldsymbol{\Gamma}_{\sigma_{ik}}{}^T \tag{52}$$

$$\dot{\hat{\boldsymbol{R}}}^T = -\eta_r e_2 \hat{\boldsymbol{W}} \boldsymbol{\Gamma}_R{}^T \tag{53}$$

$$\hat{U}_c = \hat{\psi} \tag{54}$$

$$\dot{\hat{\psi}} = -\gamma e_2 \tag{55}$$

where η_w, η_{m_j}, η_{σ_j}, $\eta_{m_{ik}}$, $\eta_{\sigma_{ik}}$, η_r are positive constant learning rate parameters; $\hat{\psi}$ represents the value of the estimated online approximated error; and γ is a positive constant.

Proof. The proposed IBSCRWFNN is designed with a Lyapunov function given by

$$\begin{aligned} &V_3\left(e_1\left(t\right), e_2\left(t\right), \widetilde{\psi}\left(t\right), \widetilde{\boldsymbol{W}}, \widetilde{\boldsymbol{m}}_j, \widetilde{\sigma}_j, \widetilde{\boldsymbol{m}}_{ik}, \widetilde{\sigma}_{ik}, \widetilde{\boldsymbol{R}}\right) \\ &= \tfrac{1}{2}{e_1}^2 + \tfrac{1}{2}{e_2}^2 + \tfrac{B_m}{2\eta_w}\widetilde{\boldsymbol{W}}\widetilde{\boldsymbol{W}}^T + \tfrac{B_m}{2\eta_{m_j}}{\widetilde{\boldsymbol{m}}_j}^T\widetilde{\boldsymbol{m}}_j + \tfrac{B_m}{2\eta_{\sigma_j}}\widetilde{\sigma}_j^T\widetilde{\sigma}_j \\ &+ \tfrac{B_m}{2\eta_{m_{ik}}}\widetilde{\boldsymbol{m}}_{ik}^T\widetilde{\boldsymbol{m}}_{ik} + \tfrac{B_m}{2\eta_{\sigma_{ik}}}\widetilde{\sigma}_{ik}^T\widetilde{\sigma}_{ik} + \tfrac{B_m}{2\eta_r}\widetilde{\boldsymbol{R}}^T\widetilde{\boldsymbol{R}} + \tfrac{B_m}{2\gamma}\left\|\widetilde{\psi}\right\|^2 > 0 \end{aligned} \tag{56}$$

The function V_3 is chosen to be positive-definite, and $\widetilde{\psi} = \psi - \hat{\psi}$. ψ is the symbol used to denote the approximated error, and it is defined by $\psi = H - F/B_m$. Furthermore, the approximated error ψ is assumed to be bounded by $|\psi| \leq F_b$. Given that the sampling interval in the experiment is considerably shorter than the fluctuations observed in H and F, the approximated error ψ is treated as a constant during the estimation process. However, it is difficult to know the upper bound F_b. Hence, a proposed adaptation law is put forth to modify the value of the online estimated approximated error $\hat{\psi}$ within the compensator. Differentiating $\widetilde{\psi}$ with respect to time yields $\dot{\widetilde{\psi}} = -\dot{\hat{\psi}}$. By utilizing Equation (12) and taking the derivative of V_3 with respect to time, the following expression can be derived:

$$\begin{aligned} &\dot{V}_3 = e_1\dot{e}_1 + e_2\dot{e}_2 - \tfrac{B_m}{\eta_w}\widetilde{\boldsymbol{W}}\dot{\widetilde{\boldsymbol{W}}}^T - \tfrac{B_m}{\eta_{m_j}}\dot{\widetilde{\boldsymbol{m}}}_j^T\widetilde{\boldsymbol{m}}_j - \tfrac{B_m}{\eta_{\sigma_j}}\dot{\widetilde{\sigma}}_j^T\widetilde{\sigma}_j - \tfrac{B_m}{\eta_{m_{ik}}}\dot{\widetilde{\boldsymbol{m}}}_{ik}^T\widetilde{\boldsymbol{m}}_{ik} - \tfrac{B_m}{\eta_{\sigma_{ik}}}\dot{\widetilde{\sigma}}_{ik}^T\widetilde{\sigma}_{ik} - \tfrac{B_m}{\eta_r}\dot{\widetilde{\boldsymbol{R}}}^T\widetilde{\boldsymbol{R}} - \tfrac{B_m}{\gamma}\widetilde{\psi}\dot{\widetilde{\psi}} \\ &= e_1[-e_2 - c_1e_1] - e_2\{B_m[U_{BSC} - U] - e_1 + c_2e_2 - F\} - \tfrac{B_m}{\eta_w}\widetilde{\boldsymbol{W}}\dot{\widetilde{\boldsymbol{W}}}^T \\ &- \tfrac{B_m}{\eta_{m_j}}\dot{\widetilde{\boldsymbol{m}}}_j^T\widetilde{\boldsymbol{m}}_j - \tfrac{B_m}{\eta_{\sigma_j}}\dot{\widetilde{\sigma}}_j^T\widetilde{\sigma}_j - \tfrac{B_m}{\eta_{m_{ik}}}\dot{\widetilde{\boldsymbol{m}}}_{ik}^T\widetilde{\boldsymbol{m}}_{ik} - \tfrac{B_m}{\eta_{\sigma_{ik}}}\dot{\widetilde{\sigma}}_{ik}^T\widetilde{\sigma}_{ik} - \tfrac{B_m}{\eta_r}\dot{\widetilde{\boldsymbol{R}}}^T\widetilde{\boldsymbol{R}} - \tfrac{B_m}{\gamma}\widetilde{\psi}\dot{\widetilde{\psi}} \\ &= -c_1{e_1}^2 - c_2{e_2}^2 - \tfrac{B_m}{\eta_w}\widetilde{\boldsymbol{W}}\dot{\widetilde{\boldsymbol{W}}}^T - e_2B_m\widetilde{\boldsymbol{W}}\hat{\boldsymbol{\Gamma}} - \tfrac{B_m}{\eta_{m_j}}\dot{\widetilde{\boldsymbol{m}}}_j^T\widetilde{\boldsymbol{m}}_j - e_2B_m\hat{\boldsymbol{W}}{\boldsymbol{\Gamma}_{m_j}}^T\widetilde{\boldsymbol{m}}_j - \tfrac{B_m}{\eta_{\sigma_j}}\dot{\widetilde{\sigma}}_j^T\widetilde{\sigma}_j \\ &- e_2B_m\hat{\boldsymbol{W}}{\boldsymbol{\Gamma}_{\sigma_j}}^T\widetilde{\sigma}_j - \tfrac{B_m}{\eta_{m_{ik}}}\dot{\widetilde{\boldsymbol{m}}}_{ik}^T\widetilde{\boldsymbol{m}}_{ik} - e_2B_m\hat{\boldsymbol{W}}{\boldsymbol{\Gamma}_{m_{ik}}}^T\widetilde{\boldsymbol{m}}_{ik} - \tfrac{B_m}{\eta_{\sigma_{ik}}}\dot{\widetilde{\sigma}}_{ik}^T\widetilde{\sigma}_{ik} - e_2B_m\hat{\boldsymbol{W}}{\boldsymbol{\Gamma}_{\sigma_{ik}}}^T\widetilde{\sigma}_{ik} \\ &- \tfrac{B_m}{\eta_r}\dot{\widetilde{\boldsymbol{R}}}^T\widetilde{\boldsymbol{R}} - e_2B_m\hat{\boldsymbol{W}}{\boldsymbol{\Gamma}_R}^T\widetilde{\boldsymbol{R}} + e_2B_m\hat{U}_c - e_2B_m\psi - \tfrac{B_m}{\gamma}\widetilde{\psi}\dot{\widetilde{\psi}} \\ &= -c_1{e_1}^2 - c_2{e_2}^2 - \left[\tfrac{B_m}{\eta_w}\widetilde{\boldsymbol{W}}\dot{\widetilde{\boldsymbol{W}}}^T + e_2B_m\widetilde{\boldsymbol{W}}\hat{\boldsymbol{\Gamma}}\right] - \left[\tfrac{B_m}{\eta_{m_j}}\dot{\widetilde{\boldsymbol{m}}}_j^T\widetilde{\boldsymbol{m}}_j + e_2B_m\hat{\boldsymbol{W}}{\boldsymbol{\Gamma}_{m_j}}^T\widetilde{\boldsymbol{m}}_j\right] - \left[\tfrac{B_m}{\eta_{\sigma_j}}\dot{\widetilde{\sigma}}_j^T\widetilde{\sigma}_j + e_2B_m\hat{\boldsymbol{W}}{\boldsymbol{\Gamma}_{\sigma_j}}^T\widetilde{\sigma}_j\right] \\ &- \left[\tfrac{B_m}{\eta_{m_{ik}}}\dot{\widetilde{\boldsymbol{m}}}_{ik}^T\widetilde{\boldsymbol{m}}_{ik} + e_2B_m\hat{\boldsymbol{W}}{\boldsymbol{\Gamma}_{m_{ik}}}^T\widetilde{\boldsymbol{m}}_{ik}\right] - \left[\tfrac{B_m}{\eta_{\sigma_{ik}}}\dot{\widetilde{\sigma}}_{ik}^T\widetilde{\sigma}_{ik} + e_2B_m\hat{\boldsymbol{W}}{\boldsymbol{\Gamma}_{\sigma_{ik}}}^T\widetilde{\sigma}_{ik}\right] - \left[\tfrac{B_m}{\eta_r}\dot{\widetilde{\boldsymbol{R}}}^T\widetilde{\boldsymbol{R}} + e_2B_m\hat{\boldsymbol{W}}{\boldsymbol{\Gamma}_R}^T\widetilde{\boldsymbol{R}}\right] \\ &+ \left[e_2B_m\hat{U}_c - e_2B_m\hat{\psi}\right] - \tfrac{B_m}{\gamma}\widetilde{\psi}\left[\dot{\hat{\psi}} + \gamma e_2\right] \end{aligned} \tag{57}$$

Moreover, by substituting (48)–(55) into (57), it can be concluded that

$$\dot{V}_3\left(e_1(t), e_2(t), \widetilde{\psi}(t), \widetilde{\boldsymbol{W}}, \widetilde{\boldsymbol{m}}_j, \widetilde{\sigma}_j, \widetilde{\boldsymbol{m}}_{ik}, \widetilde{\sigma}_{ik}, \widetilde{\boldsymbol{R}}\right) = -c_1{e_1}^2 - c_2{e_2}^2 \leq 0 \tag{58}$$

Since $\dot{V}_3\left(e_1(t), e_2(t), \widetilde{\psi}(t), \widetilde{\boldsymbol{W}}, \widetilde{\boldsymbol{m}}_j, \widetilde{\sigma}_j, \widetilde{\boldsymbol{m}}_{ik}, \widetilde{\sigma}_{ik}, \widetilde{\boldsymbol{R}}\right) \leq 0$ is negative semidefinite,

$$\dot{V}_3\left(e_1(t),\ e_2(t),\ \widetilde{\psi}(t),\ \widetilde{\boldsymbol{W}},\ \widetilde{\boldsymbol{m}}_j,\ \widetilde{\sigma}_j,\ \widetilde{\boldsymbol{m}}_{ik},\ \widetilde{\sigma}_{ik},\ \widetilde{\boldsymbol{R}}\right) < \dot{V}_3\left(e_1(0),\ e_2(0),\ \widetilde{\psi}(0),\ \widetilde{\boldsymbol{W}},\ \widetilde{\boldsymbol{m}}_j,\ \widetilde{\sigma}_j,\ \widetilde{\boldsymbol{m}}_{ik},\ \widetilde{\sigma}_{ik},\ \widetilde{\boldsymbol{R}}\right)$$

which implies that $e_1(t)$, $e_2(t)$, $\widetilde{\psi}(t)$, $\widetilde{\boldsymbol{W}}$, $\widetilde{\boldsymbol{m}}_j$, $\widetilde{\sigma}_j$, $\widetilde{\boldsymbol{m}}_{ik}$, $\widetilde{\sigma}_{ik}$, and $\widetilde{\boldsymbol{R}}$ are all bounded. By defining $\Omega(t) = c_1e_1^2 + c_2e_2^2 = -\dot{V}_3(t)$ and integrating with respect to time, one can obtain the following equation:

$$\int_0^t \Omega(\tau)d\tau = V_3(0) - V_3(t) \tag{59}$$

Since $\dot{V}_3\left(e_1(0),\, e_2(0),\, \widetilde{\psi}(0),\, \widetilde{\boldsymbol{W}},\, \widetilde{\boldsymbol{m}}_j,\, \widetilde{\sigma}_j,\, \widetilde{\boldsymbol{m}}_{ik},\, \widetilde{\sigma}_{ik},\, \widetilde{\boldsymbol{R}}\right)$ is bounded and $\dot{V}_3\left(e_1(t),\, e_2(t),\, \widetilde{\psi}(t),\, \widetilde{\boldsymbol{W}},\, \widetilde{\boldsymbol{m}}_j,\, \widetilde{\sigma}_j,\, \widetilde{\boldsymbol{m}}_{ik},\, \widetilde{\sigma}_{ik},\, \widetilde{\boldsymbol{R}}\right)$ is also bounded and nonincreasing, thus

$$\lim_{t\to\infty}\int_0^t \Omega(\tau)d\tau < \infty \tag{60}$$

Furthermore, the boundedness of $\dot{\Omega}(t)$ implies that $\Omega(t)$ is uniformly continuous. Applying Barbalat's Lemma, it can be demonstrated that $\lim_{t\to\infty}\Omega(t) \to 0$. As a result, both e_1 and e_2 will approach zero as $t \to \infty$. Consequently, the proposed IBSCRWFNN system exhibits asymptotic stability [22]. □

6. Experimentation

The experimental setup, depicted in Figure 10, comprises various components such as the PMASynRM servo drive, DSP TMS320F28075 board, and a SiC-based VSI with 4.5 kW. An industrial 7.5-kW PMSM drive is operated in torque control mode as the load. Moreover, two load torques 10 Nm (case 1) and 20 Nm (case 2), are set in the experimentation. The control of position and speed of the PMASynRM is determined using an incremental encoder, which interfaces with a quadrature encoder pulse (QEP) interface and has a sampling interval of 1 ms. The control of current operates with a sampling interval of 0.1 ms. The PMASynRM servo drive is then controlled by delivering switching commands for space vector pulse width modulation (SVPWM) to the voltage source inverter (VSI).

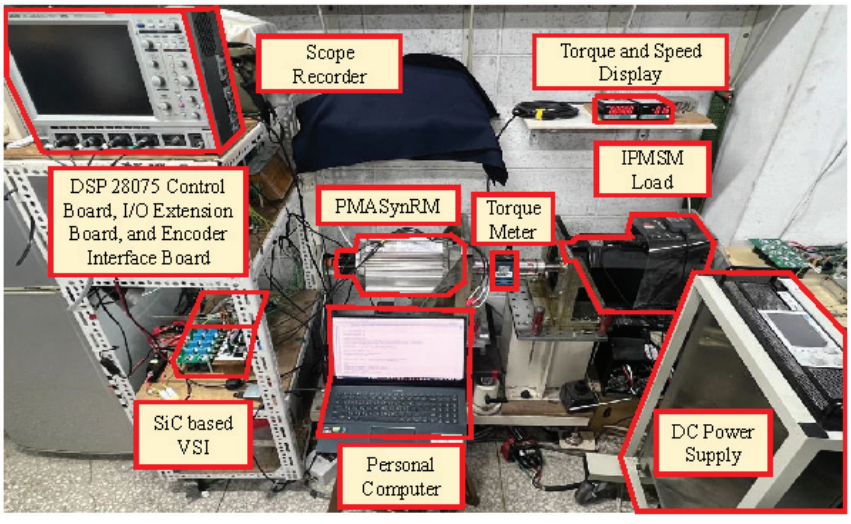

Figure 10. Experimental setup.

The suggested position control system is evaluated based on three performance metrics: T_M, T_{aver}, and T_{sd}. These metrics represent the maximum tracking error, average tracking error, and standard deviation of the tracking error, respectively. They are utilized to assess and validate the control performance.

$$T_M = \max_N(|T_{error}(N)|) \tag{61}$$

$$T_{aver} = \frac{\sum_{N=1}^{h}|T_{error}(N)|}{h} \tag{62}$$

$$T_{sd} = \sqrt{\frac{\sum_{N=1}^{h} \left(T_{error}(N) - T_{aver}(N)\right)^2}{h}} \tag{63}$$

Given that $T_{error}(N) = \theta_r^*(N) - \theta_r(N)$ and h represents the total number of iterations, the control performance of the system is demonstrated by measuring the responses of periodical step and sinusoid commands. To model the periodical step reference input, a second-order transfer function with a rise time of 0.6 s is utilized as the reference model in the following:

$$\frac{\omega_n^2}{s^2 + 2\xi\omega_n s + \omega_n^2} = \frac{30}{s^2 + 11s + 30} \tag{64}$$

In Equation (64), ξ and ω_n represent the damping ratio and undamped natural frequency, correspondingly. Moreover, the control performance of the proposed IBSCRWFNN position controller is compared with that of the BSC position controller through experimental results analysis. Furthermore, to compare the control performance, experimental results of the PI control, BSC, and the proposed IBSCRWFNN control are presented and analyzed. The parameters of PI control have been designed in Section 2.3, and the parameters of BSC and the proposed IBSCRWFNN control are provided as follows:

$$c_1 = 1.2,\ c_2 = 0.45,\ F_b = 10,\ \eta_w = 0.05,\ \eta_{m_j} = 0.15,\ \eta_{\sigma_j} = 0.3,\ \eta_{m_{ik}} = 0.01,\ \eta_{\sigma_{ik}} = 0.01,\ \eta_r = 0.02 \tag{65}$$

The parameters are iteratively adjusted to achieve optimal transient control performance while ensuring stability using a trial-and-error process. In addition, in order to strike a balance between computational resources and control performance, the network structure of the RWFNN has been designed with specific numbers of neurons in each layer: 2 in the input layer, 6 in the membership layer, 27 in the wavelet layer, 18 in the rule layer, and 1 in the output layer. Additionally, for the 32-bit floating-point DSP with 120 MHz using the "C" program, the total operation cycles and execution time for the PI controller are 60 and 0.0005 ms; the proposed BSC controller are 393 and 0.003275 ms; the proposed IBSCRWFNN controller are 9437 and 0.0786 ms. Consequently, the total execution time of the proposed IBSCRWFNN controller remains below 1 ms, which aligns with the sampling interval of the speed control loop.

In the experimentation, the objective is the control of the rotor position of PMASynRM to periodically track step and sinusoid position commands with minimum tracking errors. The test scenarios are outlined in Table 3 for the assessment of the robustness of various controllers under different operating conditions.

Table 3. Test scenarios and quantified results of experiment.

Case	Controller	Position Command (Degree)	Maximum Tracking Error (Degree)	Transient Response Time (s)	Load Torque (Nm)	Figure
Case 1	PI	periodical step	44.5	1.25	10	Figure 11a
Case 2	PI	periodical step	50.5	1.31	20	Figure 11c
Case 1	BSC	periodical step	28.3	1.15	10	Figure 12a
Case 2	BSC	periodical step	34	1.19	20	Figure 12c
Case 1	BSC	periodical sinusoid	13.2	0.82	10	Figure 13a
Case 2	BSC	periodical sinusoid	15	0.85	20	Figure 13c
Case 1	IBSCRWFNN	periodical step	14.5	0.62	10	Figure 14a
Case 2	IBSCRWFNN	periodical step	15.3	0.59	20	Figure 14c
Case 1	IBSCRWFNN	periodical sinusoid	4.9	0.32	10	Figure 15a
Case 2	IBSCRWFNN	periodical sinusoid	5.5	0.37	20	Figure 15c

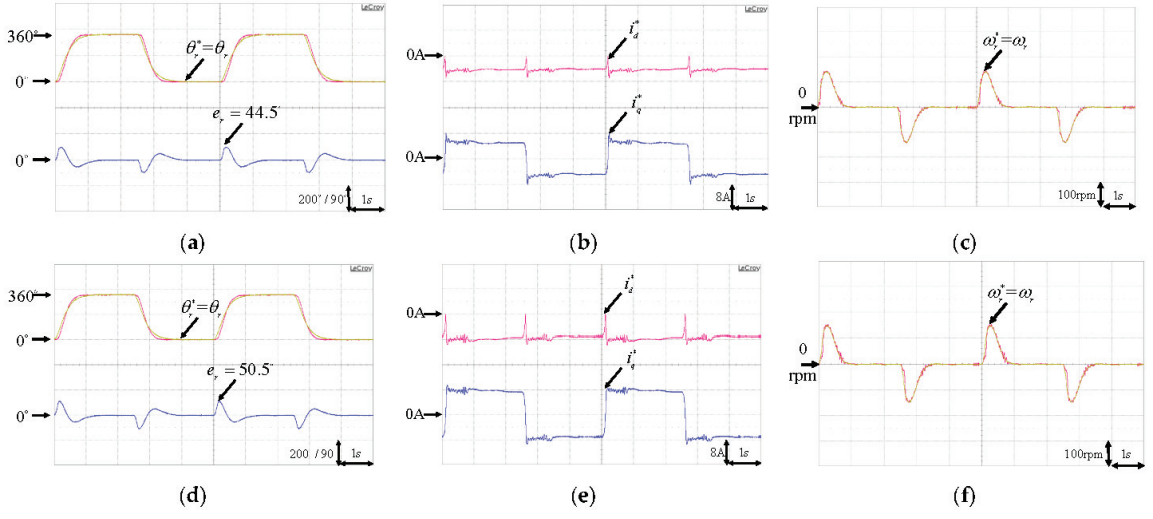

Figure 11. Experimental results of PI control with periodical step command. (**a**) Position command, response, and error at case 1; (**b**) *d*-*q* axis current commands at case 1; (**c**) Speed command and response at case 1; (**d**) Position command, response, and error at case 2; (**e**) *d*-*q* axis current commands at case 2; (**f**) Speed command and response at case 2.

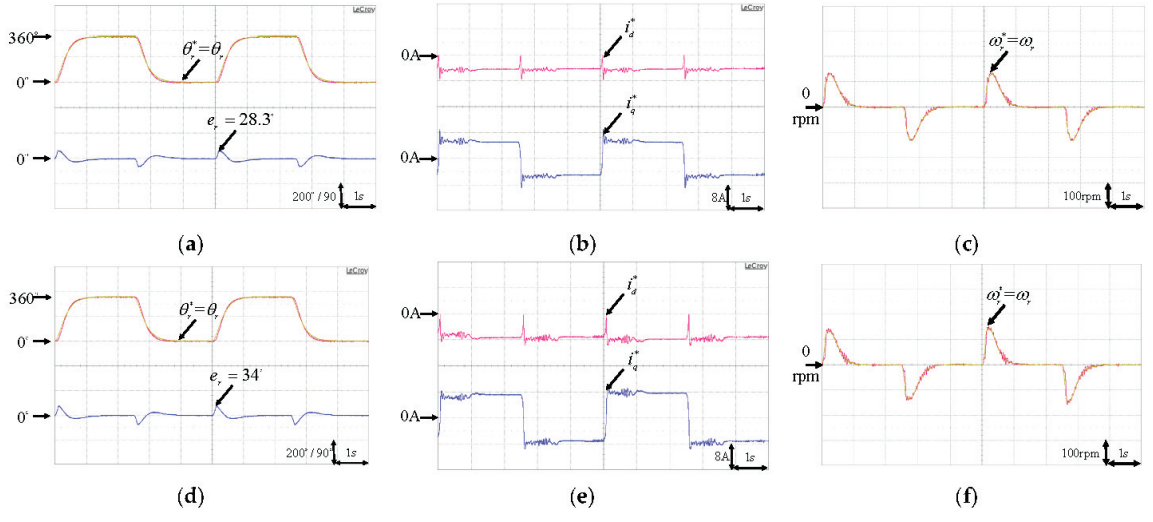

Figure 12. Experimental results of BSC control with periodical step command. (**a**) Position command, response, and error at case 1; (**b**) *d*-*q* axis current commands at case 1; (**c**) Speed command and response at case 1; (**d**) Position command, response, and error at case 2; (**e**) *d*-*q* axis current commands at case 2; (**f**) Speed command and response at case 2.

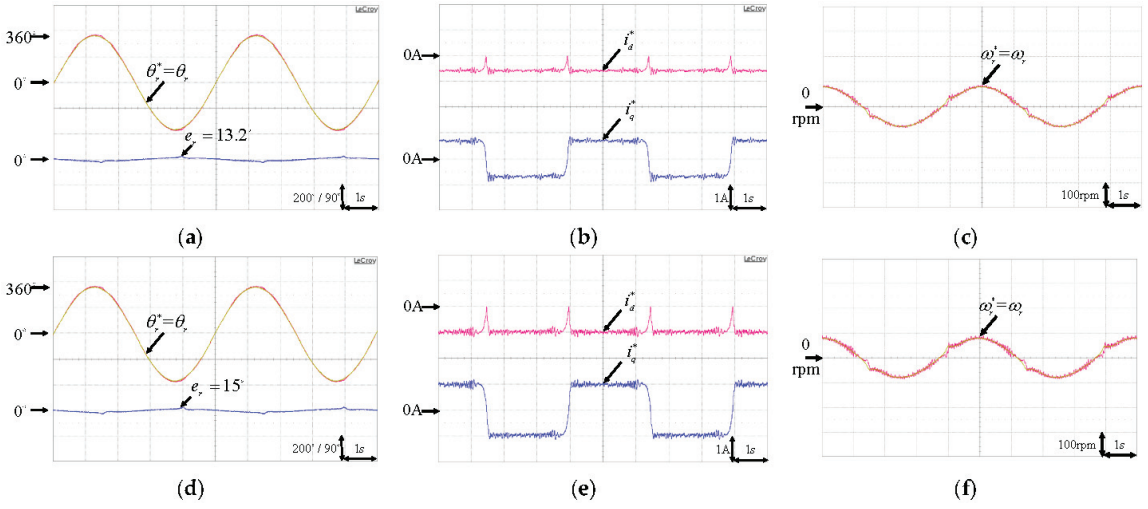

Figure 13. Experimental results of BSC control with periodical sinusoid command. (**a**) Position command, response, and error at case 1; (**b**) *d*-*q* axis current commands at case 1; (**c**) Speed command and response at case 1; (**d**) Position command, response, and error at case 2; (**e**) *d*-*q* axis current commands at case 2; (**f**) Speed command and response at case 2.

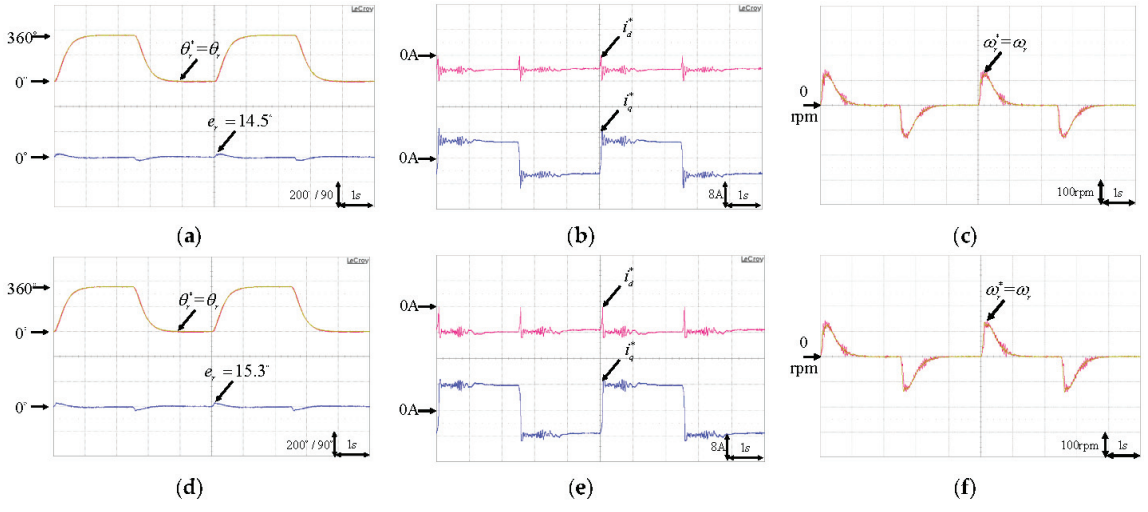

Figure 14. Experimental results of IBSCRWFNN control with periodical step command. (**a**) Position command, response, and error at case 1; (**b**) *d*-*q* axis current commands at case 1; (**c**) Speed command and response at case 1; (**d**) Position command, response, and error at case 2; (**e**) *d*-*q* axis current commands at case 2; (**f**) Speed command and response at case 2.

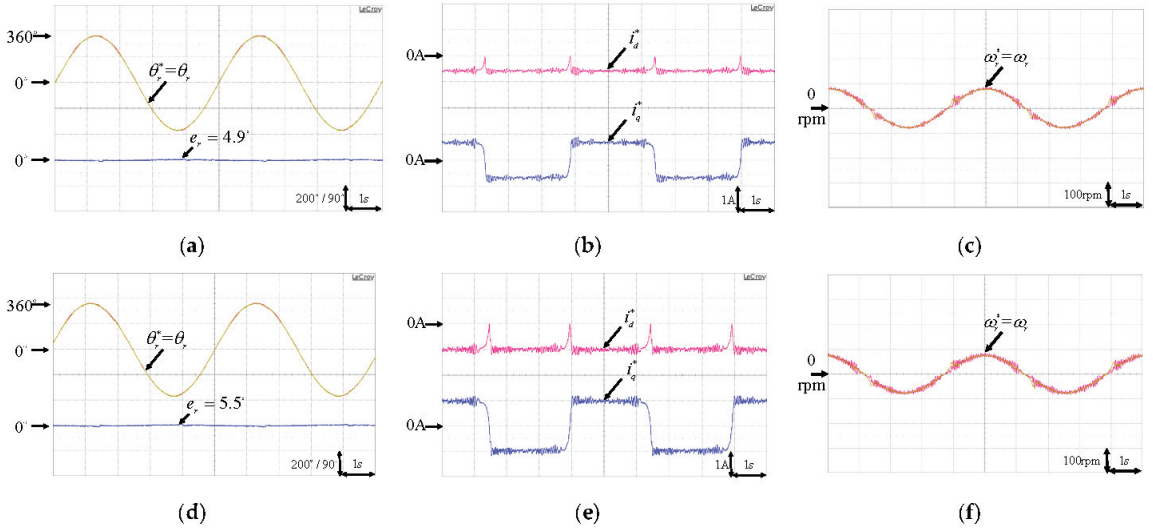

Figure 15. Experimental results of IBSCRWFNN control with periodical sinusoid command. (**a**) Position command, response, and error at case 1; (**b**) *d*-*q* axis current commands at case 1; (**c**) Speed command and response at case 1; (**d**) Position command, response, and error at case 2; (**e**) *d*-*q* axis current commands at case 2; (**f**) Speed command and response at case 2.

Figure 11 illustrates the experimental results of command tracking using periodical step commands for both case 1 and case 2 of the PI control system. The position command, response, and error are shown in Figure 11a,d; the current commands are shown in Figure 11b,e; the speed command and response are shown in Figure 11c,f. Figures 12 and 13 illustrate the experimental results of command tracking using periodical step and sinusoid commands for both case 1 and case 2 of the BSC control system. The position command, response, and error are shown in Figures 12a,d and 13a,d; the current commands are shown in Figures 12b,e and 13b,e; the speed command and response are shown in Figures 12c,f and 13c,f. In addition, Figures 14 and 15 illustrate the experimental results of command tracking using periodical step and sinusoid commands for both case 1 and case 2 of the IBSCRWFNN control system. The position command, response, and error are shown in Figures 14a,d and 15a,d; the current commands are shown in Figures 14b,e and 15b,e; the speed command and response are shown in Figures 14c,f and 15c,f.

From the experimental results, it can be observed that the d-axis current command is effectively generated using the FEA-based look-up table (LUT) for MTPA control. Moreover, the BSC position controller performs better than the PI controller, and the proposed IBSCRWFNN controller outperforms the BSC controller. The rotor response of the PMASynRM is significantly enhanced by the proposed IBSCRWFNN position controller, resulting in reduced tracking errors under different reference inputs. This improvement can be attributed to the parallel processing and online learning capabilities of the RWFNN used in the control network. In other words, the robustness of the position control is improved by employing the suggested IBSCRWFNN position controller. Furthermore, the quantified results of maximum tracking error and transient response time of all experiments are also presented in Table 3. In addition, the performance measurements of PI, BSC, and the proposed IBSCRWFNN position controllers are compared in Figure 16, considering two operating cases with periodical steps and sinusoid reference commands. The proposed IBSCRWFNN position controller exhibits lower maximum, average, and standard deviation tracking errors thanks to its faster convergence rate and improved generalization performance.

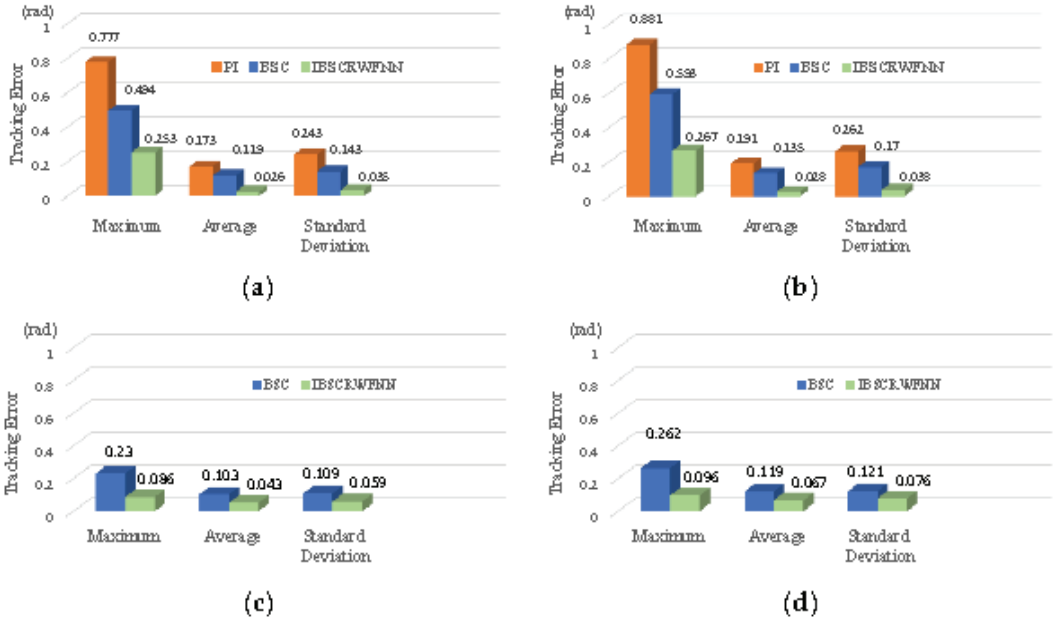

Figure 16. Maximum, average, and standard deviation of tracking errors used for the PI, BSC, and IBSCRWFNN. (**a**) Periodical step command at case 1; (**b**) Periodical step command at case 2; (**c**) Periodical sinusoid command at case 1; (**d**) Periodical sinusoid command at case 2.

7. Conclusions

In this study, an IBSCRWFNN control was proposed for a high-performance PMASynRM servo drive system. First, the dynamic model of the PMASynRM servo drive was analyzed using ANSYS Maxwell-2D capabilities. The FEA results were utilized to generate a LUT for the MTPA current angle command. Subsequently, a BSC position tracking system was developed to confront the existing lumped uncertainty of the motor drive. Moreover, the proposed RWFNN was employed as an alternative to the BSC law to address the challenges associated with the dynamic model of the motor required by the BSC in the PMASynRM servo drive. Furthermore, the Lyapunov stability method was employed to derive online learning algorithms for the RWFNN, ensuring asymptotical stability. Finally, the experimental results demonstrate that the proposed IBSCRWFNN exhibits excellent control performance in terms of position tracking control for the PMASynRM servo drive. This study presents several significant contributions, which include: (1) the successful creation of the IBSCRWFNN specifically designed for a high-performance PMASynRM position servo drive system; (2) the successful development of an online learning algorithm that allows for the real-time training of the RWFNN using the Lyapunov stability theorem; (3) the effective implementation of the IBSCRWFNN in a floating point DSP, ensuring robust position control performance for the high-performance PMASynRM.

The future works of this study are as follows: (1) in the experiment, an optical encoder was used to obtain the position of the motor rotor. Subsequently, a sensorless control method, which eliminates the need for sensors, can be further incorporated to reduce system costs. (2) In this study, the online learning rates of the intelligent control algorithm are adjusted through trial and error. In the future, it is possible to explore a self-adjusting network learning rate to optimize the intelligent control algorithm. (3) In addition to reducing motor copper losses by maximizing torque per ampere, the development of optimal efficiency control is also possible.

Author Contributions: F.-J.L. designed and developed the main parts of research work, including theory derivation and analyses of the obtained results. M.-S.H. were mainly responsible for the preparation of the paper. Y.-C.C. and S.-G.C. contributed to the DSP-based control platform and writing parts. All authors have read and agreed to the published version of the manuscript.

Funding: This research was funded by the National Science and Technology Council of Taiwan under Grant Most 110-2221-E-008-054-MY3.

Institutional Review Board Statement: Not applicable.

Informed Consent Statement: Not applicable.

Data Availability Statement: Data sharing is not applicable to this article.

Conflicts of Interest: The authors declare no conflict of interest.

References

1. Lara, J.; Xu, J.; Chandra, A. Effects of Rotor Position Error in the Performance of Field Oriented Controlled PMSM Drives for Electric Vehicle Traction Applications. *IEEE Trans. Ind. Electron.* **2016**, *63*, 4738–4751. [CrossRef]
2. Yang, Y.; Sandra, M.C.; Rong, Y.; Berker, B.; Anand, S.; Hossein, D.; Ali, E. Design and Comparison of Interior Permanent Magnet Motor Topologies for Traction Applications. *IEEE Trans. Transp. Electrif.* **2017**, *3*, 86–97. [CrossRef]
3. Fang, S.; Liu, H.; Wang, H.; Yang, H.; Lin, H. High Power Density PMSM with Lightweight Structure and High-Performance Soft Magnetic Alloy Core. *IEEE Trans. Appl. Supercond.* **2019**, *29*, 0602805. [CrossRef]
4. Kong, Y.; Lin, M.; Jia, L. A Novel High Power Density Permanent-Magnet Synchronous Machine with Wide Speed Range. *IEEE Trans. Magn.* **2020**, *56*, 7505206. [CrossRef]
5. Park, S.-H.; Lee, E.-C.; Park, J.-C.; Hwang, S.-W.; Lim, M.-S. Prediction of Mechanical Loss for High-Power-Density PMSM Considering Eddy Current Loss of PMs and Conductors. *IEEE Trans. Magn.* **2021**, *57*, 6300205. [CrossRef]
6. Bedetti, N.; Calligaro, S.; Petrella, R. Stand-Still Self-Identification of Flux Characteristics for Synchronous Reluctance Machines Using Novel Saturation Approximating Function and Multiple Linear Regression. *IEEE Trans. Ind. Appl.* **2016**, *52*, 3083–3092. [CrossRef]
7. Nikmaram, B.; Davari, S.A.; Naderi, P.; Garcia, C.; Rodriguez, J. Sensorless Simplified Finite Control Set Model Predictive Control of SynRM Using Finite Position Set Algorithm. *IEEE Access* **2021**, *9*, 47184–47193. [CrossRef]
8. Taghavi, S.M.; Pillay, P. A Mechanically Robust Rotor with Transverse Laminations for a Wide-Speed-Range Synchronous Reluctance Traction Motor. *IEEE Trans. Ind. Appl.* **2015**, *51*, 4404–4414. [CrossRef]
9. Ferrari, M.; Bianchi, N.; Doria, A.; Fornasiero, E. Design of synchronous reluctance motor for hybrid electric vehicles. *IEEE Trans. Ind. Appl.* **2015**, *51*, 3030–3040. [CrossRef]
10. Kerdsup, B.; Takorabet, N.; Nahidmobarakeh, B. Design of Permanent Magnet-Assisted Synchronous Reluctance Motors with Maximum Efficiency-Power Factor and Torque per Cost. In Proceedings of the 2018 XIII International Conference on Electrical Machines (ICEM), Alexandroupoli, Greece, 3–6 September 2018; pp. 2465–2471.
11. Wu, W.; Zhu, X.; Quan, L.; Du, Y.; Xiang, Z.; Zhu, X. Design and Analysis of a Hybrid Permanent Magnet Assisted Synchronous Reluctance Motor Considering Magnetic Saliency and PM Usage. *IEEE Trans. Appl. Supercond.* **2018**, *28*, 5200306. [CrossRef]
12. Nasiri-Zarandi, R.; Karami-Shahnani, A.; Toulabi, M.S.; Tessarolo, A. Design and Experimental Performance Assessment of an Outer Rotor PM-Assisted SynRM for the Electric Bike Propulsion. *IEEE Trans. Transp. Electrif.* **2023**, *9*, 727–736. [CrossRef]
13. Liu, Z.; Hu, Y.; Wu, J.; Zhang, B.; Feng, G. A Novel Modular Permanent Magnet-Assisted Synchronous Reluctance Motor. *IEEE Access* **2021**, *9*, 19947–19959. [CrossRef]
14. Li, K.; Wang, Y. Maximum Torque Per Ampere (MTPA) Control for IPMSM Drives Based on a Variable-Equivalent-Parameter MTPA Control Law. *IEEE Trans. Power Electron.* **2019**, *34*, 7092–7102. [CrossRef]
15. Lin, F.J.; Liu, Y.T.; Yu, W.A. Power Perturbation Based MTPA with an Online Tuning Speed Controller for an IPMSM Drive System. *IEEE Trans. Ind. Electron.* **2018**, *65*, 3677–3687. [CrossRef]
16. Li, K.; Wang, Y. Maximum Torque per Ampere (MTPA) Control for IPMSM Drives Using Signal Injection and an MTPA Control Law. *IEEE Trans. Ind. Inform.* **2019**, *15*, 5588–5598. [CrossRef]
17. Yousefi-Talouki, A.; Pescetto, P.; Pellegrino, G. Sensorless Direct Flux Vector Control of Synchronous Reluctance Motors Including Standstill, MTPA, and Flux Weakening. *IEEE Trans. Ind. Appl.* **2017**, *53*, 3598–3608. [CrossRef]
18. Dianov, A.; Tinazzi, F.; Calligaro, S.; Bolognani, S. Review and Classification of MTPA Control Algorithms for Synchronous Motors. *IEEE Trans. Power Electron.* **2022**, *37*, 3990–4007. [CrossRef]
19. Kim, H.S.; Lee, Y.; Sul, S.K.; Yu, J.; Oh, J. Online MTPA Control of IPMSM Based on Robust Numerical Optimization Technique. *IEEE Trans. Ind. Appl.* **2019**, *55*, 3736–3746. [CrossRef]
20. Lin, F.J.; Huang, M.S.; Hung, C.Y.; Chien, Y.C. Intelligent Computed Torque Control with Recurrent Legendre Fuzzy Neural Network for Permanent-Magnet Assisted Synchronous Reluctance Motor. *IEEE Access* **2023**, *11*, 54017–54028. [CrossRef]
21. Liu, T.-H.; Pu, H.-T.; Lin, C.-K. Implementation of an Adaptive Position Control System of a Permanent-Magnet Synchronous Motor and Its Application. *IET Electr. Power Appl.* **2010**, *4*, 121–130. [CrossRef]

22. Lin, F.J.; Chen, S.G.; Hsu, C.W. Intelligent backstepping control using recurrent feature selection fuzzy neural network for synchronous reluctance motor position servo drive system. *IEEE Trans. Fuzzy Syst.* **2019**, *27*, 413–427. [CrossRef]
23. Mansouri, M.M.; Hadjeri, S.; Brahami, M. New method of detection, identification, and elimination of photovoltaic system faults in real time based on the adaptive Neuro-fuzzy system. *IEEE J. Photovolt.* **2021**, *11*, 797–805. [CrossRef]
24. Dong, C.; Yu, Z.; Chen, X.; Chen, H.; Huang, Y.; Huang, Q. Adaptability Control Towards Complex Ground Based on Fuzzy Logic for Humanoid Robots. *IEEE Trans. Fuzzy Syst.* **2022**, *30*, 1574–1584. [CrossRef]
25. Chen, S.Y.; Liu, T.S. Intelligent tracking control of a PMLSM using self-evolving probabilistic fuzzy neural network. *IET Electr. Power Appl.* **2017**, *11*, 1043–1054. [CrossRef]
26. Lin, F.J.; Sun, I.F.; Yang, K.J.; Chang, J.K. Recurrent Fuzzy Neural Cerebellar Model Articulation Network Fault-Tolerant Control of Six-Phase Permanent Magnet Synchronous Motor Position Servo Drive. *IEEE Trans. Fuzzy Syst.* **2016**, *24*, 153–167. [CrossRef]
27. Fei, J.; Chen, Y.; Liu, L.; Fang, Y. Fuzzy Multiple Hidden Layer Recurrent Neural Control of Nonlinear System Using Terminal Sliding-Mode Controller. *IEEE Trans. Cybern.* **2022**, *52*, 9519–9534. [CrossRef] [PubMed]
28. Khan, M.A.; Uddin, M.N.; Rahman, M.A. A Novel Wavelet-Neural-Network-Based Robust Controller for IPM Motor Drives. *IEEE Trans. Ind. Appl.* **2013**, *49*, 2341–2351. [CrossRef]
29. Huang, W.; Oh, S.; Pedrycz, W. Fuzzy Wavelet Polynomial Neural Networks: Analysis and Design. *IEEE Trans. Fuzzy Syst.* **2017**, *25*, 1329–1341. [CrossRef]
30. Lin, F.J.; Tan, K.H.; Luo, W.C.; Xiao, G.D. Improved LVRT performance of PV power plant using recurrent wavelet fuzzy neural network control for weak grid conditions. *IEEE Access* **2020**, *8*, 69346–69358. [CrossRef]

energies

MDPI

Article

Acceleration Analysis of Canned Motors for SMR Coolant Pumps

Timothy Ngumbi Kanyolo, Harold Chisano Oyando and Choong-koo Chang *

Department of Nuclear Power Plant Engineering, KEPCO International Nuclear Graduate School (KINGS), 658-91 Haemaji-ro, Seosang-myeon, Ulju-gun, Ulsan 45014, Republic of Korea
* Correspondence: ckchang@kings.ac.kr; Tel.: +82-52-712-7303

Abstract: An SMR (small modular reactor) is expected to be able to operate flexibly in conjunction with a high renewable energy penetration grid as a result of improved safety and easy power control compared to large nuclear power plants. SMRs, such as South Korea's System-integrated Modular Advanced ReacTor (SMART), are designed to use canned motors (CMs) for their reactor coolant pumps (RCPs) to enhance their safety. CMs passively enhance the reactor's safety by preventing the leakage of radioactive reactor coolant. However, with motor sizes designed to be as small as possible, and the increased air gap of CMs between the stator and rotor, the starting torque may be insufficiently low compared to that of similar-sized induction motors (IMs). Thus, CMs may require variable frequency drives (VFDs) to start. This paper compares the torque characteristics of CMs with those of IMs for SMART's RCPs. ETAP is then used to perform a motor-starting analysis for CMs activated with and without VFDs. The results are presented and analyzed to find out if VFDs can deal with the CM starting torque issue.

Keywords: motor acceleration study; reactor coolant pump (RCP); canned motors; small modular reactor (SMR); variable frequency drive (VFD)

Citation: Kanyolo, T.N.; Oyando, H.C.; Chang, C.-k. Acceleration Analysis of Canned Motors for SMR Coolant Pumps. *Energies* **2023**, *16*, 5733. https://doi.org/10.3390/en16155733

Academic Editors: Loránd Szabó and Feng Chai

Received: 5 July 2023
Revised: 21 July 2023
Accepted: 29 July 2023
Published: 1 August 2023

1. Introduction

There is a recent increased interest in small modular reactors (SMRs) as a result of their lower initial capital investment compared to larger nuclear power plants (NPPs) and the increase in high renewable energy penetrated grids. SMRs offer small capacity, modularity, and load capabilities [1]. Similar to most modern industrial systems, motors, particularly IMs, dominate an NPP's load capacity [2]. Generally, for pressurized water reactors, reactor coolant pump (RCP) motors have the largest capacities. For enhanced safety, a good number of new SMR designs, such as KAERI's System-integrated Modular Advanced ReacTor (SMART), use passive safety systems [3], including CMs in their RCPs [4,5].

In the design of small modular reactors (SMRs), the key objective is to achieve inherent advantages, including enhanced safety, modularity, and reduced construction costs. As part of this design goal, the reactor coolant pump (RCP) and motor size must be as small as possible while still meeting the required operational and safety standards. However, one of the challenges of using canned motor technology for RCPs in SMRs is the larger air gap between the motor stator and rotor compared to similar-sized general motors. While this larger air gap allows for more cooling due to increased coolant flow, it can also result in reduced electromagnetic interlinkage between the stator and rotor fields, leading to less torque [6]. Consequently, CMs might require a larger size to produce the same starting torque as a general induction motor due to their construction.

Nonetheless, the use of variable frequency drives (VFDs) can provide a solution to this issue. VFDs allow for a smoother motor start and precise control over the torque output, which can help optimize the motor's size while still providing the necessary starting torque [7].

To further investigate the torque characteristics and to find ways to satisfy the two conflicting conditions described above, this paper conducts torque comparisons between general IMs and CMs. Additionally, motor-starting studies are performed to compare IM RCPs with CM RCPs and also to compare VFD-driven CM RCPs with CM RCPs started across the line.

To achieve the abovementioned aims, an SMR auxiliary power system (APS) is modeled in an electrical transient analyzer program (ETAP) pegged on the SMART SMR with RCP CMs.

2. Literature Review

2.1. Induction and Canned Motors

IMs work by electromagnetic induction. The interaction between the three-phase AC-supply connected stator windings' and rotor windings' electromagnetic fields produces slip according to Faraday's Law and the Lorentz force on a conductor. The most common type, the squirrel cage induction motor (SCIM), has a rotor made of conducting bars short-circuited at the ends.

The canned motor (CM) was invented in 1913 and became popular in the 1950s [8] when circumstances in the chemical and nuclear industry favored the seal-less, leak-free operations of centrifugal pumps. A CM combines and hermetically seals a centrifugal pump with an SCIM using two cans placed inside an air gap: on the stator and rotor sides, respectively, as shown in Figure 1 [9]. This leakage prevention property is immensely useful in SMRs since the CM drives RCPs that circulate radioactive reactor coolant. However, due to manufacturing limitations, the cans are made of a bulk metal material instead of laminations and this introduces eddy current losses that, in turn, interact with the air gap's magnetic field, an effect called magnetic shielding [10].

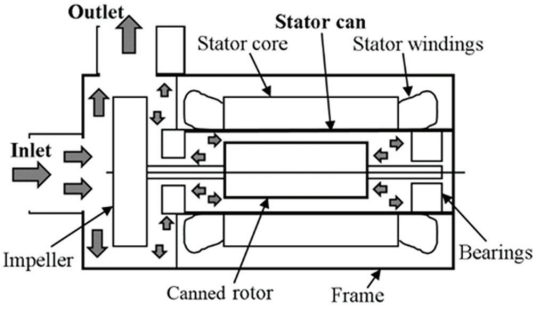

Figure 1. Outline of a canned motor.

2.2. Motor Torque Characteristics

Connecting a three-phase supply to the SCIM stator produces a rotating magnetic field (RMF) that cuts across the short-circuited rotor cage bars inducing a voltage that causes a high current flow. The current interacts with the stator's field to produce a torque that drags the rotor along the path of the RMF. Figure 2 shows a typical IM torque speed curve [7]. Notably, the torque developed at zero speed is the starting or locked rotor torque (LRT), while the one required to run a full load at a rated speed is the full load torque (FLT). In between, the maximum and minimum torques are pull-up (PUT) and breakdown torques (BDT), respectively.

The RCP motor's load torque is typical for a centrifugal pump, i.e., it follows the square law. The accelerating torque, i.e., difference between the motor torque and load torque curves, accelerates the motor to its operating speed and within its thermal limits [7]. Insufficient acceleration torque may lead to the motor overheating causing motor stator winding damage. The motor may also stall and draw high currents that may damage other motors or loads connected to the same or nearby buses.

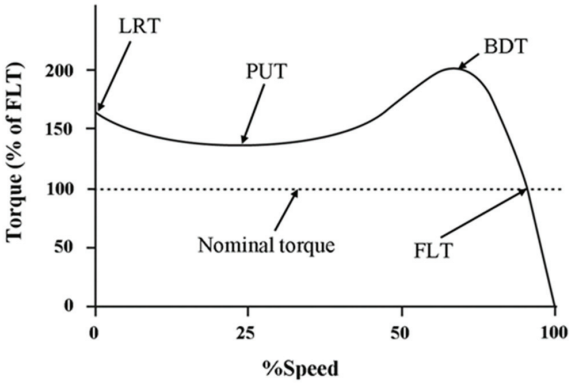

Figure 2. Typical induction motor torque–speed curve.

The CM's electromagnetic design affects eddy current losses and highly depends on air gap and can thickness. There are three factors considered in the size determination of the air gap between the cans [11]. Firstly, the clearance needs to be as small as possible such that the starting torque and the efficiency of electromagnetic conversion satisfy the pump requirements. The other two factors involve having the clearance as wide as possible to guarantee the motor cooling performance and also large enough to maintain rotor system stability.

According to studies [12], and as shown in Figure 3, the addition of cans to an IM decreases the magnetizing current ($I_{oc} < I_o$) resulting from increased magnetizing inductance ($L_{mc} > L_m$) and decreased magnetizing resistance ($r_{mc} < r_m$). Conversely, an increased slot leakage flux causes a corresponding increased stator ($l_{1c} > l_1$) and rotor ($l_{2c} > l_2$) leakage inductance. Overall, the effect is a lower power factor (PF), efficiency, and starting torque [6,10]. Stator (r_1) and rotor (r_2) resistances are mainly unchanged.

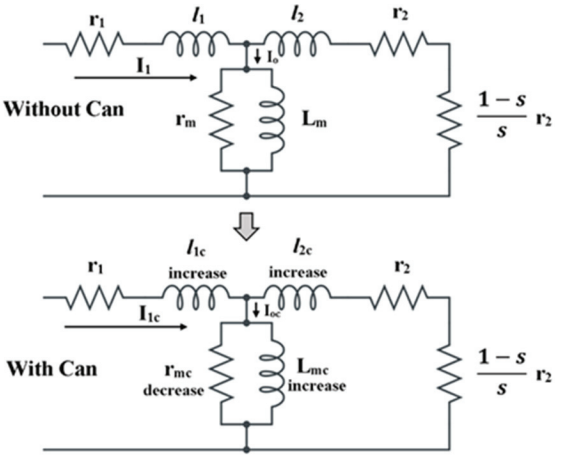

Figure 3. Equivalent circuit variation: IM vs. CM.

The usual efficiency of a CM is 50% to 70%, PF is 80%, and BDT higher than 200% of FLT. Studies [13] showed that these parameters were higher for larger-capacity CMs. A 1.9 kW CM was, for instance, shown to have a locked rotor torque that was 92.2%, that of a same-sized IM [14]. Figure 4 shows typical NEMA design letter A or B torque–speed curves for an IM and the relative curve for a similar-sized CM, i.e., CM with lower LRT and BDT values.

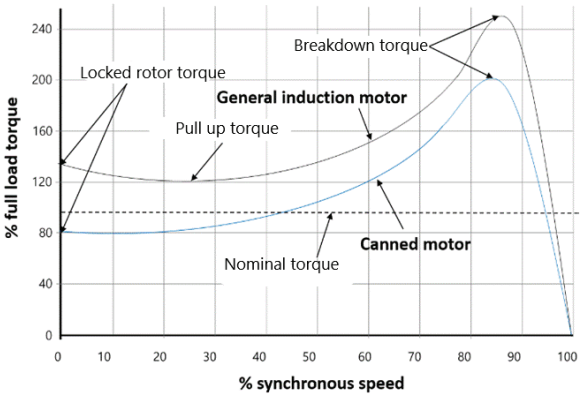

Figure 4. Relative torque–speed curve: IM vs. CM.

3. Methodology

3.1. Selection of Motor-Starting Method for Canned Motor RCP

In general, three-phase IMs of power plants are self-starting. However, a starter may be required in order to reduce the inrush current to the machine that can be as high as five to seven times the full load current (FLC) and provide overload protection. The starter method depends on various factors, such as allowable voltage drops, inrush current limitations, torque, acceleration time, cost, and compliance with standards, such as IEEE 3002.7. The major commercially used starting methods are full voltage-fixed frequency (direct online or across the line), reduced voltage-fixed frequency (wye-delta, autotransformer, and soft starter), and variable frequency drive (VFD) starts.

Across-the-line starting (direct online) is used by default. If there is a need to limit the inrush current or starting torque, reduced voltage-starting is then used.

On the other hand, variable frequency drives (VFDs) convert a fixed voltage and frequency input into a variable voltage and frequency output using power electronics. The most common VFD, the PWM-type, improves stable voltage and frequency outputs and eliminates cogging in motors [15]. A constant voltage-to-frequency (volts-per-hertz) ratio leads to a fixed flux. If the volts-per-hertz ratio is based on the rated voltage and rated frequency, and kept constant by the use of a VFD, then it follows that the rated flux and rated motor torque are maintained without the risk of magnetic core saturation. The motor thus achieves a rated torque at a rated speed with a constant rated motor flux [16]. This speed and torque control is a great advantage over the other reduced voltage-fixed frequency methods.

The main issue with the canned motor RCP is its low-torque development as a result of the smaller size of the motor (relative to larger NPPs) and the motor characteristics of a canned motor. This is particularly important when starting the motor because the voltage drop across the nearest buses (as a result of the inrush currents) is the highest. If the motor takes too long to start due to a low developed motor torque, the motor insulation may be damaged for exceeding its thermal limits and the suppressed and sustained low voltage may stall other running motors in the same system. Even though full torque can be provided by both across-the-line and VFD starts, the VFD start has the added benefit of limiting the starting current, which is the most crucial given that the RCP motor has the largest load in the SMR and thus causes the greatest voltage drops. The other benefit of using a VFD with the RCP is that it also eliminates the need for an anti-reverse rotation system [17]. The other methods (reduced voltage-fixed frequency starts) are also able to limit inrush currents but at the expense of the important torque development in the motor. This paper thus proposed the use of a VFD to start CMs, and therefore focused on direct online (DOL) and VFD starts.

However, introducing a VFD start as a motor driving method also introduced challenges [15,18,19]. Electromagnetic emissions can be produced from the VFD's output terminal and cause an interference. This can be mitigated by proper specifications, using shielded power cables to connect the VFD or using mitigation devices, such as electromagnetic interference (EMI) filters and common-mode chokes. Another issue is that of the harmonics produced by the power electronics that comprise the VFD and that have a negative impact on PF and other electronic equipment. Using adequate filtering to smoothen the input current can mitigate this and reduce the overall current harmonic distortion. Additionally, PWM pulse build-up can break down motor insulation and stress the windings, and, to mitigate the insulation damage, the motor terminal voltage can be lowered by using line reactors, resistor–capacitor snubbers, and resistor–inductor–capacitor (RLC) low-pass filters. The other challenges associated with the use of VFDs are acoustic noises produced by VFDs resonating with the system at certain speeds that shortens the life of the VFD and connected motor, high initial investment costs due to VFD complexity, and the need for reliability studies as a result of the increased failure chance of solid-state components of the VFD.

3.2. Motor-Starting Simulation Using ETAP

In order to perform this study, the SMR's auxiliary power system (APS) was designed considering physical separation, redundancy, independence, and diversity criteria. The chosen configuration is shown in the conceptual diagram in Figure 5. Additionally, and in order to compare the motor-starting performances of general induction motor RCPs with canned motor RCPs, the SMR's APS design was then summarized and modelled on ETAP as per Figure 6. This was performed because the focus of the study involved studying motor-starting and determining of motor-starting times and motor-starting torques.

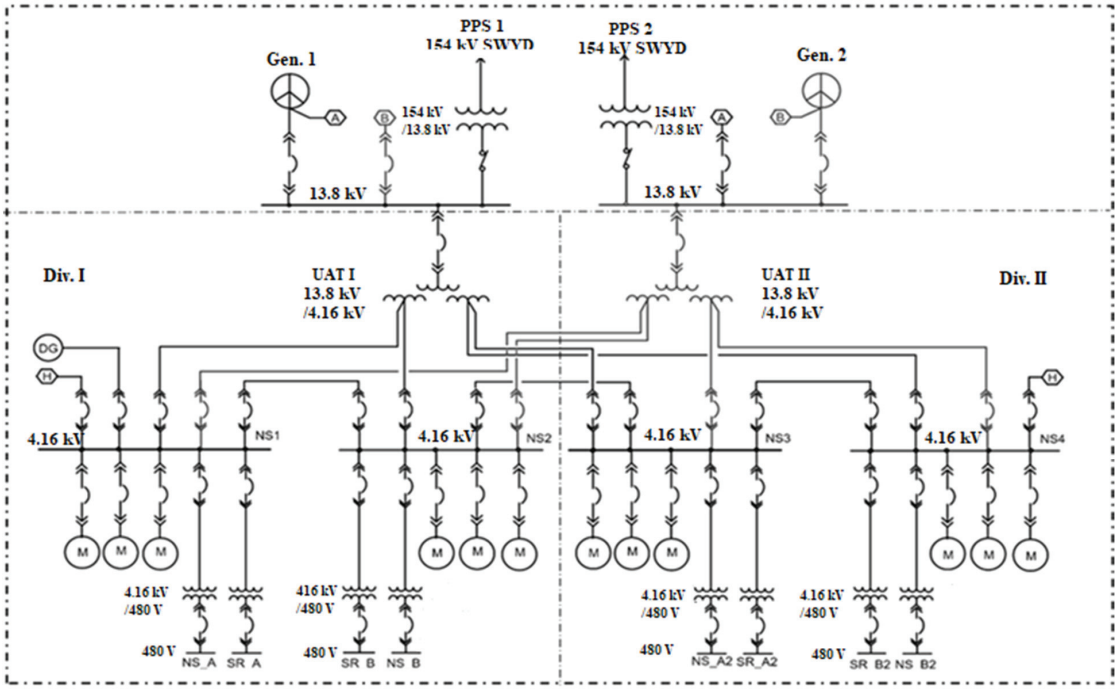

Figure 5. Concept diagram for auxiliary power system of SMR.

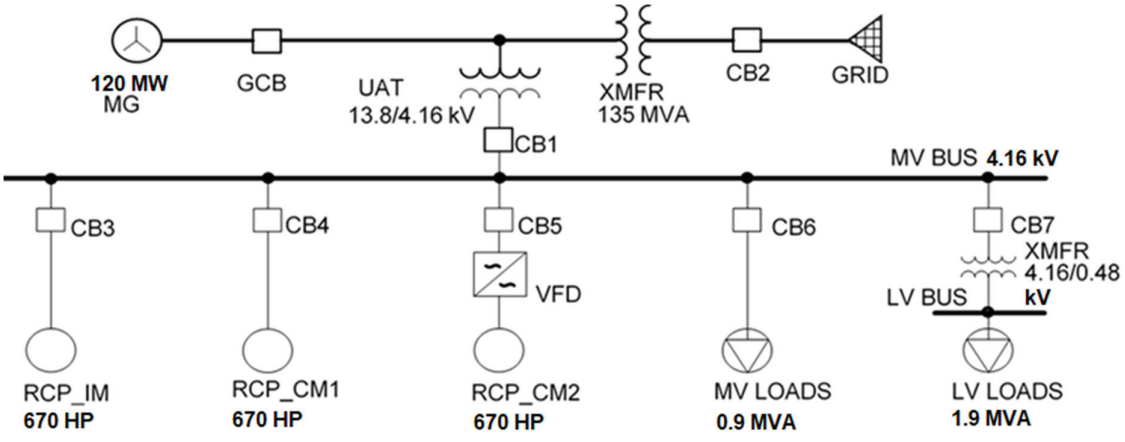

Figure 6. Partial single-line diagram for SMR auxiliary power system.

One 4.16 kV bus was conceived as enough to show voltage drops across the system, while non-RCP loads were lumped. A "Single-Cage Motor IM with deep bars" circuit model in the ETAP library (Table 1) was used to model the IM and CM RCPs by modifying equivalent circuit parameters (stator, rotor, and core inductances). From the literature reviews, the ratio between the CM LRT and that of similar-sized IMs was used as a guide [12].

Table 1. ETAP input data for RCP motors (Settings).

Setting	Induction Motor	Canned Motor
HP (kW)	500	500
Voltage rating (kV)	4	4
Torque max, BDT (%)	220.1	171.87
Locked rotor current (%)	449.92	353.14
Locked rotor torque (%)	90.05	56.48
Locked rotor PF (%)	19.52	15.21
Efficiency (%)	97.87	97.61
Full load PF (%)	92.80	91.08
Circuit design class	HV-HS-HT	HV-HS-HT
Circuit model	Estimated	Estimated

4. Results and Discussion

The study captured the comparison of direct online (DOL) starting one IM (IM), DOL starting one CM (CM1), and a variable frequency drive (VFD) starting a second CM (CM2). The total simulation time was twenty-one seconds. The results of the motor-starting study are shown in Figure 7a–e, discussed thereafter, and summarized in Table 2.

Table 2. ETAP input data for the RCP motors (settings).

Setting	DOL IM	DOL CM1	VFD CM2
Start-up time (s)	8.7	19.7	10
Locked rotor torque developed (% FLT)	88.9	56.3	110.8
Locked rotor acceleration torque (% FLT)	78.9	46.3	100.8
Maximum current (% FLC)	446.9	352.7	79.4
Bus voltage before motor start (% nominal kv)	98.1	98.1	97.9
Maximum voltage dip (% bus nominal kv)	2.6	2.1	0.2
Minimum bus voltage (% nominal kv)	95.5	96.0	97.7

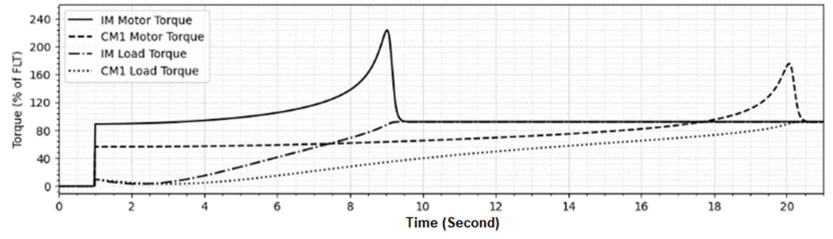

(**a**)

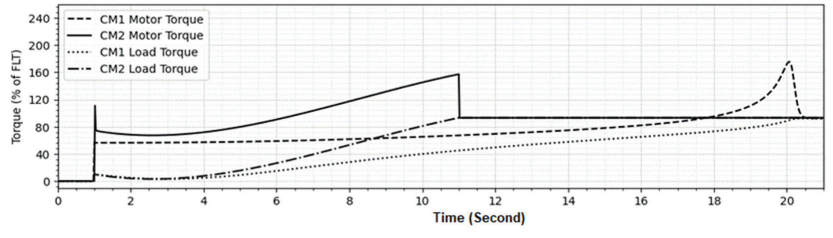

(**b**)

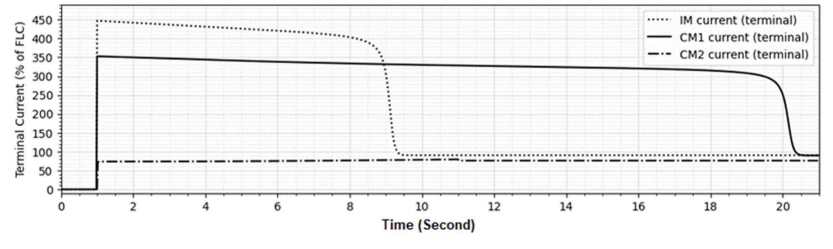

(**c**)

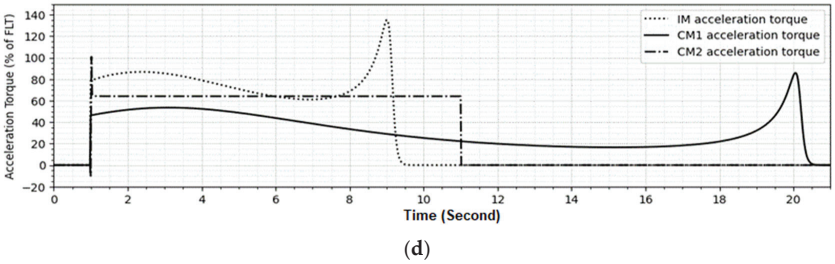

(**d**)

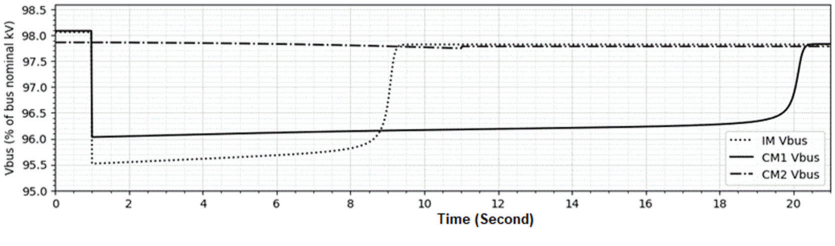

(**e**)

Figure 7. RCP motor-starting results for IM, CM1, and CM2. (**a**) Motor and load torques (IM/CM1) vs. starting time. (**b**) Motor and load torques (CM1/CM2) vs. starting time. (**c**) Motor-starting current (IM/CM) vs. starting time. (**d**) Motor acceleration torque (IM/CM) vs. starting time. (**e**) Bus voltage (IM/CM) vs. starting time.

The DOL-started IM (IM) achieved a full load torque and rated speed of 8.7 s after starting compared to the DOL-started CM (CM1) that took 19.7 s. The VFD-started CM (CM2), however, achieved a full load torque and rated speed at 10 s, compared to 19.7 s for the direct online-started CM1 (CM1).

Rated torque was achieved rapidly by the direct online-started IM (IM) compared to the direct online-started CM (CM1). This was because, even though the load torques were similar, the IM had a higher starting torque resulting in a higher accelerating torque and shorter accelerating time. The reduced starting torque of CM1 was mainly caused by eddy current losses in the canned motors. Additionally, even though both direct online-started CM (CM1) and VFD-started CM (CM2) should have had the same starting torques, employing the VFD starter resulted in a higher developed torque (almost full load torque) at the start for CM2. This was because the VFD could utilize a V/Hz control scheme to achieve a constant flux at reduced motor voltages. Consequently, for the same load torque, CM2 had a higher resultant acceleration torque compared to CM1, thus achieving a faster rated torque. All the results are illustrated in Figure 7a–c.

The bus percentage voltage drops were similar for the direct online-started IM (IM) and CM (CM1); however, the IM had a slightly greater drop (i.e., the bus voltage decreased from a 98.1% bus nominal kV to 95.5%, a difference of 2.6%) compared to CM1's (decrease from a 98.1% bus nominal kV to 96.0% bus nominal kV, a difference of 2.1%). Additionally, as shown in Figure 7d, there is a significant difference in the voltage drops for the direct online-started CM (CM1) and VFD-started CM (CM2). CM2 had no discernible voltage drop compared to CM1, i.e., CM2 bus voltage drops from a 97.9% bus nominal kV to 97.7% bus nominal kV, a difference of only 0.2%. The difference in voltage drops was attributed to IM's higher line current (inrush current of up to 446% of full load amps) compared to CM1 (352.7% of full load current) and CM2 (a maximum of 79.4% full load current), while the VFD significantly reduced the voltage drop with barely any inrush current to the motor. The VFD achieved this due to the reduced voltage applied to the motor at the start. However, even though CM1 has a lower maximum current compared to IM, the duration of its inrush current is longer and care may need to be taken to ensure the motor does not exceed its thermal limits. The inrush currents are shown in Figure 7c.

Most of the SMRs in the recent development rush around the world are adopting CMs for RCP pumps [5]. The reason for the canned motor is to increase safety by preventing coolant leakage from the motor shaft. On the other hand, due to its structural characteristics, the starting torque of a canned motor is lower than that of an IM of the same size, which means that the size of the motor must be increased to obtain the desired torque. However, since the size of the entire module must be minimized for the SMR to be manufactured as a modular type, the size of the RCP motor must also be minimized. It is necessary to take measures to handle both of these conflicting conditions.

If this problem is overlooked during the SMR development stage, the production and construction of SMRs will be greatly disrupted. The results of the study show that installing a VFD for canned motor-starting is a valid countermeasure, i.e., the operation characteristics of the same size canned motor exceed the operation characteristics of the IM motor.

5. Conclusions

In recent years, SMRs have emerged as a way to address carbon net zero. As such, more than 70 SMR models are reportedly under development worldwide [5]. In order to secure greater nuclear safety of SMR, canned motors are being adopted to drive RCP pumps. However, few auxiliary power system designs have been confirmed or proposed to include canned motor driving.

In this paper, a power system design of a two-module SMR was presented to help design the electric power system of an SMR, and based on this, an optimum motor drive system was selected and its technical feasibility was demonstrated through simulations.

The major motor in the SMR system is an RCP. However, a challenge was introduced: the smaller size of the motors due to the lower loads of the SMR meant that the motors produced lower torques. Additionally, in a bid to enhance the safety of the SMR, SMR RCPs use CMs to prevent the leakage of radioactive coolant. The low torque, as a result of these challenges, increased the risk of the RCP motor not starting or even stalling. Furthermore, SMRs are expected to perform load following to cope with variable energy sources, which means that RCPs may be required to start and stop more frequently compared to base-load nuclear power plants. Therefore, the selection of the motor-starting method was important. This study proposed using VFD-starting as a suitable motor-driving method to overcome low-torque issue. The solution also solved other challenges, such as starting the motors easily to reduce mechanical shock and increase their lifetime. However, surge protection measures must be taken as the VFD may cause voltage surges and damage to the motor.

CMs, compared to similar-sized IMs, were shown through ETAP simulations to have a reduced inrush current compared to similar-sized IMs. Further simulations showed that VFD-starts overcame the reduced starting torque issue of the CMs, thereby improving the starting torque from around 46.3% of the full load torque to 100.8% of the full load torque. In addition to this, the starting times were reduced due to the higher motor torque developed that was sufficient to guarantee starting. The paper therefore concluded that the VFD-starting of SMART SMR's RCP CMs was a viable solution to the low-starting-torque problem associated with CMs.

Further study is required to determine if additional VFD-associated costs can be justified in the long run and if the introduced electromagnetic emissions and harmonics would be within the allowable limits.

Author Contributions: T.N.K. performed the simulation and wrote this paper as the first author. H.C.O. designed the auxiliary power system of the SMR as the second author. C.-k.C. guided the design and analysis as a corresponding author. All authors have read and agreed to the published version of the manuscript.

Funding: This research received no external funding.

Data Availability Statement: Data is unavailable due to ethical restrictions.

Acknowledgments: This research was supported by the 2023 Research Fund of the KEPCO International Nuclear Graduate School (KINGS), Ulsan, Republic of Korea.

Conflicts of Interest: The authors declare no conflict of interest.

References

1. Chang, C.; Oyando, H.C. Review of the Requirements for Load Following of Small Modular Reactors. *Energies* **2022**, *15*, 6327. [CrossRef]
2. Villaran, M.; Subudhi, M. *Aging Assessment of Large Electric Motors in Nuclear Power Plants*; Nuclear Regulatory Commission: New York, NY, USA, 1996.
3. Bae, K.H.; Kim, S.D.; Lee, Y.; Lee, G.H.; An, S.; Lim, S.W.; Kim, Y.I. Enhanced safety characteristics of SMART100 adopting passive safety systems. *Nucl. Eng. Des.* **2021**, *379*, 111247. [CrossRef]
4. Carelli, M.D.; Ingersoll, D.T. *Handbook of Small Modular Nuclear Reactors: Second Edition*; Woodhead Publishing: Duxford, UK, 2020.
5. IAEA. *Advances in Small Modular Reactor Technology Developments—A Supplement to: IAEA Advanced Reactors Information System (ARIS)*; IAEA: Vienna, Austria, 2020.
6. Hu, X.; Li, Y.; Luo, L. The Influence of Air Gap Thickness between the Stator and Rotor on Nuclear Main Pump. *Energy Procedia* **2017**, *142*, 259–264. [CrossRef]
7. IEEE. *3002.7-2018—IEEE Recommended Practice for Conducting Motor-Starting Studies and Analysis of Industrial and Commercial Power Systems*; IEEE: New York, NY, USA, 2019.
8. Neumaier, R. *Hermetic Pumps: The Latest Innovations and Industrial Applications of Sealless Pumps*, 1st ed.; Gulf Professional Publishing: Woburn, MA, USA, 1997.
9. Weili, L.; Xiaochen, Z.; Wenbiao, C.; Junci, C. *Numerical Analysis of Thermal Behavior of Canned Motor*; IEEE: New York, NY, USA, 2007.
10. Hu, K.; Zhuang, H.; Yu, Q. Electromagnetic Shielding Effect of a Canned Permanent Magnet Motor. *Energies* **2020**, *13*, 4666. [CrossRef]

11. Xu, R.; Song, Y.; Gu, X.; Lin, B.; Wang, D. Research on the clearance flow between stator and rotor cans in canned motor RCP. *Ann. Nucl. Energy* **2021**, *164*, 108583. [CrossRef]
12. Yamazaki, K. Modeling and Analysis of Canned Motors for Hermetic Compressors Using Combination of 2D and 3D Finite Element Method. In Proceedings of the International Electric Machines and Drives Conference, ICEM, Seattle, WA, USA, 9–12 May 1999; p. 337.
13. Wang, Y.; Yao, Z.; Shen, H.; Xue, Y.; Cheng, D. Modeling and Analysis of Canned Motor of the Nuclear Reactor Coolant Pump. *Appl. Mech. Mater.* **2013**, *328*, 955–959. [CrossRef]
14. Yuejun, A.; Zhiheng, Z.; Ming, L.; Guangyu, W.; Xiangling, K.; Zaihang, L. Influence of asymmetrical stator axes on the electromagnetic field and driving characteristics of canned induction motor. *IET Electr. Power Appl.* **2019**, *13*, 1229–1239. [CrossRef]
15. Blair, T.H. Variable Frequency Drive Systems. In *Energy Production Systems Engineering*; The Institute of Electrical and Electronic Engineers: New York, NY, USA, 2016. [CrossRef]
16. Vandermeulen, A.H.; Natali, T.J.; Dionise, T.J.; Paradiso, G.; Ameele, K. Exploring New and Conventional Starting Methods of Large Medium-Voltage Induction Motors on Limited kVA Sources. *IEEE Trans. Ind. Appl.* **2019**, *55*, 5. [CrossRef]
17. Park, J.; Field, R.M.; Kim, T.-R. Study on the VFD (Variable Frequency Drive) for RCP (Reactor Coolant Pump) Motors of APR1400. In Proceedings of the Transactions of the Korean Nuclear Society Autumn Meeting, Pyeongchang, Republic of Korea, 30–31 October 2014.
18. Moncrief, W. *Guide to the Industrial Application of Motors and Variable-Speed Drives*; Report No. 1005983; EPRI PEAC Corporation: Palo Alto, CA, USA, 2001.
19. Khan, S. *Industrial Power Systems*; CRC Press, Inc.: Boca Raton, FL, USA, 2007. [CrossRef]

applied sciences

MDPI

Article

Analysis of the Influence of Single-Walled Carbon Nanotubes on the Fluid–Structure Interaction Vibration Control in Bionic Hydraulic Pipelines

Lingxiao Quan [1,2], Jing Gao [1], Changhong Guo [1,*] and Jiacheng Yao [1]

[1] School of Mechanical Engineering, Yanshan University, Qinhuangdao 066004, China; lingxiao@ysu.edu.cn (L.Q.); 18233510132@163.com (J.G.)
[2] Hebei Provincial Key Laboratory of Heavy Machinery Fluid Power Transmission and Control, Yanshan University, Qinhuangdao 066004, China
* Correspondence: guochanghong@ysu.edu.cn

Abstract: In previous research, a bionic hydraulic pipeline (BHP) with a three-layer structure for absorbing pulsation was invented. This paper proposes to disperse single-walled carbon nanotubes (SWCNTs) in the elastic layer material, namely silicone rubber (RTV), to enhance its ability to absorb pulsation. Firstly, the RTV-SWCNTs composite specimens with different SWCNT proportions are prepared and tested. It was found that the mechanical property is optimal when the volume content of the SWCNTs is 0.5 vol%. On this basis, BHPs with RTV-SWCNTs composite material as the elastic layer are fabricated to study the influence of the thickness and length of the elastic layer on the absorption flow pulsation. The results show that the addition of SWCNTs significantly improves the mechanical properties of silicone rubber and reduces the friction between the elastic material and oil, so that the BHP can absorb the pressure pulsation better. With the appropriate thickness and length of the elastic layer, the addition of SWCNTs can increase the pulsation suppression effect by 20%. Moreover, to analyze the influence of nanomaterials on pipeline friction, a comprehensive fourteen-equation model for describing the fluid–structure interaction (FSI) of the pipe conveying fluid considering friction coupling is established. And through numerical analysis and modal tests, the evaluation error for the modified dynamic model of the BHP is less than 5%, verifying the correctness of the proposed model and solution method.

Keywords: carbon nanotubes; pulsation absorption; bidirectional fluid–structure interaction; friction coupling; bionic pipeline

Citation: Quan, L.; Gao, J.; Guo, C.; Yao, J. Analysis of the Influence of Single-Walled Carbon Nanotubes on the Fluid–Structure Interaction Vibration Control in Bionic Hydraulic Pipelines. *Appl. Sci.* **2023**, *13*, 8862. https://doi.org/10.3390/app13158862

Academic Editor: Loránd Szabó

Received: 12 July 2023
Revised: 27 July 2023
Accepted: 28 July 2023
Published: 1 August 2023

1. Introduction

The hydraulic pipeline is considered the "blood vessel" of mechanical equipment used for hydraulic transmission. Its function is to transmit power and energy. Meanwhile, the pipeline system with excellent mechanical properties and a reasonable structure can also absorb the pressure pulsation in the hydraulic system [1]. These functions are particularly important in aviation equipment. "High speed, high pressure and high power to weight ratio" is one of the main development directions in the aviation hydraulic system and mobile machines [2]. Meanwhile, it also entails greater requirements for the stability and reliability of the hydraulic pipeline system. Due to the high speed and high pressure, as well as the complex spatial structure of the pipeline, the vibration mechanism for the aviation hydraulic system is complex, making vibration control more difficult [3].

Many scholars have conducted a lot of research on the vibration control of hydraulic systems. According to the mechanism, vibration control in the hydraulic pipeline includes passive control and active control. Passive control is realized by installing dampers, vibration absorbers, attenuators, and sticking damping materials. Zang [4] studied the vibration absorption of a functionally graded materials fluid-conveying pipe coupled with

NiTiNOL–steel, and the effects of structure parameters on the absorption performance. The results show that NiTi–steel is an effective means of vibration absorption. Jiao [5] designed a magnetic interaction-based vibration absorber for continuous beams, which has a significant role in the vibration suppression of continuous structures. Chirathalattu [6] investigated the effectiveness of passive vibration suppression for an FSI system using a nonlinear energy sink. Shu [7] proposed a vibration control method for the typical pipelines used in armored vehicles by changing the pipe diameter, bending the radius, and increasing the pipeline branches, etc. Karimi [8] used a beam-based dynamic vibration absorber (beam DVA) to analyze pipes with different sizes of harmonic excitation at different frequencies, which showed that the mass ratio and stiffness ratio, respectively, have the highest and lowest impact on pipe vibration absorption. Based on the sensitivity analysis method and the Pareto optimal multi-objective genetic algorithm, Quan [9] optimized the parameters for the pipeline support and proposed an optimization method for the passive vibration control parameters in the aviation hydraulic pipeline. Although passive control has a clear damping mechanism, a simple structure, and easy implementation, its control frequency range is narrow, the effect of damping low-frequency vibration is limited, and the control parameters are not variable. Active control acquires vibration signals through sensing elements, obtains control signals through control algorithms, and applies them to actuators to achieve vibration control in the pipeline system. Guan [10] designed a piezoelectric direct drive spool valve that could adjust the parameters with the adaptive optimal control method to reduce the pressure pulsation amplitude to a low level. Cheer [11] studied a noninvasive structure controller composed of piezoelectric laminated actuators. And the experiment proved that the controller could achieve around 20 dB of attenuation in the dominantly radiating modes. Zhang [12,13] proposed an active constrained layer damping (ACLD) system with piezoelectric materials, with the aim of investigating the vibration and damping effect of an ACLD pipeline under fixed support. Active control technology has good characteristics for pipeline vibration and a good vibration suppression effect for low-frequency vibration, but its control algorithm is relatively complex, and the parallel structure makes the fluid flow state more complicated.

Given the existing problems with pipeline vibration control technology, researchers have begun to pay attention to the application of nanomaterials for vibration control in hydraulic pipelines. Arenas [14] studied a nanocomposite made of thermoplastic polyurethane (TPU) with laponite clay filler, which can improve the impact of sound insulation performance at a resonance frequency compared with TPU. Lubecki [15] studied the application of composite materials in hydraulic hoses and conducted experimental studies on dynamic changes in the length of a microhydraulic hose under the influence of step pressure and flow load. Rafie [16] studied the vibration and damping properties of epoxy composites modified with pristine and amino-functionalized graphene nanoplatelets (GNPs) at four different nanofiller loadings. Swain [17,18] conducted viscoelastic modeling and vibration analysis on nanocomposite shell panels with different CNTs and presented a detailed mathematical formulation for the determination of viscoelastic properties. Pan [19] prepared single-walled carbon nanotubes (SWCNTs)/7075 aluminum matrix composites to investigate the effects of different SWNTs contents on the microstructure and mechanical properties. The results show that with the increase in SWCNTs, the strength and hardness of the composites increase first and then decrease. Considering the excellent properties of nanomaterials in tribology and vibration reduction applications, in this paper, SWCNTs are uniformly dispersed in the matrix material (silicone rubber) by noncovalent modification. Thus, based on the previous research on double-layer bionic hydraulic pipelines (BHPs) [20], three-layer BHPs are made and the FSI analysis and experimental verification are conducted to study the influence of nanomaterials on the damping effect of BHPs, to further promote the research on BHPs in vibration reduction.

In this paper, RTV-SWCNTs composites with different SWCNT content are prepared, and the optimal mass ratio for their performance is obtained through experiments. Based on the constitutive equation for elastic material and the effect of friction coupling, the dynamic

model of BHP is established, and the model is validated through hammering modal experiments. Through the bidirectional FSI analysis in ANSYS and experimental research, the influence of the length and thickness of the elastic layer on the pulsation suppression effect is discussed and compared with the double-layer BHP. Finally, several key issues to be further studied in the future concerning bionic hydraulic pipelines are discussed.

2. Materials and Methods

2.1. The Structure of Three-Layer BHP

The structure of the three-layer BHP has been described in detail in [20], this is just a brief introduction here. The structure of the BHP is shown in Figure 1. The outer layer is made of stainless steel for support. The middle layer is the elastic layer, which plays a role in absorbing and weakening the flow pulsation. And the inner layer is composed of nanomaterials and an elastic matrix. SWCNTs are added to the matrix to form a smooth film on the surface of the elastic layer, which can reduce the flow resistance and stabilize the flow.

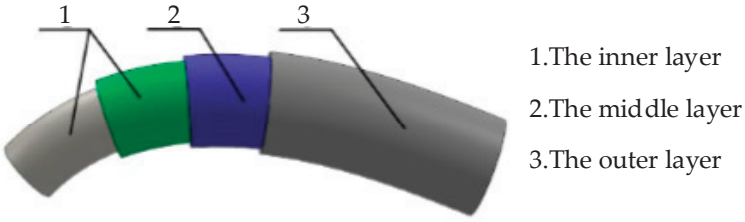

Figure 1. Structure schematic of the three-layer BHP structure.

2.2. The Preparation of RTV-SWCNTs Composite

To improve the mechanical properties of the polymer matrix, the surface modification of the SWCNTs is needed to improve its dispersion. The existing modification technologies can be roughly divided into two categories: covalent functionalization and noncovalent functionalization [21]. In this paper, noncovalent functionalization is used to modify the surface of the SWCNTs. Two-component room temperature vulcanized silicone rubber (RTV) is used as the matrix material, which consists of rubber (component A) and a cross-linking agent (component B). SWCNTs are used as the reinforced phase, and tetrahydrofuran (THF), which is a volatile solvent, is used as the dispersant. RTV-SWCNTs composites with SWCNT volume contents of 0.25 vol%, 0.5 vol%, 1 vol%, 2 vol%, and 4 vol% are prepared, respectively. Each SWCNTs-A solution is treated in a static state to observe whether there is precipitation in the solution and to preliminarily judge the dispersion of the SWCNTs in the RTV. The SWCNTs-A solution samples standing for 48 h are shown in Figure 2.

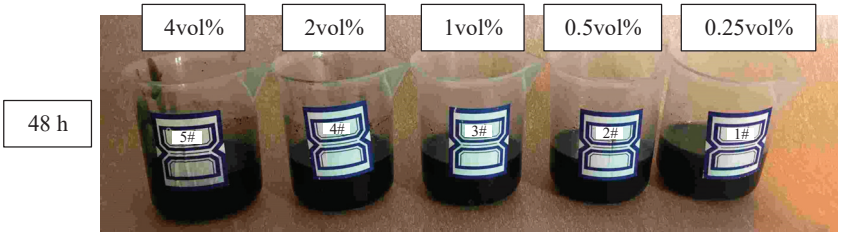

Figure 2. SWCNTs-A solution samples after 48 h of precipitation.

It could be seen that there was no precipitation of the SWCNTs in the SWCNTs-A solution, indicating that the solvent THF can disperse the SWCNTs in component A of the RTV.

2.3. Performance Test for RTV-SWCNTs Composite

Firstly, pour the prepared RTV-SWCNTs composite material solution into a dumbbell-shaped tensile mold, and cure at room temperature to prepare the tensile specimens. Then, the mechanical properties are tested using a tensile testing machine to obtain the performance parameters for the composite. Finally, the dispersion of the CNTs in the matrix material is observed through scanning electron microscope (SEM) experiments to find the RTV-SWCNTs composite material with the best performance.

2.3.1. RTV-SWCNTs Composite Tensile Test

The RTV-SWCNTs composites are subjected to tensile experiments to measure their elastic modulus, shear modulus, and Poisson's ratio. The tensile test machine used in this experiment is the Inspekt Table 100 tensile testing machine produced by Hegewald & Peschke, Germany, as shown in Figure 3. The tensile properties of the RTV-SWCNTs composites are tested at room temperature.

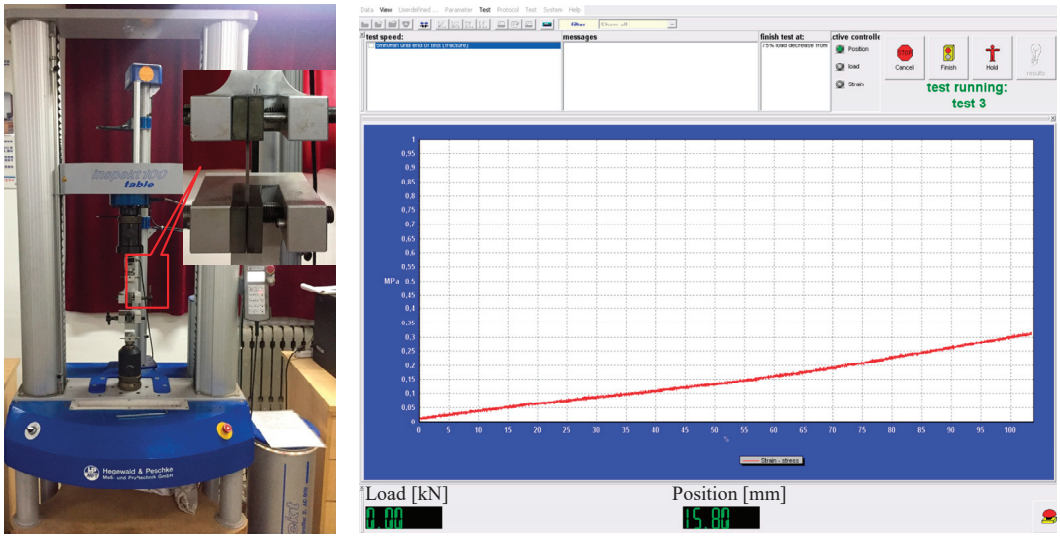

Figure 3. The tensile test bench and data acquisition program.

The mechanical properties of the RTV-SWCNTs composites with CNT contents of 0 vol%, 0.25 vol%, 0.5 vol%, 1 vol%, 2 vol%, and 4 vol% are tested. Three tensile specimens are prepared for each component group to reduce errors caused by measurement or other factors.

The stress–strain relationship of the RTV-SWCNTs composite material is non-linear. Because the elastic layer of the BHP has small deformation, the Mooney–Rivlin (M-R) constitutive model is used to describe the constitutive model of RTV-SWCNTs composites [20–25].

$$\sigma_\theta = 2C_{01}\left(3\varepsilon_\theta - 6\varepsilon_\theta^2\right) + 2C_{10}\left(3\varepsilon_\theta - 3\varepsilon_\theta^2\right) \quad (1)$$

where C_{10} and C_{01} are temperature-dependent material parameters. Then Equation (1) is simplified as:

$$\frac{\sigma_\theta}{6\left(\varepsilon_\theta - \varepsilon_\theta^2\right)} = C_{01}\left(1 - \frac{\varepsilon_\theta^2}{\varepsilon_\theta - \varepsilon_\theta^2}\right) + C_{10} \quad (2)$$

Among them, σ_θ is the stress of composite, and ε_θ is the strain of the composite. If, $x = 1 - \varepsilon_\theta^2\left(\varepsilon_\theta - \varepsilon_\theta^2\right)$, $y = \sigma_\theta / 6\left(\varepsilon_\theta - \varepsilon_\theta^2\right)$ Equation (2) can be abbreviated to,

$$y = C_{01}x + C_{10} \quad (3)$$

The tensile test data is substituted into Equation (2), and after linear fitting, the composite parameters C_{10} and C_{01} are obtained.

When the elastic material RTV is subject to small and medium deformation, the relationship between the elastic modulus E and the shear model G is as follows [26],

$$G = E/2(1+\mu) \tag{4}$$

Due to the incompressibility of RTV, Poisson's ratio μ = 0.5 can be substituted into Equation (4) to obtain E = 3G. Among them, the relationship between the shear modulus G and the parameters C_{10} and C_{01} is,

$$G = 2(C_{10} + C_{01}) \tag{5}$$

So, $E = 6(C_{10} + C_{01})$

2.3.2. Fracture Morphology Observation of Composite Materials

To better observe the fracture mechanism of the composites and the dispersion degree of the SWCNTs in the matrix material, SEM experiments are conducted on the specimens after tensile test fracture. The scanning electron microscope used in this experiment is the S-4800II cold field emission SEM by Hitachi, Japan. Table 1 shows the specific technical parameters for the SEM.

Table 1. Technical parameters of the scanning electron microscopy.

Name	Electron Beam Acceleration Voltage (kV)	Amplification (Times)	Resolution (nm)	Maximum Sample Size (mm)
value	0.5~30	30~800,000	1 (15 kV)	Φ100

3. Theoretical Modeling

3.1. Dynamic Model Considering Friction Coupling of the BHP

3.1.1. The FSI Dynamic Model

The force schematic diagram of the BHP is established according to the right-hand rule shown in Figure 4. To establish the dynamic model, we assume that the pipeline is installed parallel to the horizontal plane.

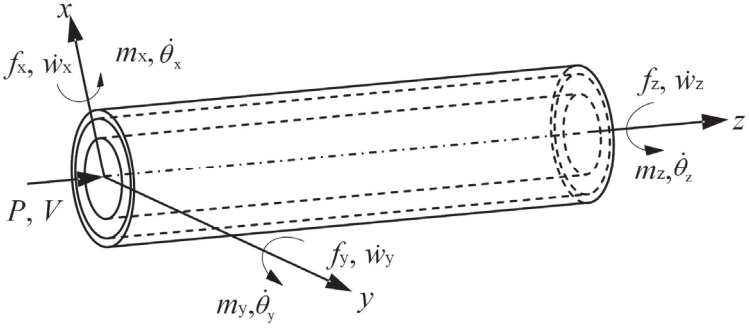

Figure 4. Force schematic diagram of the BHP.

Considering the influence of elastic material deformation, fluid viscous friction, pipeline, and fluid inertia [27], this paper establishes the FSI 14-equation for a single straight pipe as follows [20]:

Axial dynamic model:

$$\frac{1}{\rho_1}\frac{\partial P}{\partial z} + \frac{\partial V}{\partial t} + \frac{f_f}{A_1\rho_1} = 0 \tag{6}$$

$$\frac{\partial \dot{w}_z}{\partial t} + \frac{1}{\rho_t A_t + \rho_r A_r}\frac{\partial f_z}{\partial z} + \frac{f_f}{\rho_t A_t + \rho_r A_r} = 0 \tag{7}$$

$$\left[\frac{1}{K} + \frac{1}{3(C_{01}+C_{10})}\frac{r_r}{e_t+e_r}\right]\frac{\partial P}{\partial t} + \frac{\partial V}{\partial z} = 0 \tag{8}$$

$$\frac{\partial \dot{w}_z}{\partial z} + \frac{1+v_r}{6C_{10}+6C_{01}}\frac{1}{A_t+A_r}\frac{\partial f_z}{\partial t} + \frac{v_r}{6C_{10}+6C_{01}}\frac{r_r}{e_t+e_r}\frac{\partial P}{\partial t} = 0 \tag{9}$$

X-*z* plane vibration equation for the BHP:

$$\frac{\partial f_x}{\partial z} + (\rho_t A_t + \rho_r A_r + \rho_1 A_1)\frac{\partial \dot{w}_x}{\partial t} + (\rho_t A_t + \rho_r A_r + \rho_1 A_1)g = 0 \tag{10}$$

$$\frac{\partial f_x}{\partial t} + k(A_t G_t + A_r G_r)\left(\frac{\partial \dot{w}_z}{\partial z} - \dot{\theta}_y\right) = 0 \tag{11}$$

$$\frac{\partial m_y}{\partial z} + f_x + (\rho_t I_t + \rho_r I_r + \rho_1 I_1)\frac{\partial \dot{\theta}_y}{\partial t} = 0 \tag{12}$$

$$\frac{\partial m_y}{\partial t} + (E_t I_t + E_r I_r)\frac{\partial \dot{\theta}_y}{\partial z} = 0 \tag{13}$$

Y-*z* plane vibration equation for the BHP:

$$\frac{\partial f_y}{\partial z} + (\rho_t A_t + \rho_r A_r + \rho_1 A_1)\frac{\partial \dot{w}_y}{\partial t} = 0 \tag{14}$$

$$\frac{\partial f_y}{\partial t} + k(A_t G_t + A_r G_r)\left(\frac{\partial \dot{w}_y}{\partial z} + \dot{\theta}_x\right) = 0 \tag{15}$$

$$\frac{\partial m_x}{\partial z} + f_y + (\rho_t I_t + \rho_r I_r + \rho_1 I_1)\frac{\partial \dot{\theta}_x}{\partial t} = 0 \tag{16}$$

$$\frac{\partial m_x}{\partial t} + (E_t I_t + E_r I_r)\frac{\partial \dot{\theta}_x}{\partial z} = 0 \tag{17}$$

Torsional vibration equation for the BHP:

$$(\rho_t J_t + \rho_r J_r)\frac{\partial \dot{\theta}_z}{\partial t} + \frac{\partial m_z}{\partial z} = 0 \tag{18}$$

$$(G_t J_t + G_r J_r)\frac{\partial \dot{\theta}_z}{\partial z} + \frac{\partial m_z}{\partial t} = 0 \tag{19}$$

where V is the liquid flow rate (m/s), K is the liquid elastic modulus (MPa), P is the liquid pressure (MPa), ρ is the density (kg/m^3), g is the acceleration of gravity (m/s^2), E is the elastic modulus (MPa), υ is the material Poisson's ratio, G is the shear modulus (MPa), k is the shear distribution coefficient, w is the straight-line displacement (m) of the BHP, A is the cross-sectional area of each layer (m^2), θ is the angle of rotation (rad) of the BHP, f is the cross-section force of the BHP (N), m is the bending moment of the BHP (N·m), J is the polar moment of inertia (kg/m^2), r is the pipeline radius (m), e is the wall thickness for each layer (m), and I is the moment of inertia (kg/m^2). The subscripts x, y, and z are the coordinate axis direction, t is the quantity related to the stainless steel material on the outer layer of the pipeline, r is the quantity related to the elastic material in the pipeline, l is the quantity related to the fluid, and C_{10} and C_{01} are temperature-related parameters for the elastic materials, which can be obtained through experimental tests.

3.1.2. Establishment and Analysis of Friction Term of BHP

In the FSI 14-equation for the BHP, Equations (6) and (7) are the incompressible viscous fluid flow continuity equation (N-S equation) [28], which includes the friction term for the BHP. The specific form is:

$$f_{\mathrm{f}}(t) = 2\pi r_{\mathrm{r}} \tau_0(t) \tag{20}$$

τ_0 is the shear friction force of the fluid on the inner wall of the pipeline. The Laplace transform of Equation (20) is:

$$F_{\mathrm{f}}(s) = 2\pi r_{\mathrm{r}} \widetilde{\tau}_0(s) \tag{21}$$

According to the Newton friction formula, Zielke [29] established the wall shear force τ_0 in Equation (20) and obtained the relationship between the instantaneous laminar flow wall shear force τ_0 and the instantaneous average velocity and the weighted historical velocity. The specific expression is as follows:

$$\tau_{\mathrm{z}}(t) = \frac{4\rho_1 v_1}{r_{\mathrm{r}}} V(t) + \frac{4\rho_1 v_1}{r_{\mathrm{r}}} \int_0^t \frac{\partial V}{\partial t}(u) W(t-u) \mathrm{d}u \tag{22}$$

where W is the weighting function of dimensionless time τ, $\tau = v_1 t / r_{\mathrm{r}}$. The expression of $W(\tau)$ is:

$$W(\tau) = \begin{cases} \sum\limits_{i=1}^{5} e^{-m_i \tau}, \tau \geq 0.02 \\ \sum\limits_{i=1}^{6} n_i e^{(i-2)/2}, \tau < 0.02 \end{cases} \tag{23}$$

where the values for the weighted coefficients m_i and n_i are shown in Tables 2 and 3.

Table 2. Weighting coefficient m_i.

m_1	m_2	m_3	m_4	m_5
−26.3744	−70.80493	−135	−218.9216	−322.5544

Table 3. Weighting coefficient n_i.

n_1	n_2	n_3	n_4	n_5	n_6
0.2821	−1.25	1.0579	0.9375	0.3967	0.3516

Based on the theory proposed by Zielke, Brunone proposed a friction model for the turbulent flow. He believes that the wall shear force is related to the average flow velocity V, instantaneous acceleration $\partial V / \partial t$, and convection acceleration $\partial V / \partial z$ [30]. This model is widely used in the calculation of wall shear force in a turbulent flow. The expression of wall shear force in the Brunone model is:

$$\tau_B = \frac{\rho_1 f V |V|}{8} + \frac{\rho_1 D}{4} \cdot k_3 \left(\frac{\partial V}{\partial t} - \alpha \frac{\partial V}{\partial z} \right) \tag{24}$$

Among them, f is the friction coefficient under turbulent flow; α is the wave velocity of the water hammer; K_3 is the Brunson friction coefficient; this numerical value generally is an empirical value, which is determined by test or trial calculation.

Based on the Brunone friction model, Vardy established a semi-empirical and semi-theoretical formula for K_3 by introducing the assumption of global acceleration [31]:

$$k_3 = \sqrt{7.41 / Re^{k4}} / 2 \tag{25}$$

$$k_4 = \log\left(14.3 / Re^{0.05}\right) \tag{26}$$

The weighted function model by Zielke does not depend on empirical parameters, thus, it is more consistent with experimental test results on laminar flow and low Reynolds number turbulence calculations. In this paper, the fluid state in the BHP is the laminar flow, so the Zielke friction model is used as the friction term in the FSI 14-equation.

3.2. Boundary Matrix Model

The two ends of the BHP are blocked with mass blocks of m0 and mL, and the excitation force F is applied along the z-direction of the pipeline at the initial end. The overall boundary constraint equation for the BHP is consistent with [20]. It will not be repeated here, only the concrete form for the boundary matrix at both ends of the BHP is given.

$$\mathbf{D}_0 = \begin{bmatrix} 1 & 0 & -1 & 0 & & & & & & & & & & \\ 0 & A_1 & K_{z0} & 1 & & & & & & & & & & \\ & & & & Z_{x0} & 1 & 0 & 0 & & & & & & \\ & & & & 0 & 0 & -Y_{y0} & 1 & & & & & & \\ & & & & & & & & Z_{y0} & 1 & 0 & 0 & & \\ & & & & & & & & 0 & 0 & -Y_{x0} & 1 & & \\ & & & & & & & & & & & & -T_{z0} & 1 \end{bmatrix} \tag{27}$$

$$\mathbf{D}_0 = \begin{bmatrix} 1 & 0 & -1 & 0 & & & & & & & & & & \\ 0 & A_1 & -K_{zL} & 1 & & & & & & & & & & \\ & & & & -Z_{xL} & 1 & 0 & 0 & & & & & & \\ & & & & 0 & 0 & Y_{yL} & 1 & & & & & & \\ & & & & & & & & Z_{yL} & 1 & 0 & 0 & & \\ & & & & & & & & 0 & 0 & Y_{xL} & 1 & & \\ & & & & & & & & & & & & T_{zL} & 1 \end{bmatrix} \tag{28}$$

3.3. Excitation of the BHP

In the hydraulic pipeline system, the pipeline excitation form can be divided into two categories: fluid excitation and solid excitation. In this paper, the modal analysis for the BHP is carried out by solid excitation. The function form is,

$$F(t) = F_r[1(t) - 1(t - T)] \tag{29}$$

The initial end excitation vector for the BHP can be obtained by the Laplace transform of Equation (29),

$$\mathbf{Q}_0 = \begin{bmatrix} 0 & -(F_r/s)\left(1 - e^{-sT}\right) & 0 & 0 & 0 & 0 & 0 \end{bmatrix}^T \tag{30}$$

No excitation is applied at the end of the BHP, so its excitation vector is:

$$\mathbf{Q}_L = \begin{bmatrix} 0 & 0 & 0 & 0 & 0 & 0 & 0 \end{bmatrix}^T \tag{31}$$

4. Analysis Example and Methods

4.1. Frequency-Domain Characteristic Analysis and Experimental Verification of the FSI Dynamic Model

4.1.1. Analysis of Frequency-Domain Characteristics of FSI Dynamic Model

The specific parameters for the BHP are shown in Table A1 (Appendix A). A mechanical impact excitation is applied to the initial end of the BHP, where the mean value of the impact force F_r is 15,000 N and the knocking time T is 2 ms. The boundary matrix, excitation vector, and pipeline structure parameters are substituted into the FSI 14-equation for the BHP for the modal solution. The result is shown in Figure 5.

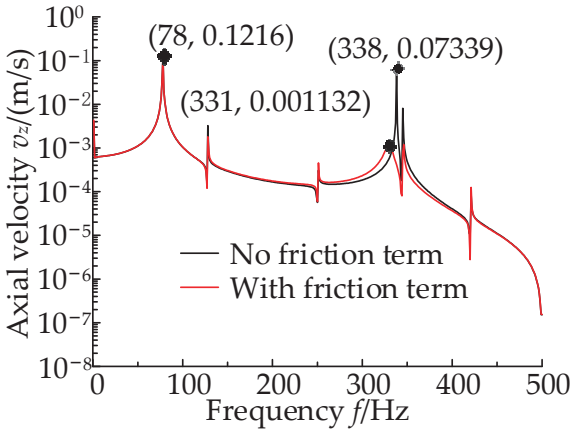

Figure 5. The curve on the effect of the friction term on the axial velocity of the BHP.

It can be observed that the frequency corresponding to each peak in the curve is the natural frequency of the BHP. By comparing the axial velocity response curve for the BHP with/without friction terms, it can be seen that friction coupling does not affect the resonant frequency, but affects its resonant peak.

4.1.2. Modal Verification Test

The modal experiment generally uses a hammer or the exciter as the excitation device. The experimental object in this paper is the BHP, which belongs to light and small equipment. The hammer is used as the excitation equipment and its specific technical parameters are shown in Figure 6a. Considering the effect of the oil on the pipeline, the oil is sealed in the pipeline. And the BHP filled with oil is suspended by a string with small rigidity. The acceleration sensor is stuck to the middle of the pipeline, as shown in Figure 6b. Then, the left end (inlet end) of the pipeline is knocked by the calibrated hammer to produce the frequency response curve.

Name	Parameter
Range	2000 N
Operating current	250 mA
Sensitivity	250 mA/N
Buffer head material	nylon
Hammer body mass	0.18 kg
Hammer head mass	0.006 kg

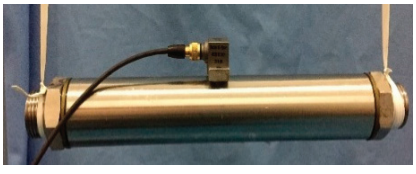

(**a**) (**b**)

Figure 6. Modal test. (**a**) Hammer used in the modal test. (**b**) The tested pipeline.

The modal experiment needs to collect the input signal and the output signal (acceleration signal). The collected input/output signals are transformed into the frequency domain using Fourier transform. Then, according to Equations (32)–(34), the auto-power spectrum of the input signal, the auto-power spectrum of the output signal, and the cross-power spectrum of the input–output signal are obtained, respectively. Finally, the frequency response curve for the axial velocity of the BHP is obtained by Equation (35), as shown in Figure 7.

$$G_{xx} = \frac{1}{N}\sum_{i=1}^{N} F_i^x F_i^{x^*} \tag{32}$$

$$G_{yy} = \frac{1}{N}\sum_{i=1}^{N} F_i^y F_i^{y^*} \tag{33}$$

$$G_{xy} = \frac{1}{N}\sum_{i=1}^{N} F_i^y F_i^{x^*} \tag{34}$$

$$H = \frac{G_{xy}}{G_{xx}} \tag{35}$$

where F is the data in the frequency domain after the Fourier transform, N is the number of sampling points, superscript $*$ represents the complex conjugate, subscript x is the input signal, and subscript y is the output signal.

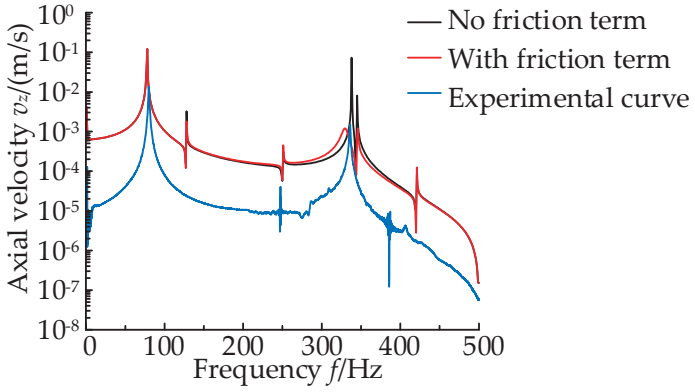

Figure 7. The frequency response curve for the BHP.

The comparison results for the experiment and simulation are shown in Table 4. The error between them is less than 5%. The validity of the FSI 14-equation dynamic model considering friction coupling is verified.

Table 4. Comparison of the modal analysis simulation and experimental data.

	Simulation (Hz)	Experimental (Hz)	Error (%)
First-order mode	78	81.26	4.01
Second-order mode	331	333.68	0.8

4.2. Bidirectional FSI Simulation and Experimental Methods for Bionic Pipelines

4.2.1. Simulation Analysis of Bidirectional FSI for the BHP

To study the influence of different types of BHP on the vibration of the pipe wall when the flow pulsation is the same, the bidirectional FSI analysis for the BHP is carried out in the ANSYS Workbench software. The grid division of the solid and fluid regions is shown in Figure 8. The structural parameters and fluid parameters are shown in Table A1; where, the parameters for the RTV are C_{01} = 1.213 MPa, C_{10} = −0.01679 MPa. The standard k-ξ, turbulence model is adopted for the fluid, the wall shear force in the BHP with RTV as the elastic layer is the wall shear force in the Brunone model, and the inner wall of the BHP with RTV-SWCNTs composite materials as the elastic layer is set as the smooth wall. The boundary condition for the pipeline inlet is set as the flow pulsation at the outlet of the axial piston pump, as shown in Figure 9. The pipeline outlet is set as the pressure outlet and the pressure is set as 2 MPa.

(**a**) (**b**)

Figure 8. Meshing in the BHP model. (**a**) Solid region sweep meshing method; (**b**) fluid region meshing method.

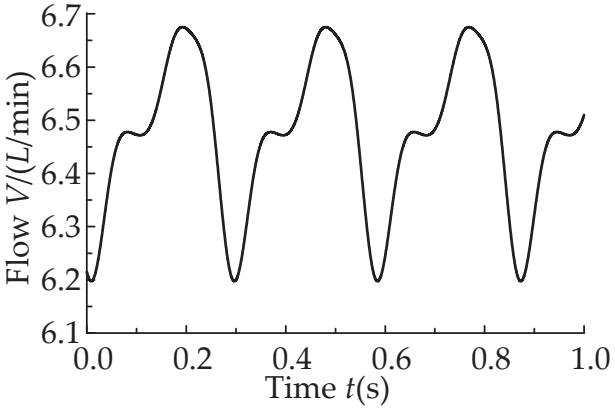

Figure 9. Flow pulsation curve for the bionic hydraulic pipeline inlet.

1. Influence of the thickness of the elastic layers on the vibration of the BHP

To study the effect of different thicknesses of the elastic layer and materials on the vibration of the pipeline wall in the BHP, the thickness of the stainless steel on the outer layer of the BHP is set at 2 mm, the length of the pipe is set at 100 mm, and the thickness of the elastic layer is, respectively, set at 5 mm, 10 mm, 20 mm, and 25 mm.

2. Influence of the length of the BHP on the vibration of the pipe wall

To study the effect of the different lengths and materials in the elastic layer on the vibration of the pipeline wall in the BHP, the thickness of the stainless steel on the outer layer of the BHP is set at 2 mm, the thickness of the elastic layer is set at 5 mm, and the length of the pipeline is, respectively, set at 100 mm, 150 mm, 250 mm, and 300 mm.

4.2.2. BHP Fabrication and Experimental System

The outer layer of the BHP is made of stainless steel and the middle layer is the elastic layer, which is composed of RTV-SWCNTs composite materials. The content of the SWCNTs in the RTV-SWCNTs composite materials is 0.5 vol%. Some of the SWCNTs adhered to the inner wall of the pipeline form a smooth film, forming the inner layer of the BHP. The double-layer BHP is used for a comparative experiment, whose outer layer is made of stainless steel and the inner layer is made of RTV. The BHP is shown in Figure 10. The structural parameters for the BHP specimens are shown in Table 5.

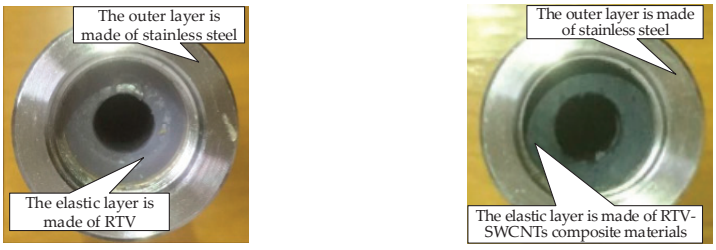

(**a**) (**b**)

Figure 10. Bionic hydraulic pipeline physical diagram. (**a**) BHP with RTV as the elastic layer; (**b**) BHP with RTV-SWCNTs composite materials as the elastic layer.

Table 5. The structural parameters for the BHP specimens.

No.	Length (mm)	Thickness of Elastic Layer (mm)	Thickness of Outer Layer (mm)	Inside Diameter (mm)
1	130	5	3	10
2	130	10	3	10
3	130	15	3	10
4	130	20	3	10
5	130	25	3	10
6	180	5	3	10
7	230	5	3	10
8	280	5	3	10
9	330	5	3	10

The experiment on the flow pulsation absorption of the BHP is to study the absorption effect of the length, the material in the elastic layer, and the thickness of the elastic layer in the BHP on the flow pulsation at the outlet of the axial piston pump, by comparing the outlet flow pulsation of the different types of BHP. The vibration experimental apparatus is shown in Figure A1 (Appendix B).

4.2.3. Experiment on the Vibration Absorption of the BHP

1. Influence of the thickness of the elastic layers on the flow pulsation

The No. 1–5 pipelines in Table 5 are installed at the outlet of the hydraulic pump, according to Figure A1. The pressure of the pipelines is set at 2 MPa.

2. Influence of the length of the BHP on the flow pulsation

The No.1, 6–9 pipelines in Table 5 are installed at the outlet of the pump, according to Figure A1. The flow pulsation curves for the different BHPs are shown in Figure 9.

3. Influence of the thickness of the elastic layers on the vibration of the BHP

The No. 1–5 pipes in Table 5 are installed at the outlet of the hydraulic pump, as shown in Figure A1. The load pressure of the pipeline is set to 2 MPa and the radial acceleration amplitude of the pipe wall at the middle node (point P) for each BHP is measured.

4. Influence of the length of the pipeline on the vibration of the BHP

The No. 1, 6–9 pipes in Table 5 are installed at the outlet of the hydraulic pump, as shown in Figure A1. The load pressure of the pipeline is set to 2 MPa and the radial acceleration amplitude of the pipe wall at point P for each BHP is measured.

5. Results and Discussion

5.1. Experimental Results on the Properties of the RTV-SWCNTs Composites

5.1.1. Tensile Test Results for the RTV-SWCNTs Composites

The tensile test results are shown in Figure 11.

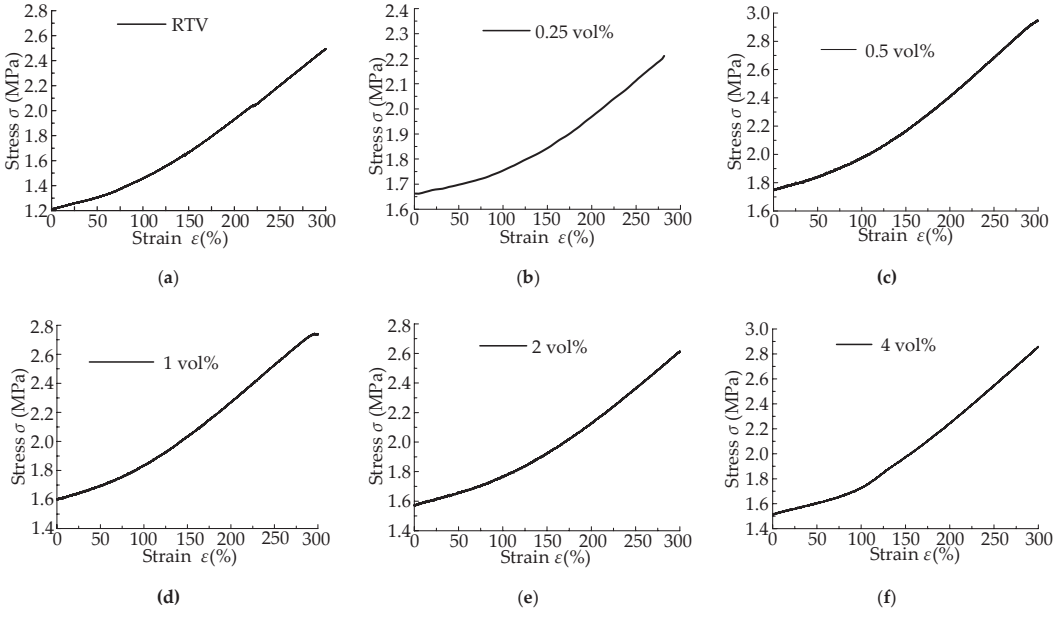

Figure 11. Stress–strain curve for the RTV-SWCNTs composites with different SWCNTs content. The content of the SWCNTs is: (**a**) 0 vol%; (**b**) 0.25 vol%; (**c**) 0.5 vol%; (**d**) 1 vol%; (**e**) 2 vol%; (**f**) 4 vol%.

Figure 12 shows the fitting curves for the composite materials under different SWC NT contents.

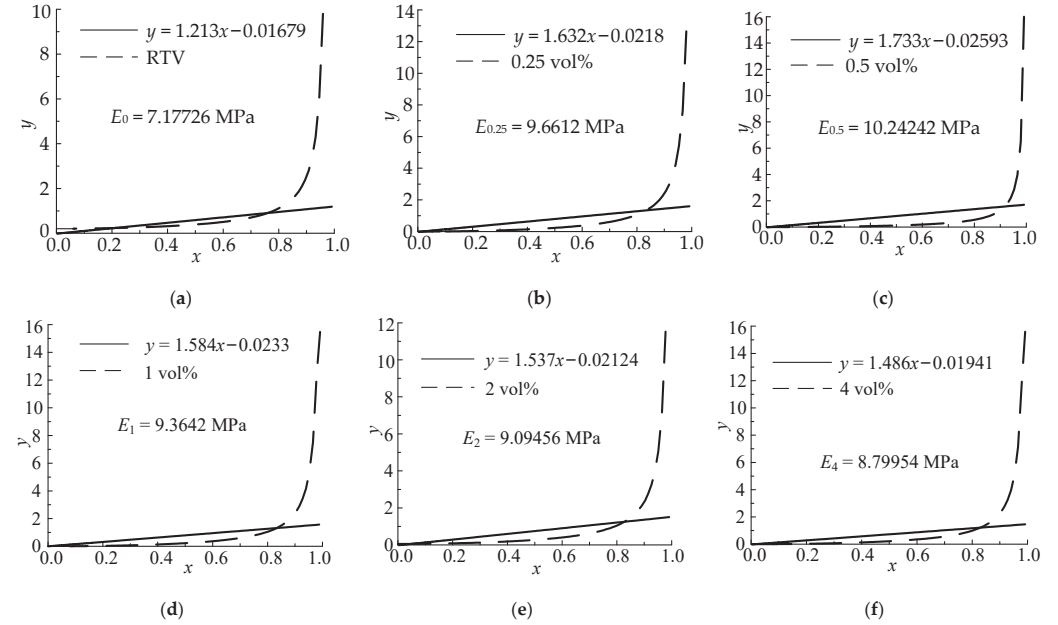

Figure 12. The fitting curve for the tensile experimental data on the composites with different SWCNTs content. The content of the SWCNTs is: (**a**) 0 vol%; (**b**) 0.25 vol%; (**c**) 0.5 vol%; (**d**) 1 vol%; (**e**) 2 vol%; (**f**) 4 vol%.

It can be seen that with the increase in the content of the SWCNTs, the elastic modulus first increases and then decreases. When the content of the SWCNTs is 0.5 vol%, the elastic modulus of the composite material reaches the maximum, which is 10.24242 MPa. And C_{10} = 1.733 MPa, C_{01} = −0.02593 MPa.

5.1.2. The Results of SEM Experiment on the Composite Materials

Under different SWCNT contents, the fracture morphology for each specimen is shown in Figure 13.

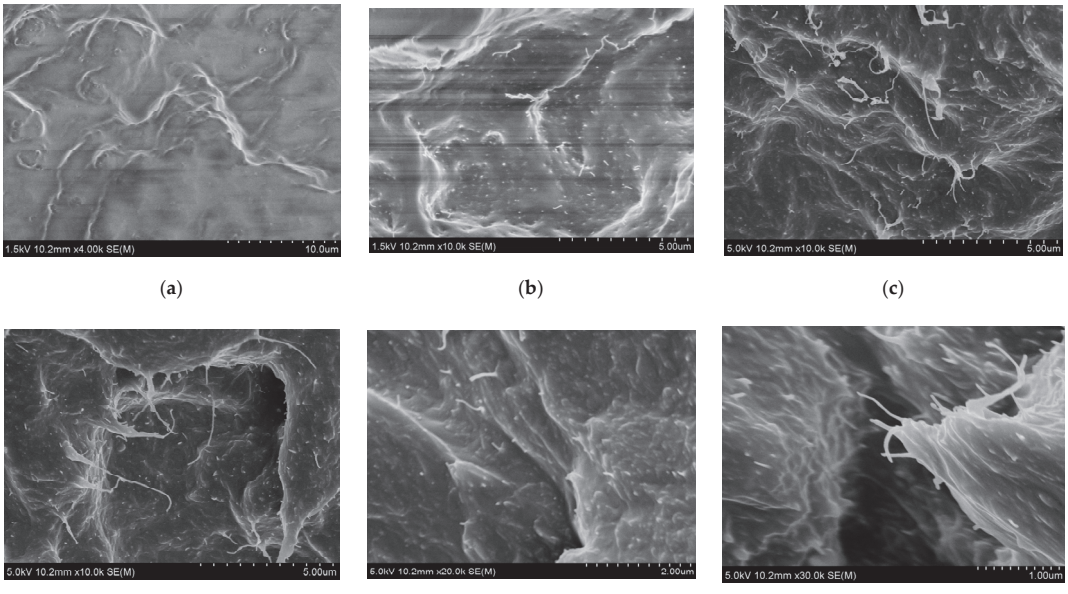

(**a**) (**b**) (**c**)

(**d**) (**e**) (**f**)

Figure 13. The fracture morphology for the specimens with different SWCNTs content under SEM. The content of the SWCNTs is: (**a**) 0 vol%; (**b**) 0.25 vol%; (**c**) 0.5 vol%; (**d**) 1 vol%; (**e**) 2 vol%; (**f**) 4 vol%.

In Figure 13a–c, when no SWCNTs are added to the matrix material, the fracture morphology is relatively smooth and has distinct folds, which is an obvious feature of a brittle fracture in the elastic material. As the content of the SWCNTs increases, the fracture morphology of the material gradually becomes rough and wrinkled, so the energy required in the stretching process increases, indicating that the tensile strength and elastic modulus of the material increase accordingly [32,33]. The surface roughness of the material in Figure 13d is similar to that in Figure 13c, but there are obvious pits on the surface. The pits are caused by the agglomeration of the SWCNTs, which indicates that the filling capacity of the SWCNTs has reached the supersaturated state. In Figure 13e,f, the pit phenomenon is more obvious, and the agglomeration is intensified, which indicates that the probability of CNTs agglomeration intensifies with the increase in the content.

Combined with the existing tensile experimental and SEM test data (the additional amount of the SWCNT is 0–4 vol%), when the content of the SWCNTs is 0.5 vol%, the mechanical properties of the RTV-SWCNTs composites are the best. Therefore, the RTV-SWCNTs composite material with the SWCNTs content of 0.5 vol% is used as the elastic layer material in the BHP.

5.2. Results from the BHP Bidirectional FSI Simulation

5.2.1. Simulation Results for the BHP Vibration with Different Elastic Layer Thicknesses

The curve for the radial acceleration at the middle node (point P) in the BHP with different thicknesses of the elastic layer is shown in Figure 14.

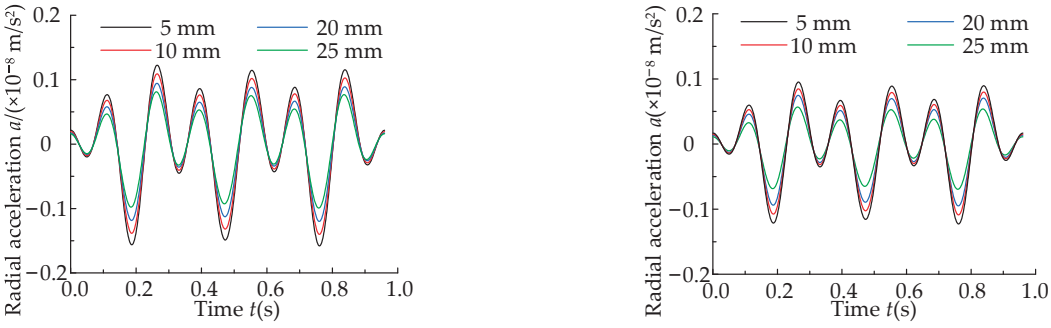

Figure 14. Radial acceleration at point P with different thicknesses of the elastic layer. (**a**) BHP with RTV as the elastic layer; (**b**) BHP with RTV-SWCNTs composite materials as the elastic layer.

As can be seen in Figure 14 that the amplitude of the radial acceleration in the BHP decreases with the increase in the thickness of the elastic layer.

Figure 15 shows the comparison curves for the radial acceleration at point P in the BHPs with RTV or SWCNTs added when the thickness of the elastic layer is the same.

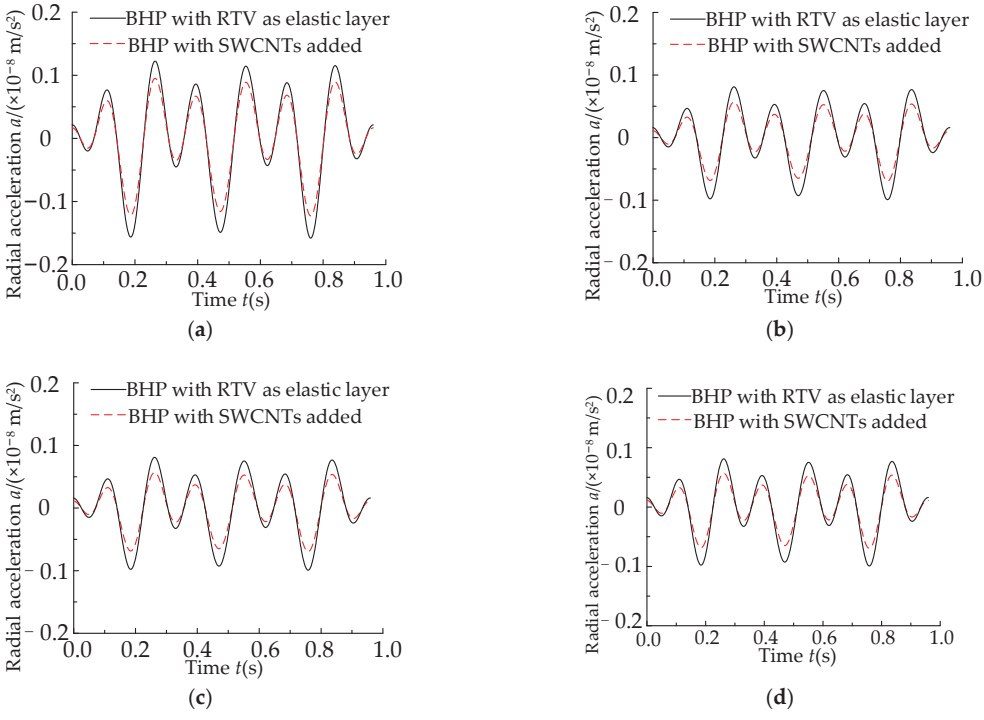

Figure 15. Radial acceleration at point P with different materials. The thickness of the elastic layer is (**a**) 5 mm; (**b**) 10 mm; (**c**) 20 mm; (**d**) 25 mm.

Figure 15 shows that when the thickness of the elastic layer is the same, the vibration acceleration in the three-layer BHP with SWCNTs added is lower than that of the double-layer BHP and the vibration absorption effect is better. Adding the SWCNTs to the elastic layer increases its tensile strength and the smooth inner wall of the pipeline can not only reduce the fluid resistance but also stabilize the flow.

The vibration reduction is 'the standard deviation of the radial acceleration of the BHP with RTV as the elastic layer minus the standard deviation of the radial acceleration of the BHP with RTV-SWCNTs composite material as the elastic layer'. The vibration reduction reflects the degree of vibration suppression in the BHP with the same elastic layer thickness and different materials, as shown in Table 6.

Table 6. The suppressive effect of the different thicknesses of the elastic layer on pipeline vibration.

Thickness (mm)	RTV	RTV-SWCNTs Composite Materials	Vibration Reduction (%)
	The Standard Deviation for the Vibration Acceleration		
5	7.58×10^{-10}	5.89×10^{-10}	22.3
10	6.73×10^{-10}	5.23×10^{-10}	22.3
20	5.775×10^{-10}	4.297×10^{-10}	25.6
25	4.82×10^{-10}	3.375×10^{-10}	29.98

It can be seen from Table 6 that the standard deviation for the radial acceleration in the three-layer BHP with SWCNTs added is significantly lower than that of the double-layer BHP with RTV as the elastic layer. And with the increase in the pipeline thickness, the suppressive effect of the vibration increases.

5.2.2. Simulation Results for BHP Vibration with Different Lengths of Pipeline

The curves for the radial acceleration at point P in the BHP with different lengths of the elastic layer are shown in Figure 16.

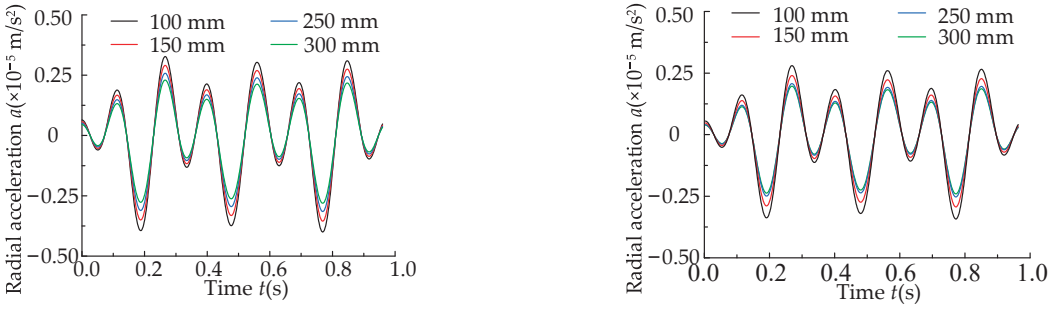

Figure 16. Radial acceleration at point P with different lengths of the elastic layer. (**a**) BHP with RTV as the elastic layer; (**b**) BHP with RTV-SWCNTs composite materials as the elastic layer.

In Figure 16, the amplitude of the radial acceleration in the BHP decreases with the increase in the pipeline length. In reference to Section 5.2.1, Figure A2 (in Appendix C) shows the radial acceleration curves for the BHPs with different elastic layer materials at P point when the pipe length is the same.

As shown in Figure A2, when the pipeline length is the same, the vibration acceleration in the three-layer BHP with SWCNTs added is lower than that of the double-layer BHP with RTV as the elastic layer, and the effect of the vibration absorption is better. The suppressive effect of the different lengths in the BHP on the vibration of the pipeline wall is shown in Table 7.

Table 7. The suppressive effect of the different lengths in the BHP on the vibration of the pipeline wall.

Length (mm)	RTV	RTV-SWCNTs Composite Materials	Vibration Reduction (%)
	The Standard Deviation for the Vibration Acceleration		
100	1.956×10^{-6}	1.675×10^{-6}	14.4
150	1.736×10^{-6}	1.435×10^{-6}	17.3
250	1.542×10^{-6}	1.237×10^{-6}	19.8
300	1.373×10^{-6}	1.176×10^{-6}	14.3

It can be seen that the standard deviation for the radial acceleration in the BHP with RTV-SWCNTs composite materials as the elastic layer is significantly lower than that of the BHP with RTV. And with the increase in the pipeline length, the suppressive effect of the vibration increases. Besides, when the length of the pipeline is 250 mm, the percentage of pulsation reduction in the pipeline is the largest and the effect of the vibration reduction is the best, which lays the foundation for further optimization in the design of the BHP.

5.3. Results from the BHP Vibration Experiment

5.3.1. Pulsation Absorption Experiment Results for the BHP with Different Thicknesses of Elastic Layer

The outlet flow pulsation curves for the different BHPs are shown in Figure 17.

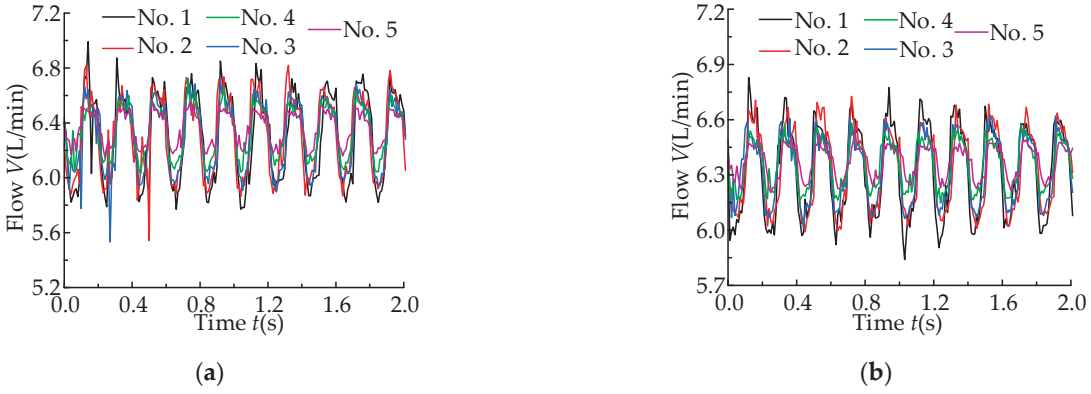

Figure 17. Effect of thickness of the elastic layer on flow pulsation. (**a**) BHP with RTV as the elastic layer; (**b**) BHP with RTV-SWCNTs composite materials as the elastic layer.

The amplitude of the flow pulsation at the outlet of the double-layer BHP with RTV as the elastic layer and the three-layer BHP with RTV-SWCNTs composite materials as the elastic layer decreases with the increase in the thickness of the elastic layer. This shows that the elastic materials (RTV and RTV-SWCNTs composite materials) have an absorption effect on the flow pulsation at the outlet of the hydraulic pump. And with the increase in the thickness of the pipeline, the absorption effect of the flow pulsation increases.

The comparison curves for the flow pulsation at the outlet of the double-layer BHP with RTV as the elastic layer and the three-layer BHP with RTV-SWCNTs composite materials as the elastic layer under the same thickness of the elastic layer are shown in Figure 18.

Figure 18 shows that the amplitude of the flow pulsation in the three-layer BHP with RTV-SWCNTs composite materials as the elastic layer is significantly lower than that of the double-layer BHP with RTV as the elastic layer.

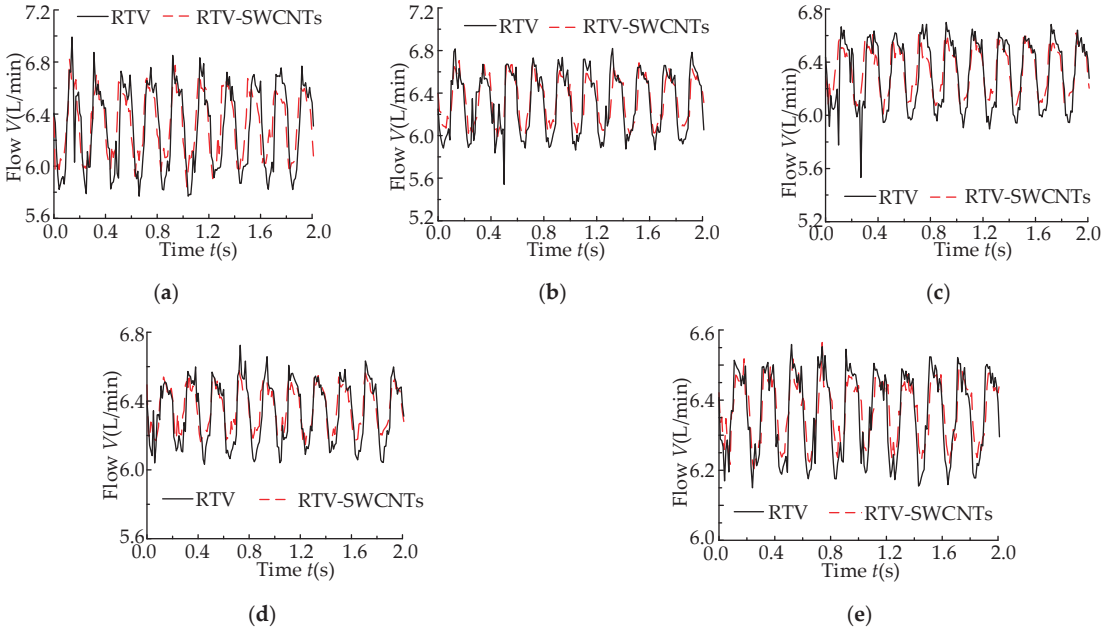

Figure 18. Effect of different elastic layer materials with the same thickness on flow pulsation. The thickness of the elastic layer is: (**a**) 5 mm; (**b**) 10 mm; (**c**) 15 mm; (**d**) 20 mm; (**e**) 25 mm.

The absorption effect of the flow pulsation in the BHPs with different thicknesses of the elastic layer is shown in Table 8. The pulsation reduction is 'the standard deviation of flow pulsation at the outlet of BHP with RTV as the elastic layer subtracts the standard deviation of flow pulsation at the outlet of BHP with RTV-SWCNTs as the composite elastic layer'. The pulsation reduction reflects the flow pulsation absorption effect for the BHP with the same pipeline thickness and different elastic layer materials.

Table 8. The absorption effect of the flow pulsation for the BHP with different thicknesses of the elastic layer.

No.	Thickness (mm)	RTV	RTV-SWCNTs Composite Materials	Pulsation Reduction (%)
		The Standard Deviation for the Flow Pulsation		
1	5	0.319	0.248	22.3
2	10	0.291	0.215	26.1
3	15	0.253	0.177	30.04
4	20	0.1802	0.128	28.97
5	25	0.1197	0.0872	27.15

The standard deviation for the flow pulsation in the three-layer BHP with SWCNTs added is significantly lower than that of the double-layer BHP with RTV as the elastic layer. With the increase in the thickness of the pipeline, the standard deviation for the flow pulsation at the outlet of the pipeline decreases, and the effect of the pulsation absorption increases. When the thickness of the elastic layer is 15 mm, the percentage of pulsation reduction is the largest and the absorption effect of the flow pulsation is the best, which lays the experimental foundation for further optimization of BHPs.

5.3.2. Pulsation Absorption Experiment Results for the BHP with Different Lengths of Pipeline

The flow pulsation curves for the different BHPs are shown in Figure 19. The amplitude of the flow pulsation at the outlet of both the double-layer BHP with RTV as the elastic layer and the three-layer BHP with RTV-SWCNTs composite materials as the elastic layer decreases with the increase in the length of the pipeline. In the limited length range of the experiment, the capacity of the BHP to absorb flow pulsation increases with the increase in its length.

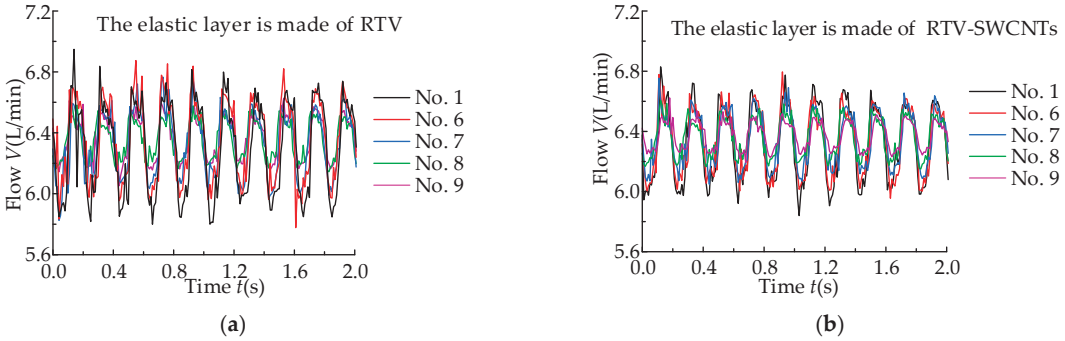

Figure 19. Flow pulsation curve for the BHP outlet. (**a**) RTV as the elastic layer; (**b**) RTV-SWCNTs composite as the elastic layer.

In reference to Section 5.3.1, the comparison curves for the flow pulsation at the outlet of the double-layer BHP with RTV or RTV-SWCNTs composite materials as the elastic layer under the same length of pipeline are shown in Figure A3 (Appendix C).

It can be seen from Figure A3 that the amplitude of the flow pulsation in the three-layer BHP with RTV-SWCNTs composite materials as the elastic layer is significantly lower than that of the double-layer BHP with RTV as the elastic layer. The absorption effect of the flow pulsation in the BHPs with different lengths is shown in Table 9.

Table 9. The absorption effect of flow pulsation in the BHPs with different lengths of pipeline.

No.	Length (mm)	RTV	RTV-SWCNTs Composite Materials	Pulsation Reduction (%)
		The Standard Deviation for Flow Pulsation		
1	130	0.319	0.248	22.3
6	180	0.301	0.216	28.2
7	230	0.2702	0.1779	34.16
8	280	0.1824	0.1296	28.9
9	330	0.128	0.0913	28.7

The standard deviation for the flow pulsation in the three-layer BHP with SWCNTs added is significantly lower than that of the double-layer BHP with RTV as the elastic layer. With the increase in the length of the pipeline, the standard deviation for the flow pulsation at the outlet of the pipeline decreases, and the effect of the pulsation absorption increases. When the length of the pipeline is 230 mm, the percentage of pulsation reduction is the largest and the absorption effect of the flow pulsation is the best, which lays the experimental foundation for further optimization of BHPs.

5.3.3. Vibration Experiment Results for the BHP with Different Elastic Layer Thicknesses

The radial acceleration amplitude for the pipe wall at the middle node (point P) in each BHP is shown in Figure 20.

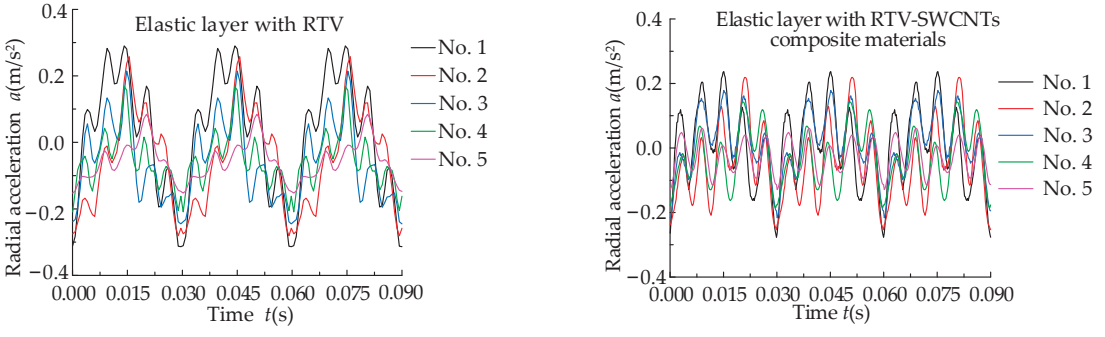

Figure 20. Effect of elastic layer thickness on the radial acceleration at point P.(**a**) BHP with RTV as the elastic layer; (**b**) BHP with RTV-SWCNTs composite materials as the elastic layer.

The radial acceleration amplitude at point P in the two-layer BHP with RTV as the elastic layer and the three-layer BHP with RTV-SWCNTs composite as the elastic layer decreases as the thickness of the elastic layer increases. This indicates that elastic materials (RTV or RTV-SWCNTs composites) can suppress pipeline vibration by absorbing the flow pulsation. With the increase in the elastic layer thickness, the effect of the vibration suppression is more obvious.

In reference to Section 5.2.1, Figure A4 (Appendix C) compares the amplitude of the radial acceleration at point P in the BHPs with RTV or RTV-SWCNTs composite as the elastic layer when the thickness of the elastic layer is the same.

In Figure A4, it can be seen that the radial acceleration at point P in the three-layer BHP with RTV-SWCNTs composite material as the elastic layer is significantly lower than that of double-layer BHP with RTV as the elastic layer. The data on the vibration suppression effect in the BHP with different thicknesses of the elastic layer is shown in Table 10.

Table 10. Suppression effect in BHPs with different thicknesses of the elastic layer on pipe vibration.

No.	Thickness (mm)	RTV	RTV-SWCNTs Composite Materials	Vibration Reduction(%)
		The Standard Deviation for Radial Acceleration		
1	5	0.179	0.162	9.5
2	10	0.143	0.106	25.9
3	15	0.1202	0.0758	36.9
4	20	0.098	0.0689	29.7
5	25	0.0892	0.0689	22.8

It can be seen that the standard deviation for the radial acceleration in the three-layer BHP with SWCNTs is significantly lower than that of double-layer BHP with RTV as the elastic layer. As the thickness increases, the standard deviation for the radial acceleration decreases, and the effect of the pulsation absorption increases. When the thickness of the elastic layer is 15 mm, the percentage of the pulsation reduction is the largest, and the vibration suppression effect in the BHP is the best. This conclusion lays the experimental foundation for the further optimization of BHPs.

5.3.4. Vibration Experiment Results for the BHP with Different Lengths of Pipeline

The radial acceleration amplitude for the pipe wall at point P for each BHP is shown in Figure 21.

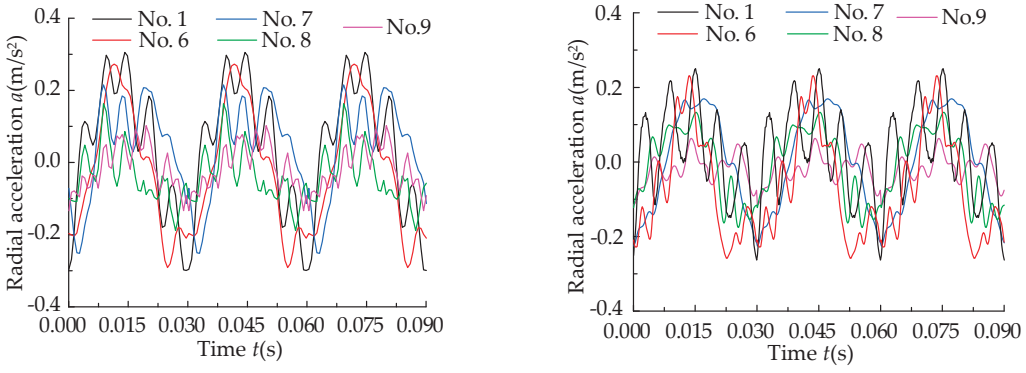

Figure 21. Effect of the length of the elastic layer on the radial acceleration at point P. (**a**) RTV as the elastic layer; (**b**) RTV-SWCNTs composite materials as the elastic layer.

The radial acceleration amplitude in the double-layer BHP with RTV as the elastic layer and the three-layer BHP with RTV-SWCNTs composite material as the elastic layer both decreased with the increase in the pipeline length. Moreover, as the length increases, the vibration suppression effect in the BHP on the pipeline system increases.

In reference to Section 5.2.1, Figure A5 (in Appendix C) compares the radial acceleration amplitude in the BHP with the same pipeline length and different elastic layers.

As shown in Figure A5, the acceleration amplitude in the three-layer BHP with RTV-SWCNTs composite as the elastic layer is significantly lower than that of the double-layer BHP with RTV as the elastic layer.

The vibration suppression effect of the BHPs with different lengths of pipeline is shown in Table 11.

Table 11. Suppression effect in the BHPs with different lengths of pipeline on pipe vibration.

No.	Length (mm)	RTV	RTV-SWCNTs Composite Materials	Vibration Reduction (%)
		The Standard Deviation for Radial Acceleration		
1	130	0.179	0.174	2.8
6	180	0.138	0.132	4.3
7	230	0.1202	0.102	15.14
8	280	0.108	0.0615	43.1
9	330	0.0712	0.03697	48.1

The standard deviation for the radial acceleration in the three-layer BHP with SWCNTs added is significantly lower than that of the double-layer BHP with RTV as the elastic layer. As the length increases, the standard deviation for the radial acceleration decreases, and the effect of the pulsation absorption increases. Moreover, when the length is 330 mm, the percentage of the pulsation reduction is the largest, and the vibration suppression effect in the BHP is the best. This lays a certain experimental foundation for further optimization of BHPs.

6. Conclusions

In this paper, based on the vibration control in the double-layer BHP to the hydraulic pump port, the BHP with a three-layer structure is made by adding the SWCNTs. The simulation analysis and experiments are carried out, and the results are compared with those for the double-layer BHPs with RTV as the elastic layer, thus the following conclusions are obtained:

1. The RTV-SWCNTs composite is prepared by surface modification of the SWCNTs with noncovalent functionalization. And through the tensile test and SEM experiment, it is found that the CNTs are saturated in the composites when the content of the CNTs is 0.5 vol%~1 vol%, and the mechanical properties of the composites are better. When the content of the CNTs exceeds 1 vol%, the CNTs will agglomerate, which will reduce the mechanical properties of the composite. By comparing the experimental data, the mechanical properties of the RTV-SWCNTs composites are the best when the content of the CNTs is 0.5 vol%.
2. Based on the previously established BHP dynamic model, considering the influence of friction coupling, the dynamic model of BHP is modified. The response curve for the BHP in the frequency domain is obtained by solving the dynamic model with MATLAB software, and the modal test verified the correctness of the modified model.
3. The BHP with nanomaterials added is prepared, and the effect of the BHP on absorbing the flow pulsation and inhibiting pipeline vibration is verified through simulation analysis and experiments. Compared with the previous test data, the effect of the BHP with nanomaterials added on inhibiting pipeline system vibration is more obvious than that of the double-layer BHP with RTV as the elastic layer material. The effect increases with the increasing thickness of the elastic layer and increases with the growing length of the BHP.
4. This paper provides new theoretical and technical support for further design optimization of BHPs and the engineering application of vibration suppression.

In the following research work, we will conduct further research on the BHP. In this paper, only THF is used as a dispersant to disperse SWCNTs in RTV. We will explore better dispersion methods and matrix materials to improve the material properties in the BHP's elastic layer. The thickness and length of the BHP's elastic layer will be further optimized to find the optimum thickness and length for absorbing pipeline vibration and flow pulsation in the pump outlet pipeline.

Author Contributions: Conceptualization, C.G. and L.Q.; methodology, J.G.; software, J.G.; validation, J.G. and L.Q.; formal analysis, C.G.; investigation, J.G.; resources, L.Q.; data curation, J.Y.; writing—original draft preparation, J.G.; writing—review and editing, J.G.; visualization, J.Y.; supervision, C.G. and L.Q.; project administration, C.G. and L.Q.; funding acquisition, L.Q. All authors have read and agreed to the published version of the manuscript.

Funding: This research was funded by the National Natural Science Foundation of China, grant numbers (51775477 and 51505410).

Institutional Review Board Statement: Not applicable.

Informed Consent Statement: Not applicable.

Data Availability Statement: The data presented in this study are available on request from the corresponding author.

Acknowledgments: The authors gratefully acknowledge the financial support from the National Natural Science Foundation of China and the testing environment provided by Hebei Provincial Key Laboratory of Heavy Machinery Fluid Power Transmission and Control. The authors also thank China Scholarship Council for supporting the two-year research experience of Lingxiao Quan at the RWTH Aachen University and Washington State University.

Conflicts of Interest: The authors declare no conflict of interest.

Appendix A. Nomenclature and Numerical Values for the Parameters in the Theoretical and Simulation Models

Table A1. Structural parameters for the BHP.

Parameter Name	Value	Parameter Name	Value
Length of the pipeline (L)	0.33 m	The bulk modulus of stainless steel (K)	1.95 GPa
Inside diameter of the pipeline (r)	0.005 m	Young's modulus of stainless steel (E)	213 GPa
The thickness of the elastic layer (e_r)	0.005 m	Shear modulus of stainless steel (G)	81.9 GPa
The thickness of the stainless steel layer (e_t)	0.002 m	The density of elastic material (ρ_r)	1150 kg/m^3
Poisson's ratio for elastic material (v_r)	0.5	Stainless steel density (ρ_t)	7800 kg/m^3
Poisson's ratio for stainless steel (v_t)	0.3	Fluid viscosity (v)	10^{-5} m^2/s
Elastic material parameters C_{10}	−0.02593 MPa	Plug quality (m_t)	0.6 kg
Elastic material parameters C_{01}	1.733 MPa		

Appendix B. The Specification for the Experimental Apparatus and Measurement System

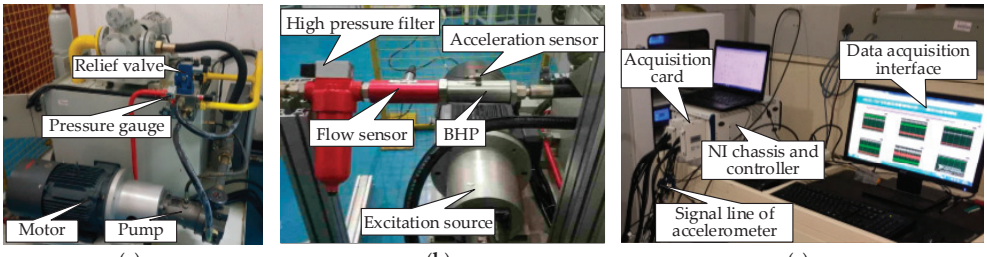

(**a**) (**b**) (**c**)

Figure A1. Installation of the vibration measurement pipeline system. (**a**) Hydraulic pump station; (**b**) installation of the BHP vibration measurement system; (**c**) measurement and control system.

Appendix C. Part of the Simulation Analysis and Experimental Data Results

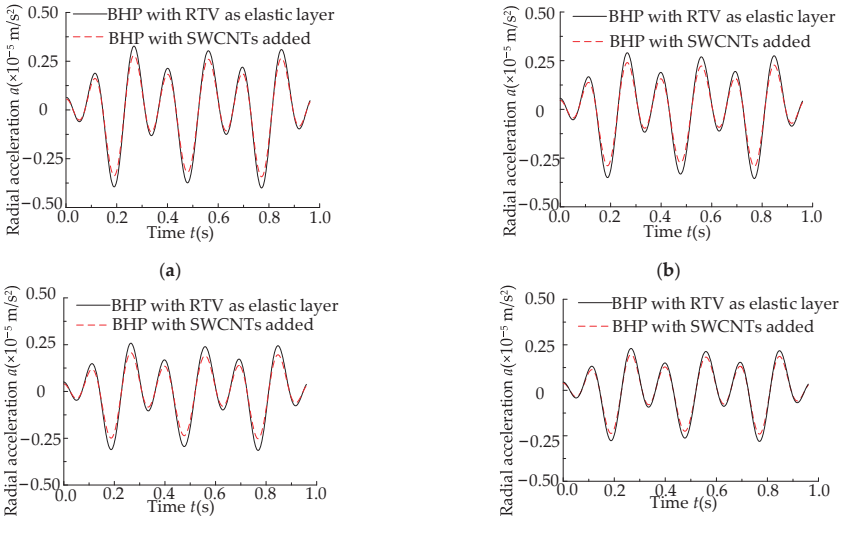

(**a**) (**b**)

(**c**) (**d**)

Figure A2. Radial acceleration at point P with different materials in the elastic layer. The length of the pipeline is: (**a**) 100 mm; (**b**) 150 mm; (**c**) 250 mm; (**d**) 300 mm.

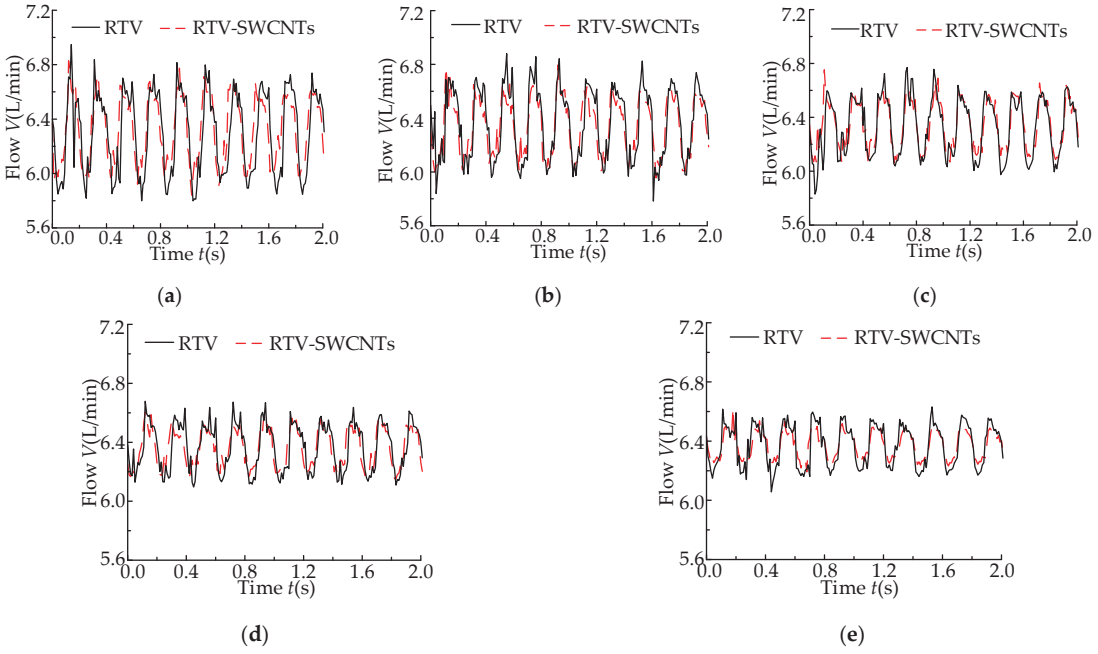

Figure A3. Effect of different materials on flow pulsation with the same length of the elastic layer. The length of pipeline is: (**a**) 130 mm; (**b**) 180 mm; (**c**) 230 mm; (**d**) 280 mm; (**e**) 330 mm.

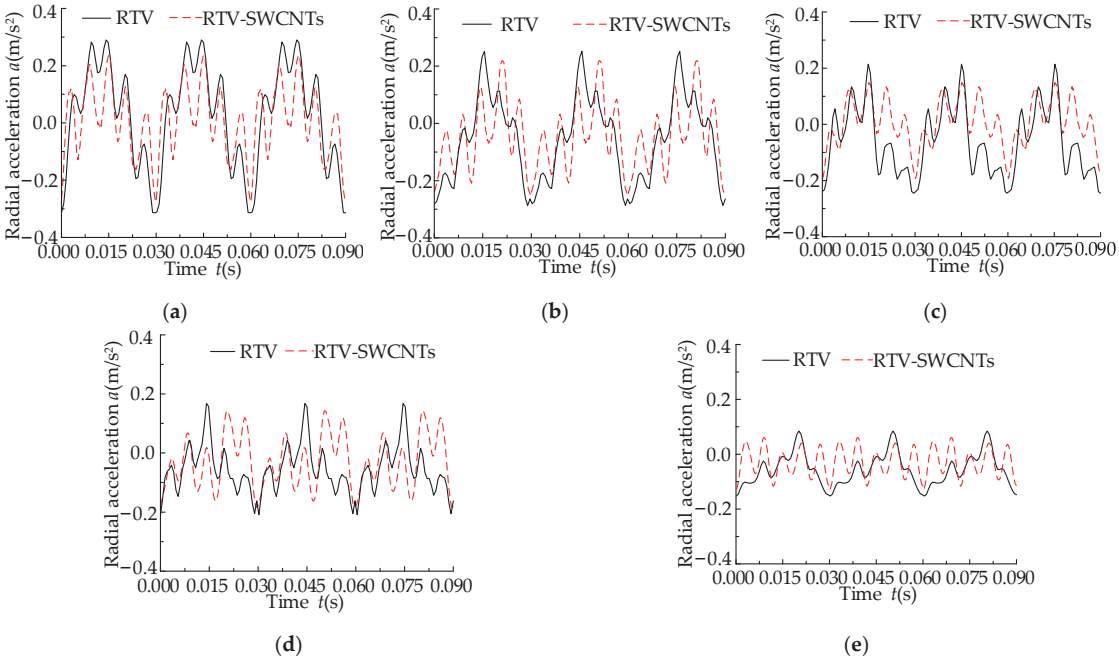

Figure A4. Influence of different materials on radial acceleration with the same thickness of the elastic layer. The thickness of the elastic layer is: (**a**) 5 mm; (**b**) 10 mm; (**c**) 15 mm; (**d**) 20 mm; (**e**) 25 mm.

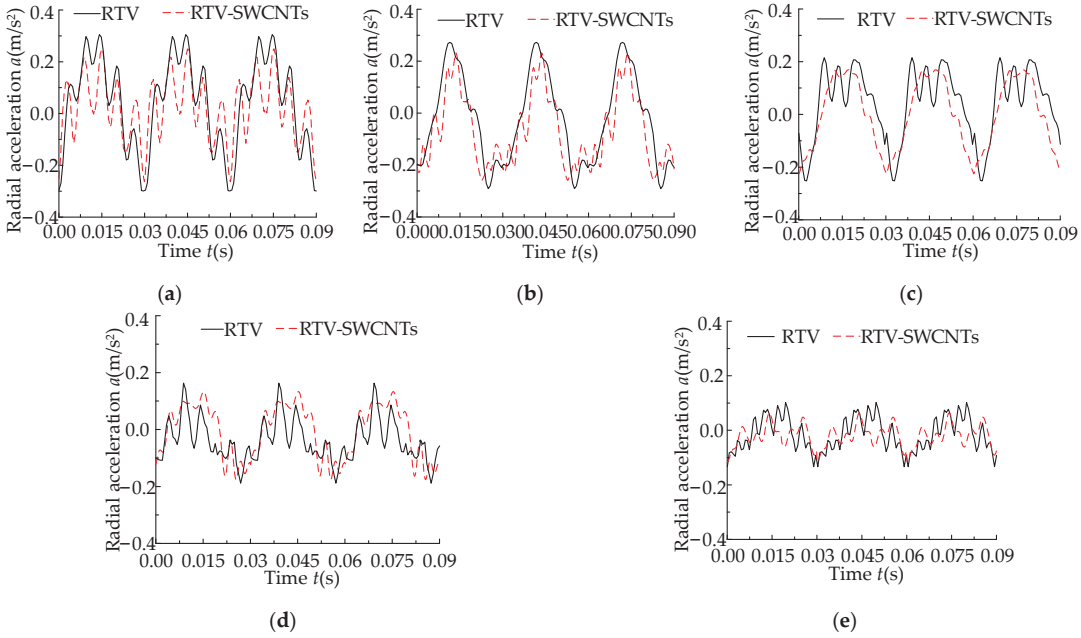

Figure A5. Effect of the elastic layer material on radial acceleration at the middle point in the pipe wall. The length of pipeline is: (**a**) 130 mm; (**b**) 180 mm; (**c**) 230 mm; (**d**) 280 mm; (**e**) 330 mm.

References

1. Zhang, L.P. *Hydraulic Transmission System and Design*; Chemical Industry Press: Beijing, China, 2005.
2. Wang, Z.L. *High-Pressure Hydraulic Energy System of Aircraft*; Beijing University of Aeronautics and Astronautics Press: Beijing, China, 2004.
3. Gao, F. Investigation into the Vibration Characteristic of the Pump and Connected Pipeline in the Aircraft Hydraulic System. Ph.D. Thesis, Zhejiang University, Hangzhou, China, April 2013.
4. Zang, J.; Xiao, R.H.; Zhang, Y.W.; Chen, L.Q. A Novel Way for Vibration Control of FGM Fluid-Conveying Pipes Via NiTiNOL-Steel Wire Rope. *Appl. Math. Mech. Engl. Ed.* **2023**, *44*, 877–896. [CrossRef]
5. Jiao, G.Y. Design of a Magnetic Interaction-Based Vibration Absorber for Continuous Beam. *Shock Vib.* **2020**, *2020*, 6384308. [CrossRef]
6. Chirathalattu, T.A.; Santhosh, B.; Bose, C.; Philip, R.; Balaram, B. Passive Suppression of Vortex-Induced Vibrations Using a Nonlinear Energy Sink—Numerical and Analytical Perspective. *Mech. Syst. Signal Process.* **2023**, *182*, 109556. [CrossRef]
7. Shu, C.L.; Yan, M.; Wang, C.; Sun, Y.; Du, F.; Chen, Q.D. Research on Typical Pipeline Design Method of Power Transmission Auxiliary System based on Vibration Control. In Proceedings of the 2022 8th International Forum on Manufacturing Technology and Engineering Materials (IFEMMT 2022), Chongqing, China, 14–16 October 2022. [CrossRef]
8. Shemshadi, M.; Karimi, M.; Veysi, F. A Simple Method to Design and Analyze Dynamic Vibration Absorber of Pipeline Structure Using Dimensional Analysis. *Shock Vib.* **2020**, *2020*, 2478371. [CrossRef]
9. Quan, L.X.; Zhang, Q.W.; Li, C.C.; Sheng, S.W. Sensitivity Analysis and Optimization for Support Parameter of Aviation Hydraulic Pipeline. *Chin. Hydraul. Pneum.* **2015**, *8*, 95–99.
10. Guan, C.B.; Jiao, Z.X.; He, S.Z. Theoretical Study of Flow Ripple for an Aviation Axial-Piston Pump with Damping Holes in the Valve Plate. *Chin. J. Aeronaut.* **2019**, *27*, 169–181. [CrossRef]
11. Cheer, J.; Daley, S. Broadband Active Control of Noise and Vibration in a Fluid-Filled Pipeline Using an Array of Non-Intrusive Structural Actuators. In Proceedings of the 44th International Congress on Noise Control Engineering, San Francisco, CA, USA, 8–11 August 2015. Available online: http://eprints.soton.ac.uk/id/eprint/380527 (accessed on 11 August 2015).
12. Zhang, Y.; Liu, X.; Rong, W.; Gao, P.; Yu, T.; Han, H.; Xu, L. Vibration and Damping Analysis of Pipeline System Based on Partially Piezoelectric Active Constrained Layer Damping Treatment. *Materials* **2021**, *14*, 1209. [CrossRef]
13. Zhang, Y.; Gao, P.; Liu, X.; Yu, T.; Huang, Z. Fluid-Induced Vibration of a Hydraulic Pipeline with Piezoelectric Active Constrained Layer-Damping Materials. *Coatings* **2021**, *11*, 757. [CrossRef]
14. Arenas, J.P.; Castano, J.L.; Troncoso, L.; Auad, M.L. Thermoplastic Polyurethane/Laponite Nanocomposite for Reducing Impact Sound in a Floating Floor. *Appl. Acoust.* **2019**, *155*, 401–406. [CrossRef]

15. Lubecki, M.; Stosiak, M.; Bocian, M.; Urbanowicz, K. Analysis of Selected Dynamic Properties of the Composite Hydraulic Microhose. *Eng. Fail. Anal.* **2021**, *125*, 105431. [CrossRef]
16. Mohammad, R.; Fred, N.; Labrosse, M.R. Processing, Manufacturing, and Characterization of Vibration Damping in Epoxy Composites Modified with Graphene Nanoplatelets. *Polym. Compos.* **2019**, *40*, 3914–3922. [CrossRef]
17. Swain, A.; Roy, T. Viscoelastic Modeling and vibration damping Characteristics of Hybrid CNTs-CFRP Composite Shell Structures. *Acta Mech.* **2018**, *229*, 1321–1352. [CrossRef]
18. Swain, A.; Roy, T. Viscoelastic Material Damping Characteristics of CNTs Based Functionally Graded Composite Shell Structures. *Proc. Inst. Mech. Eng. Part L-J. Mater. Des. Appl.* **2019**, *238*, 1510–1541. [CrossRef]
19. Pan, Y.; Liu, N.; Liu, A.; Chen, M.; Xu, W. Research on Microstructure and Mechanical Properties of Single-walled Carbon Nanotubes/7075 Composites. *Hot Work. Technol.* **2022**, *51*, 57–61. [CrossRef]
20. Quan, L.X.; Gao, J.; Guo, C.H.; Wu, S.D.; Yao, J.C. Dynamic Model and Response Analysis of Bionic Hydraulic Pipeline Based on Vascular Physiological Structure. *IEEE Access* **2019**, *7*, 67564–67575. [CrossRef]
21. Wang, J.W.; Zhang, J.; Fan, T.X. Processing Surface Treatment of Carbon Nanotubes and Its Applications to Copper Matrix Composites. *Mater. Rep.* **2018**, *32*, 2932–2939. [CrossRef]
22. Giambastiani, G.; Cicchi, S.; Giannasi, A.; Luconi, L.; Rossin, A.; Mercuri, F.; Fornasiero, P. Functionalization of Multiwalled Carbon Nanotubes with Cyclic Nitrones for Materials and Composites: Addressing the Role of CNT Sidewall Defects. *Chem. Mater.* **2011**, *23*, 1923–1938. [CrossRef]
23. Zydziak, N.; Hübner, C.; Bruns, M.; Barner, K.C. One-Step Functionalization of Single-Walled Carbon Nanotubes (SWCNTs) with Cyclopentadienyl-Capped Macromolecules via Diels-Alder Chemistry. *Macromolecules* **2011**, *44*, 3374–3380. [CrossRef]
24. Coleman, K.S.; Bailey, S.R.; Fogden, S.; Green, M.L.H. Functionalization of Single-Walled Carbon Nanotubes via the Bingel Reaction. *J. Am. Chem. Soc.* **2003**, *125*, 8722–8723. [CrossRef]
25. Huang, J.L.; Xie, G.J.; Liu, Z.W. Finite Element Analysis of Hyperelastic Rubber Materials Based on Mooney-Rivlin and Yeoh Models. *China Rubber Plast. Technol. Equip.* **2008**, *34*, 22–26. [CrossRef]
26. Freaktey, P.K.; Payne, A.R. *Theory and Practice of Engineering with Rubber*; Applied Science Publishers Ltd.: London, UK, 1978.
27. Wiggert, D.C.; Hatfield, F.J.; Stuckenbruck, S. Analysis of Liquid and Structural Transients in Piping by the Method of Characteristics. *J. Fluids Eng.* **1987**, *109*, 161–165. [CrossRef]
28. Zhang, Z.R.; Zhang, X.W. Numerical Manifold Method for Two Dimensional Steady Incompressible Viscous Flow N-S Equation. *Chin. J. Comput. Mech.* **2019**, *27*, 415–421.
29. Zielke, W. Frequency-Dependent Friction in Transient Pipe Flow. *Trans. ASME J. Basic Eng.* **1968**, *91*, 109–115. [CrossRef]
30. Brunone, B.; Golia, U.; Greco, M. Modeling of Fast Transients by Numerical Method. International Meeting on Hydraulic Transient and Water Column Separation. In *Proceedings of International Conference on Hydraulic Transients with Water Column Separation, Valencia, Spain, 4–6 September 1991*; Cabrera, E., Fanelli, M.A., Eds.; IAHR-Group: Madrid, Spain, 1991; pp. 273–280.
31. Vardy, A.E.; Brown, J.M.B. Transient Turbulent Friction in Smooth Pipe Flows. *J. Sound Vib.* **2003**, *259*, 1011–1036. [CrossRef]
32. Deng, B.C.; Li, J.S. *Rubber Plastic Blending Modification*; China Petrochemical Press: Beijing, China, 1996.
33. Yang, W.S.; Biamino, S.; Padovano, E.; Fuso, L.; Pavese, M.; Marchisio, S.; Vasquez, D.; Bolivar, C.V.; Fino, P.; Badini, C. Microstructure and mechanical properties of short carbon fibre/SiC multilayer composites prepared by tape casting. *Compos. Sci. Technol.* **2012**, 675–680. [CrossRef]

applied sciences

MDPI

Article

Performance Comparison of Traction Synchronous Motors with Ferrite Magnets for a Subway Train: Reluctance versus Homopolar Variants

Vladimir Dmitrievskii, Vadim Kazakbaev and Vladimir Prakht *

Department of Electrical Engineering, Ural Federal University, 620002 Yekaterinburg, Russia
* Correspondence: va.prakht@urfu.ru; Tel.: +7-909-028-49-25

Abstract: Due to the high cost and the predicted shortage of rare earth elements in the near future, the task of developing energy-efficient electric machines without rare earth magnets is of great importance. This article presents a comparative analysis of optimized designs of a ferrite-assisted synchronous reluctance machine (FaSynRM) and a ferrite-assisted synchronous homopolar machine (FaSHM) in a 370-kW subway train drive. The objectives of optimizing these traction machines are to reduce their losses, maximum armature current, and torque ripple. The optimization considers the characteristics of the machines in the subway train moving cycle. The problem of the risk of irreversible demagnetization of ferrites in the FaSynRM and FaSHM is also considered. To reduce the computational burden, the Nelder-Mead method is used for the optimization. It is shown that the FaSHM demonstrates better field weakening capability, which can reduce the maximum current, power, and cost of the inverter power modules. At the same time, the FaSynRM requires less permanent magnet mass for the same torque density and is more resistant to irreversible demagnetization, which can reduce costs and improve the reliability of the electric machine.

Keywords: electric machine parameter optimization; energy-efficient subway trains; extended constant power speed range; ferrite magnet electric machines; finite element analysis of electric machines; multi-objective optimization of electric machines; Nelder-Mead method; synchronous homopolar machine; synchronous motor field excitation; synchronous reluctance machine; traction motor; urban rail transportation

Citation: Dmitrievskii, V.; Kazakbaev, V.; Prakht, V. Performance Comparison of Traction Synchronous Motors with Ferrite Magnets for a Subway Train: Reluctance versus Homopolar Variants. *Appl. Sci.* **2023**, *13*, 9988. https://doi.org/10.3390/app13179988

Academic Editors: Loránd Szabó and Feng Chai

Received: 14 August 2023
Revised: 31 August 2023
Accepted: 2 September 2023
Published: 4 September 2023

1. Introduction

1.1. Disadvantages of Induction Motors and Motors with Rare Earth Magnets

At present, most traction drives, including those of trains, trams, subways, and mining dump trucks, use induction motors (IM). However, traction drives with IMs have the following disadvantages:

(1) Large loss and heating in the rotor [1,2], which can lead to unacceptably high temperatures of the rotor, shaft, and bearings, even despite the liquid cooling of the rotor [3];
(2) Continuous torque capability is significantly worse than permanent magnet synchronous motors (PMSM) [4];
(3) Higher inverter power rating with a required constant power speed range (CPSR) over 3:1 [5,6]. For example, a study [5] presents a traction drive based on an IM with a mechanical power of 50 kW and a CPSR of 3.5:1, and the power rating of the traction inverter is 125 kVA. Study [6] presents a traction drive based on an IM with a mechanical power of 50 kW and a CPSR of 4:1, and the power rating of the traction inverter is 125 kVA.

To overcome these disadvantages, rare earth permanent magnet synchronous motors (PMSM) are used, which have a larger specific torque, lower loss, and a higher power factor [7]. However, PMSMs have the following disadvantages:

(1) The production of PMSMs necessitates costly rare-earth magnets, which experience significant price fluctuations within a short span of a year or two. This variability arises due to a limited pool of magnet suppliers in the global market [8–10];
(2) In the near future, a shortage of materials for the production of rare earth magnets is predicted due to the rapid growth in the production of electric vehicles and wind turbines, which very often use rare earth permanent magnets [11];
(3) Rare-earth element extraction has an adverse environmental impact [12];
(4) The demagnetization of rare-earth magnets can occur in high-power density PMSMs due to the presence of strong magnetic fields and high temperatures;
(5) The task of maintaining high efficiency at speeds near the maximum becomes challenging when aiming for a wide constant power speed range, primarily due to increased copper loss that occurs in the field weakening mode [13];
(6) Furthermore, in electrical power applications such as subway and railway trains, the rotational motion of PMSM induces a significant uncontrolled electromotive force (EMF) in the winding. This situation presents a significant risk of fire in the event of an emergency short circuit. Given the high inertia of the trains, which makes them unable to stop in time in such critical situations, it is recommended to refrain from using the PMSM in this application.

Due to the disadvantages of IM and PMSM, the development of synchronous motors for the subway without rare earth magnets becomes relevant.

The utilization of ferrite magnets proves advantageous due to their significantly lower cost compared to rare-earth magnets and their widespread production across numerous countries worldwide [14,15].

In addition, ferrite magnets have no losses due to eddy currents and high-temperature strength [14,16]. A challenge of using ferrites in motor design is their low coercive force [14,17]. For this reason, when optimizing motors with ferrite magnets, special attention must be paid to limiting irreversible demagnetization.

1.2. Literature Overview on the Use of Ferrite-Assisted Synchronous Reluctance Motors in Traction Drives

Magnet-free synchronous reluctance motors (SynRMs) have lower losses than induction motors. However, in electric vehicles that require a wide CPSR, SynRMs have a reduced inverter utilization factor, which significantly increases the power rating and cost of the inverter power modules [6]. This drawback can be overcome, as well as the dimensions of the motor can be reduced by adding inexpensive ferrite magnets to the rotor [14]. Ferrite-assisted SynRMs (FaSynRMs) with high rotor magnetic anisotropy have proven themselves in pumping applications in which a wide CPSR is not required [18–20]. Moreover, FaSynRM is also an alternative to IPMSM in electric vehicle applications, with comparable torque capability, lower permanent magnet cost, and better field-weakening capability [21,22].

For example, in [21], the characteristics of PMSM and FaSynRM are theoretically compared in a Toyota Prius 2010 drive with a rated power of 60 kW and CPSR of 3.5:1. It is concluded that the FaSynRM has characteristics similar to the original V-shaped interior PMSM with the same overall dimensions, while the cost of its active materials is much lower, and the maximum operating temperature of the rotor is much higher. In [22], a theoretical comparison is made between V-shape rare-earth assisted SynRM and FaSynRM for a BMW i3 2016 drive with a rated power of 60 kW and CPSR of 3:1. It is shown that the use of ferrite magnets makes it possible to obtain lower peak mechanical stress, better field-weakening capability, higher peak efficiency, and comparable efficiency over the operating range.

It can be concluded that quite a lot of articles are devoted to the analysis of FaSynRM characteristics in light passenger vehicles. However, studies on optimizing FaSynRM design for a subway train drive have not been presented.

1.3. Literature Overview on the Use of Synchronous Homopolar Motors in Traction Drives and on the Use of Ferrite-Assisted Synchronous Homopolar Motors

Another alternative to PMSMs in electric vehicles is electrically excited wound rotor synchronous motors (WRSM), which solve many of the problems associated with rare earth magnets but require a solution to the problem of unreliable sliding contact [23].

By merging the advantages of permanent magnet synchronous machines (PMSMs) and wound rotor synchronous machines (WRSMs), synchronous homopolar machines (SHMs) eliminate the need for slip rings like in PMSMs and, similar to WRSMs, operate without magnets. They achieve a wide constant power speed range (CPSR) due to their adjustable excitation current. One advantage SHMs have over WRSMs is that the number of excitation coils is independent of the number of poles, whereas, in WRSMs, it increases with the number of poles, resulting in reduced excitation magnetomotive force (MMF) [14]. As a result, SHMs have lower mass and reduced losses in the excitation winding compared to WRSMs. Additionally, since SHMs have no losses in the rotor, there is no need for rotor cooling. SHMs find applications as highly reliable generators in various fields, including laser technology, pulse heating, welding units [24], automotive generators [25], railway passenger cars, ships, and aircraft [26].

In addition, the application of SHM in traction drives is being studied.

In [23,27], the utilization of SHMs as traction motors in mining trucks is discussed. Paper [27] presents and validates the computation method for the traction SHM, which relies on a set of 2D magnetostatic boundary problems. Furthermore, SHM optimization techniques for traction applications were developed [23] using the Nelder-Mead algorithm and the model proposed in [27]. Also, the performance of SHMs was compared with other types of motors. For example, in contrast to WRSMs, traction SHMs exhibit certain drawbacks, as highlighted in reference [27]. Firstly, the mass and dimensions of SHMs exceed those of WRSMs due to each rotor tooth covering roughly one pole pitch, leaving approximately half of the pole pitches unused for torque production. Secondly, SHMs necessitate a higher inverter power rating compared to WRSMs.

Several studies [28–31] have explored multi-pole SHMs that feature an excitation winding on the stator and rare-earth magnets housed in the rotor slots. These SHMs, equipped with rare-earth magnets, offer advantages over those without permanent magnets. The use of rare-earth magnets enhances the utilization of the rotor surface, while keeping the weight and dimensions comparable to conventional PMSMs. In traction drives with a wide constant power speed range (CPSR), SHMs with rare-earth magnets excel by exhibiting higher inverter utilization and lower costs for the inverter. The excitation winding enables the adjustment of the excitation flux across a wide range of speeds, utilizing the excitation winding current as an additional control signal to enhance SHM performance optimization. However, a notable drawback of SHMs with rare-earth magnets lies in their dependency on a limited number of rare-earth element suppliers, leading to high material costs. Moreover, the depth of the rotor slots in these SHMs is significantly smaller compared to those without magnets, compromising the saliency of the rotor. Consequently, although rare-earth magnets provide substantial additional torque, the primary torque generated by the interaction between the field of the excitation winding, modulated by rotor stacks, and the field of the stator winding is diminished.

To enhance the characteristics of SHMs with magnets, an alternative approach involves utilizing cost-effective ferrite magnets in their construction. Ferrite magnets are considerably less expensive than rare-earth magnets and are produced in numerous countries worldwide [10]. The application of ferrite magnets in SHMs is exemplified in [26], where they are employed as under-car generators for railway passenger cars. The use of SHM with ferrite magnets, compared with those without magnets, offers such advantages as reducing the weight and dimensions of the machine, as well as minimizing power losses.

Research on synchronous homopolar motors featuring ferrite magnets (for brevity in this paper, we call them ferrite-assisted synchronous homopolar motors, FaSHMs) is

relatively infrequent. For example, in [14], the characteristics of a FaSHM are compared with the characteristics of an SMH without magnets in the drive of a subway train bogie.

1.4. The Problem and Aim of the Study

An overview of the literature shows that although there are studies of the characteristics of FaSynRM and FaSHM in traction drives, a comparative analysis of the characteristics of these types of motors in the drive of a subway train bogie is not presented. In this paper, the characteristics of the FaSynRM and the FaSHM for a 370 kW subway train bogie drive are optimized, and their comparative analysis is provided. The optimization of the motor designs is carried out using the computationally efficient Nelder-Mead method, which makes it possible to consider the driving cycle of the train and not just the rated operating point. Optimization considers several criteria, such as cycle losses, maximum inverter current, torque ripple, and the degree of irreversible demagnetization of the permanent magnets.

We would like to highlight that although the optimization of the FaSHM for the subway drive was already considered by the authors in [14]. However, the losses in the section of the train running due to inertia (see Figure 1, "Coasting" section) that occur in the magnetic core, which are significant due to the long duration of this section of the cycle, were not taken into account. Therefore, when compared to the FaSynRM, this study re-optimized the FaSHM design to take this factor into account.

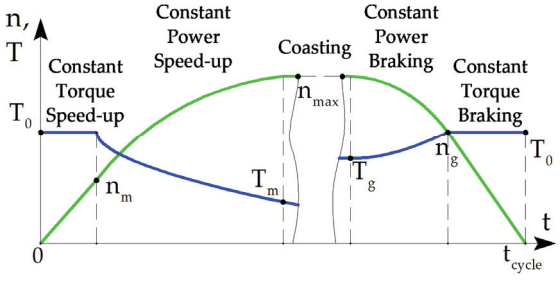

Figure 1. Dynamic speed (green line) and torque (blue line) profiles of the subway train's traction motor.

2. Representation of the Train Flow Pattern in the Motor Optimization Routine

The movement of the subway train, as depicted in Figure 1, encompasses several stages: acceleration with a constant torque, acceleration with a constant power, coasting at a steady speed (with any minimal deceleration disregarded), deceleration with a constant power, and deceleration with a constant torque. The maximum torque remains constant at T_0 = 1240 N·m for both motor and generator modes. The speed of transitioning between constant power and constant speed modes is n_m = 1427 rpm during acceleration and n_g = 2854 rpm during braking. The maximum attainable speed is n_{max} = 4280 rpm.

Figure 2 illustrates the torque dependency on rotational speed, with two separate abscissa axes representing the motor and generator modes. The optimization routine of the FaSHM for specific operating points 1, 2, 3, 4, and 5 depicted in Figure 2 is detailed in [14]. This optimization process encompasses all stages of the operating cycle, excluding coasting. The optimization function incorporates objectives such as weighted average electric losses evaluated over the cycle, with the weight coefficients w_i determined using the trapezoid quadrature formula. Building upon this research, the present study further refines the optimization procedure for traction motors with magnets in subway trains, considering the core losses during coasting mode. Despite the motor being switched off, magnetic fluxes induced by the magnets still result in coasting-related losses. Therefore, this study also considers the coasting mode (operating point 0). If coasting occupies 50% of the time

required for travel between stations, integration of the speed reveals that coasting accounts for 63.3% of the total distance. In this case, the weighting coefficients are calculated as:

$$w^{ex}{}_0 = 1/2;\ w^{ex}{}_i = w_i/2,\ i = 1, 2, 3, 4, 5. \quad (1)$$

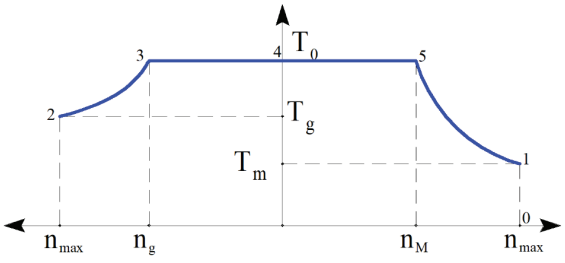

Figure 2. Demanded speed-torque characteristic of the subway train drive. The numbers 0–5 indicate the numbers of operating points of the electric machine, taken into account in the optimization process.

The average loss is calculated as:

$$<P_{loss}> = \sum(w^{ex}{}_i \cdot P_{loss\ i}), \quad (2)$$

where $P_{loss\ i}$ is the total loss at the i-th operating point.

In each operating point, denoted as V_i, the maximum allowable line-to-line voltage is approximately equal to the DC voltage, although not precisely. In the operating points of generator mode, the voltage V_i slightly surpasses the DC voltage due to the switch voltage drop, while in the operating points of the motor mode, it slightly dips below the DC voltage. To quantify this relationship, we introduce the catenary ratio ki, defined as $k_i = V_i/V_{DC\ rated}$ ($V_{DC\ rated}$ = 750 V). It is assumed that in modes 1, 2, 4, and 5, the DC voltage is equivalent to that in the catenary, resulting in ki being close to 1. The following margin values are selected: $k_2 = 1.01$, $k_1 = k_4 = k_5 = 0.97$. In operating point 3 (generator mode), k_3 can be chosen greater than in motor modes 1, 4, and 5, owing to the battery charge recuperation. For added safety, all the details pertaining to the specific modes are consolidated in Table 1.

Table 1. Points of the operating cycle of the subway train drive considered during the optimization.

Operating Point, i	Operating Point Name	Speed n_i, rpm	Torque, T_i, N·m	w_i	k_i	$w^{ex}{}_i$
0	Coasting mode; maximum speed	4280	0	-	-	0.5
1	Driving mode; maximum speed	4280	413.4	0.363	0.97	0.181
2	Braking mode; maximum speed	4280	826.9	0.091	1.01	0.046
3	Braking mode; changing from constant power to constant torque operation	2854	1240	0.182	1.1	0.091
4	Zero speed	0	1240	0.182	0.97	0.091
5	Driving mode; changing from maximum torque to constant power operation modes	1427	1240	0.182	0.97	0.091

3. Designs Features of the FaSHM and FaSynRM

The structure of the FaSynRM magnetic core is uniform along the axis of rotation; therefore, to describe it, it is sufficient to consider only its two-dimensional geometry (Figure 3a). The FaSHM consists of two pairs of stator and rotor stacks connected by axial elements that conduct the excitation magnetic flux. Therefore, to model the FaSHM, it is necessary both to consider the two-dimensional geometry of a pair of stator and rotor

packages (Figure 3b) and to consider the design of the axial elements: the stator housing and the rotor sleeve (Figure 3c).

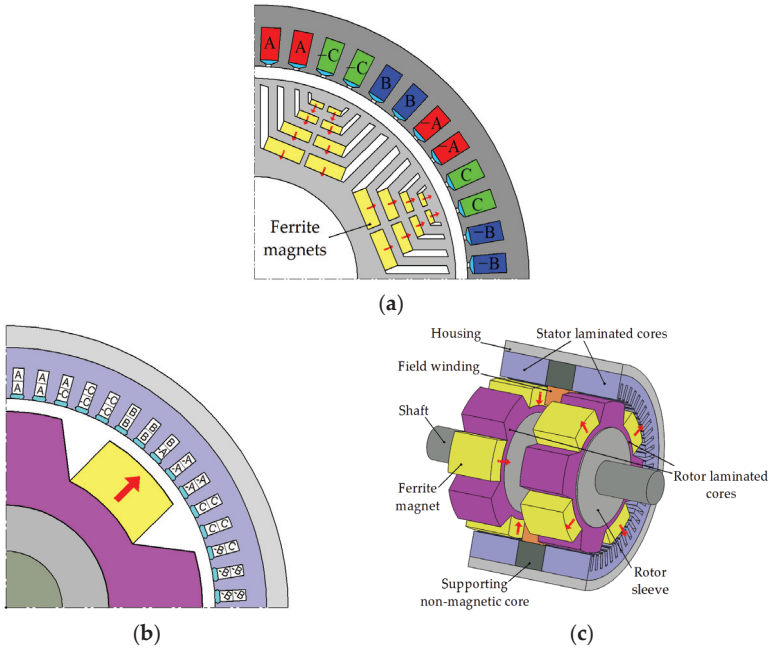

Figure 3. Motor design representation. Red arrows mark the directions of magnetization of the permanent magnets. (**a**) Ferrite-assisted synchronous reluctance motor (FaSynRM), 2-Pole area, red, blue and green colors indicate the different phases of the armature winding; (**b**) Ferrite-assisted synchronous homopolar motor (FaSHM), 1/4 cross-section and stator armature winding layout; (**c**) 3D cutout view of FaSHM with 1/2 stator cutout and unobstructed rotor.

Table 2 shows the main design parameters of the motors. Figure 3 illustrates the motor phases using capital letters A to C to indicate their order. The presence of a minus sign in Figure 3 signifies the reverse direction of the current within a winding layer. Both considered motors have a 3-phase 8-pole winding. The FaSHM stator has 60 slots, and the number of slots per pole and per phase $q = 60/(8 \cdot 3) = 2.5$. The FaSynRM stator has 48 slots, and the number of slots per pole and per phase $q = 48/(8 \cdot 3) = 2$. Unlike the FaSHM, the FaSynRM has only one set of stator and rotor stacks and does not have an excitation winding and its fastening elements, which makes it easier to assemble.

Table 2. Design features of the FaSHM and the FaSynRM.

Parameter	FaSHM	FaSynRM
Phase number	3	
Pole number	8	
Ferrite magnet grade	Y30H-2	
Excitation winding	Yes	No
Number of sets of stator and rotor stacks	2	1
Stator slot number	60	48
Number of the armature winding layers	2	1

Table 2. *Cont.*

Parameter	FaSHM	FaSynRM
Number of the stator slots per pole and phase q	2.5	2
Rotor slot number	4	-
Rotor flux barrier number per pole	-	4

Figure 4 illustrates the power supply circuit for the FaSHM, comprising a standard three-phase inverter for the multiphase armature winding and a chopper for the excitation winding. On the other hand, the FaSynRM solely necessitates a three-phase inverter without the need for a chopper.

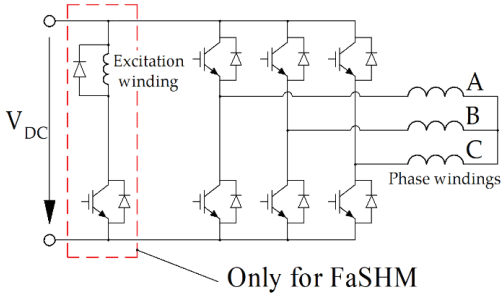

Figure 4. Layout of the three-phase inverter with a DC breaker designed to supply the excitation winding; letters A, B, and C represent the armature winding phases.

4. Objectives and Parameters of the Optimization

Since the external dimensions of the motor are essentially determined by the corresponding dimensions of the car bogie and correspond to the commercial induction motors already used in the drive under consideration, the main emphasis in optimizing the performance is on reducing losses in the duty cycle (see Figure 1) and on reducing the current rating power modules of the traction inverter. When optimizing, it is also necessary to limit torque ripple and prevent irreversible demagnetization of weakly coercive ferrite magnets. Since the applied Nelder-Mead method is an unrestricted method, the constraints are also set by additional terms of the optimization function.

Therefore, the objective function is formulated based on four objectives:

(1) Minimizing the average electrical losses, denoted as $<P_{loss\ el}>$, which is calculated as a weighted average of losses at different operating points;
(2) Minimizing the maximum armature winding current, indicated by $\max(I_{arm\ i})$, across operating points 1–5;
(3) Minimizing the maximum torque ripple, indicated by max (TR_i), across operating points 1–5;
(4) Reducing to zero δ_{demag}, which represents the cross-section area of magnets exposed to a demagnetization magnetic field stronger than the marginal demagnetization field H_0, relative to the overall cross-section area of the magnets.

When developing an electric motor, it is important to consider the discrete nature of certain parameters, such as the number of turns (N_{sec}) in the armature winding section and the standardized values of rectangular wire width and height outlined in [32]. However, this study disregards the discreteness of these values and allows them to have any positive real value, aiming to provide a more objective assessment. Random factors arising from different technical specifications in motor development can lead to optimal values of these parameters varying between designs. Specifically, the number of turns in the armature winding (N_{sec}) is chosen so that $V_{DC\ rated} = \max(V_i/k_i)$ [23].

An additional target for FaSHM is the maximum nonsymmetrized torque ripple max($TRnonsym_i$). This type of torque ripple is generated by a single pair of stator and rotor stacks, whereas a symmetrized torque ripple is produced by the entire FaSHM, involving all pairs of stator and rotor stacks. The details of the terms *TR* and *TRsym* are elaborated in [27].

In the FaSynRM, a significant contribution to the torque is generated by the reluctance torque, and the ferrite magnets play an assisting role. Therefore, when properly designed, the FaSynRM is comparatively strong to irreversible demagnetization. To ensure the strength of FaSynRM to such factors as temperature decrease, transients, or failures of the control system with an overcurrent, the maximum value of the demagnetizing field is constrained to H_0 = 2 kOe.

In [14], for the FaSHM, the demagnetizing field was not constrained in the objective function, but it was shown that the demagnetizing field does not exceed 3.2 kOe, while the coercive force of ferrite magnets can be 4 kOe. In contrast to [14], in this paper, H_0 is constrained for the FaSHM as well since it is under comparison with the FaSynRM, in which irreversible demagnetization is also possible. Moreover, in the FaSHM, the magnets make up for the disadvantage of a magnet-free SHM using only half the poles for torque production [14]. Therefore, in the FaSHM, the magnets are subjected to a greater demagnetizing effect compared to the FaSynRM. Trial runs of the optimization routine with a constraint of H_0 = 2 kOe showed an unacceptable reduction in efficiency and an increase in the maximum current of the armature winding. For this reason, a constraint of H_0 = 2.5 kOe was adopted for the FaSHM, which is somewhat larger than for the FaSynRM.

Also, in contrast to [14], when optimizing both machines, losses in the coasting mode (see Figure 1) with the motor turned off are considered. Even when the motor is turned off, the losses induced by permanent magnets in the magnetic core are not equal to zero, which is significant due to the long duration of this section of the working cycle.

Hence, the objective function of the FaSHM takes the following form:

$$F = \ln(< P_{loss} >) + 0.7\ln(\max(I_{arm\ i})) + 0.025\ \ln(\max(TRsym_i)) + \\ +0.01\ \ln(\max(TR_i)) + 150\ \max(\delta_{\text{demag}}), \quad (3)$$

where <P_{loss}> is the average total loss calculated in accordance with (2); max(I_{arm}) is the maximum armature current; max(*TRsym*) is the maximum value of the symmetrized torque ripple; max(*TR*) is the maximum value of the nonsymmetrized torque ripple; max(δ_{demag}) is the maximum ratio of the area of permanent magnets with $H > H_0$ to the total area of magnets.

The objective function for the FaSynRM is as follows:

$$F = \ln(< P_{loss} >) + 0.7\ \ln(\max(I_{arm\ i})) + 0.1\ \ln(\max(TR_i)) + \\ 0.1\ln(Mrot) + 0.1\ \ln(Mmag) + 150\ \max(\delta_{\text{demag}}), \quad (4)$$

where M_{rot} is the mass of the rotor, and M_{mag} is the mass of the permanent magnets.

The weight constants 150, 1, 0.7, 0.1, 0.025, and 0.01 in Equations (3) and (4) indicate the significance of specific objectives. These values represent the approximate relative priorities assigned to each optimization goal, drawing from the author's experience in designing comparable machines.

A coefficient of 150 at δ_{demag} ensures the selection of designs in which there is no irreversible demagnetization of permanent magnets. The next most important goal (loss <P_{loss}>) has a weight coefficient equal to unity.

The constant 0.7 signifies that a 1% decrease in the maximal current holds the same value as a 0.7% reduction in average loss. The objectives of minimizing symmetrized and unsymmetrized torque ripples hold relatively lesser significance. The constants 0.025 and 0.01 indicate that all else being equal, designs with lower torque ripples are favored. Additionally, to enhance clarity, the natural logarithm of Equations (3) and (4) is employed.

The fminsearch optimization procedure according to the Nelder-Mead method [33], implemented in the MATLAB software, is described in detail in [34]. The fminsearch (*F*, *x*0)

optimization procedure is launched to minimize the value of the objective function F by successively varying the vector x of electric machine parameters, where $x0$ is the vector of initial values of the electric machine parameters.

The procedure for calculating the objective function F, implemented in MATLAB, includes the steps shown in the flowchart in Figure 5. This flowchart is valid for both FaSHM and FaSynRM. However, for FaSHM, the objective function is calculated according to (3), and for FaSynRM, according to (4). Table 3 shows the list of variable parameters for FaSHM and Table 4 for FaSynRM. After building the geometry of the electric machine corresponding to the current value of the vector x, varied by the fminsearch function, its characteristics are calculated at operating points 0–5 (see Figure 2), necessary to calculate the terms of the objective function.

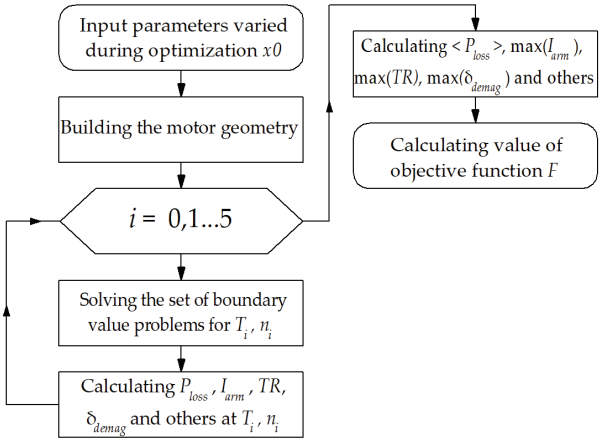

Figure 5. Objective function calculation block diagram.

Table 3. Variable FaSHM parameters.

Parameter	Before Optimization	After Optimization
Housing thickness h, mm	15.6	14.8
Total stator stacks length L_{stator}, mm	219.6	227
Stator slot depth, h_p, mm	35.9	31.0
Stator slot width, b_p, mm	9.0	7.63
Air gap width δ, mm	4.4	2.98
Rotor slot thickness, α_1	$0.423 \cdot t_z$ *	$0.547 \cdot t_z$ *
Rotor slot thickness, α_2	$0.664 \cdot t_z$ *	$0.706 \cdot t_z$ *
Current angles at operating points 1,2,3,4, electrical radians	0.943; 0.921; 0.404; 0.118	0.726; 0.834; 0.304; 0.0772
Current ratio **	10.55	9.77

Notes: * the FaSHM rotor tooth pitch $t_z = 360° / 4 = 90$ mechanical degrees; ** the current ratio is the ratio of the current in the armature winding layer to the current in the excitation winding cross-section.

Table 4. Variable FaSynRM parameters.

Parameter	Initial Design	Optimized Design
Inner stator radius R_{stat}, m	0.2	0.1943
Stator slot bottom radius R_{bot},m	0.23	0.2218
Stator slot thickness α_{stat1}	$0.4 \cdot t_{z1}$	$0.622 \cdot t_{z1}$
Air gap, mm	1	2.23
$a_{st\ i}$, mm	4	6.35
$b_{st\ i}$, mm	1	1.59
$a_{cut\ i}$, mm	4	6.95

Table 4. *Cont.*

Parameter	Initial Design	Optimized Design
$b_{cut\ i}$, mm	1	1.64
c	1.07	1.117
g	1.07	1.113
β, rad	0.01	0.021
b	$0.0777 \cdot \alpha_p$ *	$0.0755 \cdot \alpha_p$
Current angle, electrical degrees	50; 50; 50; 50	66.0; 67.7; 58.2; 55.1

Note: * α_p is the FaSynRM pole pitch; t_{z1} is the FaSynRM stator tooth pitch $t_{z1} = 360°/48 = 7.5$ mechanical degrees.

5. FaSHM Optimization Parameters and Results

5.1. FaSHM Optimization Parameters

The parameters varied during the optimization of the FaSHM, and fixed ones are shown in Figure 6. Their detailed description and the initial design are given in [14]. Table 5 provides parameters unchanged during the optimization, and Table 3 provides the initial and optimized values of varied ones.

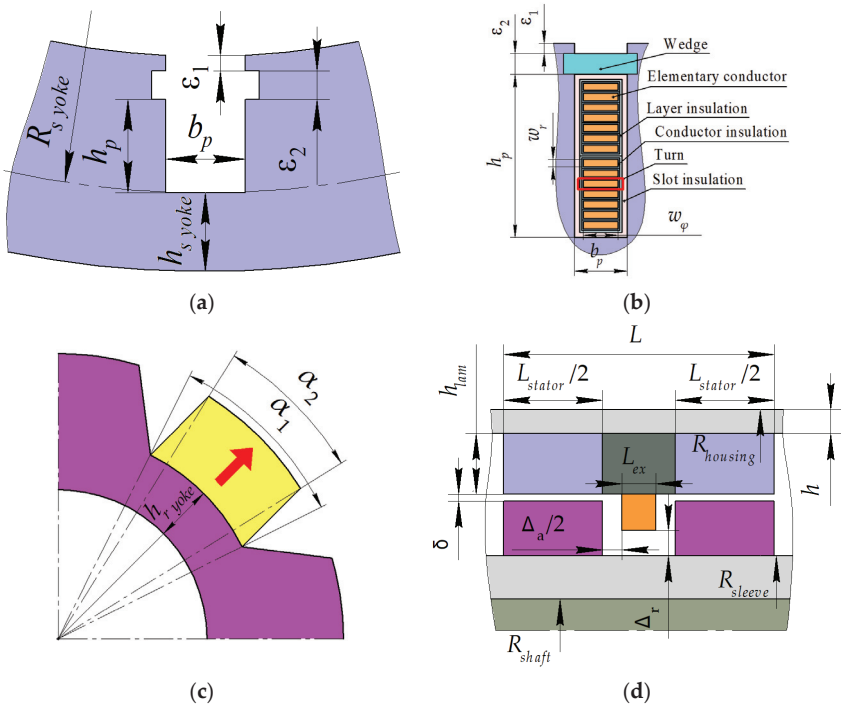

Figure 6. FaSHM parameters. (**a**) Stator, the red arrow marks the direction of magnetization of the permanent magnet.; (**b**) Armature winding; (**c**) Rotor; (**d**) Axial plane.

Table 5. FaSHM parameters were unchanged during optimization.

Parameter	Value
Machine length excluding winding end parts L, mm	260
Stator housing radius, mm	267
Axial clearance between excitation winding and rotor, Δ_a, mm	29
Radial clearance between field winding and rotor Δ_r, mm	22

Table 5. *Cont.*

Parameter	Value
Shaft radius R_{shaft}, mm	40
Stator lamination yoke $h_{s\ yoke}$, mm	21
Rotor lamination yoke $h_{r\ yoke}$, mm	17
Stator wedge thickness, ε_2, mm	2
Stator unfilled area thickness, ε_1, mm	3

5.2. FaSHM Optimization Results

As Figure 7 shows, the FaSHM optimization process took 180 calls of the objective function, and its value was significantly reduced.

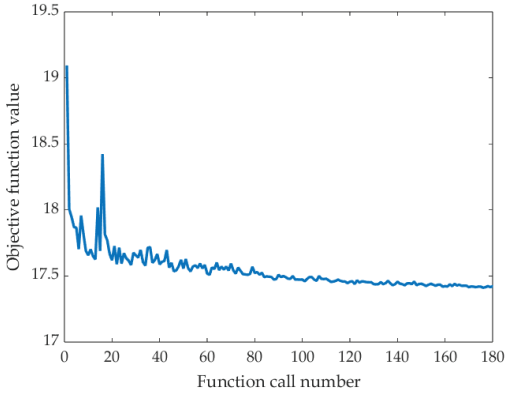

Figure 7. FaSHM optimization progress.

The losses in coasting mode are mainly concentrated in the stator laminated stacks. Its value is 705 W in the design presented in [14] and 639 W in the new design. Other motors' performance characteristics are presented in Table 6.

Table 6. FaSHM optimization results.

Parameter	Design Optimized in [14]					New Design				
Operating Point, *i*	**1**	**2**	**3**	**4**	**5**	**1**	**2**	**3**	**4**	**5**
Rotational speed n, rpm	4280	4280	2854	0	1427	4280	4280	2854	0	1427
Amplitude of the armature phase current I_{arm}, A	370	541	541	529	531	331	536	537	530	532
Efficiency, %	95.0	95.7	96.5	0	95.7	95.0	95.6	96.4	0	95.5
Output mechanical power P_{mech}, kW	185.3	−370.6	−370.6	0	185.3	185.3	−370.6	−370.6	0	185.3
Torque, N·m	413.4	−826.9	−1240	1240	1240	413.4	−826.9	−1240	1240	1240
Input electrical power, kW	195.0	−354.8	−357.7	5.6	193.6	195.0	−354.4	−357.2	6.1	194.1
Mechanical loss, kW *	3.55	3.55	1.06	0	0.14	3.55	3.55	1.06	0	0.14
Armature DC copper loss, kW	2.20	4.71	4.71	4.49	4.53	1.85	4.83	4.87	4.74	4.78
Armature eddy-current copper loss, kW	1.11	2.70	1.99	0	0.55	0.61	1.78	1.33	0	0.36
Stator lamination loss, kW	2.26	3.56	3.81	0	1.90	3.04	4.46	4.57	0	2.12
Rotor lamination loss, kW	0.04	0.09	0.07	0	0.02	0.11	0.23	0.19	0	0.05
Excitation copper loss, kW	0.55	1.21	1.21	1.13	1.14	0.51	1.37	1.38	1.32	1.33
Total loss, kW	9.72	15.81	12.85	5.62	8.27	9.68	16.22	13.41	6.06	8.77
Average losses according to Formula (2), kW			7.05					7.16		
Number of turns in armature winding			6.58					5.70		
Power factor	0.949	−0.989	−0.963	1.0	0.906	0.99	−0.99	−0.96	1.00	0.93
Line-to-line voltage amplitude V_{arm}, V	640	758	797	10	467	687	757	792	11	452

Table 6. *Cont.*

Parameter	Design Optimized in [14]					New Design				
Operating Point, *i*	**1**	**2**	**3**	**4**	**5**	**1**	**2**	**3**	**4**	**5**
Nonsymmetrized torque ripple, %	16.3	15.4	13.5	13.6	13.6	24.0	−22.6	−20.5	21.6	21.6
Symmetrized torque ripple, %	2.50	2.50	2.42	2.61	2.61	9.7	6.9	6.0	6.3	6.2
Magnetic flux density in the housing and the sleeve, T	0.30	0.71	1.04	1.15	1.15	0.36	0.76	1.29	1.43	1.43

Note: * Assuming a proportionate relationship, mechanical losses increase with the cube of speed, reaching a maximum of 3.55 kW at n_{max}.

Figure 8 shows the instantaneous magnitude of the magnetic flux density of the design presented in [14] and the new design. Figure 9 shows the minimum value (with maximum absolute value) of the demagnetization field over the machine cycle in operating point 4 since a short-term application of the demagnetization field stronger than the coercivity of the magnets results in their demagnetization. The entire magnet area in the new design is not subjected to the demagnetization field with an absolute value of more than 2.5 kOe, while the large area of the magnets in the design presented in [14] is. The absolute value of the demagnetization field does not exceed 3 kOe in this case.

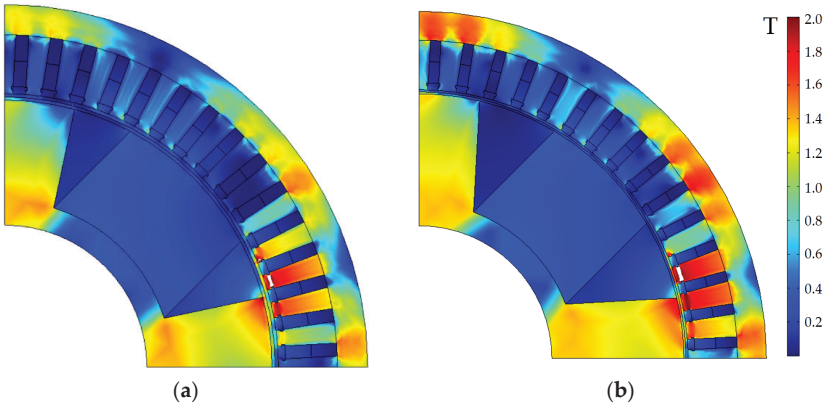

Figure 8. The cross-section of the optimized designs of the FaSHM and the plot of flux density magnitudes at operating point 4; saturation areas (>2 T) are shown with white. (**a**) Design optimized in [14]; (**b**) New FaSHM design.

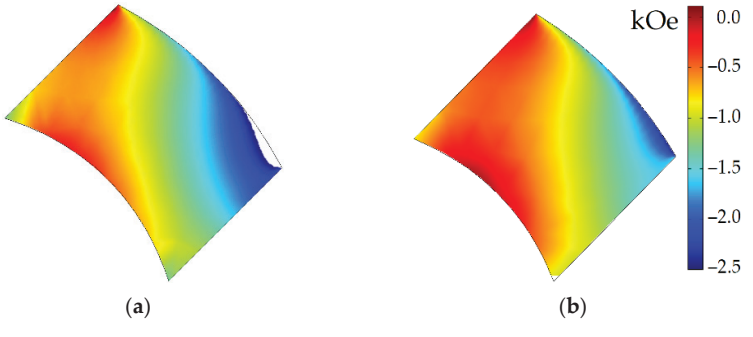

Figure 9. Operating point 4 demagnetizing force (kOe) in the FaSHM permanent magnet zone. Field stronger than −2.5 kOe is not shown (white color is used) (**a**) Design optimized in [14]; (**b**) New FaSHM design.

Figure 10 shows the calculated waveforms of the FaSHM: torque ripples at operating points with minimum and maximum torque; cogging torque; back EMF at the operating point where its maximum amplitude is reached, and back EMF at costing.

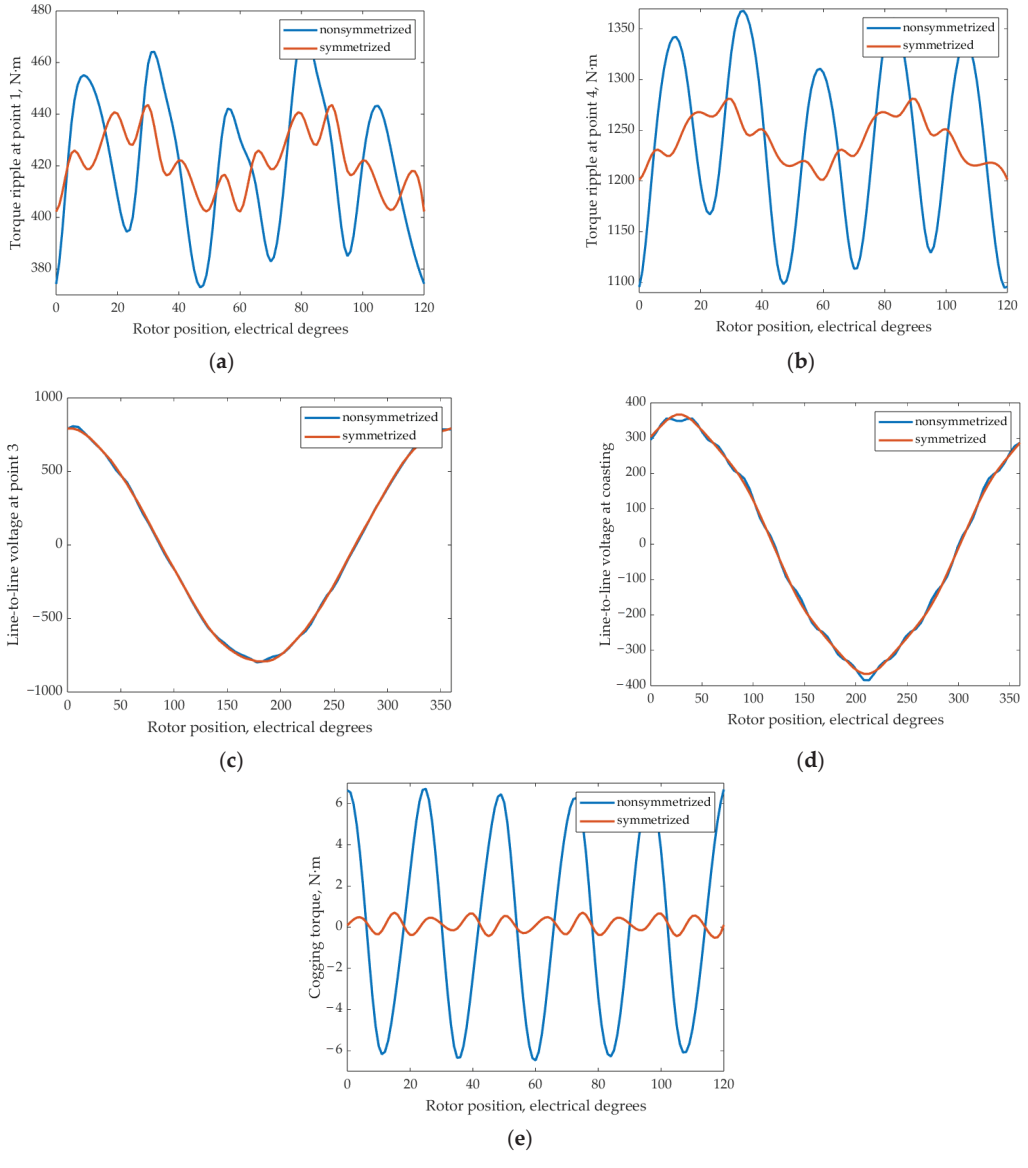

Figure 10. FaSHM calculated waveforms. (**a**) Torque ripple at operating point 1; (**b**) Torque ripple at operating point 4; (**c**) Line-to-line back EMF at operating point 3 (maximum EMF amplitude); (**d**) Line-to-line back EMF at coasting (operating point 0); (**e**) Cogging torque.

Comparing the results in Table 6, the differences in the characteristics of the FaSHM design optimized in [14] and the new design are not very large and consist of the following:

(1) The maximum current decreased slightly by $100\%(541 - 539)/541 = 0.4\%$;

(2) The main advantage of the new FaSHM design is a significantly increased resistance to demagnetization of magnets. The coercive force of the Y30H-2 magnet is about 4 kOe [35]. In the design optimized in [14], the maximum demagnetizing field is 3 kOe, and the margin is (4 − 3) = 1 kOe. In the new design, the maximum demagnetizing field is 2.5 kOe, and the margin is 1.5. Therefore, we can conclude that the new design is one and a half times more reliable for demagnetization of magnets. This is due to an increase in the width of the magnet (equal to the depth of the rotor slot) from 7.5 cm to 8.3 cm [14]. In addition, the lengths of the stator and rotor lamination have increased, which redistributed the flux over a larger area. Reducing the cross-sections of the housing and sleeve led to an increase in flux density;

(3) Core losses during coasting have been reduced by 100%(705 − 639)/705 = 9.4%, which contributes to the reduction of the average losses;

(4) However, due to achieving better reliability with respect to demagnetization, the average losses slightly increased by 100%(7.16 − 7.05)/7.16 = 1.5%.

6. FaSynRM Optimization Parameters and Results

6.1. FaSynRM Optimization Parameters

Figure 11 illustrates the parameters that define the FaSynRM geometry. The rotor has 4 magnetic flux barriers per pole. They are numbered 1, 2, 3, 4, starting from the outer barrier and ending with the inner one. The geometry of the magnetic flux barrier is shown in Figure 11b.

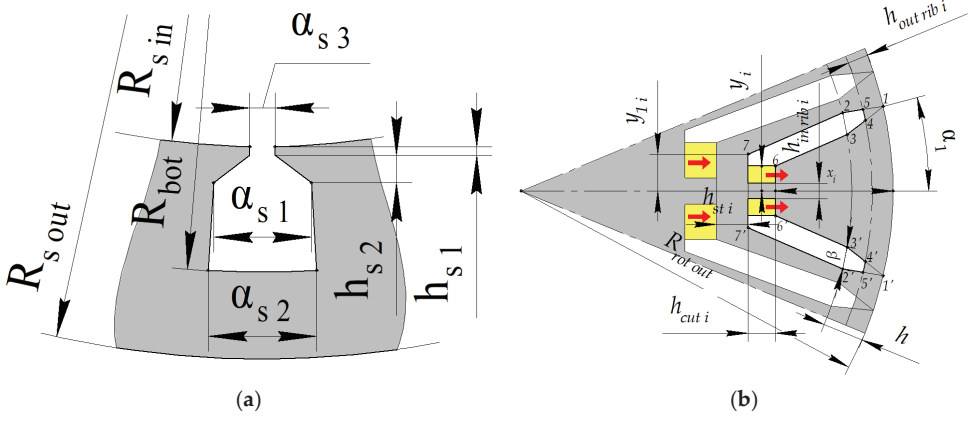

(**a**) (**b**)

Figure 11. Geometric parameters of the FaSynRM. (**a**) Stator slot; (**b**) Rotor flux barrier, red arrows mark the direction of magnetization of the permanent magnets. Areas occupied by ferrite magnets are marked in yellow.

The integrity of the rotor is ensured by internal ribs with thickness $h_{in\ rib\,i}$ in the middle of each barrier and external ribs with thickness $h_{out\ rib\,i}$, adjoining the air gap. On the surface of the rotor, points at a distance α_i of the barrier symmetry axis are 1 and 1′, which define the barrier geometry. Points 2, 2′, 3, 3′ are marked at a distance h from the surface of the rotor. The angular distance between points 2 and 3 and between 2′ and 3′ is equal to β. A circle of 455′4′ at a depth equal to the thickness of the outer ribs $h_{in\ rib\,i}$ cuts off triangles 1′4′5′ and 1′4′5′ from the barrier. For the outermost edge, points 6 and 6′ coincide with points 3 and 3′, that is, line 66′ is drawn between points 3 and 3′. With this exception, the depth x_i of the line is set to 66′, and the length of this line is $2y_i$. Line 77′ is drawn at depth $(x_i + h_{cut\ i})$, where $h_{cut\ i}$ is the width of the magnetic flux barrier. The length of this line is $2y_{1i}$. Line 77′ of the deepest gap limits the area allocated for cutouts in general. Its angular size ε is a fixed parameter. Therefore, the parameter y_{1i} is set only for three external magnetic flux barriers.

In this case, $x_{i+1} = x_i + h_{cut\ i} + h_{st\ i}$, where $h_{st\ i}$ is the steel thickness deep behind the barrier. Behind barriers 1, 2, 3 are the following barriers. Behind barrier 4 is the circumference of the inner radius of the rotor. To reduce the optimization parameters, we accept the following relations:

$$\begin{gathered} \alpha_i = a + b(i - 1/2),\ i = 1, 2, 3, 4; \\ y_{1i} = y_i \cdot c,\ i = 1, 2, 3; \\ y_i = y_{1i} \cdot g,\ i = 1, 2, 3, 4; \\ h_{cut\ i} = a_{cut\ i} + b_{cut\ i}(i - 1),\ i = 1, 2, 3, 4; \\ h_{st\ i} = a_{st\ i} + b_{st\ i}(i - 1),\ i = 1, 2, 3, 4. \end{gathered} \tag{5}$$

The ratio of the widths of the stator slot $\alpha_{stat1} / \alpha_{stat2}$ also does not change. In addition, the variable parameters include the current control angles in operating points 1, 2, 3, 4. Table 7 shows the FaSynRM parameters that are not changed during the optimization. Table 4 shows the FaSynRM parameters that are varied during the optimization.

Table 7. FaSynRM parameters were unchanged during optimization.

Parameter	Value
Machine length excluding winding end parts L, mm	240
Stator outer radius, mm	250
Stator parameter h_{stat1}, mm	1
Stator parameter h_{stat2}, mm	3
Outer rotor ribs thickness h_{outrib}, mm	1
Inner rotor ribs thickness h_{inrib_i}, mm	1.5; 2.5; 3.5; 4
Rotor parameter h, mm	3
Rotor parameter ε	$0.8 \cdot \alpha_p$
Stator slot thickness ratio $\alpha_{stat1} / \alpha_{stat2}$	1.05
Rotor parameter a	$0.4777 \cdot \alpha_p$

6.2. FaSynRM Optimization Results

As Figure 12 shows, the FaSynRM optimization process took 180 calls of the objective function, and its value was significantly reduced.

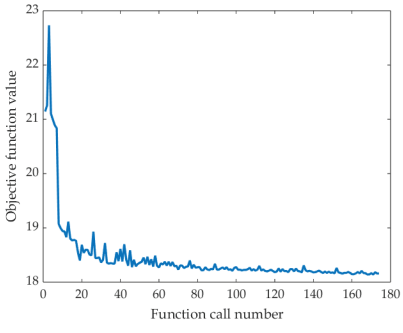

Figure 12. FaSynRM optimization progress.

Table 8 shows the characteristics of the initial and optimized FaSynRM designs. In the open-circuit coasting mode, the voltage at the motor terminals in the initial design and after optimization is 171 V and 207 V, respectively. The magnetic loss density is mainly concentrated in the stator magnetic core and is equal to 840 W and 490 W, respectively. Figure 13 shows the FaSynRM geometry and flux density amplitude at operating points 1–5 listed in Table 1. Figure 14 shows the geometry and flux density amplitude after the FaSynRM optimization. Figure 15 shows the demagnetizing field in the area of permanent magnets on the rotor before and after optimization.

Table 8. FaSynRM Optimization Results.

Parameter	Before Optimization					After Optimization				
Operating Point, *i*	**1**	**2**	**3**	**4**	**5**	**1**	**2**	**3**	**4**	**5**
Rotational speed n, rpm	4280	4280	2854	0	1427	4280	4280	2854	0	1427
Amplitude of the armature phase current I_{arm}, A	492	886	1381	1393	1402	450	693	833	832	839
Efficiency, %	91.6	93.0	94.1	0	93.4	94.7	95.4	96.0	0	95.3
Output mechanical power P_{mech}, kW	185.30	370.60	370.60	0	185.30	185.30	370.60	370.60	0	185.30
Torque, N·m	413.4	826.9	1240.0	0.2	1240.0	413.4	826.9	1240.0	0.2	1240.0
Input electrical power, kW	202.27	344.75	348.63	8.96	198.50	195.63	353.52	355.95	6.22	194.42
Mechanical loss, kW *	3.55	3.55	1.06	0	0.14	3.55	3.55	1.06	0	0.14
Armature DC copper loss, kW	1.05	3.76	8.96	8.96	8.96	1.76	4.44	6.37	6.22	6.22
Armature eddy-current copper loss, kW	-	-	-	-	-	-	-	-	-	-
Stator lamination loss, kW	11.14	16.61	10.75	0	3.80	4.25	7.88	6.89	0	2.70
Rotor lamination loss, kW	1.24	1.93	1.20	0	0.30	0.77	1.21	0.33	0	0.07
Excitation copper loss, kW	-	-	-	-	-	-	-	-	-	-
Total loss, kW	16.97	25.85	21.97	8.96	13.20	10.33	17.08	14.65	6.22	9.12
Average losses $<P_{loss}>$, kW			10.46					7.40		
Number of turns in armature winding			5.95					9.76		
Power factor	0.846	0.678	0.609	1	0.684	0.910	0.791	0.735	1	0.769
Line-to-line voltage amplitude V_{arm}, V	654	757	583	7	297	621	757	665	9	356
Torque ripple, %	27	29	33	33	33	16	16	11	10	10

Note: * The mechanical losses are assumed to be proportional to the speed with a maximum value of 3.55 kW at *nmax*.

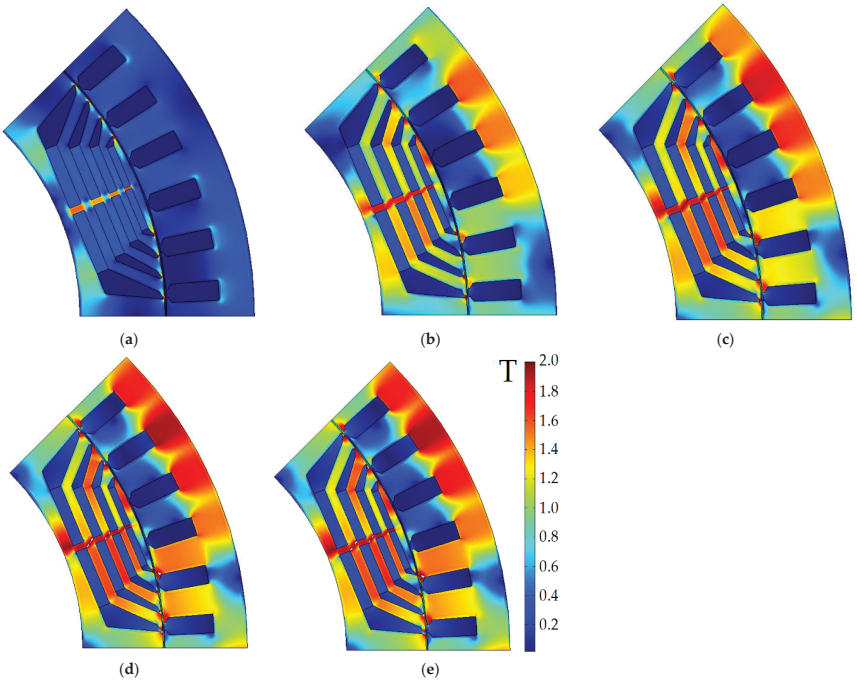

Figure 13. FaSynRM cross-section before optimization, with a plot of flux density modulus at saturation limit (>2 T) highlighted in white. (**a**) Operating point 1; (**b**) Operating point 2; (**c**) Operating point 3; (**d**) Operating point 4; (**e**) Operating point 5.

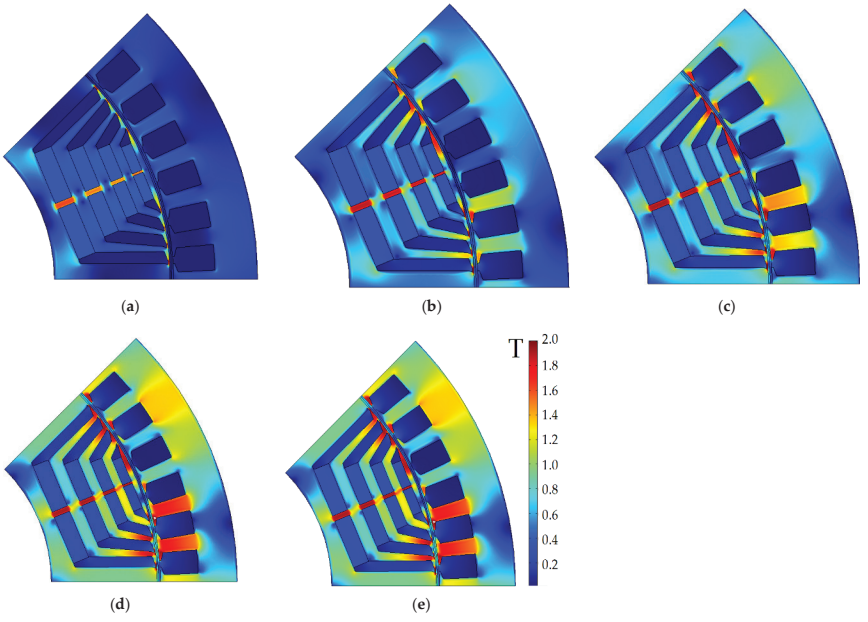

Figure 14. FaSynRM cross-section after optimization, with a plot of flux density modulus at saturation limit (>2 T) highlighted in white. (**a**) Operating point 1; (**b**) Operating point 2; (**c**) Operating point 3; (**d**) Operating point 4; (**e**) Operating point.

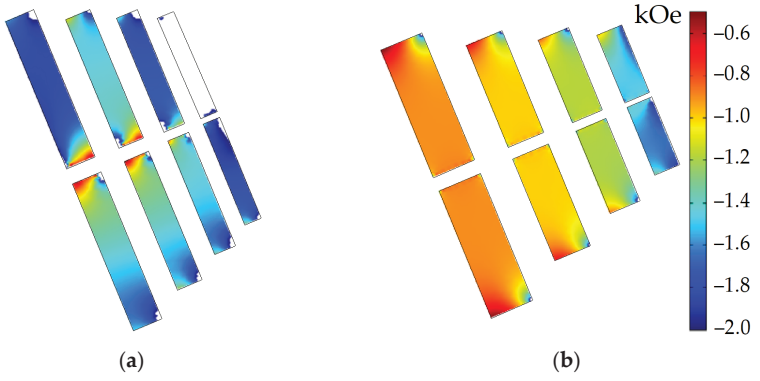

Figure 15. The demagnetizing field in the area of permanent magnets of the PMaSynRM rotor. Areas with the strongest demagnetization (<−2 kOe) are highlighted in white. (**a**) Before optimization; (**b**) After optimization.

Figure 16 shows the calculated waveforms of the FaSynRM: torque ripples at operating points with minimum and maximum torque; cogging torque; back EMF at the operating point where its maximum amplitude is reached, and back EMF at costing.

Comparing the characteristics of the FaSynRM before and after optimization, we can draw the following conclusions:

(1) Average losses were reduced by 100%(10.46 − 7.4)/10.46 = 29.3%;
(2) Maximum armature winding current decreased by 100%(1402 − 839)/1402 = 40%;
(3) Maximum torque ripple decreased by (33 − 10) = 23%;
(4) The share of magnets δ_{demag} exposed to a demagnetizing field of more than 2 kOe decreased from 8.6% to almost zero (0.06%). As can be seen from Figure 15, the −2 kOe

level is reached only in the corners of the magnets, and it can be concluded that the demagnetization of this small share of magnets is not critical. Therefore, we can conclude that with a coercive force of 4 kOe, the optimized design has a large safety margin (4 − 2) = 2 kOe. The achievement of a higher resistance to demagnetization of the design after optimization, apparently, was facilitated by an increase in the thickness of the magnets, as well as an increase in the number of turns, and hence a decrease in the turn voltage and magnetic flux in the magnetic circuits.

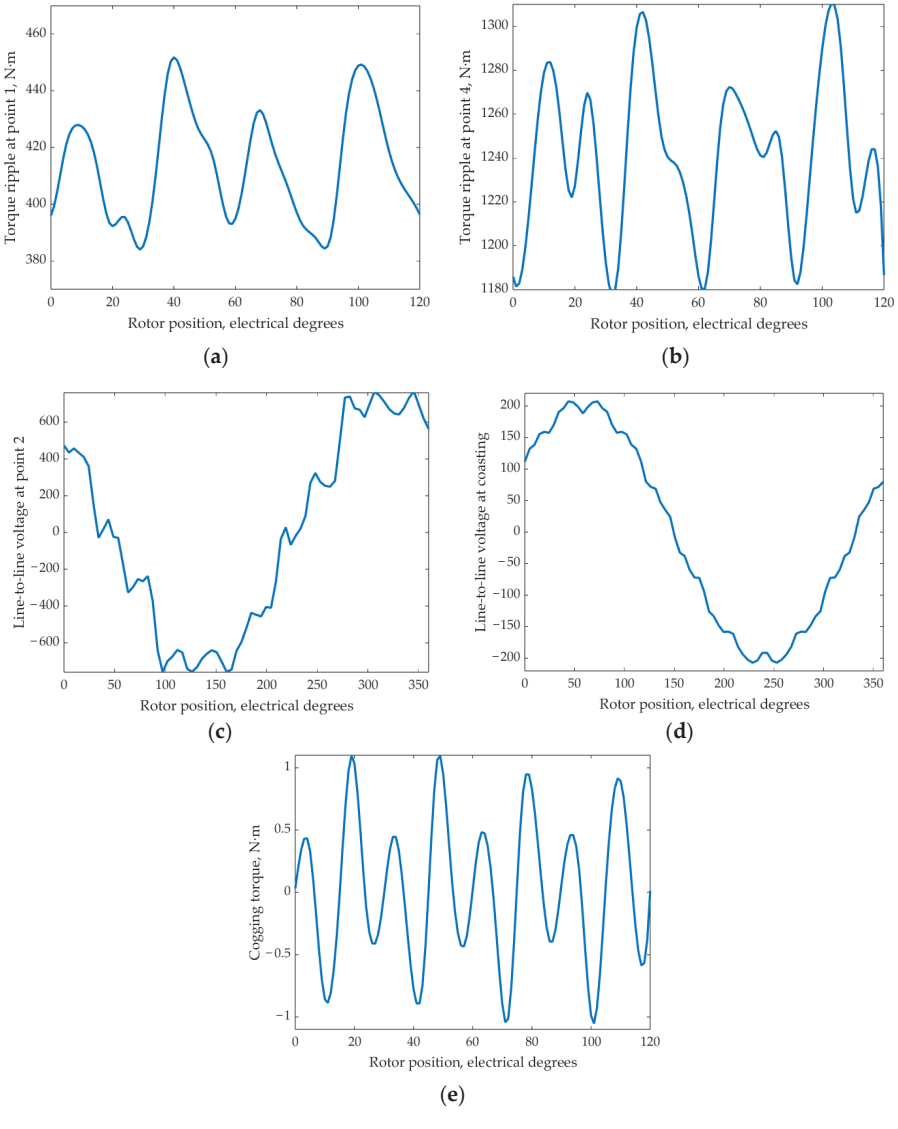

Figure 16. FaSynRM calculated waveforms. (**a**) Torque ripple at operating point 1; (**b**) Torque ripple at operating point 4; (**c**) Line-to-line back EMF at operating point 2 (maximum EMF amplitude); (**d**) Line-to-line back EMF at coasting (operating point 0); (**e**) Cogging torque.

7. Comparison of Characteristics of FaSHM and FaSynRM

This section discusses the comparison of the characteristics of the considered electrical machines after optimization. Table 9 compares the performance of the optimized FaSHM and FaSynRM. The FaSHM characteristics are taken from Table 6. The FaSynRM characteristics are taken from Table 8. Table 10 shows a comparison of masses, dimensions, and active material costs.

Table 9. Comparison of the characteristics of the optimized FaSHM and FaSynRM.

Parameter	FaSHM					FaSynRM				
Operating Point, *i*	**1**	**2**	**3**	**4**	**5**	**1**	**2**	**3**	**4**	**5**
Rotational speed n, rpm	4280	4280	2854	0	1427	4280	4280	2854	0	1427
Amplitude of the armature phase current I_{arm}, A	331	536	537	530	532	450	693	833	832	839
Efficiency, %	95.0	95.6	96.4	0	95.5	94.7	95.4	96.0	0	95.3
Output mechanical power P_{mech}, kW	185.30	370.60	370.60	0	185.30	185.30	370.60	370.60	0	185.30
Torque, N·m	413.4	826.9	1240.0	0.2	1240.0	413.4	826.9	1240.0	0.2	1240.0
Input electrical power, kW	195.0	−354.4	−357.2	6.1	194.1	195.63	353.52	355.95	6.22	194.42
Mechanical loss, kW *	3.55	3.55	1.06	0	0.14	3.55	3.55	1.06	0	0.14
Armature DC copper loss, kW	1.85	4.83	4.87	4.74	4.78	1.76	4.44	6.37	6.22	6.22
Armature eddy-current copper loss, kW	0.61	1.78	1.33	0	0.36	-	-	-	-	-
Stator lamination loss, kW	3.04	4.46	4.57	0	2.12	4.25	7.88	6.89	0	2.70
Rotor lamination loss, kW	0.11	0.23	0.19	0	0.05	0.77	1.21	0.33	0	0.07
Excitation copper loss, kW	0.51	1.37	1.38	1.32	1.33	-	-	-	-	-
Total loss, kW	9.68	16.22	13.41	6.06	8.77	10.33	17.08	14.65	6.22	9.12
Average losses $<P_{loss}>$, kW			7.16					7.40		
Power factor	0.99	0.99	0.96	1.00	0.93	0.910	0.791	0.735	1	0.769
Line-to-line voltage amplitude V_{arm}, V	687	757	792	11	452	621	757	665	9	356
Torque ripple, %	9.7	6.9	6.0	6.3	6.2	16	16	11	10	10
Maximum demagnetizing force, kOe			2.5					2		

Note: * The mechanical losses are assumed to be proportional to the speed with a maximum value of 3.55 kW at *nmax*.

Table 10. Comparison of masses, costs, and dimensions of parts of the FaSynRM.

Parameter	FaSHM	FaSynRM
Stator lamination mass, kg	110.5	104.6
Rotor lamination mass, kg	66	78.4
Armature copper mass, kg	41.7	38
Excitation copper mass, kg	8.1	-
Magnets mass, kg	34	20
Weight of the rotor sleeve and motor housing without bearing shields, kg	98.9	-
The total mass of the active materials, rotor sleeve, and motor housing, kg	359.2	241
Stator lamination cost, USD	110.5	104.6
Rotor lamination cost, USD	66	78.4
Armature copper cost, USD	291.9	266
Excitation copper cost, USD	56.7	-
Magnets cost, USD	627.64	369.2
Rotor sleeve and motor housing cost, USD	98.9	-
The total cost of the active materials (electrical steel, copper, permanent magnets), USD *	1152.7	818.2
The total cost of the active materials (electrical steel, copper, permanent magnets) and structural steel of the rotor sleeve and motor housing, USD *	1251.64	818.2
Total length of the stator lamination L, mm	227	240
Total length of the machine, excluding the winding end parts (including spaces for the excitation coils), mm	260	-
Stator lamination outer diameter D, mm	504.4	500
Air gap, mm	2.98	2.23
Active core volume $\pi \cdot L \cdot D^2/4$, liters	45.4	47.1

* In the analysis, the following material cost assumptions were considered: copper at 7 USD/kg, laminated electrical steel at 1 USD/kg, non-laminated structural steel (for housing and rotor sleeve of the FaSHM) at 1 USD/kg, and Y30H-2 grade ferrite magnet at 18.46 USD/kg [14,36].

Comparing the characteristics of the FaSHM and FaSynRM from Tables 9 and 10, we can draw the following conclusions:

(1) In this application, the average loss of the FaSHM is 100%(7.4 − 7.16)/7.4 = 3.4% less than that of FaSynRM;
(2) By adjusting the excitation flux, the maximum armature current for the FaSHM is 833/539 = 1.54 times less than for the FaSynRM, which potentially makes it possible to significantly reduce the cost of power modules of the traction inverter;
(3) The active volume of magnetic cores, excluding the stator housing, in the FaSynRM is 100%(47.1 − 45.4)/47.1 = 3.9% higher than in the FaSHM;
(4) The length of the FaSHM stator laminations is less than that of FaSynRM by 100%(240 − 227)/240 = 5.4%; the length of the FaSHM, taking into account the gap for installing the excitation winding, is greater by 100%(260 − 240)/260 = 7.7%;
(5) The mass of active materials of the FaSHM is greater than that of the FaSynRM by 100%(359.2 − 98.9 − 241)/(359.2 − 98.9) = 7.4% excluding the housing and sleeve;
(6) The cost of the FaSHM active materials is 100%(1152.7 − 818.2)/818.2 = 29.0% higher than that of the FaSynRM (excluding the housing and sleeve) due to the greater mass of copper and magnets;
(7) The maximum modulus of the demagnetizing force in the case of the FaSHM is greater than in the case of the FaSynRM by (2.5 − 2) = 0.5 kOe. In this case, the demagnetization margin for the FaSynRM is (4 − 2) = 2 kOe, and for the FaSHM is (4 − 2.5) = 1.5 kOe, where 4 kOe is the coercive force of ferrite magnets. Therefore, the FaSHM requires a more careful design of control algorithms to avoid demagnetization during failures and transients.

8. Conclusions

The article provides a comparative analysis of the optimized designs of the traction ferrite-assisted synchronous reluctance machine (FaSynRM) and the traction ferrite-assisted synchronous homopolar machine (FaSHM) in a subway train drive with a power rating of 370 kW. The machines have an approximately equal outer diameter of the stator lamination. When optimizing the machines, the train movement cycle is considered. To reduce the computational burden during optimization, the computationally efficient Nelder-Mead method is used. Moreover, each time the optimization function is called, the characteristics of one of these machines are calculated only at 6 operating points, from which, using quadrature formulas, the integral characteristics of the machines can be calculated throughout the whole moving cycle.

The goals of machine optimization are to reduce losses in the train moving cycle, the maximum current of the semiconductor inverter, and the torque ripple. In addition, the goal of optimization is to prevent irreversible demagnetization of the ferrite magnets in the rotor.

For the FaSHM, compared with the FaSynRM, the losses are reduced by 3.4%, and the maximum current of the traction inverter is reduced by 1.54 times. For the FaSynRM, compared to the FaSHM, the active core volume is higher by 3.9%. However, for the FaSynRM, the mass of active materials is reduced by 7.4%, and the cost of active materials is reduced by 29% due to the smaller mass of magnets. Also, the FaSynRM has less risk of irreversible demagnetization of the ferrite magnets in the rotor.

In general, it can be concluded that the machines in question have comparable performance. However, the FaSHM has better field weakening capability, which reduces the maximum current, power, and cost of inverter power modules, while the FaSynRM requires fewer permanent magnets at the same torque density and is more resistant to irreversible demagnetization, which reduces its cost and improves reliability.

Future work will involve conducting a comprehensive comparison of the FaSHM with other types of electrical machines utilized in subway drives and other applications.

Author Contributions: Conceptual approach, V.D. and V.P.; data curation, V.D. and V.K.; software, V.D. and V.P.; calculations and modeling, V.D., V.K. and V.P.; writing—original draft, V.D., V.K. and

V.P.; visualization, V.D. and V.K.; review and editing, V.D., V.K. and V.P. All authors have read and agreed to the published version of the manuscript.

Funding: The research funding from the Ministry of Science and Higher Education of the Russian Federation (Ural Federal University Program of Development within the Priority-2030 Program) is gratefully acknowledged.

Institutional Review Board Statement: Not applicable.

Informed Consent Statement: Not applicable.

Data Availability Statement: Data are contained within the article.

Acknowledgments: The authors thank the editors and reviewers for careful reading and constructive comments.

Conflicts of Interest: The authors declare no conflict of interest.

References

1. Matsuoka, K.; Kondo, M. Energy Saving Technologies for Railway Traction Motors. *IEEJ Trans. Electr. Electron. Eng.* **2010**, *5*, 278–284. [CrossRef]
2. De Almeida, A.T.; Ferreira, F.J.; Baoming, G. Beyond Induction Motors—Technology Trends to Move up Efficiency. *IEEE Trans. Ind. Appl.* **2014**, *50*, 2103–2114. [CrossRef]
3. Fedoseyev, L.; Pearce, E.M., Jr. Rotor Assembly with Heat Pipe Cooling System. U.S. Patent US9331552B2, 3 May 2016. Available online: https://patents.google.com/patent/US9331552B2/en?oq=US9331552B2 (accessed on 13 August 2023).
4. Guan, Y.; Zhu, Z.Q.; Afinowi, I.A.A.; Mipo, J.C.; Farah, P. Comparison between induction machine and interior permanent magnet machine for electric vehicle application. In Proceedings of the 2014 17th International Conference on Electrical Machines and Systems (ICEMS), Hangzhou, China, 22–25 October 2014; pp. 144–150.
5. Kim, B.; Lee, J.; Jeong, Y.; Kang, B.; Kim, K.; Kim, Y.; Park, Y. Development of 50 kW traction induction motor for electric vehicle (EV). In Proceedings of the 2012 IEEE Vehicle Power and Propulsion Conference, Seoul, Republic of Korea, 9–12 October 2012; pp. 142–147.
6. Zhu, Z.Q.; Chu, W.Q.; Guan, Y. Quantitative comparison of electromagnetic performance of electrical machines for HEVs/EVs. *CES Trans. Electr. Mach. Syst.* **2017**, *1*, 37–47. [CrossRef]
7. Dianov, A. Instant Closing of Permanent Magnet Synchronous Motor Control Systems at Open-Loop Start. *Sustainability* **2022**, *14*, 12665. [CrossRef]
8. Schulze, R. Reducing Environmental Impacts of the Global Rare Earth Production for Use in Nd-Fe-B Magnets. How Much Can Recycling Contribute? Ph.D. Thesis, Technical University of Darmstadt, Darmstadt, Germany, December 2018. Available online: https://tuprints.ulb.tu-darmstadt.de/8301/7/Diss%20Rita%20Schulze%2015-12-2018.pdf (accessed on 13 August 2023).
9. Dong, S.; Li, W.; Chen, H.; Han, R. The status of Chinese permanent magnet industry and R&D activities. *AIP Adv.* **2017**, *7*, 056237. [CrossRef]
10. Carraro, E.; Bianchi, N.; Zhang, S.; Koch, M. Design and Performance Comparison of Fractional Slot Concentrated Winding Spoke Type Synchronous Motors with Different Slot-Pole Combinations. *IEEE Trans. Ind. Appl.* **2018**, *54*, 2276–2284. [CrossRef]
11. The Net-Zero Materials Transition: Implications for Global Supply Chains, Report, McKinsey & Company, July 2023. Available online: https://www.mckinsey.com/industries/metals-and-mining/our-insights/the-net-zero-materials-transition-implications-for-global-supply-chains (accessed on 13 August 2023).
12. De Lima, W.I.B. *Rare Earth Industry*; Elsevier: Amsterdam, The Netherlands, 2015.
13. Papini, F.; Osama, M. Electromagnetic Design of an Interior Permanent Magnet Motor for Vehicle Traction. In Proceedings of the 2018 XIII International Conference on Electrical Machines (ICEM), Alexandroupoli, Greece, 3–6 September 2018; pp. 205–211. [CrossRef]
14. Dmitrievskii, V.; Prakht, V.; Kazakbaev, V. Design Optimization of a Synchronous Homopolar Motor with Ferrite Magnets for Subway Train. *Mathematics* **2023**, *11*, 589. [CrossRef]
15. Dobzhanskyi, O.; Grebenikov, V.; Gouws, R.; Gamaliia, R.; Hossain, E. Comparative Thermal and Demagnetization Analysis of the PM Machines with Neodymium and Ferrite Magnets. *Energies* **2022**, *15*, 4484. [CrossRef]
16. Manne, B.; Kiran Kumar, M.; B. Akuru, U. Design and Performance Assessment of a Small-Scale Ferrite-PM Flux Reversal Wind Generator. *Energies* **2020**, *13*, 5565. [CrossRef]
17. Ibrahim, M.N.; Silwal, B.; Sergeant, P. Permanent Magnet-Assisted Synchronous Reluctance Motor Employing a Hybrid Star-Delta Winding for High Speed Applications. In Proceedings of the 2018 XIII International Conference on Electrical Machines (ICEM), Alexandroupoli, Greece, 3–6 September 2018; pp. 379–385.
18. Liu, Z.; Hu, Y.; Wu, J.; Zhang, B.; Feng, G. A Novel Modular Permanent Magnet-Assisted Synchronous Reluctance Motor. *IEEE Access* **2021**, *9*, 19947–19959. [CrossRef]
19. Barcaro, M.; Pradella, T.; Furlan, I. Low-torque ripple design of a ferrite-assisted synchronous reluctance motor. *IET Electr. Power Appl.* **2016**, *10*, 319–329. [CrossRef]

20. Du, G.; Zhang, G.; Li, H.; Hu, C. Comprehensive Comparative Study on Permanent-Magnet-Assisted Synchronous Reluctance Motors and Other Types of Motor. *Appl. Sci.* **2023**, *13*, 8557. [CrossRef]
21. Liu, X.; Li, Y.; Liu, Z.; Ling, T.; Luo, Z. Analysis and design of a high power density permanent magnet-assisted synchronous reluctance machine with low-cost ferrite magnets for EVs/HEVs. *COMPEL-Int. J. Comput. Math. Electr. Electron. Eng.* **2016**, *35*, 1949–1964. [CrossRef]
22. Li, Y.; Yang, H.; Lin, H.; Fang, S.; Wang, W. A Novel Magnet-Axis-Shifted Hybrid Permanent Magnet Machine for Electric Vehicle Applications. *Energies* **2019**, *12*, 641. [CrossRef]
23. Prakht, V.; Dmitrievskii, V.; Kazakbaev, V.; Anuchin, A. Comparative Study of Electrically Excited Conventional and Homopolar Synchronous Motors for the Traction Drive of a Mining Dump Truck Operating in a Wide Speed Range in Field-Weakening Region. *Mathematics* **2022**, *10*, 3364. [CrossRef]
24. Ren, Z.; Yu, K.; Xin, Q.; Pan, Y. Performance of Homopolar Inductor Alternator with Diode-Bridge Rectifier and Capacitive Load. *IEEE Trans. Ind. Electron.* **2013**, *60*, 4891–4902. [CrossRef]
25. Lorilla, L.; Keim, T.; Lang, J.; Perreault, D. Topologies for future automotive generators. Part I. Modeling and analytics. In Proceedings of the 2005 IEEE Vehicle Power and Propulsion Conference, Chicago, IL, USA, 7 September 2005; pp. 74–85. [CrossRef]
26. Orlova, S.; Pugachov, V.; Levin, N. Hybrid Excitation of the Axial Inductor Machine. *Latv. J. Phys. Tech. Sci.* **2012**, *49*, 35–41. [CrossRef]
27. Dmitrievskii, V.; Prakht, V.; Anuchin, A.; Kazakbaev, V. Traction Synchronous Homopolar Motor: Simplified Computation Technique and Experimental Validation. *IEEE Access* **2020**, *8*, 185112–185120. [CrossRef]
28. Bekhaled, C.; Hlioui, S.; Vido, L.; Gabsi, M.; Lecrivain, M.; Amara, Y. 3D magnetic equivalent circuit model for homopolar hybrid excitation synchronous machines. In Proceedings of the 2007 International Aegean Conference on Electrical Machines and Power Electronics, Bodrum, Turkey, 10–12 September 2007; pp. 575–580. [CrossRef]
29. Asfirane, S.; Hlioui, S.; Amara, Y.; Gabsi, M. Study of a Hybrid Excitation Synchronous Machine: Modeling and Experimental Validation. *Math. Comput. Appl.* **2019**, *24*, 34. [CrossRef]
30. Hoang, E.; Lecrivain, M.; Hlioui, S.; Gabsi, M. Hybrid excitation synchronous permanent magnets synchronous machines optimally designed for hybrid and full electrical vehicle. In Proceedings of the 8th International Conference on Power Electronics—ECCE Asia, Seogwipo, Republic of Korea, 30 May–3 June 2011. [CrossRef]
31. Gandzha, S.; Chuyduk, I.; Nazarov, M. Development of a Motor-Wheel Based on a Brushless Machine of Combined Excitation for Hybrid and Electric Transport. In Proceedings of the 2021 International Ural Conference on Electrical Power Engineering (UralCon), Magnitogorsk, Russia, 24–26 September 2021; pp. 630–633.
32. IEC. *Specifications for Particular Types of Winding Wires—Part 0–2: General Requirements—Enamelled Rectangular Copper Wire*; IEC 60317-0-2:2020; IEC: Geneva, Switzerland, 2020. Available online: https://webstore.iec.ch/publication/63495 (accessed on 13 August 2023).
33. Lagarias, J.C.; Reeds, J.A.; Wright, M.H.; Wright, P.E. Convergence properties of the Nelder–Mead simplex method in low dimensions. *SIAM J. Optim.* **1998**, *9*, 112–147. [CrossRef]
34. Find Minimum of Unconstrained Multivariable Function Using Derivative-Free Method. MATLAB Documentation. © 1994–2023 The MathWorks, Inc. Available online: https://www.mathworks.com/help/matlab/ref/fminsearch.html (accessed on 30 August 2023).
35. Grades of Ferrite. The Original Online Company. Bunting. E-Magnets. Available online: https://e-magnetsuk.com/ferrite-magnets/grades-of-ferrite/ (accessed on 13 August 2023).
36. Hard Ferrite Magnets, Product Information, IBSMagnet. 2020. Available online: https://ibsmagnet.com/products/dauermagnete/hartferrit.php (accessed on 13 August 2023).

machines

MDPI

Article

High-Speed Design with Separated Tapering for Reducing Cogging Torque and Torque Ripple of a 3 kW Dry Vacuum Pump Motor for the ETCH Process

Do-Hyeon Choi [1], In-Jun Yang [2], Min-Ki Hong [2], Dong-Hoon Jung [3] and Won-Ho Kim [4,*]

[1] Department of Next Generation Smart Energy System Convergence, Gachon University, Seongnam 13120, Republic of Korea; dino0403@naver.com
[2] Department of Electrical Engineering, Hanyang University, Seoul 04763, Republic of Korea; dlswns78@naver.com (I.-J.Y.); chapcher01@naver.com (M.-K.H.)
[3] Department of Mechanical, Automotive and Robot Engineering, Halla University, Wonju 26404, Republic of Korea; dh.jung@halla.ac.kr
[4] Department of Electrical Engineering, Gachon University, Seongnam 13120, Republic of Korea
* Correspondence: wh15@gachon.ac.kr

Abstract: This paper proposes a design method to reduce cogging torque and torque ripple in the concentrated winding of IPMSMs (Interior Permanent Magnet Synchronous Motors) used in motors for the semiconductor ETCH process. IPMSMs can utilize reluctance torque through the difference in inductance between the d axis and q axis, but they are at a disadvantage in terms of reducing cogging torque while tapering the rotor and stator to reduce torque ripple. In addition, the existing single tapering can push the permanent magnets into the rotor. If the rotor's permanent magnets are embedded, the magnetic reluctance will increase, and the overall performance of the motor will decrease. However, an optimum design method was derived in which the magnets do not move during rotor tapering. This geometric design is an optimum design method that reduces cogging torque and torque ripple. This paper compares and analyzes four models, the concentrated winding model, distributed winding model, conventional tapering model, and separated tapering model, using 2D and 3D finite element analysis (FEA).

Keywords: permanent motor; torque ripple; tapering; IPMSM; ETCH process; semiconductor; dry vacuum pump; separated tapering

Citation: Choi, D.-H.; Yang, I.-J.; Hong, M.-K.; Jung, D.-H.; Kim, W.-H. High-Speed Design with Separated Tapering for Reducing Cogging Torque and Torque Ripple of a 3 kW Dry Vacuum Pump Motor for the ETCH Process. *Machines* **2023**, *11*, 991. https://doi.org/10.3390/machines11110991

Academic Editors: Loránd Szabó and Feng Chai

Received: 9 October 2023
Revised: 24 October 2023
Accepted: 25 October 2023
Published: 26 October 2023

1. Introduction

Recently, the global semiconductor market has become one of the most important markets in which to secure a global share, because competition is intensifying and developing rapidly. Therein, demand for vacuum pumps for semiconductors is rapidly increasing, centering on the ETCH (etching) manufacturing process in the semiconductor manufacturing process. Other industries, like semiconductor manufacturing, are also seeing a growing demand for vacuum pumps. Currently, semiconductor companies around the world are actively investing in the development of dry vacuum pumps for semiconductor processing. The dry vacuum pump is a technology that enables industrial production and scientific experiments by artificially creating a vacuum state. It is a pump that creates a state filled with gas molecules at a pressure lower than atmospheric pressure. These vacuum pumps require miniaturization and high-performance exhaust systems when space efficiency is considered in semiconductor and display-manufacturing processes. When the output of the motor is the same, if a high-speed design is used, the size of the motor required to produce the same output is reduced, so the high-speed motor is advantageous for miniaturization. However, when operating at high speed, the torque ripple problem of high space harmonics occurs, and a solution to this problem is required.

IPMSMs are widely used for their high torque and efficiency. An IPMSM is typically controlled by maximum torque per ampere (MTPA) at rated speed. IPMSMs suffer from torque ripple during MTPA control due to space harmonics. Although there are mechanical and electrical factors in the generation of noise and vibration of the motor, torque ripple is also one of the causes of noise and vibration. Torque ripple at high speed causes vibration. However, when operating at high speed, the torque ripple problem of high space harmonics occurs, and a solution to this problem is required. In addition, iron loss and other losses affect the performance of motors in high-speed operation, so such losses must also be reduced in the design of motors for higher speeds.

Recent research efforts to reduce the vibration and noise of motors are actively underway [1]. It is important to reduce torque ripple, a major cause of vibration and noise in motor design [1]. Among the causes of torque ripple, there are reasons related to the mechanical structure [2,3]. Research on SRM motors with altered shapes to reduce torque ripple [2], as well as studies on torque-ripple reduction through skewing, is active [3]. One of the causes of torque ripple is cogging torque. By modifying the motor's shape to reduce cogging torque, torque ripple can be minimized. By altering the surface shape of the rotor core to reduce harmonic content in the airgap flux density, cogging torque and torque ripple can be reduced [4,5]. While tapering the rotor surface can reduce cogging torque and torque ripple, it also results in a simultaneous reduction in output [6]. By applying the newly proposed method of separated tapering, which has not been suggested before this paper, it is possible to minimize output reduction while reducing cogging torque and torque ripple, thus reducing vibration and noise.

The IPMSM with the proposed separated tapering described in this paper can minimize the reduction in output and reduce cogging torque and torque ripple. Therefore, this paper proposes a high-speed design of a PM motor with separated tapering that reduces cogging torque and torque ripple for a 3 kW semiconductor-etching process.

2. Features of Concentrated Winding V-IPMSM for High Speed

When designing a motor, the rotor type will change depending on the purpose for which it is being designed. To decide about the rotor type, you must first understand the concept of torque [7].

$$\begin{aligned} &T_{total} = \tfrac{3}{2}p\{(L_d - L_q)I_qI_d + \lambda_{pm}I_q\} = T_{reluctance} + T_{magnetic}[\mathrm{N}\cdot\mathrm{m}] \\ &T_{reluctance} = \tfrac{3}{2}p(L_d - L_q)I_qI_d = \tfrac{3}{2}p(\lambda_dI_q - \lambda_qI_d)[\mathrm{N}\cdot\mathrm{m}] \\ &= \tfrac{3}{2}p(\lambda_dI_q - \lambda_qI_d)[\mathrm{N}\cdot\mathrm{m}] = {T_{reluctance}}^d - {T_{reluctance}}^q \\ &T_{magnetic} = \tfrac{3}{2}p\lambda_{pm}I_q \end{aligned} \tag{1}$$

The equation for torque is shown in Equation (1). Intuitively, torque can be generated in two ways: the first is the force between the magnet and the magnet, called magnetic torque. The second is the force between the magnet and the iron core, which is the force that causes the magnet to attach to the iron and is called reluctance torque. The rotor type that uses both magnetic torque and reluctance torque is described above as an IPMSM (interior permanent magnet synchronous motor). This is defined as a V-IPMSM because the shape of the magnet is a V. A V-IPMSM can produce higher output by concentrating the magnetic flux from the rotor into the air gap, and the IPMSM is stable even at high-speed operation because the permanent magnet is built into the rotor. For high-speed operation, the total magnetic flux is weakened by adjusting the current phase angle to achieve high-speed rotation. Such control by adjusting the current phase angle is called weak flux control, and the IPMSM is capable of this weak flux control, which is advantageous for high-speed operation [7–9].

$$P_c = P_h + P_e = K_hB^nf + K_eB^2f^2 \tag{2}$$

The equation for hysteresis loss and eddy current loss for a permanent magnet is expressed as Equation (2). Losses occurring in motors include copper loss, iron loss, and eddy current loss, and eddy current loss in permanent magnets causes temperature rise in permanent magnets and irreversible demagnetization. In Equation (2), P_h means hysteresis loss and P_e means eddy current loss. In eddy current loss, eddy currents are generated by the counter-electromotive force when a time-varying magnetic flux is generated around a magnet. In the IPM (interior permanent magnet) rotor shape, the magnetic permeability of the iron core is high, and the generation of eddy current increases by the movement of magnetic flux around the permanent magnet. Eddy current loss of the permanent magnet causes rotor heat, and efficiency may decrease, or motor failure may occur due to heat of the rotor. Therefore, a design to reduce the hysteresis loss and the eddy current loss of the permanent magnet is required [9–11].

An IPMSM uses not only magnetic torque but also reluctance torque generated by reluctance differences. Therefore, the torque generated per volume is high, but the magnetic flux density is also high and the iron loss is higher. Iron loss increases in proportion to electric frequency, and electric frequency increases with the number of poles. In addition, iron loss increases in proportion to speed. Since iron loss increases as the motor operates at higher speeds, it is necessary to design the motor to minimize iron loss. Therefore, the number of poles is designed to be four [12–14].

$$T_{cog} = -\frac{1}{2}{\Phi_g}^2\frac{dR}{d\theta} \tag{3}$$

Equation (3) is the expression for the cogging torque. Cogging torque in motors is caused by the change in reluctance between the permanent magnets of the rotor and the stator value, which is unrelated to the current. Cogging torque is one of the causes of torque ripple, and torque ripple is a cause of vibration and noise in motors. This means that the smaller the cogging torque is, the more vibration and noise will be reduced. Therefore, to reduce torque ripple, the motor should be designed to minimize cogging torque [15,16].

$$T_{ripple} = \frac{T_{peak\_to\_peak}}{T_{avg}} \times 100\% \tag{4}$$

Equation (4) is the expression for calculating the torque ripple. As expressed in Equation (4), the torque ripple increases as the range of torque fluctuation increases [1]. There are two causes of such large torque amplitudes: the input current and the mechanical structure of the motor [4,5]. First, the torque follows the peak value of the current, and the ripple frequency increases with the number of phases and rotating speed. Ripple with respect to the mechanical structure is a matter of geometry [4,5]. Ripple occurs due to the structure of the electric motor, which has slots in the stator where the windings are wound. In the PMSM described above, the cogging torque, which is the force that causes the permanent magnet of the rotor and the iron core of the stator to stick together, causes vibration and increases the torque ripple. To reduce the torque ripple in the mechanical structure, it is essential to design a shape that reduces the cogging torque to the maximum extent possible [17–20].

A high-speed design is beneficial for miniaturization because if the motors have the same power output, a higher-speed design reduces the size of the motor required to produce the same power. However, operating at high speeds introduces the problem of iron loss and eddy current loss at high frequency, which must be addressed. Torque ripple at high speeds is also an important objective function in motor design. Torque ripple is a source of heat in motors, and at high speeds it can be fatal. If the rotor generates heat or vibration at high speed, it can be fatal to the operation of the motor. Permanent magnet

motors require a design that reduces torque ripple and hysteresis loss to operate properly at high speeds [21–26].

$$(L_d I_d + \lambda_{pm})^2 + (L_q I_q)^2 \leq \left(\frac{V_{om}}{\omega_e}\right)^2 \tag{5}$$

$$I^2{}_d + I^2{}_q \leq I^2{}_{am} \tag{6}$$

$$M_{point}(I_d = -\lambda_{pm}/L_d, I_q = 0) \tag{7}$$

Equation (5) is the equation for the voltage limit circle. Equation (6) is the equation for the current limit. Equation (7) shows the M_{point}, the center of the voltage limit circle. To increase the speed of the motor, the design must place the M_{point} within the current-limiting circle. If the magnetic flux λ_{pm} of the permanent magnet is lowered by tapering, the M_{point} can be placed inside the current limit circle. Such a design is essential when designing motors for high speeds.

3. Separated Tapering Design Process and Principles for ETCH Dry Vacuum Pump Motor

Figure 1 shows dry vacuum pump and motor for the semiconductor-ETCH (etching) process. The dry vacuum pump for the semiconductor-etching processes is a crucial component in semiconductor manufacturing. This specialized vacuum pump is designed to remove gases and particles from the etching chamber without introducing moisture or other contaminants. The dry vacuum pump operates without the need for oil or lubricants, making it suitable for cleanroom environments and critical semiconductor-fabrication processes. It uses advanced technologies such as scroll, claw, or turbomolecular mechanisms to create a vacuum within the etching chamber. This vacuum ensures the removal of unwanted byproducts and gases, maintaining a stable and controlled environment for precise etching processes. The absence of oil or lubricants in these pumps reduces the risk of contamination and outgassing, which can negatively impact the quality of semiconductor devices. Therefore, dry vacuum pumps play a vital role in enabling high-quality, high-precision semiconductor-etching processes, contributing to the production of advanced microelectronics. Therefore, in vacuum pumps used for etching processes that require high precision, minimizing vibration and noise is of paramount importance.

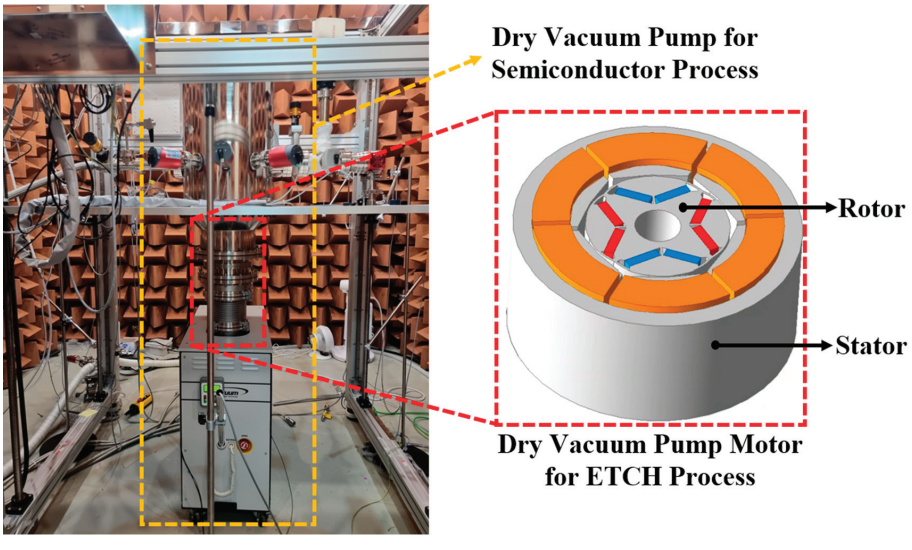

Figure 1. Dry vacuum pump and motor for semiconductor-ETCH process.

Figure 2 shows the design process for a motor with separated tapering. It looks like the general IPMSM process. However, the difference is the design of the tapering. A motor with a basic concentrated winding IPMSM can have a higher slot-fill factor than a distributed winding. However, concentrated windings are characterized by very high torque ripple. Concentrated winding has the fatal drawback of very high torque ripple, which is difficult to control and may prevent smooth operation. However, by applying tapering to the rotor and stator to make the magnetic flux flow sinusoidal and designing the iron core to shave off unnecessary saturation areas, the torque ripple can be lowered and iron loss can be reduced. Therefore, after the basic design for the motor size in Figure 2, it is necessary to apply tapering to the rotor and stator, respectively, and compare the tendencies. Torque-ripple targets for tapering length selection in the process were targeted with Model 1. After determining the tapering lengths L_{ct} and L_{st}, the stator was tapered to match the rotor geometry. The rotor and stator were shaped to minimize the torque ripple. Finally, θ_{tap} was determined and Model 4 was derived, which has very low cogging torque and torque ripple compared with the other models.

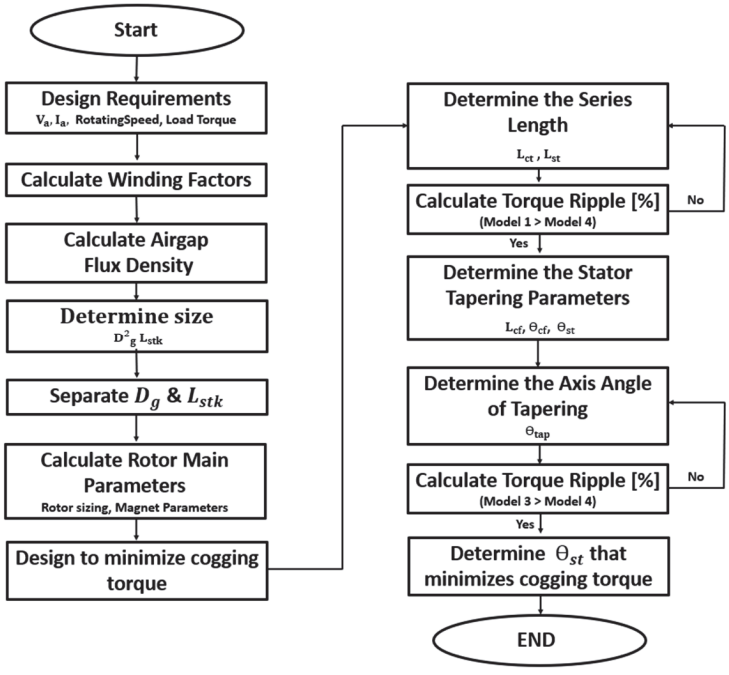

Figure 2. Process for the detailed design of 4P6S concentrated winding motor with separated tapering.

Figure 3 shows a concentrated winding model (Model 1), distributed winding model (Model 2), conventional tapering model, and separated tapering model. Figure 3 shows the parameters for separated tapering of the rotor. Applying separated tapering of the rotor can reduce the change in reluctance in the air gap, which reduces cogging torque, torque ripple, and losses. The design was changed from basic distributed winding (Model 2) to concentrated winding (Model 1). Concentrated winding can wind more coils on the stator teeth than distributed winding. It is also easy to manufacture and very advantageous for mass production. Concentrated winding is also very practical and easy to manufacture due to the short $Turn_{end}$ of the coils, which is not an area of motor performance. However, concentrated winding has the disadvantage of higher torque ripple than distributed winding. These problems can be solved by tapering the rotor and stator to make the airgap magnetic flux sinusoidal.

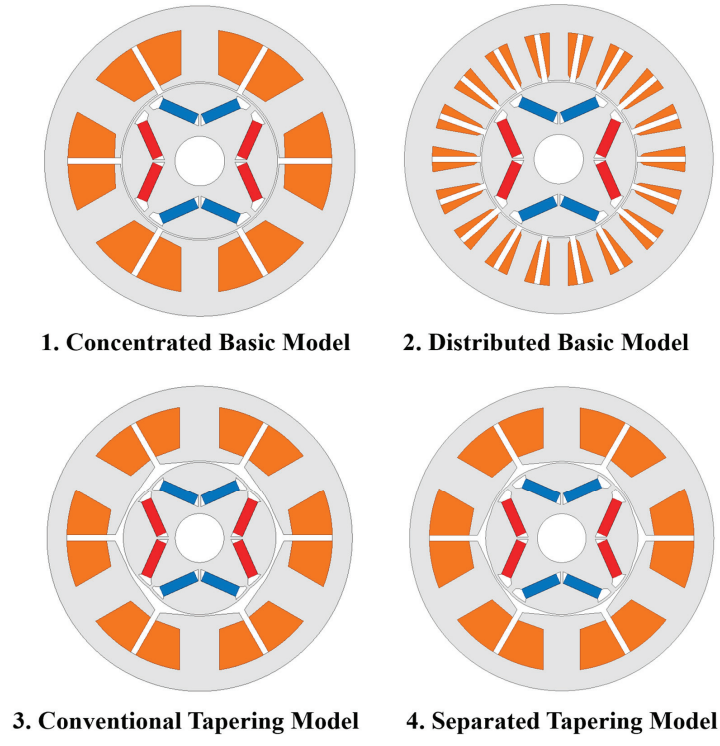

Figure 3. 2D models of the four motors used in the comparative analysis.

Figure 4a,b show a design for a separated tapering rotor. The typical rotor tapering is created by L_{ct}, as shown in Figure 4. However, this paper introduces a new tapering axis called L_{st}, which takes the form of two arcs with the axis divided into two axes. If tapering is performed only on the existing L_{ct}, it is applied even to areas where tapering is not required. However, in the case of the method in Figure 4, a design can be created that incorporates all the advantages of the conventional method along with new advantages. This tapering method in which L_{st} and L_{ct}, are applied simultaneously is defined as separated tapering. The reason for separating the axis into two on both sides is explained below [2,3].

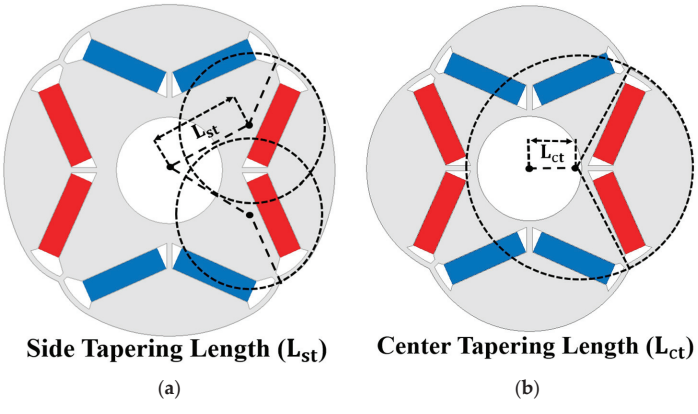

Figure 4. Rotor tapering parameters, (**a**) side tapering length, (**b**) center tapering length.

Figure 5 shows the process where magnets are pushed inside the rotor during conventional tapering. The reason for dividing the axis into two is explained in Figure 5. In the conventional tapering method, as shown in Figure 4b, where only L_{ct} is considered, increasing the value of L_{ct} for greater tapering effect necessitates pushing the magnets inside the rotor, which maintains the shape of the permanent magnets on the rotor. When the permanent magnets are pushed inside the rotor, it results in tapering that affects the output because it moves away from the air gap. However, with the application of separated tapering, an additional L_{st} axis is added on both sides to secure the ends of the permanent magnets in place. This allows tapering of only the rotor pole-piece side when tapering the rotor, without affecting the geometry of the permanent magnets, thus preventing degradation of motor output. Tapering the outer surface of the rotor without affecting the position and shape of the permanent magnets is necessary to minimize the reduction in motor output power. Additionally, since cogging torque and torque ripple can be influenced by changes in rotor geometry, tapering is required to minimize cogging torque and torque ripple.

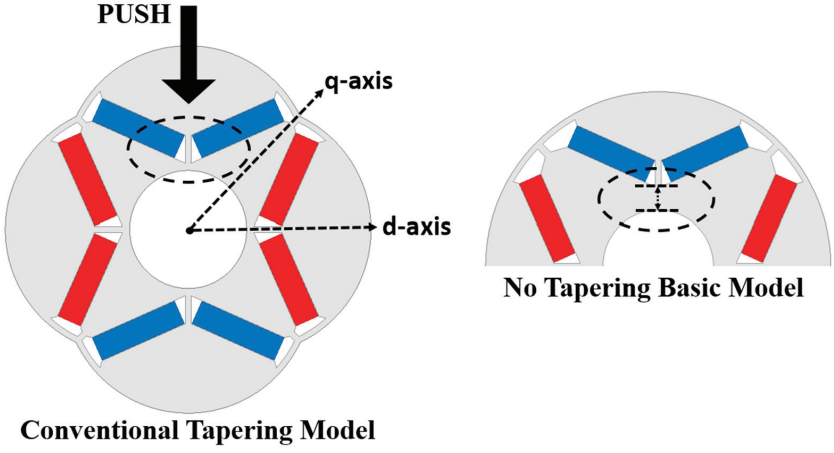

Figure 5. Problems with magnets being pushed and embedded in conventional tapering.

Figure 6a defines parameters for the angle between the two axes, L_{st} and L_{ct}. Figure 6b shows the rotor shape according to the separated axis angle. After separating the two axes, if the rotor can be finely designed according to the angle between them, it can have a significant effect in terms of cogging torque and torque ripple. In conjunction with the rotor to which separated tapering is applied as follows, conventional tapering is also applied to the stator. This maximizes the reduction of shape-sensitive cogging torque and torque ripple. The optimized design of the rotor was completed according to the θ_{tap} angle.

Figure 7 shows the stator tapering parameters. For motors with stator teeth, the change in magnetic reluctance is not constant as the rotor rotates with time. Since the change in magnetic reluctance is not constant, it is necessary to taper the unnecessary parts in the stator tooth structure. The stator shoe portion of the stator teeth was tapered with L_{cf}, θ_{cf}, and θ_{sf} parameters to match the geometry of the rotor. The rotor pole-piece tapering was designed to take the starting point according to the length of L_{cf} only in the area where the tapering was applied and taper it by the stated angle. L_{cf} is determined within half of the stator teeth, and θ_{cf} tapers the unnecessary area of the stator teeth.

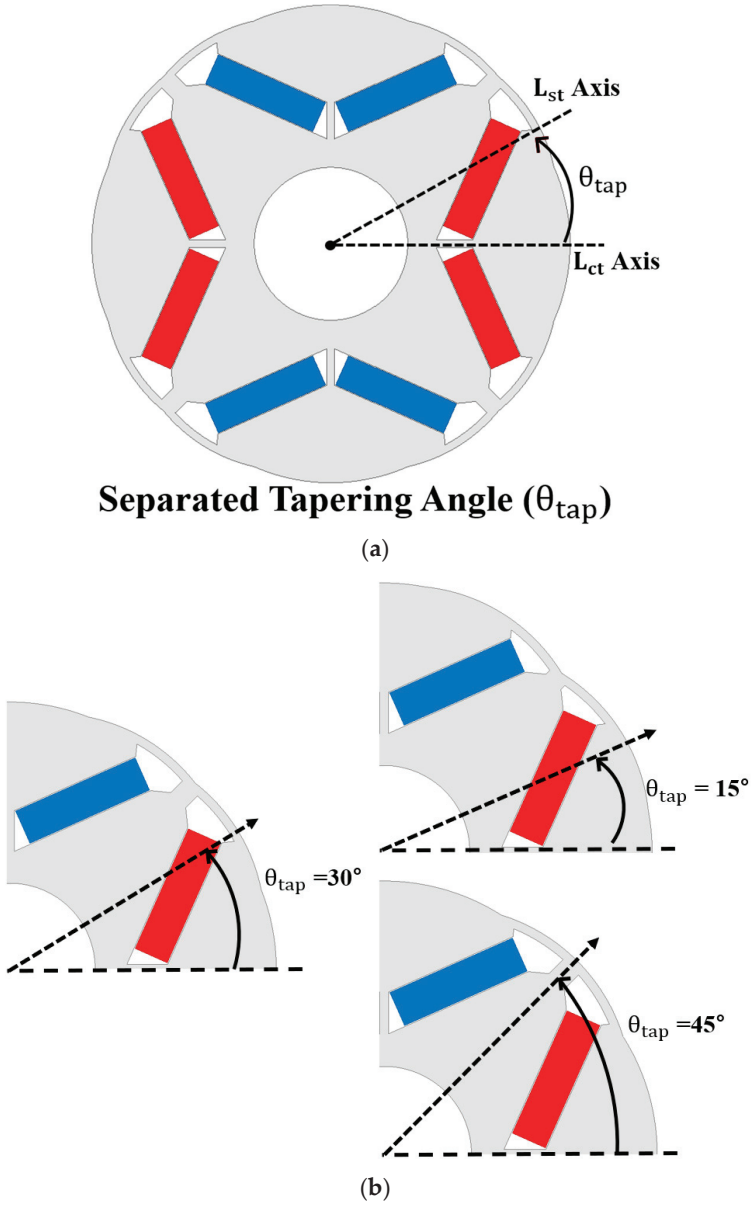

Figure 6. (**a**) Tapering in the L_{ct} and L_{st} axes, and the angle between them, θ_{tap} (**b**) changes in the rotor shape with variations in θ_{tap}.

This allows the magnetic flux emitted from the permanent magnets to be concentrated by the rotor tapering and by the stator tapering, and the magnetic flux is concentrated on the stator teeth. This design prevents leakage flux as much as possible and obtains a sinusoidal magnetic flux flow. In addition, the design does not affect the permanent magnets and does not cause reduction in output power.

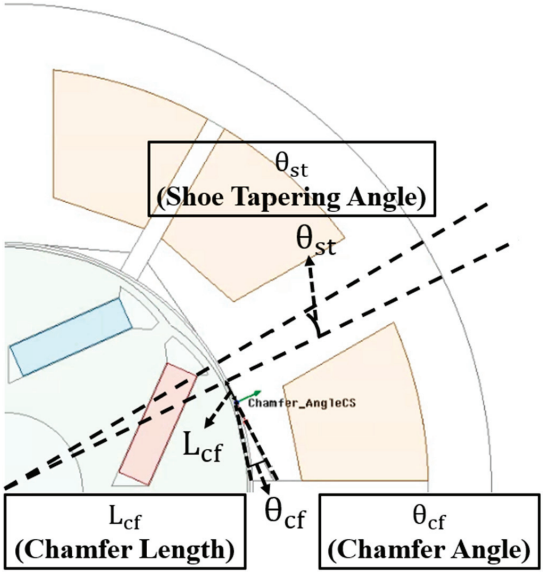

Figure 7. Stator tapering parameters.

Figure 8a shows the airgap magnetic flux density (airgap B) for the conventional model (Model 1) and the separated tapering model (Model 4), while (b) shows the harmonic distortion (THD) of the no-load line voltage by harmonic order. In (b), it can be observed that in Model 1, the fundamental component is naturally slightly larger, but there are significant increases in the 5th, 7th, 11th, and 13th harmonic components. The final model, Model 4, exhibits significantly reduced harmonics compared to the conventional Model 1, with the THD decreasing from 11.71% to 3.84%. THD stands for total harmonic distortion, and a higher THD value indicates that there are more harmonic components in the voltage waveform, signifying greater distortion from the ideal sinusoidal waveform. When harmonics distort the voltage waveform, it reduces stability. As a result, the significant reduction in THD observed in Model 4 indicates its improved stability and reliability compared with Model 1.

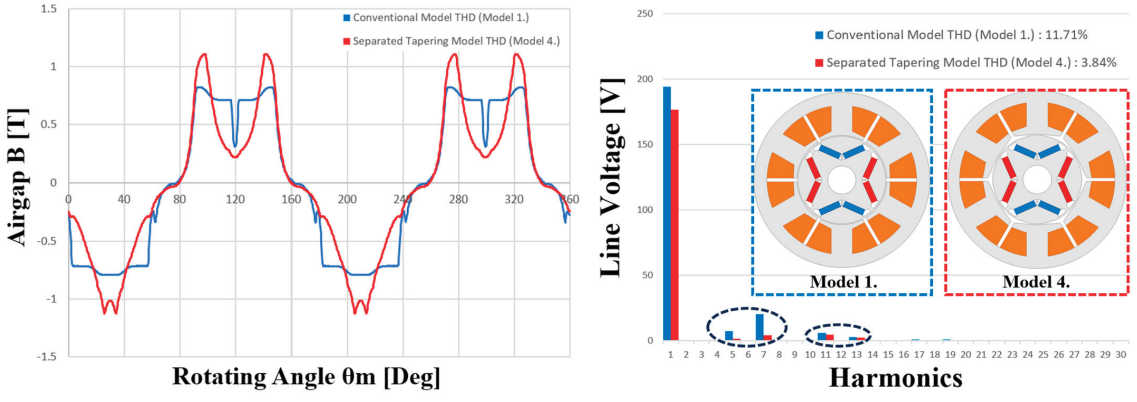

(**a**) (**b**)

Figure 8. (**a**) Airgap magnetic flux density for Model 1 and Model 4, (**b**) THD for Model 1 and Model 4.

The final model was selected based on K_{rip} values at two points, with a rated speed of 6600 rpm and a maximum speed of 9000 rpm. The existing concentrated winding model had a significant drawback, which was high torque ripple. To address this issue, this paper proposes a method to reduce torque ripple and mitigate the critical shortcomings of the existing rotor torque ripple. In this proposed approach, a new concept called "rotor separated tapering" is introduced, which can prevent output degradation and further reduce torque ripple. To complement the separated tapering of the rotor, the stator teeth are also tapered to drastically reduce torque ripple. This reduction in torque ripple is expected to minimize vibrations and noise not only at the rated speed but also at the maximum speed. Furthermore, tapering reduces the magnetic flux of the permanent magnets, allowing the center point known as the "M-point" of the voltage-limit locus to fall within the current limit area. This design offers significant advantages, especially for high-speed motor applications. It is also easy to manufacture, making it a groundbreaking production method for the electric motor industry. The design process was carried out based on the results data provided below.

4. Results

4.1. Data Analysis with Tapering Parameters

Table 1 presents the four-pole six-slot motor parameters for a 3 kW ETCH process. The final model was selected and data were analyzed at a rated speed of 6600 rpm. Additionally, a two-point design was conducted at 6600 rpm and 9000 rpm as part of the high-speed design process. While the rated operating speed is 6600 rpm, it is important to note that the instantaneous maximum speed can reach up to 9000 rpm. Therefore, a high-speed design was carried out to optimize performance at 9000 rpm. At the rated speed, the output is 4.45 Nm for a 3 kW motor. As explained earlier, the teeth-concentrated model was chosen for mass production. The rotor's permanent magnet is N42UH, a neodymium magnet, and the core material is 30PNF1600. The motor's total outer size diameter is 100 mm, and the lamination was designed at 45 mm.

Table 1. 4P6S motor parameters for a 3 kW ETCH process.

Parameter	Value	Unit
Poles/Slots	4/6	-
Speed	6600~9000	RPM
Current	11~18.4	A_{rms}
Rated power	3	kW
Rated torque	4.45	N·m
Airgap length	0.5	mm
Stator diameter (inner, outer)	25.5, 50	mm
Rotor diameter (inner, outer)	8, 25	mm
Stack length	45	mm
Material	Core	30PNF1600
	Permanent magnet	N42UH
	Coil	Copper

Figure 9 shows how the mesh settings were analyzed; the airgap mesh was divided very finely, and the data were analyzed in detail. More accurate data can be obtained when the mesh is analyzed by dividing the mesh into smaller pieces for the areas to be focused on. Since cogging torque and torque ripple are rotor- and stator-shape-sensitive, the mesh in the critical areas was finely divided to induce accurate analysis. The analysis was conducted using the 3D finite element analysis (FEA) capability of Ansys Maxwell 23.R2 software, with a total of 1,317,946 spatial elements, as shown in Figure 9. The specific area of interest in the motor, which requires a detailed analysis, is the air gap between the rotor and stator. Therefore, the number of elements in the air gap was divided into 601,250 elements. In Figure 9, each grid cell represents one spatial element.

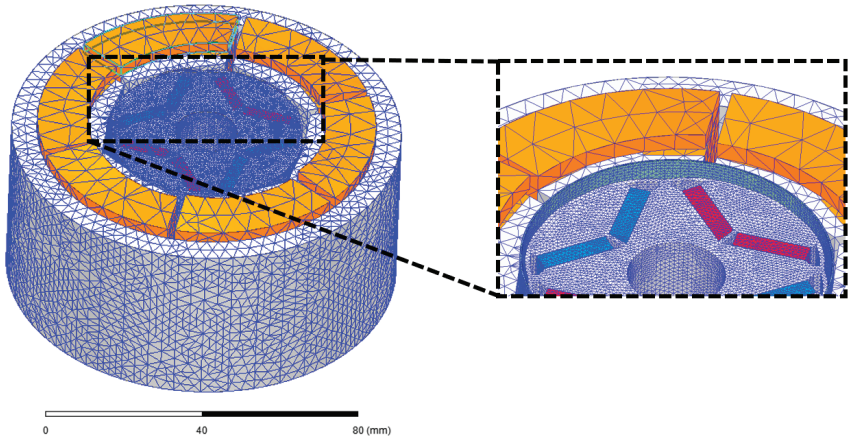

Figure 9. Mesh setting for 3D FEA (finite element analysis).

Figure 10 shows the cogging torque waveform at the rated speed of 6600 rpm. All four models were analyzed for data comparison, and finally, Model 1 was improved and designed into Model 4 to reduce the cogging torque by 88.18%. Figure 10 shows that the cogging torque is very low, at a level comparable to distributed windings. The final model was designed to reduce cogging torque at the rated operating speed of 6600 rpm. Since cogging torque is one of the causes of torque ripple, it is necessary to observe the trend of torque ripple while reducing the cogging torque. For this reason, the following data on torque ripple were analyzed [16,17,19,22].

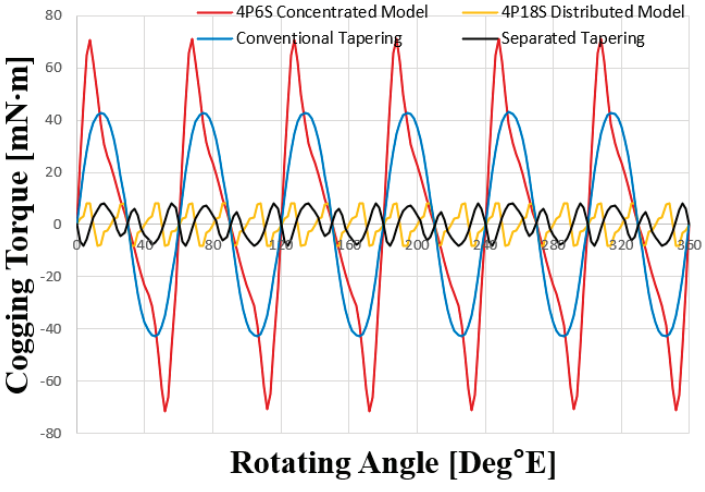

Figure 10. 6600 rpm cogging torque.

Figure 11 shows the relationship between torque ripple parameters and side tapering length. To minimize torque ripple, which is the primary objective in separated tapering, it is essential to find an optimal value that reduces torque ripple due to tapering length. Before determining this optimum value, certain factors need to be considered. The following are some of the considerations considered prior to selection [2,3,5,7,8].

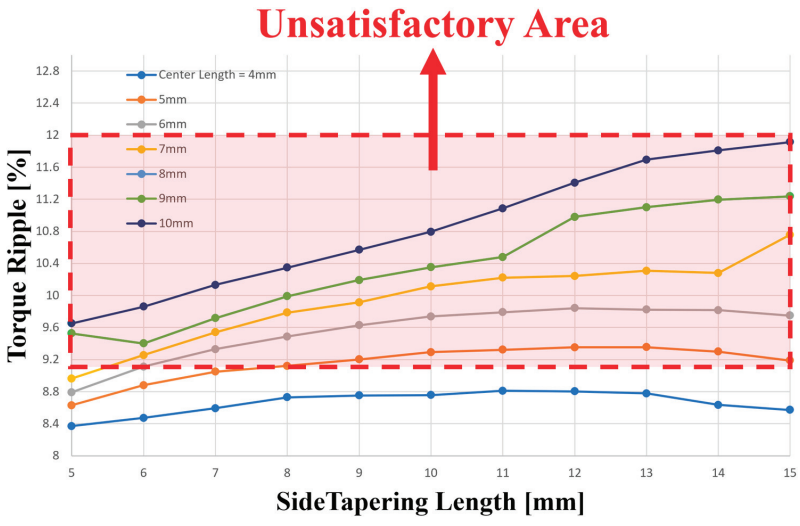

Figure 11. Variation of torque ripple with tapering length.

Considering the stiffness and the conventional model analysis with a tapering length of 5 mm, the optimal lengths of L_{ct} and L_{st} were chosen by selecting an area where the primary torque ripple target was less than 9.2%. θ_{tap} was analyzed with a temporary angle of 32 degrees that satisfied the target torque of 4.4 Nm. This angle was selected before the final shape was determined [8,22,23]. The variations in the values of L_{st} and θ_{tap} resulted in slight fluctuations in the outcomes, but these subtle differences are not significant. When designing, it is important to select the value of L_{st} within the range that satisfies the target conditions, since the primary focus is on meeting the specified design criteria.

Table 2 shows the data for the ripple factor K_{rip}. The ripple constant K_{rip} is defined as the load torque divided by the torque ripple (T_{ripple}). This design target was selected as a criterion so that K_{rip} would be greater than 1.06. The target value for the ripple constant K_{rip}, exceeding 1.06, is based on the rated speed of the conventional tapering model (Model 3) at 6600 rpm. The final model should be designed with a higher value of A than this. The angle range for θ_{tap} where K_{rip} is greater than 1.06 was determined by FEA analysis to be between 18 and 23 degrees [2,3].

Table 2. 6600 rpm FEA analysis results for the ripple factor K_{rip}.

θ_{tap}	Load Torque T_{avg} (Nm)	T_{ripple}	K_{rip} (Torque/T_{ripple})
15	4.4926	4.58977	0.978829
16	4.4898	4.530269	0.991067
17	4.4867	4.430873	1.012599
18	4.4833	4.202262	1.066878
19	4.4786	3.949895	1.133853
20	4.4736	3.683834	1.214387
21	4.4688	3.44164	1.298451
22	4.464	3.521505	1.26764
23	4.4582	3.806469	1.171217
24	4.451	4.279937	1.039969
25	4.4463	4.819738	0.922519
26	4.4402	5.420927	0.819085
27	4.4328	6.030049	0.735118

Table 2. *Cont.*

θ_{tap}	Load Torque T_{avg} (Nm)	T_{ripple}	K_{rip} (Torque/T_{ripple})
28	4.4263	6.68956	0.661673
29	4.4208	7.270177	0.608073
30	4.4139	7.816217	0.564711
31	4.4066	8.267145	0.533026
32	4.4011	8.727364	0.504287
33	4.4193	9.456249	0.467342
34	4.4141	9.700732	0.455028
35	4.4086	9.882956	0.446081
36	4.4049	10.04336	0.438588

Figure 12 shows the changes in torque ripple rate according to the side tapering angle (θ_{tap}). The data were analyzed to minimize torque ripple without degrading the output power. When optimally designed with respect to the θ_{tap} angle, the results show a significantly lower torque ripple compared with the conventional model. Additionally, implementing such a tapering method on the rotor does not affect the size of the permanent magnet, thus avoiding a reduction in power output. In conventional tapering, the permanent magnet is pushed into the rotor, leading to a drop in output. To compensate for this, the current was increased by 1.1 A to match the output. The area satisfying the goal of the torque ripple constant K_{rip}, as analyzed in Table 2, above, is intuitively depicted in Figure 12. Finally, an θ_{tap} angle was selected to achieve the target output, resulting in a reduction in torque ripple from 16.03% in the conventional model (Model 1) to 3.55%.

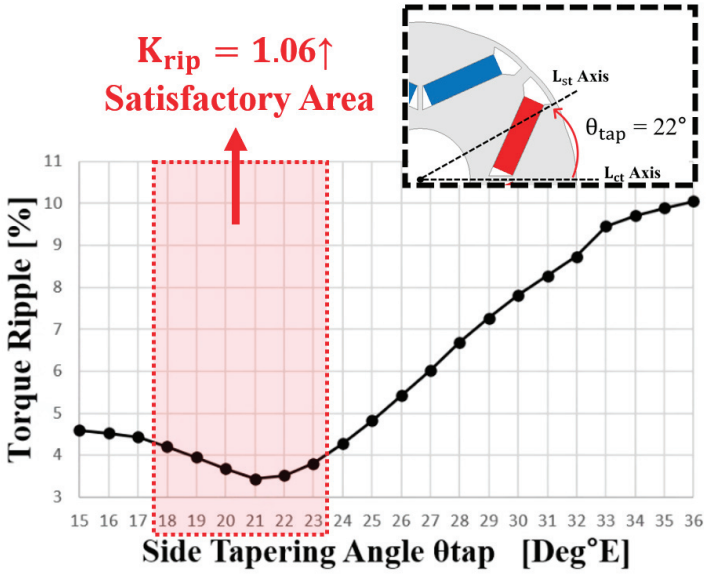

Figure 12. Analyzing torque ripple as a function of θ_{tap} angle.

4.2. Comparison of Analysis Data at Two Operation Points of 6600 rpm and 9000 rpm

Figure 13a shows the load-line voltage waveforms, indicating that voltage limits are generally considered and satisfied in the motor designs. Figure 13b shows the torque comparison at the same output for the three models when operating at the rated operating speed of 6600 rpm. The load-line voltage waveform in Figure 13a is used to monitor voltage fluctuations. Analyzing the load-line voltage waveform is crucial for evaluating the performance and stability of the motor and confirming voltage limits. As can be observed

in Figure 13a, the voltage is stable, and it satisfies the voltage limit conditions. When the torque variation (T_{pk2pk}) increases, it leads to an increase in torque ripple (T_{ripple}), which can be a source of motor vibrations. Therefore, designing to minimize torque variation (T_{pk2pk}) is essential. The separated tapering model shows less variation in torque. If the torque fluctuates significantly when the motor is running, the torque ripple becomes large, and vibration and noise are generated. Therefore, a new concept of tapering was applied to optimize the design to reduce the range of variation in torque magnitude and reduce torque ripple.

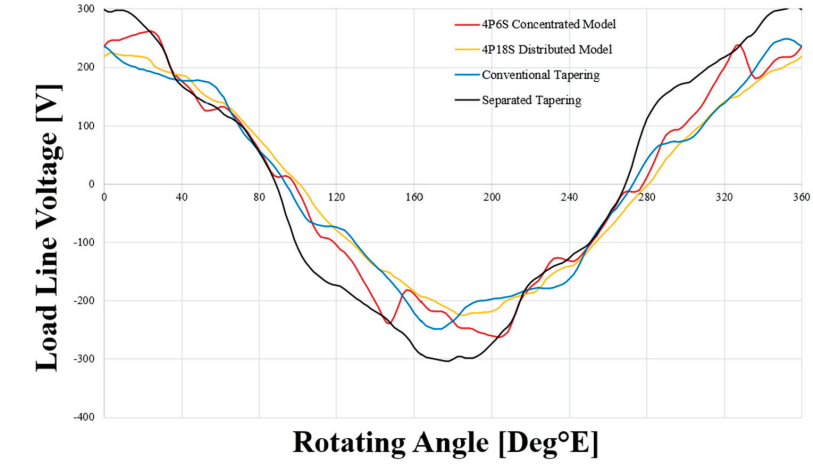

(**a**)

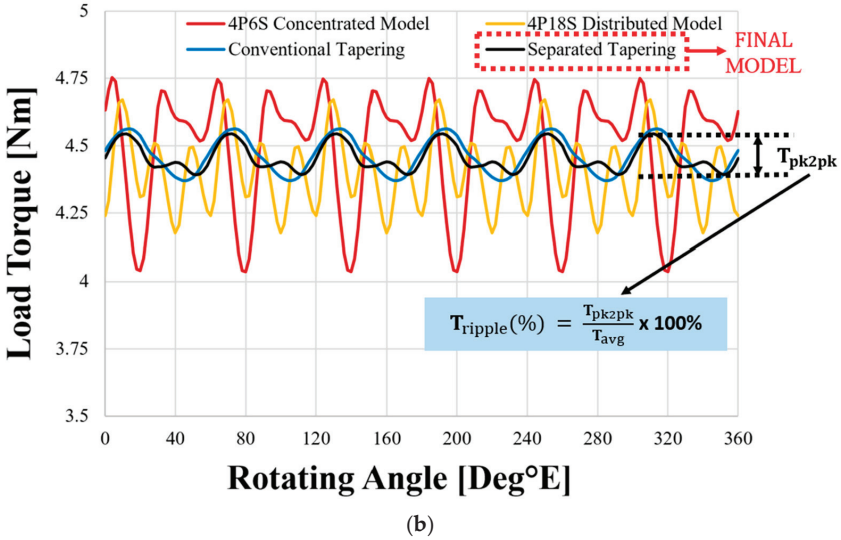

(**b**)

Figure 13. (**a**) 6600 rpm load-line voltage, (**b**) 6600 rpm load torque data.

Table 3 shows the data at 6600 rpm, the rated operating speed. It was specified that the design would proceed to reduce cogging torque and torque ripple, which are problems when changing from distributed to concentrated winding, by applying separated tapering (Model 4). As shown in Table 3, the cogging torque was reduced by 88.18%, from 142.44 mNm to 16.84 mNm, and the torque ripple was reduced by 77.85%, from 16.03% to 3.55%. The cogging torque was reduced not only in the existing model but also in the same

pole-number distribution winding model, and the torque ripple was reduced by 68.64%, from 11.32% to 3.55%.

Table 3. 6600 rpm Final Data Analysis.

Parameter	Basic Concentrated Winding Model (Model 1)	Distributed Winding Model (Model 2)	Conventional Tapering Model (Model 3)	Final Separated Tapering Model (Model 4)
Cogging torque (mNm)	142.44	16.26	176.17	16.84
Load torque (Nm)	4.49	4.44	4.45	4.46
Torque ripple (%)	16.03	11.32	4.2	3.55
K_{rip}	0.28	0.39	1.06	1.26
L2L + IR (Vmax)	238.97	216.73	224.22	228.02
Current (A)	13.4	14.2	19.5	18.4
Current density (A/mm^2)	8.53	9.42	12.35	11.71
Output power (kW)	3.01	3.01	3.03	3.04

Figure 14a shows the load-line voltage waveforms, indicating that voltage limits are generally considered and satisfied in the motor designs. Figure 14b shows the load torque at 9000 rpm. For the load-torque waveform, the black line is the separated tapering model. When the motor operates at high speed, the torque ripple increases. The red line in the basic model shows that the amplitude of the waveform is larger than the rated speed. This means that the torque ripple has increased. However, in the separated tapering model, the amplitude of the load torque is not so large. This indicates that the torque-ripple-reduction design was successful even at the maximum speed of 9000 rpm by applying separated tapering to the rotor. This new concept of tapering is very effective in reducing torque ripple when designing motors for high speeds.

Table 4 shows an analysis of the 9000 rpm data. The final model, Model 4, was confirmed to meet the target value of K_{rip} equal to or greater than 0.67 specified in Model 3, even at a maximum operating speed of 9000 rpm. Compared with the basic concentrated winding model (Model 1), the torque ripple was reduced by 78.29%, from 21.42% to 4.65%, and the efficiency was improved by 1.67%, from 93.08% to 94.64%. Thus, the separated tapering model (Model 4) is much more suitable in the high-speed operation area than the basic concentrated winding model (Model 1).

Table 4. 9000 rpm Final Data Analysis.

Parameter	Basic Concentrated Winding Model (Model 1)	Distributed Winding Model (Model 2)	Conventional Tapering Model (Model 3)	Final Separated Tapering Model (Model 4)
Load torque (Nm)	3.26	3.27	3.26	3.26
Torque ripple (%)	21.42	12.85	4.83	4.65
K_{rip}	0.15	0.25	0.67	0.7
L2L + IR (Vmax)	277.23	257.22	252.54	263.76
Current (A)	9.7	10.4	11.7	11
Current density (A/mm^2)	6.17	6.9	7.45	7
Output power (kW)	2.99	3.05	3.02	3.01

Figure 15a shows the efficiency map of Model 1, while Figure 15b displays the efficiency map of Model 4. The efficiency map allows us to intuitively see the efficiency according to rotating speed and torque. In the 6600~9000 rpm range from the rated operating speed to the maximum operating speed, it was confirmed that there was no problem, as in the below T-N curve analysis. Within the analyzed parameter range, Model 4 has an advantage at high speeds compared with Model 1. In Figure 15, the shaft torque represents the torque and considers losses such as copper loss, eddy current loss, iron loss, and so on in a PM motor. When comparing the same efficiency range in Figure 15a,b, it is intuitive to observe that Model 4, depicted in Figure 15b, exhibits higher efficiency from the rated operating speed of 6600 rpm up to the maximum operating speed of 9000 rpm, as evident from the efficiency map.

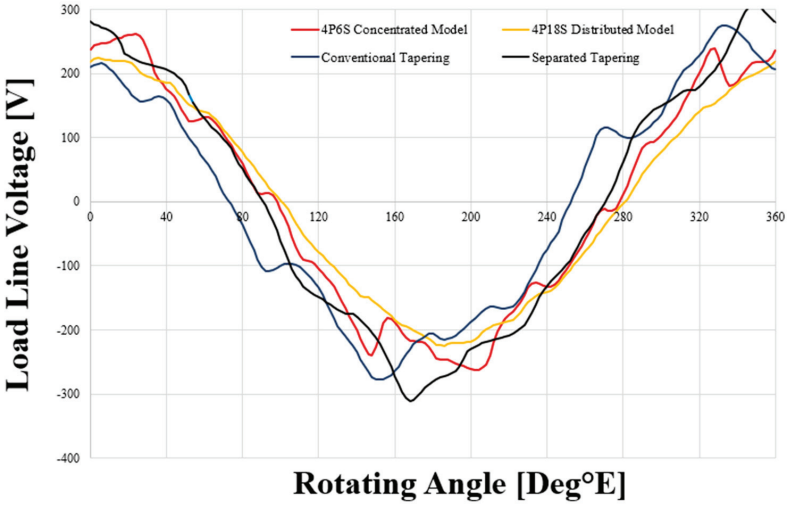

(**a**)

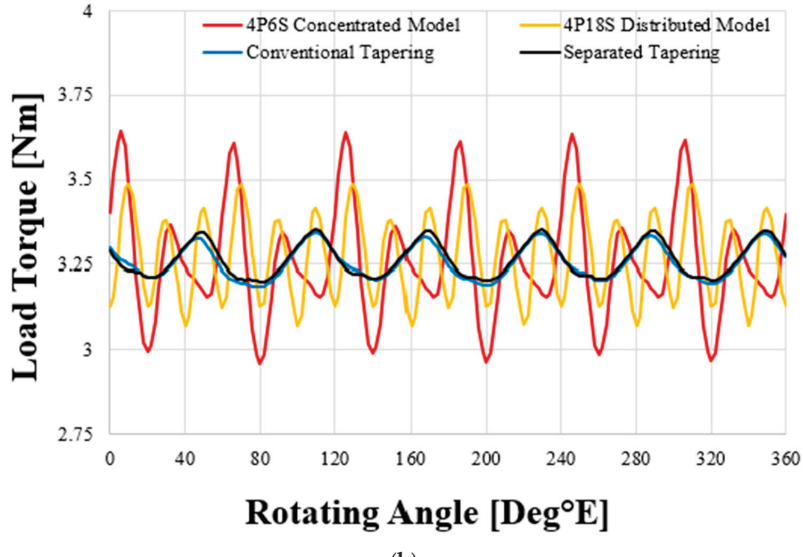

(**b**)

Figure 14. (**a**) 9000 rpm load-line voltage, (**b**) 9000 rpm load torque.

Figure 16a shows the current and voltage limits of the basic model (Model 1) and the separated tapering model (Model 4). Figure 16b shows the T-N curve comparison of the separated tapering model and the target model. Motors do not generate large, induced voltages in the low-speed range, and the voltage generated by the motor is often lower than the voltage that can be applied to the motor. When this is the case, control does not need to consider voltage limiting, only current limiting. This is MTPA control. However, in the speed range above the base speed, voltage limiting must be considered in addition to current limiting. The current vector is to be selected at the intersection where the voltage- and current-limit sources meet. The M point, the center of the current- and voltage-limit circle, is more favorable for higher speeds when it is near the center of the current-limit circle. The current- and voltage-limit circle for the separated tapering model is shown

in Figure 16, and the center point M of the voltage-limit circle for the separated tapering model is inside the current-limit circle. This is because the rotor tapering has reduced the chain flux of the permanent magnet that determines the position of the M point. It can be seen in Figure 16 that the separated tapering model also has higher base torque than the target model and is more advantageous in the high-speed area. The voltage limit is applied at 6000 rpm for the target model, but at 8300 rpm for the separated tapering model. At an operating speed of 9000 rpm, the T-N curve shows that the separated tapering model is much higher, indicating that the separated tapering model has an advantage in operating in the high-speed range. Considering the maximum speed up to 9000 rpm, the design proceeded as follows [12,14].

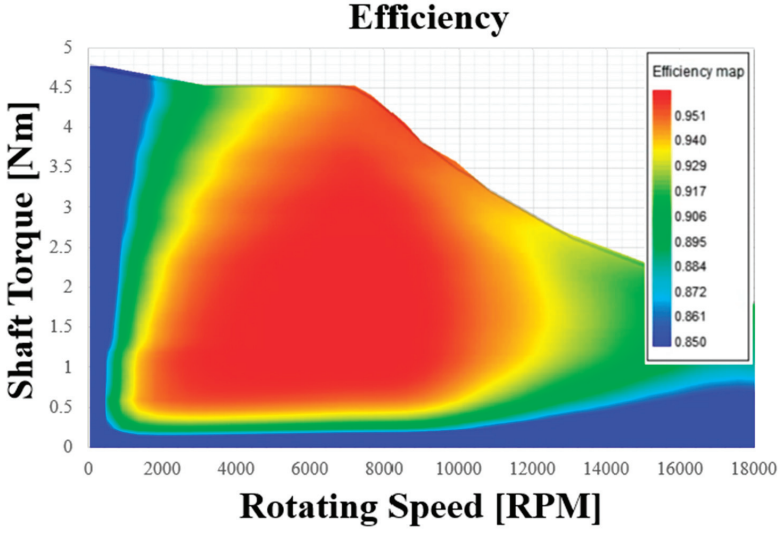

(**a**)

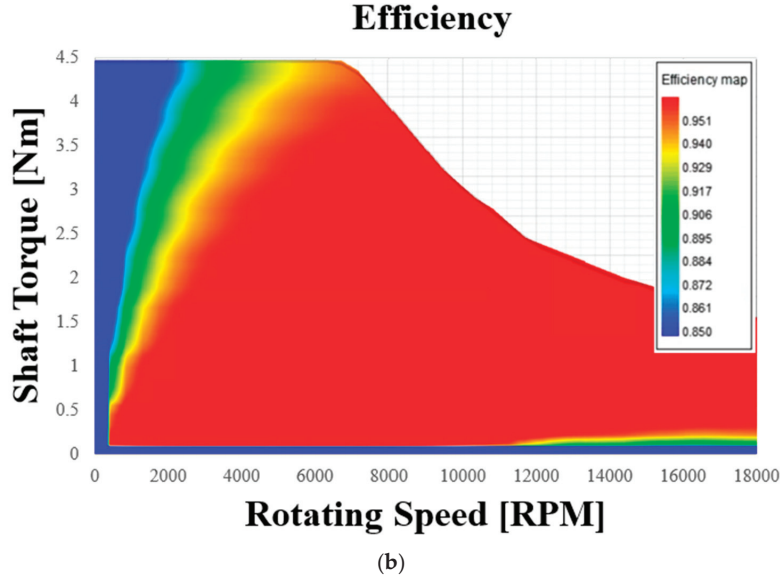

(**b**)

Figure 15. (**a**) Model 1 efficiency map, (**b**) Model 4 (separated tapering) efficiency map.

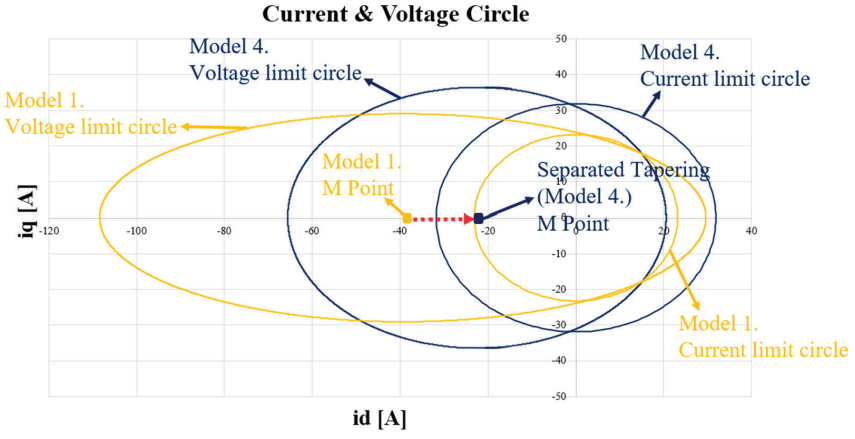

(**a**)

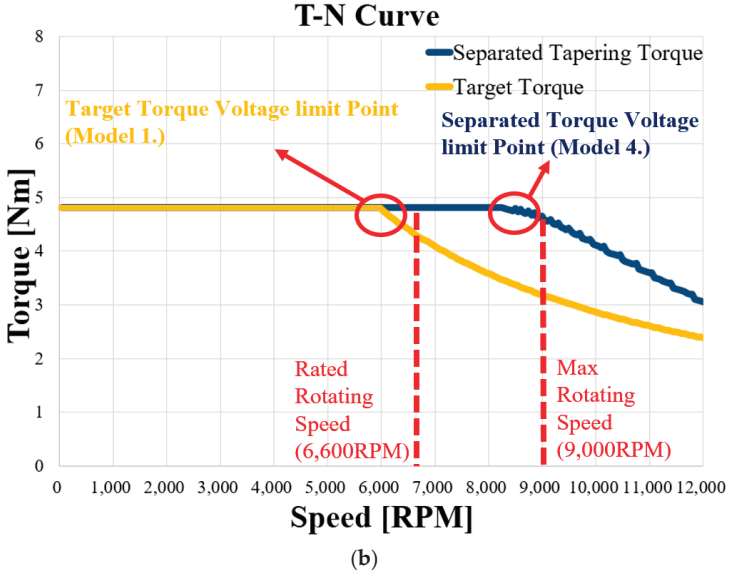

(**b**)

Figure 16. (**a**) Current- and voltage-limit circle, (**b**) T-N curve.

Figure 17a shows radial B as a function of rotor position for the conventional model (Model 1) and the separated tapering model (Model 4), while Figure 17b shows the vibration velocity [m/s] with respect to spatial distribution. In Figure 17a, when compared with the conventional model, the radial B of spatial flux density is sinusoidal, and the magnitude of the radial force is lower. Radial force refers to the force generated in the radial direction as the rotor rotates away from the center. Electromagnetic vibrations are primarily caused by the spatial distribution of radial force over time. Since radial force is expressed as the square of airgap flux density, the spatial harmonics of airgap flux density affect the spatiotemporal harmonics of radial force. The larger the radial force, the greater the motor's vibrations, leading to poor stability. The radial force of a motor can lead to vibration and noise issues, making control more challenging. Moreover, there is a significant safety risk when there is contact between the stator and rotor. In Figure 17a, Model 4 exhibits a more sinusoidal and stable waveform compared with Model 1, due to its lower radial force, and Figure 17b represents vibration velocity, showing the values of spatially distributed

vibrations by harmonic order. It can be observed that Model 4 has an overall vibration value approximately 13.18% lower than Model 1 [14,18]. As seen in Figure 17, Model 4 has a lower radial force compared with Model 1, which results in lower vibration velocity in the motor.

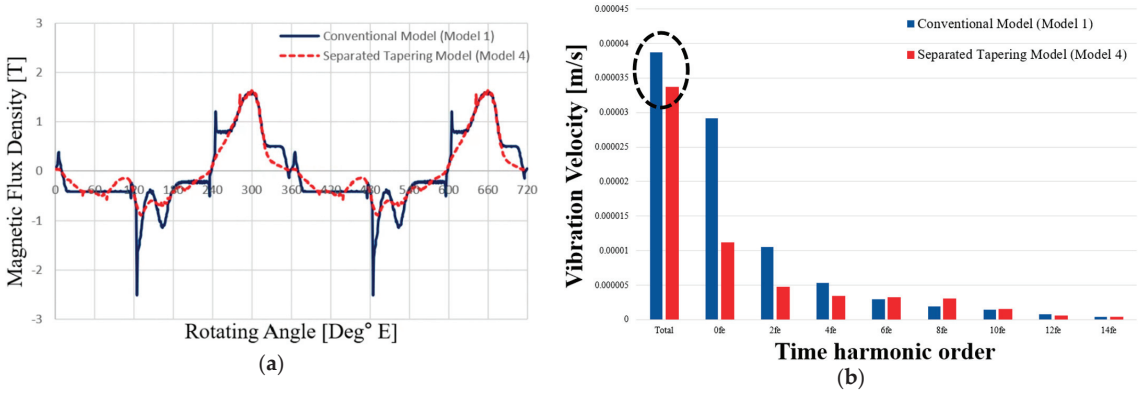

Figure 17. (**a**) Radial B for Model 1 and Model 4, (**b**) vibration velocity for Model 1 and Model 4.

4.3. Analysis of B Plots, and Demagnetization of Permanent Magnet Check

By concentrating the magnetic flux exiting the air gap as in the separated tapering model, the amount of magnetic flux received from the stator teeth increases. However, the amount of magnetic flux density that can be received by the thickness of the stator teeth is limited, and if the limit is exceeded, the teeth will become saturated. The saturation also affects the increase in iron loss, which causes heat generation and affects the overall performance. Therefore, it is important to consider the saturation of the stator teeth during the design process, and this is shown in Figure 18. As shown below, the saturation degree of the stator value is approximately 1.45 T, indicating that the design is sufficiently stable. Additionally, the stator back yoke is approximately 1.32 T and is extremely stable.

The demagnetization capability of the permanent magnet was confirmed for the improved design model, as shown in Figure 19. Demagnetization of the permanent magnets must be considered when designing electromagnetic fields; the IPMSM performs weak flux control at high speeds, and demagnetization phenomena may occur due to reverse magnetic fields. If the operating point is formed below the knee point in the B-H curve of the permanent magnet, the permanent magnet loses magnetism and demagnetization occurs. After demagnetization, even if the operating point is formed above the knee point again, the permanent magnet cannot return to the magnetic flux density it had before and has a lower flux density than before, which is called the irreversible demagnetization phenomenon. When a magnet is demagnetized, the magnetic flux density of the permanent magnet is affected, which in turn affects the performance of the motor. The next method of confirming demagnetization of a permanent magnet was to apply a current five times the rated current and confirm a demagnetization ratio of 0% for the permanent magnet. In addition, since NdFeB magnets have high-temperature demagnetization characteristics, the demagnetization ability of the permanent magnet was confirmed through 2D and 3D FEA analysis using B-H curve values of NdFeB magnets at 150 °C, considering extreme conditions at high temperatures.

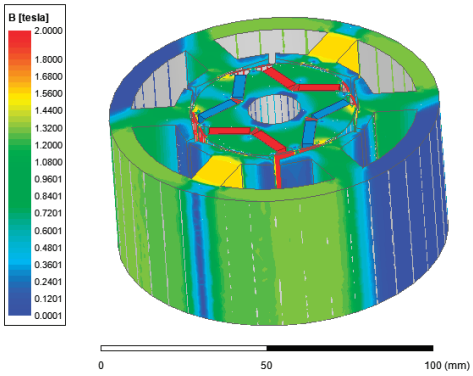

Figure 18. Separated tapering 3D-model B plot.

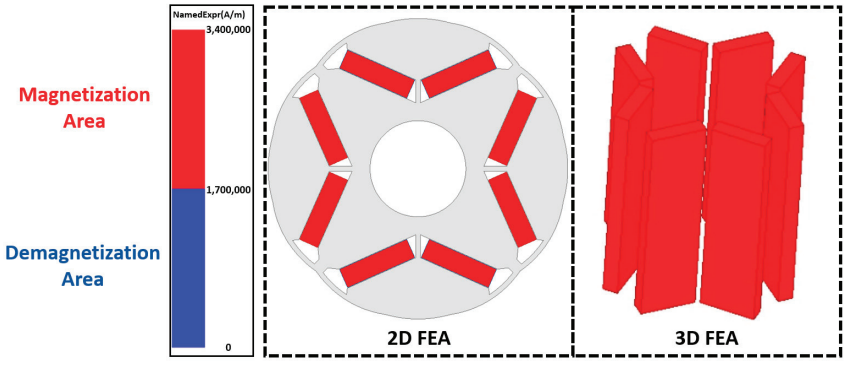

Figure 19. Magnetization and demagnetization of permanent magnet: 2D and 3D analysis.

5. Conclusions

This paper presents a new concept model of separated tapering to reduce cogging torque and torque ripple compared with the conventional concentrated model of a 3 kW semiconductor-ETCH-process vacuum pump motor. The design proceeded to reduce cogging torque and torque ripple according to the rotating angle of θ_{tap}. Since cogging torque and torque ripple are major causes of vibration and noise in motors, it is important to design motors used in vibration-sensitive semiconductor processes to reduce cogging torque and torque ripple. The final model with separated tapering (Model 4) was subjected to two-point design at a rated operating speed of 6600 rpm and a maximum operating speed of 9000 rpm. The reduction in torque ripple was confirmed for both rated and maximum speeds. The cogging torque and torque ripple of the basic concentrated model (Model 1) and the separated tapering model (Model 4) were compared and analyzed through finite element analysis (FEA). At the rated rotating speed of 6600 rpm, the cogging torque was reduced by 88.18% from 142.44 mNm in the conventional model to 16.84 mNm, and the torque ripple was reduced by 77.85% from 16.03% to 3.55%. At a maximum rotating speed of 9000 rpm, the torque ripple was reduced by 77.85%, from 16.03% in the conventional model to 3.55%, and the overall vibration, as a result of torque-ripple reduction, decreased by 13.18%. The final proposed model (Model 4) includes an innovative separated tapering design that minimizes cogging torque and torque ripple while also being advantageous at high speeds.

Author Contributions: Conceptualization, W.-H.K.; methodology, D.-H.C.; software, M.-K.H.; validation, D.-H.C.; formal analysis, I.-J.Y.; investigation, I.-J.Y.; resources, D.-H.C.; data curation, D.-H.C.; writing—original draft preparation, D.-H.C.; writing—review and editing, M.-K.H. and D.-H.J.; visualization, D.-H.C. and D.-H.J.; supervision, W.-H.K. All authors have read and agreed to the published version of the manuscript.

Funding: This research was partly supported by the Korea Institute of Energy Technology Evaluation and Planning (KETEP) grant funded by the Korea government (MOTIE) (20214000000060, Department of Next Generation Energy System Convergence based on Techno-Economics STEP) and in part by the Gachon University research fund of 2021 (GCU-202110130001)

Data Availability Statement: Not applicable.

Conflicts of Interest: The authors declare no conflict of interest.

References

1. Xu, J.; Zhang, L.; Meng, D.; Su, H. Simulation, Verification and Optimization Design of Electromagnetic Vibration and Noise of Permanent Magnet Synchronous Motor for Vehicle. *Energies* **2022**, *15*, 5808. [CrossRef]
2. Alharkan, H. Torque Ripple Minimization of Variable Reluctance Motor Using Reinforcement Dual NNs Learning Architecture. *Energies* **2023**, *16*, 4839. [CrossRef]
3. Lee, M.; Hwang, Y.; Nam, K. Torque Ripple Minimizing of Uniform Slot Machines with Delta Rotor via Subdomain Analysis. *Energies* **2021**, *14*, 7390. [CrossRef]
4. Qu, C.; Guo, Z.; Hu, Y.; Wang, X.; Han, F. Multi-Objective Optimization Design of a New Permanent Magnet Synchronous Motor Based on the Taguchi Method. *Energies* **2022**, *15*, 7347. [CrossRef]
5. Caruso, M.; Di Tommaso, A.O.; Miceli, R.; Viola, F. A Cogging Torque Minimization Procedure for Interior Permanent Magnet Synchronous Motors Based on a Progressive Modification of the Rotor Lamination Geometry. *Energies* **2022**, *15*, 4956. [CrossRef]
6. Tao, X.; Takemoto, M.; Tsunata, R.; Ogasawara, S. Novel Rotor Structure Employing Large Flux Barrier and Disproportional Airgap for Enhancing Efficiency of IPMSM Adopting Concentrated Winding Structure. *IEEE Access* **2023**, *11*, 2848–2862. [CrossRef]
7. Lee, C.-S.; Kim, H.-J. Harmonic Order Analysis of Cogging Torque for Interior Permanent Magnet Synchronous Motor Considering Manufacturing Disturbances. *Energies* **2022**, *15*, 2428. [CrossRef]
8. Akiki, P.; Hassan, M.H.; Bensetti, M.; Dessante, P.; Vannier, J.C.; Prieto, D.; McClelland, M. Multiphysics Design of a V-Shape IPM Motor. *IEEE Trans. Energy Convers.* **2018**, *33*, 1141–1153. [CrossRef]
9. Egorov, D.; Petrov, I.; Pyrhönen, J.J.; Link, J.; Stern, R.; Sergeant, P.; Sarlioglu, B. Hysteresis Loss in NdFeB Permanent Magnets in a Permanent Magnet Synchronous Machine. *IEEE Trans. Ind. Electron.* **2022**, *69*, 121–129. [CrossRef]
10. Hwang, S.-W.; Lim, M.-S.; Hong, J.-P. Hysteresis Torque Estimation Method Based on Iron-Loss Analysis for Permanent Magnet Synchronous Motor. *IEEE Trans. Magn.* **2016**, *52*, 8204904. [CrossRef]
11. Liu, G.; Liu, M.; Zhang, Y.; Wang, H.; Gerada, C. High-Speed Permanent Magnet Synchronous Motor Iron Loss Calculation Method Considering Multiphysics Factors. *IEEE Trans. Ind. Electron.* **2020**, *67*, 5360–5368. [CrossRef]
12. Yamazaki, K.; Seto, Y. Iron loss analysis of interior permanent-magnet synchronous motors-variation of main loss factors due to driving condition. *IEEE Trans. Ind. Appl.* **2006**, *42*, 1045–1052. [CrossRef]
13. Yamazaki, K.; Kumagai, M.; Ikemi, T.; Ohki, S. A Novel Rotor Design of Interior Permanent-Magnet Synchronous Motors to Cope with Both Maximum Torque and Iron-Loss Reduction. *IEEE Trans. Ind. Appl.* **2013**, *49*, 2478–2486. [CrossRef]
14. Yamazaki, K.; Ishigami, H. Rotor-Shape Optimization of Interior-Permanent-Magnet Motors to Reduce Harmonic Iron Losses. *IEEE Trans. Ind. Electron.* **2010**, *57*, 61–69. [CrossRef]
15. Kim, K.-C.; Jeon, S.-H. Analysis on Correlation Between Cogging Torque and Torque Ripple by Considering Magnetic Saturation. *IEEE Trans. Magn.* **2013**, *49*, 2417–2420. [CrossRef]
16. Dosiek, L.; Pillay, P. Cogging Torque Reduction in Permanent Magnet Machines. *IEEE Trans. Ind. Appl.* **2007**, *43*, 1565–1571. [CrossRef]
17. Seo, J.H.; Choi, H.S. Cogging Torque Calculation for IPM Having Single Layer Based on Magnetic Circuit Model. *IEEE Trans. Magn.* **2014**, *50*, 8102104. [CrossRef]
18. Hwang, S.M.; Eom, J.B.; Hwang, G.B.; Jeong, W.B.; Jung, Y.H. Cogging torque and acoustic noise reduction in permanent magnet motors by teeth pairing. *IEEE Trans. Magn.* **2000**, *36*, 3144–3146. [CrossRef]
19. Lukaniszyn, M.; Jagiela, M.; Wrobel, R. Optimization of permanent magnet shape for minimum cogging torque using a genetic algorithm. *IEEE Trans. Magn.* **2004**, *40*, 1228–1231. [CrossRef]
20. Abbaszadeh, K.; Alam, F.R.; Teshnehlab, M. Slot opening optimization of surface mounted permanent magnet motor for cogging torque reduction. *Energy Convers. Manag.* **2012**, *55*, 108–115. [CrossRef]
21. Liu, T.; Huang, S.D.; Gao, J.; Lu, K.Y. Cogging torque reduction by slot-opening shift for permanent magnet machines. *IEEE Trans. Magn.* **2013**, *49*, 4028–4031. [CrossRef]
22. Koh, C.S.; Seol, J.S. New cogging-torque reduction method for brushless permanent-magnet motors. *IEEE Trans. Magn.* **2003**, *39*, 3503–3506.

23. Bianchi, N.; Bolognani, S. Design techniques for reducing the cogging torque in surface-mounted PM motors. *IEEE Trans. Ind. Appl.* **2002**, *38*, 1259–1265. [CrossRef]
24. Bianchini, C.; Immovilli, F.; Lorenzani, E.; Bellini, A.; Davoli, M. Review of design solutions for internal permanent-magnet machines cogging torque reduction. *IEEE Trans. Magn.* **2012**, *48*, 2685–2693. [CrossRef]
25. Islam, R.; Husain, I.; Fardoun, A.; McLaughlin, K. Permanent-magnet synchronous motor magnet designs with skewing for torque ripple and cogging torque reduction. *IEEE Trans. Ind. Appl.* **2009**, *45*, 152–160. [CrossRef]
26. Ishikawa, T.; Slemon, G.R. A method of reducing ripple torque in permanent-magnet motors without skewing. *IEEE Trans. Magn.* **1993**, *29*, 2028–2031. [CrossRef]

machines

MDPI

Article

Study on Single-Phase BLDC Motor Design through Drive IC Integration Analysis

Ye-Seo Lee [1], Na-Rim Jo [1], Hyun-Jo Pyo [2], Dong-Hoon Jung [3] and Won-Ho Kim [2,*]

[1] Department of Next Generation Energy System Convergence, Gachon University, Seongnam 13120, Republic of Korea; aaabbb0127@gachon.ac.kr (Y.-S.L.); rimna22@gachon.ac.kr (N.-R.J.)
[2] Department of Electrical Engineering, Gachon University, Seongnam 13120, Republic of Korea; vdsl00700@gachon.ac.kr
[3] Department of Mechanical, Automotive and Robot Engineering, Halla University, Wonju 26404, Republic of Korea; dh.jung@halla.ac.kr
* Correspondence: wh15@gachon.ac.kr

Abstract: In this paper, a single-phase BLDC motor is applied to a cooling fan motor and a Drive IC integration analysis method of the single-phase BLDC motor is proposed. Single-phase BLDC motors have a simple structure, are easy to manufacture, and are low cost, so they are used in applications where low outputs and low costs are advantageous. Single-phase BLDC motors use a full-bridge inverter (Drive IC), and this inverter (Drive IC) has dead time due to switching. Therefore, in order to consider dead time when analyzing a single-phase BLDC motor, analysis through integration with Drive IC is necessary. This paper compares the types of single-phase BLDC motors, designs a model that satisfies target performance, and conducts research on Drive IC integration analysis through FEA. A prototype motor was manufactured and tested, and the validity of the Drive IC integration analysis was verified.

Keywords: single-phase BLDC motor; radial flux permanent magnet motor; full-bridge inverter; drive IC integration analysis

Citation: Lee, Y.-S.; Jo, N.-R.; Pyo, H.-J.; Jung, D.-H.; Kim, W.-H. Study on Single-Phase BLDC Motor Design through Drive IC Integration Analysis. *Machines* **2023**, *11*, 1003. https://doi.org/10.3390/machines11111003

Academic Editors: Loránd Szabó and Feng Chai

Received: 30 September 2023
Revised: 25 October 2023
Accepted: 28 October 2023
Published: 1 November 2023

1. Introduction

The existing microwave oven (MWO) cooling fan motor uses a 5W-rated shaded-pole induction motor (SPIM), as shown in Figure 1. The SPIM is characterized by a structure where the main concentrated winding is wound around the stator core, resulting in high losses in both copper and core, leading to low efficiency. However, due to its low cost, it is mainly used in low-power applications [1]. Although this type of induction motor has low efficiency and is unable to control variable speeds, it has the advantage of being simple to manufacture and having a stable structure. Accordingly, research has been conducted on design optimization for high performance and stable structure, as well as on cooling methods for high-loss induction motors [2] and on the accurate prediction of the stator winding temperature [3]. In the household appliance market, cost reduction has been prioritized over efficiency concerns, leading to the adoption of induction motors with low efficiency but competitive pricing. However, previously used SPIMs lacked speed control capabilities, requiring the use of different motors for fan applications that require different torque levels at different speeds. This resulted in an increase in fan motor management and operating costs. In this regard, research is needed to apply permanent magnet motors with high torque density, efficiency, and variable speed control to cooling fan motors. By replacing the existing SPIM with a permanent magnet motor, the use of variable speed control allows for the utilization of a single motor, thereby reducing management and operating costs. In addition, the higher output density in comparison to induction motors leads to a reduction in the use of magnets, windings, and cores.

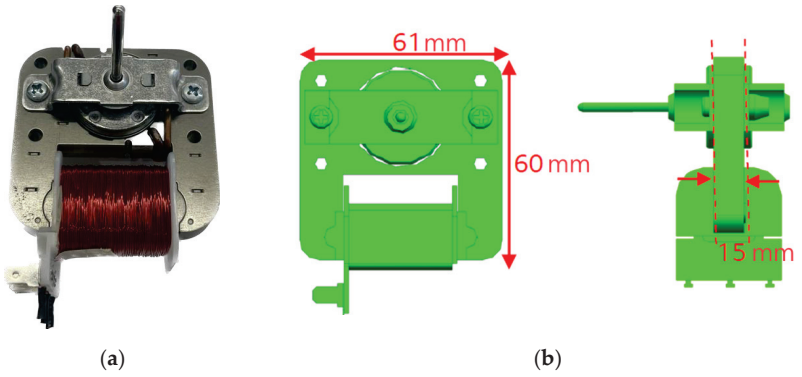

(**a**) (**b**)

Figure 1. Existing cooling fan motor (SPIM): (**a**) cooling fan motor (SPIM); and (**b**) cooling fan motor (SPIM) size.

Permanent magnet synchronous motors are classified into radial flux motors (RFM) and axial flux motors (AFM), depending on the direction of the magnetic flux. AFM is a motor that is advantageous for applications where a short axial length is crucial, especially in fields where high output density is important. However, unlike the RFM, which has a small difference in torque density depending on the number of poles in the same volume, AFM has the characteristic of increasing torque density as the number of poles increases, so RFM is advantageous with its small number of poles [4]. RFMs are largely divided based on the magnet's position into interior permanent magnet motors (IPM) and surface permanent magnet motors (SPM). An IPM has magnets positioned inside the rotor core, resulting in a higher magnetic flux density compared to SPM [5]. However, IPMs present challenges in aligning the centers of the rotor and stator due to the magnet's location inside the rotor core, and this eccentricity leads to difficulties in manufacturing and generates magnetic saturation [6,7]. On the other hand, SPM has magnets positioned outside the rotor core toward the stator, and has a simple structure, which makes it easier to manufacture, more convenient to maintain, and more cost-effective to produce [8]. In this regard, research has been conducted to reduce the costs of permanent magnet motors, especially surface permanent magnet motors (SPM), which are easier to manufacture and have lower production costs. Studies have focused on reducing the cost of magnets as a means of general costs reduction. Research has been conducted on hybrid magnets aimed at reducing the cost of magnets, resulting in a 37.9% reduction in torque cost [8]. In addition, studies have been conducted to explore magnetic shapes that allow for a reduction in magnet usage and save processing time, thereby reducing both raw material and processing costs [9].

Permanent magnet motors are mainly used in three phase or single phase. Three-phase motors are driven by a rotating magnetic field and have a high power density, high power factor, and high output density. On the other hand, single-phase motors are driven by an alternating magnetic field and have a lower output density and higher torque ripple than three-phase motors. However, they have a simple structure and are cost-effective. Furthermore, single-phase motors have the advantage of low controller costs and simple manufacturing requirements, making them suitable for mass production [10–14]. As a result, three-phase motors are preferred in applications that require high output, while single-phase motors are preferred in household applications where low output and cost-effectiveness are advantageous. This paper focuses on the research of a single-phase surface permanent magnet BLDC motor, which has a simple manufacturing process, is cost effective and suitable for low output applications.

In this paper, a single-phase BLDC motor is applied to a MWO cooling fan motor, that requires a low output and low cost characteristics in a limited volume. To meet the performance requirements in a limited volume, this paper compares four types of single-

phase BLDC motors: R-Type, C-Type, internal rotor type, and external rotor type. The performance characteristics and cost comparisons between C-Type and external rotor types are analyzed, and a proposed external rotor type that satisfies cost savings is presented. In the design of a single-phase BLDC motor, an asymmetrical air gap structure was applied to ensure the starting torque by creating a phase difference in the cogging torque according to the characteristics of the single-phase motor driven by alternating magnetic fields. In addition, to account for the impact of dead time in the full-bridge inverter (Drive IC), a design using a Drive IC was assessed to ensure the accuracy of the analysis.

This paper consists of a total of five sections. In Section 2, the design considerations of a single-phase BLDC motor are discussed, including the torque equation, Drive IC integration analysis, and the structure required for starting torque. Section 3 compares four types of single-phase BLDC motors and designs a motor to meet the target performance for C-Type and external rotor single-phase BLDC motors that are advantageous in satisfying the target torque. Additionally, a performance comparison is conducted through analysis of integrated Drive IC. Section 4 selects the motor that meets the desired performance and cost-saving standards, and validates the Drive IC integration analysis through the production of a prototype motor. Section 5 summarizes the conclusions of this paper. The design and integration of the Drive IC in this paper were performed using Ansys 2022 Maxwell software and the validity of the proposed Drive IC integration analysis is verified through finite element analysis (FEA) and the production and testing of a prototype motor.

2. Considerations in the Design of a Single-Phase BLDC Motor

2.1. Torque Equation for a Single-Phase BLDC Motor

A single-phase BLDC motor is a maintenance-free motor due to the use of an electrical commutating mechanism instead of a commutator and brushes. It is widely used in applications that require compactness due to its less complex design in comparison to three-phase motors. In a BLDC motor, the torque varies because the magnetic resistance of the air gap varies depending on the rotor's position due to the stator teeth. Equation (1) represents the torque constant as a function of rotor position, Equation (2) represents the voltage equation for a single-phase BLDC motor, and Equation (3) represents the torque equation [15].

$$k_e = n \times \frac{\Delta\lambda}{\Delta\theta} \tag{1}$$

where λ is flux linkage of a coil, θ is the rotor position in radian, n is the number of coils in the series.

$$\begin{aligned} e_b &= k_e(\theta,\ i) \times \omega \\ v_{io} &= i \times R + L \times \tfrac{di}{dt} + e_b \end{aligned} \tag{2}$$

$$T_m = k_e(\theta,\ i) \times i + T_{cg}(\theta) \tag{3}$$

where e_b is back EMF, k_e is EMF constant which is the function of the rotor position, i is winding current, ω is angular velocity, v_{io} is inverter output voltage, T_m is motor torque, and T_{cg} is cogging torque as a function of rotor position θ.

2.2. Single-Phase Drive IC Integration Analysis

For motor control, a single-phase BLDC motor can use either a single-phase half-bridge inverter or a single-phase full-bridge inverter. The half-bridge inverter circuit generates AC voltage for single-phase motors. The operation of the half-bridge inverter involves alternating the switches on and off at every half-cycle of the required AC voltage frequency period T. Equation (4) represents the fundamental and harmonic components of the inverter, and Equation (5) provides the root mean square (RMS) value of the fundamental voltage.

Based on Equation (5), the inverter can deliver 45% of the DC input voltage to the load in terms of the RMS value of the AC voltage.

$$v_p = \frac{2V_{dc}}{\pi} \sum_{n=1,3,5\cdots}^{\infty} \frac{sinn\omega t}{n} \; (n = 1,\ 3,\ 5, \cdots) \tag{4}$$

$$V_{p1-rms} = \frac{1}{\sqrt{2}} \frac{2V_{dc}}{\pi} = 0.45V_{dc} \tag{5}$$

Due to its inefficient utilization of DC voltage, the single-phase half-bridge inverter is not a suitable option for generating effective single-phase AC voltage. Therefore, the full-bridge inverter is used. Figure 2 represents the circuit and output voltage of the single-phase full-bridge inverter. In order to obtain an effective single-phase AC voltage, each voltage must be switched with a phase difference of 180 degrees. Therefore, switches D1, D2, and switches D3, D4 alternate between on and off states. The fundamental and harmonic components during that period are represented by Equation (6). The single-phase full-bridge inverter is predominantly used because it can obtain twice the AC voltage compared to the half-bridge inverter, all under the same DC voltage. The output voltage of the single-phase full-bridge inverter is provided in Equation (7), where the H Pole and L Pole represent the sections of switches as shown in Figure 2, with the H Pole corresponding to switches D_1 and D_4, and the L Pole corresponding to switches D_2 and D_3. V_H denotes the pole voltage for H Pole, V_L represents the pole voltage for L Pole, S_H is the switching function for H Pole, and S_L is the switching function for L Pole [16].

$$v_o = \frac{4V_{dc}}{\pi} \sum_{n=1,3,5\cdots}^{\infty} \frac{sinn\omega t}{n} \; (n = 1,\ 3,\ 5, \cdots) \tag{6}$$

$$\begin{aligned} v_H &= V_{dc}\left(S_H - \tfrac{1}{2}\right) \\ v_L &= V_{dc}\left(S_L - \tfrac{1}{2}\right) \\ v_o &= v_H - v_L = V_{dc}(S_H - S_L) \end{aligned} \tag{7}$$

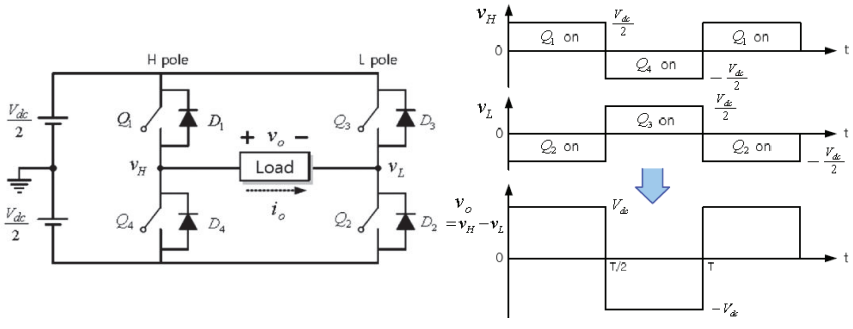

(**a**) (**b**)

Figure 2. Single phase full-bridge inverter: (**a**) circuit; and (**b**) output voltage.

A single-phase inverter experiences shoot-through time during the intervals when switching occurs. In this case, there is a momentary period when all switches are simultaneously conducting, which can lead to a short circuit incident. To prevent such accidents during switching transitions, the switching time of the switches is intentionally delayed by a certain amount of time, referred to as 'dead time'. During the dead time, an error occurs

in the output voltage, and the average error voltage is provided in Equation (8). Where, t_{dead} represents the dead time, and f_{sw} represents the switching frequency [16].

$$V_{err} = t_{dead} V_{dc} f_{sw} \tag{8}$$

Furthermore, this dead time decreases the fundamental component of the output voltage and generates harmonics in the output voltage. A study has been conducted to reduce dead time [17].

The conventional design and analysis methods for single-phase BLDC motors did not take into account the inverter's dead time and assumed the inverter's output voltage to be ideal. When analyzing without considering the inverter's dead time, it is impossible to accurately account for the decrease in the output voltage's fundamental components and the generation of harmonic components due to dead time. Therefore, when analyzing single-phase BLDC motors, it is necessary to integrate a single-phase full-bridge inverter.

Figure 3 represents the circuit of the integrated single-phase full-bridge inverter. To integrate the single-phase full-bridge inverter, four elements are required: the inverter input voltage (V_{dc}), diode specifications, switch resistance (R_{on}), and two signals for the switches On and Off. The input voltage and diode specifications can be obtained from the inverter's specifications. Switch resistance can also be determined through the inverter's specifications, and it may vary depending on the circuitry of each Drive IC. Typically, the resistance or the switch is represented as the sum of the resistances for the two switches (S_1 and S_4 in Figure 3). When designing the motor, it is essential to match the inverter's current limit. The current value is influenced by the voltage drop component resulting from the switches. Thus, it is necessary to take into account the switch resistance. Finally, two signals are required for controlling the switching of the switches on and off. Figure 4 represents the waveform of the node voltage. Signal1 is connected to switches S_1 and S_4, while Signal2 is connected to switches S_2 and S_3. When the node voltage of the signals is greater than 0 V, the switches are ON, and when it is less than 0 V, the switches are OFF. To prevent the inverter from shoot-through, the ON and OFF times of each switch need to be delayed, and therefore, T_r and T_f in Figure 4 must be greater than 0.

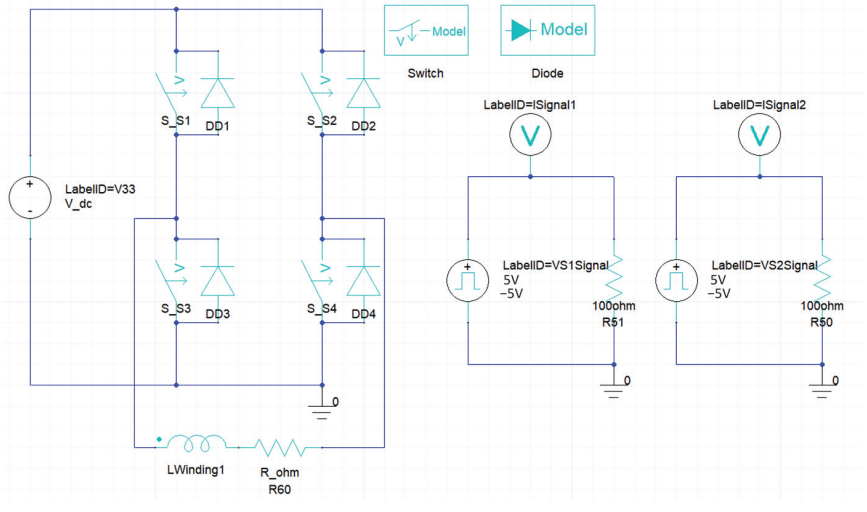

Figure 3. Single-phase full-bridge inverter circuit diagram.

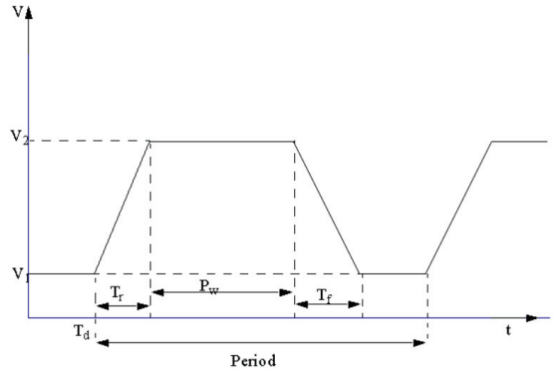

Figure 4. The T_r and T_f in the node voltage waveform.

The Drive IC's output voltage and current undergo rising segments during the dead time, which happens when the switches are toggled on and off. The soft ON and soft OFF function are used to prevent such rising phenomena. In the case of a Drive IC with the soft ON and soft OFF function, the angle of the registers can be adjusted to generate a smooth waveform for output. Figure 5 illustrates the voltage and current waveforms with and without implementation of the soft ON and soft OFF function. Where V_{OUT1} and V_{OUT2} represent the voltages when switches S_1 and S_4 are on and when switches S_2 and S_3 are on, respectively, in Figure 3. The rising portion of the output voltage is generated due to dead time, which affects the overall output. Therefore, when using a Drive IC with soft ON and OFF functionality, additional analysis is required. When using the soft ON and OFF function, the current waveform is smoothly regulated through the adjustment of the register angle. Therefore, in order to conduct an analysis, it is imperative to anticipate the scope of control. In this case, the lower magnitude of the current within the predicted range is chosen (1.63 A in Figure 6). This can be observed from the current waveform in Figure 6. Additionally, when considering the soft ON and soft OFF function, it is important to take into account the current limit of the Drive IC, which is based on the predicted current range (1.63 A to 1.71 A; shown in Figure 6).

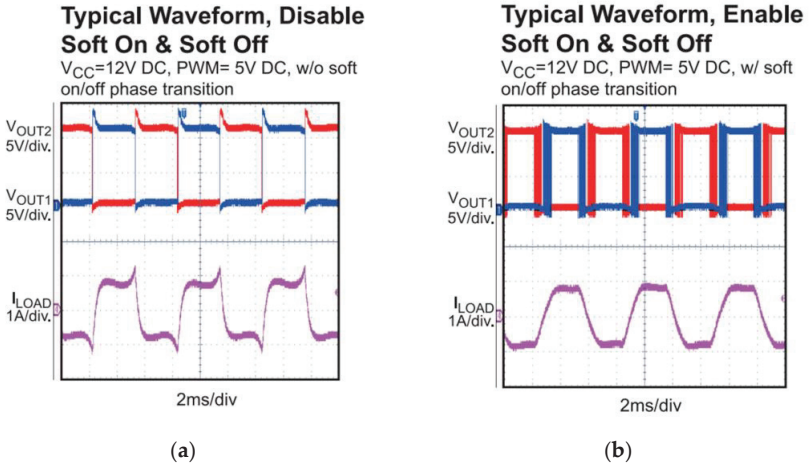

(**a**) (**b**)

Figure 5. Soft ON and soft OFF control function: (**a**) Without using soft ON and soft OFF function; and (**b**) With soft ON and soft OFF function (MPS-MP6517B datasheet).

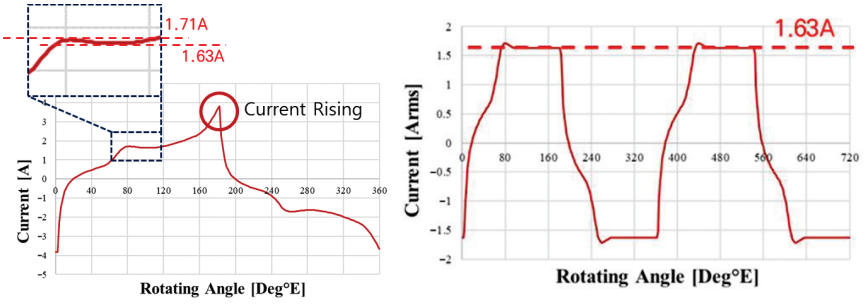

(**a**) (**b**)

Figure 6. Current waveform with soft ON and soft OFF control: (**a**) Current waveform without using soft ON and soft OFF function; and (**b**) Expected current waveform when using the soft ON and soft OFF function.

In this paper, the final selection of the Drive IC with Switch ON and OFF functionality was made considering the voltage drop due to switch resistance and motor current limitations. When selecting a Drive IC, the maximum value of the switch resistance and current limit should be considered according to the performance and specifications of the motor.

2.3. The Asymmetric Air Gap Structure of a Single-Phase BLDC Motor

A single-phase brushless DC motor operates through the use of a mechanically generated alternating magnetic field, which occurs via the winding of coils on the stator. This differs from a three-phase brushless DC motor, which utilizes a rotor in its operation. Therefore, the stator typically has an equal number of poles and slots in a 1:1 ratio. When a single-phase brushless DC motor is in operation, the interaction between the rotor magnets and the stator teeth produces cogging torque. Additionally, the interaction between the stator current and the rotor magnets results in magnetic torque. A single-phase brushless DC motor with an equivalent number of poles and slots may produce magnetic torque that matches cogging torque. Additionally, at the point where the cogging torque becomes zero, the magnetic torque can exhibit negative torque. This creates a zero-torque region referred to as the "dead point". Due to the dead point, a single-phase BLDC motor becomes unable to start its operation [14]. Therefore, for single-phase motors utilizing the alternating field mechanism, it is essential to verify the availability of starting torque. To eliminate the dead point, it is common to apply an asymmetric air-gap shape. When an asymmetric air-gap shape is applied, a phase difference occurs in the cogging torque, preventing the occurrence of zero-torque regions. Research has been conducted to propose various shapes for asymmetric air-gap and analyze their performance characteristics [18–20].

To ensure the starting torque of the single-phase BLDC motor, this design utilized an asymmetric air gap shape. Figure 7 illustrates the shapes of the symmetric air-gap model and the model with an applied asymmetric air-gap, while Figure 8 displays the cogging torque waveforms and no-load phase voltage waveforms for both the symmetric and asymmetric air-gap models. In the cogging torque waveform of Figure 8, it is clear that applying an asymmetric air-gap creates a phase difference compared to a symmetric air-gap, generating regions with no zero-torque for both the cogging and magnetic torques. However, it is noteworthy that the application of an asymmetric air-gap causes a change in the phase of the phase voltage waveform, requiring adjustment of the current phase angle to 0 degrees.

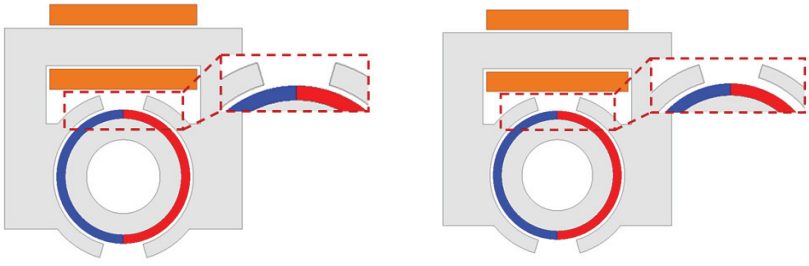

(**a**) (**b**)

Figure 7. The shapes of the symmetric air-gap model and the model with applied asymmetric air-gap are as follows: (**a**) symmetric air-gap model; and (**b**) asymmetric air-gap model.

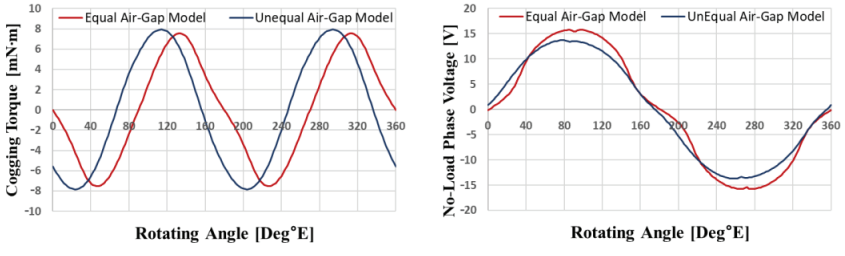

(**a**) (**b**)

Figure 8. Comparison of cogging torque and no-load phase voltage waveforms between symmetric air-gap model and asymmetric air-gap model: (**a**) cogging torque waveform; and (**b**) no-load phase voltage waveform.

Table 1 presents the torque values for the symmetrical and asymmetrical air gap models. When comparing the load torque values of the two models, the symmetrical air gap structure has a torque of 25.8 mNm, whereas the asymmetrical air-gap structure has a torque of 23.2 mNm, signifying an approximate drop of 10% in torque value. Therefore, this paper aims to review the symmetrical air-gap structure when designing a single-phase BLDC motor, including a 10% margin in the load torque, before exploring the application of the asymmetrical air-gap structure.

Table 1. Torque comparison between the symmetrical and asymmetrical air-gap models.

Parameter	Symmetrical Air-Gap	Asymmetrical Air-Gap	Unit
Torque	25.8	23.2	mNm

3. Designing a Single-Phase BLDC Motor That Meets the Target Performance

3.1. Comparison of Single-Phase BLDC Motor Types

There are four types of single-phase BLDC motors applied in this study: C-Type, R-Type, internal rotor type, and external rotor type. C-Type and R-Type have angular shapes instead of the traditional cylindrical shape, which can reduce manufacturing costs by reducing scrap during production. In the C-Type configuration, the magnetic flux crosses each pole on a singular path, whereas in the R-Type configuration, the magnetic flux crosses each pole on a split path [21]. Due to C-Type's higher magnetic flux per pole compared to R-Type at the same output, less coil is required to achieve similar results, thereby reducing

costs. As a result, C-Type was chosen for the design to meet the performance target. Figure 9 illustrates the magnetic flux patterns for both C-Type and R-Type motors.

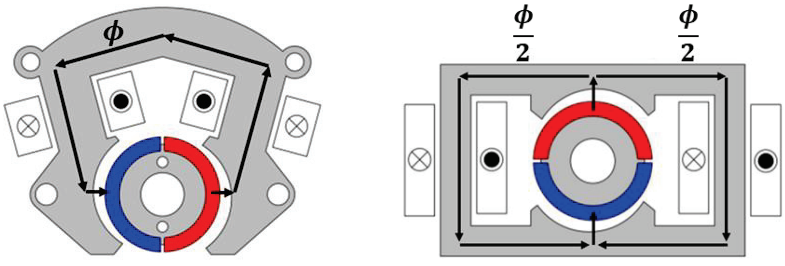

(**a**) (**b**)

Figure 9. Magnetic flux path comparison: (**a**) Magnetic flux path of C-Type BLDC motor; and (**b**) magnetic flux path of R-Type BLDC motor.

The internal rotor and external rotor types feature a cylindrical design, resulting in reduced stator core material usage. According to Equation (9), the external rotor design outperforms the internal rotor design in terms of performance. In Equation (9), *ac* represents the specific electric charge divided by the total electric charge from the void to the circumference, *k* represents the winding factor, and $\hat{B_{g1}}$ is a fundamental component of the magnetic flux density in air gap [22]. The design of a model that meets target performance parameters necessitated the selection of the external rotor type from among both internal and external rotor types. Figure 10 illustrates the variations in air-gap diameters observed between the two types.

$$T = \frac{\pi}{4}\left(k\hat{B_{g1}}accos\beta\right)D^2{}_gL_{stk} \tag{9}$$

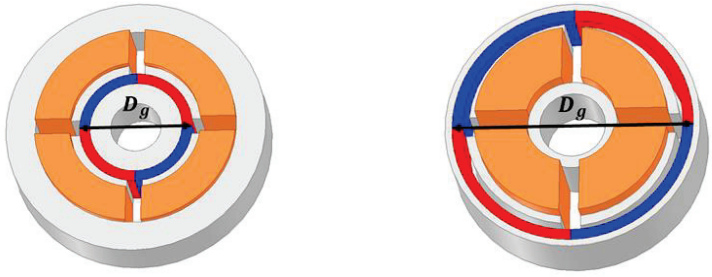

(**a**) (**b**)

Figure 10. Comparison of air-gap diameter: (**a**) internal rotor type BLDC motor air-gap diameter; and (**b**) external rotor type BLDC motor air-gap diameter.

3.2. Derivation of the Target Performance-Satisfying Model for an C-Type Single-Phase BLDC Motor

Table 2 presents the target performance and specifications of the C-Type single-phase BLDC motor. The symmetrical air-gap model will be used in this design, with consideration for a torque margin of 10% due to the asymmetric pole.

Table 2. C-Type single-phase BLDC motor target performance and specifications.

Parameter	C-Type Single Phase BLDC Motor	Unit
Poles	2	-
Slots	2	-
Rated Speed	2950	rpm
Rated Power	5	W
Rated Torque	15	mNm
Stack Length	11.2	mm
Fill Factor	50	%
Current Density	8	A_{rms}/mm^2
R_{on}	1.7	Ohm
Current Limit	1.5	A
Maximum Outer Size	61 × 60	mm
Core Material	35PN440	-
Permanent Magnet Material	HMG-12L (Nd-Bonded)	-
Coil Material	Copper	-

The single-phase C-type BLDC motor has a configuration comparable to the conventional SPIM. Accordingly, the initial design was carried out with the same dimensions as the induction motor represented in Figure 1. Figure 11 illustrates the configuration of the designed C-Type single-phase BLDC motor. The number of turns per phase required to meet the target torque was calculated. Table 3 presents the performance of the initial design model.

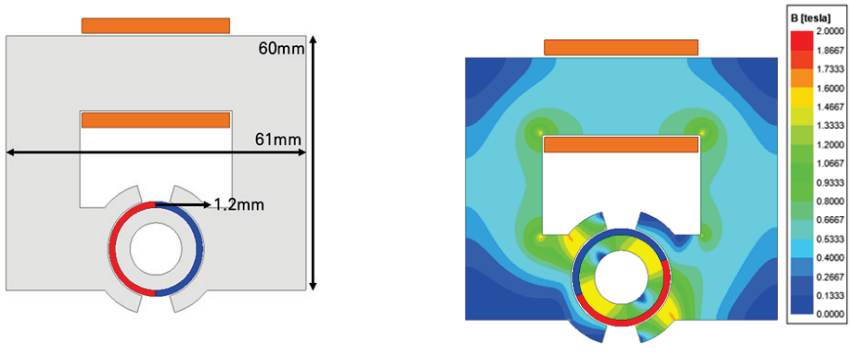

(**a**) (**b**)

Figure 11. The initial design model of the C-Type single-phase BLDC motor: (**a**) configuration of initial design model; and (**b**) the initial design model's magnetic flux density at saturation.

Table 3. Performance of the basic design model of the C-Type single-phase BLDC motor.

Parameter	C-Type Basic Design Model	Unit
Power	6.3	W
Torque	19.3	mNm
Number of Turns	495	-
Current	0.486	A
Copper Loss	2.1	W
Iron Loss	0.164	W
Efficiency	75.5	%

In the case of the initial design model, performance exceeding the target was achieved, and the stator did not saturate. Therefore, a design was conducted to increase the magnetic loading and decrease the electrical loading. Additionally, a design was carried out to reduce

the stator size based on the saturation characteristics, resulting in a model that satisfies the target performance. The use of magnets in this target performance satisfying model increased (from a previous magnet thickness of 1.2 mm to 1.9 mm), while the amount of winding and core material usage decreased.

Furthermore, in order to improve the precision of the analysis, an analysis of Drive IC integration was performed. During this process, current limitations were established, taking margins into account. When integrating the Drive IC with the model designed to meet the desired performance criteria, it was observed that due to dead time, the current limitations were exceeded, and performance exceeding the desired goals was achieved. The voltage input method utilized in the analysis of Drive IC integration leads to a decrease in current and torque as the number of turns increases. Therefore, an examination was performed on the current and torque for varying numbers of turns, and the number of turns(184Turns) that met the current constraints and the desired torque was chosen for the ultimate design. Figure 12 represents the current and torque graphs for different numbers of turns, and Figure 13 represents the configuration and magnetic flux density at saturation of the final model that meets the target performance of the C-Type single-phase BLDC motor. Figure 14 represents the current and torque waveforms of the final model during the Drive IC integration analysis. Table 4 presents the performance of the final model of the C-Type single-phase BLDC motor.

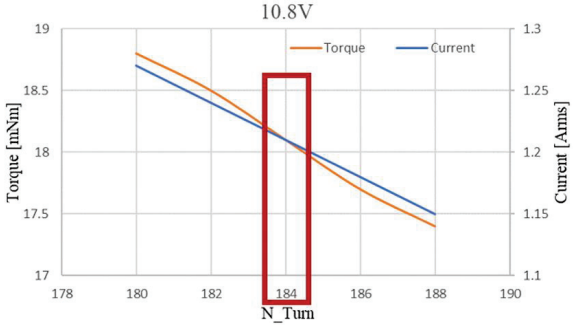

Figure 12. Current and torque graphs for different numbers of turns.

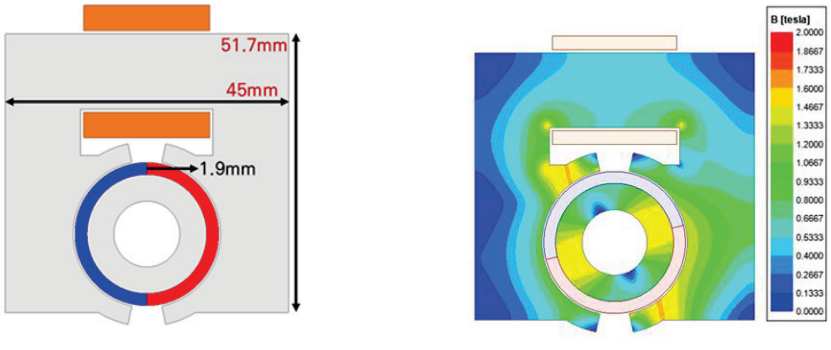

(**a**) (**b**)

Figure 13. C-Type single-phase BLDC motor final model: (**a**) final model configuration; and (**b**) final model magnetic flux density at saturation.

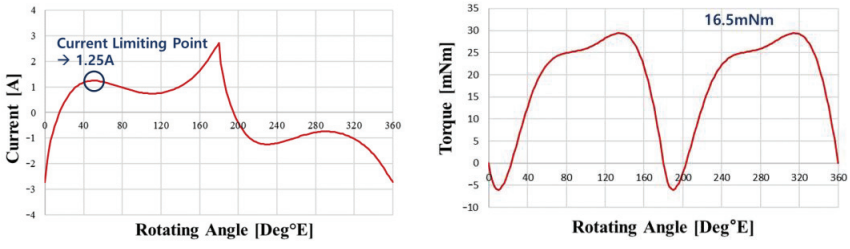

(**a**) (**b**)

Figure 14. Waveforms during Drive IC integration analysis: (**a**) current waveform; and (**b**) torque waveform.

Table 4. Performance of the final model of the C-Type single-phase BLDC motor.

Parameter	C-Type Single Phase BLDC Motor	Unit
Power	5.1	W
Torque	16.5	mNm
Number of Turns	184	-
Current	1.25	A
Copper Loss	1.86	W
Iron Loss	0.31	W
Efficiency	68.3	%

3.3. Derivation of the Target Performance-Satisfying Model for an External Rotor Single-Phase BLDC Motor

Table 5 presents the target performance and specifications for the external rotor single-phase BLDC motor. In this design, the initially considered model is a symmetrical air-gap model, taking into account a torque margin of 10% due to asymmetric air-gap. Additionally, the limitations of the selected Drive IC were used to account for current limitations.

Table 5. External rotor type single-phase BLDC motor target performance and specifications.

Parameter	External Rotor Type Single Phase BLDC Motor	Unit
Poles	2	-
Slots	2	-
Rated Speed	2950	rpm
Rated Output	5	W
Rated Torque	15	mNm
Stack Length	11.2	mm
Fill Factor	50	%
Current Density	8	A_{rms}/mm^2
R_{on}	0.71	Ohm
Current Limit	1.8	A
Maximum Outer Diameter	39	mm
Core Material	35PN440	-
Permanent Magnet Material	HMG-4 (Nd-Bonded Magnet) HMG-12L (Nd-Bonded Magnet)	-
Coil Material	Copper	-

Figure 15 illustrates the relationship between torque and cost, as related to the increase in the number of turns and magnet usage. When the cost of increasing the number of turns and the magnet thickness is equal, it is more beneficial to increase the number of turns rather

than the magnet thickness for an increase in torque. The higher residual magnetic flux density of the HMG-12L Nd-bonded magnet saturates the core, which poses a challenge in achieving the necessary number of turns to attain the desired performance target. Therefore, a comparison of the saturation densities between Nd-Bonded Magnet HMG-4 and HMG-12L was conducted for the purpose of considering a change in magnet material. Table 6 indicates the residual magnetic flux densities of the examined magnets, and Figure 16 indicates the magnet saturation densities attained by applying Nd-Bonded Magnet HMG-4 and HMG-12L Designing with HMG-4 is preferable for securing the required number of turns, considering the magnet saturation density, compared to HMG-12L. Therefore, HMG-4 is utilized in the design.

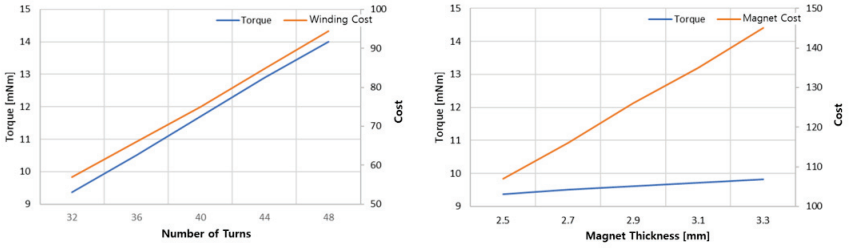

(**a**) (**b**)

Figure 15. Torque and cost comparison graph: (**a**) with equal magnet usage and increasing turns; and (**b**) with equal turns and increasing magnet usage.

Table 6. Residual magnetic flux density by magnet material.

Material	Residual Magnetic Flux Density	Unit
HMG-4	0.47	T
HMG-12L	0.75	

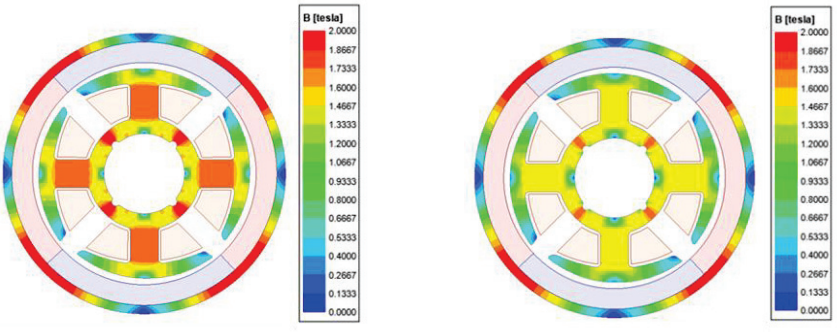

(**a**) (**b**)

Figure 16. Magnet saturation density when applying Nd-bonded magnet material: (**a**) HMG-12L; and (**b**) HMG-4.

The magnet material was replaced with HMG-4, and based on considerations of the stator core saturation characteristics and torque characteristics, a stator back yoke thickness of 1.65 mm was chosen. Figure 17 represents the torque characteristics with respect to the stator back yoke thickness. To meet the target performance, it was crucial

to secure the required number of turns. Therefore, the number of turns that satisfies the target performance was selected, considering the slot fill factor (50%) and current density (A_{rms}/mm^2 or below). Additionally, the motor outer diameter was determined accordingly.

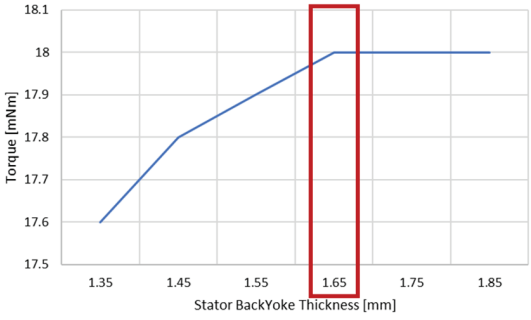

Figure 17. Torque characteristics graph with respect to stator back yoke thickness.

The target performance was achieved by selecting a total of 216 turns, taking into account the current limitation of the Drive IC, current density, and slot fill factor. To ensure the attainability of a viable phase angle for startup, an asymmetric air-gap was employed. The application of an asymmetric air-gap results in a shift in the phase of the cogging torque, allowing the magnetic torque to exceed zero at the point where the cogging torque reaches zero, enabling the motor to start. Due to the asymmetric air-gap structure, the voltage phase is changed. Therefore, the adjustment of the current phase angle to 0 degrees is necessary. Figure 18 represents the configuration of the model that meets the target performance, while Figure 19 represents the cogging torque and magnetic torque waveforms used to verify the feasibility of motor to start. Table 7 presents the performance of the target performance-satisfying model. It can be verified by Figure 19 that when the cogging torque reaches zero, the magnetic torque exceeds zero, demonstrating that the motor is capable of starting.

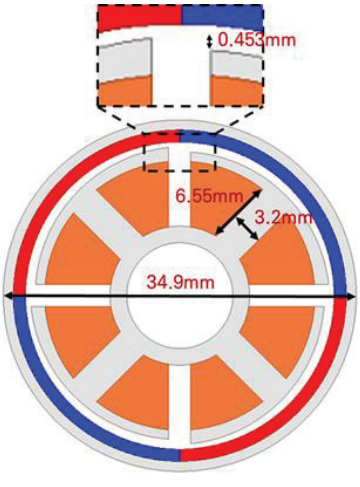

Figure 18. Configuration of the model that meets the target performance.

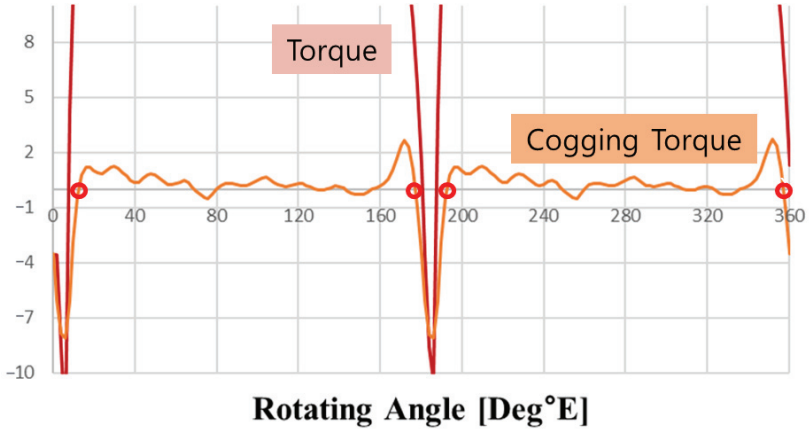

Figure 19. Cogging torque and magnetic torque waveforms for verification the feasibility of motor to start.

Table 7. Performance of the target performance-satisfying model.

Parameter	External Rotor Type Single Phase BLDC Motor	Unit
Power	4.7	W
Torque	15.2	mNm
Number of Turns	216	-
Current	1.3	A
Copper Loss	1.67	W
Iron Loss	0.215	W
Efficiency	69.3	%

Having a low shoe thickness compared to the shoe length in the stator core may potentially result in manufacturing issues in small motors. Therefore, when designing the stator for a single-phase external rotor BLDC motor, it is advantageous to have a greater shoe thickness relative to the shoe length. In designing the final model for the external rotor single-phase BLDC motor that meets the target performance, the outer diameter was set at 34.9 mm. Taking into account the maximum outer diameter of the motor as per target specifications, which is 39 mm, the minimum possible thickness of the shoe was considered during the design process. The length of the slot opening was increased by 30.4% to reduce the length of the shoe. Additionally, the thickness of the shoe was increased by 21% to confirm its manufacturability. The magnet's thickness was determined based on the torque increase rate to achieve the desired performance. Figure 20 represents the torque increase rate with respect to magnet thickness. The required number of turns per phase was calculated to achieve the desired performance. The motor's outer diameter was determined by considering the slot fill factor and current density, while increasing shoe thickness. The design of the external rotor single-phase BLDC motor was finalized by integrating a Drive IC. Figure 21 represents the configuration and magnetic flux density at saturation of the final model with applied parameter changes and Figure 22 represents the current waveform when considering the Drive IC.

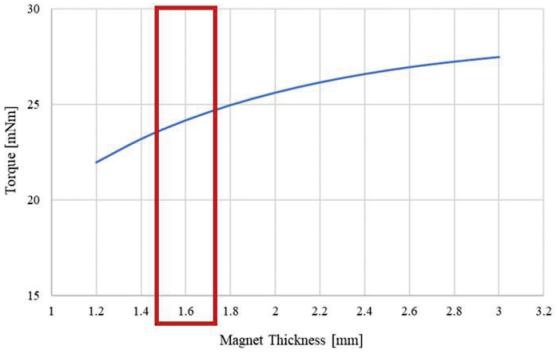

Figure 20. Torque increase rate with respect to magnet thickness.

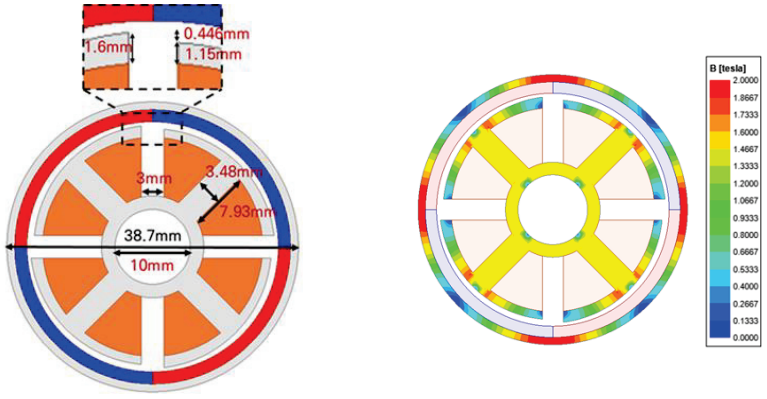

(**a**) (**b**)

Figure 21. Outer rotor single-phase BLDC motor final model with applied parameter changes: (**a**) final model configuration; and (**b**) final model magnetic flux density at saturation.

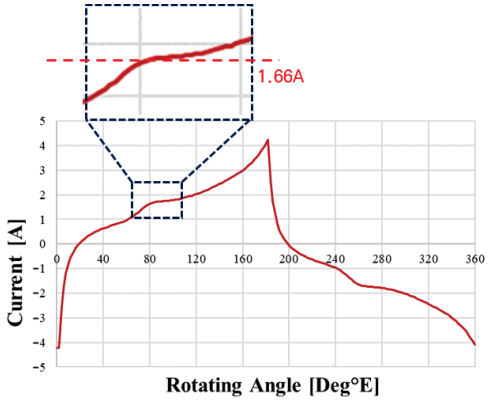

Figure 22. Current waveform when considering the Drive IC.

Incorporating the soft ON and OFF function results in reduced current, as seen in the current waveform in Figure 6. Therefore, further FEA analysis is necessary via additional current waveforms. During the assessment of the Drive IC integration, the input current

was estimated by analyzing the current waveform when implementing the soft ON and OFF features. It was confirmed through finite element analysis (FEA) that the desired performance is achieved when the input current is implemented as 1.66 A. Figure 23 represents the current waveform and torque waveform when applying the soft ON and OFF function, and Table 8 presents the performance of the final model of the external rotor single-phase BLDC motor. Figure 24 represents the operating point of the motor. The design points have been chosen based on the highest speed and torque values within this operational region.

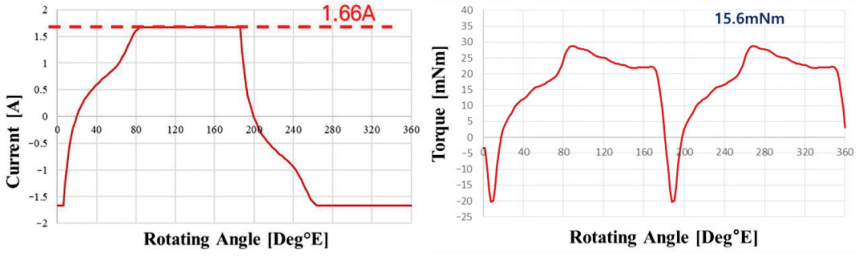

(**a**) (**b**)

Figure 23. Expected current waveform and torque waveform when applying the soft ON and OFF function: (**a**) current waveform; and (**b**) torque waveform.

Table 8. Performance of the final model of the external rotor single-phase BLDC motor.

Parameter	External Rotor Single Phase BLDC Motor	Unit
Power	4.8	W
Torque	15.6	mNm
Number of Turns	228	-
Current	1.66	A
Copper Loss	2.51	W
Iron Loss	0.192	W
Efficiency	62.4	%

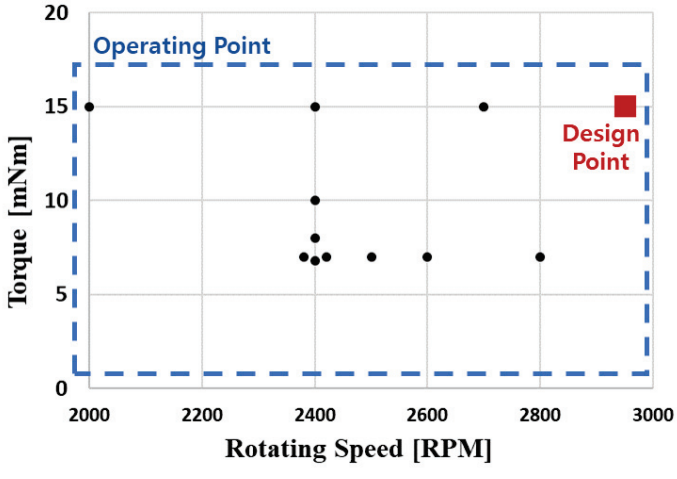

Figure 24. Operating point of the motor.

4. Selection of a Single-Phase BLDC Motor That Meets the Target Performance and Validation through the Production of a Prototype Motor

4.1. Selection of the Final Motor, Considering the Cost, for Both the C-Type and External Rotor Single-Phase BLDC Motors

Table 9 provides a comparison of the weights and costs of the final models of the C-Type and external rotor single-phase BLDC motors. The costs have been standardized based on the same year. For the C-Type motor, the magnetic flux density is higher due to the single flux path compared to the external rotor motor. Therefore, reduced copper usage is realized in the windings. However, due to the angular shape characteristics, the use of the stator core in the external rotor motor increases by approximately five times, ultimately leading to a higher final cost. Therefore, the oven fan motor requires low output and cost characteristics, and thus a single-phase BLDC motor was chosen as the optimal model.

Table 9. Comparison of the weights and costs between the C-Type and external rotor single-phase BLDC motors.

Parameter	C-Type Single Phase BLDC Motor	Outer Rotor Single Phase BLDC Motor	Unit
Stator Core (35PN440)	0.123	0.025	kg
Rotor Core (35PN440)	0.017	0.011	
Magnet(HMG-12L/HMG-4)	0.009	0.012	
Coil (Copper)	0.015	0.017	
Stator Core (35PN440)	209.4	42.1	KRW
Rotor Core (35PN440)	29.3	18.5	
Magnet (HMG-12L/HMG-4)	57.6	59.4	
Coil (Copper)	145.3	160.5	
Sum	441.6	280.4	

4.2. Prototype Motor Production and Validation

A prototype motor of the proposed external rotor single-phase BLDC motor was produced and tested to validate the feasibility of the Drive IC integration analysis. Soft ON and soft OFF functionality was utilized during the testing. To account for dead time, T_r and T_f were set to 10 μdeg. Figure 25 represents the prototype motor's configuration. Figure 26 represents the expected current waveform considering the soft ON and soft OFF function, while Figure 27 represents the current waveform obtained during the testing of the prototype motor. In Figure 27, the x-axis represents time, and the y-axis represents current. Table 10 presents the output and torque values obtained through FEA and those obtained through testing. This demonstrates the validity of the full-bridge inverter (Drive IC) integration analysis proposed in this paper.

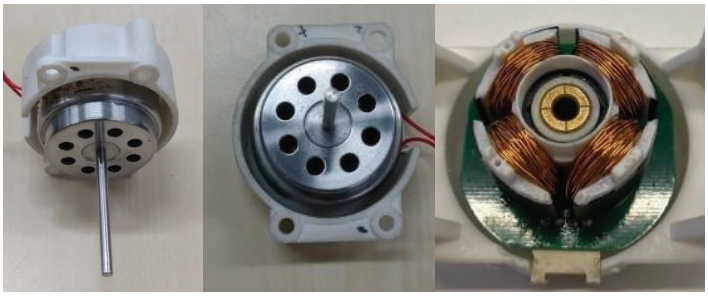

Figure 25. Prototype motor's configuration.

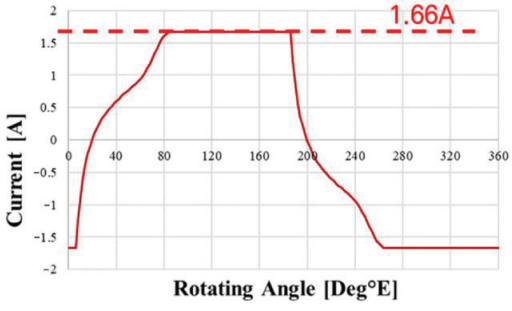

Figure 26. Expected current waveform considering the soft ON and soft OFF function.

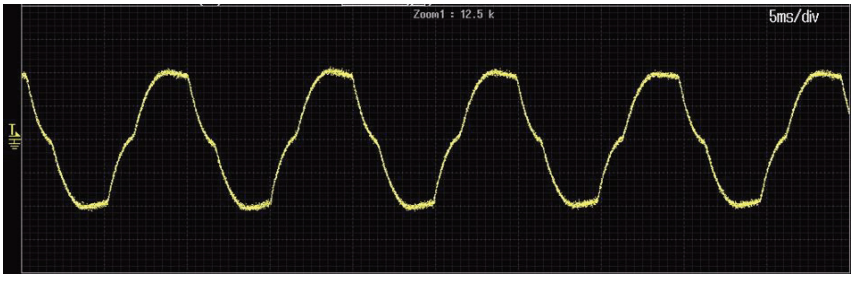

Figure 27. Current waveform obtained during the testing of the prototype motor.

Table 10. Comparison of the performance between the single-phase BLDC motor at 2950 rpm based on FEA and the prototype motor.

Parameter	FEA	Test	Unit
Power	4.8	4.7	W
Torque	15.6	15.0	mNm

5. Conclusions

This paper conducted a study on the design and analytical methods or a single-phase BLDC motor to replace SPIM. The study concentrated on an external rotor single-phase BLDC motor that meets the target performance and cost savings, enabling variable speed control. Furthermore, it is crucial to take into account the dead time of the full-bridge inverter (Drive IC) as single-phase BLDC motors mainly rely on this type of inverter. To address this concern, a Drive IC integration analysis method was proposed. The study compared various types of single-phase BLDC motors, designed models that met

performance targets, and analyzed the integration of the Drive IC. Additionally, a prototype motor was produced and verified through testing. The analysis of integrating the Drive IC through FEA and prototype motor testing revealed output discrepancies of about 2% and torque variances of approximately 4%. The test results indicate that the Drive IC integration analysis method conducted via FEA is valid.

Author Contributions: Conceptualization, W.-H.K. and D.-H.J.; methodology, Y.-S.L.; software, Y.-S.L.; validation, Y.-S.L.; formal analysis, N.-R.J.; investigation, H.-J.P.; resources, Y.-S.L.; data curation, N.-R.J.; writing—original draft preparation, Y.-S.L.; writing—review and editing, H.-J.P. and D.-H.J.; visualization, Y.-S.L. and D.-H.J.; supervision, W.-H.K. and D.-H.J.; project administration, W.-H.K. and D.-H.J. All authors have read and agreed to the published version of the manuscript.

Funding: This research was partly supported by the Korea Institute of Energy Technology Evaluation and Planning (KETEP) grant-funded by the Korea government (MOTIE) (20214000000060, Department of Next Generation Energy System Convergence based-on Techno-Economics—STEP) and in part by a grant from the Basic Research Program funded by the Korea Institute of Machinery and Materials (grant number: NK242J).

Data Availability Statement: Not applicable.

Conflicts of Interest: The authors declare no conflict of interest.

References

1. Ojaghi, M.; Daliri, S. Analytic Model for Performance Study and Computer-Aided Design of Single-Phase Shaded-Pole Induction Motors. *IEEE Trans. Energy Convers.* **2016**, *32*, 649–657. [CrossRef]
2. Sharma, U.; Singh, B. Design and Development of Energy Efficient Single Phase Induction Motor For Ceiling Fan Using Taguchi's Orthogonal Arrays. *IEEE Trans. Ind. Appl.* **2021**, *57*, 3562–3572. [CrossRef]
3. Ahmed, F.; Kar, N.C. Analysis of End-Winding Thermal Effects in a Totally Enclosed Fan-Cooled Induction Motor With a Die Cast Copper Rotor. *IEEE Trans. Ind. Appl.* **2017**, *53*, 3098–3109. [CrossRef]
4. Cavagnino, A.; Lazzari, M.; Profumo, F.; Tenconi, A. A comparison between the axial flux and the radial flux structures for PM synchronous motors. *IEEE Trans. Ind. Appl.* **2002**, *38*, 1517–1524. [CrossRef]
5. Zhao, N.; Liu, W. Loss Calculation and Thermal Analysis of Surface-Mounted PM Motor and Interior PM Motor. *IEEE Trans. Magn.* **2015**, *51*, 8112604. [CrossRef]
6. Kim, T.-J.; Hwang, S.-M.; Kim, K.-T.; Jung, W.-B.; Kim, C.-U. Comparison of dynamic responses for IPM and SPM motors by considering mechanical and magnetic coupling. *IEEE Trans. Magn.* **2001**, *37*, 2818–2820. [CrossRef]
7. Dong, J.; Huang, Y.; Jin, L.; Lin, H. Comparative Study of Surface-Mounted and Interior Permanent-Magnet Motors for High-Speed Applications. *IEEE Trans. Appl. Supercond.* **2016**, *26*, 5200304. [CrossRef]
8. Zhao, W.; Yang, Z.; Liu, Y.; Wang, X. Analysis of a Novel Surface-Mounted Permanent Magnet Motor With Hybrid Magnets for Low Cost and Low Torque Pulsation. *IEEE Trans. Magn.* **2021**, *57*, 8104804. [CrossRef]
9. Pang, Y.; Zhu, Z.Q.; Feng, Z.J. Cogging Torque in Cost-Effective Surface-Mounted Permanent-Magnet Machines. *IEEE Trans. Magn.* **2011**, *47*, 2269–2276. [CrossRef]
10. He, T.; Zhu, Z.; Eastham, F.; Wang, Y.; Bin, H.; Wu, D.; Gong, L.; Chen, J. Permanent Magnet Machines for High-Speed Applications. *World Electr. Veh. J.* **2022**, *13*, 18. [CrossRef]
11. He, C.; Wu, T. Analysis and design of surface permanent magnet synchronous motor and generator. *CES Trans. Electr. Mach. Syst.* **2019**, *3*, 94–100. [CrossRef]
12. Chen, Y.-T.; Chiu, C.-L.; Jhang, Y.-R.; Tang, Z.-H.; Liang, R.-H. A Driver for the Single-Phase Brushless DC Fan Motor With Hybrid Winding Structure. *IEEE Trans. Ind. Electron.* **2012**, *60*, 4369–4375. [CrossRef]
13. Lee, W.; Kim, J.H.; Choi, W.; Sarlioglu, B. Torque Ripple Minimization Control Technique of High-Speed Single-Phase Brushless DC Motor for Electric Turbocharger. *IEEE Trans. Veh. Technol.* **2018**, *67*, 10357–10365. [CrossRef]
14. Dunkl, S.; Muetze, A.; Schoener, G. Design Constraints of Small Single-Phase Permanent Magnet Brushless DC Drives for Fan Applications. *IEEE Trans. Ind. Appl.* **2015**, *51*, 3178–3186. [CrossRef]
15. Fazil, M.; Rajagopal, K.R. Nonlinear Dynamic Modeling of a Single-Phase Permanent-Magnet Brushless DC Motor Using 2-D Static Finite-Element Results. *IEEE Trans. Magn.* **2011**, *47*, 781–786. [CrossRef]
16. Kim, S.-H. *Electric Motor Control DC, AC, and BLDC Motors*; Elsevier Science: Amsterdam, The Netherlands, 2017; pp. 275–335.
17. Yang, Y.; Zhou, K.; Wang, H.; Blaabjerg, F. Analysis and Mitigation of Dead-Time Harmonics in the Single-Phase Full-Bridge PWM Converter With Repetitive Controllers. *IEEE Trans. Ind. Appl.* **2018**, *54*, 5343–5354. [CrossRef]
18. Fazil, M.; Rajagopal, K.R. A Novel Air-Gap Profile of Single-Phase Permanent-Magnet Brushless DC Motor for Starting Torque Improvement and Cogging Torque Reduction. *IEEE Trans. Magn.* **2010**, *46*, 3928–3932. [CrossRef]
19. Park, Y.-U.; Cho, J.-H.; Kim, D.-K. Cogging Torque Reduction of Single-Phase Brushless DC Motor With a Tapered Air-Gap Using Optimizing Notch Size and Position. *IEEE Trans. Ind. Appl.* **2015**, *51*, 4455–4463. [CrossRef]

20. Kwon, B.-I.; Yang, B.-Y.; Park, S.-C.; Jin, Y.-S. Novel topology of unequal air gap in a single-phase brushless DC motor. *IEEE Trans. Magn.* **2001**, *37*, 3723–3726. [CrossRef]
21. Choo, Y.; Hwang, H.; Cho, J.; Kim, C.; Kim, J.; Hwang, S.-H.; Choi, J.Y.; Lee, C. Investigation of Systematic Efficiency in a High-Speed Single-Phase Brushless DC Motor Using Multi-Physics Analysis for a Vacuum Cleaner. *IEEE Trans. Magn.* **2019**, *55*, 8203606. [CrossRef]
22. Aydin, M.; Huang, S.; Lipo, T. Torque quality and comparison of internal and external rotor axial flux surface-magnet disc machines. *IEEE Trans. Ind. Electron.* **2006**, *53*, 822–830. [CrossRef]

energies

MDPI

Article

Electromagnetic Performance Analysis of a Multichannel Permanent Magnet Synchronous Generator †

Mariusz Korkosz [1,*], Elżbieta Sztajmec [2] and Jan Prokop [1]

[1] Department of Electrodynamics and Electrical Machine Systems, Rzeszow University of Technology, 35-959 Rzeszow, Poland; jprokop@prz.edu.pl
[2] Department of Power Electronics and Power Engineering, Rzeszow University of Technology, 35-959 Rzeszow, Poland; e.sztajmec@prz.edu.pl
* Correspondence: mkosz@prz.edu.pl
† The publication is an extended version of the article presented at the conference Selected Issues in Power Engineering, Electrical Engineering and Industry 4.0, Rzeszów, Poland, 30 November 2022.

Abstract: In this paper, we present an analysis of the properties of the prototype three-phase Multichannel Permanent Magnet Synchronous Generator (MCPMSG) prototype designed and constructed by the authors. Each channel of the generator has electrically separated windings, which allows us to create an island system of electricity generation. The analyzed MCPMSG is intended for critical applications, and it is designed for four-channel operation. The purpose of this work is to analyze various configurations of the generator channels to improve the redundancy of the electricity generation system. The MCPMSG operation with one or two independent sources of energy consumption in the case of a dual-channel or double dual-channel operation was investigated. For the analyzed cases, the original mathematical models of the three-phase MCPMSG were developed. On the basis of numerical and laboratory tests, the influence of individual configurations on the MCPMSG output parameters was determined. An original method for diagnosing the operation of the MCPMSG channels was developed. Numerical and laboratory tests of the proposed diagnostic method based on a single voltage signal were carried out. As part of the laboratory tests, selected operating states under conditions of full winding symmetry and internal asymmetry were analyzed. The advantage of the proposed diagnostic method is the control of the operating state of the channels both under load and in the de-energized state. The proposed diagnostic method for control of the individual channel requires measurement of only one voltage signal.

Keywords: diagnostic method; dual-channel operation; fault-tolerant; harmonic analysis; multichannel generator; permanent magnet synchronous generator; redundancy; safety-critical

Citation: Korkosz, M.; Sztajmec, E.; Prokop, J. Electromagnetic Performance Analysis of a Multichannel Permanent Magnet Synchronous Generator. *Energies* **2023**, *16*, 7816. https://doi.org/10.3390/en16237816

Academic Editors: Loránd Szabó and Feng Chai

Received: 22 October 2023
Revised: 22 November 2023
Accepted: 24 November 2023
Published: 28 November 2023

1. Introduction

The use of fault-tolerant electric systems becomes unavoidable in many critical applications where failures may endanger the safety of the user or machine. Therefore, it is essential to develop structures that are resistant to damage and capable of maintaining continuity of operation. Such solutions can be achieved by redundancy of system components, for example, a multichannel three-phase system, multiple independent power converters, etc. Although multiplying components may generate higher cost, it is worth it in terms of safety.

Multichannel machines are investigated in various areas such as aviation (More Electric Aircraft—MEA) [1–3], the automotive industry (Electric Vehicles—EVs) [4–6], the marine industry [7], renewable energy resources (RESs) [8–12], and military applications [2]. In the literature, the MEA concept is the most popular in regard to multichannel machines.

An overview of electricity generation in aviation is widely presented in [2]. The authors indicate that electric power systems are progressively replacing pneumatic, hydraulic, and

mechanical power systems in MEA. Therefore, there is a need for on-board electric power generation. Over the years, reliability and power density have become more critical parameters. In [13], it is mentioned that the Permanent Magnet Synchronous Generator (PMSG) is a primary power source for modern aircraft, both civilian (Airbus and Boeing) and military (Lockheed Martin). Since the complexity of the on-board power system and its load are high, the Permanent Magnet Synchronous Machine (PMSM) is the most suitable due to its good airworthiness, autonomous work, high power density, and robust design. The authors of [1] also suggest that a favored choice for MEA applications is a dual or triple three-phase PMSM due to its balance between redundancy and complexity, while providing a balanced operation after a failure occurs. In addition to MEA, there are papers that consider the multichannel operation of EVs, since it is also essential to provide high reliability to both users and machines in the automotive field [4,5].

In addition to reliability and safety, ecology is also an essential aspect, as many countries are committed to reducing the emission of greenhouse gases [8,10,12]. In the scientific literature, tremendous work has been conducted on the development of a reduction in gas emissions and fuel cost in MEA [3]. The reduction in air pollution and the exhaustion of petroleum resources is also investigated in the area of EVs [6]. In terms of RESs, the authors focus mainly on wind power generation [9,11,12]. Recently, interest in generating energy from the movement of marine waves or marine currents, which is in an early stage of development, has been observed. Therefore, generators for use in the marine industry are investigated [7,8].

So far, a multichannel generator has not been widely investigated. There are a few papers on dual-channel generators or motors [4,5,8–10,14–17]. The tests performed refer to dual-channel work under normal conditions [4,7–13,18,19] and include failures, such as operation during failure of one or both channels [5,14], short circuit [9,18], and open circuit [4]. The starter/generator system [3,18,20] is also investigated.

Researchers have analyzed reluctance generators [14,16,17], brushless DC motors with permanent magnets [5,15], and PMSMs [4,7–13,18,19] in terms of multichannel operation. Recently, the type of generator that has been the most researched is the PMSG. Many authors in their work indicate that the PMSM is generally the preferred choice (over reluctance and induction machines) for various applications, because of its high power density, high efficiency, compact volume, and low maintenance costs, among others. Although the PMSMs have a lot of advantages, they are challenging in terms of reactive power, parallel operation, and fault tolerance [2]. In [1], it is said that in the PMSM, currents can flow in a failed lane even if it is disconnected from the power supply due to the presence of magnet-induced electromotive force (EMF). In such a case, at the design stage of the machine, the effects of a potential short circuit in the winding should be minimized by introducing, for example, thermal separation of the windings or increasing the hardiness of permanent magnets to the appearance of such a machine operating condition.

The diagnosis of generator operation and malfunctions is another important issue. There are different methods of diagnostics in terms of electric machines, and therefore, different diagnostic parameters can be used, for example, electric current, voltage, signal, temperature, noise, vibration, etc. [21–25]. Harmonic analysis can, for example, provide information on the presence of anomalies in generator operation.

The aim of this work is to analyze properties of the prototype Multichannel Permanent Magnet Synchronous Generator (MCPMSG) prototype designed and constructed by the authors for critical applications. Various configurations of the generator channels, taking into account the improvement of the redundancy of the electricity generation system, were analyzed. There are few works on the MCPMSG. Furthermore, the existing works do not address the subject of the influence of the channel configuration on the MCPMSG properties. An original mathematical model was developed for the study of the MCPMSG operation. Under laboratory conditions, the influence of the channel configuration on the output parameters of the MCPMSG was verified. An original method for diagnosing the operation of individual channels of the MCPMSG was proposed by the authors. This diagnostic

method based on a single voltage signal was tested under the conditions of numerical tests and laboratory tests. As part of these tests of the proposed diagnostic method, the capabilities of the prototype MCPMSG were used to analyze selected operating states of internal asymmetry. The advantage of the proposed diagnostic method is the control of the operating state of the channels both under load and in the de-energized state. The proposed diagnostic method for control of the individual channel requires measurement of only one voltage signal.

The paper consists of several sections. In Section 2, design and configuration analysis of the MCPMSG is presented. Section 3 contains the mathematical model of the tested MCPMSG. The operation of the MCPMSG with different sources of energy consumption is presented in Section 4. In Section 5, the proposed diagnostic method for the MCPMSG is discussed. The final Section 6 contains a summary and conclusions.

2. Design and Configuration Analysis of MCPMSG

2.1. Analysis of the MCPMSG

The designed and constructed MCPMSG is a demonstrator for testing multichannel operation. It is not optimized in terms of, for example, obtaining maximum efficiency. To reduce the cost of the prototype, components of a commercial three-phase squirrel-cage induction motor with a power of 1.5 kW were used (all components except the rotor magnetic circuit). The possibility of testing internal asymmetries, e.g., short circuits, and the introduction of temperature sensors in each phase of each channel (12 sensors) reduced the slot filling factor. The biggest drawback of the demonstrator is the use of solid steel in the magnetic circuit of the rotor instead of a package of magnetic sheets. The analyzed structure of the MCPMSG was designed to work with four independent channels. They are conventionally named A, B, C, and D. Each channel consists of three-phase windings. There are no electrical displacements between the channels, which gives much more flexibility in their configuration. However, a certain increase in the ripple of the generated braking torque is a cost of this solution. A cross-section of the geometry of the analyzed generator with locations of the windings of individual channels and prototype is shown in Figure 1. Each channel is marked with a different color.

Table 1 presents selected parameters of the analyzed MCPMSG.

Table 1. Selected parameters of the analyzed MCPMSG.

Parameter	Value
Number of phases/channels	3/4
Number of slots/rotor poles	36/4
Stator/rotor diameter	140 mm/81 mm
Active length/air-gap	140 mm/0.5 mm
Continuous output power for dual-channel operation/nominal speed	1500 W/1500 rpm
Nominal output phase voltage	73 Vrms
Nominal phase current per channel	3.8 Arms
Winding layers	2
Winding configuration	Y
Number of turns per channel phase	84
Phase resistance per channel	1.8 Ω
Number of independent coil turns in phase 1 of channel A	Coil 1 (1 + 27), coil 2 (3 + 25), coil 3 (28) (Figure 2)
Permanent magnet	N48SH

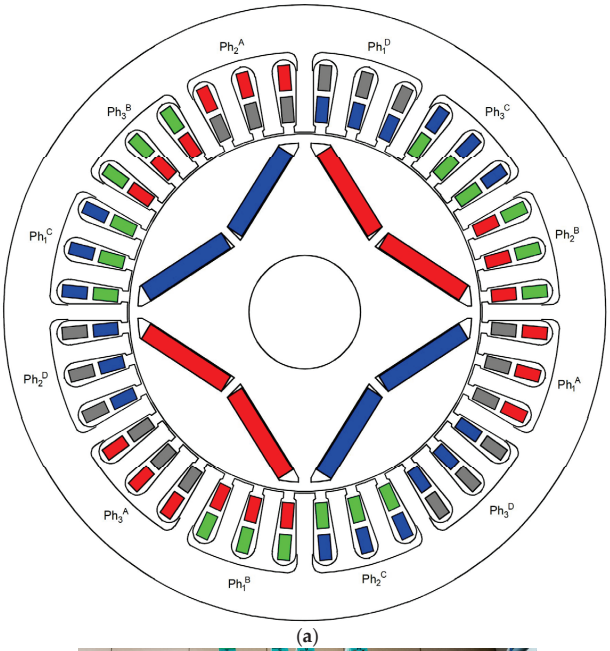

(**a**)

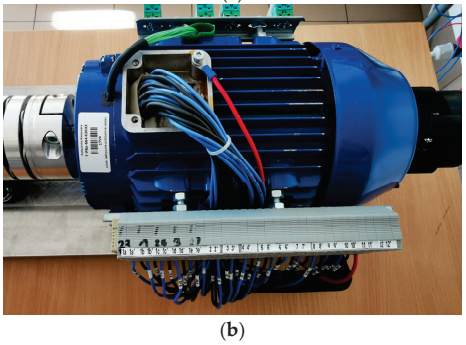

(**b**)

Figure 1. Multichannel MCPMSG: (**a**) cross-section, (**b**) prototype.

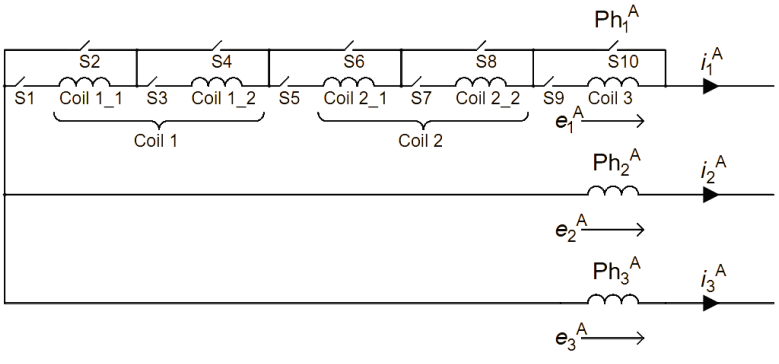

Figure 2. Diagram of the connection of windings of conventional channel A.

In the analyzed MCPMSG system, it is possible to operate in a mode of:

- QCO (quad-channel operation);
- TCO (triple-channel operation);
- DDCO (double dual-channel operation);
- DCO (dual-channel operation);
- SCO (single-channel operation).

A high safety factor in relation to the power output during the design of the machine was included. This is important in aviation or military applications [1,2].

While designing the generator, tests under unusual operating conditions were foreseen. In one of the phases of channel A, it is possible to change the number of turns of the coil within a certain range. In Figure 2, a winding connection of channel A is presented. It allows testing related to the operation of the generator under conditions of internal asymmetry to be tested. In addition, in each phase of the channel, thermocouples were installed to control the thermal condition of the machine.

Different operating states can be achieved depending on the configuration of phase 1 in channel A. Selected states analyzed in the MCPMSG are presented in Table 2.

Table 2. Analyzed operating states of channel A.

Case/Switch	S1	S2	S3	S4	S5	S6	S7	S8	S9	S10
Case I	on	off	on	off	on	off	on	off	on	off
Case II	on	off	off	on	on	off	on	off	on	off
Case III	on	off	on	off	on	off	off	on	on	off
Case IV	on	off	on	off	on	off	on	off	off	on

The variant named Case I means the operating state under the condition of electric and magnetic symmetry. The remaining variants introduce electric and magnetic asymmetry. Case II means the operating state with the lack of one turn of the coil in the winding of the generator. Case III includes the lack of three turns in the coil in the winding. A relatively insignificant asymmetry can be observed for Case II. In Case III, there is a slightly greater internal asymmetry. In Case IV, the phase winding contains only two coils (lack of 28 turns of the coil).

In the analyzed Case I (Table 2), the induced voltages in the tested MCPMSG (Figure 1a) are the same in each channel. In practice, these voltages may slightly differ. In Figure 3, an exemplary phase EMF of one of the channels obtained from the numerical model (speed at 1500 rpm) is presented (signed as "num"). Additionally, the phase EMF of phase 1 of each channel is also presented in Figure 3.

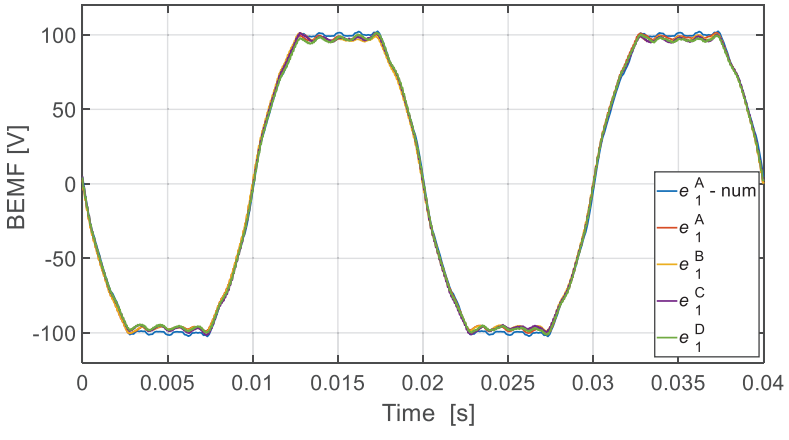

Figure 3. Phase EMF waveforms of the MCPMSG.

Good agreement is obtained between the results of numerical calculations and the laboratory tests. The received RMS (root mean square) values received from the phase EMF of the tested generator at the speed of 1500 rpm are listed in Table 3.

Table 3. RMS phase EMF of the MCPMSG—laboratory test.

Phase/Channel	Channel A	Channel B	Channel C	Channel D
Phase 1	82.476 V	81.886 V	81.963 V	81.808 V
Phase 2	80.987 V	81.429 V	80.996 V	80.622 V
Phase 3	81.262 V	81.102 V	81.506 V	81.429 V

Slight differences in the phase EMF waveforms of individual channels can be observed in the experiment results. This is a typical result for any prototype made. Even relatively small changes in the arrangement of the turns in the slots affect the value of the induced voltage. This is definitely more visible in the MCPMSG than in the classical machine with, for example, serial connection of groups of turns. It has a negative impact on the operation of the multichannel generator working in DCO, TCO, and QCO modes. The highest-value EMF occurs in phase 1 of the channel A. In this channel, additional outputs of two coils have been made (Figure 2). Table 4 summarizes the RMS values of phase EMF for DCO including the internal asymmetry of the generator (numerical).

Table 4. RMS values of phase EMF for dual-channel operation.

Case/BEMF		E_1	E_2	E_3
Case I	DCO AB	81.40 V	81.40 V	81.40 V
	DCO AC	81.44 V	81.44 V	81.44 V
Case II	DCO AB	80.91 V	81.43 V	81.43 V
	DCO AC	80.96 V	81.44 V	81.43 V
Case III	DCO AB	79.96 V	81.53 V	81.37 V
	DCO AC	79.86 V	81.43 V	81.43 V
Case IV	DCO AB	64.58 V	81.84 V	81.31 V
	DCO AC	64.56 V	81.52 V	81.52 V

The symmetry state of the two-channel DCO operation shows that the voltage at the generator terminals is identical in each phase. At the same time, for the DCO AC case, they are slightly larger. The appearance of internal asymmetry in one of the channels (phase 1 of conventional channel A) causes voltage asymmetry at the generator output. This is already visible even in Case II (one coil missing). A greater degree of asymmetry only makes the situation worse. It should be noted that the resulting asymmetry in phase 1 of conventional channel A causes a change in the voltage induced in the remaining channels. The test results show that the resulting asymmetry is better tolerated by the DCO AC configuration.

The diagram shown in Figure 2 also allows for interturn short circuits, e.g., one turn. However, this issue is not analyzed in this publication.

2.2. Analysis of the Configuration of the MCPMS Generator

The designed generator structure allows for the implementation of several independent variants of the work, for example, work with one or two sources of energy consumption. The potential possibility of the generator channel configuration while operating with one source of energy consumption is presented in Figure 4. Various configurations of the MCPMSG with one source of energy consumption are listed in Table 5. Each configuration shown in Table 5 requires the inclusion of the appropriate S_A-S_D switches shown in Figure 4.

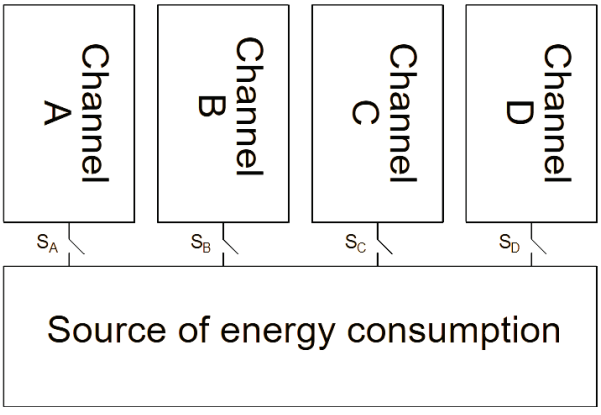

Figure 4. Analyzed configurations of the channels of the generator operating with one source of energy consumption.

Table 5. The MCPMSG with one source of energy consumption.

Mode	Channel
QCO	ABCD
TCO	ABC | ABD | ACD | BCD
DCO	AB * | AC * | AD | BC | BD | CD
SCO	A | B | C | D

For the presentation of test results, configurations are marked with an asterisk (*). The character " | " means "or", that is, a selection of the operating mode from several possible ones.

Assuming that each independent load is powered from two channels of the generator, there are two configurations that can be distinguished (*), that is, AB + CD (Figure 5a) and AC + BD (Figure 5b). In this case, each independent source of energy consumption is powered by two channels. The generator operates in a double dual-channel operation (DDCO). It allows us to increase the reliability of the dual independent electricity generation system.

The possible configuration of the MCPMSG operating with two independent sources of energy consumption is shown in Table 6. The "+" sign means a combination of the same or different operating modes.

Table 6. The MCPMSG with two sources of energy consumption.

Mode	Channel
TCO + SCO	ABC + D | ABD + C | ACD + B | BCD + A
Double DCO (DDCO)	AB + CD * | AC + BD * | AD + BC

Both the power supply system with one source of energy consumption (Figure 4) or two independent sources (Figure 5), aim to improve the safety of the operation of electricity generation systems, for example, in aviation. According to the authors, the case of DDCO MCPMSG is not considered in the literature. The results published in the rest of this work are completely original. The analysis of the impact of the channel configuration for the MCPMSG in relation to work with one reception source is also not considered in the literature. Existing work mainly focuses on the quite important problem of controlling the operation of a power electronic system. At the same time, they take into account the operation of the generator itself in a simplified way.

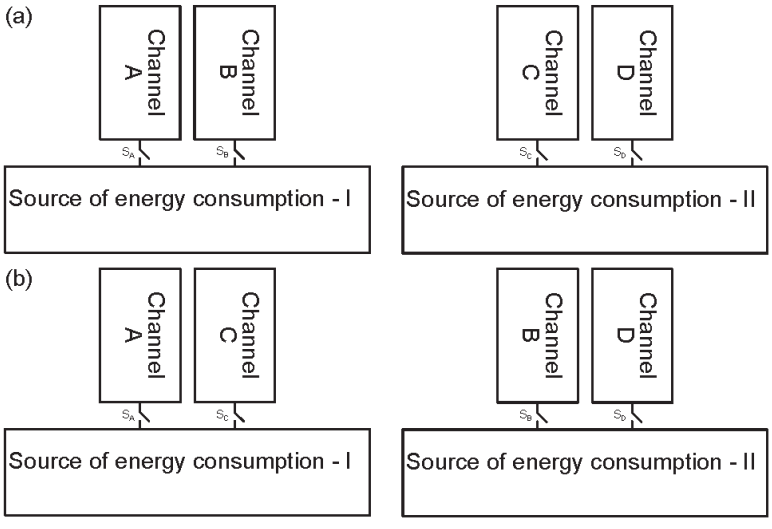

Figure 5. Analyzed configurations of the generator channels operating with two independent energy-receiving sources.

3. Mathematical Model of the MCPMSG

3.1. Model for the QCO Mode

The original mathematical model of the three-phase MCPMSG in the QCO mode developed by the authors is presented. The model was formulated by assuming the linearity of the magnetic circuit, a cylindrical symmetric stator, and a permanent magnet-type rotor (Figure 1). In the notation of the MCPMSG mathematical model, the notation for generator work is adopted. The general structure of the model for phase current vector **i** and phase generator output voltage vector **u** can be described in the following form:

$$\mathbf{e}^{\mathrm{PM}} = \mathbf{R}\,\mathbf{i} + \frac{\mathrm{d}}{\mathrm{d}t}[\mathbf{L}(\theta)\,\mathbf{i}] + \mathbf{u} \tag{1}$$

$$T_{\mathrm{m}} = J\,\frac{\mathrm{d}\omega_{\mathrm{m}}}{\mathrm{d}t} + D\omega_{\mathrm{m}} + T_{\mathrm{cog}}^{\mathrm{PM}} + T_{\mathrm{e}} \tag{2}$$

where the phase EMF voltage vector $\mathbf{e}^{\mathrm{PM}} = \mathbf{e}^{\mathrm{PM}}(\theta)$ for permanent magnet flux vector $\boldsymbol{\psi}^{\mathrm{PM}}(\theta) = \boldsymbol{\psi}^{\mathrm{PM}}$ is

$$\mathbf{e}^{\mathrm{PM}} = \omega\frac{\partial\boldsymbol{\psi}^{\mathrm{PM}}(\theta)}{\partial\theta} \tag{3}$$

and the total electromagnetic torque in the generating mode $T_{\mathrm{e}} = T_{\mathrm{e}}(\theta, \mathbf{i})$ is given by

$$T_{\mathrm{e}} = \frac{1}{\omega_{\mathrm{m}}}\left(\mathbf{e}^{\mathrm{PM}}\right)^{\mathrm{T}}\mathbf{i} + \frac{1}{2}\,\mathbf{i}^{\mathrm{T}}\frac{\partial\,\mathbf{L}(\theta)}{\partial\theta}\,\mathbf{i} \tag{4}$$

In Equations (1)–(4), vectors and matrices are defined:

$$\mathbf{e}^{\mathrm{PM}} = \begin{bmatrix}\mathbf{e}^{\mathrm{A}}\\ \mathbf{e}^{\mathrm{B}}\\ \mathbf{e}^{\mathrm{C}}\\ \mathbf{e}^{\mathrm{D}}\end{bmatrix},\ \boldsymbol{\psi}^{\mathrm{PM}} = \begin{bmatrix}\boldsymbol{\psi}^{\mathrm{A}}\\ \boldsymbol{\psi}^{\mathrm{B}}\\ \boldsymbol{\psi}^{\mathrm{C}}\\ \boldsymbol{\psi}^{\mathrm{D}}\end{bmatrix},\ \mathbf{i} = \begin{bmatrix}\mathbf{i}^{\mathrm{A}}\\ \mathbf{i}^{\mathrm{B}}\\ \mathbf{i}^{\mathrm{C}}\\ \mathbf{i}^{\mathrm{D}}\end{bmatrix},\ \mathbf{R} = \begin{bmatrix}\mathbf{R}^{\mathrm{A}} & \mathbf{0} & \mathbf{0} & \mathbf{0}\\ \mathbf{0} & \mathbf{R}^{\mathrm{B}} & \mathbf{0} & \mathbf{0}\\ \mathbf{0} & \mathbf{0} & \mathbf{R}^{\mathrm{C}} & \mathbf{0}\\ \mathbf{0} & \mathbf{0} & \mathbf{0} & \mathbf{R}^{\mathrm{D}}\end{bmatrix},$$

$$\mathbf{u} = \begin{bmatrix} \mathbf{u}^{\mathrm{A}} \\ \mathbf{u}^{\mathrm{B}} \\ \mathbf{u}^{\mathrm{C}} \\ \mathbf{u}^{\mathrm{D}} \end{bmatrix}, \ \mathbf{L}(\theta) = \begin{bmatrix} \mathbf{L}^{\mathrm{AA}}(\theta) & \mathbf{L}^{\mathrm{AB}}(\theta) & \mathbf{L}^{\mathrm{AC}}(\theta) & \mathbf{L}^{\mathrm{AD}}(\theta) \\ \mathbf{L}^{\mathrm{BA}}(\theta) & \mathbf{L}^{\mathrm{BB}}(\theta) & \mathbf{L}^{\mathrm{BC}}(\theta) & \mathbf{L}^{\mathrm{BD}}(\theta) \\ \mathbf{L}^{\mathrm{CA}}(\theta) & \mathbf{L}^{\mathrm{CB}}(\theta) & \mathbf{L}^{\mathrm{CC}}(\theta) & \mathbf{L}^{\mathrm{CD}}(\theta) \\ \mathbf{L}^{\mathrm{DA}}(\theta) & \mathbf{L}^{\mathrm{DB}}(\theta) & \mathbf{L}^{\mathrm{DC}}(\theta) & \mathbf{L}^{\mathrm{DD}}(\theta) \end{bmatrix} \tag{5}$$

The following symbols are used in Equations (1)–(4): θ—electrical rotor position angle, ω_m—the mechanical rotor speed, J—total rotor moment of inertia, D—rotor damping of viscous friction coefficient, $T_{\mathrm{cog}}^{\mathrm{PM}} = T_{\mathrm{cog}}^{\mathrm{PM}}(\theta)$—cogging torque, T_m—mechanical torque on the generator shaft. The cogging torque of PM machines produced by magnets can be expanded into a Fourier series. In Equation (1) for channels $k, l \in (A, B, C, D)$, vectors representing phase EMFs voltages $\mathbf{e}^{\mathrm{k}}$, phase permanent magnet fluxes $\boldsymbol{\psi}^{\mathrm{k}}$, phase currents $\mathbf{i}^{\mathrm{k}}$, phase output voltages $\mathbf{u}^{\mathrm{k}}$ used as sources of energy consumption, as well as matrices of stator resistances R^k and coefficients of self- and mutual inductances $\mathbf{L}^{\mathrm{kl}}(\theta)$ are defined as follows:

$$\begin{gathered} \mathbf{e}^{\mathrm{k}} = \left[e_1^{\mathrm{k}}, e_2^{\mathrm{k}}, e_3^{\mathrm{k}}\right]^{\mathrm{T}}, \ \boldsymbol{\psi}^{\mathrm{k}} = \left[\psi_1^{\mathrm{kPM}}(\theta), \quad \psi_2^{\mathrm{kPM}}(\theta), \quad \psi_3^{\mathrm{kPM}}(\theta)\right]^{\mathrm{T}}, \\ \mathbf{i}^{\mathrm{k}} = \left[i_1^{\mathrm{k}}, i_2^{\mathrm{k}}, i_3^{\mathrm{k}}\right]^{\mathrm{T}}, \ \mathbf{u}^{\mathrm{k}} = \left[u_1^{\mathrm{k}}, u_2^{\mathrm{k}}, u_3^{\mathrm{k}}\right]^{\mathrm{T}}, \ \mathbf{R}^{\mathrm{k}} = \mathrm{diag}(\mathrm{R}_1^{\mathrm{k}}, \mathrm{R}_2^{\mathrm{k}}, \mathrm{R}_3^{\mathrm{k}}), \\ \mathbf{L}^{\mathrm{kl}}(\theta) = \begin{bmatrix} \mathrm{L}_{11}^{\mathrm{kl}}(\theta) & \mathrm{L}_{12}^{\mathrm{kl}}(\theta) & \mathrm{L}_{13}^{\mathrm{kl}}(\theta) \\ \mathrm{L}_{21}^{\mathrm{kl}}(\theta) & \mathrm{L}_{22}^{\mathrm{kl}}(\theta) & \mathrm{L}_{23}^{\mathrm{kl}}(\theta) \\ \mathrm{L}_{31}^{\mathrm{kl}}(\theta) & \mathrm{L}_{32}^{\mathrm{kl}}(\theta) & \mathrm{L}_{33}^{\mathrm{kl}}(\theta) \end{bmatrix}, \end{gathered} \tag{6}$$

where for $\mathrm{i} \in (1, 2, 3)$, $\psi_{\mathrm{i}}^{\mathrm{kPM}}(\theta)$—the permanent magnet fluxes linking the stator windings, $\mathrm{L}_{\mathrm{ij}}^{\mathrm{kl}}(\theta)$—coefficients of self-end mutual inductances. The coefficients $\mathrm{L}_{\mathrm{ij}}^{\mathrm{kl}}(\theta)$ depend on the rotor construction (cylindrical or salient pole) and the internal structure of the generator windings (symmetrical or asymmetrical) and can be expanded into a Fourier series.

The phase EMFs voltage vectors $\mathbf{e}^{\mathrm{k}}$ in Equation (1) $\mathbf{e}^{\mathrm{PM}}$ for channels $\mathrm{k} \in (\mathrm{A}, \mathrm{B}, \mathrm{C}, \mathrm{D})$ are defined:

$$\mathbf{e}^{\mathrm{k}} = \omega \left[\frac{\partial \psi_1^{\mathrm{kPM}}(\theta)}{\partial \theta}, \quad \frac{\partial \psi_2^{\mathrm{kPM}}(\theta)}{\partial \theta}, \quad \frac{\partial \psi_3^{\mathrm{kPM}}(\theta)}{\partial \theta}\right]^{\mathrm{T}} \tag{7}$$

where $\omega = d\theta/dt = p\,\omega_{\mathrm{m}}$—electrical speed, p—rotor number of the pole pairs. The permanent magnet flux linking each stator winding of the MCPMS generator follows the trapezoidal profile phase EMF. The real phase EMF functions can be expressed as a Fourier series.

The total electromagnetic torque T_{e} in Equation (4) is the sum of the magnet torque $T_{\mathrm{e}}^{\mathrm{PM}}$ and reluctance torque $T_{\mathrm{e}}^{\mathrm{RE}}$. The magnet torque $T_{\mathrm{e}}^{\mathrm{PM}}$ and electrical output power $P_{\mathrm{e}}^{\mathrm{PM}}$, generated by the permanent magnets and currents, can be written in the form:

$$T_{\mathrm{e}}^{\mathrm{PM}} = \frac{1}{\omega_{\mathrm{m}}} P_{\mathrm{e}}^{\mathrm{PM}}, \ P_{\mathrm{e}}^{\mathrm{PM}} = \sum_{\mathrm{k=A}}^{\mathrm{D}} \sum_{\mathrm{i}=1}^{3} \left(e_{\mathrm{i}}^{\mathrm{k}}\, i_{\mathrm{i}}^{\mathrm{k}}\right) \tag{8}$$

Reluctance torque is produced by the interaction of the magnetomotive forces of the stator current with the angular variation in the magnetic resistance of the rotor.

Equations (1)–(4) generally constitute a mathematical model of the MCPMS generator in the QCO mode or double DCO mode, for example, DCO AB + CD or AC + BD mode.

3.2. Model for DCO Mode in Star Configuration

The voltage Equation (1) and electromagnetic torque (4) of the MCPMSG for the DCO AB mode, i.e., where only channels A and B are loaded, can be written in the form:

$$\begin{bmatrix} \mathbf{e}^{\mathrm{A}} \\ \mathbf{e}^{\mathrm{B}} \end{bmatrix} = \begin{bmatrix} \mathbf{R}^{\mathrm{A}} & \mathbf{0} \\ \mathbf{0} & \mathbf{R}^{\mathrm{B}} \end{bmatrix} \begin{bmatrix} \mathbf{i}^{\mathrm{A}} \\ \mathbf{i}^{\mathrm{B}} \end{bmatrix} + \frac{\mathrm{d}}{\mathrm{d}t} \left\{ \begin{bmatrix} \mathbf{L}^{\mathrm{AA}}(\theta) & \mathbf{L}^{\mathrm{AB}}(\theta) \\ \mathbf{L}^{\mathrm{BA}}(\theta) & \mathbf{L}^{\mathrm{BB}}(\theta) \end{bmatrix} \begin{bmatrix} \mathbf{i}^{\mathrm{A}} \\ \mathbf{i}^{\mathrm{B}} \end{bmatrix} \right\} + \begin{bmatrix} \mathbf{u}^{\mathrm{A}} \\ \mathbf{u}^{\mathrm{B}} \end{bmatrix} \tag{9}$$

$$T_e(\theta, \mathbf{i}^A, \mathbf{i}^B) = \frac{1}{\omega_m}\left\{(\mathbf{e}^A)^T\mathbf{i}^A + (\mathbf{e}^B)^T\mathbf{i}^B\right\} + \frac{1}{2}(\mathbf{i}^A)^T\frac{\partial \mathbf{L}^{AA}(\theta)}{\partial\theta}\mathbf{i}^A + (\mathbf{i}^A)^T\frac{\partial \mathbf{L}^{AB}(\theta)}{\partial\theta}\mathbf{i}^B + \frac{1}{2}(\mathbf{i}^B)^T\frac{\partial \mathbf{L}^{BB}(\theta)}{\partial\theta}\mathbf{i}^B \quad (10)$$

where for channels $k \in (A, B)$, vectors and matrices are defined in (6)–(7). Additional constraints on voltages and currents are imposed by the arrangement of generator phase windings in a star configuration (Y). The relationship of line and phase voltages and currents in a Star (Y) connection, for example, in the DCO AB mode, can be written as ($k \in (A,\ B)$):

$$\mathbf{e}_Y^k = \left[\ e_{12}^k, e_{23}^k, e_{31}^k\ \right]^T = \mathbf{K}_Y\mathbf{e}^k,\ \mathbf{i}_Y^k = \mathbf{i}^k = \left[\ i_1^k, i_2^k, i_3^k\right]^T,$$
$$\mathbf{u}_Y^k = \left[u_{12}^k, u_{23}^k, u_{31}^k\right]^T = \mathbf{K}_Y\mathbf{u}^k,\ \mathbf{K}_Y = \begin{bmatrix} 1 & -1 & 0 \\ 0 & 1 & -1 \\ -1 & 0 & 1 \end{bmatrix} \quad (11)$$

The output line voltages contained in the vectors $\mathbf{u}_Y^k$, k∈(A, B), supply one or many energy receivers of various types, alternating current (AC) or direct current (DC). For example, these voltages may be associated with a regulated direct-current load operating in voltage mode. Equations (9)–(10) with (11) constitute the mathematical model of the MCPMS generator in DCO AB mode for the star connection (Y). Similarly, equations can be written for other possible configuration cases, for example, operating in a mode DCO AC ($k \in (A,\ C)$) or DCO CD ($k \in (C,\ D)$).

4. The MCPMSG Operation with Different Sources of Energy Consumption

4.1. Generator Operation with One Source of Energy Consumption

The scope of the analysis was limited to the issue of the DCO or double DCO. The dual-channel operating state can occur with one source of energy consumption (Figure 4, for example, S_A-on, S_B-on). The experiment and numerical tests were carried out at a speed of 1500 rpm. An adjustable DC (U_{dc}) load was used as a source of energy consumption, and it was operated in voltage mode (ITECH DC Electronics Load). The laboratory test stand is shown in Figure 6. The power supply system uses a synchronous motor with permanent magnets powered by a dedicated inverter. The tested MCPMSG is coupled to the drive system through couplings and a torque converter (TS 107 by Magtrol). In the DC load range, passive diode rectifiers are used. The DC output of the rectifier is connected to the electronic loads (ITECH DC Electronics Load). A six-channel power analyzer with a motor module (WT 1600 Yokogawa) is used to record the electrical and mechanical parameters. The waveforms of current and voltage are recorded using a multichannel oscilloscope recorder (DL 850E Yokogawa) with the use of voltage and current probes.

4.1.1. Self- and Mutual Inductance

Self- and mutual inductances were determined for the SCO A, DCO AB, and DCO AC configurations. In the case of the DCO AB and DCO AC, the self-inductance is the resultant inductance of the analyzed configurations. For the DCO AB configuration, it is the resultant inductance of parallelly connected channels A and B. In the case of the DCO AC configuration, it is the resultant inductance of channels A and C. Commercial software was used to determine the inductance [26]. It offers two methods for calculating inductance, i.e., apparent and incremental. The constant current method was chosen, that is, apparent. It allows you to determine the static inductance based on the quotient of the calculated value of the coupled flux to the value of the current causing it. When determining the coupled flux, the flux from permanent magnets is omitted.

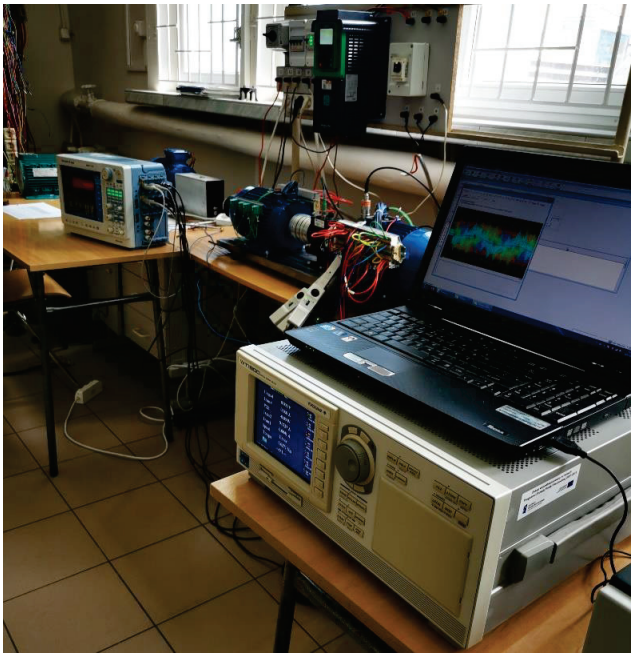

Figure 6. Test stand.

Figure 7a shows the self-inductance of the conventional band 1 of channel A. In addition, the mutual inductance with the other channels of the same phase is shown. The consequence of this for the operation of the DCO is a significant change in the self-inductance of the DCO AC channel in relation to the DCO AB (Figure 7b).

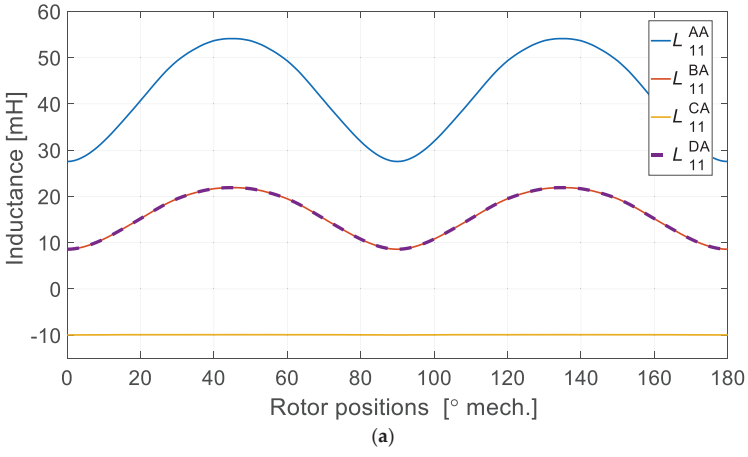

(**a**)

Figure 7. *Cont*.

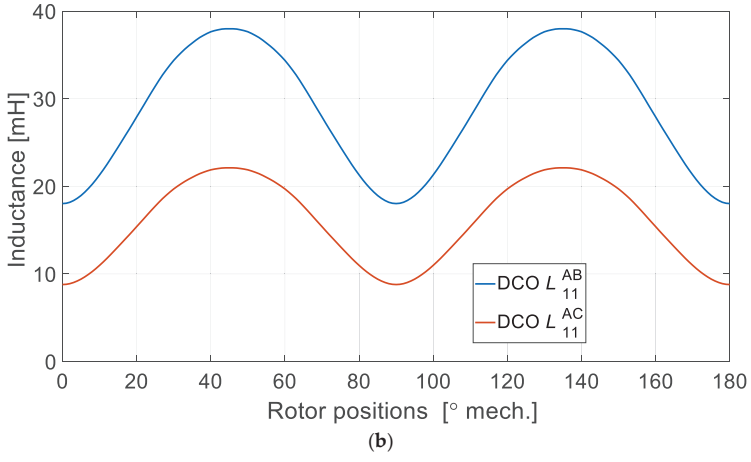

(**b**)

Figure 7. Self- and mutual inductance for (**a**) SCO A, (**b**) DCO AB, and DCO AC.

A single conventional channel A, due to the arrangement of the windings shown in Figure 1a, is substantially coupled to channels B and D (Figure 7a). In the C channel, the coupling is less due to the geometric shift of 90°. The value of the mutual inductance is practically constant and does not depend on the position of the rotor. In addition, it is negative feedback.

However, even the feedback between channels A and C is not completely negligible (Figure 7a). A significantly higher value of self-inductance of the DCO AB configuration (Figure 7b) substantially increases the values of the impedance of the channel in relation to the DCO AC configuration. This is due to the geometric distribution of the individual channels of the analyzed MCPMSG using the full pitch of the distributed winding.

4.1.2. Waveforms of Electromagnetic Torque and Currents

The electromagnetic torque of the generator operating in DCO AB and DCO AC configurations is presented in Figure 8.

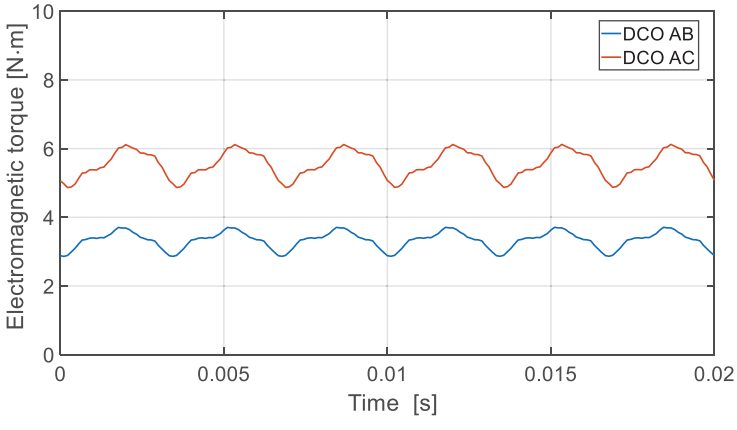

Figure 8. Electromagnetic torque for DCO AB and DCO AC for one source of energy consumption.

The DCO AB configuration generates a smaller value of the braking torque. However, it has a direct impact on the waveforms of the generator currents (Figure 9).

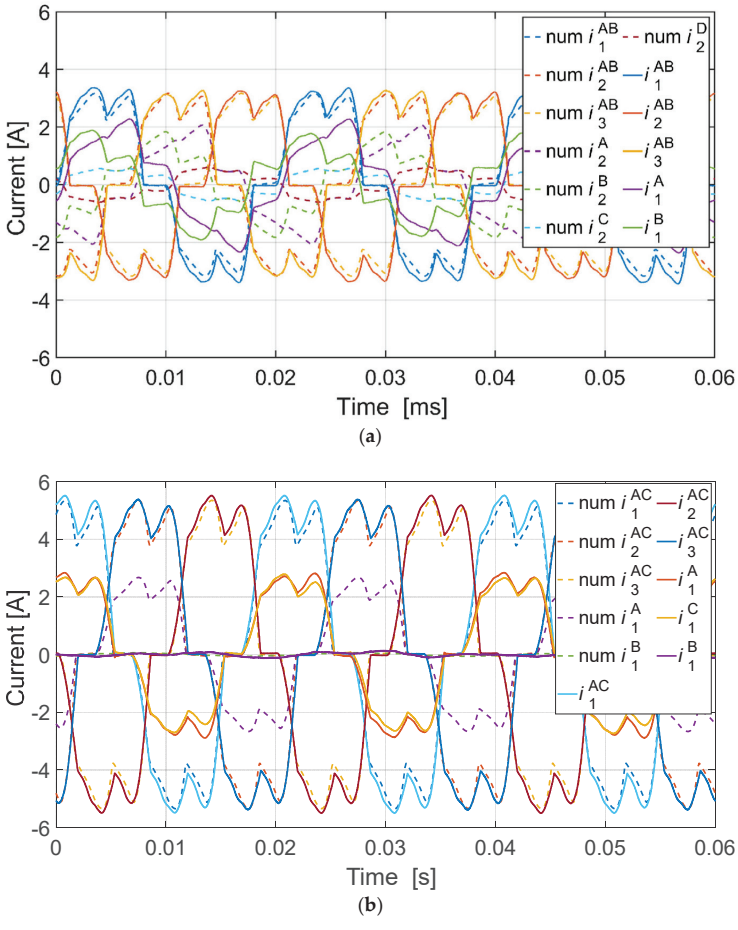

Figure 9. Current waveforms for (**a**) DCO AB and (**b**) DCO AC.

The values of the currents in the DCO AB configuration are smaller than those in the DCO AC configuration. Consequently, for the same voltage value of the load, a lower power output is obtained. Additionally, the phase shift between the currents in individual channels is observed. Despite the internal symmetry of the generator, a certain value of the equalizing current flows inside channel AB (Figure 9a). The main reason for the relatively high value of equalizing currents is the magnetic coupling between channels A and B (Figure 7a). The EMF in the individual channels (Table 3) contributes much less. In the DCO AC configuration, the visible equalization current (Figure 9b) flows mainly due to the difference in the EMF values of both channels (Table 3). The significantly lower current values of the DCO AB configuration are the result of the higher phase impedance compared to the DCO AC configuration (Figure 7b).

4.1.3. External Characteristics

In the case of the DCO AC configuration, both channel currents are identical. The results of the numerical calculations are confirmed by the experiment. The external characteristics of the efficiency of the generator in the DCO operation are determined. The external characteristics of the generator obtained in the numerical tests are shown in Figure 10a. The laboratory test results are shown in Figure 10b (DCO AB) and Figure 10c (DCO AC).

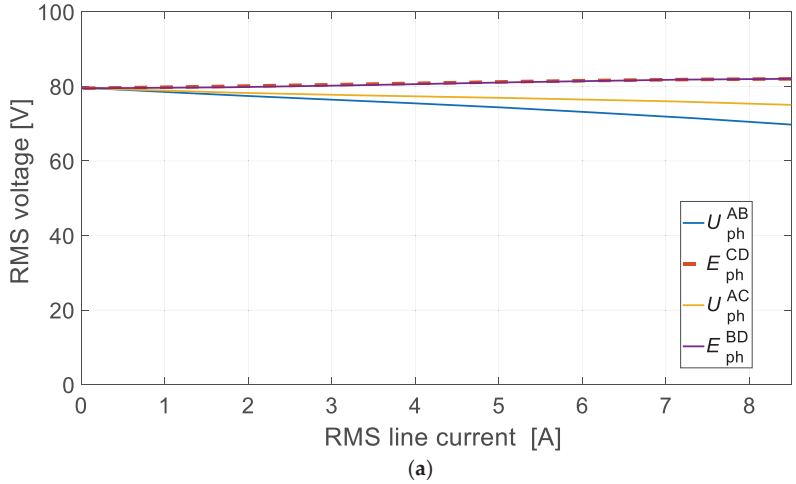

(**a**)

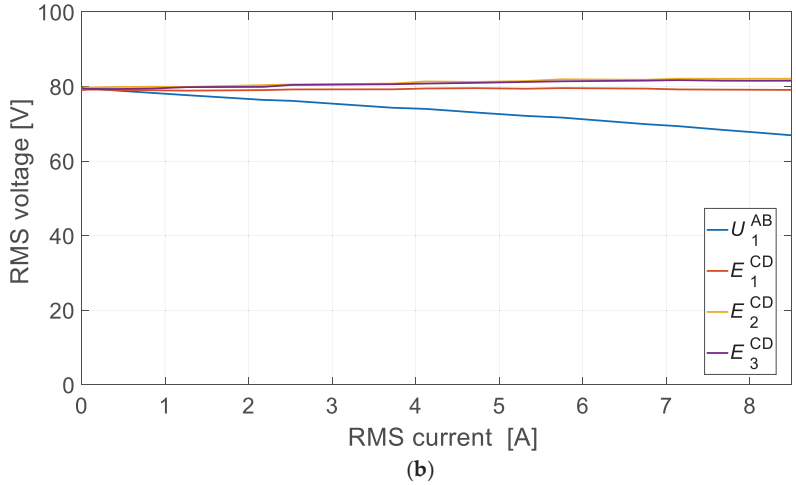

(**b**)

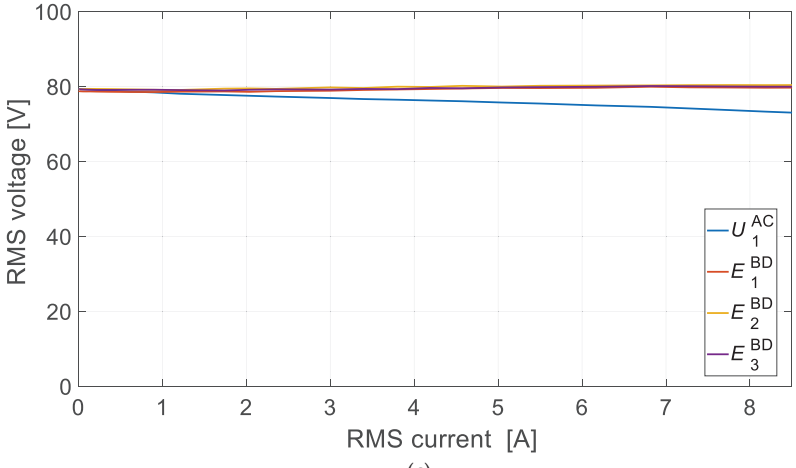

(**c**)

Figure 10. External characteristics for (**a**) numerical test, (**b**) laboratory test for DCO AB, and (**c**) laboratory test for DCO AC.

The stiffness of the external characteristic for the DCO AC operation is much higher than that for the DCO AB. The load capacity of the generator in the DCO AC mode is greater for the same output voltage variation. In both modes of operation, an increase in the value of voltages induced in unloaded channels is observed. Under laboratory conditions, a greater difference is observed in the values of induced voltages of unloaded channels in the DCO AB mode (Figure 10b). This is not visible in numerical calculations. As shown in Figure 9, in relation to the conventional channel A, there is a large magnetic coupling with channels B and D. This has a significant impact on the operation of the DCO AB configuration. Figure 11 shows the results of the numerical calculations of the RMS currents in the individual generator channels as a function of the line current of the loaded channel.

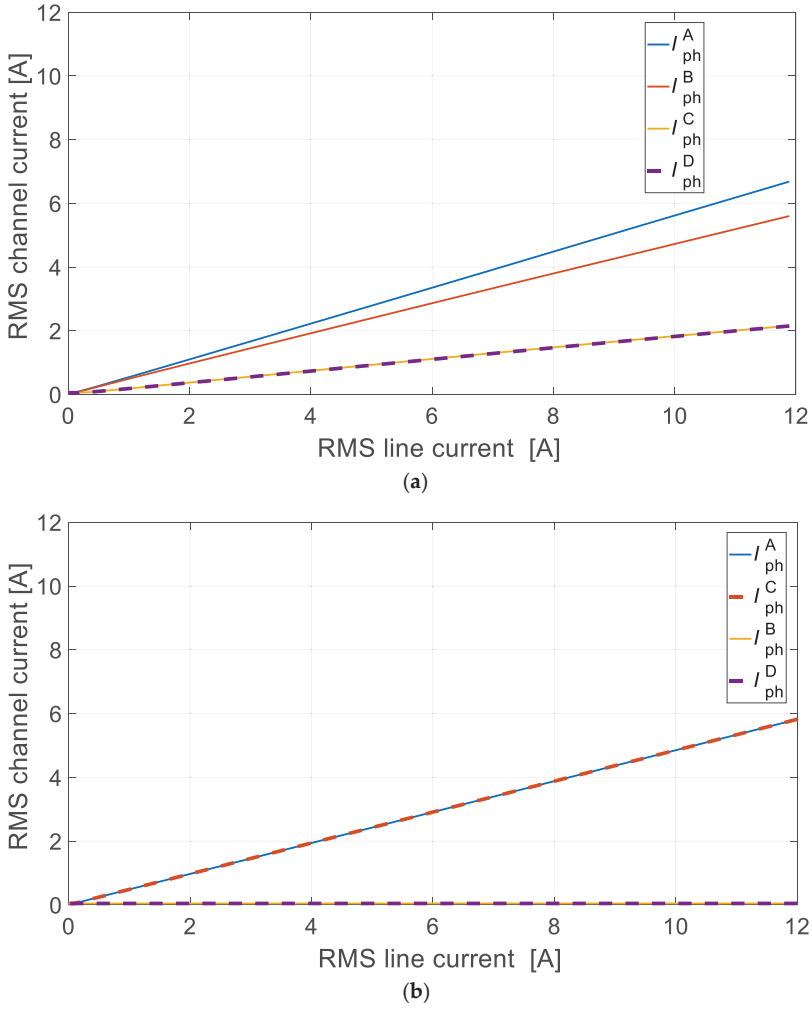

Figure 11. RMS channel current vs. RMS line current for (**a**) DCO AB and (**b**) DCO AC.

The line current is the sum of the channel currents (Figure 11). There is a significant difference between the DCO AB (Figure 11a) and the DCO AC (Figure 11b). In the case of the DCO AB, the active channels A and B are not loaded evenly. In the theoretically inactive channels C and D, due to the presence of the magnetic couplings, a high value of the equalizing current can be observed. Unfortunately, it is proportional to the currents

of the active channels. The configuration DCO AC behaves completely differently in this aspect. In the active channels A and C, the currents are identical. The currents in the inactive channels B and D equal zero.

4.2. Generator Operation with Two Independent Sources of Energy Consumption

The multichannel generator is able to work with two independent sources of energy consumption (Figure 5). In this case, the generator may be loaded evenly or unevenly. Working with only one source of consumption, as in the previous chapter, is also possible. The generator electromagnetic moment is shown in Figure 12. The current waveforms are presented in Figure 13.

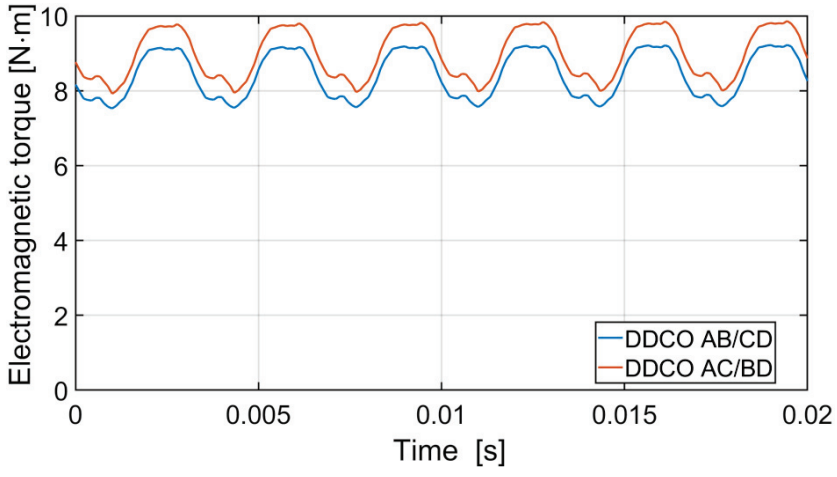

Figure 12. Electromagnetic torque for the DDCO AB/CD and the DDCO AC/BD for two independent sources of energy consumption.

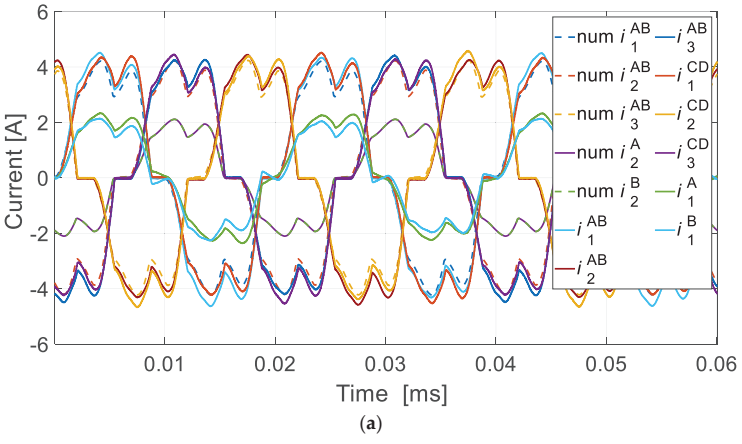

(**a**)

Figure 13. *Cont.*

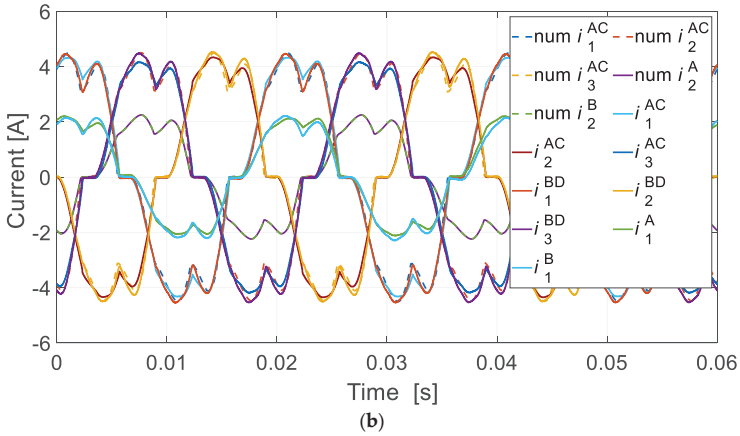

(**b**)

Figure 13. Current waveforms for (**a**) DDCO AB/CD and (**b**) DDCO AC/BD for two independent sources of energy consumption.

As in the case of the operation with one source of energy consumption, a lower value of braking torque is obtained for the DDCO AB/CD configuration. The generator current values are also lower for the DDCO AB/CD configuration. However, in the case of a symmetrical load, the currents in the individual channels are identical. It changes when the load of one pair of channels is modified. Again, for the DDCO AB/CD configuration, the equalizing currents flow in individual channels. The equalizing currents of the DDCO AB/CD configuration reach their minimum value when the load of both configurations is identical, that is, DCO AB = DCO CD. With different loads, the equalizing currents increase. In the case of DDCO AC/BD, the equalizing currents have a marginal value and are caused only by the difference in EMF of individual channels (Table 3). In the DDCO AB/CD configuration, the individual channels are practically magnetically independent. When working with two independent energy-receiving sources, the generator currents are reduced, regardless of the configuration (DDCO AB/CD or AC/BD). Increasing the load of one energy-receiving source reduces the output power of the second energy-receiving source of the tested MCPMSG (Figure 14).

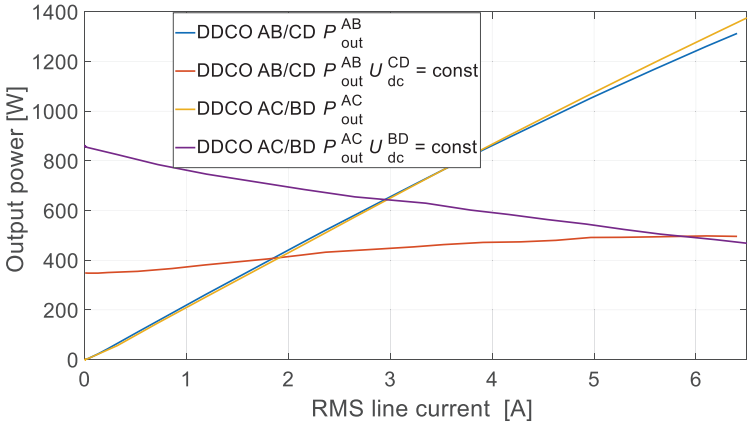

Figure 14. Output power vs. RMS value of current of the DDCO AB/CD at $U_{dc}{}^{\mathrm{CD}}$ = const and DDCO AC/BD at $U_{dc}{}^{\mathrm{BD}}$ = const.

For the MCPMSG with windings distributed in the DDCO operating mode, the DDCO AB/CD configuration shows more independence between the DCO AB and the DCO CD. Changing the load on the DCO AB causes much less impact on the DCO CD operation. There is an increase in the power output while maintaining a constant voltage value $U_{DC}{}^{CD}$. In the case of the DDCO AC/BD, the interaction between the DCO AC and the DCO BD is very large. This suggests that structures with distributed windings with a diametrical pitch are not dedicated to the implementation of the multichannel operation with different sources of energy consumption. At the same time, they work very well in a typical DCO mode with a single source of energy consumption. According to the authors, the problem of interaction of the DDCO AC/BD mode between the DCO AC and the DCO BD can be significantly reduced by using a winding with a significantly shortened pitch.

5. Diagnostic Method of the MCPMSG

5.1. Proposed Voltage Signal Method

The multichannel generator is able to work with two independent sources of energy consumption (Figure 5). In this case, the generator may be loaded evenly or unevenly. During the operation of the generator, diagnostic information about the state of individual channels is important. The paper [24] indicates the possibility of diagnostic control by performing the harmonic analysis (FFT) of the voltage signal for motor operation of the MCPMSM. In Figure 15, the authors' proposition for the location of the diagnostic voltage signal for the MCPMSG is presented [27].

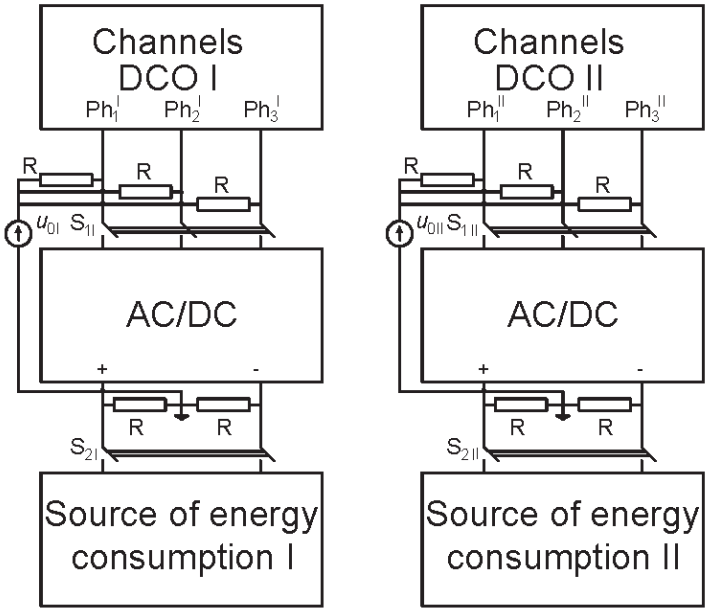

Figure 15. Proposition for the location of the diagnostic voltage signal by using the MCPMSG.

The neutral point of the generator is the neutral reference point for the generated diagnostic voltage signal u_0. However, this approach limits the diagnosis of the generator with star-connected windings only. Using the approach presented in Figure 15, the diagnostic voltage signal becomes independent of the type of the generator winding connection (star, delta, or mixed connections). While working under the condition of internal symmetry of the generator, the diagnostic voltage signal u_0 should contain only the third harmonic and its odd multiples (9th, 15th, etc.). The appearance of the internal asymmetry of the genera-

tor affects the harmonic content of the diagnostic signal u_0. The fundamental component of the voltage signal has an important role and can be determined from

$$f_1 = \frac{n \cdot p}{60}, \tag{12}$$

where f_1—frequency fundamental component, n—speed, p—number of pairs of poles.

Typical harmonics of the u_0 voltage diagnostic signal waveform should theoretically include the 3rd, 9th, 15th, and higher harmonics. This is a typical situation for the ideal u_0 diagnostic run corresponding to the analysis of a fully symmetrical typical PM or MCPMSG generator. After the appearance of the unbalanced operation (without indicating a specific cause), the emergence of a diagnostic harmonic defined by Equation (11) should be expected. Additional higher-order harmonics (fifth, seventh, etc.) should also be expected. However, its diagnostic significance is slightly smaller. Higher diagnostic harmonics (fifth, seventh, etc.) can potentially be used to determine the type of asymmetry, e.g., winding break, partial-turn short circuits, etc. According to the authors, the fundamental diagnostic harmonic f_1 and its relation to the third harmonic f_3 are the most important. The proposed diagnostic method allows us to control the operation of the MCPMSG of each pair of DCO channels (Figure 5). The diagnostic system can also be extended to direct control of each generator channel.

5.2. Results of Numerical Research and Laboratory Tests—DCO

A typical DCO operating mode will be obtained if the S_{2II} switch is open (Figure 15). In this situation, the second pair of channels remains in idle mode. At the same time, the u_{0II} diagnostic signal is available. In order to examine the MCPMSG diagnostic system mentioned above, one of the configurations (DCO AC) including the asymmetry cases listed in Table 3 was tested at a speed of 1500 rpm. The diagnostic signals obtained from the channel AC of the analyzed cases are shown in Figure 16 (numerical calculations) and Figure 17 (laboratory tests). The content of the higher-order harmonics of the voltage signal obtained from numerical calculations is presented in Figure 18. The results of the laboratory tests are shown in Figure 19.

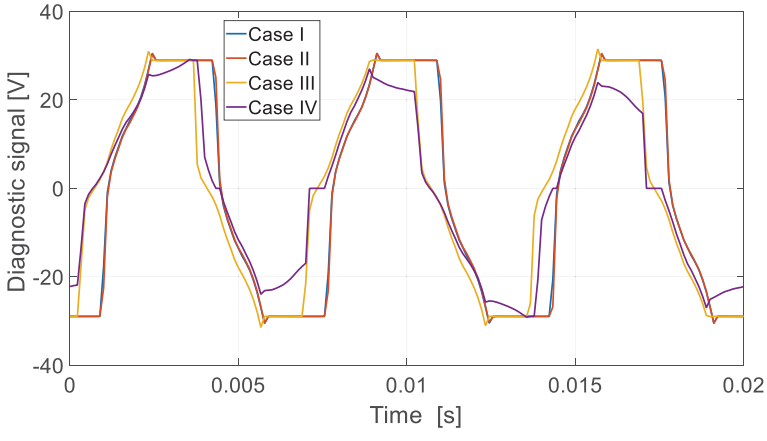

Figure 16. Diagnostic voltage signal u_{0I} of DCO—numerical calculations.

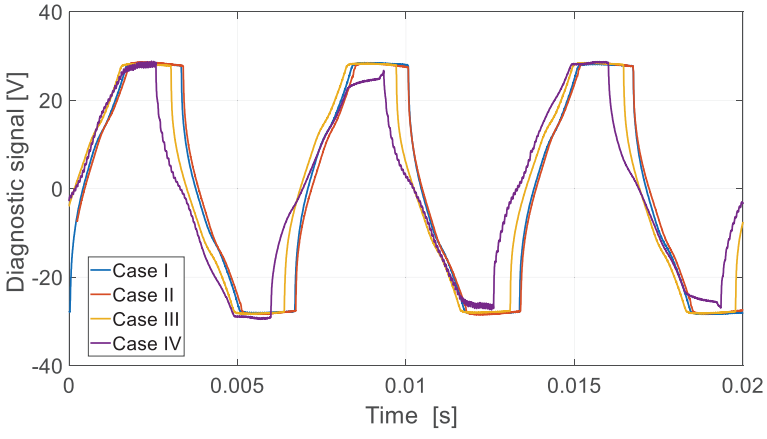

Figure 17. Diagnostic voltage signal u_{0I} of DCO—laboratory test.

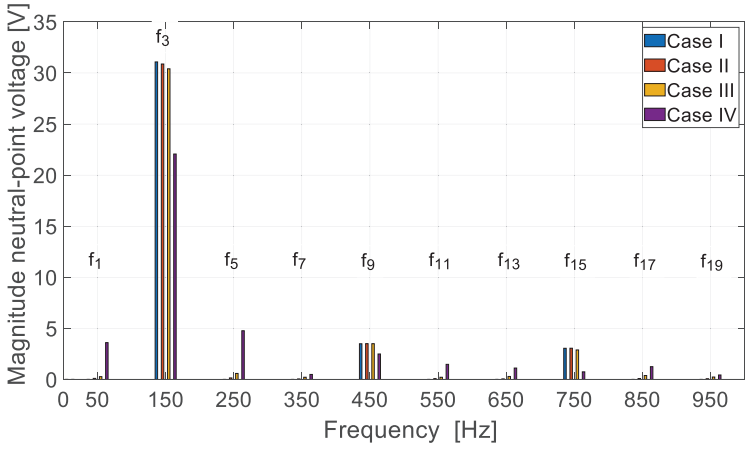

Figure 18. FFT of the diagnostic voltage signal u_{0I}—numerical calculations.

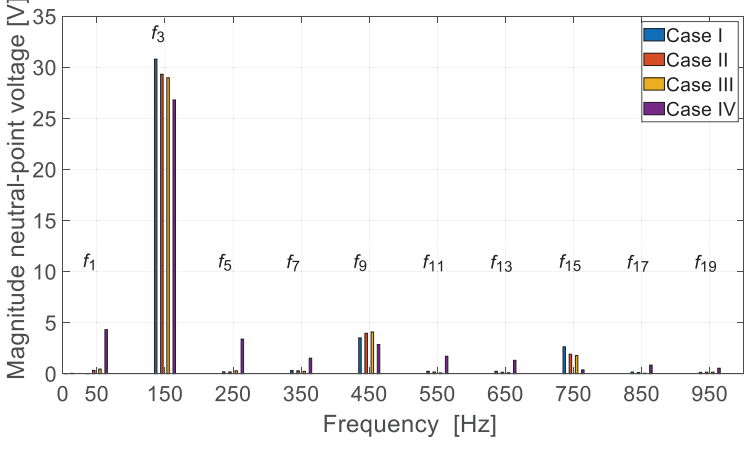

Figure 19. FFT of diagnostic voltage signal u_{0I}—laboratory test.

The numerical and laboratory tests confirmed that the proposed diagnostic approach is correct. On the basis of the diagnostic voltage signal, it is possible to control the operating status of individual channels. Any irregularities in the channel operation will result in the appearance of the fundamental component of the diagnostic signal. An increase in the fundamental component signifies an increase in internal asymmetry or other irregularities in the operation of the generator channels. As has been presented, even the lack of one turn of the coil in one of the channel windings can be observed in the diagnostic signal. In the case of operation of, e.g., redundant systems, where a multichannel mode can also be used, there is always a problem of a control of the correctness of their work.

Table 7 presents the results of the amplitudes obtained for the two most important frequencies of the diagnostic signal, i.e., f_1 and f_3.

Table 7. Amplitudes of critical diagnostic frequencies in the DCO mode.

Case/Harmonic		f_1 [mV]	f_3 [V]	f_1/f_3 [%]
Case I	num	7.7	32.83	0.023
	test	60	30.78	0.194
Case II	num	90	32.67	0.276
	test	260	29.31	0.887
Case III	num	279	32.31	0.865
	test	380	28.95	1.312
Case IV	num	3447	24.25	14.21
	test	4306	26.79	16.08

It can be seen that the laboratory test for the symmetry state (Case I) showed the existence of a significantly higher diagnostic frequency than in the case of numerical calculations. The value of the amplitude f1 of the diagnostic signal proves the existence of various internal asymmetries of the MCPMSG prototype. The introduction of, for example, the division of the phase winding of one of the channels (Figure 2) generates electrical asymmetry. One can risk a statement that the f_1 harmonic of the proposed voltage diagnostic signal can be used to assess the quality of the classical machine prototype. In the case of the MCPMSG, it is possible to assess the quality of the individual channels of the generator in this way. Regardless of the existence of a certain internal asymmetry in the real model, the tests carried out show that the appearance of internal asymmetry increases not only the diagnostic frequency f_1; in addition, the f_1/f_3 ratio also increases, which numerical and laboratory tests clearly indicate. If the amplitude of the harmonic f1 is less than 1% of the harmonic f_3, this is a situation that does not cause abnormalities in the operation of the generator channels.

Therefore, sometimes it is recommended that all channels work because only working channels can be monitored. In the case of the proposed method, it is possible to monitor the condition of the channel even when it is not involved in the generation of electricity (switch S_{2II}—off in Figure 15). The diagnostic voltage signal is available in any operating state of the multichannel generator at a speed greater than zero.

The motor current signature analysis (MCSA) method [21] was tested under numerical and laboratory conditions in relation to the possibility of detecting anomalies in the operation of the generator channels. In the MCSA method, the anomaly should be manifested by the appearance of the third harmonic component and its odd multiples. The sensitivity of the MCSA method turned out to be insufficient in relation to Case II and Case III. It was only in Case IV that the results clearly indicated a problem in the channel operation. In addition, the MCSA method is suitable for monitoring loaded generator channels.

5.3. Results of Numerical Research and Laboratory Tests—DDCO

In the case of the DDCO, the operation of both channels must be controlled. This also includes the case of a no-voltage operation of one of the DDCO systems. The analysis is limited to one configuration, i.e., the DCO AC (DCO I) and the DCO BD (DCO II). However,

in the case of the DDCO, both channels, even under conditions of internal symmetry of the generator (Case I), may be loaded differently. For the analysis, it is assumed that the DCO AC channel works with different loads. The following generator operating conditions are assumed:

- CON I: DCO I—OFF, DCO II—ON;
- CON II: DCO I—ON, DCO II—ON (LOAD DCO I < LOAD DCO II);
- CON III: DCO I—ON, DCO II—ON (LOAD DCO I = LOAD DCO II);
- CON IV: DCO I—ON, DCO II—ON (LOAD DCO I > LOAD DCO II).

The results of numerical calculations in relation to the first two diagnostic frequencies are presented in Table 8.

Table 8. The DDCO mode critical diagnostic frequency amplitudes (Case I).

Case/Harmonic		f_1 [mV]	f_3 [V]	f_1/f_3 [%]
CON I	DCO I	0.78	33.4	0.023
	DCO II	0.76	32.84	0.023
CON II	DCO I	2.34	33.87	0.069
	DCO II	2.23	33.19	0.067
CON III	DCO I	3.34	35.17	0.094
	DCO II	3.34	35.17	0.094
CON IV	DCO I	0.94	34.15	0.027
	DCO II	0.97	35.82	0.027

Under the symmetry conditions of the DDCO operation, the load change in DCO I does not affect the diagnostics of the DCO II operation. There is some interaction between DCO I and DCO II. The change in the operating conditions of the MCPMSG resulting from different loads on both channels does not affect the harmonic content of the diagnostic signals. This is the advantage of the proposed diagnostic method.

More interesting is the case of asymmetry in the DDCO operating mode. One of the cases (CON III) in which internal asymmetry appeared in DCO I (Cases II, III, and IV) is analyzed. Table 9 presents the results of the numerical calculations.

Table 9. Critical diagnostic frequency amplitudes in the DDCO mode (CON III).

Case/Harmonic		f_1 [mV]	f_3 [V]	f_1/f_3 [%]
CON I—Case I	DCO I	3.34	35.17	0.094
	DCO II	3.34	35.17	0.094
CON II—Case II	DCO I	63.8	35.09	0.182
	DCO II	56.9	35.11	0.162
CON III—Case III	DCO I	202.8	34.95	0.58
	DCO II	117.4	35.1	0.335
CON IV—Case IV	DCO I	5336	27.78	14.54
	DCO II	1109	32.45	3.441

The appearance of the asymmetry in the DCO I causes, as expected, an increase in the diagnostic harmonic f_1. Its percentage in relation to the frequency f_3 also increases. This relationship is similar to the case of the DCO I (Table 6) standalone operation with respect to percentage content. At the same time, it can be seen that in DCO II, there is also an increase in the content of the diagnostic harmonic f_1. However, this is not a diagnostic method error. The u_{0II} diagnostic signal takes into account the effect of the resulting asymmetry in DCO I. This shows the high sensitivity of the proposed method. This is also confirmed by the results of laboratory tests (Table 10).

Table 10. Amplitudes of critical diagnostic frequencies of the DDCO mode (CON III)—laboratory test.

Case/Harmonic		f_1 [mV]	f_3 [V]	f_1/f_3 [%]
CON I—Case I	DCO I	70	30.65	0.223
	DCO II	72	31.16	0.231
CON II—Case II	DCO I	296	30	0.987
	DCO II	157	30.9	0.508
CON III—Case III	DCO I	427	31.9	1.33
	DCO II	273	32.2	0.848
CON IV—Case IV	DCO I	2870	26	11.038
	DCO II	668	27.6	2.42

As shown in Section 4.1, there are relatively large magnetic couplings between the channels in the analyzed solution. This is the reason for the increase in the amplitude of the diagnostic frequency f_1. The analysis of the voltage and current waveforms shows that after the occurrence of an asymmetry event in DCO I, the shape of the current and voltage waveforms in DCO II changes. The consequence of this is a change in the time course of the diagnostic signal, manifested by an increase in the amplitude of the diagnostic frequency f_1. In practice, this means that the DCO II, despite its internal symmetry, generates asymmetric voltage waveforms at the generator terminals.

6. Summary and Conclusions

This article proposes the use of the MCPMSG for safety critical applications. In comparison to classical solutions, the use of the MCPMSG allows us to obtain an improvement in the redundancy of the power generation system. The MCPMSG can work with one energy consumption system. In this case, the two channels are treated as redundant. The other option is to work with two independent energy-receiving sources. In both cases, the configuration of the channels is important since it affects the generator operation. The analysis of the MCPMSG properties in various channel configurations is possible due to the mathematical model developed by the authors. Regardless of the type of configuration of individual generator channels, their condition should be monitored in terms of correct operation. Conclusions were formulated on the basis of the tests that were carried out.

For the DCO it is preferred to use the configuration of the channels that are not magnetically coupled. This solution provides higher efficiency of energy conversion and balanced magnetic tension. In the DCO with magnetically coupled channels, in solitary operation or with various loads, the efficiency deteriorates due to the appearance of equalizing currents.

Numerical and laboratory tests have shown that there is more interaction between the DCO AC and the DCO BD channels in the DDCO mode. The change of the DCO AC load affected the operation of the DCO BD. This problem can be reduced by reducing the pitch of the distributed winding or by using a typical concentrated winding. The proposed method of diagnosing the operating state of the channels is based on harmonic analysis of the voltage signal. The appearance of the diagnostic harmonic component in the voltage signal indicates deviations from symmetric operation. The advantage of this approach is the ability to monitor channels in a non-current state. The proposed diagnostic method can also be used under practical conditions to assess machine quality. Even small differences in the values of induced voltages, phase resistances, etc., have an impact on the increase in the diagnostic frequency f_1 of the diagnostic signal. The effects of damage to one of the channels are noticeable in the remaining efficient channels. This shows the high sensitivity of the proposed diagnostic method.

The validity of the proposed MCPMSG is verified by the experimental results.

The prototype, the extended mathematical model, and the proposed diagnostic method will allow for further testing of the MCPMSG, e.g., analysis of emergency states such as short circuits (e.g., one turn) in the windings of the band of a given channel.

Author Contributions: Conceptualization, M.K. and E.S.; methodology, M.K. and J.P.; software, M.K.; formal analysis, M.K. and J.P.; investigation, M.K. and E.S.; resources, M.K. and E.S.; data curation, M.K., writing—original draft preparation, M.K. and E.S.; writing—review and editing J.P.; supervision, M.K. and J.P.; project administration, M.K.; funding acquisition, M.K. All authors have read and agreed to the published version of the manuscript.

Funding: This research is financed in part by the statutory funds (UPB) of the Department of Electrodynamics and Electrical Machine Systems, Rzeszow University of Technology, and in part by the Minister of Education and Science of the Republic of Poland within the 'Regional Initiative of Excellence' program for the years 2019–2023. Project number 027/RID/2018/19, amount granted: 11,999,900 PLN.

Conflicts of Interest: The authors declare no conflict of interest.

References

1. Cao, W.; Mecrow, B.C.; Atkinson, G.J.; Bennett, J.W.; Atkinson, D.J. Overview of Electric Motor Technologies Used for More Electric Aircraft (MEA). *IEEE Trans. Ind. Electron.* **2011**, *59*, 3523–3531. [CrossRef]
2. Madonna, V.; Giangrange, P.; Galea, M. Electrical Power Generation in Aircraft: Review, Challenges, and Opportunities. *IEEE Trans. Transp. Electrif.* **2018**, *4*, 646–659. [CrossRef]
3. Li, J.; Zhang, Z.; Lu, J.; Liu, Y.; Chen, Z. Design and Characterization of a Single-Phase Main Exciter for Aircraft Wound-Rotor Synchronous Starter-Generator. *IEEE Trans. Magn.* **2018**, *54*, 8206805. [CrossRef]
4. Wang, Z.; Liu, B.; Guan, L.; Zhang, Y.; Cheng, M.; Zhang, B.; Xu, L. A Dual-Channel Magnetically Integrated EV Chargers Based on Double-Stator-Winding Permanent-Magnet Synchronous Machines. *IEEE Trans. Ind. Appl.* **2018**, *55*, 1941–1953. [CrossRef]
5. Bogusz, P.; Korkosz, M.; Prokop, J. A study of dual-channel brushless DC motor with permanent magnets. In Proceedings of the Selected Issues of Electrical Engineering and Electronics (WZEE), Rzeszow, Poland, 4–8 May 2016. [CrossRef]
6. Park, H.; Choi, J.; Jeong, K.; Cho, S. Comparative Analysis of Surface-mounted and Interior Permanent Magnet Synchronous Motor for Compressor of Air-conditioning System in Electric Vehicles. In Proceedings of the 2015 ICPE-ECCE Asia, Seoul, Republic of Korea, 1–5 June 2015. [CrossRef]
7. Tarnapowicz, D. Permanent magnet synchronous generators in a ship's shaft generator systems. *Sci. J. Marit. Univ. Szczec.* **2020**, *61*, 17–22. [CrossRef]
8. Kumar, R.R.; Chetri, C.; Devi, P.; Bose, S. Design and Analysis of Dual Stator Non-Magnetic Rotor Six-Phase Permanent Magnet Synchronous Generator for Marine Power Application. In Proceedings of the 2020 IEEE GUCON, Greater Noida, India, 2–4 October 2020. [CrossRef]
9. Trilla, L.; Pegueroles, J.; Urresty, J.; Muñiz, C.; Gomin-Bellemunt, O. Generator Short-Circuit Torque Compensation in Multichannel Wind Turbines. *IEEE Trans. Ind. Electron.* **2017**, *64*, 8790–8798. [CrossRef]
10. Lang, X.; Yang, T.; Enalou, H.B.; Li, C.; Bozhko, S.; Wheeler, P. A Dual-Channel-Enhanced Power Generation Architecture with Back-to-Back Converter for MEA Application. *IEEE Trans. Ind. Appl.* **2020**, *56*, 3006–3019. [CrossRef]
11. Dranca, M.A.; Chirca, M.; Breban, S.; Fodorean, D. Comparative Design Analysis of Two Modular Permanent Magnet Synchronous Generators. In Proceedings of the 2021 ISEEE, Galati, Romania, 28–30 October 2021. [CrossRef]
12. Delavari, H.; Veisi, A. Robust Control of a Permanent Magnet Synchronous Generators based Wind Energy Conversion. In Proceedings of the 2021 ICCIA, Tabriz, Iran, 23–24 February 2021. [CrossRef]
13. Setlak, L.; Kowalik, R. Model and Simulation of Permanent Magnets Synchronous Machine (PMSM) of the Electric Power Supply System (EPS), in Accordance with the Concept of a More Electric Aircraft (MEA). *ITM Web Conf.* **2018**, *16*, 03004. [CrossRef]
14. Gurleyen, H. Dual-Channel Variable Flux Reluctance Generator Design for More Electric Aircraft. In Proceedings of the IEEE GPECOM2021, Antalya, Turkey, 5–8 October 2021. [CrossRef]
15. Bogusz, P.; Korkosz, M.; Pakla, B.; Prokop, J. Comparative study of the performance of brushless DC motor with permanent magnets under classic and dual-channel operation. In Proceedings of the International Symposium on Elect. Machines (SME), Andrychow, Poland, 10–13 June 2018. [CrossRef]
16. Ding, W. Comparative Study on Dual-Channel Switched Reluctance Generator Performances Under Single- and Dual-Channel Operation Modes. *IEEE Trans. Energy Convers.* **2012**, *27*, 680–688. [CrossRef]
17. Ding, W.; Liang, D.; Sui, H. Dynamic Modeling and Performance Prediction for Dual-Channel Switched Reluctance Machine Considering Mutual Coupling. *IEEE Trans. Magn.* **2010**, *46*, 3652–3663. [CrossRef]
18. Van der Geest, M.; Polinder, H.; Ferreira, J.A.; Zeilstra, D. Design and Testing of a High-Speed Aerospace Permanent Magnet Starter/Generator. In Proceedings of the 2015 ESARS, Aachen, Germany, 3–5 March 2015. [CrossRef]
19. He, C.; Wu, T. Analysis and Design of Surface Permanent Magnet Synchronous Motor and Generator. *CES Trans. Electr. Mach. Syst.* **2019**, *3*, 94–100. [CrossRef]
20. Wang, Y.; Wang, H.; Liu, W.; Wang, Q. Modeling and Analysis of a New Voltage Regulation Method for Surface-Mounted Permanent Magnet Synchronous Generator. In Proceedings of the 2018 IEEE PEMC, Budapest, Hungary, 26–30 August 2018. [CrossRef]

21. Riera-Guasp, M.; Antonino-Daviu, J.A.; Capolino, G. Advances in Electrical Machine, Power Electronic, and Drive Condition Monitoring and Fault Detection: State of the Art. *IEEE Trans. Ind. Electron.* **2014**, *62*, 1746–1759. [CrossRef]
22. Abramov, I.V.; Abramov, A.I.; Nikitin, Y.R.; Sosnovich, E.; Božek, P.; Stollmann, V. Diagnostics of Electrical Drives. In Proceedings of the 2015 EDPE, Tatranska Lomnica, Slovakia, 21–23 September 2015. [CrossRef]
23. Gandhi, A.; Corrigan, T.; Parsa, L. Recent Advances in Modeling and Online Detection of Stator Interturn Faults in Electrical Motors. *IEEE Trans. Ind. Electron.* **2010**, *58*, 1564–1575. [CrossRef]
24. Korkosz, M.; Prokop, J.; Pakla, B.; Bogusz, P. Frequency analysis in fault detection of dual-channel BLDC motors with combined star–delta winding. *IET Electr. Power Appl.* **2021**, *15*, 824–836. [CrossRef]
25. Strangas, E.G.; Clerc, G.; Razik, H.; Soualhi, A. *Fault Diagnosis, Prognosis, and Reliability for Electrical Machines and Drives*; Wiley: Hoboken, NJ, USA, 2022; ISBN 9781119722755.
26. *Ansys Electronics Desktop 2023 R2*; Ansys Inc.: Canonsburg, PA, USA, 2023.
27. Sztajmec, E.; Korkosz, M. A study of multichannel brushless generator with permanent magnets. In Proceedings of the Conference Selected Issues in Power Engineering, Electrical Engineering and Industry 4.0, Rzeszów, Poland, 30 November 2022.

MDPI AG
Grosspeteranlage 5
4052 Basel
Switzerland
Tel.: +41 61 683 77 34

MDPI Books Editorial Office
E-mail: books@mdpi.com
www.mdpi.com/books

Academic Open
Access Publishing

mdpi.com

ISBN 978-3-7258-2310-9